

Green Energy and Technology

Akash Kumar Bhoi
Karma Sonam Sherpa
Akhtar Kalam
Gyoo-Soo Chae *Editors*



Advances in Greener Energy Technologies

 Springer

Green Energy and Technology

Climate change, environmental impact and the limited natural resources urge scientific research and novel technical solutions. The monograph series Green Energy and Technology serves as a publishing platform for scientific and technological approaches to “green”—i.e. environmentally friendly and sustainable—technologies. While a focus lies on energy and power supply, it also covers “green” solutions in industrial engineering and engineering design. Green Energy and Technology addresses researchers, advanced students, technical consultants as well as decision makers in industries and politics. Hence, the level of presentation spans from instructional to highly technical.

****Indexed in Scopus**.**

More information about this series at <http://www.springer.com/series/8059>

Akash Kumar Bhoi · Karma Sonam Sherpa ·
Akhtar Kalam · Gyoo-Soo Chae
Editors

Advances in Greener Energy Technologies

 Springer

Editors

Akash Kumar Bhoi
Department of Electrical
and Electronics Engineering
Sikkim Manipal Institute of Technology
Rangpo, Sikkim, India

Akhtar Kalam
Smart Energy Research Unit
College of Engineering and Science
Victoria University
Footscray, Melbourne, VIC, Australia

Karma Sonam Sherpa
Sikkim Manipal University
Gangtok, Sikkim, India

Gyoo-Soo Chae
Division of Information and Communication
Baekseok University
Cheonan-si, Korea (Republic of)

ISSN 1865-3529

Green Energy and Technology

ISBN 978-981-15-4245-9

<https://doi.org/10.1007/978-981-15-4246-6>

ISSN 1865-3537 (electronic)

ISBN 978-981-15-4246-6 (eBook)

© Springer Nature Singapore Pte Ltd. 2020

This work is subject to copyright. All rights are reserved by the Publisher, whether the whole or part of the material is concerned, specifically the rights of translation, reprinting, reuse of illustrations, recitation, broadcasting, reproduction on microfilms or in any other physical way, and transmission or information storage and retrieval, electronic adaptation, computer software, or by similar or dissimilar methodology now known or hereafter developed.

The use of general descriptive names, registered names, trademarks, service marks, etc. in this publication does not imply, even in the absence of a specific statement, that such names are exempt from the relevant protective laws and regulations and therefore free for general use.

The publisher, the authors and the editors are safe to assume that the advice and information in this book are believed to be true and accurate at the date of publication. Neither the publisher nor the authors or the editors give a warranty, expressed or implied, with respect to the material contained herein or for any errors or omissions that may have been made. The publisher remains neutral with regard to jurisdictional claims in published maps and institutional affiliations.

This Springer imprint is published by the registered company Springer Nature Singapore Pte Ltd. The registered company address is: 152 Beach Road, #21-01/04 Gateway East, Singapore 189721, Singapore

Preface

This edited volume comprises multidisciplinary and associative methods and approaches towards greener energy and technology. This book provides in-depth knowledge to the readers towards ongoing advancement in the area of renewable and green technology. The introductory chapter collectively discusses the evolution of modern power systems, various renewable energy sources and their interconnection in the proposed future power system. The subsequent chapters bring out the social and technological evolution topics *such as* a fuzzy-controlled single-switch DC–DC converter for PV applications with an extreme voltage ratio module, several issues and challenges to be deciphered during design, development and deployment of cyber security for smart grid, system analysis for different chemicals, their techno-economic feasibility and viability for solar fuels, Internet of things (IoT) application in green computing, solar PV, wind energy and small hydropower resources utilized to satisfy the electrical demand, framework of smart grid technology, extraction of solar module parameters, multilevel inverters for PV power system, prevention on urban heat island phenomenon, real-time smart volumetric fuel estimation system, energy efficiency and QoS evaluation, evaluation of frequency fluctuation and system stability against the intermittent fluctuation of the industrial load, smart homes with optimal energy consumption, harvesting optimal energy from solar, methods to reduce cost by introducing an asset monitoring system, solar-powered energy-efficient smart electrical vehicle based on PMSM drive, interrelationships analysis of 50 kVA class shared transformer/reactor, evaluation of proton-exchange membrane (PEM)-based fuel cells (FC), five-level switched inductor-based cascaded H-bridge quasi-switched boost inverter (SL-qSBI) for renewable energy applications, **clean energy storage**, upcoming solar energy usages, hybrid energy system for making India pollution-free, graphene-based solar cell, PWM-based phase-shift algorithm–high-voltage application, IoT–green communication, renewable energy powered home with home automation system–IoT, monitoring sustainable industrial technology—a case study, hybrid energy system to promote clean energy, supercapacitors–green energy storage, sustainable green computing, green energy management systems, MPPT for wind energy conversion system, power system analysis and control method for

energy storage system (ESS), sustainable industrial development, active vibration control system to minimize the vibration of the structure, PV degradation loss assessment of stand-alone photovoltaic, energy operation paradigm integrating information telecommunications technology, proper operating point of VSC HVDC in a large-scale meshed power system, wind power system management technologies and compensation devices, battery energy storage system (BESS) in a wind farm, real-time implementation of solar-based water irrigation system for rural areas, dual stator–dual rotor switched reluctance motor (DS-DR SRM) for sustainable green mobility, whale optimization and differential evolution (WODE) algorithm in MPPT in a PV system, an efficient and cost-effective solar power generation system for irrigation, massive MIMO for green communication and mathematical evaluation of different types of single-phase H-type transformerless inverters for PV grid system.

We hope these collected quality chapters will help the readers from different disciplines for finding new solutions by exploring and understanding the upcoming approaches and evaluation strategies in the area of greener technologies.

Rangpo, India
Gangtok, India
Cheonan-si, Korea (Republic of)
Melbourne, Australia

Dr. Akash Kumar Bhoi
Prof. (Dr.) Karma Sonam Sherpa
Prof. (Dr.) Gyoo-Soo Chae
Prof. (Dr.) Akhtar Kalam

Contents

An Overview on Structural Advancements in Conventional Power System with Renewable Energy Integration and Role of Smart Grids in Future Power Corridors	1
Nil Patel, Deepak Porwal, Akash Kumar Bhoi, D. P. Kothari, and Akhtar Kalam	
Cybersecurity for Smart Grid: Threats, Solutions and Standardization	17
L. Chhaya, Paawan Sharma, Adesh Kumar, and Govind Bhagwatikar	
Solar Fuels via Two-Step Thermochemical Redox Cycles	31
Azharuddin Farooqui, Marta Boaro, Jordi Llorca, and Massimo Santarelli	
Internet of Things (IoT) Application in Green Computing: An Overview	85
Sameer Kumar Das and Hemanta Kumar Palo	
A PSO-Based Multi-objective Optimization to Satisfy the Electrical Energy Demand Through Renewable Energy Integration: A Case Study	103
Mahesh Wagh and Vivek Kulkarni	
EMI Concerns, Measurements and Standards for Smart Grid	123
L. Chhaya, Paawan Sharma, Adesh Kumar, and Govind Bhagwatikar	
Extraction of Solar Module Parameters Using Jaya Optimization Algorithm	137
P. Anandhraj, K. Mohana Sundaram, P. Sanjeevikumar, and Jens Bo Holm-Nielsen	
A Multilevel Inverter-Controlled Photovoltaic Generation	149
Neeraj Priyadarshi, Farooque Azam, Akash Kumar Bhoi, and Amarjeet Kumar Sharma	

A Study on the Airflow Variation and Energy Consumption of Apartment Complexes in Medium Cities	157
Jun-Gi Lee, Sung-Hoon Kim, and Kyung-Hee Lee	
Real-Time Smart Volumetric Fuel Estimation System for Automobiles Under All Road Conditions	167
Priyanshi Singhal, Nivedita Singh, Rajkumar Viral, Saket Kumar, Divya Asija, P. M. Tiwari, and Pallavi Choudekar	
Energy Efficiency and QoS Evaluation of Radio Resource Management Techniques for M2M Communications in LTE-Based Cellular Systems	181
Mariyam Ouaisa, Mariya Ouaisa, and Abdallah Rhattoy	
An Influence Analysis on the Power System by Load Fluctuation of Large-Scale Industrial Steel Load	199
Hyun-Chul Lee, Yong-Gi Roh, and Byoung-Jo Jung	
Dynamic Operation of Grid-Connected Photovoltaic Power System	211
Neeraj Priyadarshi, Farooque Azam, Akash Kumar Bhoi, and Amarjeet Kumar Sharma	
Case Study of the Asset Monitoring Focused on Facility Management	219
Sangchul Kim and Shinjo Eom	
A State-of-the-Art Review on Solar-Powered Energy-Efficient PMSM Drive Smart Electric Vehicle for Sustainable Development	231
Chiranjit Sain, Atanu Banerjee, Pabitra Kumar Biswas, and Sanjeevikumar Padmanaban	
Green Energy Generation Using Renewable Energy Technologies	259
Sanghita Baidya and Champa Nandi	
Characteristic Analysis of 50 kVA Class Shared Transformer/Reactor	277
Jae-hyeon So, Young-Un Park, Su-Yong Kim, Kyung-il Woo, and Dae-Kyong Kim	
A Proton Exchange Membrane-Based Fuel Cell Integrated Power System	285
Neeraj Priyadarshi, Farooque Azam, Akash Kumar Bhoi, and Amarjeet Kumar Sharma	
Application of IoT in Green Computing	295
T. Poongodi, S. R. Ramya, P. Suresh, and Balamurugan Balusamy	

Five-Level Switched Inductor-Based Cascaded H-Bridge Quasi-Switched Boost Inverter for Renewable Energy Applications 325
 Rahul Kumar, Sneha, Rahul Rambhad, P. Sriramalakshmi, and V. T. Sreedevi

Green Synthesis of rGO/Ag Nanocomposite for Clean Energy Storage Application 337
 Naorem Aruna Devi and Bibhu Prasad Swain

An Investigation on the Outcomes of Rail-Based Solar Tracking System Incorporating Minimum Torque Condition for Increasing the Photovoltaic Energy Capture on Sunny Days 357
 Arun A. Yadav and P. V Ramana

An Optimization Case Study of Hybrid Energy System in Four Different Regions of India 399
 Somudeep Bhattacharjee, Samrat Chakraborty, and Champa Nandi

Graphene for the Potential Renewable Energy Applications 439
 Sayantan Sinha and Bibhu Prasad Swain

A Closed-Loop Control of Fixed Pattern Rectifier for Renewable Energy Applications 451
 Neeraj Priyadarshi, Farooque Azam, Akash Kumar Bhoi, and Amarjeet Kumar Sharma

DC–DC Converter with High Conversion Ratio for Transmission 463
 Jae-Ha Ko, Chun-Sung Kim, Jong-Cheol Kim, Seong-Mi Park, and Sung-Jun Park

Narrowband-IoT Base Station Development for Green Communication 475
 Subhankar Shome and Rabindranath Bera

Design and Prototype Implementation of a Renewable Energy-Powered Home with Home Automation System Using Internet of Things (IoT) 489
 Dherendra Bhattacharai, Amit Kumar Singh, Sanjeev Newpaney, and Pawan Pyakurel

A Four-Switch-Type Converter Fed Improved Photovoltaic Power System 505
 Neeraj Priyadarshi, Farooque Azam, Akash Kumar Bhoi, and Amarjeet Kumar Sharma

Impact of Power Factor Correction Methods on Power Distribution Network—A Case Study 513
 Sudeep Pradhan, Dipanjan Ghose, and Amit Kumar Singh

Design of a Smart Energy Management Controller for Hybrid Energy System to Promote Clean Energy	527
Somudeep Bhattacharjee and Champa Nandi	
ZnO/rGO Nanocomposite for Supercapacitor Energy Storage Applications	565
Sumitra Nongthombam and Bibhu Prasad Swain	
Green IoT (G-IoT): An Insight on Green Computing for Greening the Future	579
T. Suriya Praba, S. Pooja Laxmi, T. Sethukarasi, R. D. Harshitha, and Veeramuthu Venkatesh	
An Overview of Green Energy Management Systems	601
J. Ajayan, P. Prakasam, and P. Mohankumar	
Two-Stage DC-AC Quadratic Boost Inverter for Renewable Energy Applications	617
Rajat Kumar Sah, Namit Wadhawan, Akansha, and P. Sriramalakshmi	
Maximum Power Point Tracking for Wind Energy Conversion System	631
Monika Vardia, Neeraj Priyadarshi, Irfan Ali, Farooque Azam, and Akash Kumar Bhoi	
A Study on Frequency Regulation Energy Storage System Design in Island Power System	641
Jaewan Suh, Seungmin Jung, and Minhan Yoon	
A Fuzzy Logic Control Based Vibration Control System for Renewable Application	651
Tarunkumar Choudhary, Neeraj Priyadarshi, Piyush Kumar, Farooque Azam, and Akash Kumar Bhoi	
Experimental Investigation and Fuzzy-Based Modeling of Micro-EDM Process Parameters	665
I. Shivakoti, G. Kibria, B. B. Pradhan, and A. Sharma	
Experimental Study on PV Degradation Loss Assessment of Stand-Alone Photovoltaic (SAPV) Array in Field: A New Simplified Comparative Analytical Approach	685
Rohit Tripathi, Rakhi Sharma, and G. N. Tiwari	
Design of Wind Energy Conversion System Under Different Fault Conditions	707
Monika Vardia, Neeraj Priyadarshi, Irfan Ali, Farooque Azam, and Akash Kumar Bhoi	
A New Wake-Up Modem for Low-Power Communications	717
Gun-Ho Lee and Eui-Rim Jeong	

Effective and Reactive Power Measurement Technique Using a Phase Angle of Voltage-Based Current DFT 727
 Ji-Hoon Yang, Seong-Mi Park, and Sung-Jun Park

A Preventive Control Strategy of Embedded VSC HVDC in a Large-Scale Meshed Power System 739
 Jaehyeong Lee, Sungchul Hwang, Soseul Jung, Gilsoo Jang, Seungmin Jung, and Minhan Yoon

Development of BESS Design Plan for Wind Power System Using Short-Term Capacity Factor 749
 Minhan Yoon, Jaewan Suh, and Seungmin Jung

A Feasibility Study About Capacity Factor-Based BESS Design Plan by State of Charge Analysis 761
 Yunhwan Lee, Minhan Yoon, Jaewan Suh, and Seungmin Jung

Design and Implementation of DC–DC Boost Converter for Solar Application 773
 Ashutosh Jha, Anilanshu Singh, and S. Angalaeswari

Real-Time Implementation of Solar-Based Water Irrigation System 781
 S. Angalaeswari, Suvasom Mookherjee, and K. Jamuna

MPPT in Partially Shaded PV System with the Use of WODE Technique 795
 K. R. Sugavanam, A. Mutharasan, J. Prakash, P. Gowtham, M. Ramprasanth, and U. Vinay Sahoo

A Case Study on Implementation of an Efficient and Cost-Effective Solar Power Generation System for Irrigation Purpose 807
 K. S. Tamilselvan, G. Mageshkumar, S. Suthagar, and G. Murugesan

Augmented Yield Productivity of Solar Still Using Energy Storage Materials: Experimental Investigation Under the Climatic Conditions of Rajasthan 817
 Amrit Kumar Thakur, M. Ponrajan Vikrama, and S. Christopher

Massive MIMO for Green Communication 833
 Samarendra Nath Sur

Evaluation of Leakage Current in Single-Phase H-Type Transformerless Inverters for PV Grid System 843
 Mohammed Imran and Manjula Mane

About the Editors

Dr. Akash Kumar Bhoi (Ph.D., M.Tech., B.Tech.) is currently an Assistant Professor in the Department of Electrical and Electronics Engineering at Sikkim Manipal Institute of Technology (SMIT), SMU, India. He has specialized in the field of Biomedical Engineering and Renewable Energy. His areas of research are Biomedical Signal Processing, Renewable Energy, Computational Approaches and Patter Recognition, etc. He is also a reviewer of journals of national and international repute. He has published several papers in national and international journals and conferences. He has also served on numerous organizing panels for international conferences and workshops. He is currently editing several books with Springer Nature and is also the Guest editor for special issues in Springer Nature journals.

Prof. (Dr.) Karma Sonam Sherpa completed his B.E. (Electrical Engineering) from MREC, Jaipur, and M.Tech. in Power Electronics and Machine Drives from IIT Kharagpur in 1996 and 2003, respectively. He has a doctorate from Sikkim Manipal University. Currently, Prof. Sherpa is Dean of Research & Development and a Professor in the Department of Electrical & Electronics Engineering. His areas of research are DC power conversion and nonlinear dynamics, voltage stability and load management in power distribution systems and electromagnetic levitation systems, electric power distribution system, power electronics and electrical drives. He has published papers in national and international journals and conferences. He has organized workshop, seminars and conference.

Prof. (Dr.) Akhtar Kalam has been at Victoria University, Melbourne since 1985 and is currently the Head of Engineering and the Chair of the Academic Board and lectures in the Master's by coursework program at Engineering Institute of Technology, Perth, Australia. Further, he has Distinguished Professorship position at the University of New South Wales, Sydney and 5 Malaysian universities. He received his B.Sc. and B.Sc. Engineering from Calcutta University and Aligarh Muslim University, India. He completed his M.S. and Ph.D. at the University of Oklahoma, USA and the University of Bath, UK. His major areas of interests are

power system analysis, communication, control, protection, renewable energy, smart grid, IEC61850 implementation and cogeneration systems. He has conducted research, provided industrial consultancy and published over five hundred publications on his area of expertise and written over 29 books in the area.

Prof. (Dr.) Gyoo-Soo Chae received his Ph.D. (Electrical Engineering) from Virginia Polytechnic Institute and State University (Virginia Tech), Blacksburg, VA. After receiving the Ph.D., he shortly worked at Amphenol Mobile, Korea as a RF manager. He has been a Professor at Baekseok University in Korea since 2003. He has been granted a department scholarship (Kyungpook National University grant) and is associated with IEEE Antennas and Propagation Society. He serves as the editor-in-chief of The Korea Institute of Information, Electronics, and Communication Technology since 2013. His research interests are antennas and dual-band inverted-F antenna.

An Overview on Structural Advancements in Conventional Power System with Renewable Energy Integration and Role of Smart Grids in Future Power Corridors



Nil Patel, Deepak Porwal, Akash Kumar Bhoi, D. P. Kothari, and Akhtar Kalam

Abstract Renewable energy (RE) sources are gaining popularity in mainstream power system. A conventional vertical power system is being seen as in need of modification to meet the strong requirements of uninterruptible power, growing consumption of electricity in rural and urban areas, mitigating voltage fluctuation problems for far-end loads and overall cost reduction of erecting huge long power transmission networks for feeding remote areas. The concept of one-way power transmission is slowly being replaced in renewable energy sources connected to power system. The renewable energy sources are generally low inertia small machines, driven by renewable sources like solar, water, hydro and waves. These are preferred to be connected near to load points to fulfill local load demands. Nowadays, the power system is a distributed network energy system, with several renewable energy sources along with communication and automatic control, in practice. In this chapter, the evolution of modern power system, various renewable energy sources and their interconnection in the proposed future power system is discussed with schematic diagrams.

N. Patel (✉)

Power Electronics and Drives Department, Research and Development Centre,
Cimac Solution Pvt. Ltd., Ahmedabad, India
e-mail: nilpatel792@gmail.com

D. Porwal

Department of Electrical Engineering, MNIT, Jaipur, India
e-mail: deepakporwal1512@gmail.com

A. K. Bhoi

Department of Electrical and Electronics Engineering, Sikkim Manipal Institute of Technology,
Sikkim Manipal University, Majhitar, India
e-mail: akash730@gmail.com

D. P. Kothari

Department of Electrical Engineering, VNIT, Nagpur, India
e-mail: dpkvits@gmail.com

A. Kalam

Smart Energy Research Unit, Victoria University, Melbourne, Australia
e-mail: akhtar.kalam@vu.edu.au

© Springer Nature Singapore Pte Ltd. 2020

A. K. Bhoi et al. (eds.), *Advances in Greener Energy Technologies*,

Green Energy and Technology, https://doi.org/10.1007/978-981-15-4246-6_1

Keywords Modern power system · Renewable energy sources · RE integration · Distributed generation · Smart grid · Micro-grid

1 Introduction

Nowadays, the power system is being seen as distributed power delivery system which consists of several controllers, sensors, IED devices and measuring and controlling devices along with bidirectional power flow capability. This allows the renewable energy sources to feed the load in case of source station having deficiency of power and allows the power to flow toward the source when there is excess power between load demand and renewable energy generation. The excess power can also be stored in storage systems like batteries. The new hybrid power system is a combination of various energy sources like thermal, hydropower, nuclear, tidal, wave, photovoltaic and wind energy generation in coordinated manner to meet the load demand in optimal manner with minimum devices. The optimal power flow analysis in such a system is of utmost importance. The voltage at the point of coupling is a function of power delivered by the renewable energy generation. The reverse power flow from coupling point toward source needs careful planning of the power transmission corridor. It requires active functioning of various monitoring and controlling devices. Modern power system is heading toward distributed generation-based power system. The smart grids and micro-grids are the future small-scale automated intelligent power system. The modern power system can be viewed as multi-component hierarchical system [1–4].

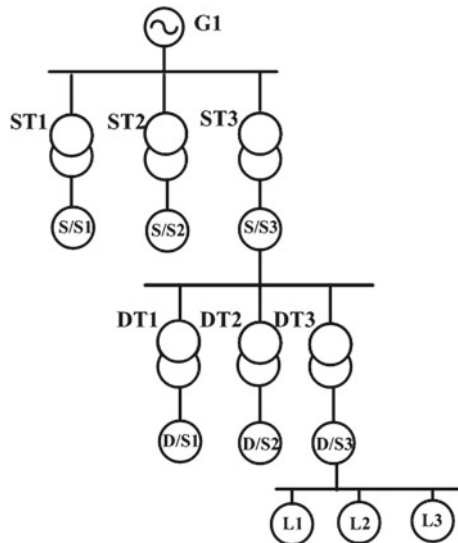
Over the years, the power system has evolved with catalytic changes in its both structural and operational forms. The developed countries as well as developing countries are aiming for an advanced version of power system to meet the future power demands with added features of security, reliability and optimal operational cost. Conventional power system structure is discussed in Sect. 2. A traditional power system has bulk generation, transmission, sub-transmission, distribution and customers as its components. The conventional power system is a large central generating power-type system with ancillary services such as frequency control, voltage control, and active and reactive power control. Today's requirements from power system have changed and are mostly governed by end consumers like uninterruptible power, better power quality and security at optimal unit cost. Therefore, the need for restructuring of power system has come as an immediate requirement. Various renewable sources present in customers' premises are also being thought as an innovative scheme to meet the local power requirements. The modern power system architecture and its functions are discussed in Sect. 3. It also explains about constraints in the prospective architecture. The renewable sources present in customers' premises are mainly solar, wind and small hydro like ponds or rivers. These are clean, green and abundant sources of energy present in nature. The mechanism of extraction of energy from renewable sources is discussed in Sect. 4. This also highlights the challenges for large-scale commercial power generation from these

sources. The small independent low-voltage grids are the future of power system. These grids are enabled with automatic sensing devices and intelligent monitoring, control, recording devices. This also allows bidirectional flow of power in case of excess power available from renewable energy sources connected in the smart grid. The smart grids are being rigorously tested at laboratory scale and being planned at commercial applications. Section 5 discusses the role of smart grids in today’s power system.

2 Conventional Power System Structure

The power system is growing in size and complexity because of increasing load demand, addition of new power units, expansion of existing structure, employing various voltage and reactive power compensation techniques. Thus, the power system is being seen as in great demand of restructuring and modification. The conventional power system consists of large generators, transformers, high- and medium-voltage transmission lines, distribution system, commercial and residential loads in radial manner. This enables only a one-way transfer of power from source station to loads. Any abnormal conditions can cause power continuity. It can also reflect on the generator sides and thus cause the overall system to shut down. Generator classification can be done as: Generators greater than >50 MW can be classified as large power generators. Generators beyond 25–50 MW can be classified as medium power generators. The conventional radial power system topology is shown in Fig. 1. The share

Fig. 1 Schematic diagram of conventional power system



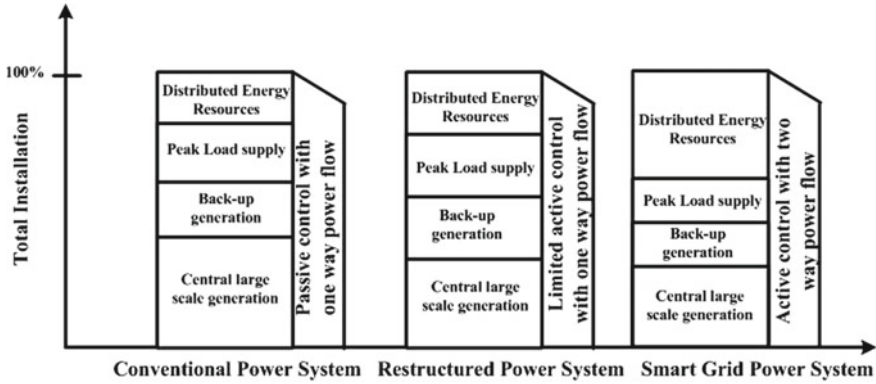


Fig. 2 Share of power sources in various power system topologies

of large central power stations in existing power system and future power system is shown in Fig. 2.

Where

- G1: Generation (11 kV, 20 kV).
- ST1, ST2, ST3: Step-up transformers; S/S1, S/S2, S/S3: transmission substations (220 kV, 400 kV, 765 kV, with HVDC, shunt compensators, FACTS devices).
- DT1, DT2, DT3: Secondary transmission; D/S1, D/S2, D/S3: sub-transmission substations (132 kV, 110 kV, 66 kV).
- Distribution (33 kV, 11 kV).
- L1, L2, L3: Consumption (11 kV, 415 V, 230 V)—with various PQ, DG and power electronic loads.

Conventional distribution system has:

1. Simple and easy-to-operate system with adequate power quality.
2. Unidirectional power flow structure from source to load only.
3. Simple and robust protection system with coordination of the protection scheme.
4. Lower cost of existing distribution system.

The existing conventional power system has various issues from security, reliability as well as economic point of view. The radial power transfer system suffers from frequent interruptions causing the complete shutdown of the system. It has mainly large generators connected at source point. These generators are generally located very far from load centers, thus making the overall system less efficient. The far-end load points also suffer from significant voltage drops in the transmission and distribution lines [5–7].

3 Modified Power System Structure

The growing independent small load centers based on their geographical areas are willing to fulfill their needs from locally available clean and green energy sources, e.g., solar, wind, wave, tidal, small hydro, biomass and waste management. Small topological areas require very small amount of power for household and agricultural activities. These can be completed by local available resources. Thus, the entire power system needs restructuring to facilitate the expansion and meet future requirements [8, 9]. The prospective future power system design is shown in Fig. 3.

3.1 Merits of Restructured Modern Power System

Figure 4 shows the restructured modern power system. This elaborates the traditional one-directional vertical power delivery network being transformed into an advanced automated bidirectional power distribution network. The power system in today’s context is being visualized as more secure, reliable network equipped with advanced management and control devices. Another benefit of having local distributed generation is to have optimal utilization of natural available resources present in the territory of interest, indirectly increased employment to locals and overall contribution to boost the economy. The present power system is in direct need of structural modifications. The need to improve voltage profile at far end from the substation is of paramount importance. All these factors have led the power system to undergo tremendous change from past few decades [10–13].

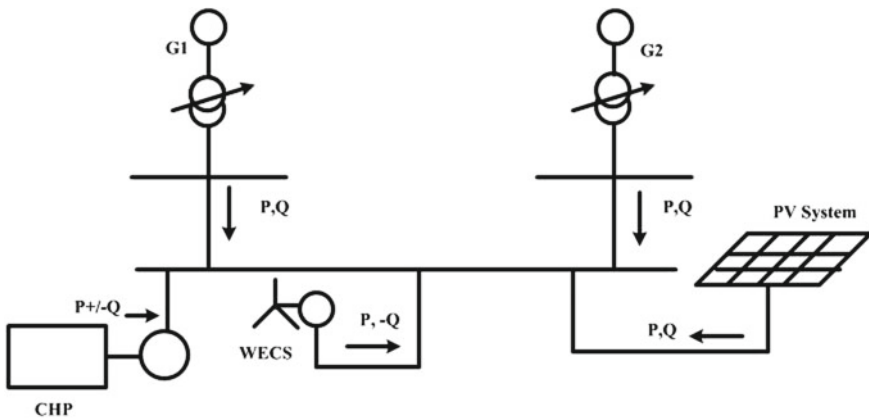


Fig. 3 Schematic of prospective future power system

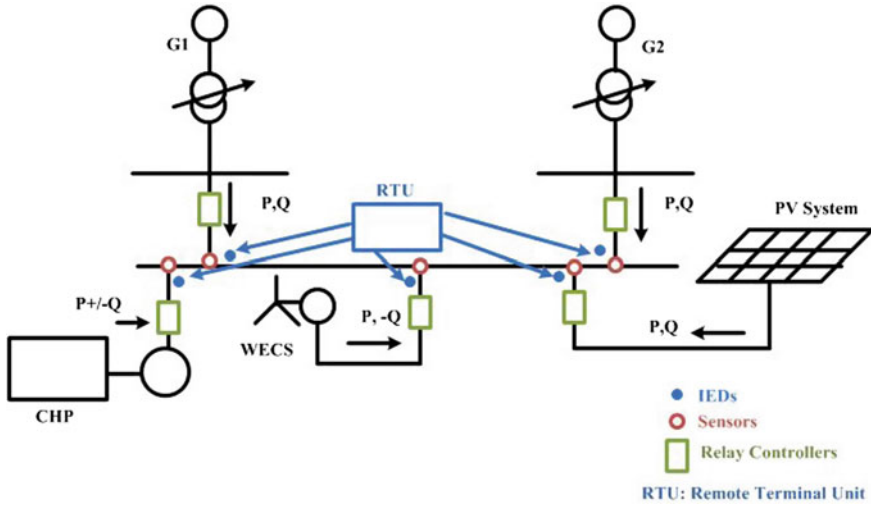


Fig. 4 Power system with advanced intelligent and automatic system

3.2 Insights of Modern Power System

At present, the margin between the highest consumption and the likely available production is very small. This creates a huge burden on the utilities to charge heavily for any units outside the allotted tariff block. Several countries are facing this problem of utmost importance. The restructuring in modern times has challenges of less time of infrastructure erection and installations, lack of adequate investments, general public awareness and policy guidelines for reliable and secure operation. The design paradigm of large power production units connected at high voltage levels with several subsequent lower voltage utilities and consumers is being shifted to small independent low-voltage power units connected more closely to the load points. Several terms are coming like, “Embedded generation”, “distributed generation”, “small-scale generation” “renewable energy sources”, “distributed energy resources” [14]. All these differ only in the topology and methodology adopted, but from macroscopic view all are same in terms of their objectives and outline. Distributed generation refers to production units connected to the distribution network as well as large production units based on renewable energy sources. Small-scale generation is another one such term for connecting very low power generation units for power production mainly to feed a small geographical area or quantifiable amount of load. Embedded generation is a topology used for units, which can work as both generators and loads based on the requirements. These allow the bidirectional flow of active/reactive power or both from/to the units. “Renewable energy sources”, as the name suggest is a renewable energy sources enabled generation like solar, wind, small hydro, wave, tidal etc. [15–17].

DG also refers to the power plants that are compatible with the existing distribution feeders or point of common coupling.

Distributed generation:

1. Power coming from multiple sources.
2. Devices are controllable loads/generators.
3. Intelligent automated communication-enabled system.

3.3 Challenges in Prospective Modern Power System

The main problem with renewable energy source-based generation is the variation in production capacity at different time intervals, the size of individual units, flexibility in choosing the locations and control of operation. In distributed generation, we have power converters or any other converter in general being used as an interface between the energy source and the connecting grid. Machines, in this generation, are electronically controlled by these power converters. The power electronic-enabled controllers are called as power conditioners. The power conditioners improve both reliability and efficiency of the whole system. With the known high variable nature of renewable energy sources, a term commonly used is hosting capacity approach, which is the maximum amount of generation from such units that can be integrated into the power system, while still maintaining its performance within acceptable limits.

Power system issues:

- Transient state behavior of DG units and its impact on the power system.
- Faults occurring in DG units.
- Modifications required in integrating the DG units in the existing power system.
- Protection control strategy for DG-integrated power system.
- Islanding of DG-integrated power system in case of severe faults or trips.

These highly intermittent sources of energy if connected with some storage mechanism provide solution for meeting uncertain demand and remote area demand fulfillment.

The islanding event in such a renewable energy-integrated power system occurs due to voltage variations, frequency variations or rate of change of voltage/frequency exceeding a threshold value. Various islanding detection techniques have been proposed earlier [18, 19]. The active islanding techniques study small perturbations in the system, which suffers from small non-detecting zones and large time of detection. The active methods are also applicable to single DG unit system. This makes the system to suffer for longer time. Other techniques involve passive islanding techniques. The passive methods realize current and voltage signals. The passive techniques analyze voltage variations and its derivatives, frequency variations and

its derivatives and active and reactive power excursions. However, the passive detection techniques suffer from large non-detection zones. Other methods like modified islanding detection techniques have been exercised in recent times. This method uses voltage deviation, rate of change of voltage, variation of frequency, rate of change of frequency, variation of active power, rate of change of active power, voltage–active power sensitivity. The voltage and frequency are cross-coupled with active power and reactive power to analyze the sensitivity. A definitive participation coefficient is then calculated to identify the most vulnerable buses. Thus, these indices help to avoid undesirable islanding events [20–22].

Distributed generation is getting attention nowadays with objectives to:

- Increase market competition, boost the investment, increase production capacity and thus reduce the price of electricity per unit.
- Reduce the environmental effects, carbon and other harmful emissions.
- Avail the local demand fulfillment by local resources, reduce losses and avoid heavy, bulky transmission structure.

To attract the investors for new proposed power system, several incentive mechanisms are being prepared. Various government agencies and other technical bodies are trying to redesign the framework of policies, which governs this power system planning and erection model [23–26].

Constraints:

- Sophisticated information is required to control the source and load.
- Physical circuit constraints and thermal loading limit.
- Thermal management is required to allow the power to actually come through [27].

4 Renewable Energy Sources

Renewable energy generation is going to play an important role in the future power system. The renewable energy generation includes:

1. **Solar Photovoltaic Power Generation:** This is a clean energy generation example. Solar radiation coming from the Sun is made to fall on the semiconductor material. The photovoltaic process causes the electrons to flow from n-type semiconductor to p-type semiconductor and thus causes the current to flow in an external connected load. The irradiance level, temperature and material of PV cell are the factors, which affect the energy generated. Solar has other applications like solar thermal, solar space heating, cooling and refrigeration, solar distillation, solar drying and solar cooking. The power output of solar PV system is DC. This is enough to power local small necessary loads. It is emission free, and less maintenance is required. The demerits of solar PV generation are its high installation and commissioning cost and a storage mechanism like batteries

required in grid-connected solar PV system. The solar PV system also includes charge controller, battery storage, inverter and controllable loads. Though the efficiency of solar cells is low, significant research is going on to improve cell efficiency. The batteries account for significant amount in total system cost and suffer from quick discharge and frequent replacements [28].

2. **Wind Energy Generation:** The energy is extracted from wind. The wind flows due to pressure difference between the ground and at appropriate height from the ground. The wind rotates the wind turbine blades, which are coupled through a shaft and gearbox mechanism to the induction generation. The generator is rotated at a particular speed by adjusting the pitch angle of the blades and gear ratio in gearbox such that useful power above cut in speed can be achieved. The advantage of wind energy generation is that it is available in both day and nights. It is one of the most developed technologies in recent times, thus leading the renewable energy. The output of induction generator is AC, which can be conditioned by suitable power electronics converters for required output. The only disadvantage of wind energy conversion system is that it suffers from large intermittent nature of the wind. Thus, proper storage mechanism is further required for a given load demand. This makes the overall system expensive.
3. **Small Hydropower Generation:** The water is stored in small ponds or reservoir built with small dams. The water is made to flow on the turbines by opening the gates, and the generators coupled to the turbines generate the electricity. Sometimes, the water at outlet is fed back through the pumps to the ponds or reservoirs in nights when the rate of electricity consumption is low. Thus, this way the water can be again utilized through a closed-loop feedback system. The generators in small hydropower generation are generally alternators whose output is AC, which can be transmitted through the transmission lines to longer distances. The hydropower generation is considered environmental-friendly because there are no harmful emissions. It has low upfront cost. However, the time taken to build a hydropower plant is quite large and overall cost of the whole system is higher. The scheduled maintenance is also required. It is useful for meeting the peak load demands because of quick time of starting up. The demerits of hydropower plants are that a suitable location of erection is required and it is difficult to expand once built and operation started (Fig. 5).

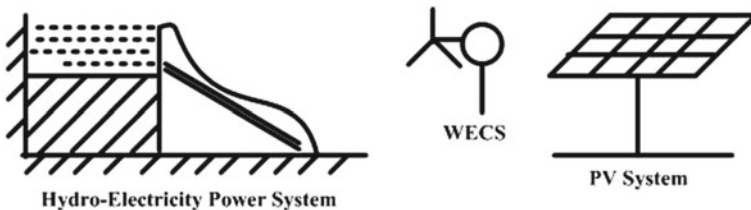


Fig. 5 Various renewable energy source symbols

4.1 Primary Energy Sources and Their Scope

The various sources of electricity are from coal, oil, natural gas, nuclear, hydro, etc. Human waste, animal excretion and plants are decomposed in the presence of atmospheric conditions. They are accumulated below the earth with continuous air and soil mixture forming layer, they get deeply in the earth surface. Later, with the high pressure and temperature present in the earth surface at several meters depth. These deposits get converted into solid, liquid or gaseous fuels, rich in carbon and hydrogen mainly. These are called hydrocarbons. The pressurized deposits are fuels containing energy when properly processed and refined. The fuels since obtained from fossil woods, plants and human/animal waste are known as fossil fuels. The energy obtained by chemical combustion of these fossil fuels is known as fossil fuel energy. The fossil fuels are made to be burnt at high temperature and pressure to produce enough heat energy. This heat energy is utilized to raise the temperature of water or other fluids like synthesized oil to get the high-pressure, high-temperature steam which is made to fall on turbine generator set, which ultimately produces the electric power. The other form of energy is oil. Natural oil is a hydrocarbon obtained from chemical process and refining of petroleum crude oil. The natural oil is processed in various steps to get the appropriate form to be used as liquid fuel. The efficiency of these processes is very low around 25–30% overall. Maximum efficiency of such plants is reported to have 40% efficiency. The overall efficiency is product of turbine efficiency and generator efficiency along with boiler efficiency. Natural gas is another form of energy obtained from hidden underground gas reserves, and these gas resources are more commonly found to be around river basins, lakes or sea coastal areas. Apart from these, there are some other sources like large hydropower plants with runoff river or pond storage system. All these sources are non-renewable energy sources. The sources once used cannot be recycled. Thus, the problem existing for future is the growing depletion of these conventional energy sources. Modern power system needs other energy sources to be discovered to meet the future demands. These sources also pollute the environment. Coal, oil and natural gas are rich in carbon content. The carbon reacts with oxygen present in the atmosphere and forms carbon dioxide and carbon monoxide, thus polluting the environment of the nearby locations near to generating plant. The hydroelectricity generation is though a well-adopted system; it involves great risks of flooding, soil erosion and other danger to aquatic species. The hydro-plants are large structure, which have the potential to cause a significant damage to the environment during any malfunction. Nowadays, new and renewable energy sources are getting popularity because of their cleanliness, abundance and presence in the required geographical topological location. The renewable energy sources are thus the sources of future energy system. The renewable energy sources involve solar, wind, hydro, tidal, ocean, wave, biomass and other small-scale pilot generation techniques like friction and waste management energy techniques. These resources are going to fulfill the future energy demands. The environmental effects pose a limit on the usage of conventional energy sources. The biological concerns have given stringent limitations in the new policy frameworks for optimal usage of

fossil fuel and other conventional energy sources. The rising global warming has put a pressure on leading countries to give renewable energy sources a boost.

5 Smart Grid and Its Scope in the Future Power System

SMART GRIDS: Smart grids are important potential means at demand-side management for increasing flexibility and controllability in the power system. Controllable loads such as charging electric vehicles and heat pumps with thermal storage will allow the increased utilization of renewable energy sources.

A smart grid is an intelligent automatic power delivery mechanism to enable bidirectional power flow capability with advanced monitoring, recording, measuring and controlling abilities. This also performs billing operation and other functions for consumers to keep record of units consumed scheduled maintenance and avoid any troubleshooting.

The other definition of smart grid is: A smart grid is an innovative sophisticated power delivery and control mechanism, which allows active participation of utilities as well as consumers. This allows the end user of electricity to take active participation in power purchasing and thus price controlling. It also has its several components such as bulk generation, transmission distribution and consumers like conventional power system structure along with operators, marketers, power managers, service providers, etc.

Smart grids are the future of power system. Smart grid is referred to as:

According to European Technology platform for smart grids (2006): Smart grid is the electrical system that can be connected the actions of all consumers and connected it. Producers and users and those who do the both. A smart grid offers novel products and services together with meticulously monitoring, control, communications and self-healing technologies to it.

According to Department of Energy (DoE), USA: Grid 2030 envisions a fully automated power delivery network that monitors and controls every customer and node, ensuring two-way flow of information and electricity between the power plants and the appliances, and the points in between.

According to International Electrotechnical Commission (IEC): The smart grid is a developing network of transmission lines, equipment, control and new technologies working together to respond immediately to our twenty-first-century demand for electricity.

Smart grid has the following functions [29–33]:

1. Better utilization of existing power system.
2. Quicker restoration of electricity after power disturbances.
3. Reduced operation and management costs for utilities and ultimately lower price of power for consumers.
4. Reduced peak demand, which will also help lower electricity rates.

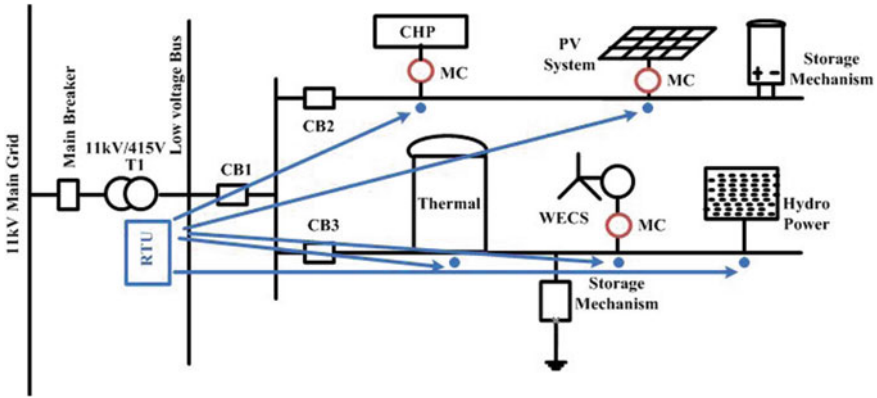


Fig. 6 Smart grid architecture

5. Increased integration of large-scale renewable energy systems.
6. Better integration of customer-owned power generation systems including renewable energy systems.
7. Increase active participation of consumers and thus reducing the cost of per-unit power.
8. Provide consumers with greater level of information and penetration in the existing passive power system.
9. Significantly reduce the environmental of large central power stations by replacing some amount of power by renewable energy sources.
10. Maintain or even increase reliability and security of power system at optimal cost.
11. Maintain and improve the existing system services efficiently.
12. Encourage investors in the modern infrastructure building by assuring the benefits of integrated power system.
13. Foster market toward a competitive bidding system for power purchase selling (Fig. 6).

5.1 Smart Grid Architecture Components: [34–37]

Major components of smart grid are classified as follows: (1) smart infrastructure, (2) smart information and communication system, (3) smart management and (4) smart protection and control.

In smart infrastructure, system is divided into the following two parts:

1. Smart energy system: This includes bulk generation, transmission and distribution with advanced and intelligent control.

2. Smart information and measurement system: This includes smart meters, measuring and other auxiliary control, measurement units like PMUs and RTUs, GPS-enabled protection, smart meters, sensors and other ancillary services.

6 Conclusion and Summary

In this chapter, the challenges in existing power system are discussed and analyzed. The modern-day power system needs a whole lot of planning for redesign, expansion and successful operation. The various renewable energy sources available near to remote-end loads can be major sources of local demand fulfillment. The renewable energy sources as discussed in this chapter are available in abundance, clean and green but suffer from high variability in their source energy. The storage mechanism is required to fill up this gap. The storage mechanism along with the renewable energy sources equipped with automatic and intelligent smart controlling and monitoring devices can together form a smart grid. The low-voltage smart grids with independent operation features are the future of modern power system.

References

1. Tønne E, Sand K, Foosnæs JA, Paulsen R (2012) Integration of distributed generation into MV distribution grid in Norway—the Namsskogan case. In: CIRED workshop- integration of renewables into the distribution grid
2. Strbac G, Ramsay C, Pudjianto D (2007) Integration of distributed generation into the UK power system. Imperial College London, Summary Report
3. Cheng Y, Lataire P (2005) New concepts for distributed power generation and power quality for large-scale integration of renewable energy sources. In: European conference on power electronics and applications
4. Krishans Z, Mutule A, Kutjuns A (2005) Integration of distributed generation in the networks of Latvian power system. In: IEEE Russia Power Tech
5. Bollen M, Hassan F, Integration of distributed generation in the power system. Wiley-IEEE Press
6. Kashfi AR, El-Hawary ME (2014) Controller for demand side management. In: Electrical power and energy conference
7. Chiradeja P (2005) Benefit of distributed generation: a line loss reduction analysis. In: IEEE/PES transmission and distribution conference & exhibition. Asia and Pacific Dalian, China
8. Dang K, Yu J, Dang T, Han B (2011) Benefit of distributed generation on line loss reduction. In: International conference on electrical and control engineering
9. Bopp T, Shafiu A, Cobelo I, Chilvers I, Jenkins N, Strbac G (2003) Commercial and technical integration of distributed generation into distribution networks. In: 17th international conference on electricity distribution
10. Ratra S, Tiwari R, Niazi KR (2017) Voltage stability enhancement by the coordinated operation of OLTCs in the presence of wind turbines using Taguchi method. In: The 6th international conference on renewable power generation (RPG), October 2017

11. Matvoz D, Leskovec R, Maksić M (2017) Optimized reactive power characteristics for distributed generation sources in the low voltage network. In: IEEE Manchester PowerTech
12. Perez GA, Kagan N (2015) Integration of distributed generation in power distribution networks and its structure as an intelligent generation system. In: IEEE PES Innovative Smart Grid Technologies Latin America (ISGT LATAM)
13. Fozdar M, Arora CM, Gottipati VR (2007) Recent trends in Intelligent techniques to power systems. In: 42nd international universities power engineering conference
14. Eroshenko SA, Khalyasmaa AI (2017) Intelligent model of decision support system of distributed generation integration. In: 8th IEEE international conference on software engineering and service science (ICSESS)
15. Kashfi AR, El-Hawary ME (2014) Distributed generation integration with enhanced power system protection. In: Electrical power and energy conference
16. Menchafou Y, El Markhi H, Zahri M, Habibi M (2015) Impact of distributed generation integration in electric power distribution systems on fault location methods. In: 3rd international renewable and sustainable energy conference (IRSEC)
17. Scheepers M, van Werven M, Mutale J, Strbac G, Porter D (2006) Distributed generation in electricity markets, its impact on distribution system operators, and the role of regulatory and commercial arrangements. *Int J Distrib Energy Resour*
18. Narayanan K, Siddiqui SA, Fozdar M (2017) Detection and operation of unintentional islands in the presence of distributed generation units. <https://dx.doi.org/10.5772/intechopen.68859>
19. Narayanan K, Siddiqui SA, Fozdar M (2016) Optimal placement of distributed generators in radial distribution system for reducing the effect of islanding. *J Electr Eng Technol*
20. Narayanan K, Siddiqui SA, Fozdar M (2016) Hybrid islanding detection method and priority-based load shedding for distribution networks in the presence of DG units. *IET Gener Transm Distrib*
21. Narayanan K, Fozdar M, Siddiqui SA (2015) An improved hybrid method to reduce the effect of islanding in the presence of optimally located DGs. In: IEEE INDICON
22. Narayanan K, Fozdar M, Siddiqui SA (2015) Identification and reduction of impact of islanding using hybrid method with distributed generation. IEEE power & energy society general meeting
23. Kamps K, Mohrke F, Zdrallek M, Awater P, Schwan M (2018) Modelling of smart grid technologies for reliability of distribution grids. In: Power systems computation conference (PSCC)
24. Mahesh C, Josh FT (2017) A comprehensive study on distributed energy generation integration technology. In: Proceedings of IEEE international conference on innovations in electrical, electronics, instrumentation and media technology ICIEEIMT 17
25. Lorena Tuballa M, Lochinvar Abundo M (2016) A review of the development of Smart Grid technologies. *Renew Sustain Energy Rev* 59:710–725
26. Reliability considerations from the integration of Smart Grid. North American Electric Reliability Corporation, 2010
27. Purchala K, Belmans R, Exarchakos KL, Hawkes AD (2006) Distributed generation and the grid integration issues. Imperial College London
28. Schenkman BL, Wilson DG, Robinett III RD (2010) PhotoVoltaic distributed generation for Lanai Power Grid real-time simulation and control integration scenario. In: International symposium on power electronics, electrical drives, automation and motion, SPEEDAM
29. Kumar DS, Savier JS (2017) Impact analysis of distributed generation integration on distribution network considering smart grid scenario. In: IEEE region 10 symposium (TENSYPMP)
30. Hernando-Gil I, Ilie I-S, Djokic SZ (2012) Reliability performance of smart grids with demand-side management and distributed generation/storage technologies. In: 3rd IEEE PES Innovative Smart Grid Technologies Europe (ISGT Europe)
31. Deng R, Yang Z, Chow M-Y, Chen J (2015) A survey on demand response in smart grids: mathematical models and approaches. *IEEE Trans Ind Inf* 11(3)
32. Dupont B, Vingerhoets P, Tant P, Vanthournout K, Cardinaels W, De Rybel T, Peeters E, Belmans R (2012) LINEAR breakthrough project: large-scale implementation of smart grid technologies in distribution grids. In: 3rd IEEE PES Innovative Smart Grid Technologies Europe (ISGT Europe)

33. Momoh JA (2009) Smart grid design for efficient and flexible power networks operation and control. In: IEEE/PES power systems conference and exposition
34. Flamillillareesh, Pramod CP (2015) Distributed generation integration with enhanced power system protection. In: IEEE international conference on technological advancements in power & energy
35. Marashi K, Sarvestani SS (2014) Towards comprehensive modeling of reliability for smart grids: requirements and challenges. In: IEEE 15th international symposium on high-assurance systems engineering
36. Arnold GW (2011) Challenges and opportunities in Smart Grid: a position article. Proceedings of the IEEE 99(6)
37. Hassan R, Radman G (2010) Survey on Smart Grid. In: Proceedings of the IEEE SoutheastCon

Cybersecurity for Smart Grid: Threats, Solutions and Standardization



L. Chhaya, Paawan Sharma, Adesh Kumar, and Govind Bhagwatikar

Abstract Smart grid technology is developing at a very rapid pace. Energy sector is going under massive transformation as a result of smart grid design and development. It is characterized by full duplex communication of information along with bidirectional flow of electricity. Smart grid is an amalgamation of power and communication infrastructures. It is a complex hierarchical architecture with heterogeneous communication networks. Smart grid is an automated network with self-healing capability. A central controller manages an entire operation. A robust and secured infrastructure is inevitable for enormous amount of data communication. Cybersecurity is an indispensable constituent of smart grid technology. Limited spectrum availability, communication delays, interoperability between various protocols and network scalability are major challenges for the deployment of secured infrastructure. Smart grid is being transformed from idea to actual execution and deployment. There are several issues and challenges to be deciphered during design, development and deployment process. Cybersecurity is one of the key challenges for secured and reliable operation of smart grid technology. Cyber security can be defined as protection from exactions transported by computer network and/or terminals and the safety of assets from intentional or unintentional alterations or damage from malicious use of software-based control services. Smart grid communication infrastructure integrates WSN, communication transceivers, AMI, SCADA, electronics devices with firmware and various network devices used for hierarchical communication network

Present Address:

L. Chhaya (✉)
Gandhinagar, Gujarat, India

P. Sharma
Department of Computer Science and Engineering, School of Technology, PDP, U,
Gandhinagar, Gujarat, India
e-mail: paawan.sharma@gmail.com

A. Kumar
Department of Electronics, Instrumentation and Control Engineering,
University of Petroleum & Energy Studies, Dehradun, Uttarakhand, India
e-mail: adeshkumar@ddn.upes.ac.in

G. Bhagwatikar
SANY Group, Pune, Maharashtra, India

© Springer Nature Singapore Pte Ltd. 2020

A. K. Bhoi et al. (eds.), *Advances in Greener Energy Technologies*,
Green Energy and Technology, https://doi.org/10.1007/978-981-15-4246-6_2

layers. All these components are crucial and inevitable for smart grid communication infrastructure. These components are susceptible to cyberattacks. NIST has provided strategy for standardization of cybersecurity. Cybersecurity is a ubiquitous notion as smart grid is an always ON network comprising of IoT. This paper is anticipated to serve as a survey and study of various cybersecurity concerns pertaining to smart grid and possible elucidations.

Keywords Cyber security · Network · Smart grid · Standards

1 Introduction

Smart grid technology is transforming from concept to real implementation. There are enormous challenges to be solved during deployment process. Cybersecurity is one of the key challenges. Cybersecurity can be described as protection from extortions conveyed by computer or peripherals and the security of resources from modifications or impairment from unintentional or vindictive use of software-based control services [1]. Smart power grid comprises full duplex communication network. There is a bidirectional flow of power between utilities and customers. Smart grid uses supervisory control and data acquisition, wireless sensor networks, various communications protocols and hierarchical network layers. All these components are susceptible to malfunction as a result of cyberattacks. Cybersecurity is a prevalent concept for efficiency, reliability and security of smart grid network. Security of local network data, stored data and Internet data is a crucial priority. National Institute of Standards and Technology (NIST) has defined seven smart grid provinces [2] as shown in Fig. 1.

Many stakeholders have developed different models for efficient grid management. IBM has developed the model which gives more emphasis on communication

Fig. 1 Smart grid provinces

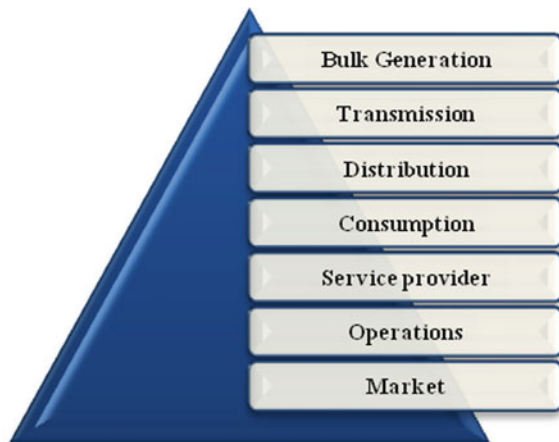




Fig. 2 Conceptual model of smart grid

networks and software packages [3]. Figure 2 shows the integration of IBM and NIST models.

As shown in above conceptual diagram, communication network is an imperative component of smart grid. Communication architecture requires various hardware and software modules which makes the system more vulnerable to cyberthreats. This paper depicts an all-inclusive analysis of cybersecurity threats, existing solutions and standards.

2 Cybersecurity Threats in Smart Grid

Siemens SIMATIC-WinCC system was attacked by the Stuxnet worm in 2010. It was the first cyberattack which affected the industrialized structures. As per Symantec's information, approximately 45,000 networks had been destructed through the worms till time in entire world, and around 60% of the targeted hosts are based at Iran. It is also confirmed by the government [4]. This example shows the significance of cybersecurity in hierarchical smart grid network. Security of cyberspace is important for data integrity during exchange of information. Authentication, availability of real-time information and confidentiality of data are the most important aspects of smart grid security. Furthermore, security aspects for smart grid network are more complex and critical due to heterogeneity of the network. The threats and attacks are unexplored and diverse. This section addresses the cybersecurity threats.

2.1 Intrusion

Intrusion is the attack of illicit user on the system to control the behavior of system. It leads to malfunction of devices as well as desecration of integration and confidentiality of the system [5]. Port scans and IP scans are the typical tools for realization of this attack [6].

2.2 Password Stealing

This attack is a despoliation of confidentiality. This attack can be technical or social engineering attack like password sniffing and dictionary attacks, respectively.

2.3 Malware Attack

Malware is malicious software which may contain worms, Trojan horses, viruses, logic bomb, backdoors or trapdoors [6]. Malicious software attack violates the integrity of system. Backdoors, trapdoors and logic bombs can be pre-inserted into software or programs which may generate attacks in future [7].

2.4 Eavesdropping

This attack is generated by sniffing IP packets on the networks or by interrupting the wireless transmission at various network layers. This attack violates the confidentiality of smart grid communication network.

2.5 Denial of Service Attack

Smart grid comprises IP-based applications and services. TCP-IP is vulnerable to denial of service attacks [6]. Attacker or trespasser can utilize the restricted network resources and make them unoccupied for authentic users.

An encryption and other characteristics must be secret. Any modifications or alterations made by intruders make the system unapproachable for users. Denials of service attacks reduce the availability of system by altering its configuration. Various types of denial of service attacks are described below.

2.5.1 Side-Channel Attacks

This type of attack utilizes the cryptographic information. Typical side-channel attacks include timing attack, electromagnetic analysis attack, power analysis attack to obtain control and administrative rights of smart grid power system. These attacks encroach upon consumer privacy.

2.5.2 Identity Spoofing

In identity spoofing attack, intruder impersonates legitimate user without password. Some of the common identity attacks are network spoofing, man in the middle attack, software exploitation, message replays, etc.

2.6 Cybersecurity Threats Allied with AMI

Advanced metering infrastructure (AMI) is an assimilation of power grid and ICT infrastructure [8]. It includes various software as well as hardware for operation and management of hierarchical and heterogeneous Smart grid network. Applications of AMI include metering, billing, distribution and consumer support. Various attacks on AMI can intrude upon the confidentiality, authenticity and availability of metering as well as billing information. It can be termed as sophisticated energy theft.

2.7 WSN Security

Wireless sensor network can be defined as assimilation of sensor nodes to obtain and communicate an information pertaining to different measured parameters such as current, temperature and humidity. Real instance management of various heterogeneous and hierarchical networks is the most decisive feature of smart grid technology. WSN forms the base of smart grid communication infrastructure. WSN comprises power supply unit (mostly battery), transceivers, memory, processor and location finding system.

The security concerns and issues for WSN must be differently addressed and solved due to complexity and restrictions of design and functionality. In a usual communication network, the addresses of transmitter and receiver are significant for data communication, but WSN comprises redundant nodes for data communication, and so, the transfer of data is more important than the address of a specific node. For instance, the real-time readings pertaining to humidity, temperature or current may be sent from any of the nodes placed in a specific region, and thus, data collection becomes more significant. WSN is different from rest of the communication networks in terms of its data-oriented approach compared to address-oriented approach of

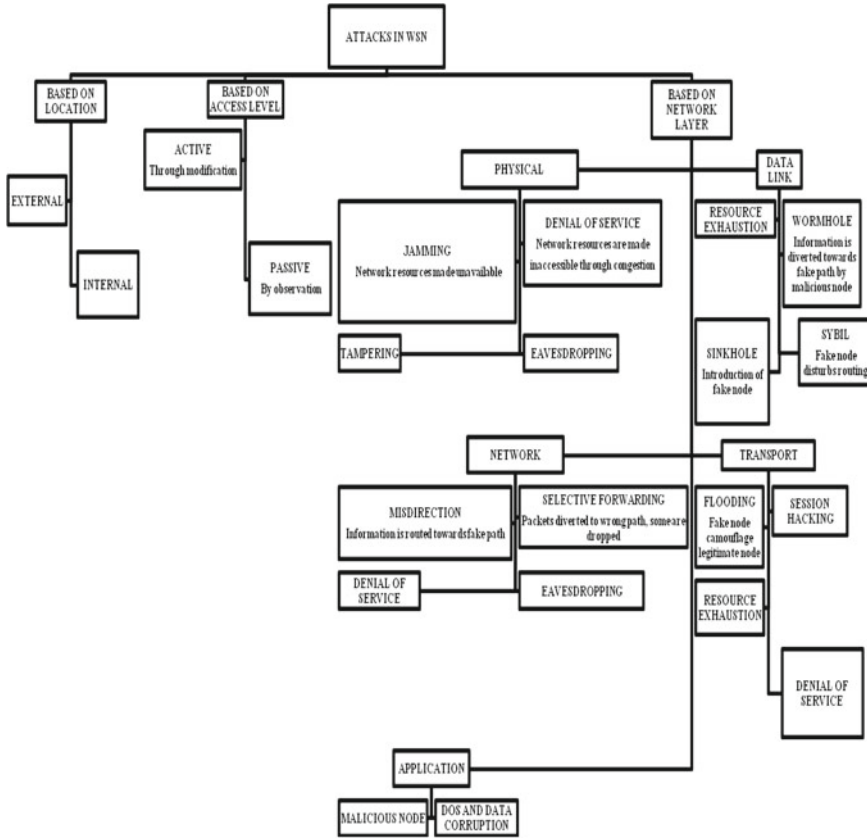


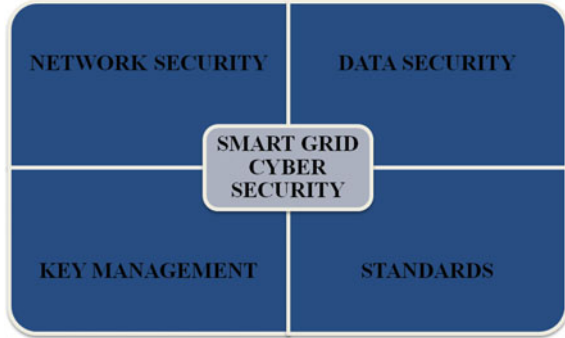
Fig. 3 Classification of WSN attacks

conventional communication network. Moreover, the computational ability of WSN node is quite inadequate which prevents the use of advanced and memory consuming algorithms for security measures. This restriction enhances the security concern for redundant nodes. WSN security is the most decisive, susceptible, complicated and mystifying aspect of smart grid security. Various cyberattacks for WSN network can be categorized as shown in Fig. 3.

3 Cybersecurity Solutions

Cybersecurity is a crucial issue to be addressed for smart grid infrastructure. It has gained attention of researchers and industries, and many solutions have been developed so far. Internet of things (IoT) can be an effective solution as everything will be connected to Internet, and data communication will not be aggregated through

Fig. 4 Important aspects of smart grid cybersecurity



enormous points before reaching application layer. This section depicts the survey of existing solutions. As shown in Fig. 4, the fundamental aspects of smart grid cybersecurity such as network security, data security, key management and standards are described in this section.

3.1 Network Security

Denial of service (DNS) attack is the usual attack in the context of cyberattacks. This attack makes the service unavailable. So, the detection and mitigation of this attack are essential for smart grid security [8].

3.1.1 Detection of Denial of Service Attack

The detection of denial of service attack is very essential to take appropriate action against attack. Detection of distributed denial of service attack is essential as mere detection of source IP is not a solution for this type of attacks. Many methods are developed for attack detection based on contents of packets, pattern of attack, etc. Some contemporary methods are as follows.

- Use of flow entropy
In this method, the router samples some of the packets to create a flow and then measure source entropy, quantity of packets per second and average entropy. Then, the counted value and known values are compared to detect the attack [9–11].
- Using signal strength information
Use of signal strength information for detection of attack is applicable for wireless communication devices. Jamming attack can be detected using this method. Each wireless device comes with its specified values of receiver sensitivity and threshold value of noise. Jamming devices do not have these unique values. Jamming attack can be done by either sending continuous amplified signal or by sending a noise

resembling signal. Above attacks must be detected by detector. Another approach is to check the output of decoder. If the decoder output is not appropriate, then it can be jamming attack [12].

- **Use of Signatures**
Denial of service attacks is generated using identified attack features. Any attack related action is matched with signatures, and the outcomes are matched to detect the attack.
- **Measurement of sensing time**
Wireless networks use carrier sense multiple access method. In this technique, the channel is sensed by transmitter to ensure that it is unoccupied before it proceeds for data transmission. During jamming attack, this sensing duration is very high, an attack can be detected once the sensing time duration is not matched with the threshold value, and the transmitter declares it as a denial of service attack.
- **Counting transmission failure**
Jamming attack causes failure of transmission. When a transmission failure reaches a threshold value, the decision can be taken that it is due to jamming attack. Counting of transmission failures can be detected at transmitter or receiver.

3.1.2 Mitigation of Denial of Service Attacks

As soon as the denials of service attacks are detected, the countermeasures must be taken in order to prevent outages or disruption in communication process. The denial of service attacks either disrupt the communication process of victim's network or exhaust the victim network's resources. Thus, the countermeasures are taken at either physical layer or network layer due to nature of attacks. Following mitigation approaches can be taken.

- **Reconfiguration of network topology**
Network reconfiguration is done by changing a topology of a network. This method isolates attacker from victim network. For complex smart grid network, this method is very expensive.
- **Pushback**
After the detection of denial of service attack, the attacker's characteristics like source IP address and attack patterns can be pushed back in uplink direction to block the IP address of attacker.
- **Filter Method**
The IP address of black listed or distrustful packet is filtered out by router so that only authentic packets can move further.
- **Limitation of data rate**
After detection of higher false detection rate, the data rate of a particular user is restricted by the router so that the denial of service attack can be mitigated. In

case the user is authentic and legitimate, the complaint can be sent, and the data rate can be again increased.

- **Cleaning center**
This mitigation approach is a combination of filtering and reconfiguration methods. After the DNS attack, a packet is diverted to a cleaning center node which is capable to perform filtering [12].
- **Mitigation at physical layer**
The jamming attacks are performed at physical layer which is responsible for transmission and reception. Different techniques like direct sequence and frequency hopping spread spectrum can be used for prevention of these attacks. In these techniques, the carrier frequency keeps changing, so jamming attack can be prevented as it is based on generating the same frequency to cancel the actual transmission [13–15].

Various personal area networks Bluetooth, Zigbee, etc., already use frequency hopping spread spectrum technologies [13–16].

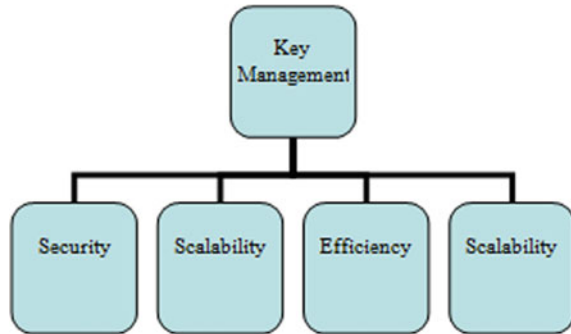
3.2 *Data Security*

Security of gigantic amount of data is an inevitable part of smart grid cybersecurity. During transmission and reception processes, the data must be secured. The user must be authenticated. Data security and authenticity are the integral parts of secured communication framework. Various encryption techniques are developed for data security. Public key cryptography and symmetric key cryptography can be used for smart grid applications. Symmetric key requires less computational capacity of devices. Public key requires more computational capabilities, but it facilitates easier key management. However, smart grid is a complex network, and use of encryption technique depends on various factors like bandwidth availability, security requirements, authentication, multicast, fault resilience, etc. For multicast applications, authentication is done using following techniques [16].

3.2.1 **Timing Asymmetry**

In this method, transmitter generates an authentication key after sending a message. But the key is transmitted only when all the nodes receive the message. In this scenario, if any attack has been generated, then the attacker will not be able to use the key and will be identified immediately.

Fig.5 Key management aspects



3.2.2 Secret Information Asymmetry

In this method, each transmitter authenticates itself by a unique authentication key. The drawback of this method is increased overhead which can be considered as redundant information.

3.2.3 Hybrid Asymmetry

This technique is a combination of timing asymmetry as well as secret information asymmetry. It generates temporary authentication keys for various transmitters.

3.3 Key Management

Key management is an indispensable part of cybersecurity. It includes the management of symmetric and public keys. Public key infrastructure confirms the security of the system by receiving a certificate of authenticity of receiver through certifying authority. Symmetric key is fast, efficient and requires less computational capabilities. However, for the complex smart grid network, new aspects for key management can be developed as shown in Fig. 5.

Despite many security techniques, a reliable and efficient framework for complex network like smart grid is still a challenge. The security techniques for physical layer should be developed by developing different modulation and coding schemes.

3.4 Regulations and Standards

The crucial role of cybersecurity is realized by many regulators and institutions. The organizations like NIST, IEEE and NERC-CIP have developed some regulations and

standards for smart grid cybersecurity framework. NIST has recognized the following basic IEC standards as follows [17–20].

- 60870-6
- 61850
- 61968
- 61970
- 62351

Above five standards are also recommended by IEC as the basic requirement of smart grid cybersecurity using IEC 62357 in place of IEC 60870-6. Moreover, there are primarily following regulations and reports aiming on smart grid cybersecurity.

3.4.1 North American Electric Reliability Corporation-Critical Infrastructure Protection (NERC-CIP)

The NERC-CIP cybersecurity standards [17] include cybersecurity defense of the most crucial power generation, transmission and distribution infrastructures.

3.4.2 Nist 800-53

NIST publication 800-53. This is a revised document suggested for security of federal information systems [18].

3.4.3 Nistir 7628

This document describes strategies for smart grid cybersecurity [6]. It endeavors to evaluate the security of entire smart grid infrastructure.

3.4.4 IEEE 1686

This standard is developed by IEEE for the cybersecurity of intelligent electronic devices (IEDs) at substations. This standard instigated from an IED security endeavors of the NERC-CIP. The standard is appropriate to any IED where security and liability are required in IED operation. IEDs will be safeguarded by user identity and password protection. It will monitor all security-related activities and make it available on real-time basis [19].

3.4.5 IEC 62351

This standard is developed for data security related to power management. IEC 62351 is a sequence of official papers which describe the types of security actions for communication networks. It also includes profiles such as TCP/IP and manufacturing message specification (MMS). It will facilitate data security through digital signatures. Some of the features of this standard are confidentiality through encryption, avoidance of spoofing and observation of communication infrastructure [19].

3.4.6 IEC/ISO-15408

This standard is developed for assessment of cybersecurity of smart grid by considering uncertainties of generations and loads. It includes introductory general model for information technology security, functional requirements and security assurance requirements [20].

4 Conclusion

Smart grid is a multifaceted and diverse network comprising of various intelligent devices and communication technologies. It is susceptible to cyberattacks at different layers of heterogeneous network. Detection of attack is inevitable for its mitigation.

The nature as well as countermeasures of attacks are still unknown and unprecedented. A framework for attacks and their solutions is important and necessary for cybersecurity purpose. This paper describes a comprehensive survey of cybersecurity threats, countermeasures and standards. Cybersecurity issues require rigorous research as solutions must be developed for various types of attacks. Smart grid is a huge network comprising of hierarchical sub-networks. Several protocols, technologies and standards are incorporated for conceptualization and realization of smart grid architecture. Smart grid network architecture must be adaptable as well as reconfigurable to endure a variety of dynamics. The network must be robust enough to deal with uncertainties and complexities of operation and management. Reliability of smart grid is a massive challenge to overcome. Amalgamation of renewable energy resources for energy generation has introduced novel challenges and issues such as consistency of power supply, load profile, scattered resources, forecasting pertaining to steadfastness of power grid. Efficiency of smart grid technology is also one of the foremost challenges to conquer due to complex architecture of smart grid comprising of diverse energy sources, EV, PHEV, microgrid, WSN, distinct loads, AMI and SCADA. Internet of things (IoT) model can be a prominent way out as it avoids vulnerability by reducing points of attacks.

References

1. Appendix B2 (2007) A systems view of the modern grid-sensing and measurement. National Energy Technology Laboratory
2. NIST (2010) Introduction to NISTTR 7628 guidelines for smart grid cyber security
3. Garner G (2010) Designing last mile communications infrastructures for intelligent utility networks (smart grid). IBM Intelligent Utility Network (IUN) Communication Services
4. Antiy CERT (2010) Report on the worm Stuxnet's attack. Antiy Corp, Harbin, China
5. Dzung D, Naedele M, Von Hoff TP, Crevatin M (2005) Security for industrial communication systems. Proc IEEE 93:1152–1177
6. Wang J (2009) Computer network security. Higher Education Press, Beijing, New York, Springer, Berlin, pp 3–24
7. Can O, Sahingoz OK (2015) A survey of intrusion detection systems in wireless sensor networks. In: International conference on modeling, simulation, and applied optimization, pp 1–6
8. NIST framework and roadmap for smart grid interoperability standards. Release 3, Nat'l Institute of Standards and Technology (2014)
9. Jun J-H, Lee D, Ahn C-W, Kim S-H (2014) DDoS attack detection using flow entropy and packet sampling on huge networks. In: International conference on networks, Nice
10. Meng G, Wang N (2014) A network intrusion detection method based on improved K-means algorithm. Adv Sci Technol Lett 53(I):429–433
11. Shin S, Lee S, Kim H, Kim S (2013) Advanced probabilistic approach for network intrusion forecasting and detection. Expert Syst Appl 40:315–322
12. Lin D (2013) Network intrusion detection and mitigation against denial of service attack. WPE-U Report, University of Pennsylvania
13. Popper C, Strasser M, Capkun S (2010) Anti-jamming broadcast communication using uncoordinated spread spectrum techniques. IEEE J Sel Areas Commun 28:703–715
14. Lee EK, Gerla M, Oh SY (2012) Physical layer security in wireless smart grid. IEEE Comm Mag 50:46–52
15. Cyber security in the smart grid (2013) W. Wang and Z. Lu. Survey and challenges. Comput Netw 57:1344–1371
16. Shapsough S, Qatan F, Aburukba R, Aloul F, Al Ali AR (2015) Smart grid cyber security: challenges and solutions. In: International conference on smart grid and clean energy technologies (ICSGCE), Offenburg, Germany, pp 170–175
17. NERC CIP Cyber Security Standards (2011) NERC Reliability Standards, CIP
18. NIST Special Publication 800-53 (2009) Revision 3: recommended security controls for federal information systems and organizations. NIST, Gaithersburg, MD
19. Momoh J (2012) Interoperability, standards, and cyber security. In: Smart grid: fundamentals of design and analysis. Wiley-IEEE Press, pp 160–175
20. Wang Y, Gao J (2011) Analysis of smart grid security standards. In: IEEE international conference on computer science and automation engineering, Shanghai, pp 697–701

Solar Fuels via Two-Step Thermochemical Redox Cycles



Azharuddin Farooqui, Marta Boaro, Jordi Llorca, and Massimo Santarelli

Abstract With the advent of green technologies, solar fuel has gained particular interest that helps in producing syngas which is the primary feedstock for many of the synthetic chemicals using emissions (CO_2 and H_2O). Thermochemical redox cycles use metal oxides as oxygen carriers that are capable of oxygen diffusion during continuous reduction and oxidation cycles. In the chapter, the focus has been derived in many aspects such as metal oxides and their evolution, reactor design and their scope of large-scale modularity, and lastly its application in fuel, chemicals and power plants. The chapter also highlights the system analysis for different chemicals, their techno-economic feasibility, and viability.

Keywords Thermochemical redox cycle · Oxygen carriers · $\text{CO}_2/\text{H}_2\text{O}$ splitting · CO_2 utilization · Solar fuels

1 Introduction

CO_2 emissions by burning fossils are the main contributor to the most discussed issue of the decade, with 35.2 Gt being emitted in 2017 [1]. Even though there are a substantial investment and a decrease in energy price by renewables in the last few years, fossil fuels will continue to serve as a major contributor in global energy [2]. It is reported that one of the major sources of the increase in carbon dioxide emissions is from power plants and followed by the transportation sector.

A. Farooqui (✉)

Institute of Engineering Thermodynamics, German Aerospace Center (DLR), Stuttgart, Germany
e-mail: azhar.uddin@dlr.de; azharuddin0613@gmail.com

A. Farooqui · J. Llorca

Institute of Energy Technologies, Universitat Politècnica de Catalunya, Barcelona, Spain

M. Boaro

Polytechnic Department of Engineering and Architecture (DPIA), Università di Udine, Udine, Italy

M. Santarelli

Department of Energy, Politecnico di Torino, Torino, Italy

© Springer Nature Singapore Pte Ltd. 2020

A. K. Bhoi et al. (eds.), *Advances in Greener Energy Technologies*,

Green Energy and Technology, https://doi.org/10.1007/978-981-15-4246-6_3

In a recent report by International Energy Agency (IEA), the estimated global energy demand grew by 2.1% in 2017 which was twice the growth rate in the previous year. Fossils such as natural gas demand grew by an unprecedented value of 3% followed by oil which rose by 1.6%. It is also important to mention electricity demand increased by 3.1%. Even though renewables have seen the highest growth which accounted for one-fourth of global energy demand in 2017, overall 70% of global energy demand was met by fossil-based fuels, out of which natural gas share was of 22% [1]. Therefore, the demand for hydrocarbons as primary fuel will continue to grow as shown in Fig. 1. This will eventually lead to an increase in carbon dioxide emissions unless measures of fast transition are not adopted [3].

In the recent report of International Panel on Climate Change (IPCC) which paves the path of changing, the goal of limiting the global warming rise of 2–1.5 °C within by 2040 has been posted as mandatory. This leads to a global call to make some stringent efforts in changing energy policies to reduce further usage of fossil fuels [4] otherwise the consequences will be irreversible in terms of ecological imbalance and environmental damage. Primarily apart from renewable energy-based power production, there was an extensive drive for carbon capture and sequestration (CCS)-based power plants and call for retrofitting the existing power plants to adopt CCS. Adopting CCS-based power generation system would not completely solve the problem. As the amount of CO₂ generation from them is also huge that it is not possible to store all of it in a depleted oil well or geological formations which also have safety implications to store in a long-term basis. Other alternatives such as CO₂ used enhanced oil recovery also have limitations as the recovery rates are as low as 10% [5].

In this perspective, the efforts to sequestrate CO₂ emissions should proceed together with a policy of re-utilization of the high amount of recovered CO₂. In terms of re-utilization, one possibility is to produce synthetic fuels from carbon

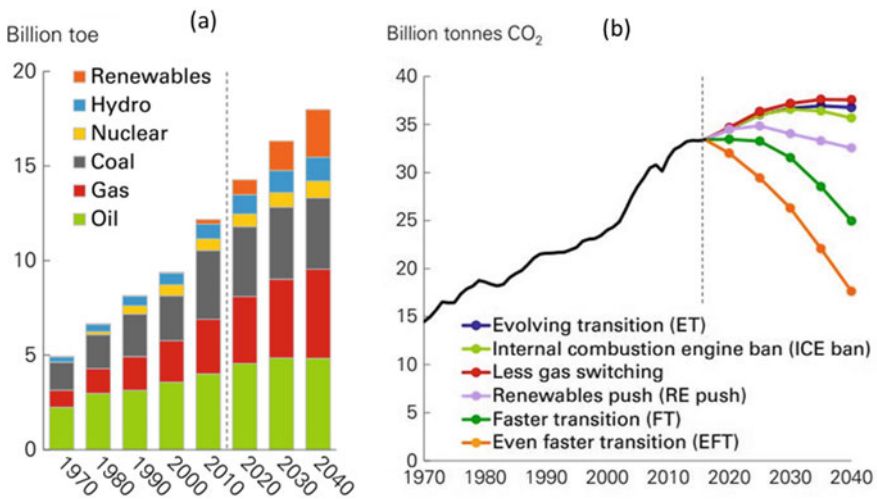


Fig. 1 a Fuels as primary energy demand; b CO₂ emission forecast with different scenarios [3]

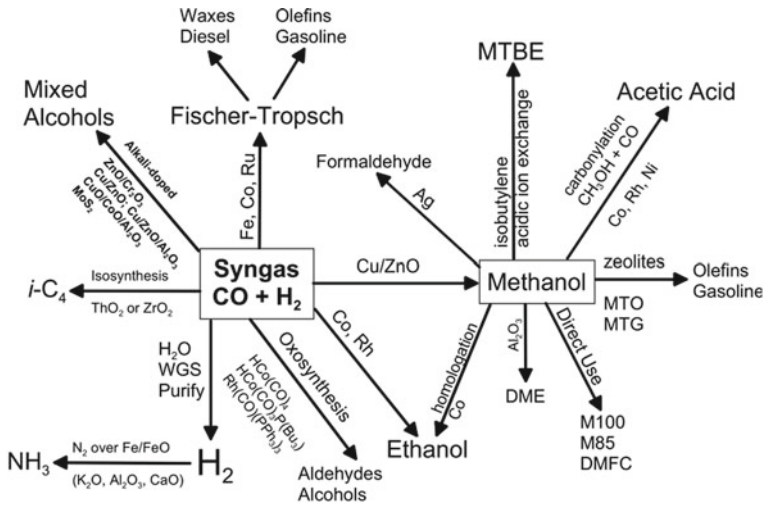


Fig. 2 Syngas as feedstock for different chemical products [6]

dioxide emissions. Syngas is considered the target fuel because there is a large availability of CO₂ and H₂O from the flue gases of carbon capture-based power plants, available for its production. Secondly, the syngas serves as the feedstock for multiple chemical productions such as methanol, dimethyl ether (DME), ethanol to just name few [6]. The downstream possibility of usage of syngas is shown in Fig. 2. At the moment, syngas is produced using biomass, natural gas, and coal commercially. The natural gas is converted into syngas by partial oxidation, autothermal, solar methane reforming, and steam reforming which are few to name [7].

Since the reforming reactions for syngas production are endothermic in nature and require external heat, their combination with solar energy is an attractive option to improve such processes [8]. What makes solar energy even more attractive to the production of fuels or chemicals, is the fact that solar energy is readily available almost everywhere. Fuel production with the use of solar energy is termed as Solar Fuels [9, 10].

Conversion of solar energy and CO₂ by thermochemical processes to produce solar fuels was initially investigated to produce hydrogen as it was considered as the fuel of the future. Further processing can lead to the production of methanol, gasoline diesel, and kerosene, which are the liquid hydrocarbon feedstock for chemical processes, contributing to a sustainable circular economy in the fuel and power industry as shown in Fig. 3 [11]. Therefore, solar fuels considered as carbon neutral if they are produced from waste gas (H₂O + CO₂), represent a viable way of storing intermittent renewable energy.

There are many pathways suggested for solar fuels based on the mechanism, process, and temperature range required (Fig. 4). The processes are broadly classified as a photochemical or photobiological, electrochemical, and lastly thermochemical group, which requires a very high temperature that can be attained by concentrated

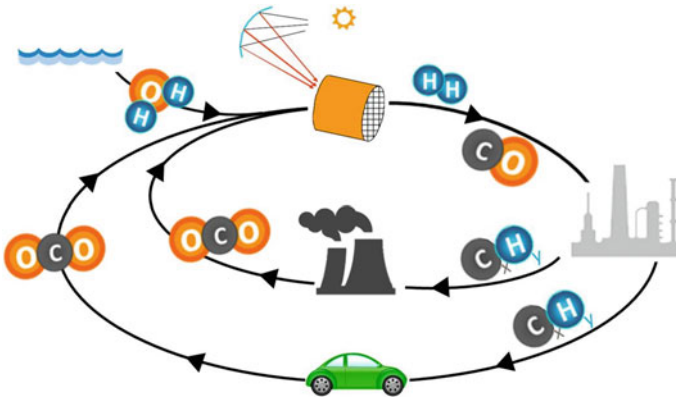


Fig. 3 Circular economy by solar fuels from renewable energy. CO₂ and H₂O are captured from power plants and fed to a solar thermochemical process and converted into hydrocarbons in chemical plants [11]

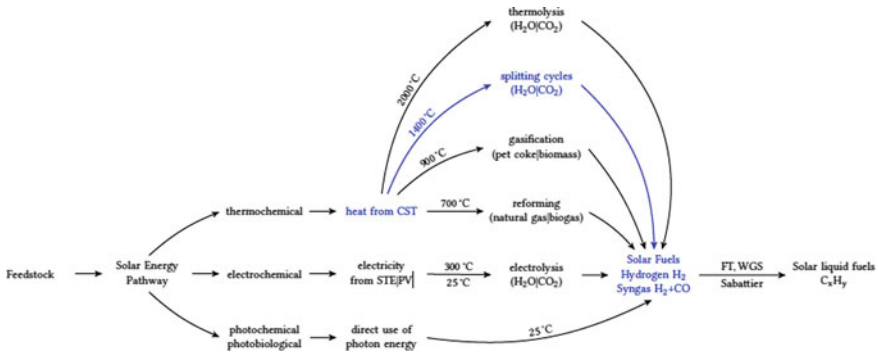


Fig. 4 Solar fuel’s major pathways [16]

solar power technologies. Photochemical and photobiological pathway requires photon energy from solar energy, but the scale of the process is very small. In the electrochemical pathway, the solar energy is initially converted into electricity, which by electrolysis produces hydrogen or syngas depending on the feed.

Thermochemical cycles associated with concentrated solar energy constitute one of the cheapest solutions in terms of cost among those mentioned above to produce syngas and hydrogen [12]. It is comparable with the most developed and widespread process which is steam methane reforming (SMR). The problems associated with it are the degree of development of the technology which does not allow to reach higher efficiency and the use of a fossil fuel as raw material, which is a greenhouse gas emitting process [13]. Anyway, the demand for clean and cheap hydrogen is pushing the research toward the development of alternative technologies [14, 15].

Theoretically, the simplest reaction to obtain syngas from the mixture $\text{H}_2\text{O}/\text{CO}_2$ is the direct thermal splitting. Unfortunately, the temperature needed of $2400\text{ }^\circ\text{C}$ is not achievable with the current technology, and the problem of the separation of H_2 and O_2 to avoid explosive mixtures is a major issue. Alternatively, the process of thermochemical dissociation is carried out in two steps (reduction and oxidation) by using metal oxides, which tremendously lowers the temperature required for syngas production.

In two-step thermochemical redox cycles, heterogeneous chemical reactions take place. The solid reactant is usually a metal oxide (also called an oxygen carrier) that changes its oxidation state stripping and releasing oxygen in a cyclic way. Many materials have been investigated to maximize the syngas production, minimize the degradation, and to reduce the operating temperature. The most interesting was found to be ferrites, ceria-based materials, and perovskites. For all these materials, there is the possibility of tuning their redox properties and improve their behavior thank to appropriate doping of their lattice [16].

2 Carbon Capture and Sequestration

In the late 1970s, after the global crisis, Carbon capture was proposed to enhance the oil recovery. Later, the use of CCS was shifted to capture CO_2 emitted from fossil fuel for tackling climate change. At the current status, there are 26 facilities integrated with CCS technology, which account for more than 30 Mtpa of CO_2 emission avoided [17]. The CO_2 produced in a power or industrial plant is previously captured, conditioned, and transported through pipeline, railways, or roadways and stored in a suitable body for several decades. According to the point where CO_2 is separated, CCS is referred to as pre-combustion, oxy-fuel or post-combustion as shown in Fig. 5.

In post-combustion carbon capture, CO_2 is separated downstream from the flue gases after the combustion of fossil fuel [18]. The major benefit lies in the adaptability to retrofit the existing fossil fuel plants such as coal power plant. However, its use implies a plant efficiency penalty and cost addition as CO_2 in the flue gases. In addition, flue gases coming from the combustion chamber are at ambient pressure, making the CO_2 separation highly energy inefficient [19]. The most used separation process is physical and chemical absorption in which CO_2 is scrubbed through a liquid solvent. In physical adsorption, CO_2 is physically captured at the surface of the solvent, which has an increased absorption ability at high pressure [20]. In general, physical absorption is used when CO_2 content in flue gas is higher than 15 vol% [21]. In chemical absorption process, the flue gases are scrubbed through an aqueous alkaline solvent (MEA, DEA, MDEA, etc.) in an absorber, where CO_2 is captured by the solvent via chemical reactions. A subsequent stripper column is used to regenerate the rich in CO_2 solvent through heating up and release a high content CO_2 stream (>85%) [22]. When the flue gas from fossil fuel power is at ambient pressure and CO_2 content is lower than 15 vol%, chemical absorption is preferred.

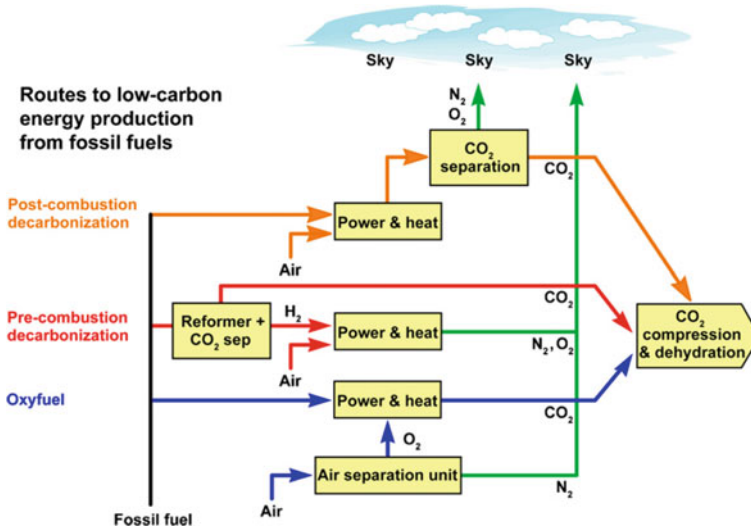


Fig. 5 Main route for carbon capture [19]

An oxy-fuel CCS-based process consists in burning the fuel in a pure oxygen atmosphere (>95%) so that the flue gas is not diluted in nitrogen but is only composed of mixture of H₂O and CO₂. Water is separated by condensation to obtain a pure CO₂ stream. Differently, from air combustion plant, where N₂ absorbs the heat of combustion, in oxy-fuel combustion plant, to control the adiabatic flame temperature, a recirculation of the exhausted gases is proposed (>80%) [23]. This technology can be used for novel plants or can retrofit existing power plants with few modifications [24]. The main drawback of the process is the energy required to produce a pure oxygen stream in an air separation unit (ASU); it is estimated a consumption of 0.16–0.25 kWh per kg of O₂ for the production of a 95% pure O₂ stream [25]. Separation of oxygen from nitrogen can be either obtained by cryogenic and non-cryogenic processes. For industrial process where a high amount of O₂ is required, cryogenic separation is used. Nevertheless, most of the research is direct to non-cryogenic technology, such as membrane separation, whose adoption will reduce the energy penalty [21, 24]. Cryogenic separation takes advantage of the different condensation temperatures of gases. The air is firstly compressed (4–6 bar), cooled down to its condensation temperature (–172 °C at 6 bar), and sent continuously to two stripper columns where N₂ and O₂ are separated [26]. The energy cost of this cycle is due to the air compression, which is required to have an appropriate level of cooling power to drive the separation [27]. In the current state of the art, big scale oxy-fuel combustion is not yet in the commercial status, and most of the projects are pilot or demonstrative plants based on coal combustion [28]. As shown in Fig. 6, after the construction of pilot plants of 1 MWe and lower size in the first decade of the 2000s, larger size demonstration plants such as White Rose in the UK [29] or Shenhua in China [30] are now in the phase of projection and construction. Regarding

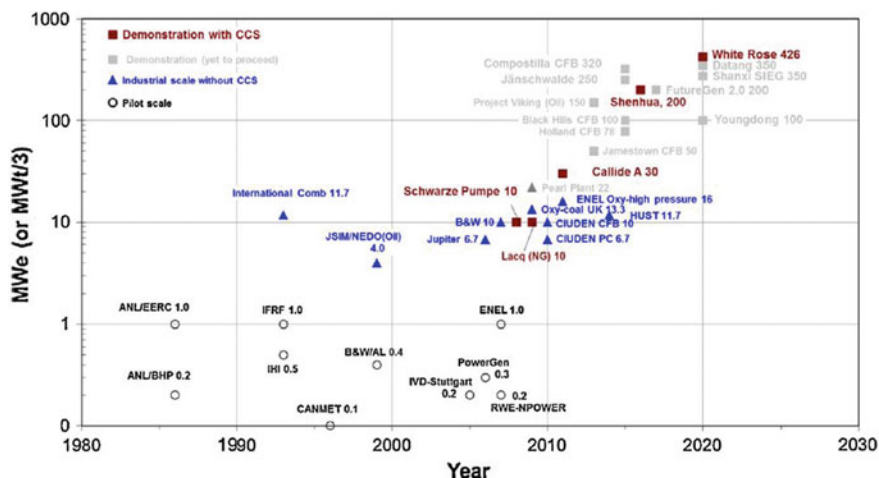
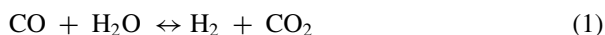


Fig. 6 Historical progression of oxy-fuel combustion technology [33]

the oxy-fuel combustion process integrated with the natural gas-driven cycle, they are in a lower stage of development with respect to above-listed coal-fed projects. Few proposed plants such as the one from Allam et al. [31] or Anderson et al. (CES) [32] have reached the demonstrative phase.

In pre-combustion CCS process, pre-treatment of the relevant fuel (coal or natural gas) would be necessary. For coal, it firstly undergoes low O_2 gasification process which produces a syngas composed of H_2 and CO . A water–gas shift (WGS) reaction is secondly used to increase the H_2 content converting CO into CO_2 (reaction 1). In the case of methane, which is in gaseous form, it undergoes steam reforming (reaction 2), and then, the H_2 content is increased by a WGS reaction [18]



Finally, CO_2 and H_2 are separated via physical, chemical absorption or using membrane separation and H_2 is burnt producing as a product just water [34]. After sequestration, CO_2 is dehydrated, conditioned, and pressurized at a pressure of 110 bar and sent to storage location via pipeline, railways, or roadways [18]. Especially for large plants, pipeline transportation is the main solution, since it has been used for decades, especially in the USA, for oil recovery (EOR) [35].

There are several options for CO_2 storage. At present, the most corroborate option is the storage in geological bodies such as deep saline aquifers, unmined coal bed or oil and gas depleted reservoir [17, 36]. A suitable geological site can hold a million tonnes of CO_2 for several decades or centuries by different physical and chemical mechanism [37]. An alternative is to store CO_2 in the oceans. Injecting

carbon monoxide at depths higher than 3 km, it is demonstrated that it can be stocked for several centuries due to the CO₂ higher density with respect to the surrounding [38]. Moreover, oceans cover 70% of the earth's surface, so they can represent a sink for a huge amount of CO₂. However, there is some controversy about the potential risk of acidification of water due to CO₂ storage that would be disastrous for the marine ecosystem [38]. For this reason, although the high potential, ocean storage is not considered in the near term.

To conclude, CCS technologies are one of the most attractive solutions to climate change tackling, especially in the middle term where fossil fuel is still the main source for power generation. However, it presents many drawbacks such as energy efficiency drop for the power plant when it is integrated. It is estimated that the energy penalty might range from 7–15% drop in efficiency depending on the carbon capture technology [18]. In addition, CO₂ storage is seen as a controversial and critical part of whole CCS chain due to higher risk of potential leakage, earthquakes, global capacity, engineering feasibility, and economic expenditure issues [39, 40]. For this reason, rather than a pollutant to be stored or eradicate carbon dioxide can act as primary ingredient for the production of new fuels and chemicals [41]. This concept opens to a new branch referred to as carbon capture and utilization (CCU), which will be discussed in the following subsection.

3 Carbon Capture and Utilization

As an alternative to storage, CO₂ utilization has achieved a great attention in the scientific and industrial field in last years [42]. In fact, the concept of CCU not only permits to make fuel exploitation cleaner but also gives the opportunity for a more sustainable energy economy [43]. CO₂ can be recycled and used as a product directly or converted into a new one. Several industries use directly CO₂ for their applications. For example, in the food and beverage sector, it is used as a carbonating agent, packaging gas, or in the pharmaceutical sector as an intermediate for drug synthesis [44]. However, these markets do not have a potential size to be considered a valid solution in limiting CO₂ emissions in a crucial way. Vice versa, the conversion of CO₂ into chemicals and fuels is a promising and attractive market as it allows to cut a portion of the capture cost and create a closed-loop carbon cycle [45]. CO₂ conversion into fuel or chemicals initially received criticism for various reasons. Since the CO₂ embedding time into fuel is not so long, it will eventually from fuel to CO₂ and then again into the atmosphere if it is not captured again. Other reasons being the stringent high temperatures required for thermochemical dissociation. With scientific advancement, capturing CO₂ and retrofitting existing plants would solve the issue of emitting CO₂ directly to the atmosphere.

It is estimated that the CO₂ recycle can contribute to a 7% reduction in overall emissions [46]. The main drawback of CO₂ is that it is thermodynamically highly stable, and so, its conversion requires high-energy input, active catalyst, and optimum reaction conditions [47]. CO₂ can be used as co-reactant in carboxylation reactions,

in which all carbon dioxide molecules are built into products without entirely cut the C=O bonds [48]. Among carboxylation processes, mineral carbonation and utilization of CO₂ as a precursor to organic carbonates, carbamates, acrylates, carboxylic acids, and polymers can be cited [49]. For example, the production of urea, for fertilizers and polymers synthesis, is an organic carboxylation reaction that is already present at industrial scale (more than 100 Mt of urea are produced yearly) [42]. Alternatively to carboxylation, CO₂ can be reduced, breaking one or both the C=O bonds and used for the synthesis of new species like syngas. Syngas, a mixture of H₂ and CO, is one of the most valuable resources in the industry field since its versatility. As shown in Fig. 2, the syngas can be used in multiple processes for either chemical, fuel, or power generation.

Nevertheless, as already stated, CO₂ is a highly stable molecule, so in order to break one of the C=O bonds, a high-energy carrier is required. Of great interest, it is when this energy vector, either heat, electricity, or high-energy reactants (H₂, CH₄, etc.), is produced by renewable resources. In this way, the renewable energy used for the reaction of dissociation acts as a chemical storage [48]. Several processes have been proposed for CO₂ dissociation, one that has received great consideration in the research, especially for its application at a large scale, is the chemical looping [50, 51].

4 CO₂ Utilization Using Chemical Looping Processes

Due to the limitation of electrochemical or photochemical or other modes of conversions of CO₂, thermochemical conversions of CO₂ are being currently studied as cheaper alternatives. There are primarily two ways for such thermochemical dissociation of CO₂, namely: (a) direct dissociation and (b) chemical looping.

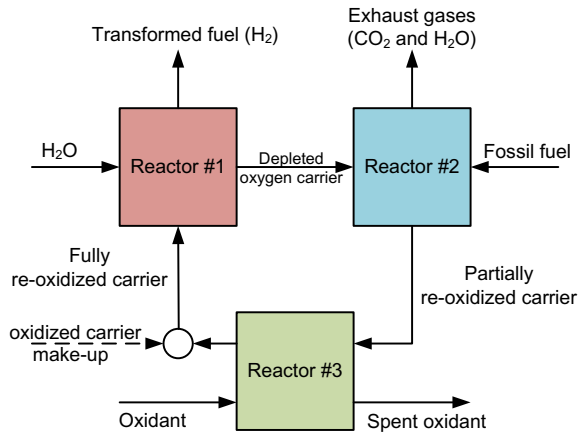
Direct dissociation of CO₂ at extremely high temperatures of 1900–2400 °C has been investigated by Traynor and Jensen in USA [52]. The process yielded around 6% of CO₂ into CO. Multiple other studies have been conducted to define the working parameters of such thermochemical conversions [53, 54]. However, with very high temperature and quenching process requirement, direct dissociation of CO₂ has so far been considered as difficult and unprofitable.

Chemical looping is a process based on the principle of a set of chemical reactions occurring in multiple reactors, whereby one of the reactants constantly circulates between reactors forming a closed loop as shown in Fig. 7.

Indeed, for practical application, losses occur, requiring makeup of the reactants into the closed-loop system, as indicated by the dashed lines in Fig. 7. In general, depending on the individual reactions being either endothermic or exothermic, such systems do not operate in isothermal conditions. Temperature swings between the reactors often over hundreds of degrees, requiring regenerative heat exchangers to be frequently incorporated into the system.

A wide variety of processes in the power engineering and petrochemical engineering currently use chemical looping as their main principle of operation, one of the

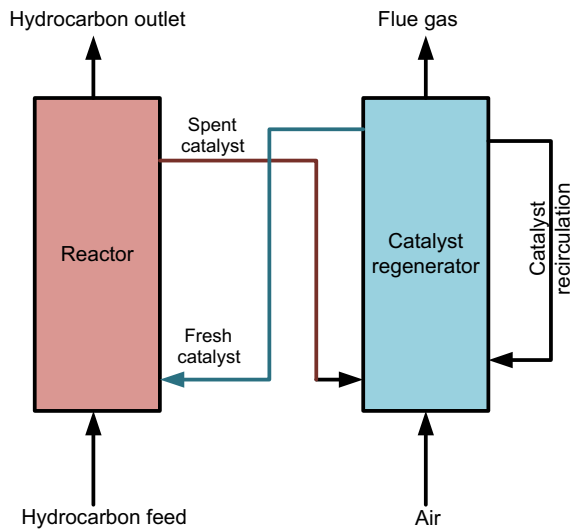
Fig. 7 Chemical looping diagram of a three-reactor setup for fuel decarbonization



most mature processes being the fluid catalytic cracking (FCC). In this process, the catalyst is first used in the cracking reactor to break up higher-order hydrocarbons to shorter chains, however, by losing its own potential, requiring regeneration. Therefore, it is sent to a regeneration reactor and back to the cracking process, thereby completing a chemical loop. In this process, the regenerator reactor is of a circulating fluidized bed type, whereby the catalyst resides for a couple of cycles in the regenerator (Fig. 8). This configuration of the system helps in temperature control of the regeneration process which otherwise is highly exothermic [55].

Another example of an industrial chemical looping process is the monoethanolamide (MEA) reactor for carbon capture and storage (CCS) systems.

Fig. 8 FCC process chemical loop with indicated recirculation of part of the catalyst in the regenerator



Though used in relatively small scale due to primary reason of lack of economic feasibility of the CCS process in current market condition, the technology is well developed. A general layout of the amine-based capture systems is presented in Fig. 9. In this process, the exhaust gas is rinsed with chilled monoethanolamide in the counterflow reactor, where the amines absorb the CO_2 , SO_2 , and other oxides available in the flue gas. Later, the lean mixture is heated up, releasing the absorbed gases. Amines leaving desorption reactor are cooled down, first in the regenerative heat exchanger and in the additional cooler, and then, they are directed into the scrubber. The MEA system is used as a post-combustion method of the CO_2 separation, by which existing plants can be retrofitted to incorporate it.

However, new approaches are being developed for carbon capture, one of the recent developments being the separation of the exhaust gases from the oxidant through the chemical looping combustion (CLC) process [56, 57]. In such a system as opposed to the concept of direct interaction between oxidant and fuel, the oxygen required for the combustion process is transported in between them by metal oxides.

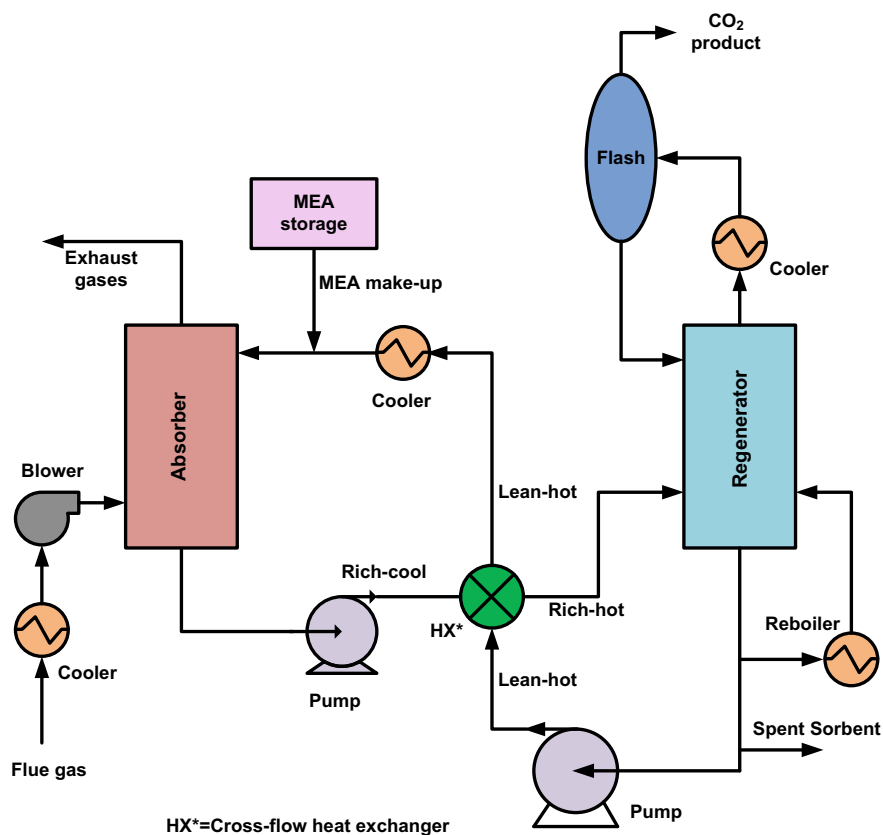


Fig. 9 Monoethanolamine-based carbon capture chemical loop diagram

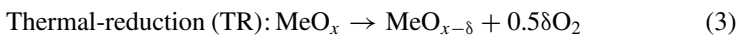
In fact, Fig. 7 represents diagrammatically a CLC system layout. Even though it is not necessary to have the three-reactor setup, some of the oxygen carriers might not be re-oxidized to their initial state within the first oxidation reactor (reactor #2, Fig. 7), thus requiring additional oxidation reactor, fed with air or pure oxygen. Such a process has also been proposed to be used for fuel decarbonization.

In the CLC, the chemical energy of a carbonaceous fuel (coal, hydrocarbons, etc.) is converted into chemical energy of hydrogen, as reported in processes studied by Chiesa et al. [20]. In the study by Chiesa, iron oxide-based redox pair (hematite–wustite–magnetite) was considered as the oxygen carrier in three-reactor configuration as shown in Fig. 7. The complete reaction chain is exothermic, allowing the production of high-quality steam. Chemical looping CO₂ or H₂O splitting investigated in this work has similar configuration, though energy required to drive the process is not strictly limited being from fossil fuel combustion, it can come from absorption of the solar irradiation or reduction via methane.

4.1 CO₂/H₂O Dissociation by Chemical Looping

Chemical looping (CL) syngas production is an innovative fuel production technology based on splitting CO₂/H₂O into CO/H₂, respectively. In the most common two-reactor setup of the CL, two interconnected reactors (reduction reactor and oxidation reactor), containing metal oxides particles, form a circulating closed loop, being alternately reduced and oxidized, respectively. The principle of its operation is based on the spontaneous release of oxygen from the metal oxide's crystalline lattice either by thermal reduction at high temperatures (above 1300 °C) or by fuel reduction, which leads to the creation of oxygen vacancies in the material. Subsequently, this reduced metal oxide is re-oxidized in the low-temperature oxidation reactor (around 1000 °C) with use of water vapor or carbon dioxide. It is important to mention that the thermal reduction is favorable at a very low partial pressure of oxygen (vacuum pressures). Therefore, in the solar thermochemical redox cycle, there would be a pressure and temperature swing between the two steps unlike fuel reduction redox cycles can operate at near atmospheric pressure as well as at isothermal mode.

Indeed, as mentioned, two fundamentally different pathways of the reduction reaction are possible. Thermal reduction using concentrated solar energy is one of the most studied processes. The energy required to sustain the otherwise endothermic reduction reaction and to maintain such high temperatures is derived from the concentrated solar radiation. The complete reaction chain occurring via thermal reduction of metal oxide can be presented as per Eqs. (3–4a, 4b). A schematic of solar-based thermochemical and fuel reduction chemical looping CO₂/H₂O splitting redox cycle is shown in Fig. 10.



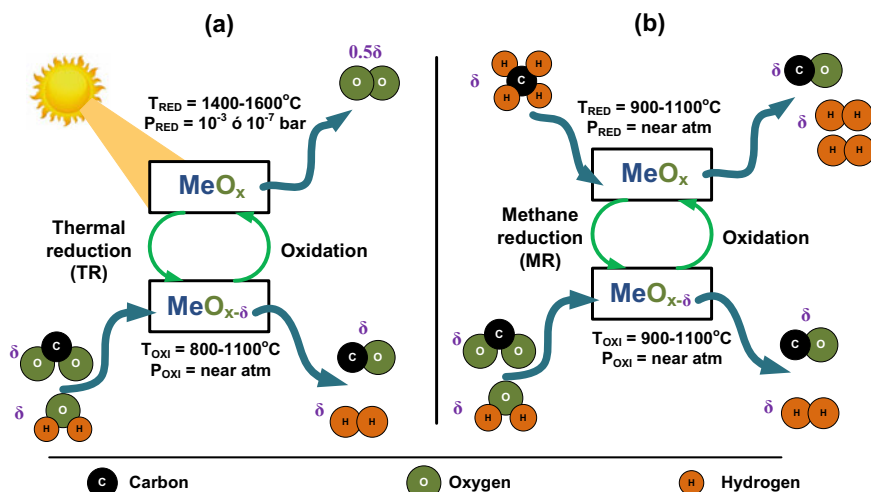
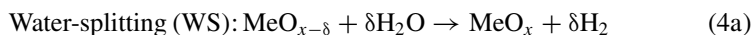


Fig. 10 **a** Solar thermochemical redox cycle for syngas production, **b** methane reduction chemical looping $\text{CO}_2/\text{H}_2\text{O}$ splitting for syngas production



However, an alternative approach to operating the redox cycle at a lower temperature, thereby decreasing the temperature swing between reduction and oxidation, is to combine the redox cycle with the methane reforming [58, 59] according to Eqs. (5 and 3). Several sources of methane, a primary constituent of natural gas, can be identified. Besides the abundant supply of locally available natural gas, increased access to natural gas reserves, through technological innovations like hydraulic fracturing has resulted in an increased access to methane for multiple industrial processes [60]. Additionally, current development in power to gas (P2G) technologies, with a well-established natural gas network, can be speculated to provide an abundant supply of methane in the future. Moreover, also considering the importance of bio-methane in the renewable energy mix, the utility of synthetic methane would increase in the future. Apart from lowering the temperature of the entire cycle, this approach also enables the production of two streams of syngas, one from the reduction and the oxidation reactor steps as shown in Fig. 10, together with the possibility of the system to operate round the clock, without the need of the fluctuating renewable resource like the sun.



In both the schemes, either a thermal reduction of fuel reduction (given by Eqs. 3 and 5), the oxygen carrier is often reduced to a non-stoichiometric extent (δ), meaning that 0.5δ moles of oxygen are released from the oxygen carrier during thermal reduction which should be taken away by a vacuum pump. Similarly, by partial oxidation of CH_4 forming CO and H_2 (Eqs. 4a, 4b). For oxidation reaction, $\text{Me}_{x-\delta}$ would react with incoming $\text{H}_2\text{O}/\text{CO}_2$ to H_2/CO by oxygen and vacancy diffusion in the lattice of the oxygen carrier.

In addition, the partial oxidation of methane (POM) by chemical looping considering metal oxide provides multiple benefits listed as follows:

1. It provides an alternative to the current high-energy-intensive industrial process of steam reformation of methane (SRM) for syngas generation for subsequent chemical production.
2. It also provides an alternate to catalytic partial oxidation of methane (CPOM), which, even though advantageous compared to SRM, suffers from the drawback of direct contact of fuel and oxidant near the auto-ignition temperature of the fuel, raising safety concerns [61]
3. It also negates the need for a separate air separation unit (ASU) for pure oxygen requirement in the CPOM process, whereby the oxygen is supplied by an oxygen carrier directly during the partial oxidation process, simplifying the entire chemical cycle greatly.
4. Since the thermal reduction requires vacuum pressures and fuel reduction is possible to reduce the metal oxide at atmospheric pressure, this would eliminate the pressure swing between the thermally reduced two-step redox cycles.

5 Oxygen Carriers for Solar Fuels via Chemical Looping $\text{CO}_2/\text{H}_2\text{O}$ Splitting

Oxygen carriers are essentially the species of metal oxides which have at least two states of oxidation or one metallic and oxidized state. Examples include ZnO/Zn , $\text{Fe}_3\text{O}_4/\text{FeO}$, etc. that has the ability to release oxygen during high-temperature reduction process [62]. Numerous studies exist on the determination of the suitable metal oxide for the chemical looping splitting cycle, the overview of which can be found in the literature [56, 62–64]. Such wide variety of metal oxides requires them to be categorized specifically, based on the temperature of the reduction and oxidation reactions, the potential for oxygen storage or whether the metal oxide undergoes phase transformation during the redox cycle.

5.1 Volatile Oxygen Carriers

Among the different categories that exist, the oxygen carriers for the two-step chemical looping applications can be technically differentiated into volatile and non-volatile oxygen carriers (also referred as metal oxides). Volatile redox usually exhibits a phase transition in the reduction reaction, especially during thermal reduction. The metal gets vaporized during the reduction step due to its lower boiling temperatures than its higher valence state. The vaporized metal is then quenched (rapid cooling) to eliminate the possibility of recombination with oxygen (reverse reaction) [63]. The most common volatile oxygen carriers (OCs) include ZnO/Zn, GeO₂/GeO, CdO/Cd, and SnO₂/SnO as metal oxide/metal redox pair [65].

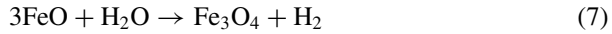
The thermal reduction of the volatile metal oxides are usually highly endothermic, with the ΔG of reaction going below zero only at temperatures above 1723 °C, for instance, zinc dissociation from zinc oxide, the temperature is 1980 °C [63]. However, at this high temperature, the recombination of the reduced volatile metals with the released oxygen is the major problem. Therefore, a quenching process to fast cool the metal is an indispensable step for such redox pairs. Nevertheless, during the quenching process, a certain amount of oxygen recombines with the metal oxide reducing the overall effectiveness and efficiency of the cycle [62]. Multiple studies have focused on the research and development of working with the volatile metal [66–68]. However, the drawback of the quenching remains as the major issue for such redox pairs. Hence, this type of metal/metal redox pairs was not further considered in recent times.

5.2 Non-volatile Oxygen Carriers

Non-volatile oxygen carriers, unlike the volatile oxygen carriers, do not undergo phase transformation upon reduction, either thermally or chemically, i.e., they remain solid during the entire thermochemical cycle. Hence, no quenching step is necessary. Most often, specifically for thermal reduction, the non-volatile carriers are carried out from the reactor via sweep gases only as solids. Therefore, the separation of the reduced metals, usually in a cyclone, is much easier, lowering the system complexity and also system losses. Nevertheless, non-volatile cycles usually utilize those metal oxides having a lower storage capacity than their volatile oxygen carrier (OC) [62]. It is worth mentioning that due to the lower molecular weights of the volatile OC, they tend to have a larger share of oxygen atoms by weight. Thus, often, the storage capacity of the volatile metal oxides is 2–5 times higher than in the case of magnetite/wustite or ceria/cerium oxide (III) pairs.

Several non-volatile OCs were investigated in the literature including hercynites and ferrites of the multiple valence state, Co₃O₄, Nb₂O₅, WO₃, SiO₂, Ir₂O₃, CdO to name few [69–73]. The magnetite/wustite redox cycle was firstly proposed in 1977 by Nakamura [74], while Roeb et al., in 2006, were one of the first to propose the

same metal pair for the water dissociation [75]. In this redox cycle, the magnetite was first thermally reduced to wustite by simultaneously releasing oxygen, while the water reacted back with the wustite (FeO) to form magnetite (Fe₃O₄) and H₂, as per the following Eqs. (6 and 7).

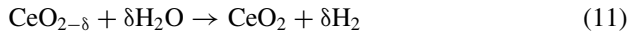
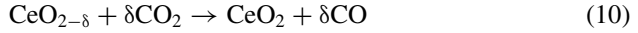
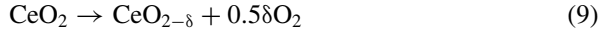
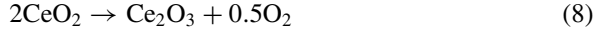


In chemical looping combustion (CLC), Fe-based oxygen carriers have been investigated. Iron oxides have been historically investigated as oxygen carriers. However, unlike the three-step CLC, the iron oxide-based cycles used for H₂O/CO₂ splitting are two-step cycles, whereby the oxygen carrier (OC) goes through the magnetite/wustite cycle, without being fully re-oxidized to hematite. In his thermodynamic analysis carried by Nakamura [76] developed the reaction system for alternate redox reaction at temperatures of 2200 °C (reduction) and 1000 °C (oxidation), respectively. The thermal reduction was evaluated to occur in air. However, the thermal reduction temperature, being higher than the melting point of the OC of that oxidation state, limits the applicability of this process. Multiple strategies are suggested to improve the redox behavior which includes decreasing the cycle operation pressure [76]; doping of the iron oxide either with transition metal such as Mn, Co, Ni, or Zn, forming a ferrite oxide (Fe_{1-x}M_x)₃O₄ or with a reduced form (Fe_{1-x}M_x)_{1-y}O with the aim of decreasing the reduction temperature, and improving the reactivity. However, as can be noticed from the reactions (4a, 4b) and (5), these OCs essentially operate between two thermodynamically stable stoichiometric conditions (FeO and Fe₃O₄). Hence, such non-volatile oxygen carriers can be also be referred to as stoichiometric oxygen carriers as a sub-category.

Indeed, there exists one another sub-category within non-volatile OCs. This is formed by those oxygen carriers, which usually release oxygen to a particular non-stoichiometric extent. One of the most studied metals in this category is cerium oxide. Cerium (Ce⁺⁴) oxide has been extensively studied for different applications as a catalyst for being structurally stable due to its elevated optical and electrochemical properties [77]. Furthermore, ceria is known for its stable crystal structure, even after several redox cycles are well documented [78]. Ceria is also known for rapid reaction kinetics and having good mechanical strength and resistant to agglomeration and attrition. It is also shown that ceria has resistant to sintering at higher temperature as well which makes it as one of the most interesting materials for the chemical looping CO₂/H₂O splitting applications [59].

Indeed, temperature plays one of the most important roles in determining the stoichiometric extent of reduction. Abanades and Flamant [79] have reported almost stoichiometric reduction of cerium (Ce⁺⁴) oxide to cerium (Ce⁺³) oxide at very high temperatures of around 2000 °C, however, often leading to problems of sublimation of the reduced OC. Nevertheless, the focus on the later stages of material development was shifted too much lower temperatures, around 1300–1500 °C, even though

this yielded non-stoichiometric reduction of ceria. Both the stoichiometric and non-stoichiometric thermal reduction reactions, followed by the splitting with CO_2 and H_2O , are shown in the following Eqs. (8) and (9), respectively.



As can be understood, at lower temperatures and at non-stoichiometric conditions, the removal of the oxygen by thermal or chemical reduction is essential while ensuring no change in the crystalline structure even after repeated cyclic redox operation. Therefore, this results in a limiting non-stoichiometric parameter δ , which has been reported in the literature to be 0.35 by Buffin et al. [80, 82], Kümmerle et al. [81], and Knoblouch et al. [83]. The corresponding maximum available oxygen storing capacity of CeO_2 , therefore, can be calculated as $0.033 \text{ kgO}_2/\text{kgCeO}_2$ before the material loses its lattice configuration.

The performance of pure and doped ceria has been studied in the literature quite extensively. Gokon et al. [84] evaluated the comparative performance of ceria and NiFe_2O_4 , both supported and unsupported on ZrO_2 . Results showed a superior thermal stability and yield rates of ceria over six consecutive cycles. Better ceria oxygen was reported with a non-stoichiometric coefficient (δ) varying between 0.034 and 0.11 at a thermal reduction temperature of $1450 \text{ }^\circ\text{C}$. However, no significant improvement was observed with the increase in temperature to $1550 \text{ }^\circ\text{C}$ [84].

Doping ceria has been investigated for improving the extent of reduction by increasing the intrinsic vacancies that affect its electronic structure which in turn influences the ionic conductivity, resulting in the redox cycle to be achieved at lower temperatures. Abanades et al. [85] reported significant improvements in the thermal reduction behavior of zirconia-doped ceria, $\text{Zr}_{0.5}\text{Ce}_{0.5}\text{O}_2$ powder, in comparison with pure Ceria. It was obtained that the reduction started already at $900 \text{ }^\circ\text{C}$ in comparison with $1150 \text{ }^\circ\text{C}$ for pure ceria with a 70% increase in yield of oxygen release from the doped OC. However, this increases the oxidation temperature, with water splitting reactions starting in temperatures above $800 \text{ }^\circ\text{C}$ [85]. In a second study performed in 2011, the same research group reported the rapid decrease in the performance of the doped metal oxide for re-oxidation [86]. Sheffe et al. [87] carried out thermodynamic analyses for $\text{CO}_2/\text{H}_2\text{O}$ splitting on differently doped ceria oxides. The general trend showed a reduction reaction which starts at temperatures of $930 \text{ }^\circ\text{C}$ with simultaneous enhancement of oxidation reactions with an increase in the dopant concentration.

Table 1 Redox temperature range for general OCs

Material cycle	Temperature range (°C)
Tin cycle	600–1600
GeO ₂ /GeO cycle	1400–1800
CdO/Cd cycle ^a	1150–1723
Ferrite cycle	927–1327
Zinc cycle	1127–1727
Ceria	700–1600
Perovskites	1000–1600

^aCd is toxic and has very few studies

Results from the evaluation of thermochemical cycles for CO₂ dissociation utilizing doped ceria were also reported by Jiang et al. [88]. Similar improvement to the thermal reduction, as obtained by Abanades et al. [85], was reported utilizing Ce_{x-0.25}Zr_xO₂ ($x = 0.25$) [88]. A doubling of the CO yields from CO₂ splitting for Ce_{x-0.25}Zr_xO₂ ($x = 0.25$) (10.6 ml/g) than ceria (4.5 ml/g) [88]. The temperature range for redox cycles for some of the volatile and non-volatile OCs is listed in Table 1.

Otsuka et al. [89] were one of the initial researchers to investigate the δ phase of ceria, i.e., non-stoichiometric ceria for water splitting application. Panlener et al. [90] reported the oxygen non-stoichiometry of ceria at different ranges of oxygen partial pressures and temperatures by thermodynamic analysis. At 1550 °C, thermal reduction gives a non-stoichiometry of 0.066 at vacuum pressure of 10⁻⁵ bar giving neat to stoichiometric hydrogen in oxidation step [78]. As stated earlier, ceria has faster oxidation kinetics than reduction. Therefore, several metal cations and oxides have been doped to improve the reactivity and kinetics. In doing so, divalent (Mg, Sr, Ca), trivalent cations (La, Y, Cr, Sm) [86, 91–95], and tetravalent cations (Zr, Ti, Hf, and Sn) [93] have been doped to ceria into its fluorite structure to create intrinsic vacancies. This helps in improving oxidation rate by faster oxygen diffusion.

The divalent cations such as Ca and Mg cations doping will increase the ability of fuel production and lower the thermal reduction temperature.

The trivalent cations M=La, Cr, Sm, Y doping to ceria show a negative impact for both O₂ release and CO production [88]. Though, La doping improves thermal stability for multiple redox cycles and Cr doping decreases the oxidation temperature for water splitting.

Among tetravalent cations, Zr doping decreases oxygen molar enthalpy which deforms the lattice structure of CeO₂ [91] and thereby increasing the reduction capability. Thermodynamic data calculations were confirmed with experimentation performed by Hao et al. [96] on oxygen non-stoichiometry in Zr_xCe_{1-x}O₂ ($x = 0-0.2$), which shows the increasing of reduction non-stoichiometry with increase in Zr doping at 1350 °C. Among other tetravalent cations doped to ceria, the order of release of oxygen is as follows Ti < Sn < Hf < Zr during reduction step. Similarly, CO₂ splitting rate is seen to increase for 2.5 times for Zr-doped ceria compared to undoped

ceria. It is also reported that CO and O₂ are released when the redox temperature is increased above 1100 °C for Hf_{0.25}Ce_{0.75}O₂ and Zr_{0.25}Ce_{0.75}O₂. For Sn and Ti-doped ceria, oxygen release rate is very much higher, but CO₂ splitting rate is very low due to formation of pyrochlore structure (Ce₂Sn₂O₇ and Ce₂Ti₂O₇) even at very high reduction temperature [88].

Takalkar et al. [97] reported a study on doping of ceria Ce_xM_{1-x}O_{2-δ} (M=Ni, Zn, Mn, Fe, Cu, Cr, Co, Zr) considering thermal reduction at 1400 °C and CO₂ splitting at (1000 °C) to evaluate the effect of doping transition metals to the ceria using thermogravimetric analyzer (TGA). The doping of Zn and Fe showed the higher capability to release O₂/g of oxygen carrier during thermal reduction. Similarly, the CO₂ splitting rates were higher for the reported doped oxygen carrier. The O₂ release rate for these doped ceria is reported as Ce_{0.9}Zr_{0.1}O_{2-δ} < Ce_{0.9}Mn_{0.1}O_{2-δ} < Ce_{0.9}Cu_{0.1}O_{2-δ} < Ce_{0.9}Co_{0.1}O_{2-δ} < Ce_{0.9}Ni_{0.1}O_{2-δ} < CeO₂ < Ce_{0.9}Cr_{0.1}O_{2-δ} < Ce_{0.9}Fe_{0.1}O_{2-δ} < Ce_{0.9}Zn_{0.1}O_{2-δ} for the average values for ten cycles. Similarly, the CO production ability reported is as follows: Ce_{0.9}Zr_{0.1}O_{2-δ} < Ce_{0.9}Mn_{0.1}O_{2-δ} < Ce_{0.9}Cu_{0.1}O_{2-δ} < Ce_{0.9}Cr_{0.1}O_{2-δ} < Ce_{0.9}Co_{0.1}O_{2-δ} < Ce_{0.9}Ni_{0.1}O_{2-δ} < CeO₂ < Ce_{0.9}Fe_{0.1}O_{2-δ} < Ce_{0.9}Zn_{0.1}O_{2-δ}. The results for CO₂ splitting rate are higher for doping of Zn and Fe which is higher than undoped ceria with highest being Ce_{0.9}Zn_{0.1}O_{2-δ} with CO/O₂ of 2.31 ratio of release for oxidation and reduction step. Ni and Co doping showed not much effect giving similar CO₂ splitting rates as that of undoped ceria.

5.3 Perovskites Carriers

Besides metal oxides, perovskites, as alternative OCs, have gained significant research interest in recent years. Even though the most significant share of the research for the applicability of such OCs is in the CLC and methane reforming processes [33, 71], many studies have reported the outcomes of the use of perovskite in chemical looping CO₂/H₂O splitting [98]. Perovskites have higher oxygen carrying capacities compared to OC and doped OCs at lower temperature. Perovskites with general formula ABO_{3-δ} have large non-stoichiometry at high temperatures and also the oxidation reversibility, which is essential for thermochemical application of H₂O/CO₂ splitting to give higher solar to fuel efficiency. Perovskites have been popular as oxygen separation membranes in the last decade, with multiple options of substituting A and B sites to improve the properties based on the application.

La_{1-x}Sr_xMO₃ (M=Mn, Fe) was tested for conversion of methane and water to syngas at a temperature of around 1000 °C [88]. Transition metals such as Ni, Co, Cu, and Cr in La_{1-x}Sr_xFeO₃ have significantly improved performance. A-site substitution of Sr and Ce and B-site substitution of Co and Mn to La_xA_{1-x}Fe_yB_{1-y}O₃ (0 ≤ x, y ≤ 1) perovskites with different supports were tested for different temperatures [99]. For unsupported perovskites, there is no significant CO production reported even with a higher O₂ release during reduction cycle at a lower temperature. Different supports such as ZrO₂, Al₂O₃, and SiO₂ were tested and found SiO₂ to be the best candidate. By substituting A site and B site, the reduction temperature or oxygen

release temperature gets lowered by 200–300 °C and also increasing product yield by 2–3 times. $\text{LaFe}_{0.7}\text{Co}_{0.3}\text{O}_3/\text{SiO}_2$ shows 4 times higher CO production compared to undoped $\text{LaFeO}_3/\text{SiO}_2$ at a reduction temperature of 1300 °C.

5.3.1 A-Site Substitution by Alkaline Earth Ions

For $\text{La}_{1-x}\text{Sr}_x\text{MnO}_3$ (LSM $_x$), perovskite non-stoichiometry is investigated by extrapolating the low-temperature experimental non-stoichiometry data using a defect model. It was reported that higher non-stoichiometry was observed when compared to ceria under similar oxygen partial pressures and reduction temperatures (1500 °C) for LSM35 ($\text{La}_{0.65}\text{Sr}_{0.35}\text{MnO}_3$). It was also reported that the Gibbs free energy for LSM is negative in magnitude than ceria at similar temperature conditions. Yang et al. [100] reported that for LSM $_x$ ($x = 0-0.5$) resulted in giving H_2/O_2 ratio of 2 during redox steps, but this ratio drops if the percentage of Sr doping increases which increases the reduction extent simultaneously decreasing the oxidation capability, thereby reducing the H_2 production. A new class of perovskites $\text{La}_{1-x}\text{Ca}_x\text{MnO}_3$ (LCM $_x$, $x = 0.35, 0.5, 0.65$) has been tested for WS and CDS [101]. It is also seen that with an increase in Ca, the non-stoichiometry increases during reduction, and it lowers the reduction temperature by a significant margin. But the increase in Ca in LCM $_x$, oxidation ability decreases. The reduction temperature was set to 1400 °C and oxidation temperature of 1100 °C. It is observed that O_2 production was calculated for LCM35 (109 $\mu\text{mol/g}$), LCM50 (315 $\mu\text{mol/g}$), and LCM65 (653 $\mu\text{mol/g}$). LCM50 produces 1.6 times more oxygen than LSM50 (201 $\mu\text{mol/g}$) and 5 times more oxygen than ceria (112 $\mu\text{mol/g}$) under similar conditions.

For oxidation step, 40% of CO_2 is used as reactant for splitting reaction. Thus, LCM50 (525 $\mu\text{mol/g}$) shows higher CO production rates by 1.6 times than LSM50 (325 $\mu\text{mol/g}$) and 5 times more than ceria (112 $\mu\text{mol/g}$). Similar is the case of H_2 production, and the WS was shown at 1000 °C with LCM50 (272 $\mu\text{mol/g}$), which is lower than LSM50 (308 $\mu\text{mol/g}$) [100]. In both WS and CDS, reaction kinetics for oxidation was little slower. Similarly, $\text{La}_{1-x}\text{Ba}_x\text{MnO}_3$ (LBM $_x$, $x = 0.35, 0.5$) was tested thermochemical CO_2 splitting reaction [102]. During reduction, O_2 evolution rate is higher for LCM50 than LSM50 with least for LBM50. The CO production with LBM $_x$ did not show improvement. LCM50 has an orthorhombic atomic structure, and LSM50 has a rhombohedral structure. The stoichiometry is the same, but the difference in the reactivity is due to structural difference. It is indicated by tolerance factor (τ) which is smaller for LCM 50 (0.978) than LSM50 (0.996).

5.3.2 A-Site Substitution by Rare Earth Ions

Two perovskite families with rare earth ions were tested— $\text{L}_x\text{Sr}_{(1-x)}\text{MnO}_3$ (LSMO) and $\text{L}_x\text{Ca}_{(1-x)}\text{MnO}_3$ (LCMO) ($\text{L}=\text{La, Nd, Sm, Gd, Dy, Y}$; $x = 0.5$)—for two-step thermochemical decomposition to WS and CDS [101]. It was reported that from La to Y, the oxygen release rate increases with the reduction in the size of the rare earth

Table 2 Perovskites and ceria and doped ceria oxygen carriers and their operating conditions

Oxide	T_{RED} (°C)	T_{OXI} (°C)	O ₂ ($\mu\text{mol/g}$)	CO(H ₂) ($\mu\text{mol/g}$)	Refs.
Y _{0.5} Sr _{0.5} MnO ₃ (YSM50)	1400	800	483	757 ^a	[95]
Y _{0.5} Sr _{0.5} MnO ₃ (YSM50)	1300	800	389	624 ^a	[95]
Y _{0.5} Sr _{0.5} MnO ₃ (YSM50)	1200	800	258	418 ^a	[95]
Y _{0.5} Ca _{0.5} MnO ₃ (YCM50)	1400	1100	575	671 ^a	[95]
La _{0.5} Ca _{0.5} MnO ₃ (LCM50)	1400	1100	315	525 ^a	[86]
La _{0.5} Sr _{0.5} MnO ₃ (LSM50)	1400	1100	201	325 ^a	[86]
La _{0.5} Sr _{0.5} MnO ₃ (LSM50)	1400	1000	298	298 ^b	[88]
La _{0.5} Sr _{0.5} MnO ₃ (LSM50)	1400	873	236	224 ^a	[96]
La _{0.6} Sr _{0.4} MnO ₃ (LSM40)	1400	700	205	397 ^c	[94]
La _{0.6} Sr _{0.4} Al _{0.4} Mn _{0.6} O ₃	1350	1000	120	247 ^a	[97]
CeO ₂	1400	1000	53	105 ^a	[86]
Ce _{0.75} Zr _{0.25} O ₂	1400	1000	193	241 ^a	[98]
Ce _{0.75} Zr _{0.25} O ₂	1400	1000	179	323.9 ^b	[98]

^aTGA study for CDS^bTGA study for WS^cAlumina tube reactor was used for WS with an infrared furnace heating rate of 500 °C/min

ion. This is due to the decrease in tolerance factor which is smaller for smaller rare earth cation. The oxygen production by YSM50 (481 $\mu\text{mol/g}$) is higher than LSM50. It was also reported that YCM50 even has higher O₂ release rate (0.575 mmol/g), and the temperature for reduction decreases with the size of cation substituted (with order La to Y). The size difference in Ln and A cations is described by a size variance factor σ^2 which creates a disorder in the perovskite motif structural pattern, which in turn influences the reduction temperature required. The variance factor of LCMO is smaller compared to LSMO (therefore it has lower reduction temperature) [101]. YSM50 has a higher variance factor and begins to release O₂ around 860 °C and YCM50 at 970 °C. Similar to reduction, CO₂ splitting rate also enhances by smaller size rare earth ion size with Yttrium-based perovskites which show the highest CO production (671 $\mu\text{mol/g}$) at 1100 °C. It was also reported that YSM50 produces fuel production in constant levels with multiple cycles, making it one of the promising perovskites for energy applications. The reduction and oxidation temperature reported being low as compared to other perovskites. Table 2 lists temperatures and performances of several perovskites and, for comparison, of ceria-based materials.

5.3.3 B-Site Substitution

Apart from perovskites, ceria was reported to have the highest fuel production rate and conversion efficiency, and therefore, all the comparisons of new material were

reported to compare with ceria for non-stoichiometric and non-volatile redox cycles. Aluminum was substituted in LSMx, and this enhances the H₂O splitting rate at least 9 times and for CO₂ splitting rate at least 6 times higher than ceria with no change in reaction kinetics [103]. In La_{0.5}Sr_{0.5}Al_{1-x}Mn_xO₃ with an increase in Al content, there is an increase in O₂ release, which reaches 322 μmol/g for $x = 0.5$. Similar is the case with La_{0.5}Ca_{0.5}Al_{1-x}Mn_xO₃ increase in Al content, for which the O₂ release increases as well as CO production. It was also reported that Al doping reduces the formation of carbonate on the surface, which deactivates the perovskite characteristics [104]. Mg doping shows no improvement in oxidation (splitting rate) even though it exhibit sintering resistance at higher temperature compare to LSMx [105]. Other transition metals such as iron, cobalt, and chromium were also tested for B-site substitution [88, 99, 106]. Ga and Sc-substituted LSMx showed higher CO production rate [106].

Using Sr_{0.4}La_{0.6}Mn_{0.4}Al_{0.6}O₃, McDaniel et al. [107] obtained an increase in 8 times the yield of hydrogen at 1350 °C than pure Ceria, with a subsequent higher yield of H₂ and CO from the H₂O/CO₂ split reactions, respectively. A high cyclic stability of the perovskite was also reported, with no noticeable decrease in the performance after 80 redox cycles. These results were subsequently confirmed through the studies by Jiang et al. [99], in 2010, where the performance of lanthanum–ferrite-based perovskites doped with Co and Mn on the ferrite side was evaluated. Experimental results on the thermal reduction of both LaFe_{0.7}Co_{0.3}O₃ and LaFe_{0.7}Mn_{0.3}O₃ revealed the high oxygen carrying capacity of such materials. However, a poor performance of the CO₂ splitting was reported, which were considerably improved by the addition of supporting materials like SiO₂ [99]. Another study by Galinsky reported significant improvements to the reduction rate utilizing iron oxide supported La_{0.8}Sr_{0.2}FeO_{3-d} (LSF) [108].

5.3.4 Spinel Structured Oxygen Carriers

Recent studies have also indicated that there is much focus on the spinel structured OCs for the chemical looping splitting application through the modification of physio-chemical properties. The selection of the right cation enables the synthesis of an OC with a high structural and mechanical stability under high-temperature operations [109, 110]. Aston et al. [111] reported the performance of two mixed metal oxide spinels, NiFe₂O₄, and CoFe₂O₄ prepared by the incipient wetness method, with ZrO₂ as substrate. Results indicated a high yield of hydrogen through water splitting (7–9 times per gram of OC than iron oxide), however, at a much lower rate compared to that of iron oxide. Similar studies were performed on CoFe₂O₄ by Cocchi et al. [112]. Even though a faster reaction rate was seen, there was significant carbon deposition for CO₂ splitting, which would often limit the applicability of the tested material over several cycles. Also, due to the corresponding oxidation and reduction reactions, the applicability of this metal oxide to a two-step cycle is limited, with a three-step cycle being a more preferred solution [98].

With the in-depth review of different oxygen carriers for thermochemical redox application, it is evident that there is huge interest in the material development with respect to its reactivity, stability to operate at high temperature and pressure swing. Apart from these important aspects, other physical properties need attention, such as attrition rate, agglomeration, and sintering behavior due to continuous cyclic redox operation. The reactivity properties of the oxygen carrier can be improved by finding ways to improve the oxygen carrying capacity by means of doping or with appropriate supports, which need further research on new materials. At present, if the $\text{CO}_2/\text{H}_2\text{O}$ dissociation could be implemented at industrial scale, then it could only be possible by an oxygen carrier which has good properties, and at the same time, it is abundantly available. Out of the above-mentioned OCs, ceria stands as reliable and good candidate showing good splitting ability and stability. The next section describes the reactors that have been designed, tested, and investigated for $\text{CO}_2/\text{H}_2\text{O}$ splitting through thermochemical redox cycles.

All the oxygen carriers reported in the literature demonstrated the redox ability of $\text{CO}_2/\text{H}_2\text{O}$ splitting as well as O_2 release during the reduction step. The broad classification of metal oxides into volatile and non-volatile and the sub-category of non-volatile into the stoichiometric and non-stoichiometric redox metal oxides have shown a broad mapping of the suitable metal oxides that could lower the reduction temperatures. Volatile metal oxides have the issue of quenching and sublimation, and therefore, the research for the quest of most suitable oxygen carrier is drifted to non-volatile oxygen carrier category. Ferrites and hercynites have been investigated with different doping and supports. The slow kinetics and lower oxygen carrying capacity have motivated the researchers to investigate the non-stoichiometric metal oxides such as ceria which showed higher ability to participate in redox reactions with mechanical stability and maintaining the uniformity in the structure. Ceria has been studied with different doping and supported for the benefit of H_2O and CO_2 splitting along with O_2 release rates during the reduction step. Of all the metal oxides, even though doped ceria and perovskites have shown very high reaction kinetics for redox recycling, CeO_2 is only commercially available oxygen carrier at a cheaper price and could satisfy the need to an industrial-scale plant that undergoes ceria redox recycling.

6 Reactors for $\text{CO}_2/\text{H}_2\text{O}$ Splitting

Based on the type of reduction mechanism, the reactor design can be fundamentally different between the concentrated solar-driven cycle and the methane driven cycle. Also, based on the two-reactor or three-reactor design (splitting or CLC cycle), the reactor designs change significantly. In order to present a state of the art of the reactor designs, studied and/or operated for chemical looping $\text{CO}_2/\text{H}_2\text{O}$ splitting for the two-reactor design model, the typology is divided between reactors for solar thermochemical cycles and those for fuel reduction cycles.

6.1 Reactors for Solar Thermochemical Splitting Cycles

The most commonly used technique to achieve the high temperature of thermal reduction required is the use of concentrated solar energy. Most often, the conventional forms of concentrated solar power generation systems, as used for electricity generation, are employed, which includes: the linear Fresnel (line focus), parabolic trough (line focus), heliostat field (point focus), and the parabolic dish (point focus) solar concentrators. A detailed discussion of the solar thermal reactors is provided in the subsequent section [113].

The four reactors above-mentioned have been listed in the increasing order of achievable concentration ratio, and thereby of maximum operating temperatures. Obviously, the concentrators with line focus are unable to generate a high temperature due to a much lower concentration ratio. Since a temperature of over 1200 °C is usually employed for thermal reduction of OCs, heliostat field or central tower systems and parabolic dish technologies are the preferred choices. However, due to the limitation of the scale of parabolic dishes, state of the art of solar concentrators for thermal reduction of OCs have focused on the central tower as the most suitable technological alternative. In addition to the type of concentrators, many other categories of reactors exist and are discussed below.

Based on the mechanism of heat transfer from the concentrated solar heat generator to the working fluid and the reactor, the solar reactor configurations can be categorized as (a) direct process and (b) indirect process [114]. For the direct process, the reactor forms a single unit with the receiver. They are the so-called volumetric receivers, and volumetrically absorb the solar radiation on the oxygen carriers. On the other hand, the indirect process employs an additional thermal fluid that exchanges heat with the receiver (usually in a tubular receiver).

Since the primary reaction occurs on a solid (the OC) in the presence of a gas (usual fuel for fuel reduction or vacuum created in the reactor), reactor's classification can be based on the arrangement of the metal oxide in the reactor. Accordingly, two reactor types can be defined [114]:

1. **Structured reactors**—In the structured reactors, the metal oxides are most often arranged in a particular ordered structure within the reactor. The reactor design ranges from a single reactor chamber to a modular dual chamber reactor for the simultaneous production of O₂ and H₂ [115]. The most common type of reactors belonging to this category is the honeycomb, foam, or membrane reactor [114, 116].
2. **Non-structured reactors**—In these type of reactors, the metal oxide is distributed randomly without a particular order, with the fluidized bed, moving bed, and packed bed reactors being the most common reactors of this category [114].

Indeed, yet another classification exists for the reactor based on the possibility to perform the two-step cycle in a single reactor or separate reactors for the reduction and the oxidation reactions. As mentioned, structured reactors can usually be designed to perform simultaneously the two reactions of the two-step cycle.

The efficiency of the reactor is an important parameter, which might limit the productiveness of the entire cycle, even with a very active OC. To maintain optimal thermodynamics, kinetics, and durability, together with economic and efficient design for the production of the desired product, the reactor must be able to deliver solar thermal heat and reactant gases to the oxygen carrier without dissipating heat energy which may need external work, by maintaining structural integrity [115]. For any high-temperature process to be efficient, heat losses have to be minimal. The primary necessities to ensure an adequate system design while minimizing system heat losses can be summarized as follows [117]:

1. Minimizing the multiple solar reflections, as the efficiency of commercially available reflectors is limited, and it is of prime importance to restrict the solar reflections.
2. A rapid transfer of heat from the solar radiation to the active material.
3. By maintaining the temperature of the reactor system and the oxygen carrier material to avoid inefficient heat recuperation between solids.
4. By efficient removal of all reactants and products to ensure that there is no back reaction.
5. By ensuring an effective transport of solids and at the same time maintaining the structure of active oxygen carrier.

Besides efficient management of parasitic losses from mass transport and heat transfer, there are several other parameters which are considered essential to ensure adequate system performance of the entire cycle. These factors can be summarized after Muhich et al. as follows [115]:

1. The reactor should be modular and scalable to ensure the economy of the scale.
2. Both the reactors should be able to operate separately as the reaction kinetics is not identical in reduction and oxidation step.
3. The reactors should be able to effectively decouple the reduction and oxidation steps, both spatially or temporally to separate the O₂ and the product gases (H₂ and CO).
4. The design should minimize moving parts, thereby also preventing high-temperature operation failure of the reactors.
5. Reactor materials should be compatible with the OCs, as well as be stable under the high-temperature operating conditions.
6. The reactors should be designed in such a way that it minimizes the attrition of the OC and should have sufficient residence time in both reactors.

Based on such design goals, significant work has been performed and the reactors can be broadly classified into monolithic (structured) or particle systems based (non-structured) reactors. A brief discussion on some of the developed reactors for the solar thermochemical redox cycles for syngas production follows.

6.2 Monolith or Structured Reactors

The basic feature of this type of solar thermal reactors is that the design is based on a self-supported active material [115]. Many designs of the monolithic type of reactors have been studied in the literature.

The simplest of the monolithic or structured reactors is the stationary monolith cavity (SMC) [118], as shown in Fig. 11. Here, the active material, present in a porous cavity, was irradiated from the top through a quartz window. The gases were proposed to be introduced radially, flowing through the OCs and exiting from the bottom. The tested metal oxide was monolithic porous ceria collected in cylinder form. The peak solar to fuel efficiency obtained was 0.8%, without any heat recovery [118]. In further experiments by Furler et al. [119], the active metal oxide from monolithic form was replaced to porous felt, which led to the doubling of the solar to fuel efficiency. An energy balance reported that majority of the losses was from the reactor wall by conduction (nearly 50%) which can be decreased by improving reactor insulation. The remaining losses of nearly 41% were due to reradiation from the windows which are limited by the current technology of window materials. However,

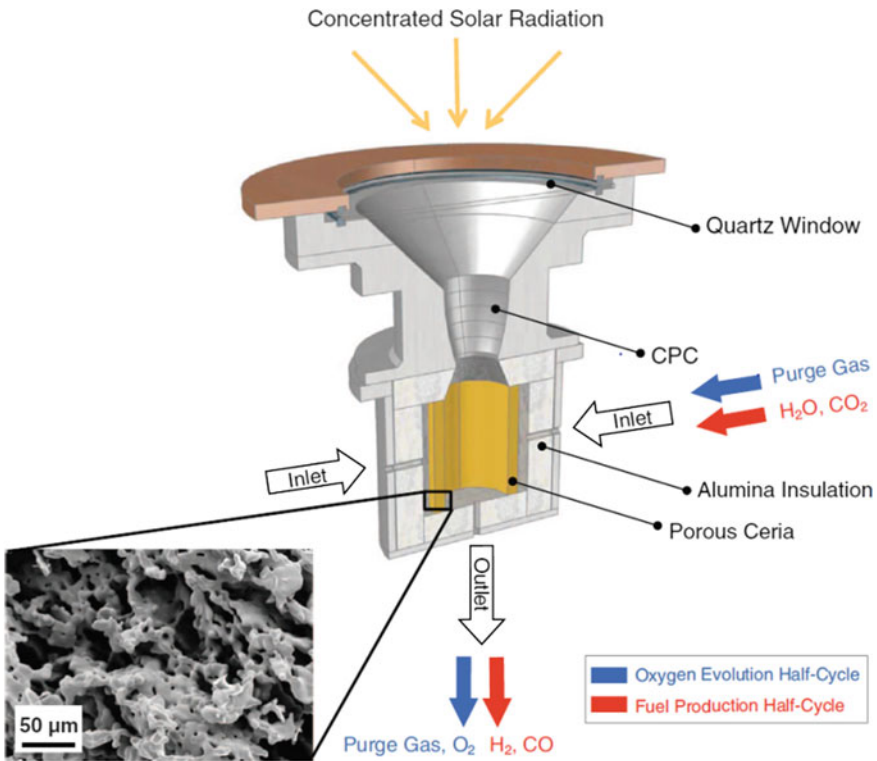


Fig. 11 Stationary monolith cavity (SMC) reactor by Chueh et al. [118] for $\text{H}_2\text{O}-\text{CO}_2$ dissociation

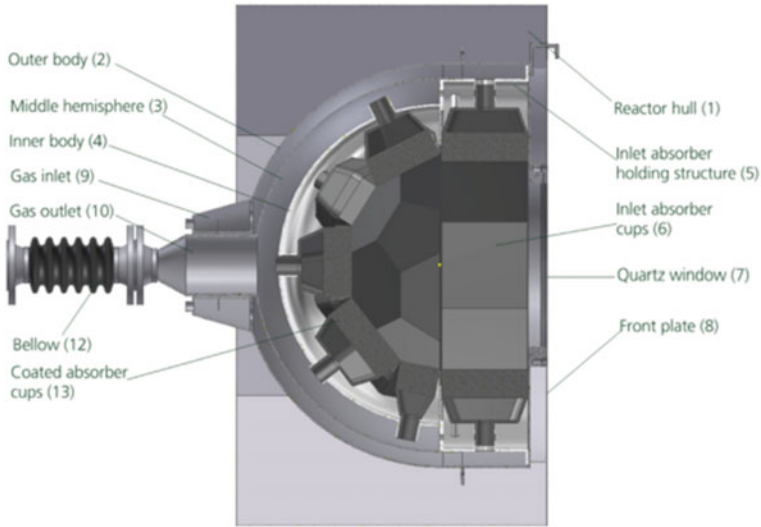


Fig. 12 Sectional view of the spherical stationary monolith cavity (SMC) reactor as proposed by Houaijia et al. [120]

a good cyclability of the reactor was obtained, where the reactor was able to operate continuously for 500 cycles, the steady state being achieved after 200 cycles.

Other types of monolithic cavity reactors have been proposed with one or more reaction chambers for the alternate reactions of the redox cycle to occur. Houaijia et al. [120] proposed a multi-cavity reactor to enhance the performance of the whole reactor system thermally. A modular reactor design for 1 MW thermal output was proposed with conical and spherical geometries being obtained as the most promising absorber geometries. However, spherical geometry was simulated as the most suitable and the design of the reactor developed is presented in Fig. 12. A net cycle efficiency of 0.88% was obtained for the complete solar receiver–reactor system including hydrogen production. Radiation losses were predominated the overall losses, contributing to over 50% of the net thermal losses, close to 100 kW. In this design also, windows continued to impact significantly in the overall system losses, resulting in the poor system efficiency of such reactor designs.

In majority of the solar cavity reactors designs, the oxygen carrier is like a honeycomb structure [121]. In addition, the active metal oxide is directly heated by solar irradiation through quartz window. Even though the simplicity of design makes such cavity reactors less prone to mechanical failure, the heat exchange between gas–solid between the two steps of redox cycles is not available unless both the reactors are kept in single cavity. This leads to the lowering of the system losses. Additionally, the use of a window system for introduction of concentrated solar radiations limits the size of the whole reactor system which indirectly limits to a small scale.

As opposed to a cavity reactor, the rotating piston reactor has been proposed. Even though the primary principle of the reactor design is the same as that of the

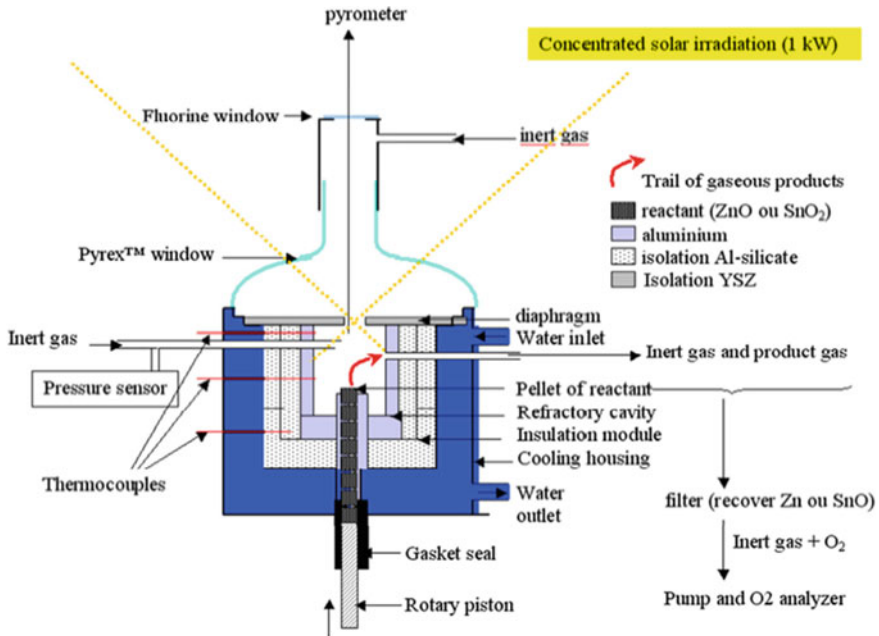


Fig. 13 Rotating piston reactor as proposed by Chambon et al. [122]

cavity reactor, this reactor design particularly suits well for application to volatile stoichiometric reaction chemistries [122] (Fig. 13). For volatile metal oxides, as the OC involves volatilization during reduction which swept to quenching in a separate chamber by an inert gas, while the fresh material is continuously fed into the reactor. The rotating monolith reactors have only one advantage of using volatile OCs, and all other characteristics are same as of SMC type of reactors [120].

The Counter-Rotating-Ring Receiver Reactor Recuperator (CR-5) was proposed by Diver et al. [123], where counter-rotating rings with metal oxide fins are stacked will be irradiated in the upper part by solar beams. In this reactor, the active OC is introduced into the heated area of the reactor with the help of a piston in the form of pallets as shown in Fig. 14. As explained for SMC reactors, OC reduced by getting volatilizing and swept to quenching chamber [122]. In this reactor, the circumferentially placed rings rotate in opposite directions at a very low speed of 1 rpm to enhance the heat recovery between redox steps. As the rings rotates, the metal oxide alternately passes from higher temperature reduction zone to lower temperature oxidation zone and back again as a continuous cycle. The calculated solar to fuel efficiency was 29% [123]. The scalability of such reactors was also evaluated, as Kim et al. [124] proposed the use of the CR5 reactor for H₂O/CO₂ splitting for liquid fuel generation within the “Sun to Petrol” (S2P) project.

Yet another reactor design for structured reactors was developed as the Surround-Sun reactor, using a “tube within a tube” design concept, could potentially avoid

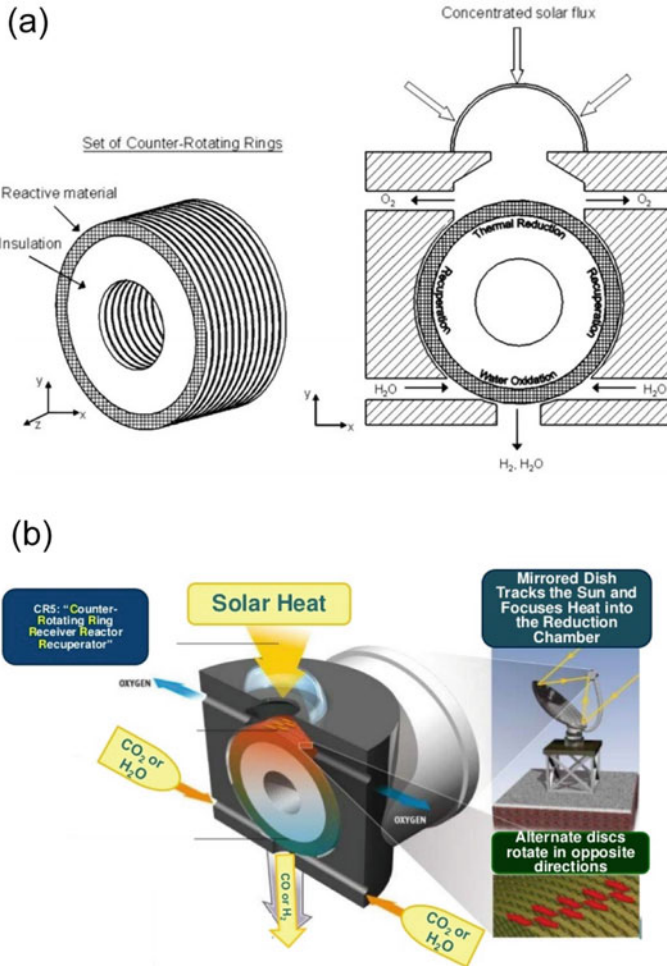


Fig. 14 CR5 reaction proposed by Diver et al. [123]

the quartz window usage to limit the heat losses, which by far was found to be one of the most inefficient components of such solar reactors [115]. As proposed by Melchior et al. [125], and followed by other studies by Martinek et al. [126], one or more tubular reactors packed with the OC housed in an insulated cavity similar to shell and tube format. The concentrated sunlight would enter through an open aperture and the overall operation would occur in a temperature swing mode. While half of the tubes would be subject to concentrated solar energy, thereby undergoing reduction, the other half would be exposed to steam or CO₂ to undergo oxidation. The reactor operation and geometry are pictorially depicted in Fig. 15. Additionally, the reactor gives the flexibility to operate in isothermal condition. Not having a transparent material, in the form of a window, nor having rotating mechanical

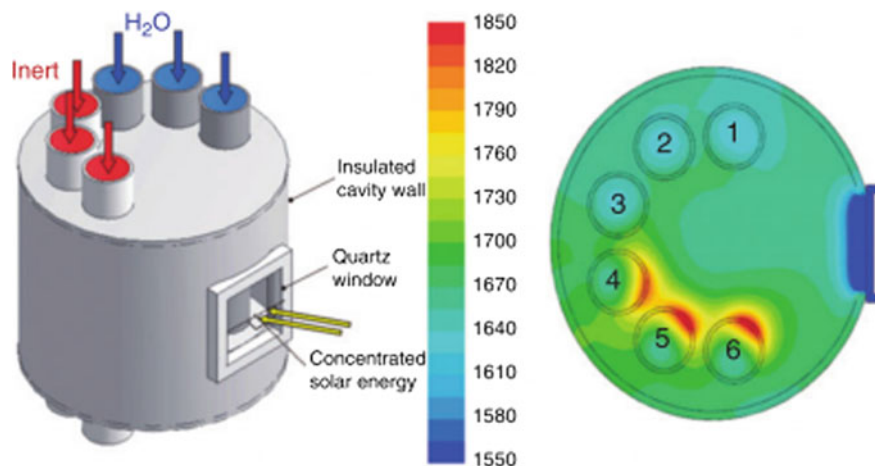


Fig. 15 Surround-sun reactor design proposed by Melchior et al. [125]

parts represent significant advantages in such reactor designs, allowing them to be potentially scalable, subject to the availability of a suitable containment materials [115]. However, one serious drawback of this type of reactor design seen is the non-uniform transport of temperature within the bed due to uneven radial illumination [126]. This eventually lowers the reaction rates in both redox reactions leading to lower CO and H₂ yield [125]. Other problems like pumping gases and pressure loss across through the packed bed, development of hot spots within the reactor bed, poor heat conductivity, etc. pose challenges to the commercial-scale development of this type of reactors [115].

Different prototype reactors incorporating fixed coated ceramics in a structured reactor form have been developed within the HYDROSOL project. Roeb et al. [75] proposed a structured solar reactor for simultaneous reduction and dissociation, implementing a honeycomb monolith reactor made by a plurality of channels. As shown in Fig. 16, each of the channels was coated by a surface of the active metal oxide compound and comprises a siliconized silicon carbide (SiSiC) coating with ferrite oxide. The metal oxide has been chosen to be directly irradiated by the concentrated sun rays. The reactor was tested within a solar furnace at 1200 °C for reduction and in between 800–1200 °C for oxidation step for six cycles [75]. A better output from oxidation reactions was obtained at a higher reduction temperature of 1200 °C, which, nevertheless, results in precipitation, leading to a faster degradation of the support material. Around 80% productivity of the water splitting reaction was obtained, at an efficiency of 40%, however producing hydrogen intermittently.

To improve on the discontinuity in the production of hydrogen, due to the application of the same reactor for alternate reduction and oxidation, Roeb et al. [127] further proposed a quasi-continuum reactor for hydrogen synthesis. The honeycomb structures developed in their previous study were used, but employing two parallel chambers that made it possible to perform reduction and oxidation together (Fig. 17a).

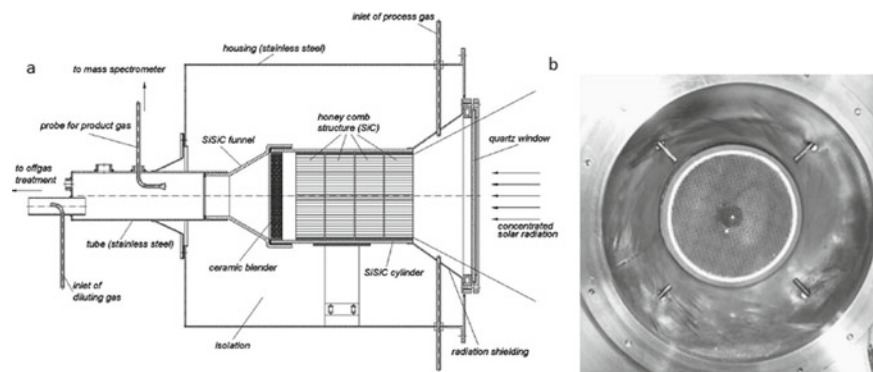


Fig. 16 Honeycomb multi-channel solar reactor as proposed by Roeb et al. [75]

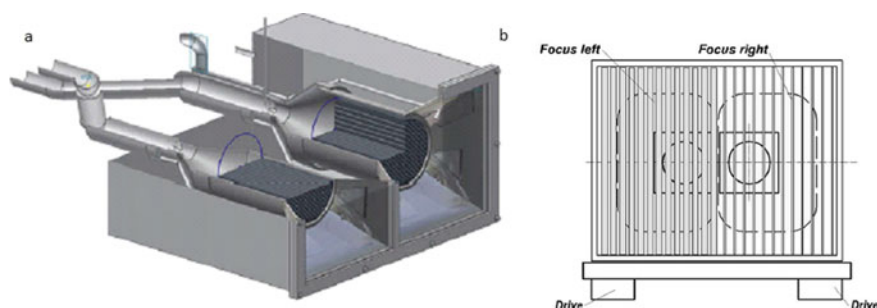


Fig. 17 a Multi-chamber reactor proposed by Roeb et al. [127], b lamellae shutter for temperature regulation

Similar to the previous study, they were assessed at 1200 and 800 °C for reduction and oxidation, utilizing a lamellae shutter to regulate the different temperatures in the respective reactors, as shown in Fig. 17b.

A scale-up plant of 100 kW, based on the multi-chamber reactor design with the honeycomb structure, as proposed by Roeb et al. [127], with a solar tower as a concentrator [128] was installed on “Plataforma Solar de Almeria facility.” About 35 g per cycle of H₂ was measured which resulted in the production of around 500 g of hydrogen per day, even though the objective was set at a daily production of 3 kg. Deactivation of the metal oxide during the cycles and non-homogeneous temperature distribution inside the coated channels were some of the challenges observed.

As an alternative to the design proposed by Roeb et al. [127], for the continuous H₂ production in a honeycomb monolith structure, Kaneko et al. [129] proposed a rotary reactor which would be able to perform both reduction and oxidation continuously. A rotating reactor between two chambers was proposed, where water splitting was simultaneously performed in one reactor, to that of reduction in another, as shown

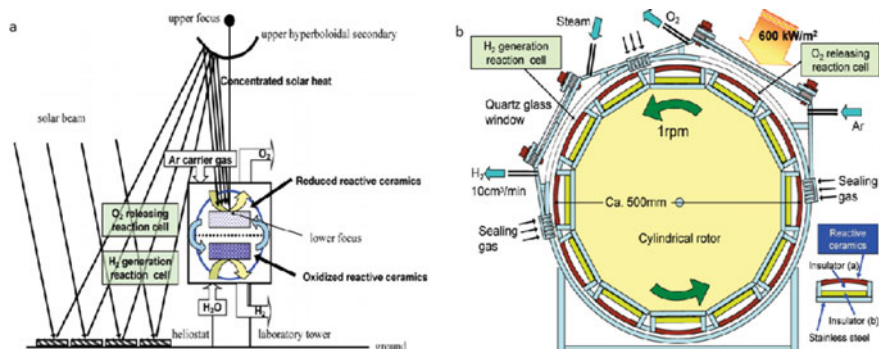


Fig. 18 a Rotary reactor concept proposed by Kaneko et al. [129], b pilot scale rotating reactor

in Fig. 18. Like the previous study by Roeb et al. [127], both laboratory- and pilot-scale applications were studied using a Ni-ferrite oxide coated reactor [129]. At the reported optimum temperatures for oxidation and reduction (900 and 1200 °C, respectively), 2.1 cm³ of O₂ was produced in 30 min [129].

6.3 Particle or Non-structure Reactors

This category of reactors essentially utilizes the movement of particles (i.e., the OCs), rather the reactor itself. This results in the reactors to be non-structured, in relation to the arrangement of the metal oxides within the reactor [114, 115]. Such movement of the OCs enables the easy decoupling between the oxidation and reduction reactions, which often have much dissimilar reaction kinetics.

One of the first reactors to be proposed of this kind was a tubular packed bed reactor in 1995 by Tamaura et al. [130]. It comprised a 2-cm-diameter quartz tubular packed bed reactor heated by a solar furnace. As shown in Fig. 19, secondary concentrator is used to ensure uniform irradiation. The reactor was tested using an OC that comprised 5 g of Ni_{0.5}M_{0.5}Fe₂O₄ powder mixed with 7.5 g of Al₂O₃ support. Alternate streams of argon and water were used for reduction and oxidation, respectively [130]. Low amount of oxygen produced, together with the limitations with respect to the use of oxygen-free atmosphere for reduction step, was reported as significant disadvantages.

A comprehensive reactor design, overcoming multiple challenges of the non-structured class of reactors is the rotating cylinder type reactor by Müller et al. [131]. In this reactor design, sunlight would enter the rotating cylinder, where the OCs are contained longitudinally along the length of the reactor, as shown in Fig. 20. The design of such reactors has specifically focused on the use of volatile stoichiometric oxygen carriers. Therefore, the reduced OC is taken away by a vacuum pump to the quenching and then to the oxidation units. Screw feeders are employed for the feeding in fresh OCs [132]. These reactors show higher heat and mass transfer capabilities,

Fig. 19 Tubular packed bed solar reactor for H₂ production proposed by Tamaura et al. [130]

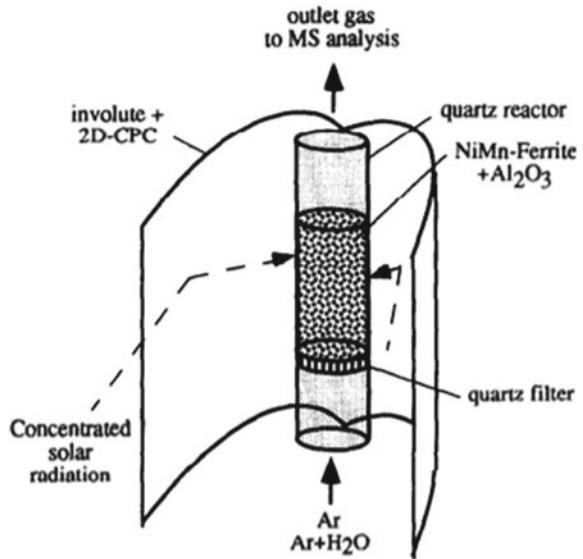
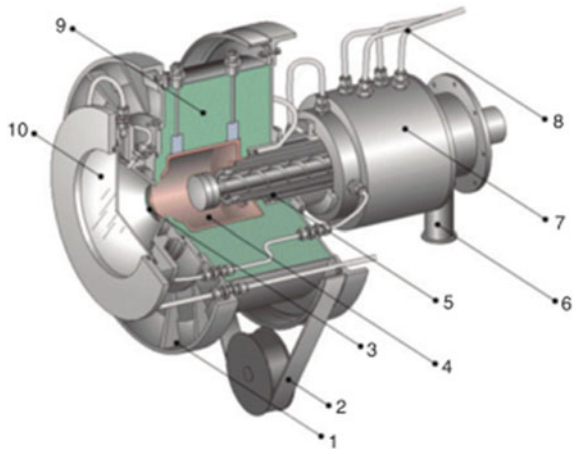


Fig. 20 Rotating particle flow reactor proposed by Muller et al. [131]



but due to the quartz window use for solar irradiation, it suffers the scalability of the system. Moreover, the presence of the rotary elements at high temperatures of more than 1500 °C creates significant operational challenges to the proposed design. Nevertheless, a reactor efficiency of 14% and a process efficiency of 12% was obtained by employing ZnO as the OC. Optimal operating conditions and feed conditions were also studied and reported in the same study [131].

To overcome the issues of moving elements in the reactor, several reactor designs, especially relating to material feeding, have been proposed in this category. Initially,

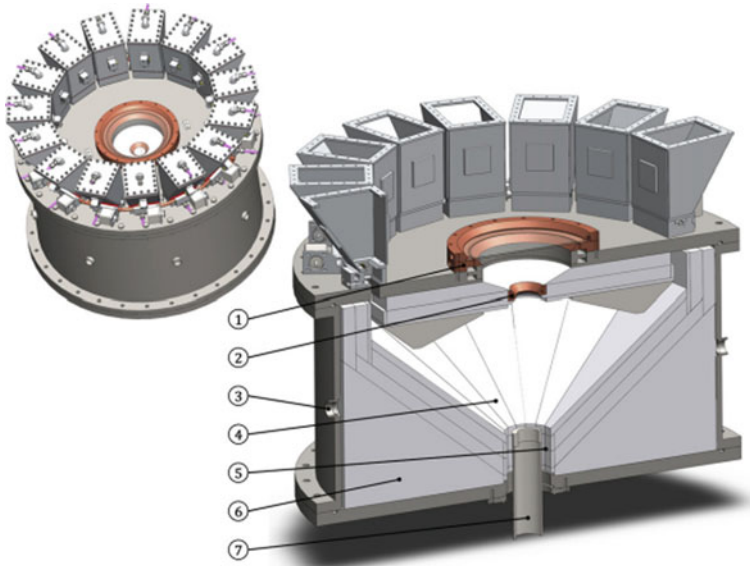
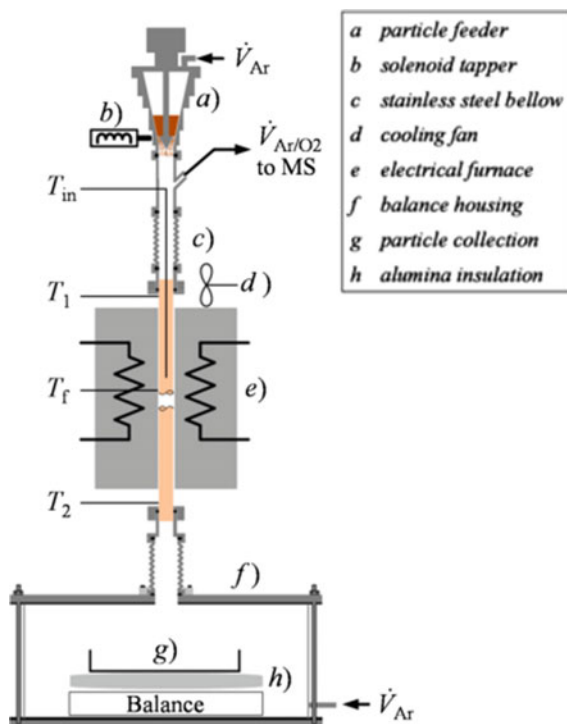


Fig. 21 Proposed beam-down solar thermochemical reactor by Koepf et al. [133]

a simple beam-down reactor was developed on an experimental scale, which was further aimed to improve by incorporating vortex flow in a two separate chambered solar beam-down reactor by Koepf et al. [133, 134]. “Gravity-Fed Solar-Thermochemical Receiver/Reactor (GRAFSTRR)” consists of inverted conical-shaped reaction surface, as shown in Fig. 21. The OCs were fed from the top, and the particles were gravitationally transported through the incident concentrated solar radiation, essentially depicting a moving bed. A highly concentrated sunlight is achieved in the reaction cavity for a thermochemical reaction where the particle residence time is based on the inclination of the surface. The reactor showed a thermal stability and smooth operation with ZnO as OC.

Particle reactors, essentially focusing on non-volatile metal oxide redox pairs, have also been developed in recent years. Based on aerosol reactor, Scheffe et al. [135] proposed a reactor, where the OCs were proposed to be loading from the top of tubular reactor to allow a free-flow gravity based motion through the heated zone of the reduction chamber, as shown in Fig. 22. It essentially resembles a moving bed reactor. The inert sweep gas in the reduction reactor is fed from the bottom, countercurrent to the reducing OC particles to increase residence time which in turns to increase the reaction rates [115, 135]. For volatile metal oxide redox pairs, the released oxygen and metal oxide vapor are taken away from the top of the reactor to the quenching chamber. However, for non-volatile OCs, the reduced metal oxide is accumulated at the bottom before being transferred to the oxidation reactor through a conveying arrangement [135]. This reactor type essentially employs the indirect heating of metal oxide particles, where the heat is conducted and radiated onto

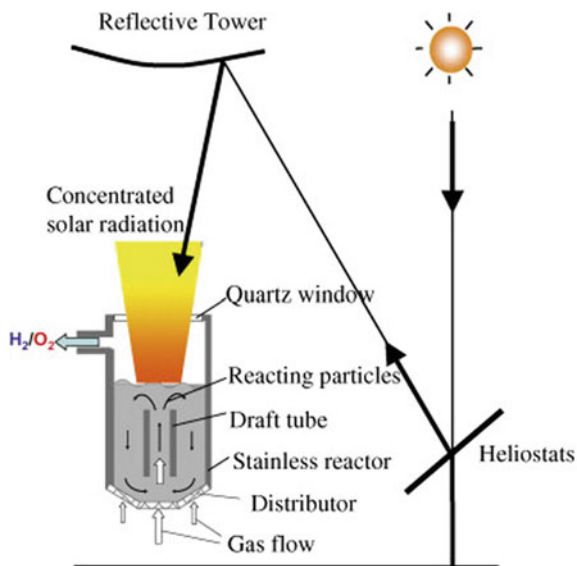
Fig. 22 Schematic of the aerosol reactor [135]



the metal oxide particles from the walls of the reactor, which directly absorbs the concentrated solar radiations. Ceria was tested as the OC, and the entire setup was heated to a temperature of 1500–1600 °C and a very low O_2 partial pressure (5–12 pa). A very high yield of ceria reduction was obtained but low mass flow with respect to the reactor size. An isothermal operation of the reactor has been envisaged, and together with effective decoupling of the reduction and oxidation reactors, would result in a potential twenty-four hour syngas generation from CO_2/H_2O splitting [135].

Even though the above model of reactor design would benefit in terms of lower mass transfer limitation, the essential drawback is there is no direct connection to the oxidation reactor or heat recuperation heat exchanger from solids for temperature swing redox reactions and the metal oxide conveyor system to return the oxidized OC to top of the aerosol reactor [115]. To overcome such barriers, Gokon et al. [136] tested an fluidized bed reactor with a draft tube for internal recirculation for thermochemical processes and for CO_2/H_2O splitting redox cycles by combining solar beam-down concept, as shown in Fig. 23. The reactor design attempts to have the same benefit of the aerosol reactor of maintaining low mass transfer limitation with both the redox reactions occur in the same chamber [136]. The OCs are loaded into a reaction chamber making it a fluidized bed with a draft tube in the center to enhance intermixing, while the inert sweep gases are fed at the bottom through a

Fig. 23 Internally circulating bed proposed by Gokon et al. [136]



distributor. The OC particles fluidizes and allowing them to rise and fall through the central annulus. A quartz window allows the solar irradiation to raise the temperature for reduction. The reactor performance was evaluated with unsupported NiFe_2O_4 and supported $\text{NiFe}_2\text{O}_4/\text{ZrO}_2$ on a laboratory scale, equipped by a high-powered sun simulator having three 6 kW xenon lamps. Non-uniform heat distribution within the reactor was obtained, with only the upper part of the draft tube measuring sufficient temperatures required for the reduction step [136]. On an overall 30 min cycle, a 35% reduction of the supported ferrite oxide was obtained, however, with a subsequent complete re-oxidation of water splitting reaction. The need for a quartz window and the presence of the oxidation reactor within the same chamber, limiting the space for reduction reactor, and unequal heat distribution are the primary disadvantages for efficient use of concentrated sunlight.

A moving bed reactor for thermochemical redox cycle was patented by Sandia laboratories developed by Ermanoski et al. [137] that decouple the reduction and oxidation reactions, also capable of solid heat recuperation between the redox steps [137]. The reactor comprises a reduction chamber which can be directly illuminated as shown in Fig. 24a.

A screw elevator is designed to lift the oxidized OCs from the bottom of the reduction reactor, after which a casing (which rotates) conveys the OCs up to a stationary ceramic screw which act as heat exchanger.

The reduction step occurs on the upper side of the reactor where OCs get heated up by concentrated solar light before dropping through the hollow center of the screw elevator [137]. The O_2 released would be taken away by a vacuum pump. The oxidation zone is roughly atmospheric, while the reduction zone would operate at a low pressure, the screw acting as a pressure buffer between the two. The oxidation

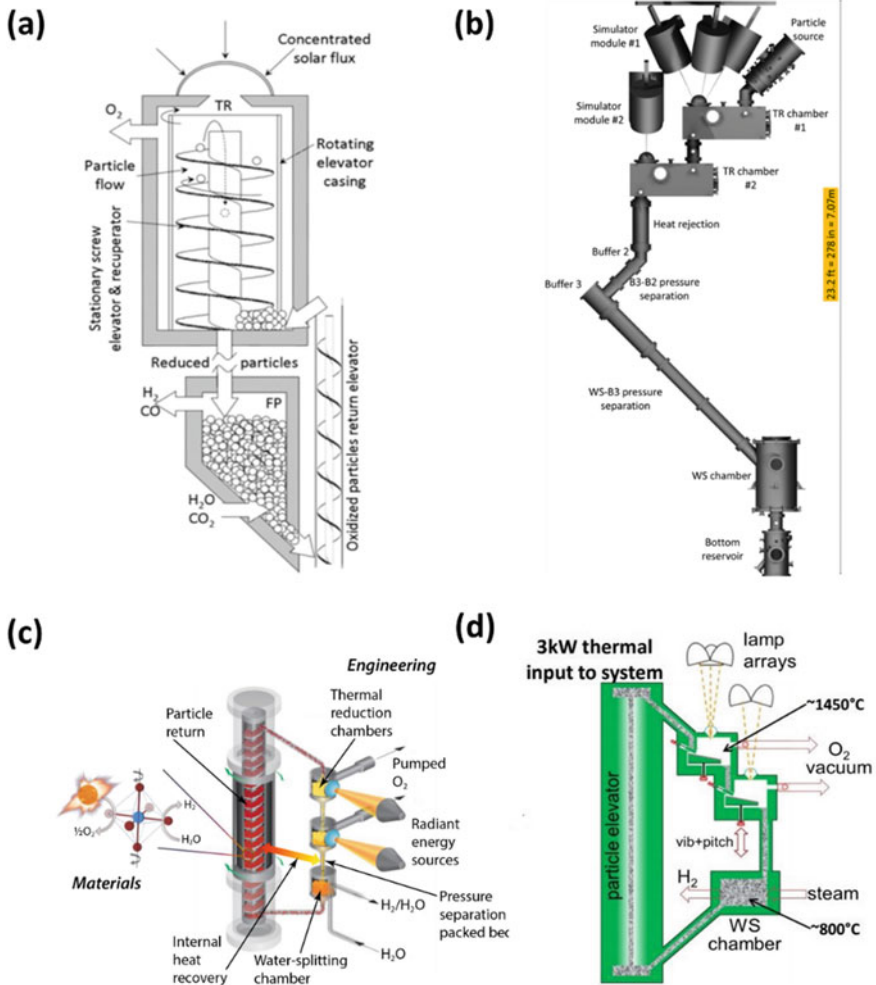


Fig. 24 Moving bed reactors proposed by Sandia laboratories [137–139]

chamber forms a secondary moving bed through which $\text{H}_2\text{O}/\text{CO}_2$ can be pumped, thus oxidizing the OC, thereby generating syngas. While decoupling the oxidation and reduction reactions, this reactor design also simplifies the solid–solid heat transfers and provides colocation of both the redox steps, enabling continuous reaction. A design update has also been proposed by Ermanoski et al. [137] and Ermanoski [138] (Cascading Pressure Receiver–Reactor, CPR2) at Sandia laboratories, USA, whereby a staged pressure reduction has been proposed to facilitate oxygen removal while de-emphasizing the heat exchange through gas–solid and solid–solid heat recovery. However, the use of the quartz window presents the familiar drawback stated earlier which limits the size of the reactor system and also increases the probability of

attracting fine particles through thermophoretic deposition. This could potentially result in a diminished transparency of the window. The heated particles may come in contact with the window producing hot spots leading to catastrophic failure. Moreover, the rotating parts at high temperatures are also a negative aspect, straining the vacuum seals and stressing the casing of the reactor [115].

Another recent development in reactor configuration conceptualized by Muhich et al. [115] was the “Solar Thermal Particle Flow Reactor.” Beam-up approach was used in the design that comprises of multiple reduction/oxidation reactors which are arranged in a circumferential inner and outer periphery. The reduction reactors have been arranged to form the inner ring of the reactor, while the oxidation reactors are on the outside. The reactor system is proposed to be placed on a central tower, with concentrated sunlight being directed up through the gap in the bottom of the receiver, as illustrated in Fig. 25. Due to the need of only one reflection by the downward-facing cavity receiver, a minimal convective heat loss from the hot gases that rise out of aperture is envisaged.

The reduction reactor forms a moving bed reactor, indirectly heated through the reactor wall, and oxygen is evacuated by a vacuum pump. The reduced oxygen carriers at the bottom forms a loosely held packed bed which acts as pressure buffer and gives a pressure swing before entering the oxidation reactor [115]. Here, oxidation occurs in a fluidized bed reactor, the particles being transported up by steam entrainment through a longer steam conveying tube. The design claims the possibility to run in near-isothermal temperatures for redox reactions eliminating the heat of solid-to-solid heat recuperation which in turns eliminates the thermal stresses in

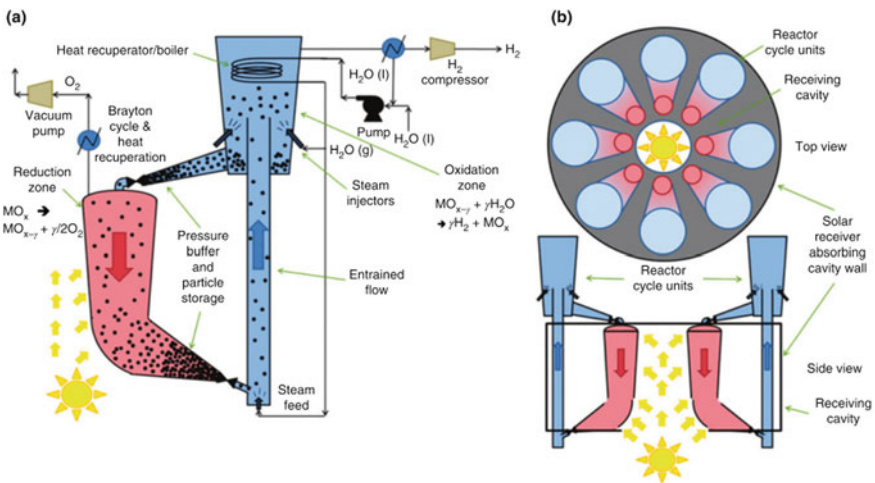


Fig. 25 Interconnected solar-based particle flow reactor based on fluidized bed and moving bed reactor by Muhich et al. [115]. **a** Single unit of reduction and oxidation reactor with a vacuum pump system for the removal of oxygen from the reduction reactor and **b** multiple oxidation and reduction reactor configuration with solar receiver concept. Reactors are not shown to scale

the OC due to temperature swing. Use of the fluidized bed results in a better heat distribution and gas/solid heat recuperation, resulting in a potential increase in the overall reactor and system efficiency. However, key challenges like the development of high-temperature ceramic heat exchangers, development of novel oxygen carriers, reactor lining material compatible with reactive OCs, efficient solar tower, heliostat systems, and receiver system remains an open area for research that needs to be addressed [115]. It is important to mention that the selectivity of the fuel in these types of reactors is limited to the fluidization regime in which the reactor operates and by the downstream usage of the product gas.

6.4 Reactors for Chemical Looping Splitting Cycles with Carbonaceous Fuels

Experimental setup using fixed bed reactors for studying the behavior of methane partial oxidation using metal oxides has been made and reported in multiple studies in the literature [60, 61]. Solar aided methane reforming using ceria as the OC has been proposed and studied by Welte et al. [59]. The reactor design concept is a particle-transport reactor, whereby the heat required for the endothermic reaction has been proposed to be supplied via a solar concentrator. The schematic of the reactor, as proposed by Welte et al., is shown in Fig. 26. Both counter- and co-current reactor configurations have been evaluated. The maximum non-stoichiometry of 0.25 during reduction was obtained solar to fuel efficiency of 12%. Indeed, the primary concept of the reactor was to use methane as an aid to enhance the thermal reduction and not as a primary reactant. The authors also reported the simultaneous upgrade of the calorific value of methane by 24% through the use of concentrated solar energy.

However, unlike thermal reduction of metal oxides for chemical looping cycles, no commercial-scale reactor design exists for methane partial oxidation coupled to CO₂ and H₂O splitting. Multiple reactor designs based on the fluidized or moving bed have proposed reactors for three-step chemical looping combustion cycles with complete combustion of methane aiming to produce CO₂ and H₂O [98]. However, being a fundamentally different process to what the present study aims to explore, such reactors have not been further elaborated in detailed.

7 Modeling of Reactors

Efficiency is of fundamental importance in determining the performance of both the reduction and oxidation reactors for any chemical looping processes. It is necessary to not only determine the possible losses and limitations of the reactor design but also to improve the understanding of the selection of the reactor design based on the peculiar downstream applications of the generated products. Therefore, modeling the

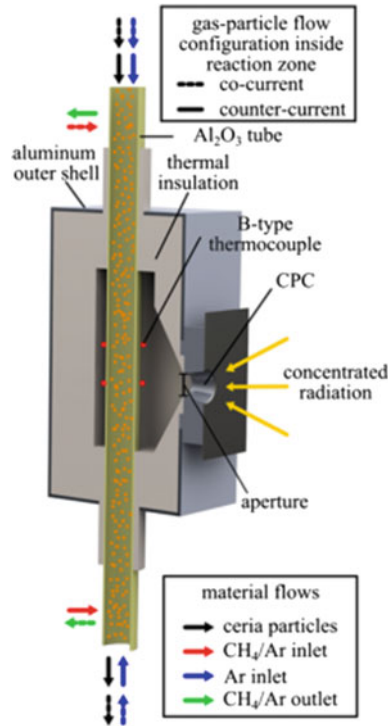


Fig. 26 Schematic of the proposed solar particle-transport reactor by Welte et al. [59] showing both countercurrent and co-current gas–solid flow configurations

reactors would aid in optimized design for scale-up of the process, also to increase the reduction extent and gas conversion rates in both redox steps together with identifying the challenges deriving from the scale-up of such proposed reactor systems. Most of the advanced reactor design modeling has been performed for chemical looping combustion [140, 141]. As mentioned, non-structured reactors have shown the highest potential for scale-up, of which moving bed and fluidized bed reactors are the most commonly studied [142].

7.1 Fluidized Bed Reactors

Fluid bed reactors are an industrially commercialized technology being used in the industry for many years now [143], with the first industrial-scale devices developed for coal gasification, known as Winkler’s coal gasifier. Since then, the concept has

been expanded to different catalytic processes and synthesis of the hydrocarbon-based fuels in the Fischer–Tropsch process [143]. A significant development in scaling up of the reactor has taken place, especially for coal combustion and metallurgical processes. Commissioned at the end of the 2000s, the newest unit of Łagisza power plant in Poland uses the circulating fluidized bed (CFB) boiler that supplies supercritical steam to the 480 MWe turbine.

Fluidized bed reactor modeling can be categorized into three categories after Abad et al. [140], based on the fundamental principles followed for the respective design and evaluation.

- Simplistic models neglecting the complex fluid dynamic behaviors taking place in the fluidized bed [144, 145];
- Macroscopic models considering experimentally developed semi-empirical correlations for the hydrodynamics of a fluidized bed [146]; and
- Multi-phase computational fluid dynamic (CFD) models [147, 148].

Each of the different principles followed have their individual advantages and disadvantages. While the simplistic models lack accuracy, they provide relatively faster results in comparison with CFD models that are restricted from the large computational power necessary for evaluating the same.

To reduce the complexity of the mechanistic modeling approaches, the development of simplistic models incorporating the principles of the chemical reactions occurring in the reactors (e.g., chemical equilibrium or reactions kinetics) is necessary. Such an approach may be conveniently realized using the process simulator Aspen Plus, a chemical design tool. It is widely used and accepted in the industry for its versatility, ease of use and ability to simulate a wide range of steady-state processes ranging from single unit operation to complex processes involving many units [149]. Legros et al. [149] studied the modeling of circulating fluidized bed reactors for coal combustion in ASPEN Plus, by essentially utilizing the first principle of the reactor modeling stated above. Since no in-house fluidized bed model existed at that time in the ASPEN Plus reactor directory, a model of a circulating fluidized bed, using conventional reactor models of ASPEN Plus integrating Fortran blocks and user kinetic subroutines, was used to develop the desired model with satisfactory results. The proposed model is shown in Fig. 27. Similar models have been extensively used for modeling coal and biomass gasification or combustion processes, with results being reported in the literature [150].

However, with the addition of the in-house fluidized bed model to the ASPEN Plus directory (v8.8), the need to develop own model to replicate fluidized bed hydrodynamics would no longer be there. Of course, kinetic modeling for reactions in the reactor is essential to be included to obtain accurate results. Indeed, the present in-house fluidized bed model in ASPEN Plus, that is simulated as a series of stirred reactors (RCSTR), utilizes the second principle of modeling fluidized bed reactors using empirical relations for the hydrodynamics of the fluidized bed [151]. It is understood that the fluidized bed reactors for $\text{CO}_2/\text{H}_2\text{O}$ dissociation could be questionable with respect to the selectivity of the syngas produced as it requires a huge amount of reactant gases for the fluidized bed to operate. Another issue is the mode

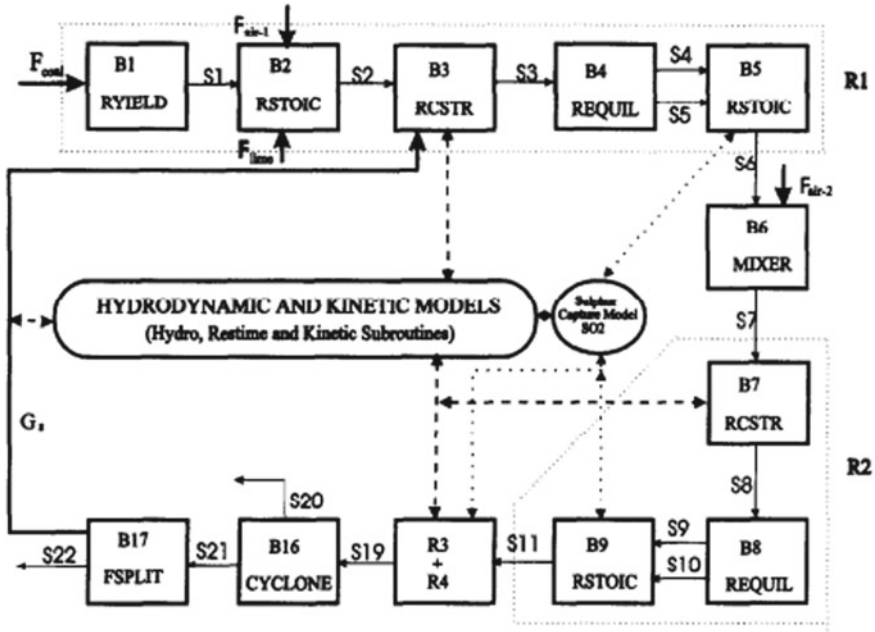


Fig. 27 Proposed hydrodynamic and kinetic model of a circulating fluidized bed reactor in ASPEN Plus as proposed by Legros et al. [149]

of fluidization regime in which it could operate as it is inherently linked with the solid inventory of the bed. $\text{CO}_2/\text{H}_2\text{O}$ gas at the inlet distributor cannot be diluted with an inert such as in case of CLC due to the limitation of the downstream usage of the syngas. The separation of the inert would increase tremendous effort and decrease the efficiency as a whole.

7.2 Moving Bed Reactors

Similar to the fluidized bed, moving bed reactors have been extensively used in the chemical industry. One of the most used is the countercurrent moving bed reactor comprising two different phases moving countercurrent to each other and thereby transferring mass and/or energy between the phases along with chemical reaction in one or both phases [152]. The most famous example is the blast furnace, followed by calcination of limestone, etc. [152]. Though there are economic and operational benefits of the moving bed reactors, it received relatively less attention in comparison with the packed or fluidized bed reactors due to non-availability of general model to solve the governing equations [153].

Most of the studies for modeling moving bed reactors have focussed on selecting the ideal reaction mechanism to increase the accuracy of prediction of the products

from the designed reactors [153]. While Parisi and Laborde [154] and Negri et al. [155] studied the applicability of the shrinking core reaction model, Dussoubs et al. [156] extensively analyzed the additive characteristic times model for formulating accurately the gas–solid reaction rates. Another kinetic model, the extended grain model was adopted and extended for the moving bed reactor introduced by Rahimi and Niksiar [153]. The reported comprehensive numerical model of a moving bed reactor is used for reduction of Fe_2O_3 pellets via an in-house methodology developed using fundamental principles of thermodynamics and chemical kinetics. An average error of 1.2% was reported from the obtained results of the simulation [153]. Reactor modeling using commercial software ASPEN plus provides multiple benefits and advantages, as already mentioned earlier. Since no moving bed reactor model exists in Aspen Plus, similar to past modeling of fluidized bed reactors, the development of a comprehensive model using the available in-built reactor models of Aspen Plus is necessary. Benjamin [157], proposed a built-in model for a countercurrent moving bed coal gasifier. However, the results showed that the solution was time-consuming and an analysis of the proposed model can be found in the Aspen Plus guide to moving bed gasifier modeling [158]. An alternative, as proposed by Aspen Plus [158], to utilize multiple RCSTRs in series, results in a considerably simpler model. This also allows the direct use of the built-in algorithms of Aspen Plus.

Such a reactor model for the thermodynamic assessment of the moving bed reactor was implemented by Tong et al. [159] for a moving bed in a chemical looping combustion cycle with $\text{Fe}_3\text{O}_4/\text{Fe}$ redox pair and methane as fuel. Five RGIBBS reactors were modeled in series to replicate the countercurrent moving bed reactor model, employing minimization of the Gibbs free energy for thermodynamic analysis. A good match for both the solid and gas conversion was obtained with respect to the experimental results conducted and reported in the same literature [159]. He et al. [160] developed a steady-state kinetic model of a moving bed gasifier using a similar technique in Aspen Plus, however, to model a Lurgi coal gasifier for synthetic natural gas (SNG) production. In the same study, he went on to demonstrate the methodology of optimizing the number of RCSTRs in series, necessary to provide a convergence to the obtained results. The results were also compared with industrial data, with good agreement.

8 System Modeling

Besides generating CO or H_2 from splitting CO_2 or water, respectively, system modeling for further use of the proposed chemicals is crucial not only to investigate the probable integration of the all the units (like the chemical looping unit) but also to identify the need of advancement for the balance of plant for effective integration. Integrating the chemical looping unit effectively within process layouts design for power or chemicals production has been studied mostly for the chemical looping combustion technology [161, 162].

Nevertheless, two-step water and CO₂ splitting cycles have been simulated for integration into industrial-scale processes by Gençer et al. [163], whereby the Fe₃O₄/FeO redox pair was used for water splitting in a solar-driven cycle for round the clock power generation. An average efficiency of 35% was obtained including energy storage. de la Calle and Bayon [164] modeled 1 MW solar thermochemical redox cycle plant that produces H₂ based on the solar tower with a heliostat-based field of 2.7 km² could reach 1850–1950 °C reduction temperature and oxidation temperature of 1000–1100 °C with peaking non-stoichiometry of 0.25. Besides water splitting, also CO₂ splitting provides considerable opportunities for carbon dioxide utilization (CCU) as an alternative to CCS with potential system integration for chemicals or electricity production.

9 Concluding Remarks

The thermochemical redox cycles for splitting of CO₂ and H₂O into CO and H₂ are a relatively easy way to produce fuel. It will certainly help in a way of CO₂ utilization of the ever-increasing carbon emissions and will help in reducing the carbon tax. The process has many important factors, being one of the most important the metal oxide or the material which undergoes reactions with CO₂ and H₂O for their splitting, another is the reactor design.

During the two-step cycles, the thermal reduction is thermodynamically favored at higher temperatures and lower partial pressures of oxygen and the oxidation step, i.e., the splitting step (CO₂/H₂O splitting) is favoured by relatively lower temperatures. In order to achieve high reaction rates, high temperatures are needed but limited to avoid the reduction (backward reaction) simultaneously during oxidation or splitting reactions. There is a cyclic temperature and pressure swing with a parallel swing of CO₂/H₂O with inert gas during the redox process. The heat rejection at thermal reduction is associated with heat losses and lowers the efficiency of the system. Also due to the high specific heat of metal oxides and continuous swing of temperatures creates thermal stress on the reactive substrate.

The reactor design is essentially important, as it has to handle very high temperatures. In the past, many directly radiated solar reactors have been proposed and tested, and still, significant improvements are needed to implement these reactors for large-scale applications. Reaction kinetics also plays an important role in designing material oxide for the process, which includes supports.

Since the materials tested in the past are classified into volatile and non-volatile, the research is driven toward non-volatile and non-stoichiometric material oxides due to their higher valence characteristics that exhibit high oxygen evolution and higher splitting efficiency. Volatile materials listed in the above sections have the issue of reactions occurring above the melting points and have issues with recombination. The potential candidate for the metal oxide redox cycles later shifted to ceria, as it has higher conversion efficiency and operates at lower temperatures relative to other materials. The efficiency is generally improved by doping ceria lattice with trivalent

and tetravalent cations. The increasing interest in perovskites in the last decade for many different applications drew also attention in the thermochemical application as well. Many perovskite families were tested with many substitutions of A sites and B sites. Perovskites showed very high oxygen release and CO₂ and H₂O splitting rates, and it was reported to have 6 times higher than ceria for CO₂ splitting and 9 times for O₂ release. Of all the oxygen carriers tested, even though other materials such as perovskites and doped metal oxides showed high oxygen carrying capacity, ceria is one of the most suitable candidates for large-scale industrial application for the CO₂/H₂O splitting.

Of all the reactor concepts, the reactor that would be industrially developable for both reduction and oxidation steps will be a moving bed reactor. It is, therefore, relatively easier to control the residence time of the metal oxide that is an important parameter due to the different reaction kinetics of reduction and oxidation. The analysis also aims at developing schemes for an industrial-scale power plant and performs a feasibility study for percentage efficiency again after a solar-based (or fuel reduced) CO₂/H₂O splitting unit.

References

1. IEA (2018) IEA, global energy & CO₂ status report 2017. <https://www.iea.org/publications/freepublications/publication/GECO2017.pdf>
2. Le Quéré C, Andrew RM, Friedlingstein P, Sitch S, Hauck J, Pongratz J, Pickers PA, Korsbakken JI, Peters GP, Canadell JG (2018) Global carbon budget 2018. *Earth Syst Sci Data* 10:2141–2194. <https://doi.org/10.5194/essd-10-2141-2018>
3. BP Energy Economics (2018) BP energy outlook 2018. <https://doi.org/10.1088/1757-899X/342/1/012091>
4. IPCC (2019) IPCC special report on global warming of 1.5 °C
5. Liu G, Sorensen JA, Braunberger JR, Klenner R, Ge J, Gorecki CD, Steadman EN, Harju JA (2014) CO₂-based enhanced oil recovery from unconventional reservoirs: a case study of the Bakken formation. In: SPE unconventional resources conference, 7. <https://doi.org/10.2118/168979-MS>
6. Spath PL, Dayton DC (2003) Preliminary screening—technical and economic assessment of synthesis gas to fuels and chemicals with emphasis on the potential for biomass-derived syngas. <https://doi.org/10.2172/15006100>
7. Simbeck DR, Karp AD, Dickenson RL (1998) Syngas production for gas-to-liquids applications: technologies, issues and outlook. https://web.anl.gov/PCS/acsfuel/preprint%20archive/Files/Merge/Vol-45_1-0003.pdf
8. Sheu EJ, Mokheimer EMA, Ghoniem AF (2015) A review of solar methane reforming systems. *Int J Hydrogen Energy* 40:12929–12955. <https://doi.org/10.1016/j.ijhydene.2015.08.005>
9. Bulfin B, Vieten J, Agrafiotis C, Roeb M, Sattler C (2017) Applications and limitations of two step metal oxide thermochemical redox cycles: a review. *J Mater Chem A* 5:18951–18966. <https://doi.org/10.1039/c7ta05025a>
10. Graves C, Ebbesen SD, Mogensen M, Lackner KS (2011) Sustainable hydrocarbon fuels by recycling CO₂ and H₂O with renewable or nuclear energy. *Renew Sustain Energy Rev* 15:1–23. <https://doi.org/10.1016/j.rser.2010.07.014>
11. Konstandopoulos AG, Pagkoura C, Dimitrakis D, Lorentzou S, Karagiannakis G (2015) Solar hydrogen production. In: Production of hydrogen from renewable resources, pp 283–311

12. Detz RJ, Reek JNH, Van Der Zwaan BCC (2018) The future of solar fuels: when could they become competitive? *Energy Environ Sci* 11:1653–1669. <https://doi.org/10.1039/c8ee00111a>
13. Hosseini SE, Wahid MA (2016) Hydrogen production from renewable and sustainable energy resources: promising green energy carrier for clean development. *Renew Sustain Energy Rev* 57:850–866. <https://doi.org/10.1016/j.rser.2015.12.112>
14. Lemus RG, Duart JMM (2010) Updated hydrogen production costs and parities for conventional and renewable technologies. *Int J Hydrogen Energy* 35:3929–3936. <https://doi.org/10.1016/j.ijhydene.2010.02.034>
15. Ruth M, Laffen M, Timbario T (2009) Hydrogen pathways: cost, well-to-wheels energy use, and emissions for the current technology status of seven hydrogen production, delivery, and distribution scenarios. DoE EERE. <https://doi.org/10.2172/1107463>
16. Dimitrakis DA (2017) Thermochemical water and carbon dioxide redox splitting for neutral carbon footprint solar fuels: from material to reactor. Aristotle University of Thessaloniki, Thessaloniki
17. Global CCS Institute (2017) The global status of CCS: 2017, 43. <https://doi.org/978-0-9944115-2-5>
18. Leung DYC, Caramanna G, Maroto-Valer MM (2014) An overview of current status of carbon dioxide capture and storage technologies. *Renew Sustain Energy Rev* 39:426–443. <https://doi.org/10.1016/j.rser.2014.07.093>
19. Merkel TC, Lin H, Wei X, Baker R (2010) Power plant post-combustion carbon dioxide capture: an opportunity for membranes. *J Membr Sci* 359:126–139. <https://doi.org/10.1016/j.memsci.2009.10.041>
20. Chiesa P, Lozza G, Malandrino A, Romano M, Piccolo V (2008) Three-reactors chemical looping process for hydrogen production. *Int J Hydrogen Energy* 33:2233–2245. <https://doi.org/10.1016/j.ijhydene.2008.02.032>
21. IEA (2004) Energy technology analysis: prospects for CO₂ capture and storage, 249. <https://doi.org/10.1016/B978-1-85617-710-8.00010-8>
22. Wang M, Lawal A, Stephenson P, Sidders J, Ramshaw C (2011) Post-combustion CO₂ capture with chemical absorption: a state-of-the-art review. *Chem Eng Res Des* 89:1609–1624. <https://doi.org/10.1016/j.cherd.2010.11.005>
23. Buhre BJP, Elliott LK, Sheng CD, Gupta RP, Wall TF (2005) Oxy-fuel combustion technology for coal-fired power generation. *Prog Energy Combust Sci* 31:283–307. <https://doi.org/10.1016/j.pecs.2005.07.001>
24. Habib MA, Nemitallah M, Ben-Mansour R (2013) Recent development in oxy-combustion technology and its applications to gas turbine combustors and ITM reactors. *Energy Fuels* 27:2–19. <https://doi.org/10.1021/ef301266j>
25. Pfaff I, Kather A (2009) Comparative thermodynamic analysis and integration issues of CCS steam power plants based on oxy-combustion with cryogenic or membrane based air separation. *Energy Procedia* 1:495–502. <https://doi.org/10.1016/j.egypro.2009.01.066>
26. Lockwood T (2014) Developments in oxyfuel combustion of coal. IEA Clean Coal Centre, CCC/240, London, United Kingdom, pp 1–122
27. Chorowski M, Gizicki W (2015) Technical and economic aspects of oxygen separation for oxy-fuel purposes. *Arch Thermodyn* 36:157–170. <https://doi.org/10.1515/aoter-2015-0011>
28. Nemitallah M, Habib M, Badr H, Said S, Aqil J, Rached B, Mokheimer EM, Mezghani K (2017) Oxy-fuel combustion technology: current status, applications, and trends. *Int J Energy Res* 41:1670–1708. <https://doi.org/10.1002/er.3722>
29. White Rose Project (n.d.) <https://www.zeroco2.no/projects/developers/alstom>. Accessed 1 Mar 2018
30. Xiuzhang W (2014) Shenhua Group’s carbon capture and storage (CCS) demonstration. *Min Rep* 150:81–84. <https://doi.org/10.1002/mire.201400006>
31. Allam RJ, Palmer MR, Brown GW, Fetvedt J, Freed D, Nomoto H, Itoh M, Okita N, Jones C (2013) High efficiency and low cost of electricity generation from fossil fuels while eliminating atmospheric emissions, including carbon dioxide. *Energy Procedia* 37:1135–1149. <https://doi.org/10.1016/j.egypro.2013.05.211>

32. Anderson R, Brandt H, Doyle S, Viteri F (2003) A demonstrated 20 MWt gas generator for a clean steam power plant. In: 28th international technical conference on coal utilization and fuel systems, p 916
33. Stanger R, Wall T, Spörl R, Paneru M, Grathwohl S, Weidmann M, Scheffknecht G, McDonald D, Myöhänen K, Ritvanen J (2015) Oxyfuel combustion for CO₂ capture in power plants. *Int J Greenhouse Gas Control* 40:55–125. <https://doi.org/10.1016/j.ijggc.2015.06.010>
34. MacDowell N, Florin N, Buchard A, Hallett J, Galindo A, Jackson G, Adjiman CS, Williams CK, Shah N, Fennell P (2010) An overview of CO₂ capture technologies. *Energy Environ Sci* 3:1645. <https://doi.org/10.1039/c004106h>
35. Metz B, Ogunlade D, de Heleen C, Manuela L, Leo M (eds) (2005) IPCC, 2005: IPCC special report on carbon dioxide capture and storage. Prepared by Working Group III of the Intergovernmental Panel on Climate Change
36. Van Der Zwaan B, Smekens K (2009) CO₂ capture and storage with leakage in an energy-climate model. *Environ Model Assess* 14:135–148. <https://doi.org/10.1007/s10666-007-9125-3>
37. Doughty C, Freifeld BM, Trautz RC (2008) Site characterization for CO₂ geologic storage and vice versa: The Frio Brine Pilot, Texas, USA as a case study. *Environ Geol* 54:1635–1656. <https://doi.org/10.1007/s00254-007-0942-0>
38. House KZ, Schrag DP, Harvey CF, Lackner KS (2006) Permanent carbon dioxide storage in deep-sea sediments. *Proc Natl Acad Sci* 103:12291–12295. <https://doi.org/10.1073/pnas.0605318103>
39. Jenkins CR, Cook PJ, Ennis-King J, Undershultz J, Boreham C, Dance T, de Caritat P, Etheridge DM, Freifeld BM, Hortle A, Kirste D, Paterson L, Pevzner R, Schacht U, Sharma S, Stalker L, Urosevic M (2012) Safe storage and effective monitoring of CO₂ in depleted gas fields. *Proc Natl Acad Sci* 109:E35–E41. <https://doi.org/10.1073/pnas.1107255108>
40. Zöback MD, Gorelick SM (2012) Earthquake triggering and large-scale geologic storage of carbon dioxide. *Proc Natl Acad Sci* 109:10164–10168. <https://doi.org/10.1073/pnas.1202473109>
41. Yuan Z, Eden MR, Gani R (2016) Toward the development and deployment of large-scale carbon dioxide capture and conversion processes. *Ind Eng Chem Res* 55:3383–3419. <https://doi.org/10.1021/acs.iecr.5b03277>
42. Alessandra QE, Gabriele C, Jean-Luc D, Siglinda P (2011) Carbon dioxide recycling: emerging large-scale technologies with industrial potential. *Chemsuschem* 4:1194–1215. <https://doi.org/10.1002/cssc.201100473>
43. Tour JM, Kittrell C, Colvin VL (2010) Green carbon as a bridge to renewable energy. *Nat Mater* 9:871. <https://doi.org/10.1038/nmat2887>
44. Cuéllar-Franca RM, Azapagic A (2015) Carbon capture, storage and utilisation technologies: a critical analysis and comparison of their life cycle environmental impacts. *J CO₂ Util* 9:82–102. <https://doi.org/10.1016/j.jcou.2014.12.001>
45. Huang CH, Tan CS (2014) A review: CO₂ utilization. *Aerosol Air Qual Res* 14:480–499. <https://doi.org/10.4209/aaqr.2013.10.0326>
46. Aresta M (2010) Carbon dioxide: utilization options to reduce its accumulation in the atmosphere. *Carbon Dioxide Chem Feed* 1–13. <https://doi.org/10.1002/9783527629916.ch1>
47. Song C (2006) Global challenges and strategies for control, conversion and utilization of CO₂ for sustainable development involving energy, catalysis, adsorption and chemical processing. *Catal Today* 115:2–32. <https://doi.org/10.1016/j.cattod.2006.02.029>
48. von der Assen N, Jung J, Bardow A (2013) Life-cycle assessment of carbon dioxide capture and utilization: avoiding the pitfalls. *Energy Environ Sci* 6:2721–2734. <https://doi.org/10.1039/C3EE41151F>
49. Peters M, Köhler B, Kuckshinrichs W, Leitner W, Markewitz P, Müller TE (2011) Chemical technologies for exploiting and recycling carbon dioxide into the value chain. *Chemsuschem* 4:1216–1240. <https://doi.org/10.1002/cssc.201000447>
50. Spallina V, Shams A, Battistella A, Gallucci F, Annaland MVS (2017) Chemical looping technologies for H₂ production with CO₂ capture: thermodynamic assessment and economic comparison. *Energy Procedia* 114:419–428. <https://doi.org/10.1016/j.egypro.2017.03.1184>

51. Bayham SC, Tong A, Kathe M, Fan L-S (2016) Chemical looping technology for energy and chemical production. *Wiley Interdisc Rev Energy Environ* 5:216–241. <https://doi.org/10.1002/wene.173>
52. Traynor AJ, Jensen RJ (2002) Direct solar reduction of CO₂ to fuel: first prototype results. *Ind Eng Chem Res* 41:1935–1939. <https://doi.org/10.1021/ie010871x>
53. Nigara Y, Cales B (1986) Production of carbon monoxide by direct thermal splitting of carbon dioxide at high temperature. *Bull Chem Soc Jpn* 59:1997–2002. <https://doi.org/10.1246/bcsj.59.1997>
54. Lyman JL, Jensen RJ (2001) Chemical reactions occurring during direct solar reduction of CO₂. *Sci Total Environ* 277:7–14. [https://doi.org/10.1016/S0048-9697\(01\)00829-4](https://doi.org/10.1016/S0048-9697(01)00829-4)
55. Sadeghbeigi R (2012) Fluid catalytic cracking handbook: an expert guide to the practical operation, design, and optimization of FCC unit, 3rd edn. Butterworth-Heinemann. <https://doi.org/10.1016/B978-0-12-386965-4.X0001-8>
56. Tang M, Xu L, Fan M (2015) Progress in oxygen carrier development of methane-based chemical-looping reforming: a review. *Appl Energy* 151:143–156. <https://doi.org/10.1016/j.apenergy.2015.04.017>
57. Dilmaç N, Dilmaç ÖF, Yardımcı E (2017) Utilization of Menteş iron ore as oxygen carrier in chemical-looping combustion. *Energy* 138:785–798. <https://doi.org/10.1016/j.energy.2017.07.126>
58. Krenzke PT, Davidson JH (2014) Thermodynamic analysis of syngas production via the solar thermochemical cerium oxide redox cycle with methane-driven reduction. *Energy Fuels* 28:4088–4095. <https://doi.org/10.1021/ef500610n>
59. Welte M, Warren K, Scheffe JR, Steinfeld A (2017) Combined ceria reduction and methane reforming in a solar-driven particle-transport reactor. *Ind Eng Chem Res* 56:10300–10308. <https://doi.org/10.1021/acs.iecr.7b02738>
60. Warren KJ, Scheffe JR (2018) Kinetic insights into the reduction of ceria facilitated via the partial oxidation of methane. *Mater Today Energy* 9:39–48. <https://doi.org/10.1016/j.mtener.2018.05.001>
61. Bhavsar S, Vesper G (2014) Chemical looping beyond combustion: production of synthesis gas via chemical looping partial oxidation of methane. *RSC Adv* 4:47254–47267. <https://doi.org/10.1039/c4ra06437b>
62. Agrafiotis C, Roeb M, Sattler C (2015) A review on solar thermal syngas production via redox pair-based water/carbon dioxide splitting thermochemical cycles. *Renew Sustain Energy Rev* 42:254–285. <https://doi.org/10.1016/j.rser.2014.09.039>
63. Yadav D, Banerjee R (2016) A review of solar thermochemical processes. *Renew Sustain Energy Rev* 54:497–532. <https://doi.org/10.1016/j.rser.2015.10.026>
64. Smestad GP, Steinfeld A (2012) Review: photochemical and thermochemical production of solar fuels from H₂O and CO₂ using metal oxide catalysts. *Ind Eng Chem Res* 51:11828–11840. <https://doi.org/10.1021/ie3007962>
65. Vishnevetsky I, Berman A, Epstein M (2011) Features of solar thermochemical redox cycles for hydrogen production from water as a function of reactants' main characteristics. *Int J Hydrogen Energy* 36:2817–2830. <https://doi.org/10.1016/j.ijhydene.2010.11.027>
66. Carrillo RJ, Scheffe JR (2017) Advances and trends in redox materials for solar thermochemical fuel production. *Sol Energy* 156:3–20. <https://doi.org/10.1016/j.solener.2017.05.032>
67. Gael L, Stéphane A, Jumas J, Olivier-fourcade J (2014) Characterization of two-step tin-based redox system for thermochemical fuel production from solar-driven CO₂ and H₂O splitting cycle. *Ind Eng Chem* 53:5668–5677
68. Zhang Y, Nie T, Wang Z, Liu J, Zhou J, Cen K (2016) Splitting of CO₂ via the heterogeneous oxidation of zinc powder in thermochemical cycles. *Ind Eng Chem Res* 55:534–542. <https://doi.org/10.1021/acs.iecr.5b02407>
69. Furler P, Scheffe JR, Marxer D, Steinfeld A (2014) Solar reactors for thermochemical CO₂ and H₂O splitting via metal oxide redox reactions. In: SFERA II Summer School 2014, Odeillo, France. [https://sfera2.sollab.eu/uploads/images/networking/SFERA%](https://sfera2.sollab.eu/uploads/images/networking/SFERA%2014%20Summer%20School%202014%20Odeillo%20France.pdf)

- [20SUMMER%20SCHOOL%202014%20-%20PRESENTATIONS/Solar%20Reactor%20Reduction%20-%20Philipp%20FURLER.pdf](#)
70. Hartley UW, Ngoenthong N, Cheenkachorn K, Sornchamni T (2015) CO₂ to syngas: metal oxides on stainless steel 316L for micro-channel reactor application. In: International conference on chemical and biochemical engineering, Paris (France), 20–22 July 2015, pp 8–11. https://www.researchgate.net/profile/Mahdi_Belguidoum/publication/289540155_AbstractsBook_ICCBE2015/links/5690232b08aec14fa557e115/AbstractsBook-ICCBE2015.pdf
 71. Tesconi S, Agrafiotis C, Breuer S, De Oliveira L, Neises-Von Puttkamer M, Roeb M, Sattler C (2013) Thermochemical solar energy storage via redox oxides: materials and reactor/heat exchanger concepts. *Energy Procedia* 49:1034–1043. <https://doi.org/10.1016/j.egypro.2014.03.111>
 72. Jiang Q, Chen Z, Tong J, Yang M, Jiang Z, Li C (2016) Catalytic function of IrO_x in the two-step thermochemical CO₂-splitting reaction at high temperatures. *ACS Catal* 6:1172–1180. <https://doi.org/10.1021/acscatal.5b01774>
 73. Gokon N, Suda T, Kodama T (2015) Oxygen and hydrogen productivities and repeatable reactivity of 30-mol%-Fe-, Co-, Ni-, Mn-doped CeO_{2-δ} for thermochemical two-step water-splitting cycle. *Energy* 90:1280–1289. <https://doi.org/10.1016/j.energy.2015.06.085>
 74. Nakamura T (1977) Hydrogen production from water utilizing solar heat at high temperatures. *Sol Energy* 19:467–475. [https://doi.org/10.1016/0038-092X\(77\)90102-5](https://doi.org/10.1016/0038-092X(77)90102-5)
 75. Roeb M, Sattler C, Klüser R, Monnerie N, de Oliveira L, Konstandopoulos AG, Agrafiotis C, Zaspalis VT, Nalbandian L, Steele A, Stobbe P (2006) Solar hydrogen production by a two-step cycle based on mixed iron oxides. *J Sol Energy Eng* 128:125. <https://doi.org/10.1115/1.2183804>
 76. Darken LS, Gurry RW (1946) The system iron-oxygen. II. Equilibrium and thermodynamics of liquid oxide and other phases. *J Am Chem Soc* 68:798–816. <https://doi.org/10.1021/ja01209a030>
 77. Liu F (2013) Cerium oxide promoted oxygen carrier development and scale modeling study for chemical looping combustion. University of Kentucky. https://uknowledge.uky.edu/cgi/viewcontent.cgi?article=1029&context=me_etds
 78. Chueh WC, Haile SM (2010) A thermochemical study of ceria: exploiting an old material for new modes of energy conversion and CO₂ mitigation. *Philos Trans R Soc A Math Phys Eng Sci* 368:3269–3294. <https://doi.org/10.1098/rsta.2010.0114>
 79. Abanades S, Flamant G (2006) Thermochemical hydrogen production from a two-step solar-driven water-splitting cycle based on cerium oxides. *Sol Energy* 80:1611–1623. <https://doi.org/10.1016/j.solener.2005.12.005>
 80. Bulfin B, Lowe AJ, Keogh KA, Murphy BE, Lübben O, Krasnikov SA, Shvets IV (2013) Analytical model of CeO₂ oxidation and reduction. *J Phys Chem C* 117:24129–24137. <https://doi.org/10.1021/jp406578z>
 81. Kümmerle EA, Heger G (1999) The structures of C-Ce₂O_{3+δ}, Ce₇O₁₂, and Ce₁₁O₂₀. *J Solid State Chem* 147:485–500. <https://doi.org/10.1006/jssc.1999.8403>
 82. Bulfin B, Hoffmann L, De Oliveira L, Knoblauch N, Call F, Roeb M, Sattler C, Schmücker M (2016) Statistical thermodynamics of non-stoichiometric ceria and ceria zirconia solid solutions. *Phys Chem Chem Phys* 18:23147–23154. <https://doi.org/10.1039/c6cp03158g>
 83. Knoblauch N, Simon H, Schmücker M (2017) Chemically induced volume change of CeO_{2-δ} and nonstoichiometric phases. *Solid State Ionics* 301:43–52. <https://doi.org/10.1016/j.ssi.2017.01.003>
 84. Gokon N, Sagawa S, Kodama T (2013) Comparative study of activity of cerium oxide at thermal reduction temperatures of 1300–1550 °C for solar thermochemical two-step water-splitting cycle. *Int J Hydrogen Energy* 38:14402–14414. <https://doi.org/10.1016/j.ijhydene.2013.08.108>
 85. Abanades S, Legal A, Cordier A, Peraudeau G, Flamant G, Julbe A (2010) Investigation of reactive cerium-based oxides for H₂ production by thermochemical two-step water-splitting. *J Mater Sci* 45:4163–4173. <https://doi.org/10.1007/s10853-010-4506-4>

86. Le Gal A, Abanades S (2011) Catalytic investigation of ceria-zirconia solid solutions for solar hydrogen production. *Int J Hydrogen Energy* 36:4739–4748. <https://doi.org/10.1016/j.ijhydene.2011.01.078>
87. Scheffe JR, Steinfeld A (2012) Thermodynamic analysis of cerium-based oxides for solar thermochemical fuel production. *Energy Fuels* 26:1928–1936. <https://doi.org/10.1021/ef201875v>
88. Jiang Q, Zhou G, Jiang Z, Li C (2014) Thermochemical CO₂ splitting reaction with Ce_xM_{1-x}O_{2-δ} (M=Ti⁴⁺, Sn⁴⁺, Hf⁴⁺, Zr⁴⁺, La³⁺, Y³⁺ and Sm³⁺) solid solutions. *Sol Energy* 99:55–66. <https://doi.org/10.1016/j.solener.2013.10.021>
89. Otsuka K, Hatano M, Morikawa A (1985) Decomposition of water by cerium oxide of δ-phase. *Inorganica Chim Acta* 109:193–197. [https://doi.org/10.1016/S0020-1693\(00\)81768-5](https://doi.org/10.1016/S0020-1693(00)81768-5)
90. Panlener RJ, Blumenthal RN, Garnier JE (1975) A thermodynamic study of nonstoichiometric cerium dioxide. *J Phys Chem Solids* 36:1213–1222. [https://doi.org/10.1016/0022-3697\(75\)90192-4](https://doi.org/10.1016/0022-3697(75)90192-4)
91. Le Gal A, Abanades S, Flamant G (2011) CO₂ and H₂O splitting for thermochemical production of solar fuels using nonstoichiometric ceria and ceria/zirconia solid solutions. *Energy Fuels* 25:4836–4845. <https://doi.org/10.1021/ef200972r>
92. Singh P, Hegde MS (2010) Ce_{0.67}Cr_{0.33}O_{2.11}: a new low-temperature O₂ evolution material and H₂ generation catalyst by thermochemical splitting of water. *Chem Mater* 22:762–768. <https://doi.org/10.1021/cm9013305>
93. Scheffe JR, Jacot R, Patzke GR, Steinfeld A (2013) Synthesis, characterization, and thermochemical redox performance of Hf⁴⁺, Zr⁴⁺, and Sc³⁺ doped ceria for splitting CO₂. *J Phys Chem C* 117:24104–24114. <https://doi.org/10.1021/jp4050572>
94. Ihara S (1980) On the study of hydrogen production from water using solar thermal energy. *Int J Hydrogen Energy* 5:527–534. [https://doi.org/10.1016/0360-3199\(80\)90059-2](https://doi.org/10.1016/0360-3199(80)90059-2)
95. Le Gal A, Abanades S (2012) Dopant incorporation in ceria for enhanced water-splitting activity during solar thermochemical hydrogen generation. *J Phys Chem C* 116:13516–13523. <https://doi.org/10.1021/jp302146c>
96. Hao Y, Yang CK, Haile SM (2013) High-temperature isothermal chemical cycling for solar-driven fuel production. *Phys Chem Chem Phys* 15:17084–17092. <https://doi.org/10.1039/c3cp53270d>
97. Takalkar GD, Bhosale RR, Kumar A, AlMamani F, Khraisheh M, Shakoor RA, Gupta RB (2018) Transition metal doped ceria for solar thermochemical fuel production. *Sol Energy* 172:204–211. <https://doi.org/10.1016/j.solener.2018.03.022>
98. Voitic G, Hacker V (2016) Recent advancements in chemical looping water splitting for the production of hydrogen. *RSC Adv* 6:98267–98296. <https://doi.org/10.1039/C6RA21180A>
99. Jiang Q, Tong J, Zhou G, Jiang Z, Li Z, Li C (2014) Thermochemical CO₂ splitting reaction with supported La_xA_{1-x}Fe_yB_{1-y}O₃ (A=Sr, Ce, B=Co, Mn; 0 ≤ x, y ≤ 1) perovskite oxides. *Sol Energy* 103:425–437. <https://doi.org/10.1016/j.solener.2014.02.033>
100. Yang CK, Yamazaki Y, Aydin A, Haile SM (2014) Thermodynamic and kinetic assessments of strontium-doped lanthanum manganite perovskites for two-step thermochemical water splitting. *J Mater Chem A* 2:13612–13623. <https://doi.org/10.1039/c4ta02694b>
101. Dey S, Naidu BS, Govindaraj A, Rao CNR (2015) Noteworthy performance of La_{1-x}Ca_xMnO₃ perovskites in generating H₂ and CO by the thermochemical splitting of H₂O and CO₂. *Phys Chem Chem Phys* 17:122–125. <https://doi.org/10.1039/C4CP04578E>
102. Rao CNR, Dey S (2016) Generation of H₂ and CO by solar thermochemical splitting of H₂O and CO₂ by employing metal oxides. *J Solid State Chem* 242:107–115. <https://doi.org/10.1016/j.jssc.2015.12.018>
103. McDaniel AH, Miller EC, Arifin D, Ambrosini A, Coker EN, O'Hayre R, Chueh WC, Tong J (2013) Sr- and Mn-doped LaAlO_{3-δ} for solar thermochemical H₂ and CO production. *Energy Environ Sci* 6:2424. <https://doi.org/10.1039/c3ee41372a>
104. Gálvez ME, Jacot R, Scheffe J, Cooper T, Patzke G, Steinfeld A (2015) Physico-chemical changes in Ca, Sr and Al-doped La-Mn-O perovskites upon thermochemical splitting of CO₂ via redox cycling. *Phys Chem Chem Phys* 17:6629–6634. <https://doi.org/10.1039/c4cp05898d>

105. Demont A, Abanades S (2015) Solar thermochemical conversion of CO₂ into fuel via two-step redox cycling of non-stoichiometric Mn-containing perovskite oxides. *J Mater Chem A* 3:3536–3546. <https://doi.org/10.1039/c4ta06655c>
106. Dey S, Naidu BS, Rao CNR (2016) Beneficial effects of substituting trivalent ions in the B-site of La_{0.5}Sr_{0.5}Mn_{1-x}A_xO₃ (A=Al, Ga, Sc) on the thermochemical generation of CO and H₂ from CO₂ and H₂O. *Dalton Trans* 45:2430–2435. <https://doi.org/10.1039/c5dt04822b>
107. McDaniel AH, Ambrosini A, Coker EN, Miller JE, Chueh WC, O’Hayre R, Tong J (2013) Nonstoichiometric perovskite oxides for solar thermochemical H₂ and CO production. *Energy Procedia* 49:2009–2018. <https://doi.org/10.1016/j.egypro.2014.03.213>
108. Galinsky NL, Huang Y, Li F (2013) Iron oxide with facilitated O₂—transport for facile fuel oxidation and CO₂ capture in a chemical looping scheme. *ACS Sustain Chem Eng* 1:364–373. <https://doi.org/10.1021/sc300177j>
109. Mathew DS, Juang RS (2007) An overview of the structure and magnetism of spinel ferrite nanoparticles and their synthesis in microemulsions. *Chem Eng J* 129:51–65. <https://doi.org/10.1016/j.cej.2006.11.001>
110. Ferreira TAS, Waerenborgh JC, Mendonça MHRM, Nunes MR, Costa FM (2003) Structural and morphological characterization of FeCo₂O₄ and CoFe₂O₄ spinels prepared by a coprecipitation method. *Solid State Sci* 5:383–392. [https://doi.org/10.1016/S1293-2558\(03\)00011-6](https://doi.org/10.1016/S1293-2558(03)00011-6)
111. Aston VJ, Evanko BW, Weimer AW (2013) Investigation of novel mixed metal ferrites for pure H₂ and CO₂ production using chemical looping. *Int J Hydrogen Energy* 38:9085–9096. <https://doi.org/10.1016/j.ijhydene.2013.05.078>
112. Cocchi S, Mari M, Cavani F, Millet JMM (2014) Chemical and physical behavior of CoFe₂O₄ in steam-iron process with methanol. *Appl Catal B Environ* 152–153:250–261. <https://doi.org/10.1016/j.apcatb.2014.01.040>
113. Different Types of Solar Concentrators-KTH Roy Institute of Technology Energy Department (n.d.) https://energy.kth.se/compedu/webcompedu/webhelp/S9_Renewable_Energy/B5_Solar_Energy/C3_Advanced_Solar_Thermal/ID107_files/Different_Types_of_Solar_Concentrators.htm. Accessed 2 June 2018
114. Rao CNR, Dey S (2017) Solar thermochemical splitting of water to generate hydrogen. *Proc Natl Acad Sci* 20171700104. <https://doi.org/10.1073/pnas.1700104114>
115. Muhich CL, Ehrhart BD, Al-Shankiti I, Ward BJ, Musgrave CB, Weimer AW (2016) A review and perspective of efficient hydrogen generation via solar thermal water splitting. *Wiley Interdisc Rev Energy Environ* 5:261–287. <https://doi.org/10.1002/wene.174>
116. Lorentzou S, Pagkoura C, Zygogianni A, Karagiannakis G, Konstandopoulos AG (2017) Thermochemical cycles over redox structured reactors. *Int J Hydrogen Energy* 42:19664–19682. <https://doi.org/10.1016/j.ijhydene.2017.06.109>
117. Siegel NP, Miller JE, Ermanoski I, Diver RB, Stechel EB (2013) Factors affecting the efficiency of solar driven metal oxide thermochemical cycles. *Ind Eng Chem Res* 52:3276–3286. <https://doi.org/10.1021/ie400193q>
118. Chueh WC, Abbott M, Scipio D, Haile SM (2010) High-flux solar-driven thermochemical dissociation of CO₂ and H₂O using ceria redox reactions. *Science* 63(80): 1797–1801. <https://doi.org/10.1126/science.1197834>
119. Furler P, Scheffe JR, Steinfeld A (2012) Syngas production by simultaneous splitting of H₂O and CO₂ via ceria redox reactions in a high-temperature solar reactor. *Energy Environ Sci* 5:6098–6103. <https://doi.org/10.1039/C1EE02620H>
120. Houaijia A, Sattler C, Roeb M, Lange M, Breuer S, Säck JP (2013) Analysis and improvement of a high-efficiency solar cavity reactor design for a two-step thermochemical cycle for solar hydrogen production from water. *Sol Energy* 97:26–38. <https://doi.org/10.1016/j.solener.2013.07.032>
121. Agrafiotis C, Roeb M, Konstandopoulos AG, Nalbandian L, Zaspalis VT, Sattler C, Stobbe P, Steele AM (2005) Solar water splitting for hydrogen production with monolithic reactors. *Sol Energy* 79:409–421. <https://doi.org/10.1016/j.solener.2005.02.026>

122. Chambon M, Abanades S, Flamant G (2011) Thermal dissociation of compressed ZnO and SnO₂ powders in a moving-front solar thermochemical reactor. *AIChE J* 57:2264–2273. <https://doi.org/10.1002/aic>
123. Diver RB, Miller JE, Allendorf MD, Siegel NP, Hogan RE (2008) Solar thermochemical water-splitting ferrite-cycle heat engines. *J Sol Energy Eng* 130:041001. <https://doi.org/10.1115/1.2969781>
124. Kim J, Miller JE, Maravelias CT, Stechel EB (2013) Comparative analysis of environmental impact of S2P (sunshine to petrol) system for transportation fuel production. *Appl Energy* 111:1089–1098. <https://doi.org/10.1016/j.apenergy.2013.06.035>
125. Melchior T, Perkins C, Weimer AW, Steinfeld A (2008) A cavity-receiver containing a tubular absorber for high-temperature thermochemical processing using concentrated solar energy. *Int J Therm Sci* 47:1496–1503. <https://doi.org/10.1016/j.ijthermalsci.2007.12.003>
126. Martinek J, Viger R, Weimer AW (2014) Transient simulation of a tubular packed bed solar receiver for hydrogen generation via metal oxide thermochemical cycles. *Sol Energy* 105:613–631. <https://doi.org/10.1016/j.solener.2014.04.022>
127. Roeb M, Neises M, Säck JP, Rietbrock P, Monnerie N, Dersch J, Schmitz M, Sattler C (2009) Operational strategy of a two-step thermochemical process for solar hydrogen production. *Int J Hydrogen Energy* 34:4537–4545. <https://doi.org/10.1016/j.ijhydene.2008.08.049>
128. Roeb M, Säck JP, Rietbrock P, Prah C, Schreiber H, Neises M, de Oliveira L, Graf D, Ebert M, Reinalter W, Meyer-Grünefeldt M, Sattler C, Lopez A, Vidal A, Elsberg A, Stobbe P, Jones D, Steele A, Lorentzou S, Pagkoura C, Zygogianni A, Agrafiotis C, Konstandopoulos AG (2011) Test operation of a 100 kW pilot plant for solar hydrogen production from water on a solar tower. *Sol Energy* 85:634–644. <https://doi.org/10.1016/j.solener.2010.04.014>
129. Kaneko H, Miura T, Fuse A, Ishihara H, Taku S, Fukuzumi H, Naganuma Y, Tamaura Y (2007) Rotary-type solar reactor for solar hydrogen production with two-step water splitting process. *Energy Fuels* 21:2287–2293. <https://doi.org/10.1021/ef060581z>
130. Tamaura Y, Steinfeld A, Kuhn P, Ehrensberger K (1995) Production of solar hydrogen by a novel, 2-step, water-splitting thermochemical cycle. *Energy* 20:325–330. [https://doi.org/10.1016/0360-5442\(94\)00099-O](https://doi.org/10.1016/0360-5442(94)00099-O)
131. Müller R, Haerberling P, Palumbo RD (2006) Further advances toward the development of a direct heating solar thermal chemical reactor for the thermal dissociation of ZnO(s). *Sol Energy* 80:500–511. <https://doi.org/10.1016/j.solener.2005.04.015>
132. Muhich C, Steinfeld A (2017) Principles of doping ceria for the solar thermochemical redox splitting of H₂O and CO₂. *J Mater Chem A* 5:15578–15590. <https://doi.org/10.1039/C7TA04000H>
133. Koepf E, Advani SG, Steinfeld A, Prasad AK (2012) A novel beam-down, gravity-fed, solar thermochemical receiver/reactor for direct solid particle decomposition: design, modeling, and experimentation. *Int J Hydrogen Energy* 37:16871–16887. <https://doi.org/10.1016/j.ijhydene.2012.08.086>
134. Koepf EE, Lindemer MD, Advani SG, Prasad AK (2013) Experimental investigation of vortex flow in a two-chamber solar thermochemical reactor. *J Fluids Eng* 135:111103. <https://doi.org/10.1115/1.4024965>
135. Scheffe JR, Welte M, Steinfeld A (2014) Thermal reduction of ceria within an aerosol reactor for H₂O and CO₂ splitting. *Ind Eng Chem Res* 53:2175–2182. <https://doi.org/10.1021/ie402620k>
136. Gokon N, Mataga T, Kondo N, Kodama T (2011) Thermochemical two-step water splitting by internally circulating fluidized bed of NiFe₂O₄ particles: successive reaction of thermal-reduction and water-decomposition steps. *Int J Hydrogen Energy* 36:4757–4767. <https://doi.org/10.1016/j.ijhydene.2011.01.076>
137. Ermanoski I, Siegel NP, Stechel EB (2013) A new reactor concept for efficient solar-thermochemical fuel production. *J Sol Energy Eng* 135:031002. <https://doi.org/10.1115/1.4023356>
138. Ermanoski I (2014) Cascading pressure thermal reduction for efficient solar fuel production. *Int J Hydrogen Energy* 39:13114–13117. <https://doi.org/10.1016/j.ijhydene.2014.06.143>

139. Mcdaniel A, Randolph K (2015) High efficiency solar thermochemical reactor for hydrogen production. Annual progress report: 2015. https://www.hydrogen.energy.gov/pdfs/progress15/ii_c_1_mcdaniel_2015.pdf
140. Abad A, Gayán P, de Diego LF, García-Labiano F, Adánez J (2013) Fuel reactor modelling in chemical-looping combustion of coal: 1. Model formulation. *Chem Eng Sci* 87:277–293. <https://doi.org/10.1016/j.ces.2012.10.006>
141. Schnellmann MA, Scott SA, Williams G, Dennis JS (2016) Sensitivity of chemical-looping combustion to particle reaction kinetics. *Chem Eng Sci* 152:21–25. <https://doi.org/10.1016/j.ces.2016.05.028>
142. Fan DL-S (2017) *Chemical looping partial oxidation: gasification, reforming, and chemical syntheses*. Cambridge University Press, Cambridge
143. Yates JG, Lettieri P (2016) Fluidized-bed reactors: processes and operating conditions. <https://doi.org/10.1007/978-3-319-39593-7>
144. Kramp M, Heinrich S (2012) Carbon stripping—a critical process step in chemical looping combustion of solid fuels. *Chem Eng Technol* 35:497–507. <https://doi.org/10.1002/ceat.201100438>
145. Cuadrat A, Abad A, Gayán P, De Diego LF, García-labiano F, Adánez J (2012) Theoretical approach on the CLC performance with solid fuels: optimizing the solids inventory. *Fuel* 97:536–551. <https://doi.org/10.1016/j.fuel.2012.01.071>
146. Brown TA, Dennis JS, Scott SA, Davidson JF, Hayhurst AN (2010) Gasification and chemical-looping combustion of a lignite char in a fluidized bed of iron oxide. *Energy Fuels* 24:3034–3048. <https://doi.org/10.1021/ef100068m>
147. Mahalatkar K, Kuhlman J, Huckaby ED, Brien TO (2011) CFD simulation of a chemical-looping fuel reactor utilizing solid fuel. *Chem Eng Sci* 66:3617–3627. <https://doi.org/10.1016/j.ces.2011.04.025>
148. Zhang Y, Chao Z, Jakobsen HA (2017) Modelling and simulation of chemical looping combustion process in a double loop circulating fluidized bed reactor. *Chem Eng J* 320:271–282. <https://doi.org/10.1016/j.cej.2017.03.046>
149. Legros R, Chaouki J, Paris J (1998) Simulation of circulating fluidized bed reactors using ASPEN PLUS. *Fuel* 77:327–337. [https://doi.org/10.1016/S0016-2361\(97\)00211-1](https://doi.org/10.1016/S0016-2361(97)00211-1)
150. Sathwani N, Li P, Eden MR, Adhikari S (2017) Process modeling of fluidized bed biomass-CO₂ gasification using ASPEN plus. In: 27th European symposium on computer aided process engineering, ESCAPE 27, Elsevier B.V., Barcelona, Spain, pp 2509–2514. <https://doi.org/10.1016/B978-0-444-63965-3.50420-7>
151. Fluidization in Aspen Plus—Aspen Technology tutorial (2013)
152. Schaefer RJ (1974) Steady state behaviour of moving bed reactors. *Chem Eng Sci* 29:119–127
153. Rahimi A, Niksiar A (2013) A general model for moving-bed reactors with multiple chemical reactions part I: model formulation. *Int J Miner Process* 124:58–66. <https://doi.org/10.1016/j.minpro.2013.02.015>
154. Parisi DR, Laborde MA (2004) Modeling of counter current moving bed gas-solid reactor used in direct reduction of iron ore. *Chem Eng J* 104:35–43. <https://doi.org/10.1016/j.cej.2004.08.001>
155. Negri ED, Alfano OM, Chiovetta MG (1995) Moving-bed reactor model for the direct reduction of hematite. Parametric study. *Ind Eng Chem* 34:4266–4276. <https://doi.org/10.1021/ie00039a017>
156. Dussoubs B, Jourde J, Patisson F, Houzelot JL, Ablitzer D (2002) Mathematical modelling of uranium dioxide conversion in a moving bed furnace. *Powder Technol* 128:168–177
157. Benjamin BW (1985) Great plains ASPEN model development: gasifier model. Final topical report. Scientific Design Co., Inc., New York, p 180
158. Aspen Plus model for moving bed coal gasifier—Aspen Technology tutorial (2010)
159. Tong A, Zeng L, Kathe MV, Sridhar D, Fan L (2013) Application of the moving-bed chemical looping process for high methane conversion. *Energy Fuels* 27:4119–4128. <https://doi.org/10.1021/ef3020475>

160. He C, Feng X, Hoong K (2013) Process modeling and thermodynamic analysis of Lurgi fixed-bed coal gasifier in an SNG plant. *Appl Energy* 111:742–757. <https://doi.org/10.1016/j.apenergy.2013.05.045>
161. Mukherjee S (2015) Chemical looping combustion for solid fuels—development and optimisation of industrial scale flowsheet models for power generation. University of Surrey. <https://doi.org/10.13140/2.1.2554.1442>
162. Porrazzo R, White G, Ocone R (2016) Techno-economic investigation of a chemical looping combustion based power plant. *Faraday Discuss* 192:437–457. <https://doi.org/10.1039/C6FD00033A>
163. Gençer E, Mallapragada DS, Maréchal F, Tawarmalani M, Agrawal R (2015) Round-the-clock power supply and a sustainable economy via synergistic integration of solar thermal power and hydrogen processes. *Proc Natl Acad Sci* 112:15821–15826. <https://doi.org/10.1073/pnas.1513488112>
164. de la Calle A, Bayon A (2017) Annual performance of a solar-thermochemical hydrogen production plant based on CeO₂ redox cycle. In: Proceedings of 12th international modelica conference, 15–17 May 2017, Prague, Czech Republic, pp 857–866. <https://doi.org/10.3384/ecp17132857>

Internet of Things (IoT) Application in Green Computing: An Overview



Sameer Kumar Das and Hemanta Kumar Palo

Abstract The aim of the paper is to investigate the application domain of the Internet of Things (IoT) for efficient and sustained Green Computing (GC). The essence of this research attributes to many IoT and GC issues that need to be addressed in the creation and maintenance of smart society. A lack of strict adherence to these factors may hamper the very application domain of IoT and threatens their environmental sustainability. An effort is made to segment the entire application domain of IoT-based GC (IoTGC) into five relevant categories for better understanding and clarity. These segments are based on factors such as hardware, software, policy, awareness, and recycling. Detail investigations have been made on these segments to highlight the potential issues that may benefit future researchers in this field.

Keywords Internet of Things · Green computing · Energy efficient · Data center · Environmental sustainability

1 Introduction

There are few information technology buzzwords not possible for the technocrats and industries to neglect or avoid in the coming years. These are the mobile first, artificial intelligence, blockchain, immersive experience, micro-service architecture, Zettabyte Era, robotic process automation, 3D alteration, Internet of Things (IoT), quantum computing, etc. These things are going to change the way we leave today and will rule the future world. Among these trending technologies, this work focuses on the IoT and its application in Green Computing in the current scenario [1].

S. K. Das
Arihant Junior College, Berhampur, Odisha, India
e-mail: sameerdas.gate@gmail.com

H. K. Palo (✉)
Department of ECE, Institute of Technical Education and Research, Siksha 'O' Anusandhan (Deemed to be University), Bhubaneswar, Odisha, India
e-mail: hemantapalo@soa.ac.in

The IoT is associated with the smart technologies that connect almost everything and everybody in this world. The washing machines, refrigerators, microwaves, clocks, water taps, homewares, cooking vessels, or pots are all connected with the digital world. These IoT devices need to be eco-friendly, economically viable, and energy efficient to be environmentally sustainable [2]. The IoT-based Green Computing (IoTGC) is destined for such services for a greener and smarter world. The thrust area has been the design, development, operation, maintenance, and control of energy-efficient IoT systems which are economical and easily acceptable to the end user. The area creates a genuine interest among researchers due to the many challenging issues like global climate change, energy crisis, environmental issues, etc. [3]. As per the International Federation of Global and Green ICT (IFGICT), the Green IoT (IoTGC) or green IT needs to maintain a healthy environment by optimal use of the Internet, computers, and their resources. The computing systems and its peripherals must be economically viable, energy-efficient, safe, easily disposable/recyclable, and environmental-friendly [4, 5]. The technology must be handheld and large-scale data centers. suit all classes of systems, including the handheld and large-scale data centers.

2 Internet of Things (IoT)

The IoT comprises a set of devices, machines or equipment, such as home appliances, vehicles, medical, or agricultural equipment, containing hardware (printers, monitors, servers, actuators, sensors, etc.), software, and connecting network (i.e., Internet) for interaction and communication among these devices effectively and remotely. The application domain of IoT is broadly segmented into the following categories as shown in Fig. 1 [6–9].

Most consumer applications of IoT have been in the area of home automation, smart vehicles, wearable technologies (related to health and sensor appliances by remote control, and monitor capabilities), agriculture, home or smart city, etc. [10–12]. The major areas of focus in these applications are the provision of efficient heating, lighting, air conditioning, security, media systems, etc. For example, one of the application domains of the smart home system using IoT is to provide care for the elderly or disabled individuals. The application domain can be enhanced to tag the IoT devices to emotional speech recognition systems [13, 14]. Use of assistive technologies with voice control systems, pacemakers, Fitbit electronic wristbands, or advanced hearing aids can help people with sight or mobility disabilities. Use of sensors to deal with a sudden fall or an immediate seizure or similar sort of emergency condition of a patient in these homes with additional security devices to alert nearby attendants/medicos can enhance his/her quality of life.

IoT can be used in many commercial applications by collecting and analyzing data related to medical and health care, transportation, agriculture, building, and home automation, etc. Further, monitoring, control, and research on these inputs may provide new insights into these fields. A smart system that creates a link between the

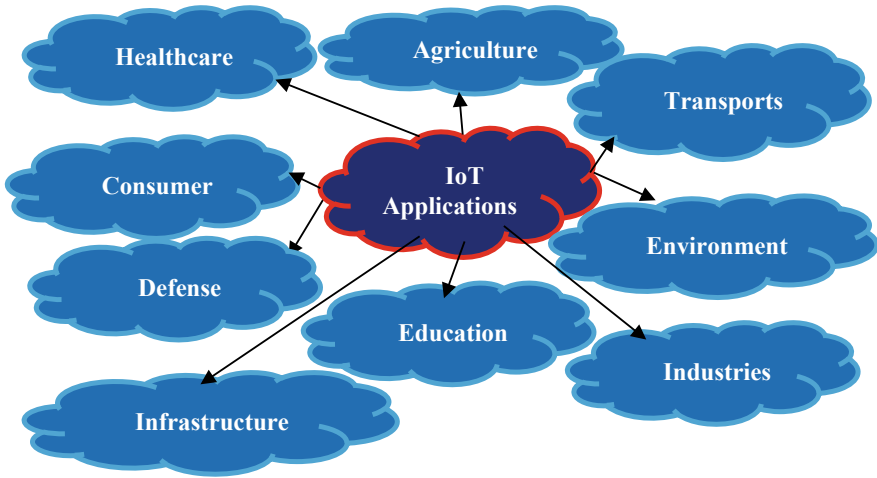


Fig. 1 Applications of IoT

healthcare services, medical resources, physicians, and patients can provide greater freedom and reliability of such systems [15–17]. Another possible approach can be the use of smart beds that are equipped with sensors that tell the monitoring authority when the beds are occupied or vacated. These beds can also be fitted with automatic and appropriate support and pressure devices to eliminate or reduce manual assistance to a patient.

The use of IoT in the transportation system must include an efficient framework that integrates, communicates, controls, and processes information among various devices and sensors attached to such systems and borders. For fruitful interaction and coordination among smart traffic systems, vehicle control, logistics and packaging systems, parking, toll collection, safety, and road assistance, the IoT-based technology remains unparalleled today.

The IoT devices remain essential in any smart infrastructure systems to be it a smart home or an apartment, a campus, or a smart city. Using these devices, it is possible to monitor and control different electrical/electronic and mechanical equipment and devices as per user preferences. Further, the technology is found useful in many service-based industries, product and manufacturing companies, agriculture, infrastructure applications, metropolitan-scale development, energy management, environmental monitoring, living laboratories, security and intelligence, and many similar other fields.

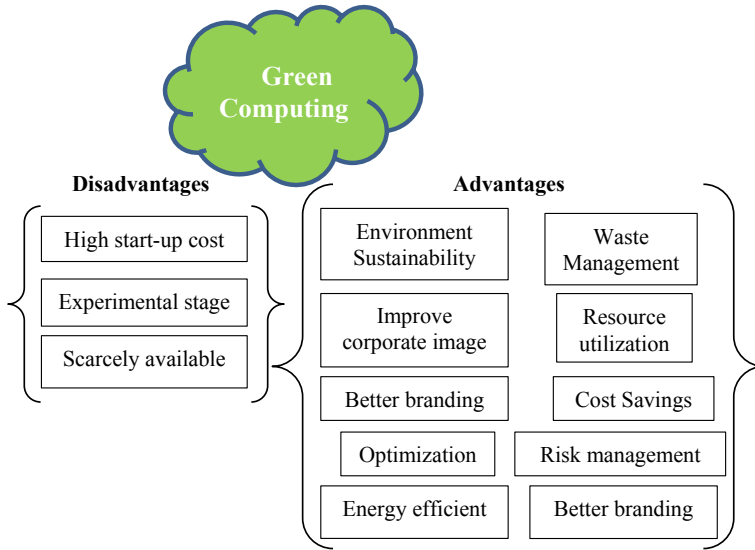


Fig. 2 Advantages and disadvantages of green computing

3 Green Computing

Green Computing deals with efficiency and eco-friendly use of computing machines, peripherals, and associated resources economically. The objective is to design, develop, manufacture, use, and disposal of biodegradable computing machines to maintain a smart world environment [10–12]. The goal of GC is to minimize the energy consumption, reduce greenhouse effect, disposal or recycling of hazardous materials, the biodegradability of defunct materials, and minimization of industrial wastes efficiently. The advantages and limitations of the GC are summarized in Fig. 2.

4 Application of IoT in Green Computing (IoTGC)

The IoTGC has been quite efficiently applied in many vivid application domains that include low-energy-aware communication process and sensors [10], mobile communication and smart phones [6], cloud computing [8], IoT ecosystem formation [9], agricultural and health application [3], and constructing the Green Campus [11]. These IoTGC application areas can be broadly segmented into the following sub-categories as shown in Fig. 3.

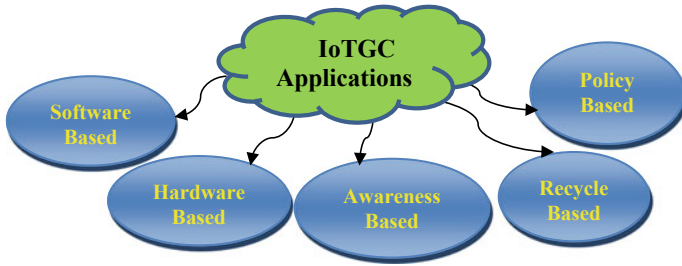


Fig. 3 IoTGC taxonomy and applications

4.1 Policy-Based IoTGC Applications

The policies and strategies in planning and implementation of IoTGC devices based on the real-time data can provide inputs on its future impact on the environment. Further, there can be a considerable amount of energy savings if the policies are decisive at different levels. Policies on energy consumption, automation system, data management, and user feedback, etc. can help both the end user and the industries to take necessary corrective steps for better IoTGC. One such example is the *City Explorer*. It is a home automation solution having layers such as the data collection, data processing, and services that reduce the level of energy consumption by 20% in a real-life scenario [12, 15–17]. The policy-based IoTGC applications are shown in Fig. 4.

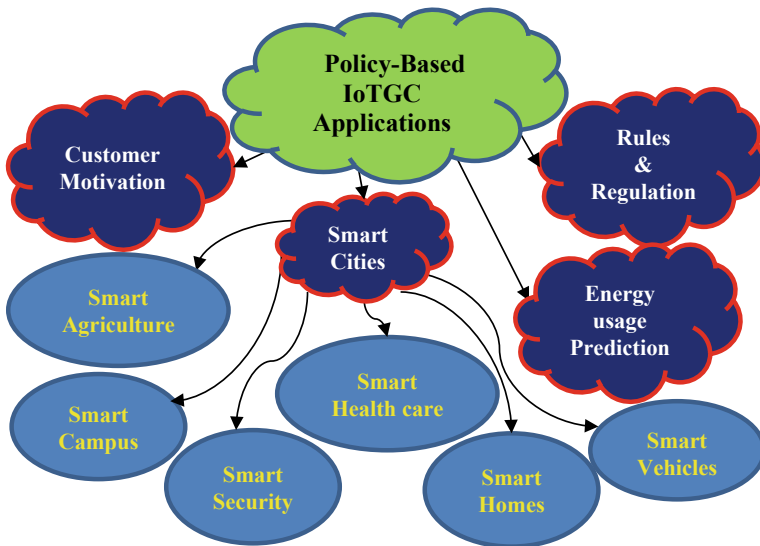


Fig. 4 Policy-based IoTGC applications

4.1.1 Green Campus or Smart Campus

The resources in this world are scarce and limited. It is depleting rapidly with the growth of our global population. For example, the CO₂ concentration in the atmosphere has been below 320 ppm in 1955, whereas the industrialization has increased its level of concentration to 25% by mid-2013 [8]. It is an indication of an unhealthy world which is degraded and polluted very rapidly. In this situation, we cannot afford other environmental crises such as climate change, global warming, soil erosion, and acid rain that may imbalance the world's ecosystem further. This has made many government agencies, and NGOs ponder on ways and means to reduce the carbon footprints for a better environment. This also demands a greater awareness among designers, manufacturers, service providers, and end users to emphasize energy-efficient systems that benefit the society in many ways. In this regard, the intellectuals and educational institutions can play a pivotal role in providing the green world by promoting Green Campus or residence. These smart campuses using IoTGC are essential to counter the curse of depleted resources. It requires the implementation and adaptation of advanced information communication technologies (ICTs) by every institution. The smart campus in these institutions must have the desired automatic monitor and control system to manage all the facilities on these campuses economically and with ease. The smart campus is destined to reduce the energy consumption to the minimum and utilization of the facilities optimally [10]. With the planned IoTGC system, the smart society is capable to manage the computer laboratories, the air conditioners, and the sensor network efficiently and save energy.

4.1.2 Green Health Care and Green Agriculture

The use of an IoT-based GC will provide a context-aware linking system that can change the health care and agriculture, and environment quite effectively [10, 11]. It remains an ambient, working in concert to support people in their day-to-day life using information and intelligence of the IoTGC network. Some of the healthcare applications of IoTGC are the remote health monitoring system, handling of huge data both in time and quantity using the data mining and visualization techniques, etc. The integration of the IoTGC paradigm to these systems will arguably enhance flexibility, intelligence, and interoperability. These devices exchange information through different modules of the system via the Internet, thus significantly simplifying and reducing the administration tasks. For example, the use of an automatic alarm system that intimates the nearest healthcare institute in case of emergency. On similar lines, the IoTGC-based smart agriculture requires the integration of many of the heterogeneous objects such as the humidity sensors, wearable sensing devices, temperature sensors, mobile phones, communication technologies, etc. that offer specific services to make it successful [3].

4.1.3 Smart Vehicles

The development of a smart transport system based on IoTGC has been an area where still research has been going on in recent years. Important features such as e-notification, automated accident detection, and traffic and weather updates using remote servers to vehicle owners and drivers can help save up on time and energy. Similarly, it is possible to restrict the speed of a vehicle using the IoT under adverse weather condition and dense traffic. These IoT devices take into consideration the driver's reaction time and distance traveled and analyze the data to intimate the driver for possible mishaps. Similarly, the use of the GPRS tracking system, GSM modem, prioritization of emergency vehicles, setup of infrared proximity sensors, embedded processor, and XBee-PRO mounted on either side of the roads is few attributes of smart vehicle management [15]. This processor controller updates the delays in traffic light by accounting the number of vehicles passing on the road. The smart vehicular management system must consider traffic congestion as it results in air pollution, frequent idling, and acceleration of vehicles [16]. This, in turn, causes frequent braking, more energy consumption, and wear and tear of the vehicles. Similarly, vehicles equipped with recognition systems to detect the affective states of the driver or its occupant can provide timely assistance by alerting the controlling agencies in disastrous situations [18, 19].

4.1.4 Smart Homes

The IoTGC application for the design and development of a smart home or green home can provide the end-user the facilities to cope up with the busy schedule which he/she is occupied today. Such an intelligent home can be considered as a network of physical devices comprises electronic gadgets, sensors, software, and communication setups inside the home [20]. All the devices such as the mobile phone, computer, air conditioner, heating mechanism, lighting, ventilation, hardware, and security systems in a smart home communicate effectively and seamlessly with each other using sensors and a central axis called the gateways. This technology based on IoTGC has brought a revolution in human life by connecting and communicating with everyone irrespective of time and place. However, these devices need to be manufactured using biodegradable materials for a cleaner environment and should be energy efficient.

4.1.5 Smart Security

The use of the Internet has reduced the gaps between the individuals and between things or both irrespective of time and place. This leads to an exposure of vital and secured information both at private and government entities to the public domain due to the interconnected network and application layers. It is hence highly desirable to take preventive measures to pilferage or leakage of sensitive information to people

or a organization of malicious intention. To prevent any unwanted threats to social, national, environmental, and personal entities, the smart security needs the judicious use of the IoT-based gateways [21]. It must cover these systems with password protection, jumbling, ciphering or cryptographic technologies, and secure routing mechanism by strengthening key management system, etc. to maintain an effective and user-friendly network. Further, the information integrity, authenticity, confidentiality, usability point of departure in the perception layer and its sub-layers should be strictly confined to specific application requirements with the desired security clearance at each level. Similarly, the use of authentication and access control system can eliminate the accessibility of an unauthorized user to the IoT. Another mechanism is the application of an effective intrusion tolerance or fault-tolerant mechanism to maintain normal operation of the communication network.

4.2 Software-Based IoTGC Applications

A few of the software-based IoTGC applications are shown in Fig. 5 and have been explained briefly here.

4.2.1 Cloud Computing

The major function of cloud computing is the delivery of services. Cloud computing has three specific characteristics. These are (a) virtual, (b) dynamic provision on demand, and (c) negotiation. It offers the software and hardware resources as services across a parallel and distributed system. These systems comprise dynamically provisioned interconnected and virtualized computers [7, 8]. These virtues enable cloud computing to reduce carbon emissions. It also helps to reduce energy consumption significantly. The IoTGC data center by moving a few on-premises applications into

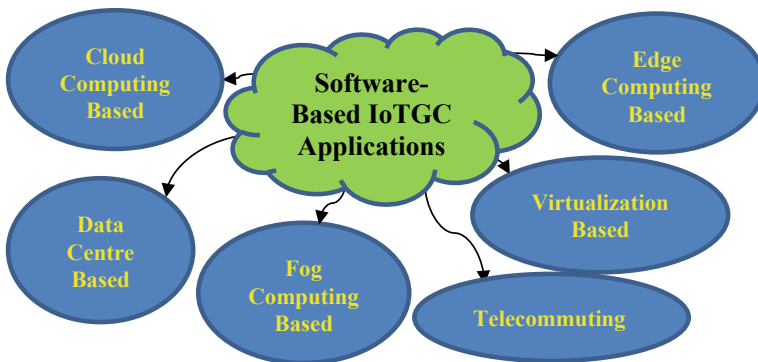


Fig. 5 Software-based IoTGC applications

the cloud can lower the carbon emissions and the energy consumption to a great extent. A very real-life example of cloud computing is the purchase of goods and services online without physically going to the shop floor. The omission of transports by individual reduces greenhouse gas and makes the environment clean.

4.2.2 Edge Computing

It has been observed that cloud computing remains an inefficient approach to process the data when the data reduces at the network edge. New technologies such as the edge and the fog computing replace cloud computing with lower-energy consumption [22, 23]. Edge computing allows the enabling technologies to perform the computation at the edge of the network. On downstream data, it has accomplished on behalf of cloud services, while on upstream data, it is accomplished on behalf of IoT services. The concept of edge signifies to the computing and network resources that are maintained between the path of data sources and cloud data centers. As an example, the smart phone can be considered as an edge between the body things and the cloud. Similarly, a gateway in a Green Campus can be an edge between campus things and cloud. Likewise, the cloudlet and the micro-data center are the edge between the cloud and the mobile device. Although edge computing should be performed at the proximity of data sources, it can be interchangeable with fog computing. However, edge computing is pivotal toward the thing side, whereas fog computing is oriented more toward the infrastructure side. This has made the edge computing an emerging technology similar to cloud computing that benefits the formation of a better green world.

Both edge and fog computing enable the redistributing of computation thus are energy efficient [23]. Edge computing requires a small data center for its efficient function, and thus, the use of refrigerating and maintenance is minimized. This helps in lower-energy utilization and e-waste. It has been used for face recognition with a built a proof-of-concept platform [24]. The response time has been reduced to 169 ms with edge computing as compared to 900 ms with cloud computing as observed by these researchers. In a similar application involving offload computing, the cloudlets prove more efficient for wearable cognitive assistance with an improved response time between 80 and 200 ms. It also reduces energy consumption to approximately 40% by means of cloudlet offloading.

4.2.3 Fog Computing

The fog computing enhances the efficiency and minimizes the amount of data to be transported to the cloud for processing, analysis, and storage. It helps in data security and compliance and is a non-trivial extension of cloud computing. It acts as a platform to bridge various sensing gadgets appeared at the network edge to the core computing structure of the cloud [25]. It has the ability to provide low latency, better quality of services, security, location awareness, privacy protection, and reliability and is

more suitable in real-time applications than cloud computing. In this, the processing generally occurs either in the data hub of the mobile device or on the network edge of a router or a gateway device [26, 27]. Thus, such schemes help the IoTGC when the sensor generates an immense amount of data and remains inefficient to transmit these data via the cloud. Further, the transmission of data between the sensors and the cloud or vice versa requires a large bandwidth that makes the cloud computing inefficient. Thus, in the future, the fog computing is going to replace the cloud computing in the field of low-energy consumption, smart grid, smart transportation system, management systems, smart traffic, health care, and agriculture system, etc.

4.2.4 Telecommuting

Tele-presence or teleconference application can be implemented with ease and efficiency using the IoTGC initiatives. It provides satisfaction for workers and helps to minimize the greenhouse gas effects which occur due to traveling. As a result, the profit margin increases since the office overhead costs are reduced due to a requirement of less space, heat, and lighting for an office [7]. For example, a significant average annual energy savings of 23 kW hours per square foot, i.e., 70% of all energy consumed due to heat, air conditioning, and lighting in a US office building has been reported [28]. Similarly, other related initiatives such as hoteling, consulting, sales, and field service integrated with telecommuting are going to benefit from such a system. The following are a few new avenues that need careful attention for the future researchers of IoTGC to make it more effective. These are broadly extended to

- The energy consumption
- Identification of the key energy indices for efficient utilization of different network elements
- Device and network optimization for carrier telecommunication
- Effective management of the link between the environment and the network technology.

4.2.5 Data Center Based

Data centers remain the biggest consumer of energy and hence need to be optimized to be energy efficient. Thus, these centers need to have context-aware sensing mechanism so as to approach the selective sensing for optimal use of power sources. An effective power scheduling algorithm can energize the useful sensor and cut off the idle sensors as these consume unnecessary power [29]. Effective management of the data center requires meeting the following challenges.

- Evaluation and optimum distribution of workload to different servers' judiciously.
- Identification of potential ideal servers and redistribution of workload.

- The use of renewable power generators.
- An economic consumption of the electricity and the resource.

4.2.6 Virtualization Based

The virtualization-based IoTGC application reduces the number of hardware resources in computing architecture, and hence, the technique can reduce a significant consumption of energy. It is a software-based or virtual process to represent something, such as virtual applications, networks, storage, and servers. It minimizes IT expenses, boosts efficiency, flexibility, scalability, and agility for all size businesses. Use of the Mixed-Integer Linear Programming (MILP) in the virtualization framework with four-layer architecture has resulted in a saving of 36% energy consumption in IoT devices [8]. Few of the benefits of virtualization are:

- Simplified and efficient data center management.
- Greater business continuity and disaster recovery.
- Accessibility of a true software-defined data center.
- Fast provisioning of applications and resources.
- Enhancement of efficiency, productivity, responsiveness, and agility.
- Reduction in the capital and operating cost.
- Elimination or minimization in downtime.
- More workload mobility, availability of resources, improved performance, and automated operations.

Virtualization works on the principle of partitioning, isolation, encapsulation and hardware independence. Similarly, there are different types of virtualizations such as desktop, server, and network.

4.3 *Hardware-Based IoTGC Applications*

The design and developments of computing hardware are paramount in the IoTGC framework to make it eco-friendly, energy efficient and to maintain the environmental sustainability. A brief on few of the IoTGC hardware modules have been discussed below and are shown in Fig. 6.

4.3.1 RFID Based

The radio frequency identification (RFID) remains pivotal in IoTGC application. These are the wireless microchips that help to tag different objects for their identification automatically. These devices can capture data with reduced costs across a wide scale of business activities. Since the IoTGC network consists of different

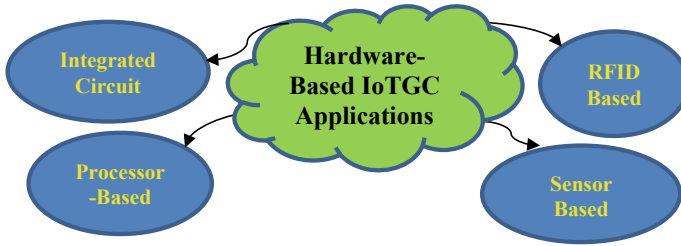


Fig. 6 Hardware-based IoTGC applications

things and objects that need to be identified for a specific function to be performed, the use of RFID is a prerequisite in such network. In such a system, everyday life objects can be radio-tagged for identification and information retrieval for real-time database procurement and storage. These databases so obtained can be used for planning, analysis, research, and many other similar activities [30]. The use of RFID in IoTGC can be extended to many application domains such as manufacturing, health care, agriculture, telemedicine, payment transactions, marine operations, military and defense, and warehousing and distribution systems [31]. However, there are few issues that RFID technology needs to tackle to make its effective implementation in IoTGC applications. These issues are:

- **Collision problems:** The problems occur due to the electromagnetic interference among multiple transmissions, readers, and tags. A few of the reliable and efficient collision avoidance protocols such as the binary tree, query tree, and Frame Slotted Aloha protocol have been used to solve such issues. However, the efficiency of these protocols is below 50% that requires the design and development of new and efficient protocols.
- **Privacy and security concerns:** Inappropriate protection of tags can lead to DoS attacks and eavesdropping of targets besides creating problems in traffic analysis. Many pieces of research are aimed to obtain and implement privacy and security protocols that are economical, reliable, and maintain the applicability of RFID systems.
- **Other challenges:** One of the important challenges in the use of the RFID tags is they are costly. The design and development of engineer tags and readers with guaranteed reliability in identification are other issues which need consideration. Further, the effective integration of RFID into existing systems must be made for the IoTGC application domain successfully. In this regard, suitable RFID middleware that serves as links between the RFID systems and the existing back-end infrastructures can play a major role.

4.3.2 Integrated Circuit (IC) Based

The design and the development of an integrated circuit (IC) for the function of an IoTGC network remain a vital issue in the conservation of energy resources. The integration of sensors, traffic e-waste processing power on a single chip to minimize carbon footprint, and the energy consumption are a few major steps toward the concept of the green sensor in IoTGC domain [8]. A wide portfolio and balanced IC technologies based on logic platforms such as the SOI, CMOS, FinFET, and IPs with specific qualities like power management, NVM, MEMS, CIS, and RF are few immediate requirements of future smart IoTGC devices.

4.3.3 Processor Based

An efficient processor that can be recommended of used in the IoTGC application is the CoreLH. The processor is a dual-core energy-efficient processor with the CoreL which is intended for low-computation tasks, while the CoreH is used for high-computation tasks [8]. In this processor, different tasks are assigned to different cores using an efficient scheduling mechanism to minimize the energy consumption. On the other hand, the mobile application processor such as deep learning (DL) allows the incorporation of advanced attributes on smart phones not possible earlier [32]. For example, Apple's neural engine integration into A11 Bionic chip allows the addition of more accurate face locking feature on the iPhone X. Similarly, the emergence of the neuromorphic processors new to this field can approximate the human neuron mechanism and synapses [33]. The processor can realize the Spiking Neural Network (SNN) to learn both in the spatial as well as the temporal domains. These processors are more energy efficient than the DL and can also tackle different issues of machine learning online. For example, IBM's TrueNorth and Intel's Loihi processors are designed using the neuromorphic architecture. However, it is not yet clear, whether such processors can be efficiently used for broad commercial applications. The Applied Brain Research and Brainchip are few new startup processors where some researches have been done to develop tools and IPs.

4.3.4 Sensor Based

Sensors are essential to detect health status, such as the heartbeat, home security, and air quality. Thus, sensors form an integral part in the industries relying on IoTGC to monitor different systems and processes [5]. In general, a sensor detects the physical changes in an environment, things, or objects such as pressure, temperature, and humidity. It transforms the physical, chemical, or mechanical changes into an electric signal for further processing by the computing machine. A few common sensors that we encounter in daily life include the pressure sensors, thermometers, gas sensors, light sensors, gyroscopes, accelerometers, motion sensors, and many more. A

good sensor should have the desired range (maximum-minimum), sensitivity, and resolution. Sensors can be classified into three major categories [5, 10, 12, 31].

- Active or passive: While active sensors require a source of external power to energize and operate the passive sensors which do not such source.
- Based on the property: Sensors are classified as mechanical, thermal, chemical, etc. based on the purpose a sensor is used for.
- Digital or analog: Based on the type of signals, the sensor generates, and it can be considered as an analog or a digital sensor.

While choosing a sensor to integrate with an IoTGC application, several important factors need to be considered for greater benefit. These factors are the sensor accuracy, its applicability to the task in hand, durability, and the operating environment. To reduce energy consumption in IoTGC sensors, one of the most effective ways is to schedule the power on and off of the sensor according to its use. The use of sensor-on-chips is another way to reduce energy consumption and can be used in different IoTGC-based applications by minimizing traffic and communication overheads. There are other efficient sensors with their own limitations and advantages. However, the design and development of a cost-effective, eco-friendly, energy efficient, and bio-disposable sensor still remain a challenge that suits the application in hand.

4.4 Awareness-Based IoTGC Applications

Although the IoTGC is destined to support smart vehicles and smart spaces, much of its smartness remains invisible to the end user. This is because the user is either unaware or not understand how the IoT can function more effectively. It fails to communicate its purpose, presence, analysis, or practice to the wider audience due to a lack of monitoring. Further, such discrepancies cause obvious privacy and transparency concerns including loss of opportunities for users to provide the desired feedback [8].

The absence of adequate awareness or understanding among the users results in a poor experience/frustration, suspicion, mistrust, inability to capitalize on the benefits as well as the security vulnerabilities [31]. Thus, the scheduled campaigns at regular interval to create awareness among the manufacturer, network providers, and end users to stress on energy-efficient system for better IoTGC application are an area needing further consideration. However, a major issue pertaining to these awareness campaigns is that its effectiveness varies among cultures, countries, and the adaptability of people to such campaigns [34]. The use of smart metering for power conservation must be incorporated into the mind of homeowners, office buildings with regular circulars, and notices. Further, the methods of energy control and its economic use based on that real-time data should be fed to the customers, homeowners, builders, etc. for greater awareness in the society. Few of the areas that the

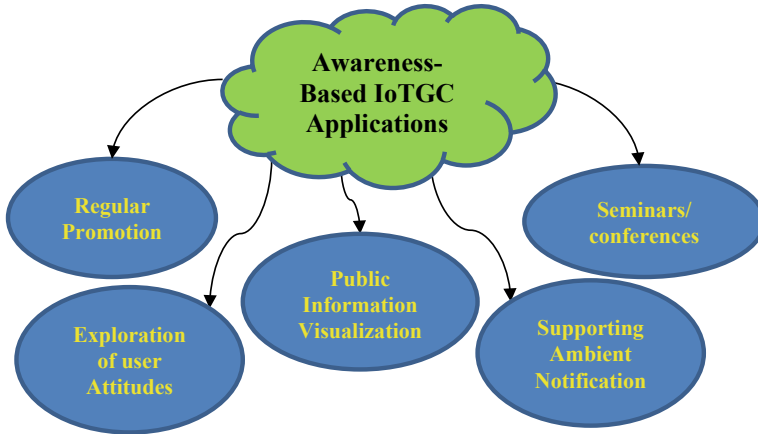


Fig. 7 Awareness-based IoTGC applications

authors feel to be focused to achieve the desired awareness among the end users for the efficient IoTGC system are shown in Fig. 7.

4.4.1 Supporting Ambient Notification

Use of a fixed pervasive display is an easy and effective way to gather awareness of green IoT or IoTGC in an ambient fashion. It will be more appealing than the use of any personal display device such as a smart watch or a mobile phone. The visible display device allows one to capture awareness campaigns while in transit.

4.4.2 Public Information Visualization

Information visualization in a specific domain has been used to disseminate information to experts in earlier days so that they can use their skills to interpret the intended purpose. However, ambient visualizations can be used to inform a broader audience who resides in the periphery of IoT devices. These can also be used for the public who are curious or interested. Few such attempts can be a notice, information percolator (aesthetically pleasing decorative object), the information displayed using air balloons, ambient and embedded displays (LEDs integrated into a Nabaztag rabbit as a visualization component), etc. [30, 31].

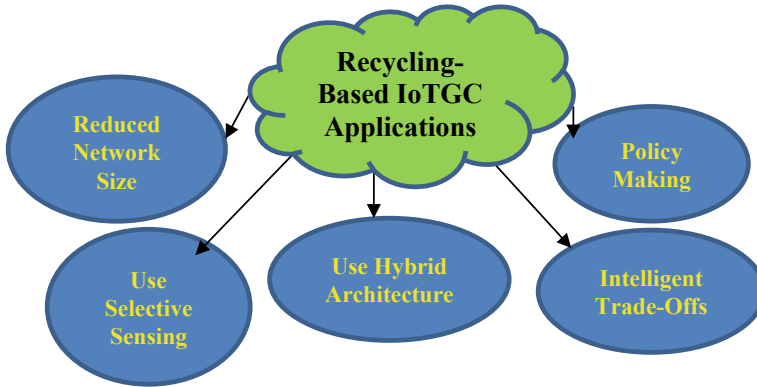


Fig. 8 Steps for recycle-based IoTGC

4.5 *Recycle-Based IoTGC Applications*

To achieve an environmental-friendly IoTGC application, it is highly imperative the materials used to manufacture the IoT devices which are easily recyclable. For example, the use of non-biodegradable materials that worsen the greenhouse effect in the manufacturing of mobile phones like plastic, copper, etc. should be avoided [8]. Similarly, the use of solar energy as a source of a battery can remove many problems in the use of other energizing sources of batteries. Few steps to minimize carbon footprints for a better IoTGC are summarized in Fig. 8.

For energy-efficient IoTGC application, it is mandatory to place the nodes and allocate the routing mechanism judiciously, thereby reducing the network size. Similarly, gathering the data that are essential for a particular framework will promote selective sensing. This way a lot of energy can be saved due to the removal of redundant data. Further, the use of both active and passive sensors, i.e., the hybrid architecture to accomplish various IoTGC tasks, can minimize the consumption of energy. In this regard, the formulation of suitable procedures or policies for users of smart homes, buildings, smart vehicles, or similar application to reduce the energy can help the environment equipped with IoT devices [3]. Finally, the intelligent trade-offs among mostly deciding factors such as the cost, energy consumption, data usage, compressive sensing, and the location of servers and data centers will allow the functioning of IoTGC in a better way.

5 Conclusion

The paper attempts to provide the impact of IoT in today's world and its obligations toward Green Computing. As observed, the IoTGC domain is still in its infant stage and is not readily available to common people due to a high initial setup cost. Further,

it is not applicable to everyone as it needs awareness, knowledge, and willing to accept the technology by the end user. By considering these factors, this work overviews the current trends of IoTGC toward the development of a smart world. It has shown better competence in the field of smart transportation, health care, and the education system. It makes our living area smart by the inclusion of sensors, actuators, and control or monitoring features to many systems such as heating, air conditioning, ventilation, and ambient light sensing control and adjustments. However, the system will die a natural death in case it does not consider the living environment and contaminate it by non-biodegradable wastes. As the system is going to consume a tremendous amount of energy, it requires robust mechanisms and be energy efficient. Greater awareness among users, manufacturers, and network providers of green IoT may lead to better environmental protection with more freedom in its application. Similarly, the introduction of adequate policies and procedures by government agencies and statutory bodies will assist the application domain by reducing the greenhouse effect and optimum utilization of energies and scarce resources.

References

1. Zhu C, Leung VC, Shu L, Ngai EC (2015) Green internet of things for the smart world. *IEEE Access* 3:2151–2162
2. Visalakshi P, Paul S, Mandal M (2013) Green computing. *Int J Mod Eng Res*. In: Proceedings of the national conference on architecture, software systems and green computing (NCASG), pp 63–69
3. Nandyala CS, Kim HK (2016) Green IoT agriculture and healthcare application (GAHA). *Int J Smart Home* 10(4):289–300
4. Kallam S, Madda RB, Chen CY, Patan R, Cheelu D (2017) Low energy-aware communication process in IoT using the green computing approach. *IET Netw* 1–7
5. Mekala MS, Viswanathan P (2018) A survey: energy-efficient sensor and VM selection approach in green computing for X-IoT applications. *Int J Comput Appl* 1–6.
6. Kamilaris A, Pitsillides A (2016) Mobile phone computing and the internet of things: a survey. *IEEE Internet of Things J* 3(6):885–898
7. Curry E, Guyon B, Sheridan C, Donnellan B (2012) Developing a sustainable IT capability: lessons from Intel's journey. *MIS Q Executive* 11(2):61–74
8. Arshad R, Zahoor S, Shah MA, Wahid A, Yu H (2017) Green IoT: an investigation on energy saving practices for 2020 and beyond. *IEEE Access* 5:667–681
9. Mineraud J, Mazhelis O, Su X, Tarkoma S (2016) A gap analysis of internet-of-things platforms. *Comput Commun* 89:5–16
10. Wang HI (2014) Constructing the green campus within the internet of things architecture. *Int J Distrib Sens Netw* 10(3):1–8
11. Wang K, Wang Y, Sun Y, Guo S, Wu J (2016) Green industrial internet of things architecture: an energy-efficient perspective. *IEEE Comm Mag* 54(12):48–54
12. Moreno MV, Ábeda B, Skarmeta AF, Zamora MA (2014) How can we tackle energy efficiency in IoT based smart buildings? *Sensors* 14(6):9582–9614
13. Palo HK, Mohanty MN, Chandra M (2018) Speech emotion recognition of different age groups using clustering analysis. *Int J Inf Retrieval Res* 8(1):69–85
14. Palo HK, Mohanty MN, Chandra M (2017) Emotion analysis from speech of different age groups. In: Proceedings of the second international conference on research in intelligent and computing in engineering, vol 10, pp 283–287

15. Keertikumar M, Shubham M, Banakar RM (2015) Evolution of IoT in smart vehicles: an overview. In: IEEE international conference on green computing and internet of things (ICGCIoT), pp 804–809
16. Md. AbdusSamad K, Jun I, Tomohisa H, Akira O, Kazuyuki A (2014) Smart driving of a vehicle using model predictive control for improving traffic flow. *IEEE Trans Intell Transp Syst* 15(2):1–11
17. Izquierdo MZ, Santa AJ, Gómez-Skarmeta AF (2010) An integral and networked home automation solution for indoor ambient intelligence. *IEEE Pervasive Comput* 9(4):66–77
18. Palo HK, Chandra M, Mohanty MN (2018) Recognition of human speech emotion using variants of mel-frequency cepstral coefficients. In: *Advances in systems, control and automation, lecture notes in electrical engineering*, vol 442. Springer Nature Singapore, pp 491–498
19. Palo HK, Kumar P, Mohanty MN (2017) Emotional speech recognition using optimized features. *Int J Res Electron Comput Eng* 5(4):4–9
20. Galinina O, Mikhaylov K, Andreev S, Turlikov A, Koucheryavy Y (2015) Smart home gateway system over Bluetooth low energy with wireless energy transfer capability. *EURASIP J Wireless Comm Netw* 1:1–18
21. Gou Q, Yan L, Liu Y, Li Y (2013) Construction and strategies in IoT security system. In: IEEE international conference on green computing and communications and IEEE internet of things and IEEE cyber, physical and social computing, pp 1129–1132
22. Shi W, Cao J, Zhang Q, Li Y, Xu L (2016) Edge computing: vision and challenges. *IEEE Internet of Things J* 3(5):637–646
23. Sun X, Ansari N (2016) EdgeIoT: mobile edge computing for the internet of things. *IEEE Comm Mag* 54(12):22–29
24. EPA Office Building Energy Use Profile (PDF). EPA. August 15, 2007. Archived from the original (PDF) on 6 Mar 2009, Retrieved 17 Mar 2008
25. Yi S, Hao Z, Qin Z, Li Q (2015) Fog computing: platform and applications. In: *Proceedings of 3rd IEEE workshop hot topics web system and technology (HotWeb)*, Washington, DC, USA, pp 73–78
26. Atlam H, Walters R, Wills G (2018) Fog computing and the internet of things: a review. *Big Data Cogn Comput* 2(2):10
27. Al-Azez T, Lawey AQ, El-Gorashi TEH, Elmighani JMH (2015) Virtualization framework for energy efficient IoT networks. In: *Proceedings of IEEE 4th international conference on cloud network (CloudNet)*, pp 74–77
28. Colella R, Catarinucci L, Tarricone L (2016) Improved RFID tag characterization system: use case in the IoT arena. In: *IEEE international conference on RFID technology and applications (RFID-TA)*, Foshan, pp 172–176
29. Peoples C, Parr G, McClean S, Scotney B, Morrow P (2013) Performance evaluation of green data center management supporting sustainable growth of the internet of things. *Simul Model Pract Theory* 34:221–242
30. Mirlacher T, Buchner R, Förster F, Weiss A, Tscheligi M (2009) Ambient rabbits likeability of embodied ambient displays. In: *European conference on ambient intelligence*. Springer, Berlin, pp 164–173
31. Mikusz M, Houben S, Davies N, Moessner K, Langheinrich M (2018) Raising awareness of IoT sensor deployments
32. Mohammadi M, Al-Fuqaha A, Sorour S, Guizani M (2018) Deep learning for IoT big data and streaming analytics: a survey. *IEEE Commun Surv Tutor* 20(4):2923–2960
33. Venkataramani S, Roy K, Raghunathan A (2016) Efficient embedded learning for IoT devices. In: *21st Asia and South Pacific design automation conference (ASP-DAC)*. IEEE, pp 308–311
34. Ghimire S, Luis-Ferreira F, Nodehi T, Jardim-Goncalves R (2017) IoT based situational awareness framework for real-time project management. *Int J Comput Integr Manuf* 30(1):74–83

A PSO-Based Multi-objective Optimization to Satisfy the Electrical Energy Demand Through Renewable Energy Integration: A Case Study



Mahesh Wagh and Vivek Kulkarni

Abstract In the pathway of sustainable development, the energy consumption achieves crest and becomes a global issue. Several countries are trying to tackle this problem of increase in demand of energy and limited reserves of fossil fuel-based resources. Also, the energy consumption giving rise to the environmental issues is another big concern. Researchers, all over the globe, are very keen about this problem and suggesting solutions in the form of energy efficiency, conservation and renewable energy technology. Nowadays, larger penetration of renewable energy resources in grid is getting much more lead and importance. This paper reveals a particle swarm optimization (PSO) technique in Microsoft XL optimizer and is utilized to satisfy the electrical demand for the case study of Kolhapur in Maharashtra state in India. The 40% of total electrical the demand is tried to satisfy due to lack of supportive grid capability to accommodate the renewable electricity more than this. Solar PV, wind energy and small hydropower resources are utilized to satisfy the electrical demand. An optimization problem based on multi-objective is formulated for the integrated combination of resources to satisfy the average single-day electrical demand of first of each month for the whole year. Mainly, cost and CO₂ emission reduction are the objectives considered to solve the constant optimization problem.

Keywords Particle swarm optimization (PSO) · Multi-objective optimization · Integrated renewable energy sources · Electrical demand satisfaction

M. Wagh (✉)

Department of Technology, Shivaji University, Kolhapur, Maharashtra 416004, India
e-mail: waghmahesh2006@gmail.com

V. Kulkarni

Department of Mechanical Engineering, Sanjay Ghodawat Group of Institutions, Atigre, Kolhapur, Maharashtra, India
e-mail: vvku20@rediffmail.com

© Springer Nature Singapore Pte Ltd. 2020

A. K. Bhoi et al. (eds.), *Advances in Greener Energy Technologies*,

Green Energy and Technology, https://doi.org/10.1007/978-981-15-4246-6_5

Abbreviations

PSO	Particle Swarm Optimization
MOO	Multi-Objective Optimization
ACO	Ant Colony Optimization
DE	Differential Evolution
LT/HT	Low Tension/High Tension
IRES	Integrated Renewable Energy Sources
PV	Photovoltaic
FY	Fiscal Year
SA	Simulated Annealing
MLD	Million Litres per Day

1 Introduction

Energy is one of the important parameters in the discussions of sustainable development. As crest of energy consumption is coming, the energy conservation becomes a worldwide concern. Various nations are initiating and promoting energy conservation and energy efficiency. The rising energy requirement and restricted supply of the conventional sources have upstretched the worries of the researchers all over the world to search for unconventional resources. Moreover, to the growing energy requirement concerns, the red alarms of environment have led to the development of renewable energy technologies in energy sector. Renewable or unconventional energy resource technologies comprise the energy generation from unpolluted and inexhaustible sources like solar, wind, hydro, biomass, etc. [1]. In developing countries like India, the formation of energy policy begins with an energy security and climate change mitigations. Renewable energy has become a significant chunk of the energy policy formation in India. Due to intermittency in availability of the renewable energy resources, there are many restrictions to use these resources as an alternative to the conventional grid energy. However, integration of renewable energy systems consisting of two or more renewable energy resources has been recommended to overcome the restrictions in the use of individual renewable energy sources and to reduce the cost and increase the reliability. Optimal design of an integrated renewable energy sources (IRES) requires correct selection and sizing of different options based on an appropriate optimization strategy. Without considering the design optimization, there is a possibility that the selected size of these energy generators is above the required capacities and consequently resulting in a higher cost. Hence, in the design phase of these generators, it is desired to evaluate any possible configuration to get the optimal alternative and the corresponding optimal capacity of selected generators based on a set of predefined criteria [2]. The targets of 175 GW of generation from renewable energy resources are set by Government of India, by year 2022. It consists of 100 GW of solar, 60 GW of wind, 10 GW of biomass power

and 5 GW of small hydropower. The fastest economically growing state of Maharashtra in India has the largest base of electricity consumers in the country, with per capital energy consumption of 1239 kWh. For fiscal year (FY) 2019, the energy requirement of the Maharashtra state is expected to go from 132,700 GWh in FY15 to nearly 18,315 GWh in FY19, translating into a total peak power requirement of 26,432 MW in FY19 [3]. Considering high potential of RE in the Maharashtra state, Indian government has set objective of achieving 22 GW RE capacity to Maharashtra by 2022 [4]. Maharashtra also has set objective of achieving 14.4 GW of RE capacity by 2020 under its RE policy 2015. To achieve these targets, there is need for growth of generation through renewable [4]. Most of the existing literature has been reviewed, and it is found that the modelling of IRES based on the requirement of the demand and availability of those resources in optimal manner is performed to a certain limits. Because of the uncertain nature of renewable energy sources, multi-objective models are used by researchers, and reduction in energy generation cost, reduction in total life cycle of CO₂ emissions and maximization of use of locally available renewable energy resources are the main objectives. Researchers have used the traditional mathematical techniques like linear programming, non-linear programming, stochastic mathematical programming, interval mathematical programming and fuzzy mathematical programming. Many of the researchers were fond of newly advanced techniques and have utilized the techniques like Pareto optimal frontier (POF), particle swarm optimization (PSO), analytical hierarchical process (AHP), genetic algorithm, and evolutionary algorithms for modelling and optimization. Hybrid Optimization Model for Electric Renewable (HOMER), HOGA, iHOGA are some popular software used by many researchers in cost optimization of renewable energy systems. The impact of large-scale integration of intermittent energy sources is studied by some researchers by using WASP-IV model (Wien Automatic System Planning) software tool. Regression analysis, Long-range Energy Alternatives Planning (LEAP) system and MARKAL simulations also have been used by many of the researchers for the long-term and short-term energy and demand forecasting. Particle swarm optimization algorithm was used by many researchers to solve linear, nonlinear and mixed-integer optimization problems. Compared to other optimization techniques, PSO can achieve global minimum in less time. PSO technique is applied to solve the urban energy planning issues in minimum generation costs. In this paper, a case study of Kolhapur is considered to satisfy the electrical energy demand. A multi-objective optimization problem is developed and solved with the help of PSO algorithm by using Microsoft XL optimizer. Solar photovoltaic (PV), wind energy and micro-hydro are the renewable energy resources utilized to fulfil the electrical energy demand of Kolhapur. The methodology of the study is explained in following flowchart in Fig. 1.

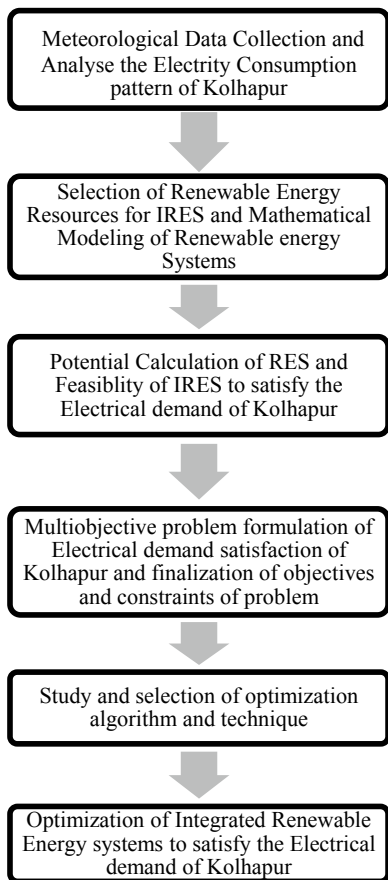


Fig. 1 Methodology of the proposed case study of Kolhapur

2 Study Area Scenario

Kolhapur district is situated in the south-west part of Maharashtra state in the Sahyadri mountain region. Out of the total area available, 28% is allotted for residential use, 4.45% for commercial and 1.52% for industrial sectors. The remaining 27.63% is allotted for agricultural use, the rest for utilities and 1.07% for water bodies at Kolhapur. It gets a raw water supply of 128 MLD, of which the corporation supplies 120 MLD; 8 MLD is obtained through groundwater sources [3]. Kolhapur city has groundwater sources of Panchganga River 6 km via Bawada and 11 km via Shingnapur [5]. Table 1 furnishes the detailed information about the sector-wise area usage in Kolhapur, Table 2 provides information of climatic data collected from NASA GEOS-4 model elevation, and Fig. 2 furnishes the detailed map of Kolhapur in ArcGIS.

Table 1 Sector-wise area distribution of Kolhapur

Sector	Area in km ²
Residential	18.75
Commercial	2.97
Industrial	1.02
Public/semi-public	9.41
Road and transport	2.07
Open space	7.67
Public services and crematories	1.07
Defence	1.2
Water bodies	0.72
Agriculture	18.46
Barren land	0.11
Undeveloped	3.37
Total	66.82

Table 2 Climatic data of Kolhapur city from the NASA GEOS-4 model elevation

Monthly averaged direct insolation incident on a horizontal surface (kWh/m ² /day)	5.16
Monthly averaged diffuse radiation incident on a horizontal surface (kWh/m ² /day)	1.81
Monthly averaged diffuse radiation incident on a horizontal surface (kWh/m ² /day)	3.79
Monthly averaged relative humidity (%)	58.54
Monthly averaged atmospheric pressure (kPa)	95.7
Monthly averaged precipitation (mm/day)	3.36



Fig. 2 Topographic map of Kolhapur (ArcGIS)

3 Electricity Consumption of Kolhapur

Energy consumption data of Kolhapur district is collected from Kolhapur subdivision of Maharashtra State Electricity Distribution Company Limited (MSEDCL). The electricity is used by various types of consumers, and they are broadly classified into domestic, commercial, industry and agriculture. The low-tension, LT (low-voltage) line supplies electricity to domestic sector, group housing, commercial complexes, temporary connections, hoardings/advertisements and crematorium/burial. The high-tension, HT (high-voltage) line supplies electricity to commercial complexes. Both LT and HT lines supply electricity to industrial and agricultural sectors depending upon their electrical demand. For simplification, it is necessary to merge some sectors as HT industrial, HT seasonal, HT group housing, HT temporary supply, HT public services, LT industrial, LT power room, LT poultry will merge into industrial sector, HT commercial, HT complex, LT commercial, LT prepaid commercial in to commercial sector, HT agriculture, LT agriculture into agricultural sector and LT domestic, hoardings, street lightening, temporary connection, LT public services, LT prepaid residential, LT prepaid commercial, LT prepaid temporary into residential sector. Figure 3 reveals the average month-wise electrical consumption of Kolhapur in 2016.

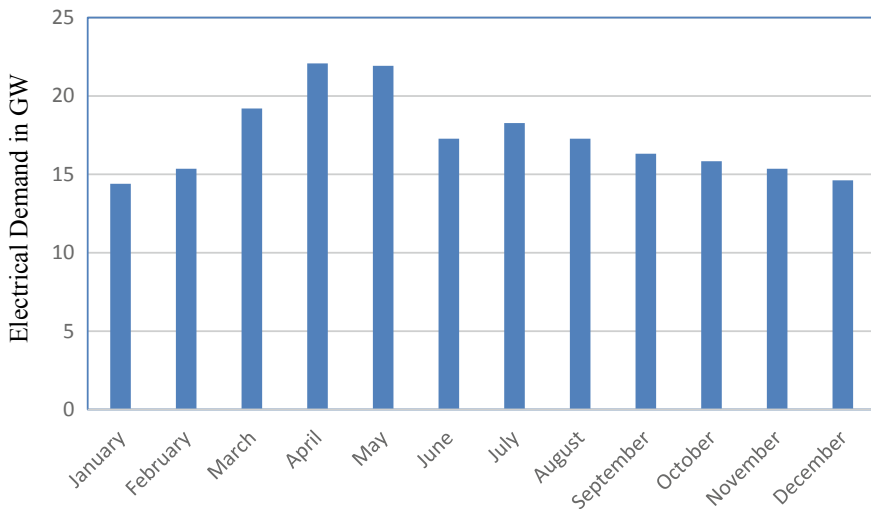


Fig. 3 Average month-wise electricity consumption of Kolhapur

4 Mathematical Modelling of Renewable Energy Systems

The advancement in the exploitation of renewable energy can certainly expand the diversity in the energy generation scenario and can be influential in gaining continual and sustainable energy supply. Following are the renewable energy sources which are taken into consideration to fulfil the electrical demand of Kolhapur.

4.1 Solar Photovoltaic Energy System

The intensity of solar radiation decide the amount of electrical power generation from solar photovoltaic energy systems. On a fixed and inclined solar PV panel, the total hourly solar radiation (H_T) can be calculated as [6]

$$H_T = H_b R_b + H_d R_d + (H_b + H_d) R_r \quad (1)$$

where H_T is in kWh/m², H_b is the beam part of solar radiation (kWh/m²), H_d is diffused part of solar radiation (kWh/m²), R_b is tilt factor for beam radiation, R_d is tilt factor for diffused radiation and R_r is tilt factor for reflected part of solar radiations [6]. Hourly power output of PV system (P_{PV}) is calculated as

$$P_{PV} = \eta \cdot H_T \cdot A \quad (2)$$

where η is the conversion efficiency of PV system and A is the surface areas of PV system. Annual energy output of PV system E_{PV} is estimated as

$$E_{PV} = \sum_{i=1}^{8760} P_{PV}(i) \quad (3)$$

4.2 Wind Energy System

The output of wind energy system principally depends upon the swept area of the rotor blade and cube of the wind speed. Power available in the wind P_{wind} is given by [7]

$$P_{wind} = \frac{1}{2} \rho A V_{wind}^3 \quad (4)$$

where ρ is air density (kg/m³), A is a swept area by blades (m²) and V_{wind} is wind velocity (m/s). It was proved that the maximum power extraction from the wind is

not more than 60% for an ideal wind turbine, but in the practical case, including all the efficiencies of transmission and electrical power conditioning equipment, it is up to 35% [7]. The extractable power from the wind turbine is given by

$$P_{\text{wind}} = \frac{1}{2} C_p \rho A V_{\text{wind}}^3 \quad (5)$$

Annual energy output of wind energy system E_{wind} is estimated as

$$E_{\text{wind}} = \sum_{i=1}^{8760} P_{\text{wind}}(i) \quad (6)$$

4.3 Micro-hydro Energy System

In the run-off river, if the rainfall data and catchment area are known, then the power generation from the micro-hydro power plant can be estimated. In the modelling of the micro-hydro system, the first step is to find out the flow rate [8]. The hydropower potential can be written as

$$Q_{\text{site}} = K \cdot \frac{A_{\text{site}}}{A_{\text{gauge}}} \cdot Q_{\text{gauge}} \quad (7)$$

where A_{site} is catchment area of power plant (m^2), A_{gauge} is catchment area of gauge (m^2), Q_{site} is discharge at site (m^3/s), Q_{gauge} is discharge at gauge (m^3/s) and K is scaling constant or function. The mechanical power generated by the turbine is given by [8]

$$P = \eta_{\text{total}} \cdot \rho \cdot Q \cdot g \cdot H \quad (8)$$

where P is mechanical power output produced at the turbine, η_{total} is hydraulic efficiency of the turbine, ρ is density of water ($1000 \text{ kg}/\text{m}^3$), g is acceleration due to gravity ($9.81 \text{ m}/\text{s}^2$) and H is effective pressure head (m).

5 Potential Calculation of RES to Satisfy the Electrical Demand of Kolhapur

As three renewable energy resources are selected, which are solar photovoltaic, wind and micro-hydro, the theoretical calculation of potentials is required to check the feasibility of RES to satisfy the electrical demand.

5.1 Solar Photovoltaic Energy Potential Calculation

Photovoltaic module installation in urban areas is usually done on building rooftops, because of more resource availability, less visual impact and even for safety reasons. In Fig. 4, by knowing the total gross rooftop area, the next essential and required step is to quantify the amount of useful rooftop area, capable of accommodating photovoltaic systems [9, 10].

From Fig. 4, total roof top area available for solar PV = 1.926 km². Monthly average direct solar insolation is 5.16 kWh/m²/day. Considering a polycrystalline solar panel having a module efficiency of 13.5%, the solar potential available is calculated using Eq. (2) as follows:

$$\begin{aligned} \text{Solar PV potential available} &= \text{Solar insolation at tilted} \\ &\quad \text{surface with } 17^\circ \times \text{Solar panel} \\ &\quad \text{Efficiency} \times \text{Area Available} \end{aligned}$$

$$\therefore \text{Solar potential available} = 58.46 \text{ MW}$$

$$\text{Actual energy produced per year} = 697,678 \text{ MWh/year}$$

$$\text{Daily energy production} = 1911.44 \text{ MWh/day}$$

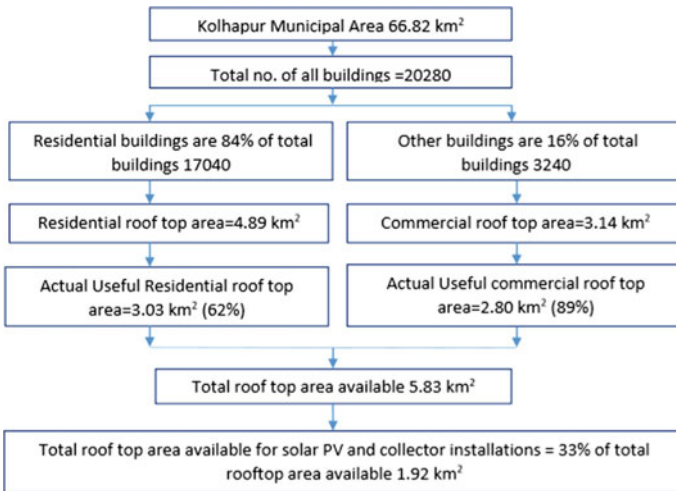


Fig. 4 Gross rooftop area available for solar PV system

5.2 Wind Energy System Potential Calculation

Wind energy exploitation in urban areas is not so advanced as solar PV or solar thermal for hot water. Using the System Advisor Model (SAM) developed by National Renewable Energy Laboratory (NREL), the area required for 1 kW wind energy system is calculated as 20 m². Industrial and barren lands and defence areas are considered for installation. Area available from industrial sectors is the area other than building footprint area and is considered as 0.7 [9]; therefore, total land area available summarizes to 1.59 km², and total of 4529.4 kW potential is calculated using mean wind velocity of 3.79 m/s for 50 m height. Available wind energy potential is 84.15 MW, and extractable wind energy potential is 4.53 MW.

5.3 Micro-hydro System Potential Calculation

Hydro projects up to 1 MW are recognized as micro-hydro power plants. Kolhapur has river banks of Panchganga River, 6 km via Bawada and 11 km via Shingnapur. Discharge and head data of Panchganga River is taken from Real-Time Data Acquisition System for Krishna basin, and hydropower potential is calculated. Annual average discharge rate of Panchganga River is 0.044 m³/s, and four 10 kW of micro-hydro systems can be installed on Panchganga River for the 50-m head, which summarizes to available potential of hydropower system is 2303.43 MW and extractable potential is 21.5 MW.

6 Multi-objective Problem Formulation

When there are simultaneous conflicting objectives to satisfy, the multi-objective optimization (MOO) problem formulation plays an important role. In the single-objective optimization, a Pareto optimal solution is generated and they are called as equally efficient solutions instead of single solution. A MOO problem comprises a set of objective functions that can be either maximized or minimized. A solution space is generated with the help of constraints which are given in the problem formulation. The multi-objective optimization problem formulation is as follows:

$$x = (a, b)^c$$

where a = first objective function, b = second objective function, c = constraints.

Table 3 Levelized costs of renewable resources

Renewable resource	Levelized cost of electricity (Rs./kWh)
Solar PV	6.79
Wind	5.33
Hydro	3.76

6.1 Economic Objective

Minimization of cost is always a first objective of any project. Minimization of levelized cost of electricity is considered as an economic objective, and the objective function is formulated as follows [11–13]:

$$\text{Total daily cost of generation} = \min \sum_{i=1}^N E_i \times C_i \tag{9}$$

where i is for energy system, $i = 1$ for solar photovoltaic energy system, $i = 2$ for wind energy system, $i = 3$ for small hydro energy system, $N =$ number of energy system, $E_i =$ total number of unit generated and $C_i =$ levelized cost of energy system.

For Kolhapur, Maharashtra Electricity Regulatory Commission is the supreme body for deciding the renewable energy costs [8, 14]. Table 3 depicts the levelized cost of renewable energy systems.

6.2 Emission Minimization Objective

Second objective is selected as minimization of CO₂ emissions and is defined. The entire life cycle emissions of the renewable energy generation systems are taken into considerations, and second objective function $f_2(x)$ is formulated, which are given in Table 4.

$$\text{Total daily CO}_2 \text{ emission} = \min \sum_{i=1}^N \text{CO}_{2i} \times E_i \tag{10}$$

Table 4 CO₂ Emissions by renewable energy systems

Renewable resource	Embedded emission gCO ₂ /kWh
Solar PV	5.34
Wind	3
Hydro	4.6

where CO_{2i} = CO_2 emission from energy system, E_i = total number of unit generated, N = number of energy system and CO_2 emissions by renewable energy systems are given as in Table 4 [15].

7 Constraints

The decision variables are confined to the values of the lower- and upper-bound limits. This is called as constraint optimization [16]. The lower- and upper-bound limits create a decision variable space. To obtain a feasible solution, the constraint limits should not be violated. In the practical design problems of IRES, one or more constraints can also be considered and satisfied [12].

7.1 Supply–Demand Constraint

IRES must be able to satisfy the demand of study location Kolhapur. Supply should match the demand at any time of the project life. As the generation of renewable energy resources is dependent on climatic condition, the result of the model should give an optimum combination of three generating resources which are solar PV, wind and small hydro in order satisfy the demand of study area [11–13].

$$\sum_{i=1}^N E_i \geq D \quad (11)$$

D = Peak demand of energy at that time and E_i = total electricity generated by combination of IRES.

7.2 Potential Constraint

The energy flowing in the component in every time $E_i(t)$ must be less than the component's capacity. Potential available for the components is dependent on climatic conditions [11–13]

$$\sum_{i=1}^N E_i \leq \sum_{j=1}^N P_j \quad (12)$$

P_j = Potential of resource and generated electricity by solar, wind and small hydro must not be greater than available potential.

7.3 Emission Constraint

The target emission is set as average of the three CO₂ emissions by solar, wind and small hydro. Target emission is set as 4.3133 gCO₂/kWh.

$$\sum_{i=1}^N \text{CO}_{2i} \times E_i \leq T_e \quad (13)$$

T_e = Target emission level. The following vector defines the decision variables [9]

$$D = [IVHQ] \quad (14)$$

where I = solar radiation (kWh/m²/day), V = wind speed (m/s), H = head (m) and Q = discharge (m³/s).

8 Optimization Algorithm

Optimization algorithms are classified as deterministic algorithms and probabilistic algorithms. For a given problem, if a clear relation between the characteristics of the possible solutions and their utility exists, the deterministic algorithms are utilized [17]. Different optimization algorithms are studied, and their comparison is summarized in Table 5 to finalize the optimization algorithm technique for modelling of IRES to satisfy the electrical demand in Kolhapur.

From the above comparison table, PSO algorithm is selected, because it does not require ranking of solution, has less computation time, mutation and overlapping is restricted, and has more effective memory capability and simplified calculations. The selected PSO algorithm is applied with following selected parameters as shown in Table 6.

9 Multi-objective Optimization Using PSO

To obtain an optimized combination of IRES to satisfy the electrical demand of Kolhapur using XL optimizer tool, first step is the input to the model. Input to the model is variables of mathematical models of RES's, which are solar insolation for solar photovoltaic energy system, wind speed for wind energy system and water head and discharge rate for small hydro energy system. Solar radiation and wind speed input is taken from the NASA-SSE which gives a 22-year averaged value of parameters. Water head and discharge rate required for the small hydro energy system is taken from the Krishna–Bhima basin online. Various scenarios are generated to satisfy the electrical demand of Kolhapur. First day of each month is considered as

Table 5 Comparison of optimization algorithms

Algorithms	GA	Memetic	PSO	ACO	SA	DE
Optimization method	Metaheuristic population based	Metaheuristic population based	Metaheuristic population based	Metaheuristic population based	Metaheuristic trajectory based	Metaheuristic population based
Objective function	Multi-objective	Multi-objective	Multi-objective	Multi-objective	Multi-objective	Multi-objective
Parameters affecting performance	Population size, no. of generations, crossover rate, mutation rate	Population size, no. of generations, crossover rate, mutation rate	Population size, no. of generation cycles, maximum change of velocity and positions, inertia constant (ω)	No. of ants, no. of iterations, pheromone evaporation rate, pheromone reward factor	Temperature, no. of iterations, imbalance factor (α), size factor	Population size, mutation factor
Influence of population size on solution processing time	Exponential	Exponential	Linear	Linear	Linear	Linear
Type of variable	GA study is steady state, and variables taken are real-coded	Real coded	Real no.	Real coded	Real no.	
Inspiration from nature	Survival of fittest	Survival of genetically fittest and most experienced	Flock migration, fish schooling	Shortest path to food source	NA	
Ability to reach good solution without local search	Less	Less	More			More

(continued)

Table 5 (continued)

Algorithms	GA	Memetic	PSO	ACO	SA	DE
Requires ranking of solution	Yes	Yes	No	No		No
Effect of homogeneous sub-grouping	Yes		Yes	Yes	NA	NA
Tendency for premature convergence	Medium	Medium	High			Low
Average fitness cannot get worse	False		False			True
Applications	Electrical engineering and circuit design, networking and communications, economics and finance, data mining and data analysis, image processing, combinatorial optimization, etc.	Combinational optimizations, operations research, biochemistry, engineering, structural optimization and design, etc.	Function optimization, combinatorial optimization, networking and communication, geometry and physics, machine learning, electrical engineering and circuit design, chemistry and chemical engineering, etc.	Combinational optimization, networking and communication, scheduling, etc.	Image processing, chemistry and chemical engineering, combinational optimization, function optimization, etc.	Engineering, structural optimization and design, function optimization, scheduling, electrical engineering and circuit design, etc.

(continued)

Table 5 (continued)

Algorithms	GA	Memetic	PSO	ACO	SA	DE
Objective function	Minimization of power loss, reliability of the system while minimizing the system cost, compromised non-inferior solution is obtained		Reduce THD losses and improve voltage profile, power loss reduction, AHPS optimal sizing, multi-criteria design of HPGS	DG investment in DG and its operating cost minimization		
Advantages	Very useful for complex problem. It can rapidly locate for complex search space and provides feasible solutions, derivative not required		Mutation and overlapping restricted. More effective memory capability, and simplified calculations	Inherent parallelism		
Disadvantages	Dynamic data set operation is difficult, and absolute optimum finding is not efficient		Scattering and optimization problem is very difficult to find	Theoretical analysis is very tough. Uncertain in time convergence, but absolute convergence can be found out		

Table 6 PSO algorithm parameters

S. No.	Parameter	Selected value
1	Inertia weight (w)	0.8
2	Self-confidence factor ($C1$)	2
3	Swarm confidence factor ($C2$)	2
4	Population	20

an example, and 40% of the total demand of that day is satisfied. One example of month of July is explained in detail. Electricity consumption on first of July was 1903.433 MWh. To obtain the optimal combination of IRES to satisfy this electrical demand, PSO algorithm using XL optimizer is applied, and Table 7 explains the details of demand satisfaction on the same day.

Table 7 Optimal combination of IRES to satisfy the demand for July

Electricity consumption (MWh)	Variables	Values	Electricity units generated (MWh)	Total units generated from IRES (MWh)
1903.43	Solar radiation (I) kWh/m ² /day	3.66	1256.34	3262.68
	Wind speed (V) m/s	5.39	687.47	
	Water head (H) m	50	1318.85	
	Discharge (Q) m ³ /s	155.76		

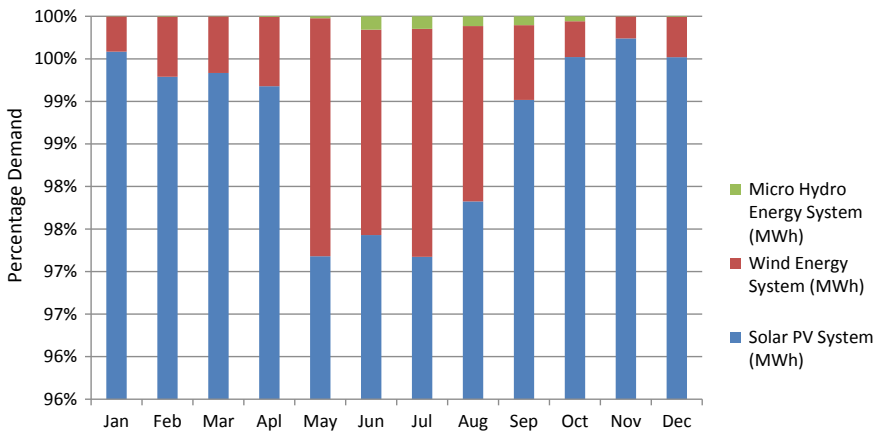


Fig. 5 Yearly graph of optimal combination of IRES to satisfy electrical demand of Kolhapur

Likewise, Fig. 5 reveals the optimal combination of RES for 40% electricity demand satisfaction of Kolhapur. Each month's first-day demand is considered for optimization, and thus, whole year's optimized combination has been represented.

From the above graph, it is clear that economic and environmental objectives for Kolhapur electricity demand satisfaction are satisfied. It is seen from the outputs that 40% of electrical demand of Kolhapur city can be satisfied with the renewable energy systems alone by the combination of solar PV, wind and micro-hydro.

10 Conclusion

To satisfy the electrical demand of Kolhapur, various renewable energy sources are considered and potential of each source is estimated depending on their dependency on climatic conditions at Kolhapur. Solar photovoltaic potential available for Kolhapur city is calculated by using with the real-time data input from NASA-SSE and is around 14,245.49 MWh/day. Wind energy potential available is calculated using real-time input of wind speed at Kolhapur, which is around 1874.81 MWh/day. Small hydro energy system potential is calculated using online real-time data of Panchganga River using Krishna–Bhima basin which is around 5525.85 MWh/day. Depending upon the climatic data available, the extractable potentials of RES are calculated, which summarizes to 861.36 MWh/day of solar photovoltaic system, 108 and 0.969 MWh/day of micro-hydro energy system. It can be concluded from the results that the electrical demand can be very well satisfied with the help of renewables. Also, it is found that, in tropical country like India, the solar energy can be utilized in large quantity, and more penetrations of solar PV can be possible up to 40%. Almost, for the nine months in a year, solar energy is available to its fullest extent. Real-time simulations of this system and spatial distribution of the renewable can be the future work of the study.

References

1. Bansal M, Khatod DK, Saini RP (2014) Modeling and optimization of integrated renewable energy system for a rural site. In: International conference on reliability, optimization and information technology, pp 25–28
2. Gupta S, Saurabh S, Akella AK (2014) Modelling, simulation and optimization of integrated alternative source of energy system with grid substation. *IOSR J Electr Electron Eng (IOSR-JEEE)* 56–63
3. Central Electricity authority New Delhi, Executive Summary for the Month of Jan 2017
4. Government of Maharashtra—Maharashtra Electricity Regulatory Commission Annual Report 2012–2013
5. City Development plan for 2031 of Kolhapur city, Minister of State for Urban Development Maharashtra (2013)
6. Akella AK, Sharma MP, Saini RP (2007) Optimum utilization of renewable energy sources in a remote area. *Renew Sustain Energy Rev* 894–908

7. Saif A, Elrab KG, Zeineldin HH, Kennedy S, Kirtley JL (2010) Multi-objective capacity planning of a PV-wind-diesel-battery hybrid power system. In: IEEE international energy conference and exhibition, energy conference, pp 217–222
8. Bhandari B, Poudel SR, Lee KT, Ahn SH (2014) Mathematical modeling of hybrid renewable energy system: a review on small hydro-solar-wind power generation. *Int J Precis Eng Manuf-Green Technol Korean Soc Precis Eng* 157–173
9. Filipe Carreira Serra (2011) Renewable energy sources implementation in urban area—case study on electricity generating potential from renewables in Portela civil parish
10. Singh R, Banerjee R (2015) Estimation of rooftop solar photovoltaic potential of a city. *Solar Energy* 589–602
11. Sharafi M, ELMekaway TY (2014) Multi-objective optimal design of hybrid renewable energy systems using PSO-simulation based approach. *Renew Energy* 68:67–79
12. Maheshwari Z (2013) An approach to modeling and optimization of integrated renewable energy systems (IRES)
13. Ko MJ, Kim YS, Chung MH, Jeon HC (2015) Multi-objective optimization design for a hybrid energy system using the genetic algorithm. *Energies* 8(4):2924–2949
14. U. N. ESCAP (2005) Urban environmental governance: for sustainable development in Asia and the pacific. United Nations, New York, p 65
15. Bhargava SK, Das SS, Paliwal P (2014) Multi-objective optimization for sizing of solar-wind based hybrid power system: a review. *Int J Innov Res Sci Eng Technol* 3(3):195–201
16. Bussar C, Stöcker P, Cai Z, Moraes L, Alvarez R, Chen H, Sauer DU (2015) Large-scale integration of renewable energies and impact on storage demand in a European renewable power system of 2050. *Energy Procedia* 73:145–153
17. Afzal A, Mohibullah M, Sharma VK (2010) Optimal hybrid renewable energy systems for energy security: a comparative study. *Int J Sustain Energy* 29(1):48–58

EMI Concerns, Measurements and Standards for Smart Grid



L. Chhaya, Paawan Sharma, Adesh Kumar, and Govind Bhagwatikar

Abstract An existing electrical grid is being transformed at a very rapid pace. Smart Grid comprises of heterogeneous and complex infrastructure. An integration of various communication technologies is inevitable for sensing, automation, control and metering applications in Smart Grid. Power electronic interface has a vital role to play in the deployment of Smart Grid. Therefore, the sources of radiated and conducted electromagnetic interference (EMI) must be identified and their effects can be mitigated for the prevention of EMI-related hazards. The safe operation of devices and components operating in the electromagnetic environment is must be ensured in terms of their electromagnetic compatibility according to various standards. EMI issues must be rigorously addressed as there are multiple causes and effects of these interferences. Moreover, the existing standards for measurement and prevention of EMI effects are based on primitive power grid infrastructure. Smart Grid is itself a developing technology which demands painstaking research endeavors. Safety of Smart Grid infrastructure is a crucial issue to be addressed due to its heterogeneous infrastructure. In this paper, the possible electromagnetic interferences are classified and analyzed for future interference mitigation research endeavors. This paper is anticipated to serve as an extensive survey of EMI issues, impacts, measurement procedures and standards in the framework of Smart Grid technology.

L. Chhaya (✉)
Gujarat, India
e-mail: lipi.chhaya@gmail.com

P. Sharma
Department of Computer Science and Engineering, School of Technology, PDPU, Gandhinagar,
Gujarat, India
e-mail: paawan.sharma@gmail.com

A. Kumar
Department of Electronics, Instrumentation and Control Engineering, University of Petroleum
& Energy Studies, Dehradun, India
e-mail: adeshkumar@ddn.upes.ac.in

G. Bhagwatikar
SANY Group, Pune, India
e-mail: gowind.india@gmail.com

© Springer Nature Singapore Pte Ltd. 2020

A. K. Bhoi et al. (eds.), *Advances in Greener Energy Technologies*,
Green Energy and Technology, https://doi.org/10.1007/978-981-15-4246-6_6

Keywords Communication equipment · Communication network · Electromagnetic compatibility · Electromagnetic interference · Electrostatic discharge · Immunity testing · Smart Grid · Standards

1 Introduction

A power grid is a complex system that carries electricity from generation units to consumer premises. The grid is called intelligent by the amalgamation of electrical and communication infrastructures.

As shown in Fig. 1, Smart Grid is characterized by bi-directional flow of data and electricity with self-healing capability.

Three significant features of Smart Grid are communication technologies, distribution automation and automated control systems [1–4].

The deployment of Smart Power Grid is essential for reduced emissions, energy efficiency, reliability, outage minimization, active consumer participation and integration of renewable energy sources. The communication infrastructure of Smart Power Grid is a combination of various heterogeneous and hierarchical communication networks like home area network, neighborhood area network and wide area network. These networks are designed to facilitate various applications and services like supervisory control and data acquisition, generation and distribution network automation, real-time monitoring, energy management system, cyber security and effective spectrum utilization by spectrum sensing technology [2–4]. The use of numerous entities like power system components and devices, transmission lines, conductors and communication network devices makes Smart Grid network vulnerable to radiated as well as conducted electromagnetic emissions. In the existing

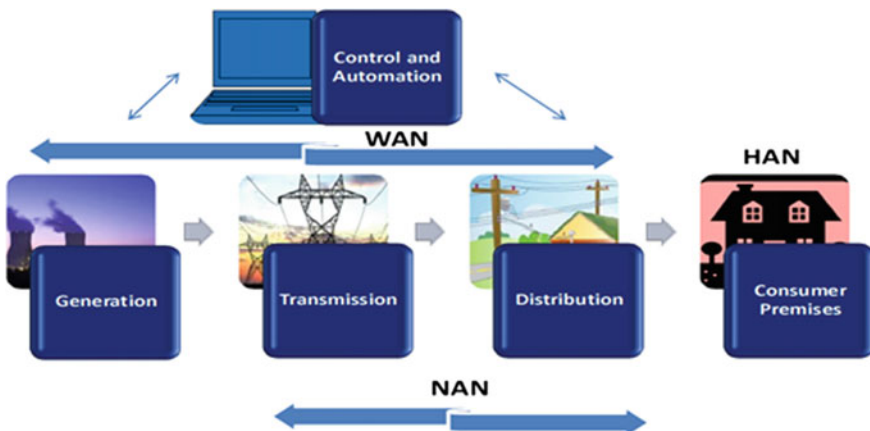


Fig. 1 Architecture of Smart Grid

power grid, the electromagnetic environs are considered for low to medium frequencies lower than 1 GHz. Power system components, transmission lines and conductors emit strong electric and magnetic fields. The electromagnetic interference occurs at operating frequencies and their harmonics. Partial discharges and corona due to high voltages also cause high-frequency interferences [5]. The existing standards for testing and measurements of electromagnetic interferences and compatibility are suitable for traditional power grid components and devices. In Smart Grid network, various microcontrollers, power electronic converters, renewable energy components and communication network devices will be installed. These devices and components will further increase electromagnetic interference [5–8]. The components of Smart Grid network must be compatible with electromagnetic interferences as well as safe for the operation of other devices operating in their vicinity. The innovative sets of standards are being established for safe and robust operation of Smart Grid.

2 EMI Concerns in Smart Grid

Electromagnetic interference is a disturbance which adversely affects the operation of various apparatus due to conducted and/or radiated electromagnetic radiation generated from internal or external source [6–8]. Smart Power Grid network is an assimilation of various electronics devices and wired as well as wireless communication networks. Integration of renewable energy resources with hierarchical and heterogeneous Smart Grid network also creates EMI and EMC issues. Smart Grid is vulnerable to conducted as well as radiated EMI. EMI can destruct or damage the power system and cause blackouts and hazards. Figure 2 shows the main causes of electromagnetic interference in Smart Grid. In this section, various causes of EMI and their impacts are discussed.

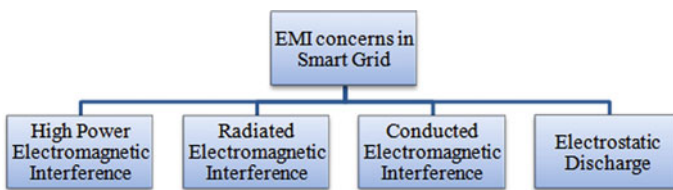


Fig. 2 EMI concerns in Smart Grid

2.1 High Power Electromagnetic Interference

High power electromagnetic interference can be due to excessive geomagnetic storms initiated by solar activity, intentional electromagnetic interference caused by delinquents and high altitude electromagnetic pulse. This can be referred as the triple threat [8] as discussed below.

2.1.1 Excessive Geomagnetic Storms

Solar noise is an extraterrestrial noise generated by the Sun. Under quiet conditions, the Sun constantly radiates over a very broad frequency range which is used for various communication applications. However, the Sun is a persistently changing star which undergoes cycles of peak activities which may cause electromagnetic interferences such as sunspots and corona flares. The solar cycle disturbances are repeated every 11 years. The solar supercycle is in operation when the peaks of solar cycles reach at maximum point every 100 years. An excessive electromagnetic storm is demarcated as a 1 in 100 year storm [8]. An interaction of charged particles evicted from the Sun with Earth's magnetic field produces geomagnetic disturbances at the surface of the Earth. Geomagnetic storms induce time-varying currents in the high voltage grid through neutral of the transformer. This time-varying currents can adversely affect the power grid by heating of transformers, greater inductive load and excessive harmonics.

2.1.2 Intentional Electromagnetic Interference (IEMI)

An IEMI is the term used to indicate a premeditated attempt to damage the device or network through radiated and/or conducted electromagnetic emissions. This type of attack is used for illicit offenses. This attack can be formed by high power microwaves (HPM), non-nuclear electromagnetic pulse (NNEMP) or electromagnetic weapons [8]. Standardization work to deal with IEMI is initiated by the EMC society of IEEE, ITU-T and IEC SC 77C [8]. IEMI attack can cause jamming, denial of service or damage of equipment. It can affect solar installations, wind installations, distribution devices, smart meters and substation devices due to its high-frequency characteristics.

2.1.3 High Altitude Electromagnetic Pulse (HEMP)

HEMP is formed by electromagnetic burst at altitude above 30 km over the Earth's surface. The burst is created by intense electromagnetic fields. There are three types of HEMP radiations [9].

Early Time (E1)-High Altitude Electromagnetic Pulse (HEMP)

E1-HEMP reaches field level of 50 kV/m in 10 ns and travels at a speed of light. It is a rapid rising short duration pulse with high frequency. These pulses can interrupt the operation of solid-state electronics devices. They can also penetrate through walls of substations and damage the devices. Smart Grid electronics devices and antennas can be adversely affected by E1-HEMP. E1-HEMP can also couple with distribution lines above the ground and can cause mechanical damage and insulator flashover [9]. It is also harmful to SCADA system located at control centers.

Intermediate Time (E2)-High Altitude Electromagnetic Pulse (HEMP)

E2-HEMP reaches field levels 100 V/m between the time interval of 1 microsecond and 1 s. On the basis of research done over the years, it is concluded that E2-HEMP is comparatively less harmful than E1 and E3 pulses due to its limited coverage, coupling efficiency and field levels [9].

Late Time (E3)-High Altitude Electromagnetic Pulse (HEMP)

E3-HEMP reaches field levels of 40 V/km between 1 and quite a few hundred seconds [6, 9]. The radial coverage of E3-HEMP is thousand kilometers which can efficiently couple with the transmission lines. It causes the saturation of transformer and potential damage to grid assets [8]. E3-HEMP can also produce severe power harmonics and destruct various devices [9]. It can also cause malfunction of devices and affect accuracy of monitoring and control units.

2.1.4 Classification of HPEM on the Basis of Frequency Bands

HPEM intentional EMI can be classified in terms of frequency bands. Band ratio is the ratio of upper frequency point and lower frequency point [9].

$$br = f_H/f_L.$$

The sources creating HPEM are classified in Table 1. This classification is important for threat analysis of IEMI sources.

2.2 Radiated Electromagnetic Interference

Smart Grid comprises of hierarchical and heterogeneous communication infrastructure [10]. Interoperability of diverse communication standards is unavoidable for

Table 1 HPEM classification on the basis of bandwidth

Type of band	Bandwidth in percentage Percentage bandwidth (pbw) = $200 \cdot (br - 1/br + 1)\%$	Band ratio (br)
Narrowband	$<1\%$	<1.01
Mesoband	$1\% < pbw \leq 100\%$	$1.01 < br \leq 3$
Subhyperband	$100\% < pbw \leq 163.6\%$	$3 < br \leq 10$
Hyperband	$163.6\% < pbw \leq 200\%$	$br \geq 10$

reliable operation [11]. Amalgamation of power and communication networks makes the grid more vulnerable to EMI. The study of radiated EMI is essential for the design and development of robust Smart Grid infrastructure which can operate competently in most severe electromagnetic environmental conditions. The various sources of radiated EMI are as follows.

2.2.1 Radiated EMI from Wireless Communication Devices

Smart Grid communication infrastructure is an integration of various hierarchical networks like HANs, NANs and WANs [10]. These networks are formed by the integration of different communication standards operating at various frequencies. Smart Grid communication infrastructure also comprises of wireless sensor networks (WSNs) for sensing and communication of different parameters [11]. Numerous base stations, WSN nodes, terminals and transceivers operating at different frequency bands can cause EMI problems as they also contains inter-modulation products, harmonics and frequency conversion products. Interference is also generated from various digital electronics components, power supplies and sensor nodes. Co-existence of diverse communication standards is also a key concern for safe and reliable operation of Smart Grid.

2.2.2 Radio Frequency Radiated Interference from High Voltage Discharges

The high voltage components and apparatus operating are above 100 kV produce EMI as a result of corona discharges and surface arcing. Corona discharges produce interferences in the range of few kHz to 100 MHz [5–8]. Gap sparks also produce EMI in the range of GHz. An EMI caused by air-insulated switches is very strong in terms of frequency and magnitude. For the lines below 70 kV, gap sparks are the prime source of EMI and the spectrum is up to 1 GHz. For the lines beyond 110 kV, corona discharges as well as gap sparking are the principle sources [6–8].

2.2.3 Radio Frequency Radiated Interference from Inverters, Integrated Circuits, Switches and Oscillators

An integration of renewable energy resources is a promising aspect of Smart Grid. Switching operations in converters used to convert renewable power into usable form produce EMI. In solar photovoltaic system, an inverter is used for DC to AC conversion. This conversion takes place by means of fast switching by generally using pulse width modulation (PWM). The switching frequency is in terms of kHz. This switching operation causes EMI on AC as well as DC lines. Oscillatory impulses and fluctuations in voltages also cause interferences [5–7]. Bus bars located in substations produce damped oscillations which can potentially damage or cause malfunction on other electronic devices. Integrated circuits (ICs) processing high frequencies are also produced EMI.

2.2.4 Radiated Electromagnetic Interference from Smart Meters

Smart meter is an imperative part of advance metering infrastructure (AMI). Smart meters communicate energy consumption data to a central node. An operating environment of smart meters must be safe and secure for reliable communication of information. This communication is possible by using various licensed or unlicensed bands. Various communication standards, such as Zigbee, WLAN, Bluetooth, GSM, CDMA, GPRS, EDGE, WiMAX, LTE, [10] can be used for data communication. Use of these heterogeneous communication technologies may produce intended and unintended radiated EMI effects. Intended emissions are related to data transmission. Unintended emissions are spurious signals which may not fall into the allocated frequency bands [10–14]. Co-existence of various communication technologies such as Zigbee and Wi-Fi working in industrial, scientific and medical band in home area networks (HANs) can also cause EMI effects. Standardization and legal compliance are inevitable for the integrity and reliability of smart meters. The electronic devices in the vicinity of smart meters must be technically compatible with smart meters for safe operation.

2.2.5 Modeling of Radiated EMI

Radiated electromagnetic interference includes differential mode interference and common-mode interference. Differential mode radiating interference can be assumed as a small current loop by considering ground plate reflection [12] (Figs. 3 and 4).

An equation for equivalent far-field differential mode interference strength can be written as,

$$E_{DM} = 2.63 * 10^{-14} * f^2 * (AI_{DM}) * (1/r)$$

Fig. 3 Electric dipole radiation model [28]

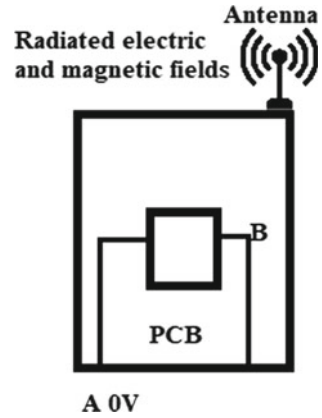
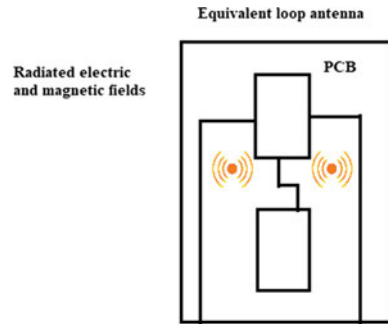


Fig. 4 Magnetic dipole radiation model



In the equation, f is the signal frequency, IDM is differential mode current, A is the loop area size in the circuit and r is distance of measurement. From the above equation, it is evident that the strength of differential mode interference is proportional to the square of frequency, loop area and differential mode current, and it is inversely proportional to the distance [12].

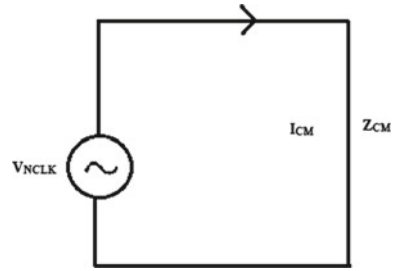
As per Maxwell’s equations and radiated model of electric dipole, a common-mode model can be assumed as a shortwave dipole driven by a single voltage source. Equivalent far-field common-mode radiated interference strength can be termed as,

$$E_{CM} = 12.6 * 10^{-7} * (fLI_{CM}) * (1/r)$$

The common-mode interference strength is directionally proportional to frequency of the signal, length of cable and common-mode current. It is inversely proportional to distance of measurement.

Furthermore, Smart Grid technology is an assimilation of various electronics and electrical devices working through the combination of hardware and software. Integrated circuit is the key component of Smart Grid network architecture for its diverse functionalities. The integrated circuit to be used in Smart Grid architecture

Fig. 5 Equivalent chip interference model



is required to function at high frequency in terms of MHz and even more than that with tremendous processing capabilities [12]. Figure 5 shows the equivalent chip interference model. V_{NCLK} is the transmission signal in the cable, I_{CM} is the current and Z_{CM} is impedance for common-mode interference.

$$I_{CM} = V_{NCLK}/Z_{CM}$$

V_{NCLK} is a single clock frequency signal. But the processing is done at high speed so this single high frequency consists of harmonics. Thus, it is a combination of multiple signals. This can be represented as,

$$V_{NCLK} = V_0 + \sum_{(i=1)}^k V_i$$

$$i = 1, 2, 3, 4 \dots$$

V_0 is the main interference signal while rest is the multiple of main signal.

2.3 Conducted Electromagnetic Interference Due to Renewable Energy Resources and Power Electronics Devices and Converters

Conducted EMI is routed through power supplies, signal lines and cables. The coupling mechanism can be capacitive, inductive or common impedance [13–17]. There are enormous sources of conducted EMI. Harmonics from power line, surges due to lightning and switching transients, bursts and transients due to inductive DC circuits, etc., are some of the factors which can cause conducted EMI. Various power electronic interfaces also have an adverse interference effects on different subsystems. Integration of renewable energy resources and use of power electronics converters, interfacing between various electronics components, integrated circuits, etc., are the major contributors of conducted EMI in Smart Grid environments [14–18]. The amount of EMI effect depends on the type of coupling mechanism. When the solar

panel is connected in a microgrid or mini-grid architecture, EMI is produced at both AC as well as DC side of the system. The specific issues related to conducted EMI caused by power electronics converters such as aggregation of multiple EMI sources, influence of EMI sources on the performance of other devices and the flow of EMI over distance circuits at input and output terminals of power electronics converter are the major issues to be addressed for electromagnetic compatibility [19–24]. The rectifiers and inverters in high voltage substations produce significant broadband EMI. There are two types of conversion technologies in practice: thyristor-based converters and voltage source converter (VSC)-based converters. The VSC-based power converters use IGBTs with faster switching [25–27]. Thus, the VSC-based converters have broader EMI spectrum up to few MHz.

2.4 Electrostatic Discharge

Electrostatic discharge (ESD) can be described as a phenomenon in which a transfer of electrical charge takes place between bodies of dissimilar electrostatic potential placed in vicinity or through direct contact [28]. ESD can occur when a moving electronic device comes in contact or proximity of stationary conducting object or when the equipment with cable connection is moved from one location to the other [28]. ESD can disrupt the operation of electronic devices. It occurs due to differences in static voltages of devices or surfaces [13–16, 24]. ESD effects can be mitigated by controlling the difference between static voltages of different surfaces. Data centers will play a pivotal role in Smart Grid applications. High level of humidity may cause ESD in data centers. Controlling the humidity by setting a certain threshold level can be beneficial to mitigate the occurrence of ESD.

3 EMI Measurement Procedures for Smart Grid

The primitive EMI measurement procedures can be considered as a reference but they are insufficient for the complete electromagnetic analysis of complex Smart Grid system. Smart Grid is a combination of various power electronic converters, sensors, communication standards, smart meters, renewable energy sources and electricity generation, transmission and distribution network components. A complex heterogeneous and hierarchical Smart Grid architecture require a painstaking research of EMI issues by considering even a smallest component of the network. Conducted EMI can be measured by measuring voltage at the input of the superhetrodyne receiver. The specific supplementary devices such as line impedance stabilization network, field probe, current probe, absorbing clamps can be used to convert the physical quantities like radiated power, electromagnetic field and current. The receiver parameters are normalized to ensure the comparability of results. The measurement of EMI can be conducted in frequency domain as well as time domain. The frequency-domain

measurement conducted using superhetrodyne receiver determines an effect of interference on communication signal. For reliability of control system, the real-time information in time-domain information is more suitable. Frequency-domain measurement must be supplemented with statistical study of repetitive measurements as well as time-domain measurement. In time-domain measurements, the common and differential mode measurements can be used for the analysis of EMI influence on control signals. For meticulous analysis of effect of parasitic couplings on various levels of cross talk, the measurement of EMI voltage and current both are inevitable [22–26].

4 Standards for Electromagnetic Compatibility in Smart Grid

Some of the important standards [29–31] for electromagnetic interference and compatibility testing and measurements are as follows.

- IEC 61000-6-5: This standard depicts the immunity requirements of devices and components used for generation, transmission and distribution of power and associated communication network. Equipment placed at power stations, and substations are included in this standard. High power apparatus used in primary systems of electricity network is not covered in this standard.
- IEC 61000-4-2: This standard describes the immunity requirements and test levels for electronic devices in the presence of electrostatic discharge (ESD) from human body or metal object in the proximity of that device. According to this standard, ESD tests should be performed on fully operational and configured equipment containing all necessary hardware, software and firmware.
- IEC 60255-26: This standard is applicable to power system monitoring and control interface devices and protection apparatus. This standard specifies electromagnetic compatibility requirements for protection devices used in power plants and substations in open-air conditions.
- IEC 60439-1: This standard is applicable to type tested and partly type tested control gear and switch gear assemblies with low voltages up to 1 kV AC or 1.5 kV DC. This standard is developed for assemblies used for generation, transmission, distribution and conversion of energy.
- IEC 62052-11: This standard includes type tests for indoor and outdoor metering devices for voltage up to 600 V and frequencies of 50 and 60 Hz. This standard is applicable for advance metering infrastructure (AMI).
- ANSI C12.1: This standard provides performance guidelines for auxiliary equipment, pulse apparatus, AC watt-hour meters, and demand meters used for revenue metering.
- ANSI C63.12: This standard provides guidelines for conducted and radiated emission levels and test levels for individual electronic instruments in controlled environment [29].

- IEEE-C-37.90: This standard specifies testing and performance requirements, standard ratings and service conditions for relays, and relay systems used for the protection of power system equipment and control systems. A relay system may consist of communication interface, computer interface and components used for audio systems. It does not include the relay system for switching and industrial control.
- IEEE 1613: This standard describes the guidelines for performance and testing conditions, standard ratings, environmental conditions and service conditions for communications and networking apparatus. It covers communication ports, sensors and protective relays. It does not include devices included in IEEE-C-37.90.
- IEEE 60870-2-1: This standard is related to tele-control systems and equipment. It is applicable for encrypted serial data transmission for the management of widespread system. Moreover, it is applicable to equipment in distribution automation systems. This standard specifies minimum immunity and emission requirements and test values as well as characteristics of power supplies connected to the mentioned devices.
- IEEE 1642: This standard describes risk levels, safety methods, monitoring techniques and experiment techniques for the protection of publicly accessible computer systems from IEMI.
- IEEE 1909.1: This standard provides guidelines for testing and installation of Smart Grid communication equipment. It includes electromagnetic compatibility (EMC) testing for communication devices installed in generation, transmission and distribution domains of Smart Grid infrastructure [29–31].
- OIML R 46-1 and 2: These guidelines are developed by International Organization of Legal Metrology (OIML). It describes technical and metrological specification applicable to energy meters subject to legal metrological controls. It is applicable for smart meter immunity testing.
- CISPR-24: It is applicable to information technology-related products which use microprocessors. It is basically a product immunity testing standard. The devices at consumer premises in Smart Grid are covered in this standard. It also contains testing of DC ports as well as DC power.

5 Conclusion

Smart Grid can be described as the most revolutionary technology in the current era. Integration of communication technology with existing passive power grid is a critical and crucial aspect of this revolution. An integration of various wireless communication technologies makes Smart Grid network vulnerable to EMI threats. Adverse effects of EMI may result in severe consequences such as component failure, performance degradation or grid failure. Electromagnetic compatibility testing

is essential for each and every component of the Smart Grid network for operational reliability and safety. Harmonization between different existing standards is also inevitable and can be conscientiously explored in further research. Future work may include EMC testing of various components of Smart Grid communication network. Researchers can explore various techniques to mitigate the adverse effects of EMI. Prototype EMC testing in laboratory can also provide plethora of design solutions. This survey paper is anticipated to serve as an extensive study and analysis of EMI considerations and standardization process which may lead toward enormous research problems and exploration of solutions.

References

1. Hashmi M, Hänninen S, Mäki K (2011) Survey of smart grid concepts, architectures, and technological demonstrations worldwide. In: IEEE PES conference innovative smart grid technologies (ISGT Latin America), p 7
2. Yan Y, Qian Y, Sharif H, Tipper DA (2013) Survey on Smart Grid communication infrastructures: motivations, requirements and challenges. *IEEE Comm Surv Tutor* 15:5–20
3. Gungor VC (2011) Smart Grid technologies: communication technologies and standards. *IEEE Trans Ind Info* 7:529–539
4. Yu R, Zhang Y, Gjessing S, Yuen C, Xie S, Guizani M (2011) Cognitive radio based hierarchical communications infrastructure for smart grid. *IEEE Net* 25(5):14
5. Rao DAVK, Veerabhadraiah S (1990) Effects of EMI/EMC on electronic devices. *IETE Tech Rev* 7:70–74
6. Ganesan R, Kini KR (2003) Electromagnetic interference/compatibility measurement. *IETE Tech Rev* 20:415–424
7. Hikita M, Yamashita H, Hoshino T, Kato T, Hayakawa N, Ueda T, Okubo H (1998) Electromagnetic noise spectrum caused by partial discharge in air at high voltage substations. *IEEE Trans Power Deliv* 13(2):434–439
8. Radasky WA (2009) Protection of commercial installations from the triple threat of HEMP, IEMI, and severe geomagnetic storms. *Interference Technology EMC Directory and Design Guide. Report of the Commission to Assess the Threat to the United States from Electromagnetic Pulse (EMP) Attack, vol 1, pp 1–6*
9. Giri DV, Tesche FM (2004) Classification of intentional electromagnetic environments (IEME). *IEEE Trans Electromagnetic Compat* 46:329–334
10. Chhaya L, Sharma P, Bhagwatikar G, Kumar A (2017) Wireless sensor network based smart grid communications: cyber-attacks, intrusion detection system, and topology control. *Electronics* 6(1):1–22
11. Chhaya L, Sharma P, Bhagwatikar G, Kumar A (2017) Communication theories and protocols for smart grid hierarchical networks. *J Elec Electr Engg* 10:43–48
12. Zhao Y, Deng Y, Yan W, Qiu X, Liu Y (2014) The radiated EMI noise modeling and features analysis on the basis of Smart Grid Equipments. In: *International symposium on electromagnetic compatibility*, pp 1–4
13. Radasky WA, Hoard R (2012) An overview of the impacts of three high power electromagnetic (HPEM) threats on Smart Grids. In: *International symposium on electromagnetic compatibility*, pp 1–6
14. Yu Q, Johnson RJ (2011) Integration of wireless communications with modernized power grids: EMI impacts and considerations, *Electromagnetic Compatibility (EMC)*. In: *International symposium on electromagnetic compatibility*, pp 329–334
15. CISPR 18–1, 2, 3, *Radio interference characteristics of overhead power lines and high-voltage equipment, Ed. 2.0, (2010–06)*

16. Pakala WE, Chartier VL (1971) Radio noise measurements on overhead power lines from 2.4 to 800kV. *IEEE Trans Power App Syst PAS-90* 3:1155–1165
17. Hanigovszki N, Landkildehus J, Spiazzi G, Blaabjerg F (2006) An EMC evaluation of the use of unshielded motor cables in AC adjustable speed drive applications. *IEEE Trans Power Electron* 21(1):273–281
18. Konefal T, Dawson J, Denton A, Benson T, Christopoulos C, Marvin A, Porter S, Thomas D (2001) Electromagnetic coupling between wires inside a rectangular cavity using multiple-mode-analogous-transmission-line circuit theory. *IEEE Trans Electro Comp* 43(3):273–281
19. Koyama Y, Tanaka M, Akagi H (2010) Modeling and analysis for simulation of common mode noises produced by an inverter-driven air conditioner. In: *International Power Electronics Conference (IPEC)*, pp 2877–2883
20. Ogasawara S, Akagi H (1996) Modeling and damping of high-frequency leakage currents in PWM inverter-fed AC motor drive systems. *IEEE Trans Ind Appl* 32(5):1105–1114
21. Ogasawara S, Akagi H (2000) Analysis and reduction of EMI conducted by a PWM inverter fed AC motor drive system having long power cables. In: *IEEE 31st annual power electronics specialist's conference*, vol 2, pp 928–933
22. Evans IC, Limpaecher R, Dillon A (2008) Powering the way—a paper on AC LinkTM technology for 21st century HVDC transmission. In: *IEEE Energy 2030 Atlanta*, pp 1–11
23. Maas J (2012) Smart Grid and electrostatic discharge: cause for new concerns? In: *International symposium on electromagnetic compatibility (EMC EUROPE)*, pp 1–6
24. Koepke G (2012) White paper on electromagnetic compatibility and smart grid interoperability issues
25. Smolenski R, Kempfski A, Benysek G (2009) Aggregated conducted EMI generated by group of frequency converter-fed drives. In: *Compatibility and power electronics*, pp 381–385
26. Smolenski R, Kempfski A, Bojarski J, Lezynski P (2012) EMI generated by power electronic interfaces in Smart Grids. In: *International symposium on electromagnetic compatibility*, pp 1–6
27. Luszcz J, Smolenski R (2015) Low frequency conducted emissions of grid connected static converters. *IEEE Electro Comp Mag* 4:86–94
28. Sadiku MNO, Akujuobi CM (2004) Electrostatic discharge (ESD). *IEEE Potentials* 22:39–41
29. American National Standard Recommended Practice for Electromagnetic Compatibility Limits and Test Levels (2016) In: *ANSI C63.12-2015 (Revision of ANSI C63.12-1999)*, p 46
30. IEEE Recommended Practice for Protecting Publicly Accessible Computer Systems from Intentional Electromagnetic Interference (IEMI) (2015) In: *IEEE Std. 1642*, p 39
31. IEEE Recommended Practice for Smart Grid Communications Equipment-Test Methods and Installation Requirements (2014) In: *IEEE Std. 1909.1*, pp 1–40

Extraction of Solar Module Parameters Using Jaya Optimization Algorithm



P. Anandhraj, K. Mohana Sundaram, P. Sanjeevikumar,
and Jens Bo Holm-Nielsen

Abstract The electricity gained from photovoltaic array increased the attention of researchers due to its diminishing cost over the years, moreover environment-friendly nature and renewability. Prior to the installation part of the solar module, precise modeling is required for investigation. However, precise modeling is a tedious task since certain parameters are not mentioned in the manufacturer's datasheets. In this article, a method based on Jaya algorithm is projected and implemented numerically in MATLAB software to find the unknown parameters in 250 W_p SVL0250P photovoltaic module nonlinear equations by varying the curve at different environmental conditions. Also, the comparative study is done between proposed and flower pollination algorithm and find the best optimization technique based on the speed of convergence and accuracy. The proposed Jaya algorithm has attained the fitness function within 30 iterations.

Keywords Photovoltaic (PV) · Jaya algorithm · Optimization · Flower pollination algorithm (FPA) · Irradiance · Convergence curve

1 Introduction

Hazardous greenhouse effect and global warming, rendered by conventional power generating methods using fossil fuels, insist the benign and renewable energy sources produce electricity, as they are profuse in nature and reliable alternative for fossil fuels. Among the non-conventional energy sources, the energy obtained from solar is identified as the mainly feasible source due to inexhaustibility, non-polluting nature,

P. Anandhraj · K. Mohana Sundaram (✉)
Department of Electrical and Electronics Engineering, Vel Tech Multi Tech
Dr. Rangarajan Dr. Sakunthala Engineering College, Chennai 600062, India
e-mail: kumohanasundaram@gmail.com

P. Sanjeevikumar · J. B. Holm-Nielsen
Center for Bioenergy and Green Engineering, Aalborg University, 6700 Esbjerg, Denmark

© Springer Nature Singapore Pte Ltd. 2020
A. K. Bhoi et al. (eds.), *Advances in Greener Energy Technologies*,
Green Energy and Technology, https://doi.org/10.1007/978-981-15-4246-6_7

and maintenance free [1]. The Direct Current (DC) output from the solar module is directly fed into the load or through the power electronic converters when it is connected into the sophisticated applications. The impeccable modeling of solar cells is needed prior to the installation part being deployed for greater power generation. The worldwide researchers found that MATLAB and PSPICE are the most appropriate software for solar cell modeling. Generally, solar cell manufacturers furnish only a limited number of parameters. To model the solar panel using single diode model, the parameters such as shunt resistance (R_p), series resistance (R_s), ideality factor (a), diode saturation current (I_0), and photogenerated current (I_{pv}) are mandatory, but these mentioned parameters will not be provided in the datasheets [2–5]. The double diode model was preferred for better accuracy and other purposes, in which, the extra diode represents the recombination of carriers [6–8]. In 2001, Jervase has described a numerical method to extract five unknown parameters using Gauss-Seidal algorithm [9]. However, this method is complex and time consuming. The Newton–Raphson method is utilized to optimize unknown parameters of solar cells [10]. This method was also difficult to implement since the number of instances to find the optimized point is found to be extremely high. Besides these two methods, there are several other optimization techniques involved in the parameter estimation, i.e., (i) genetic algorithm [11], (ii) particle swarm optimization [12], (iii) bird mating [13], (iv) harmony search [14], and (v) pattern search [15]. Among which, the selection of chromosomes from the initial population is difficult in the genetic algorithm. The selected pattern may be incorrect in the pattern search algorithm, which can lead to the prematuration of the result. Further, the researchers have adopted the bio-inspired algorithms to neglect complex mathematical calculations, thereby diminish time. The Differential Evaluation (DE) and Evolutionary Algorithms (EA) were used by some researchers and they found the similar limitations of PSO and GA method in the DE and EA. The common limitations found in the algorithms are large computation time, and diversity has been lost when the global optimal is achieved [16–18]. In 2013, the best bio-inspired algorithm called Bacterial Foraging Algorithm (BFA) applied for the optimization of unknown values in the solar cells and proved that BFA is the best bio-inspired algorithm when compared to other two algorithms based on the convergence speed, absolute error, and accuracy [19]. In 2017, the enhanced flower pollination algorithm that is applied to optimize unknown values from the PV panel was implemented [20]. However, in literary works, Jaya algorithm was not used for extracting the unknown parameters of PV module. Since 2016, Rao [21–25] is retaining Jaya algorithm for optimization problems to find the best result. Hence, in this article, the Jaya algorithm is proposed for parameter extraction. In addition to this, the algorithm is compared with flower pollination algorithm on the basis of the speed of convergence and the best-favored technique is obtained.

2 Solar Cell Mathematical Modeling

For less complexity, the model with one diode is analyzed in this article and it is shown in Fig. 1. In an ideal PV cell, anti-parallel diode is connected across the current source even though the practical solar model has series and parallel resistance across the diode. The resistance between the *p* semiconductor layer and metal base is represented by R_s . The R_p represents the manufacturing method of the solar cell and the leakage current [10].

Applying KCL, solar cell output current Eq. (1) is given by:

$$I = I_{PV} - I_D - \frac{V_D}{R_p} \tag{1}$$

The expanded solar current Eq. (2) [9–12] is given as:

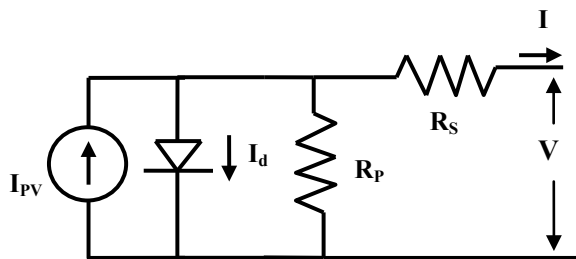
$$I = I_{PV} - I_0 \left[\exp\left(\frac{V + R_s I}{V_t a}\right) - 1 \right] - (V + R_s I)/R_p \tag{2}$$

As a result of the above discussion, five unknown parameters such as I_{PV} , R_p , R_s , a , I_0 in the one diode model are required for exact solar cell modeling. In order to reduce complexity, in this proposed work, ' I_{PV} ' and ' I_0 ' are calculated analytically. The diode ideality factor ' a ' is chosen arbitrarily between 1 and 2 which is based on the other parameters of the PV model [26, 27]. The remaining two parameters of ' R_s ' and ' R_p ' are computed using Jaya algorithm. It is found that these parameters are varied with respect to irradiance and temperature, and then adjusted to an optimum point which is built on the minimized error between computed and actual power. The photogenerated current of single diode solar cell [10] is given by Eq. (3).

$$I_{PV} = (I_{SC} + k_i dT) * G/G_n \tag{3}$$

where I_{SC} represents short-circuit current, G and G_n represent actual solar irradiance and irradiance at standard test condition, k_i represents current temperature coefficient. The I_0 for the one diode model has relied on the photogenerated current and open-circuit voltage [11] and it is represented in Eq. (4).

Fig. 1 One diode solar cell model



$$I_0 = I_{PV} / \exp\left(\frac{(V_{OC} + k_v dT) * V_t}{a}\right) - 1 \quad (4)$$

where V_{OC} is the open-circuit voltage, k_v represents voltage temperature coefficient. When the PV curve is at the maximum power point (MPP), the voltage V is V_{mp} , and the current I is I_{mp} . Further, at this point, the differentiation of power as a function of voltage becomes zero [11]. With this condition, the unknown parameters are extracted in this article.

Equation (5) represents the derivation of current as a function of the voltage at the MPP.

$$\left.\left(\frac{dI}{dV}\right)\right|_{(V_{mp}, I_{mp})} = (I_0 \psi \exp\{\psi(V_{mp} + I_{mp} R_S)\} - Z_P) / (1 + I_0 \psi R_S \exp\{\psi(V_{mp} + I_{mp} R_S)\} - Z_P R_S) \quad (5)$$

where $G_P = 1/R_P$ represents the reciprocal of shunt resistance, $\psi = 1/aV_t$ reciprocal of diode ideality factor and thermal voltage. Equation (6) represents the fitness function.

$$J = \left.\left(\frac{dI}{dV}\right)\right|_{V_{mp}, I_{mp}} + \left(\frac{I_{mp}}{V_{mp}}\right) \quad (6)$$

The optimized solution is achieved when the fitness function (J) reaches zero approximately [11].

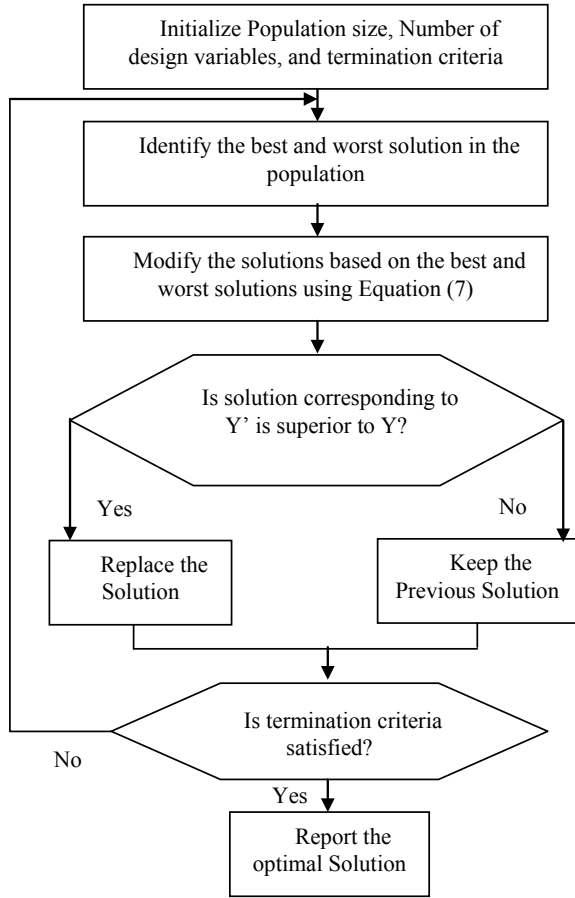
3 Jaya Algorithm-Based Solar Cell Parameter Extraction

Jaya algorithm Fig. 2 was proposed by Prof. Dr. Hab. Ravipudi Venkata Rao. In this technique, 'n' number of random initial solutions are selected that should be able to meet the lower and higher limit of the design variables. Afterward, all the variables in the solution are updated based on the Eq. (7).

$$Y' = Y + r_1[(Y_{best}) - Y] - r_2[(Y_{worst}) - Y] \quad (7)$$

where r_1 and r_2 indicate the random values which are in the limit [0 1]. By updating all the values, it assists to transform each fitness function into the best solution [25].

Fig. 2 Flowchart of the Jaya algorithm



4 Results and Its Discussion

A PV modeling has been done in order to examine the algorithms presented in this article. A 250 W_p SVL 0250P solar module datasheet provides the values of V_{oc} , I_{sc} , I_{mp} , and V_{mp} . Nevertheless, these parameters are inadequate for precise PV characteristics modeling and it needs values of R_s , R_p , a . The unknown parameters are optimized by Jaya algorithm. The initial value of R_s is choosing randomly within the range of [0 2] and initial boundary limit for parallel resistance (R_p) between 50 and 500. The selected value of diode ideality factor (a) ranges from 1 to 2.

From Table 1, it can be observed that the magnitude of R_s is very small and the magnitude of R_p is high. According to which, a smaller value of R_s and higher value of R_p move the PV curve toward maximum power point.

With all the above data, PV modeling has been done for two algorithms. After several instances, the finest convergence curve is achieved for each method and

Table 1 Solar model parameters estimated with Jaya algorithm for different temperature and irradiance

Parameters	SVL 0250P
$T = 25\text{ }^{\circ}\text{C}$ & $G = 1000\text{ W/m}^2$	0.213
R_s	288
R_p	
$T = 47.40\text{ }^{\circ}\text{C}$ & $G = 525\text{ W/m}^2$	0.0295
R_s	156.9646
R_p	
$T = 45.90\text{ }^{\circ}\text{C}$ & $G = 368\text{ W/m}^2$	1.1984
R_s	402.6458
R_p	

minimum fitness value in that curve determines the accuracy of the algorithm. The fitness curve of Jaya algorithm is depicted in Fig. 3. From the curve, the finest fitness value attained is 0.14 which is small and also it is achieved within thirty iterations.

The computed electrical characteristics of the 250 Wp solar module (SVL0250P) at standard test condition and two other environmental conditions are depicted in Figs. 4, 5 and 6.

With the help of the graph, it is found that position V_{mp} and I_{mp} varied based on the insolation. Figure 7 represents the variation of the fitness function with the number of iteration for Jaya and FPA, and it can be observed that the convergence speed of the proposed method is superior to FPA.

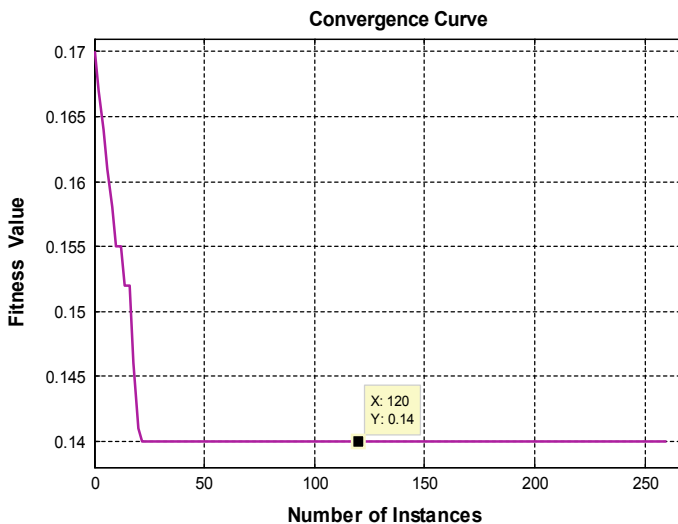


Fig. 3 Convergence curve of Jaya algorithm

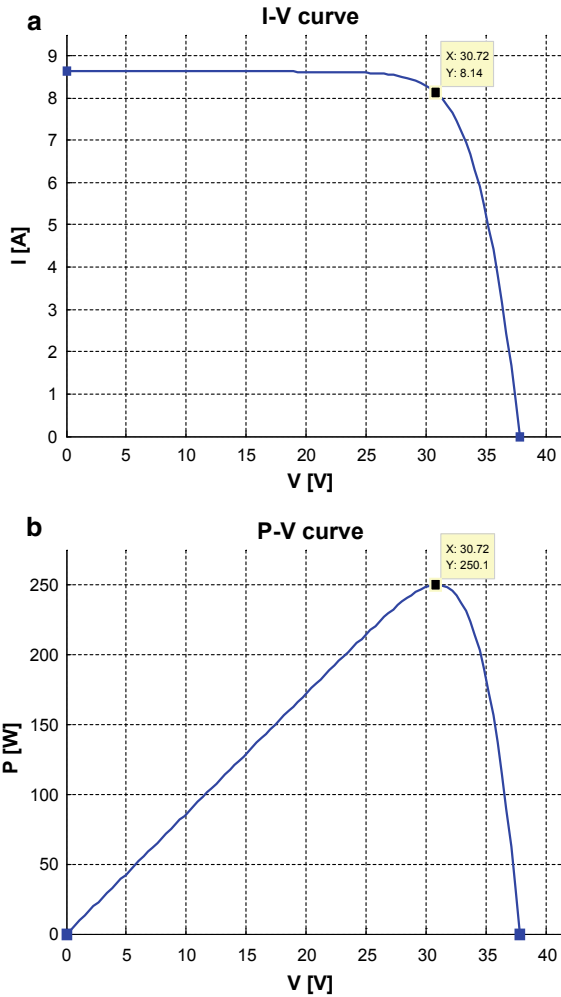


Fig. 4 a, b Electrical characteristics at standard test condition

5 Conclusion

In this article, Jaya algorithm was proposed successfully to calculate solar cell's unknown parameters R_s and R_p precisely without sub-optimal traps. These parameters have been extracted with a fitness function of differentiation of power as a function of V_{mp} . The SVL0250P PV module electrical characteristics obtained for different environmental conditions using Jaya algorithm and its outcomes are compared to FPA. It can be observed that the speed of convergence and consistency of the

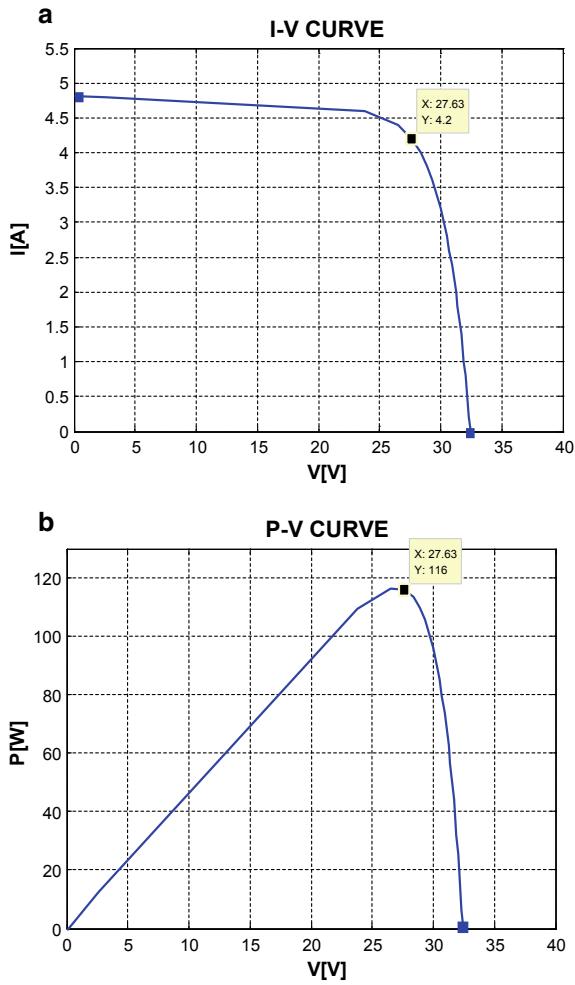


Fig. 5 a, b Electrical characteristics for irradiance (G) = 525 W/m² and T = 47.4 °C

fitness function of Jaya algorithm is efficient when compared with flower pollination algorithm. The complexity of computation in Jaya algorithm is lower compared to FPA. Hence, Jaya algorithm is an appropriate and fast computational algorithm for PV module parameters extraction.

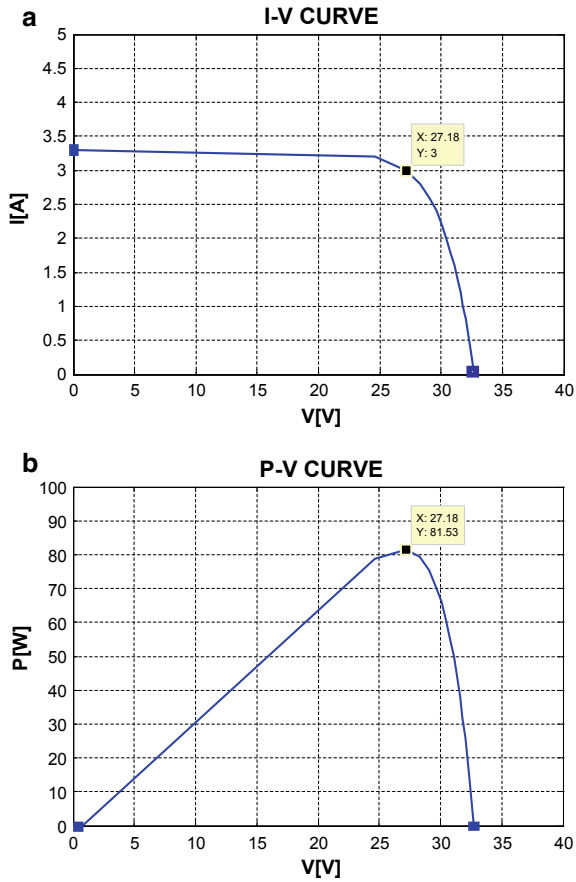
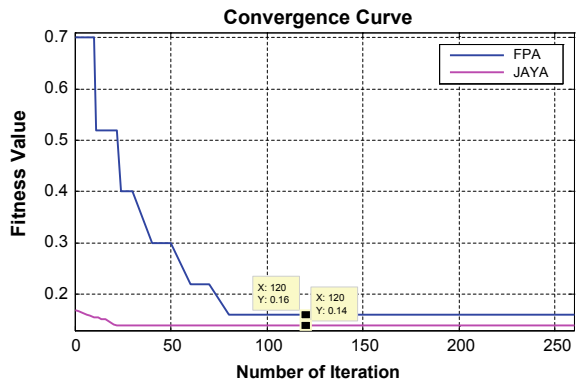


Fig. 6 a, b Electrical characteristics for irradiance (G) = 368 W/m² and T = 45.9 °C

Fig. 7 Convergence curve of Jaya and FPA



Acknowledgements The DST-TSDP (No.DST/TSG/WM/2015/557/G) Government of India has supported financially to carry out this research work.

References

1. Chan DSH, Phang JCH (1987) Analytical methods for the extraction of solar-cell single and double-diode model parameters from I-V characteristics. *IEEE Trans Electron Dev* 34:286–293
2. Ishaque K, Salam Z, Syafaruddin (2011) A comprehensive MATLAB Simulink PV system simulator with partial shading capability based on two-diode model. *Solar Energy* 85:2217–2227
3. Sachin VR, Vivek JP (2015) Simulation and comparison of perturb and observe and incremental conductance MPPT algorithms for solar energy system connected to grid. *Sadhana* 40:139–153
4. Liu C-C, Chen C-Y, Weng C-Y (2008) Physical parameters extraction from current–voltage characteristic for diodes using multiple nonlinear regression analysis. *Solid-State Electron* 52:839–843
5. Aurobinda P, Pathak MK, Srivastava SP (2016) A single phase photovoltaic inverter control for grid connected system. *Sadhana* 41:15–30
6. Gow JA, Manning CD (1999) Development of a photovoltaic array model for use in power-electronics simulation studies. *IEE Proc Elect Power Appl* 146:193–200
7. Gow JA, Manning CD (1996) Development of a model for photovoltaic arrays suitable for use in simulation studies of solar energy conversion systems. In: *Proceedings of 6th international conference on power electronics and variable speed drives*, pp 69–74
8. Pongratananukul N, Kasparis T (2004) Tool for automated simulation of solar arrays using general-purpose simulators. *Proceedings of IEEE workshop computer power electronics*, pp 10–14
9. Jervase JA, Bourdoucen H, Al-Lawati A (2001) Solar cell parameter extraction using genetic algorithms. *Meas Sci Technol* 12:1922–1925
10. Marcelo GV, Jonas RG, Ernesto RF (2009) Comprehensive approach to modelling and simulation of photovoltaic arrays. *IEEE Trans Power Electron* 24:1198–1208
11. Ismail M, Moghavvemi M, Mahlia T (2013) Characterization of PV panel and global optimization of its model parameters using genetic algorithm. *Energy Convers Manage* 73:10–25
12. Jing JS, Kay-Soon L (2012) Photovoltaic model identification using particle swarm optimization with inverse barrier constraint. *IEEE Trans Power Electronics* 27:3975–3983
13. Askarzadeh A, dos Santos Coelho L (2015) Determination of photovoltaic modules parameters at different operating conditions using a novel bird mating optimizer approach. *Energy Convers Manage* 89:608–614
14. Alhajri MF, El-Naggar KM, Alrashidi MR (2012) Optimal extraction of solar cell parameters using pattern search. *Renew Energy* 44:238–245
15. Askarzadeh A, Rezazadeh A (2012) An innovative global harmony search algorithm for parameter identification of a PEM fuel cell model. *IEEE Trans Ind Electron* 59:3473–3480
16. Wang W, Wu JM, Liu JH (2009) A particle swarm optimization based on chaotic neighborhood search to avoid premature convergence. In: *Third international conference on genetic and evolutionary computing*
17. Jacob B, Balasubramanian K, Sudhakar Babu T, Mohammed Azharuddin S, Rajasekar N (2015) Solar PV modeling and parameter extraction using artificial immune system. *Energy Procedia* 75:331–336
18. Ishaque K, Salam Z, Taheri H, Shamsudin A (2011) A critical evaluation of EA computational methods for Photovoltaic cell parameter extraction based on two diode model. *Solar Energy* 85:1768–1779

19. Rajasekar N, Neeraja K, Rini V (2013) Bacterial Foraging algorithm based solar PV parameter estimation'. *Sol Energy* 97:255–265
20. Prasanth RJ, Sudhakar BT, Tomislav D, Rajasekar N (2017) A new hybrid bee pollinator flower pollination algorithm for solar PV parameter estimation. *Energy Convers Manage* 135:463–476
21. Venkata RR, More KC (2017) Design optimization and analysis of selected thermal devices using self-adaptive Jaya algorithm. *Energy Convers Manage* 140:24–35
22. Venkata Rao R, Saroj A (2017) Constrained economic optimization of shell and tube heat exchangers using elitist-Jaya algorithm. *Energy* 128:785–800
23. Venkata Rao R, Saroj A (2017) Economic optimization of shell-and-tube heat exchanger using Jaya algorithm with maintenance consideration. *Appl Therm Eng* 116:473–487
24. Venkata RR, Dhiraj P, Joze B (2017) A multi-objective algorithm for optimization of modern machining processes. *Eng Appl Artif Intell* 61:103–125
25. Venkata RR (2016) A simple and new optimization algorithm for solving constrained and unconstrained optimization problems. *Int J Ind Eng Comput* 7:19–34
26. Carrero C, Amador J, Arnaltes S (2007) A single procedure for helping PV designers to select silicon PV module and evaluate the loss resistances. *Renew Energy* 32:2579–2589
27. Walker G (2001) Evaluating MPPT converter topologies using a matlab PV model. *J Elect Electron Eng* 21:45–55

A Multilevel Inverter-Controlled Photovoltaic Generation



Neeraj Priyadarshi, Farooque Azam, Akash Kumar Bhoi,
and Amarjeet Kumar Sharma

Abstract Distributed power systems have been broadly diagnosed as an intermittent source nowadays. The photovoltaic (PV) systems have been considered for grid integration as per rapid developed market. The main advantages such as abundant amount, noiseless and pollution-less features with reliable operations make the PV system more acceptable. The maximum disbursed power can be utilized for PV-based system among all renewable sources. Multilevel inverters (cascaded H-bridge) have been considered as dispensed power electronics system for PV power system. In this work, fuzzy logic-based control system has been employed for monitoring grid integration continuously which is also responsible to regulate cascaded H-bridge inverter.

Keywords PV · Multilevel inverters · H-bridge

1 Introduction

Among various forms of renewable energy assets, sun power has turn out to be very famous and annoying. The solar grants strength to the earth on the price of one.2 × one zero five TW, which is ready 104 instances of what mankind currently produces and consumes. Solar electricity may be gathered and used in many approaches. A photovoltaic (PV) tool makes use of semiconductor substances to convert daylight to

N. Priyadarshi (✉) · A. K. Sharma

Department of Electrical Engineering, Birsa Institute of Technology (Trust), Ranchi 835217, India
e-mail: neerajrjd@gmail.com

A. K. Sharma

e-mail: ermaxamar@gmail.com

F. Azam

School of Computing & Information Technology, REVA University, Bangalore 560064, India
e-mail: farooque53786@gmail.com

A. K. Bhoi

Department of Electrical & Electronics Engineering, Sikkim Manipal Institute of Technology,
Sikkim Manipal University, Gangtok, India
e-mail: akash730@gmail.com

© Springer Nature Singapore Pte Ltd. 2020

A. K. Bhoi et al. (eds.), *Advances in Greener Energy Technologies*,

Green Energy and Technology, https://doi.org/10.1007/978-981-15-4246-6_8

strength [1–5]. Thermo-photovoltaic uses the energy of warmth, or infrared radiation, to generate power. Concentrating sun electricity (CSP) systems use the concentrated warmth of the solar as the heat supply for traditional strength plants. Solar heating technologies make use of the solar heat to satisfy a ramification of desires, which includes heating swimming pools and heating water or air for residential and business use. Sunlight structures collect sunlight and use optical fibers to transmit it within the building to complement traditional lights. There may be brilliant marketplace growth in sun electricity. The Ministry of New and Renewable Energy (MNRE) is helping the sun power through countrywide sun task. The authorities of India have set up a goal to put in one hundred GW with the aid of 2022 through the investment of Rs. 6.3 trillion (\$a hundred billion) in five years. Determine 1.1 shows the growth of photovoltaic in India.

A grid-integrated PV system is interfaced with utility grid in which solar arrays, inverters and power-conditioning systems are major components. These systems are integrated to stand-alone systems to high power utility systems, and extra power can be transferred to loads through grid power systems [6–11]. The generated PV power must be conditioned through inverter before injecting into utility grid which converts DC to AC power and interfaces between solar system and utility grid. This inverter employed to review the level of grid voltage, current and frequency automatically gets cutoff during fault conditions as well as able to synchronize with utility grid voltage (Fig. 1).

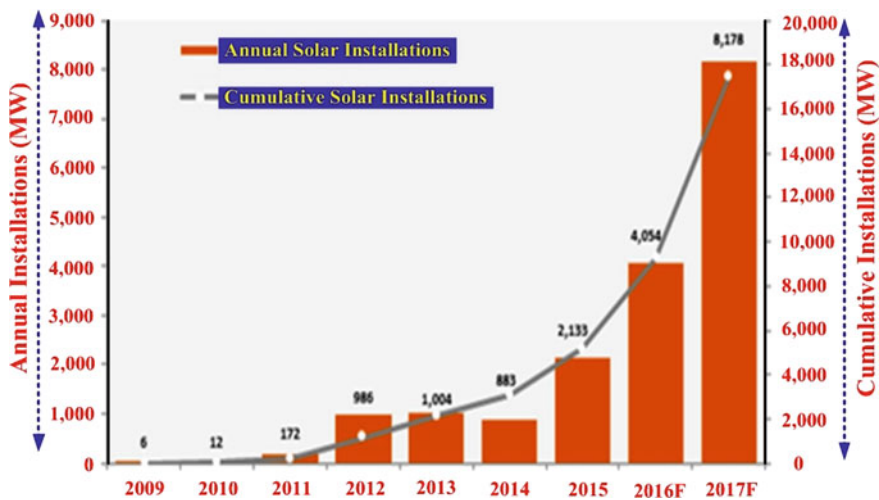


Fig. 1 Installed PV capacity in India (in MW)

2 Multilevel Inverter

Various initiatives have been taken to begin high power equipments in the past years. Motor drives with medium power applications need voltage and energy levels. However, it is very difficult to associate semiconductor-based power devices with it. Therefore, multilevel inverter has been provided for high and medium power applications. This topology provides high ratings of power with renewable source integration such as PV, wind and fuel cell with multilevel inverter to the utility grid.

In 1975, the concept of multilevel inverter has been introduced which begun with three-degree inverter. Recently, various multilevel topologies of inverter have been described which works with sequence of semiconductor devices, decrement in DC voltage level and synthesized staircase voltage level to produce higher level of electrical power. Capacitors, batteries and renewable sources are employed as multi DC voltage regulators, and DC assets are produced by commutating of these sources.

A multilevel inverter comprises many advantages compared to conventional inverters which work on sequence switched frequency with PWM strategy. The multilevel inverter produces low total harmonics, lesser dv/dt stresses, reduced electromagnetic compatibility and satisfactory wave nature of staircase. It also works on fundamental and high switching which reveals that decrement in switching frequency infers lower switching loss and good performance.

Nevertheless, the multilevel inverter has some shortcomings as more semiconductor-based power switches and switches with lower voltage rating that can also be utilized for multilevel inverter. Moreover, each power switch needs separate gate pulse generation circuitry which results in complexity of the design.

Several topologies of multilevel inverters have been discussed by various researchers during the past decades. Nowadays, various researches are carried out especially on recent converter topology and its control strategy. Cascaded H-bridges with different DC supply, diode-clamped and capacitor-clamped-based multilevel inverter topologies have been discussed by researchers. Additionally, sinusoidal pulse width modulation, space vector modulation and selective harmonic elimination methods are frequently used as modulation techniques for multilevel inverters. The multilevel inverters are used for various applications as motor drives, renewable energy integration, AC transmission system as well as traction systems.

3 MATLAB/Simulink Model for Proposed System

The multilevel-based inverter for PV power generation has been evaluated using MATLAB simulation environment. The complete sets of simulation responses are presented for PV grid integration, and Simulink responses have been analyzed. Figure 2 presents the inverter voltage produced that varies with time scale. Inverter current is presented in Fig. 3 with time. Figures 4, 5 and 6 explain the waveforms

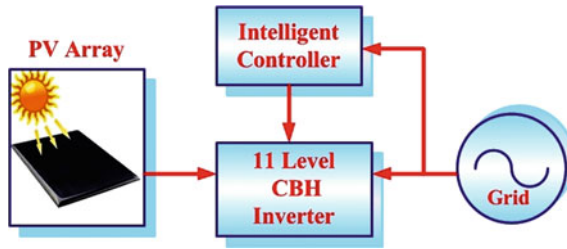


Fig. 2 Block diagram of grid-connected PV power system

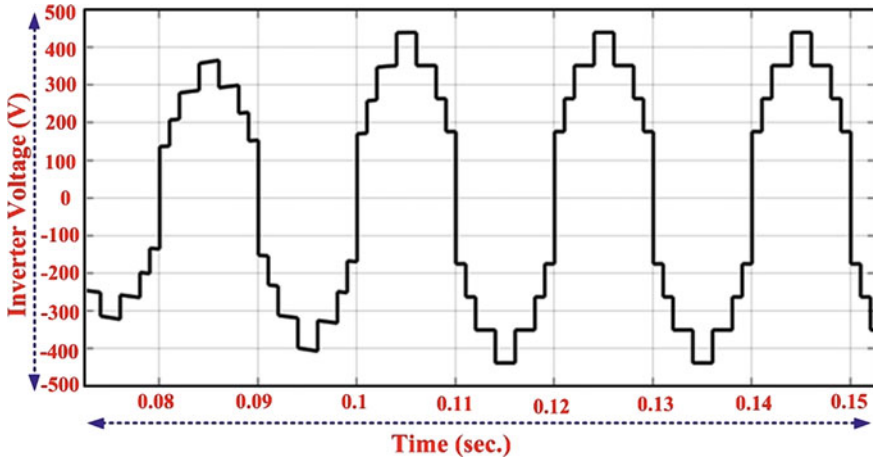


Fig. 3 Inverter voltage varies with time

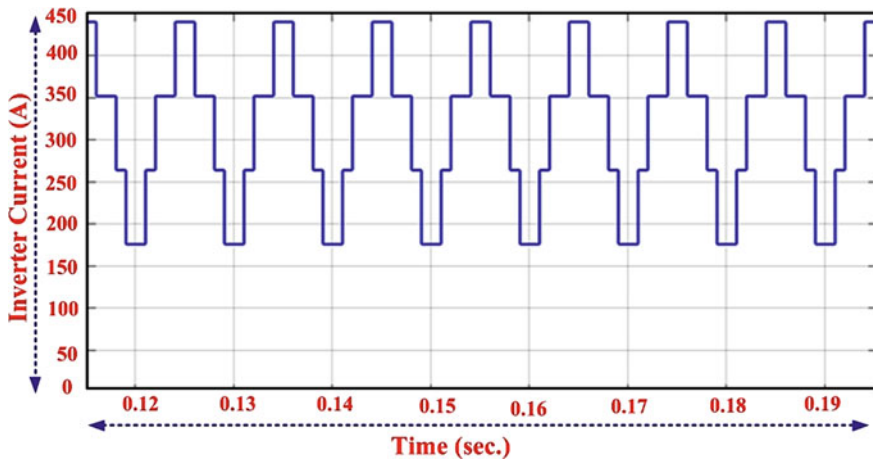


Fig. 4 Inverter current varies with time

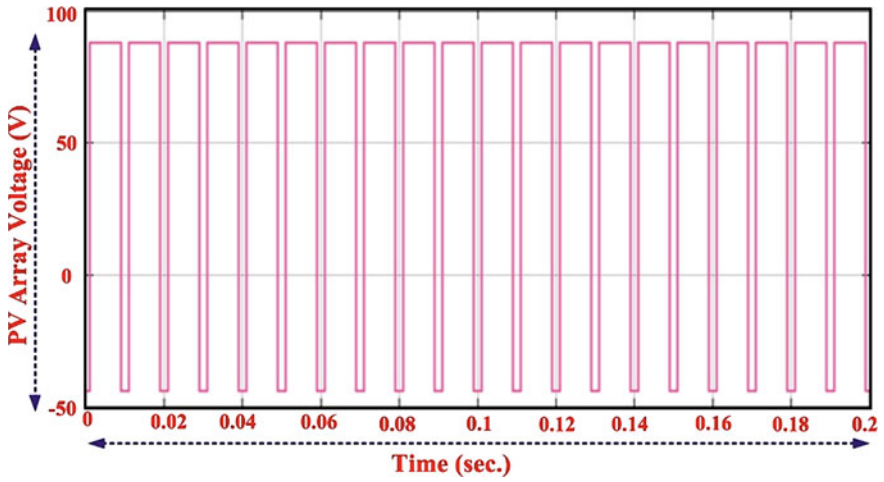


Fig. 5 PV Array voltage varies with time

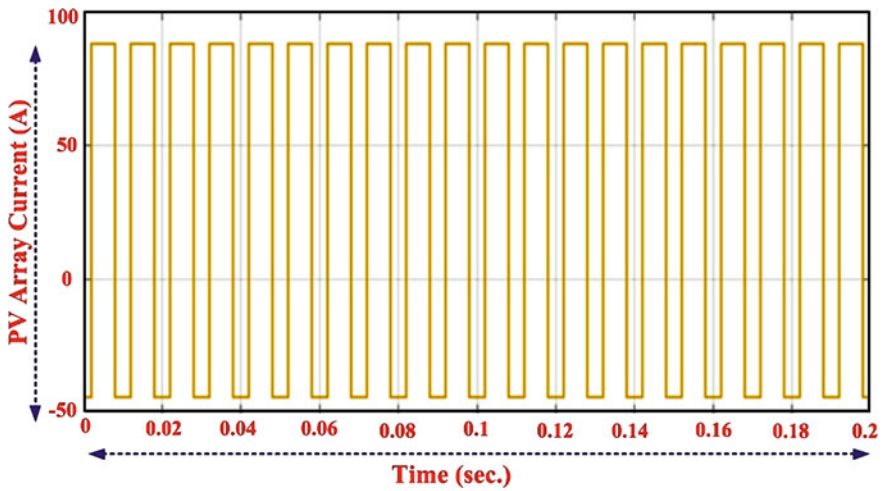


Fig.6 PV current varies with time

of PV voltage, current and multilevel 11 level inverter output voltages, respectively (Fig. 7).

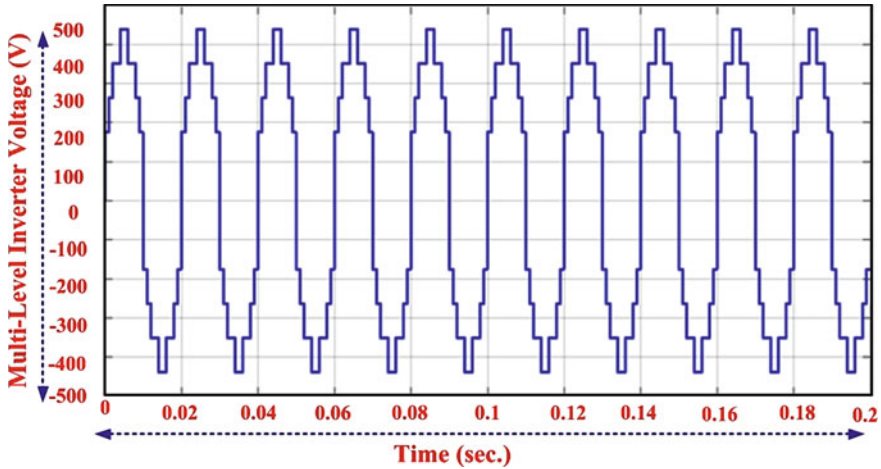


Fig. 7 Multilevel inverter voltage waveforms

4 Conclusion

In this research work, multilevel inverters (cascaded H-bridge) have been considered as dispensed power electronics system for PV power system. Intelligent fuzzy logic-based control system has been employed for monitoring grid integration continuously and is also responsible to regulate cascaded H-bridge inverter. The simulated responses validate the designed control system for PV power generation.

References

1. Priyadarshi N, Padmanaban S, Maroti PK, Sharma A (2018) An Extensive practical investigation of FPSO-based MPPT for grid integrated PV system under variable operating conditions with anti-islanding protection. *IEEE Syst J* 1–11
2. Priyadarshi N, Padmanaban S, Bhaskar MS, Blaabjerg F, Sharma A (2018) A fuzzy SVPWM based inverter control realization of grid integrated PV-wind system with FPSO MPPT algorithm for a grid-connected PV/wind power generation system: hardware implementation. *IET Electr Power Appl* 1–12
3. Priyadarshi N, Anand A, Sharma AK, Azam F, Singh VK, Sinha RK (2017) An experimental implementation and testing of GA based maximum power point tracking for PV system under varying ambient conditions using dSPACE DS 1104 controller. *Int J Renew Energy Res* 7(1):255–265
4. Hong L, Duo Y, Wenzhe S, Jinhu L, Xinghuo Y (2019) An overall distribution particle swarm optimization MPPT algorithm for photovoltaic system under partial shading. *IEEE Trans Industr Electron* 66:265–275
5. Sanjeevi P, Neeraj P, Jon BH-N, Mahajan B, Farooque A, Amarjeet KS, Eklos H (2019) A novel modified sine-cosine optimized MPPT algorithm for grid integrated PV system under real operating conditions. *IEEE Access* 7:10467–10477

6. Priyadarshi N, Sharma AK, Azam F (2017) A hybrid firefly-asymmetrical fuzzy logic controller based MPPT for PV-wind-fuel grid integration. *Int J Renew Energy Res* 7(4)
7. Priyadarshi N, Sharma AK, Priyam S (2017) Practical realization of an improved photovoltaic grid integration with MPPT. *Int J Renew Energy Res* 7(4)
8. Nishant K, Ikhlaq H, Bhim S, Bijaya KP (2017) Maximum power peak detection of partially shaded PV panel by using intelligent monkey king evolution algorithm. *IEEE Trans Ind Appl* 53:5734–5743
9. Kinattungal S, Peddapati S, Padmabhan SRN, Sishaj PS, Sanskaran P (2015) Enhanced energy output from a PV system under partial shaded conditions through artificial bee colony. *IEEE Trans Sustain Energy* 6:198–209
10. Priyadarshi N, Padmanaban S, Mihet-Popa L, Blaabjerg F, Azam F (2018) Maximum power point tracking for brushless DC motor-driven photovoltaic pumping systems using a hybrid ANFIS-FLOWER pollination optimization algorithm. *MDPI Energies* 11(1):1–16
11. Hugues R, Fabrizio D, Julien F, Giovanni P, Giovanni S, Jean PM, Serge P (2015) A PSO-based global MPPT technique for distributed PV power generation. *IEEE Trans Ind Electron.* 62:1047–1058

A Study on the Airflow Variation and Energy Consumption of Apartment Complexes in Medium Cities



Jun-Gi Lee, Sung-Hoon Kim, and Kyung-Hee Lee

Abstract The relationship between the urban heat island and the change of the airflow before and after the apartment house which is provided as a measure to secure the residence and the energy consumption of the apartment house at a specific time are analyzed. Obtain the wind roses and average temperature of the Korea Meteorological Administration to determine the climate characteristics of the target area. After that, the energy consumption of the apartment house is analyzed by collecting and analyzing the energy consumption for cooling and heating at a specific time by utilizing the private data system of building data. The airflow change is divided into the before and after using the Ecotect analysis program. In the analysis of energy consumption of apartment houses, it was confirmed that the insulation performance of the apartment was affected by energy consumption for cooling and heating over time. The analysis of the change of the airflow by the construction of the apartment house shows that the summer and winter air low in the area, can not escape to another place and it will rise and cause that heat island phenomenon. In the future, research will be carried out to prevent the occurrence of urban heat island phenomenon in areas with low airflow.

Keywords Airflow · Energy consumption · Urban heat island phenomenon · Building insulation performance · Apartment complex

1 Introduction

The industrialization and urbanization have increased the number of people who come into the city, and cities have been proving medium- and large-sized apartment

J.-G. Lee

Research Institute of Industrial Technology, Pusan National University, Busan, Republic of Korea
e-mail: jk_junki@pusan.ac.kr

S.-H. Kim · K.-H. Lee (✉)

Department of Architectural Engineering, Pusan National University, Busan, Republic of Korea
e-mail: samlgh@pusan.ac.kr

S.-H. Kim

e-mail: police0215@hanmail.net

© Springer Nature Singapore Pte Ltd. 2020

A. K. Bhoi et al. (eds.), *Advances in Greener Energy Technologies*,

Green Energy and Technology, https://doi.org/10.1007/978-981-15-4246-6_9

complexes as a measure to secure residences following the population growth. Even small cities, which are not large cities as special cities and metropolitan cities, have been also building apartment houses when they develop housing sites, redevelop houses, or provide new houses on their own. The acts as a cause may induce the urban heat island phenomenon, which could be seen in the downtowns of large cities, in small cities, and affect the microclimate of existing regions. In particular, being small and medium-sized complexes are constructed on existing field where low-rise houses or paddy field or field is placed, it has an effect on greening ration, sunshine amounts, isolation and air current to existing field or environs [1, 2]. The influence of each other in the same complex varies depending on the spacing and arrangement type of the building [3]. In addition, the increase in the number of newly built apartment due to land development of housing redevelopment projects consumes energy for summer cooling and winter heating. Energy consumption for summer cooling lowers the temperature inside the apartment and raises the temperature of the outside air, which is a major cause of the urban heat island phenomenon [4]. Existing researches have studied the effect of urban heat island phenomenon on the urban area, the point or the time of occurrence, the temperature change, and the energy consumption to the apartment generation location, layout type, or configuration [6–8]. In addition, even if the actual energy consumption is collected, it is possible that the user of the building is informed that experiment is being performed and data is collected, which may differ from the actual energy usage data [9, 10].

In this study, the change of the airflow and the energy consumption of the specific period where analyzed according to the season before and after the construction of the small complex apartment. Analysis of the change in airflow may suggest ways to minimize air pollution that may occur in area scheduled for future construction. And the need for the analysis is argued for comfortable atmospheric environment in the area where artificial structure can be excessively densely distributed. The energy consumption analysis compares the energy consumption when the apartment is newly built and the energy consumption after the period. The result of this analysis can be used as a resource to identify change in energy consumption and the time of green remodeling. And the result of this study can be used as a basic data to analyze the urban heat island phenomenon that can occur in small and medium cities through the construction of apartment complexes.

2 Materials and Methods

In order to conduct this study, areas where the development activities have occurred were selected as shown in Fig. 1, and analysis models were set separately for before and after the development activities. The selected area is located in the center of the inland province and is likely to be vulnerable to urban heat island phenomenon. With the analysis models set as above, air current analysis was carried out in the Ecotect analysis program. And apartment energy consumption was collected using the private data system of building data [11].

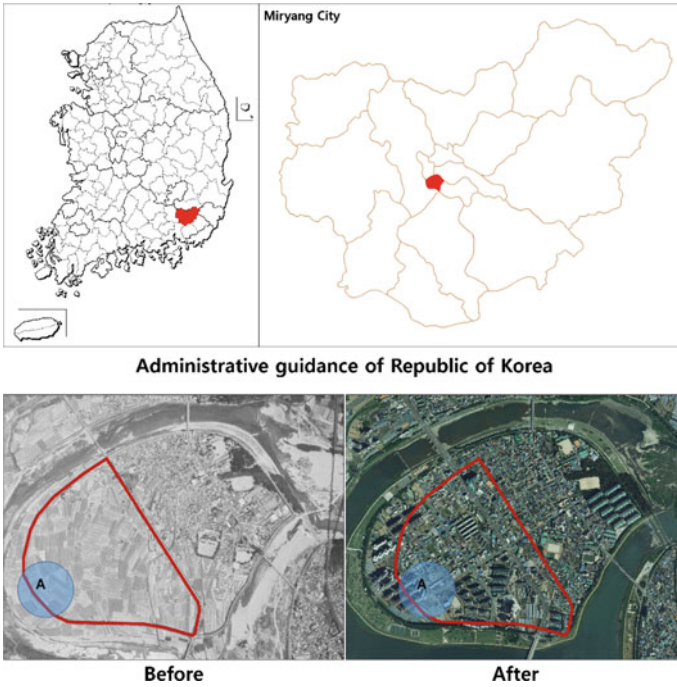


Fig. 1 Before and after development of analysis area in Republic of Korea

2.1 Overview of the Energy Consumption Analysis

To compare climate change and apartment energy consumption, the meteorological agency provided to local climate data for the analytical model, as shown in Fig. 2

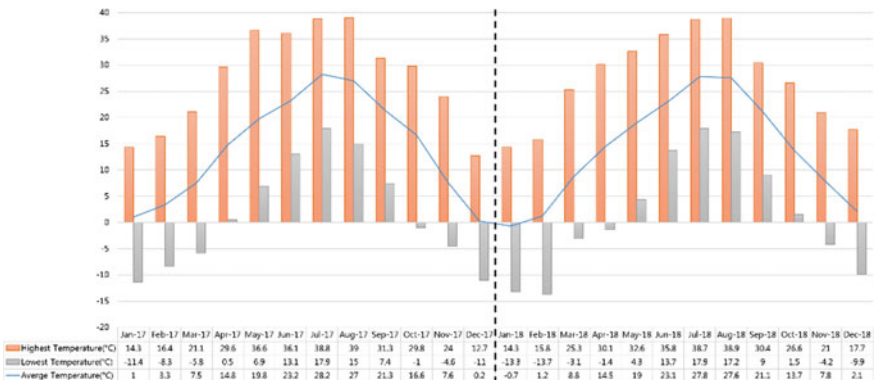


Fig. 2 Temperature change between 2017 and 2018

[12]. The lowest temperature in winter, 2017, was minus 11.4 °C, and the highest temperature in summer was 35.9 °C. The lowest temperature in winter, 2018, is minus 13.7 °C, and the highest temperature in summer is 39.0 °C. Winter and summer temperature in 2018 are higher than in 2017, and are less cold in winter and hotter in summer. When the heating period and the cooling period are distinguished, the heating from other areas is identified by local characteristics located in the inland areas.

The location of the selected apartment to analyze energy consumption is as shown in Fig. 3. The orientation facing the living room window of the apartment was set as the main orientation, and the entire analysis model was confirmed to be South-East, South-West, and the construction period differs from 2006, 2007, and 2009. Hyumeonsia apartments are rented houses, while Koarlu and Puleujio apartment are for sale. Basic information about apartment is shown in Table 1. Energy consumption analysis divides residential area by monthly energy consumption, and finds energy consumption per unit area and divides into electricity and gas consumption. Electricity is divided into energy for summer cooling and energy for winter heating and gas is set as energy consumption for winter heating.



Fig. 3 Location of selected apartment for energy consumption analysis

Table 1 Apartment basic information for energy consumption analysis

Division	Data of use approval	Heating method	Household number	Corridor type	Residential area (m ²)
1. Humeonsia apart.	October 09, 2009	Individual	861	Corridor	39,376.18
2. Koalu apart.	July 31, 2006	Individual	344	Terraced	29,794.69
3. Puleujio apart.	January 10, 2007	Individual	457	Terraced	42,511.76

2.2 Overview of the Airflow Analysis

As for wind rose chart for air current analysis as shown in Fig. 4, the seasonal wind directions and wind speed form 2017 and 2018 provided by the Meteorological Administration were analyzed and the analyzed average wind directions and wind speeds are as shown in Table 2. The average wind speed in spring is 1.47 m/s, in summer is 1.73 m/s, in autumn is 1.53 m/s, and in winter is 1.42 m/s; it has been confirmed that the wind in the area is relatively small. The low airflow speed in the area can cause a heat island phenomenon where the heat does not move in the

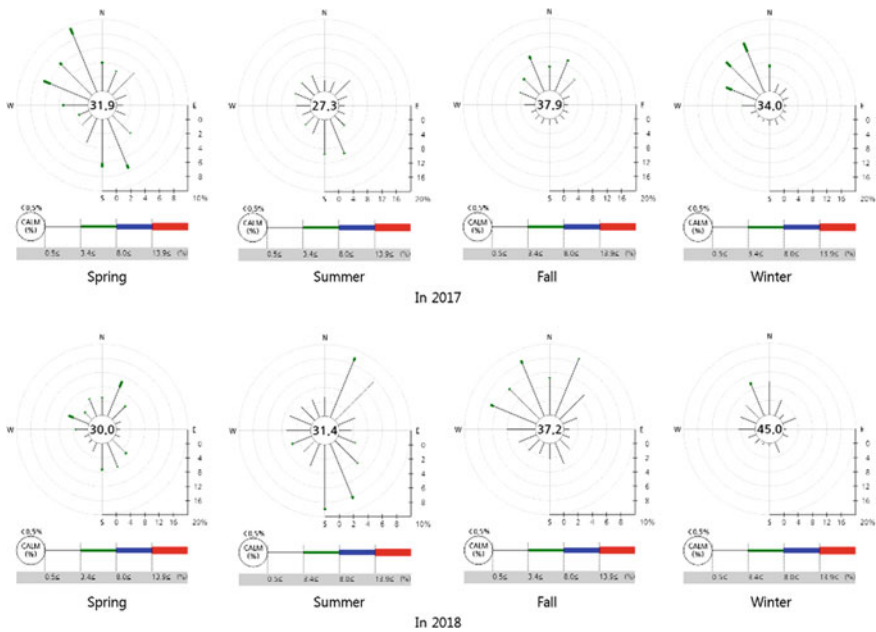


Fig. 4 Wind directed and wind speed in 2017 and 2018

Table 2 Average wind directions and wind speeds

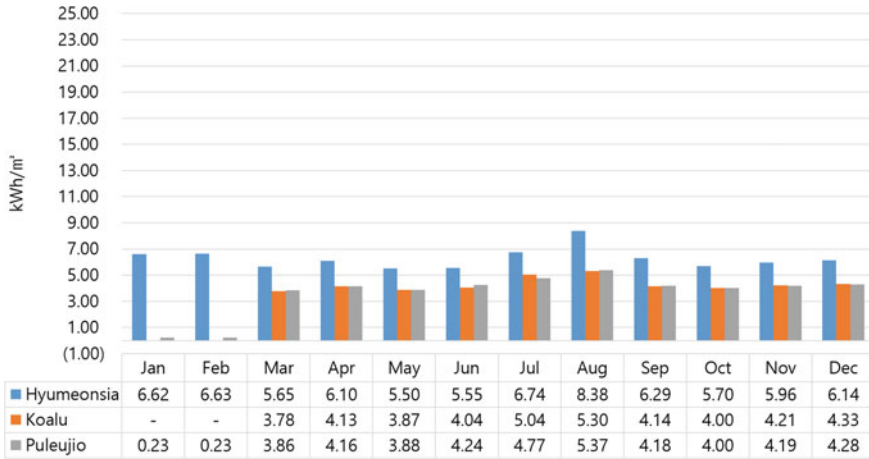
Division	Spring	Summer	Fall	Winter
Direction	NNW	NNW	SSE	NNW
Speed (m/s)	1.47	1.73	1.53	1.42

downtown area due to the difficulty of moving or diluting the hot heat generated by equipment that operates for summer cooling to another area.

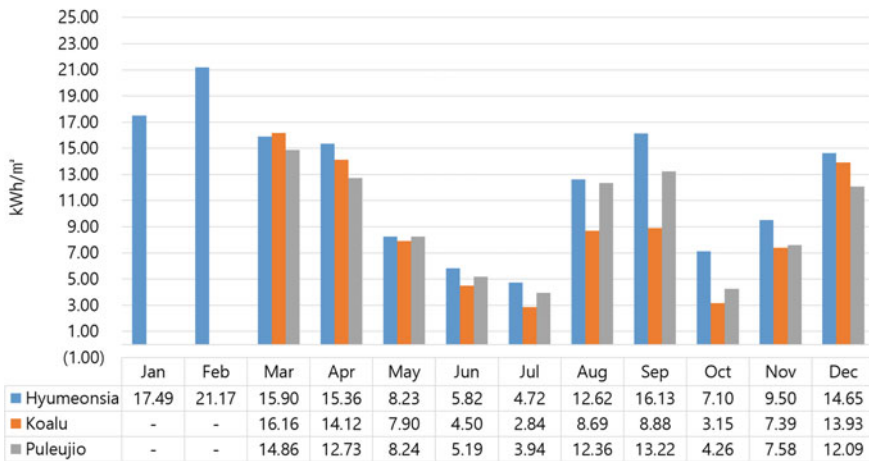
3 Results and Discussion

3.1 Energy Consumption Analysis

The electricity and gas energy consumption data for January–February 2017 were not included in the comparative analysis. In addition, August–September data of 2017 gas energy consumption are confirmed as unreliable data. In August–September, the outside temperature is high; therefore, the amount of electricity used for cooling should be higher than the amount of gas used for heating. As shown in Fig. 5, the gas consumption in August–September seems to be abnormal. To analyze the results of this study, we compare the electricity and gas energy consumptions in Fig. 6 by 2018. The construction times of three apartments selected for energy consumption comparison are 2006, 2007, and 2009. The closer the building time is the better the insulation performance in order of 2009 (Hymneonsia), 2007 (Puleujio), and 2006 (Koalu). Depending on the building year of the building, the insulation performance of the applied structure is different, which has an effect on energy consumption. In addition, the hypothesis that the recently built building's thermal insulation performance is better than the previously built building's thermal insulation performance, it is possible to establish the hypothesis that the recently built building consumes less energy. Electric energy consumption was the lowest in March, April, and May, which means less energy is used for cooling or heating. Electricity is used for cooling from June to September, and electric energy is used for heating in October, November, December, January, and February. Among the three selected apartments, Hymneonsia apartments use the most electric energy on average to compare energy consumption. It was built two to three years later than other two apartments, but the energy consumption was high. This is not only in the case of electric energy but also in gas energy consumption. The cause can be found in the method of housing sale. The apartments that were sold in 2009 are rental apartment, and the other two apartments are available for sale. Rental apartment can not be traded and the tenant can not repair or change the interior at will. On the other hand, sale apartments are available for sale, and after the sale, the inside of the buyer can be repaired or changed at will. In the process of repairing or interiors, window replacement is considered to be the biggest factor to improve the insulation performance of the apartment.



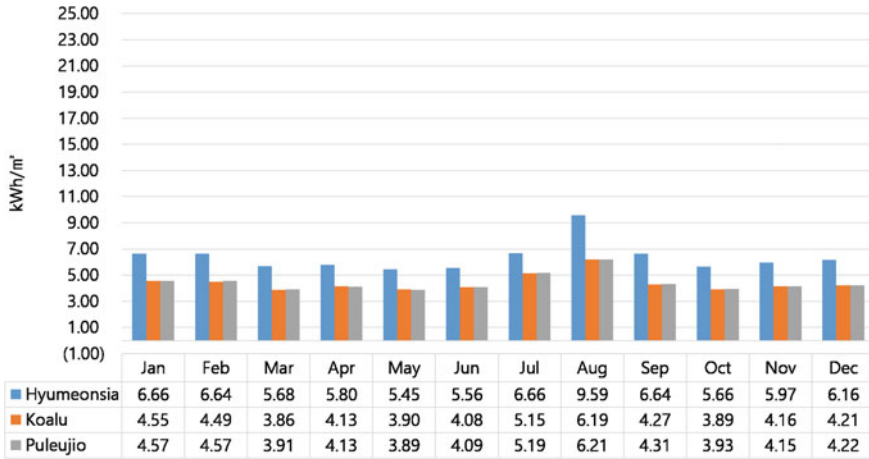
Electric Energy Consumption in 2017



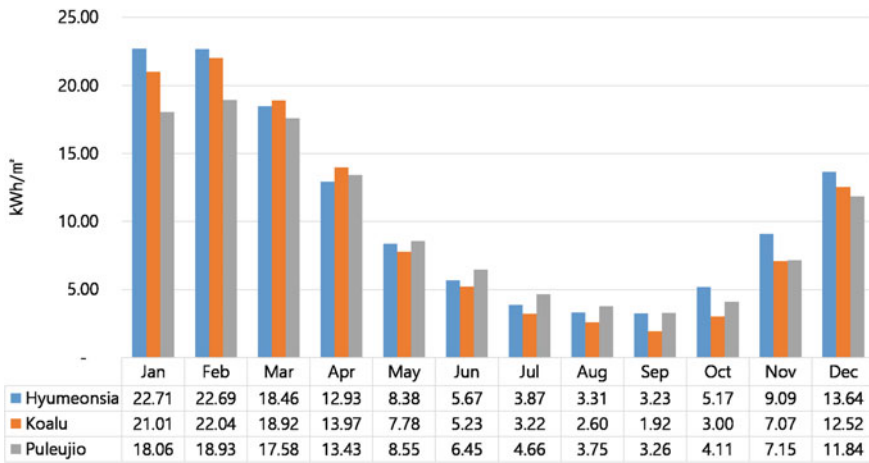
Gas Energy Consumption in 2017

Fig. 5 Electric and Gas energy consumption in 2017

Energy consumption for cooling and heating has many variables such as the number of electronic products in the household, frequency of use, generation members, generation member’s schedule, age, and efficiency of air-conditioning equipment. Among them, the insulation performance of a building is more important than other variables when building a new apartment. Good insulation performance means that heat is blocked from outside of the summer and heat is blocked from the inside of the winter. The interruption of heat reduces the use time of equipment for cooling and heating energy consumption. And more research is needed in this part.



Electric Energy Consumption in 2018



Gas Energy Consumption in 2018

Fig. 6 Electric and Gas energy consumption in 2018

3.2 Airflow Analysis

The results of the analysis of changes in air flow according to the development actions are as follows. It can be seen that before development activities, airflow was flowing smoothly in blocks consisting of paddy fields or dry fields. When the blocks of paddy fields or dry field were constructed into low-rise house and small- and medium-sized apartment complexes, airflow were shown to be stagnant in low-rise house block and were shown to relatively smoothly flow in apartment complexes but as shown in Figs. 7 and 8.

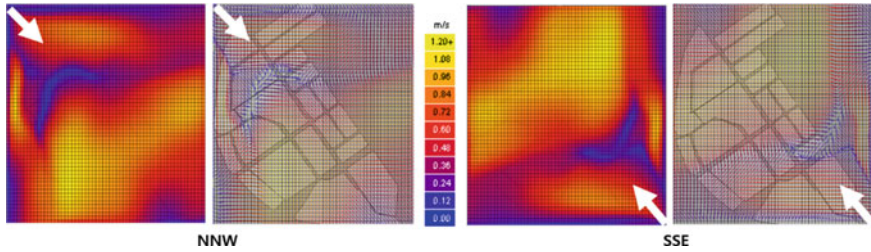


Fig. 7 Analysis of the airflow change before development

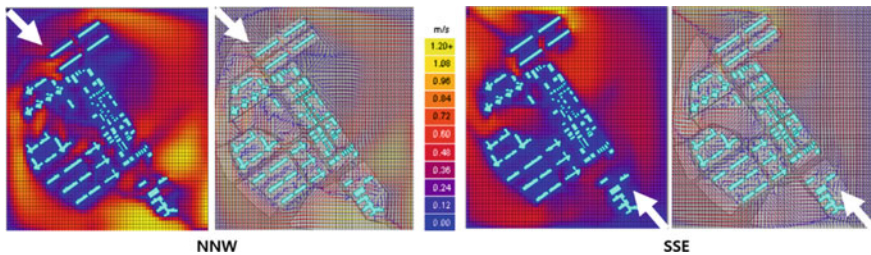


Fig. 8 Analysis of the airflow change after development

The vortices were shown to occur in internal spaces between buildings. In addition, it was identified that the airflow was not flowing smoothly in general and this is judged attributable to the fact that the average wind speed in the selected analysis area was not higher than 1.47 m/s. In future studies, when air currents are stagnant at less than 1m/s, we want to analyze the effect of changes in green ground rate on land or building surface temperature to determine whether urban heat island phenomena occur.

4 Conclusion

The purpose of this study is to analyze the change of airflow and apartment energy consumption when a new apartment is built or redeveloped in a small city. In the analysis of energy consumption of apartment houses, it was confirmed that the insulation performance of the apartment was affected by energy consumption for cooling and heating over time. This will require a lot of the data to be verified in the future. The analysis of the change of the airflow by the construction of the apartment house shown that the summer and winter air currents are stagnated due to the arrangement of the building. Especially, when the average airflow rate is low in the area, it can not escape to another place and it will rise and cause the heat island phenomenon. In the future, research will be carried out to prevent the occurrence of urban heat island phenomenon in areas with low airflow.

References

1. Jung EH, Son KS, Ryu JW, Kim DW, Cha GC (2008) Evaluation of spatial characteristic of wind corridor formation in Daegu area using satellite data. *J Korean Assoc Geogr Inform Stud* 11:73–84. <https://kiss.kstudy.com/thesis/thesis-view.asp?key=2740735>
2. Park JH (2003) Air temperature reduction effects of small green spaces in Urban blocaks of Seoul. Seoul National University, Seoul. <https://s-space.snu.ac.kr/handle/10371/124962>
3. Jung HE, Han BH, Kwak JI (2015) A study on air temperature reduction effect and the functional improvement of street green areas in Seoul, Korea. *J Korean Inst Landscape Archit* 43:37–49. <https://www.ndsl.kr/ndsl/commons/util/ndslOriginalView.do?dbt=JAKO&cn=JAKO201527358962261&oCn=JAKO201527358962261&pageCode=PG11&journal=NJOU00290624>
4. Geoff L, John P, Lee K, Patrick L, Sarah L (2018) The increasing trend of the urban heat island intensity. *Urban Clim* 24:360–368. <https://doi.org/10.1016/j.uclim.2017.02.004>
5. Ling J, Li Q, Xing J (2015) The influence of apartment location on household space heating consumption in multi-apartment buildings. *Energy Buildings* 103:185–197. <https://www.sciencedirect.com/science/article/pii/S0378778815300840?via%3Dihub>
6. Jung HJ, Kang J (2018) An energy model of high-rise apartment building integrating variation in energy consumption between individual units. *Energy Buildings* 158:656–667 (2018). <https://doi.org/10.1016/j.enbuild.2017.10.047>
7. Jin HS, Choi BH, Kang JK, Kim SI, Lim JH, Song SY (2016) Measurement and normalization methods to provide detailed information on energy consumption by usage in apartment buildings. *Energy Procedia* 96:881–894. <https://www.sciencedirect.com.ssl.eproxy.pusan.ac.kr/science/article/pii/S1876610216308001>
8. Suh DJ, Yoo YS, Lee IW, Chang SJ (2012) An electricity energy and water consumption model for Korean style apartment buildings. In: 12th international conference on control, automation and systems, pp 113–117. <https://ieeexplore.ieee.org.ssl.eproxy.pusan.ac.kr/document/6393329/authors#authors>
9. Jan HJ, Kang JA (2018) An energy model of high-rise apartment buildings integrating variation in energy consumption between individual units. *Energy Buildings* 158:656–667. <https://www.sciencedirect.com/science/article/pii/S0378778817334266?via%3Dihub>
10. Jang HJ, Kang JA (2016) A stochastic model of integrating occupant behavior into energy simulation with respect to actual energy consumption in high-rise apartment buildings. *Energy and Buildings* 121:205–216
11. Energy Consumption of apartment buildings [Data on Internet] Building data open system. Available from: <https://open.eais.go.kr/nbemifm/OpenInfoList.do#> (website)
12. Average temperature data collection in Miryang City [Data on Internet] Meteorological office: Miryang city temperature 2017 and 201812. Available from: <https://data.kma.go.kr/data/grmd/selectAsosRltmList.do?pgmNo=36> (website)

Real-Time Smart Volumetric Fuel Estimation System for Automobiles Under All Road Conditions



Priyanshi Singhal, Nivedita Singh, Rajkumar Viral, Saket Kumar, Divya Asija, P. M. Tiwari, and Pallavi Choudekar

Abstract Due to the rapid development of the automobile industries, fuel estimation and its indication are very significant and become crucial in order to make the automobile owner conscious about the distance it could cover. Thus, sometimes it becomes essential for the driver to discern the available quantity of fuel remain in the vehicle to refill the vehicle tank within time. Imprecise fuel level indications lead to incorrect estimations and uneasiness to the user. Monetary loss can be incurred due to this. To prevent this, an accurate and efficient alternative technology is suggested. This paper presents the uses of turbine type of flow sensors for the accurate measurement of the fuel present in vehicle. Two turbine types of flow sensors are fixed at fuel tank inlet and carburettor outlet so that fuel input and consumption are recorded instantaneously to measure balance fuel in tank. Further, to ensure accuracy in the measurement, both the sensors are calibrated at various calibration factors. At calibration factor 9, the proposed system is shown 2% error in inflow of fuel, and at 6 calibration factor, 0% error is shown in out flow of fuel from tank, respectively. The flow rate is also an important parameter because it can change error rate of fuel. The considered flow rate for the proposed system is about 12–50 ml/s approximately.

P. Singhal · N. Singh · R. Viral · S. Kumar (✉) · D. Asija · P. M. Tiwari · P. Choudekar
Amity University Uttar Pradesh, Noida, UP, India
e-mail: skumar39@amity.edu

P. Singhal
e-mail: astroshivi22@gmail.com

N. Singh
e-mail: ditas2801@gmail.com

R. Viral
e-mail: rviral@amity.edu

D. Asija
e-mail: dasija@amity.edu

P. M. Tiwari
e-mail: pmtiwari@amity.edu

P. Choudekar
e-mail: pachoudekar@amity.edu

The proposed method shows accurate estimation of remaining fuel. Additionally, the proposed method is cost effective and easy to implement.

Keywords Fuel · Gauge · Fuel indicator · Measurement · Sensors · Accuracy · Calibration factor

1 Introduction

Fuel measurement indication turns out to be vital in vehicles as it facilitates the user for distance estimation that may be travelled with the available fuel. False measurements of the fuel left cause uneasiness and discomfort to the user [1]. In most of the vehicles, real fuel data loaded, and the vehicle's fuel utilization maintenance poses a problem sometimes. The basic explanation behind extending a vehicles fuel range is definitely the fuel check, which is given on the dashboard panel of the vehicle, which helps the driver to identify that the vehicle has less amount of fuel left. Though, there is a lot of fuel available. Subsequently, the conventional fuel systems utilized are very inappropriate measurement and incorrect [2].

Most widely recognized and customary fuel measurement system generally uses resistive or potentiometre type flow sensors in order to measure the quantity of fuel inside the vehicle's tank. These kinds of system have two units, i.e. (i) the sender unit responsible to measure the quantity of fuel inside the tank (ii) the gauge unit capable to show the known level of fuel to the user/driver [3]. The smart fuel measure system is another process, which is already available in markets [4]. Additionally, makes utilization of installed system, for instance, microcontrollers or chip for giving better accuracy. The sending and the measurer are the two important units that are available in fuel indicating system. The sending unit usually mounted inside the fuel tank of vehicle slightly above the level of fuel, normally made of froth, connected with a thin metal flexible bar or wire. The end point of this metal bar/wire is arranged so that it can move over a variable resistor or potentiometre. This varying resistor has a small contact segments of resistive metal which is in touch with the sliding arm of variable resistor and resulting current enable to flow causes the deflection of the indicator. The indicator deflection is directly proportional to the fuel quantity in the tank. When the fuel tank is unfilled, there is a movement of the float to the base of the tank, which further moves the strip through the resistor in the same manner, which again produces the opposition and flow of the current indicate the fuel remain to measure [5]. In most of the fuel measurement system, a fuel bimetallic strip is used having a thermal coefficient of expansion, which is different from one another [6]. When an obstruction is observed, the current increases, and the strip is heated that cause the expansion of metal leading to bend of the strip, and this action tends to the movement of the needle over the fuel gauge [7]. With the increase in resistance, amount of the current passing through it decreases coils causing the bimetallic strip to cool. The strip attaches with a pointer which can move full to null as soon as the strip cools. However, recent vehicles have been equipped with the

advanced fuel measure system in which a centralized microcontroller board/chip is implemented. The controller chip communicates with changing value of resistor and shows this value digitally on the dashboard display of vehicle. Therefore, in easiness of corresponding voltage measurement, the accuracy of fuel measurement in these systems improved [8].

A major area in fuel degree estimation of vehicle is to provide the one on time exact value of fuel. The calculation to evaluate the level of fuel should be rigid and enough vigorous with the aim that it can estimate to measure the amount of fuel present in car's fuel tank.

Most of the available car manufacturers provide a sign which can show the fuel measured in a repository. This device also finds many applications in fuel measurement of buried tank such as at petrol pumps, gas stations and oil refineries. The accessible fuel is estimated in tank by detecting the height of the level of fuel taken from marked place like the tank base. However, the level of fuel is steady on the vehicle, when tank placed on it is not moving.

Whenever, level of tank is at full capacity or it show the maximum current flowing in the circuit and the indicator needle points to "F" signify the full level of tank. However, when the tank is empty and at low level, the needle points to "E" that indicates an empty tank. The level of fuel might consistently vary with street surface conditions, e.g. slant, vehicle inclination, vibration or bad road conditions. When the indicator moves in an opposing direction, the sensor displays different quantity of the fuel. Some of the new vehicles have a fuel check device. The fuel level sensors are normally based on variable motion which has a gliding part that deflects and moves alongside the level of fuel [9]. The system has two essential hardware components where one is for detecting and another is for sign of level of fuel. The detecting unit normally utilizes a flow measuring sensor to know the level of fuel. Though, the indicating system estimates the measure of electric current situated across the detecting unit and display the level of fuel. Numbers of other methods are also reported to show fuel measurement using different apparatus [10]. Moreover, as the advanced technologies growing rapidly, the new and sophisticated equipments are available and thus make fuel measurement system more accurate and effective [11].

Therefore, the proposed system is capable in overcoming the drawbacks of currently available fuel measurement system. This system can be used to measure the fuel volume whatever the conditions of road such as slant, slope, vehicle inclination, vibration and bumps. Here, two turbine flow sensors are used for taking the inlet and outlet fuel volume values. The measured value of fuel is sent to Arduino controller in the form of signals. Based on the programming of the Arduino controller and mathematical formulation, it estimates the exact quantity of fuel inside the tank for under different road conditions. This volume can be visualized by means of any display units such as the proposed system used a liquid crystal display (LCD). Thus, this accurate fuel measurement can enhance the vehicle's performance [12].

2 System Description

In the proposed method, an Arduino controller is used, which is connected to the flow sensors, and the LCD is connected to the Arduino and flow sensors to show the results of the flow rate. The sensor is placed in the tank and will give the results when fuel is flown in it. Two turbine type flow sensors are used in the proposed system.

Figure 1 shows the connection between the Arduino, LCD and sensors. A 5 V VCC and GND of flow metre is connected to Arduino's VCC and GND. The pulse line of flow sensors is connected to the Arduino's digital PIN 2, and rest is interfaced with LCD. Figure 1 shows the LCD starting input, connection between Arduino and LCD, similarly the entire connection of the circuit with sensors connected to the tank. The value is displayed after the increment of each ml or litre.

2.1 Arduino

Atmega328P based Arduino controller is used as a brain of the instrument. The device is controlled by this controller. Every sensor and display unit is connected through this controller. It generally consists of 14 digital pins, six analog inputs, a 16 MHz quartz crystal, a USB connection, a power jack, an ICSP header and a reset button [13].



Fig. 1 Proposed system description and connection

2.2 *Flow Sensor*

The proposed system uses two turbine flow sensors to measure to flow rate [14]. To measure fuel volume, it is the best practice to use flow sensors that have high reliability and accuracy in nature [15]. The sensor is set accordingly with the liquid flow and consists of a wheel type small sensor to calculate the fluid that has travelled through it. It also has a combined magnetic hall impact sensor that yields an electrical beat with each transformation. Except this, a plastic valve body, a water rotor and a hall impact sensor are the major part of liquid flow sensor. When liquid moves inside the rotor, then the rotor rotates. The speed of the rotor keeps changing with various rate of stream. The result of the correlated pulse signal is generated by the Hall effect sensor. This is reasonable to find the flow in liquid container. The Hall effect liquid flow sensor is YFS201, which has three wires; Red/VCC (5–24 V DC Input), Black/GND (0 V) and Yellow/OUT (pulse output). In order to estimate the liquid flow rate (in l/h or l/h or in ml/s), the generated pulse has to be recorded [16]. This sensor in some applications shows the measured quantity of fuel in percentage or in volume using analog output. In proposed system, the sensor gives it output in ml/s or l/h, which is suitable to measure fuel of vehicle [17]. Flow sensors provide various pulses corresponding to the immediate flow rate change [18]. Additionally, features of this sensor are that it is compact and easy to install. It generally gives high sealing performance [19].

2.3 *Liquid Crystal Display*

It is used to show the results or amount of volume that is measured by flow sensor. The LCD used 16×2 display, ground (0 V), VCC (4.7–5.3 V) [20].

2.4 *Fuel Tank*

The tank is referred to the tank of the vehicle. In proposed method, the volume of the tank is displayed on the LCD.

The ratings and technical specifications of each are given in Table 1.

3 **Proposed Methodology**

When the automobile is on a slope, this method may be very accurate. It reminds the driver to get the tank refilled only when required and provides the accurate value. The fuel flow rate of a vehicle is a key indicator of engine execution. Accurate displaying

Table 1 Technical specifications

S. No.	Specifications	Values
1	Min. working voltage	4.5 V DC
2	Max. working current	15 mA
3	Working voltage	5–24 V DC
4	Flow rate	1–30 l/min
5	Load capacity	10 mA
6	Operating temperature	80
7	Liquid temperature	120
8	Operating humidity	35–90% RH
9	Water pressure	1.75 MPa
10	Storage temperature	–25 to + 80
11	Storage humidity	25–95% RH

of the fuel flow rate is critical to examine engine execution and can be used to assessing vehicle's emissions. Knowledge of fuel consumption is also required for finding the running expenses of vehicle [21].

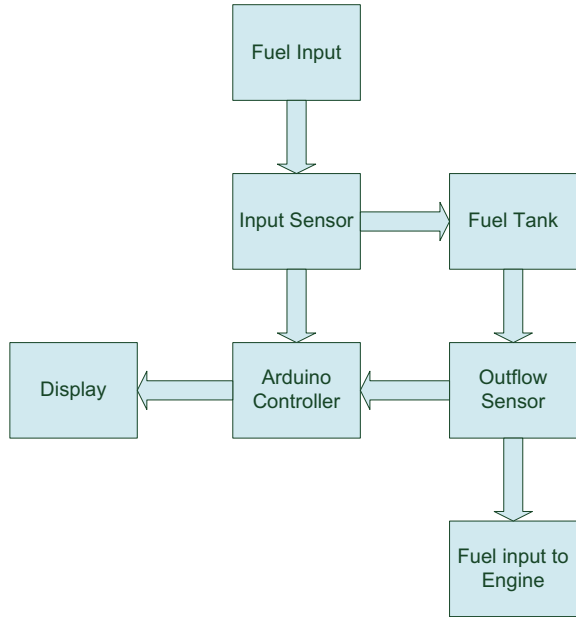
The methodology adopted in this paper provides the accurate rate of oil flow (petrol or diesel) by utilizing flow sensors at the fuel outflow nozzle and carburettor tank. It will exactly estimate the appropriate amount of fuel left in the tank. Also, the Arduino is coded for displaying the left-over quantity of fuel and rest amount of fuel filled in the tank. A suitable LCD display is used to display the readings.

Figure 2 shows the block diagram of the proposed method. As per block diagram, the first flow sensor is placed on the inlet of the nozzle which will detect the fuel going in the tank and continuously sends the signal to the Arduino, whereas the second flow sensor is placed at the outlet of the tank, it also sends the signals to the Arduino. Using the data received from both the flow sensors, Arduino calculates the final quantity present in the tank which is displayed on the LCD.

The computational procedure could be seen in the flow chart shown in Fig. 3. It represents the working of the flow sensor with Arduino uno and LCD. It can be seen that the first step is to initialize the LCD and flow sensor is calibrated. After that, flow rate is calculated and further total litres flowed since starting is calculated. This process goes on until the tank becomes empty.

In the proposed methodology, turbine flow sensors are used which works on the principle of Hall effect. As per the Hall effect principle, a voltage change is observed in a conductor with the magnetic area perpendicular to it and horizontal to the electric current. Flow metre, which is a small fan/propeller-shaped rotor, is placed in the path of the liquid flowing and utilizes the Hall effect. A small fan/Propeller-formed rotor, is located inside the route of the liquid flowing and uses the hall effect applied inside the flow metre [22]. The rotor rotates due to the pushing of the liquid against the fans of the rotor. The Hall effect sensor is connected to the shaft of the rotor. The current-carrying coil and the shaft of the rotor that are connected to a magnet constitute the sensor, thus inducing a pulse with the rotation of the rotor. For every litre of

Fig. 2 Block diagram of proposed method



liquid passing via it per minute, the output is approximately 4.5 pulses. The change in magnetic area as a result of the magnet connected to the rotor shaft is the major reason for pulse production [23].

In order to find out an optimal value of flow rate and minimize the errors in measurement, various calibration factors (C.Fs.) are used. It helps to choose the volume at different flow rates and CFs. The calculation of the flow rates in litres per hour (l/h) is carried out with the following empirical formulae given in Eqs. (1–5).

$$C.F. = \left[\frac{\{1000 / (\text{new time} - \text{old time})\} \times \text{Pulse Count}}{\text{Flow Rate}} \right] \tag{1}$$

$$\text{Flow Millilitre} = \left[\frac{\text{Flow Rate} \times 1000}{60} \right] \tag{2}$$

$$\text{Total Value} = \frac{\text{Flow(Millilitre)}}{1000} \tag{3}$$

$$\text{Flow Rate} = \frac{1}{4} \times \pi \times (\text{pipe diameter})^2 \times \text{Velocity} \tag{4}$$

$$\text{Velocity} = \left[\frac{\text{Pulse Count}}{\text{new time} - \text{old time}} \right] \tag{5}$$

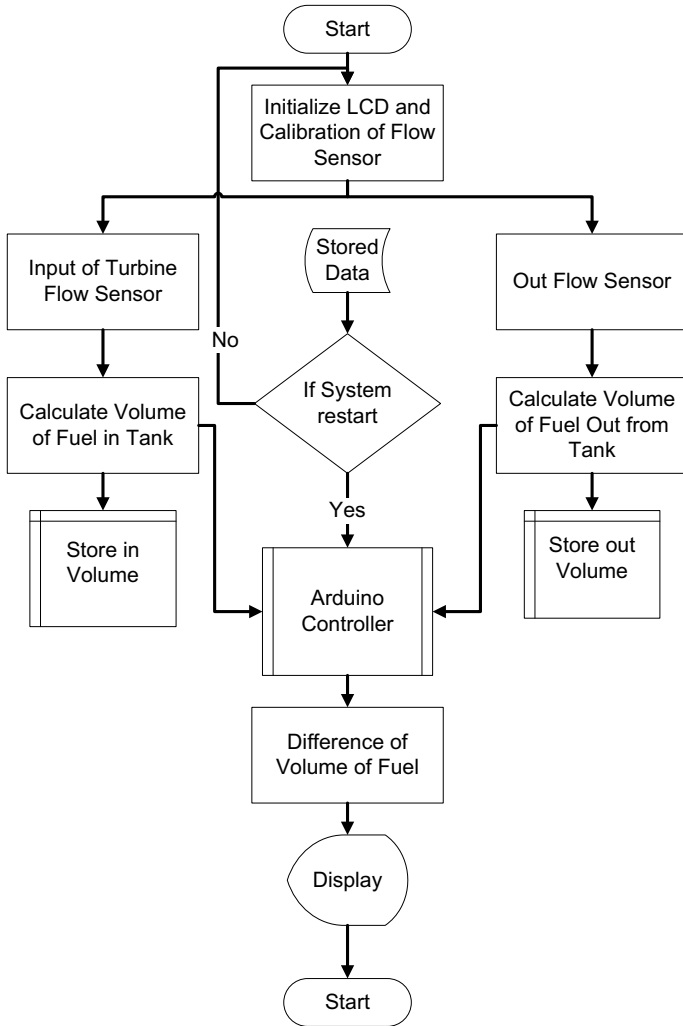


Fig. 3 Flow chart of proposed fuel measurement system

where pulse count is the pulse obtained from turbine flow sensor. New time and old time estimate the time to complete a cycle of turbine flow sensor between one pulse to another pulse.

- Flow Rate Total volume flow from a cross section of pipe
- Flow millilitre Volume of fuel in ml
- Total volume Volume of fuel in Litre
- C.F. Calibration Factor.

4 Results and Discussions

The proposed method shows the reading of liquid intake in the tank. Results shown in Table 2 are dependent upon different flow rate and calibration factor. According to the experimental set-up, calibration factor is dependent upon flow rate, and flow rate is depending upon pipe cross section area. Two approximation of flowrate is assumed according to experimental set-up in Table 2. Different calibration factors are assumed, and it is used to estimate the errors in quantity of liquid fuel.

In Table 2, calibration factor is assumed 4.5, and it is experimentally performed for 500 ml liquid fuel. It is clearly illustrated in Table 2 that for 12.5 ml/s flow rate, the quantity of fuel has different readings, and for increased flow rate 54 ml/s, the reading of liquid is different. Error observed in Table 2, with calibration factor 4.5 is average approximate 25.96% for 12.5 ml/s flow rate down from volume taken and 40.65% for 54 ml/s flow rate above the volume taken, respectively.

According to cross section area of pipe implanted in experimental set-up, the value observed for calibration factor is 9. For same quantity of liquid fuel with same flow rate 12.5 ml/s, the error observed 9% down from the values taken. And with flow rate 54 ml/s, observed error is approximately 1.56% above the measured quantity.

It is observed from Fig. 4 the least error is approximately 0.2% which is for 500 ml fuel with calibration factor 9. This observation can be useful for the experimental set-up, and it can be used as product in different vehicles.

With the highlighted observation in Table 2, the proposed system is giving less error than 10% down from volume taken and 1.56% up from volume under consideration. This error is further reduced to 0% after assuming the value in four decimal places and converted it in litres. Then, this error is reduced to 0% after applying the volume of 1 and 1.5 l.

Table 3 illustrates the reading from experimental set-up of proposed system with calibration factor 9, and error observed from Table 3 from 1 l of fuel is negligible approx. 3.75% down from the value taken and 6% approximately above the volume taken, respectively.

As per the data observed in Table 4, for 1.5 l of fuel, the average error observed 2.7% approximate down from volume observed with slow flow rate, and with fast flow rate 54 ml/s, the error is reduced to 0.86%. The error observed for higher volume is lower, and with volume of fuel for large tank, the error is reduced and near to zero. Consequently, after considering at 9 calibration factors, the least error, i.e. 0.86% is estimated. Hence, C.F 9 is chosen as the optimal values for flow rate measurement for considered area of cross section of pipe connected to sensor.

Similarly, in Table 5, gross estimation of available fuel is calculated based on incremental value of 1 l of fuel at each time. The corresponding estimation results such as Initial Fuel (I) (A), Consumed Fuel (B), Available Fuel (I) (C) and Incremental Fuel (D) are shown. The corresponding measurement is also illustrated in Table 5. It can be observed that the 0% error is attained when the available fuel quantity is 13.4 l. Based on the observation made in Table 5, the graphical representation is shown in Fig. 5.

Table 2 Illustration of measured fuel volume at different CFs

C.Fs	F.Rs. (ml/s)	For fixed volume (ml)	Volume (ml) measure from flow sensor	Estimated error (%)
2.5	12.5	500	1092	118.4
			1221	144.2
			1284	156.8
			1188	137.6
			1376	175.2
	54		1318	163.6
			1422	184.4
			1467	193.4
			1562	212.4
			1566	213.2
4.5	12.5	500	353	-29.4
			379	-24.2
			336	-32.8
			346	-30.8
			437	-12.6
	54		624	24.8
			731	46.2
			676	35.2
			729	45.8
			755	51
9	12.5	500	477	-4.6
			439	-12.2
			432	-13.6
			427	-14.6
			475	-5
	54		503	0.6
			502	0.4
			528	5.6
			506	1.2
			501	0.2
10	12.5	500	607	21.4
			602	20.4
			632	26.4
			595	19
			610	22

(continued)

Table 2 (continued)

C.Fs	F.Rs. (ml/s)	For fixed volume (ml)	Volume (ml) measure from flow sensor	Estimated error (%)
	54		605	21
			598	19.6
			591	18.2
			584	16.8
			611	22.2

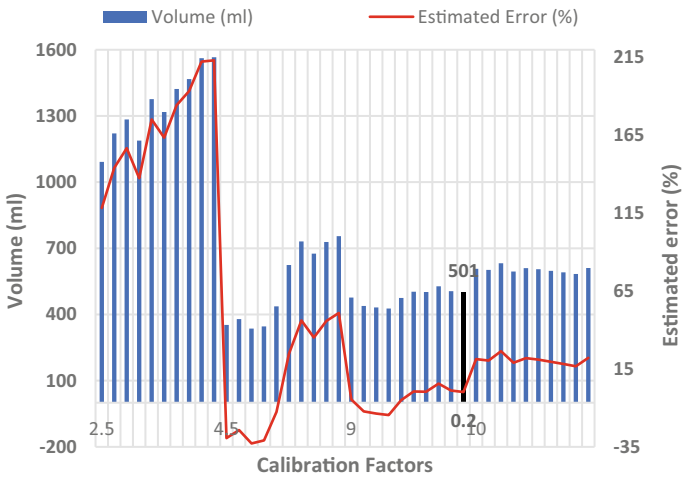


Fig. 4 Graphical representation of CF, volume and estimated error

Table 3 Percentage error estimation at various flow rate with fixed Volume of 1000 mL

For fixed volume (ml)	F.Rs. = 12.5 ml/s		F.Rs. = 54 ml/s	
	Volume (ml)	Error (%)	Volume (ml)	Error (%)
1000	971	2.9	982	1.8
	966	3.4	1057	5.7
	955	4.5	1073	7.8
	958	4.2	1093	9.3

5 Conclusion

The device helps to estimate the quantity of fuel available in the fuel tank. Flow sensors measure the amount of fuel flowing into the fuel tank and the amount of fuel flowing out from the fuel tank. The algorithm applied calculates the amount of fuel present inside the fuel tank in litres. An alarm system helps the driver to

Table 4 Percentage error estimation at various flow rate with fixed Volume of 1500 mL

For fixed volume (ml)	F.Rs. = 12.5 ml/s		F.Rs. = 54 ml/s	
	Volume (ml)	Error (%)	Volume (mL)	Error (%)
1500	1449	3.4	1510	1
	1467	2.2	1508	0.533
	1432	6.8	1518	1.2
	1502	0.13	1522	1.47
	1510	1	1502	0.133

Table 5 Gross estimation of available fuel inside the vehicle tank

Initial fuel (l) (A)	Consumed fuel (B)	Available fuel (l) (C)	Incremental fuel (D)	% Error (A)	% Error (B)	% Error (C)	% Error (D)
17.8	4.7	13.1	1.1	5.617	19.148	4.2	100
18.9	5.7	13.3	2.2	5.82	17.54	1.5	50
19.9	6.6	13.3	3.2	5.025	13.63	0	31.25
20.9	7.5	13.4	4.2	4.78	12	0.74	23.8
21.9	8.5	13.4	5.2	4.56	11.76	0	19.23

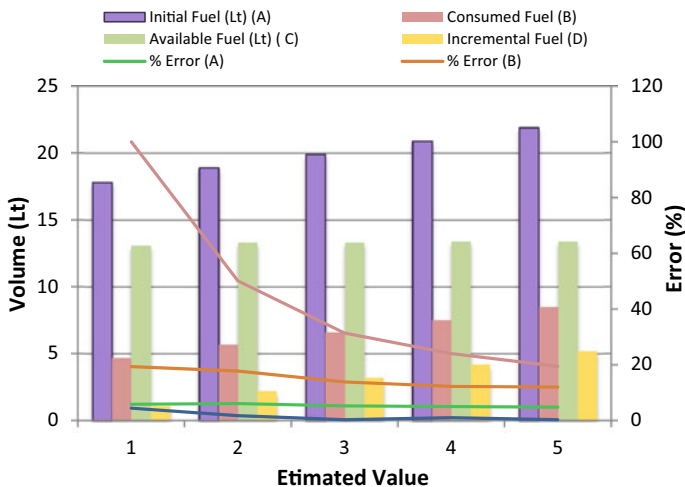


Fig. 5 Graphical representation of gross estimation of available fuel

know, when to fill the fuel. Vehicle bumping and vibration have negligible effect on the system which is an advantage over traditional fuel gauges. The vehicle owner may keep his vehicle fuel tank completely filled at all times as it reduces the risk of explosion. The present system applied in all type of vehicle is just about potentiometre

fuel gauge which only displays the level of fuel in fuel tank. The proposed system displayed reading with accuracy of 98–100%. After few adjustment and calibration, the proposed system illustrates 0% error. The practical task is performed on the set-up designed, and it has shown 0% error till 10 l of fuel.

References

1. Biswas P, Sivakumar A (2016) Accurate fuel level measurement system with tilt compensation using tilt sensor. *Int J Sci Eng Res* 7(3):759–762
2. Aher SS, Kokate RD (2012) Fuel monitoring and vehicle tracking. *Int J Eng Innov Technol (IJEIT)* 1(3):162–169
3. Gautam DK, Modwel G, Kumar A, Tiwari A (2015) Fuel level management in automotive system: solving fuel sloshing issues. In: International conference on green computing and internet of things (ICGCIoT), Noida, pp 1399–1401
4. Divakar V (2014) Fuel gauge sensing technologies for automotive applications. *Int J Adv Res Comput Eng Technol (IJARCET)* 3(1):40–42
5. Botha S, Meijnsen L, Hancke G, Silva B (2016) Design of a water flow and usage meter. In: IECON 2016—42nd Annual conference of the IEEE industrial electronics society, Florence, pp 6211–6215
6. Chati YS, Balakrishnan H (2016) Statistical modeling of aircraft engine fuel flow rate. In: 30th Congress of the international council of the aeronautical sciences, Daejeon, Korea, pp 1–10
7. Fathollahzadeh H, Mobli H, Jafari A, Mahdavejhad D, Tabatabaie SMH (2011) Design and calibration of a fuel consumption measurement system for a diesel tractor. *Agric Eng Int CIGR J* 13(2):1–12
8. Avinashkumar A, Singaravelan U, Premkumaran TV, Gnanaprakash K (2014) Digital fuel level indicator in two-wheeler along with distance to zero indicator. *IOSR J Mech Civ Eng (IOSR-JMCE)* 11(2):80–84
9. Dhande KD, Gogilwar SR, Yele S, Gandhewar V (2014) Fuel level measurement techniques: a systematic survey. *Int J Res Advent Technol* 2(4):81–84
10. Patel R, Pungalia H, Mahajan S (2016) Flow meter and Arduino based fuel gauge for automotive vehicles. *IOSR J Mech Civ Eng (IOSR-JMCE)* 13(5):85–92
11. Skwarek V, Eggers T (2013) A low-cost capacitive fuel-level and quality sensor for automotive applications. In: AMA Conferences, Bremen, Germany, pp 680–685
12. Gogawale R, Sonawane S, Swami O, Nikam SS (2016) Petrol level detection using ultrasonic sensor. *Int Eng Res J (IERJ)* 2(2):1–3
13. Vignesh J, Nijanthan V, Venkateshwaran J, Suresh Kumar K, Vidhya B (2017) Digital fuel level indicator for motor bikes using Arduino microcontroller. *SSRG Int J Electron Commun Eng (SSRG-IJECE)* 4(3):31–34
14. Gokul LS, Sivashankar S, Srinath M, Sriram Kathirayan M, Sudharsan M (2017) Digital indication of fuel level in litres in two wheelers. *Int J Innov Res Sci Eng Technol* 6(7):31–37
15. Kocher MF, Wold MT, Hoy RM, Lammers A, Blankenship EE (2016) Calibration procedure for fuel flow meters, Nebraska Tractor Test Lab. *Appl Eng Agric* 32(3):319–326
16. Kolmanovsky I, McDonough K, Gusikhin O (2011) Estimation of fuel flow for telematics-enabled adaptive fuel and time efficient vehicle routing. In: 11th International conference on ITS telecommunications, St. Petersburg, pp 139–144
17. Daingade PS, Patil AS, Nikam DB, Rokade MR, Kharade SS, More AJ (2018) The quality and quantity testing of gasoline fuel using sensing method. *Int Res J Eng Technol (IRJET)* 5(3):2949–2953
18. Prakash M, Raguna V, Sowmitha K, Thamilzamudham P, Nandhini P (2018) Intelligent digital fuel gauge along with engine locking system using Arduino. *Asian J Appl Sci Technol (AJAST)* 2(2):641–648

19. Senthil Kumar R, Ganapathi M, Arunkumar D, Goutham G, Karthick M (2017) Fuel monitoring system for fuel management. *Int J Sci Eng Technol Res (IJSETR)* 6(4):565–571
20. Skog I, Händel P (2014) Indirect instantaneous car-fuel consumption measurements. *Trans Instrum Meas (IEEE)* 63:3190–3198
21. Kuan Y, Septiani A, Yuliane A (2018) Development of the diagnostic system for fuel cell vehicle using lab view. In: *International conference on system science and engineering (ICSSE)*, pp 1–6
22. Mingjie C, Zhenhua J, Qingchun L, Xiao Y, Maodong F, Kongjian Q (2010) A chassis dynamometer laboratory for fuel cell hybrid vehicles and the hydrogen consumption measurement system. In: *Vehicle power and propulsion conference*, pp 1–5
23. Ogawa K, Yamamoto T, Hasegawa H, Furuya T (2009) Development of the fuel-cell/battery hybrid railway vehicle. In: *Vehicle power and propulsion conference*, pp 1730–1735

Energy Efficiency and QoS Evaluation of Radio Resource Management Techniques for M2M Communications in LTE-Based Cellular Systems



Mariyam Ouaisa, Mariya Ouaisa, and Abdallah Rhattoy

Abstract The recent cellular wireless networks must not only ensure the communication between users known as human to human (H2H) but also between a huge number of machines for machine-type communication (MTC) or machine to machine (M2M). M2M can be considered as devices that can establish communications with other devices without any human intervention. M2M is also seen as the base of the vision of connected objects. It tempts a lot of attention because it can be seen as a new opportunity for network operators and Internet of Things (IoT) service. Today, there are several types of MTC-based applications spanning multiple domains, such as health, transport, smart meters and surveillance. The deployment of this kind of application in mobile cellular networks, particularly Long-Term Evolution (LTE) and LTE-Advanced (LTE-A), cannot be effective without controlling the challenges posed by the deployment of a large number of MTC devices in the same cell. Indeed, the deployment of a myriad of MTC devices will cause the challenge of resource allocation for assuring the quality of service (QoS). As MTC devices are equipped with a non-rechargeable battery, power consumption is also among the main challenges facing M2M communications over Long-Term Evolution networks. In this article, we focused on the radio resource management in downlink LTE networks for M2M communication by a study of scheduling techniques that are: proportional fair (PF), exponential proportional fair (EXP)/PF, maximum-largest weighted delay first (MLWDF) and frame-level scheduler (FLS). We considered the video and VoIP services as real-time (RT) streams as well as best effort (BE) as non-real-time (NRT) streams, considering the QoS criteria in terms of throughput, fairness and energy, in order to conclude a distinct vision on the quality of experience provided by these

M. Ouaisa (✉) · M. Ouaisa

LMMI Laboratory ENSAM, ISIC High School of Technology, Moulay-Ismaïl University, Meknes, Morocco

e-mail: mariyam.ouaisa@edu.umi.ac.ma

M. Ouaisa

e-mail: mariya.ouaisa@edu.umi.ac.ma

A. Rhattoy

Department of Computer Engineering, High School of Technology, Moulay-Ismaïl University, Meknes, Morocco

e-mail: rhattoy@gmail.com

© Springer Nature Singapore Pte Ltd. 2020

A. K. Bhoi et al. (eds.), *Advances in Greener Energy Technologies*,

Green Energy and Technology, https://doi.org/10.1007/978-981-15-4246-6_11

algorithms. The results of analysis indicate that MLWDF scheduler is the best according to the energy and spectral efficiency than PF, EXP-PF and FLS techniques, while FLS is better in terms of quality of service (QoS) metrics for RT services.

Keywords M2M · H2H · LTE · QoS · Scheduling algorithms · Energy efficiency

1 Introduction

Today, the optimization of energy consumption for connected objects was considered as a critical need, imposed by the physical constraint that is the life of batteries of embedded equipment such as mobile phones and sensors [1]. Indeed, works dedicated to reducing energy consumption in the next-generation networks have emerged to address a critical issue related to the limitation of resources in smart grids. Machine to machine (M2M) communications [2, 3] are characterized by low computing capacity, memory and especially energy. This limitation of the energy capacity is more problematic because of the use cases of this type of network since the deployment of the nodes is generally carried out in hostile and inaccessible environments such as uneven ground and fields of battles. This directly impacts the service life of this type of network and makes energy consumption a major key for the design and use of sensor networks [4].

The problem of energy consumption in M2M communication presents at different levels. Among them, we can mention the minimization of interferences to improve the quality of service (QoS), the level of radiation to limit the impact on health and the reduction of energy consumption to reduce costs and to minimize the Carbonne borrowing. Various optimization approaches affecting several aspects related to energy consumption in networks are proposed. They concern the technological, architectural and network management aspects. Indeed, among the aspects that are the subject of works minimizing the energy consumption of access networks, we can mention: planning and sizing, user association and scheduling [5].

Packet scheduling mechanisms play a fundamental role in the radio resource management (RRM) over cellular systems in that they aim to optimize according to specific criteria and reach the time and frequency resources. These mechanisms allow the allocation of radio resources by taking into consideration certain parameters relating to the state of the transmission channels and the user requirements in terms of QoS. In addition, new generation cellular networks, including Long-Term Evolution (LTE) and LTE-Advanced (LTE-A) networks [6, 7], raise optimization issues with several elements that must be considered simultaneously. Also, they aim to enhance the spectral efficiency and the capacity of the network while taking into account the requirements of the applications in terms of QoS and the need to guarantee a minimum of equity between users whose number is in a constant increase [8, 9].

In this work, we propose a performance analysis of some downlink scheduling algorithms for LTE systems in a hybrid scenario combined with the M2M and human to human (H2H) communications. This evaluation not only concerns the performance

of these schedulers in terms of QoS, but it also includes an analysis of their spectral and energy efficiency.

The organization of this paper is as follows: In Sect. 2, we present the M2M system architecture, the scheduling process for M2M communications and the characteristics of radio resources. Section 3 describes the downlink radio resource allocation in LTE, as well as the scheduling algorithms considered in this article. We evaluate and analyze in Sect. 4 the performances of the existing algorithms and we conclude the more efficient scheduler in term of average throughput, fairness index, spectral and energy efficiency.

2 Energy Consumption for M2M Communication Over LTE Access Network

Among the constraints of mobile terminals reside on the fact that the capacity of the onboard batteries is low, which has the consequence of reducing the duration of its use between two refills. Although battery technologies are evolving, this limitation is accentuated by the rapid evolution of mobile uses in terms of number of applications and data volumes. The standards that define radio networks and technologies, such as Institute of Electrical and Electronics Engineers (IEEE) and 3rd Generation Partnership Project (3GPP) [10], have very early considered the problem of energy conservation on mobile terminals by introducing the notion of states for radio interfaces, according to the mobile activity [11].

M2M devices are characterized by low computing capacity, memory and especially energy. This limitation of the energy capacity is more problematic because of the use of M2M system since the deployment of the nodes is generally carried out in hostile and inaccessible environments such as hilly terrain and battlefields. This directly impacts the service life of this type of network and makes energy consumption a major criterion in the design and use of this type of network.

The problem of energy consumption in wireless networks is present at different levels. New constraints are increasingly considered. These include minimizing interference to improve QoS, the level of radiation to limit the impact on health and reducing energy consumption to reduce costs. Various optimization approaches affecting several aspects related to energy consumption in networks are proposed. They concern the technological, architectural and network management aspects. Among the aspects that are the subject of work minimizing the energy consumption of access networks, we can mention, sleep techniques, user association approaches and scheduling mechanisms [12].

2.1 Sleeping Techniques

Slumbering nodes during periods of inactivity is probably one of the most studied and recommended techniques for global energy conservation on radio access networks. Since a base station having nothing to transmit still consumes a significant amount of energy, the idea is to sleep (sleep) these nodes as soon as possible. This obviously affects the coverage of the network but complementary solutions can be used such as, for example, the temporary extension of the coverage areas of neighboring cells or inter-operator cooperation. The main difficulties of these techniques concern the choice of cells to fall asleep and the right moment to fall asleep or wake up a radio station.

2.2 User Association

In cellular networks, the number of active users on a base station has a significant impact on the power consumption thereof. This implies that the user association policy is a decisive element for the energy conservation of base stations and therefore in a global manner, radio access networks.

2.3 Scheduling Mechanisms

Limiting resources, fluctuating radio conditions and data flows, pose significant challenges for the radio resource management techniques. The scheduling mechanisms have been extensively studied for resource management and in particular for dynamically allocating on shared channels to different users. These mechanisms can be based on a multitude of criteria and are one of the determining factors in the behavior and performance of the system in operation. Generally, it is the operators themselves (and not the equipment manufacturers) who choose and parameterize these algorithms, according to their commercial strategies. In addition to the QoS parameters, these mechanisms can therefore include business criteria such as subscription types and priorities between users or flows.

In this paper, we focus on scheduling techniques as an approach for energy conservation in access networks and the guarantee of system quality of service.

3 Radio Resource Management of M2M Communication

Resource management is the most important function of base stations in wireless systems. Indeed, it is on this function that a wireless system, such as LTE systems, counts most to guarantee a certain QoS, offers a maximum capacity in terms of

throughput and improves the equity between the users that seek to acquire radio resources. These objectives often tend to be contradictory, since the improvement of one aspect, in some cases, is paid for by the deterioration of another, for example, the overall flow in a cell could be increased but at the expense of a reduction equity between users or a decrease in QoS [13].

RRM mechanisms aim to control the use of radio resources by satisfying QoS metrics and the massive number of users in an environment characterized by limited spectrum availability, distortion signal due to multipath channel, fading and interference, user mobility. To achieve its objectives, the RRM plays on four main axes:

- **Admission control:** The admission control regulates the operation of the network in such a way as to guarantee the continuity of the services provided and the reception of the new connection requests.
- **Power control:** This point is an important element in mobile networks that due to the problem of battery life and the safety causes.
- **The control of handover:** The mobility of the user equipment (UE) sometimes requires that they change the serving Evolved Node B (eNodeB). This process of taking care of the mobility of the UEs is called handover.
- **Scheduling:** This is the entity responsible for the allocation of radio resources; the packets are allocated to the UEs following the execution of a scheduling algorithm at the MAC layer.

3.1 Concept of Scheduling

Scheduling is one of the most important resource management mechanisms in LTE networks; it determines which user should be transmitted in a given time interval. This is a critical design element since it allocates the allocation of the channel among users and thus, in general, determines the overall behavior of the system. An optimal system throughput can be achieved by assigning all radio resources to the user with the best radio conditions of the channel, nevertheless scheduling, in practice, should have several levels of equity. Thus, by choosing different scheduling algorithms, operators can tailor the system behavior to their needs. So, there is no need to standardize the algorithms used; instead, operators can choose different criteria. Prediction of channel quality, cell capacity and different classes of traffic priorities are examples of information on which the scheduler could base decisions [14].

3.2 Scheduling Process for M2M Communication

The classifications of LTE scheduling techniques are based on M2M communication requirements to achieve optimal integration. Based on these characteristics,

we can conclude that M2M communications require four primary requirements. First, energy-efficient scheduling uses single-carrier frequency-division multiple access (SC-FDMA) for the uplink and orthogonal frequency-division multiple access (OFDMA) for the downlink. Second, QoS-based scheduling is required to handle different QoS requirements such as latency, jitter, error rate, and guaranteed bit rate (GBR). Thirdly, multi-hop scheduling uses several hops to send data over short distances instead of sending them over long distances using a single hop, which saves energy. Finally, scalable network scheduling uses the native IP connectivity feature in LTE to support a considerable number of M2M communications [15].

The design of downlink or uplink scheduling techniques for M2M communications should take into account that machine-type communication device (MTC) in M2M communications may have strict delay requirements. In addition, scheduling should take into account the fact that a significant number of MTCs can compete for limited radio resources. Scheduler is the functional entity for obtaining fast packet scheduling and the basic medium access control (MAC) layer function in the LTE eNodeB. This has a major impact on system performance. It contains an uplink scheduler and a downlink scheduler, which support the allocation of physical layer resources for the uplink shared channel (UL-SCH) and the downlink shared channel (DL-SCH). The physical layer resources mainly include the PRB physical resource block, the modulation and coding scheme (MCS), the power allocation schemes and the antenna selection schemes for multiple antennas. Figure 1 shows the position of the scheduler in the LTE protocol and its relation to key techniques such as hybrid automatic repeat request (HARQ) and adaptive modulation and coding (AMC). Its key function is to determine how to correctly allocate the resource to users in order to maximize the system throughput, as long as the delay and QoS of packets are guaranteed [16].

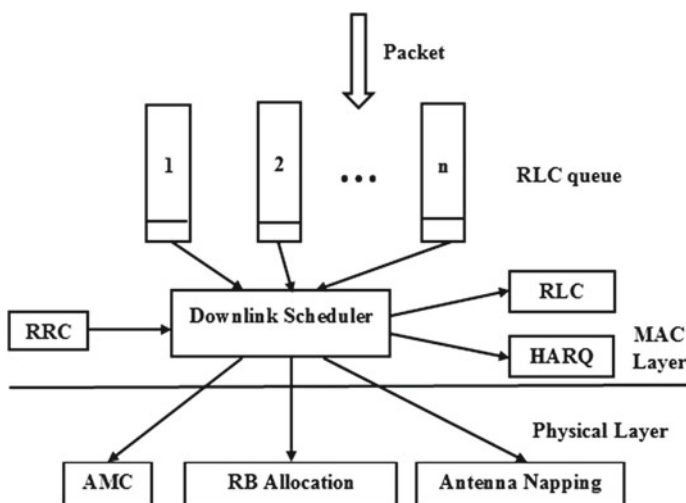


Fig. 1 Architecture scheduling in the LTE system

4 LTE Downlink Resource Allocation

Scheduling represents a fundamental part in optimizing the management and allocation of radio resources, which results in the allocation of radio spectrum in the form of channels according to a number of criteria, such as the state channels, the number of block resources (RBs) available and constraints in terms of quality of service. The distribution of RBs is managed by a base station scheduling function; for each transmission time interval (TTI) of 1 ms, a scheduling decision is made based on scheduling algorithms to enable the sharing of radio channels between the active users during this TTI. These algorithms are the subject of our research and take into account several criteria, namely the condition of the user channel, interferences, criteria relating to the quality of service and energy, priorities of services, etc. A radio resource block RB corresponds to 12 subcarriers of 15 kHz each of 180 kHz in the frequency domain and to a time slot of 0.5 ms in the time domain, each slot is composed of 6 or 7 orthogonal frequency-division multiplexing (OFDM) symbols, depending on whether the cyclic prefix is extended or normal [17].

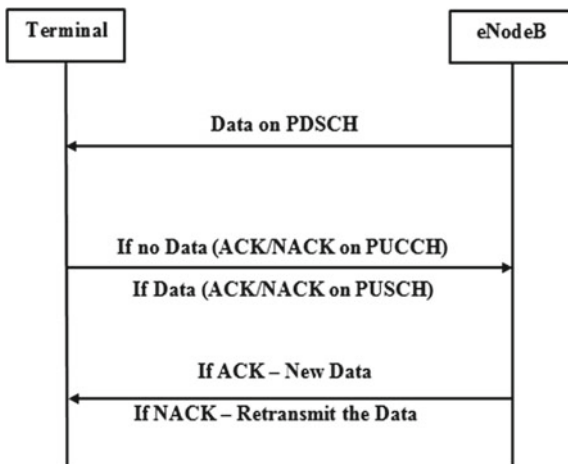
4.1 Downlink Scheduling Procedure

Scheduling is a procedure that allows eNodeB to allocate physical resources to terminals, either UE or MTC, according to a certain algorithm, so that they can send or receive data in each TTI. In the downlink direction, once the scheduler has made a decision, the RBs are allocated to each device. In addition, a MCS is also assigned to each of them taking into account the channel quality indicator (CQI) and potentially all the other information available to the scheduler. Users must then be notified which resources have been allocated so that they can decode the data correctly. This announcement of resource allocation is implemented using allocation reports. Downlink data transmission is understood to mean the data transmitted from the network to the terminals, namely layers higher than the lower layers. In LTE, DL data is transmitted from the network to the terminal via PDSCH. The terminal decodes the data and verifies all error conditions during transmission. The terminal sends HARQ feedback (ACK/NACK) to the eNodeB in two ways (Fig. 2):

- If the terminal has data to transfer to eNodeB, it sends HARQ feedback via the PUSCH channel.
- If the UE does not have any data to transfer to the eNodeB, it sends HARQ feedback via the PUCCH channel.

On the basis of the HARQ, the return network decides on the transmission or retransmission of data. If ACK is received, the eNodeB sends new data to the terminal. If NACK is received, eNodeB retransmits the same data to the terminal with different revisions [18].

Fig. 2 Downlink data transmission procedure



Scheduling thus enters the class of functions designed according to an inter-layer optimization, the exploitation of which is one of the strong characteristics of modern communication systems and in particular of LTE. The scheduler is brought to exploit the temporal and frequency dimensions.

4.1.1 Temporal Dimension

The data is transmitted on shared channels between the UEs of the system. The reason for this choice is twofold. On the other hand, the radio resource requirements of the UE can vary considerably over time depending on the type of service required. During a voice call, for example, periods of silence are numerous; during these periods, no data is transmitted. Reserving radio resources for the duration of a voice call is thus wasted by the system, since it could be allocated to another UE during periods of silence. It is therefore more efficient for the system to pool radio resources into shared channels and allocate them to the UE according to their instant needs.

The scheduling that can exploit the rapid variations of the channel is called dynamic. To do this, the temporal resources allocated must be very brief. In LTE, the granularity of the allocation of time resources, or TTI, is of a subframe, i.e., 1 ms. In other words, the scheduler is free to choose the UEs to serve as well as their allocation of PRB to each subframe.

For the scheduling to follow the channel fading, the eNodeB must have information on the quality of the UE channel, which allows estimating the rate that it can reach in the radio conditions that he meets. This information is obtained by means of the UEs return of a CQI.

4.1.2 Frequency Dimension

The allocation of resources is always done in pairs of PRB, a PRB of the pair being allocated on each slot of a subframe or is served. The allocation reported on the PDCCH thus always carries both slots of the target subframe. The scheduler allocates to each user PRBs with favorable radio conditions. Scheduling implies that the UE returns information in frequency dimension according to the quality of the channel. This information takes the form of a CQI.

4.2 Channel Condition Information (CQI)

The CQI is an indicator of the state of the channel measured by the UE and returned to the eNodeB in a downlink. It corresponds to an UE commitment to the bandwidth that it considers to be able to receive in the current radio conditions. It is also used to determine which UEs to serve at a given time and which PRBs to allocate to the UE when allocating frequency resources. It is used to calculate the scheduler metric. The decisions of resource allocations are communicated to the UE via the PDCCH, using Scheduling algorithms execution [19].

5 Downlink Scheduling Algorithms

Many studies have sought to correct the problems for current and future networks. These have led to the conclusion that an inter-layer approaches “MAC/PHY” is a solution particularly suitable for making optimal use of radio resources. Built on this inter-layer approach, new and particularly efficient schedulers have emerged called opportunistic schedulers. The goal of this type of algorithm is to enhance the system performance in order to improve spectral efficiency fairness between users. In this work, we considered the following algorithms, proportional fair (PF), exponential proportional fair (EXP-PF), maximum-largest weighted delay first (MLWDF) and frame-level scheduler (FLS) [20, 21].

5.1 Proportional Fair

This scheduler combines the radio resources by jointly taking into account the quality of the channel and the bit rate consumed by each user in the previous TTI. Its purpose is to try to increase the rate of the network by maximizing the throughput of each user; it tries to guarantee equity between users. For this algorithm, the metric is defined as the ratio between the instantaneous rate available and the average rate.

$$k^* = \operatorname{argmax}_k \frac{R_k(t)}{T_k(t)} \quad (1)$$

where $T_k(t)$ is the instantaneous rate of the user k and $R_k(t)$ is the average rate calculated at time $t-1$ of the user k .

5.2 Maximum-Largest Weighted Delay First

This algorithm is based on the same principle as the PF except that it takes into consideration the requirements of different applications in terms of QoS. Indeed, the choice metric of the PF is multiplied by a parameter α_k which takes into consideration the maximum delay τ_k and the maximum probability δ_k so that the delay of the first packet of the queue does not exceed τ_k .

$$k^* = \operatorname{argmax}_k \alpha_k \cdot D_{\text{HOL},k} \cdot \frac{R_k(t)}{T_k(t)} \quad (2)$$

where $D_{\text{HOL},k}$ is the delay tolerated by the flow.
 α_k is given by:

$$\alpha_k = \frac{-\log(\delta_k)}{\tau_k} \quad (3)$$

Thus, this type of scheduling favors RT streams and users having good conditions of the radio channel.

5.3 Exponential Proportional Fair

This scheduler gives more priority to the RT streams having the greatest delay while respecting other non-real-time (NRT) streams. The EXP-PF algorithm chooses the user k to allocate the resources, via the following equation:

$$k^* = \operatorname{argmax}_k \beta_k \frac{R_k(t)}{T_k(t)} \quad (4)$$

β_k is given by:

$$\beta_k = e^{\frac{\alpha_k D_{\text{HOL},k} - X}{1 + \sqrt{X}}} \quad (5)$$

With:

$$X = \frac{1}{N} \sum_k \alpha_k D_{\text{HOL},k}(t) \quad (6)$$

where the symbols have the same meanings as the previous ones and N is the number of RT streams active in the DL direction.

5.4 Frame-Level Scheduler

This scheduler considers flow classes where the processing is different for each RT and NRT class. This type of algorithm favors RT versus NRT flows, which makes it more appropriate and more efficient for LTE scheduling, but equity is not really considered. The scheduling schema of FLS is divided into two levels, in the upper level, a less complex algorithm based on a linear control loop and discrete over time; this level specifies the number of bits contained in the packet to be transmitted by the source in the LTE frame. In the lower level, the radio resources are contributed to the users using the scheduling strategy PF taking into account the bandwidth required by the FLS. This two-level modeling provides a compromise between the throughput offered by the system and equity. For the scheduler PF, the volume of the data $u_i(k)$ for the i th flux in the k th LTE frame is calculated according to the following formula:

$$u_i(k) = h_i(k) * q_i(k) \quad (7)$$

6 Evaluation of Scheduling Algorithms

In this section, the downlink schedulers already mentioned will be evaluated and compared using an open-source simulator LTE-Sim [22]. To evaluate the energy and QoS of a network, many parameters must be analyzed as throughput, fairness index, spectral and energy efficiency [23–25].

6.1 Evaluation Metrics

This evaluation makes it possible to analyze and understand the behavior of these schedulers and can be the basis for proposing a new algorithm or for improving existing ones. The metrics used for the evaluations are:

6.1.1 Throughput

This is the total bit rate in reception; the measurement of this bit rate is one of the important operations which make it possible to identify the average success rate of transfer of the messages on a communication channel. Its value is calculated for a time interval, by dividing the total amount of information received during this interval, by the duration of the interval in question. The general formula for the calculation of the useful flow is:

$$\text{Throughput} = \frac{N_p * T_p}{T} \quad (8)$$

6.1.2 Fairness Index

This metric is a criterion that must be taken into consideration to ensure a minimum performance threshold for users, especially those penalized by poor channel conditions. In this case, the scheduler is not concerned about how the resources are used by the UEs, nor about the state of the transmission channel. Level of equity received by each flow according to Jain's Equity Index is given as follows:

$$\text{Fairness}_{\text{index}} = \frac{(\sum x_i)^2}{n \times \sum x_i^2} \quad (9)$$

where x_i is the user's rate i and n is the number of enabled flows.

6.1.3 Spectral Efficiency

The efficient use of radio resources is one of the main objectives to be achieved. Several types of performance measures can be considered:

- Maximizing the number of users served in a given time interval.
- Maximization of spectral efficiency (expressed in bit/s/Hz) by always serving users who enjoy the best channel conditions.
- One of the most used indicators of effectiveness is the user's goodput.

$$\text{Spectral Efficiency} = \frac{D_{\text{max}}}{W_c} \quad (10)$$

With D_{max} —the maximum rate of the user and W_c —the bandwidth of the channel.

6.1.4 Energy Efficiency

This metric makes it possible to evaluate the bit rate offered in the cell compared to the power consumed by the eNodeBs. It involves using less energy to produce the same service or the same useful output. The definition of current energy efficiency is the ratio between spectral efficiency and power output.

We consider in our case that the energy efficiency of a network is the amount of bits of information transmitted or received by users per unit of energy consumption in bit/Joule.

$$\text{Energy Efficiency} = \frac{D}{P_c} \quad (11)$$

With D —the bit rate and P_c —the power consumed.

6.2 Simulation and Results

In this part, we propose a performance evaluation of some downlink scheduling algorithms for LTE system which are PF, MLWDF, EXP-PF and FLS. This assessment concerns not only the performance of these schedulers in terms of QoS such as throughput and fairness index, but it also includes an assessment of their spectral and energy efficiency.

The implementation of our scenario in high congestion is made in a LTE downlink transmission for a hybrid M2M and H2H communication developed with C++ using the LTE-Sim simulator, in order to evaluate the QoS metrics and energy for existing downlink scheduling techniques. We consider in our simulation that the number of M2M devices varies between [20–100], while the H2H terminals are fixed in 30. The devices used are uniformly distributed in a single cell with a radius of 1 km and modeled according to a random mobility model. We also considered in this simulation two types of traffic, RT traffics (video and VoIP) and NRT traffic [best effort (BE)]. The simulation parameters are mentioned in Table 1.

Figures 3 and 4 present the average throughput for the four scheduling techniques according to the number of MTCDs varied from 20 to 100 and the number of H2H users is fixed at 30, for different types of traffics. The results indicate that the FLS offers higher throughput for the video traffic at high load compared to the PF, MLWDF and EXP-PF algorithms according to Fig. 3a. While for VoIP traffic, Fig. 3b illustrates that for the four scheduling techniques, the average throughput is increased with the same behavior according to the variation in the number of devices. However, for the BE streams of an NRT service, as the number of devices increases in the cell, the throughput of the four algorithms decreases appreciably. PF, MLWDF and EXP-PF schedulers offer equivalent bit rates; this is explained by the fact that they have a similar behavior for the NRT traffic, while FLS is the less performer according to this type of traffic (Fig. 4).

Table 1 Simulation parameters

Simulation Parameters	Values
Simulation duration	120 s
Flow duration	120 s
Frame structure	FDD
Mobility	Fixed for M2M 3 km/h for H2H
Cell radius	1 Km
System bandwidth	20 MHz
RB bandwidth	180 kHz
Time slot	0.5 ms
Scheduling time (TTI)	1 ms
Number of RBs	100 RBs
Maximum delay	0.1 s
Traffic model	Video VoIP Best effort
Video bit rates	242 kbps
VoIP bit rates	8.4 kbps
Number of H2H users	30
Number of M2M users	20 à 100

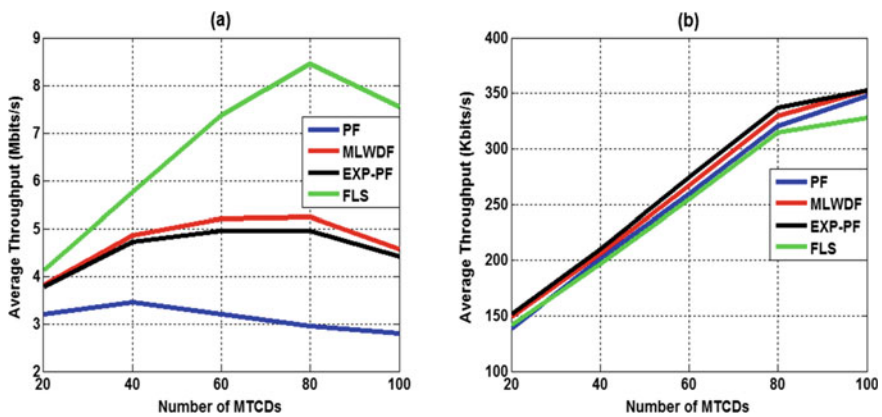


Fig. 3 Average throughput for video flow (a) and VoIP flow (b)

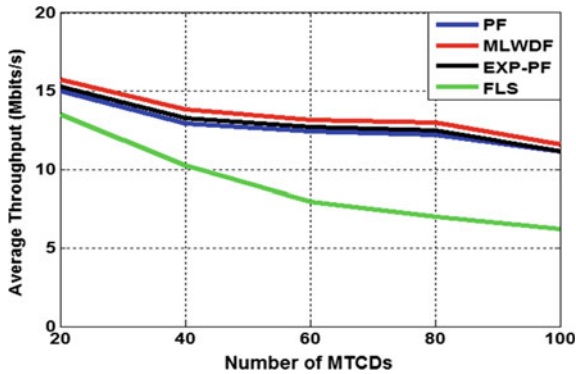


Fig. 4 Average throughput for BE flow

Figures 5 and 6 present the Jain fairness index of the scheduling algorithms studied according to the number of MTC devices. We find that for video flow in Fig. 5a, the PF scheduler has the least fairness index while the FLS has the largest one. Figure 5b illustrates that the techniques have a similar index fairness when we increase the number of devices in the same cell for VoIP traffic. However, Fig. 6 shows that the behavior of PF, MLWDF et EXP-PF schedulers in terms of equity is similar for BE flows, while the FLS is the least fair one.

In Fig. 7, the spectral efficiency decreases for all the algorithms as the number of devices increases. The MLWDF algorithm is the efficient compared to other algorithms for this metric. For the energy efficiency, as shown in Fig. 8 when we varied the number of devices, the energy efficiency of all scheduling algorithms decreases. This decrease is due to the fact that when the flow reaches its maximum capacity, the power consumed by the eNodeB continues to increase as a function of the load.

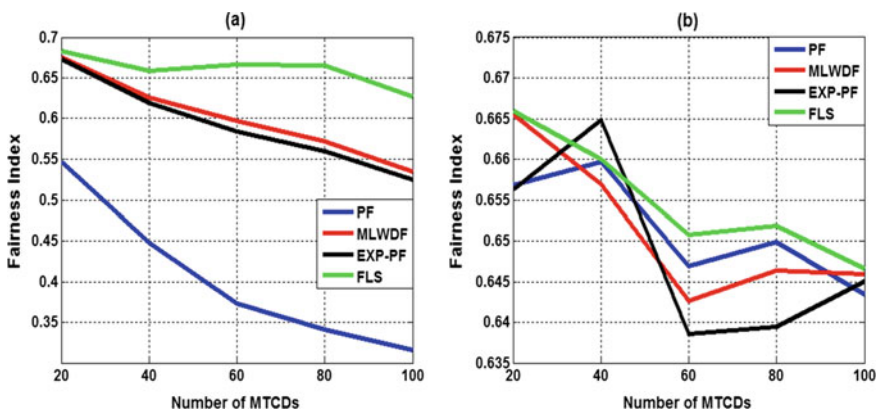


Fig. 5 Jain fairness index for video flow (a) and VoIP flow (b)

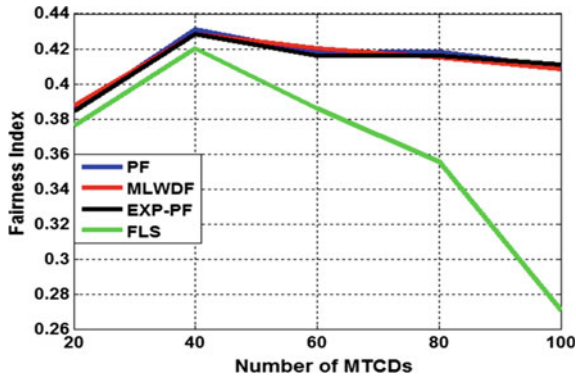


Fig. 6 Jain fairness index for BE flow

Fig. 7 Spectral efficiency (Bits/s/Hz)

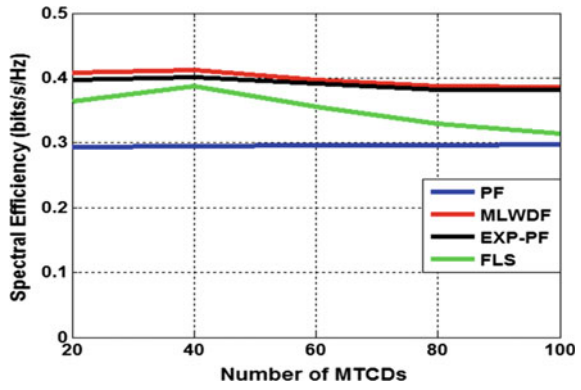
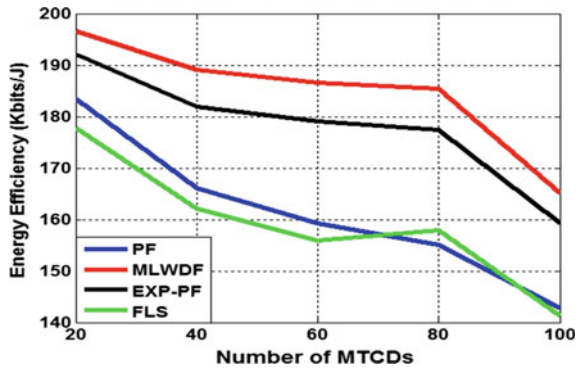


Fig. 8 Energy efficiency (Kbit/J)



The power of emission, which depends on the load, increases and becomes predominant and the energy efficiency thus continues to decrease slightly. According to these results, we can conclude that MLWDF scheduler has the better energy efficient compared to other scheduling techniques.

7 Conclusion

In this paper, we analyzed the performance of downlink scheduling algorithms in the LTE network for a hybrid scenario M2M and H2H communications. We proposed a performance evaluation of four packet scheduling algorithms (PF, MLWDF, EXP-PF and FLS). For these assessments, we considered several criteria that combine throughput, fairness, energy and spectral efficiency for RT and NRT services. The results of this evaluation showed that FLS mechanism is the best in terms of throughput and fairness for RT traffics. The MLWDF scheduler is the best in terms of energy and spectral efficiency compared to PF scheduling algorithm, that offers much lower throughput and equity than other schedulers for video and VoIP flows. This evaluation makes it possible to compare the scheduling algorithms and to analyze the impact of these algorithms on the energy consumed by the users. These algorithms seek to achieve equity among users in terms of QoS. However, one of the constraints of today's mobile devices is the limited capacity of the battery in the face of ever-growing data traffic. Taking into account, the state of the battery can achieve certain energy equity between the users. For future work, we will propose a scheduling algorithm whose goal is to decrease the energy consumption of users with the low battery level.

References

1. Wang K, Alonso-Zarate J, Dohler M (2013) Energy-efficiency of LTE for small data machine-to-machine communications. In: IEEE international conference on communications (ICC), pp 4120–4124
2. Ouaisa M, Benmoussa M, Rhattoy A, Lahmer M, Chana I (2016) Impact of M2M traffic in random access channel over LTE networks. In: Advances in electronics, communication and computing, ETAEERE, pp 11–19
3. Ouaisa M, Rhattoy A, Lahmer M (2018) New method to control congestion for machine to machine applications in long term evolution system. *Int J Commun Antenna Propag (I.Re.C.A.P.)* 8(4)
4. Biral A, Centenaro M, Zanellari A, Vangelista L, Zorzi M (2015) The challenges of M2M massive access in wireless cellular networks. *Digit Commun Netw*
5. Salman MI, Ng CK, Noordin NK, Ali BM, Sali A (2012) Energy efficient transmission for LTE cellular system. In: International conference on computer and communication engineering (ICCCE), pp 222–227
6. Ouaisa M, Rhattoy A, Lahmer M (2016) Analysis of authentication and key agreement (AKA) protocols in long-term evolution (LTE) access network. *Advances in Electronics, Communication and Computing, ETAEERE*, pp 1–9

7. Ouaisa M, Rhattoy A (2018) A new scheme of group-based AKA for machine type communication over LTE networks. *Int J Electric Comput Eng (IJECE)* 8(2):1169–1181
8. Zheng K, Hu F, Xiangy W, Dohler M, Wang W (2012) Radio resource allocation in LTE-A cellular networks with M2M communications. *IEEE Commun Mag*
9. Ouaisa M, Benmoussa M, Rhattoy A, Lahmer M, Chana I (2016) Performance analysis of random access mechanisms for machine type communications in LTE networks. In: *International conference on advanced communication systems and information security 2016 (ACOSIS'16)*
10. Ouaisa M, Rhattoy A, Lahmer M (2017) Group access authentication of machine to machine communications in LTE networks. In: *The second international conference on Internet of Things, data and cloud computing (ICC 2017)*
11. Ouaisa M, Rhattoy A, Chana I (2018) New security level of authentication and key agreement protocol for the IoT on LTE mobile networks. In: *6th international conference on wireless networks and mobile communications (WINCOM)*, IEEE, pp 1–6
12. Videv S, Thompson JS, Haas H, Grant PM (2012) Resource allocation for energy efficient cellular systems. *EURASIP J Wirel Commun Netw* 2012(1):1–15
13. Bouguen Y, Hardouin E, Wolff FX (2012) LTE et les réseaux 4G
14. 3GPP TS 36.300. V15.2.0 (2018) Evolved universal terrestrial radio access (E-UTRA) and evolved universal terrestrial radio access network (E-UTRAN); overall description; Stage 2 (Release 15)
15. de Andrade TP, Astudillo CA, da Fonseca NL (2016) Allocation of control resources for machine-to-machine and human-to-human communications over LTE/LTE-a networks. *IEEE Internet Things J* 3(3):366–377
16. 3GPP TS 36.211. V8.0.0 (2018) Evolved universal terrestrial radio access (E-UTRA); physical channels and modulation
17. Fritze G (2012) SAE: the core network for LTE. Ericsson, Technical white paper
18. Coupechoux M, Martins P (2013) Vers les systèmes radio mobiles de 4e génération - de l'UMTS au LTE
19. 3GPP TS 36.321. V15.2.0 (2018) Evolved universal terrestrial radio access (E-UTRA); medium access control (MAC) protocol specification (Release 15)
20. Fouziya SS, Nakkeeran R (2014) Study of downlink scheduling algorithms in LTE networks. *J Netw* 9(12)
21. Ouaisa M, Rhattoy A, Lahmer M (2018) Comparative performance study of QoS downlink scheduling algorithms in LTE system for M2M communications. In: *International conference Europe Middle East & North Africa information systems and technologies to support learning*. Springer, Cham, pp 216–224
22. Piro G, Grieco LA, Boggia G, Capozzi F, Camarda P (2010) Simulating LTE cellular systems: an open source framework. *IEEE Trans Veh Technol* 6(2):498–513
23. Ouaisa M, Rhattoy A (2018) New method based on priority of heterogeneous traffic for scheduling techniques in M2M communications over LTE networks. *Int J Intell Eng Syst* 11(6)
24. Mahmud SA, Khan F, Ali M, Khan GM, Yousaf FZ (2014) Fairness evaluation of scheduling algorithms for dense M2M implementations. In: *Proceedings of IEEE WCNC 2014—workshop on IoT communications and technologies*
25. ETSI TR 103 117 (2012) Environmental engineering (EE); principles for mobile network level energy efficiency, V1.1.1

An Influence Analysis on the Power System by Load Fluctuation of Large-Scale Industrial Steel Load



Hyun-Chul Lee, Yong-Gi Roh, and Byoung-Jo Jung

Abstract Power system should adjust the supply capacity power by load fluctuation. This paper has been examined the frequency fluctuation and system stability against the intermittent fluctuation of the industrial load. Load fluctuation should be examined the effects on the power supply service in the power system. The load fluctuation would be a factor that increases the reserve power. In order to reflect, the system has been analyzed according to period, season and load level. The method has been analyzed load fluctuation to power system frequency by using the Fourier transform. It has been calculated the power capacity operating by load fluctuation of short period, seasonal and load level. As a result of frequency analysis for the load fluctuation, the reserve capacity power was needed to the short period than the load capacity calculation according to the load fluctuation time used in the power system. The maximum fluctuation rate has been shown in the off-peak load and fall seasonal load of 208%. The minimum fluctuation rate has been shown in the mid-peak load and in the winter seasonal load of 35%. It could be considered which should be analyzed the effect on the power supply service and suggest countermeasures against system instability.

Keywords Power system · Reserve power · Load fluctuation · Industrial load · Frequency analysis

H.-C. Lee · Y.-G. Roh
Department of Electrical Control, JHRDI, Seoul, South Korea
e-mail: Oneye1@hotmail.com

Y.-G. Roh
e-mail: ygroh@korcham.net

B.-J. Jung (✉)
Department of Lift Engineering, Korea Lift College, Geochang, South Korea
e-mail: bjjung@klc.ac.kr

1 Introduction

The power supply and demand have been based on the electricity demand forecasted for the pricing power generation plan. It was used the demand forecasting system according to the daily power demand forecasting procedure of the electricity market operating rule under the cost-based pool (CBP). Therefore, the short-term fluctuation was not reflected in the demand forecast. However, the power supply and demand have been largely fluctuating the load during the real power system operation within 1 h due to the load fluctuation. In particular, steel and mill industries, which are intermittent loads with large fluctuations in short-term periods, have been operating as high-level short-term load fluctuation exceeding the contracted capacity of the demand meter (DM) for 15 min [1–3].

There is a frequency reserve power and a standby reserve power in response to the load fluctuation within 1 h. The frequency adjustment reserve power could be corresponded to the real-time load fluctuation by operating the governor free control (GFC) of the participating generator and the automation generator control (AGC). The reserve power could be operated into the power system in case of sudden stoppage of power generation facilities, demand forecast error, stoppage of power plant and transmission facility failure. The alternative/standby reserve power could be reacted within 10 min after the power supply instruction and could be operated by the power supply command within 20 min during the supply and demand period and 120 min in other periods [4–7].

In this study, it would be proposed a possible method for frequency fluctuation and power system instabilities due to short-term fluctuation of large-scale capacity industrial loads by using the reserve power in the power system.

2 Industrial Load in the Power System

It was the contracted power, sales power, sales revenue and unit price of each contract type in Korea in 2014 with more than 20 million customers as shown in Table 1 [8]. By type of contract, industrial power was accounted for 64,371 MW, which was 57% of total contract power. Therefore, ancillary services (such as frequency control) have been trading in market other than electricity trading.

2.1 Control Method of the Reserve Power Due to Load Fluctuation

It should be required real-time operation to maintain stability and quality in the power system. Domestic electricity market has been separated to related functions for maintaining various power quality. The power control was shown by the type

Table 1 Customer Status by use in the Korea for 2014

		Number of house	Contract power (kW)	Sales power (MWh)	Sales revenue (₩1000)	Unit price (₩/kWh)
Residential	Residential	14,117,000	8,612,424	64,457,263	8,066,377,000	125
	Late night	822,000	598,598	14,657,873	986,847,000	67
Normal	Type A	2,882,000	33,111,045	52,305,163	6,929,603,000	132
	Type B	73,000	16,690,196	48,455,716	6,143,718,000	127
Education		20,000	4,231,061	7,438,374	849,079,000	114
Commercial	Type A	342,000	12,769,509	20,707,356	2,500,277,000	121
	Type B	45,000	51,601,493	251,844,216	26,616,721,000	106
Agricultural	Type A	85,000	414,992	901,050	22,908,000	25
	Type C	1,480,000	10,928,553	13,602,985	663,269,000	49
	Street lamp	1,605,000	1,077,707	3,221,008	365,234,000	113
Total	21,471,000	140,035,578	477,591,004	53,144,033,000		

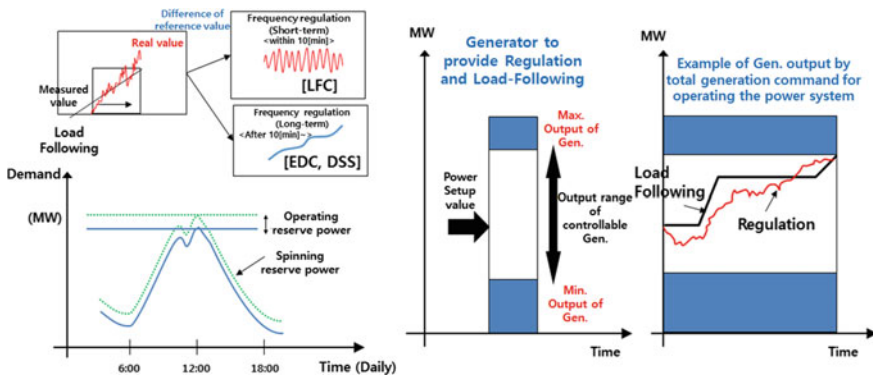


Fig. 1 Method of generator control for stability in power system

of power supply of the generator due to the load fluctuation in the power system as shown in Fig. 1 [8]. The small demand fluctuation could be compensated by frequency fluctuation to respond to short-term regulation. There would be power supply services such as regulation, load-following and energy unbalance in order to balance power supply and demand.

2.1.1 Load Fluctuation by Using the Power System Frequency

The time of average load fluctuation time was determined by fast Fourier transform (FFT) analysis of the spring, winter and summer periods [9]. The present load measurement of the large capacity customer has been using the 15 min of average load value although the frequency analysis for the load fluctuation was calculated for 1

Table 2 Range of frequency by load fluctuation

No	Load fluctuation time	Frequency range (Hz)
1	10–15 min	0.001–0.002
2	1–5 min	0.003–0.015
3	50–40 s	0.002–0.030
4	~30 s	0.040–0.050

min, 30 s and 10 s. The frequency operating range was shown according to the load fluctuation period as shown in Table 2.

2.1.2 Load Fluctuation by Using the Statistics

Statistical analysis was used to analyze the load fluctuation of large capacity customers. The probability distribution was using the normal distribution for load fluctuation analysis. It is used to calculate the reserve power range according to the load fluctuation because the normal distribution was the range of variance with respect to the average data. It was used the frequency distribution curve to calculate the reserve power by confirming at the statistical load fluctuation. The analytical method has been the statistical function (σ : sigma) to analyze the load capacity as a measure of the frequency of the load fluctuation by following Eq. 1.

$$\sigma = \sqrt{\frac{N \sum_{i=1}^N (\Delta \bar{P}_i)^2 - \left(\sum_{i=1}^N \Delta \bar{P}_i\right)^2}{N^2}} \quad (1)$$

Here, N is the average load time (1, 5, 15 min), ΔP is load variation capacity, and i is the real-time load fluctuation.

2.2 Load Fluctuation Analysis

It was investigated the industries with low load factor, high power consumption and high load fluctuation by in the power system. The daily load curve has been analyzed by the seasonal domestic power system as shown in Fig. 2.

The daily load value of winter and summer was increased up to about 75 GW, and spring was increased up to about 60 GW. The daily load curve was presented for the purpose of roughly analyzing the power consumption of the domestic power system. It has been shown the minimum change rate was 20%, and the maximum change rate was 50% of steel/mill load in the power system [10] (Fig. 3).

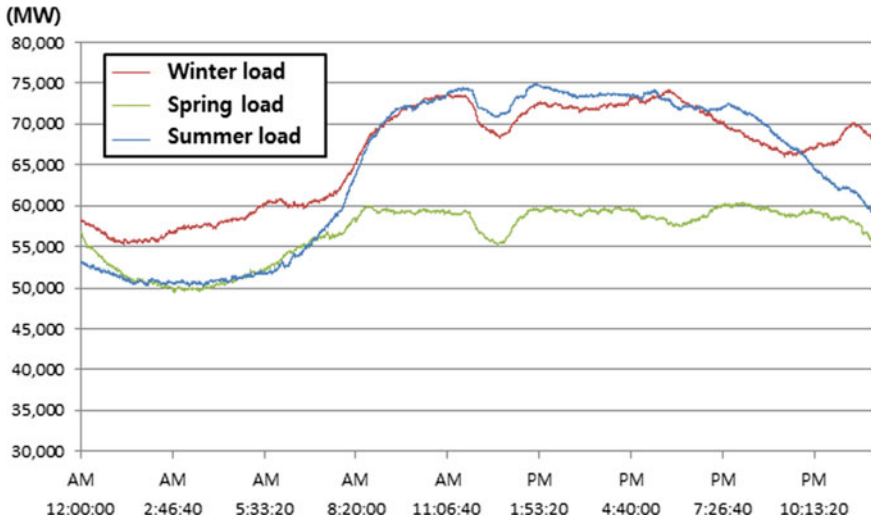


Fig. 2 Load curve by the seasonal in the power system

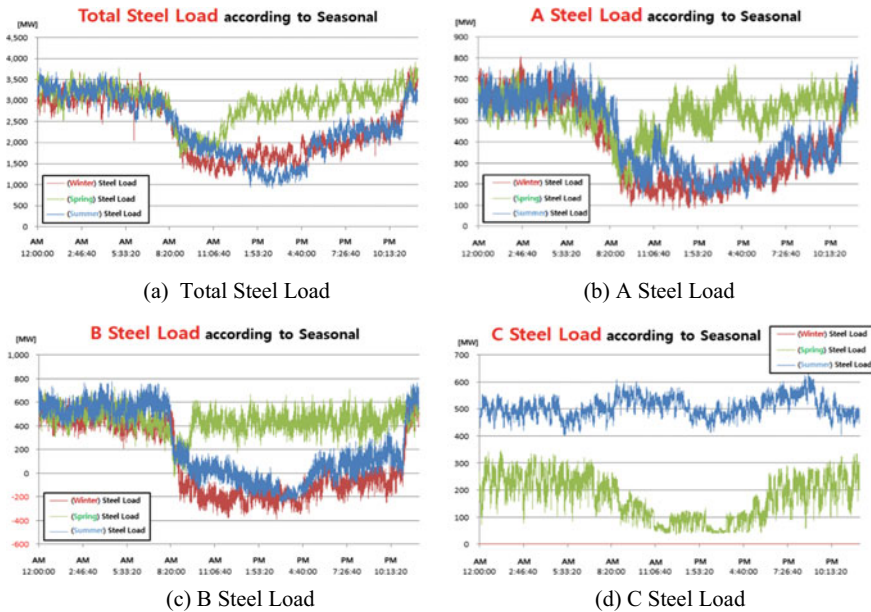


Fig. 3 Each steel load according to seasonal in the power system

Table 3 Load analysis of steel loads according to season

Load type (MW)		Power system load	Total Steel load	Each Steel loads		
				A Steel	B Steel	C Steel
Winter load	Average	66,400.5	2330.9	381.2	101.9	–
	Peak	74,188.0	3785.3	805.6	705.5	–
	Off-peak	55,288.0	1131.0	78.5	–390.5	–
Summer load	Average	64,530.5	2360.7	421.6	228.3	507.3
	Peak	74,980.0	3766.5	794.9	773.2	634.7
	Off-peak	50,186.0	907.8	108.2	–259.8	403.2
Spring load	Average	56,683.4	2934.6	530.4	446.1	173.4
	Peak	60,416.0	3917.9	770.7	727.8	347.9
	Off-peak	49,464.0	1629.7	175.3	–30.7	35.6

2.2.1 Power Capacity Variation Due to Seasonal Load

It was analyzed the result of the Korea Power Exchange (KPX) seasonal 2 s load fluctuation data as shown in Table 3. The seasonal loads were classified according to the average, peak and off-peak loads of the steel industry load.

It has been shown the daily load curve according to each steel loads of seasonal load as shown in Fig. 4. The curves have been partial downward curve on the large load fluctuation in the short period of the seasons. The daily characteristics were showed similar patterns in the winter and the summer load. However, it was showed different patterns in the spring and autumn load. It has been considered as a result of the differentiated charge and demand adjustment of the electricity rate charge.

It has been resulted of analyzing the seasonal load fluctuation levels of total steel load as shown in Figs. 4, 5 and 6. It was shown numeric value by the load fluctuation level of industry steel load. The use pattern of the daily load was similar showed off-peak load and peak load in winter load and summer load. Spring load has been needed to much load fluctuation capacity. The industry load was considered to control the demand power capacity. It was operating by reducing the load capacity due to the demand power in winter and summer steel load. Spring load was increasing the load fluctuation level as a result of analyzing the load level of off-peak, middle peak and peak load.

2.2.2 Frequency Characteristic Due to the Seasonal Load

It has been shown the FFT analysis according to seasonal and load level of total industrial steel load and a steel load. The magnitude of the frequency is large in the specific frequency band (15 min, 5 min, 1 min, 30 s, 10 s). The seasonal load fluctuation was analyzed by using FFT in the total industrial steel load by winter, summer and spring as shown in Figs. 7 and 8. As a result of the FFT analysis,

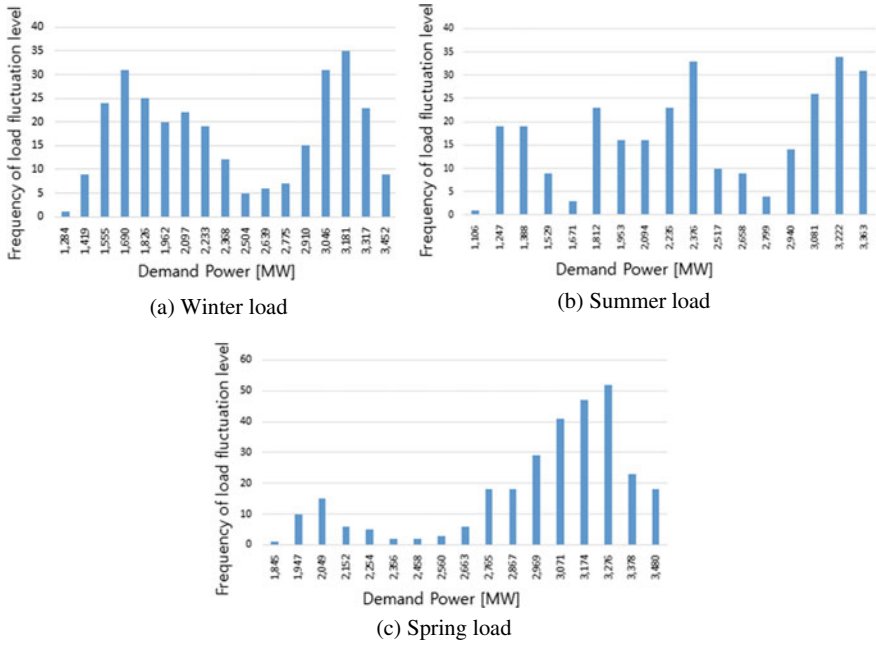


Fig. 4 Frequency of load fluctuation level in the total steel industrial load

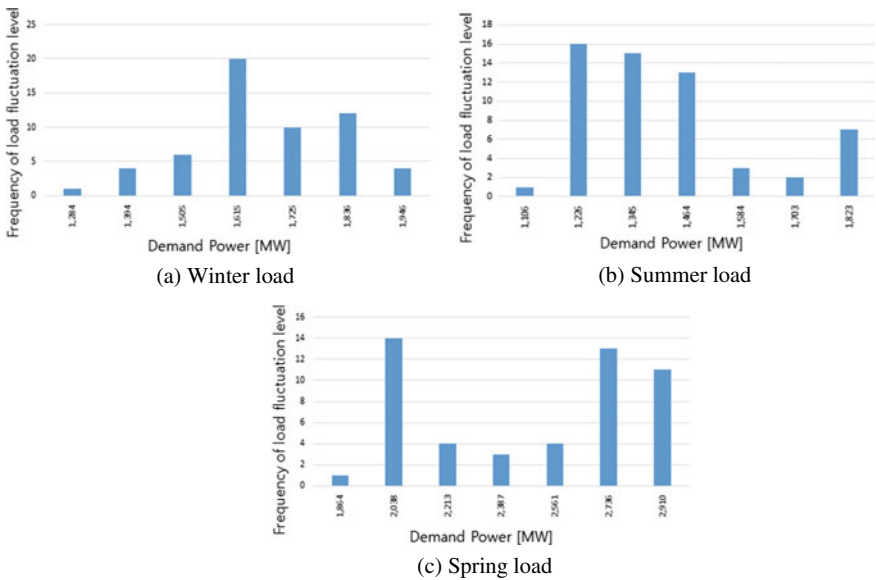


Fig. 5 Frequency of load fluctuation level about peak in the total steel industrial load

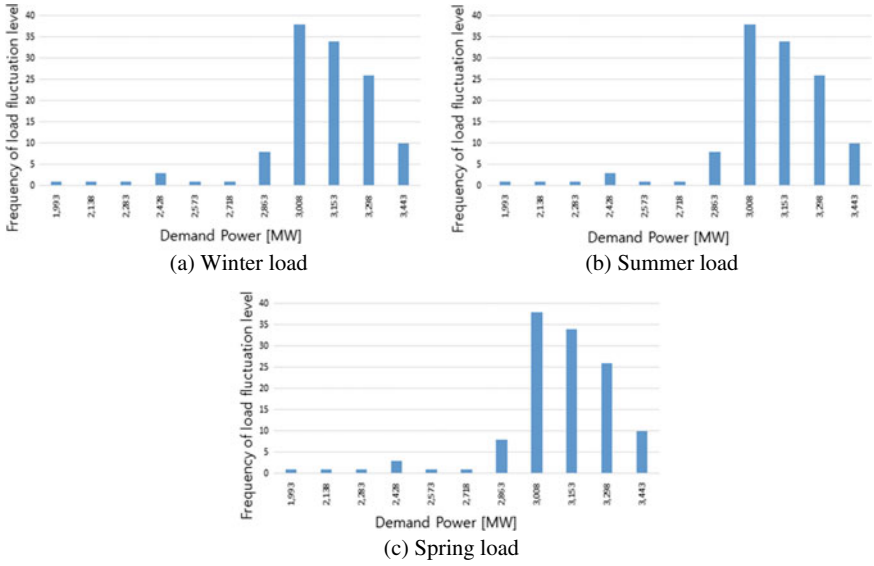


Fig. 6 Frequency of load fluctuation level about off-peak in the total steel industrial load

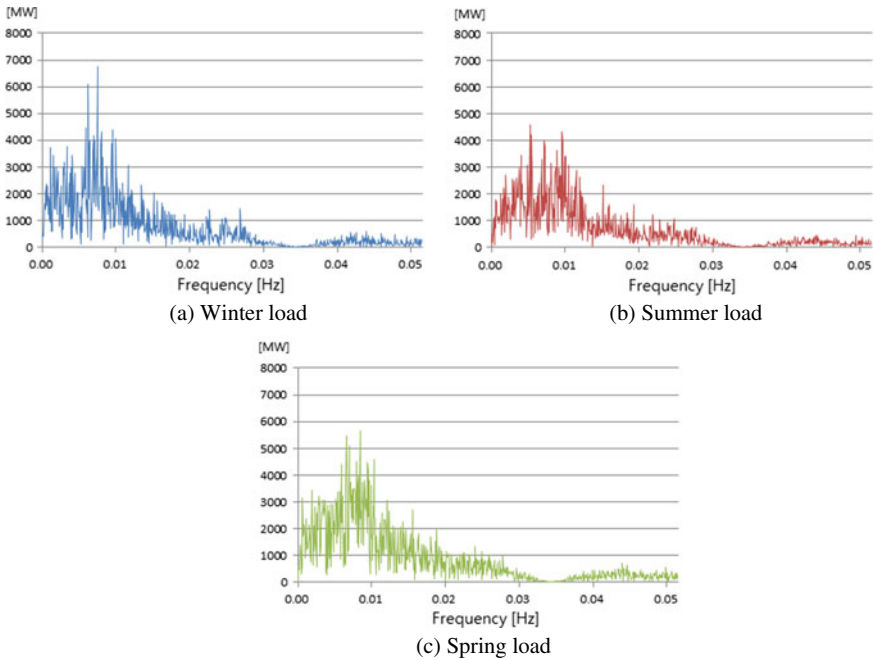


Fig. 7 FFT analysis by load fluctuation about peak in the total steel industrial load

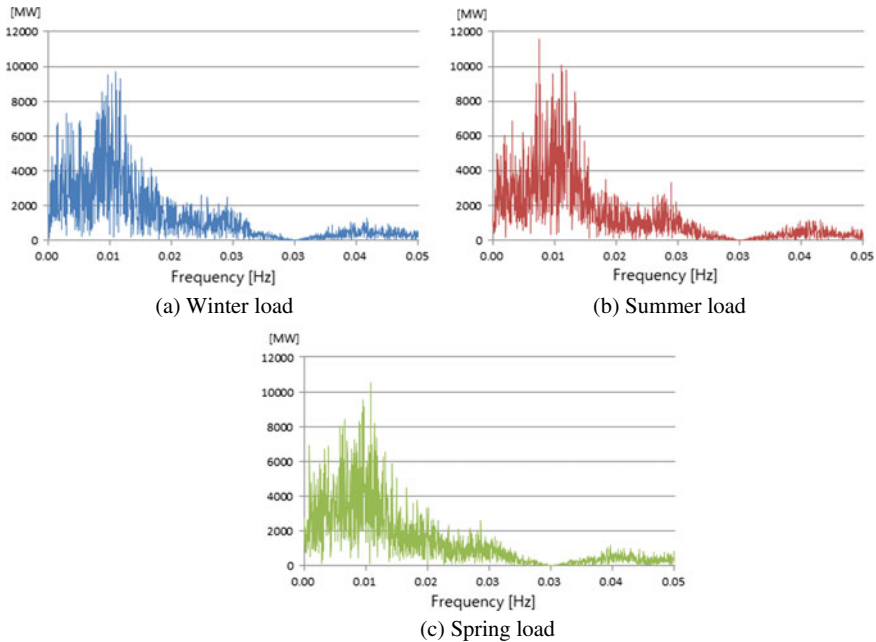


Fig. 8 FFT analysis by load fluctuation about off-peak in the total steel industrial load

the frequency magnitude was shown large from before 0.03 Hz. It has been the load fluctuation of the seasonal load greatly fluctuation after 40 s with reference to Table 2.

It has been shown the FFT analysis according to seasonal and load level of a steel load. The seasonal load fluctuation was analyzed by using FFT in the industrial steel load by winter, summer and spring as shown in Figs. 9 and 10. As a result of the FFT analysis, the frequency magnitude was shown large from before 0.02 Hz. It has been the load fluctuation of the seasonal load greatly fluctuation after 1 min with reference to Table 2.

The steel industrial load has been increased by 50% (1783 MW/3547 MW) from the average 20% (514 MW/2531 MW) according to a rough analysis of the power consumption in the power system. The load fluctuation was showed a high change. The frequency variation characteristics were derived by analyzing the winter, summer and spring data based on the 2 s instantaneous value measured by power exchange energy management system (EMS) for seasonal load and the load fluctuation by FFT analysis.

As a result, the fluctuation was showed large in the range of 5–10 min of the steel load. The short-term fluctuation of the total seasonal load was large in 1 min (508 MW in summer), 10 min (445 MW in spring), 15 min (608 MW in summer). This result should be noted in terms of the safety of operating short-term power system. It has been simulation method for reserve power and cost according to load fluctuation

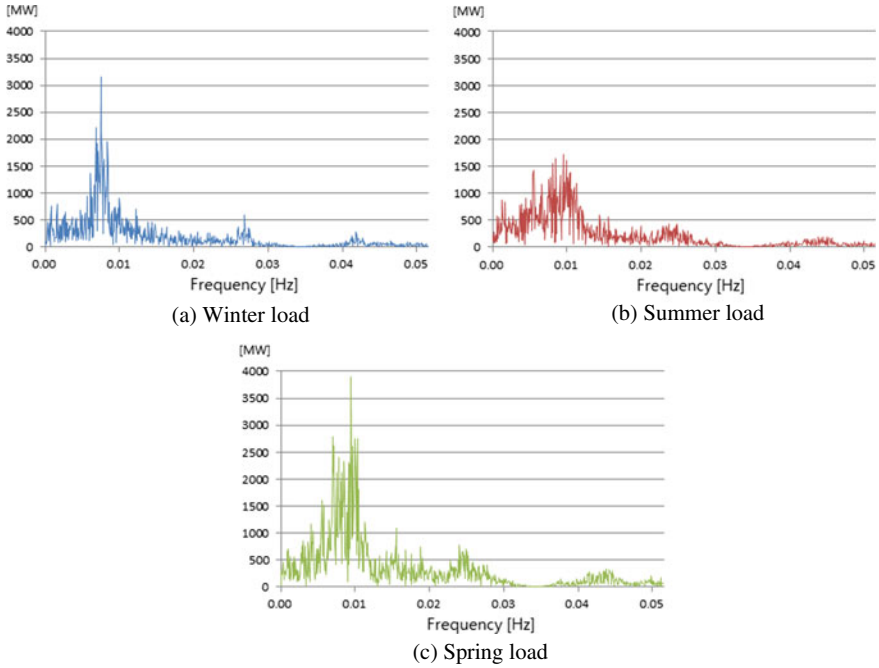


Fig. 9 FFT analysis by load fluctuation about peak load in the A steel industry

as shown in Fig. 11. The frequency variation characteristic has been calculated the frequency adjustment secure reserve power by the GF control and the AGC. If the load fluctuation was exceeded the maintenance range, the secure control capacity by the reserve power additional method was added to converge the system frequency within the maintenance range.

The mean load of steel/mill load fluctuation was calculated by the following Eqs. (2) and (3).

$$P_{L-avg}(t) = \frac{1}{T} \sum_{t=t_1}^T P_L(t) \tag{2}$$

$$\Delta P_{L-avg}(t) = P_{L-avg}(t) - P_{L-avg}(t + \Delta t) \tag{3}$$

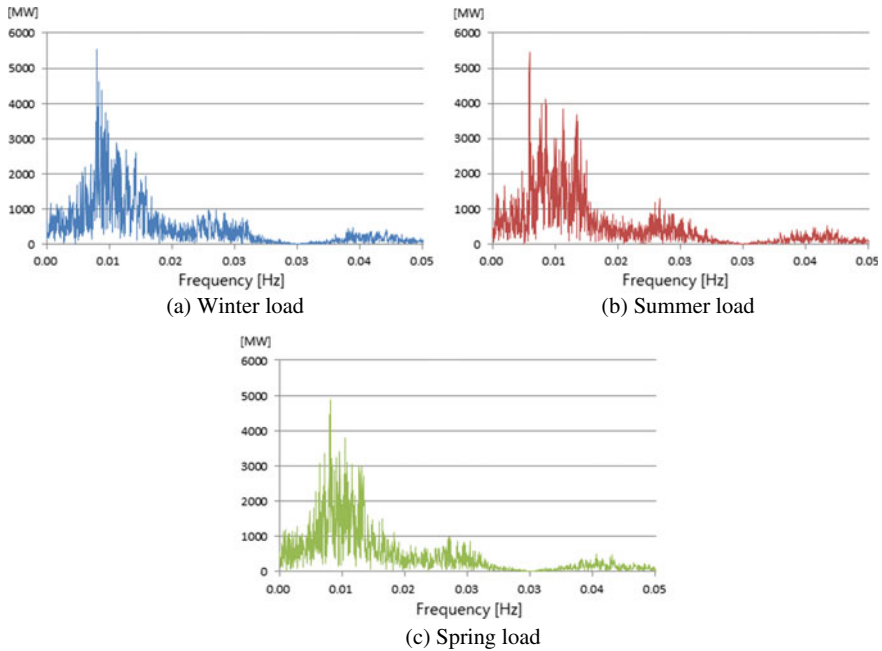


Fig. 10 FFT analysis by load fluctuation about off-peak load in the A steel industry

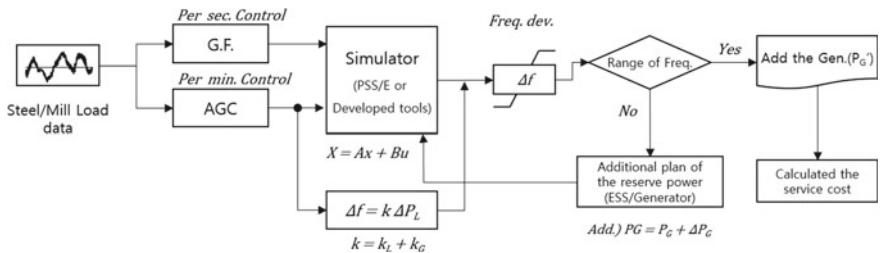


Fig. 11 Block diagram for securing reserve power by load fluctuation

3 Conclusion

Load fluctuation and frequency have been analyzed by seasonal and load level. Load fluctuation was large in spring and off-peak load with small power use. Load fluctuation was relatively small in summer and winter due to the plenty of power use. If fluctuation load was small, it would be reduced by securing reserve power in the power system. It could be considered to be reliable operation in the power system.

The improvement of the intermittent fluctuation load of the power system should be handled in relation to the uneven power by the grid connection of the renewable

energy to be introduced in the future. It is expected that it will be very important to build technical and economic infrastructure to apply demand response system.

References

1. Customer-Specific Metrics for the Regulation and Load-Following Ancillary Services (2000) Oak ridge National Lab, Jan 2000, Available from: <https://citeseerx.ist.psu.edu/viewdoc/download?doi=10.1.1.154.1661&rep=rep1&type=pdf>
2. Wolak FA (2011) An ancillary services payment mechanism for the Chilean electricity supply industry. Stanford University. July 2011, Available from: https://web.stanford.edu/group/fwolak/cgi-bin/sites/default/files/files/Ancillary_Services_Chile_Wolak_sept.pdf
3. Chu W-C, Chen Y-P (2009) Feasible strategy for allocating cost of primary frequency regulation. *IEEE Trans Power Syst* 24(2): 508–515. Available from: <https://ieeexplore.ieee.org/abstract/document/4797822>
4. Korea Power Exchange (2010) Operation standard of ancillary service for Power System operation
5. Korea Power Exchange (2011) Evaluation of supply reserve and operating reserve requirements considering enlargement of power system scale
6. Hirst E, Kirby B (1996) Electric power ancillary services, Feb 1996, ORNL/CON-426. Available from: https://www.consultkirby.com/files/con426_Ancillary_Services.pdf
7. Electric Power Charge by Contract type in the Korea for 2014 (2014) EPSIS. Available from: <https://epsis.kpx.or.kr/epsisnew/selectEksaCscCscGrid.ajax?menuId=0904050100>
8. Load Frequency Control in the power system at all times and in emergency (2002) CREPI Technical Report No. 869, Mar. 2002, pp. 148, Available from: https://www.bookpark.ne.jp/cm/ieej/detail.asp?content_id=IEEJ-GH869-PRT
9. Lee H-C, Roh Y-G, Jung B-J (2019) A study on the power system analysis by steel and mill load. *ICNCT* 2019, pp 153–155
10. Lee H-C, Jung B-J, Roh Y-G, Ryu I-H (2018) A study on load pattern of large capacity load variation in the power system. *J Eng Appl Sci* 13(Special Issue 3):3348–3352

Dynamic Operation of Grid-Connected Photovoltaic Power System



Neeraj Priyadarshi, Farooque Azam, Akash Kumar Bhoi,
and Amarjeet Kumar Sharma

Abstract Recently, the market of grid-connected photovoltaic (PV) systems is growing rapidly, and therefore, grid-connected PV inverters are in more demand. Now, various researchers are working on cost optimization and tracking efficiency of PV system and hence increase the power quality of the grid-connected PV system. The main objective of this research paper is to harvest optimal energy from solar which has reduced cost of inverter, and for this, cascaded inverter has been selected for grid integration with improved performance.

1 Introduction

The current PV inverter has \$0.25 as per watt in the USA, and government has taken initiative to make PV structures of \$1 in keeping with watt by means of year 2020, in which simplest \$0.10 with watt for electrical–electronics applications. The objective can be achieved by harvesting maximum energy from sun which reduced cost of inverter, and for this, cascaded inverter has been selected for grid integration and reduces the cost to improve performance. Moreover, maximum power point tracking has also been used to extract extra solar electricity from solar arrays [1–5]. Various inverters are associated to generate higher level of electrical power in case of cascaded inverter topology which reduces the voltage stress of the power switches. Moreover, MOSFETs with lower voltage stress can also be utilized for high scale PV generation which results in the reduction of PV inverter prices. In equated with other inverter

N. Priyadarshi (✉) · A. K. Sharma

Department of Electrical Engineering, Birsa Institute of Technology (Trust), Ranchi 835217, India
e-mail: neerajrjd@gmail.com

F. Azam

School of Computing & Information Technology, REVA University, Bangalore 560064, India
e-mail: farooque53786@gmail.com

A. K. Bhoi

Department of Electrical & Electronics Engineering, Sikkim Manipal Institute of Technology,
Sikkim Manipal University, Majhitar, India
e-mail: akash730@gmail.com

© Springer Nature Singapore Pte Ltd. 2020

A. K. Bhoi et al. (eds.), *Advances in Greener Energy Technologies*,

Green Energy and Technology, https://doi.org/10.1007/978-981-15-4246-6_13

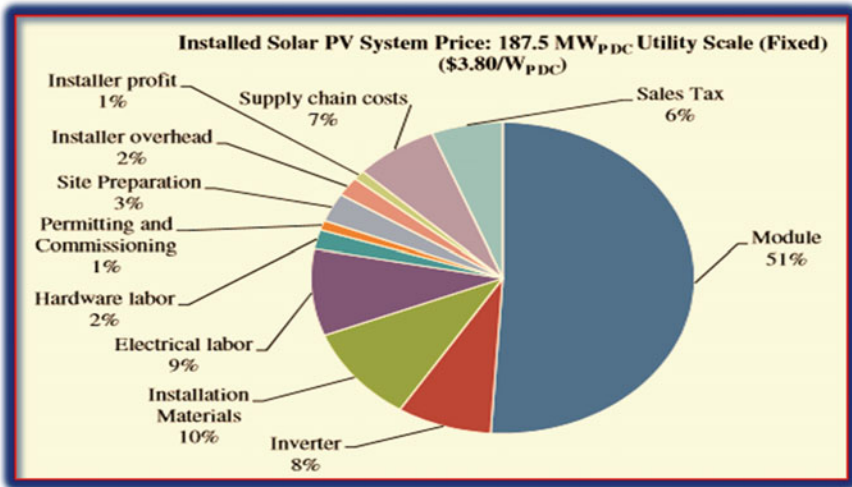


Fig. 1 Global PV system price breakdown

topologies, the cascaded inverter has lower switching frequency and can work on high level of energy which does not affect the PV arrays, and consequently, high efficiency is achieved [6–11] (Fig. 1).

2 Control Strategy for Controlling Inverter

The traditional proportional-integral controllers are unable to solve steady-state error issues present in grid current for grid integrated PV system, and phase-locked loop (PLL) has been employed to solve these problems. It can translate using Clark transformation (ABC to $\alpha\beta$ frame) which processed to Park's conversion with dq rotation frame. Moreover, dq translation cannot be used for direct quadrature zero while used for three-phase network. These transformations have been employed to make the calculations simpler. The calculated results have been translated to abc reference frame and fed to real-time applications which makes the design complexity simpler.

A PLL controller makes the phase of output and reference signal same which compares the phase of these two signals and provides the adjustment of oscillator frequencies for phase synchronization. The obtained phase detector signal regulates the oscillator as a feedback signal in the network. As frequency is calculated mathematically as phase derivative, the PLL locks phase of output and reference signal which results in locking of both signals and synchronization is possible.

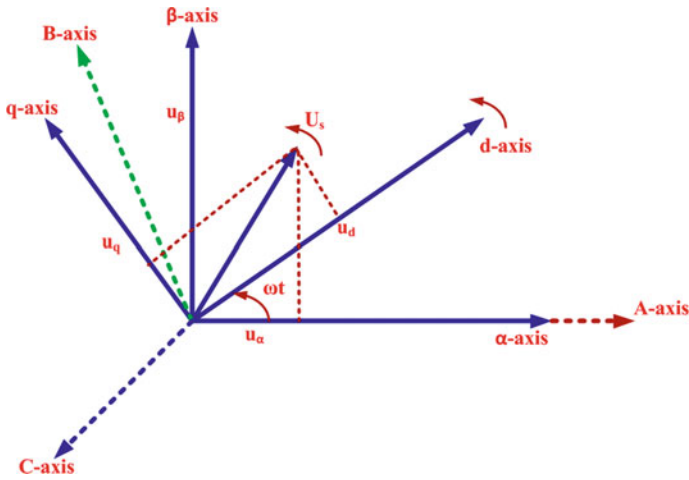


Fig. 2 Principle of *abc* to *dq* transformation

2.1 Principle of *ABC* to *dq* Transformation

Sinusoidal-based parameters are oriented using two rotating axes equivalent to three axes sine parameters with similar angular velocity after *dq* transformation. And these transformed axes are named as *d-q*-axis in which *d*-axis leads to *q*-axis by 90° (Fig. 2).

3 Dynamic Operation of Grid-Connected PV System

The PV grid tied dynamic behavior can be evaluated under varying solar insolation and surrounding temperature. The 200 W PV power systems operate at 25 V and 8 A operating voltage and current, respectively. MATLAB simulation has been performed to obtain the performance under changing operating conditions. These operations can be created by cloud passing and blocking which associated to PV panels. The solar insolation level varies from 1000 to 200 W/m² at time 0.005 s, and corresponding variations of PV voltage and current have been noted, and result is depicted in Fig. 3.

Figures 3 and 4 present the variable temperature and irradiance level at $t = 0.005$ s in dynamic state condition, respectively.

Figures 5, 6 and 7 depict the simulated results of PV voltage, current and power for 100 W grid-connected PV system in dynamic state condition. Simulated results reveal that PV parameters are operated near to maximum power point under changing operating conditions (Figs. 8, 9 and 10).

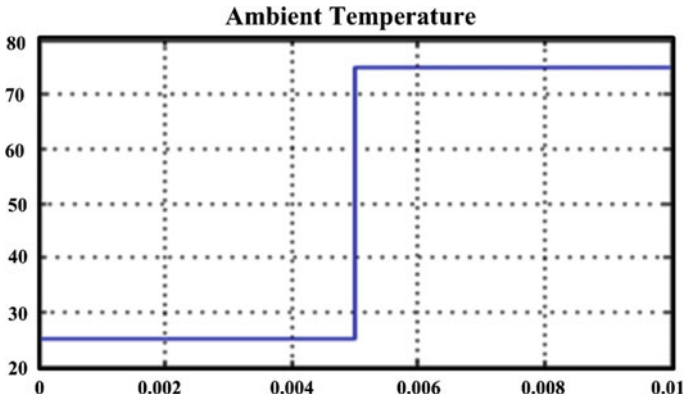


Fig. 3 Variable ambient temperature at dynamic state operation

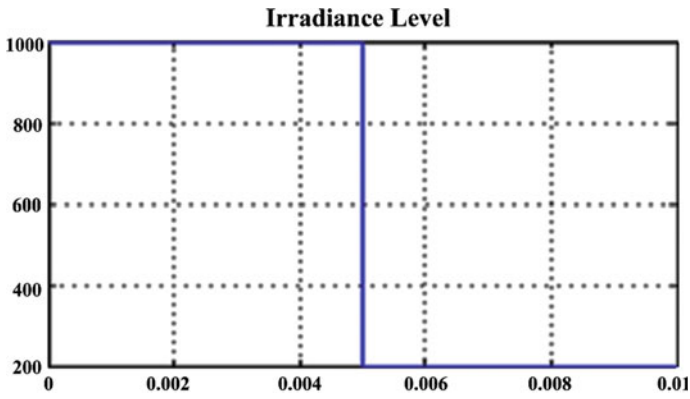


Fig. 4 Variable irradiance level at dynamic state operation

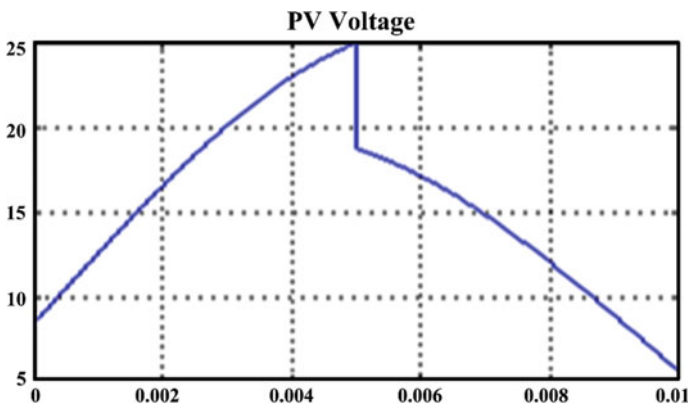


Fig. 5 Transient condition PV voltage

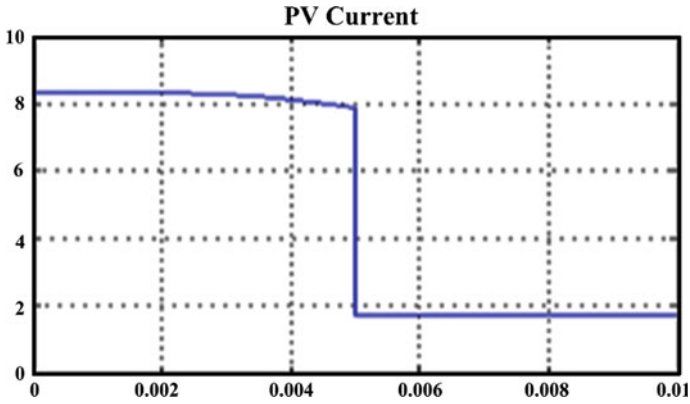


Fig. 6 Transient condition PV current

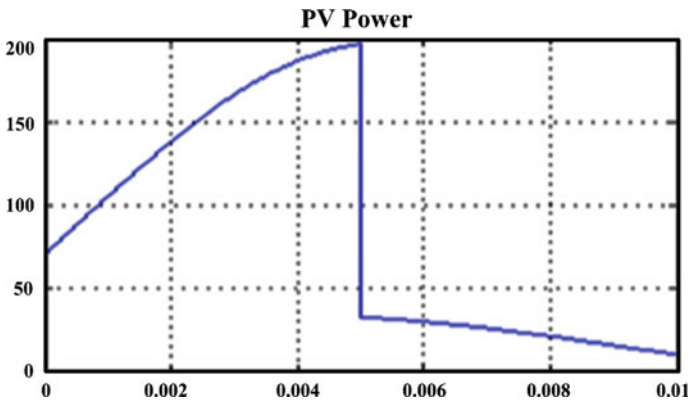


Fig. 7 Transient condition PV power

Figures 11 and 12 present PV grid tied performance in dynamic state condition. The sine wave obtained inverter current fed to the grid which is responsible for unit power factor behavior. The active/reactive powers maintained under dynamic state condition which is presented by Fig. 13.

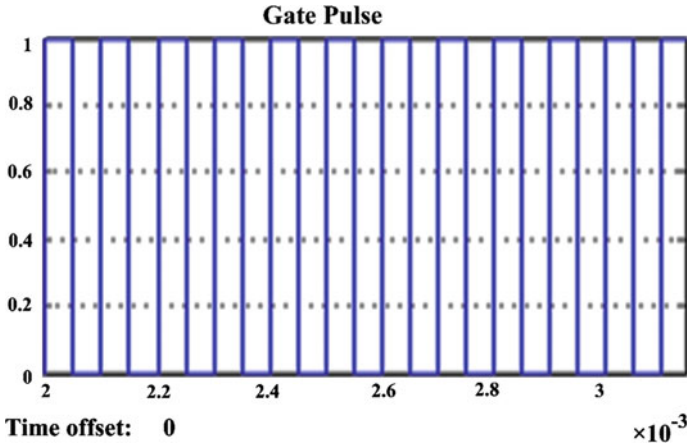


Fig. 8 Gating pulses for DC-DC converter

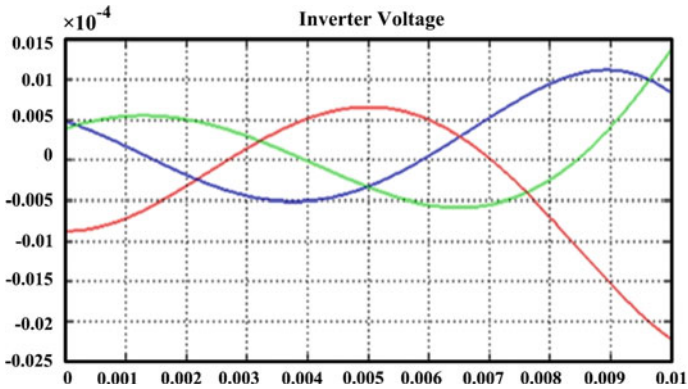


Fig. 9 Inverter voltage under dynamic conditions

4 Conclusion

PV grid dynamic performance of photovoltaic systems varies with different operating conditions. The PV associated parameters are obtained and realized using MATLAB simulation tools. Proposed inverter fed sine wave-shaped inverter current to utility grid and power factor unity has been maintained. The active/reactive powers are well maintained in dynamic state condition which validates the accurate design of PV power system.

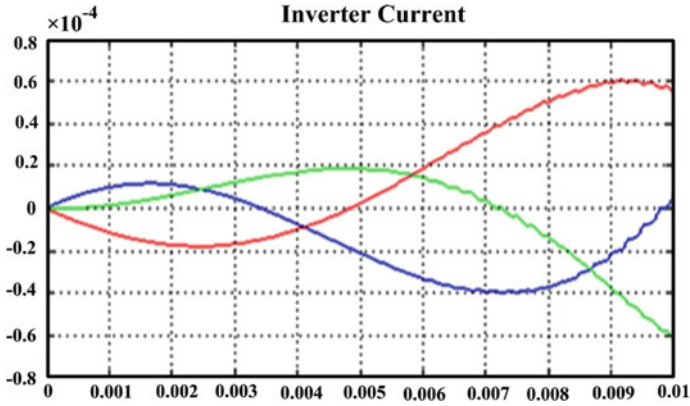


Fig. 10 Inverter current under dynamic conditions

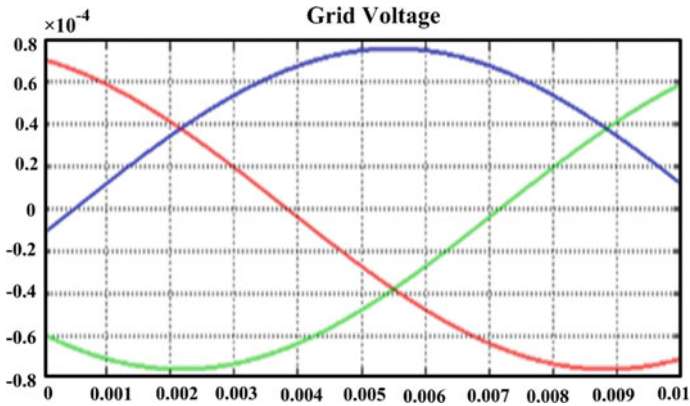


Fig. 11 Grid voltage under dynamic conditions

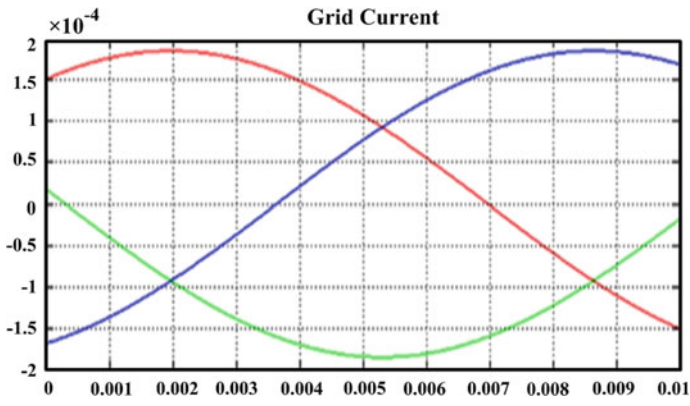


Fig. 12 Grid current under dynamic conditions

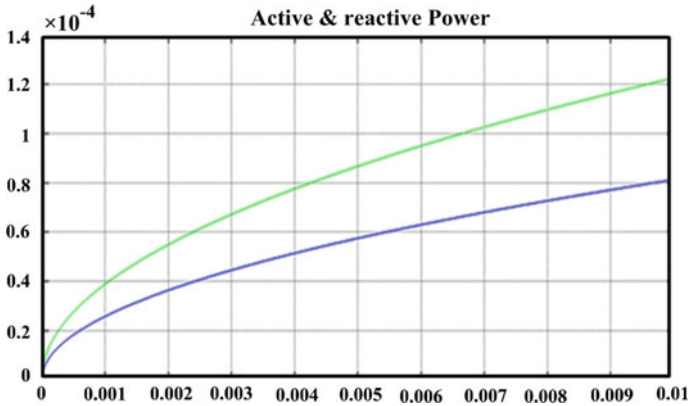


Fig. 13 Active and reactive power at dynamic state

References

- Priyadarshi N, Padmanaban S, Maroti PK, Sharma A (2018) An extensive practical investigation of FPSO-based MPPT for grid integrated PV system under variable operating conditions with anti-islanding protection. *IEEE Syst J* 1–11
- Priyadarshi N, Padmanaban S, Bhaskar MS, Blaabjerg F, Sharma A (2018) A fuzzy SVPWM based inverter control realization of grid integrated PV-wind system with FPSO MPPT algorithm for a grid-connected PV/wind power generation system: hardware implementation. *IET Electr Power Appl* 1–12
- Priyadarshi N, Anand A, Sharma AK, Azam F, Singh VK, Sinha RK (2017) An experimental implementation and testing of GA based maximum power point tracking for PV system under varying ambient conditions using dSPACE DS 1104 controller. *Int J Renew Energy Res* 7(1):255–265
- Nishant K, Ikhlaq H, Bhim S, Bijaya KP (2018) Self-adaptive incremental conductance algorithm for swift and ripple free maximum power harvesting from PV array. *IEEE Trans Ind Inf* 14:2031–2204
- Satyajit M, Bidyadhar S, Pravat KR (2016) A new MPPT design using grey wolf optimization technique for photovoltaic system under partial shading conditions. *IEEE Trans Sustain Energy* 7:181–188
- Priyadarshi N, Sharma AK, Azam F (2017) A hybrid firefly-asymmetrical fuzzy logic controller based MPPT for PV-wind-fuel grid integration. *Int J Renew Energy Res* 7(4)
- Priyadarshi N, Sharma AK, Priyam S (2017) Practical realization of an improved photovoltaic grid integration with MPPT. *Int J Renew Energy Res* 7(4)
- Mahdi J, Seyed HF (2017) A new approach for photovoltaic arrays modeling and maximum power point estimation in real operating conditions. *IEEE Trans Ind Electron* 64:9334–9343
- Prasanth RJ, Rajasekar N (2017) A novel flower pollination based global maximum power point method for solar maximum power point tracking. *IEEE Trans Power Electron* 32:8486–8499
- Priyadarshi N, Padmanaban S, Mihet-Popa L, Blaabjerg F, Azam F (2018) Maximum power point tracking for brushless DC motor-driven photovoltaic pumping systems using a hybrid ANFIS-FLOWER pollination optimization algorithm. *MDPI Energies* 11(1):1–16
- Bhim S, Chinmay J, Anmol B (2018) An improved adjustable step adaptive neuron based control approach for grid supportive SPV system. *IEEE Trans Ind Appl* 54:563–570

Case Study of the Asset Monitoring Focused on Facility Management



Sangchul Kim and Shinjo Eom

Abstract Background/Objectives. This study aims to propose an asset monitoring solution for company's facility management. Asset monitoring is an end-to-end solution that collects, analyzes, and transmits various data related to business operations. Methods/Statistical analysis: Asset monitoring embedded devices or smart machines through detectors or controllers connected by wired/wireless. The validity of the study was verified by analyzing the difference between supervisory control and data acquisition (SCADA) and asset monitoring through a literature survey on SCADA that was used in the past. Then, in order to propose the advantages and application of asset monitoring, we conducted a case study on asset monitoring. Findings: The research on three different fields was conducted, and the final result of the asset monitoring was derived. First, we studied asset monitoring of the pipeline company. We can find several meaningful propositions like (1) take multiple networks to one network and (2) local intelligence to react quickly to local events. Second, a result of the investigation of chemical and petroleum is abstracted like (1) reduced energy costs through better management of energy consumers (e.g., forecourt lights) and (2) less downtime of money generators. Finally, we analyzed the automated meter reading/advanced metering technology (AMR/AMT). As same as the previous two cases: (1) interval billing to incent energy conservation and (2) demand response to remotely turn-off devices using high consumption during peak times were important to the company. What we intend to pursue through asset monitoring, in general, is to improve the value of business through convergence with other systems in the company, and it is confirmed that efficiency can be pursued through asset monitoring. Improvements/Applications: Asset monitoring solutions are predictable and cost-effective compared to post-maintenance. Therefore, this paper shows a method to reduce cost by introducing asset monitoring for the facility management section.

S. Kim

School of Architecture, Hankyong National University, Anseong, South Korea
e-mail: sckim08@hknu.ac.kr

S. Eom (✉)

School of Architecture, Kyungil University, Gyeongsan, South Korea
e-mail: creed@kiu.kr

© Springer Nature Singapore Pte Ltd. 2020

A. K. Bhoi et al. (eds.), *Advances in Greener Energy Technologies*,

Green Energy and Technology, https://doi.org/10.1007/978-981-15-4246-6_14

Keywords Asset monitoring · SCADA · Facility management · Case study · Maintenance

1 Introduction

Data mining asset monitoring enables the remote monitoring of essential electromechanical and electronic equipment for problems and of environmental data like temperature and vibrations [1]. The key functions performed by asset monitoring are to aggregate data locally from installed sensors, to analyze the data locally or at a central location against predefined criteria, and to act on the data analysis when necessary by integrating into an application [2]. Supervisory control and data acquisition (SCADA) had used in many years, but collected business operations data are analyzed, and the appropriate action is taken based on the analyzed results [3]. For example, a field service automation (FSA) application can be used to send urgent service request messages to service personnel. Asset monitoring also enables more efficient integration with back-end business processes for enterprise resource planning (ERP) or customer relationship management (CRM). Therefore, this study aims to propose an asset monitoring solution for company’s facility management. Asset monitoring is an end-to-end solution that collects, analyzes, and transmits various data related to business operations.

2 Literature Review

2.1 SCADA System

The rapid development of hardware and software technologies enables us to develop a new generation of supervisory control and data acquisition (SCADA) systems as shown in Fig. 1. The Web-based SCADA system described here is composed of intelligent RTUs, and each module supports a hardware architecture and HTTP protocol, has a Web server/browser structure, and supports a distributed master station that decomposes SCADA functionality into multiple sets of Web site components. Based on a well-proven architecture module, Web-based SCADA hardware design

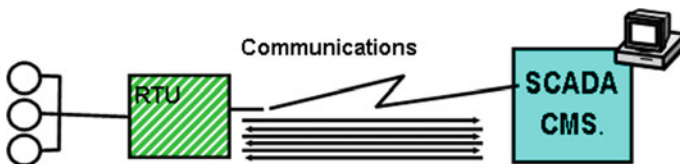


Fig. 1 SCADA connecting diagram

and software development can benefit from the numerous technologies available in the system and add flexibility and scalability [3].

But, SCADA had been used many years, and it had lots of benefits; however, it had disadvantage in several aspects such as [3, 4];

- Poll/response paradigm uses 100% of available bandwidth
- ‘Transport’ is the ‘application.’ You cannot break them apart
- One protocol for all field equipment limits new/mixed technologies
- It is not ‘managed’ network
- SCADA system goes down ... monitoring is down
- End point is normally a terminal or user monitoring data
- Plus, typically, these systems are not connected, or not easily connected, to back-end e-business applications
 - Between host and field equipment, data related by one-to-one
 - Custom application is required to access data for other applications
 - If data is needed for multiple applications, multiple custom connections are needed.

2.2 Asset Monitoring

2.2.1 Asset Monitoring Hierarchy

And the maintenance of facility assets consists of asset management (AM), which analyzes investment risks through portfolio management, property management (PM), which helps to maximize profits by reducing vacancy through real estate management, and management of expenses, and there is facility management (FM) to carry out. Details about this are shown in Fig. 2.

2.2.2 Overview of Asset Monitoring System

Asset monitoring enables the remote monitoring of essential electromechanical and electronic equipment for problems and of environmental data like temperature and vibrations. The key functions performed by asset monitoring are (1) to aggregate data locally from installed sensors, (2) to analyze the data locally or at a central location against predefined criteria, and (3) to act on the data analysis when necessary by integrating into an application as shown in Fig. 3 [5].

Modern asset monitoring adds ‘intuitive intelligence’ to the above functions and is built on a ‘plug-and-play’ infrastructure for (1) trend analysis against past history and experience, (2) a flexible infrastructure based on ‘open standards’ that can

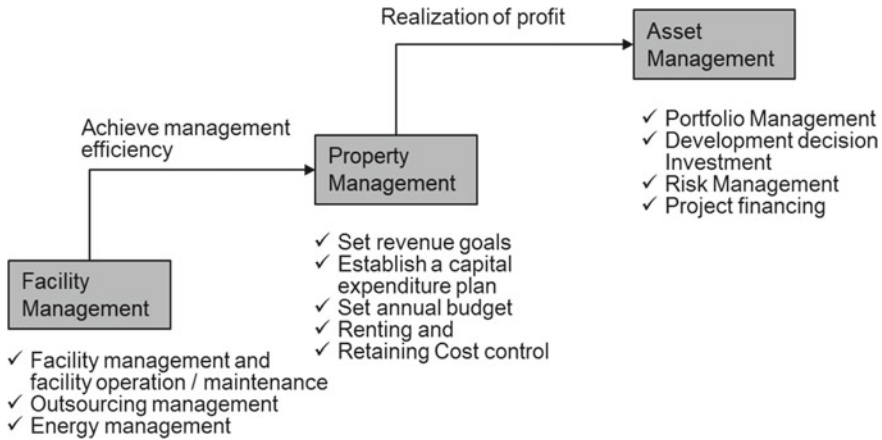


Fig. 2 Hierarchy of facility asset monitoring

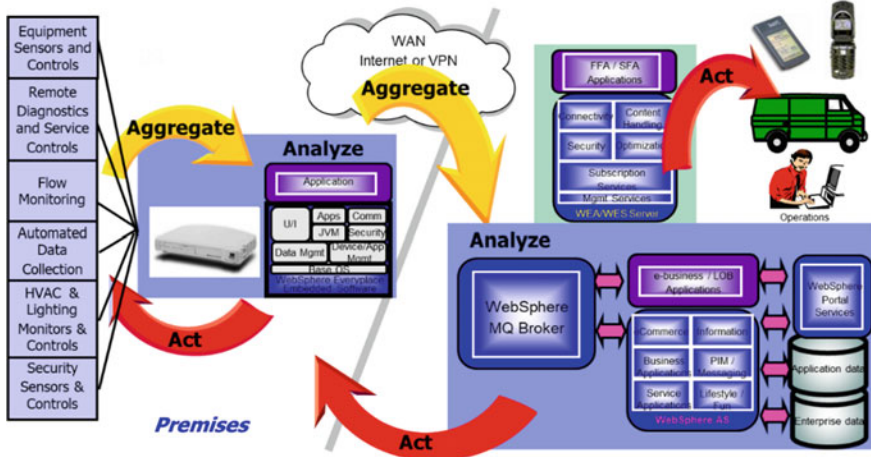


Fig. 3 Concept diagram of asset monitoring solution

be upgraded, and (3) productivity improvements via enterprise-level integration of data/knowledge, processes, and applications.

Unlike the existing supervisory control and data acquisition (SCADA), asset monitoring detects the state of itself by the managed system, and the data such as the state is relayed to the system of the back-end in real time through the residential gateway, and the processing is transferred [5], and integrated process optimization is possible through real-time machine links across enterprise value chain.

Asset monitoring as shown in Fig. 4 has three parts: (1) intelligent gateway, (2) intelligent sensors, and (3) asset monitoring server.

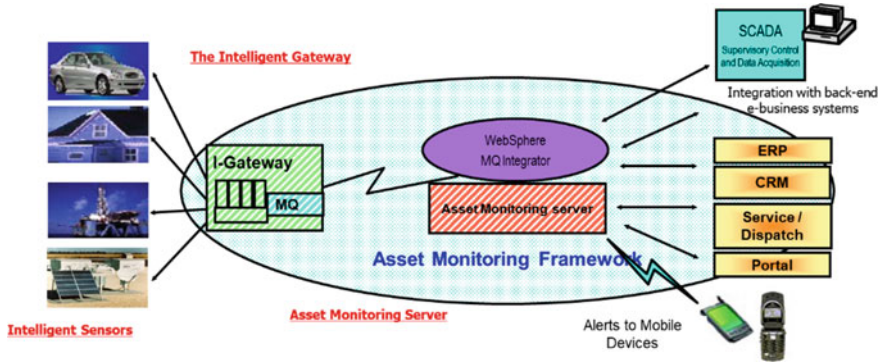


Fig. 4 Asset monitoring overview

1. Intelligent Gateway

An embedded computing platform is hosting a Java execution environment, applications and, APIs, enabling the gateway to:

- collect asset data, report status, and operation characteristics
- analyze device input with diagnostic algorithms locally
- control assets locally based on local input, even aggregating and analyzing data received from multiple local device
- receive and load code updates and parameters remotely
- support multiple device types and protocols simultaneously.

2. Intelligent Sensors

Actuators send and receive data converting dumb sensor information into a format that is readily readable by other systems.

3. Asset Monitoring Server

A bundling of e-business and pervasive computing technologies: A comprehensive solution that monitors and controls assets provides device management, security, offers and manages notification services, data synchronization, messaging, and performs diagnostic analysis.

2.2.3 Asset Monitoring Benefit

Tangible benefits of asset monitoring system are:

1. Reduction in downtime of essential equipment
 - preventive versus corrective maintenance
 - remote upgrades of software components.
2. Reduction in cost of customer service and field engineers

- reduced need for training (less wastage)
- reduced energy consumption
- reduced scrap on production floors.

And another aspect, intangible benefits are gained by asset monitoring:

- Improved customer satisfaction and loyalty for equipment sold to third parties
- Better data on performance feeds into R&D and next-generation products
- Contact with customer and equipment throughout the life cycle
- ‘Service’-based recurring revenue from both own and competitors’ products
- Reduced risk of human errors
- Reduced paper administration
- Ability of customers to monitor ‘their batch’ at third-party contract manufactures.

Also, it has technical and financial benefits:

- No more custom applications for ERP such as SAP/ORACLE to acquire data
- Central point of data
- Protocol neutrality to transfer all types of data over the network
- Event-based data for near real-time updates
- One-to-many topology
- Equipment and application neutrality
- Reduce costs and shorten implementation cycles
- Capital structure is maintained
- Communication path and cost reduction
- Improved accuracy of system performance modeling
- Real-time data for business logic and asset management
- Billing data is collected in near real time by reducing billing cycles without cost savings
- Benefit from the spot market with real-time data
- Reduce communication costs due to event-driven data
- Reduce time to deploy greenfield applications and asset acquisitions in the business infrastructure
- Reduce hardware costs by competing against price versus performance rather than proprietary applications
- Resale or competitive advantage to use real-time data in customer resource management (CRM) systems and case study of asset monitoring.

3 Case Study of Asset Monitoring

3.1 Pipeline Monitoring Case

3.1.1 Solution Description

Petroleum companies have vast networks of pipelines moving crude, gas, and processed products as shown in Fig. 5. They already have some level of SCADA network monitoring and controlling the flow and operation of the pipelines and associated equipment [6, 7]. Samples of the instrumentation included: flow meters, temperature, pressure, vortex, cathodic detection, density, etc. So, asset monitoring can enhance and supplement the current SCADA systems with new technology based on transmission control protocol/Internet protocol (TCP/IP), intelligent gateways, and message queue (MQ) messaging broker.

3.1.2 Technology Value Propositions

- Potential to lower infrastructure and common costs
- Take numerous networks to one network
- Event-driven messaging (to reduce bandwidth needs)
- Local intelligence to react quickly to local events
- Publish and subscribe messaging format allows data to flow easily to multiple back-end systems and applications
- Better SCADA data security
- Predictive maintenance.

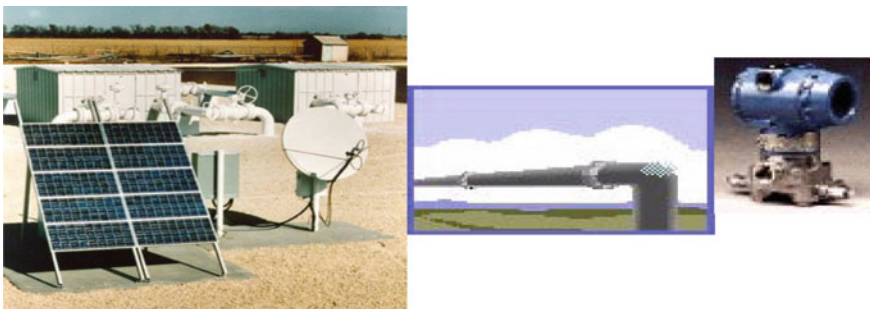


Fig. 5 Major facility of pipeline company

3.2 Chemical and Petroleum Case

3.2.1 Solution Description

A subset of retail petroleum concentrates on the point of sales (POS), retail sale of goods and related back-office infrastructure, and i-Gas Station adds sensors on gas station equipment such as gas pumps, tanks, car wash, power meter, and forecourt lights to better monitor and manage gas station operations as shown in Fig. 6 [8, 9].

3.2.2 Value Propositions

- Reduced energy costs through better management of energy consumers (e.g., forecourt lights)
- Less downtime of money generators (e.g., gas pumps or car wash, through predictive maintenance)
- Reduce theft (a major problem in some countries)
- Better inventory control
- Combine multiple station management systems into one hub
- Provides infrastructure for new revenue opportunities, such as potentially, multimedia deliver to customers via Wi-Fi hot spot
- Data for regional and mobile management
- Data for FSA application.



Fig. 6 Major facility of gas station company



Fig. 7 Major facility of AMR/AMT company

3.3 Automated Meter Reading/Advanced Metering Technology (AMR/AMT) Case

3.3.1 Solution Description

AMR is automating existing meter reading for billing (low additional value) [10, 11], and AMT (high additional value) monitoring and control of meters and connected electric devices adding connection to new applications and capabilities (e.g., demand response, load balancing, interval charging) as shown in Fig. 7.

3.3.2 Value Propositions

- Theft detection
- Interval billing to incent energy conservation
- Demand response to remotely turn-off devices using high consumption during peak times
- Load management.

3.4 End Vision of Asset Monitoring System

The end vision is transparency of information by integrating asset monitoring at the enterprise level, and this leads to business value improvement as shown in Fig. 8.

4 Conclusion

Asset monitoring is an efficient technique that has been proven to be effective by the three. First, we performed asset monitoring of the pipeline company. We can find several meaningful propositions like (1) to take multiple networks to one network and (2) local intelligence to react quickly to local events. Second, as a result

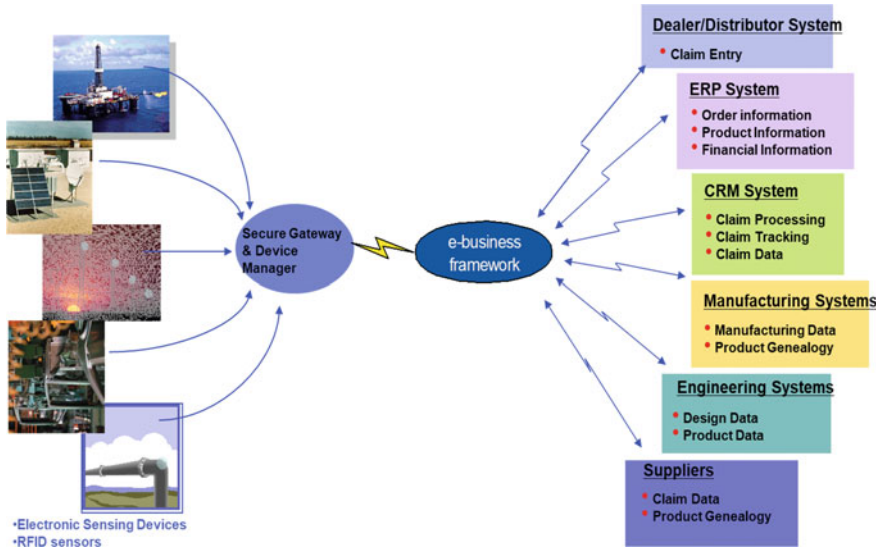


Fig. 8 Completion goal of asset monitoring system

of the investigation of chemical and petroleum is abstracted like (1) reduced energy costs through better management of energy consumers (e.g., forecourt lights) and (2) less downtime of money generators. Finally, we analyzed the automated meter reading/advanced metering technology (AMR/AMT). As same as the previous two cases: (1) interval billing to incent energy conservation and (2) demand response to remotely turn-off devices using high consumption during peak times were important to the company. Asset monitoring is spreading to other industries as it has the advantage of remotely monitoring power sales and facility management as well as oil sales volume in real time. This paper is a preliminary study to apply asset monitoring to the facility management area. If you take advantage of the advantages of asset monitoring, you can reduce equipment downtime and increase sales in the facility construction industry. Monitoring IT architecture, construction plan, and operational process can reduce maintenance cost and minimize downtime of enterprise assets and facilities. And what we intend to pursue through asset monitoring, in general, is to improve the value of business through convergence with other systems in the company, and it is confirmed that efficiency can be pursued through asset monitoring.

Acknowledgements This work was supported by the National Research Foundation of Korea (NRF) grant funded by the Korea Government (MSIP) (2017R1D1A1B03036308).

References

1. Baird GM (2011) Defining public asset management for municipal water utilities. *J Am Water Works Assoc* 103(5):30. <https://doi.org/10.1002/j.1551-8833.2011.tb11449>
2. Agarwal V, Lybeck NJ, Pham BT, Rusaw R, Bickford R (2013) Online monitoring of plant assets in the nuclear industry. In: Annual conference of the prognostics and health management society 2013
3. Li D, Serizawa Y, Kiuchi M (2002) Concept design for a web-based supervisory control and data-acquisition (SCADA) system. In: IEEE/PES transmission and distribution conference and exhibition, vol 1, Yokohama, Japan, pp 32–36. <https://doi.org/10.1109/TDC.2002.1178256>
4. Khadraoui D, Feltus C (2013) Critical infrastructures governance exploring SCADA cybernetics through architected policy semantic. In: IEEE international conference on systems man and cybernetics (SMC) 2013, pp 4766–4771. <https://doi.org/10.1109/SMC.2013.811>
5. John NA (2010) Physical asset management. Springer publication, p 45
6. Taylor JH, Sayda AF (2008) Prototype design of a multi-agent system for integrated control and asset management of petroleum production facilities. In: 2008 American control conference, Seattle, WA, pp 4350–4357. <https://doi.org/10.1109/ACC.2008.4587179>
7. Taylor JH (2016) Intelligent control and asset management: an event-based control road map. In: 2016 Second international conference on event-based control, communication, and signal processing (EBCCSP), Krakow, pp 1–4. <https://doi.org/10.1109/EBCCSP.2016.7605269>
8. Sayda AF, Taylor JH (2008) A multi-agent system for integrated control and asset management of petroleum production facilities—part 1: prototype design and development. In: 2008 IEEE international symposium on intelligent control, San Antonio, TX, pp 162–168. <https://doi.org/10.1109/ISIC.2008.4635950>
9. Sayda AF, Taylor JH (2008) A multi-agent system for integrated control and asset management of petroleum production facilities—part 2: prototype design verification. In: 2008 IEEE international symposium on intelligent control, San Antonio, TX, pp 169–175. <https://doi.org/10.1109/ISIC.2008.4635951>
10. Foudeh HA, Mokhtar AS (2015) Automated meter reading and advanced metering infrastructure projects. In: 2015 9th Jordanian international electrical and electronics engineering conference (JIEEEEC), Amman, pp 1–6. <https://doi.org/10.1109/JIEEEEC.2015.7470753>
11. Zheng W, Yin H, Wang A, Fu P, Liu B (2017) Development of an automatic reading method and software for pointer instruments. In: 2017 First international conference on electronics instrumentation & information systems (EIIS), Harbin, pp 1–6. <https://doi.org/10.1109/EIIS.2017.8298626>

A State-of-the-Art Review on Solar-Powered Energy-Efficient PMSM Drive Smart Electric Vehicle for Sustainable Development



Chiranjit Sain, Atanu Banerjee, Pabitra Kumar Biswas,
and Sanjeevikumar Padmanaban

Abstract Energy and electric vehicles are closely related for the sustainable development in the environment. In this proposed study, an extensive review of the different technologies towards solar-powered energy-efficient smart electrical vehicle based on permanent magnet synchronous motor (PMSM) drive have been addressed. To reduce the emissions of greenhouse gasses and to maintain the environmental sustainability, solar-powered electric vehicles create a vital role in a modern energy-efficient environment. The different existing as well as modern technologies based on Internet of Things (IoT) tools for smart electric vehicles to be required in several smart cities is represented. An efficient as well as economic design of a solar-powered electric vehicle to communicate between the industry and the environment is proposed in this article. Eventually, PMSM motors are broadly employed in typical solar-powered electric vehicles due to the rapid advancements in permanent magnet materials and several improved constructional features like high torque to weight ratio, higher power density, lesser noise and vibration. Furthermore the impact of solar energy and the recent developments in the aerodynamic design of an electric vehicle is also addressed. The emerging trends of Information and Communication Technology (ICT) related with environmental concern are well established to meet the different smart technologies. The outcome of the article would be an enormous interest for the researchers as well as technologists to explore such future scope of work in the respective field.

C. Sain (✉) · A. Banerjee
Department of Electrical Engineering, National Institute of Technology Meghalaya,
Bijni Complex, Laitumukhrah, Shillong, Meghalaya 793003, India
e-mail: chiranjitsain@nitm.ac.in

A. Banerjee
e-mail: atanu_banerjee@nitm.ac.in

P. K. Biswas
Department of Electrical & Electronics Engineering, National Institute of Technology Mizoram,
Aizawl 796012, India
e-mail: pabitra.biswas2009@gmail.com

S. Padmanaban
Department of Energy Technology, Aalborg University, Esbjerg, Denmark
e-mail: san@et.aau.dk

© Springer Nature Singapore Pte Ltd. 2020

A. K. Bhoi et al. (eds.), *Advances in Greener Energy Technologies*,
Green Energy and Technology, https://doi.org/10.1007/978-981-15-4246-6_15

Keywords Electric vehicle · Energy efficiency · Environment · Permanent magnet synchronous motor · Solar power · Smart technology

1 Introduction

With the advancement of Industrial Engineering, a holistic interpretation for the innovation and growth of latest technologies has enriched. In the present years, the utilization of Information and Communication Technology (ICT) has reflected the industrial process and the production system in a significant manner [1]. Basically, industrial engineering emerges as a new scientific and industrial planning that uses information technology as well as industrial automation to enhance the overall industrial productivity [2]. Society and mankind have been promisingly aware regarding the destruction it is effecting to the atmosphere, and the role of electric vehicles has been distinguished to act as a vital role in retrieving the balance. Presently, the green energy sources generate lowers than 10% of the energy utilized in the electric grid, since majority of the electrical energy utilized for charging electric vehicles shall be generated from burning fossil fuels, such as coal, gas and oil, at the various generating units [3–5]. The transformation in the global atmosphere is one of the major environmental concerns in present day's scenario. The only initiative to overcome this critical hazardous is to reduce the level of greenhouse gases. In many developing countries, several measures have been adopted to maintain the emission of harmful gasses such as carbon dioxide, carbon monoxide, nitrous oxides to a sustainable limit. The overall economic growth and environmental sustainability of a country depend upon the utilization of electric power [6, 7]. Therefore, to meet with the energy efficient and clean energy environment, utilization of renewable energy sources is one of the promising interests throughout the world. Out of the entire non-conventional sources of energy, solar is one of the economic, environments friendly, easy maintenance and one of the largest energy sources in view of the renewable energy sector. In conventional vehicles, fuel consumption, emission of harmful gases lead to the incremental pollution as well as hazardous for the society and environment. Basically, the energy efficiency of an electric propulsion system depends upon the different losses, harmonic distortion, torque pulsations, noise and vibration, etc. [8–10]. Usage of clean energy sources could be helpful to draw the apprehension of using a vehicle due to environmental concern. Energy consumption of an electric vehicle is solely depended upon aerodynamic details. It is obvious that the more aerodynamic is, vehicle energy consumption will be lower. At high-speed operation of the modern electric vehicles, aerodynamics is much important on the basis of electrical energy consumption and utilization [11, 12]. Depending upon the designing aspect, the mass of the vehicle, aerodynamic drag, rolling resistance, motor/engine efficiency, transmission efficiencies need to be considered while expecting optimum energy efficiency. Hence, the transmission efficiency of a modern electric vehicle can be enhanced by incorporating an energy-efficient electric motor, thus eliminating the use of the gearbox and clutch as the electric motor generates

torque from standstill onwards [13]. In case of an energy-efficient vehicle, the efficiency for the conversion of electrical energy provided on vehicle charging at the wheels varies nearly 45–55%. The optimum efficiency for a merchant solar cell is presently about 16%, may lowered to approximately 13% while surrounded. The maximum power that can be obtained from solar dissipation on the earth's surface is 1000 Wm^{-2} , which is generally smaller caused by the presence of cloud and dust in the environment [14–16].

With the advancement of Internet of Things (IoT) technology, electric vehicles can be promisingly established as an advanced type of mobile intelligent power consumption device. In a typical smart grid technology, electric vehicles can be used as energy storage protocol. Smart grid technology can provide intelligent monitoring and a wide area communicating the network with greater control on all aspects of operations [8, 17]. As a result, charging system, monitoring system, billing system, entire data collection technology of a typical electric vehicle can be transformed into a smart system. Hence, this robust and intelligent control technology using IoT tools can be incorporated in a solar-powered electric vehicle for enhancing the environmental sustainability and future demand in a smart city [18]. PMSM machines are vastly employed in an electric vehicle technology because of its high dynamic response, better torque speed characteristics, noiseless operation, high power density, high efficiency compared to other conventional motors. Basically, the design of power electronic converter and sophisticated control technique plays an important role in energy-efficient electric vehicles. Therefore, different control strategies of PMSM drives have been addressed towards the application of an electric vehicle in a modern energy-efficient environment [19, 20].

Robinson et al. in [4], have been highlighted towards the impact of recharging attitude of an electric vehicle driver and also the effect in the current policy of recharging demand profiles in northeast of England. The authors are also described about the required financial supports and possible smart tolls for greater management of vehicle recharging unit for maximum demand. In [5], authors have discussed about the recent developments of electric vehicles, the integration of renewable energy and electric grid. In this article, the economic, environmental and the impact of the grid for electric vehicles are also discussed. In [6], Daziano and Chiew demonstrated about the invention of electric vehicles as an alternative solution for the sustainable transportation system. In this article, one generalized discrete model for the purchasing of an electric vehicle is proposed and the corresponding data analysis is also introduced. Ewing and Sarigöllü [7] discussed about the protocol for consumer choices in clean fuel vehicles against the conventional vehicles employing the discrete choice methodology. They also established three market segments for achieving the target for such clean fuel vehicles. In [8], Taylor et al. demonstrated about the analytical framework to monitor the influence of plug-in electric vehicles on the functioning of distribution systems. Basically, the impact of plug-in electric vehicles on one utility distribution feeder is summarized. Galus et al. in [9] discussed about some smart management system to reduce the possible congestion issues in energy networks for the integration of plug-in electric vehicles. In [10], Garimella et al. proposed the concept about electromechanical heat generation in a lithium-ion

battery. The amount of heat generated in this process is a robust function of current and temperature, and the entropic function in charge depletion is analyzed. Glerum et al. in [15] proposed a dynamic discrete–continuous model of car proprietorship and its use. In this article, the methodology used to describe the model can specify the annual travelled distance, type of fuel, car state, ownership status, etc. In [16], Parks et al. described some efficient methodologies about cost analysis, modelling approaches, environmental needs, security interests to evaluate the performance of plug-in hybrid electric vehicles on utility system operations. Soares et al. in [17] discussed some stochastic solutions for the future charging of electric vehicles and also addressed a tool based on Monte Carlo method for distribution of grid planning. In [18], Zakariazadeh et al. developed one fruitful method for the operational planning of an integrated distribution system. Moreover, in this solution, scheduling of electric vehicles and non-conventional generators are integrated to suppress the negative effects associated with the renewable generation.

Considering the above discussions, the main contribution of the proposed work is given below:

1. To establish the environmental impact of solar energy in energy-efficient electric vehicles for the sustainable development. Some statistical analysis about the usage of energy and emissions of greenhouse gasses in the environment is considered.
2. To discuss the proposed aerodynamic design for energy-efficient electric vehicles for high-performance applications. In this study, some recent developments in the aerodynamic design of modern electric vehicles are also incorporated for sustainable industrial developments.
3. To describe little mathematical analysis and some real-time implementation for the installation of solar-powered smart electric vehicles for maintaining good energy efficiency. In this study one practical design of the solar-powered electric vehicle using professional tools is proposed.
4. To carry out some proposed design considerations of a PMSM machine for energy-efficient electric vehicles.
5. To identify and discuss some proposed smart technologies based on ICT infrastructure for solar-powered electric vehicles in recent smart cities.
6. To ensure the utilization of Industrial Information Engineering in smart electric vehicles for enhancing new employment and infrastructures.

This article is organized as follows: Sect. 2 represents the impact of solar energy utilized in an electric vehicle, Sect. 3 reports the proposed design considerations of an energy-efficient electric vehicle, Sect. 4 describes the smart technology-based solar-powered electric vehicle, Sect. 5 represents the industrial integration in a smart electric vehicle, Sect. 6 establishes the endorsement and future scope of research, and Sect. 7 represents the conclusion part accordingly.

2 Impact of Solar Energy Utilized in an Electric Vehicle

In addition to the conventional energy sources, solar energy sources take a vital part for the utilization in an electric vehicle. Basically, photovoltaic cells transform solar energy into direct current electricity. In fact, solar dissipation hits the higher atmosphere having a range of 1300 Wm^{-2} while some radiation has been strayed in the surrounding atmosphere, and at the same instant, it meets the Earth’s surface which is lower than 1000 Wm^{-2} . If a solar panel has been located on the roof of the car, the sun will touch the plate at various angles as the sun rotates all over the sky, which decreases to 50%, the mass of energy dropping on the layer [21, 22]. Basically, there are two techniques of using the solar panel either on-board or off-board the vehicle. It is observed that if entire area of the car has been covered with solar cells, a minimum amount of power can be gained. Carbon dioxide discharging and the impact of exhaust gas discharged on health have been a critical issue on the environmental aspect. With the recent technological advancements in the electric vehicle infrastructure, incorporated into the passion for less environmentally detrimental transport system, recent progress for solar-powered electric vehicles shows a promising interest [23, 24]. In the present electric vehicles, selection of an electric motor is one of the major concerns due to production of noise and vibration in the environment. During the design of a solar-powered smart electric vehicle, the typical considerations in the design of power converters, design of the proposed electric motor, design of control unit, design of battery charging unit have been taken care to reduce the acoustic noise, vibration and some critical issues in the environmental concern [25–27].

Basically, solar panels used for the generation of electricity have been installed on the ground or on different constructions. Moreover, the mass of solar energy reflecting on all the infrastructures in the UK is about 1600 TWh in every year, as measured to fossil fuel utilize of approximately 1500 TWh in a year. In Fig. 1, some typical analysis about the amount carbon dioxide emissions of different vehicles

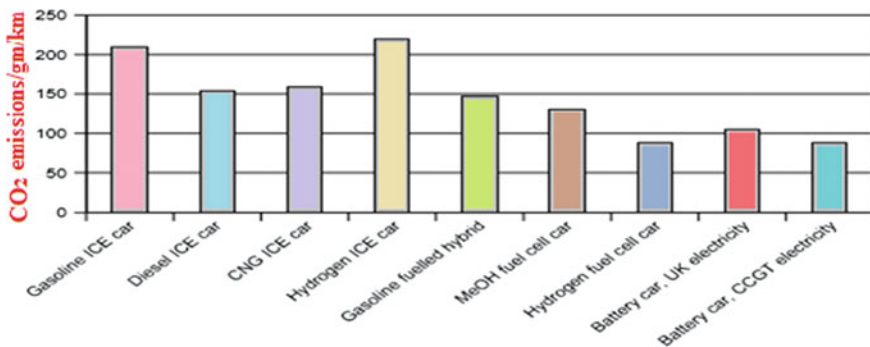


Fig. 1 Statistical analysis for carbon dioxide emissions from various classifications of vehicle. *Source* Electric vehicle technology explained

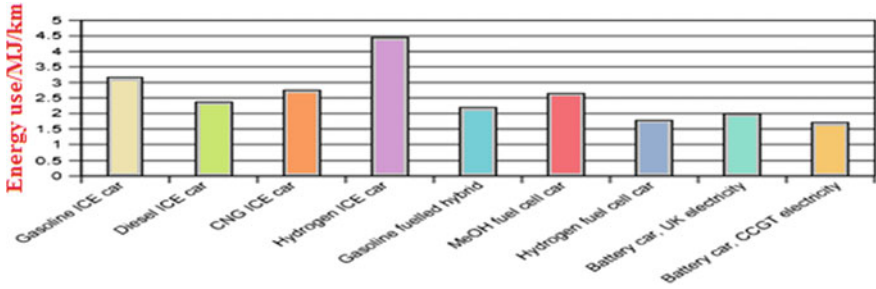


Fig. 2 Amount of energy use obtained from various kinds of vehicle. *Source* Electric vehicle technology explained

Table 1 Some typical case studies

Kind of vehicle	Efficiency	Remarks
Petrol car	28%	
Battery electric car	Efficiency of car = 80%, power station efficiency = 40%	Pollutions has been switched from car to power station
Hybrid car	Electrical energy to mechanical power = 90%, overall efficiency = 40.5%	Percentage of pollution lowered by 55% while consumption of fuel is 70%
Fuel cell electric car	Conversion from hydrocarbon into hydrogen = 80%, electricity to mechanical power = 90%	Pollution lowered by 90%

has been depicted. Furthermore, in this discussion, the amounts of energy used for different types of vehicles have been represented [28–30] (Fig. 2).

Some typical case studies about the study of efficiency and percentage of pollution of different vehicles are represented in Table 1. This study basically represents a comparative performance analysis for energy conversion of different vehicles.

3 Proposed Design Aspects of an Energy-Efficient Electric Vehicle

The typical energy efficiency of an electric vehicle depends truly upon the aerodynamic design, especially at high-speed operation. The magnitude of aerodynamic force on an electric vehicle can be represented as $F_{ad} = 0.5 \rho AC_d v^2$ and the net power consumed at the wheels.

$$P_{adw} = 0.5 \rho AC_d V^3 \tag{1}$$

where ρ is air density factor, A is the frontal area, v is the velocity and C_d is the drag coefficient [31, 32]. Teardrop is the exact aerodynamic structure. The value of drag coefficient changes with the length-to-diameter ratio, and minimum value of C_d can be determined as 0.04, while the length-to-diameter ratio is 2.4. In real time, the value of drag coefficients is relatively larger due to different circumstances such as the ground presence, wheel effects and mechanical design that may change from the reference and non-uniformities such as air inlets and eminence. As an example, Honda Civic hatchbacks possess a frontal area of 1.9 m² with the value of drag coefficient of 0.36. Furthermore, this can be lowered by such prominent interest for the design of aerodynamic structure [33, 34]. Few examples can be taken as Honda Insight hybrid electric car which has a C_d value of 0.25, while the General Motors EV1 vehicle has a lesser C_d of 0.19. The amount of power required in battery P_{adb} to compensate aerodynamic drag is determined by the ratio of entire power transmitted to move the wheels to the system efficiency. Therefore,

$$P_{adb} = \frac{P_{adw}}{\lambda_0} = \frac{0.5\rho AC_d V^3}{\lambda_0} \tag{2}$$

The mass of the battery m_b with specific energy needed to conquer the aerodynamic drag with a velocity v for a distance d can be represented as m_b

$$P_{adb} = \frac{P_{adw} * d}{V * SE * 3600 \text{ kg}} \tag{3}$$

The switching of battery power needed and battery mass for achieving the aerodynamic drag at various speeds have been represented in Fig. 3 and in Fig. 4 having

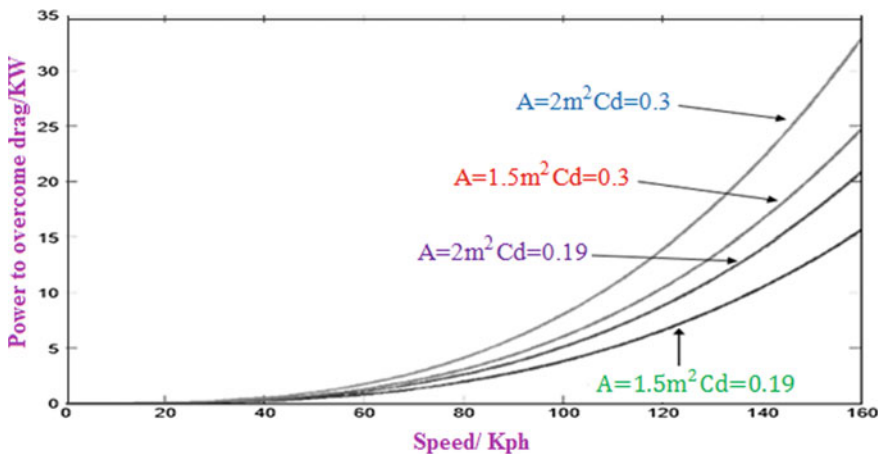


Fig. 3 Representation of power needed to achieve aerodynamic drag of various frontal areas and drag coefficients. *Source* Lightweight electric/hybrid vehicle design

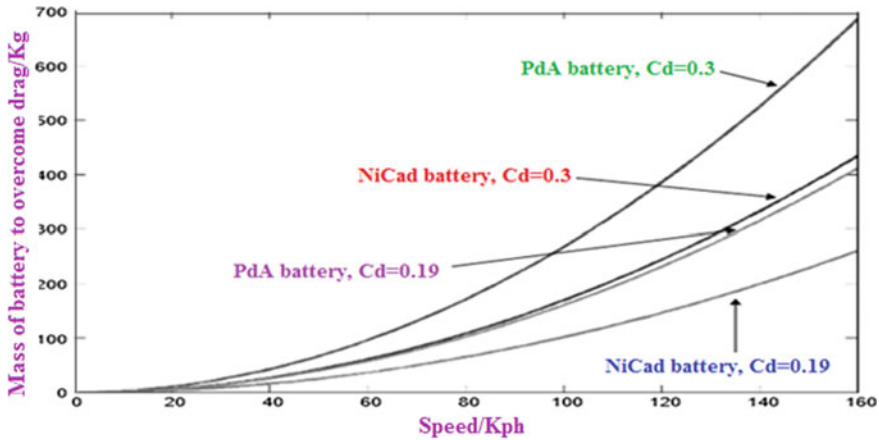


Fig. 4 Representation of drag coefficient and corresponding speed on battery mass. Source Lightweight electric/hybrid vehicle design

various drag coefficients and frontal areas [35, 36]. In Fig. 5, variation of drag coefficient for different electric vehicles in different periods is represented. It is observed in Fig. 5 that the value of drag coefficient is getting reduced from its earlier days due to advancements in the aerodynamic design of modern electric vehicles.

Chassis Design: The chassis represents the robustness of the car when the entire body as well as glazing operated as a cocoon to maintain the passengers and the associated loads secured from the external sources. In present days, the combinations of body and chassis are coupled to form it as monocoque by which whole part, including the glazing connects to the robustness and firmness, which in turn much lighter vehicles are obtained [37]. The chassis/body should have the following characteristics: stronger, lighter, rigid, lesser harmonics as well as reduction of noise and vibration,

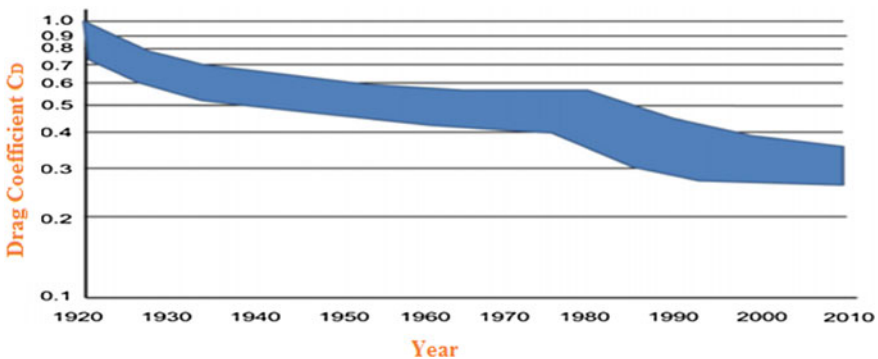


Fig. 5 Statistical approach towards the reduction in drags coefficient. Source Design of hybrid Electric vehicles (NPTEL online material)

more aerodynamic, minimizations of force in passengers/drivers, cheaper, protected from corrosion, etc. During the chassis design, optimization of clashing arrangements such as price and robustness, and energy efficiency. Some electric vehicles have been adjusted from an IC engine operated vehicle and utilize an existing vehicle chassis/body [38–40]. It carries few benefits as much as the entire vehicle is accessible and in a common way has to be adjusted, that is definitely an economic opinion than constructing a complete new vehicle. However, these vehicles frequently offer a flexible distance and performance; the superior performances are determined while the body chassis is made for specific purpose. Most modern electric vehicles utilize aluminium material as the supreme structure regardless the lesser strength/mass of aluminium compared to carbon fibre blends. The panels of such vehicles can also be constructed from composites [41, 42].

3.1 Recent Developments in the Aerodynamic Design of Electric Vehicles

To meet with the advancement in the technological aspect and for environmental concern, several mechanisms have been taken into consideration for the aerodynamic design of recent electric vehicles. Government as well as automobile industries jointly framed such regulations for manufacturing of more developed aerodynamic vehicles. An active aerodynamic method as well as passive method has been incorporated in the historical growth of electric vehicles. In the year of 2013, Mercedes-Benz manufactured the lowest drag coefficient vehicles in the market [43–45]. The value of the drag coefficient in this proposed model was 0.23. The image of the proposed car has been represented in Fig. 6. In this proposed vehicle, active as well as passive method of design was adopted. The prime characteristics of this proposed model are the active grille shutter system. This proposed system utilizes flaps placed inside the front grille which turned into a closed entity while activate. This methodology makes engine and brakes need not to be cooled. In the year of 2016, the American electric car company Tesla INC pioneered a facelift on their flagship model which has been depicted in Fig. 7. The drag coefficient of this particular value taken as



Fig. 6 Mercedes CLA released in 2013. *Source* Google Image Library



Fig. 7 2016 Tesla Model S manufactured in 2016. *Source* Tesla INC, 2017

0.24 and closed front design has been proposed [46–48]. As a result, this proposed design does not require much cooling like conventional vehicles. In this design, air curtains have been placed in the front bumper to monitor the airflow passes across the front tires and a flat structure in the lower body pane [49]. As compared to the previous two models in the year of 2017, BMW has been manufactured an advanced electric vehicle with a drag coefficient of 0.22, and it is so called 5 Series Sedan. This proposed model uses both active as well as passive aerodynamic features. In this design, some modifications in the active front grille shutter have been considered [50–52]. As a result, huge areas of lower part panel are covered in the rear axle area, and front-end air curtains are proposed. The proposed model of the electric vehicle is depicted in Fig. 8.

The entire aerodynamic features, i.e. active as well as passive components, located over a whole body of the vehicle have been represented in Fig. 9.

It is well described from both the figures that several advantages can be obtained if the value of aerodynamic resistance as well as frontal area of the vehicle can be maintained as low as possible. In addition to this on economic aspect battery weight and cost of battery can also be played a major concern while considering the aerodynamic details [53, 54].

Some technical specifications for electric bicycle and low-speed electric vehicles are represented in Tables 2 and 3, respectively. Designers or manufacturers



Fig. 8 2017 BMW 5 Series Sedan. *Source* BMW AG, 2017

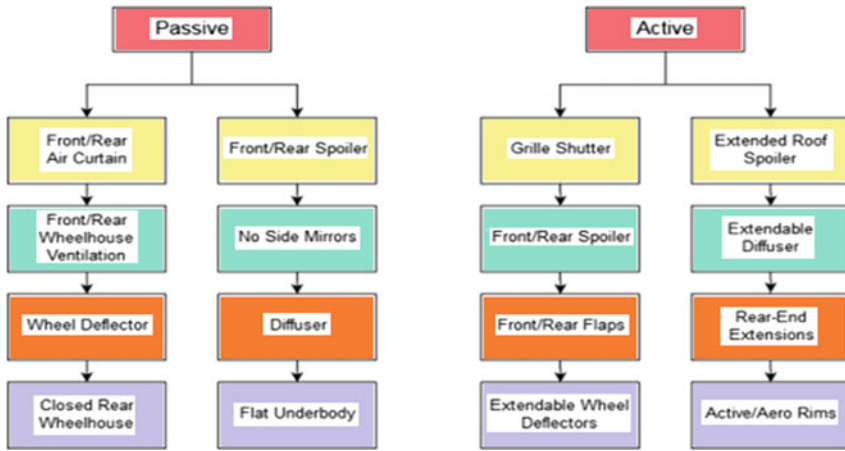


Fig. 9 Presentation of aerodynamic features located all over a vehicle body

Table 2 Some technical details of electric bicycle

Dimensions of wheels	23 or 25 inch
Size of frame	18 inch
Motor rating	150 W hub motor
Kind of speed variation	Handlebar-mounted twist throttle
Range, pedal-assist mode	Desired 45 km, nearly
Rating of battery	36 V, 15 Ah valve regulated lead acid battery
Peddalling gears	5, 22 or 24 speed
Battery charging time and capacity	8 h, 36 V
Overall weight	41 kg
Recent price	Approximately £686 depends on technical rating

Source Lightweight electric/hybrid vehicle design

Table 3 Technical specifications for a low-speed electric vehicle

Length	3060 mm
Weight	1350 mm
Height	1650 mm
Wheelbase	2525 mm
Payload	355 kg
Ground clearance	155 mm at curb weight
Minimum radius while turning	4060 mm
Distance	64 km
Acceleration	0–35 kph, 5 s
Hill climbing capacity	22%

Source Lightweight electric/hybrid vehicle design

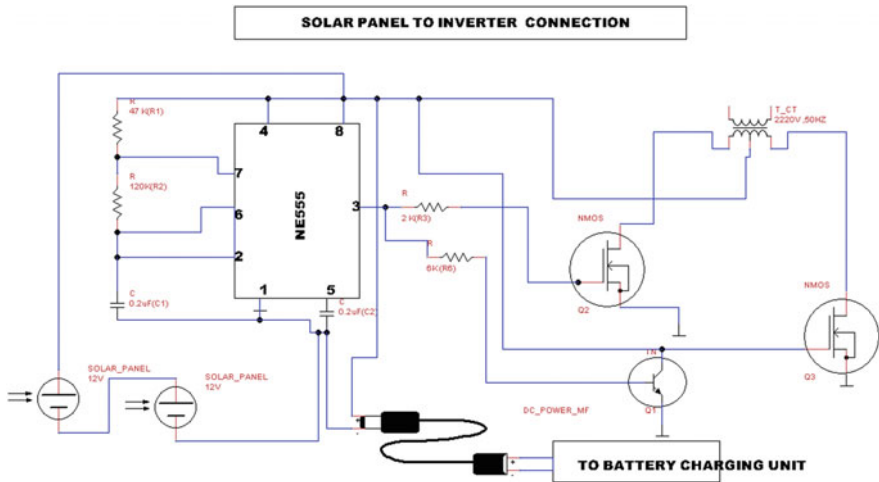


Fig. 10 Proposed design layout for the installation of solar PV panel for electric vehicle (Part-1)

can select some proposed specifications in specific applications in energy-efficient environment.

In Fig. 10, proposed layout design for solar panel to inverter connection has been depicted. On keeping in view making project economic, we use NE555 timer IC in astable mode for pulse generation. Here, input signal (voltage) comes from the solar panel, i.e. 24 V (12 V + 12 V in series) and goes to pin-8 (Vcc); resistor R1 is connected between Vcc (pin-8) and discharge pin-7. Another resistor R2 is attached between the discharge pin-7 and trigger pin-2, and pin-6 shares a common mode of operation. Here the capacitor is charged through resistance R1 and R2 and discharge only through R2. Since pin-7 has low impedance to ground during output flow inverter of cycle and therefore for discharging goes on [55–57]. Now, output PWM comes from pin 3 which is fed to gate of MOSFET (Q2) and drives to transformer; this time gate, voltage is max, similarly at this time. There is no gate voltage in MOSFET (Q3), and it is off-state. Now, when there is no gate voltage in MOSFET (Q1), reverse voltage flows through the transistor Q1 and on the MOSFET (Q3). In these ways, it is operating and drives the transformer to give the desire output of 220 V AC-50 Hz [58].

Here, we use N-CHANNEL MOSFET because for high switching speed. The driving requirement for MOSFET is much better, much simpler as compared to BJT.

In case of light electric vehicles, the proposed layout design for the installation of the solar panel with inverter circuitry has been represented in Fig. 11. Here, the proposed mini power inverter has been designed with SCR as we are considering lightweight vehicle. The design concept of the proposed circuit is easier and inexpensive [59, 60]. To design the proposed circuit with SCR as the major part, behave as oscillator generator with a frequency of 400 Hz. The output obtained from this

no tool options

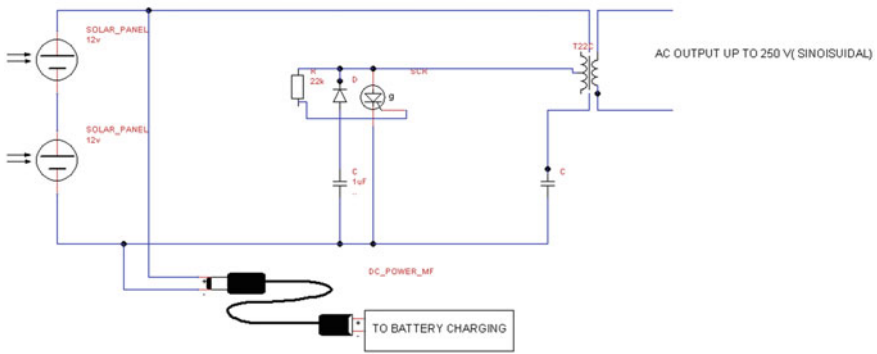


Fig. 11 Proposed design layout for the installation of solar PV panel for electric vehicle (Part-2)

proposed power inverter is about 300 V having a voltage input 12 V and current rating of 0.8 A.

The limitation observed in this proposed circuit is that it might latch in the conducting state whether the load is much heavier or if the output is shorted; this needs some sort of protection on the input line like a fuse or similar [61, 62]. The transformer considered is a 10 W mains type with centre tap 6 V + 6 V rating of windings on the thyristor side and a 110 V + 110 V rating of windings connected in series at the output. Efficiency is near about 50%, and the actual load is equivalent to a 22 k resistor, 5 W. The output response is nearly sinusoidal at a frequency of 400 Hz.

A simple yet accurate automatic regulated 24 V lead acid battery charger circuit is discussed in this proposed discussion. Suitable design layout is shown in Fig. 12. The current in this proposed circuit goes switched off as soon as battery gains full charge [63]. Here, we use IC LM338; it is actually a series of adjustable three terminals positive voltage regulator which is proficient of providing in excess of 5 A over 1.2 V to 32 V output span. In real analysis, they are easily and exceptional to use and require only two resistors to set output voltage. An input DC supply of range 24 V is applied to the input of IC, which is coming from the solar panel. The voltage can be obtained from transformer bridge and capacitor network. If we need to charge 6-V battery, R2 is chosen to generate voltage around 7 V, but we are considering of 24 V battery unit so we selected R2 around 28 V. However, tripping voltage or at voltage where the circuit is cut off, we select 10 k ohm POT or preset. The output supply from IC LM338 is connected to the positive terminal of the battery for charging purpose. This voltage also behaves as the sensing as well as the operating voltage for IC741 [64, 65].

The input capacitor is used; i.e., C1 is used to filter the unwanted noise, especially if regulator located far from power supply. The output capacitor is used to improve

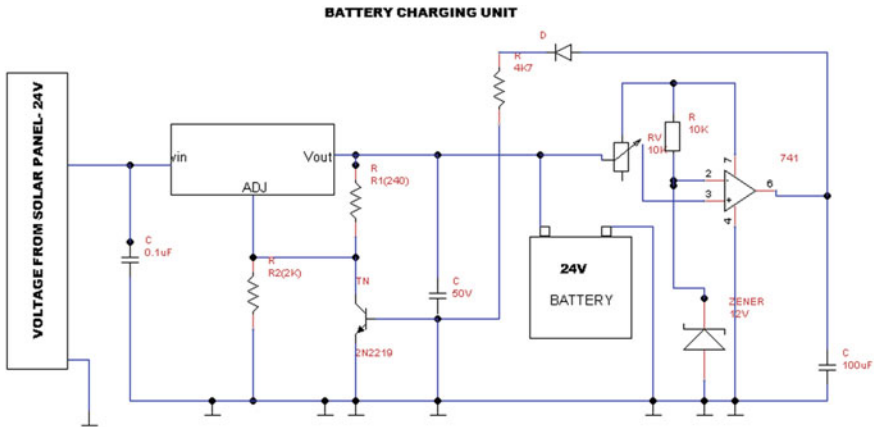


Fig. 12 Proposed design layout for the installation of battery charging unit for solar-powered electric vehicle

the transient response. Diode D is used for providing lower impedance discharge path to block capacitor from discharging into the output regulator [66].

4 Smart Technology-Based Solar-Powered Electric Vehicle

With the rapid progress of Internet of Things (IoT) technology and the renewable energy integration, electric vehicles play a significant role for the sustainable development in the environment [67]. The technology so-called self-monitoring analysis and reporting technology (SMART) has been an innovative interest in the industries as well in research institutions for such strong foundation and robust control. To meet the latest vision, a huge change in the power supply infrastructure and traffic systems need to be incorporated. In fact, drivers are supposed to get the reliability that they will be able to conveniently recharge their vehicle wherever they are [68, 69]. The required closely meshed network of charging stations will only be obtained at sustainable cost with very smart and cost-effective electric charging systems that can be installed anywhere [70, 71]. Electricity is available everywhere, so that electric mobility can configure on a sound infrastructural basis. The charging stations are only energized after a registered user has activated the charging function. Thus, there is no danger of live cables being exposed even when a smart charging station is destroyed or knocked over in an accident. The proposed charging station can also be installed to display additional information such as road map, tourist guidance in nearby places, etc. [72, 73]. A typical layout representation for a solar-powered smart electric vehicle is depicted in Fig. 14 (Fig. 13).

Recently, SIEMENS Technology Solution has been proposed and designed smart technology-based charging solution for a modern electric vehicle which is shown in

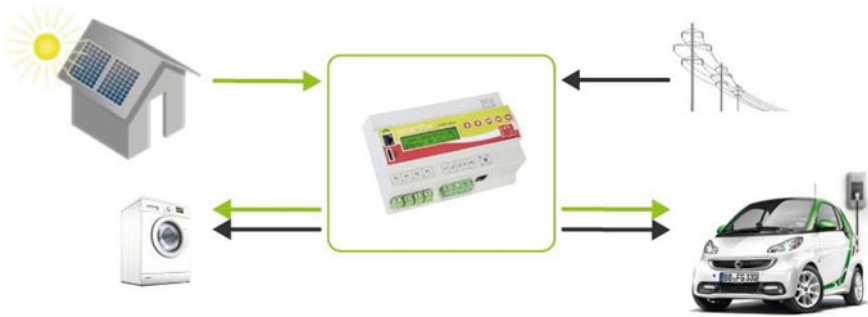


Fig. 13 Layout representation of a solar-powered smart electric vehicle. *Source* The Mobility House



Fig. 14 Smart technology-based charging solution for a modern electric vehicle. *Source* SIEMENS Technology Solution

Fig. 15. The real-time image of a solar-powered smart electric vehicle developed by the Mobility House has been represented in Fig. 16. Here, solar panels have been utilized for the charging purpose in the proposed electric vehicles, and some novel IoT tools are incorporated for such sophisticated control and environment-friendly [74, 75]. In a typical smart city application, integration of an electric grid and the vehicles can be an efficient approach for security, economy and energy storage environment.

In Fig. 16, a typical IoT-based architecture for a smart electric vehicle has been represented. Generally, the entire architecture comprises of several elements like different sensors (motion sensor, optical sensor, smart sensor), network having wireless connectivity for communication, cloud computing, data storage devices and some



Fig. 15 Image of a solar-powered smart electric vehicle. *Source* The Mobility House

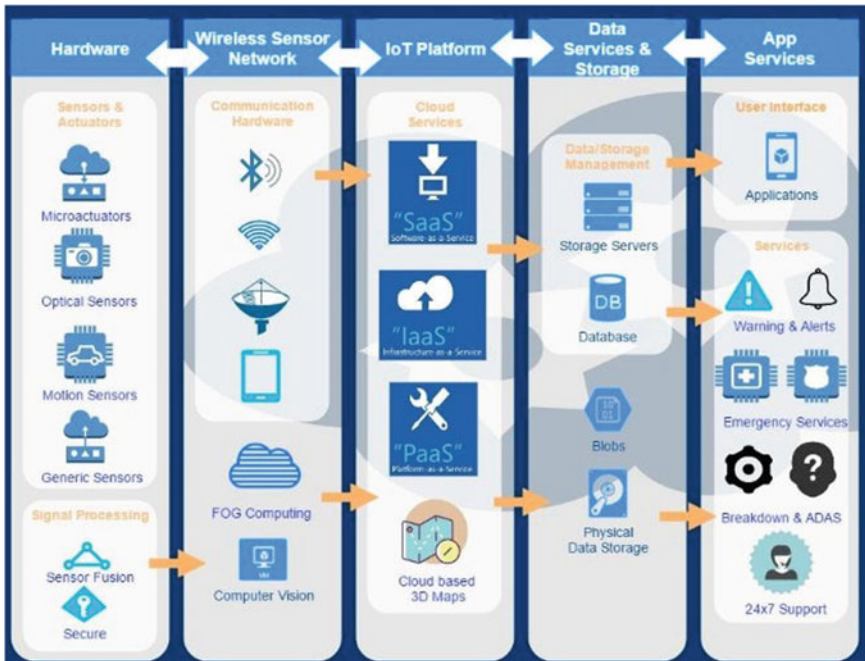


Fig. 16 IoT-based architecture for a smart electric vehicle. *Source* Internet of Things for Smart Cities

security as well as safety devices [76, 77]. Moreover, the Internet of Things technology has been integrated in electric vehicles in different smart cities to monitor and implement such mechanisms like IoT-enabled charging station, modern communication system integrated with charging station to communicate with central control unit, smart transformer as well as smart energy metre for metering, billing, etc. Such topologies based on IoT tools in modern electric vehicles are described in the following manner [78].

Air quality: A world-wide vision has already been undertaken by the different government as well as private organizations to maintain the climate change for the next decade. The target is taken under such circumstances that at least 20% cut down in the greenhouse gas discharges by 2020 compared with 1990 [79, 80]. A reduction in 20% energy absorption through enhanced energy efficiency by 2020 utilizations of renewable energy will be enhanced by 20% [81]. Therefore with the advancement of IOT technology better monitoring system for checking the quality of air in the atmosphere.

Monitoring of Noise: Noise has been generated through acoustic pollution as much as carbon oxide (CO) in the air. Different countries have been taken some measures to reduce the level of noise due to environmental concern. In a smart city, IoT can provide a noise measuring device to calculate the quantity of noise generated at any specified time in the respective regions to meet such facilities [82, 83]. With the promising concept of IoT tools, the production of acoustic noise and vibration in a typical electric vehicle can be well monitored, recorded and depending upon the level of noise it can minimized for protecting the environment [84].

Traffic congestion management: IoT technology enables the monitoring of traffic congestion in the developed countries. Traffic monitoring may be adopted by mounting the modern sensory systems in the electric vehicle and GPS-based modern communication protocol based on IoT technology [85, 86]. By incorporating this proposed technology, huge congestion in traffic may be reduced during peak hours in a day.

Smart parking system: The topology of smart parking is basically based upon the installation of different sensors in the roadside and a typical intelligent monitoring system [87]. By establishing lower-range communication methodologies, such as radio frequency identifiers or near-field communication, it can be realized an electronic monitoring system for a car parking. Furthermore, the concept of IoT tools in a typical electric vehicle enables the reduction of greenhouse gasses generated by conventional vehicle architecture [89, 90].

5 Proposed Design Considerations of PMSM for Solar-Powered Electric Vehicle

With the advancement of permanent magnet materials such as samarium cobalt, alnico, rare earth magnets, economic construction, better dynamic response,

improved speed range, high torque to weight ratio, PMSM motors are vastly employed in modern electric vehicles [91, 92].

Here, we are optimizing the 45/70 kW drive motor for the medium size electric vehicle of the future. This incorporates improvements in basic working mechanisms while more attentions need to incorporate in material construction and construction technology. The technology of hybrid vehicles provides greater flexibility on the motor performance [93, 94]. An electric vehicle establishes a discrete torque-speed characteristic with fixed power operation from reference speed to maximum speed. The current carrying capability by the stator and rotor winding will be lesser for overall shape of structure in operation [95]. The most significant advancement presently for PMSM machines is the invention of the Daido magnet tube in magnequench material. This magnetic material serves the advantage of the high-energy magnet and containment tube. The surface-mounted motors generally provide a containment sleeve to maintain the several millimetres of the air gap to the magnetic circuit. The typical important specifications for the design of the magnetic circuit are weight and minimum core losses while lowering the slot leakage to reduce the winding inductance. The proposed design is assumed for the selection of high power drives [96, 97]. The rotor structure comprises of a steel sleeve where the magnets are mounted, and a containment band has been combined on the outside. Majority of industrial motors utilize samarium cobalt which has excellent mechanical properties. In general, alloys of magnesium oxide are in common use and the tendency to design rotors located on standard size blocks, $1 \times 0.5 \times 5.5$ inches thick. Vector control or field-oriented control makes PMSM machine more sophisticated and flexibility for high-performance applications [98]. A typical constructional requirement for the proposed PMSM machine has been represented in Fig. 17. In this diagram, the different parts of PMSM, i.e. stator, rotor, position of magnets along with different paths for flux distribution, has been demonstrated. Some practical economic design considerations for the high-speed heavy electric vehicles driven by PMSM are depicted

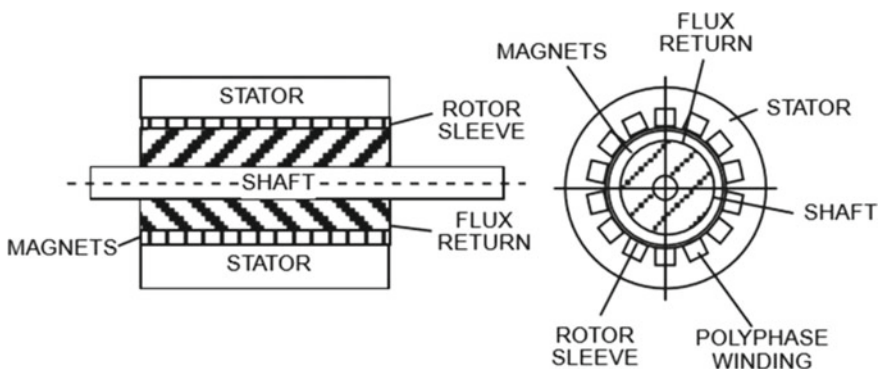


Fig. 17 Typical constructional features of PMSM machine. *Source* Permanent magnet motor technology (Jacek F. Gieras, M. Wing)

Power (3.5:1 CPSR) (kW)	45	70	70	70	150
Speed max	12 000	10 000	13 500	20 000	20 000
Stator OD (mm)	218	200	220	200	225
Rotor OD (mm)	141	113	141	113	145
Active length (mm)	80.5	190	97	110	160
Overall length (mm)	141	260	157	170	230
Stator voltage (V)	150	360	460	360	460
Max Efficiency	96%	96%	98%	96.5%	98.6%
Winding L (mH)	0.1	1.78	1.37	0.85	0.28
Winding R (mW)	9.6	66	116	38	13.4
Poles	16	8	8	8	8
Stator/rotor mass (kg)	19	40	21	24	44

Fig. 18 Recent economic design of PMSM (35 KW is continuous rating, 70 KW is short time rating). *Source* Electric motor drives, R. Krishnan

in Fig. 18. This proposed technical specification for the designing of PMSM for electrical vehicles can be used by the designer or manufacturer in automobile industries [99]. In [60], a comprehensive discussion is established between an induction motor, PMSM motor and a switched reluctance motor for electric vehicle applications. A fast finite element analysis has adopted for such analytical design of IM. Finally, various kinds of analysis such as noise and vibration, harness have been done, and a suitable comparative performance analysis is achieved. Few authors in [63] proposed a solid rotor topology for high-speed interior PMSM constructed with a semimagnetic stainless still. The proposed methodology has been validated using dynamic structural, static structural finite element method to meet the feasibility of the present design method. Authors in [65] described a computational method for the design of an interior PMSM applicable for the traction systems. Additionally, the introduction of FEM-based technique saves the CPU time drastically without interrupting such accuracies. In [67], authors have addressed on multi-objective optimal design procedure of IPMSM for high-performance applications. In this section, Taguchi method has been introduced while incorporating five multi-objective functions for a V-shaped PMSM rotor.

Recently, with the advancement of technology, energy-efficient motors are extensively used in electric vehicles technology as they operate at highest efficiency at some specified operating regions. In case of energy-efficient motor, some characteristics like power factor, efficiency, effect of noise and vibration, temperature rise, dynamic behaviour are the main considerations while designing the machine [100, 101]. Production of noise and vibration in electric vehicles possess several inconveniences for high-performance applications. Therefore, reduction of acoustic noise and vibration in PMSM has a major concern in recent electric vehicles [102]. During the designing of electric vehicles, some important factors such as lamination structure, materials

used for lamination, elimination of cogging torque, winding configuration, magnetic permeability, length of the air gap are taken into consideration for such better performance of modern electric vehicles in an energy-efficient environment [103].

6 Industrial Linkage in Smart Electric Vehicles

With the introduction of Information and Communication Technology, the systematic progress of industrial engineering facilitates a huge infrastructural development for industrial sectors. Specifically, industrial engineering interacts with the every recent advancement in the environment for solving such complex problems [40]. A wide variety of methods have been adopted by the use of information technology and industrial electronics to enhance the environmental safety in recent days. The use of renewable energy such as solar, wind, etc., and the smart grid integration improves the industrial sustainability in a wide area network. The use of smart electric vehicles tremendously decreases the urban emissions which improve the charging patterns. Basically, electric vehicles play as a decentralized energy resource establishing a storage capacity in the electricity demand [40, 104]. Smart charging infrastructure improves flexibility in the energy scenario which in turn increases stability and maximum capacity investment. In fact, the urban establishment and the mobility follow innovative business policies to improve the energy efficiency for industrial integration. The rapid progress of renewable energy sources signifies large quantity of non-dispatchable sources of generation into the energy management system [105]. Smart charging system is used to control the power of charge to synchronize with the system capacity, use of optimized renewable energy and the customer demands. Digitization helps customer communication such as their involvement in the programme and the charging infrastructure. In few countries, the communication between the electric vehicles and grid supports frequency regulation facility to the grid electricity and generates funding [106, 107]. However, in most of the countries, the particular facility is yet to be tested for commercialization. The charging infrastructures of smart electric vehicles integrate the decentralized generation and storage capacity for optimum load profile. Furthermore, the impact of Internet of Things (IoT) and the industrial integration enhances the energy efficiency of smart electric vehicles and maximizes the grid infrastructure. In [88], authors have been addressed towards the structure and capacity of a grid-interactive energy system comprises of a PV source, plug-in electric vehicles and some local loads. In this article, vehicle to grid infrastructure for future demand response operation and the necessary measurements are available. Authors in [89] have been investigated the concept of real-time structure for controlling electrical demand and to support the energy demand [108, 109]. In fact, the integration of electric vehicles and decentralized energy storage system is also described. In [90], few authors demonstrated about the cost analysis of public transportation system for wireless charging system. Basically, the outcome of the article is to analyse and identify the recent market cost for such wireless charging solution. Authors in [91] discussed about the charging infrastructure of electric vehicles and

the concept of renewable energy sources for the development of smart microgrid structure. The typical energy management system in a smart city for enhancing the flexibility of charging infrastructure is also established. In the recent days, with the advancement of ICT tools, different kinds of wireless charging system for electric vehicles have been adopted. Various charging methods such as near-field wireless technology, magnetic resonance-based wireless charging and the permanent magnet coupling-based wireless charging have been recently attracted in various smart cities for industrial information integration [110, 111]. For the sake of sustainability and environmental safety, the role of wireless charging system plays a major role in the recent electric vehicles. Wireless power transfer (WPT) reduces the utilization of battery which in turn reduces the overall weight and the installation cost. Interfacing of a grid for wireless charging infrastructure in hybrid electric vehicles is also a crucial protocol for future energy demand and sustainable industrial development [112].

7 Discussions and Endorsement (Future Scope of Research)

At the end of the study, few points can be discussed and recommended for exploring future scope of research in this field.

1. The introduction of industrial integration amplifies the awareness towards sustainable industrial developments.
2. Utilization of renewable energy such as solar energy in recent electric vehicles optimizes the environmental concern. However, the feasibility and overall efficiency for solar-powered electric vehicles for large-scale applications is under investigation.
3. Aerodynamic structure of recent electric vehicles plays a major role for improving energy efficiency. For future sustainable industrial development, automation industries should take more attention about the vehicle infrastructure.
4. The availability of permanent magnet materials such as rare earth magnets, alnico and its construction take a vital concern for such economic design of PMSM motor. Additionally, several merits such as large power density, greater torque to volume ratio PMSM can be successfully utilized in recent electric vehicles in most of the countries.
5. There is a suitable relationship between the Internet of Things (IoT) and the impact of Industrial Engineering. Hence, IoT-based smart electric vehicles can integrate the charging system, communication system and security system in a more efficient way for enhancing the industrial development. However, more research is going on in this field to validate the topology.

8 Conclusion

This paper significantly describes the comprehensive review of different technologies for the development of solar-powered smart electric vehicles. To protect the environment from the emission of greenhouse gasses and for the sustainable development, solar-powered electric vehicles are the promising technology used in different developed countries. The proposed mathematical analysis and economic design considerations for the installation of a solar-powered energy-efficient electric vehicle can be considered in recent automobile industries as well as in various research organizations to meet the future goal. Furthermore, this comprehensive report demonstrates such fruitful methodologies and associated advancements to meet with smart technologies. Applications of ICT-based IoT tools in solar-powered electric vehicles would be an innovative and sophisticated technology in recent days in different smart cities for sustainable industrial developments. A manufacturer or designer can choose a suitable aerodynamic design of recent electric vehicles with robust construction of a permanent magnet synchronous motor with the help of various control strategies would be an emerging trend for the need of industrial engineering. Moreover, the summary of all recent and emerging technologies related to electric vehicles infrastructure would be a promising need for the overall growth of society and the environment.

References

1. Denis N, Dubois MR, Desrochers A (2015) Fuzzy-based blended control for the energy management of a parallel plug-in hybrid electric vehicle. *IET Intell Transp Syst* 9(1):30–37
2. Padhi S, Pati UC, Mahapatra K (2018) Overview of high-step-up DC–DC converters for renewable energy sources. *IETE Tech Rev* 35(1):99–115
3. Mondal M, Kumbhar GB (2018) Detection, measurement, and classification of partial discharge in a power transformer: methods, trends, and future Research. *IETE Techn Rev* 35(5):483–493
4. Robinson AP, Blythe PT, Bell MC, Hübner Y, Hill GA (2013) Analysis of electric vehicle driver recharging demand profiles and subsequent impacts on the carbon content of electric vehicle trips. *Energy Policy* 61:337–348
5. Richardson DB (2013) Electric vehicles and the electric grid: a review of modeling approaches, impacts, and renewable energy integration. *Renew Sustain Energy Rev* 19:247–254
6. Daziano RA, Chiew E (2012) Electric vehicles rising from the dead: data needs for forecasting consumer response toward sustainable energy sources in personal transportation. *Energy Policy* 51:876–894
7. Ewing G, Sarigöllü E (2000) Assessing consumer preferences for clean-fuel vehicles: a discrete choice experiment. *J Public Policy Mark* 19:106–118
8. Taylor J, Maitra A, Alexander M, Brooks D, Duvall M (2000) Evaluation of the impact of plug-in electric vehicle loading on distribution system operations. In: *Power & Energy Society General Meeting, 2009 (PES'09)*. IEEE, pp 1–6
9. Galus MD, Andersson G (2009) Integration of plug-in hybrid electric vehicles into energy networks. In: *PowerTech 2009*. IEEE, Bucharest, pp 1–8
10. Bandhauer TM, Garimella S, Fuller TF (2014) Temperature-dependent electrochemical heat generation in a commercial lithium-ion battery. *J Power Sources* 247:618–628

11. On-site electric vehicle fire investigation. US Department of Transportation—National Highway Traffic Safety Administration (2013)
12. IEC 62133-2 (2017) Secondary cells and batteries containing alkaline or other non-acid electrolytes—safety requirements for portable sealed secondary cells, and for batteries made from them, for use in portable applications—Part 2: Lithium systems
13. German Association of the Automotive Industry (VDA) (2013) Accident assistance and recovery of vehicles with high-voltage systems
14. Kapoor K, Pandey KK, Jain AK, Ashish N (2014) Evolution of solar energy in India: a review. *Renew Sustain Energy Rev* 40:475–487
15. Glerum A, Frejinger E, Karlström A, Beser Hugosson M, Bierlaire M (2013) Modeling car ownership and usage: a dynamic discrete-continuous choice modeling approach. Presented at the international choice modelling conference, Sydney, Australia
16. Parks K, Denholm P, Markel T (2007) Costs and emissions associated with plug-in hybrid electric vehicle charging in the Xcel Energy Colorado Service Territory. NREL Report No. TP-640-41410
17. Soares FJ, Pecos Lopes JA, Rocha Almeida PM, Moreira CL, Seca L (2011) A stochastic model to simulate electric vehicles motion and quantify the energy required from the grid. Presented at the power systems computation conference (PSCC), Stockholm, Sweden
18. Zakariazadeh A, Jadid S, Siano P (2015) Integrated operation of electric vehicles and renewable generation in a smart distribution system. *Energy Convers Manag* 89:99–110
19. Energy Community (2015) Policy guidelines by the energy community secretariat on reform of the support schemes for promotion of energy from renewable energy sources, PG 05/2015/21
20. IEA (2014) Renewables grid integration and variability session 1: introduction, variable generation, flexibility and netload. IEA Training and Capacity Building-Latin America, Santiago de Chile
21. Hung YH, Wu CH (2013) A combined optimal sizing and energy management approach for hybrid in-wheel motors of EVs. *Appl Energy* 108:236–243
22. Hung YH, Wu CH (2012) An integrated optimization approach for a hybrid energy system in electric vehicles. *Appl Energy* 98: 479–490
23. Ye YH, Shi YX, Cai N (2012) Electro-thermal modeling and experimental validation for lithium ion battery. *J Power Sources* 199:227–238
24. Lin YX (2015) Electromechanical system design and control of hybrid cooling module. Master Thesis, Department of Industrial Education, National Taiwan Normal University, Taipei, Taiwan
25. Zhang Y, Ouyang M, Lu Q (2004) A model predicting performance of proton exchange membrane fuel cell stack thermal systems. *Appl Thermal Eng* 24:501–513
26. Barnard R (2009) Road vehicle aerodynamic design, 3rd edn. MechAero Publishing, St. Albans, p 54. ISBN 978-09540734-7-3
27. Hucho WH (1998) Aerodynamics of road vehicles, 4th edn. SAE International, Warrendale, PA. ISBN 978-0-7680-0029-0
28. Buchheim R, Leie B (1982) The development of the Audi 100—a new approach in aerodynamic passenger car design. In: Vehicle aerodynamics symposium organised by VW, Dec 2–3
29. Kumar A, Singh A, Regin AF (2015) Study on Effect of ground clearance on performance of aerodynamic drag reduction devices for passenger vehicle using CFD simulations. SAE Technical Paper
30. Lennart L, Jesper M, Hakan D, Gunnar O (2013) Performance of an automotive under-body diffuser applied to a sedan and a wagon vehicle. Technical Paper
31. Esser M (2016) Standardization and vehicle regulation aspect of camera monitor system. Technical Paper, Springer International Switzerland
32. Kounenis C, Bonitz S, Ljungskog E, Sims-Williams D (2016) Investigations of the rear-end flow structures on a sedan car. SAE Technical Paper 2016-01-1606
33. Bonetto R, Bui N, Lakkundi V, Olivereau A, Serbanati A, Rossi M (2012) Secure communication for smart IoT Objects: protocol stacks, use cases and practical examples. In: Proceedings of IEEE IoTSoS, San Francisco, CA, USA, pp 1–7

34. Dohler M, Vilajosana I, Vilajosana X, Llosa J (2011) Smart cities: an action plan. In: Proceedings of Barcelona smart cities congress, Barcelona, Spain, pp 1–6
35. Nuortio T, Kytöjoki J, Niska H, Bräysy O (2006) Improved route planning and scheduling of waste collection and transport. *Expert Syst Appl* 30(2):223–232
36. Corley MJ, Lorenz RD (1998) Rotor position and velocity estimation for a salient-pole permanent magnet synchronous machine at standstill and high speeds. *IEEE Trans Ind Appl* 34:784–789
37. Zhou Z-y, Xu Z, Li T-c (2004) FPGA implementation of a new hybrid rotor position estimation scheme based on three symmetrical locked Hall effect position sensors. In: The 4th international power electronics and motion control conference, 2004. IPEMC 2004, vol 3, pp 1592–1596
38. Zheng B, Wu L, Lin A, Li L, Yuan C, Dang J (2011) Study of a new detection technology for sensorless PMSM drive with flux linkage observer. In: 2011 international conference on consumer electronics, communications and networks (CECNet), pp 1691–1694
39. Thiemann P, Mantala C, Hordler J (2011) PMSM sensorless rotor position detection for all speeds by direct flux control. In: 2011 IEEE international symposium on industrial electronics (ISIE), pp 673–678
40. Zeraoulia M, El Hachemi Benbouzid M, Diallo D (2006) Electric motor drive selection issues for HEV propulsion systems: a comparative study. *IEEE Trans Veh Technol* 55(6):1756–1764
41. Yamazaki K, Fukushima Y, Sato M (2008) Loss analysis of permanent magnet motors with concentrated windings—variation of magnet eddy current loss due to stator and rotor shapes. *IEEE Trans Ind Appl* 45(4):1334–1342
42. de Santiago J, Bernhoff H, Ekergård B, Eriksson S, Ferhatovic S, Waters R, Leijon M (2012) Electrical motor drivelines in commercial all-electric vehicles: a review. *IEEE Trans Veh Technol* 61(2):475–484
43. Un-Noor F, Padmanaban S, Mihet-Popa L, Mollah MN, Hossain E (2017) A comprehensive study of key electric vehicle (EV) components, technologies, challenges, impacts, and future direction of development. *Energies* 10:1217
44. Li S, Li Y, Choi W, Sarlioglu B (2016) High-speed electric machines: challenges and design considerations. *IEEE Trans Transp Electrific* 2(1):2–13
45. Wang Z, Lu K, Blaabjerg F (2012) A simple start-up strategy based on current regulation for back-EMF-based sensor less control of PMSM. *IEEE Trans Power Electron* 27:3817–3825
46. Febin Daya JL, Sanjeevikumar P, Blaabjerg F, Wheeler PW, Ojo JO (2015) Implementation of wavelet-based robust differential control for electric vehicle application. *IEEE Trans Power Electron* 30(12):6510–6513
47. Chen HC, Huang H (2013) Design of buck-type current source inverter fed brushless DC motor drive and its application to position sensor less control with square wave current. *IET Electr Power Appl* 7(5):416–426
48. Tiwari R, Padmanaban S, Neelakandan RB (2017) Coordinated control strategies for a permanent magnet synchronous generator based wind energy conversion system. *Energies* 10:1493
49. Ying L, Ertugrul N (2003) A novel, robust DSP-based indirect rotor position estimation for permanent magnet AC motors without rotor saliency. *IEEE Trans Power Electron* 18(2):539–546
50. Biswas PK, Banerjee A, Sain C (2015) Design and development of a closed loop model of an adjustable speed permanent magnet synchronous motor (PMSM) drive using PI controller. In: International conference on power electronics systems and applications, Hong Kong Polytechnic University, Hong Kong, pp 1–5
51. Kim T, Lee HW, Parsa L, Ehsani M (2006) Optimal power and torque control of a brushless DC (BLDC) motor/generator drive in electric and hybrid electric vehicles. In: Conference record of the 2006 IEEE industry applications conference forty-first IAS annual meeting, vol 3, pp 1276–1281
52. Banerjee A, Biswas PK, Sain C (2015) The Comparative study between different performance indices of a permanent magnet synchronous motor (PMSM) drive on variable sensor angle.

- In: International conference on power electronics systems and applications (PESA), Hong Kong Polytechnic University, Hong Kong, pp 1–6
53. Lin CH (2012) A novel hybrid recurrent wavelet Neural network control for a PMSM drive electric scooter using rotor flux estimator. *Int Rev Electr Eng—IREE* 7(3):4486–4498
 54. Singh B, Murthy SS, Reddy AHN (2000) A micro controller based speed controller for permanent magnet brushless DC Motor. *IETE Tech Rev* 17(5):299–310
 55. Ng K, Zhu ZQ, Howe D (1996) Open-circuit field distribution in a brushless motor with diametrically magnetized PM rotor, accounting for slotting and eddy current effects. *IEEE Trans Magn* 32(5):5070–5072
 56. De Belie F, Melkebeek J (2010) Seamless integration of a low-speed position estimator for IPMSM in a current controlled voltage-source inverter. In: *IEEE international conference on sensor less control for electrical drives (SLED)*, pp 50–55
 57. Sain C, Biswas PK, Banerjee A (2015) Design and analysis of open loop model of a permanent magnet synchronous motor (PMSM) drive. In: *International conference on energy, power and environment (ICEPE)*
 58. Chinthamalla R, Sanjeevikumar P, Karampuria R, Jain S, Ertas AH, Fedak V (2016) A solar PV water pumping solution using a three-level cascaded inverter connected induction motor drive. *Eng Sci Technol Int J (JESTECH)* 19(4):1731–1741
 59. Jain S, Chinthamalla R, Karampuri R, Sanjeevikumar P (2017) Effective dual solar PV fed three-phase open-end winding induction motor drive for water pumping system application. *J Mod Power Syst Clean Energy (MPCE)*
 60. Yang Z, Shang F, Brown IP, Krishnamurthy M (2015) Comparative study of interior permanent magnet, induction, and switched reluctance motor drives for EV and HEV applications. *IEEE Trans Transp Electric* 1(3):245–254
 61. Rini Ann Jerin A, Palanisamy K, Sanjeevikumar P, Umashankar S, Ramachandramurthy VK (2017) Improved fault ride through capability in DFIG based wind turbines using dynamic voltage restorer with combined feed-forward and feed-back control. *IEEE Access J*
 62. Awasthia A, Karthikeyan V, Sanjeevikumar P, Rajasekar S, Blaabjerg F, Singh AK (2017) Optimal planning of electric vehicle charging station at the distribution system using hybrid optimization algorithm. *Energy* 133:70–78
 63. Arumugam P (2016) High-speed solid rotor permanent magnet machines: concept and design. *IEEE Trans Transp Electric* 2(3):391–400
 64. Liu X, Zhu ZQ, Wu D (2014) Evaluation of efficiency optimized variable flux reluctance machine for EVs/HEVs by comparing with interior PM Machine. In: *Proceedings of IEEE 17th international conference on electrical machines and systems*, pp 2648–2654
 65. Fujishima Y, Wakao S, Kondo M (2004) An optimal design of interior permanent magnet synchronous motor for the next generation commuter train. *IEEE Trans Appl Supercond* 14(2):1902–1905
 66. Duan S, Zhou L, Wang J (2014) Flux weakening mechanism of interior permanent magnet synchronous machines with segmented permanent magnets. *IEEE Trans Appl Supercond* 24(3)
 67. Kim K, Lee J, Kim H (2009) Multi-objective optimal design for interior permanent magnet synchronous motor. *IEEE Trans Magn* 45(3):1780–1783
 68. Sanjeevikumar P, Blaabjerg F, Wheeler P, Lee K, Mahajan SB, Dwivedi S (2016) Five-phase five-level open winding/star-winding inverter drive for low voltage/high-current applications. In: *2016 IEEE transportation electrification conference and expo, Asia-Pacific (IEEE-ITEC'16)*, Busan (Korea), pp 66–71
 69. Sanjeevikumar P, Pecht M (2016) An isolated/non-isolated novel multilevel inverter configuration for dual three phase symmetrical/asymmetrical converter. *Eng Sci Technol Int J (JESTECH)* 19(4):1763–1770
 70. Choi UM, Blaabjerg F, Lee KB (2015) Method to minimize the lowfrequency neutral-point voltage oscillations with time-offset injection for neutral-point-clamped inverters. *IEEE Trans Ind Appl* 51(2):1678–1691

71. Choudhury A, Pillay P, Williamson SS (2014) DC-link voltage balancing for a 3-level electric vehicle traction inverter using an innovative switching sequence control scheme. *IEEE J Emerg Sel Topics Power Electron* 2(2):296–307
72. Choi UM, Lee JS, Lee KB (2014) New modulation strategy to balance the neutral-point voltage for three-level neutral point clamped inverter systems. *IEEE Trans Energy Convers* 29(1):91–100
73. Xia C, Zhao J, Yan Y, Shi T (2014) A novel direct torque and flux control method of matrix converter-fed PMSM drives. *IEEE Trans Power Electron* 29(10):5417–5430
74. Niu F, Wang B, Babel AS, Li K, Strangas EG (2016) Comparative evaluation of direct torque control strategies for permanent magnet synchronous machines. *IEEE Trans Power Electron* 31(2):1408–1424
75. Krishnan R (2010) Permanent magnet synchronous and brushless DC motor drives. CRC Press, Boca Raton, FL, USA
76. Geyer T, Papafotiou G, Morari M (2009) Model predictive direct torque control—Part I: concept, algorithm and analysis. *IEEE Trans Ind Electron* 56(6):1894–1905
77. Dost P, Sourkounis C (2014) On influence of various modulation schemes on a PMSM within an electric vehicle. In: Proceedings of the IEEE industry application society annual meeting, pp 1–10
78. Dost P, Sourkounis C (2011) Effects of the control-process-structure to the drivability in electric vehicles. In: 19th Mediterranean conference on control & automation (MED), pp 365–370
79. EC (2011) Smart Grids: from innovation to deployment—Communication from the Commission to the European Parliament, the Council, the European Economic and Social Committee and the Committee of the Regions
80. Jiang Z, Dougal RA (2008) Hierarchical microgrid paradigm for integration of distributed energy resources. In: 2008 IEEE power and energy society general meeting—conversion and delivery of electrical energy in the 21st century. IEEE, pp 1–8
81. El-Hawary ME (2014) The smart grid—state-of-the-art and future trends. *Electr Power Compon Syst* 42:239–250
82. Frankfurt School-UNEP Centre/BNEF (2016) Global trends in renewable energy investment 2016: analysis of trends and issues in the financing of renewable energy
83. Ji L, Zhang XPP, Huang GHH, Yin JGG (2015) Development of an inexact risk-aversion optimization model for regional carbon constrained electricity system planning under uncertainty. *Energy Convers Manag* 94:353–364
84. Fuss S, Szolgayová J, Khabarov N, Obersteiner M (2012) Renewables and climate change mitigation: irreversible energy investment under uncertainty and portfolio effects. *Energy Policy* 40:59–68
85. Cheng X, Hu X, Yang L, Husain I, Inoue K, Krein P (2014) Electrified vehicles and the smart grid: the ITS perspective. *IEEE Trans Intell Transp Syst* 15:1388–1404
86. Rahimi F, Ipakchi A (2010) Demand response as a market resource under the smart grid paradigm. *IEEE Trans Smart Grid* 2010(1):82–88
87. Haidar AMA, Muttaqi KM, Sutanto D (2014) Technical challenges for electric power industries due to grid-integrated electric vehicles in low voltage distributions: a review. *Energy Convers Manag* 86:689–770
88. Cvetkovic I, Thacker T, Dong D, Francis G, Podosinov V, Boroyevich D, Wang F, Burgos R, Skutt G, Lesko J (2009) Future home uninterruptible renewable energy system with vehicle-to-grid technology. In: Energy conversion congress and exposition, 2009 (ECCE 2009). IEEE, pp 2675–2681
89. Becker B, Allerding F, Reiner U, Kahl M, Richter U, Pathmaperuma D, Schmeck H, Leibfried T (2010) Decentralized energy-management to control smart-Home architectures. In: Muller-Schloer SYC, Karl W (eds) Architecture of computing systems—ARCS 2010, vol 5974. Lecture notes in computer science. Springer, Berlin/Heidelberg, pp 150–161
90. Jang YJ, Jeong S, Lee MS (2016) Initial energy logistics cost analysis for stationary, quasi-dynamic, and dynamic wireless charging public transportation systems. *Energies* 9(7):483

91. Ahmad F, Alam MS, Asaad M (2017) Developments in xEVs charging infrastructure and energy management system for smart micro grids including xEVs. *Sustain Cities Soc* 35:552–564
92. Fisher TM, Farley KB, Gao Y, Bai H, Tse ZTH (2014) Electric vehicle wireless charging technology: a state-of-the-art review of magnetic coupling systems. *Wireless Power Transf* 1(2):87–96
93. Zaheer A, Hao H, Covic GA, Kacprzak I D (2015) Investigation of multiple decoupled coil primary pad topologies in lumped IPT systems for interoperable electric vehicle charging. *IEEE Trans Power Electron* 30(4):1937–1955
94. Yilmaz T, Hasan N, Zane R, Pantic Z (2017) Multi-objective optimization of circular magnetic couplers for wireless power transfer applications. *IEEE Trans Magn* 53(8), Art. no. 8700312
95. Ko YD, Jang YJ (2013) The optimal system design of the online electric vehicle utilizing wireless power transmission technology. *IEEE Trans Intell Transp Syst* 14(3):1255–1265
96. Throngnumchai K, Kai T, Minagawa Y (2011) A study on receiver circuit topology of a cordless battery charger for electric vehicles. In: *Proceedings of the energy conversion congress and exposition (ECCE)*, pp 843–850
97. Vekic MS, Grabic SU, Majstorovic DP, Celanovic IL, Celanovic NL, Katic VA (2012) Ultralow latency HIL platform for rapid development of complex power electronics systems. *IEEE Trans Power Electron* 27(11):4436–4444
98. Inaba Y, Cense S, Bachir TO, Yamashita H, Dufour C (2011) A dual high-speed PMSM motor drive emulator with finite element analysis on FPGA chip with full fault testing capability. In: *Proceedings of the 2011 14th European conference on power electronics and applications*, pp 1–10 (2011)
99. Saied SA, Abbaszadeh K, Fadaie M (2010) Reduced order model of developed magnetic equivalent circuit in electrical machine modelling. *IEEE Trans Magn* 46(7):2649–2655
100. Carpiuc SC, Lazar C (2015) Fast real-time constrained predictive current control in permanent magnet synchronous machine-based automotive traction drives. *IEEE Trans Transp Electrification* 1(4):326–335
101. Kabir MA, Husain I (2016) Design of mutually coupled switched reluctance motors (MCSRMs) for extended speed applications using 3-phase standard inverters. *IEEE Trans Energy Convers* 31(2):436–445
102. Jack AG, Mecrow BC, Haylock JA (1996) A comparative study of permanent magnet and switched reluctance motors for high-performance fault-tolerant applications. *IEEE Trans Ind Appl* 32(4):889–895
103. Boldea I, Tutelea LN, Parsa L, Dorrell D (2014) Automotive electric propulsion systems with reduced or no permanent magnets: an overview. *IEEE Trans Ind Electron* 61(10):5696–5711
104. El-Refaie AM, Jahns TM (2004) Optimal flux weakening in surface PM machines using concentrated windings. In: *Proceedings of the IAS annual meeting, Oct 2004*, pp 1038–1047
105. Dorrell DG, Knight AM, Evans L, Popescu M (2012) Analysis and design techniques applied to hybrid vehicle drive machines—assessment of alternative IPM and induction motor topologies. *IEEE Trans Ind Electron* 59(10):3690–3699
106. Wang J, Yuan X, Atallah K (2013) Design optimization of a surface mounted permanent-magnet motor with concentrated windings for electric vehicle applications. *IEEE Trans Veh Technol* 62(3):1053–1064
107. Torregrossa D, Peyraut DO, Fahimi D, M’Boua J, Miraoui A (2011) Multiphysics finite-element modeling for vibration and acoustic analysis of permanent magnet synchronous machine. *IEEE Trans Energy Convers* 26(2):490–500
108. Liu N, Chen Q, Lu X, Liu J, Zhang J (2015) A charging strategy for PV-based battery switch stations considering service availability and self-consumption of PV energy. *IEEE Trans Ind Electron* 62:4878–4889
109. Wandhare RG, Agarwal V (2015) Novel integration of a PV-wind energy system with enhanced efficiency. *IEEE Trans Power Electron* 30(7):3638–3649
110. Abt V, Vigier F, Schneider M (2009) Enterprise business modelling languages applied to farm enterprise: a case study for IDEFO, GRAI Grid, and AMS languages. In: *Advances in modelling agricultural systems*. Springer, US, pp 167–191

111. Ahmed MR, Cui HY, Huang X (2014) Smart integration of cloud computing and MCMC based secured WSN to monitor environment. In: Proceedings of the 4th international conference on wireless communications, vehicular technology, information theory and aerospace & electronic systems (VITAE)
112. Blomqvist E, Thollander P (2015) An integrated dataset of energy efficiency measures. *Energy Effi* 8(6):1125–1147

Green Energy Generation Using Renewable Energy Technologies



Sanghita Baidya and Champa Nandi

Abstract The sustainable development of energy market is depending on the improvement of renewable energy technologies. The renewable technologies are eco-friendly, green, and clean resources for power generation. Conventional sources for generating energy are limited on earth which creates scarcity and they are also producing harmful gases to atmosphere. The technologies based on renewable energy sources are providing a great opportunity to minimize the global warming by reducing the production of greenhouse gases (like CO₂). Some renewable energy sources are useful for minimizing the wastes from the locality (like biogas). In rural areas, renewable technologies are offering employment opportunities. Though earth is plenty with renewable sources, they are dramatically depending on the geographical positions and environmental situations. This creates several challenges for the development of renewable technologies. This chapter gives a concise overview on merits and limitations of renewable energy sources. For monitoring and controlling the renewable technologies, Internet of things (IoT) can play a vital role. The chapter mainly focuses on the different types of renewable technologies. The implementation of this green energy technology offers a sustainable development of the energy market. In this chapter monitoring of solar PV is also briefly discussed with IoT technology.

Keywords Background of renewable energy · Different types of renewable energy · Environment protection · Difficulties with renewable energy technologies · IoT on renewable energy technology

1 Introduction

To face the increasing demand for electricity, renewable energy-based technologies are providing a great opportunity. It also helps in economic field as well as employment sector. Being a clean energy technology, it has a good impact on human

S. Baidya · C. Nandi (✉)
Tripura University, Agartala, India
e-mail: cnandi@tripurauniv.in

S. Baidya
e-mail: sanghita.ee@tripurauniv.in

© Springer Nature Singapore Pte Ltd. 2020

A. K. Bhoi et al. (eds.), *Advances in Greener Energy Technologies*,

Green Energy and Technology, https://doi.org/10.1007/978-981-15-4246-6_16

health and environment. Recently, the use of renewable energy-based technologies is increased tremendously for energy security. Instead of solar, wind, and water, India has abundant biomass which can provide a great scope of employment in rural areas [1]. But there are some challenges with these technologies which are built based on the renewable energy. Different weather conditions make their influence on renewable energy production and the frequent changing conditions of climate cannot be forecasted accurately. Another problem regarding renewable energy generation is that it is available in fewer amounts when the demand is high and the amount of it more at the time of low demand, i.e., the fluctuation of renewable energy over the day causes difficulties in planning of power system as well as scheduling. The role of renewable energy over the conventional energy is extremely prominent as it has several good effects not only on industries but also environment. Though capital cost for renewable energy-based technologies is more expensive than that of conventional power, renewable energy generation technologies are abundant, clean, and now, pervasive. Hence, to maintain a tie up between renewable energy and grids, Internet of things (IoT) devices are used widely which have the ability of managing different levels of demand flexibly [2].

The present scenario of energy management has various objectives which make it more complex on the eve of sustainability. The sustainable development of energy management to mitigate the rising energy demand needs proper planning for renewable energy technologies [3].

Global warming due to green house gasses (CO_2 , CO SO_2 , etc.) is another matter of concern now. Different firms along with electricity generation plants are responsible for providing greenhouse gases to environment. Therefore, renewable energy-based technologies are preferred to these firms and electricity generating stations. Thus, investigating these technologies can help to mitigate greenhouse gases and it has an important insinuation for both the climate policy and the renewable energy technology development [4].

The propagation of new energy technologies has challenges and also has opportunities for operators. It is shown that the waste or unused part of Indian land (approximately 32,000 km^2), when installed with solar power plants, can produce 2,000 billion KWh of electricity, which is two times the total generation in the year 2013–14. Wind power is one of the largest sources of renewable energy in India and India ranked fifth-largest country on the World on installed wind power plant. The second-largest source of renewable energy is biomass energy which is nearly 12% of total installed capacity of renewable energy in our country [5].

In this chapter, the review of different types of renewable energy and its technologies are discussed. The sustainable growth of renewable energy-based technologies for increasing the use of clean energy in various fields is capable to minimize the problems which are stated here. Protection of environment from greenhouse gases by using renewable energy sources is also mentioned in this chapter. At last, the barriers for installation of renewable energy technologies are enlightened and remote monitoring for the development of these installations is also highlighted here.

1.1 Background of Renewable Energy Technologies

To improve the quality of our day-to-day life, energy plays an important role. Challenges are arising due to lack of energy production which creates a burning issue for modern civilization. To maintain a smoothly running life, huge amount of energy is required. It has been seen that most of the people on the earth face the scarcity of electricity daily. The increasing population of any country needs to fill up their basic requirements. Thus, the demand of energy generation along with consumption is increasing rapidly in developed and developing countries. To meet the excessive power demand, more fossil fuels should be used which causes ozone-layer depletion, maximize the health risk of living beings, changes in atmosphere, environmental problems, etc. The amount of solar energy which is absorbed by earth at day time by solar radiation should be returned back at night through longer wavelengths to the universe for maintaining the thermodynamic balance of the planet. But the presence of green house gases on the atmosphere prevents the energy to go back which increased the temperature of the earth surface very high, i.e., known as global warming. It has been shown from several surveys that the conventional energy sources for power generation (fossil fuels) are sharing CO₂ to the atmosphere which further maximized the level of CO₂ in the environment. It is found that the CO₂ level is increased from 280 to 390 ppm. Therefore, to meet the increasing energy demand in a clean way, renewable energy sources are very significant. The technologies based on the non-conventional energy sources to generate power are used widely in most of the countries. Though three types of energy sources (fossil fuels, renewable energy sources, and nuclear resources) are available in the earth, renewable energy sources are most abundantly used for power generation as they are environment-friendly and do not have limitation. The commonly used renewable energies are wind energy, marine energy, solar energy, biofuels, geothermal energy, biomass energy, etc. The renewable energy sources can be used as an independent decentralized small-scale power generating units for rural areas. The present scenario shows that approximately 23.7% energy demand of whole over the world is satisfied by renewable energy sources.

The modern renewable energies are more reliable, comparatively the existing energies. They are concentrated solar, bio-energy, shore wind, geothermal, etc. Surprisingly, in 2015, the share of hydropower as a renewable energy is placed on the top by securing 16.6% out of 22.7% of the total share. The investments over the renewable energy-based technologies were gradually increased from 2004 to 2011. But, a dramatically decay of the investments was shown after 2011 due to lack of modern technologies for installation of solar photovoltaic units. According to the Global Status Report (GSR) of 2016, the top most countries of the world of renewable energy-based installations are the USA, Canada, China, Brazil, and Germany. From last few years, it had been shown that the investment toward renewable energy is gradually developed. In 2014, the solar and wind energies provided 46 GW and 49GW power from the installations, respectively.

Mainstream renewable energy technologies and emerging energy technologies are the two important part of the renewable energy technologies. The solar energy, hydropower, biomass energy, wind energy, etc., belong to the mainstream renewable energy sources. A vast part of power generation is depending on the mainstream energy technologies. On the other hand some new emerging energy technologies (such as marine energy, tidal energy etc.) are now involved in energy market which attracted great interest of the researchers. The marine energy technique used wave energy of ocean, tidal currents, temperature gradients, and tidal power. The benefits of marine energy are high potential wave energy, consistency, and predictability. But as lack of better technology, only a little bit of these vast energy sources can be utilized. The wave energy of ocean is also dependent on the wind that blows through the ocean surface. These waves have much strength that they loosed very small amount of energy while travelling from long distance over the ocean surface. These waves also efficiently transferred the energy. Here, converters are used to renovate the wave energy into electrical energy. The concentration of energy is very high for this wave energy. The potential and strength of the wave with its energy are mainly dependent on the geographical location of the ocean. Another emerged energy source is tidal energy which is produced due to rise and fall of waves in the ocean. The movement of earth, sun, and moon is responsible for this raise and fall of waves. The effect of gravitational force also makes an impact on this. The advantage of this energy is that it is predictable and continuous. Since 1966, tidal power station has been built to utilize the energy. The potential energy of tidal wave is depended on the specific geographical location of ocean. Hydrokinetic turbines are used for extracting energy from the tides [6].

The renewable energy technologies are not separately capable to meet the overall demand of the increasing worldwide population. Hence, these approaches have to integrate with the existing grids. The power electronic equipments are used to interconnect the smart grids based on renewable energies with the existing power grids. The communication setup is very important for the integration of renewable energy technologies with the existing power grids. Because transferring of information and data from one unit to other unit should be safe and secure. Previously, the controlling of the energy consumption and other relevant parameters of grid was done in a centralized way. But now, decentralized approaches are more preferable to controlling the system based on renewable energy sources. For better communication with the interconnected grids, information and communication technology (ICT) plays an important role. SCADA technology is the most used ICT for monitoring and controlling the grid parameters along with power consumption remotely. Smart metering technologies (which also include monitoring of power quality, remote switching of connected loads, load profiling, etc.) are used for smaller stage grids. The further technologies are designed based on Internet connection to enhance the communication way, monitoring, and controlling of the grids. Unfortunately, it is seen that some grid owners are wishing to restrict the communicating resources on their own control. Wireless communication systems are also a new approach for better communication among the integrated grids [7].

1.2 Necessity of Renewable Energy Technologies Use

The matter of concern for today's world is the security of energy system along with the pollution of environment. It is necessary to find out a solution to generate energy using the renewable resources without harming the environment. The technologies based on renewable energy are basically in the decentralized configuration and centralized in the form of supply. One of the most easily available renewable energy resources is solar and wind. The technologies build-up based on those resources have to face several challenges on the field of energy consumption. It is observed that most of the energy markets are not suitable for these technologies. Thus, it requires sum up of new technologies with the existing one for better energy utilization. The new approaches for improvement of energy system include energy Internet. It can integrate the different energy technologies with information technology to find the solutions of environmental issues as well as energy emergency. The energy Internet scheme is advantageous for increasing the consumption of energy produced from renewable resources and for making a mutual coordination between raising energy demand and present supply strategy of energy [8].

To reduce carbon emissions into the environment, renewable energy resources are playing an important role. The global warming is the worst result of carbon emission on the atmosphere. Thus, the use of renewable energy technologies for energy generation is very beneficial for environmental issues. But the main problems with this approach are weather and position of system installation. These technologies provided different ways to increase the consumption of energy produced from renewable resources. The power generation process from renewable resources and its increased consumption provided a great impact on environment by reducing carbon emission on the whole. The modern renewable technologies are basically based on the Internet which helps the end-users to access the system information from anywhere on the world via Web connection of any computer. The Web of things technology is one of them which have several interconnected device via Internet [9].

The renewable resources can use to generate electricity in the rural areas. But the main challenge is proper monitoring and controlling the connected tools with the system. Thus, modern communication technologies are integrated with the existing system to make them smart. A smart grid can easily control the operations of the whole system by providing monitoring facilities and optimization of energy. The previous monitoring schemes have different types of limitations and most of the times also need extra construction for monitoring purpose as the plants are installed in farther locations. But the modern technologies used the Internet connection for communication. Arduino, Raspberry-pi, Rabbit, etc., are the devices which helped for interfacing the whole system or plant to the Internet. RET SB5 the scarcity of fossil fuel on the energy market increased the use of renewable energy resources for power generation. Due to the high penetration of non-conventional energy sources in the existing power grids, different types of challenges are shown like frequency oscillation, fluctuation of power flow, disturbance on converter output, unstable operations, etc. Interfacing the power electronic converters also leads to instability of the

generated power and ultimately not suitable to integrate with a vast renewable energy source. Virtual synchronous generator and synchronous power controller are used to maintain the stability of the power grid and to make connection with large power grids of renewable energy sources. Thus, the renewable energy technologies are more effective for accurate sharing of active and reactive power. The new technologies can also give a quick response to any change in frequency and voltage profile of the power grid [10].

The modern generation gives priority on making smart grids instead of traditional power grids. These smart grids are very economical for energy market and also environment-friendly as they used renewable energy sources to generate power. The smart grid approach faces different kinds of issues when integrating with existing grids. The smart grid also provided bidirectional flow of current which needs proper protection. The previous schemes for protection purpose are commonly centralized which needs a system-wide or region-wide configuration for data collection and maintain the communication with the whole unit. Undesirable low strength and low quality of signals are the other issues of communication with those schemes. To overcome these issues, new distributed wide area differential protection scheme is used which also maintain the penetration of renewable energy sources and will provide necessary bandwidth with proper communication configuration [11].

2 Different Types of Renewable Energy Technologies

Recently, the distributed form of energy generation is adopted for renewable energy generation because it is one of the most admired techniques in present days. The distributed energy generation technology can work with small-scale power plants as well as the large-scale power plant and users can also benefit for this technology as it is nearer to the users. The renewable energy technologies reduced the burden of tradition grids. They also increase the efficiency of energy generation and consumption by using local resources for power generation, i.e., renewable energy resources. This also helps on economic factor of energy market.

The conventional energy sources give a negative or harmful effect on environment such as environment pollution, global warming, depletion of ozone layer, acid rain, etc., at the time of electric power generation. Hence, renewable energy sources are abundantly used for generation of electricity because of their environment friendliness. Its cost effectiveness also developed the energy market. But the renewable energy sources are totally dependent on location. These sources are also facing the issues of unpredictability, variability, and intermittency. To overcome those challenges, new renewable energy technologies are required [12].

The renewable energy technologies have several varieties from which some are listed here.

2.1 HVDC Transmission Line and Renewable Energy Technologies

The clean energy technologies are rapidly developing in most of the countries. But the sources of renewable energy are located in large distance from the locality where loads are connected. Therefore, the transmission lines have to travel more distance from source to load. The high-voltage DC (HVDC) transmission is, hence, more suitable in this case. But the nature of existing electricity grids is not all-time adjustable with the new technologies based on power electronics. It may suffer from system instability and several operating issues. The use of power electronic-based approaches are beneficial as they are flexible in nature and also they have quick controlling capacity on the grid power quality and stability. It also enhances the supplying ability of electricity with better efficiency. In addition, they are fault sensitive, quick process controlling, and can manage other abnormalities of the grid. An industry based on power electronic equipments should have the LCC and MMC technologies in HVDC converters. The multi-terminal HVDC systems also have DC circuit breakers. The main issue related to the power electronics approaches is designing of equipments which will connect to the existing grid system technology and integration of large units of renewable energy sources with HVDC transmission. Sun et al. in 2017 demonstrated the uniqueness of power electronics for generating electricity from renewable energy sources. They have also mentioned the impacts of their approach on the stability of the power grids, transmission of HVDC, and operational necessities [13].

2.2 Energy Storage and Operation Management of Power Grids with Renewable Energy Technologies

The energy storage system is a backup for the whole system when intermittency, position dependency, inconsistency, and irregularity issues are arising in the renewable energy sources-based power generating stations. The time of energy production may not be the time of energy consumption that creates a mismatch to maintain the balance between production and consumption. Hence, energy storage system is necessary to manage the electricity network by providing flexible energy supply to meet the demand. Storage of energy also improved the efficiency and integration of different renewable energy sources. To store the generated energy, battery storage technology is widely used due to its different kinds of advantages like maturity, modularity, high energy density, reliability, easy transportation, etc. Batteries are easily available in the market with different ranges. They also have a wide application area such that aerospace operation, marine, electric grids, wireless network system, and many more. Besides that, the battery-based energy storage technology is also used for off-grid electrification in rural areas along with demand shifting. The solar radiation is very high at the day time and zero at the evening to night [12]. The countries near

to the equator have a quite suitable geographical position for solar energy utilization. Sudan is one of those countries which have a huge amount of non-conventional green energy sources. The wind speed of Sudan per month is up to 8 m/s which are very apposite for electricity generation through wind. Yet, the demand of energy consumption has not filled up. On the other hand, the load is increasing on the transmission lines which also raising the economical issues. The crisis of fossil fuels and their increasing price also enhancing the significance of renewable energy sources for generation of electricity. The areas far away from the traditional grids use their own small independent power grids for meeting the demand like Nyala power plant. Another issue with the existing standalone grids is their diesel generators are needed time to time maintenances. Therefore, storage system is required on the grids based on the renewable energy system. The solar radiation and the wind speed are not same for each day. Thus, generation of power is interrupted. Thus, storage is necessary to meet the sudden demand of customers [14]. There are so many studies about the storage system but they have their own advantages and disadvantages. Some of those installations may suffer from economic dispatch, instability, and poor quality of generation. On the other hand, some are facing the insecurity issues, optimization problems and cost issue. From the further studies, it has been shown that renewable energy is preferable on the standalone systems with battery storage because the areas are farther from the grids and the production cost may be minimum for those systems. The fuzzy-adaptive particle swarm optimization technology is also adopted to determine the numbers of wind turbine, solar plate, and battery storage unit. Another challenge is the integration of renewable energy sources (wind, solar, etc.) to the diesel grid with vanadium redox flow battery. It should be designed in such a manner that the ESS will charge at the time of low demand and discharge during pick hours. Ahmed et al. in 2018 proposed a system based on renewable energy sources for operation management of the grids with battery storage system. The proposed scheme is the integration of wind and solar PV energy sources with the existing diesel grid. It will decrease the power generation cost and save fossil fuel. The emission of carbon dioxide may also minimize. The renewable energy sources-based power generation is considering here for maintaining the power demand in remote areas. The simulation results show that the new technology is useful to minimize the power generation cost and carbon dioxide emission. The CAES is used to store the wind energy. Thus, the proposed scheme provides backup for the system with whom it is integrated and also it is managing the operation of the grid system [15]. Matthew Simeon, Adoghe et al. in 2018 proposed a technology based on smart battery energy storage system for addressing the drawback of solar radiation. At the time of minimum solar radiation, a supplementary battery is used to charge the main battery. In their work, a voltage-level sensor is used to control the operations of both the primary and secondary batteries automatically. Two relays are connected to the whole system. The relays are operating depending up on the signals of the voltage-level sensors. The working of connected relays (i.e., alternating on-off of the main and auxiliary battery) enables the sustainable electrical power supply to the load [12].

2.3 Ocean Thermal Energy Conversion (OTEC) Technology

The OTEC is coming from the concept of absorbing solar energy by the upper layer of ocean water. This makes the upper-layer water warm. But the water layer below 800–1000 m remains cold. The absorbed energy is taken out through OTEC cycle. In this cycle, the temperature variation between the hot water and cold water is used to generate electricity. For driving the turbine, a sufficient amount of vapor with high pressure is required that can be provided by the vapors formed from the hot upper-layer seawater. These vapors are condensed via the cold water layer. The OTEC cycle has three techniques such that closed cycle, hybrid cycle, and open cycle to haul out energy from OTEC plants. Seawater is used as a working fluid for turbines of open-cycle OTEC technology for extracting energy from OTEC. On the other way, CFC, ammonia or propane are used for closed-cycle. The hybrid cycle used both the open-cycle and closed-cycle technologies. For considering the OTEC resource as a regular source of power supply, the main challenge is the variation of temperature due to weather change. Theoretically, compared to the other ocean energy resources, OTEC has the highest potential. The minimum criteria of heat diversity between hot and cold seawater layer are 20 °C for operating a small commercial-scale power plant to utilize OTEC resources. Though the growth of OTEC-based power plants is shown in islands, the major problem to make OTEC fully commercial is per unit cost [6].

2.4 Renewable Energy Technologies for Microgrids

Microgrids have small units for power generation based on the distributed generation system. Most commonly, renewable energy resources are used for power generation on microgrids as the non-renewable resources are responsible for emitting harmful gases (like CO₂) on the atmosphere. But these non-renewable energy resources are used as backup system on the grids for facing the sudden energy demand. The renewable energy technologies based on sustainable energies like geothermal energy, solar energy, bio-energy, wind energy, etc., are used on the microgrids for generating power. To expand the utilization of renewable energy sources as well as its technologies, various policies are taken by the different countries. The main endeavor for these kinds of initiatives is reducing the production of green house gases to save the environment and enhancing the use of renewable energy sources as they are easily and abundantly available in the earth. Though several renewable sources are available, microgrids are usually preferred solar and wind energy to produce electricity due to their easy installation and continuous developing technology. As the microgrids have small-sized generating units, range of generating power is normally from less than a kW to tens of MW. The generating units are allied comparatively close or nearer to the load demand [16].

2.4.1 Wind Energy Technologies

The renewable energy technology based on wind energy is growing rapidly due to its unique advantages. Figure 1 represents the wind energy generation technology. Wind energy is a non-polluting energy which is also known as green energy. Some of its reimbursements are it is sustainable, restored by nature, eco-friendly, cost effective, and easily available whole over the world. But the wind speed is quite unpredicted because of sudden weather change. Another issue with this renewable energy is low power density. The power generated by the wind turbine generators is limited in few MWs. Thus, the cost of investment initially remains very high. The main problem with wind farm installation in largescale is the location. Most of the places where wind speed is very suitable for power generation are situated far away from the locality (where the load is required most). Hence, the transmission-line structure also hampered. For better power generation, improvement of wind turbine system is very essential. In the past, the output power obtained from the wind energy installations was nearly 200 kW. The average output power shows some increase upto 600 kW in 1999. Due to the improvement of technologies, today, approximately 2–3 MW power can be generated by the wind energy installations for onshore applications. The wind farms based on sea area can be produced three times more energy than standard onshore structure [16].

The biggest wind turbine in the world is the Sea Titan 10 MW wind turbine. It is designed by American Superconductor (AMSC) Company which is based on energy technologies. The turbine has 190 m diameter for rotor with directly driven turbine and 125 m hub height. The capacity of the turbine is 10 MW. The Norwegian technology company Sway has also designed the second-largest wind turbine in the world named as the ST10 offshore wind turbine. The output power from the turbine is also 10 MW. The rotor has 164 m diameter and 2 rpm nominal speed. The length of the blades is 67 m. And the third-biggest wind turbine is Areva's 8 MW designed by the French energy company.

There are three types of wind generators normally available in the energy market. The first one has standard squirrel-cage induction generator (SCIG). It can be directly integrated into the grid system. Also, it is a constant-speed wind turbine. The next type of wind generator has variable speed and a doubly fed induction generator (DFIG). The power supplied to the rotor windings is fed by power electronics converters which is 30% of the rated power. The stator winding of the DFIG is directly connected to the grid. The last (third) type of wind turbine also has variable speed and asynchronous generator (SCIG). The supply power forms electronics converters that are similar to



Fig.1 Electricity generation from wind energy

the fully rated power on this type. The first type and second type of wind turbines have multi-stage gear box [16].

2.4.2 Solar PV Technologies

One of the most abundantly available renewable energy is solar energy. Solar energy is a non-depleting sustainable energy source on the earth. Huge amount of solar energy is naturally available every day on the earth surface. Figure 2 illustrated a grid-connected scenario of solar energy technologies. This energy is also ubiquitous and non-polluting green energy resource for power generation. In fact, it is one of the cheapest renewable energy technologies among the others after the wind energy. In one word, solar energy is very cost effective for present power generation situation. The main advantage of solar energy is the solar photovoltaic modulation. The PV plates are very flexible in size for integrating them on any buildings or rooftops or power plants. It is also very suitable for decentralized application near the load demand. The PV plates have no moving parts and no specific thermal stresses. Thus, the photovoltaic systems can bid long lifetime, tremendously high reliability, operate calmly, and required low maintenance. The solar radiations used on the PV panels are diffuse radiation. The PV panels are also functional in moderate climates with superior fractions of diffuse radiation.

The challenges with solar energy-based installations are that the unpredictability of solar radiation, limited control over variability, lower density of power, and higher initial capital cost. The main issue with the solar PV modules is low efficiency (in the range of 14–25%) which is comparatively very squat than other renewable energy system’s efficiency. Solar PV cells are four different types; they are thin film, crystalline silicon which can categorize again in two types, i.e., mono-crystalline, polycrystalline and hybrid cells, which are presented.

The growth rate of solar PV energy can be graphically represented as an exponential curve. This solar technology is gradually expanded from small-scale niche market to a grid-connected power source. For further development of the PV technology, researchers are trying to introduce better technologies with the collaboration of industrialization that brings maturity to the solar energy system. The concentrating

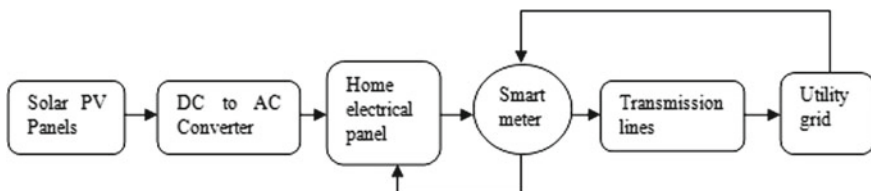


Fig.2 Grid-connected solar energy technology

photovoltaic (CPV) solar systems are integrated with organic solar cells for improvement of the solar energy technologies. It is a very effective way to increase the performance of the PV plates in solar energy system and reduce the costs of the system. Different levels of solar PV technologies are available in the energy market starting from low-cost and low-efficiency technologies to high-cost and high-efficiency technologies. The main drawback of solar energy-based technologies is the higher investment cost.

In 1996, the USA had installed solar photovoltaic of 77 MW total capacities, which ranked highest at that time in the world. After that Japan took the lead for producing power from solar energy until 2005. Germany was the third country who also made a record by approaching to 40,000 MW of power production using solar energy. Surprisingly, China is now reached to the highest position of producing solar PV energy in the world from 2017.

The 7.0 and 7.9% of power are contributed from solar PV for domestic consumption of total requirement of energy annually in Germany and Italy, respectively. It is predicted that by 2050, the most valuable source for electric power generation will be the solar energy. Approximately, 11% and 16% of power can be easily produced from concentrated solar energy and solar PV, respectively [16].

3 Environmental Protection with Renewable Energy Technologies

It has been seen that 14% of the total energy demand of whole over the world can be supplied by renewable energy sources. Different types of renewable energies are available in the energy market like hydropower, solar, biomass, wind, geothermal, etc. The clean renewable energy resources are domestic and inexhaustible in nature. Power generation using hydro renewable resources is providing 20% of electricity of total power demand. The developed lifestyle of people required more power consumption. The fossil fuels are not sufficient to meet this increasing demand of power. Moreover, the use of fossil fuels to produce electricity provides a negative impact on atmosphere which also maximized the health issues. It is also responsible for climate change by increasing green house gases in the environment [17]. The problem with sustainable development using renewable resources is sluggish movement of society toward waste management, minimizing green house gases, reducing vehicles generated air pollution, etc. In the Kyoto Protocol, some agreements were taken for preventing the pollution caused by greenhouse emissions [18]. The renewable energy sources are abundantly available on the desert and mountain regions of the earth (especially, solar and wind). Hence, it can be used for sustainable development in those remote locations. Another advantage of improving renewable energy technologies is that it provided several jobs under different projects of renewable energy in rural areas. For most of the small-scale power generation units, decentralized scheme is taken to produce electricity from renewable energy.

It is shown that in last 200 years, 31% of CO₂ level is increased in the atmosphere. Destruction of forests and enrichment of methane gas in the environment cause depletion of O₃ layer around the earth surface. Thus, the temperature of earth surface is increased gradually which causes rise of sea water levels from last few years. Approximately, 37% of harmful green house gases are emitted from industries either directly or indirectly via electrical energy utilization purpose. Therefore, renewable energy sources have a great scope to build an energy market which can produce clean power and minimized the level of green house gases. On this approach, solar energy plays an important role for generating power or electricity from solar radiation. It basically works on thermal application. Cooking, crop drying, water heating, etc., are the usual applications of solar energy. An analysis between solar water heating scheme for domestic purpose and conventional water heating system shows that 1237 kg of CO₂ production can be controlled by using renewable energy technology (i.e., using solar water heater). Approximately, 2085 kg and 1860 kg of carbon dioxide produced from diesel and petrol operating pumps, respectively, can be eliminated by solar PV-based pump (the solar radiation is required 5.5 kWhm⁻²). Another technology based on solar energy helps to process fruits and different vegetables in sanitized, hygienic, and clean condition. This is named as solar-drying technology. It also has several benefits like less time consumption, smaller area, saves energy, and quality improvement of goods which helps for environment protection. Though the cost associated with solar energy for generation of electricity is more than that of conventional ways, it has zero amount of carbon emission to the environment. The solar PV modules are capable to produce electricity from solar radiations without any vibration, noise, and emissions. The grid-connected solar PV system converted DC power to AC power. Generally, silicon solar cells are used widely. The solar cells along with the system are based on recycled materials which satisfy the energy demand and minimize harmful gas production [19].

In case of continuous wind energy utilization, an integrated power generation unit with other methods is needed. As wind speed may vary whole over the day as well as it depends on the weather condition. An analysis shows that wind energy potential is about 26,000 TWh/year but only 9000 TWh/year capacity of wind energy is used. The wind energy technology for power generation is virtually free from pollution. The wind technology converted the wind energy into electrical energy using wind turbines.

Bio-gas technology is considered as one of the most efficient energy sources which is also environment-friendly. The wastes from agricultural field, food industry, households (unused or damaged vegetables, food, fruits, etc.), animal slurries, and manure are causing continuous pollution risk and make a harmful effect on the environment. Therefore, proper management of this garbage is required to minimize greenhouse gas emission and recycle the nutrients of the environment. The advantage of biogas is that it can be easily produced and stored. The bio-gas technology is used for cooking and space heating (stoves) in rural areas. Cooking using firewood, lighting using kerosene, chemical fertilizers, heating using wood, coal, dried animal manure, etc., are responsible for increasing the greenhouse gases which causes global warming. In this point of view, bio-gas technology is providing a better substitute

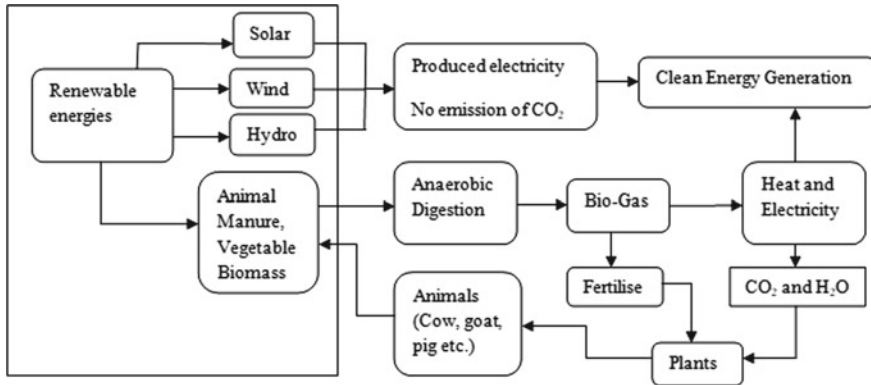


Fig.3 Environment protection with renewable energy technologies

for above-mentioned issues. Though bio-gas has CO_2 and CH_4 , use of it can offer a better chance to minimize the greenhouse gas emanation [19]. Figure 3 illustrated the different renewable energy technologies for environmental protection.

Bio-diesel technology is also providing a great opportunity to reduce production of harmful gases from transport industries, as huge amount of green house gases are emitting from this industry. On the other hand, use of bio-diesel can prevent the environment from the particulates released from burning fuels. Bio-diesel has oxygen which helps in combustion that decreases the amount of CO , hydrocarbons, and emission of other particulates, thus, making benefit to the health of human as well as animals. It is shown that approximately 79,782 tons of carbon dioxide emission can be eliminated by transesterified 10% of castor seed oil into biodiesel. The main advantage of using bio-diesel technology is that the amount of CO_2 released at the time of ignition can be recycled using crop cultivation, thus making the environment harm-free [19].

4 Difficulties with Renewable Energy Technologies Utilization

Renewable energy technologies are widely used as an alternative source of power generation in whole over the world. The conventional energy resources like coal, natural gas, crude oil, etc., have finite amount in the earth. Thus, for maintaining the developed lifestyle of people and for further improvement of energy market use of non-conventional energy sources are required. Also to reduce the emission of greenhouse gases renewable energy technologies are very beneficial. But the installation of renewable energy technologies has faced several barriers such as financial issues, weather change, social challenges, location, transmission, techniques and many more [20]. Some of these are listed here.

4.1 Huge Initial Investment Cost

With the improvement of industrialization and technology based on renewable energy the developed countries also have to pay high capital cost. Thus, the main drawback of renewable energy installation is very high initial investment cost. Hence, most of the consumers are not satisfied with the adoption of those approaches because of higher tariff.

4.2 Losses Regarding Transmission and Distribution Lines

Usually, the losses of electricity include power theft and low efficiency of plant. It needs constant monitoring and controlling the whole system. Apart from this, the renewable energy-based generating stations are situated farther from the locality or load. Thus, long transmission and distribution lines are required which may lead to more losses.

4.3 Irregularity of Solar Radiation and Wind Speed

Solar radiation is varied with the variation of geographical locations on the earth due to the position of earth rotational axis and constant movement of sun–earth. Similarly, the wind speed also dramatically depends on the geographical position of earth. Another issue is that lack of accuracy on collection of solar radiation data.

4.4 Poor Communication and Information Technology

The important issue regarding the development of renewable energy technologies is lack of communication and information of data. As the power generating units are installed far away from the locality, proper and regular monitoring is required for better performance of these networks. The problem of power theft can also be controlled with continuous monitoring. The monitoring should be done on-line as manual monitoring for the installation farther from locality may have poor accuracy and time consuming.

4.5 Requirement of Backup/Storage System

As most of the renewable energy sources are depended on the geological patchy distribution, the power generation may blink. In case of cloudy days, solar energy is not available. Also, at night solar radiations are not present. On the other hand, wind speed is also varied with sudden change of weather. Therefore, to make a constant power supply backup system or energy storage devices should present on the overall scheme.

4.6 Issues with Infrastructure

The infrastructure of any grid or generating station includes physical conveniences along with essential tools and service of power companies. Lack of institutional mechanisms in case of after-scale support regarding the renewable technologies is also a big matter of concern. The main challenge is integrating the renewable energy technologies with the existing grid. Most of the existing grid infrastructures are not suitable to amalgamate new technologies. Less involvement of private sectors and less motivation toward target program also make a barrier on the way of renewable energy technology development.

5 Internet of Things with Renewable Energy Technologies

The large-scale solar power plants are designed typically in some inaccessible places. Therefore, it is very difficult to monitor those plants regularly. This clam for automation of monitoring and controlling system of those installations. Today's generation widely used the advance technologies based on the Internet link with wired or wireless networks. The progress of Internet facilities enlightens the conception of Internet of Things (IoT). IoT basically works for sharing information among the connected devices as well as the connected systems. The IoT is now implemented in smart cities, smart homes, smart cars, healthcare, energy system, and industries for security purpose [21].

The solar energy is becoming the future sustainable energy source gradually. Rooftop solar PV approaches are generally used and they also associated with existing traditional grids. Thus, the total system on-line monitoring is required for getting information on real-time data so that grid stability can be maintained. The large-scale solar power plants which are installed far away from load station are also need on-line monitoring to make a regular observation on those units. The solar irradiance along with the temperature of solar radiation also varies from time to time, which increase the demand of remote monitoring. Thus, implementing IoT on solar power plants improved the performance of the plants, enhanced the monitoring system, and also

useful for maintenance. This also helps to detect faults in the power plants. Several issues of traditional-wired monitoring system can be solved by using IoT due to its user-friendly nature and cost effectiveness. IoT approach is suitable for renewable energy-based power market due to its flexible behavior and decentralized real-time monitoring nature. The initial PV monitoring systems have reduced real time and little automaticity. Solar PV plant monitoring and controlling with Zigbee technology is not suitable for large distance. All these issues can be solved by integrating IoT with solar energy technology. The other wireless Internet-connected public networks or communication networks are not cost effective on the area of maintenance and operation. Adhya et al. in 2016 demonstrated a cost-effective scheme using IoT for on-line monitoring of solar PV power plants. The new scheme has sensors for transmitting data through mobile radio network. It has GPRS element for sharing the information to the remote area. Their approach can be further modified by integrating remote shut down and remote management of solar PV plants [22].

6 Conclusion

Renewable energy technologies are widely used whole over the world for supplying the increasing demand for clean energy. The small-scale renewable technologies are integrated with existing grids. It is a green energy technology which reduced the emission of greenhouse gases into the atmosphere. Various types of renewable technologies are discussed in this chapter. A brief review on renewable energy technologies with their advantages and limitations are discussed in this chapter. Though all renewable energy sources are beneficial, solar energy and wind energy are typically used in microgrids. The large-scale solar power plants are located on inaccessible areas, thus required on-line monitoring. The on-line monitoring becomes more flexible by using IoT technology. This chapter exactly pointed out the different types of renewable technologies and the merits and limitations of renewable energy sources. The main aim of this chapter is to enlighten the various ways to generate green energy.

References

1. Ahmad MM, Kumar A, Ranjan R (2018) Current trends in renewable energy: an overview. *Int J Eng Res Adv Technol (IJERAT)* 04:1–15
2. Finco L, Minoli D (2018) Implementing the internet of things for renewable energy. *Internet of Things A to Z: technologies and applications*. Wiley Online Library. <https://doi.org/10.1002/9781119456735>. Chap. 15
3. Wang DD, Sueyoshic T (2018) Climate change mitigation targets set by global firms: overview and implications for renewable energy. *Renew Sustain Energy Rev* 94:386–398
4. Hansena JP, Narbelb PA, Aksnesc DL (2017) Limits to growth in the renewable energy sector. *Renew Sustain Energy Rev* 70:769–774

5. Daisy IJ, Manimekalai V, Hari Prasaath S (2017) An overview of power generation and scope for renewable energy in India. In: 2nd international conference on communication and electronics systems (ICCES 2017), pp 996–999
6. Hussain A, Arif SM, Aslam M (2017) Emerging renewable and sustainable energy technologies: state of the art. *Renew Sustain Energy Rev* 71:12–28
7. Liserre M, Sauter T, Hung JY (2010) Future energy system. *IEEE Ind Electron Mag* 18–37
8. Zhu J, Xie P, Xuan P, Zou J, Yu P (2017) Renewable energy consumption technology under energy internet environment. In: 2017 IEEE conference on energy internet and energy system integration (EI2)
9. Mohanty S, Panda BN, Pattnaik BS (2014) Implementation of a web of things based smart grid to remotely monitor and control renewable energy sources. In: 2014 IEEE students' conference on electrical, electronics and computer science
10. Poursmaeil E, Mehrasa M, Vechiuan I, Catalão JPS (2017) Double synchronous controller for integration of large-scale renewable energy sources into a low-inertia power grid. In: 2017 IEEE PES innovative smart grid technologies conference Europe (ISGT-Europe)
11. Dustegor D, El Mezayani T, Srivastava SK (2011) A distributed fault protection method for power grid with high penetration of renewable energy sources. In: 2011 IEEE international conference on smart grid communications (SmartGridComm)
12. Simeon M, Adoghe AU, Wara ST, Oloweni JO (2018) Renewable energy integration enhancement using energy storage technologies. In: 2018 IEEE PES/IAS power Africa, pp 864–868
13. Sun J, Li M, Zhang Z, Tao Xu, He J, Wang H, Li G (2017) Renewable energy transmission by hvdc across the continent: system challenges and opportunities. *CSEE J Power Energy Syst* 3:353–364
14. Tran TTD, Smith AD (2019) Stochastic optimization for integration of renewable energy technologies in district energy systems for cost-effective use. *Energies* 12(3):533. <https://doi.org/10.3390/en12030533>
15. Ahmed A, Jiang T (2018) Operation management of power grid system with renewable energy sources and energy storage system integrations. In: 2018 2nd IEEE conference on energy internet and energy system integration (EI2)
16. Molina MS, Mercado PE (2018) Renewable energy technologies for microgrids. Microgrids design and implementation. Springer, Cham, pp 27–67. https://doi.org/10.1007/978-3-319-98687-6_2
17. Nandi C, Bhattacharjee S, Chakraborty S (2019) Climate change and energy dynamics with solutions: a case study in Egypt. In: Climate change and energy dynamics in the middle east. Springer, Berlin, pp 225–257
18. Holm-Nielsen JB, Al Seadi T, Oleskowicz-Popiel P (2009) The future of anaerobic digestion and biogas utilization. *Bioresour Technol* 100:5478–5484
19. Panwar NL, Kaushik SC, Kothari S (2011) Role of renewable energy sources in environmental protection: a review. *J Renew Sustain Energy Rev* 15:1513–1524
20. Luthra S, Kumar S, Garg D, Haleem A (2015) Barriers to renewable/sustainable energy technologies adoption: Indian perspective. *J Renew Sustain Energy Rev* 41:762–776
21. Nandi C, Debnath R, Debroy P (2019) Intelligent controller design for carbon monoxide detection in IoT environment. In: Guide to ambient intelligence in the IoT environment. Springer, Berlin, pp 153–176
22. Adhya S, Saha D, Das A, Jana J, Saha H (2016) An IoT based smart solar photovoltaic remote monitoring and control unit. In: 2016 2nd international conference on control, instrumentation, energy and communication (CIEC), pp 432–436

Characteristic Analysis of 50 kVA Class Shared Transformer/Reactor



Jae-hyeon So, Young-Un Park, Su-Yong Kim, Kyung-il Woo,
and Dae-Kyong Kim

Abstract A major advantage of shared transformer/reactor is their ability to reduce weight and volume. It is characterized by the fact that it can use only one support for each device. At this time, the distances between the transformer and the reactor that are apart from each other become very close to each other, and an obstacle element is generated. We found a difference in the value of the inductance and the part where the output decreases slightly. However, if it solves this little problem, it can use the devices with a slightly lighter weight and smaller volume for the desired output and efficiency. The core of this paper is presented a new form of existing devices, and the study of interrelationships is presented.

Keywords Passive elements · Shared transformer/reactor · Transformer characteristic analysis · Transformer inductance · Transformer weight

1 Introduction

Fossil fuels, such as oil, coal, and natural gas, are commonly used energy sources. The world faces environmental pollution problems. Therefore, interest in renewable energy has increased [1]. Renewable energy technologies, such as solar power and wind power generation, have been improving. Based on research on improving technology and good efficiency, it will soon be possible to produce electricity without fossil fuels [2, 3]. At this time, increasing the efficiency of power generation as a renewable energy is an important issue. These issues are presented in a range of solutions. Research on energy storage systems (ESS), which is a power storage system, has been conducted actively to achieve uniform power supply of distributed power

J. So · Y.-U. Park · D.-K. Kim (✉)
Green Energy Institute, Suncheon National University, Suncheon, Korea
e-mail: dkkim@sunchon.ac.kr

S.-Y. Kim
Korea Electronics Technology Institute, Gwangju, Korea

K. Woo
Pukyong National University, Busan, Korea

sources (solar and wind power) [4, 5]. The appropriate use of the ESS requires a power conditioning system (PCS) to achieve the proper power output [6, 7]. PCSs contain transformers and reactors. The transformer is a device that receives the power converted by an alternating current and converts it to a voltage suitable for the use by the customer using electromagnetic induction action. The reactor is an element used to improve the harmonics, noise reduction, and power factor generated by the switching operation of the PCS. In order to use such passive elements (transformers, reactors), a steel support must be used for each element. This steel support takes up a lot of space and is heavy. In addition, the volume of the device increases as the used power capacity increases. As the volume increases, the space utilization becomes inefficient and research has been conducted to reduce the power and weight of the device [8, 9]. One way to supplement this is to use a shared transformer/reactor that combines the transformer and reactor [10]. The advantage of the shared transformer/reactor is that the devices that occupied two spaces can be resolved into a single space. Using a shared transformer/reactor, the user can exploit the weight and volume using only one of the two steel supports. On the other hand, the results of the study on the interrelationship of shared transformer/reactor and the problems were not analyzed sufficiently. Therefore, this paper presents the results of an analysis of the difference between the shared transformer/reactor and individual model. The research items are the voltage, current, capacity, inductance, and flux comparison analysis.

2 System and Shared Transformer/Reactor Configuration

The studied transformers and reactors in this paper are components of solar PCS. Figure 1a shows the overall system configuration from the battery to the grid connection. Table 1 shows the specifications of the transformer, reactor, and inverter in the PCS system.

The core material is selected considering the frequency and saturation magnetic flux density. The size and shape of the transformer and reactor were designed as follows:

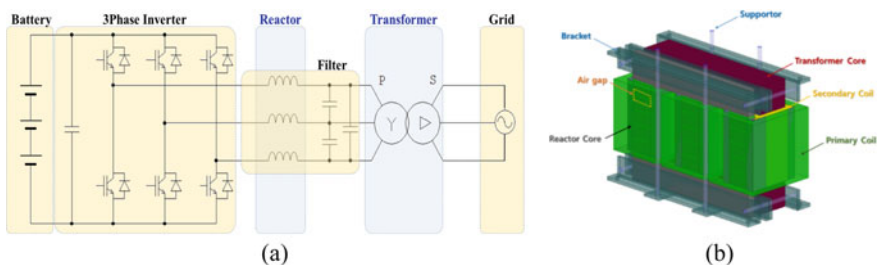


Fig. 1 System configuration and shared transformer/reactor **a** System configuration. **b** Shared transformer/reactor

Table 1 Specification of PCS system

Component		Unit	Value		
Inverter	Rated output power	kVA	50		
	Input voltage	V _{dc}	364 ~ 480		
	Output voltage	V _{ac}	380		
	Switching frequency	Hz	8000		
	Output frequency	Hz	60		
Transformer	Core (29PH090)	Width	mm	920	
		Thickness	mm	144	
		Height	mm	760	
		Max flux density	T	2.2	
	Coil (copper)	Primary	Number of turns	Turn	150
			Voltage	V _{ac}	380
		Secondary	Number of turns	Turn	150
			Voltage	V _{ac}	380
Inductor	Core (29PH090)	Width	mm	920	
		Thickness	mm	40	
		Height	mm	760	
		Max flux density	T	2.2	

$$P_{in} = \frac{P_{out}}{\eta} I_{dc} = \frac{P_{in}}{V_{in(min)}} I_{pm} = \frac{P_{in}}{V_{in(min)} \times K_t} \tag{1}$$

$$N_p = \frac{A_{wp} \times J}{I_{pm}} \tag{2}$$

$$N_p = \frac{A_w \times K_p \times K_u \times J \times V_{in(min)} \times K_t}{P_{in}} \tag{3}$$

$$A_e = \frac{V_{in} \cdot t_{on(max)}}{N_p \cdot \Delta B} \tag{4}$$

$$A_p = \left(\frac{11.1 \times P_{in}}{K_t \times K_u \times K_p \times K_p \times \Delta B \times f} \right)^{1.143} \tag{5}$$

$$A_p = A_e A_w = \left(\frac{11.1 \times P_{in}}{\Delta B \cdot f \cdot K'} \right)^{1.143} \tag{6}$$

$$R_m = \frac{F}{\Phi} = \frac{MPL}{\mu_r \mu_0 A_C} \tag{7}$$

$$R_g = \left(\frac{1}{\mu_0} \right) \left(\frac{l_g}{A_c} \right) \tag{8}$$

$$R_{mt} = R_m + R_g \quad (9)$$

$$L = \frac{N^2}{R_{mt}} \quad (10)$$

Equations (1–10) are the formulas of design for transformer and reactor, respectively. Here, P_{in} is input power, P_{out} is output power, η is efficiency, I_{dc} is DC current, $V_{in(min)}$ is minimum input voltage, K_t is topology factor, N_p is number of transformer's primary turns, A_{wp} is primary wire area, J is current density, f is frequency, K_p is core window utilization factor (primary), K_u is total core window utilization factor, A_e is core cross-sectional area, $t_{on(max)}$ is maximum on time, ΔB is change in flux, A_p is area product, and A_W is core window area.

The DC power output from the battery is converted into three-phase AC power by a three-phase inverter using PWM control. The reactor's role is to eliminate harmonics for the AC waveform output from the inverter. The transformer operates like an isolation transformer that separates the PCS from the grid to protect the system when a surge occurs. The reactor winding and primary winding of the transformer can be combined. Therefore, it is possible to design by a shared transformer/reactor structure as shown in Fig. 1b. In this case, the primary winding of the transformer shares with the reactor core and the transformer core. Design of shared transformer/reactor reduces the weight that the coil and supporting structure for the inductor and also saves the amount of space that transformers and reactors.

Figure 2 shows the transformer, reactor and shared transformer/reactor in 3D structure. The purpose of this paper is to compare and analyze the characteristics of transformer, reactor, and shared transformer/reactor, respectively. So, the condition should be the same. Therefore, the analysis of individual models was performed as shown in Fig. 2b, c by removing only each the cores of transformer and reactor in a shared transformer/reactor.

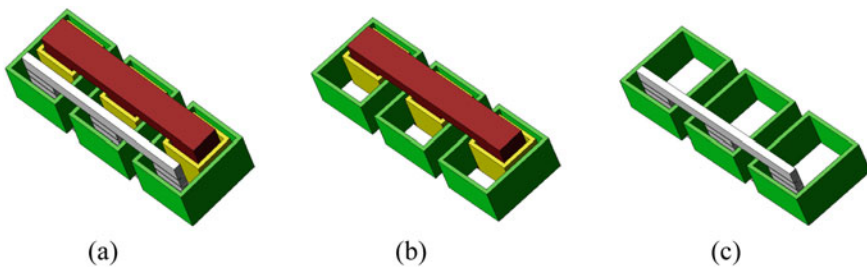


Fig. 2 Trans model shape **a** Shared transformer/reactor, **b** Transformer, **c** Reactor

3 Results of Characteristic Analysis for Transformer, Reactor, and Shared Transformer/Reactor

Characteristic analysis for transformer, reactor, and shared transformer/reactor is performed by FEA. Circuit for transformer is composed delta-delta connection. Also, the transformer is purposed for insulation type. The turns ratio of the primary coil and secondary coil is 1:1. FEA analysis was performed that the load was adjusted so that the output power was 50 kVA. The characteristics analyzed and are voltage, current, inductance of shared coil (primary coil), and saturation flux density at peak current when steady state.

3.1 Results of Transformer and Reactor

The results of transformer characteristics analysis are shown in Fig. 3. The input and output voltage of transformer is about 381 and 380 V_{rms} . The current was about 48 A_{rms} . As a result, output power is 54 kVA and that results show that the specifications are satisfied. The inductance analyzed the primary coil of the transformer. Because parts that require inductance are shared with inductors, inductance is 200mH in primary coil of transformer. The saturation magnetic flux density is 2.14 T, which was not saturated because it was lower than the permissible flux of 2.2 T of core.

The results of reactor characteristics analysis are shown in Fig. 3f. The inductor should be interpreted as a current source to extract the inductance value. Therefore, the same as transformer input current. As a result, inductance is about 7.4 mH.

3.2 Results of Shared Transformer/Reactor

The same specifications and materials were used to compare the characteristics of the transformer and reactor with those of the shared transformer/reactor. The analysis results are shown in Fig. 4. The input and output voltage of the shared transformer/reactor was about 381 and 379 V_{rms} . The input and output current was about 63 and 47.2 A_{rms} . Therefore output power is 53.6 kVA. The saturation magnetic flux density is about 2.15 T. Inductance is 346 mH in primary coil. The characteristics of the shared transformer/reactor are similar to those of the transformer and reactor models. However, there is a 40% difference in inductance. In the case of the shared transformer/reactor model, the gap between the transformer and the reactor core is narrow and interaction occurs with each other. Therefore, the mutual inductance for the shared transformer/reactor model should be considered. Also, consideration should be given to the mutual, flux linkage between the primary coil and the secondary coil.

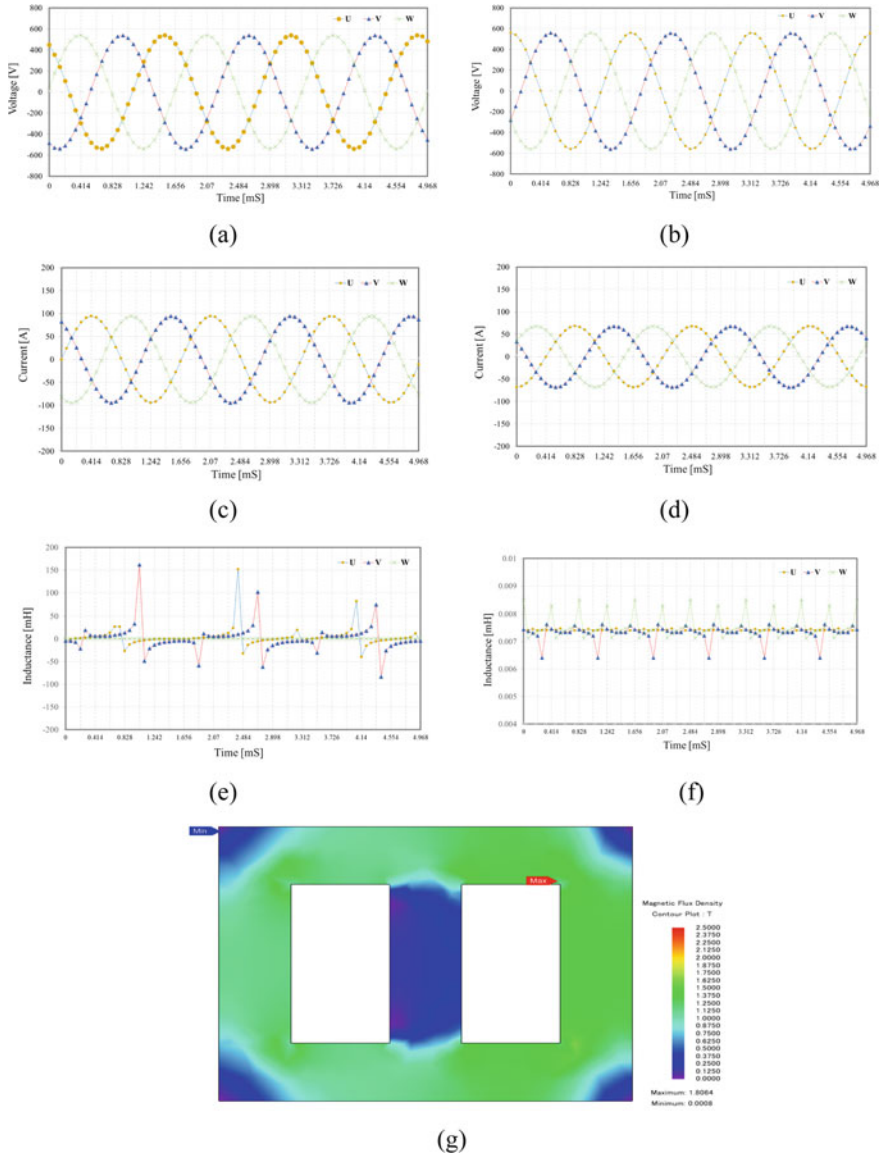


Fig. 3 Analysis of characteristics for transformer and reactor **a** Input voltage, **b** Output voltage, **c** Input current, **d** Output current, **e** Transformer inductance, **f** Reactor inductance, **g** Saturation magnetic flux density

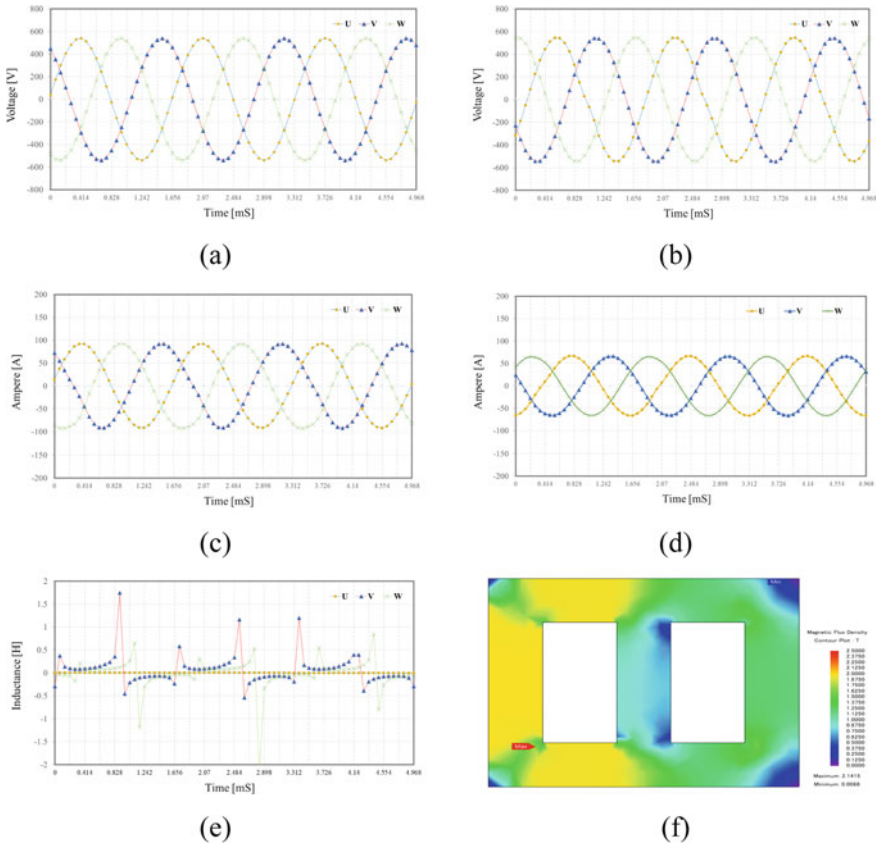


Fig. 4 Analysis of characteristics for shared transformer/reactor **a** Input voltage, **b** Output voltage, **c** Input current, **d** Output current, **e** Shared model inductance, **f** Saturation magnetic flux density

4 Conclusion

This paper revealed a lack of research results on the interrelationship of all-in-one transformers. In the above results, the power of the shared transformer/reactor and the power transformer of the individual transformer were similar. This proves that there is no need to use individual devices in two separate spaces. On the other hand, as the distance between the two devices decreases, changes in inductance and magnetic flux may be problems that need to be solved. Future studies will examine the causes and solutions for the efficiency of shared transformer/reactor transformers in terms of the mutual inductance and magnetic flux.

Acknowledgements This research was supported by the Korea Electric Power Corporation. (Grant number: R18XA06-44).

References

1. Rahbar K, Chai CC, Zhang R (2018) Energy cooperation optimization in microgrids with renewable energy integration. *IEEE Trans Smart Grid* 9(2):1482–1493
2. Munoz FD, Mills AD (2015) Endogenous assessment of the capacity value of solar PV in generation investment planning studies. *IEEE Trans Sustain Energy* 6(4):1574–1585
3. Du E, Zhang N, Hodge B-M, Wang Q, Kang C, Kroposk B et al (2018) The role of concentrating solar power toward high renewable energy penetrated power systems. *IEEE Trans Power Syst* 33(6):6630–6641
4. Holmes J (2013) A more perfect union: energy systems integration studies from Europe. *IEEE Power Energ Mag* 11(5):36–45
5. Byrne RH, Nguyen TuA, Copp DA, Chalamala BR, Gyuk I (2017) Energy management and optimization methods for grid energy storage systems. *IEEE Access* 6(1):13231–13260
6. Koran A, LaBella T, Lai J-S (2014) High efficiency photovoltaic source simulator with fast response time for solar power conditioning systems evaluation. *IEEE Trans Power Electron* 29(3):1285–1297
7. Moon S, Yoon S-G, Park J-H (2015) A new low-cost centralized MPPT controller system for multiply distributed photovoltaic power conditioning modules. *IEEE Trans Smart Grid* 6(6):2649–2658
8. Chou S-F, Lee C-T, Ko H-C, Cheng PT (2014) A low-voltage ride-through method with transformer flux compensation capability of renewable power grid-side converters 29(4):1710–1719
9. Behara S, Sandeep N, Yaragatti UR (2018) Simplified transformer-based multilevel inverter topology and generalisations for renewable energy applications. *IET Power Electron* 11(4):708–718
10. Kim SY, Cho JH, Soo LH, Lee J (2017) 50 kW-class integral transformer/reactor design for solar PCS to improve power density. In: ICEMS. <https://doi.org/10.1109/ICEMS.2017.8056134>

A Proton Exchange Membrane-Based Fuel Cell Integrated Power System



Neeraj Priyadarshi, Farooque Azam, Akash Kumar Bhoi,
and Amarjeet Kumar Sharma

Abstract A fuel cell as electrochemical apparatus can convert chemical energy to electrical power. Recently, proton exchange membrane (PEM)-based fuel cells (FC) are widely used for future advancements. In this research work, PEMFC-based systems have been realized mathematically as well as MATLAB simulation environment which has various socioeconomic advantages. Based on the V-I characteristics of fuel cells, the behavior of fuel cell has been evaluated. Nevertheless, these characteristics are not sufficient to evaluate electrode interfacing mechanism of membrane.

N. Priyadarshi (✉) · A. K. Sharma

Department of Electrical Engineering, Birsa Institute of Technology (Trust), Ranchi 835217, India
e-mail: neerajrjd@gmail.com

A. K. Sharma

e-mail: ermaxamar@gmail.com

F. Azam

School of Computing & Information Technology, REVA University, Bangalore 560064, India
e-mail: farooque53786@gmail.com

A. K. Bhoi

Department of Electrical & Electronics Engineering, Sikkim Manipal Institute of Technology,
Sikkim Manipal University, Masjitar, India
e-mail: akash730@gmail.com

© Springer Nature Singapore Pte Ltd. 2020

A. K. Bhoi et al. (eds.), *Advances in Greener Energy Technologies*,

Green Energy and Technology, https://doi.org/10.1007/978-981-15-4246-6_18

1 Introduction

Fuel cells as a renewable source of energies are treated as future power source. Nowadays, the researchers are taken more intention on sustainable-based eco-compatible technology for future growth as it is clean, effective, and pollution-less behavior [1–7]. The electrical power can be generated by oxidizing hydrogen gas and can be used for distributing generation, transportation, portable as well as automotive applications. Because of its higher energy density, efficiency and working on lower operated temperature [8–11]. Because of the depletion of conventional energy sources, the demand for fuel cell-based renewable energy sources has been increased in past decades. The fuel cell-based renewable technology has low polluting products with unlimited fuel cell supply which makes this technology more efficient. Moreover, this technology moves near to commercialization which fulfills required power demand globally with higher efficiency and environmental friendliness.

In this paper, the complete mathematical expressions governing electrolytic membrane, layer of cathode catalyst, backing of electrode with flow channel have been described which explain the working of single polymer electrolyte membrane fuel cell. Electrical empirical model as well as transient electrical response has been discussed for finding PEM output and PEMFC responses, respectively. Additionally, power flow, transient responses, and efficiency have been realized with varying loading conditions by designing simpler PEMFC mathematical modeling.

2 Equivalent Circuit of PEMFC

PEMFC comprises of charged double layer at the top of cathode terminal of fuel cell which provides simpler design of the equivalent network and electric capacitor works as charged layer nearer to interfaced electrolytic electrode responsible for charge and energy storing as shown in Fig. 1.

Equivalent resistance (R_a) is the summation of activation (R_{act}) as well as concentration equivalent resistance (R_{con}). Also, equivalent capacitance (C) provides smother potential differences along R_a . Mathematically, the dynamic behavior of single fuel cell can be derived by considering v_d entire voltage drop across R_a as:

$$\frac{dv_d}{dt} = \frac{i}{c} - \frac{v_d}{\tau} \quad (1)$$

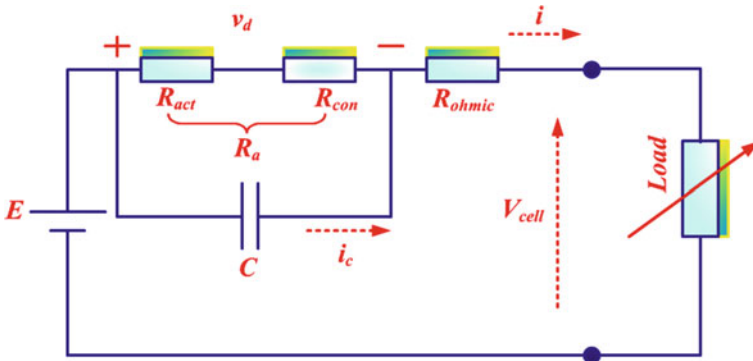


Fig. 1 Equivalent PEMFC network

Here time constant (τ) varies as per varying loading condition and affecting the transient voltage. Also, R_a can be expressed as association of activation losses, concentration losses, and current (i_c) and value of C is not taken in account in steady-state conditions as:

$$\tau = CR_a = \frac{C(V_{act} + V_{con})}{i - i_c} \tag{2}$$

Also, the voltage across PEMFC can be expressed mathematically by taking thermal characteristic, momentum characteristic, and the mass transportation into account as:

$$V_{cell} = E_{nernest} - V_{ohmic} - V_d \tag{3}$$

Stack output voltage can be evaluated by combining N identical individual fuel cells as:

$$V_{stack} = NV_{cell} \tag{4}$$

The output power of PEMFC expressed as:

$$P_{stack} = V_{stack}i \tag{5}$$

The power consumed by the polymer electrolyte membrane fuel cell stack is

$$p_{consumed} = (V_d + V_{ohmic}) \tag{6}$$

The efficiency of PEMFC is calculated as:

$$\eta = \frac{i V_{\text{stack}}}{E_{\text{nernest}} i} = \frac{V_{\text{stack}}}{E_{\text{nernest}}} \quad (7)$$

3 Mathematical Model Calculations

Fuel cell output can be expressed empirically and mathematically based on polymer electrolyte membrane fuel cell output characteristics according to Amphlettetal and Kimetal.

$$V_{\text{cell}} = E_{\text{nernest}} - V_{\text{act}} - V_{\text{ohmic}} - V_{\text{con}} \quad (8)$$

The activation loss of polymer electrolyte membrane fuel cell can be generated by slow kinetic reactions occurred at electrode active surface and mathematically derived as:

$$\left. \begin{aligned} V_{\text{act}} &= \xi_1 + \xi_2 T + \xi_3 T [\ln(\text{CO}_2)] + \xi_4 T [\ln(i)] \\ \xi_1 &= -\frac{\Delta G_c}{2F} - \frac{\Delta G}{\alpha_c n F} \\ \xi_2 &= \frac{RT}{\alpha_c n F} \{ \ln [n F A K_c^0 (C_{\text{H}^+})^{1-\alpha_c} (C_{\text{H}_2\text{O}})^{\alpha_c}] \} \\ \xi_3 &= \frac{R(1 - \alpha_c)}{\alpha_c n F} \\ \xi_4 &= -\left(\frac{R}{2F} + \frac{R}{2F} \right) \end{aligned} \right\} \quad (9)$$

$$\text{CO}_2 = \frac{\text{PO}_2}{5.08 \times 10^6 \exp(-498/T)} \quad (10)$$

Total ohmic resistance is the combination of equivalent membrane impedance (R_M), and contact resistances (R_c) and potential difference produced by ohmic losses are described mathematically as:

$$V_{\text{ohmic}} = i R_{\text{ohmic}} = i (R_M + R_c) \quad (11)$$

4 Simulation Results

This section explains, in detail, the modeling and simulated response of the proposed PEMFC-based fuel cell using MATLAB/Simulink simulation software. Fuel cell power system has been designed by using different tool parameters in which fuel current and voltage are treated as input and output models, respectively. Steady and dynamic models are designed by assuming isothermal and impedance transfer connected in shunt to the nonlinear model of steady state, respectively.

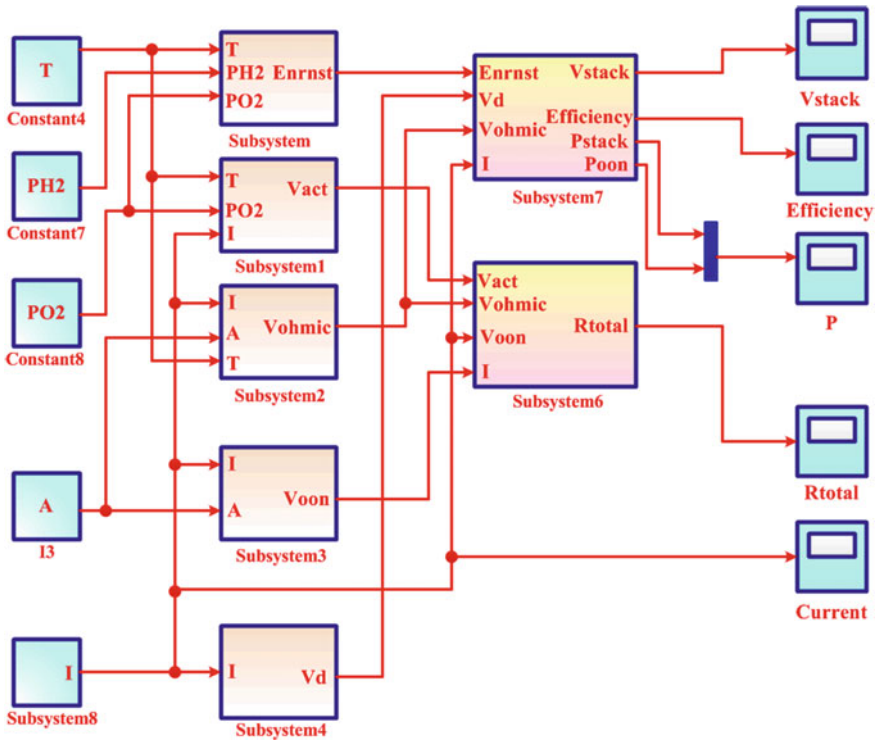


Fig. 2 Dynamic model simulation PEMFC diagram

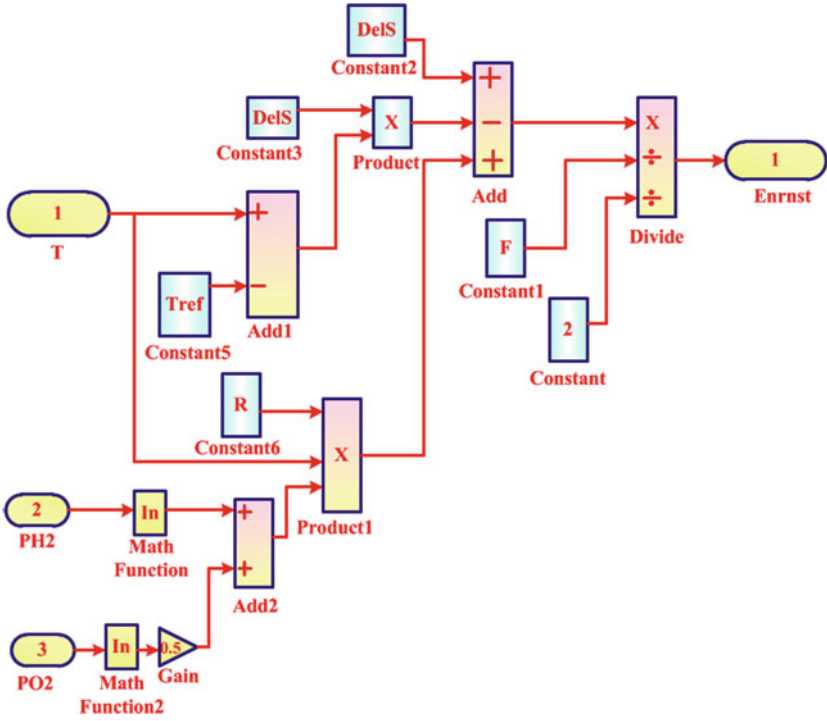


Fig. 3 PEMFC of electrode potential

4.1 Dynamic Model Simulation

Figure 2 depicts the dynamic model of PEMFC which can be designed using mathematical and empirical derivations. Figures 3, 4, 5, 6, 7, 8 and 9 depict the designed Simulink PEMFC models using mathematical derivations of electrode potential, Activation losses, Ohmic losses, concentration losses, voltage drop, output power, efficiency, voltage, resistance for performance evaluation which are optimizing the accurate modeling of system designed.

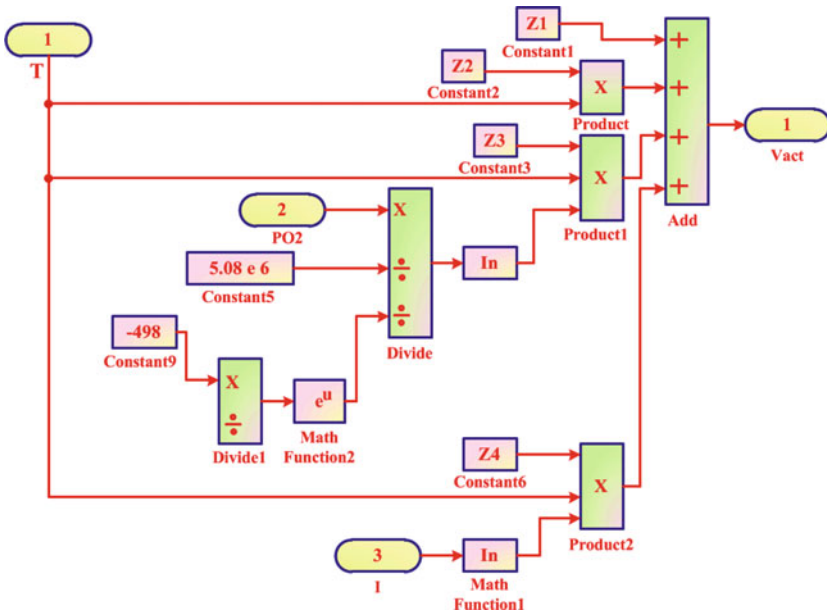


Fig. 4 PEMFC activation losses

5 Conclusion

This research work explained, the complete mathematical expressions governing electrolytic membrane, layer of cathode catalyst, backing of electrode with flow channel has been designed and modeling, and simulated response of the proposed PEMFC-based fuel cell using MATLAB/Simulink simulation software has been presented. Fuel cell power system has been designed using different tool parameters and electrode potential, activation losses, Ohmic losses, concentration losses, voltage drop, output power, efficiency, voltage, resistance models of PEMFC have been realized effectively using Simulink environment.

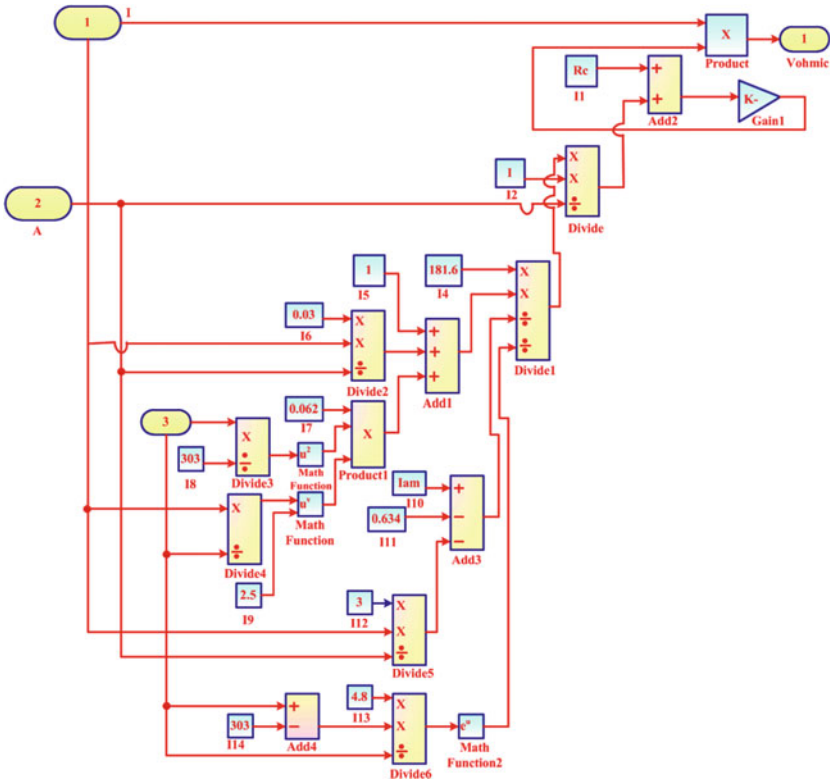


Fig. 5 PEMFC ohmic losses

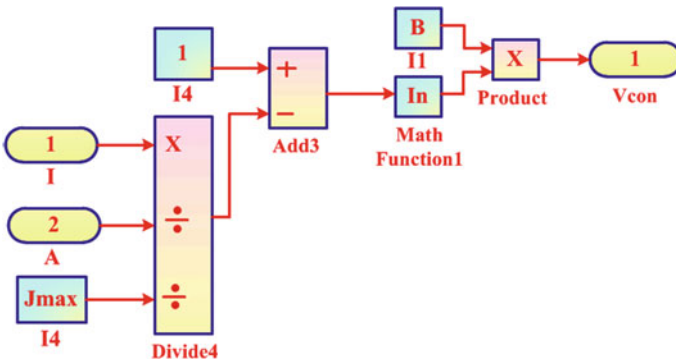


Fig. 6 PEMFC concentration losses

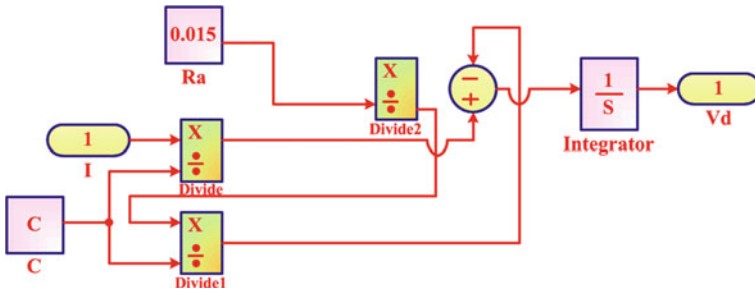


Fig. 7 PEMFC voltage drop

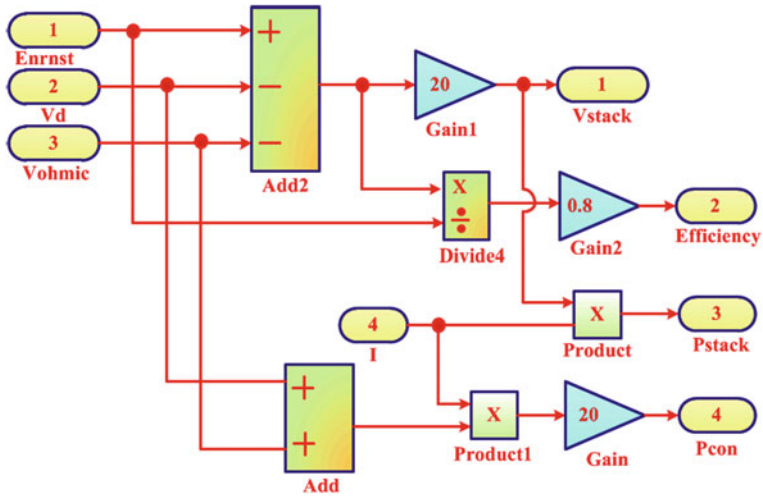


Fig. 8 PEMFC output power, efficiency, voltage

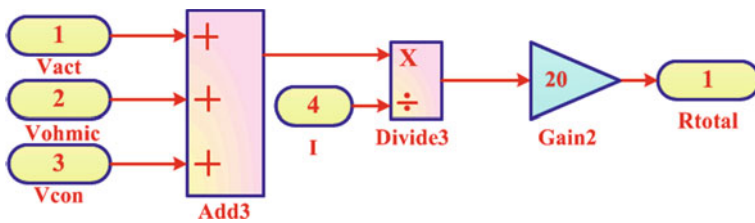


Fig. 9 PEMFC resistance

References

1. Abderazak L, Dezso S, Josep MG, Laszlo M, Aissa B (2018) Discrete model predictive control-based maximum power point tracking for PV systems: overview and evaluation. *IEEE Trans Power Electron* 33:7273–7287
2. Nishant K, Ikhlaiq H, Bhim S, Bijaya KP (2017) Rapid MPPT for uniformly and partial shaded PV system by using Jayade algorithm in highly fluctuating atmospheric conditions. *IEEE Trans Ind Info* 13:2406–2416
3. Priyadarshi N, Anand A, Sharma AK, Azam F, Singh VK, Sinha RK (2017) An experimental implementation and testing of GA based maximum power point tracking for PV system under varying ambient conditions using dSPACE DS 1104 controller. *Int J Renew Energy Res* 7(1):255–265
4. Priyadarshi N, Kumar V, Yadav K, Vardia M (2017) An experimental study on zeta buck-boost converter for application in PV system. In: *Handbook of distributed generation*. Springer, Cham. DOI https://doi.org/10.1007/978-3-319-51343-0_13
5. Priyadarshi N, Sharma AK, Priyam S (2018) An experimental realization of grid-connected PV system with MPPT using dSPACE DS 1104 control board. In: *Advances in smart grid and renewable energy*. Lecture notes in electrical engineering, vol. 435, Springer, Singapore
6. Priyadarshi N, Sharma AK, Azam F (2017) A hybrid firefly-asymmetrical fuzzy logic controller based MPPT for PV-wind-fuel grid integration. *Int J Renew Energy Res* 7(4)
7. Priyadarshi N, Sharma AK, Priyam S (2017) Practical realization of an improved photovoltaic grid integration with MPPT. *Int J Renew Energy Res* 7(4)
8. Nishant K, Ikhlaiq H, Bhim S, Bijaya KP (2017) MPPT in dynamic condition of partially shaded PV system by using WODE technique. *IEEE Trans Sustain Energy* 8:1204–1214
9. Ahmed ASM, Alberto B, Osama AM (2017) Design and hardware implementation of FLMPPT control of PV systems based on GA and small-signal analysis. *IEEE Trans Sustain Energy* 8:279–290
10. Priyadarshi N, Padmanaban S, Mihet-Popa L, Blaabjerg F, Azam F (2018) Maximum power point tracking for brushless dc motor-driven photovoltaic pumping systems using a hybrid ANFIS-flower pollination optimization algorithm. *MDPI Energies* 11(1):1–16
11. Hong L, Duo Y, Wenzhe S, Jinhu L, Xinghuo Y (2019) An overall distribution particle swarm optimization MPPT algorithm for photovoltaic system under partial shading. *IEEE Trans Ind Electron* 66:265–275

Application of IoT in Green Computing



T. Poongodi, S. R. Ramya, P. Suresh, and Balamurugan Balusamy

Abstract The Internet of things (IoT) enables global connectivity over the world-wide physical objects. The world is made smart with the development of science and technology, by people collaborating automatically with heterogeneous devices. The exchange of massive information between the devices gives rise to enormous energy requirements. The IoT is interconnected to big data analytics and cloud computing to predict the behavior of smart devices, provide useful business insights, and act as a feedback control. In addition, most of the organizations would adapt to the growing interest of smart world which in turn energy demand increases more rapidly. Moreover, there is a never-ending increase in number of vendors and users of various technologies. Green IoT prominently focuses on reducing the environmental problems and creating a sustainable environment related to IoT. It has been emphasized that the utilization of energy-efficient technologies in IoT either reduces the impact of greenhouse gases or inhibit greenhouse effect in various IoT applications. Green IoT assists in maintaining the climatic condition by introducing low energy consumption devices or electrical appliances, minimizing greenhouse gas emissions, utilizing carbon-free materials, and promoting reusability. In order to achieve sustainable environment, an outline of Green IoT and its applications are described in the perspective of minimizing the energy utilization in IoT. The designing of green data centers, sensor network, and cloud computing is discussed with certain policies in order to save energy. In addition, the different Green IoT strategies are analyzed

T. Poongodi (✉) · B. Balusamy

School of Computing Science and Engineering, Galgotias University, Greater Noida, Uttar Pradesh, India

e-mail: tpoongodi2730@gmail.com

B. Balusamy

e-mail: kadavulai@gmail.com

S. R. Ramya

Department of Computer Science and Engineering, PPG Institute of Technology, Coimbatore, Tamil Nadu, India

e-mail: srramyacse@gmail.com

P. Suresh

School of Mechanical Engineering, Galgotias University, Greater Noida, Uttar Pradesh, India

e-mail: psuresh2730@gmail.com

© Springer Nature Singapore Pte Ltd. 2020

A. K. Bhoi et al. (eds.), *Advances in Greener Energy Technologies*,

Green Energy and Technology, https://doi.org/10.1007/978-981-15-4246-6_19

and the principles that can be adapted to attain Green IoT also discussed. Finally, various applications of IoT are described such as smart home which allows the user to control the smart devices like automated doors, smart locks, security cameras, electrical appliances with the application on a smart phone or any other connected devices. Smart e-health is useful in monitoring and tracking patients, and smart city assists people by interconnecting systems, thereby offers required services in order to provide a smarter view for the present scenario and which in turn makes the IoT greener.

Keywords Green IoT · Sensor objects · Cloud computing · Smart world · RFID · Data center

1 Introduction

The Internet of things (IoT) aims to connect the physical world with the digital world with the help of sensors and actuators that sense, collect, and transmit information from the environment through the Internet. The world is become smart with the development of science and technology, by collaborating people automatically with various devices. It provides an opportunity for devices to be seamlessly connected and provide intelligent insights into human beings [1–5]. In particular, all the devices will be equipped with secondary sensors and additionally, so that they can respond to each other, thereby requiring more energy. Most of the devices have embedded radio-frequency identifier (RFID) tags through which the data is transmitted. In recent years, there is an increase in the sales of RFID and they seem to grow exponentially. The exchange of massive information between the devices gives rise to enormous energy requirements [6, 7]. The Internet of things is interlinked to big data analytics, cloud computing to predict and analyze the behavior of smart devices which provide useful business insights and acts as a feedback control. Cloud computing enables the interaction and integration of data in the cloud. In addition, most of the organization would adapt to the growing interest of smart world and the energy demand increases more rapidly. It is predicted by 2025, the IoT nodes may reside in everything like food packages, furniture, paper documents, and so on. However, for a smart world as such to be sustainable, energy efficiency should be considered.

In the recent years, the utilization of ICT has grown up rapidly and several areas getting better life with numerous benefits. The widespread adoption and advances in ICT have contributed to environmental problems where most of the people are unaware of it. All IoT devices consume significant amount of energy placing a great burden on electric grids and greenhouse gases. The constant increase in the accumulation of greenhouse gases has changed weather patterns and the world's climate causing drought in some regions and floods in others. The global temperatures are slowly pushed higher, posing serious problems to the world. Global data depicts the weather-related disasters—storms and droughts occur more frequently and have increased in magnitude. To inhibit the collection of greenhouse gases in the earth zone, global

emissions should be prevented in further increasing. Furthermore, energy is also a major cause in the environmental change, as coal or oil that helps to produce power releases such as carbon dioxide, pollutants, and harmful chemicals into the environment. Thereby, reducing electric power consumption would pave a way for the reduction of CO₂ emissions that have an acute impact on global warming and the environment. Nevertheless, CO₂ emissions cause respiratory diseases and acid rain. Hence, on the roadmap of moving toward Green IoT, state-of-the-art technologies and practices that satisfy the energy hunger and billions of devices have to be evolved more.

Moreover, there is a never-ending increase in number of vendors and users of various IoT technologies. Green IoT can be assisted by formulating green policies and regulations, which stimulate the interest in users to use green products. Nevertheless, to build a green environment, the old way of doing things has to be eradicated and new adaptable methodologies have to be defined. Furthermore, Green IoT comprises the dimension of environmental inter-dependability, cost-effectiveness of energy efficiency, and the total cost of ownership which includes the cost of removal and recycling.

1.1 Internet of Things

Internet of things is a computing device that connects physical objects to the Internet, and it is capable to convey the identity to other devices. It includes sensor technologies, RFID, and wireless technologies. Moreover, it carries an immense amount of information that is helpful to make intelligent decision making and it enables security, resilient, convergent, efficient, and transparent in operations.

According to Cisco report, the number of interconnected devices will reach 50 billion by 2020 and the Gartner IoT estimates that IoT will have 26 billion units by 2020. The general view of IoT key elements is given in Table 1 where data is collected from the target, processed, and analyzed to offer intelligence services to the users. The hardware segment refers to the interconnection of sensors, actuators, or any embedded hardware that is used for communication such as RFID [8–10].

Sensors are devices that convert physical parameter to electrical output, whereas actuators are the devices that convert electrical signal to physical output. Wireless

Table 1 General view of IoT key elements

Elements	Description
Hardware	Embedded hardware, sensors, actuators, tags
Middleware	Data storage, computing, and context awareness
Internet	Provide communication anytime, anywhere between everything
Presentation	Processing, interpretation, and visualization of data

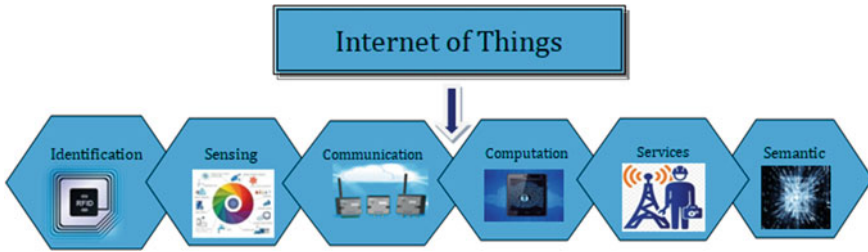


Fig. 1 Elements of Internet of things

sensor networks play a key role in the hardware layer. Middleware refers to the cloud environment, where data is being stored, processed, and various analyses are performed on the data to gain useful insights. Nevertheless, recent advancements in technology have brought forth fog computing and edge computing, where data can be processed locally to avoid latency and fast processing. On the other hand, the presentation segment interprets and visualizes the data in a form that is understandable by the user. The Internet segment is responsible for communication and cooperation between various segments anytime, anywhere, and between everything that is connected to the Internet of things. The six common elements in IoT are described, and it is shown in Fig. 1.

Identification: IoT provides an interaction among users and things where devices have to be uniquely identified to enable the interaction within a specific context, for instance, ubiquitous code (ucode), Electronic Product Code (EPC), radio-frequency identifier (RFID), automatic identification and data capture (AIDC), Host Identity Protocol (HIP), etc.

Sensing: The sensors collect data and share it with the connected devices in the network. It makes devices to function automatically, and the entire ecosystem becomes “smarter.” The sensing devices can sense the temperature, humidity, proximity, pressure, water quality, chemical, gas, physical movement, acceleration, angular velocity, light rays, etc.

Communication: Communication technologies interrelate heterogeneous objects together to provide the various set of services. The protocols for communication in IoT can be Bluetooth, IEEE 802.15.4, LTE-Advanced, Wi-Fi, ultra-wide bandwidth (UWB), near-field communication (NFC), etc.

Computation: The software applications and hardware processing units (micro-processor, microcontroller, system on a chip (SoC), and field-programmable gate arrays (FPGAs)) perform the computational task. Various hardware platforms such as UDOO, Raspberry Pi, Arduino, Gadgeteer, and software platforms, such as RIOT OS, LiteOS, TinyOS, are used.

Services: IoT services are categorized into four types: information aggregation services, identity-related services, collaborative-aware services, and ubiquitous services. Identity-related services provide the base for other types of services, which help in relating the real-world objects to the virtual world.

Semantics: It is essential to extract the knowledge meaningfully so that the desired services can be offered. The steps involved in semantics are to discover and utilize resources, model and analyze the data. Some of the commonly used semantic technologies are Efficient XML Interchange (EXI), Resource Description Framework (RDF), Web Ontology Language (WOL), etc.

IoT offers a framework for interconnecting devices to permit the communication seamlessly. Most of the IoT applications are highly focused on the middleware layer of IoT architecture for information processing. Initially, IoT architecture is basically designed as a three-layered architecture which comprises of perception, network, and application layers. Further, it has been extended to five-layered architecture, where the basic architecture is not ample to face challenges of various IoT applications. The five-layered IoT architecture is shown in Fig. 2 which includes perception, network, middleware, application, and business layer.

1. Perception layer: The perception layer also known as device layer consists of different physical objects and sensor devices. The sensor devices can be the 2D barcode, RFID, or infrared sensor depends on object identification method. Such sensor device in this layer identifies the object, senses the environment, and collects information about the identified object. Any other smart objects can also be identified by sensing some physical parameters in the same environment. The gathered information is about location, vibration, motion, orientation, temperature, chemical changes, acceleration, humid level in the air, etc., depending on the type of sensors, and it is sent to the network layer for transmission.
2. Network layer: The network layer is also called as “transmission layer.” The main functionality of this layer is to interconnect different network devices,

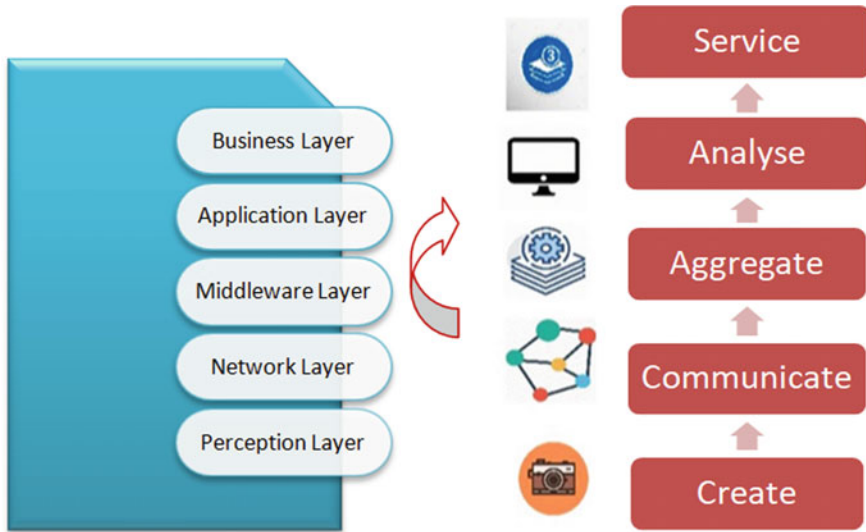


Fig. 2 IoT architecture

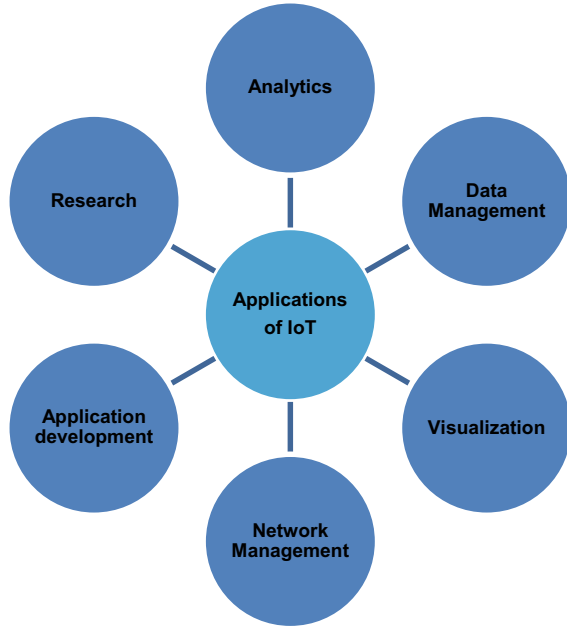
smart objects, and servers. It transmits and processes the data which is gathered already from sensor devices. The transmission medium can be either wired or wireless, and the technology can be infrared, Wi-Fi, Bluetooth, ZigBee, 3G, etc. Further, the information is transmitted to the processing layer.

3. **Middleware layer:** It is the main “processing layer.” The middleware layer stores, analyzes, and processes a large amount of data which is received from the network layer. The responsibility of this layer also lies in the service management and sustaining the connection with the database. Since it is behaving as the middle layer, the devices in IoT provide various services to the lower layers. The devices can be connected and communicated easily with the devices that are designed to provide the same type of services. It may be interlinked with various technologies like big data, cloud computing, and databases for processing the huge volume of information. It plays a major role in automatic decision making, ubiquitous computation, and information processing. Processing layer gathers and stores the information received from the network layer.
4. **Application layer:** The main responsibility of the application layer is to deliver application-oriented services to the IoT end users. This layer directly communicates with the end-user application with its application layer protocols.
5. **Business layer:** Finally, the business layer has a control over the entire IoT system including business models, user’s privacy, and applications. Based on the information received from the previous layer, it deals with the formation of different business models, graphs, flowcharts. Moreover, for IoT technology the real achievement lies in well-constructed business models. After analyzing data, the business layer helps in decision making about upcoming activities and business strategies.

The key technologies involved in IoT are RFID, M2M, WSN, addressing schemes, data storage, and visualization. In general, IoT has various application domains such as data analytics, data management, visualization, network management, application development, and research as shown in Fig. 3. Application development refers to the launch of IoT-enabled products by the industry. With the hype around IoT, many applications that ease the day-to-day life of humans, namely smart home, wearables, smart grids, connected cars, smart health, smart retail, smart supply chain, smart agriculture, smart city, have been introduced and developed. With the advent of many useful IoT products, frequent communication happens between the things or devices are the key elements of application design and development.

The network management domain plays a vital role in establishing the mode of communication that has to be deployed between various entities involved. The network could be wireless or wired, and in most of the scenarios, a hybrid model of both wired and wireless communication is used. The key technologies used are Bluetooth Low Energy (BLE), ZigBee, Z-Wave, Wi-Fi, near-field communication (NFC), LoRaWAN, and cellular communications—GSM, 4G, 5G. Initially, data transmission was event-driven but today data is transmitted periodically. Thereby, there is a constant increase in the quantity of data that is being generated every second. Data management refers to the adaptation of state-of-the-art technologies on

Fig. 3 Application domains of IoT



handling data. Many cloud vendors provide infrastructure and storage capabilities. Nevertheless, the major concern is on how the data is to be stored as the information transmitted from IoT devices come in various formats and varying sizes. Managing the immense amount of data is still a challenge that needs to be addressed. Data analytics is a domain that has attracted interest toward many academicians. The primary element in apprehending data analytics includes the datasets that are generated by sensors. Clustering, classification, and predictive analytics can be performed on data depending on the application use cases. Visualization deals with presenting the analyzed data in a format that is understandable and convenient to the user in the form of graphs or tables. All the above-mentioned application domains of IoT have involved significant research attraction in the past decades. Current research and development are focused on transforming IoT to Green IoT for sustainability and providing an eco-friendly environment [11, 12].

1.2 Green Computing

With the increase in number of devices, subscribers and digital content, the rise in energy utilization level is also obvious. It is expected that the number of connected devices will be around 50 billion by 2020 and 100 billion by 2030. There is an exponential increase in the amount of data generated, thereby increases the levels of carbon dioxide as well. The literature reveals that 345 million tons of CO₂ will

be emitted by cellular devices in 2020 and the same will increase in the decades to come. Tremendous emissions of CO₂ are a threat to the environment and poses health hazards. Therefore, to ensure the sustainability of the environment and make the world a better place to live in all computing capabilities have to be made green. Green computing also focuses on various domains such as energy-efficient computing and power management, design and layout out of data center with server virtualization, responsible removal and recycling, green metrics assessment tools and methodology, usage of renewable sources of energy, environmental-related risk mitigation, and regulatory compliance [13].

2 Green IoT

To create a sustainable environment, IT sector and in fact every computer user should green their devices and the way the devices are used. Green IoT uses energy-efficient technologies either to reduce the impact of greenhouse gases or to inhibit the greenhouse effect in IoT applications. In the former case, the effect of greenhouse gases will be reduced [14–18].

On the other hand, the later would optimize IoT. Thereby, from the design to implementation of IoT everything should be green. Framework for Green IoT is discussed and may be implemented with Green RFID tags, data centers, sensor network, cloud computing. Using Green IoT, the greenhouse gas emission is lowered, and energy efficiency is improved by the utilization of less harmful materials and encouraging reuse and recycling. The large-scale consumption of energy resources consumed by IoT to make our lives easy and sustainable on this planet has to be efficiently handled. It is predicted to change the human's life in the future and would definitely lead to a green and smart environment which is shown in Fig. 4. Green IoT provides low carbon solutions and sustainability.

Green IoT is gaining more attention as the usage of energy is increasing and the available energy resources are decreasing rapidly. Different strategies are used to conserve energy in smart buildings, and the data is gathered with IoT devices [19]. It is inferred that an enormous amount of energy can be saved if the air-conditioning and ventilation strategies are efficiently implemented in the described systems. Wireless sensor network (WSN) plays a significant role in the deployment of IoT devices. In [20], the list of techniques with various environmental resources is described to conserve energy in WSN. Yet, instead of batteries if the different medium is used for storage it could improve energy efficiency. Data center is a vital component in energy-efficient IoT-based WSN. In the proposed system [21], orchestration agent (OA) in a client–server model is designed for context evaluation of servers in terms of resource consumption and the designated server manages data centers. The chosen server transmits the processed information to client systems. OA is installed on each device of client and server sides to ensure reliability, which automatically leads to high energy consumption.

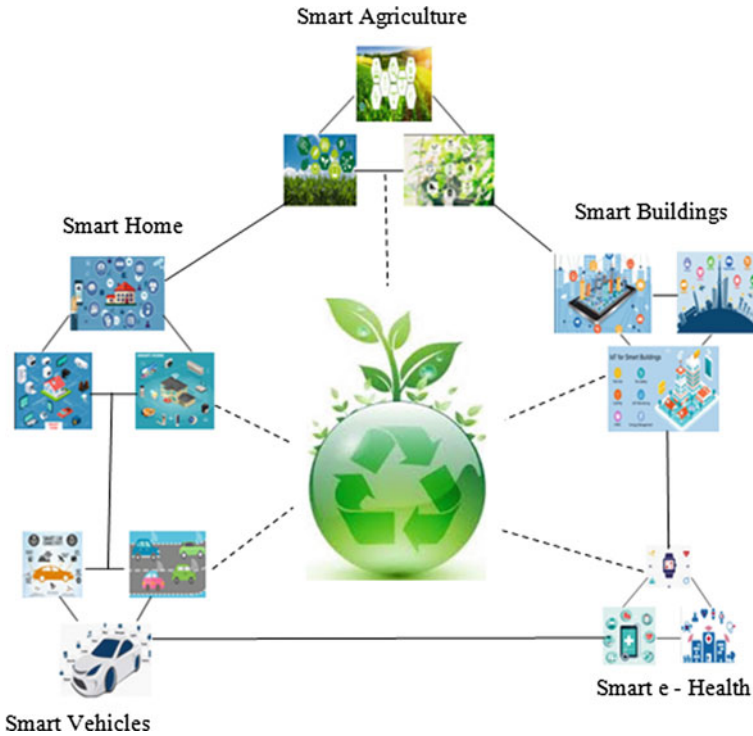


Fig. 4 Green Internet of things

In [22], C-MOSDEN is proposed as a context-aware sensing platform which implements selective sensing to obtain energy efficiency. However, it reduces the energy consumption but creates overhead and the model can be efficient if the overhead is minimized. An efficient scheduling algorithm is proposed to conserve energy in sensors if they are idle but are switched on. Reconfiguring virtual objects (VO) during run-time on three different operating modes, such kind of energy-efficient model is proposed. To estimate the energy consumption of the operating modes, analytical model was introduced and the outcome of one mode is resulted in 47.9% less energy consumption than the other. A green and scalable IoT is proposed to deploy IoT on a very larger scale, minimal consumption algorithm, and an optimized model supports the model to operate an energy-efficient way. The system works well with heterogeneous networking environment and achieves better level of energy efficiency [21]. Nowadays, medical industry prefers IoT devices to store real-time data of patient's due to its scalability and robustness [23]. In [24], dynamic packet downloading algorithm with cloud storage and access point (AP) is proposed for energy-efficient data communication. If APs are equipped with passive RFIDs for generating its own energy instead of battery-powered, the consumption of energy can be considerably reduced. In case of smart phones, sensing power is a major driving

force in the emerging IoT sector even though the energy efficiency in mobile devices is a challenging issue. A novel solution is proposed in [7], uses prediction models, resource behavior analysis, and data logging records data in various aspects such as contexts, applications, time, and location to predict the consumption of energy in smart phones.

2.1 Green IoT Principles

Green IoT is an emerging technology in ICT research as the energy requirement raises exponentially and the traditional sources of energy are depleting. The following principles are suggested to achieve the benefits in Green IoT:

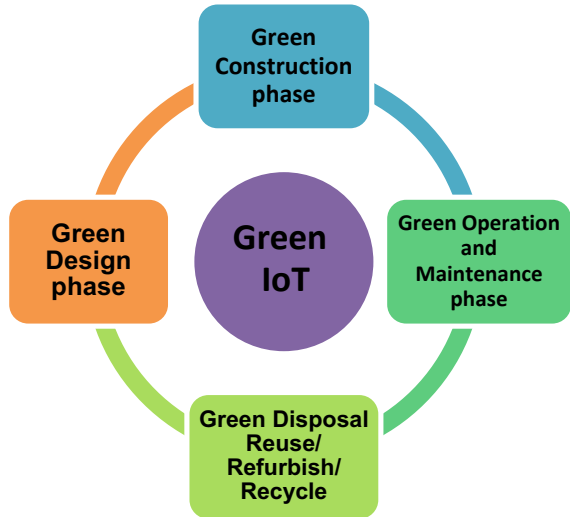
1. **Reduced network size:** Nodes have to be efficiently placed in the network and efficient routing mechanisms have to be used to save energy.
2. **Selective sensing:** It collects only required relevant data, thereby eliminates unwanted or irrelevant data energy loss.
3. **Hybrid architecture:** Deploy passive and active sensors depending on the application can reduce energy.
4. **Policy making:** Effective policies have to be framed to reduce energy consumption in various IoT application areas such as smart buildings.
5. **Intelligent trade-off:** Trade-off must be chosen based on the scenario. Cost, communication, and processing have to be intelligently prioritized.

2.2 Green IoT Architecture

Green IoT focuses on the three main concepts, namely design, leverage, and enabling technologies. In the design phase, the technologies such as energy-efficient devices, network architectures, communication protocols, and interconnection are considered. In the leveraging phase, it refers to how to enhance the energy efficiency and minimize carbon emissions. By enabling green ICT technologies, Green IoT preserves natural resources by reducing hazardous emissions, energy, pollution, and resource consumption. Hence, Green IoT focuses on green design, green construction, green operation and maintenance, and green disposal.

To effectively notify the environmental impact of IoT, a holistic approach that addresses all issues must be formulated. In general, with the moving pace of technology and adaptation to the latest improvements in the field of ICT, the number of connected devices increases gradually. Nevertheless, energy consumption needs to be reduced for the reliability of Green IoT. By focusing on the above principles, total environmental sustainability can be achieved. Figure 5 shows the lifecycle of Green IoT, which has four phases—green design, green construction, green operation and

Fig. 5 Life cycle of Green IoT



maintenance, and green disposal such that the impact of environmental hazards could be minimized and the phases are described below in detail.

1. **Green design:** Component design should focus on the use of environment-friendly materials to be implemented in design. Hardware and software characteristics of the key components of an IoT system such as RFIDS, devices, sensors, and actuators that are the key role players of an IoT system should be designed to minimize resource utilization and produce less heat without reducing the performance. Hardware components could be reduced in size while the software characteristics ensure environment sustainability.
2. **Green construction:** IoT devices and sensors that are manufactured should be environment-friendly and the components must be made of biodegradable materials. As the number of devices grows rapidly, the construction sector ensures the compliance of green products. Standards and policies have to be framed for assessing the durability and quality of the components. All manufacturing firms should use only biodegradable materials and follow the efficient design.
3. **Green operation and maintenance:** Energy consumption of all devices should be reduced. Devices can be programmed to automatically power down, when they are not being used. Moreover, power saving mode can be established as the default mode must be enabled to reduce the emission of greenhouse gases. Utilization of IoT components can be significantly enhanced by making simple changes in the way it is used. Sensors can work on the principle of “awake and sleep” to prolong its lifetime. Moreover, energy consumption of the devices has to be reduced to minimize the impact of hazardous gases in the environment. The energy cost savings as per component may not seem much, whereas the cost of collective components within an enterprise would not be considered in determining the cost.

4. **Green disposal:** Recycling is the method of applying some technology to the existing devices or materials in order to remake the same device or some other devices. Old devices and equipment should be recycled and refurbished to reduce the amount of electronic wastes. In China, the rate of recycling of mobile phones is very less, since most of the devices are reused in the secondhand market which does not affect the environment. Around 15% of mobile phones are recycled in industrialized countries.

Green recycling refers to the use of recyclable materials in the manufacture of IoT devices. For instance, let us consider a mobile phone which is a commonly used device, and it contains copper, plastic, and some non-biodegradable elements. As per the survey conducted in Australia, it is found that 23 million mobile phones are no longer usable. Moreover, 90% of materials used in the manufacture of mobile phones are recyclable. The need for recycling increases and automatically reduces the energy consumption and the effect of greenhouse gases. Electric and Electronic Equipment (EEE) recently introduced the recovery and collection of metals that come under EEE-type. Furthermore, the use of solar energy for charging has been proposed by authors in that around 20% of the consumed energy is reduced [25].

2.3 Green IoT Technologies

The technologies that are pushing Green IoT forward are shown in Fig. 6. These are the major enablers and begin right from design to recycling as discussed in the Green IoT lifecycle.

Fig. 6 Green IoT technologies

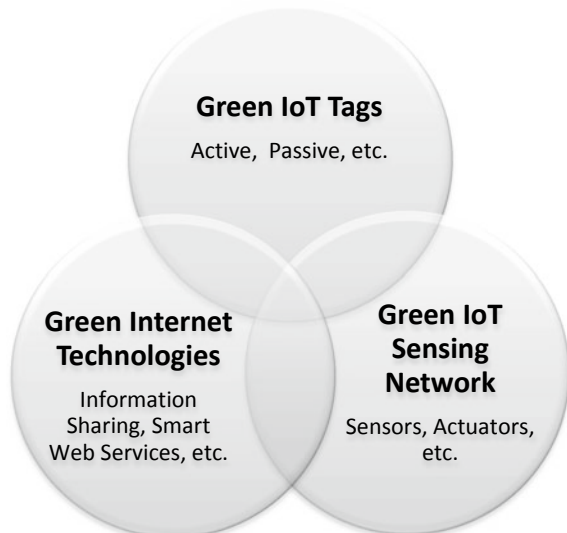


Table 2 Functionalities of sensing network

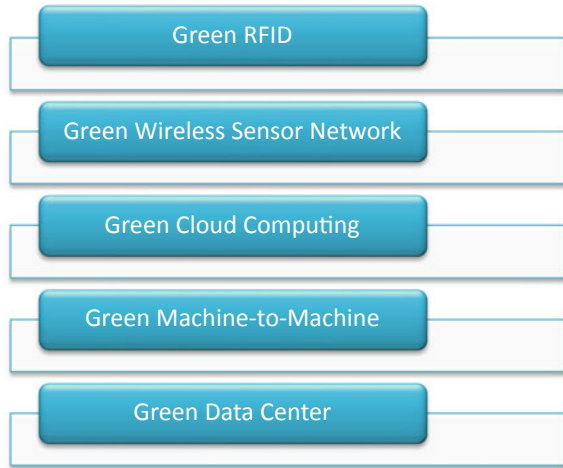
Sensing network	Functionalities
WPAN	Low range wireless network for connecting devices within the workspace of an individual
WBAN	Wearable or portables sensors and actuators are placed inside the body
HAN	A local area network that connects the devices in the vicinity of a home
NAN	Wi-Fi hotspots and wireless local area networks that allow users to connect to the Internet with low cost

1. Green tags: These are biodegradable RFID tags that are reduced in size to minimize the amount of non-biodegradable materials. In addition, there are various protocols which are designed to achieve energy efficiency. The RFID could be active, where the tags are powered by a battery, and they transmit data automatically, where passive RFID tags do not require to be powered by a battery; they transmit data only when they receive energy from an RFID Reader and work on the principle of induction.
2. Green sensing network: Sensing networks include WSN, wireless personal area network (WPAN), wireless body area network (WBAN), home area network (HAN), neighborhood area network (NAN). The functionalities of different sensing network are described in Table 2. The sensing network should employ energy management techniques by enabling power saving mode. Moreover, the size of the data may be reduced for efficient storage mechanism and conservation of electric power. Moreover, it is expected that 5G will appear in 2020 and handle mobile data 1000 times faster than the present cellular systems. It would link fixed and mobile devices at affordable rates with reliability leading to an economic industrial revolution. However, there are emerging challenges that need to be resolved in the horizon of 5G with Green IoT [26].
3. Green Internet technologies: Current scenario demands the manufacture of devices that consume less energy without compromising the performances in both hardware and software. In addition to that, software solutions should minimize the resource utilization to reduce energy consumption. Also, IoT devices transmit small packets with the connection between the devices; hence, the communication needs to be delay tolerant [27].

3 Green ICT to Enable Green IoT

The growth of ICT increases the rate of energy consumption and the rise in the number of environmental issues that need to be addressed. The green technologies that enable Green IoT are called as Green Information and Communication Technologies (Green ICTs). These technologies refer to the facilities and storage that allows devices and users to collect, store, access, and manage information with the new resources that

Fig. 7 Green ICT



do not affect the health of humans and environment. The core green technologies that construct a smart green world are shown in Fig. 7.

3.1 *Green Radio-Frequency Identification (RFID)*

RFID is a small electronic device with a unique identifier consisting of a microchip and antenna. The microchip is used to transmit and receive signals. It automatically identifies and tracks object that has the RFID tag. Collectively, they include numerous RFID tags and a small number of RFID Readers. The RFID tags come in various forms such as printable, paper-based and biodegradable RFID tags. Information flow is triggered when the RFID Reader transmits a query signal for which the RFID tags in the region respond. The transmission range of RFID signals is a few meters, and they have various frequency bands ranging from 124–135 kHz to 860–960 MHz. RFID plays a significant role in making the world greener by saving energy, improving the waste management process, and minimizing the emissions of the vehicle. In [26], Green RFID antennas provide solution for embedded sensors. The flexible design in antenna affords the sufficient calibration of the humidity sensor. RFID components include tag, reader, antenna, and station. RFID usage impacts directly and positively on both operational performance and logistics [28]. In [29], the lifetime of unmanned aerial vehicle (UAV) battery is enhanced and RFID Reader detection range also improvised. To achieve more benefits, RFID and UAV can be combined together and implemented in supply chain management systems. In an environmental monitoring operation, the recharging process of multipurpose RFID tag using UAV is examined [30]. In [31], UAV indoor localization technique using passive RFID is discussed and tracking, and localization activities are considered to reduce cost and provide more simplicity.

On the contrary, Green RFID emphasizes the following:

1. Reduction in size: Reduction in size would directly reduce the amount of non-biodegradable materials used in the manufacture, as it is difficult to recycle RFID tags.
2. Design of energy-efficient algorithms: Energy-efficient algorithms dynamically adjust to transmission power, optimize tag estimation, avoid tag collision, and overhearing should be designed and implemented.

3.2 Green Wireless Sensor Network

A wireless sensor network (WSN) consists of autonomous sensors that are spatially distributed and collaboratively monitor the various environmental conditions such as temperature, pressure, motion, and sound from the surroundings. The sensor nodes are incorporated only with limited power and storage capacity. They cooperatively work with the other sensors and collectively transmit sensory data to the base station, which is also called as a sink node in an ad hoc manner. IEEE 802.15.4 is a commercial WSN solution for low transmission and bit rate communications in the physical and MAC layer.

On the other hand, Green WSN should focus on the following techniques:

1. Power saving mode: Sensor nodes should transmit information only when it is required. The sensor nodes should be in sleep mode if they are idle, thereby saving energy consumption.
2. Energy depletion: Energy harvesting mechanisms that harvest the natural renewable sources of energy (Sun, kinetic energy, etc.) should be deployed. Traditional approaches such as wireless charging would deplete energy.
3. Radio optimization techniques: Energy-efficient cognitive radio, directional antennas, cooperative communication, and transmission power optimization techniques should be used for information transmission to the base station.
4. Data reduction mechanisms: The sampling rate of IoT sensors would be high, and the depletion of energy is very fast. Hence, data reduction techniques such as adaptive sampling, aggregation, compression, and network sampling have to be adapted.
5. Energy-efficient routing techniques: Routing algorithms with energy as a metric, multipath routing to have information transmitted in multiple paths with relay node placement and mobility should be deployed.

3.3 Green Cloud Computing

It provides on-demand network access in a shared pool of resources such as networks, storage, applications, and services that can be configured and customized based on the user requirement—infrastructure as a service (IaaS), platform as a service (PaaS), software as a service (SaaS), and with the latest improvement of everything as a service (XaaS). Elasticity is offered as resources are managed in a large pool with convenient access times. With the growing number of applications that require to be hosted in the cloud as private, public or community based, more resources are deployed and power is consumed causes environmental issues with the increase of CO₂ emission. On offloading data processing and storage tasks in mobile devices such as tablets and smart phones, cloud computing is integrated in the mobile environment introducing Mobile Cloud Computing (MCC). Nevertheless, on migrating to green cloud computing, the following would be the potential solutions:

1. Promoting reduced energy consumption in both hardware and software: Manufacturing units must design hardware that consumes less energy. Moreover, software solution should utilize minimum resources which consume less amount of energy with efficient design.
2. Power saving virtual machine techniques: Green initiative includes power saving VM consolidation, migration, placement, and allocation to reduce energy consumption in data centers.
3. Energy-efficient resource allocation: Various resource allocations such as auction-based resource allocation, gossip-based resource allocation and scheduling mechanisms should be implemented for energy efficiency.
4. Energy-saving policy: By drafting effective accurate models and evaluation approaches regarding energy-saving policies for cloud computing.

Recent advancement in cloud computing has led to the inception of sensor cloud, which is a powerful unique data storage platform that influences cloud computing technologies to provide rapid elasticity, excellent visualization, and user programmable analysis. It is capable of ever existing data sensing and gathering with powerful data storage and processing facilities. Sensor cloud model as shown in Fig. 8 and the sensor network provider (SNP) have a ubiquitous variety of sensors that could be static or mobile and to collect data from the environmental surroundings. The role of cloud service provider (CSP) is to store and process the transmitted sensor data with the data centers. The processed data is provided to the cloud service user (CSU) on demand. With the integration of cloud and sensor networks, there are many advantages. Users can access their sensor data from the cloud with a network connection in a pervasive manner. The utility of WSN is enriched as it can serve multiple applications such as healthcare monitoring and environmental monitoring. The services provided by cloud are enhanced with respect to speed, processing speed, and performance. Statistics reveal that sensor cloud outperforms than traditional WSN and cloud data centers with prolonged sensor life by 3.25% and reduction in energy consumption by 36.68%. These are seen as required characteristics for a smart world

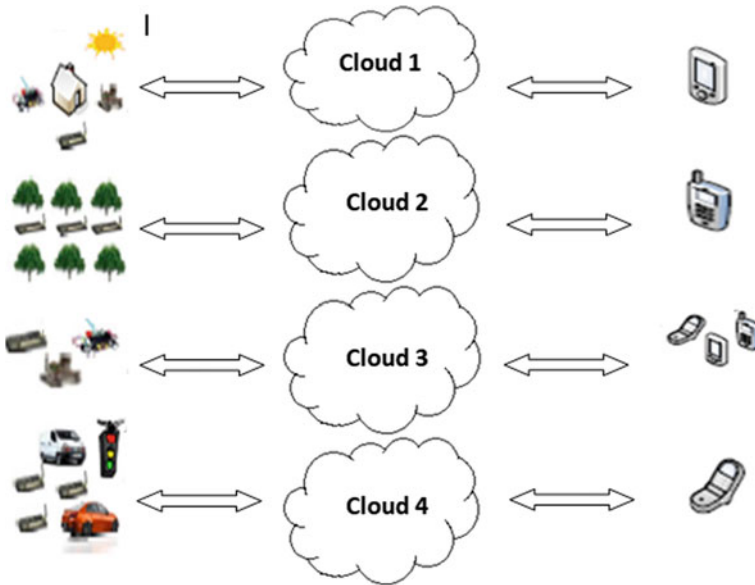


Fig. 8 Sensor cloud model

with green cloud. Nevertheless, security of sensor cloud continues to be a threat due to lack of trust and reputation between the CSP and SNP; as a result, any CSU may choose a fake CSP.

3.4 Green Machine-to-Machine

It allows both the wired or wireless devices of the same type to communicate with one other. Large number of M2M devices that are deployed in M2M domain collect the monitored data in IoT. The wired or wireless networks relay gathered data to the base station. As many devices are deployed in the M2M domain and the enormous growth of device to device communication and automation, energy usage has rapidly increased. Furthermore, the following mechanisms have to be implemented for Green M2M to reduce the consumption of energy:

1. Intelligent adjustment of transmission power: A threshold needs to be determined to ensure that the minimal range of transmission power is ensured for communication.
2. Design efficient communication protocols: Routing algorithms that focus on distributed computing techniques should be designed for M2M communication.
3. Activity scheduling: Switching devices to the low power operation mode called as sleeping mode should be scheduled. It implies that only a small subset of the

nodes will be active during the data-gathering phase. Thereby, around 40% of power can be saved and the negative impact of greenhouse gases is minimized.

4. Joint energy-saving mechanisms: Energy can be saved among the devices by following resource allocation and energy harvesting mechanisms such as spectrum sensing and management with interference mitigation and power optimization.

3.5 Green Data Center

Data center is physical or virtual repository for storage, management, and dissemination of data and applications that are created by various users or things. By continuing the development of Web services, many organizations are installing more servers for storage capacity and policy expansion. Besides cost, the availability of electric power is a critical aspect to be tackled by companies. Data centers consume enormous of energy with high operational costs and increased emissions of CO₂. With the increase in demand for IoT applications, massive amount of data is being generated by ubiquitous applications. Thereby, a vital requirement for efficient data centers and the urge for energy efficiency become much more significant. Data efficiency in data centers has to be improved by deploying energy-efficient equipment with proper airflow management for cooling purposes. Moreover, environment-friendly energy management software may be deployed in the data centers.

Green data center can become a reality by following the below-listed mechanisms:

1. Use of renewable or green energy sources such as water, wind, and solar.
2. Utilization of efficient power management technologies like vSphere, Turbo Boost.
3. Modeling of energy-efficient hardware by making use of the advantages of dynamically varying voltage and frequency. Server virtualization has saved energy consumption by 50%. Moreover, power down feature of servers should be enabled when not in use.
4. Design and implement energy-efficient data center architecture such as nano-data centers that achieve power conservation.
5. Design energy-aware routing algorithms and protocols that consider the traffic flow, network power, and state of sleeping nodes.
6. Draw support for sensing and analytical techniques such as optical communication and virtual machine migration.

3.6 Green ICT Principles

The Green ICT principles are described below in the objective of providing a sustainable environment for smart living [32–34].

1. Turn off devices/facilities when not in use: Devices or facilities are turned ON only when required. If these devices are always working (in ON mode always) enormous energy is consumed. Sleep scheduling is implemented in WSN, where sensor nodes dynamically turn awake (ON) and sleep (OFF).
2. Transmission of data only when required: Large-sized data consumes a lot of energy. Intelligent algorithms have to be deployed that send data only when required. For example, predictive data delivery sends data based upon the behavior of the user.
3. Minimize the length of data path: Routing algorithms that take the path size as a metric is a straightforward mechanism to reduce energy consumption. In addition to it, algorithms that consider the traffic flow in a path and effectively route paths in multiple paths have to be designed. Nevertheless, cooperative relaying in wireless networks has achieved significant gains with respect to energy consumption.
4. Advanced communication techniques: Data fusion with compressive sensing enhances energy efficiency by combining data from multiple sources and transmitting accurate data. Spectrum usage and efficiency can be improved with the use of cognitive radio which sense the environment and dynamically changes its modes of operation [35].
5. Renewable green power sources: Traditional sources of energy such as solar, wind, water, and biomass can be used as they can be renewed naturally and repetitively utilized. Renewable sources of energy have a vital role in energy efficiency and minimization of CO₂ [36].

4 Applications of Green IoT

Green IoT significantly makes remarkable changes in the surroundings due to the development of IoT devices and potentially reduces the cost of managing hazardous emissions, e-waste, and energy utilization. Green IoT is a good practice of designing, producing, using and disposing of servers, computers and some subsystems such as monitors, communication equipments, and storage devices more frequently and efficiently but with less impact on the environment and society. Optimizing the available resources and designing new IoT devices reduce the negative effect on human health and without perturbing the environment drives the force toward Green IoT. The main goal of Green IoT is to utilize environmental conservation, minimize the harmful effect of pollution and CO₂ emission, and reduce the cost of power consumption of IoT devices. Green IoT has a high potential with green ICT technologies to support environmental sustainability and economic growth which makes the world smarter and greener [13, 14]. In [37], industrial emission influence environmental changes for varying time and region is described and analyzed in detail. IoT devices with minimum energy consumption are required in order to form a healthier environment.

Many sensors, machines, devices, and drones are involved to communicate with each other for completing the task intelligently in the green environment. Moreover,

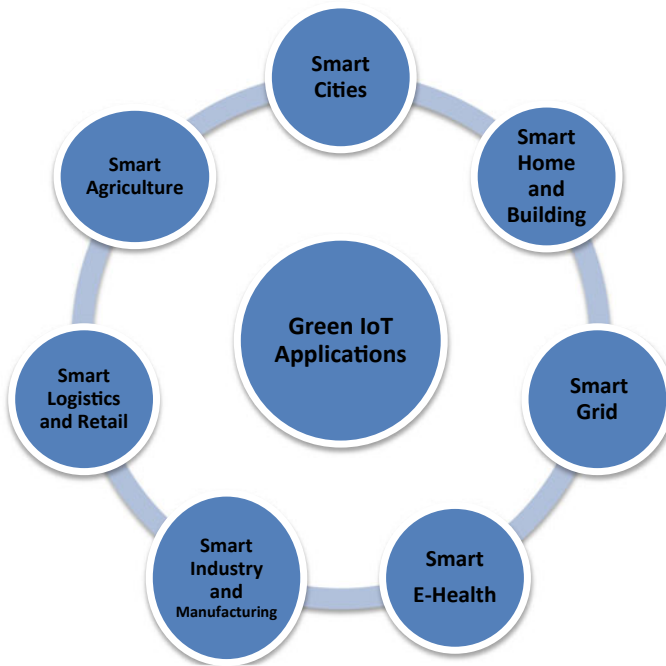


Fig. 9 Applications of Green IoT

Green IoT makes IoT to be benefitted in minimizing the harm, forming eco-friendly environment an exploring various energy sources. Therefore, many applications of Green IoT are economically, environmentally meaningful, and sustainable which preserves natural resources and reduces the harmful impact on human health. The various applications of Green IoT such as smart cities, smart home and buildings, smart grid, smart e-health, smart industry and manufacturing, smart logistics and retail, smart agriculture are shown in Fig. 9.

4.1 Smart Cities

Smart city market is predicted to reach 100 billion dollars by 2020, based on the annual report reaching nearly 16 billions every year. The interconnected systems provide the required services in regard to various needs of the users. The applications of Green IoT are smart transportation, smart security, and smart energy-saving mechanisms. Interconnected systems offer the required services to the users, and it is more convenient, easier to obtain the information according to their interest. The most upcoming applications for Green IoT are smart cities which have gained more attention in the last few years. It is a prominent and promising IoT application, where

Green IoT is characterized by efficient energy utilization to make the world smarter. Green ICT technologies should be enabled with sensors and communication add-ons to form a sustainable smart world. The devices can sense the environment, and data can be communicated with other devices as well. The smart city includes smart light lamp, smart parking, high-quality air, smart traffic management, smart vehicle, and so on [38, 39]. The quality of human life would be enriched by employing various applications of smart cities and introducing novel technologies for smart connected communities [40, 41]. Internet of things consists of Internet-connected devices where human uses it to make their life more comfortable and convenient. IoT plays a vital role in forming smart cities too eco-friendly.

1. **Traffic management:** It is an annoying experience for the persons who are being stuck in heavy traffic, and it creates too much emissions lead to global warming. For instance, IoT sensors fixed on traffic lights can alert if the traffic jam is heavy. After analysis, the big data platform could suggest the alternative routes to handle the situation. The person can be directed to find out the nearby parking places. The entering and leaving the parking places are monitored by IoT sensor, and the updated information will reach the person who is using application and connected to smart city. The application directs the user to the parking area nearer to their destination; thus, the person who caught in traffic jam gets assistance and could reach the destination earlier.
2. **Waste management:** Everyday 3.5 million tons of waste are generated and that too increasing continuously. Hence, the ways should be found to limit the waste production with recycling process to maintain the environmental sustainability for smart cities. The IoT sensors can track the level of recycling bins and give alarm to empty the container. The process should be tracked continuously by the relevant representative to check the waste level either increasing or decreasing. Waste management officials should take proper measures to prevent the illegal dumping of waste.
3. **Evaluating the sustainability level of smart city:** The factors which are affecting the planet negatively should be identified clearly to make the smart city more sustainable. Initially, the city officials can start the process with commercial off-the-shelf (COTS) sensor equipment and proceed with the customized sensors for rapid technological implementation. It is recommended to use IoT data along with big data to determine the city's present sustainability level, and how it is updated over time. The utilization of IoT technology in green computing will surely have a positive impact on smart cities [38].
4. **Minimize resource consumption:** The smart meter gauge typically tracks the consumed energy level in home and regarding fluctuations in energy usage over time. The users would manage the utility charges, and the environment is also protected simultaneously. 47% people said obtaining information via IoT sensors would assist the user in carrying predictive maintenance and cut down on energy usage. IoT-connected lights can be activated or deactivated automatically according to the premises busy or empty. IoT sensors can be fixed in water management system to measure the water flow rate, detect leaks, and a statistical report can

be generated to check the overall water usage. Some significant strategies can be followed to prevent the water wastage with the help of IoT sensors.

4.2 Smart Home and Buildings

IoT-connected devices are used for remote monitoring and managing home appliances such as heating and lighting. Smart home automation allows the user to control the smart devices like automated doors, smart locks, security cameras, electrical appliances (washing machine, refrigerator, air conditioner, dishwasher, microwave oven, etc.) with the application on a smart phone or any other connected devices. In a smart home, the temperature in air conditioner would be automatically adjusted according to the weather forecast. Security surveillance, door unlocking, thermostat, lighting, etc., can be covered. The renewable energy sources like solar panels and wind turbine are incorporated into already existing energy sources for automating the home appliances to reduce the amount of electric charge. If the refrigerator works continuously, the fluctuation in the power load might occur due to the cooling process and compressor system. The compressor will function till the temperature is below or equal to the threshold level.

Today's lifestyle is changed even to be more efficient and smarter by remote access of home appliances such as air conditioner, microwave, refrigerator, geyser, and robotic devices. Green IoT enables home as a smart home where lighting, heating appliances, and various electronic devices are controlled remotely by using a smart phone. The centralized mobile in-house receives voice commands and gives responses to the connected devices. In a smart home, a model is formulated QoS provisioning of different IoT devices based on channel assigned optimization. Scheduling the execution of all home appliances is based on the weather condition, resident behavior, discomfort index, etc., and it can be done either statically or dynamically. In static scheduling, the profile of home appliances is defined based on user activities. Scheduling is prepared based on the amount of received power supply, power generation capacity, and energy demand of all electrical and electronic appliances. Suppose the forecasted data and user activities vary, rescheduling is done to meet the energy demand. This is the process called run-time scheduling. With the tremendous increase in population, digital transformation, automation, and modern lifestyle the globe is facing a very big energy crisis because of climate change, depletion of fossil fuels, and a lot of carbon emission. IoT-enabled smart home is essential to conserve sustainable and renewable energy resources, where it provides connectivity, convenience, and comfort.

4.3 Smart Grid

The power resources should be controlled in such a way that it can be provided proportionally to the population growth. Thus, the energy consumption of different building premises could be reduced. The services offered by them can be enhanced once the area is connected to the network and is monitored persistently [42]. The capability of grid should be dynamically adjustable to afford energy at low cost and high quality. A low-cost remote memory proof for smart grid is proposed [43, 44]. Furthermore, the approaches to increase data validity for smart cities are proposed. In the future, the smart grid can monitor the energy consumption level and able to construct full energy-based systems [45].

Smart grid is a network of substations, transmission lines, and transformers that provides electricity from the power station to the residential or office premises. It allows two-way communication between the sensor devices and users via transmission lines. If some appliances such as washing machine or dishwasher are used during peak hours, the pay is more at that time. Smart thermostats and smart meters will suggest the best time to use the appropriate home appliances in such a way the utility bills can be minimized. In addition, smart surveillance allows the safety of elderly people and children to be watched continuously using applications.

4.4 Smart E-Health

The performance of healthcare applications is enhanced by implanting sensors in human body for monitoring. Data is gathered and analyzed to provide suitable treatment for the patients in real time. The various types of sensors and actuators can be fixed in human body for tracking the human body [46, 47]. Advanced IoT sensors are introduced to produce real-time data about human health makes a drastic revolution in the healthcare industry [48–50]. It improves quality, access and cost in efficient healthcare services.

Due to the emission of CO₂ from decentralized data centers, the environment is polluted and data can be shared with personal health record (PHR) by reusing data centers. Flexibility, compatibility, and availability are increased, and the high emission of CO₂ is avoided. Due to flexibility, the updated information can be shared with other data centers for reusable resources and e-healthcare services [49].

4.5 Smart Industry and Manufacturing

With minimal human intervention, robots are designed to complete the manufacturing task. The functionalities are automatically tracked and handled in a controlled manner. Hence, industries are automated with automatic functioning of machines with

little or without human intervention [51]. The industrial Green IoT converges smart manufacturing systems and IoT architecture which enables remote access and reduces downtime. It also enables efficient data sharing among industrial firms, factory floor and extensively improves market agility, equipment efficiency, labor productivity, etc.

4.6 Smart Logistics and Retail

RFID and smart shelves play a significant role in retail and logistics which draws the attention in achieving accuracy and providing the required customer services. A pallet fixed on a truck or in a warehouse can send messages which include the detail about the product such as sizes and style variations. Juniper's research estimates that the investment of IoT in retail will reach \$2.5 billion by 2020. The interconnected physical devices in retail industry significantly modify the operational way of supply chain. The requirements for digitally transformed logistics are energy saving, contextual data analysis, cost efficiency, integrated end-to-end management, real-time activity oversight, and remote tracking.

GPS can be attached with sensors to track the functionality of every part in the logistics exercise and predictive maintenance for climate and atmospheric changes, vehicle, route optimization, and complete traceability. Data should be available to the customers and there should be an option for tracking their purchases in real time.

4.7 Smart Agriculture

In smart agriculture, all devices should be equipped with sensors and communication add-ons for effective sensing and communication; in fact, it requires more energy. The energy demand is further increased greatly because of the remarkable interest from several organizations. Hence, the Green IoT recently focuses on decreasing the energy consumption by satisfying the smart world with sustainability. Energy-efficient algorithms with IoT facilitate the reduction of the greenhouse effect in various applications. The strategies should be followed by industries to deal with limited land availability, water scarcity, and cost management factors. IoT and cloud computing can reduce the power consumption in smart agriculture. Green IoT and Green nanotechnology in combination can create the sustainable smart agricultural industry [52].

With smart agriculture gadgets, the smart farming gained in the process of growing farms and rising livestock. According to the BI intelligence report, the number of connected IoT devices will reach 75 million by 2020 and global smart agriculture market size prediction says it will reach \$15.3 billion by 2025. Some of the benefits are

1. Immense amount of data is collected by agriculture sensors, and it senses soil quality, crop's growth progress, cattle health, or weather condition.
2. Able to plan for the better product distribution by having the control over the internal process.
3. Anticipate the risk of losing the yield.
4. The multiple processes such as fertilizing, pest control, and irrigation are automated.
5. Easy to maintain good standards for growth capacity and crop quality with the automation.

IoT sensors of agriculture:

1. Smart farming sensors monitor the climate condition for choosing the suitable crops, and the appropriate steps are taken to improve the capacity. Smart agriculture IoT devices are smart elements, allMETEO, Pynco, etc.
2. Greenhouse automation uses smart agriculture sensors which have smart sprinkler controller to manage the lighting systems and irrigation remotely.
3. The significant element of precision farming is crop management where the sensors collect data about the temperature, leaf water potential, and crop health for improving the farming practices.
4. Smart agriculture sensors (collar tags) are used to observe the physical conditions such as temperature, nutrition insight, and activity about the herd.

The quality of sensors is significant for the product to be hit, and it depends on its reliability and accuracy of the gathered data. The efficient data analytic techniques and predictive algorithms are required to gain deep insight into the gathered information. The maintenance of sensors is a challenge in smart agriculture because the sensors fixed in the field can be easily damaged. The farm owner should have a control over the field remotely via smart phone. The adequate wireless range is required for proper communication and to transmit the data to the server through the connected devices are autonomous. The concrete internal infrastructure is compulsory for handling the immense load to ensure the performance of smart farming application [53, 54].

5 Open Challenges and Future Research Direction

The Green IoT is recently focused on most exciting areas, namely green design and implementations, Green IoT services and applications, green communication and networking, mobility and network management, energy-saving mechanisms, smart objects, integrating RFIDs with sensor networks, green localization, and compatibility of heterogeneous networks. Some of the key challenges in searching of optimal solutions for Green IoT are as follows:

- Achieving acceptable performance by integrating energy-efficient mechanisms across IoT architecture.

- Smart applications should be focused on green technologies to decrease the impact on the atmosphere.
- Green IoT infrastructure should be designed in such a way that it affords ease of accessibility.
- Context awareness applications of energy-efficient Green IoT system can be designed.
- Energy-efficient devices and protocols with low power consumption should be used for communication.
- There should be a trade-off between the efficiency of spectrum sensing and management techniques.
- Reliable power use models of Green IoT systems are needed.
- Energy-efficient system architecture and service composition strategies should be clearly investigated.
- Achieving efficient energy-saving scheduling techniques for Green IoT communications.
- Users should have ease of access and control of their virtual private IoT.
- There is a demand for UAV to restore huge amount of IoT devices in various fields such as traffic monitoring, agriculture in order to minimize the toxic waste and energy utilization. Hence, UAV is a hot and prominent technology that leads Green IoT with high efficiency and less cost.
- Sensor cloud is a technology which transmits information from sensor to mobile cloud by integrating WSN and mobile cloud. Green social network as a service (SNaaS) clearly examines the energy efficiency of WSN, cloud management, and its services.
- M2M plays a vital role in reducing hazardous emissions and energy usage by enabling automated systems. The delay in machine automation should be reduced in traffic management system to take immediate necessary action.
- Devising suitable techniques with improved QoS parameters such as delay, bandwidth, and throughput for the effective contribution of Green IoT.
- The radio-frequency energy harvest should be considered to support green communication among IoT devices.
- For smart and green environmental life, reduce the energy usage and CO₂ emission by designing smarter IoT devices.

6 Conclusion

In this chapter, the major challenges in IoT and its elements to produce intelligence services to the users have been discussed. Furthermore, in order to solve environmental problems, energy-efficient IoT and its technology have been discussed. Green IoT helps the environment by improving energy efficiency, minimizing greenhouse gas emissions, using carbon-free materials, and promoting reusability. With respect to Green IoT, principles have been suggested to save energy. Moreover, the lifecycle

of Green IoT focuses on green design, green construction, green operation and maintenance, and green disposal to have very minimal consequences in the atmosphere which have been discussed. The Green IoT technologies include hot green ICT such as green tags that are reduced in size to minimize the amount of non-biodegradable materials and green sensing networks should deploy energy management by enabling power saving mode and green Internet technologies that consume less energy without compromising performance should be manufactured have been discussed in this chapter. Also, potential solutions are suggested on migrating to green cloud computing and later move on to the topic of green ICT principles for a sustainable environment with smart living. Finally, headed over applications of Green IoT such as smart home which helps to monitor and operates the home appliances with more easier and convenient manner, smart health care for monitoring and tracking patients in real time, smart grid to control and manages resources so that power can be offered and smart city helps to obtain information of interest for residents by making it more convenient and easier have been discussed.

References

1. Atzori L, Iera A, Morabito G (2010) The Internet of things: a survey. *Comput Netw* 54:2787–2805
2. Miorandi D, Sicari S, De Pellegrini F, Chlamtac I (2012) Internet of things: vision, applications and research challenges. *Ad Hoc Netw* 10(7):1497–1516
3. Al-Fuqaha A, Guizani M, Mohammadi M, Aledhari M, Ayyash M (2015) Internet of things: a survey on enabling technologies, protocols, and application. *Commun Surv Tutor IEEE* 17(4):2347–2376
4. Botta A, De Donato W, Persico V, Pescapé A (2016) Integration of cloud computing and Internet of things: a surve. *Futur Gener Comput Syst* 56:684–700
5. Chase J (2013) The evolution of the Internet of things, Texas Instrum. Dallas, TX, USA, White Paper, p 7
6. Rani S, Talwar R, Malhotra J, Ahmed SH, Sarkar M, Song H (2015) A novel scheme for an energy efficient Internet of things based on wireless sensor networks. *Sensors* 15:28603–28626
7. Sathyamoorthy P, Ngai E (2015) Energy efficiency as a orchestration service for the Internet of things. In: *Proceedings of 11th Swedish national computer networking workshop*, pp 41–44
8. Evangelos AK, Nikolaos DT, Anthony CB (2011) Integrating RFIDs and smart objects into a unified Internet of things architecture. *Adv Internet Things* 1:5–12
9. Zhang D, Yang LT, Chen M, Zhao S, Guo M, Zhang Y (2014) Realtime locating systems using active RFID for Internet of things. *IEEE Syst J* 10(3):1226–1235
10. Juels A (2006) RFID security and privacy: a research survey. *IEEE J Sel Areas Commun* 24(2):381–394
11. Xiaojun C, Xianpeng L, Peng X (2015) IOT-based air pollution monitoring and forecasting system. In: *International Conference on Computer and Computational Sciences (ICCCS)*. IEEE, pp 257–260
12. Da Xu L, He W, Li S (2014) Internet of things in industries: a survey. *IEEE Trans Ind Inform* 10(4):2233–2243
13. Huang J, Meng Y, Gong X, Liu Y, Duan Q (2014) A novel deployment scheme for green Internet of things. *IEEE Internet Things J* 1:196–205
14. Gapchup A, Wani A, Wadghule A, Jadhav S (2017) Emerging trends of Green IoT for smart world. *Int J Innov Res Comput Commun Eng* 5:2139–2148

15. Arshave R, Zahoor S, Shah MA, Wahid A, Yu H (2017) Green IoT: an investigation on energy saving practices for 2020 and beyond. *IEEE Access* 5:15667–15681
16. Doknić V (2014) Internet of things greenhouse monitoring and automation system
17. Wang HI (2014) Constructing the green campus within the Internet of things architecture. *Int J Distrib Sens Netw* 10:804627
18. Prasad R, Ohmori S, Simunic D (2010) *Towards green ICT*. River Publishers, Gistrup
19. Akkaya K, Guvenc I, Aygun R, Pala N, Kadri A (2015) IoT-based occupancy monitoring techniques for energy-efficient smart buildings. In: *Proceedings of IEEE wireless communications and networking conference workshops*, pp 58–63
20. Peoples C, Parr G, McClean S, Scotney B, Morrow P (2013) Performance evaluation of green data center management supporting sustainable growth of the Internet of things. *Simul Model Pract Theory* 34:221–242
21. Perera C, Talagala DS, Liu CH, Estrella JC (2015) Energy-efficient location and activity-aware on-demand mobile distributed sensing platform for sensing as a service in IoT clouds. *IEEE Trans Comput Soc Syst* 2(4):171–181
22. Murugesan S (2008) *Harnessing green IT: principles and practices*. IT Prof 10
23. Rohokale VM, Prasad NR, Prasad R (2011) A cooperative Internet of things (IoT) for rural healthcare monitoring and control. In: *Proceedings of 2nd wireless communication, vehicular technology, information theory and aerospace and electronic systems technology (Wireless VITAE)*, pp 1–6
24. Kim J (2015) Energy-efficient dynamic packet downloading for medical IoT platforms. *IEEE Trans Ind Inform* 11(6):1653–1659
25. Zink T, Maker F, Geyer R, Amirtharajah R, Akella V (2014) Comparative life cycle assessment of smart phone reuse: repurposing vs. refurbishment. *Int J Life Cycle Assess* 19(5):1099–1109
26. Zhu C, Leung V, Shu L, Ngai ECH (2015a) Green Internet of Things for smart world. *Access IEEE* 3:2151–2162
27. Shaikh FK, Zeadally S (2016) Energy harvesting in wireless sensor networks: a comprehensive review. *Renew Sustain Energy Rev* 55:1041–1054
28. Zelbst PJ, Sower VE, Green KW Jr, Abshire RD (2011) Radio frequency identification technology utilization and organizational agility. *J Comput Inf Syst* 52:24–33
29. Hubbard B, Wang H, Leasure M (2016) Feasibility study of UAV use for RFID material tracking on construction sites. In: *Proceedings of 51st ASC annual international conference proceedings college station, TX, USA*
30. Allegretti M, Bertoldo S (2015) Recharging RFID tags for environmental monitoring using UAVs: a feasibility analysis. *Wirel Sens Netw* 7:13
31. Choi JS, Son BR, Kang HK, Lee DH (2012) Indoor localization of unmanned aerial vehicle based on passive UHF RFID systems. In: *9th international conference on ubiquitous robots and ambient intelligence (URAI)*. IEEE, pp 188–189
32. Prasad SS, Kumar C (2013) A green and reliable Internet of things. *Commun Netw* 5:44–48
33. Zhu C, Leung VC, Shu L, Ngai ECH (2015b) Green Internet of things for the smart world. *IEEE Access* 3:2151–2162
34. Upadhyay AP, Bijalwan A (2015) Climate change adaptation: services and role of information communication technology (ICT) in India. *Am J Environ Prot* 4:70–74
35. Uddin M, Rahman AA (2012) Energy efficiency and low carbon enabler green IT framework for data centers considering green metrics. *Renew Sustain Energy Rev* 16:4078–4094
36. Shaikh FK, Zeadally S, Exposito E (2015) Enabling technologies for green internet of things. *IEEE Syst J* 11(2):983–994
37. Lü YL, Geng J, He GZ (2015) Industrial transformation and green production to reduce environmental emissions: taking cement industry as a case. *Adv Clim Change Res* 6:202–209
38. Petrolo R, Loscrì V, Mitton N (2015) Towards a smart city based on cloud of things, a survey on the smart city vision and paradigms. *Trans Emerg Telecommun Technol*
39. Heo T, Kim K, Kim H, Lee C, Ryu JH, Leem YT, Jun JA, Pyo C, Yoo SM, Ko J (2014) Escaping from ancient Rome! Applications and challenges for designing smart cities. *Trans Emerg Telecommun Technol* 25:109–119

40. Maksimovic M (2017) The role of Green Internet of things (G-IoT) and big data in making cities smarter, safer and more sustainable. *Int J Comput Digit Syst* 6
41. Jiang D, Zhang P, Lv Z, Song H (2016) Energy-efficient multiconstraint routing algorithm with load balancing for smart city applications. *IEEE Internet Things J* 3:1437–1447
42. Liu Y, Weng X, Wan J, Yue X, Song H, Vasilakos AV (2017) Exploring data validity in transportation systems for smart cities. *IEEE Commun Mag* 55:26–33
43. Yanti H (2015) The applications of WiFi-based wireless sensor network in Internet of things and smart grid. *Buletin Inovasi ICT & Ilmu Komputer* 2
44. Yang X, He X, Yu W, Lin J, Li R, Yang Q, Song H (2015) Towards a low-cost remote memory attestation for the smart grid. *Sensors* 15:20799–20824
45. Karnouskos S (2010) The cooperative internet of things enabled smart grid. In: *Proceedings of the 14th IEEE international symposium on consumer electronics (ISCE2010)*, June 2010
46. Kalarthi ZM (2016) A review paper on smart health care system using Internet of things. *Int J Res Eng Technol (IJRET)* 5:80–83
47. Islam SR, Kwak D, Kabir MH, Hossain M, Kwak KS (2015) The Internet of things for health care: a comprehensive survey. *IEEE Access* 3:678–708
48. Niewolny D (2013) How the Internet of things is revolutionizing healthcare. White paper, pp 1–8
49. Hassanaliereagh M, Page A, Soyata T, Sharma G, Aktas M, Mateos G, Andreescu S (2015) Health monitoring and management using Internet-of-things (IoT) sensing with cloud-based processing: opportunities and challenges. In: *IEEE international conference on services computing (SCC)*, pp 285–292
50. Ullah F, Habib MA, Farhan M, Khalid S, Durrani MY, Jabbar S (2017) Semantic interoperability for big-data in heterogeneous IoT infrastructure for healthcare. *Sustain Cities Soc* 34:90–96
51. Kulkarni N, Abhang S (2017) Green industrial automation based on IOT: a survey. *Int J Emerg Trends Sci Technol* 4:5805–5810
52. Maksimovici M, Omanovic-Miklicanin E (2017) Green Internet of things and green nanotechnology role in realizing smart and sustainable agriculture. In: *VIII international scientific agriculture symposium “AGROSYM 2017”*, Jahorina, Bosnia and Herzegovina
53. Nandyala CS, Kim HK (2016) Green IoT agriculture and healthcare application (GAHA). *Int J Smart Home* 10:289–300
54. Sala S (2009) Information and communication technologies for climate change adaptation, with a focus on the agricultural sector. Think piece for CGIAR science forum workshop on ICTs transforming agricultural science, research, and technology generation, Wageningen, Netherlands, pp 16–17

Five-Level Switched Inductor-Based Cascaded H-Bridge Quasi-Switched Boost Inverter for Renewable Energy Applications



Rahul Kumar, Sneha, Rahul Rambhad, P. Sriramalakshmi, and V. T. Sreedevi

Abstract This research article proposes a five-level switched inductor-based cascaded H-bridge quasi-switched boost inverter (SL-qSBI) for renewable energy applications (REA) based on ripple input current-based SLBI topology. The switching pulses are generated using phase-shifted triangular carrier sinusoidal modulation (PS-PWM) strategy. The input DC voltage of 36 V is boosted and inverted to 155 V peak AC load voltage. The stiff DC source is considered for understanding the modes of operation of the inverter topology proposed. The simulation is performed in MATLAB/Simulink environment, and the simulated waveforms are presented to validate the operation of this topology. In addition, the performance of five-level cascaded H-bridge switched inductor-based qSBI (SLBI) is compared with the conventional five-level qSBI topology.

Keywords Switched Boost Inverter (SBI) · Voltage-Source Inverter (VSI) · Switched Inductor Boost Inverter (SLBI) · Total Harmonic Distortion (THD) · Quasi SBI (qSBI) · Impedance Source Inverter (ZSI) · Pulse-Width Modulation (PWM) · Phase Shifted Sine Pulse Width Modulation (PS-PWM)

R. Kumar · Sneha · R. Rambhad · P. Sriramalakshmi (✉) · V. T. Sreedevi
School of Electrical and Electronics Engineering, Vellore Institute of Technology, Chennai,
Tamil Nadu 600127, India
e-mail: sriramalakshmi.p@vit.ac.in

R. Kumar
e-mail: rahulzonline191@gmail.com

Sneha
e-mail: sk4sneha75@gmail.com

R. Rambhad
e-mail: rahulrambhad421@gmail.com

V. T. Sreedevi
e-mail: sreedevi.vt@vit.ac.in

1 Introduction

The conventional method of converting power from DC to AC requires a voltage-source inverter (VSI) [1, 2] in which the inverted alternating voltage is always less than the input DC voltage. An additional DC–DC boost converter is placed in between the DC power supply and the inverter module to obtain a high peak AC output. It forms a dual-stage power conversion configuration in which the efficiency is reduced and the cost is high. In the conventional VSIs, both switches of an H-bridge leg should not be gated simultaneously. It would result in a short circuit of the input source. Hence, to overcome this limitation, Z-source inverters (ZSIs) and its modified topologies are introduced which can provide both boost and inversion in single stage [3–22]. The conventional ZSI [3] has two inductors and two capacitors connected like an X network. The shoot-through technique is employed to trigger both the switches of one leg simultaneously to boost the available DC voltage. Various pulse-width modulation (PWM) control techniques are incorporated with the conventional ZSIs as well as other ZSI derived topologies.

In order to obtain high boost factor for fuel cells, photovoltaic applications, etc., where it is required to convert a low input DC voltage to a high AC output voltage, impedance network is formed in association with SC cell and SL cell, transformer assisted. But Z-network makes the ZSI more bulky and increases the overall cost of the circuit. If the passive elements are not symmetrical, it will lead the entire system to unstable region. To reduce these parameters, SBI is proposed in [23, 24]. The SBI is similar to the ZSI where the shoot-through state is utilized to boost the DC input. The conventional SBI has lesser number of passive elements and an additional active switch when compared to ZSI. In traditional SBIs, a large value of duty ratio (D) is used to get high boost voltage gain. But when it is incorporated, modulation index (M) value gets reduced as governed by the equation $M \leq 1 - D$. The small value of M causes high THD. To overcome the drawbacks of SBI, SLBI topology is introduced with additional three diodes and an inductor to boost the available input voltage.

In this paper, a novel topology of a five-level SL-based cascaded H-Bridge qSBI is proposed. The SLBI inverter has a boost factor which is $(1 + D)$ times greater than the conventional SBI [25]. Since the five-level inverter has two identical cascaded SLBIs, the overall output voltage of the cascaded network is superior to one SLBI module. Hence, it is used in connection with fuel cells and solar cells where a low DC voltage needs to be boosted to meet the grid voltage. Also, an improved THD profile can be obtained in the output AC voltage without using any filter circuit.

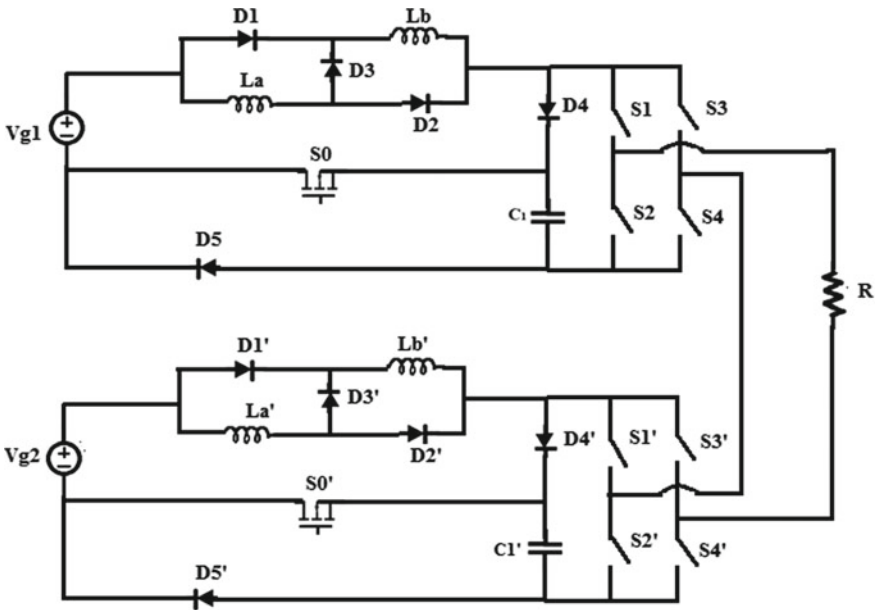


Fig. 1 SL-based five-level cascaded H-bridge qSBI

2 Five-Level Switched Inductor-Based Cascaded H-Bridge QSBI Topology

Figure 1 illustrates the proposed topology of five-level switched inductor-based cascaded H-bridge qSBI.

The five-level cascaded H-bridge SLBI inverter topology is obtained by connecting two identical SLBI modules in cascaded form. The same voltage supply is given to both identical modules of SLBI. The DC voltage supply can be given from solar cells or batteries with desired value. This topology is based on ripple input current type SLBI topology proposed in [25] to achieve the required five-level output voltages. Since the inductor is connected in series with DC source, the source current contains the ripple content. Hence, it is called as ripple input current type SLBI topology [25]. There are some other type of SLBI topologies are proposed in [25].

3 Working Principle of Five-Level SL-qSBI

The operation of ripple current SLBI topology is explained in [25]. It has two working modes, i.e., shoot-through and active state. Both shoot-through and active states are shown in Figs. 2 and 3, respectively.

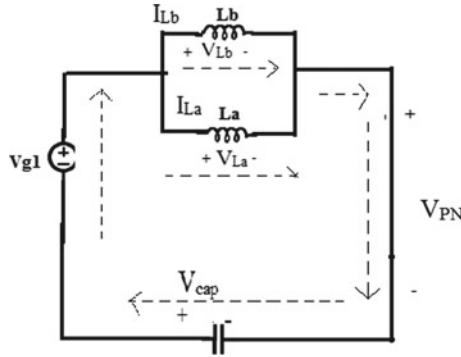


Fig. 2 Shoot-through state

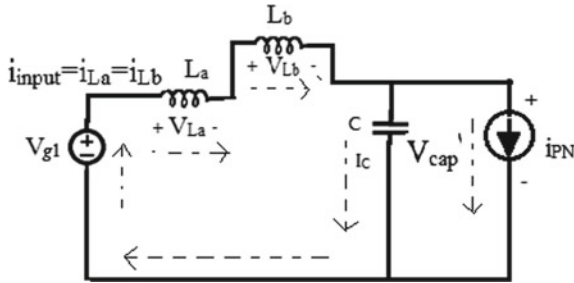


Fig. 3 Active state

3.1 Shoot-Through Stage

The shoot-through stage is shown in Fig. 2. During this state, the capacitor is assumed as fully charged, and inductors are uncharged. Due to this, diode D_4 and diode D_5 will be reverse biased and will not conduct. The pulses are generated in such a way that the boost network switch S_0 is fired along with both the switches (S_1 and S_2). During this instant, the capacitor will start to discharge as the charges get a complete close path (diodes D_1 and D_2 are on), and the inductors will get charged.

During shoot-through mode, the inductor voltages and capacitor current values are obtained as follows:

$$L_a \frac{di_{La}}{dt} = L_b \frac{di_{Lb}}{dt} = V_{g1} + V_{cap} \tag{1}$$

$$C_1 \frac{dV_{cap}}{dt} = I_{La} - I_{Lb} = -i_{input}, i_{input} \text{ is the input current} \tag{2}$$

3.2 Active State

Figure 3 shows the active through stage. During this state, inductors are charged with polarity as shown in Fig. 3. The diodes D_4 and D_5 will be forward biased, whereas diodes D_1 and D_2 will be reverse biased. The switch S_0 is closed as no pulse is given to it. The pulses produced by PS-PWM are given to the inverter switches so that the current flows through the load when the inductor discharges (in addition to source the current). The capacitor gets charged, and the load current passes as shown in Fig. 3.

In the course of active state, the inductor voltage and capacitor current values are obtained as

$$L_a \frac{di_{La}}{dt} = V_{g1} - V_{cap} - V_{Lb_non}, \quad V_{Lb_non} \text{ is the inductor voltage during non-text state} \quad (3)$$

$$L_b \frac{di_{Lb}}{dt} = V_{Lb_non} \quad (4)$$

$$C \frac{dV_{cap}}{dt} = I_{La} - i_{PN} = I_{Lb} - i_{PN} = i_{input} - i_{PN} \quad (5)$$

Applying volt-second balance to L_b , using Eqs. (1–5) gives inductor voltage V_{Lb_non} during the shoot-through state,

$$V_{Lb_non} = \frac{d_1}{1 - d_1} (V_{g1} + V_{cap}), \quad d_1 \text{ is the duty ratio of the first module} \quad (6)$$

Similarly, applying volt-second balance to inductor L_a and charge second balance to capacitor C , it gives,

$$V_{cap} = \frac{1 - d_1}{1 - 3d_1} V_{g1} \quad (7)$$

$$I_{La} = I_{Lb} = \frac{1 - d_1}{1 - 3d_1} i_{PN} \quad (8)$$

$$i_{input} = (1 + d_1) I_L \quad (9)$$

During the non-shoot-through state, the DC link voltage (V_{PN1}) across the inverter module 1 is given by,

$$V_{PN1} = V_{cap} = \frac{1 + d_1}{1 - 3d_1} V_{g1} = B V_{g1} \quad (10)$$

The boost factor (B) of module 1 five-level CHB-based SL-qSBI is given by,

$$B = \frac{1 + d_1}{1 - 3d_1} \tag{11}$$

The output voltage of five-level SLBI inverter is the addition of output voltage of both modules.

4 Phase-Shifted Sine PWM Strategy [26]

The PWM technique used to produce the firing pulses is depicted in Fig. 4. In the figure, V_{tri} refers to a high-frequency triangular carrier waveform of amplitude V_p . $V_{control}$ and $-V_{control}$ are two control waveforms of amplitude $M * V_p$ (M is the modulation index) which has a switching frequency of f_0 . And $V_{control}$ and $-V_{control}$ are two constant voltage levels. The two voltage levels $V_{control}$ and $-V_{control}$ are calculated by using the formulae $(1 - d_1)$ and $(1 - d_2)$, where d_1 and d_2 are the duty ratios of the first and second module of proposed five-level SLBI topology. It should also satisfy the following conditions: $M + d_1 = 1$ and $M + d_2 = 1$, where M is the modulation index.

Figure 4 illustrates the phase-shifted carrier PWM technique. Here, the shoot-through pulses are produced by comparing the high-frequency triangular carrier signals with (V_{tri}) the positive envelope and the negative envelope. This shoot-through pulse is given to boost network switch. The shoot-through pulse is then added with the Sine PWM switching sequence to obtain the switching sequence for H-bridge so that the inverter bridge switches can operate along with the boost network switch S_0 . For second module, the PWM signal generation for switches S_B, S_5, S_6, S_7, S_8 is almost same as signal generation for switches $S_A, S_1, S_2, S_3,$ and S_4 , respectively,

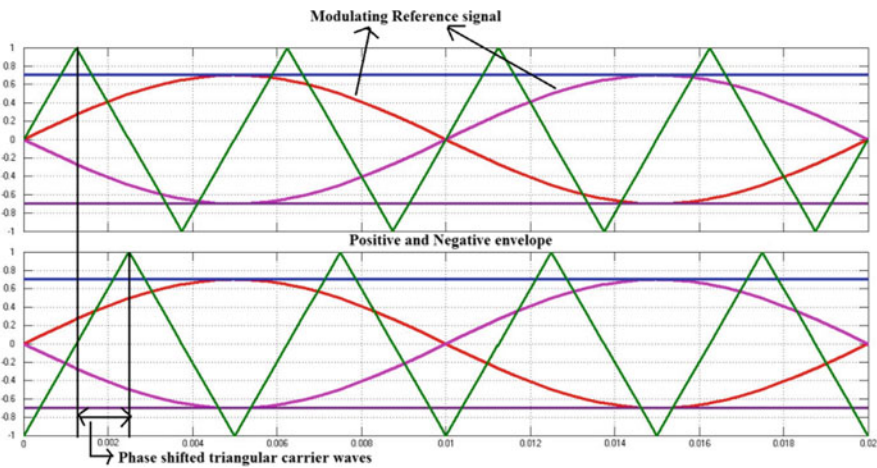


Fig. 4 Phase-shifted carrier Sine PWM [26]

with a difference that the high-frequency triangular carrier wave has to be phase shifted by 90° . But output from each module will be phase shifted by 90° , and hence, five-level output voltage is obtained.

5 Simulation Results

In the proposed topology, an input supply of 18 V is given to each module so as to obtain 100 W output across a resistive load. The component specifications used for simulation are listed below in Table 1.

The analysis of this novel topology is performed in MATLAB/SIMULINK. Figure 5a–e exhibit the simulated results of the five-level SLBI topology.

Figure 5a shows the source voltage and source current waveforms of one module. Input voltage of 18 V is applied across each module, and peak input ripple current flows through the input side.

Figure 5b shows the waveform of both the inductors current I_{La} and I_{Lb} . The optimum selection of inductor can improve the input current ripple. Otherwise, to eliminate the low frequency in the inductor current ripples, feedback techniques need to be used.

The DC link voltages of both the modules are made equal by controlling the duty ratio of the shoot-through state. Both the modules provide a DC link voltage of 75 V each with a phase shift of 90° between both the modules which is seen in Fig. 5c.

The peak voltage of 75 V appears at the output of each module which is shown in Fig. 5d.

A peak unfiltered five-level output voltage of 150 V and the peak load current of 1.3A are obtained across the load which is seen in Fig. 5d.

Table 1 Simulation parameters

Parameters	Attributes
Input voltage (V_g)	18 V
Reference wave frequency (f_0)	50 Hz
Carrier frequency (f_s)	20 kHz
Duty ratio (d_1, d_2)	0.26
Modulation index (M)	0.74
Inductance (L)	1 mH
Capacitance (C)	100 μ F
Load resistance (R_L)	121 Ω

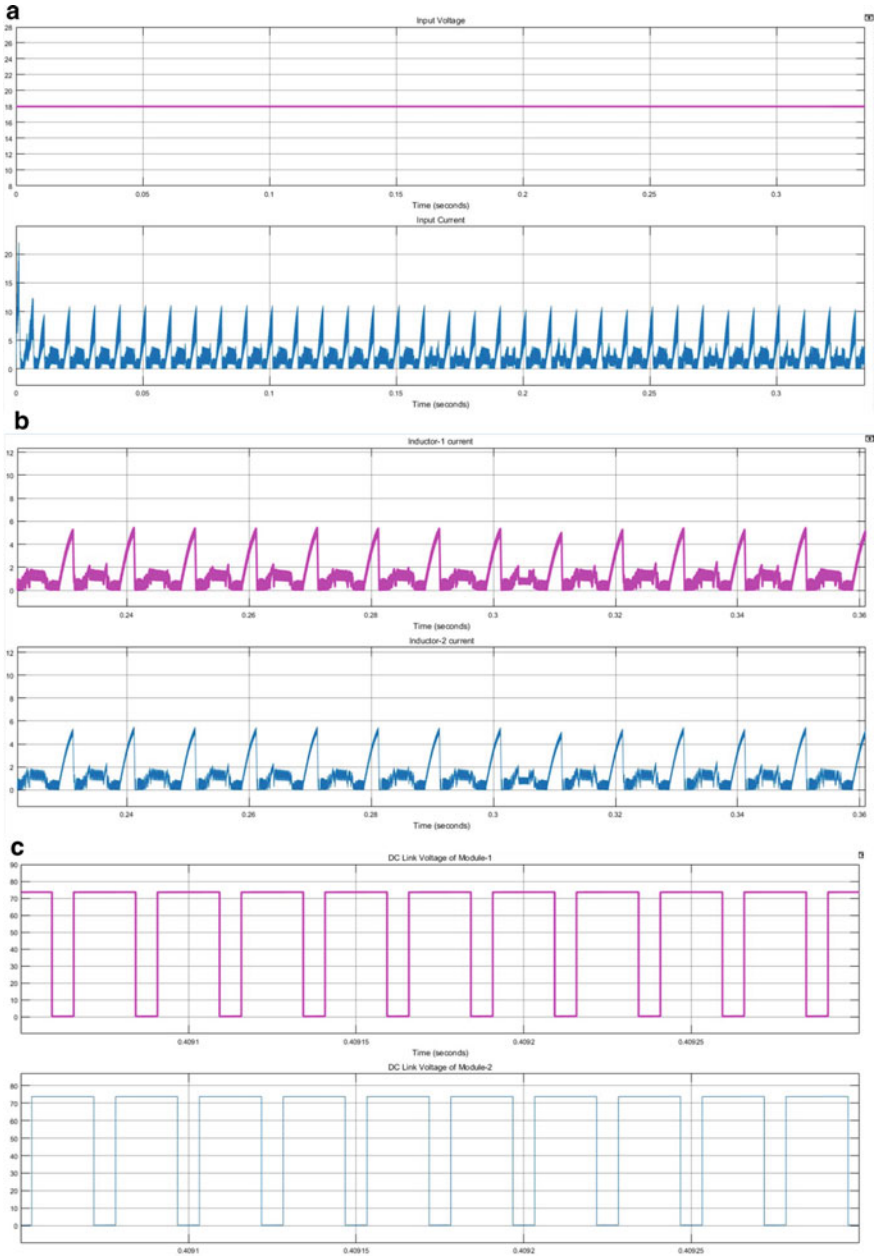


Fig. 5 **a** Waveforms of source voltage and source current, **b** inductor currents of one module, **c** DC link voltage waveforms of both modules, **d** output voltages of the modules, **e** output load voltage and load current

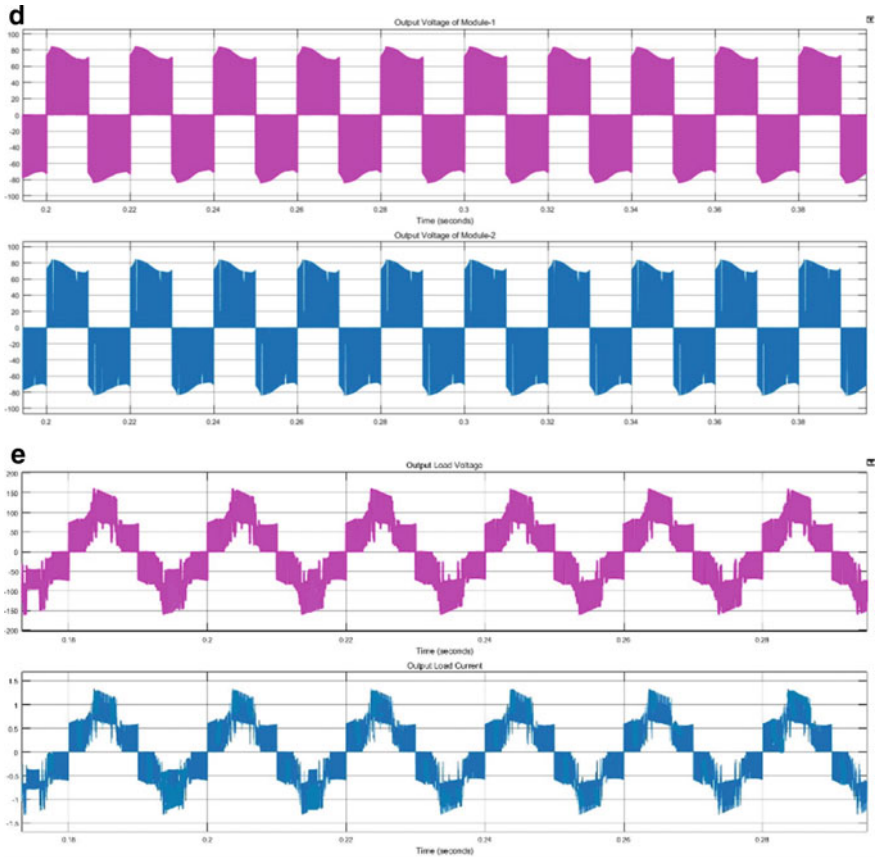


Fig. 5 (continued)

6 Performance Comparison of Five-Level SLBI and Five-Level qSBI

The performance comparison of five-level SLBI and five-level qSBI is presented in Figs. 6 and 7. The graphs are plotted between the boost factor (B) versus duty ratio (D), and gain (G) versus modulation index (M), of both SLBI and qSBI topologies. Table 2 consists of the necessary expressions used for obtaining the plots between the five-level qSBI and five-level SLBI.

It is understood from Fig. 6 that the boost factor is high for five-level cascaded H-bridge SLBI when it is compared to five-level qSBI for the same value of shoot-through duty ratio.

For the given range of modulation index, the voltage gain is high for five-level SLBI when it is compared to five-level qSBI as it is shown in Fig. 7.

Fig. 6 Boost factor (B) versus duty ratio (D)

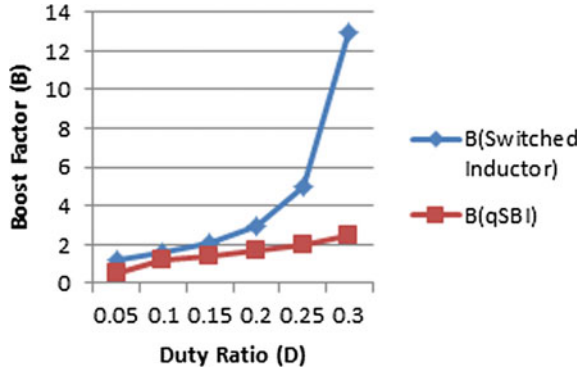


Fig. 7 Voltage gain (G) versus modulation index (M)

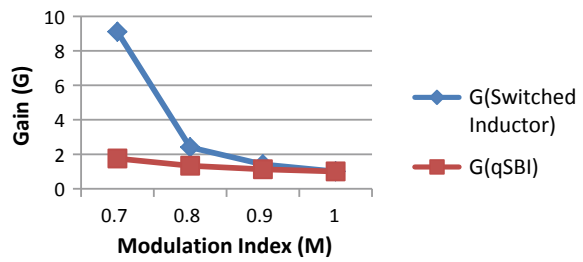


Table 2 Expressions for boost factor and voltage gain of SLBI and qSBI

S. No.	Parameters	SLBI [25]	qSBI [26]
1	B (in terms of D)	$\frac{1+D}{1-3D}$	$\frac{1}{1-2D}$
2	G (in terms of M)	$\frac{M(2-M)}{3M-2}$	$\frac{M}{2M-1}$

7 Conclusion

The operating principle, steady state analysis, and PS-PWM control strategy of the proposed topology of five-level switched inductor-based cascaded H-bridge qSBI are presented in detail. Each module with input voltage of 18 V produces five-level peak AC load voltage of 150 V. A small value of shoot-through duty ratio of d_1, d_2 , of 0.26 can provide a high gain of 4.16. The voltage stress across the devices is less, and so, higher efficiency is obtained. The performance comparison is presented between five-level qSBI and five-level SLBI. Hence, the topology is suitable whenever a small DC voltage needs to be boosted and inverted to meet the demand of low voltage and medium power applications. Further, the work can be extended to closed-loop control of five-level SL-qSBI-based topology for grid connected and renewable energy-based applications.

References

1. Chen S, Lai YM, Tan SC, Tse CK (2009) Fast response low harmonic distortion control scheme for voltage source inverters. *IET Power Electron* 2(5):574–584
2. Dasgupta S, Sahoo SK, Panda SK (2011) Single-phase inverter control techniques for interfacing renewable energy sources with microgrid—part I: parallel-connected inverter topology with active and reactive power flow control along with grid current shaping. *IEEE Trans Power Electron* 26(3):717–731
3. Peng FZ (2003) Z-source inverter. *IEEE Trans Ind Appl* 39(2):504–510
4. Tang Y, Xie S, Ding J (2014) Pulsewidth modulation of Z-source inverters with minimum inductor current ripple. *IEEE Trans Power Electron* 61(1):98–106
5. Liu JB, Hu JG, Xu LY (2007) Dynamic modeling and analysis of Z-source converter-derivation of AC small signal model and design-oriented analysis. *IEEE Trans Power Electron* 22(5):1786–1796
6. Liu Y, Ge B, Abu-Rub H, Peng FZ (2014a) Modelling and controller design of quasi-Z-source inverter with battery-based photovoltaic power system. *IET Power Electron* 7(7):1665–1674
7. Liu Y, Ge B, Abu-Rub H, Peng FZ (2014b) Phase-shifted pulse-width-amplitude modulation for quasi-Z-source cascade fivelevel inverter-based photovoltaic power system. *IET Power Electron* 7(6):1444–1456
8. Sun D, Ge B, Yan X et al (2014) Modeling, impedance design, and efficiency analysis of quasi-Z source module in cascade fivelevel photovoltaic power system. *IEEE Trans Ind Electron* 61(11):6108–6117
9. Liu H, Liu P, Zhang Y (2013) Design and digital implementation of voltage and current mode control for the quasi-Z-source converters. *IET Power Electron* 6(5):990–998
10. Ellabban O, Mierlo JV, Lataire P (2012) A DSP-based dual-loop peak DC-link voltage control strategy of the Z-source inverter. *IEEE Trans Power Electron* 27(9):4088–4097
11. Hanif M, Basu M, Gaughan K (2011) Understanding the operation of a Z-source inverter for photovoltaic application with a design example. *IET Power Electron* 4(3):278–287
12. Calzo GL, Lidozzi A, Solero L, Crescimbeni F (2012) Three-phase Z-source power supply design. *IET Power Electron* 5(8):1270–1281
13. Rajaei AH, Mohamadian M, Dehghan SM, Yazdian A (2010) Single-phase induction motor drive system using z-source inverter. *IET Electr Power Appl* 4(1):17–25
14. Banaei MR, Dehghanzadeh AR, Salary E, Khounjahan H, Alizadeh R (2012) Z-source-based fivelevel inverter with reduction of switches. *IET Power Electron* 5(3):385–392
15. Gao F, Loh PC, Blaabjerg F, Teodorescu R, Vilathgamuwa DM (2010) Five-level Z-source diode-clamped inverter. *IET Power Electron* 3(4):500–510
16. Rymarski Z, Bernacki K (2014) Influence of Z-source output impedance on dynamic properties of single-phase voltage source inverters for uninterrupted power supply. *IET Power Electron* 7(8):1978–1988
17. Qian W, Peng FZ, Cha H (2011) Trans-Z-source inverters. *IEEE Trans Power Electron* 26(12):3453–3463
18. Nguyen MK, Lim YC, Park SJ (2013) Improved trans-Z-source inverter with continuous input current and boost inversion capability. *IEEE Trans Power Electron* 28(10):4500–4510
19. Zhu M, Yu K, Luo FL (2010) Switched-inductor Z-source inverter. *IEEE Trans Power Electron* 25(8):2150–2158
20. Nguyen MK, Lim YC, Cho GB (2011) Switched-inductor quasi-Z-source inverter. *IEEE Trans Power Electron* 26(11):3183–3191
21. Nguyen M-K, Lim Y-C, Choi J-H (2012) Two switched-inductor quasi-Z-source inverters. *IET Power Electron* 5(7):1017–1025

22. Nguyen MK, Lim YC, Park SJ, Shin DS (2013) Family of high-boost Z-source inverters with combined switched-inductor and transformer cells. *IET Power Electron* 6(6):1175–1187
23. Mishra S, Adda R, Joshi A (2012) Inverse Watkins-Johnson topology-based inverter. *IEEE Trans Power Electron* 27(3):1066–1070
24. Ravindranath A, Mishra S, Joshi A (2013) Analysis and PWM control of switched boost inverter. *IEEE Trans Ind Electron* 60(12):5593–5602
25. Lim Y-C, Yoo J-Y, Park S-J, Le T-V, Nguyen M-K (2015) Class of high boost inverters based on switched-inductor structure. *IET Power Electron* 8(5):750–759
26. Tran T-T, Nguyen M-K (2017) Cascaded five-level quasi-switched-boost inverter for single-phase grid-connected system. *IET Power Electron* 10(14):1896–1903

Green Synthesis of rGO/Ag Nanocomposite for Clean Energy Storage Application



Naorem Aruna Devi and Bibhu Prasad Swain

Abstract Recently, many researchers are having more interest in developing eco-friendly synthesis methods for the production of metal nanoparticles. Nanoparticles play very important role in developing sustainable technologies for future, for humanity and the environment. Various techniques are reported for the production of nanoparticles such as physical, biological, chemical and hybrid techniques (Mohanpuria et al in *J Nanopart Res* 10:507–517 2008 [33]; Tiwari et al in *Curr Sci* 95:647–655, 2008 [34]; Luechinger et al in *Chem Mat* 22:155–160, 2010 [35]). Physical and chemical methods have been used for the synthesis of metal nanoparticles for a long time, but due to their use of high radiation and toxic reagents, this method is very unsafe for the environment as well as for the health of human. Therefore, there is a need of environmentally friendly technique. Among the various methods, green synthesis of nanoparticles is environmental-friendly technique, in which toxic, expensive chemicals and hazardous reagents were not used. Synthesis of metal nanoparticles using plants extract is seemed to be the best candidate as the synthesized nanoparticles are more stable and production rate is high than the nanoparticles produced by microorganisms (Irvani in *Green Chem* 13:2638, 2011 [37]). Green synthesis method is gaining much importance as it is simple and economic. Graphene and graphene-based nanocomposites are raised outstandingly in various research areas for applications such as catalysis, sensing and energy storage. The biological, strong mechanical strength, thermal and electrical properties make graphene-based nanocomposites of metallic nanoparticles effective in various applications. In this chapter, attempts are made in reviewing the properties of the metal nanoparticle, synthesized metal nanoparticles using various methods of green synthesis and its application for clean energy storage. Further, a green synthesis process using the extracts of *Tilia amurensis* plant for the production of rGO/Ag nanocomposites is also discussed.

Keywords Green synthesis · Environmental-friendly · Metal nanoparticles · GO · rGO/Ag nanocomposites · Clean energy storage

N. A. Devi · B. P. Swain (✉)

Department of Physics, National Institute of Technology Manipur, Imphal, India
e-mail: bibhuprasad.swain@gmail.com

© Springer Nature Singapore Pte Ltd. 2020

A. K. Bhoi et al. (eds.), *Advances in Greener Energy Technologies*,

Green Energy and Technology, https://doi.org/10.1007/978-981-15-4246-6_21

1 Introduction

The science which deals with controlling matter at the molecular level is called nanotechnology [1]. The study of nanomaterials has opened up new possibilities of application in material science and engineering such as applied microbiology, surface-enhanced Raman scattering (SERS) [2], bionanotechnology [3], quantum dots [4] and nanobiotechnology [5]. Optics, electrics, mechanics, chemical sciences, space industries, biomedical sciences, drug-gene delivery, catalysis [6, 7], photo-electrochemical applications [8], energy science, nonlinear optical devices [9, 10], optoelectronic devices [11, 12] are some fields which find the application of nanotechnology important. A peculiar property of nanomaterial is its very minute size and huge surface to volume ratio. This makes nanoparticles unique in that there is a difference of chemical and physical properties (e.g. mechanical properties, melting point, catalytic activity, optical absorption, sterical and biological properties, electrical conductivity and thermal properties.) as compared with bulk material containing composition of same chemical [13–15]. It is because of this that the interest in the study of nanomaterials has been increasing tremendously. Controlling shape and size at nanometre scale can help in achieving design and production of nanomaterials with novel applications. The size and shape-dependent properties of nanoparticles are also useful for various applications such as biosensing and catalysts, computer transistors, antimicrobial activity, chemical sensors, optics electrometers and wireless electronic logic and memory schemes. Also, the nanoparticles are useful in various fields namely hyperthermia of tumours, filters, medical imaging and drug delivery [16–19]. Medicine and pharmacy is another field where application of nanotechnology is important.

Particles whose structural dimensions are of the range of 100 nm or less are defined as nanoparticles. A green chemistry approach that links nanotechnology and plant biotechnology is the nanoparticles synthesized by plants. Nanoparticles are obtained by metal ion bioreduction using plant extracts such as alkaloids, sugar, phenolic acids, terpenoids, proteins and polyphenol. The property of the nanometric materials atoms differs from that of the bulk materials. Nanomaterials synthesized using chemical methods are dangerous to human health and not eco-friendly. Therefore, biological synthesis has started to substitute the chemical method for a more eco-friendly approach where extracts derived from plants are used to synthesize nanoparticles, and this has superiority over chemical method. Nanomedicines have opened up to new possibilities of fighting against dreadful diseases like cancer, neurodegenerative disorders and many more effectively with less adverse effect. There has been an increase in the use of natural products and plant extracts being tested for new drug discovery because of their superiority over chemicals method of synthesis. Physical and chemical methods have been used in synthesizing nanomaterial for a very long time. However, recently, researchers have started developing new ways of synthesizing nanomaterials using microorganisms and biological methods because of its eco-friendly nature and less harmful to human and environment as no harsh, toxic

chemicals are being used. Chemical reduction of silver nanoparticles is an example which may lead to absorption of toxic chemicals on the surface of nanoparticles.

The synthesis of nanoparticles using biological ways which involves plants, viruses and microorganisms, and their by-products using biotechnological tools is called green nanobiotechnology. Nanoparticles synthesized using this method have various advantages over those synthesized using chemical and physical methods in many aspects. They consume less energy, generate eco-friendly products and by-products, and also there is no use of expensive chemicals. Therefore, for these reasons, many scientists, chemists, researchers and chemical technologists have started to opt for the green synthesis method of nanoparticles. Thus, green nanobiotechnology has become the alternate ways of synthesizing biocompatible stable nanoparticles. Dried biomass of plants and metallic salts are used as bio-reducing agent and precursor, respectively, for synthesizing metallic nanoparticles in the green biotechnology method.

Recently, the appearance of graphene has been attracting a considerable research interest because of its various unique properties like high electron mobility ($200,000 \text{ cm}^2 \text{ V}^{-1} \text{ s}^{-1}$) [20], two-dimensional one atom thick sp^2 bonded single-layer carbon atom which are arranged in hexagonal honeycomb lattice [21–23], high electrical conductivity ($10^3\text{--}10^4 \text{ Sm}^{-1}$) [24], good mechanical, thermal and chemical properties [25] and large theoretical surface area ($2630 \text{ m}^2 \text{ g}^{-1}$) [26]. On account of these properties, graphene metal/metal oxide nanocomposites are considered as a potential solution in application in various technological fields such as energy storage devices, solar cells, nanoelectronics and transparent electrodes for displays. It also helps in enhancing efficiency, lifetime and selectivity of the core functioning materials in the electrocatalysis and electrosensing setups [27–29]. Various methods can be used to synthesize the graphene metal/ metal oxide nanocomposites like co-reduction, in-situ green synthesis, wet chemical, radiation, etc. These synthetic procedures are toxic to environment due to the use of harsh reducing agents like sodium borohydride, formaldehyde, strong alkaline solution (KOH and NaOH) which are harsh enough to cleave the hexagonal framework of graphene resulting in some unwanted and unrestorable chemical changes and structural damage in the graphene sheets. In order to avoid such results, we prefer the most efficient and clean technology method that is the green synthesis method among the various methods. The preparation of graphene from graphite has been done using various methods like micro mechanical exfoliation of graphite, solvo-thermal analysis, chemical vapour deposition (CVD), epitaxial growth on electrically insulating surface and solution-based chemical reduction of graphene oxide at moderate temperature. The last method which is also called solvo-thermal chemical reduction of GO is cost effective in the preparation of rGO in bulk scale. In the preparation of rGO from GO by chemical, different reductants have been used such as hydroquinone, hydrazine, sodium borohydride and dimethyl hydrazine. Disadvantages of these reductants are that the reaction is slow and can also be hazardous in nature. However, capping agents are required for strong π - π interactions between reduced graphene plates and low solubility in water or other organic solvents to prevent formation of irreversible agglomerates. These capping agents can

bring change in the properties of the graphene sheets and thus limiting in its application fields [30, 31]. So, an environment-friendly, highly productive and rapid method for the production of graphene has been endeavoured by researchers nowadays. In particular, Ag nanoparticles (AgNPs) coated rGO (AgNPs/rGO) has become famous among researchers on account of its unique electrochemical and optical properties and also its high catalytic activity [32]. There are many obstacles in the fabrication of metal nanoparticles/ rGO composites which are yet to be overcome. For instance, hazardous reducing agents like hydrazine, NaBH₄ and formaldehyde are being used in many synthesis methods. Also, there is strong absorption of other molecules or surfactants which are being used on the metal nanoparticle's surface and thus decreasing the performance of the metal nanoparticles/rGO composites. Among the various methods, green synthesis of nanoparticles is environmental-friendly technique, in which toxic, expensive chemicals and hazardous reagents were not used.

1.1 Green Synthesis of Metal Nanoparticles

Several studies have been reported in order to produce metal nanoparticles. Various techniques are reported for the production of nanoparticles such as physical, biological, chemical and hybrid techniques [33–35]. Some of the physical methods are molecular beam epitaxy, lithographic techniques, sputter deposition, spray pyrolysis, thermal evaporate, plasma arcing and ball milling, etc. In chemical methods, synthesis of nanoparticles was done by electrodeposition, sol–gel method, chemical vapour deposition, hydrolysis co-precipitation method, chemical solution deposition, wet chemical method and Langmuir Blodgett method [36]. Due to use of high radiation and toxic reagents in chemical and physical methods, this method is very unsafe for the environment as well as for the health of human. Among the various methods, green synthesis of nanoparticles is environmental-friendly technique, in which toxic, expensive chemicals and hazardous reagents were not used. Since a one-step procedure was used in the green synthesis of nanoparticles, it has different nature, possess proper size and great stabilization of nanoparticles.

Recently, the micro-organisms and biological systems are playing a vital role for the production of metal nanoparticles. It is developing at the great rate due to their easy formation of nanoparticles and over the chemical synthesis methods where harsh chemicals were used that lead to adsorption on the nanoparticle's surface which may create toxic in environment. A fresh approach has come for the production of metal nanoparticles by the use of organisms to develop the natural nano-factories. For the production of well-defined nanoparticles and high stabilization of nanoparticles, the following important aspects may be considered:

1. *Choosing of good organisms*: The best organisms for the production of metal nanoparticles were chosen depending to the organism's properties [37]. Plants having great potential in heavy metal accumulation and detoxification were considered as a perfect candidate to use in production of nanoparticles.

2. *Optimization on growth of cell and activity of enzyme*: Optimal condition is needed for the buffer strength, light, mixing speed, inoculum size, pH, temperature and nutrients. The enzyme activity increases due to the substrates present in subtoxic levels [37].
3. *Optimal reaction conditions*: Yield and productivity rate are the two important things that are to be considered for preparing metal nanoparticles using organisms [37].

Hence, bioreduction conditions need optimization in the reaction mixture. Control of pH, temperature, mixing speed, time and concentration of the substrate are needed. By optimizing these crucial components, the nanoparticle's properties and morphologies could be controlled.

At recent, many researchers proved that the extracts of plant act as potential precursor in order to produce nanoparticles in environmental-friendly and non-toxic ways. The green synthesis with the use of plant extracts exhibits more attention than chemical methods and physical techniques. Using the extracts of plant in the preparation of metal nanoparticles is easy and low cost, and thus, it can be used to produce metal nanoparticles in a large scale economically. In the synthesis of nanoparticles, plants extract functions as the reducing agent as well as the capping agent also. Therefore, the reduction process of metal nanoparticles containing biomolecules of different combinations such as amino acids, vitamins and enzymes that are found in plant extracts is not harmful to environment.

Several biosynthesis methods of using plant leaf extracts in production of metal nanoparticles have been reported by many researchers. Sastry et al. investigated the reduction of Ag and Au nanoparticles with using *Pelargonium graveolens* leaf broth [38, 39] and broth of *Azadirachta indica* leaves [40]. Shankar et al. [40] investigated on the reduction of aqueous Ag⁺ and AuCl₄ ions using neem leaf (*A. indica*) broth for biosynthesis of pure metallic nanoparticles and simultaneously also for bimetallic core-shell nanoparticles (i.e. for synthesized gold and silver nanoparticles). The author reported that even after keeping for four weeks in solution after the synthesis, stability of the metal particles was observed. Further, they reported that it might be due to the presence of terpenoids or reducing agents in the leaf broth of neem. Synthesized silver nanoparticles are mostly appeared to be in spherical form and polydispersed having a range of diameter 5–35 nm. Gold nanoparticles synthesized with the use of broth leaf of neem are seemed to have a tendency of forming thin planar structures instead of just having particles of spherical form. Mostly, the formation of the planar particles is in triangular shaped with little hexagonal-shaped particles [40]. Jha et al. [41] confirmed that with the use of *Cycas* leaf extract, the stable silver nanoparticles can be produced. XRD shows the structure of silver nanoparticles having fcc crystal structure. Vilchis-Nestor et al. [42] studied the production of silver and gold nanoparticles at ambient conditions using aqueous solution of the extract of green tea (*Camellia sinensis*). Further investigation on tea extract as controlling components, metal ions concentrations and optical properties of nanostructure, morphology and size were also reported. They found that the obtained nanomaterials become slightly bigger and more spherical when *C. sinensis* extract amount

increases. Further demonstrated that the synthesis and stabilization of Ag and Au nanoparticles were obtained due to the presence of phenolic acid-type biomolecule that are found to be present in the extract of *C. sinensis*. Another investigation was done using leaf extract of black tea for synthesis of silver and gold nanoparticles [43]. They found stable nanoparticles and nanoparticles having different shapes like prisms, rods, trapezoids and spheres. The author explained that synthesis of nanoparticles might have resulted due to polyphenols and flavonoids. Mude et al. [44] have used callus extract of *Carica papaya* in preparing silver nanoparticles having sphere shape structure of diameter ranging from 60 to 80 nm. It was reported that for being stable, metal nanoparticles and synthesis proteins and other ligands might be responsible. Moreover, with the use of *Jatropha curcas* latex which acts as both capping as well as reducing agent were also have been reported for the synthesis of Ag nanoparticles [45]. Investigation on preparation of nanoparticles by using the extracts of fruit was also been reported. A new approach of using banana peel (*Musa paradisiaca*) extract was reported by Bankar et al. [46] in order to produce Ag nanoparticles. After washing the banana peels, it was boiled at a particular temperature viz. 90 °C for around 30 min in distilled water. It is a well-known fact that when we incubate the reaction mixture at a particular temperature, and the reduction process of metal will be affected at that temperature. The reactants are consumed rapidly with the increase in temperature which leads to produce small nanoparticles.

1.2 *rGO/Ag Nanocomposite for Clean Energy Storage Application*

The concern about the environment to meet the increasing energy demand has led to the birth of a quest for sustainable energy storage device having high density of energy and power. Super capacitor is considered as a clean energy storage device among the energy storage devices. Super capacitors exhibit a large specific capacitance (capacitance per unit mass), high energy and power density, dynamic storage capacity along with a long life for many cyclic operations [47, 48]. For example, a chemically modified graphene-based super capacitor with aqueous electrolyte has a specific capacitance of 135 Fg⁻¹, and it can be increased up to 205 Fg⁻¹ by hydrazine reduction of graphene [49]. The improvement in specific capacitance leads to the various improvements in the electrochemical properties of graphene resulting in an ultrahigh density of energy [50]. Although many different kinds of carbon and carbon metal oxides have been introduced as electrode material in the past few years, but the search for newer electrode materials for better specific capacitance with a greater cyclic stability is still in progress. Although graphene is an excellent choice for super capacitor application for its high surface area, superior electrochemical and mechanical properties, but pure graphene nanosheets deliver a specific capacitance much lower than the theoretical value. This happens due to the agglomeration of single graphene sheet [51–53]. One way to solve this issue is synergistic coupling

of graphene with metal oxide nanoparticles. The hybrid nanocomposite materials exhibit a much higher specific capacitance with enhanced cyclic stability. A wide range of metal oxides which includes SnO_2 , Co_3O_4 , MnO_2 , Fe_2O_3 , ZnO , Fe_3O_4 , RuO_2 and CeO_2 has been studied in laboratory by anchoring them with the support of graphene sheet [54]. A further improvement is seen enhancing the electrocatalytic activity when the nanocomposites were doped with some novel metals like silver, lead, gold [55]. Zhenyuan et al. establish such a ternary composite of reduced graphene oxide (rGo)/Ag/ CeO_2 with an enhanced capacitive performance. Ag decorated MnO_2 /rGO nanocomposite is another of ternary composite where the Ag nanoparticles enhance the electrical conductivity by acting like a bridge for the electrons [56]. In recent studies, it is found that the two-step hydrothermal process is an effective way to synthesize Ag grafted ternary nanocomposites with good capacitive performance. In the following context, a green synthesis process using *Tilia amurensis* plant extracts (TAPE) for the production of rGO/Ag nanocomposites is discussed.

2 Experimental Procedures

2.1 Synthesis of AgNPs

Synthesis of AgNPs has already been done using several green synthesis methods. In this case, *T. amurensis* leaves were collected, and until it was needed should be stored at 4 °C. Wash 20 g of *T. amurensis* leaves using double distilled water thoroughly. After washing it properly, a sharp stainless steel knife is to be used to make a slice of the leaves into fine pieces of about 1–5 cm. Now, the shredded *T. amurensis* leaves are to be put in sterile distilled water (100 mL) and then kept it for 5 min to boil. By using a Whatman number 1 filter paper, the mixture which has obtained is to be filtered. For the synthesis of AgNPs, the filtered extract was used, and 5 mM of aqueous AgNO_3 of about 10–100 mL were added. Then, incubate the mixture for another 6 h at particular temperature viz. 60 °C, and the pH of the mixture was controlled at 8 [57].

2.2 Synthesis of GO

Modified hummer's method was used for the synthesis of GO. In this synthesis process, at 0 °C, add 2 g of natural graphite powder to 350 mL of H_2SO_4 , and then, gently add 8 g of KMnO_4 and 1 g of NaNO_3 while stirring. Now, transfer the mixture to a 40 °C water bath, and stirring is done for about 60 min. Slowly add 250 mL of deionized water, and there should be an increase in temperature, i.e. 98 °C. The mixture was heated at particular temperature (98 °C) for 30 min. By adding deionized

water (500 mL) and 30% of H_2O_2 solution (40 mL), the reaction was terminated. The product changes its colour to brilliant yellow which indicates the oxidation of pristine graphite to graphite oxide. Later filter the product and wash it by using diluted HCl to take off the metal ions. Until a pH of 7 is achieved, wash the product repeatedly with distilled water, and to obtain exfoliated graphene oxide, the obtained powder was further sonicated for 15 min [57].

2.3 Synthesis of rGO

In this procedure, add 10 mL of *T. amurensis* plant extract in the aqueous GO of 90 mL 1.0 mg/mL, and the solution is transferred to a tightly sealed glass bottle. After that, the mixture is stirred and heated at 30 °C for about 12 h. Afterwards, with the use of the magneto stirrer heater, stirring is done for the rGO suspension for around 30 min at 400 rpm at a particular temperature viz. 30 °C. Without aggregation, a homogeneous suspension of *T. amurensis* plant extract with rGO was formed. Now, by using the distilled water, the obtained product is to be washed for many times in order to confirm the removal of the excess *T. amurensis* plant extract residue, and by sonication, the product is again dispersed in water. Finally, the obtained suspension is to be done centrifugal for another 30 min at 5000 rpm, and later in vacuum, the sonicated mixture is to be filtered and dried to obtain the required rGO [57].

2.4 Synthesis of rGO/Ag Nanocomposite

Figure 1 (a, b) and Fig. 2 (a, b) show the rGO/Ag nanocomposites have been synthesized by using *T. amurensis* plant extracts. Aqueous GO solutions of about 100 mg and AgNO_3 (5 mM) were the precursors used. At first, by using sonicator, 100 mg of GO is to be dispersed in water (60 mL) for 60 min. In a round bottom flask of about 250 mL, 5 mM of AgNO_3 were to be dissolved in 30 mL water to prepare the reaction mixture. And then, 60 mL of GO was dispersed in the solution and aqueous TAPE of about 10 mL were added. The mixture is stirred for around 12 h and heated at a particular temperature (90 °C). The colour of the mixture will be changed after 12 h when the reaction is stopped. Finally, the obtained mixture is to be centrifuged with water for three times in order to remove unreacted reagents. The obtain powder was black in colour [57].

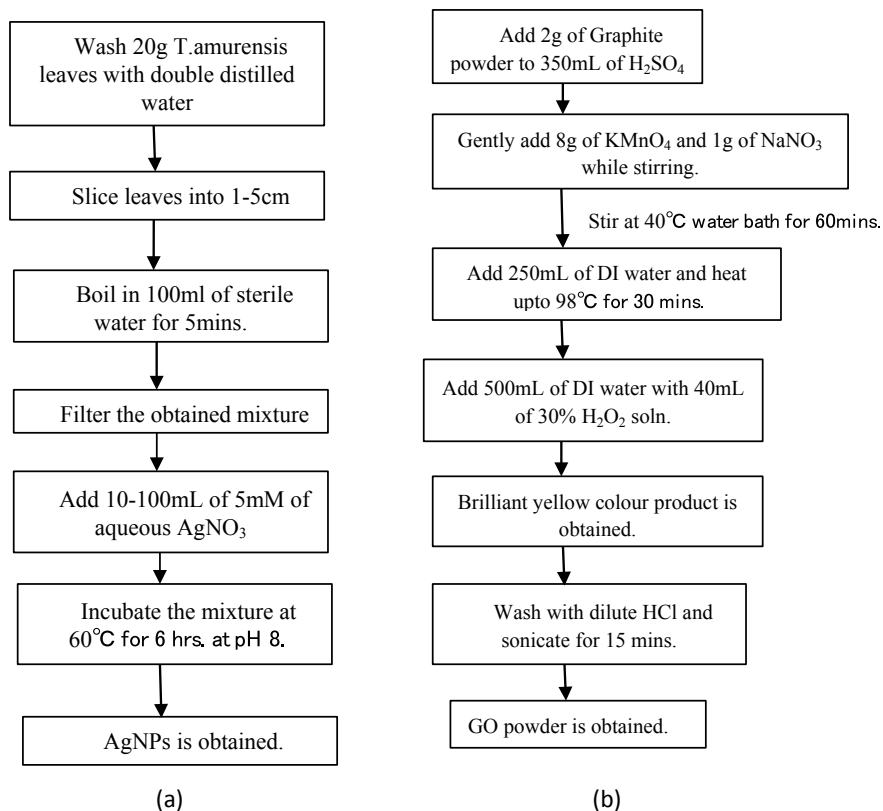


Fig. 1 a Synthesis of AgNPs and b Synthesis of GO

3 Structural Characterization Technique

3.1 XRD

X-ray diffraction is a non-destructive analytical technique mainly used for phase identification and structural characterization of crystalline materials. Bragg's Law is expressed as

$$2d_{hkl} \sin \theta = n\lambda$$

where θ is the incident angle, λ is the wavelengths of the x-rays, and d (hkl) is spacing between two crystal lattice planes.

XRD shows a number of peaks in the diffraction patterns. By comparing their positions and relative intensities with the known structure database, their patterns are to be identified. The extra peaks might sometimes appear due to the impurity or

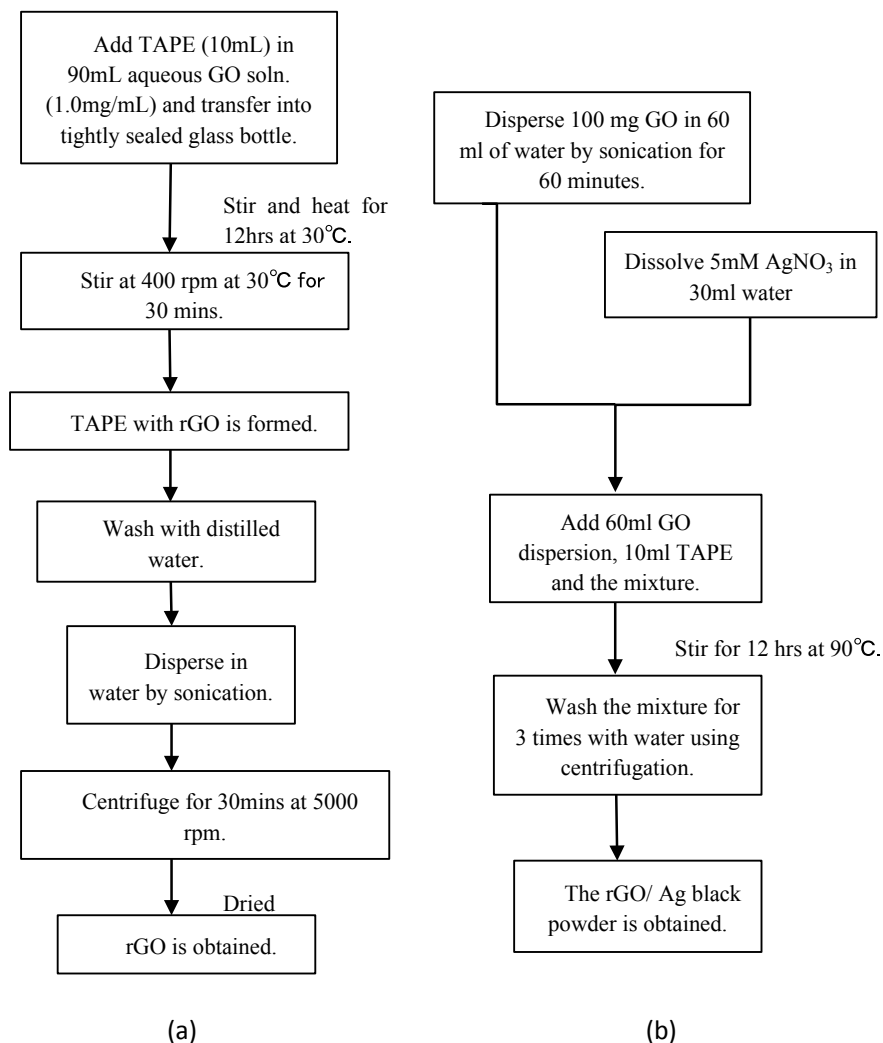


Fig. 2 **a** Synthesis of rGO and **b** synthesis of rGO/Ag nanocomposite

structural information after the thermal treatment. Gurunathan et al. [57] reported that the XRD patterns of GO, rGO and rGO–Ag confirm the crystalline nature of the rGO–Ag nanocomposites which are shown in Fig. 3. They also demonstrated that at a low angle, GO shows a reflection (i.e. $2\theta = 10.9^\circ$) as compared to graphite (i.e. $2\theta = 26.5^\circ$). A new reflection arises after disappearance of reflection in GO that indicates the rGO which is at angle $2\theta = 26.4^\circ$. But in spite of the XRD pattern obtained for rGO and GO, the rGO–Ag nanocomposites show two easily distinguishable reflections. One of the diffraction peaks which appears at 33.1° that corresponds to the plane (111), and the another diffraction peak is located at 45.3° which corresponds to the

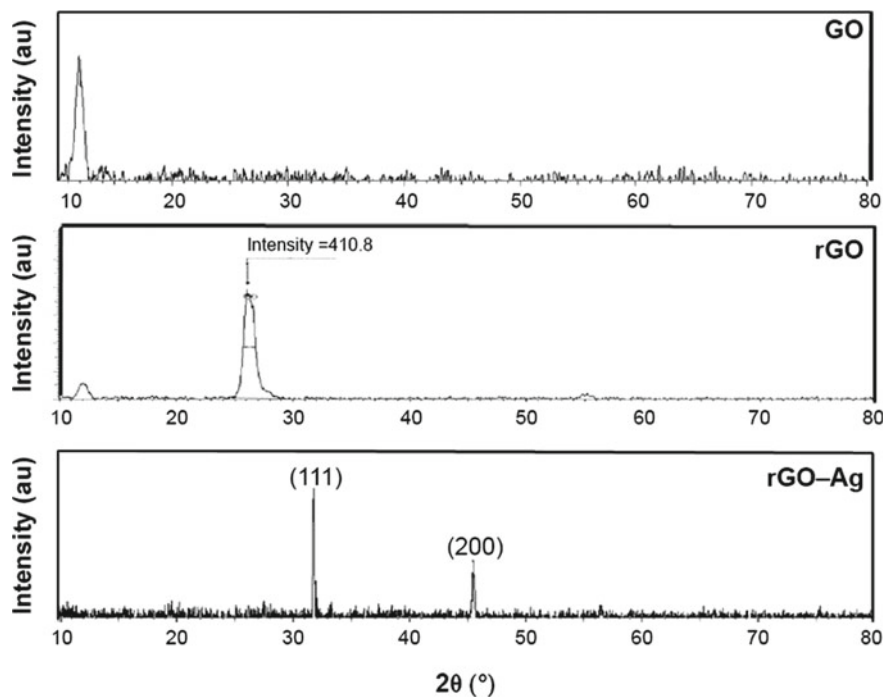


Fig. 3 a XRD pattern of GO, b rGO and c rGO/Ag nanocomposite [57]

plane (200) of Ag having fcc crystalline structure [58]. Thus, XRD confirms the structure of AgNPs having fcc crystal structure. Any other reflections have not been seen in addition to that of Ag and graphene, in a clear manner indicating the reduction graphene oxide and silver ions. This also gives the idea that the other molecules in the extract of plant do not affect the lattice of rGO–Ag nanocomposite.

3.2 SEM

SEM is a type of electron microscope that is used to determine the composition and the surface topography of the sample. The images obtained by SEM are shown in Fig. 4, where Fig. 4a is for GO, Fig. 4b is for rGO, and Fig. 4c is for rGO/AG nanocomposite. A structure of closely packed arranged in lamellae, and brittle structure is seen in the SEM image of GO Fig. 4a, indicating microstructure having multilayer. Many aggregated layers and crumpled sheets having shape of square were present in the sample of GO which are closely related to each other in order to form a conducting network continuously [59]. The GO sheets edges get folded, crumpled and restack closely when exfoliation of GO from Gt occurs. Moreover, it also gives the idea about the morphology of GO surface which is seen to have carpet-like soft structure.

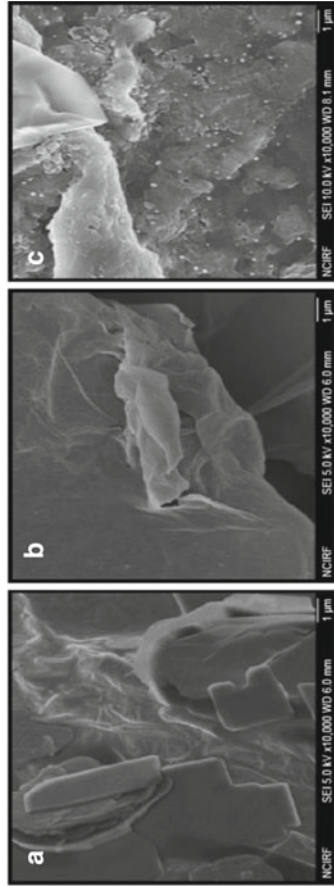


Fig. 4 SEM images of GO, rGO and rGO/Ag nanocomposite [57]

The group of carboxyl or hydroxyl and the remaining molecules of water might be responsible for it [57]. But rGO is in contrast with GO, it shows transparent rippled silk-like waves or a flaky, scale-like, layered structure [57]. The SEM images of rGO–Ag nanocomposite are shown in Fig. 4c, which reveals that AgNPs were dispersed well having size ranging from 10 to 20 nm which are transferred on the graphene. The SEM image of rGO/Ag nanocomposite shows a wavy and curled morphology. The AgNPs are well dispersed and distributed homogeneously on the surface of rGO.

3.3 TEM

The morphology of the prepared rGO–Ag along with GO and rGO is characterized by TEM analysis. A typical image obtained from TEM is shown in Fig. 5 [57]. From the image of GO, it is seen that GO has a plate and lamellar structure packed closely having a clean surface. In case of rGO, it shows a structure like sheets of 100 nm in size. The image of rGO–Ag shows that many nanoparticles are attached to the surfaces of both of the samples. The anchored NPs show spherical morphology and are mostly of the size of 20 nm; they are distributed evenly and dispersed homogeneously on the surface of rGO. It can also be observed that the rGO sheets are distributed in evenly spread silky, wave-like structure. For anchoring of Ag NPs, the rGO sheet should not be aggregated, and it can be seen in the image that aggregation did not occur. In the image of rGO–Ag, it is clearly defined that almost all the silver NPs are residing on the GO support leaving only a very few in outside of the GO structure. This indicates that strong interactions are present between AgNPs and GO [60].

In a recent work of Yuan and co-workers, graphene/AgNPs (GNS/AgNPs) is fabricated employing a simple green synthesis technique. The precursors which were used in this synthesis are as follows: GO for graphene, AgNO₃ for AgNPs. Sodium citrate was used as stabilizer and reducing agent. Chook and co-workers fabricated Ag–GO nanocomposites and AgNPs using a green way of microwave irradiation. By analysing the Ag–GO samples obtained in this way, it is found that the AgNPs have a size of 40.7 ± 7.5 nm on average, and they are deposited on the GO sheet layers [61]. In another work of Hu et al., AgNPs and rGO were synthesized using a reducing and stabilizing agent poly (N-vinyl-2-pyrrolidone) [60]. The TEM image of the resulting rGO–Ag nanocomposite shows that the AgNPs are having a diameter of 13 nm average and are well-dispersed and distributed within the almost transparent GO sheets.

de Faria and co-workers demonstrated another green synthesis technique for GO–Ag employing biomolecules. In this method, metal NPs surrounded by protein can interact with oxygenated-groups which allow the AgNPs to attach to the GO surface [62].

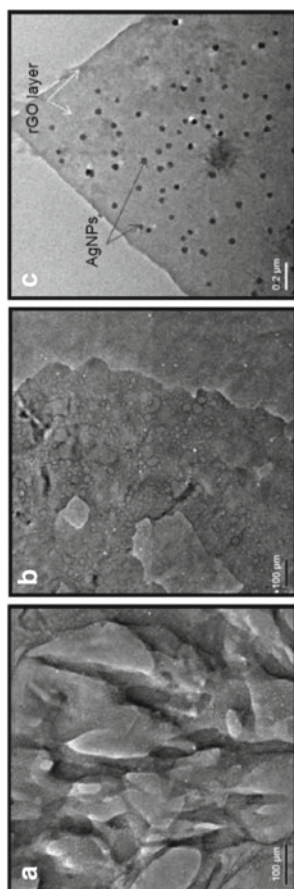


Fig. 5 TEM images of GO, rGO and rGO/Ag nanocomposite [57]

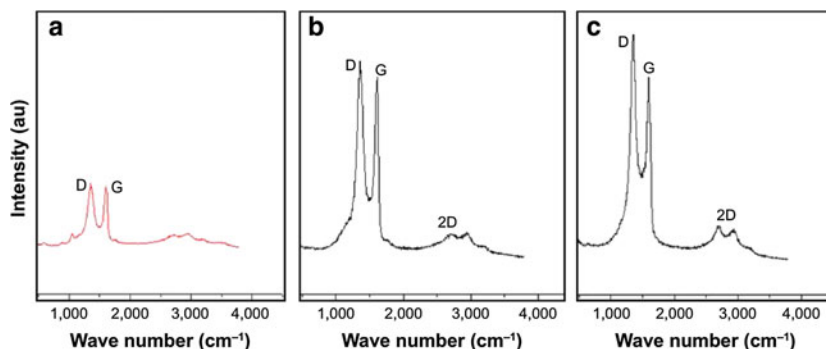


Fig. 6 Raman spectrum for GO, rGO and rGO/Ag nanocomposite [57]

3.4 Raman Spectroscopy

Raman spectroscopy technique provides us the information about the structural and electronic properties of graphene-based composite. It gives the fingerprint by which molecules can be identified. Gurunathan et al. [57] observed that it gives further confirmation of the reducing ability of TAPE for AgNO_3 and GO. The author observed a broad G band in Raman spectra for GO shifted to 1599 cm^{-1} , and the appearance of D band at 1347 cm^{-1} was observed (Fig. 6a). In case of rGO, it shows that the G band is found to be at 1584 cm^{-1} , and the D band was appeared at 1351 cm^{-1} as shown in Fig. 6b. The D band was attributed to the breathing mode of the k-point phonons of A_{1g} symmetry, which shows the disorder or defects in carbon atoms formed due to the attachment of epoxide and hydroxyl groups on the basal plane of the carbon, whereas G band brings out the E_{2g} phonon of the carbon sp_2 atoms. Gurunathan et al. also demonstrated the broadening of G bands that occur in Raman spectra for rGO/Ag nanocomposite and rGO that may be due to the intensify isolated double bonds while also suggested for the intensification of the D bands, the disorder enhancing of the rGO/Ag nanocomposite and rGO might be responsible. Raman spectra for rGO/Ag nanocomposite found a G band around 1611 cm^{-1} (Fig. 6c), which is upshifted by 27 cm^{-1} as compared to Raman spectra obtained for rGO. Other researchers have also reported that the upshift of the G band occurs due to the coupling of electron-coupling in the presence of Au. Hui et al. [32] also showed the D band in Raman spectra for the composite of GO and Ag was found at 1351 cm^{-1} , whereas the G band was appeared at 1602 cm^{-1} approximately. Dinh et al. also showed the typical feature of GO in Raman spectra where a D band appeared at 1351 cm^{-1} and a G band at 1602 cm^{-1} . Moreover, the G band for the AgNPs/rGO sample was found to be shifted to 1589 cm^{-1} . The ratio of the intensities (I_D/I_G) is generally used in order to measure the defect levels in graphitic systems. The ratio of these intensities for rGO/Ag increases to 2.09 as compared to that of the rGO's intensity ratio 1.74 and GO obtaining intensity ratio as 1.54 [57], suggesting that during the treatment of Ag nanoparticles, the graphene sheet was broken into fragments which leads to decrease

the sp_2 domain size. The ratio of the intensity of the bands increases when there is introduction of rGO/Ag nanocomposite which indicates the degree of disorder. To distinguish the thickness of the sheet of the graphene, the 2D band is commonly known. The 2D band was observed at 2672 cm^{-1} for the composite of rGO and Ag indicating that there presents a small amount of graphene sheet layers.

4 Summary/Conclusion

In this context, we studied rGO/Ag nanocomposite prepared by green synthesis method using TAPE. Green synthesis of nanoparticles is environmental-friendly technique in which toxic, expensive chemicals and hazardous reagents were not used. Nanoparticles synthesized using green synthesis method has various advantages over those synthesized using chemical and physical methods on many aspects. They consume less energy, generate eco-friendly products and by-products, and also, there is no use of expensive chemicals. Characterizations of synthesized rGO/Ag nanocomposite were carried out using XRD, SEM, TEM and Raman spectroscopy. The XRD pattern of these compositions confirmed the formation of fcc crystal structure. Synthesized AgNPs appear to be in spherical form and well dispersed having a range of diameter around 10–20 nm. Furthermore, even after keeping for three months, stability and solubility of rGO/Ag nanocomposite were observed outstandingly. Synthesis of metal nanoparticles using plants extract is seemed to be the best candidate, as the synthesized nanoparticles are more stable and production rate is high than the nanoparticles produced by microorganisms. Reduction of metal ions using plants acts fast than using bacteria or fungi. The stabilization and formation of AgNPs obtained might be due to the presence of vitamins, alcoholic compounds, proteins, alkaloids, polysaccharides and amino acids biomolecule that are found to be present in the plant. Thus, green synthesis method is gaining much importance as it is simple and economic. Moreover, the biological, strong mechanical strength, thermal and electrical properties make graphene-based nanocomposites of metallic nanoparticles effective in various applications.

References

1. Senapati S (2005) Biosynthesis and Immobilization of nanoparticles and their applications. PhD thesis, University of Pune, pp 2–174, (2005).
2. Klefenz H (2004) Nanobiotechnology: From Molecules to Systems. *Eng. Life Sci.* 4:211–218
3. Goodsell D (2004) The quest for nanotechnology. *Bionanotechnology: lessons from Nature* pp 1–8 (2004)
4. Chan WCW, Nie S (1998) Quantum Dot Bioconjugates for ultrasensitive nonisotopic detection. *Science* 281:2016–2018
5. Tian Z, Ren B (2004) Adsorption and reaction at electrochemical interfaces as probed by surface-enhanced raman spectroscopy. *Annu Rev Phys Chem* 55:197–229

6. Schmid G (1992) Large clusters and colloids—metals in the embryonic state. *Chem Rev* 92:1709–1727
7. Hoffman AJ, Mills G, Yee H, Hoffmann MR (1992) Q-sized CdS: synthesis, characterization, and efficiency of photoinitiation of polymerization of several vinylic monomers. *J Phys Chem* 5546–5552
8. Colvin VL, Schlamp MC, Alivisatos A (1994) Light-emitting diodes made from cadmium selenide nanocrystals and a semiconducting polymer. *Nature* 370:354–357
9. Wang Y, Herron N (1991) Nanometer-sized semiconductor clusters: materials synthesis, quantum size effects, and photophysical properties. *J Phys Chem* 95:525–532
10. Mansur HS, Grieser F, Marychurch MS, Biggs S, Urquhart RS, Furlong DN (1995) Photoelectrochemical properties of ‘Q-state’ CdS particles in arachidic acid Langmuir–Blodgett films. *J Chem Soc Faraday Trans* 91:665–672
11. Wang Y (1991) Nonlinear optical properties of nanometer-sized semiconductor clusters. *Acc Chem Res* 24:133–139
12. Yoffe AD (1993) Low-dimensional systems: quantum size effects and electronic properties of semiconductor microcrystallites (zero-dimensional systems) and some quasi-two-dimensional systems. *Adv Phys* 42:173–266
13. Daniel MC, Astruc D (2004) Gold nanoparticles: assembly, supramolecular chemistry, quantum-size-related properties, and applications toward biology, catalysis, and nanotechnology. *Chem Rev* 104:293–346
14. Bogunia-Kubik K, Sugisaka M (2002) From molecular biology to nanotechnology and nanomedicine. *BioSystems* 65:123–138
15. Zharov VP, Kim JW, Curiel DT, Everts M (2005) Self-assembling nanoclusters in living systems: application for integrated photothermal nanodiagnostics and nanotherapy. *Nanomed.: Nanotechnol. Biol Med* 1:326–345
16. Tan M, Wang G, Ye Z, Yuan J (2006) Synthesis and characterization of titania-based monodisperse fluorescent europium nanoparticles for biolabeling. *J Lumin* 117:20–28
17. Lee HY, Li Z, Chen K, Hsu AR, Xu C, Xie J, Sun S, Chen X (2008) PET/MRI dual-modality tumor imaging using arginine-glycine-aspartic (RGD)-conjugated radiolabeled iron oxide nanoparticles. *J Nucl Med* 49:1371–1379
18. Pissuwan D, Valenzuela SM, Cortie MB (2006) Therapeutic possibilities of plasmonically heated gold nanoparticles. *Trends Biotechnol* 24:62–67
19. Panigrahi S, Kundu S, Ghosh S, Nath S, Pal T (2004) General method of synthesis for metal nanoparticles. *J. Nanopart. Res.* 6:411–414
20. Bolotin KI, Sikes KJ, Jiang Z, Klima M, Fudenberg G, Hone J, Kim P, Stormer HL (2008) Ultrahigh electron mobility in suspended graphene. *Solid State Commun* 146:351–355
21. Rao CNR, Biswas K, Subrahmanyam KS, Govindaraj A (2009) Graphene, the new nanocarbon. *J Mater Chem* 19:2457–2469
22. Allen MJ, Tung VC, Kaner RB (2010) Honeycomb carbon: a review of graphene. *Chem Rev* 110:132–145
23. Pereg-Barnea T, Refael G (2012) Inducing topological order in a honeycomb lattice. *Phys Rev B* 85:075127
24. Novoselov KS, Geim AK, Morozov SV, Jiang D, Zhang Y, Dubonos SV, Grigorieva IV, Firsov AA (2004) Electric field effect in atomically thin carbon films. *Science* 306:666–669
25. Lee C, Wei XD, Kysar JW, Hone J (2008) Measurement of the elastic properties and intrinsic strength of monolayer graphene. *Science* 321:385–388
26. Stoller MD, Park SJ, Zhu YW, An JH, Ruoff RS (2008) Graphene-based ultracapacitors. *Nano Lett* 8:3498–3502
27. Jeon EK, Seo E, Lee E, Lee W, Um MK, Kim BS (2013) Mussel-inspired green synthesis of silver nanoparticles on graphene oxide nano sheets for enhanced catalytic applications. *Chem Commun* 49:3392–3394
28. Li SS, Lv JJ, Teng LN, Wang AJ, Chen JR, Feng JJ (2014) Facile synthesis of PdPt@Pt nanorings supported on reduced graphene oxide with enhanced electrocatalytic properties. *ACS Appl Mater Interfaces* 6:10549–10555

29. Wang H, Wang C, Yang B, Zhai C, Bin D, Zhang K, Yang P, Du Y (2015) A facile fabrication of copper particle-decorated novel graphene flower composites for enhanced detecting of nitrite. *Analyst* 140:1291–1297
30. Si Y, Samulski ET (2008) Synthesis of water soluble graphene. *Nano Lett* 8:1679–1682
31. Gupta B, Kumar N, Titovich KA, Ivanovich KV, Vyacheslavovich SA, Dash S (2017) Lubrication properties of chemically aged reduced graphene-oxide additives. *Surf Interfaces* 7:6–13
32. Hui KS, Hui KN, Dinh DA, Tsang CH, Cho YR, Zhou W, Hong X, Ho-Hwan C (2014) Green synthesis of dimension-controlled silver nanoparticle–graphene oxide with in situ ultrasonication. *Acta Mater* 64:326–332
33. Mohanpuria P, Rana NK, Yadav SK (2008) Biosynthesis of nanoparticles: technological concepts and future applications. *J Nanopart Res* 10:507–517 (2008)
34. Tiwari DK, Behari J, Sen P (2008) Time and dose-dependent antimicrobial potential of Ag nanoparticles synthesized by topdown approach. *Curr Sci* 95:647–655
35. Luechinger NA, Grass RN, Athanassiou EK, Stark WJ (2010) Bottom-up fabrication of metal/metal nanocomposites from nanoparticles of immiscible metals. *Chem Mat* 22:155–160
36. Parveen K, Banse V, Ledwani L (2016) Green synthesis of nanoparticles: their advantages and disadvantages. *AIP* 1724:020048
37. Iravani S (2011) Green synthesis of metal nanoparticles using plants. *Green Chem* 13:2638
38. Shankar SS, Ahmad A, Pasricha R, Sastry M (2003) Bioreduction of chloraurate ions by geranium leaves and its endophytic fungus yields gold nanoparticles of different shapes. *J Mater Chem* 13:1822–1826
39. Shankar SS, Absar A, Mural S (2003) Geranium leaf assisted biosynthesis of silver nanoparticles. *Biotechnol Prog* 19:1627–1631
40. Shankar SS, Rai A, Ahmad A, Sastry M (2004) Rapid synthesis of Au, Ag, and bimetallic Au core-Ag shell nanoparticles using Neem (*Azadirachta indica*) leaf broth. *J Colloid Interface Sci* 275:496–502
41. Jha AK, Prasad K (2010) Green synthesis of silver nanoparticles using cycas leaf. *Int J Green Nanotechnol: Phys Chem* 1:110–117
42. Vilchis-Nestor AR, Mendieta VS, Camacho-López MA, Gómez-Espinosa RM, Camacho-López MA, Arenas-Alatorre JA (2008) Solventless synthesis and optical properties of Au and Ag nanoparticles using *Camellia sinensis* extract. *Mater Lett* 62:3103–3105
43. Begum NA, Mondal S, Basu S, Laskar RA, Mandal D (2009) Biogenic synthesis of Au and Ag nanoparticles using aqueous solutions of Black Tea leaf extracts. *Colloids Surf B* 71:113–118
44. Mude N, Ingle A, Gade A, Rai M (2009) Synthesis of silver nanoparticles using callus extract of *Carica papaya*. *J Plant Biochem Biotechnol* 18:83–86
45. Bar H, Bhui DKr, Sahoo GP, Sarkar P, De SP, Misra A (2009) Green synthesis of silver nanoparticles using latex of *Jatropha curcas*. *Colloids Surf A Physicochem Eng Asp* 339:134–139
46. Bankar A, Joshi B, Kumar AR, Zinjarde S (2010) Banana peel extract mediated novel route for the synthesis of silver nanoparticles. *Colloids Surf A Physicochem Eng Asp* 368:58–63
47. Vanitha M, Balasubramanian N (2013) Waste minimization and recovery of valuable metals from spent lithium-ion batteries—a review. *Environ Technol Rev* 2:101–115
48. Kotz R, Carlen M (2000) Principles and applications of electrochemical capacitors. *Electrochim. Acta* 45:2483–3498
49. Du X, Guo P, Song H, Chen X (2010) Graphene Nanosheets as electrode material for electric double-layer capacitors. *Electrochim Acta* 55:4812–4819
50. Zhu Y, Murali S, Stoller MD, Ganesh KJ, Cai W, Ferreira PJ, Pirkle A, Wallace RM, Cychosz KA, Thommes M, Su D, Stach EA, Ruoff RS (2011) Carbon-based supercapacitors produced by activation of graphene. *Science* 332:1537–1541
51. Geim AK (2009) Graphene status and prospects. *Science* 324:1530–1534
52. Hou JG, Yang C, Wang Z, Jiao SQ, Zhu HM (2013) Bi₂O₃ quantum dots decorated anatase TiO₂ nanocrystals with exposed (001) facets on graphene sheets for enhanced visible light photocatalytic performance. *Appl Catal B* 129:333–341

53. Antolini E (2012) Graphene as a new carbon support for low temperature fuel cell catalysts. *Appl Catal B* 123:52–68
54. Vanitha M, Keerthi CP, Balasubramanian N (2015) Ag nanocrystals anchored CeO₂/graphene nanocomposite for enhanced supercapacitor applications. *J Alloys Compd* 644:534–544
55. Shuping Y, Qiubo L, Wensheng Y, Kefei H, Zhongming W, Hong Z (2013) Graphene-CeO₂ hybrid support for Pt nanoparticles as potential electrocatalyst for direct methanol fuel cells. *Electrochim Acta* 94:245–251
56. Lianbo M, Xiaoping S, Zhenyuan J, Guoxing Z, Hu Z (2014) Ag nanoparticles decorated MnO₂/reduced graphene oxide as advanced electrode materials for supercapacitors. *Chem Eng J* 252:95–103
57. Gurunathan S, Han JW, Park JH, Kim E, Choi YJ, Kwon DN, Kim JH (2015) Reduced graphene oxide–silver nanoparticle nanocomposite: a potential anticancer nanotherapy. *Int J Nanomedicine* 10:6257–6276
58. Zhang Z, Xu FG, Yang WS, Guo MY, Zhang BL, Tang JL (2011) A facile one-pot method to high-quality Ag-graphene composite nanosheets for efficient surface-enhanced Raman scattering. *Chem Commun* 47:6440–6442
59. Gurunathan S, Han JW, Dayem AA, Eppakayala V, Kim JH (2012) Oxidative stress-mediated antibacterial activity of graphene oxide and reduced graphene oxide in *Pseudomonas aeruginosa*. *Int J Nanomed* 7:5901–5914
60. Hu CF, Liu YL, Qin JL, Nie GT, Lei BF, Xiao Y, Zheng MT, Rong JH (2013) Fabrication of reduced graphene oxide and silver nanoparticle hybrids for raman detection of absorbed folic acid: a potential cancer diagnostic probe. *ACS Appl Mater Interfaces* 5:4760–4768
61. Chook SW, Chia CH, Zakaria S, Ayob MK, Chee KL, Huang NM, Neoh HM, Lim HN, Jamal R, Rahman RMFRA (2012) Antibacterial performance of Ag nanoparticles and AgGO nanocomposites prepared via rapid microwave-assisted synthesis method. *Nanoscale Res Lett* 7:541
62. de Faria AF, Martinez DS, Meira SM, de Moraes AC, Brandelli A, Filho AG, Alves OL (2014) Anti-adhesion and antibacterial activity of silver nanoparticles supported on graphene oxide sheets. *Colloids Surf B Biointerfaces* 113:115–124

An Investigation on the Outcomes of Rail-Based Solar Tracking System Incorporating Minimum Torque Condition for Increasing the Photovoltaic Energy Capture on Sunny Days



Arun A. Yadav and P. V Ramana

Abstract The effectiveness of each solar-operated system mostly depends upon its orientation with respect to sunbeams, and for this, there do plethora of system exist, but as per the ecological and geometrical circumstances, the efficiency of conventional systems varies, and for the reason that, the overall yield is deteriorated. It has known that an external energy source is essential for driving the solar tracking unit. Somehow, if one could minimize or dispense with this external energy source, the effectiveness of the photovoltaic panel would increase. An approach is made to develop the rail-based solar tracking system, which could dispense the external energy source by incorporating minimum torque condition. This study comprises an investigational corroboration of a perception to be used in optimum tracking stratagem during the sunny days in India. The work also insights experimental and simulation studies of incident sun insolation and energy yield of PV module in different conformations. The data analysis was performed for the city of Vasad (22.5° N, 73.1° E). The study outcomes obtained here have corroborated the method that employs the perception of “rail-based solar tracking incorporating the minimum torque condition” to determine feasibility of the scheme. The outcomes of this paper may aid as valuable consideration for upcoming solar energy usages.

Keywords Solar energy · Solar angles · Minimum toque condition · Rail-based solar tracking · Optimal tracking strategy · Tracking efficiency

A. A. Yadav (✉)

Department of Mechanical Engineering, Neotech Institute of Technology,
Vadodara 390022, GJ, India
e-mail: er.arun.yadav1911@gmail.com

P. V Ramana

Department of Mechanical Engineering, Sardar Vallabhbhai Patel Institute of Technology,
Vasad 388306, GJ, India

© Springer Nature Singapore Pte Ltd. 2020

A. K. Bhoi et al. (eds.), *Advances in Greener Energy Technologies*,

Green Energy and Technology, https://doi.org/10.1007/978-981-15-4246-6_22

1 Introduction

The quantity of solar energy acquired is the role of solar collector configuration [1–3]. Solar collector platform plays a vital role for the growth of solar-operated systems, particularly in high temperature concentrating solar power (CSP) systems [4] and flat photovoltaic (PV) systems [5] that straightway transform the sun energy into electrical or thermal energy [6]. The quantity of power obtainable from PV module is affected by three constraints, namely orientation of solar tracker, materials of solar module and intensity of sunlight [7–9]. In order to boost up the power gain, solar collector system is essential to track the sun on its path as it travels across the blue. Nevertheless, such platforms or systems can be provident only if additional cost associated with the solar tracking platform is lesser than the cost of the added PV modules which will have to the equal power generation with the platform having a fixed configuration [10–14]. It is found that energy consumption of driving motors should be within 2–3% of gained energy [15, 16].

In this study, four configurations of solar tracking system, dual axes, two single axis (X -axis or Y -axis) and fixed axes have been deliberated. For each of the two deliberated single-axis tracking systems, an annually optimum slope has been considered, whereas for traditional PV systems, one fixed tilt system has been used and tilted according to annually optimum slope. The annually optimum slope is measured equivalent to latitude (Φ) of the place [17–21]. Starting from the current state of the art, the work aims at: (a) reducing the degree of structural and constructive complexity, corroborated with increasing reliability in operation and maximizing the solar energy captured by the photovoltaic platform served; (b) validation of an optimal geometrical synthesis algorithm of my previous work [22] that uses a concept of “rail-based solar tracking incorporating minimum torque condition”; (c) design, construction, location and testing of the demonstrator in the built environment. By solving the problems, there are significant contributions regarding the validation of conceptual functional model and maximizing of tracking efficiency of PV platform.

2 The Used Configurations of PV Platform

The various configurations of PV platform taken in this study are briefed and enumerated below:

- Fig. 1d represents a fixed tilt PV module system, configured to the equator and tilted according to yearly optimum slope (FA).
- Figure 1a represents a module mounted on single axis solar tracking configuration with vertical rotating axis ψ^* (X -axis tracking) and tilted according to yearly optimum slope $\alpha^* = 22.5^\circ$ (E–W).
- Figure 1b represents a module mounted on single axis solar tracking configuration with horizontal rotating axis α^* (Y -axis tracking) and tilted according to yearly optimum slope $\psi^* = 180^\circ$ due North (N–S).

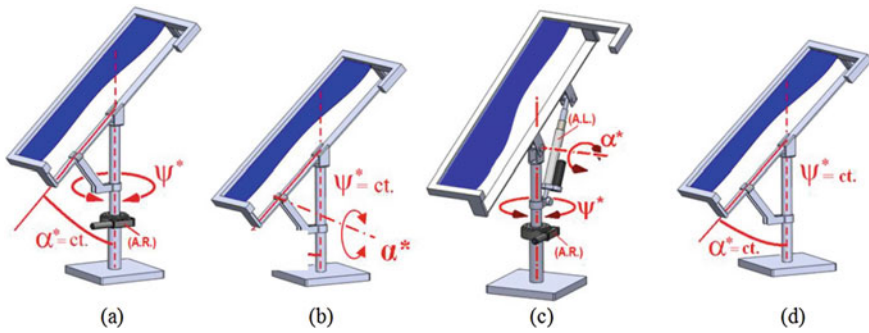


Fig. 1 Various configurations of PV platform: **a** X-axis (E–W); **b** Y-axis (N–S); **c** Dual axes (DT); **d** Fixed tilt (FA)

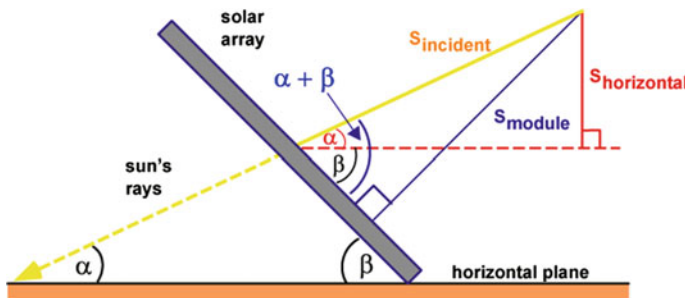


Fig. 2 Solar radiation on tilted surface

- Figure 1c represents a dual axes sun tracking configuration (DT).

Furthermore, the solar insolation absorbed by PV module depends not only on the intensity of the sunlight but also on the orientation angle between the sun and the module, namely solar beam incident angle (α), the instantaneous slope of PV module (β) and azimuth angle (ψ) [23–25]. The solar insolation on inclined PV panel surface is the component vector of the solar insolation which is vertical to the PV panel surface. Figure 2 illustrates how to estimate the solar insolation on inclined surface (S_{module}) specified either the solar insolation considered on horizontal surface (S_{horiz}) or the solar insolation calculated vertical to the sun (S_{incident}) [26–28].

3 Working Model

In this section, the main role of the proposed rail-based solar tracking system is to have the PV module always directed to sun (DTS) from dawn to evening. To achieve this, the light-dependent resistors (LDRs) based sensing unit [29], comparator and

driving unit with relay are incorporated in control system of solar tracking mechanism. Furthermore, the control strategy of solar tracking mechanism is detailed in succeeding section. The device would be activated when the sunlight is incident on LDRs. Whenever PV module comes out of orientation with the sun, initiating the PV platform such a way that it would be fetched back toward the sun. Once, DTS situation would be couth, the mechanical actuator would be ceased to turn until the PV module again missed the aim point to certain degrees, noticeable by LDRs.

The first step to comprehend this objective is the creation and assembly of a tabletop conceptual model that could be made up later to practical model in order to check the performance of system. This work includes the validation of a concept “rail-based solar tracking system incorporating minimum torque condition.” The conceptual model and mathematical study of method that uses rail-based tracking system have already been developed by author itself in [30]. The optimized dimensions required to build up the functional model for validation and feasibility purpose have also been presented by author himself in [22]. In the current paper, a design of closed-loop control system has predicted, where LDRs sensing unit perceives the location of the sun if there is no disruption. One has to consider also the fact that somehow if sunlight may not strike on LDRs sensing unit due to clouds in the sky. Additional adjustments (that has not addressed here) might be essential to put up such disruption to striking sunbeams on the LDRs sensing unit.

3.1 Mechanical System: Drive Speed and Gear Ratios

The complete design with optimized dimensions [22] and working principle [30] have been discussed by author itself in his research article. This section includes the selection of driving motors and components required to build up working functional model with its pros and cons. The solar angle scheme for the azimuth angle ψ^* (and elevation angle α^*) is here being used to govern the speed of sun tracker and gear ratio necessities. It is known from Fig. 3 that speed of sun tracker (degree per minute) is equivalent to the partial derivatives of the solar angles (slope at each point). The sun trajectory for azimuth angle (X -axis tracking) particularly moves faster, and it is recognized from the graph that it attains maximum sun speed.

According to Fig. 3, one can fix the movement of the sun in degree/min by means of the constraints attained from the graph (at the point of maximum sun speed) in the given formula.

$$\text{Sunspeed (degree/min)} = \frac{\Delta_{\text{SunAngle (degree)}}}{\delta_{\text{time (minutes)}}} \quad (1)$$

Equation 1 calculates the sun’s speed in degree/min. Nevertheless, to commune the sun speed to the speed of motor, it is necessary to convert sun speed into revolution/min (RPM). However, stating to Fig. 3, one can thus compute the sun speed in revolution/min (RPM) by dividing it with 360° .

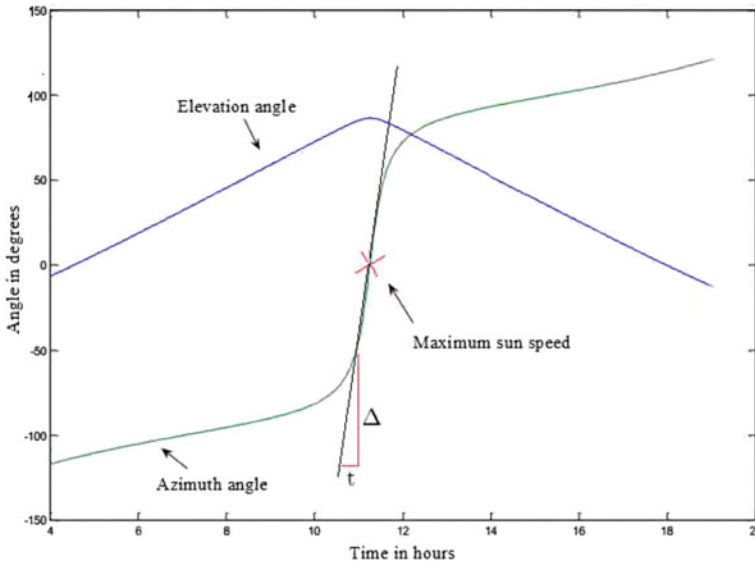


Fig. 3 Sun elevation and azimuth angles of the daytime sun path for Vasad (India), illustrating the maximum sun speed on azimuth angle curve superimposed

$$\text{Sunspeed}(\text{degree}/\text{min}) = \frac{\text{Sunspeed}(\text{degree}/\text{min})}{360^\circ} \tag{2}$$

As per the location of the observer, the above equation illustrates the sun speed around an average of $0.25^\circ/\text{min}$. Hence, the azimuth angle ψ^* , a fastest moving solar tracking axis (see Fig. 3), should attain at least $0.25^\circ/\text{min}$ to cope up with apparent motion of the sun. To attain this speed, a least rotational speed of 0.000694 RPM ($0.25^\circ/360^\circ = 0.000694 \text{ RPM}$) is essential for fruitful solar tracking. But electrical motors naturally rotate in range of $1750\text{--}2000 \text{ RPM}$. This speed is not suitable to drive the solar tracker. Therefore, an intermediate system is required to reduce the motor speed and also provide adequate torque to the solar tracker. This can be accomplished by means of gear drive or transmission system.

With a reducer on the azimuth axis, the speed of the motor shaft can be determined by the following equation because the speed of the motor shaft must rotate at certain minimum speed in order to cope up with the sun speed. This can be computed with the help of sun speed (RPM) when multiplied to the gear ratio of the reducer.

$$\text{Motor Shaft}_{\text{min}}(\text{rpm}) = \text{SunSpeed}(\text{rpm}) \times \text{Gear}_{\text{ratio}} \tag{3}$$

where the $\text{Gear}_{\text{ratio}}$ can be computed as follows:

$$\text{Gear}_{\text{ratio}} = \frac{\text{Motor}_{\text{input speed}}}{\text{Gearbox}_{\text{output speed}}} \tag{4}$$

If one could not find minimum desired speed by the combination of reducer and motor as computed in Eq. 3, an alternate high-speed motor or a gear ratio will be selected. For example, if an electrical motor of 1750 rpm would be chosen, the maximum permissible reduction gear ratios would have been around 2,000,000:1 (1750/0.000694). With such high gear ratio, a reducer and a motor of 1750 RPM will just cope up with the sun movement during maximum sun speed. Practically, the gear drive ratios are between 10,000:1 and 30,000:1. But, this gear ratio would not be sufficient to track the sun, and sun tracker moves faster than the sun speed itself (0.000694 RPM). As per literature survey, the continuous tracking is not fruitful for energy gain. Hence, the ON/OFF type control system is desired in order to synchronize the speed of the sun tracker with the sun speed itself. The more practical or genuine way of choosing a driving motor for solar tracking platform is that first choose the feasible available gear ratio and then choose a motor with adequate torque to meet the condition in Eq. 3.

The following equation is used to relate speed of the motor shaft and the speed of the sun tracker in RPM. This equation is useful for calculating the speed of the sun tracker on either direction. It is very practical when the speed of motor shaft is kept fix or gear drive work within the determined rpm range.

$$\text{Sun Tracker Speed (rpm)} = \frac{\text{Motor Shaft (rpm)}}{\text{Gear}_{\text{ratio}}} \quad (5)$$

From Eq. 5, an example is solved in order to illustrate how to calculate the RPM of sun tracker. If it is assumed that a gear ratio is 15,000:1 and the speed of the motor is approximately 1750 rpm, the speed of sun tracker will be around 0.175 RPM. This implies that the speed of the sun tracker is approximately 250 times faster than maximum sun speed (see Fig. 3). Continuing further, the speed of the sun tracker can be computed by choosing lower RPM-based motor or by reducing the motor speed with pulse width modulation (PWM) or variable frequency drive (VFD) to operate at a different efficiency point (see Fig. 4). Say if the motor speed reduces down to 20 RPM and uses a reducer with gear ratio of 15,000:1, sun tracker speed computed from Eq. 5 will be 0.00133 RPM. This implies that RPM will be twice than maximum sun speed (see Fig. 3). The combination of reducer (or gearbox) and a motor will thus be practically possible to meet the sun speed as per Eq. 3.

Furthermore, the optimum solution for sun tracking motor/reducer should be selected such that it could carry adequate sun tracking and motor speed (see Eq. 5) so that electrical motor runs close to its maximum efficiency or maximum torque (see Fig. 4). The designer should confirm that sun tracking speed is at higher than sun speed or within the same order at the point of maximum sun speed on azimuth curve. This can be concluded with the help of motor performance curve and solar angles curve (see Fig. 3 and Eq. 1). As per the literature survey, continuous tracking is not economical solution to keep up with sun speed. The best solar tracking motor with gearbox combination [6], which causes minimum electrical losses and also reduces power consumption, has been chosen for solar tracking system. Hence, the speed of DC motor is reduced through gearbox under the ratio of 1:10:10:5:5.

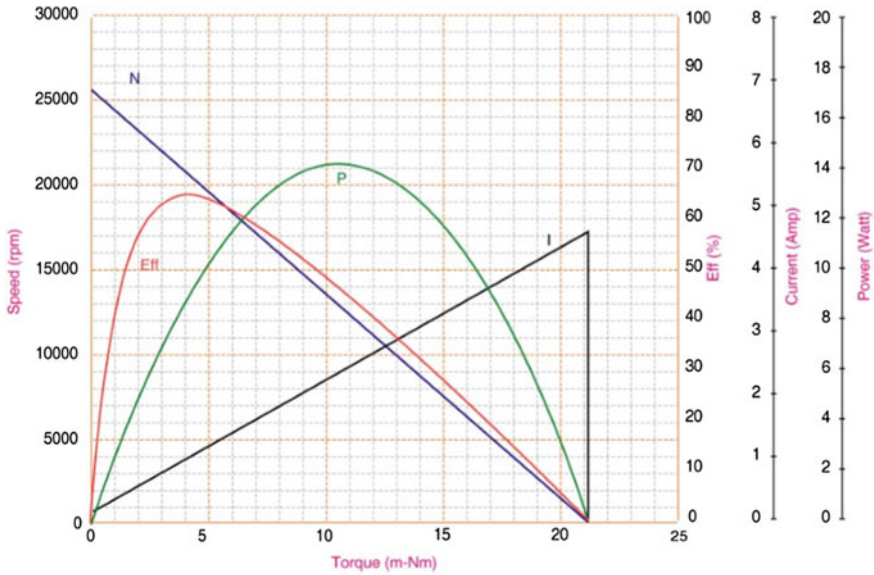


Fig. 4 Performance curve and optimal operation points for typical DC motor for proposed rail-based solar tracking system

3.2 Electrical System: Hardware Design and Power Consumption

The system locates the sun autonomously in azimuth angle ψ^* and elevation angle α^* . The maximum power can be extracted from the PV module when both azimuth axis (X -axis) and elevation axis (Y -axis) concurrently advance till the PV module is aligned in DTS. The PV configurations setting up is not constrained to the geographical site. Figure 5 illustrates the block diagram sun tracking system, describing the interconnection and composition of the system. This section deals with whole working algorithms that are summed up with flowcharts as illustrated in Fig. 6.

Figure 8 illustrates the complete control circuit diagram for azimuth direction. The control system comprised of two hardware circuits for either direction in order

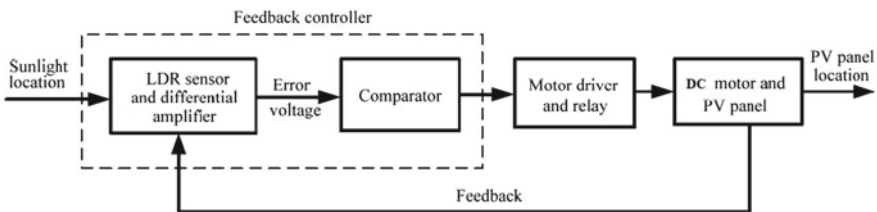


Fig. 5 Building block diagram of control system for used PV tracking system

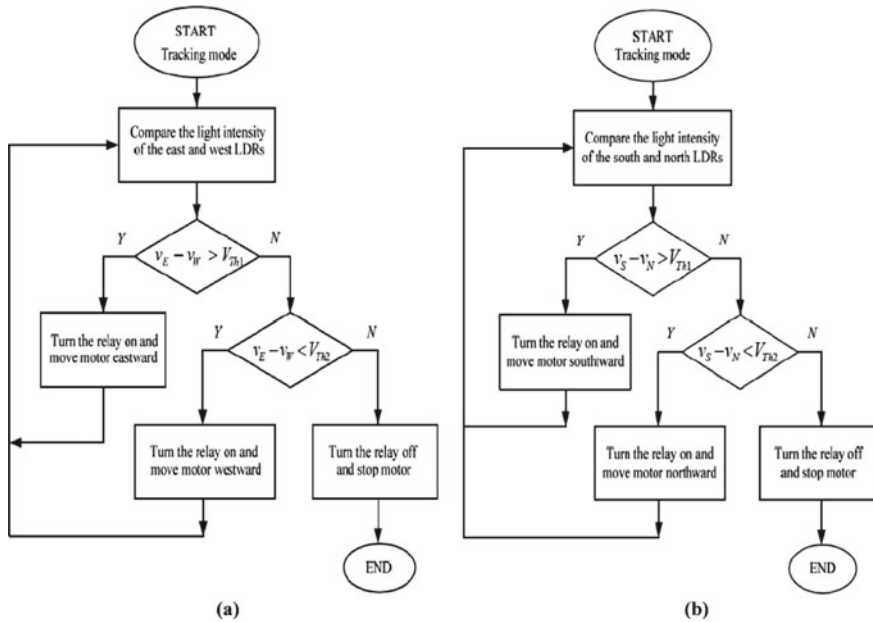


Fig. 6 Flowchart of tracking algorithms of (a) azimuth axis; (b) elevation axis control

to actuate the DC geared motor (see Fig. 7). The proposed solar tracking is divided into three sections, namely LDR-based sensing unit, comparator and motor driver with relay. The following subsection details about the design procedure of making the three sections for solar tracking mechanism.

3.2.1 LDR-Based Photosensor Unit

It is essential to sense the location of the sun in order to track the sunlight, and for that, photosensor is desired. The easiest photosensor is a photoresistor. The materials for this can be either a cadmium sulfide (CdS) type or a gallium arsenide (GaAs) type. In next step, the complexity is increased when the photodiode is followed by the phototransistor. The proposed solar tracking system used CdS photocell for photosensor because of its low cost and less complexity. Although CdS photocell is passive in nature, its resistance decreases when the amount of sunlight incident on it. That means that resistance of this photocell is inversely proportional to the quantity of sunlight light intensity incident on it. This photocell is used here as a voltage divider by placing it in series with a resistor. The output of this voltage divider at the junction is computed with the help of two resistors (see Fig. 8). The artificial light is used for calibration of the tracker under front edge or top edge of pyramid (see Fig. 9). During this process, the DC motor is disconnected and digital millimeter is placed. The two variable resistors (trimmer) of 100 kΩ is used to balance the zero

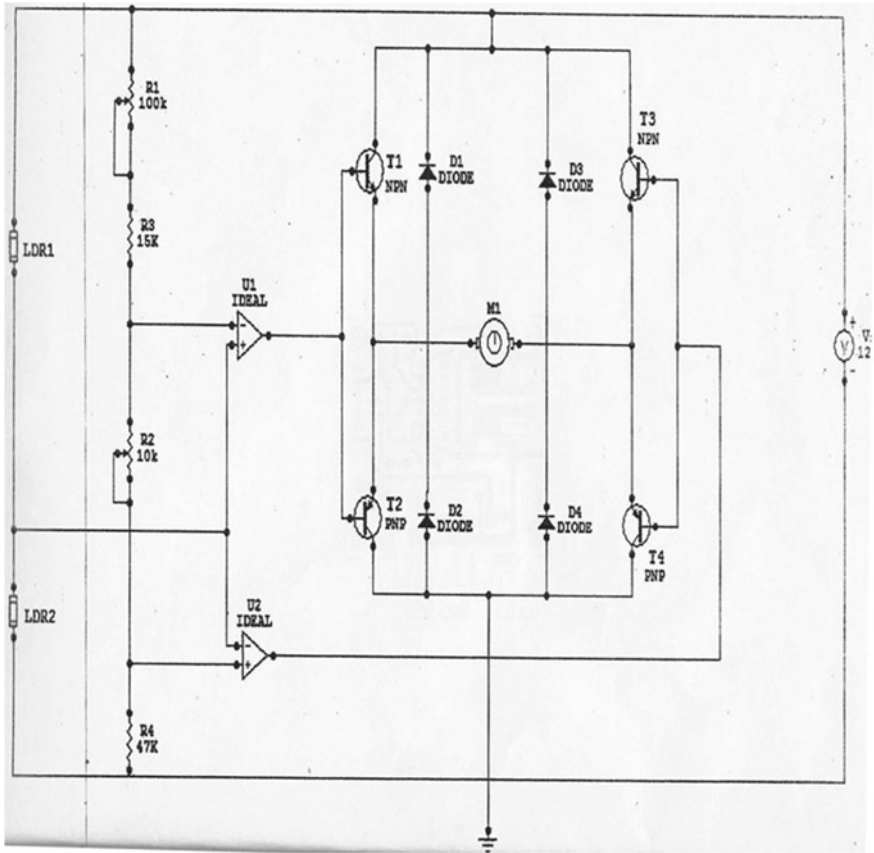


Fig. 7 Circuit diagram of solar tracking system

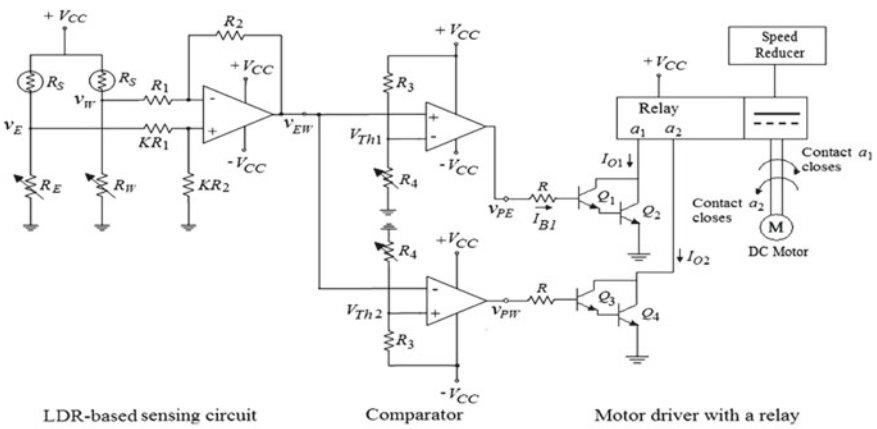


Fig. 8 Control circuit diagram for azimuth axis (X-axis) of solar tracking system

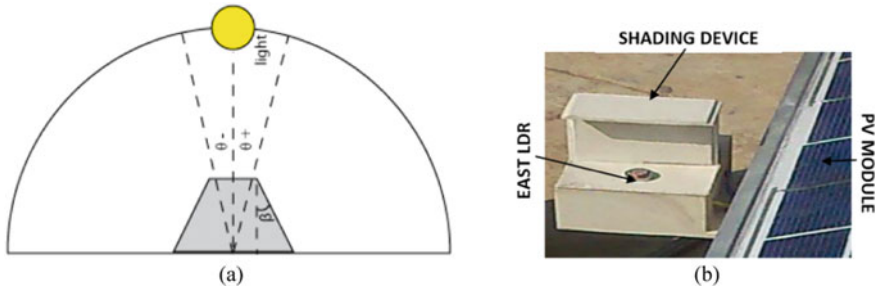


Fig. 9 a Set-up for calibration of solar tracker; b Device of sun location for azimuth axis (X-axis)

volt. After calibrating the zero volts at ideal position of light source, a DC motor is connected and checked for movement in accordance with changing the direction of light source.

The paper presents the LDRs based photosensor with a separator shade as a Sun sensor. Figure 9b illustrates the photosensor device, which encompasses a two-quadrant LDR sensor with separator mounted on a device for either direction. This photosensor device is fixed on the frame of PV module. The LDR photocells in East-West (see Fig. 9b) and in North-South help in the recognition of X-axis and Y-axis motion of the PV module, respectively. The Sun sensor works on the principle of shadow, which is created by a separator. If the sunlight does not incident on PV module perpendicularly, the shadow created by the separator covers one of the LDRs. Due to this, varying amount of sunlight intensity is captured by the Sun sensor. The first part of Fig. 8 illustrates simplest error voltage circuit. It is quite reasonable that if an LDR is shadowed, the output voltage of corresponding LDR of voltage divider is lesser than an output voltage of unshaded LDR. This creates an error voltage which later the differential amplifier magnifies it. The following Eq. 6 describes the feedback error voltage.

$$V_{EW} = -\frac{R_2}{R_1} V_W + \left(1 + \frac{R_2}{R_1}\right) \frac{K R_2}{K R_1 + K R_2} V_E \tag{6}$$

which can be reorganized in the following manner:

$$V_{EW} = \frac{R_2}{R_1} (V_E - V_W) \tag{7}$$

If west LDR is shadowed, $V_E > V_W$ and $V_{EW} > 0$.

This is how error voltage of Sun sensor LDRs in either direction rotates DC motors in forward and reverse order. The power transistors and four diodes are accompanied by DC motor to compensate load on it and damp the ripple, respectively (see Fig. 7). The four diodes also surge the voltage, which is generated while rotation of DC motor, due to back EMF. The working of solar tracking system with the help of LDRs is illustrated in Fig. 8. The details of the components used for making solar

Table 1 Components used in solar tracking system

Sr. No.	Components used	Ratings/Model No.	Quantity
1.	Diode	1N4007	04
2.	IC	7812	01
3.	Capacitor	1.0 nF and 470 μF, 25 V	02
4.	Comparator	100 k and 10 k	02
5.	Transistor	BD 140 and BD 139	04
6.	Resistor	47 k and 150 k	02
7.	IC	LM329	01

tracking circuit are given in Table 1. Figure 15 illustrates the printed circuit board (PCB) design which is used later to develop complete prototype of proposed solar tracking system.

3.2.2 Comparator Unit

The comparator unit compares the error voltage of LDRs with threshold values and functions like switch. This causes to turn on the relay and triggered to rotate the DC motors. It is generally an operation amplifier (op-amp), which runs in open-loop mode. This op-amp converts a time-varying analog signal into a binary output. The threshold value implies here as input voltage and the states of output change corresponding to this threshold value as illustrated in Fig. 10. As depicted in the second part of Fig. 8, the two threshold values are expressed as follows:

$$V_{Th1} = \frac{R_4}{R_3 + R_4} V_{CC} \tag{8}$$

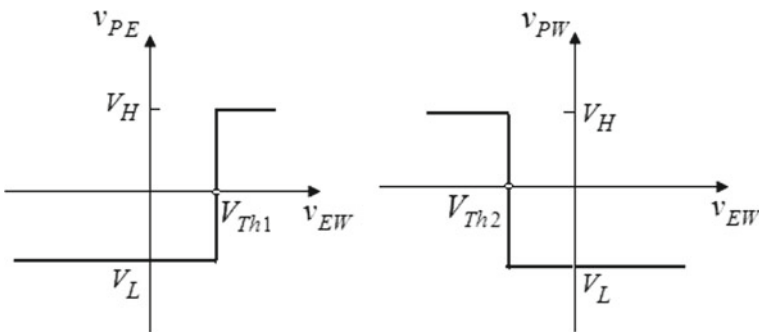


Fig. 10 Voltage transfer characteristics of open-loop comparator

$$V_{Th2} = \frac{R_4}{R_2 + R_4} (-V_{cc}) \quad (9)$$

The comparator has either of two output states, namely a low saturated state V_L or a high saturated state V_H . The high saturated state V_H and low saturated state V_L should be equal to the supply voltages $+V_{cc}$ and $-V_{cc}$, respectively. This can be stated as follows:

$$\begin{aligned} V_{PE} &= V_H \text{ for } V_{EW} > V_{Th1} \\ &= V_L \text{ for } V_{EW} < V_{Th1} \end{aligned} \quad (10)$$

$$\begin{aligned} V_{PW} &= V_L \text{ for } V_{EW} > V_{Th2} \\ &= V_H \text{ for } V_{EW} < V_{Th2} \end{aligned} \quad (11)$$

Figure 10 depicts the voltage transfer characteristics of a comparator in open-loop mode. The threshold values dominate the sensitivity of tracking mechanism, which can be controlled with the help of the variable resistor R_4 . The sensitivity of tracking is inversely proportional to variable resistance value R_4 . Nevertheless, the response of tracking system will be progressively oscillatory.

3.2.3 Relay Allied Motor Driver Circuit

The last part of Fig. 8 illustrates the designed relay allied motor driver circuit. It offers increased current gain and triggers a relay by means of two Darlington pairs. A feedback error voltage V_{EW} is created when west LDR has shadowed. If $V_{EW} > V_{Th1} > V_{Th2}$, the comparator gives two outputs V_{PE} and V_{PW} in high saturated state and low saturated state, respectively. This causes transistors Q_3 and Q_4 in the cut-off state, and Q_1 and Q_2 will therefore conduct. This means that transistors Q_1 and Q_2 work in forward-active mode. For that, the following equation can be derived to find out the input current or the base current of Q_1 .

$$I_{B1} = \frac{V_H - V_{BE1} - V_{BE2}}{R} \quad (12)$$

where V_{BE} is the base-emitter voltage in forward-biased mode. Hence, the output current can be formulated as:

$$\begin{aligned} I_{O1} &= I_{C1} + I_{C2} = \beta_1 I_{B1} + \beta_2 (1 + \beta_1) I_{B1} \\ &= [\beta_2 + \beta_1 (1 + \beta_2)] I_{B1} \cong \beta_1 \beta_2 I_{B1} \end{aligned} \quad (13)$$

where the constants β_1 and β_2 are the current gains in common-emitter mode.

This output current activates the relay, and contact a_1 closes in normally open (NO) mode. This causes a clockwise movement of DC motor shaft in X -axis direction or

azimuth direction, which in turn moves the PV module toward eastward DTS. More precisely, the used PV tracking platform moves PV module until all LDRs error voltage is zero in both directions, which in turn generate high energy from PV module by orienting the sunlight vector perpendicular to PV surface.

3.2.4 Design of Solar Charge Controller

Figure 11 depicts the design and working of solar charge controller, which plays an important role in batteries allied solar power systems. It regulates power going into a battery from PV module. It simply avoids an overcharging of a battery, which causes abominable effects such as reduction in battery life or damage the battery at worst case (see Fig. 13). It generally monitors the voltage of battery by opening the circuit. This means that it charges the battery until voltage of battery reaches to maximum rated voltage. In this work, the solar charge controller circuit is essential in order to store electrical energy from PV module.

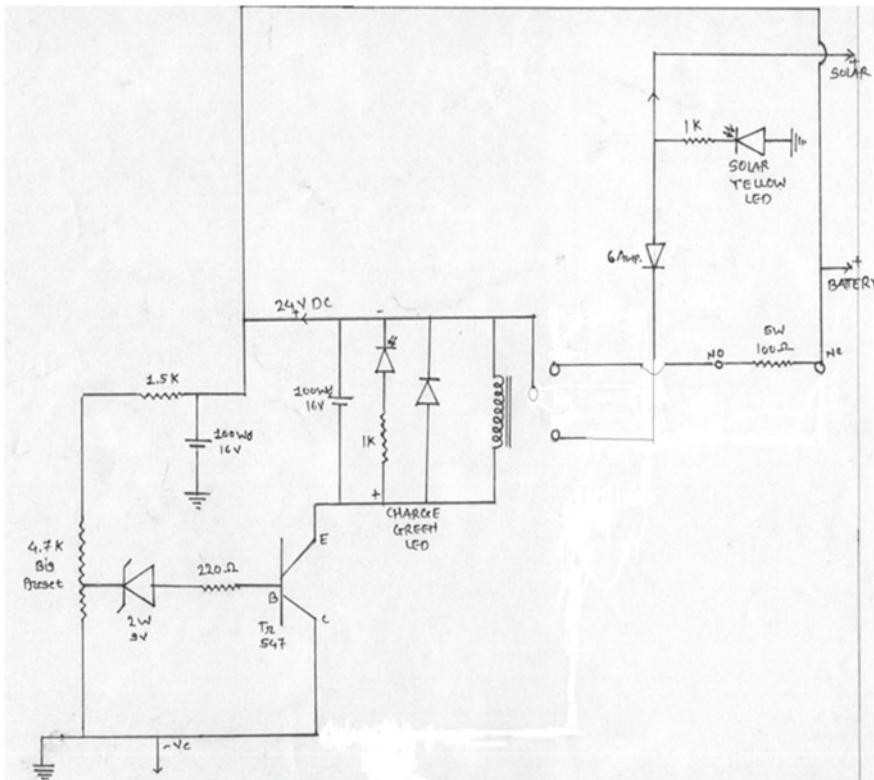


Fig. 11 Circuit diagram of solar charge controller

Fig. 12 PCB of solar charge controller



Table 2 Components used in solar charge controller

Sr. No.	Components used	Ratings/Models	Quantity
1	Preset	4.7 k	01
2	Resistor	1.5 k	02
3	Zener diode	9 V, 2 W	01
4	Relay	12 V	01
5	Diode	6 A	01
6	Diode	1N4007	03
7	Yellow LED	2 V, 20 mA	01
8	Green LED	2.1 V, 20 mA	01
9	Capacitor	100 μ F, 16 V	01

To sense the overvoltage of battery, a switching transistor is used in solar charge controller. For that, base of the transistor is connected with 9 V Zener diode, which in turn goes in breakdown mode. The breakdown mode causes to switch ON the relay circuit, which in turn stops the direct charging from PV module. In this way, the battery can be saved from overcharging and heating. A 100 Ω low resistance allied contact relay allows very low current to pass through battery that reduces the self-discharging rate of battery in ideal mode. The printed circuit board (PCB) design and list of components are shown in Fig. 12 and Table 2, respectively (Fig. 13).

3.2.5 Power Consumption

In order to ensure whether the sun tracker actually produces more energy than it consumes, practical readings are obtained for each component of sun tracking system. For that, a 0.49 Ω resistor working as power shunt is used to gauge the current departing from the battery to various electrical components of solar tracking platform (see Fig. 14). The voltmeter measures the voltage (V_{R_i}), which in turn divided by resistance gives the current flowing into the sun tracker system. The supply voltage

Fig. 13 Impact of charging regime of battery capacity

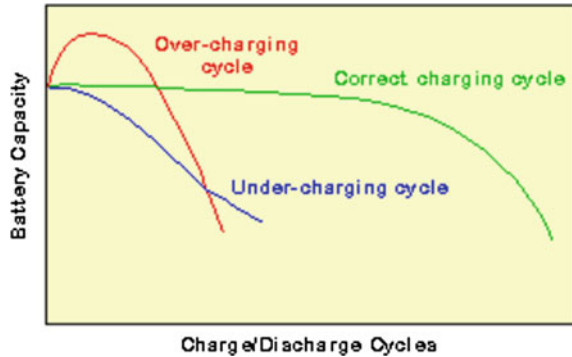
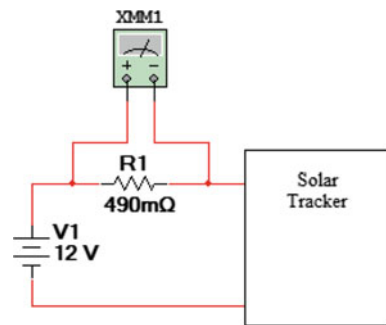


Fig. 14 Test circuit for power consumption



(12 V) when multiplied with this obtained the current, estimates the power consumption. In order to find individual current drawn by each PV tracking configurations, the several practical readings are taken. The first readings are measured to the whole system including shunt resistance as depicted in Fig. 14. The current is measured for each system, namely FA (non-tracking), E–W tracking (X-axis direction), N–S tracking (Y-axis direction) and DT. The obtained results are given in Table 3. The following things are deduced from the obtained results in Table 3. The control circuit for solar tracking system consisted of four indicator LEDs, two motor driving circuits and a battery charge controller devour 0.18 W when the used PV configuration system is FA. The N–S (Y-axis tracking) orientation devours $1.2 - 0.18 = 1.02$ W when moving sensors during the utmost point load. The E–W (X-axis) orientation

Table 3 Power consumption of different configuration of rail-based dual axes solar tracking system

Sr. No.	Tracking type	V_{R_1} (mV)	Current (mA)	Power (W)
1.	FA (Non-tracking)	7.350	15.0	0.18
2.	N–S (Y-axis)	49.00	100.0	1.2
3.	E–W (X-axis)	73.50	150.0	1.8
4.	DT (Dual axis)	98.0	200.0	2.4

Fig. 15 PCB design of solar tracking



devours $1.8 - 0.18 = 1.62$ W at its utmost load point because of friction in mechanical parts. The total power consumption is equal to $0.18 + 1.02 + 1.62 = 2.82$ W at maximum load point. The total power consumption is not always the case because the sun tracker does not move simultaneously through both axes at maximum load points. It is concluded from the above calculations that DT system consumes 2.82 W in worst-case scenario, while FA system consumes just less than a quarter of a watt (Fig. 15).

4 Energy Assessment: Simulation

The simulation study for different orientation types of solar tracking systems is made in MATLAB R2017a software via simulating the global radiation of specific location. Before that the derivations are made for different components of solar radiation with certain assumptions in order to simplify the mathematical formulation for orientation mechanism of PV-based tracking systems. The derivations and detailing are made in the following sub-section.

4.1 *Solar Radiation Absorbed by Various Configurations of PV System*

The following assumptions are made for the derivation of amount of solar radiation absorbed by various configurations of PV system.

- The planet earth is considered perfectly spherical, and this causes elevation of PV module platform free from participation.
- The apparent movement of the sun, which happened by means of earth's rotation about own axis, is taken from east to west exactly each day in a year.

- One year is taken equivalent to 365 days, i.e. 24 h in a day or 8760 h.
- The PV module faces the sun at noon, i.e., the sun is exactly between east and west or 0° to the zenith, and the sun is exactly behind the earth at midnight, i.e., 180° to the zenith.
- The average daily solar insolation is 1 kW/m^2 at air mass 1.5 [31].

Figure 16 illustrates the variation of solar insolation at various zenith angle. The solar insolation is maximum (1000 W/m^2) at zenith angle 0° and minimum (0 W/m^2) at zenith angle 90° on horizontal surface. This implies that inclined PV panel to the sunlight decreases PV panel output as depicted in Fig. 2. It is known that earth makes 360° in one revolution about own axis, i.e., takes 24 h in movement from east to west direction. This direction henceforth is called as X-axis direction ($-180^\circ < \psi < 180^\circ$), which describes position of the sun with respect to zenith (see Fig. 17). The zenith angle in X-direction can be expressed as follows:

$$Z_X = 15^\circ (T - 12) \tag{14}$$

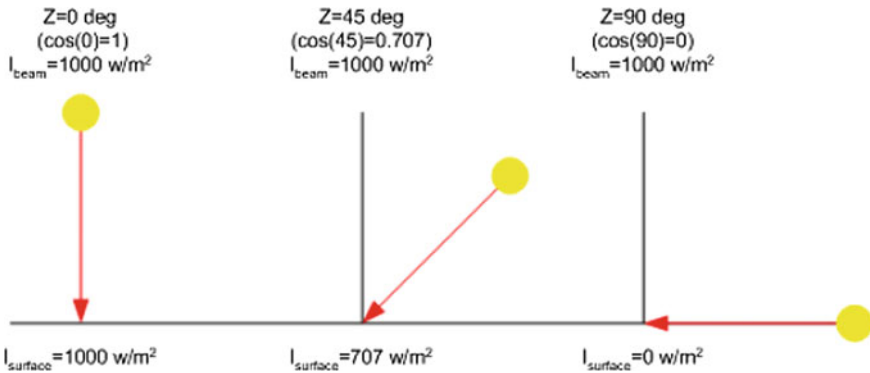


Fig. 16 Variation of solar insolation at different zenith angles (Z)

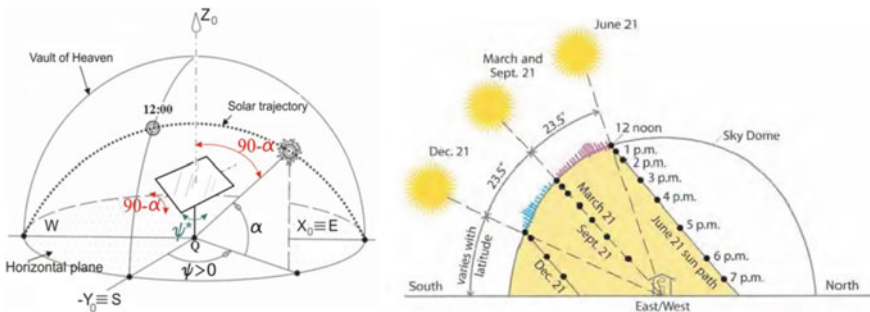


Fig. 17 Sun position with respect to point Q in east to west and north to south direction in different seasons

where T is time variable in hours.

The zenith angle in X -direction can be calculated from Eq. 14 which is as follows starting from midnight of the first day. The cycle repeats at every 24 h.

$$\begin{aligned} T = 0 \text{ h (at midnight of 1st day), } & Z_X = 15^\circ(0 - 12) = -180^\circ \\ T = 12 \text{ h (at noon of 1st day) } & Z_X = 15^\circ(12 - 12) = 0^\circ \\ T = 24 \text{ h (at midnight of 2nd day) } & Z_X = 15^\circ(24 - 12) = 180^\circ \\ T = 36 \text{ h (at noon of 2nd day), } & Z_X = 15^\circ(36 - 12) = 360^\circ = 0^\circ \end{aligned}$$

The second axis is called Y -axis direction ($0^\circ < \alpha < 90^\circ$), which describes the solar angle to the zenith on the equator while moving from north to south direction (see Fig. 17). Nevertheless, the Earth is inclined by 23.5° and equator's Y angle fluctuates between $+23.5^\circ$ and -23.5° . This angle becomes 0° at vernal equinoxes. Figure 17 depicts the Earth's rotation around the sun allied with Y angle changes. The values of Y angle change over a year, and henceforth, it can be expressed as follows:

$$Z_{Y \text{ equator}} = 23.5^\circ \sin\left(\frac{2\pi}{8760}T\right) \quad (15)$$

The variable T is the time in hours, measured from and at midnight on vernal equinox. Nevertheless, the selected point may not be at the equator. This is because the latitude of the place also effects on Eq. 15 (see Fig. 17). The latitude may be positive and negative and depends on location on the Earth. In this paper, positive latitude is taken because the chosen place is in the northern hemisphere. Finally, the angle to zenith in Y -direction (Z_Y) is the difference of the latitude angle (Φ) of the place and Eq. 15.

$$Z_Y = \Phi - Z_{Y \text{ equator}} = \Phi - 23.5^\circ \sin\left(\frac{\pi}{4380}T\right) \quad (16)$$

Thus, the two angles of the sun in both directions with respect to zenith have derived for given location. Now, the solar radiation absorbed corresponding to computed angles (X , Y) for specified location is derived in the following section. The solar radiation absorbed by PV platform depends on its orientation to the zenith (Z_X and Z_Y) [32]. Hence, the percentages of available solar radiation for both the zenith angles are expressed as follows:

$$R_X = \cos(Z_X) = \cos(15^\circ(T - 12)) \quad (17)$$

$$R_Y = \cos(Z_Y) = \cos\left(\Phi - 23.5^\circ \sin\left(\frac{\pi}{4380}T\right)\right) \quad (18)$$

The total radiation absorbed on the surface of the globe can be computed for given location over time period T starting from and at midnight of vernal equinox as follows:

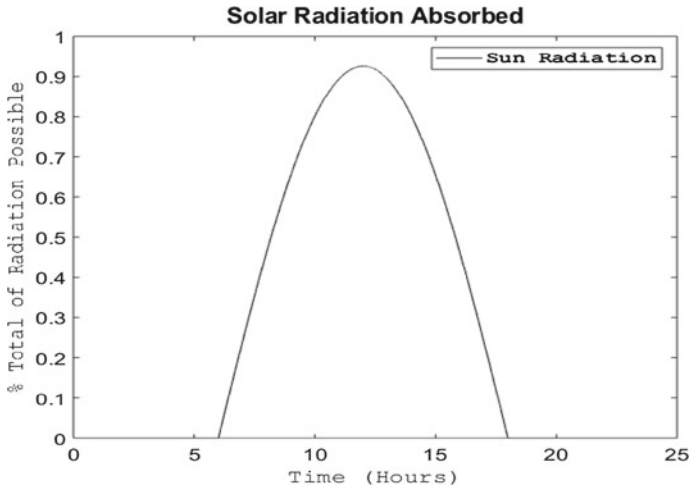


Fig. 18 Percentage total radiation in Vasad, IN on vernal equinox

$$R_T = R_X \times R_Y = \cos(15^\circ(T - 12)) \times \cos\left(\Phi - 23.5^\circ \sin\left(\frac{\pi}{4380}T\right)\right) \tag{19}$$

In order to know the variation of sun radiation on the vernal equinox throughout the day, the above equations are put into MATLAB R2017a. The graph is plotted against the solar radiation hitting on the surface for Vasad, India ($\Phi = 22.5^\circ$) over the time period $T (= 24 \text{ h})$ and discarding all negative values (see Fig. 18). From Fig. 18, it is concluded that the solar radiation never reaches to the 100%. This is because of latitudinal effect of the location, i.e., the sun is offset by $\Phi = 22.5^\circ$.

The above plot time is widened to check the variation of solar radiation corresponding to angle Z_Y correctly over the time period of 365 days or 8760 h. The above graph is replotted into MATLAB R2017a over time period of 8760 h. The plot depicts the fluctuation of solar radiation throughout the year. From Fig. 19, it is validated the equation for Z_Y as the percentage of solar radiation varies over a year and comes back to the same point. Again, the total solar radiation never goes beyond the 100% validating the 4th condition of the assumption. Figure 19 also depicts the percentage total radiation on different days. Here, X and Y denote hours and the percentage maximum sun radiation on that day at noon, respectively, for example June 21st ($X: 2220, Y: 0.9998$).

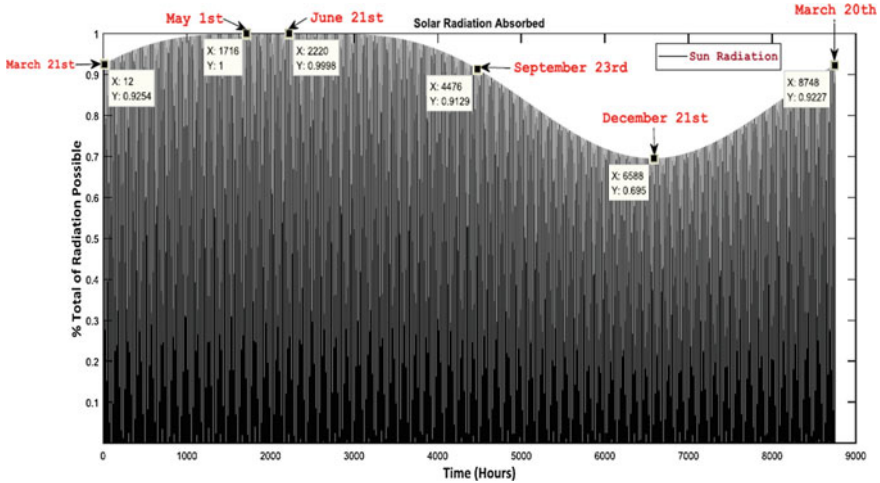


Fig. 19 Percentage total radiation in Vasad, IN over a year ($T = 8760$ h)

4.2 Performance of Used PV Systems

This subsection deals with calculation of percentage of sun radiation absorbed by different configurations of the PV sun tracking platform. Certain remarks are considered for motion of solar tracking platform. First, the tracker’s movement always lags the sun’s movement by 2° in both directions corresponding to tracking error. Due to this tracking error, the tracker would absorb only cosine of tracking error times available sun radiation, i.e. 99.93% in one direction. For both directions, the amount would be squared and bring the percentage closer to 99.87% of available sun radiation. Second, the tracker always orients any PV module in DTS in clear sky. Henceforth, the following equation can be derived for DT system, which captures the amount of incoming sun radiation striking on the PV platform.

$$R_{DT} = 0.9993^2 \times R_T \tag{20}$$

Put the value of Eq. 19 into Eq. 20, which can be now represented as follows:

$$R_{DT} = 0.9987 \times \cos(15^\circ(T - 12)) \times \cos\left(\Phi - 23.5^\circ \sin\left(\frac{\pi}{4380}T\right)\right) \tag{21}$$

Before plotting the graph in MATLAB R2017a for DT system, the other configurations of sun tracking system are also desired to be derived for equations of solar radiation absorption in order to check performance among them. First, E–W tracking (X -axis) allied PV platform that traces the sun from east to west direction for solar angles $\psi = \psi^*$ and $\alpha = \Phi = 22.5^\circ$. As it is single axis tracking system, it

can only absorb 99.97% of the available sun radiation. But another angle is fixed at 22.5° in *Y*-direction. That is why this angle is directed toward the zenith. The amount of solar radiation striking on E–W tracking equipped PV platform also depends on this *Y* angle and it is not compensated for. That is why the total radiation percent absorption affects $\cos(Z_Y)$ component, which fetches the equations as follows:

$$R_{EW} = 0.9993 \times \cos(Z_X) \times R_T \tag{22}$$

$$R_{EW} = 0.9993 \times \cos^2\left(15^\circ(T - 12) \times \cos\left(\Phi - 23.5^\circ \sin\left(\frac{\pi}{4380}T\right)\right)\right) \tag{23}$$

Similarly, the same equations can be proposed to N–S tracking configuration system. It also absorbs 99.93% of available sun radiation due to single axis sun tracking system in *Y*-direction ($\psi = 180^\circ$ due North and $\alpha = \alpha^*$). It also depends on the amount of solar radiation percent in *X*-direction. That is why, it is not compensated for. Hence, the amount of solar radiation percent affects $\cos(Z_X)$ component, which fetches the equations as follows:

$$R_{NS} = 0.9993 \times \cos(Z_Y) \times R_T \tag{24}$$

$$R_{NS} = 0.9993 \times \cos(15^\circ(T - 12)) \times \cos^2\left(\Phi - 23.5^\circ \sin\left(\frac{\pi}{4380}T\right)\right) \tag{25}$$

Final PV configuration system is fixed axis (FA) system also known as non-tracking system. The FA system ($\psi = 180^\circ$ due North and $\alpha = 22.5^\circ$) is put on the ground such that the normal vector of PV module is directed toward zenith. Hence, the percent amount of sun radiation striking on FA equipped PV system is the function of the $\cos(Z_X)$ and $\cos(Z_Y)$ components, which fetch the equation as follows:

$$R_{FA} = \cos(Z_X) \times \cos(Z_Y) \times R_T \tag{26}$$

$$R_{FA} = \cos^2\left(15^\circ(T - 12) \times \cos^2\left(\Phi - 23.5^\circ \sin\left(\frac{\pi}{4380}T\right)\right)\right) \tag{27}$$

After deriving equations for all four PV tracking configured systems, they put into MATLAB R2017a to create vectors over time period ($T = 24$ h) on vernal equinox. The following graph yields by plotting in MATLAB.

Figure 20 depicts that the DT system absorbs all available solar radiation despite its tracking error. E–W (*X*-axis tracking) equipped with PV platform appears to be improved tracking configuration in morning. But, the *Y* angle, which is not compensated for, falls down certain percent amount of solar radiation at noon. That is why the E–W configuration lags in percent absorption of solar radiation compared with N–S configuration at noon. At last, FA system (non-tracking) shows the minimum

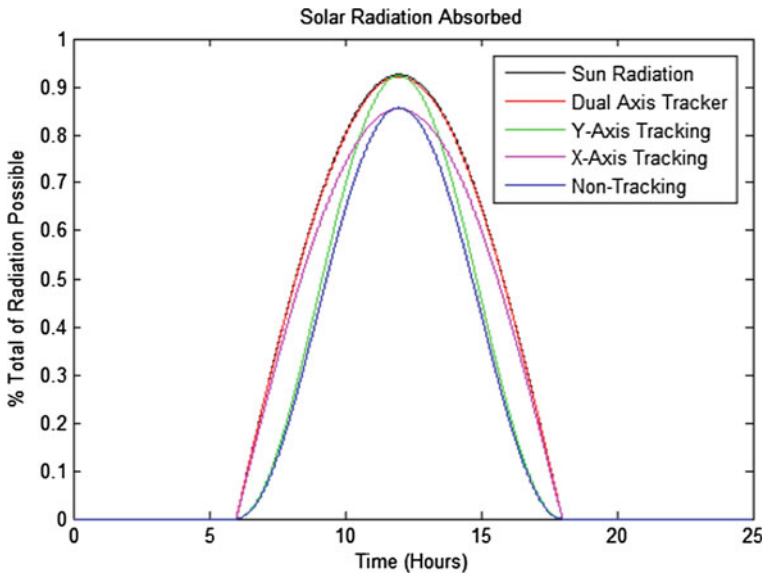


Fig. 20 Percent of total radiation for various configurations of PV tracking system on vernal equinox in Vasad, IN

percent amount of solar radiation absorption as it cannot indemnify the tracking error in both directions. Figure 20 depicts only percent of total radiation captured by various configurations of PV platform on vernal equinox. But, if it plotted over a year, the outcomes might be a little changed. If it has plotted over a year, the result would have yielded in an undecipherable like in Fig. 19. So, this action is evaded. However, if the integral of the power absorbed has taken over 365 days, it would have yielded numerical values for energy gained for relating the profits of a tracking mechanism over a year. This objective can be fulfilled after putting further assumptions into action. First, the days continued to be clear and cloudless for transmitting solar energy. Second, the PV module mounted to each sun tracking platform would be perfectly selfsame and had a power absorption and generation would be also of 1000 W/m^2 . The reason for doing this would be twofold. One is to streamline the mathematics without making any changes in the above equations of different solar tracking configurations. Second, if two sun trackers are compared, the value drops out and becomes impertinent anyhow.

After making certain assumptions to simplify the mathematics, however, an issue is arisen about integration of the following mathematical terms.

$$\cos\left(\Phi - 23.5^\circ \sin\left(\frac{2\pi}{8760} T\right)\right)$$

Table 4 Simulated kWh yielding from various PV tracking configurations over a year in Vasad, IN

Step size	Total available sun radiation	FA system (Non-tracking)	E–W system (X-axis tracking)	N–S system (Y-axis tracking)	DT system (Dual axes tracking)
1 h	2456.131934	1745.066224	2204.342652	1934.650393	2443.866625
1/10 h: (6 min)	2469.376646	1745.066130	2216.266226	1934.650292	2457.045196
1/100 h: (36 s)	2469.446826	1745.066130	2216.332433	1934.650291	2457.115024
1/1000 h: (3.6 s)	2469.446873	1745.066130	2216.332487	1934.650291	2457.115073

The mathematical terms cannot be converted into elementary mathematical problem. However, this term is integrated over a definite integral with the help of Mathematica software. But, this causes a program crash after a long period of waiting. The integration is made in discrete data points in MATLAB R2017a. This is because the discrete data points could be accessible from previously available simulation in MATLAB R2017a and the numerical values could be approached by addition. Approach by addition exemplify that software is adding up all the discrete data values over the whole year. After that, these data values are multiplied with step size, which is nothing but fraction of an hour. This procedure is repeated for further smaller step sizes until the numerical values yields almost similar. The yields are tabulated in the following Table 4, and all the values are in kWh over a year T .

Table 4 depicts that the numerical values for the 1/1000th step size and the 1/100th step size are almost similar and practically negligible. So, the numerical value obtained for the 1/1000th step size is good for approximation of the integral. However, each PV tracking configurations consumes certain amount of energy in order to trace the position of the sun precisely. The power consumption of different configurations of PV tracking systems are measured and detailed in previous Sect. 3.2.5. According to that, DT system consumes 2.82 W during tracking and either of E–W system or N–S system would consume 1.8 W at worst case. Else, it consumes 0.18 W for FA system. The sun tracker is scheduled to move once in every 2 min for one millisecond. This can be achieved by adjusting the variable resistor R_4 (see Fig. 8). This implies that DT system consumes 2.82 mWs for only one millisecond. Similarly, E–W/N–S system consumes 1.8 mWs. Multiplying these values by 120 s interval time, i.e., the tracker moves around 360 times over 12 h of the sunshine. Again, multiplying this value to DT system consumes 1.0152 Ws over 12 h of sunlight in a day; it devours less than 0.000282 Wh/day or 0.000103 kWh/year. Similarly, E–W or N–S system consumes less than 0.00018 Wh/day or 0.0000657 kWh/year, which is insignificant with respect to FA system. FA system consumes 0.18 W/day, i.e., 4.32 Wh/day or 1.5768 kWh/year. Thus, a net energy gain for DT system is 1.576903 kWh less, while it is 1.576866 kWh for E–W or N–S system. A model PV module is chosen for comparison in order to get approximate

Table 5 Net Energy Generated (NEG) kWh yielding from 10 W PV module over a year in Vasad, IN

	FA system	E–W system	N–S system	DT system
Net Energy Generated (kWh)	17.45066	20.58638	17.76964	22.99425

Table 6 Percentage gains of tracking systems (PGTS) for 10 W module over a year in Vasad, IN

Configurations of PV tracking system	% gain over FA system	% gain over E–W system	% gain over N–S system
E–W system	17.96907	–	15.85141
N–S system	1.827873	–	–
DT system	31.76720	11.69640	29.40190

power gained by sun tracking. A 10 W PV module is picked up. This is because the weight and size are precise to anticipate the load limit on PV platform structure. The weight of PV module is counterbalanced in such a way that load on the shaft of DC motor remains the same. 10 W implies that 0.01 of the maximum sun radiations, which was computed in Table 4, is transformed into electricity. Hence, the electricity generated by various PV tracking configuration would be approximated over a year when they are multiplied by 0.01 as follows (Table 5).

The NEG (kWh) are compared among various configurations of PV systems in Table 6. The numerical involves here are the results of the 1/1000th step size. Each configuration of PV system uses selfsame 10 W PV module.

Table 6 clearly depicts that DT system benefits more than 31% energy gain over selfsame PV module mounted on FA system. DT system also benefits large difference of energy gain of 11% and 29% over E–W system and N–S system respectively. The above table also depicts that the E–W system generates large amount of energy over N–S system. But, this benefit declines and ultimately vanishes if the tracker’s location gets farther and farther from the equator. Again, the same simulated MATLAB coding with minor changes is used to plot the graph over various latitudes. The following result yields from MATLAB plot.

Above Fig. 21 clearly depicts that E–W system (*X*-axis tracking) predominates over the N–S system (*Y*-axis tracking) at latitudes closer to equator whereas *Y*-axis tracking generates more power than *X*-axis tracking for latitudes farther to the equator. They intersect each other around 47° in graph. The exact location may not be computed without derivation of equations for power production. Henceforth, the plot illustrates that DT system generates more amount of energy over the other tracking systems across the entire surface of the Earth.

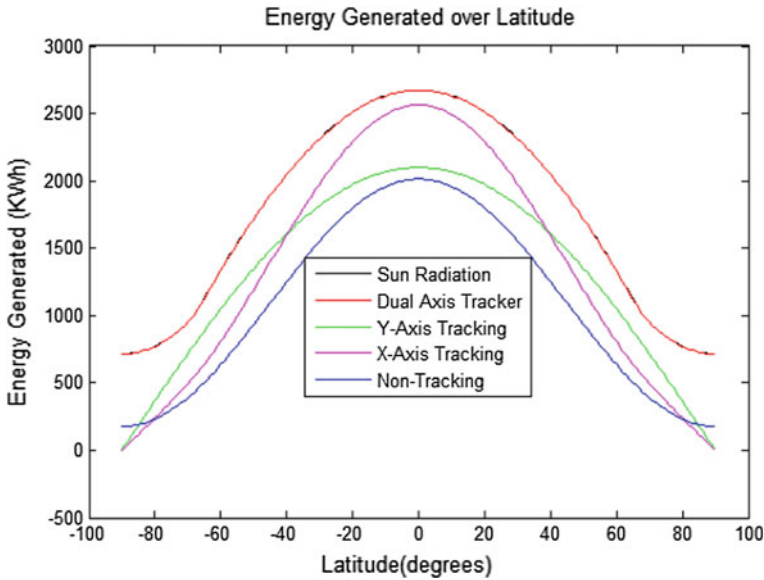


Fig. 21 Energy generated (kWh) over different latitudes

5 System Analysis: Data Collections and Testing Results

The section describes the prototype building and tracking accuracy testing. It describes also the feasibility of the functional model and performance of prototype for various configurations of PV system. As the prototype uses the method of rail-based solar tracking mechanism incorporating the minimum torque condition, the working prototype model reveals the validation of the functional model. The work is done at Sardar Vallabhbai Patel Institute of Technology (SVIT), Vasad GJ in India. The latitude of the city is 22.5° N so that optimum tilt angle (β) is chosen equal to latitude (Φ) of the city facing the south ($\psi = 180^\circ$) for optimum solar radiation as discussed in previous Sect. 1. The experiments are performed in twofold. First, it compares the tracking efficiency of different configurations of PV system among them and validated with simulated results. Second, it compares the tracking efficiency of DT system with FA system in different seasons, namely winter (25 December), vernal equinox (21 March) and summer (21 June). The experimental set-up of rail-based dual axes solar tracking system is illustrated in Fig. 22 along with list of components in Table 7. The following subsection deals with accuracy test of DT system. Figure 22 depicts the scale-down working prototype of conceptual functional model as discussed in Sect. 3. This prototype can be scale up for 500 Wp PV system with scale ratio of 5:1. Table 7 depicts the scale-down optimized dimension of conceptual function model. The actual optimized dimension of functional model proposed by the author himself is discussed in detail in [22].

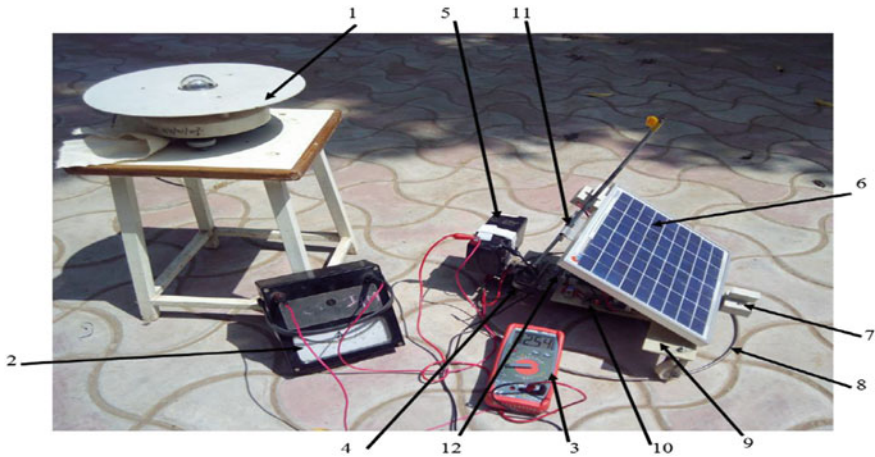


Fig. 22 Experimental set-up: 1 pyranometer, 2 A-meter, 3 multimeter, 4 DC geared motor, 5 lead-acid battery, 6 PV module, 7 LDR sensing device, 8 circular rail track, 9 crossbar, 10 control circuit, 11 leadscrew and adjustable nut mechanism and 12 railbar

5.1 Accuracy Tests on Dual Axes Solar Tracking Prototype

This subsection presents the measurements of tracking error in either direction. The experimental values are compared with theoretically calculated solar angles (α , ψ) on the same day. First, the elevation angle or altitude angle (α^*) is measured by means of a simple magnetically based angle meter (see Fig. 23a). Second, the azimuth angle (ψ^*) is determined by means of a simple measurement technique known as compass quadrant bearings is illustrated in Fig. 24. In this technique, the directions, namely North (N), South (S), East (E) and West (W), are assigned a certain angle 0° , 180° , 90° and 270° , respectively. To measure azimuth angle (ψ^*), the green arrow is considered as a pointer. Then, an angle with respect to North (N), which corresponds to 0 , is computed. It shows the angle 103° (shown in parentheses) as illustrated in Fig. 24b. This technique can be followed in three steps. First, it should be checked whether the green arrow is closer to N or S. From Fig. 24b, it can easily be interpreted that it is closer to S. Second, measure that angle between the green arrow and the S (e.g. 77°). Third, it should be checked whether it is closer to the E or the W. In our case, it is closer to the E. Hence, the azimuth angle is designated by means of compass quadrant bearing method as S 77° E in red color. In this way, azimuth angle is measured. The big circular sheet is designed based on compass quadrant bearing method and kept below the circular rail track (8). To locate the angle on this sheet, a pointer is attached beneath of LDR sensing device (7) as illustrated in Fig. 22. Hence, the azimuth and elevation angle of DT system are measured every 15 min from 9:30 to 16:00. These values are compared with theoretically calculated solar angles (α , ψ) and difference between those values provide tracking error in the proposed prototype. Some computed azimuth angles as shown in parentheses in

Table 7 List of components used in solar tracking system

Sr. No.	Name of components	Description	Optimized scale down dimensions
1	PV module (SES1210)	Material: Polycrystalline Maximum power voltage (V_{pmax}): 18 V Maximum power (P_{max}): 10 W _P at 1 kW/m ²	Length (L_m): 300 mm Width (W_m): 360 mm Thickness (t_m): 22 mm
2	Circular rail track	Material: SS410	Diameter (D): 464 mm C/s diameter (d): 8 mm
3	Crossbar	Material: ABS fibre plastic sheet	Length (L_c): 373 mm Width (W_c): 45 mm Thickness (t_c): 12.5
4	Railbar	Material: Wrought iron plate (L-shaped)	Length (L_R): 420 mm Width (W_R): 30 mm Thickness (t_R): 12 mm
5	Fully threaded stud rod (Right handed)	Material: SS304 Size: M8×1.25 – 4g6g	Length (L_R): 468 mm Diameter (D_n): 8 mm
6	Hexagonal nut	Material: SS304 Size: M8×1.25 Thread class: 6H	Width (W_h): 12 mm Thickness (t_h): 6.5 mm
7	Centre distance between front wheels across	–	234 mm
8	Centre distance between front and rear wheels across	–	328 mm
9	DC geared motor	Voltage (V_{dc}): 12 V Speed (S_m): 10 RPM Weight (W_m): 125 gms Torque (T_m): 12 kg-cm	–
10	Lead acid storage battery	Voltage (V_B): 12 V Capacity (C_B): 7 Ah Weight (W_B): 2.5 kg	–

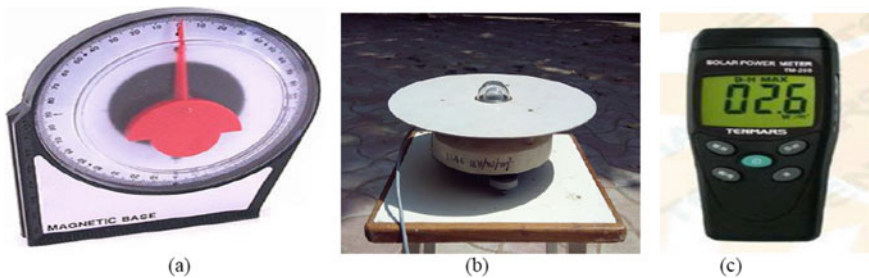


Fig. 23 Measuring instruments (a) magnetic base pendulum angular meter (Mfg. Part No. DZ803); (b) pyranometer with resolution 11.46 μ V/W/m²; (c) digital solar power meter with resolution, range and sampling time of 1 W/m², 1999 W/m² and 0.25 s, respectively

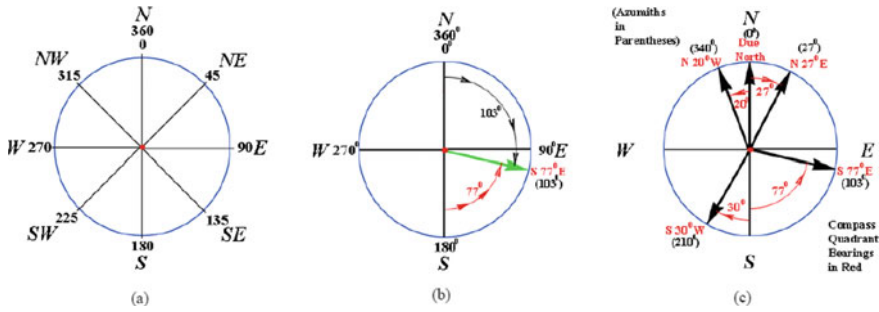


Fig. 24 Compass quadrant bearings method for azimuth angle (ψ^*) measurement

black color are illustrated in Fig. 24 with designation by means of compass quadrant bearing in red color.

The tracking error is determined on January 15, March 21 and June 21 as illustrated in Fig. 25. It can be easily interpreted from the graph that the tracking error is found less than 1° at solar noon (12:45 pm) and within 2° in the morning and evening. The experimental results are good in accordance with theoretical results. The minimum and maximum tracking errors occur at solar noon (12:45 pm) and in the morning and evening, respectively. This is because the availability of sunlight intensity is least in the morning and evening. The proposed prototype is scale-down model with 10 W PV module so that the lower intensity of sunlight is not sufficient to transform sun energy into electricity. The sufficient amount of power is not generated from 10 W PV module if a certain amount of sunlight does not cross the threshold value of sunlight intensity. Because it is scale-down prototype of DT system, a certain thing must be constrained to gain useful power output from PV module. As LDR system works on the principle of photoconductivity, the movement of DT system depends upon incidence of intensity of the sunlight on the LDRs sensing device corresponding to degree of the detectability of it. In order to reduce unnecessary losses in DT system while tracking the sun, a threshold value of intensity of sunlight that is detectable by LDRs sensing device is decided. The threshold value of LDR sensing device is constrained by adjusting the variable resistance R_4 (see Fig. 8). As per specification of 10 W PV module, it would generate maximum power output ($P_{max} = 10 W_p$) when intensity of sunlight and temperature would be 1 kW/m^2 and 25°C , respectively. That is why the maximum tracking errors occur in the morning and evening time due to intensity of sunlight falls below the threshold value, i.e., 400 W/m^2 , and this amount of sunlight intensity would not participate in generation of electrical energy from PV module.

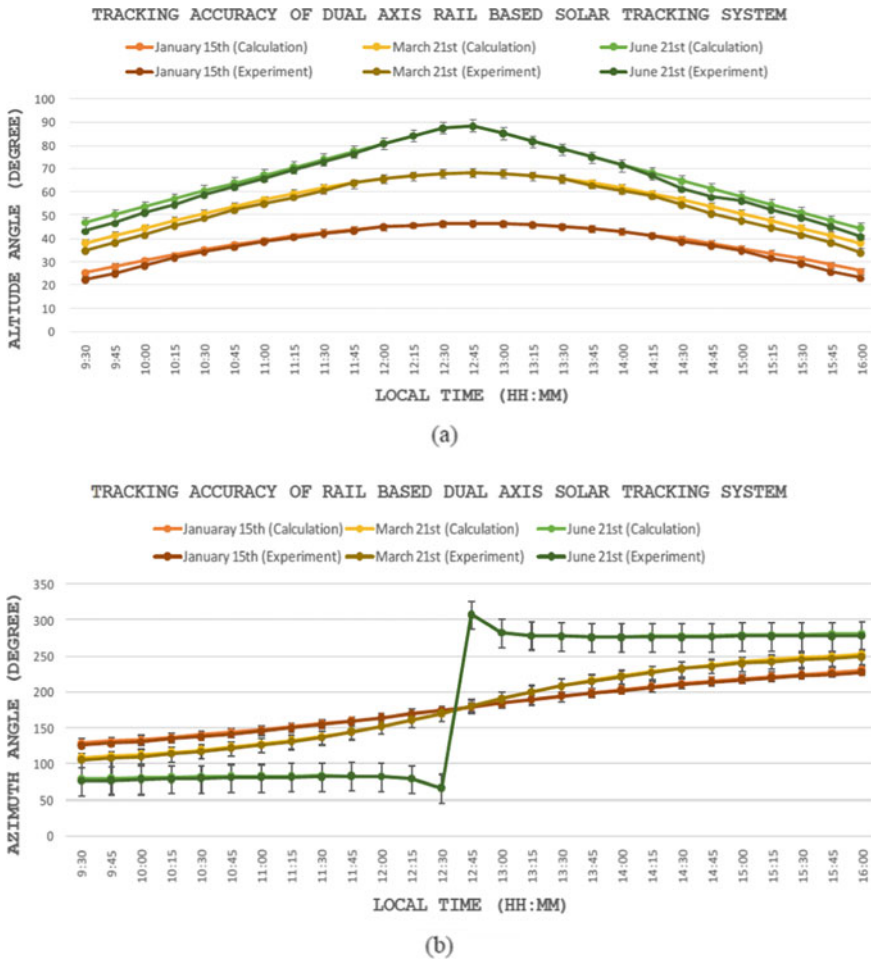


Fig. 25 Tracking accuracy of DT system on January 15, March 21 and June 21 for (a) altitude angle (α^*); (b) azimuth angle (ψ^*)

5.2 Performance Tests on Used PV Systems

This sub-subsection deals with the performance tests on different configured PV systems, namely FA (non-tracking) system, E-W system (X-axis tracking), N-S system (Y-axis tracking) and DT system (dual axis tracking). The tests are performed in two sets. Set I describes the performance analysis by different configured solar tracking systems on March 21, 2016. Set II describes the performance analysis between DT system and FA system on January 15, March 21 and June 21. Table 9 depicts the variation of power output (W) for four systems, i.e. DT system, E-W system, N-S system and FA system using polycrystalline material for PV module on March 21,

2016. Table 8 illustrates the data collections for global solar radiation on March 21, 2016, in Vasad, IN. The global radiation data is collected by means of two measuring instruments as depicted in Fig. 23b and Fig. 23c. The accuracy of both instruments, namely pyranometer (see Fig. 23b) and digital solar power meter (KM SPM 11), are $11.46 \mu\text{V/W/m}^2$ and $\pm 10 \text{ W/m}^2$ ($\pm 5\%$), respectively.

Table 8 depicts the global radiation data collection on March 21, 2016, measured by means of two separate instruments, namely pyranometer and solar power meter. The simulated results of global radiation are also tabulated in it. The simulated data can be attained by using the same MATLAB code as discussed in Sect. 1.7.1 (see Fig. 18). The maximum global radiation occurs at 12:45 pm. This maximum global

Table 8 Global radiation data collection on March 21, 2016, in Vasad, IN

Time (GMT + 5.5)	Pyranometer			Solar power meter	Simulation
	Equivalent voltage (V)	Conversion factor ($\mu\text{V/W/m}^2$)	Equivalent radiation (W/m^2)	Global radiation (W/m^2)	Global radiation (W/m^2)
9:30	0.0054	11.46	471.2042	465.0 ± 10	560.2753
9:45	0.0058	11.46	506.1082	501.0 ± 10	580.7938
10:00	0.0061	11.46	532.2862	528.0 ± 10	601.3123
10:15	0.0065	11.46	567.1902	563.0 ± 10	627.4346
10:30	0.007	11.46	610.8202	607.0 ± 10	653.5568
10:45	0.0074	11.46	645.7243	641.0 ± 10	679.6790
11:00	0.0078	11.46	680.6283	676.0 ± 10	705.8013
11:15	0.008	11.46	698.0803	692.0 ± 10	760.7013
11:30	0.0082	11.46	715.5323	709.0 ± 10	815.6013
11:45	0.0085	11.46	741.7103	735.5 ± 10	870.5013
12:00	0.008	11.46	698.0803	693.5 ± 10	925.4013
12:15	0.0088	11.46	767.8883	763.0 ± 10	870.5013
12:30	0.009	11.46	785.3403	790.5 ± 10	815.6013
12:45	0.0099	11.46	863.8743	871.0 ± 10	760.7013
13:00	0.0095	11.46	828.9703	837.5 ± 10	705.8013
13:15	0.009	11.46	785.3403	780.0 ± 10	679.6790
13:30	0.0088	11.46	767.8883	773.0 ± 10	653.5568
13:45	0.0086	11.46	750.4363	745.5 ± 10	627.4346
14:00	0.0083	11.46	724.2583	719.5 ± 10	601.3123
14:15	0.0078	11.46	680.6283	686.0 ± 10	580.7938
14:30	0.0074	11.46	645.7243	652.5 ± 10	560.2753
14:45	0.0071	11.46	619.5462	625.5 ± 10	539.7568
15:00	0.0065	11.46	567.1902	561.0 ± 10	519.2383
15:15	0.0062	11.46	541.0122	544.5 ± 10	495.8256
15:30	0.006	11.46	523.5602	517.0 ± 10	472.4128
15:45	0.0058	11.46	506.1082	498.0 ± 10	449.0000
16:00	0.0052	11.46	453.7522	449.0 ± 10	425.5872

radiation received by all configured PV systems resulting in maximum power output is given in Table 9. The maximum power outcomes from various configurations of PV systems are 9.506 W, 8.422 W, 7.138 W and 7.072 W for DT system, E–W system, N–S system and FA system, respectively. The output of PV module is recorded every 15 min from 9:30 to 16:00 on March 21, 2016. The overall production from PV module is calculated by taking sum of recorded readings for various configuration during 9:30 to 16:00. Then, it is multiplied by 15 min of time interval resulting in 2900.59 Wh/day, 2594.86 Wh/day, 2232.36 Wh/day and 2199.95 for DT system, E–W system, N–S system and FA system, respectively. Similarly, the average equivalent radiation can also be obtained when the summation of all equivalent radiation is multiplied to 15 min of time interval resulting in around 265 kWh/m². With respect to this average equivalent solar radiation, the overall production from various configurations of PV systems is given in Table 10 (Set I). In order to calculate the tracking efficiency [33] for various configurations of PV system can be expressed as follows:

$$\eta = \frac{E_T - (E_F + E_C)}{E_F} \times 100 \tag{28}$$

where E_T is power output from tracking system; E_F is power output from FA system (non-tracking) and E_C is power consumption by PV tracking system. The power production from each tracking configurations of PV system is obtained by multiplying the 15 min of time interval to the summation of the measured data. (see Table 10). The exact energy consumption E_C is cumbersome to gain, but its maximum limit can be determined as follows:

$$E_C \leq P_r \times \Delta t \tag{29}$$

where P_r is DC motor’s rated power, i.e., 1.2 W; Δt is DC motor’s working time, i.e., 6.5 h (9:30–16:00). For DT system configuration, the working time would be less than 6.5 h (9:30–16:00). Thus, the maximum limit of power consumption by DT system is obtained, $E_C \leq 1.2 \times 6.5 \times 2 = 15.6$ Wh/day. For E–W or N–S system, the working time would be less than 1 h that is determined by cross multiplying the number N ($N = \frac{6.5 \times 60}{2} = 195$) of tracking steps by motion step duration Δt ($\Delta t \leq 6$ s). Consequently, the maximum limit of power consumption by E–W or N–S system is also attained, $E_C \leq 1.2 \times 1 = 1.2$ Wh/day. Thus, the maximum limits of energy efficiencies for all configurations of PV system are obtained according to Eq. 29. Thus, tracking efficiencies for used PV systems are summarized in Table 10 with simulated data.

Table 10 depicts the validation of experimental results with simulated data. In Set I, the DT system emerges higher power output than others configurations of PV systems. The experimental results are in good accordance with simulated results. Similarly, the same procedure is followed for determining the tracking efficiency of DT system with respect to FA system. Again, the tracking efficiency of dual axes rail-based tracking system (DT system) emerges higher power output with respect to fixed system (FA system) in Set II. Table 11 shows that the tracking efficiency

Table 9 Variation of power output for four systems using polycrystalline module on clear sunny day (March 21, 2016)

Time (GMT + 5.5)	DT System			E-W System			N-S System			FA System		
	Voltage (V)	Current (A)	Power (W)	Voltage (V)	Current (A)	Power (W)	Voltage (V)	Current (A)	Power (W)	Voltage (V)	Current (A)	Power (W)
9:30	12.200	0.402	4.904	12.000	0.391	4.692	11.820	0.348	4.113	11.600	0.346	4.014
9:45	12.300	0.412	5.068	12.100	0.389	4.707	11.880	0.370	4.396	11.640	0.367	4.272
10:00	12.400	0.446	5.530	12.200	0.406	4.953	11.910	0.390	4.645	11.690	0.388	4.536
10:15	12.500	0.463	5.788	12.300	0.424	5.215	11.920	0.402	4.792	11.710	0.400	4.684
10:30	12.700	0.490	6.223	12.400	0.442	5.481	11.940	0.418	4.991	11.760	0.415	4.880
10:45	12.800	0.520	6.656	12.500	0.468	5.850	11.960	0.432	5.167	11.810	0.431	5.090
11:00	12.900	0.541	6.979	12.700	0.495	6.287	11.980	0.452	5.415	11.850	0.450	5.333
11:15	13.000	0.571	7.423	12.500	0.525	6.563	11.990	0.473	5.671	11.900	0.472	5.617
11:30	13.200	0.589	7.775	12.600	0.541	6.817	12.000	0.486	5.832	11.940	0.488	5.827
11:45	13.300	0.619	8.233	12.600	0.568	7.157	12.030	0.498	5.991	11.990	0.497	5.959
12:00	13.400	0.645	8.643	12.700	0.583	7.404	12.050	0.535	6.447	12.000	0.534	6.408
12:15	13.600	0.654	8.894	12.800	0.612	7.834	12.080	0.556	6.716	12.050	0.555	6.688
12:30	13.800	0.671	9.260	12.800	0.629	8.051	12.100	0.567	6.861	12.090	0.565	6.831
12:45	14.000	0.679	9.506	13.200	0.638	8.422	12.140	0.588	7.138	12.130	0.583	7.072
13:00	13.800	0.668	9.218	13.100	0.632	8.279	12.110	0.565	6.842	12.080	0.563	6.801
13:15	13.600	0.647	8.799	13.000	0.614	7.982	12.090	0.548	6.625	12.040	0.546	6.574
13:30	13.500	0.634	8.559	12.800	0.597	7.642	12.080	0.539	6.511	11.960	0.538	6.434
13:45	13.400	0.625	8.375	12.700	0.575	7.303	12.060	0.508	6.126	11.900	0.506	6.021
14:00	13.300	0.602	8.007	12.600	0.565	7.119	12.040	0.491	5.912	11.880	0.489	5.809
14:15	13.100	0.586	7.677	12.500	0.545	6.813	12.000	0.470	5.640	11.830	0.468	5.536

(continued)

Table 9 (continued)

Time (GMT + 5.5)	DT System			E-W System			N-S System			FA System		
	Voltage (V)	Current (A)	Power (W)	Voltage (V)	Current (A)	Power (W)	Voltage (V)	Current (A)	Power (W)	Voltage (V)	Current (A)	Power (W)
14:30	13.000	0.569	7.397	12.400	0.528	6.547	11.990	0.458	5.491	11.770	0.456	5.367
14:45	12.800	0.538	6.886	12.300	0.501	6.162	11.970	0.442	5.291	11.760	0.440	5.174
15:00	12.700	0.498	6.325	12.200	0.477	5.819	11.930	0.402	4.796	11.700	0.401	4.692
15:15	12.600	0.462	5.821	12.000	0.452	5.424	11.910	0.395	4.704	11.620	0.393	4.567
15:30	12.400	0.439	5.444	11.900	0.425	5.058	11.890	0.375	4.459	11.540	0.381	4.397
15:45	12.200	0.417	5.087	11.800	0.408	4.814	11.870	0.358	4.249	11.490	0.364	4.182
16:00	12.000	0.408	4.896	11.700	0.393	4.598	11.840	0.338	4.002	11.400	0.342	3.899

Table 10 Comparison of tracking efficiencies of various configurations of PV systems

Set I (21/03/2016)						
Total Global Radiation ($G_h = 265 \text{ kWh/m}^2$)						
PV tracking configuration	E_T (Wh/day)	E_F (Wh/day)	E_C (Wh/day)	η (%) (Experimental)	η (%) (Simulated)	Δ_η (Difference)
DT system (Dual axis)	2900.59	2199.95	≤ 15.60	≥ 31.14	31.77	0.63
E-W system (X-axis)	2594.86	2199.95	≤ 1.20	≥ 17.90	17.97	0.07
N-S system (Y-axis)	2232.36	2199.95	≤ 1.20	≥ 1.42	1.83	0.41

Table 11 Assessment of tracking efficiency of DT system with FA system in different seasons

Set II						
Date	E_T (Wh/day)	E_F (Wh/day)	E_C (Wh/day)	η (%) (Experimental)	η (%) (Simulated)	Δ_η (Difference)
15/01/2017 (Winter)	2747.325	2119.575	≤ 15.60	≥ 28.888	≥ 29.36510	0.4770
21/03/2017 (Spring equinox)	2858.730	2198.115	≤ 15.60	≥ 29.344	≥ 31.76720	2.4232
21/06/2017 (Summer)	3222.57	2454.405	≤ 15.60	≥ 30.662	≥ 32.18124	1.5132
Average	2942.875	2257.365	≤ 15.60	≥ 29.678	≥ 31.10451	1.4265

of DT configured system is more than 31% over FT configured system in different seasons, namely Winter (15/01/2017), Spring equinox (21/03/2017) and Summer (21/06/2017). It is concluded from Table 11 that the average power gain from DT system over FA system is more than 29% including the energy consumption of driving motors. The energy consumption is less than 1% of increased power gain, which conforms to the required condition of tracking mechanism as mentioned in [15]. The performance analysis of DT system over FA system is also illustrated in Fig. 26. Table 12 depicts the overall production of DT system over FA system for different seasons from 9:30 to 16:00. It also shows the variation of tracking efficiencies with respect to time duration from 9:30 to 16:00. The tracking efficiency is found to be maximum at 12:00 noon and shows the maximum variation of tracking efficiency from 11:15 to 13:00. This is because the minimum torque acting on the shaft of motors. The minimum torque condition is explained in details in the following subsection.

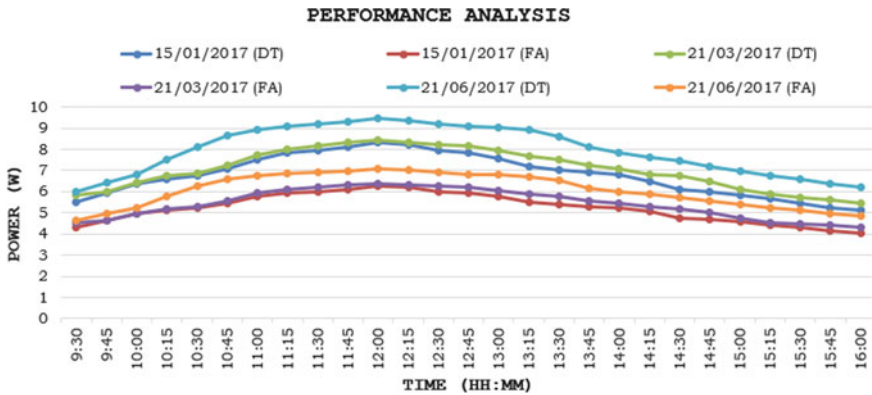


Fig. 26 Variation of power curves of polycrystalline module mounted on DT system and FA system for different seasons

5.3 Optimal Torque Testing

This section deals with optimal torque design of the proposed rail-based solar tracking platform, and associated electronic circuitry is tested by rotating the PV module at the rate corresponding to the speed of DC motor. The angular rotation rate can be attained from the slope of the graph (see Fig. 27). The minimum torque condition implies that the maximum energy gain can be obtained when there would be minimum load on the shaft of the motors. As the sun’s apparent movement is from east to west direction, the location of it can be determined by the combinations of elevation and azimuth angles (α, ψ) at given specified time from the graph of sun path (see Fig. 28). From Fig. 28, the solar angles (α, ψ) on January 15, March 21 and June 21 at 12:00 are ($46^\circ, 180^\circ$), ($67^\circ, 180^\circ$) and ($88^\circ, 180^\circ$). The solar angles are calculated at 12:00 noon because the maximum tracking efficiency or power output is obtained at noon (see Table 12) in all seasons in clear-sky days. The elevation angle α^* changes 0° – 90° and azimuth angle ψ^* changes 90° – 270° due North (see Fig. 24).

The DC motors have their current proportional to the torque. The two DC motors are used for controlling each axes of rail-based dual axis tracking platform. Although PV module is mounted on rail-based tracking platform, the total deadweight is distributed on guiding wheels. One of the wheels is connected with DC motors (see Fig. 22). Hence, a comparatively entire structure can be driven by a small torque-based DC motor. The second DC motors which are attached to the leadscrew and nut mechanism drive the elevation axis. The torque for both the motors is tested. Therefore, the minimum torque on DC motor is achieved when PV module is approached to maximum elevation angle. Hence, the minimum torque is obtained by DC motors at 12:00 noon resulting in maximum energy gain (see Table 12). Table 12 depicts that the tracking efficiency increases when time approaches toward 12:00 noon and then decreases. This is because the center of gravity (CG) of PV module shifts on the front wheels while motors are mounted on rear wheels. If torque is not optimized,

Table 12 Power output of values of two systems using polycrystalline module and percentage difference between DT system and FA system

Time (GMT + 5.5)	15/01/2017			21/03/2017			21/06/2017		
	DT	FA	η (%)	DT	FA	η (%)	DT	FA	η (%)
9:30	5.504	4.320	27.40741	5.812	4.532	28.2436	5.989	4.642	29.0177
9:45	5.931	4.648	27.60327	5.978	4.656	28.3935	6.412	4.963	29.1961
10:00	6.378	4.985	27.94383	6.428	4.974	29.232	6.800	5.252	29.4745
10:15	6.564	5.120	28.20313	6.725	5.200	29.3269	7.500	5.782	29.7129
10:30	6.741	5.245	28.5224	6.845	5.285	29.5175	8.102	6.240	29.8397
10:45	7.085	5.474	29.43003	7.242	5.564	30.1582	8.645	6.569	31.603
11:00	7.501	5.792	29.50622	7.747	5.947	30.2674	8.925	6.761	32.0071
11:15	7.845	5.962	31.58336	7.998	6.100	31.1148	9.100	6.861	32.6337
11:30	7.934	6.010	32.01331	8.187	6.221	31.6026	9.210	6.924	33.0156
11:45	8.090	6.105	32.51433	8.299	6.290	31.9396	9.298	6.988	33.0567
12:00	8.310	6.253	32.89621	8.452	6.345	33.2072	9.489	7.055	34.5004
12:15	8.220	6.205	32.47381	8.302	6.301	31.7569	9.378	7.010	33.7803
12:30	7.925	6.000	32.08333	8.218	6.251	31.467	9.212	6.900	33.5072
12:45	7.812	5.954	31.20591	8.164	6.220	31.254	9.102	6.831	33.2455
13:00	7.580	5.782	31.09651	7.960	6.070	31.1367	9.040	6.791	33.1174
13:15	7.187	5.512	30.38824	7.671	5.887	30.3041	8.900	6.712	32.5983
13:30	7.000	5.378	30.15991	7.491	5.756	30.1425	8.610	6.520	32.0552
13:45	6.900	5.312	29.89458	7.261	5.583	30.0555	8.104	6.149	31.7938
14:00	6.785	5.232	29.68272	7.050	5.423	30.0018	7.841	5.991	30.8797
14:15	6.505	5.070	28.30375	6.810	5.281	28.9528	7.628	5.858	30.2151

(continued)

Table 12 (continued)

Time (GMT + 5.5)	15/01/2017			21/03/2017			21/06/2017		
	DT	FA	η (%)	DT	FA	η (%)	DT	FA	η (%)
14:30	6.115	4.768	28.25084	6.745	5.200	29.71115	7.459	5.731	30.1518
14:45	6.010	4.697	27.95401	6.458	4.989	29.44448	7.200	5.547	29.79999
15:00	5.810	4.554	27.58015	6.118	4.742	29.0173	6.982	5.395	29.4161
15:15	5.654	4.445	27.1991	5.864	4.551	28.8508	6.752	5.242	28.8058
15:30	5.451	4.295	26.91502	5.699	4.463	27.6944	6.567	5.100	28.7647
15:45	5.218	4.123	26.55833	5.600	4.400	27.2727	6.375	4.958	28.5801
16:00	5.100	4.064	25.49213	5.458	4.310	26.6357	6.218	4.855	28.0742

Bold significance indicates the power production, from PV module held on various configurations of PV platform, are maximum during those time range

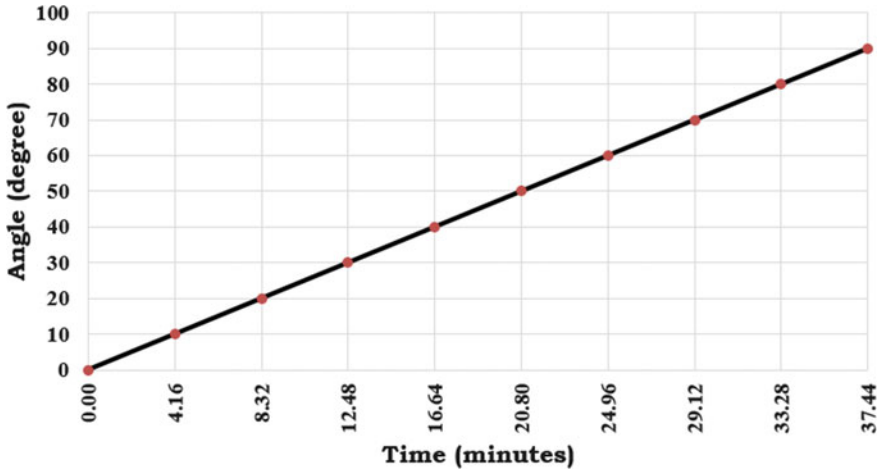


Fig. 27 Variation of angle versus time

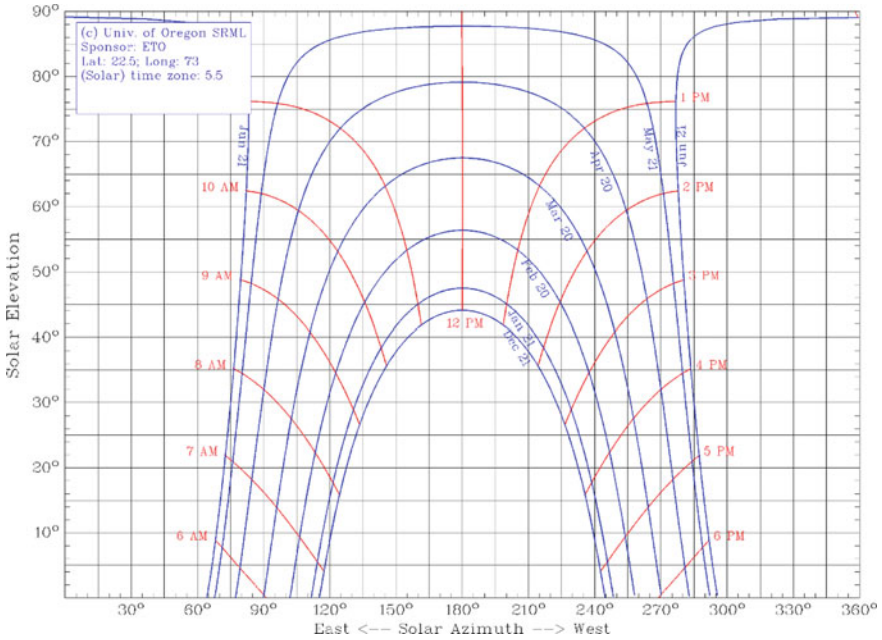
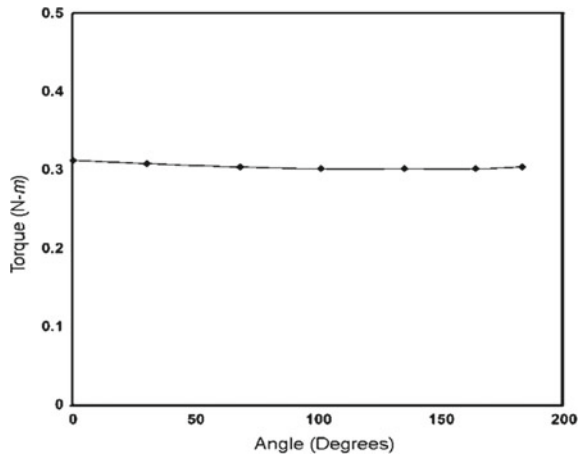


Fig. 28 Variation of solar angles throughout the year in different seasons in Vasad, IN ($\Phi = 22.5^\circ$)

Fig. 29 Variation of torque versus angle



there would be a least or a maximum torque as PV module undergoes rotation. The maximum value would be greater than the torque values as illustrated in Fig. 29. The range of the torque is between 0° and 180° that is suitable to estimate the variability of the torque.

6 Conclusion

In this paper, the PV solar tracking system that uses the concept of “rail-based tracking mechanism incorporating the minimum torque condition has been presented. It employs four configurations of PV system. The following conclusions are deduced on the basis of the above study:

- The rail-based solar tracking system employs the design study of LDRs sensor-based control system with motor driving circuitry. It also includes the battery charge controller to avoid overcharging of it. Experimental results show that tracking accuracy is within 1° .
- The proposed mechanism offers the stability of the system incorporating minimum torque condition on driving motor. It reduces the energy consumption up to less than 1% of increase energy gain. The maximum tracking efficiency is obtained at noon due to minimum torque condition.
- The performance results show that rail-based dual axes solar tracking configuration has greater power gain than 29% over fixed system at tilt angle of 22.5° . These results have validated with simulated results.

The proposed rail-based PV tracking system is feasible and can be used for further improved tracking efficiency. This can be achieved by using single DC motor, which drives both the axes.

References

1. Fernandez-Ahumada LM, Casares FJ, Ramirez-Faz J, Lopez-Luque R (2017) Mathematical study of the movement of solar tracking systems based on rational models. *Sol Energy* 150:20–29
2. Obara S, Matsumura K, Aizawa S, Kobayashi H, Hamada Y, Suda T (2017) Development of a solar tracking system of a nonelectric power source by using a metal hydride actuator. *Sol Energy* 158:1016–1025
3. Burduhos BG, Visa I, Neagoe M, Badea M (2015) Modeling and optimization of the global solar irradiance collecting efficiency. *Int J Green Energy* 12(7):743–755
4. Yang C, Cheng T, Cheg C, Wang C, Lee C (2017) Open-loop altitude-azimuth concentrated solar tracking for solar-thermal applications. *Sol Energy* 147:52–60
5. Sumathi V, Jayapragash R, Bakshi A, Akella P (2017) Solar tracking methods to maximize PV system output—a review of the methods adopted in recent decade. *Renew Sustain Energy Rev* 74:130–138
6. Prinsloo GJ, Dobson RT (2015) *Solar tracking*. SolarBooks, Stellenbosch. ISBN 978-0-620-61576-1, pp 1–542. <https://doi.org/10.13140/2.1.2748.3201>
7. Duffie JA, Beckman WA (2013) *Solar engineering of thermal processes*. Fourth eds. Wiley, USA. ISBN: 9780470873663
8. Venkateswari R, Sreejith S (2019) Factors influencing the efficiency of photovoltaic system. *Renew Sustain Energy Rev* 101:376–394
9. Loschi HJ, Iano Y, Leon J, Moretti A, Conte FD, Braga H (2015) A review on photovoltaic systems: mechanisms and methods for irradiation tracking and prediction. *Smart Grid Renew Energy* 6:187–208
10. Sungur C (2009) Multi-axes sun-tracking system with PLC control for photovoltaic panels in turkey. *Renew Energy* 34:1119–1125
11. Senpinar A, Cebeci M (2012) Evaluation of power output for fixed and two-axis tracking PV arrays. *Appl Energy* 92:677–685
12. Bahrami A, Okoye CO (2018) The performance and ranking pattern of PV systems incorporated with solar trackers in the northern hemisphere. *Renew Sustain Energy Rev* 97:138–151
13. Bahrami A, Okoye CO, Atikol U (2017) Technical and economic assessment of fixed, single and dual-axis tracking PV panels in low latitude countries. *Renew Energy* 113:563–579
14. Lazaroiu GC, Longo MR, Roscia M, Pagano M. Comparative analysis of fixed and sun tracking low power PV systems considering energy consumption
15. Mousazadeh H, Keyhani A, Javadi A, Mobli H, Abrinia K, Sharifi A (2009) A review of principle and sun-tracking methods for maximizing solar systems output. *Renew Sustain Energy Rev* 13:1800–1818
16. Yao Y, Hu Y, Gao S, Yang G, Du J (2014) Multipurpose dual-axis solar tracker with two tracking strategies. *Renew Energy* 72:88–98
17. Despotovic M, Nedic V (2015) Comparison of optimum tilt angles of solar collectors determined at yearly, seasonal and monthly levels. *Energy Convers Manag* 97:121–131
18. Jacobson MZ, Jadhav V (2018) World estimates of PV optimal tilt angles and ratio of sunlight incident upon tilted and tracked PV panels relative to horizontal panels. *Sol Energy* 169:55–66
19. Dananeh MA, Mousavi SM (2018) Solar irradiance estimation models and optimum tilt angle approaches: a comparative study. *Renew Sustain Energy Rev* 92:319–330
20. Ahmad MJ, Tiwari GN (2009) Optimum tilt angle for solar collectors used in India. *Int J Ambient Energy* 30(2):73–78. <https://doi.org/10.1080/01430750.2009.9675788>
21. Jamil B, Siddiqui AT, Akhtar N (2016) Estimation of solar radiation and optimum tilt angles for south-facing surfaces in Humid Subtropical Climate Region of India. *Int J Eng Sci Technol* 19(4):1826–1835. <https://doi.org/10.1016/j.jestch.2016.10.004>
22. Yadav AA, Yadav CO, Ramana PV (2018) Kinematical synthesis and numerical analysis of rail-based dual-axis solar tracking system. In: Sengupta S, Zobaa A, Sherpa K, Bhoi A (eds) *Advances in smart grid and renewable energy*. Lecture notes in electrical engineering, vol. 435. Springer, Singapore, pp 167–175. https://doi.org/10.1007/978-981-10-4286-7_17

23. Hafez AZ, Soliman A, El-Metwally KA, Ismail IM (2017) Tilt and azimuth angles in solar energy applications—a review. *Renew Sustain Energy Rev* 77:147–168
24. Parkin RE (2010) Solar angles revisited using general vector approach. *Sol Energy* 84(6):912–916. <https://doi.org/10.1016/j.solener.2010.02.005>
25. Kelly NA, Gibson TL (2011) Increasing the solar photovoltaic energy capture on sunny and cloudy days. *Sol Energy* 85:111–125
26. Cheng CL, Chan CY, Chen CL (2006) An empirical approach to estimate monthly radiation on south-facing tilted planes for building application. *Energy* 31(14):2940–2957. <https://doi.org/10.1016/j.energy.2005.11.015>
27. Li DHW, Lam TNT, Chu VWC (2008) Relationship between the total solar radiation on tilted surfaces and the sunshine hours in Hong Kong. *Sol Energy* 82(12):1220–1228
28. Pandey CK, Katiyar AK (2014) Hourly solar radiation on inclined surfaces. *Sustain Energy Technol Assessments* 6:86–92. <https://doi.org/10.1016/j.seta.2014.01.007>
29. Salgado-Conrado L (2018) A review on sun position sensors used in solar applications. *Renew Sustain Energy Rev* 82:2128–2146. <https://doi.org/10.1016/j.rser.2017.08.040>
30. Yadav A, Yadav C, Ramana PV (2017) A study on mathematical modeling of dual axes photovoltaic tracking mechanism for maximizing solar system output. *Int J Emerg Technol Adv Eng* 7:61–67. http://www.ijetae.com/files/Volume7Issue9/IJETAE_0917_11.pdf
31. Rai GD (1980) Solar energy utilization. Khanna Publishers, p 44
32. Fatemi SA, Kuh A (2013) Solar radiation forecasting using zenith angle. *Global Conf Signal Inf Process (GlobalSIP)*. <https://doi.org/10.1109/globalsip.2013.6736930>
33. Catalin A, Nicoleta T (2013) Optimal design of the tracker used for a photovoltaic string. *J Renew Sustain Energy* 5:1–16

An Optimization Case Study of Hybrid Energy System in Four Different Regions of India



Somudeep Bhattacharjee, Samrat Chakraborty, and Champa Nandi

Abstract With a large and growing population, the demand for electricity is increasing which results in the emissions of greenhouse gases that also increasing. In India, a major portion of the power is generated from fossil fuel-based conventional resources which emit greenhouse gases. The Indian electricity sector is a major contributor to greenhouse gases, and these greenhouse gases are responsible for the dangerous impacts of climate change like floods, drought, storms, etc. In order to reduce the impacts of climate change, the use of clean energy sources needs to be increased. In this chapter, a grid-connected hybrid energy system is designed utilizing solar power, wind power, battery, and gas generator as a backup system. This hybrid system is analyzed for four different areas of India based on their real-time data of climatic conditions. This hybrid system is deliberately planned, so that there will be a little emanation of carbon, as carbon emanation is one of the primary causes behind the environmental change. This chapter also explains the role of renewable energy-based hybrid power system to combat climate change. This optimization analysis estimates the amount of production of electrical energy, per unit cost of energy, and the total installation cost of the hybrid energy system. The proposed hybrid system is most profitable in Kavaratti, where its levelized cost of energy is 0.688 \$/kWh. This chapter will contribute toward the dream of making India pollution free.

Keywords Clean energy · Hybrid energy system · Solar power plant · Wind farm · Optimization · Climate change

S. Bhattacharjee · S. Chakraborty · C. Nandi (✉)
Department of Electrical Engineering, Tripura University, Agartala, India
e-mail: cnandi@tripurauniv.in

S. Bhattacharjee
e-mail: somudeep.ee@tripurauniv.in

S. Chakraborty
e-mail: 1995samchakraborty@gmail.com

1 Introduction

India is situated on the Indian Plate, which is situated on the north of the Indo-Australian Plate. The nation is located north of the equator somewhere in the north latitude of between $8^{\circ} 4'$ and $37^{\circ} 6'$ and $68^{\circ} 7'$ and in the east longitude of between $68^{\circ} 7'$ and $97^{\circ} 25'$. The Indian atmosphere involves a wide scope of climatic conditions over an immense geographic scale and changed geology, making speculations troublesome. Specifying the span through the Himalayan mountains, narrows of Bengal, Bedouin Ocean, and the Indian Sea, which borders India in all four directions, an incredible variety of warmth and rain dissemination exists [1]. Being an emergent country, India is progressively helpless against the impacts of environmental change because of its reliance on atmosphere delicate divisions like horticulture and ranger service. Low per capita salaries and little open spending plans likewise lead to a low monetary versatile limit. The country is powerless against the prompt financial impacts of environmental change. A recent report showed that the temperature over the nation expanded at around 0.57° per 100 years.

Lacking foundation likewise implies that individuals are increasingly uncovered and less flexible to environmental change. For instance, starting in 2015, just 0.124 billion residents of India are associated with gutter and 0.297 billion with drain. The rest is dependent on pit lavatories or open excretion, which makes significant dangers of waterborne malady during floods—that turn out to be increasingly serious with environmental change. These dangers are increasingly extreme in urban zones, where the higher thickness of individuals implies that essential framework alternatives probably will not be sufficient. Also, numerous metro cities of India are flood-prone, and is exposed to atmospheric dangers, for example, ocean level ascent, storm floods, and violent winds. In spite of the fact that India pays small normal wages for each individual, the nation currently is third biggest producer which produces ozone-harming substance emanations after China and the USA [1].

The Indian electricity sector is a major contributor to greenhouse gases. In the present world, many people are without access to electricity. On the other hand, Asian countries like India have reached the electrification rate up to 89% as of 2016 [2]. The main advantage of a country like India is that it receives solar irradiance of 5000 trillion kWh annually [3], not only that India enjoys wind speed which ranges annually on an average from 6 to 7 m/s [4]. Use of renewable resources for generating electricity is one of the best options in India, not only to save the environment but also to combat situations like a massive grid failure which took back in the year 2012. In India, a major portion of power is supplied from coal thermal power plant, i.e., 58.3% [5], and this results in a huge amount of pollution. Hence, the use of renewable for making hybrid power plant is gaining importance for their prospective advantages [6]. The hybrid power plant uses the combination of different renewable resources like solar, wind, hydro, etc., and also consists of backup and storage components [7]. The federal government has vowed to lessen the discharge force of total national output by 20–25%, with respect to 2005 dimensions, by 2020 [1]. In general, hybrid power plants can be used to mitigate the load requirements of countryside areas. India has

likewise made real promises to extend its sustainable power source supply, improve power efficiency, and assemble mass travel and different measures to diminish its discharges. There is proof that a significant number of these atmosphere activities could produce considerable advantages notwithstanding diminishing the impression of carbon in India. Some less carbon-emitting actions are monetarily alluring, which cover progressively effective climate control systems, leaving request the board, gasification and vehicle execution guidelines. Others offer social advantages: For instance, Indian urban communities may see significant enhancements in air quality if the nation were to advance sustainable power source advances rather than non-renewable energy sources and strolling/cycling/open transport rather than private vehicles [1].

In this chapter, a grid-connected hybrid energy system is designed utilizing solar power, wind power, gas generator, and battery backup system. The gas generator is used only in extreme conditions when no other options are left. This hybrid system is deliberately planned, so that there will be a little emanation of carbon, and tries to utilize the cheapest possible energy resource for reducing the energy bills. This hybrid system is strategically analyzed in four different areas of India for the case study. These areas enjoy good solar irradiance and high wind speed which helps to generate electricity to serve load demand. In this chapter, a fixed amount of residential electrical load is assumed for every area, and the extra power is sold to the grid whenever there is an excess generation of electricity. The design and the optimization study of the hybrid model are done in HOMER Pro[®] software with the use of real-time data of solar irradiance and wind speeds of those areas. The result of this study shows that the overall hybrid system is profitable and helps in reducing pollution by utilizing pollution-free sources. The chief purpose of this work is to reduce the environmental pollution by fulfilling a fixed portion of the load demand of those four different areas and sell the generated power in excess to the main grid. This chapter also includes a detailed discussion about the scenario of the climate change in India and the role of clean energy-based hybrid system to combat climate change. This chapter contributes toward the dream of making India pollution free by suggesting an idea of utilizing all those locations where the possibility of renewable power generation is very high by placing solar–wind hybrid power plant in different parts of India and uses it for generating electricity. This hybrid power plant helps to reduce the use of thermal power plant and the pollution made by those plants if placed strategically at suitable locations in India.

The chapter comprises the following sections apart from the introduction. Section 2 introduces the scenario of climate change in India. Section 3 focuses on the role of the hybrid energy system to promote green energy. Section 4 focuses on system description. Section 5 describes the methodology that is used in this chapter. Section 6 shows the simulation model. Section 7 indicates the optimization results of four chosen areas. Section 8 focuses on the discussion and implication. Sections 9 indicates the conclusion, and Sect. 10 depicts open research directions.

2 The Scenario of Climate Change in South Asia Including India

The Indian atmosphere involves a wide scope of climatic conditions over an immense geographic scale. In light of the Köppen framework, the mean month-to-month temperature, mean month-to-month precipitation, and mean yearly precipitation are taken into account. India has six noteworthy climatic situations, going along parched desert situated in the western part of the country, high expanse along with icy masses in the northwestern part of the country, and moist sultry districts sustaining vegetations in the southwestern part along with island domains. Numerous locales possess obviously extraordinary climates. The Meteorological Office of Government of India separates the seasons as follows: winter, summer, stormy, and withdrawing rainstorm [1]. Environmental change is responsible for making the monsoon uncertain.

Presently, there is a worldwide accord about the danger presented in the environmental change. The difference is just on the best way to approach, adjusting human exercises that release ozone-depleting substances, fueling an unnatural weather change. The worst part is ozone-depleting substances, eminently CO_2 , CH_4 , and N_2O . These collect for uncommon dimensions to climate because of the reprobate consuming of non-renewable energy sources. The ozone-harming substances (greenhouse gases) act as a cover around the earth, catching a lot of the warmth that would some way or another have gotten away into space [8].

The extensive scale utilization of conventional-based energy was the main target of the Industrial Revolution which happened in the nineteenth century. Non-renewable energy sources, for example, oil, coal, and petroleum gas, supply the vast majority of the energy which are expected to run vehicles, create power for enterprises, family units, and so forth. The energy segment is in charge of about three-fourths of the carbon dioxide outflows, one-fifth of the methane emanations, and an extensive amount of nitrous oxide. It additionally creates nitrogen oxide (NO_x) and carbon monoxide (CO) which are not ozone-depleting substances but rather cause an effect on the compound cycles in the air that produces or demolishes ozone-harming substances [9].

The Intergovernmental Panel on Climate Change (IPCC) in its report says that “Warming of the Climate Change is unequivocal,” indicating the expanded worldwide, air and sea temperatures, across the board softening of snow and ice and rising ocean levels. In case if the introduction of the greenhouse substances continued to increase at a very high level, the overall temperature could climb by 2.4–6.4 °C before the century ends, with far-reaching climatic effects. It is less astonishing that the board found inferable from human action and gas emanations; basically, CO_2 is raised by 70% somewhere in the range of 1970–2004. Quite a bit of that challenge lies in executing carbon catch and capacity advances in the energy supply area, which in the previous three and a half decades has been in charge of a 145% expansion in gas discharges [8].

There are numerous effects of environmental change in South Asia. A few impacts of a dangerous atmospheric deviation, including an unflinching ocean level ascent,

expanded the cyclonic movement, and changes in surrounding temperature and precipitation designs have influenced or are anticipated to influence the subcontinent [10]. According to the IPCC, contingent on the situation envisioned the anticipated worldwide normal warm of the plane consequences in heat increments around the globe toward ending of the twenty-first centenary with respect as far as possible of the twentieth centenary varies starting 0.6–4 °C. As the heat increases, the IPCC picture anticipated moderate yearly increment of warmth before the centenary over in the South Asia result to 3.3 °C [10].

Later investigation of various semi-observational models predicts an ocean level ascent of around 1 m in the 2100 year. Progressing ocean level ascents have officially submerged a few low-lying islands in the Sundarbans, uprooting a large number of individuals. Temperature ascends on the Tibetan level, which is making a Himalayan icy masses retreat. Expanded avalanches with flood anticipated having an effect on provinces, for example, Assam. Natural calamities, for example, a 1998 coral fading occasion that executed off over the seventy percentage of underwater biological systems of the Island of Lakshadweep and Andaman, expediting through raised sea temperature fixing in the direction of a worldwide temperature alteration, are additionally anticipated to end up progressively normal [10].

India bears the world's most noteworthy community carbon expenditure. The Indira Gandhi Foundation of Improvement Exploration announced, if expectations, identifying with an unnatural weather change made by the Intergovernmental Board of Environmental Change happen as intended, atmosphere related components could make India's Gross domestic product decreased by up to 9%; adding to this would move developing seasons for significant yields, for example, rice, creation of which reduced to forty percent. Around seven million individuals are anticipated to be uprooted due to, among different elements, submersion of parts of Mumbai and Chennai, if worldwide temperatures were to ascend by an insignificant 2 °C (3.6 °F). Residents in India's northeastern territory of Meghalaya are likewise worried that rising ocean levels will submerge neighboring low-lying areas, bringing about an inundation of evacuees into Meghalaya—which has a couple of assets to deal with such a circumstance [10].

3 Role of Hybrid Energy System to Promote Green Energy

Interest in energy and related administrations, to meet social and monetary advancement and improve human welfare and well-being, is expanding. Since around 1850, worldwide utilization of non-renewable energy sources (coal, oil, and gas) has expanded to rule energy supply, prompting a quick development in carbon dioxide (CO₂) outflows. There are various choices for bringing down greenhouse gases (GHGs) outflowing from the energy framework while as yet fulfilling the worldwide interest for energy administrations. A portion of these conceivable choices, for example, energy protection and effectiveness, petroleum product exchanging,

renewable energy (RE), atomic and carbon capture and storage (CCS), were evaluated in the IPCC Fourth Assessment Report (AR4). A complete assessment of any arrangement of moderation choices would include an assessment of their particular alleviation potential just as their commitment to maintainable advancement and all related dangers and expenses. This report will focus on the job that the sending of RE advancements can play inside such an arrangement of relief alternative. The arrangement of RE advancements has expanded quickly lately, and their offer is anticipated to increment generously under most aspiring alleviation situations. Extra arrangements would be required to pull in the important increments in interest in innovations and foundation [11].

Thus, the sustainable power source is a standout among the best instruments in the battle against environmental change. Wind- and sunlight-based energy have encountered wonderful development and enormous cost upgrades over the previous decade without any indications of backing off. Costs are declining quickly, and the sustainable power source is winding up progressively focused on petroleum derivatives all around the nation. In certain spots, the new sustainable power source is now less expensive than proceeding to work old, wasteful, and filthy non-renewable energy source terminated or atomic power plants [12].

Actually, the venture firm Lazard calculates that the expense of producing power from wind and sun oriented has declined by 58 and 78%, individually, since 2009. Those cost patterns are relied upon to proceed and combined with the ongoing expansion of government charge credits for a sustainable power source, wind- and sun-based development is broadly expected to quicken throughout the following quite a long while, with limit anticipated to twofold from 2015 dimensions by 2021. With cautious arranging, sustainable power source and clean energy alternatives like to expand energy production, and putting away energy for utilizing later will help make ready [12]. In the more extended term, the U.S. Environmental Protection Agency's Clean Power Plan to build up the principal national cutoff points on carbon contamination from power plants will keep on driving sustainable power source development. Wind- and sunlight-based energy will assume a focal job in accomplishing the out-flow cuts required, and carbon approaches like the Clean Power Plan will be basic to guaranteeing that low-carbon assets are organized over higher-emanating power plants [12].

Most of the places in India not only have good access to solar irradiation and wind speed but also have a suitable environment to set up a hybrid power plant in those places. These areas can not only provide a huge amount of power to the grid but also can serve the load demand of those areas. Thus, through investigations of those places, hybrid power plants can be set up according to the renewable resources available. In India, these places needed to be investigated and connected to the main grid, but still, the energy demand is mainly fulfilled by a thermal power plant. This generates pollution in that area in large which needs to be stopped. It is true that backup conventional source is required for maintaining continuity of supply, but still it is better to use a hybrid system than large-sized thermal power plants.

In this chapter, four areas are selected based on solar irradiance and wind speed. These areas are Alipur in Andaman and Nicobar Islands, Badabenakudi in Odisha,

Yaingangpokpi in Manipur, and Kavaratti in Lakshadweep. For these areas as well as states, the demand for power is mainly fulfilled by coal, gas, and distributed generation (DG) power sources. The state of Andaman and Nicobar Islands is mainly dependent upon thermal power generation, whereas the generation of power from renewable sources here is merely low [13]. Figure 1 shows the availability of energy in the state of Andaman and Nicobar Islands. The state of Odisha is mainly dependent upon thermal power plant, and here, also the generation of power from a renewable resource is very low [14]. Figure 2 shows the availability of energy in Odisha. The state of Manipur is not only dependent upon gas power plant, but here, the generation of power from a renewable resource like hydro is mostly high. Other renewable sources of power generation in this state are very low [15]. Figure 3 shows the availability of energy in Manipur. The state of Lakshadweep mainly depends on the DG set, but here, also the generation of power from a renewable resource like solar is there. Other renewable sources of power generation in this state are very low [16]. Figure 4 shows the availability of energy in Lakshadweep.

Fig. 1 Energy availability in Andaman and Nicobar Islands [13]

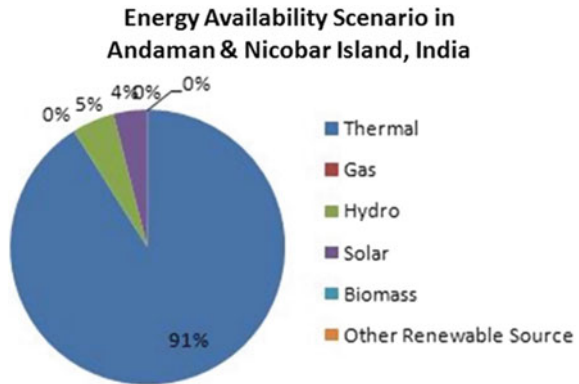


Fig. 2 Energy availability in Odisha [14]

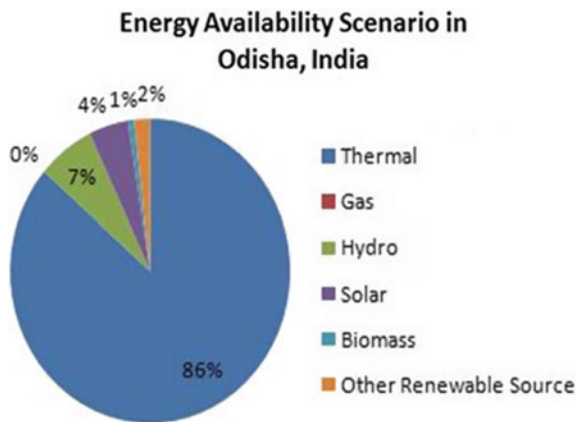


Fig. 3 Energy availability in Manipur [15]

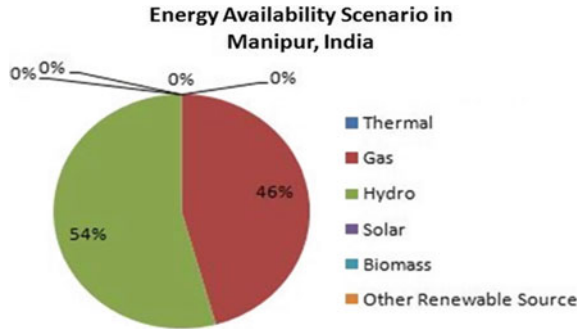
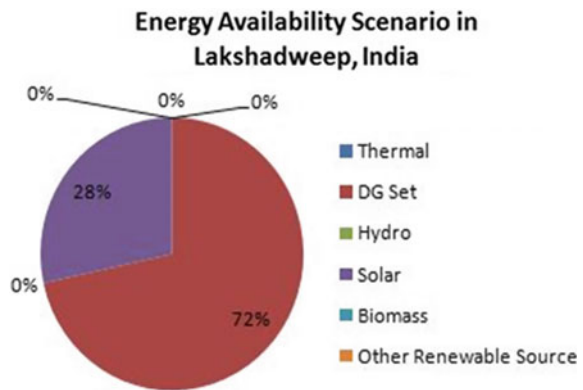


Fig. 4 Energy availability in Lakshadweep [16]



Thus, it is very important that the dependency on conventional energy sources needs to be stopped because of increasing air pollution. These states, especially those areas which we selected, have a large possibility of generation of power from non-conventional renewable sources, especially solar and wind. This chapter discusses the solar irradiance and wind speed of these areas as well as design of hybrid energy system using these sources and shows the results. This would be proof to be a big step toward the clean environment in India if these kinds of areas are utilized and used for energy generation. It reduces pollution to a large extent.

Using renewable energy sources, many research works have been done in many different regions which may help for a better environment. Kumar et al. [17] proposed a simulation-based model to set up a rural micro-grid system with renewable sources like solar and wind, along with diesel generator and battery bank in Leporiang, Papum Pare, India. The model provides an efficient way for the management of energy. Kumari et al. [18] proposed a model of a hybrid power system using various renewable resources like wind, biomass, hydrogen fuel, solar, etc., to ensure continuous electricity supply in Perumal Kovil Pathy, Tamil Nadu, India. The optimization results show that the stand-alone hybrid power model minimizes not only the cost of energy but also CO₂ emission. Swarnkar et al. [19] proposed hybrid

power system optimization using solar and wind for Rajasthan Technical University, Kota, Rajasthan, India. This model optimizes the system costs, clean energy usage percentage, emission of carbon, and demand for the load on a yearly basis. The result shows suitable energy cost optimization with the reduction in emission because of the low utilization of energy from the main grid. Lal et al. [20] proposed an integrated power scheme which comprises PV, wind, micro-hydro, and diesel for remote area function. The optimization result reveals that renewable energy sources are better in comparison to non-renewable energy sources, and replacing them is the best way for electric power distribution for off-grid remote areas. Bhattacharjee et al. [21] proposed a grid-connected solar battery system for Tripura University campus. The result shows that the system totally fulfills the load demand of the campus, and during necessity, it takes some power from the main grid but at a very low leveled cost.

4 Description of the System

The grid-integrated renewable energy-based power plant is modeled using HOMER Pro[®]. The model is analyzed in favor of four different locations: Alipur, Badabenakudi, Yaingangpokpi, and Kavaratti. HOMER Pro[®] software needs some data for input in order to find the result of optimization [22], which obtains as of NASA surface meteorology and solar energy database for four specific areas. The block diagram of the grid-connected hybrid system is shown in Fig. 5. This system consists of three main sources of power, solar, wind, and gas generator, where the gas generator is only for backup. There is a battery backup provided for an emergency situation. A grid is connected in this hybrid system to sell extra power as well as to purchase power during requirement. This hybrid system is designed and analyzed using HOMER Pro[®] software for four different areas of India where it is mainly required.

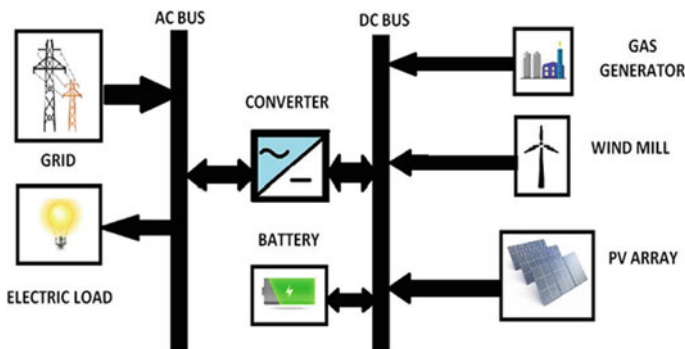


Fig. 5 Block diagram of grid-connected hybrid system

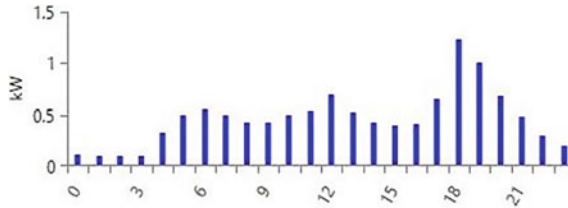


Fig. 6 Daily profile for load (average) [23]

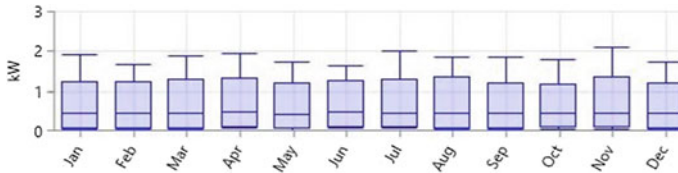


Fig. 7 Monthly profile for load (average) [23]

4.1 Load Profile

In this chapter, it is assumed that the average consumption of energy in all the four areas is 11.13 kWh/d, which is the same for all four areas. Figure 6 portrays everyday's mean profile for demand, in which the maximum demand has been found between the intervals from 17:00 to 21:00 h [23]. Figure 7 portrays the monthly mean load where the maximum demand for the load is 2.07 kW [23]. In the selected locations, the population of people is not very high due to which this normal average electrical load is assumed for each location. The main reason for selecting these locations is that they have a good possibility of renewable power generation. The population of Alipur in Andaman and Nicobar Islands is only 50 [24], the population of Badabenakudi is 3282 [25], the population of Yaingangpokpi is 684 [26], and the population of Kavaratti is 11,221 [27] as per Government of India Census 2011 report.

4.2 Solar Radiation and Wind Speed

The latitude and longitude of Alipur in Andaman and Nicobar Islands are $11^{\circ} 45.7' N$ and $92^{\circ} 41.9' E$, which is found by using HOMER Pro[®] software. The average yearly solar radiation of Alipur area is 5.30 kWh/m²/day. Figure 8 portrays the mean data in favor of solar irradiance in the Alipur area for monthly basis. The data for the speed of wind flow is taken at 50 m over the earth's surface in the Alipur area. Figure 9 indicates the wind data for the Alipur area whose wind speed data varies from 3.93

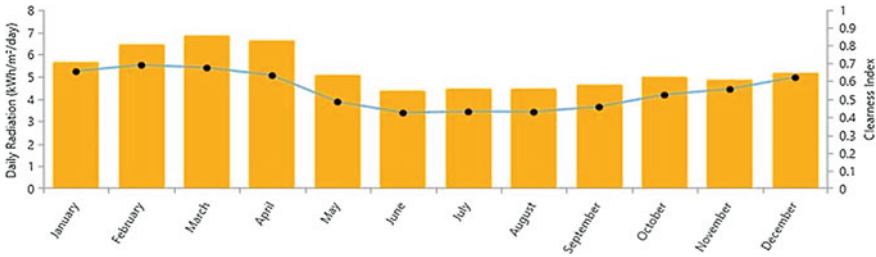


Fig. 8 Solar radiation and clearness index of Alipur (monthly average) [23]



Fig. 9 Wind speed of Alipur (monthly average) [23]

to 8.81 m/s. The mean yearly speed of the wind is 6.24 m/s with the month of June having the maximum speed of the wind for the Alipur area.

The latitude and longitude of Badabenakudi in Odisha are 19° 48.1' N and 85° 33.6' E, which is found by using HOMER Pro® software. The average yearly solar radiation of Badabenakudi area is 4.97 kWh/m²/day. Figure 10 portrays the average monthly data for solar radiation of Badabenakudi area. The data for the speed of wind flow is taken at 50 m over the earth’s surface in the Badabenakudi area. Figure 11 indicates the wind data of Badabenakudi area where the speed of the wind ranges

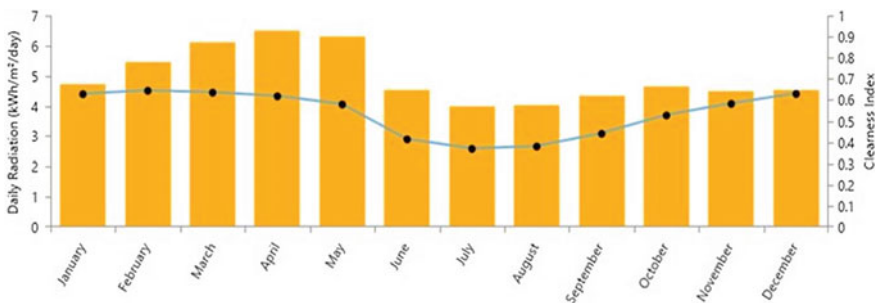


Fig. 10 Solar radiation and clearness index of Badabenakudi [23]



Fig. 11 Wind speed of Badabenakudi [23]

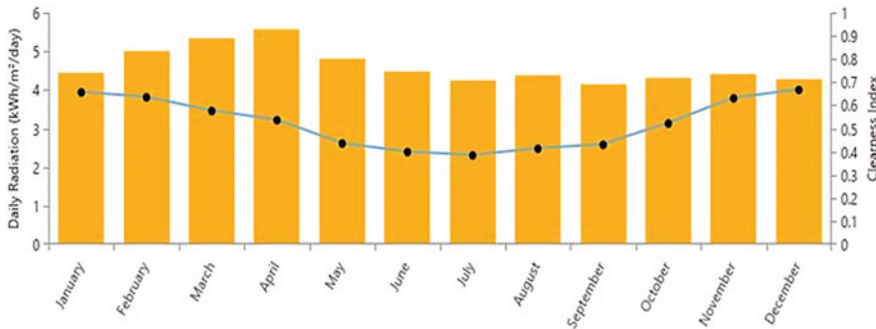


Fig. 12 Solar radiation and clearness index of Yaingangpokpi [23]

between 3.64 and 5.89 m/s. The mean yearly speed of the wind is 4.82 m/s with the month of July having the maximum speed of the wind for Badabenakudi area. The latitude and longitude of Yaingangpokpi in Manipur are 24° 39.8' N and 93° 50.8' E, which is found by using HOMER Pro software. The average yearly solar radiation of Yaingangpokpi area is 4.61 kWh/m²/day. Figure 12 portrays the average monthly data for solar radiation of Yaingangpokpi area. The data for the speed of wind flow is taken at 50 m over the earth's surface in the Yaingangpokpi area. Figure 13 indicates the wind data of Yaingangpokpi area where the speed of the wind ranges between 2.04 and 2.86 m/s. The mean yearly speed of the wind is 2.45 m/s with the month of February having the maximum speed of the wind. The latitude and longitude of Kavaratti in Lakshadweep are 10° 33.6' N and 72° 38.6' E, which is found by using HOMER Pro software. The average yearly solar radiation is 5.76 kWh/m²/day of Kavaratti area. Figure 14 portrays the average monthly data for solar radiation of Kavaratti area. The data for the speed of wind flow is taken at 50 m over the earth's surface in the Kavaratti area. Figure 15 indicates the wind data of Kavaratti area where the speed of the wind ranges between 3.49 and 8.99 m/s. The mean yearly speed of the wind is 5.21 m/s with the month of June having the maximum speed of the wind for Kavaratti area. The data for the speed of the wind and radiation from



Fig. 13 Wind speed of Yaingangpokpi [23]

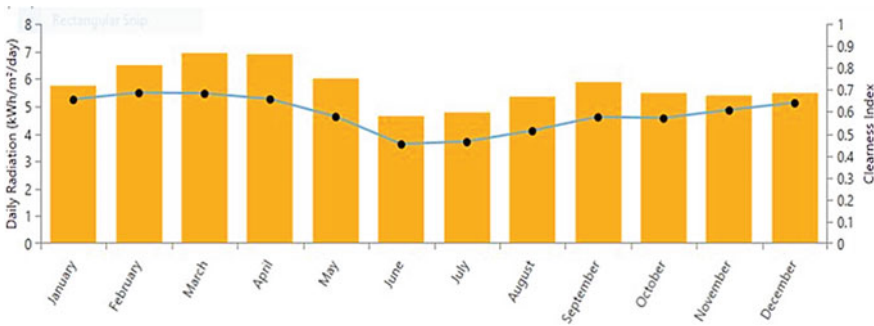


Fig. 14 Solar radiation and clearness index of Kavaratti [23]



Fig. 15 Wind speed of Kavaratti [23]

sun is fetched from the NASA surface meteorology and solar energy database [28]. This data helps in the analysis of the hybrid system more accurately, especially in terms of cost optimization and power generation.

5 Methodology

5.1 About HOMER Pro[®] Software

HOMER Pro software was developed by Dr. Peter Lilienthal in National Renewable Energy Laboratory (NREL) in the USA [29]. Later in 2009, the software was commercialized by Dr. Lilienthal [29]. This software is meant for modeling, optimization, and study of any hybrid energy plant which uses renewable sources of energy. The design of models and analysis of both island and grid-connected hybrid energy system are done using HOMER Pro [30]. Depending upon the input parameters like a profile of the load, solar radiance, and speed of the wind, which is used in this chapter, all possible configurations are simulated. The results are displayed according to the most economical manner in which the loads are satisfied [30]. Results are also displayed in HOMER Pro in graphs and table formats [31].

5.2 Economic Evaluation by HOMER Pro[®]

5.2.1 Net Present Cost (NPC)

NPC comprises setting up charge and operating charge for the model all over its life span, analyzed by the subsequent formula [32]:

$$\text{NPC} = \text{TAC}/\text{CRF}(i, \text{Rpr}_j) \quad (1)$$

Here, TAC indicates the total annualized cost in terms of \$, CRF indicates the capital recovery factor, i indicates the rate of interest in terms of %, and Rpr_j indicates the project lifetime in terms of a year.

5.2.2 Total Annualized Cost

The total annualized cost comprises the addition of the cost of all equipment used in power system which is comprised of capital cost, operation cost, maintenance cost, replacement cost, and fuel cost calculated annually [32].

5.2.3 Capital Recovery Factor

The capital recovery factor is also known as CRF which calculates the series of cash flow annually in ratio with respect to the present value [32].

$$\text{CRF} = \frac{i \times (1 + i)^n}{(1 + i)^{n-1}} \quad (2)$$

Here, n indicates the years, and i indicates the rate for real interest annually.

5.2.4 Annual Real Rate

The annual real interest rate represents the nominal interest rate as a function [32].

$$i = \frac{i' - F}{1 + F} \quad (3)$$

Here, i indicates the real interest rate, i' indicates nominal interest rate, and F indicates annual inflation rate.

5.2.5 Cost of Energy

The cost of energy also known as COE represents the average cost/kWh of the system producing electrical energy which is useful in practice. The calculative formula for COE is as follows [32]:

$$\text{COE} = \frac{\text{TAC}}{L_{\text{prim,AC}} + L_{\text{prim,DC}}} \quad (4)$$

Here, $L_{\text{prim,AC}}$ indicates primary AC load, and $L_{\text{prim,DC}}$ indicates the primary DC load.

6 Simulation Model

The system is modeled by choosing different apparatus of the HOMER Pro[®] software. In this chapter, the simulation system is the same for four different areas: Alipur, Badabenakudi, Yaingangpokpi, and Kavaratti. The model consists of a PV array, windmill, generator, power converter, load, battery storage, and grid connection which is shown in Fig. 16. The lifetime of this project is 25 years for every location.

The full name of the PV array which has been utilized for this chapter is Generic flat plate PV and is synthesized by Generic. The labeled capability of this PV array is 50,000 kW with temperature for operation about 47 °C. The capitalized expenditure is 3000 \$/kW with operation and preservation expenditure of 10 \$/year. The life span of the array PV array is 25 years with an effectiveness of 13%. These are

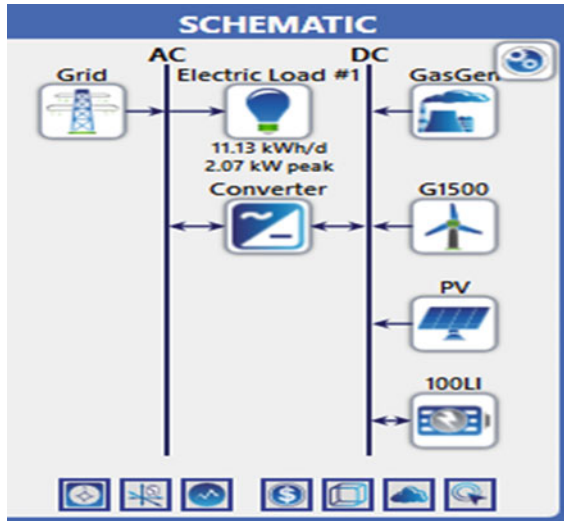


Fig. 16 HOMER Pro[®] model of grid-connected hybrid power system

unequivocally modeled with maximum power point tracker with the labeled capability of 100,000 kW. The capitalized expenditure of maximum power point tracker is 3000 \$/kW with functional and repair expenditure of 10 \$/year. The substitution expenditure of maximum power point tracker is 3000 \$/kW. The life span of the tracker is 15 years having effectiveness of 95%. The full name of the wind-based turbine employed in this chapter is Generic 1.5 MW contrived by Generic. The labeled capability for one windmill is 1500 kW with a capitalized expenditure of \$3,000,000 and functional and repair expenditure of 60,000 \$/year. The total installed capacity is 750 MW. The name of the gas generator used is Generic 200 kW Gas Microturbine manufactured by Generic. The rated capacity is 200 kW with lifetime of 40,000 h. The fuel used in this generator is natural gas with fuel curve intercept 0 m³/h and fuel curve slope 0.290 m³/h/kW. The initial capital cost is \$340,000, and functional and repair expenditure (per op. hour) cost is \$4. The generator is used here only as a backup if the PV array, wind turbine, battery, and grid fail to provide electricity. The name of the power converter is System Converter manufactured by Generic. The life span of the converter is 15 years having effectiveness of 95%. The capitalized expenditure is 300 \$/kW with functional and repair expenditure of 0 \$/year. The total capacity is 850 MW. The full name of the battery is Generic 100 kWh Li-Ion manufactured by Generic. The capacity of one battery is 100 kWh with a voltage of 600 V. The life span for the battery is 15 years with the effectiveness of 90%. Its capitalized expenditure is \$70,000 with functional and repair expenditure of 10 \$/year. In this hybrid system, ten such batteries are used. The overall hybrid system is designed in such a way that it chooses the cheapest possible configuration of energy sources for fulfilling the electric load demand.

7 Optimization Results

7.1 Optimization Results for Alipur

Table 1 shows the NPC of the integrated energy scheme. Table 2 shows the annual expenditure of the integrated energy scheme. After optimization, the leveled COE obtained is \$0.7165 and the total NPC is \$2807.031 M. Table 4 indicates the information for production history showing whole non-conventional power produced for every year which is 322,591,414 kWh/year. Table 5 indicates the information related to the consumption of power in which AC primary load consumption is 4062 kWh/year. Therefore, the integrated energy system fulfills the demand and generates more than the required demand. Table 3 indicates the purchase from the grid (kWh) on a monthly basis and grid sales (kWh) on a monthly basis. This shows that the integrated energy system injects huge excess power to the grid than what it consumes.

Figure 17 indicates the graph of the solar irradiance in kW/m² per month and PV output in kW for each month, where it can be seen that the solar irradiance is as high as 1.2 kW/m² mainly in the months of March and November, and the PV power output is high as nearly 40,000 kW mainly in the months of March and November. Figure 18 indicates the plot of the speed of wind in m/s for each month and wind turbine output in kW for each month, where the highest wind speed is nearly 12 m/s in the months of June and July, and the highest wind power output is 700,000 kW in the months of June and July. Table 6 indicates the pollutants' discharge from an integrated energy system which shows that very minimal emissions of pollutants are there.

Table 1 Net present costs of Alipur

Name	Capital	Operating	Replacement	Salvage	Resource	Total
Generic 1.5 MW	\$1.50 B	\$384 M	\$468 M	-\$262 M	\$0.00	\$2.09 B
Generic 100 kWh Li-Ion	\$700,000	\$1278	\$233,668	-\$43,493	\$0.00	\$891,454
Generic 200 kW gas microturbine	\$340,000	\$0.00	\$0.00	\$59,065	\$0.00	\$280,935
Generic flat plate PV	\$150 M	\$6.39 M	\$0.00	\$0.00	\$0.00	\$156 M
Grid	\$0.00	-\$196 M	\$0.00	\$0.00	\$0.00	-\$196 M
PV dedicated converter	\$300 M	\$12.8 M	\$125 M	-\$23.3 M	\$0.00	\$415 M
System converter	\$255 M	\$0.00	\$106 M	-\$19.8 M	\$0.00	\$342 M
system	\$2.21 B	\$207 M	\$700 M	-\$305 M	\$0.00	\$2.81 B

Table 2 Annualized costs of Alipur

Name	Capital	Operating	Replacement	Salvage	Resource	Total
Generic 1.5 MW	\$117 M	\$30.0 M	\$36.6 M	−\$20.5 M	\$0.00	\$163 M
Generic 100 kWh Li-Ion	\$54,759	\$100.00	\$18,279	−\$3402	\$0.00	\$69,735
Generic 200 kW gas microturbine	\$26,597	\$0.00	\$0.00	−\$4620	\$0.00	\$21,977
Generic flat plate PV	\$11.7 M	\$500,000	\$0.00	\$0.00	\$0.00	\$12.2 M
Grid	\$0.00	−\$15.3 M	\$0.00	\$0.00	\$0.00	−\$15.3 M
PV dedicated converter	\$23.5 M	\$1,000,000	\$9.79 M	−\$1.82 M	\$0.00	\$32.4 M
System converter	\$19.9 M	\$0.00	\$8.32 M	−\$1.55 M	\$0.00	\$26.7 M
System	\$173 M	\$16.2 M	\$54.7 M	−\$23.9 M	\$0.00	\$220 M

Table 3 Grid purchase (kWh) each month and grid sales (kWh) each month of Alipur

Month	Energy purchased (kWh)	Energy sold (kWh)	Net energy purchased (kWh)	Peak demand (kW)	Energy charge	Demand charge
January	124	25,835,902	−25,835,779	1.91	−\$1.29 M	\$0.00
February	138	11,964,541	−11,964,403	1.67	−\$598,220	\$0.00
March	167	8,091,438	−8,091,271	1.88	−\$404,564	\$0.00
April	157	6,980,349	−6,980,192	1.92	−\$349,010	\$0.00
May	117	13,681,697	−13,681,579	1.73	−\$684,079	\$0.00
June	66.7	59,025,987	−59,025,920	1.61	−\$2.95 M	\$0.00
July	81.6	43,663,231	−43,663,149	1.97	−\$2.18 M	\$0.00
August	65.6	54,051,465	−54,051,399	1.57	−\$2.70 M	\$0.00
September	112	18,003,242	−18,003,130	1.85	−\$900,157	\$0.00
October	141	9,830,804	−9,830,662	1.77	−\$491,533	\$0.00
November	107	19,185,035	−19,184,928	2.07	−\$959,246	\$0.00
December	99.8	36,145,468	−36,145,368	1.51	−\$1.81 M	\$0.00
Annual	1377	306,459,157	−306,457,781	2.07	−\$15.3 M	\$0.00

7.2 Optimization Results for Badabenakudi

Table 7 shows the NPC of the integrated energy scheme. Table 8 shows the annual expenditure of the integrated energy scheme. After optimization, the leveled COE

Table 4 Production summary of Alipur

Component	Production (kWh/year)	Percent
Generic flat plate PV	67,136,109	20.8
Generic 200 kW gas microturbine	0	0
Generic 1.5 MW	255,455,305	79.2
Grid purchases	1377	0.000427
Total	322,592,791	100

Table 5 Consumption summary of Alipur

Component	Consumption (kWh/year)	Percent
AC primary load	4062	0.00133
DC primary load	0	0
Grid sales	306,459,157	100
Total	306,463,220	100

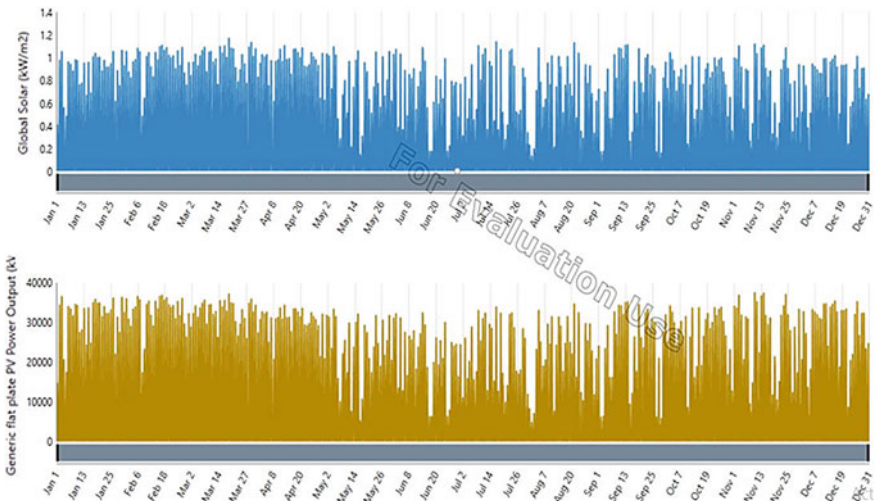


Fig. 17 Plot of global solar irradiance (kW/m^2) per month and generic flat plate PV output (kW) per month of Alipur

obtained is \$0.7341 and the total NPC is \$2811.425 M. Table 10 indicates the information for production history showing whole non-conventional power produced for every year which is 315,355,298 kWh/year. Table 11 indicates the information related to the consumption of power in which AC primary load consumption is 4062 kWh/year. Therefore, the integrated energy system fulfills the demand and generates more than the required demand. Table 9 indicates the purchase from the grid (kWh) on a monthly basis and grid sales (kWh) on a monthly basis. This shows

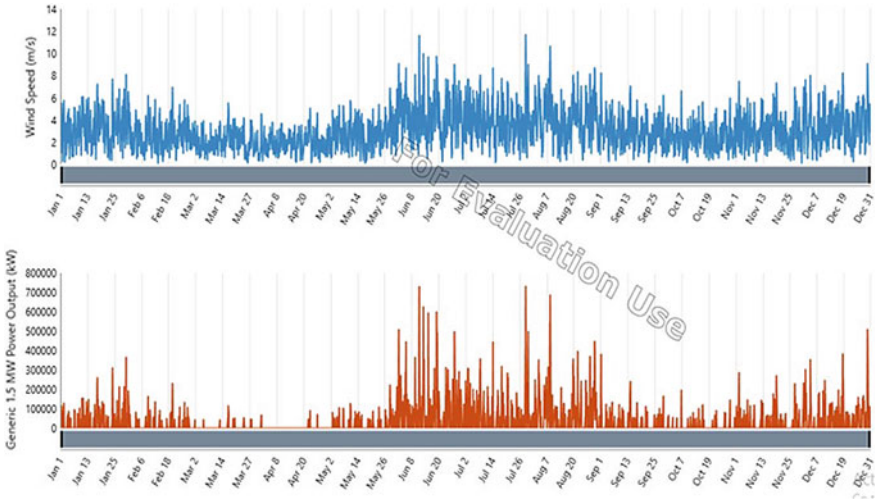


Fig. 18 Plot of wind speed (m/s) per month and generic 1.5 MW power output (kW) per month of Alipur

Table 6 Emission summary of Alipur

Pollutant	Quantity	Unit
Carbon dioxide	870	kg/year
Carbon monoxide	0	kg/year
Unburned hydrocarbons	0	kg/year
Particulate matter	0	kg/year
Sulfur dioxide	3.77	kg/year
Nitrogen oxide	1.84	kg/year

that the integrated energy system injects huge excess power to the grid than what it consumes. Figure 19 indicates the graph of the solar irradiance in kW/m² per month and PV output in kW for each month, where it can be seen that the solar irradiance is as high as 1.2 kW/m² mainly in the month of July and the PV power output is high as nearly 40,000 kW mainly in the month of November. Figure 20 indicates the plot of the speed of wind in m/s for each month and wind turbine output in kW for each month, where the highest wind speed is nearly 11 m/s at the end of June and the highest wind power output is 700,000 kW at the end of June. Table 12 indicates the pollutants’ discharge from an integrated energy system which shows that very minimal emissions of pollutants are there.

Table 7 Net present costs of Badabenakudi

Name	Capital	Operating	Replacement	Salvage	Resource	Total
Generic 1.5 MW	\$1.50 B	\$384 M	\$468 M	−\$262 M	\$0.00	\$2.09 B
Generic 100 kWh Li-Ion	\$700,000	\$1278	\$233,668	−\$43,493	\$0.00	\$891,454
generic 200 kW gas microturbine	\$340,000	\$0.00	\$0.00	−\$59,065	\$0.00	\$280,935
Generic flat plate PV	\$150 M	\$6.39 M	\$0.00	\$0.00	\$0.00	\$156 M
Grid	\$0.00	−\$191 M	\$0.00	\$0.00	\$0.00	−\$191 M
PV dedicated converter	\$300 M	\$12.8 M	\$125 M	−\$23.3 M	\$0.00	\$415 M
System converter	\$255 M	\$0.00	\$106 M	−\$19.8 M	\$0.00	\$342 M
System	\$2.21 B	\$211 M	\$700 M	−\$305 M	\$0.00	\$2.81 B

Table 8 Annualized costs of Badabenakudi

Name	Capital	Operating	Replacement	Salvage	Resource	Total
Generic 1.5 MW	\$117 M	\$30.0 M	\$36.6 M	−\$20.5 M	\$0.00	\$163 M
Generic 100 kWh Li-Ion	\$54,759	\$100.00	\$18,279	−\$3402	\$0.00	\$69,735
Generic 200 kW gas microturbine	\$26,597	\$0.00	\$0.00	−\$4620	\$0.00	\$21,977
Generic flat plate PV	\$11.7 M	\$500,000	\$0.00	\$0.00	\$0.00	\$12.2 M
Grid	\$0.00	−\$15.0 M	\$0.00	\$0.00	\$0.00	−\$15.0 M
PV dedicated converter	\$23.5 M	\$1,000,000	\$9.79 M	−\$1.82 M	\$0.00	\$32.4 M
System converter	\$19.9 M	\$0.00	\$8.32 M	−\$1.55 M	\$0.00	\$26.7 M
System	\$173 M	\$16.5 M	\$54.7 M	−\$23.9 M	\$0.00	\$220 M

7.3 Optimization Results for Yaingangpokpi

Table 13 shows the NPC of the integrated energy scheme. Table 14 shows the annual expenditure of the integrated energy scheme. After optimization, the leveled COE obtained is \$0.7202 and the total NPC is \$2807.959 M. Table 16 indicates the information for production history showing whole non-conventional power produced

Table 9 Grid purchase (kW) each month and grid sales (kW) each month of Badabenakudi

Month	Energy purchased (kWh)	Energy sold (kWh)	Net energy purchased (kWh)	Peak demand (kW)	Energy charge	Demand charge
January	161	10,785,547	-10,785,385	1.91	-\$539,269	\$0.00
February	116	13,768,720	-13,768,604	1.67	-\$688,430	\$0.00
March	116	27,716,856	-27,716,741	1.88	-\$1.39 M	\$0.00
April	103	37,399,119	-37,399,016	1.92	-\$1.87 M	\$0.00
May	94.1	29,744,148	-29,744,054	1.73	-\$1.49 M	\$0.00
June	80.3	32,928,990	-32,928,910	1.48	-\$1.65 M	\$0.00
July	82.7	42,647,513	-42,647,430	1.97	-\$2.13 M	\$0.00
August	103	34,433,555	-34,433,452	1.84	-\$1.72 M	\$0.00
September	133	14,361,654	-14,361,521	1.61	-\$718,076	\$0.00
October	140	14,832,625	-14,832,484	1.77	-\$741,624	\$0.00
November	123	24,219,037	-24,218,915	2.01	-\$1.21 M	\$0.00
December	142	16,747,101	-16,746,959	1.72	-\$837,348	\$0.00
Annual	1394	299,584,864	-299,583,470	2.01	-\$15.0 M	\$0.00

Table 10 Production summary of Badabenakudi

Component	Production (kWh/year)	Percent
Generic flat plate PV	65,565,846	20.8
Generic 200 kW gas microturbine	0	0
Generic 1.5 MW	249,789,452	79.2
Grid purchases	1394	0.000442
Total	315,356,692	100

Table 11 Consumption summary of Badabenakudi

Component	Consumption (kWh/year)	Percent
AC primary load	4062	0.00136
DC primary load	0	0
Grid sales	299,584,864	100
Total	299,588,927	100

for every year which is 321,062,856 kWh/year. Table 17 indicates the information related to the consumption of power in which AC primary load consumption is 4062 kWh/year. Therefore, the integrated energy system fulfills the demand and generates more than the required demand. Table 15 indicates the purchase from the grid (kWh) on a monthly basis and grid sales (kWh) on a monthly basis. This shows that the integrated energy system injects huge excess power to the grid than what it consumes. Figure 21 indicates the graph of the solar irradiance in kW/m² per month

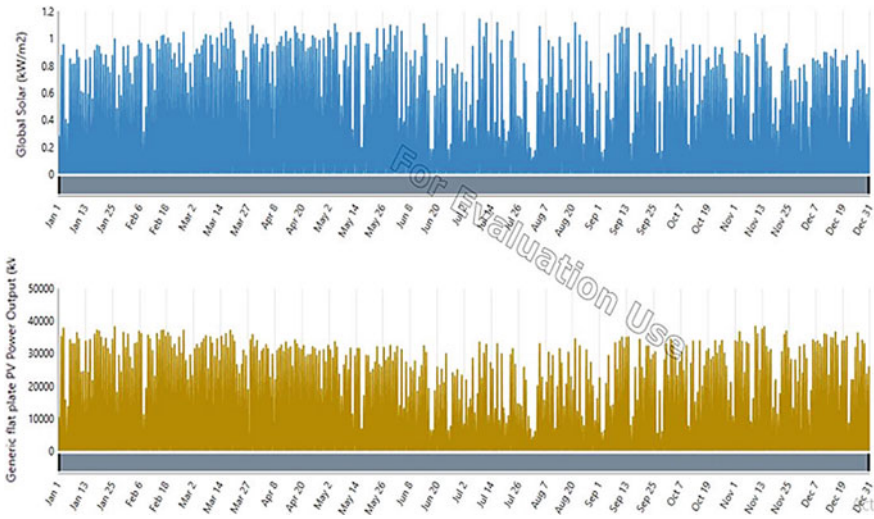


Fig. 19 Plot of global solar irradiance (kW/m^2) per month and generic flat plate PV output (kW) per month of Badabenakudi

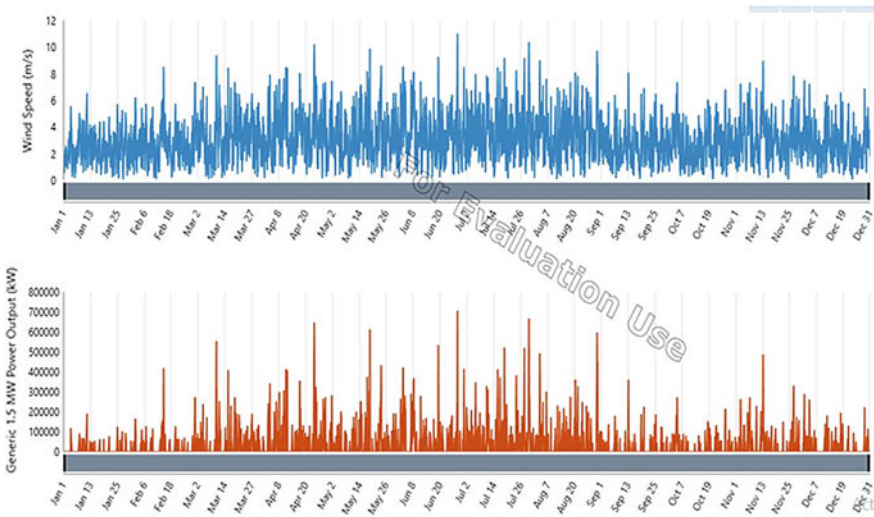


Fig. 20 Plot of wind speed (m/s) per month and generic 1.5 MW power output (kW) per month of Badabenakudi

and PV output in kW for each month, where it can be seen that the solar irradiance is as high as 1.2 kW/m^2 mainly in the month of July and the PV power output is high as nearly 40,000 kW mainly in the months of January and November. Figure 22 indicates the plot of the speed of wind in m/s for each month and wind turbine output

Table 12 Emission summary of Badabenakudi

Pollutant	Quantity	Unit
Carbon dioxide	881	kg/year
Carbon monoxide	0	kg/year
Unburned hydrocarbons	0	kg/year
Particulate matter	0	kg/year
Sulfur dioxide	3.82	kg/year
Nitrogen oxide	1.87	kg/year

Table 13 Net present costs of Yaingangpokpi

Name	Capital	Operating	Replacement	Salvage	Resource	Total
Generic 1.5 MW	\$1.50 B	\$384 M	\$468 M	−\$262 M	\$0.00	\$2.09 B
Generic 100 kWh Li-Ion	\$700,000	\$1278	\$233,668	−\$43,493	\$0.00	\$891,454
Generic 200 kW gas microturbine	\$340,000	\$0.00	\$0.00	−\$59,065	\$0.00	\$280,935
Generic flat plate PV	\$150 M	\$6.39 M	\$0.00	\$0.00	\$0.00	\$156
Grid	\$0.00	−\$195 M	\$0.00	\$0.00	\$0.00	−\$195 M
PV dedicated converter	\$300 M	\$12.8 M	\$125	−\$23.3 M	\$0.00	\$415 M
System converter	\$255 M	\$0.00	\$106 M	−\$19.8 M	\$0.00	\$342 M
System	\$2.21 B	\$208 M	\$700 M	−\$305 M	\$0.00	\$2.81 B

Table 14 Annualized costs of Yaingangpokpi

Name	Capital	Operating	Replacement	Salvage	Resource	Total
Generic 1.5 MW	\$117 M	\$30.0 M	\$36.6 M	−\$20.5 M	\$0.00	\$163 M
Generic 100 kWh Li-Ion	\$54,749	\$100.00	\$18,279	−\$3402	\$0.00	\$69,735
Generic 200 kW gas microturbine	\$26,597	\$0.00	\$0.00	−\$4620	\$0.00	\$21,977
Generic flat plate PV	\$11.7 M	\$500,00	\$0.00	\$0.00	\$0.00	\$12.2 M
Grid	\$0.00	−\$15.3 M	\$0.00	\$0.00	\$0.00	−\$15.3 M
PV dedicated converter	\$23.5 M	\$1,000,00	\$9.79 M	−\$1.82 M	\$0.00	\$32.4 M
System converter	\$19.9 M	\$0.00	\$8.32 M	−\$1.55 M	\$0.00	\$26.7 M
System	\$173 M	\$16.2 M	\$54.7 M	−\$23.9 M	\$0.00	\$220 M

in kW for each month, where the highest wind speed is nearly 11 m/s in the month of March and the highest wind power output is 700,000 kW in the month of March. Table 18 indicates the pollutants' discharge from an integrated energy system which shows that very minimal emissions of pollutants are there.

Table 15 Grid purchase (kW) each month and grid sales (kW) each month of Yaingangpokpi

Month	Energy purchased (kWh)	Energy sold (kWh)	Net energy purchased (kWh)	Peak demand (kW)	Energy charge	Demand charge
January	115	36,002,425	-36,002,310	1.71	-\$1.80 M	\$0.00
February	99.1	37,534,049	-37,533,950	1.67	-\$1.88 M	\$0.00
March	107	40,478,125	-40,475,019	1.88	-\$2.02 M	\$0.00
April	108	28,580,838	-28,580,730	1.92	-\$1.43 M	\$0.00
May	110	21,397,378	-21,397,269	1.73	-\$1.07 M	\$0.00
June	98.8	22,382,510	-22,382,411	1.61	-\$1.12 M	\$0.00
July	95.3	22,493,059	-22,492,964	1.97	-\$1.12 M	\$0.00
August	115	17,379,572	-17,379,458	1.81	-\$868,973	\$0.00
September	131	13,145,631	-13,145,500	1.85	-\$657,275	\$0.00
October	122	18,125,757	-18,125,634	1.77	-\$906,282	\$0.00
November	126	21,744,723	-21,744,596	2.01	-\$1.09 M	\$0.00
December	144	25,742,953	-25,742,809	1.57	-\$1.29 M	\$0.00
Annual	1371	305,007,021	-305,005,650	2.01	-\$15.3 M	\$0.00

Table 16 Production summary of Yaingangpokpi

Component	Production (kWh/year)	Percent
Generic flat plate PV	65,238,984	20.3
Generic 200 kW gas microturbine	0	0
Generic 1.5 MW	255,823,872	79.7
Grid purchases	1371	0.000427
Total	321,064,226	100

Table 17 Consumption summary of Yaingangpokpi

Component	Consumption (kWh/year)	Percent
AC primary load	4062	0.00133
DC primary load	0	0
Grid sales	305,007,021	100
Total	305,011,083	100

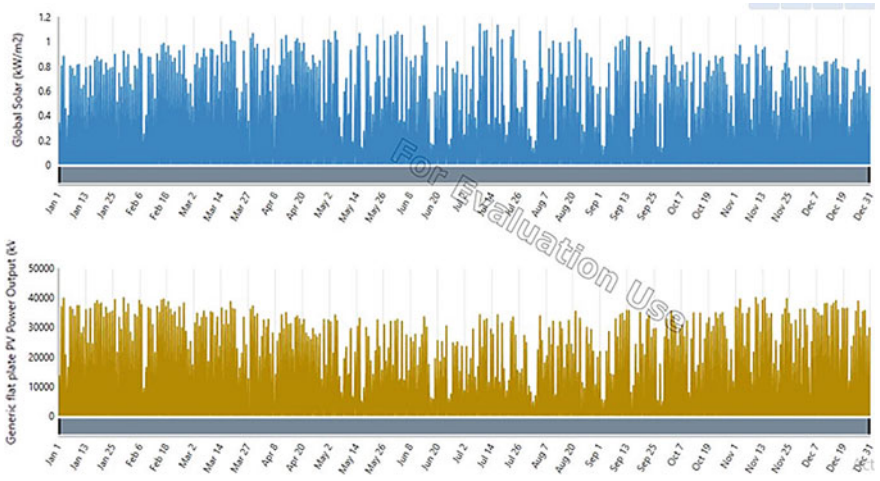


Fig. 21 Plot of global solar irradiance (kW/m^2) per month and generic flat plate PV output (kW) per month of Yaingangpokpi

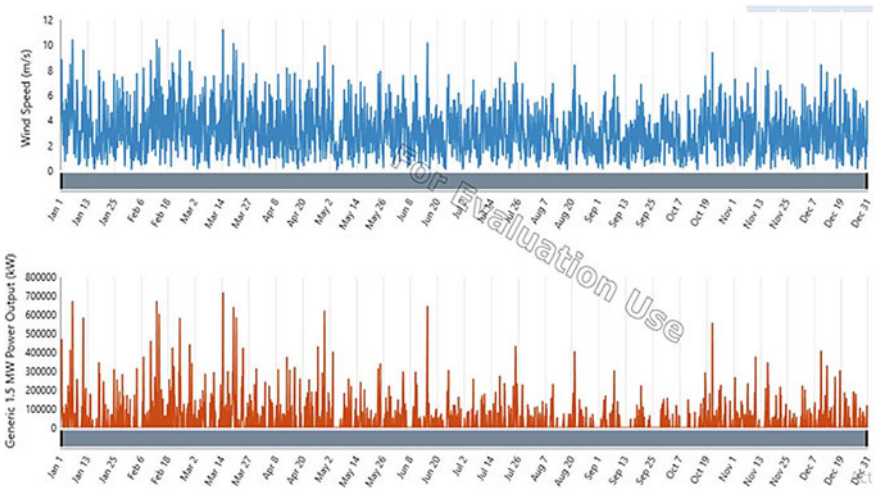


Fig. 22 Plot of wind speed (m/s) per month and generic 1.5 MW power output (kW) per month of Yaingangpokpi

7.4 Optimization Results for Kavaratti

Table 19 shows the NPC of the integrated energy scheme. Table 20 shows the annual expenditure of the integrated energy scheme. After optimization, the leveled COE obtained is \$0.6881, and the total NPC is \$2799.502 M. Table 22 indicates the information for production history showing whole non-conventional power produced

Table 18 Emission summary of Yaingangpokpi

Pollutant	Quantity	Unit
Carbon dioxide	866	kg/year
Carbon monoxide	0	kg/year
Unburned hydrocarbons	0	kg/year
Particulate matter	0	kg/year
Sulfur dioxide	3.76	kg/year
Nitrogen oxide	1.84	kg/year

Table 19 Net present costs of Kavaratti

Name	Capital	Operating	Replacement	Salvage	Resource	Total
Generic 1.5 MW	\$1.5 B	\$384 M	\$468 M	-\$262 M	\$0.00	\$2.09 B
Generic 100 kWh Li-Ion	\$700,000	\$1278	\$233,668	-\$43,493	\$0.00	\$891,454
Generic 200 kW gas microturbine	\$340,000	\$0.00	\$0.00	-\$59,065	\$0.00	\$280,935
Generic flat plate PV	\$150 M	\$6.39 M	\$0.00	\$0.00	\$0.00	\$156 M
Grid	\$0.00	-\$203 M	\$0.00	\$0.00	\$0.00	-\$203 M
PV dedicated converter	\$300 M	\$12.8 M	\$125 M	-\$23.3 M	\$0.00	\$415 M
System converter	\$255 M	\$0.00	\$106 M	-\$19.8 M	\$0.00	\$342 M
System	\$2.21 B	\$199 M	\$700 M	-\$305 M	\$0.00	\$2.80 B

for every year which is 334,991,373 kWh/year. Table 23 indicates the information related to the consumption of power in which AC primary load consumption is 4062 kWh/year. Therefore, the integrated energy system fulfills the demand and generates more than the required demand. Table 21 indicates the purchase from the grid (kWh) on a monthly basis and grid sales (kWh) on a monthly basis. This shows that the integrated energy system injects huge excess power to the grid than what it consumes. Figure 23 indicates the graph of the solar irradiance in kW/m² per month and PV output in kW for each month, where it can be seen that the solar irradiance is as high as 1.2 kW/m² mainly in the months of March and September and the PV power output is high as nearly 40,000 kW mainly in the month of November. Figure 24 indicates the plot of the speed of wind in m/s for each month and wind turbine output in kW for each month, where the highest wind speed is nearly 13 m/s in the month of June and the highest wind power output is 800,000 kW in the month of June. Table 24 indicates the pollutants' discharge from an integrated energy system which shows that very minimal emissions of pollutants are there.

Table 20 Annualized costs of Kavaratti

Name	Capital	Operating	Replacement	Salvage	Resource	Total
Generic 1.5 MW	\$117 M	\$30.0 M	\$36.6 M	−\$20.5 M	\$0.00	\$163 M
Generic 100 kWh Li-Ion	\$54,759	\$100.00	\$18,279	−\$3402	\$0.00	\$69,735
Generic 200 kW gas microturbine	\$26,597	\$0.00	\$0.00	−\$4620	\$0.00	\$21,977
Generic flat plate PV	\$11.7 M	\$500,00	\$0.00	\$0.00	\$0.00	\$12.2 M
Grid	\$0.00	−\$15.9 M	\$0.00	\$0.00	\$0.00	−\$15.9 M
PV dedicated converter	\$23.5 M	\$1,000,000	\$9.79 M	−\$1.82 M	\$0.00	\$32.4 M
System converter	\$19.9 M	\$0.00	\$3.32 M	−\$1.55 M	\$0.00	\$26.7 M
System	\$173 M	\$15.6 M	\$54.7 M	−\$23.9 M	\$0.00	\$219 M

Table 21 Grid purchase (kW) each month and grid sales (kW) each month of Kavaratti

Month	Energy purchased (kWh)	Energy sold (kWh)	Net energy purchased (kWh)	Peak demand (kW)	Energy charge	Demand charge
January	151	7,422,516	−7,422,366	1.71	−\$371,118	\$0.00
February	120	6,564,956	−6,564,865	1.37	−\$328,243	\$0.00
March	138	7,852,562	−7,852,425	1.56	−\$392,621	\$0.00
April	123	8,472,518	−8,472,395	1.47	−\$423,620	\$0.00
May	106	14,716,550	−14,716,444	1.59	−\$735,822	\$0.00
June	42.7	95,044,663	−95,044,620	1.17	−\$4.75 M	\$0.00
July	42.6	67,031,208	−67,031,165	0.958	−\$3.35 M	\$0.00
August	63.7	57,561,010	−57,560,946	1.47	−\$2.88 M	\$0.00
September	96.6	28,455,172	−28,455,075	1.61	−\$1.42 M	\$0.00
October	152	9,126,634	−9,126,482	1.77	−\$456,234	\$0.00
November	165	6,490,665	−21,744,500	2.07	−\$324,525	\$0.00
December	167	9,500,626	−9,500,458	1.72	−\$475,023	\$0.00
Annual	1368	318,239,110	−318,237,742	2.07	−\$15.9 M	\$0.00

Table 22 Production summary of Kavaratti

Component	Production (kWh/year)	Percent
Generic flat plate PV	72,131,024	21.5
Generic 200 kW gas microturbine	0	0
Generic 1.5 MW	262,860,349	78.5
Grid purchases	1368	0.000408
Total	334,992,741	100

Table 23 Consumption summary of Kavaratti

Component	Consumption (kWh/year)	Percent
AC primary load	4062	0.00128
DC primary load	0	0
Grid sales	318,239,110	100
Total	318,243,172	100

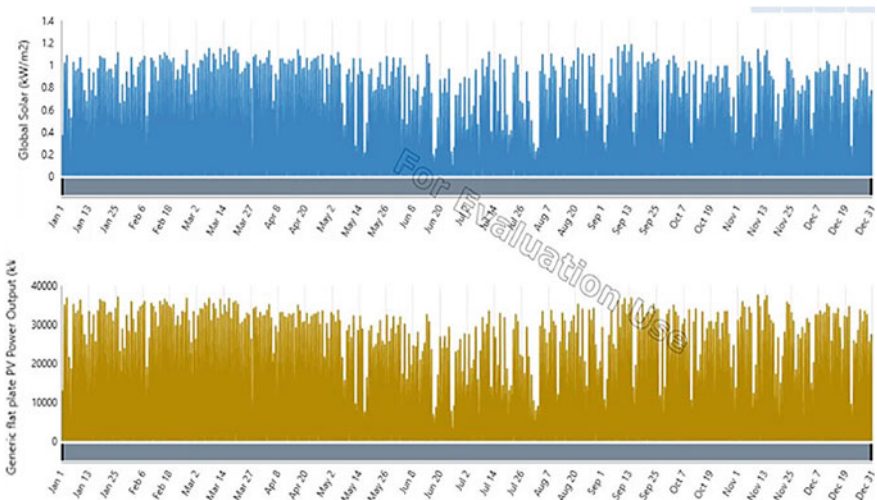


Fig. 23 Plot of global solar irradiance (kW/m^2) per month and generic flat plate PV output (kW) per month of Kavaratti

7.5 Comparative Case Study Analysis of the Optimization Results of Four Different Locations

Table 25 shows the comparison of optimization results of four different locations, and it indicates that the hybrid system is most profitable in Kavaratti. But it does not indicate that it was not profitable in other parts. It is profitable in every area. This table helps us to understand the variation of total net present cost, operating

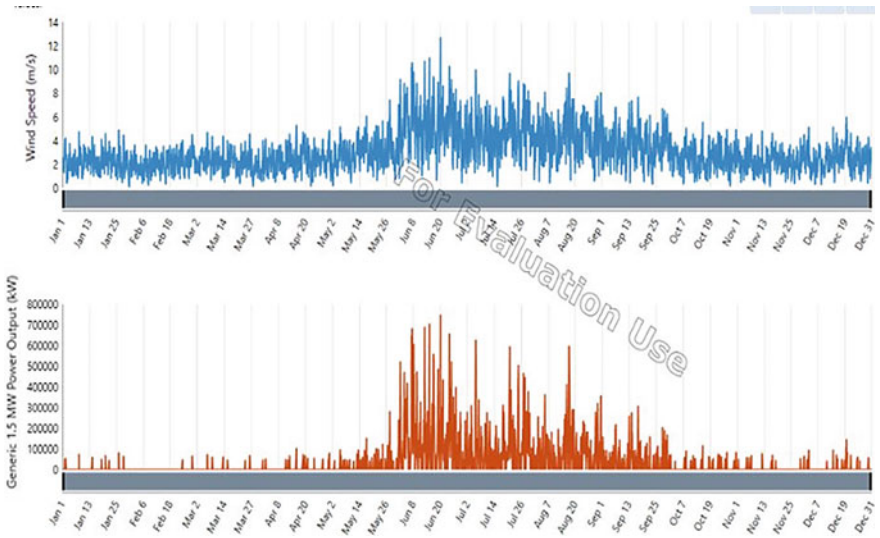


Fig. 24 Plot of wind speed (m/s) per month and generic 1.5 MW power output (kW) per month of Kavaratti

Table 24 Emission summary of Kavaratti

Pollutant	Quantity	Unit
Carbon dioxide	864	kg/year
Carbon monoxide	0	kg/year
Unburned hydrocarbons	0	kg/year
Particulate matter	0	kg/year
Sulfur dioxide	3.75	kg/year
Nitrogen oxide	1.83	kg/year

cost, leveled cost of energy, PV leveled cost, wind leveled cost, grid sales, grid purchases, yearly PV array production, yearly wind turbine production, maximum PV output, PV penetration, PV mean output, maximum wind output, wind penetration, and wind mean output in four different locations of India. Figure 25 shows the hourly solar power generation in kW of Alipur, Badabenakudi, Yaingangpokpi, and Kavaratti. Figure 26 shows the hourly windmill power generation in kW of Alipur, Badabenakudi, Yaingangpokpi, and Kavaratti. Figure 27 shows the hourly grid purchase power in kW of Alipur, Badabenakudi, Yaingangpokpi, and Kavaratti. Figure 28 shows the hourly grid sales power in kW of Alipur, Badabenakudi, Yaingangpokpi, and Kavaratti. Figures 25, 26, 27, and 28 are based on the 24-h real-time data of the day of April month. These figures help to understand the hourly variation of solar power generation, wind power generation, grid purchase power, and grid sale power of four different areas on a particular month. This case study analysis is based on 24-h duration, and it aims to understand all the different situations that the

Table 25 Comparison of optimization results of four different locations

Cost type	Locations			
	Alipur, Andaman and Nicobar Islands 744,206, India (11° 45.7' N, 92° 41.9' E)	Badabenakudi, Odisha 752,011, India (19° 48.1' N, 85° 33.6' E)	Yaingangpokpi, Manipur 795,132, India (24° 39.8' N, 93° 50.8' E)	Kavaratti, Lakshadweep 682,555, India (10° 33.6' N, 72° 38.6' E)
Total net present cost (\$)	\$2,807,031,000.00	\$2,811,425,000.00	\$2,807,959,000.00	\$2,799,502,000.00
Levelized cost of energy (\$/kWh)	\$0.717	\$0.734	\$0.720	\$0.688
Net operating cost (\$)	\$207 M	\$211 M	\$208 M	\$199 M
Annual operating cost (\$)	\$16.2 M	\$16.5 M	\$16.2 M	\$15.6 M
PV levelized cost (\$/kWh)	0.665	0.681	0.685	0.619
Wind levelized cost (\$/kWh)	0.640	0.654	0.639	0.622
Grid sales (kWh/year)	306,459,157	299,584,864	305,007,021	318,239,110
Grid purchases (kWh/year)	1377	1394	1371	1368
PV array production (kWh/year)	67,136,109	65,565,846	65,238,984	72,131,024
Wind turbine production (kWh/year)	255,455,305	249,789,452	255,823,872	262,860,349
Maximum PV output (kW)	37,452	38,285	40,039	37,546
PV penetration (%)	1,652,601	1,613,948	1,605,902	1,775,555

(continued)

Table 25 (continued)

Cost type	Locations			
	Alipur, Andaman and Nicobar Islands 744,206, India (11° 45.7' N, 92° 41.9' E)	Badabenakudi, Odisha 752,011, India (19° 48.1' N, 85° 33.6' E)	Yaingangpokpi, Manipur 795,132, India (24° 39.8' N, 93° 50.8' E)	Kavaratti, Lakshadweep 682,555, India (10° 33.6' N, 72° 38.6' E)
PV mean output (kW)	7664	7485	7447	8234
Maximum wind output (kW)	731,157	703,183	714,752	746,915
Wind penetration (%)	6,288,208	6,148,739	6,297,281	6,470,488
Wind mean output (kW)	29,162	28,515	29,204	30,007

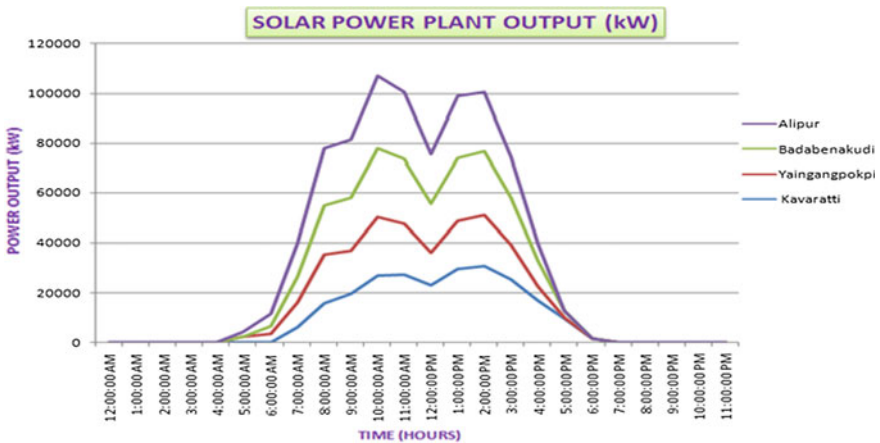


Fig. 25 Hourly solar power generation in kW of Alipur, Badabenakudi, Yaingangpokpi, and Kavaratti

hybrid system could face. This analysis is carried out using the optimization results of the proposed hybrid system. The availability of solar power is good at daytime as solar power is not available at night. In addition, wind power may not be available at night. In this situation, both the battery backup power and grid power are used as backup power to fulfill the load demand. If the grid power and battery backup power are not present at that time, then the gas generator is present to maintain the continuity of power supply. In this way, continuity of power supply is maintained in

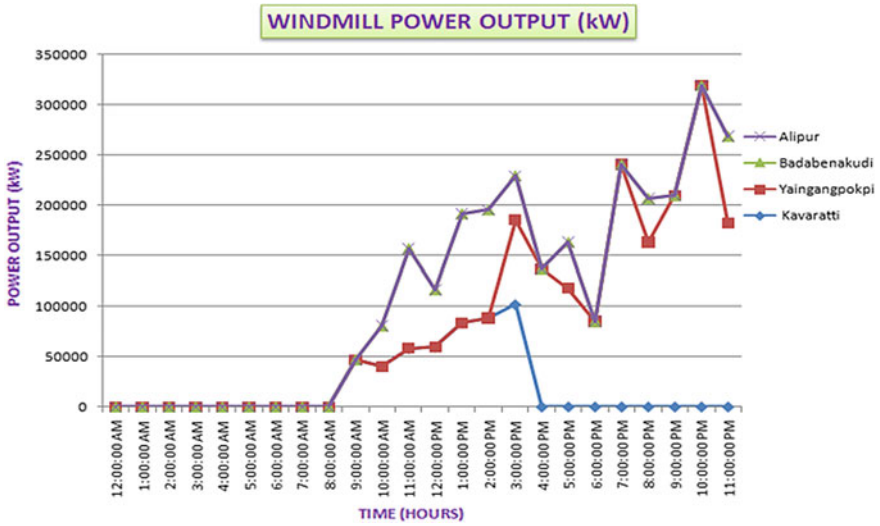


Fig. 26 Hourly windmill power generation in kW of Alipur, Badabenakudi, Yaingangpokpi, and Kavaratti

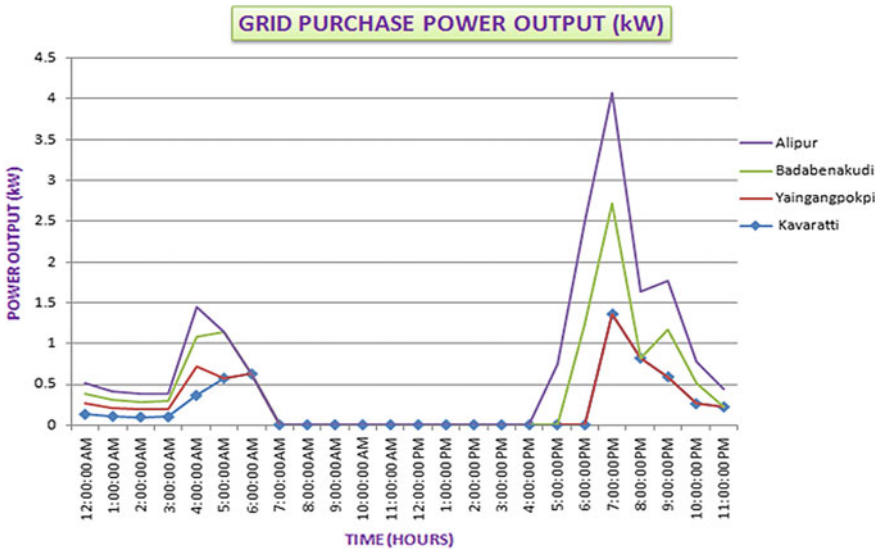


Fig. 27 Hourly grid purchase power in kW of Alipur, Badabenakudi, Yaingangpokpi, and Kavaratti

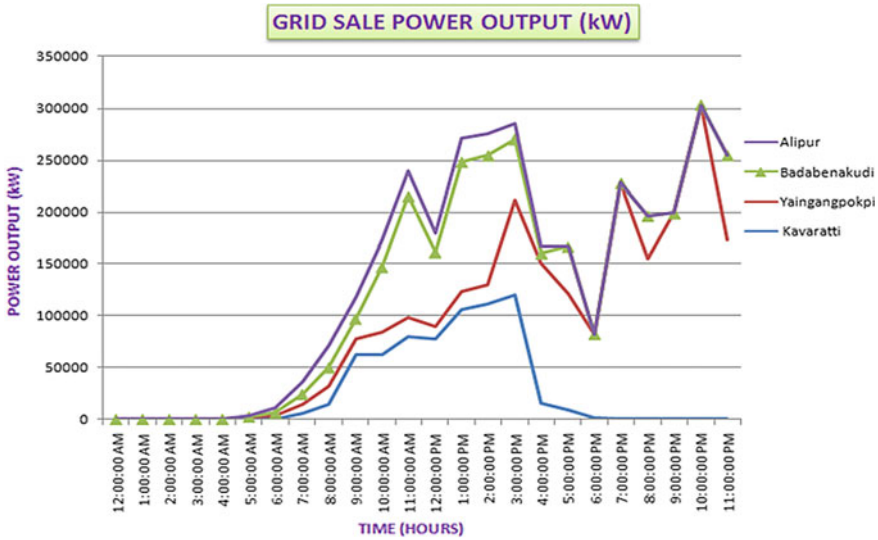


Fig. 28 Hourly grid sale power in kW of Alipur, Badabenakudi, Yaingangpokpi, and Kavaratti

every situation. The overall hybrid system is designed to select the cheapest possible configuration for maintaining continuity of power supply.

Figures 25 and 26 demonstrate the hourly solar and wind power production in kW. The hourly grid power purchase in kW is demonstrated in Fig. 27. The hourly grid power sale in kW is demonstrated in Fig. 28. All these figures are based on the 24-h real-time information of April month. From Figs. 25, 26, 27, and 28, it is easy to understand all the different conditions. In the first condition, i.e., from 7:00 AM to 4:00 PM time duration, both the solar power and wind power are available in a large amount in all areas, so grid power purchase is zero at that time and grid power sale is very high. In the second condition, i.e., from 4:00 PM to 12:00 AM time duration, solar power generation is reduced to zero. During this time duration, the wind power is available in large quantity only for three areas (Alipur, Badabenakudi, and Yaingangpokpi), and for Kavaratti location, wind power is zero. This results that grid power purchasing was increasing at that time and grid sales is decreasing. In the third condition, i.e., from 12:00 AM to 4:00 AM time duration, both the solar power generation and wind power generation are zero, as a result the hybrid system purchase power from grid, and power sale to grid is zero. Due to the presence of battery backup, grid purchase is less in amount. At the time duration of 4:00 AM to 7:00 AM, solar power generation is increasing and wind power is zero, which results in decreasing of grid purchase and increasing of grid sales. All these conditions are based on the proposed hybrid system. Based on this case study analysis, it is simple to understand that the proposed locations of India possess a huge scope of solar power production and wind power production which is desirable to be utilized. Solar

power production is possible at a bigger amount as well as the scope of wind power production is present in a large quantity which is proved by the case study analysis.

8 Discussion

As India is a progressing country, it is much more exposed to climate change because of its reliance on agriculture and forestry. The Indian electricity sector is a major contributor to greenhouse gases, and these greenhouse gases are responsible for the dangerous impacts of climate change like floods, drought, storms, etc. In order to reduce the impacts of climate change, the use of renewable energy sources needs to be increased. In this chapter, a grid-connected hybrid energy system is designed utilizing solar power, wind power, gas generator, and battery backup system. This chapter chiefly focuses on the optimization analysis of the proposed hybrid system by utilizing real-time information. This optimization analysis estimates the amount of production of electrical energy, per unit cost of energy, and the total installation cost of the hybrid energy system. This chapter includes a 24-h case study analysis to understand all the different situations that the hybrid system could face. The research toward the proposed system illustrates its results using the following points:

- This chapter explains the scenario of climate change in India. It explains the role of renewable energy-based hybrid system to combat climate change. It explains the electricity generation scenario of Andaman and Nicobar Islands, Odisha, Manipur, and Lakshadweep, where the use of renewable energy sources is not very high. In each state, one location is selected for analyzing.
- The average yearly solar radiation of Alipur area is 5.30 kWh/m²/day. The mean yearly speed of the wind is 6.24 m/s. The average yearly temperature of Alipur area is 27.27 °C. These results signify that the chosen area is appropriate for solar and wind power production.
- The average yearly solar radiation of Badabenakudi area is 4.97 kWh/m²/day. The mean yearly speed of the wind is 4.82 m/s. The average yearly temperature of Badabenakudi area is 26.43 °C. These results signify that the chosen area is appropriate for solar and wind power production.
- The average yearly solar radiation of Yaingangpokpi area is 4.61 kWh/m²/day. The mean yearly speed of the wind is 2.45 m/s. The average yearly temperature of Yaingangpokpi area is 21.06 °C. These results signify that the chosen area is appropriate for solar and wind power production.
- The average yearly solar radiation of Kavaratti area is 5.76 kWh/m²/day. The mean yearly speed of the wind is 5.21 m/s. The average yearly temperature of Kavaratti area is 27.33 °C. These results signify that the chosen area is appropriate for solar and wind power production.
- The proposed hybrid system generates 67,136,109 kWh/year of solar energy in Alipur, which is approximately 20.8% of the total generated energy every year. The proposed hybrid system generates 65,565,846 kWh/year of solar energy in

Badabenakudi, which is approximately 20.8% of the total generated energy every year. The proposed hybrid system generates 65,238,984 kWh/year of solar energy in Yaingangpokpi, which is approximately 20.3% of the total generated energy every year. The proposed hybrid system generates 72,131,024 kWh/year of solar energy in Kavaratti, which is approximately 21.5% of the total generated energy every year.

- The proposed hybrid system generates 255,455,305 kWh/year of wind energy in Alipur, which is approximately 79.2% of the total generated energy every year. The proposed hybrid system generates 249,789,452 kWh/year of wind energy in Badabenakudi, which is approximately 79.2% of the total generated energy every year. The proposed hybrid system generates 255,823,872 kWh/year of wind energy in Yaingangpokpi, which is approximately 79.7% of the total generated energy every year. The proposed hybrid system generates 262,860,349 kWh/year of wind energy in Kavaratti, which is approximately 78.5% of the total generated energy every year. These results signify that the possibility of wind power production is very high.
- The electric load consumed 4062 kWh/year of energy for every location. The total energy sell to the grid is high in every location, and grid purchase is low in every location. The levelized cost of energy is low in every location. This indicates that the system is effective and economical. Kavaratti is the most suitable location for this hybrid system due to its lowest levelized cost of energy.

The above key points essentially signify that the chosen areas are wealthy in the potential outcomes of wind and solar power production. In addition, the total production of renewable energy is very high which demonstrates that the proposed hybrid system is effectively using these potential outcomes. After the optimization analysis, it is obvious that the proposed hybrid system is effectively satisfying the electric load demand throughout the year by utilizing renewable power principally. Grid purchases are very low. Grid sales are very high. The levelized cost of energy is very less. In addition, the emissions of the proposed hybrid system are very less. Therefore, the proposed hybrid system is not only profitable but also environmentally friendly.

9 Conclusion

In order to reduce the bad impacts of climate change, the utilization of renewable energy sources needs to be increased. One of the most common limitations of renewable energy is its fluctuation. Renewable energy sources are not able to maintain the continuity of power supply all over the day and also show variation with season along a year. In order to solve this problem, there is a need to utilize a hybrid energy system of two or more energy sources. In this chapter, a grid-connected hybrid energy system is designed utilizing solar power, wind power, gas generator, and battery backup system. The gas generator is used only in extreme conditions

when no other options are left. This hybrid system is deliberately planned, so that there will be a little emanation of carbon. The proposed hybrid indicates the huge possibility of energy generation from wind sources. This hybrid system always tries to use the cheapest possible energy source for fulfilling the load demand and for reducing the energy bills. For increasing the reliability and efficiency of the proposed hybrid system, different components are strategically connected using AC and DC buses. In order to analyze the feasibility of the hybrid system, it is examined in four different locations and it is found to be profitable in all locations. The proposed hybrid system is most profitable in Kavaratti where its levelized cost of energy is 0.688 \$/kWh. The proposed hybrid system generates 72,131,024 kWh/year of solar energy in Kavaratti, which is approximately 21.5% of the total generated energy every year. The proposed hybrid system generates 262,860,349 kWh/year of wind energy in Kavaratti, which is approximately 78.5% of the total generated energy every year. Therefore, the final conclusion of this chapter is that the proposed hybrid system is cost-effective, nature-friendly, and efficient in keeping up the continuity of power supply. If the utilization of the proposed hybrid system increases in other parts of India, it can replace the thermal power plant by renewable energy-based hybrid system which helps to combat climate change.

10 Open Research Directions

To lessen the effect of the environmental change, this chapter proposes a thought of introducing the sustainable power source-based hybrid energy system in those regions areas where renewable potential outcomes are great. This opens new research areas which incorporate looking of every one of those places where the possibility of renewable energy generation is great [33]. It likewise incorporates new research areas of investigating different combinations of various sustainable power sources depending on the area. A few spots of India are wealthy in some other sustainable power sources like hydro and so forth, which can be utilized as the main source of the hybrid system. Hydroelectric power plants are the most proficient plants when combined with solar power plants. Similarly, the biogas plant can be used as an additional source of energy as it is helpful in the reduction of the dangerous impacts of environmental change. These ideas also provide a cost-effective business if implemented with suitable preparation.

References

1. Environment of India, https://en.wikipedia.org/wiki/Environment_of_India. Accessed on 14 Jan 2019
2. Energy Access Outlook 2017—from poverty to prosperity, https://www.iea.org/publications/freepublications/publication/WEO2017SpecialReport_EnergyAccessOutlook.pdf. Accessed 14 Jan 2019

3. Krupali's Blog, <https://www.eai.in/club/users/krupali/blogs/627/>. Accessed on 15 Jan 2019
4. Tank V, Bhutka J, Harinarayana T (2016) Wind energy generation and assessment of resources in India. *J Power Energy Eng* 4(10):25–38
5. Power Sector at a Glance ALL INDIA, <https://powermin.nic.in/en/content/power-sector-glance-all-india>. Accessed on 16 Jan 2019
6. Rohani A, Mazlumi K, Kord H (2010) Modeling of a hybrid power system for economic analysis and environmental impact in HOMER. In: 18th Iranian conference on electrical engineering (ICEE), IEEE, pp 819–823
7. Kavali J (2013) Hybrid solar PV and biomass system for rural electrification. In: International conference on global scenario in environment and engineering, vol 5, no 2. IEEE, pp 802–810
8. Climate change and its impact on India, <https://www.rediff.com/money/2007/jun/05clim.htm>. Accessed on 16 Jan 2019
9. Causes of climate change, <https://edugreen.teri.res.in/explore/climate/causes.htm>. Accessed on 17 Jan 2019
10. Effects of global warming on South Asia, https://en.wikipedia.org/wiki/Effects_of_global_warming_on_South_Asia. Accessed on 17 Jan 2019
11. Edenhofer O, Pichs-Madruga R, Sokona Y, Seyboth K, Kadner S, Zwickel T, Eickemeier P, Hansen G, Schlömer S, von Stechow C, Matschoss P (eds) (2011) Renewable energy sources and climate change mitigation: special report of the intergovernmental panel on climate change. Cambridge University Press, Cambridge
12. Renewable Energy Is Key to Fighting Climate Change, <https://www.nrdc.org/experts/noah-long/renewable-energy-key-fighting-climate-change>. Accessed on 18 Jan 2019
13. Power for All Andaman and Nicobar, https://powermin.nic.in/sites/default/files/uploads/joint_initiative_of_govt_of_india_and_andman_nicobar.pdf. Accessed on 19 Jan 2019
14. 24 × 7 Power for All Odisha, https://powermin.nic.in/sites/default/files/uploads/joint_initiative_of_govt_of_india_and_Orissa.pdf. Accessed on 19 Jan 2019
15. 24 × 7 Power for All—Manipur, https://powermin.nic.in/sites/default/files/uploads/joint_initiative_of_govt_of_india_and_manipur.pdf. Accessed on 19 Jan 2019
16. 24 × 7 Power for All Lakshadweep Islands, https://powermin.nic.in/sites/default/files/uploads/joint_initiative_of_govt_of_india_and_lakshadweep.pdf. Accessed 19 Jan 2019
17. Kumar A, Deng Y, He X, Kumar P, Bansal RC (2017) Energy management system controller for a rural microgrid. *J Eng* 2017(13):834–839
18. Kumari J, Subathra P, Moses JE, Shruthi D (2017) Economic analysis of hybrid energy system for rural electrification using HOMER. In: International conference on innovations in electrical, electronics, instrumentation and media technology (ICEEIMT). IEEE, pp 151–156
19. Swarnkar NM, Gidwani L, Sharma R (2016) An application of HOMER Pro in optimization of hybrid energy system for electrification of technical institute. In: International conference on energy efficient technologies for sustainability (ICEETS). IEEE, pp 56–61
20. Lal K, Dash BB, Akella AK (2011) Optimization of PV/wind/micro-hydro/diesel hybrid power system in HOMER for the study area. *Int J Electr Eng Inform* 3(3):307–325
21. Bhattacharjee S, Chakraborty S, Thakur BN, Ali MS (2018) Modelling, optimization and cost analysis of grid connected solar-battery system for Tripura University Campus. *Int J Adv Sci Res Manag* 3(9):23–31
22. Kellogg WD, Nehrir MH, Gerez V, Venkataramanan GV (1998) Generation unit sizing and cost analysis for stand-alone wind, photovoltaic and hybrid wind/PV systems. *IEEE Trans Energy Convers* 13(1):70–75
23. HOMER Energy, <https://www.homerenergy.com/>. Accessed on 20 Jan 2019
24. Census of India 2011 Andaman and Nicobar, https://censusindia.gov.in/2011census/dchb/3500_PART_A_DCHB_ANDAMAN%20&%20NICOBAR%20ISLANDS.pdf. Accessed on 20 Jan 2019
25. Census of India 2011 Odisha, https://censusindia.gov.in/2011census/dchb/DCHB_A/21/2118_PART_A_DCHB_PURI.pdf. Accessed on 20 Jan 2019
26. Census of India 2011 Manipur, https://censusindia.gov.in/2011census/dchb/1407_PART_B_DCHB_IMPHAL%20EAST.pdf. Accessed on 20 Jan 2019

27. Census of India 2011 Lakshasweep, https://censusindia.gov.in/2011census/dchb/3101_PART_B_DCHB_LAKSHADWEEP.pdf. Accessed on 20 Jan 2019
28. NASA Surface Meteorology and Solar Energy, <https://eosweb.larc.nasa.gov/cgi-bin/sse/homer.cgi?email=skip@larc.nasa.gov>. Accessed on 20 Jan 2019
29. About HOMER Energy LLC, <https://www.homerenergy.com/company/index.html>. Accessed on 20 Jan 2019
30. Rezzouk H, Mellit A (2015) Feasibility study and sensitivity analysis of a stand-alone photovoltaic–diesel–battery hybrid energy system in the north of Algeria. *Renew Sustain Energy Rev* 43:1134–1150
31. Lambert T, Gilman P, Lilienthal P (2006) Micropower system modeling with Homer. In: *Integration of alternative sources of energy*, Wiley, New York, pp 379–418
32. Nurunnabi M, Roy NK (2015) Grid connected hybrid power system design using HOMER. In: *International conference on advances in electrical engineering (ICAEE)*. IEEE, pp 18–21
33. Nandi C, Bhattacharjee S, Chakraborty S (2019) Climate change and energy dynamics with solutions: a case study in Egypt. In: *Climate change and energy dynamics in the Middle East*. Springer, Berlin, pp 225–257

Graphene for the Potential Renewable Energy Applications



Sayantana Sinha and Bibhu Prasad Swain

Abstract To combat the challenge of the upcoming energy crisis due to the shortage of fossil fuel and the global warming issue, it is evidently needed to use the non-conventional energy sources. Among the many sources, solar energy is the most popular alternative source since it is cheapest and convenient to harvest energy from sunlight. Although the conversion efficiency of the generally used conventional solar cells are not very good, in recent advancement of solar cell technology, the use of graphene has shown a 20% reduction in the reflectance of solar irradiation causing a significant increase in efficiency up to 20%. Based on the application of graphene, many different types of graphene solar cells have been developed. Basically, graphene is applied to photovoltaic cells as transparent electrode, catalytic counter electrode, Schottky junction, and electron or hole or both electron–hole transport layers. The overall power conversion efficiency also changes according to the application type. For example, with graphene/silicon solar cells, the highest efficiency obtained is 15.6% whereas in solar cell made with graphene quantum dot and P3HT, the efficiency achieved is up to 1.28%. With perovskite-based graphene solar cells, the conversion efficiency can be reached up to as high as 23.3%. So, various types of solar cells and what are the roles of graphene there are discussed in this chapter.

Keywords Renewable energy · Graphene-based solar cell · Graphene photovoltaic cell · Green energy harvesting · van der Waals Schottky diode · Perovskite solar cell

1 Introduction

In today's world, the most burning issue is the probable upcoming depletion of conventional energy sources and also the huge carbon emission due to the usage of fossil fuels. To make our civilization safe from the grave danger of energy depletion, it has been a great interest of research for many researchers across the world to develop some efficient alternative energy conversion and storage mechanism for last few decades. Among the alternate non-conventional sources of energy, solar power is the

S. Sinha · B. P. Swain (✉)

Department of Physics, National Institute of Technology Manipur, Imphal, India
e-mail: bibhuprasad.swain@gmail.com

© Springer Nature Singapore Pte Ltd. 2020

A. K. Bhoi et al. (eds.), *Advances in Greener Energy Technologies*,

Green Energy and Technology, https://doi.org/10.1007/978-981-15-4246-6_24

most superior candidate having a huge possibility; because, in a normal day, in the country like India, the solar irradiation can go as high as 200 MW per km² but the problem with the solar cell is its poor conversion efficiency. However, with the continuous contributions of the researchers, many materials are coming out day by day which can increase the conversion efficiency. Likewise, new efficient, long-lasting, and cost-effective solutions are coming out for storing the energy electrochemically. Although various materials have been studied in search for a good energy conversion and storing device material, it was a major breakthrough in this field when the graphene was discovered. Graphene, which is a flat two-dimensional honeycomb-like crystalline carbon structure, provides some excellent features like high specific surface area (~2600 m²/g) [1], high chemical stability, high electrical conductivity, bio compatibility, etc. Since graphene is a form of carbon, it is economically cheap and environment-friendly. With the two attractive characteristics of graphene, high specific surface area and good chemical stability (i.e., it can withstand both acidic and basic media for a long time), it became a very suitable supercapacitor electrode material which can store energy in a very efficient way.

1.1 Overview of Graphene

After the experimental discovery of graphene by Hans-Peter Boehm in 1961 [2], it becomes the prophet of a new branch of science, “nanotechnology.” In the year 2004, two scientists from Manchester University Professor Andre Geim and Professor Kostya Novoselov by repeatedly fragmenting the layer of graphite flake using sticky tapes were finally able to separate a single carbon atom layer which was the first hands-on development of graphene. It is a two-dimensional flat single layer of carbon atoms with sp² bonding which has a honeycomb-like crystal structure. It is the base material of all the nanostructures viz. quantum dot (0D), carbon nanotube (1D), graphene sheet (2D), and graphite (3D). After the first isolation of graphene by scotch-tape method in 2004, many other techniques have been discovered for good quality graphene. The preparation technique is also very important because the characteristics of graphene are highly dependent on the process steps.

Nowadays, graphene has found so many applications that it cannot be listed wholly with guarantee nevertheless some major applications are being mentioned here. Graphene-based semiconductor devices like the nanoscaled field effect transistors (FETs) are being fabricated using the graphene nanoribbons (GNR) [3–5]. Since a single layer of graphene is highly transparent (a single-layer graphene film has an opacity of 2.3% only), this is considered to be a suitable substitute for indium tin oxide (ITO) layer [6, 7] which is a commonly used material for transparent electrodes. Thus, graphene can be used in solar cell [8, 9], LCD [10], LED [11], etc. Graphene is also reported as to be a suitable material in sensor applications. Many graphene-based sensors including NH₃, NO₂, CH₄ gas sensors, PH sensors, etc., have been reported with a good sensitivity.

The graphene-based device fabrication methods are majorly classified into two groups the “top-down approach” and the “bottom-up approach” [12]. The top-down approach is started with a bulk material and by some mechanical processes like ablation or lithography, the desired structure is formed. On the other hand, in bottom-up approach, the structure is grown with atoms or molecules.

1.2 Graphene Solar Cell

Due to the very high optical transparency in the infrared to violet region, good thermal stability, good chemical and mechanical properties, graphene has become a very good choice for photovoltaic applications. In solar cell applications, graphene finds its use in the transparent electrode, catalytic counter electrode, Schottky junction, and electron or hole or both electron–hole transport layers, etc. [11, 13]. The performance of a graphene-based photovoltaic (PV) cell can be improved by using multiple number of graphene layers and or by adding dopant.

1.2.1 Effects of Graphene Layers in Solar Cells

The sheet resistance of one single graphene layer is high enough to make a solar cell with it. So, we need to stack up multiple layers of graphene. For example, the sheet resistance for one layer of graphene is 2100 Ω/sq while that of a three-layered graphene structure is 350 Ω/sq . Adding one layer of graphene reduces the transmittance by 2.3% only but by stacking the multiple layers, the transmittance can be reduced significantly. For example, a three-layered structure of graphene has a transparency of 90.8%. So, there is a tradeoff between the sheet resistance and the transparency level, and we need to find an optimum point so that the optical to electrical energy conversion efficiency becomes the highest.

1.2.2 Effects of Doped Graphene in Solar Cells

Although by many researchers, it is found that the indium tin oxide (ITO) can be substituted by graphene, still there is some provision of improvement because the overall power conversion efficiency (PCE) for graphene-based cells is less than that of the ITO-based cell and graphene-based solar cells are also having greater failure rate due to the surface wetting problem between the electrode and the hole transport layer [14]. One way to improve the performance is by using some dopant with the graphene. By adding AuCl_3 dopant, the wetting surface of graphene can be changed and thus, an enhancement can be obtained in the rate of success [14]. The doping also increases the conductivity and it further helps to increase the overall PCE.

1.2.3 Graphene–Silicon Solar Cells

Schottky junction solar cells are made by depositing graphene layer on n-type silicon wafer [15, 16]. Generally, to make such type junction cells, first an n-type silicon wafer is taken (~300 nm thick) and a SiO₂ layer is deposited on it. Then, a junction area (~0.1 cm²) is etched in the SiO₂ layer and graphene is then deposited on it. The thickness of the graphene layer becomes typically around 10–100 nm. Two contacts are made, one in the backside of Si wafer and another on the front side, i.e., in the graphene side. The backside contact is made by depositing silver/titanium/lead deposition and the front side contact can be made by depositing gold (Au) on the SiO₂ by sputtering on which the graphene is deposited. The graphene sheet here works as the transparent electrode. It is seen that the graphene layer also serves as separator for the photo-generated electron–hole pairs by means of the intrinsic electric field within the graphene sheet. The intrinsically developed electric field guides the photo-generated electrons and holes through the n-Si wafer and the graphene sheet, respectively. Although the PCE of graphene-based Schottky junction-type solar cells is not very good at that time, there is a lot of possibility of improving it by increasing the transparency and the conductivity of the graphene films and improving the interface region between graphene and n-Si using the surface passivation property of silicon. Apart from this, many other improvisations are also suggested by researchers like by optimizing the SiO₂ layer thickness, using the physical vapor deposition (PVD) technique instead of the chemical vapor deposition (CVD) process to deposit the graphene film, adding antireflective coating, etc. [16]. After these improvisations, researchers could achieve a quite good fill factor and they have found that the efficiency of this type cell can go up to 15.6% which is significantly good [16].

1.2.4 Graphene/Polymer Solar Cells

The graphene-based polymer solar cells have become popular since last few years because it is cheap, mechanically flexible, light weight, and easy to produce in largescale in the industries. Moreover, in recent studies, the PCE up to 10% could be reached with graphene polymer solar cell, while the theoretical predictive value is 12% [18].

A structure of polymer solar cell (PSC) has been shown in Fig. 1 which has been taken from an article by Yin et al. [19]. Here, a reduced graphene oxide film on a substrate made of polyethylene glycol terephthalate (PET) is used as the transparent electrode. In Fig. 1a, the mechanical flexibility of the cell has been depicted. If the electrode was the traditional indium tin oxide (ITO) film, then it has been cracked on bending like that.

1.2.5 Graphene Quantum Dot (GQD) Solar Cells

Graphene quantum dots (GQDs) are the zero-dimensional nanostructure having nanoscale fragments of graphene in which the electron transport is confined by all three dimensions in space. Owing to the excellent electrical and optical properties particularly, the high optical transmittance of graphene GQD have been an attractive choice for making photovoltaic cells. Typically, the size or the diameter of the GQDs is below 20 nm. The GQDs also shows photoluminescence effect on excitation and it has an exciting feature; the tunability of its band gap is by modifying the size. For example, the band gap of benzene is 7 eV and that becomes 2 eV for a GQD having 20 aromatic rings [20].

These GQDs have been synthesized broadly in two ways, the top-down approach and bottom-up approach. A large graphene sheet is successively fragmented into a nano-dimensional structure in top-down approach whereas in bottom-up approach, many different types of processes like cage-opening of fullerene, solution chemistry method, etc., are used [21–23]. The GQDs obtained in bottom-up approach are molecules having a conjugate structure of few carbon atoms [23].

On analyzing the absorption spectra of the GQDs, a noticeable peak is found in 230 nm due to the $\pi \rightarrow \pi^*$ interaction. The functional groups and the surface chemistry further modify the absorption spectra and the photoluminescence [24]. The main difference in the photoluminescence between the semiconductors and the GQDs is that the quantum dots have much wider spectrum and the peak shifts toward red and goes down when the wavelength is increased.

It has been seen that by changing the orientation of colloidal GQDs on a polar model surface like water and mica, the PCE of the solar cell can be increased. It is shown schematically in Fig. 2; here, water acts like a substrate and the orientation of the GQDs was determined by the interaction between co-facial intermolecular attraction like π -stacking and molecule–water interactions [29].

One interesting field of research in the GQD-based photovoltaic cell domain is the dye-sensitized solar cell (DSSC). A DSSC is typically made of three parts: A sensitized photoelectrode (usually TiO_2 is used), a counter electrode (CE), and an

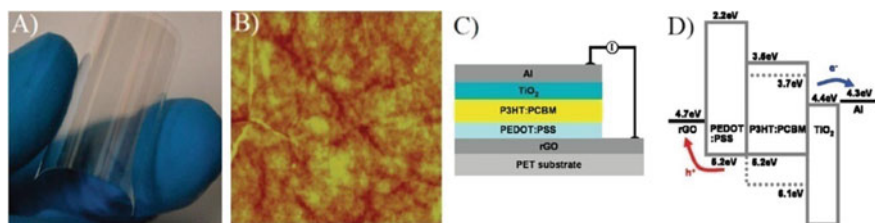


Fig. 1 a Photograph of the PSC (rGO/PET); b picture of rGO/PET obtained by atomic force microscope (AFM); c schematic representation of different layers of the PSC; and d schematic diagram of energy levels for the PSC, fabricated with rGO/PEDOT:PSS/P3HT:PCBM/ TiO_2 /Al, and rGO transparent electrode [19]

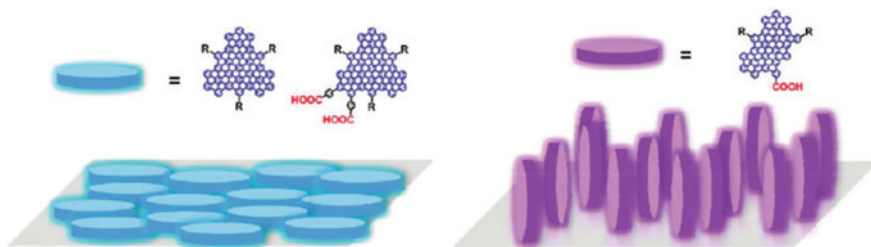


Fig.2 Schematic representation of the GQDs oriented in parallel and perpendicular directions with respect to the polar surface [25]

electrolyte. GQDs can be used both as the photoanode and the counter electrode to improve the efficiency of the DSSCs [26–28].

Another way of making photovoltaic cell is by using green luminescence GQDs and poly (3-hexylthiophene) (P3HT). With this combination, a bulk heterojunction polymer is constructed. With this addition of GQD layer to the active polymer layer (P3HT), the cell efficiency is increased. An open-circuit voltage of 0.67 V is observed with a photoelectric conversion efficiency of 1.28%. The performance enhancement after the addition of GQD is explained as a result of the higher electron mobility in GQD.

1.2.6 Graphene–Tandem Solar Cells

Graphene–tandem solar cell is also known as multi-junction solar cell. It is made by stacking two or more subcells connected in parallel or series. Theoretical maximum conversion efficiency of a single solar cell is 40% while that can be reached up to 86% with tandem solar cell. The graphene-based tandem cells have the highest PCE among the other photovoltaic cells having same structure. The PCE for tandem cell is found to be as high as 18.1% [29].

For example, graphene oxide and polymer tandem cell are made by stacking two subcells. To make the solar cell, a layer of Cs-neutralized GO (graphene oxide) is stacked with a pure GO layer. The layers are connected via a MoO_3 and an aluminum layer which acts as a charge recombinant layer. Such cells exhibit a PCE in the range of 2.92–3.91% that depends on the blend of polymer used as well as the thickness of the various components inside the cell. The cell can develop an open-circuit voltage in the range of 1.23–1.69 V, depending on the resistance of the interconnecting layers between the GO sheets which varies with the layer thickness.

Another example of tandem solar cell consists of graphene and single-walled carbon nanotubes. That kind of cells exhibits a PCE between 2.9% and 3.5%. The cells having graphene interconnecting layers in the subcells show more PCE than that of without having it.

1.2.7 Graphene–Perovskite Solar Cells (PSCs)

Any material can be called as perovskite material if it has a crystal structure similar to calcium titanium oxide (CaTiO_3), and the structure is called the perovskite structure. Apart from the CaTiO_3 -like structure, $\text{XIIA}^{2+}\text{VIB}^{4+}\text{X}^{2-}_3$ having the oxygen in the edge centers are also can be referred to as the perovskite materials. The generic chemical formula of perovskite is ABX_3 . Here, A is an organic or metal cation with larger size and B is a metal cation having comparatively smaller size and X is a halide anion [30]. In Fig. 3, a general perovskite structure is shown.

If a perovskite structure-based material, typically a hybrid organic–inorganic lead- or halide-based material, is used in a solar cell, then it is called a perovskite solar cell. The first perovskite solar cell (PSC) was developed by Kojima and coworkers in 2009 and that was a PCE of 3.8% only while the PSC made by Meng et al. in December 2018 was proposed to have a highest reported PCE up to then, which was 23.3% [32]. So much efficiency increment in just nine years tells how fast is the advancement of this photovoltaic technology. Due to the high efficiency and comparatively low production cost, it became a commercially attractive solar cell.

A commonly used perovskite material is methylammonium lead trihalide ($\text{CH}_3\text{NH}_3\text{PbX}_3$) where X denotes a halogen atom, i.e., iodine, bromine, or chlorine. Depending on the halide atom content, the optical band gap of the material differs between 1.5 and 2.3 eV. Another perovskite material studied by many researchers in PV application is formamidinium lead trihalide ($\text{H}_2\text{NCHNH}_2\text{PbX}_3$) which has an optical band gap in the range of 1.5–2.2 eV depending on which halide atom is there in the place of X. The 1.48 eV band gap is considered as the most suitable for single-junction solar cell since it provides the long range in electron and hole diffusion lengths which also makes it suitable for fabricating the planar heterojunction

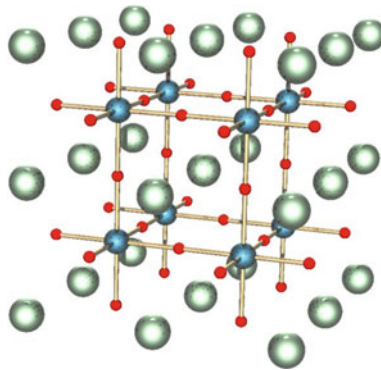


Fig. 3 A perovskite structure having general chemical composition ABX_3 . The red dots denote the halide (X) atoms (generally oxygen), the spheres in blue denote the B atoms (metal cation with smaller size, e.g., Ti^{4+}), and the spheres in green denote the A atoms (metal cation with larger size, e.g., Ca^{2+}) [31]

solar cells [33]. The contains of lead in both the popular perovskite materials mentioned above lead to an issue and in attempt to overcome it, tin-based material has been developed, $\text{CH}_3\text{NH}_3\text{SnI}_3$ although it has a lesser power conversion efficiency [34, 35].

In some recent studies, transition metal oxide-based perovskite material and their heterojunction (e.g $\text{LaVO}_3/\text{SrTiO}_3$) shows highly efficient solar cells [36].

However, the use of lead has made the perovskite materials unstable in the ambient air. To reduce the chance of instability, double perovskite material has been studied, the chemical formula of one such double perovskite is Cs_2SnI_6 which was proposed by Ren Ke et al. As in Cs_2SnI_6 , the Sn is in a tetravalent bond, it cannot be oxidized further [37], thus Cs_2SnI_6 poses better stability in oxygen and water vapor-contained environment. One more advantage of Cs_2SnI_6 is the 1.3 eV band gap, with high absorption coefficient, 10^{-5} cm^{-1} for wavelengths less than 730 nm [37].

The synthesis process of perovskite is much simpler than the preparation of silicon for solar cell where high temperature, clean room, and expensive apparatus are needed. Perovskite materials can be easily prepared by wet chemical processes in laboratory environment. For making methylammonium and formamidinium lead trihalides, many coating techniques have been adopted such as spin coating, spray coating, blade coating, slot-die coating, inkjet printing and screen printing, vapor deposition, and electrodeposition techniques.

1.2.8 Graphene–Organic Solar Cells

Organic solar cells have got the attention of the researchers because they are cheaper, lighter, more flexible, and environment friendlier than the inorganic solar cells. The organic solar cell is one in which all the materials involved in light absorption and charge transport are organic only. Among the various organic materials, graphene has an excellent optoelectric characteristic which made it suitable for use in organic solar cells (OSCs). Although graphene has a very good optical transparency, still in case electrical conductivity, it has a poor performance in comparison to the conventional transparent electrode material ITO which results in a lower performance of OSCs [38]. In OSCs, ITO has been a dominant material but it has some limitations such as the metal ions can diffuse into the active organic layer of the OSC leading to a decrease in the mechanical property. That's why ITO is not used in flexible OSCs [39]. The performance of an organic solar cell using a graphene-film grown with chemical vapor deposition in place of the ITO has been studied and graphene is found to be a suitable substitute for the TIO layer only with the lack of electrical conductivity.

To overcome the problem of poor conductivity, doping can be done to the graphene. Generally, three types of different approaches are followed to improve the electrical conductivity: (i) electrostatic doping of graphene with ferroelectric polymers [40], (ii) “multilayer stack” method of graphene films [41, 42], and (iii) “chemical doping” methods by using wet chemical dopants like nitric acid [43], tetracyanoquinodimethane (TCNQ) [44], and AuCl_3 [14].

1.2.9 Graphene–GaAs Solar Cell

If graphene is layered over a semiconductor, then a van der Waals Schottky diode is formed and this Schottky diode can be used as a solar cell. The specialty of van der Waals Schottky diode is that unlike a standard Schottky diode, its barrier height can be adjusted because the Fermi level of graphene semiconductor is tunable. Among the semiconductor, GaAs is a good choice for PV application because it has a direct band gap of 1.42 eV and high electron mobility ($8000 \text{ cm}^2 \text{ V}^{-1} \text{ s}^{-1}$ in room temperature).

To prepare such a cell, first grow a graphene thin film on a copper sheet. Then, take a GaAs wafer and clean it by dipping into 10 wt% HCl solution for about 3 min. After cleaning, form a gold contact of 60 nm on the back of the wafer by thermal evaporation. Now, in the front of the wafer, deposit a SiN_x layer of 80 nm thickness by plasma-enhanced CVD (PECVD) which acts as the insulating layer between the graphene layer and the semiconductor. After that etch a window on the nitride layer to define the active area of graphene/GaAs contact. Clean the active area by dipping the wafer into 10 wt% HCl for 5 min followed by rinsing it with DI water. Treat the active area with NH_3 plasma for 5 min using a 120 V and 27.5 MHz RF source. Roughness has no effect on plasma treatment on the GaAs surface and Ga–As–N compound formed on the surface. Transfer the graphene layer on to the GaAs substrate using a support layer of polymethyl methacrylate (PMMA). Remove the PMMA using acetone and paste a silver layer over graphene on the SiN_x -coated areas. Spin coat a layer of bis(trifluoromethanesulfonyl)amide[$((\text{CF}_3\text{SO}_2)_2\text{NH})$] (TFSA) over the substrate for p-type doping the graphene. Deposit an Al_2O_3 film by electron beam evaporation as an antireflective coating. To make the gate electrode, deposit another layer of graphene over the active area by the previously described method and paste a silver layer on it. Remove the PMMA and anneal the whole thing in 120°C for 5 min [45].

1.2.10 Graphene Photoactive Layers

Graphene and graphene oxide can be used in a solar cell as any of the following four: electron–hole separation layer, active interfacial layer, electron transport layer, and hole transport layer. The PCE of PV cell having graphene photoactive layer lies in the range of 0.4–10.3% and the PCE depends on the type of photoactive layer and which derivative of graphene is used. The photoactive layers consisted of few layers of graphene grown by CVD technique, pyrolysis or any other methods can form an n-type heterojunction in conjugation with n-doped Si. These types of heterojunctions exhibit a PCE in the range of 1.01–2.88%. The PCE can be increased up to 4.35% by doping the graphene with nitric acid. It is also possible to make solar cells by depositing graphene layer on nanowires. Nanowires can harvest the sunlight in a better way in comparison to the planer structure; however, planer heterojunctions show a better PCE than that of the nanowires.

1.2.11 Graphene Solar Cells Future Advancements

The solar cell is a great point of interest for both the academic researchers and the industry. But the use of Si or other inorganic materials in solar cells defined a limitation in the advancement of future solar cell technology. The introduction of organic molecules like graphene or low band gap polymers has brought a revolution in the industry and can yield many commercially successful advanced solar cell architectures. A lot of progress has already been taken place in the graphene-based solar cell technology and this progress will continue in the future also. The possibility of optimization and tuneability of many parameters makes graphene very suitable for overcoming the future challenges in solar cell industry. For the advancement of the existing non-graphene-based PV cells or the new graphene-based solar cells, graphene has an obvious dominant role in the fast-growing solar cell industry.

2 Conclusion

A lot of advancement in graphene-based solar cell has been taken place during last few years. With graphene tandem solar cells, the PCE could be achieved upto 18.1% and by employing perovskite material/graphene-based solar cells, 23.3% conversion efficiency is reported by Meng and coworkers. As described in the context of various research works, graphene layer is a good alternative for TiO₂ layer. Hence, it shows that the graphene has enough potential to replace the conventional silicon-based solar cells nevertheless there are a lot of provisions for further improvements in the PCE as well as the mechanical properties such as flexibility. Thus, a numerous research works is going on in this field across the world.

References

1. Bonaccorso F, Colombo L, Yu G, Stoller M, Tozzini V, Ferrari AC, Ruoff RS, Pellegrini V (2015) Graphene, related two-dimensional crystals, and hybrid systems for energy conversion and storage. *Science* 347
2. Boehm HP, Clauss A, Fischer GO, Hofmann U (1962) Das Adsorptionsverhalten sehr dünner Kohlenstoff-Folien. *Zaac* 316:119–127
3. Mohammad R, Mohammad M, Kamyar HS, Mohammad S, Kazem MF (2012) Electronic properties of a dual-gated GNR-FET under uniaxial tensile strain. *Microelectron Reliab* 52:2579–2584
4. Khalid A, Sampe J, Majlis BY, Mohamed MA, Chikuba T, Iwasaki T, Mizuta H (2015) Towards high performance graphene nanoribbon transistors (GNR-FETs). In: 2015 IEEE regional symposium on micro and nanoelectronics (RSM)
5. Akhavan ND, Jolley G, Membreno GU, Antoszewski J, Faraone L (2013) Study of uniformly doped graphene nanoribbon transistor (GNR) FET using quantum simulation. *COMMAD 2012* (2013)
6. Varela-Rizo H, Martín-Gullón I, Terrones M (2012) Hybrid films with graphene oxide and metal nanoparticles could now replace indium tin oxide. *ACS Nano* 4565–4572

7. Arvidsson R, Kushnir D, Molander S, Sandén BA (2016) Energy and resource use assessment of graphene as a substitute for indium tin oxide in transparent electrodes. *J Clean Prod* 132:289–297
8. Wang X, Zhi L, Müllen K (2007) Transparent, conductive graphene electrodes for dye-sensitized solar cells. *Nano Lett* 323–327
9. Li X, Zhu H, Wang K, Cao A, Wei J, Li C, Jia Y, Li Z, Li X, Wu D (2010) Graphene-on-silicon Schottky junction solar cells. *Adv Mater* 22:2743–2748
10. Arvidsson R, Kushnir D, Molander S, Sandén BA (2016) Energy and resource use assessment of graphene as a substitute for indium tin oxide in transparent electrodes. *J Clean Prod* 132:289–297
11. Allen MJ, Tung VC, Kaner RB (2010) Honeycomb carbon: a review of graphene. *Chem Rev* 110:132–145
12. Tour JM (2014) Top-down versus bottom-up fabrication of graphene-based electronics. *Chem Mater* 26:163–171
13. Feng T, Xie D, Lin Y, Zang Y, Ren T, Song R, Zhao H, Tian H, Li X, Zhu H, Liu L (2011) Graphene based Schottky junction solar cells on patterned silicon-pillar-array substrate. *Appl Phys Lett* 99
14. Park H, Rowehl JA, Kim KK, Bulovic V, Kong J (2010) Doped graphene electrodes for organic solar cells. *Nanotechnology* 21
15. Miao X, Tongay S, Petterson MK, Berke K, Rinzler AG, Appleton BR, Hebard AF (2012) High efficiency graphene solar cells by chemical doping. *Nano Lett* 12:2745–2750
16. Song Y, Li X, Mackin C, Zhang X, Fang W, Palacios T, Zhu H, Kong J (2015) Role of interfacial oxide in high-efficiency graphene-silicon Schottky barrier solar cells. *Nano Lett* 15:2104–2110
17. Linab XF, Zhangab ZY, Yuanab ZK, Li J, Xiao XF, Hongab W, Chenab XD, Yu DS (2016) Graphene-based materials for polymer solar cells. *Chin Chem Lett* 27:1259–1270
18. Yong V, Tour JM (2010) Theoretical efficiency of nanostructured graphene-based photovoltaics. *Small* 6:313–318
19. Yin Z, Sun S, Salim T, Wu S, Huang X, He Qi, Lam YM, Zhang H (2010) Organic photovoltaic devices using highly flexible reduced graphene oxide films as transparent electrodes. *ACS Nano* 4:5263–5268
20. Kittiratanawasin L, Hannongbua S (2016) The effect of edges and shapes on band gap energy in graphene quantum dots. *Integr Ferroelectr* 175:211–219
21. Qin Y, Cheng Y, Jiang L, Jin X, Li M, Luo X, Liao G, Wei T, Li Q (2015) Top-down strategy toward versatile graphene quantum dots for organic/inorganic hybrid solar cells. *ACS Sustain Chem Eng* 3:637–644
22. Bacon M, Bradley SJ, Nann T (2014) Graphene Quantum Dots. *Particle* 31:415–428
23. Shen J, Zhu Y, Yanga X, Li C (2012) Graphene quantum dots: emergent nanolights for bioimaging, sensors, catalysis and photovoltaic devices. *Chem Com* 48:3686–3699
24. Zhu S, Zhang J, Tang S, Qiao C, Wang L, Wang H, Liu X, Li B, Li Y, Yu W, Wang X, Sun H, Yang B (2012) Surface chemistry routes to modulate the photoluminescence of graphene quantum dots: From fluorescence mechanism to up-conversion bioimaging applications. *Adv Funct Mater* 22:4732–4740
25. Hamilton IP, Li B, Yan X, Li L (2011) Alignment of colloidal graphene quantum dots on polar surfaces. *Nano Lett* 11:1524–1529
26. Liu F, Jang MH, Ha HD, Kim JH, Cho YH, Seo TS (2013) Facile synthetic method for pristine graphene quantum dots and graphene oxide quantum dots: origin of blue and green luminescence. *Adv Mat* 25:3657–3662
27. Chen L, Guo CX, Zhang Q, Lei Y, Xie J, Ee S, Guai G, Song Q, Li CM (2013) Graphene quantum-dot-doped polypyrrole counter electrode for high-performance dye-sensitized solar cells. *ACS Appl Mater Interfaces* 5:2047–2052
28. Liu T, Yu K, Gao L, Chen H, Wang M, Hao L, Li T, Hea H, Guo Z (2017) A graphene quantum dot decorated SrRuO₃ mesoporous film as an efficient counter electrode for high-performance dye-sensitized solar cells. *J Mater Chem A* 5:17848–17855

29. Zhou J, Ren Z, Li S, Liang Z, Sury C, Shen H (2018) Semi-transparent Cl-doped perovskite solar cells with graphene electrodes for tandem application. *Mat Let* 22:82–85
30. Eperon GE, Stranks SD, Menelaou C, Johnston MB, Herza LM, Snaith HJ (2014) Formamidinium lead trihalide: a broadly tunable perovskite for efficient planar heterojunction solar cells. *Energy Environ Sci* 7:982–988
31. Navrotsky A (1998) Energetics and crystal chemical systematics among ilmenite, lithium niobate, and perovskite structures. *Chem Mater* 10:2787–2793
32. Meng L, You J, Yang Y (2018) Addressing the stability issue of perovskite solar cells for commercial applications. *Nat Commun* 9
33. Eperon GE, Stranks SD, Menelaou C, Johnston MB, Herz LM, Snaith HJ (2014) Formamidinium lead trihalide: a broadly tunable perovskite for efficient planar heterojunction solar cells. *Energy Environ Sci* 7:982–988
34. Noel NK, Stranks SD, Abate A, Wehrenfennig C, Guarnera S, Haghghirad AA, Sadhanala A, Eperon GE, Pathak SK, Johnston MB, Petrozza A, Herz LM, Snaith HJ (2014) Lead-free organic–inorganic tin halide perovskites for photovoltaic applications. *Energy Environ Sci* 7:3061–3068
35. Hao F, Stoumpos CC, Cao DH, Chang RPH, Kanatzidis MG (2014) Lead-free solid-state organic–inorganic halide perovskite solar cells. *Nat Photonics* 8:489–494
36. Assmann E, Blaha P, Laskowski R, Held K, Okamoto S, Sangiovanni G (2013) Oxide heterostructures for efficient solar cells. *Phys Rev Lett* 110
37. Ke JCR, Lewis DJ, Walton AS, Spencer BF, O'Brien P, Thomas AG, Flavell WR (2018) Ambient-air-stable inorganic Cs₂SnI₆ double perovskite thin films via aerosol-assisted chemical vapour deposition. *J Mater Chem A* 6:11205–11214
38. Kim K, Bae SH, Toh CT, Kim H, Cho JH, Whang D, Lee TW, Özyilmaz B, Ahn JH (2014) Ultrathin organic solar cells with graphene doped by ferroelectric polarization. *ACS Appl Mater Interfaces* 6:3299–3304
39. Kumar A, Zhou C (2010) The race to replace Tin-Doped indium oxide: which material will win? *ACS Nano* 4:11–14
40. Ni GX, Zheng Y, Bae S, Tan CY, Kahya O, Wu J, Hong BH, Yao K, Özyilmaz B (2012) Graphene-ferroelectric hybrid structure for flexible transparent electrodes. *ACS Nano* 6:3935–3942
41. Bae S, Kim H, Lee Y, Xu X, Park JS, Zheng Y, Balakrishnan J, Lei T, Kim HR, Song YI, Kim YJ, Kim KS, Özyilmaz B, Ahn JH, Hong BH, Iijima S (2010) Roll-to-roll production of 30-inch graphene films for transparent electrodes. *Nat Nanotechnol* 5:574–578
42. Kasry A, Kuroda MA, Martyna GJ, Tulevski GS, Bol AA (2010) Chemical doping of large-area stacked graphene films for use as transparent, conducting electrodes. *ACS Nano* 4:3839–3844
43. Jung YU (2012) Organic photovoltaic devices with low resistance multilayer graphene transparent electrodes. *J Vac Sci Technol A* 30
44. Hsu CL, Lin CT, Huang JH, Chu CW, Wei KH, Li LJ (2012) Layer-by-layer graphene/TCNQ stacked films as conducting anodes for organic solar cells. *ACS Nano* 6:5031–5039
45. Li X, Chen W, Zhang S, Wu Z, Wang P, Xu Z, Chena H, Yin W, Zhong H, Lin S (2015) 18.5% efficient graphene/GaAs van der Waals heterostructure solar cell. *Nano Energy* 16:310–319

A Closed-Loop Control of Fixed Pattern Rectifier for Renewable Energy Applications



Neeraj Priyadarshi, Farooque Azam, Akash Kumar Bhoi,
and Amarjeet Kumar Sharma

Abstract In this paper, closed-loop control of fixed pattern rectifier for renewable power applications has been proposed. This method explains the dual-loop control as voltage and current controller makes unity power coefficient. The main advantage of this control strategy has rapid dynamic response and better static nature. Dc-link voltage regulation and power factor maintenance have been achieved using voltage and current controller, respectively. MATLAB simulation has been employed to justify the responses for fixed pattern rectifier which maintains modulating index fixed.

1 Introduction

Recently, various issues related to power factor corrections and harmonic distortion present in supply current have been arisen by designers for diode rectifiers. However, power electronics systems are playing a vital role in solving problems related to industrial as well as consumer sectors. In this regard, pulse width modulated (PWM) inverters are best suited and have less harmonic distortions in supply current because they make the sine nature of the current waveform. This unity power coefficient can be achieved by making power supply in phase with supply current and ac–dc

N. Priyadarshi (✉) · A. K. Sharma
Department of Electrical Engineering, Birsa Institute of Technology (Trust),
Ranchi 835217, India
e-mail: neerajrjd@gmail.com

A. K. Sharma
e-mail: ermaxamar@gmail.com

F. Azam
School of Computing & Information Technology, REVA University, Bangalore 560064, India
e-mail: farooque53786@gmail.com

A. K. Bhoi
Department of Electrical & Electronics Engineering, Sikkim Manipal Institute of Technology,
Sikkim Manipal University, Gangtok, India
e-mail: akash730@gmail.com

conversion can be utilized for battery charging applications. Renewable energy-based control technologies are widely used for power generation [1–6]. Conventionally, rectifiers are made by silicon-controlled rectifiers (SCR) and diodes and work as a controlled/uncontrolled rectifiers which act as natural commutating inverters and comprise of reactive power generation and harmonic distortion as main shortcomings.

The electrical power control and operation are the key factor for designers to prevent from harmonic distortion. Moreover, PWM converters have been used with better static behavior, rapid transient response, and pure sine waveforms of supply current and has unity power coefficient which is employed for battery charging of electrical vehicle. This PWM-based control strategies are frequently used in renewable power applications-based control [7–9]. In this control strategy, proportional-integral controllers have been employed as outer loop and mathematical analysis as well as current-controlled strategy has been targeted. Simulation as well as practical analysis has been done which justify good static, transient behavior, fast dynamicity, and better robust nature of the closed-loop control of designed fixed pattern rectifier. Compared to natural commutated converters which are switching *ON* and *OFF* only once a cycle, the force commutating converters provide switching whenever is required and have full control on converters switching and comprise of least harmonic distortion and unity power factor operations. Moreover, voltage/current source with reversal power can be possible by using dc-link regulation.

2 Mathematical Analysis of Closed-Loop Controlled Fixed Pattern Rectifier

The θ acts as a phase angle between V_m and V_r with supply current I and total impedance Z , and current can be expressed as.

$$I = \frac{V_m - V_r}{Z} \quad (1)$$

Also, the original component of voltage (V_m) is translated along V_r -axis, then $V_m = V_r$, and Eq. (1) becomes:

$$I = \frac{V_m - K_v V_{dc} e^{j\theta}}{Z} \quad (2)$$

The general schematic of three-phase rectifier is constructed with IGBTs as shown in Fig. 1 and the general block diagram that shows the entire operation in the simple way is also presented in Fig. 2 as following.

For making supply current continuous, the inducting impedance is considered as $Z = R + j\omega L = R + jX$ which makes the overall system highly efficient and requires for $X/R \gg 1$ is needed with negligence of RFI filter effect. Figure 3 denotes the overall closed-loop control of fixed pattern rectifier for renewable energy applications.

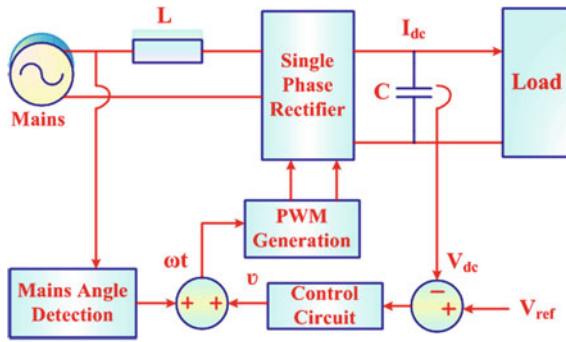


Fig.1 General block diagram

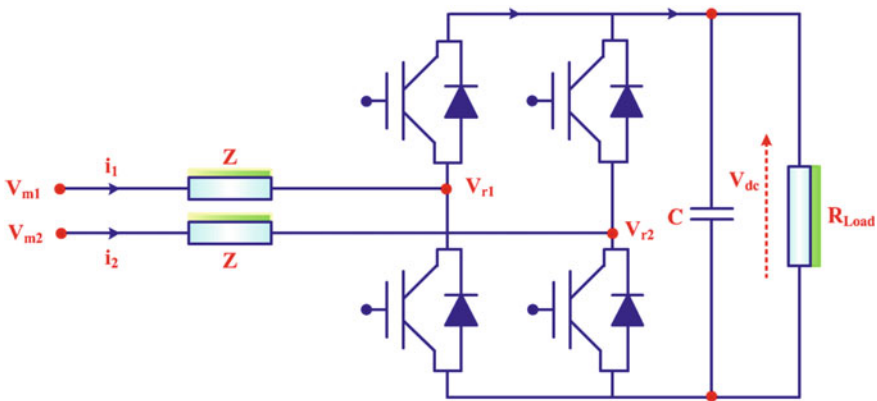


Fig. 2 General topology of classical active rectifier

3 Implementation Methodology

The method of implementation is based on software simulation and hardware implementation of fixed pattern rectifier. Before hardware implementation, software simulation will help to identify the problems and gives solution to solve the problems. This solution will help to implement the circuit in the hardware. In software simulation, MATLAB/Simulink is used in this project. It is the most widely used tool in the electrical engineering community. It is one of the powerful tools. All the necessary materials of the project can be got from sim power systems block. Figures 4, 5, 6, 7, 8, and 9 present the generation of pulses for IGBT, pulses for IGBT converter, open-loop simulation, input current and input voltage waveform, closed-loop simulation, and rectified output, respectively. Moreover, the hardware results of Figs. 10, 11, 12, 13, 14, and 15 depict the invert sine pulse generation and comparator, triangle and sine comparison, PWM pulses for converter (switch 1, 3), PWM pulses for converter

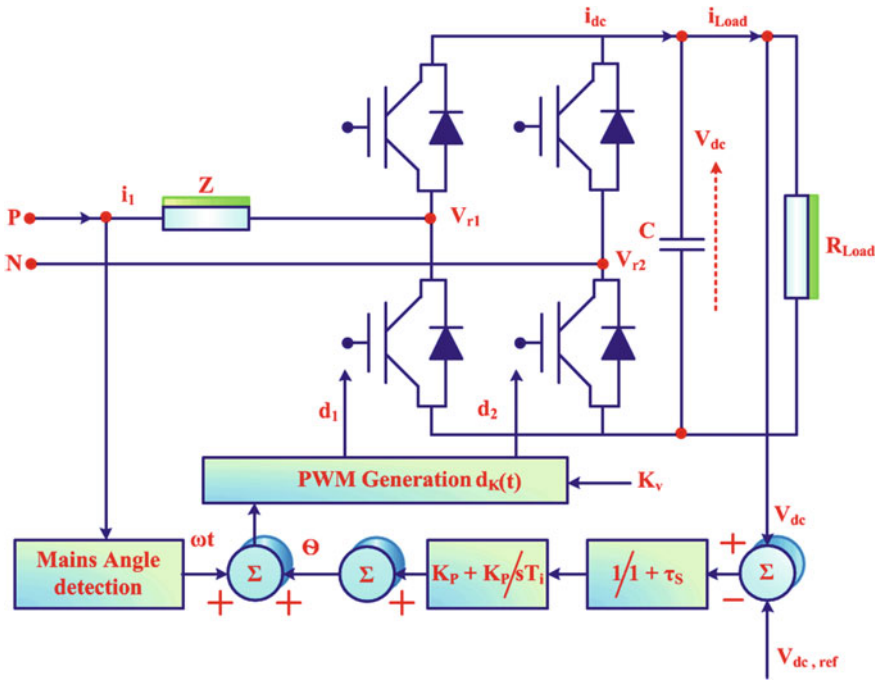


Fig. 3 System control configuration

(switch 2, 4), hardware setup, and rectified output, respectively, which validate the simulation design for closed-loop control of fixed pattern rectifier.

To compare the two signals, comparators are used. When two signals are given to a comparator, it will compare and gives the output. In this project, the triangular wave is compared with the sine wave using LM330 comparator. The hardware circuit of comparator is shown. Here, the triangular input is given to the one terminal and sine wave is given to the another terminal. It compares both signals and it produces pulses at output.

4 Conclusion

In this research work, a closed-loop control of fixed pattern rectifier for renewable power applications has been designed and validated through simulation and practical implementation. The modulation index is constant throughout the operation and control strategy works in dual-loop control as voltage and current controller which makes unity power coefficient which comprises rapid dynamic response and better

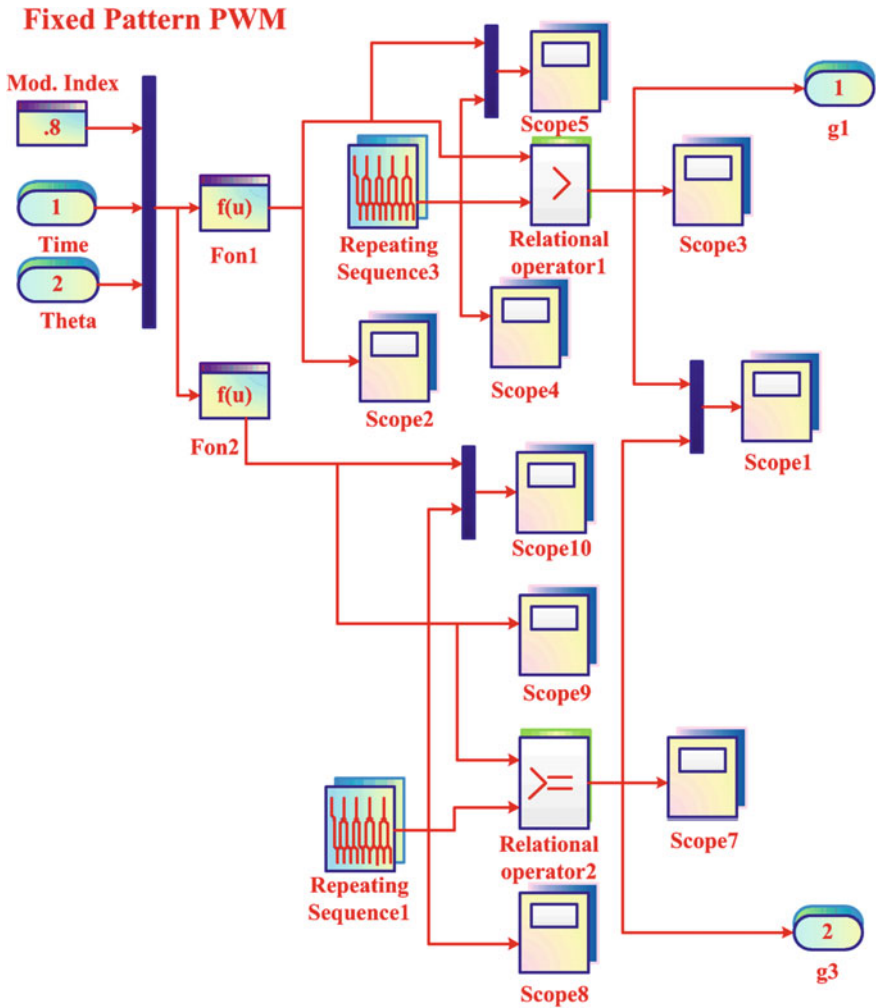


Fig. 4 Generation of pulses for IGBT

static nature as major benefits. Dc-link voltage regulation and power factor maintenance have been achieved using voltage and current controller, respectively, which makes the designed systems best suited for renewable power applications.

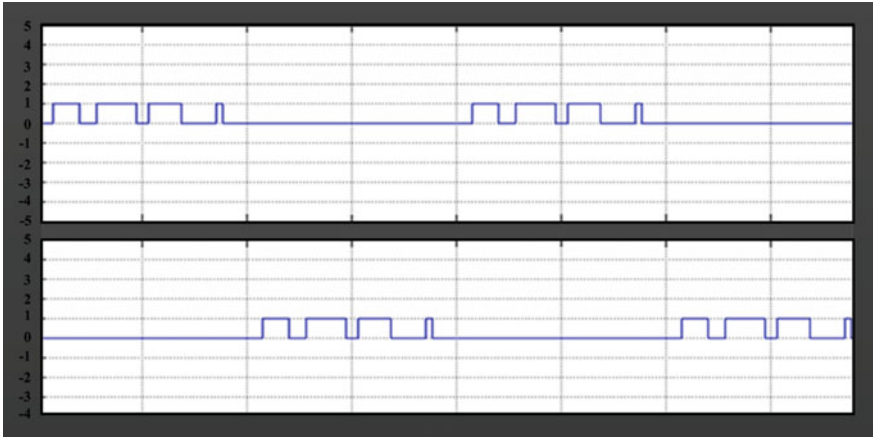


Fig. 5 Pulses for IGBT converter

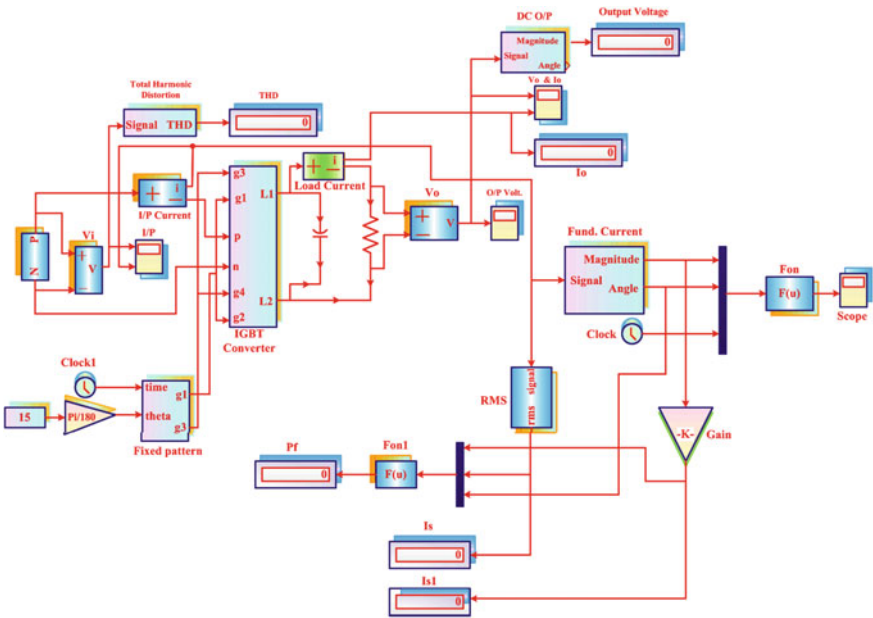


Fig. 6 Open-loop simulation

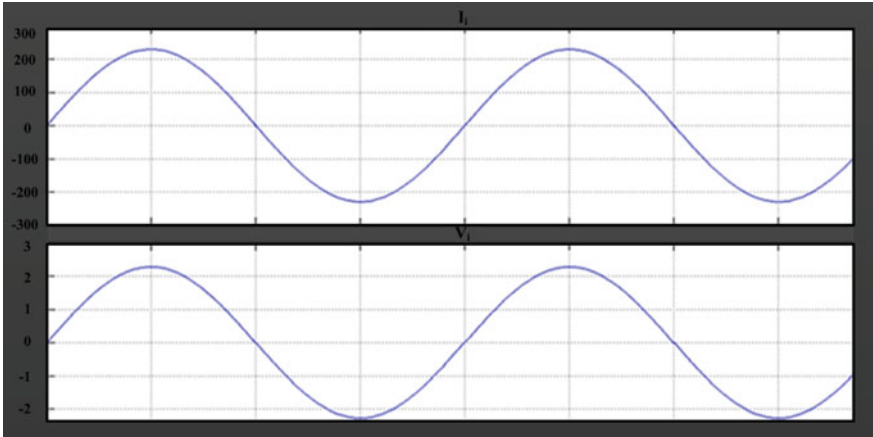


Fig. 7 Input current and input voltage waveform

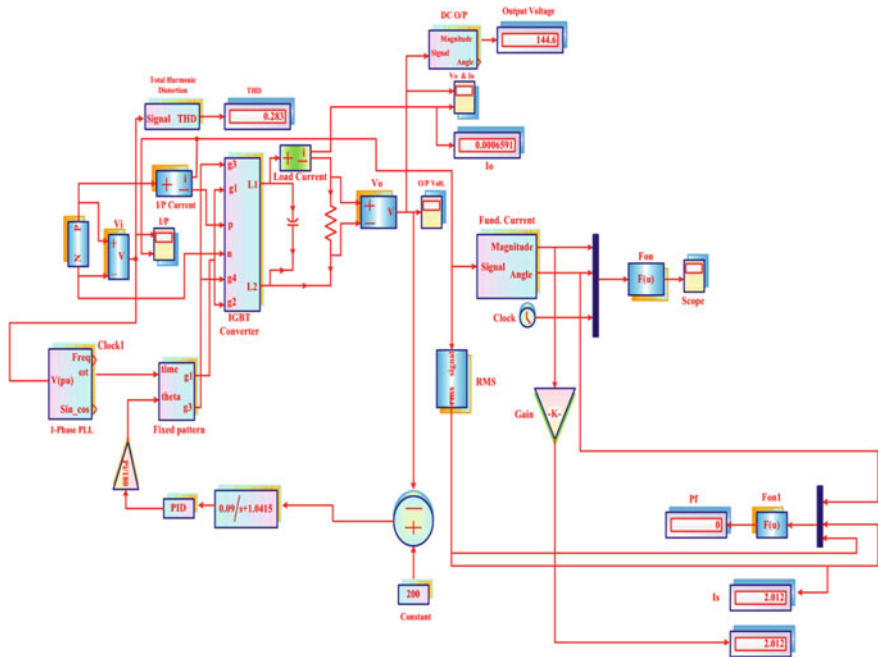


Fig. 8 Closed-loop simulation

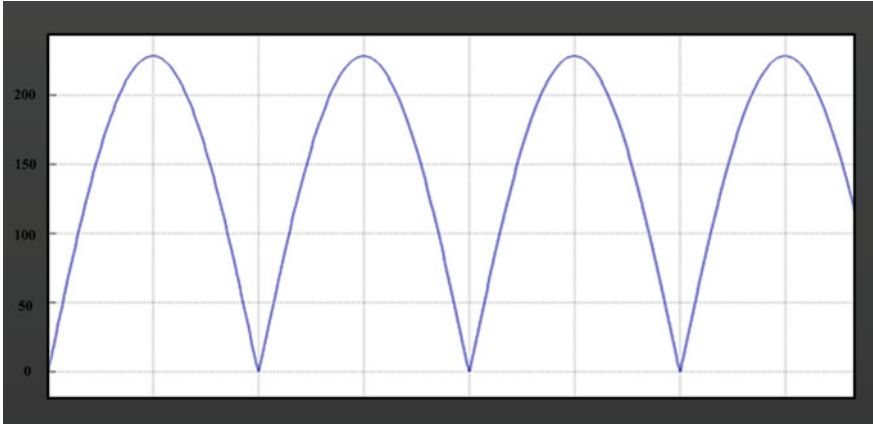


Fig. 9 Rectified output

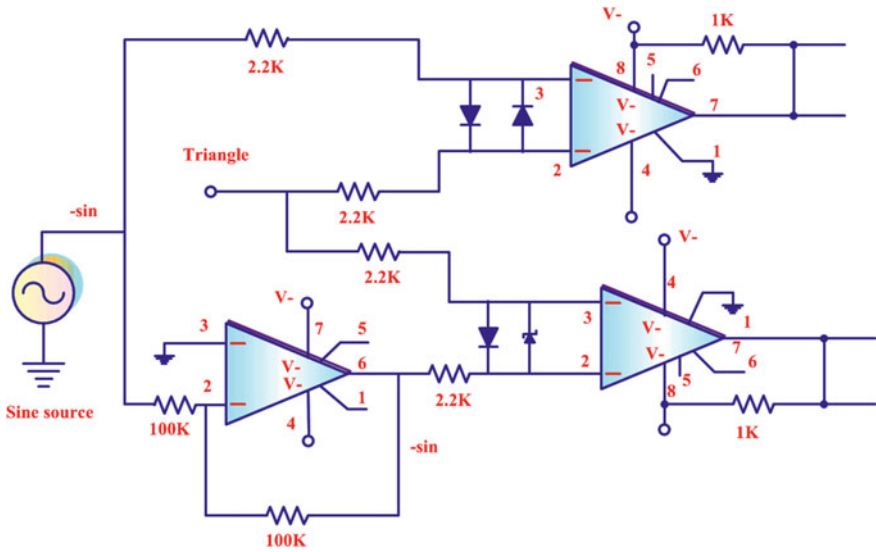


Fig. 10 Invert sine pulse generation and comparator

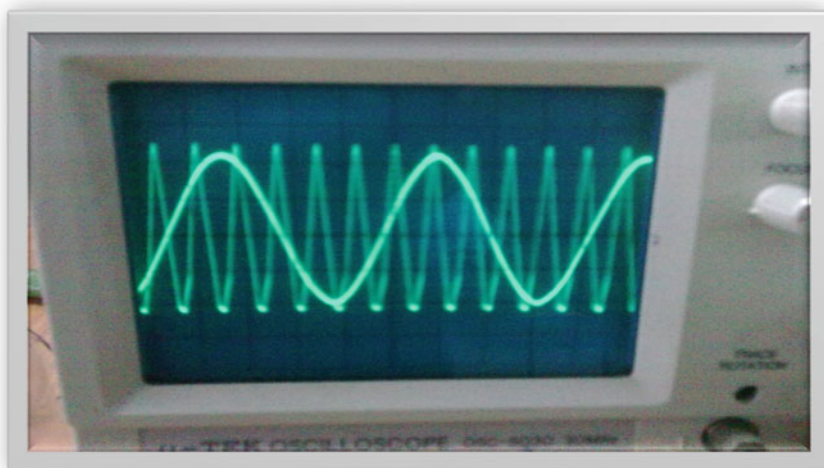


Fig. 11 Triangle and sine comparison



Fig. 12 PWM pulses for converter (switch 1, 3)

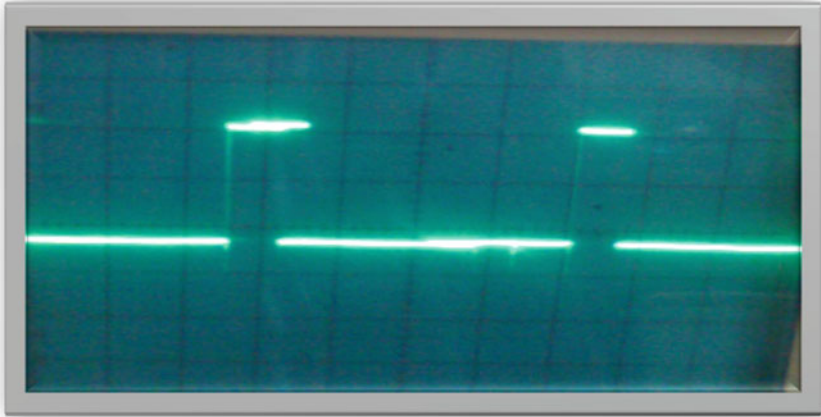


Fig. 13 PWM pulses for converter (switch 2, 4)

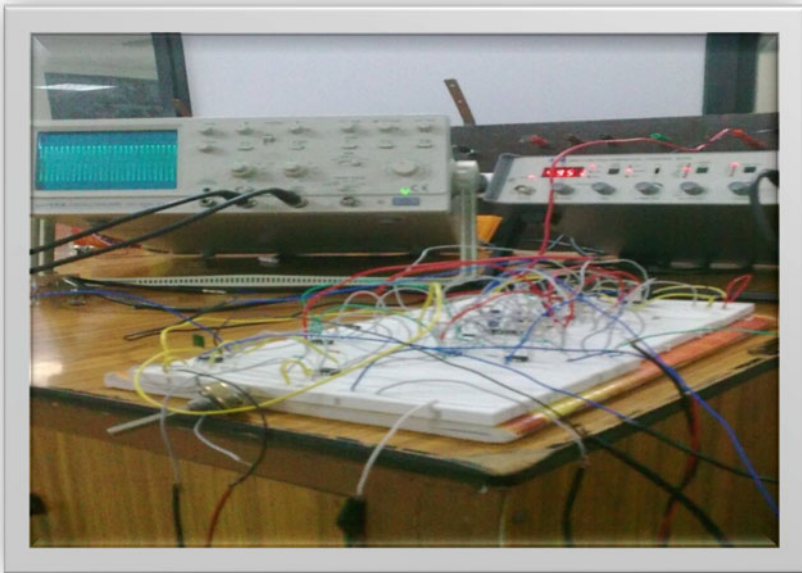


Fig. 14 Hardware setup

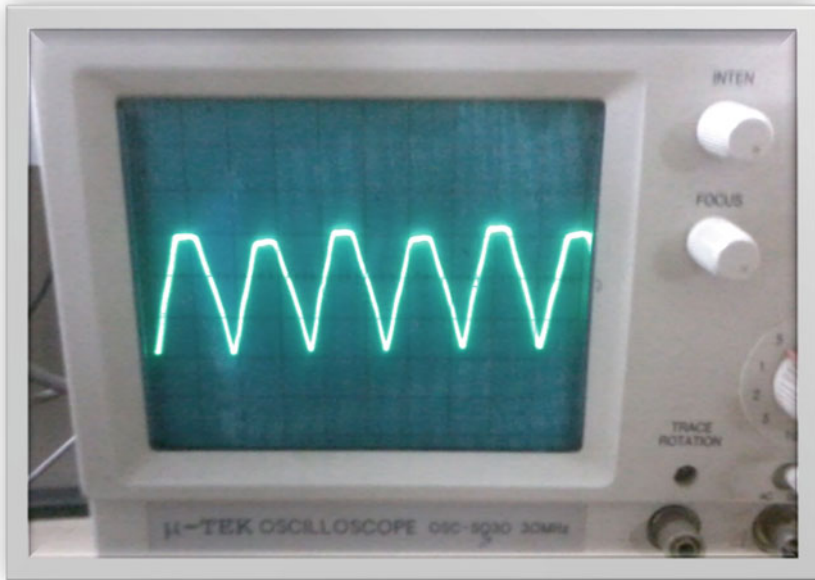


Fig. 15 Rectified output

References

1. Padmanaban S, Priyadarshi N, Holm-Nielsen JB, Bhaskar MS, Azam F, Sharma AK, Hossain E (2019) A novel modified sine-cosine optimized MPPT algorithm for grid integrated PV system under real operating conditions. *IEEE Access* 7:10467–10477
2. Li H, Yang D, Su W, Lü J, Yu X (2018) An overall distribution particle swarm optimization MPPT algorithm for photovoltaic system under partial shading. *IEEE Trans Ind Electron* 66(1):265–275
3. Priyadarshi N, Anand A, Sharma AK, Azam F, Singh VK, Sinha RK (2017) An experimental implementation and testing of GA based maximum power point tracking for PV system under varying ambient conditions using dSPACE DS 1104 controller. *Int J Renew Energy Res* 7(1):255–265
4. Priyadarshi N, Kumar V, Yadav K, Vardia M (2017) An experimental study on zeta buck-boost converter for application in PV system. In: *Handbook of distributed generation*. Springer, Heidelberg. https://doi.org/10.1007/978-3-319-51343-0_13
5. Priyadarshi N, Sharma AK, Priyam S (2018) An experimental realization of grid-connected PV system with MPPT using dSPACE DS 1104 control board. In: *Advances in smart grid and renewable energy. Lecture notes in electrical engineering*, vol 435. Springer, Singapore
6. Priyadarshi N, Sharma AK, Azam F (2017) A hybrid firefly-asymmetrical fuzzy logic controller based MPPT for PV-wind-fuel grid integration. *Int J Renew Energy Res* 7(4)
7. Priyadarshi N, Sharma AK, Priyam S (2017) Practical realization of an improved photovoltaic grid integration with MPPT. *Int J Renew Energy Res* 7(4)
8. Michael B, Jason W, Steven Z, Petr M (2018) Design considerations for IoT-based PV charge controllers. In *Proceeding of IEEE World Congress on Services*, pp 59–60
9. Mohamed AA, Berzoy A, Mohammed OA (2016) Design and hardware implementation of FL-MPPT control of PV systems based on GA and small-signal analysis. *IEEE Trans Sustain Energy* 8(1):279–290

DC–DC Converter with High Conversion Ratio for Transmission



Jae-Ha Ko, Chun-Sung Kim, Jong-Cheol Kim, Seong-Mi Park,
and Sung-Jun Park

Abstract *Background/Objectives:* Nowadays, demand for power converters in high-voltage applications such as wind power, electric locomotives, BESS, and HVDC has increased rapidly. However, high-voltage applications have great problems in the limited ability of power electronic devices. Because of this reason, numerous studies have been conducted to find solutions that can increase the operating voltage of new semiconductor power switching devices. *Methods/Statistical analysis:* In this paper, we propose a circuit configuration for a high-voltage-isolated DC–DC converter. Since the operating voltage range of the switching device is limited, research on a DC–DC configuration operating at a high voltage has hardly been conducted. The proposed configuration of converter is divided into two parts: the high-voltage side consists of a serial modular multilevel converter (MMC) and the other is a low voltage, rectifier diode bridge, both connected to a high-frequency transformer. *Findings:* A novel configuration of a DC–DC converter that can be applied to high voltage is mentioned. This is largely divided into two sides, consisting of a high-voltage MMC, a low-voltage H-bridge rectifier, and a high-frequency transformer connecting the two sides. The circuit configuration will be presented and verified by modeling and experimental results that can determine the practicality of the new phase with pulse width modulation (PWM). *Improvements/Applications:* The proposed converter is suitable for high-voltage applications with high step ratio and insulation characteristics between the source and load. A PWM-based phase shift algorithm is provided to control the output voltage. The cell rotation selection is applied to achieve the self-balancing capacitor voltage level.

J.-H. Ko · C.-S. Kim · J.-C. Kim
Green Energy Institute, Mokpo-si, Korea
e-mail: jhko@gei.re.kr

S.-M. Park
Department of Lift Design, Korea Lift College, Geochang 50141, Korea
e-mail: soengmi@klc.ac.kr

S.-J. Park (✉)
Department of Electrical Engineering, Chonnam National University, Gwangju 61186, Korea
e-mail: sjpark1@jnu.ac.kr

Keywords Phase shift · DC–DC converter · High-voltage application · MMC · H-bridge rectifier

1 Introduction

Nowadays, the spread of clean energy is growing rapidly. The International Energy Agency (IEA) estimates that worldwide electricity consumption will reach 30,000 TWh per year by 2030. Fossil fuel-burning thermal power plants are still a major source of power worldwide. According to the Renewable Energy Policy Network (REN21) in the twenty-first century, 73.5% of the world's electricity was generated from fossil fuels in 2017 [1].

Demand for power converters in high-voltage applications such as wind power, electric locomotives, BESS, and HVDC has increased rapidly in recent years [2–7]. However, high-voltage applications have great problems in the limited ability of power electronic devices. Hundreds of studies have been conducted to find solutions that can increase the operating voltage of new semiconductor power switching devices. On the other hand, the multistage configuration has been found to be effective in increasing the rated voltage with conventional power switches [8]. Modular structures [9, 10] appear as conventional multilayer transducers such as diode clamps [11, 12] or cascaded H-bridges. Today, multistage configurations for DC–DC converters are prevalent in high-voltage application fields. Such a converter is used for step-up or step-down, but the higher the step rate the larger the size of the topology.

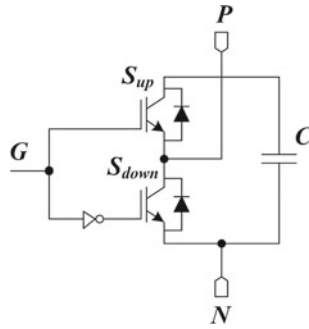
In this paper, a new configuration of a DC–DC converter for high-voltage applications is proposed. The high-voltage section is composed of MMC, the low-voltage section is the H-bridge rectifier, and the high-frequency transformer connects the two parts. The proposed transducer is suitable for high-voltage applications with high step ratio and isolation between power supply and load. A PWM-based phase shift algorithm is proposed to control the output voltage. The cell rotation selection is applied to achieve the self-balanced capacitor voltage. The circuit configuration is presented and verified by modeling and experimental results that can demonstrate the practicality of the proposed pulse width modulation (PWM).

2 Materials and Methods

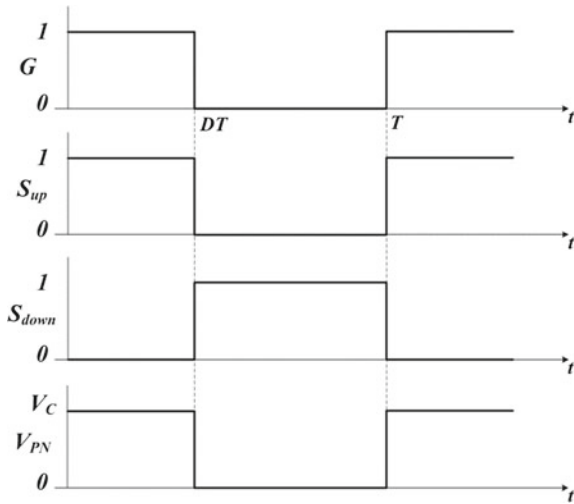
2.1 Conventional MMC

As shown in Fig. 1a, the conventional MMC consists of two power switches (S_{up} , S_{down}), which can carry positive current with a power supply or a capacitor. The power switch is controlled by a switching function G with two possible states.

$$G = 1$$



(a) Conventional MMC



(b) switching pattern of the MMC

Fig. 1 Conventional MMC and PWM

$$G = 0 \tag{1}$$

When switching function is 1, S_{down} is OFF and S_{up} is ON. Meanwhile, when the switching function is 0, S_{up} is OFF while S_{down} is ON. The output voltage of the MMC is measured between nodes P and N and is defined by the switching function. Assuming that the voltage change in capacitor C is negligible when compared to the average V_C , the output voltage is shown as follows

$$V_{PN} = GV_C \tag{2}$$

The conventional MMC has two voltage levels determined by the switching function. Where $G = 0$ defines a 0 V output voltage and $G = 1$ defines an output voltage

equal to V_C . Figure 1b shows the switching pattern of the MMC with the corresponding output voltage. This method of indicating the switching state of a converter provides a concise representation of converter behavior in a more complex topology.

2.2 Configuration of Proposed MMC

Figure 2 shows a circuit and waveform of the proposed DC–DC converter and PWM. For the high voltage (HV) side, the upper group has N MMCs, and the lower group also has N MMCs and is connected in series. Assuming all components are ideal and the circuit is in a stable state, the voltage of the capacitor is the same. At the A-linking point of the upper group and the lower group, it is possible to generate a

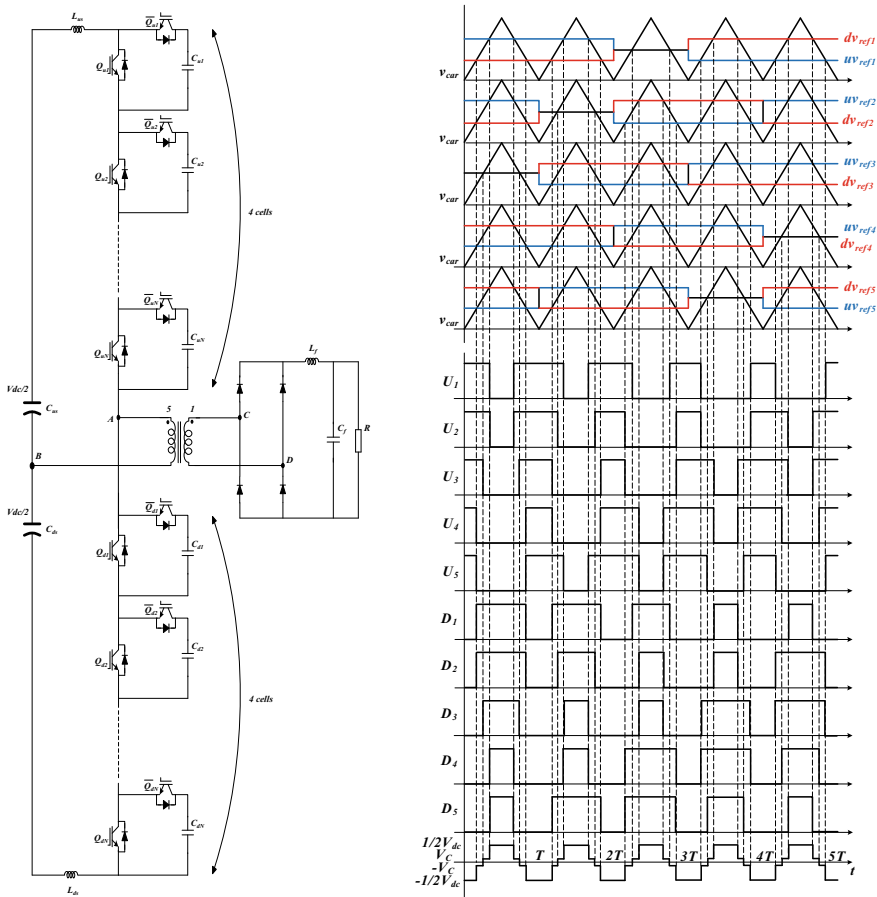


Fig. 2 Configuration of proposed DC–DC converter and PWM

higher voltage level, a smaller voltage level, or a voltage equal to the voltage level of the B-neutral point of the source. Thus, the voltage between A and B may be a negative voltage, a positive voltage, or a zero voltage. The N value also determines the type of the proposed converter.

$$\text{Even topology type: } N = 2n \quad (n = 1, 2, 3, 4, 5, \dots) \quad (3)$$

$$\text{Odd topology type: } N = 2n + 1 \quad (n = 1, 2, 3, 4, 5, \dots) \quad (4)$$

There are little differences between the instantaneous voltage across the MMC and the voltage across C_{us} , C_{ds} . And, it is offset by including the inductors L_{ds} , L_{us} . The low-voltage part consists of an H-bridge rectifier and a low-pass filter L_f , C_f is generally present at the output of the converter. The high-frequency transformer uses and isolate both parts as well as deliver energy between the high and low voltages parts.

In general, the operation of the DC–DC converter is similar to that of an isolated. Where the series MMC on the high-voltage side represents the half-bridge configuration and the low-voltage side is the active H-bridge rectifier. The control methods for both configurations are identical and operate with a phase-shift PWM mechanism. However, special PWM algorithms are used within the MMC to ensure phase-shift PWM mechanisms, as well as to stabilize the MMC's capacitor voltage balancing.

2.2.1 Even Topology Configuration

In the even configuration, the MMC numbers of the upper group and the lower group are even numbers in the $2k$ format, where k is a natural number and greater than 1.

All three transition modes are shown in Fig. 4. Here, the detailed circular diagram in Fig. 3 will explain how the mode works. The capacitors of each MMC compensate for the reactive current and each operating mode ensures that the $2k$ MMC is switched on for stable voltage supply. Therefore, it is assumed that all components are ideal and that the circuit is in stable condition. Each capacitor V is same that $V_{dc}/2k$. The voltage at point B is $V_{dc}/2k$, and by varying the voltage at point A , three-level voltages can be obtained in the input primary voltage waveform with three operating modes per cycle.

The voltage applied to the primary side of the transformer shall be positive and negative symmetrical. This means that mode 1 and mode -1 have the same duration. Therefore, the output voltage of the converter is controlled by the ratio of mode 1, -1 and mode 0 in one cycle. Figure 5 shows that the output voltage of the converter proposed in the even phase is controlled by the variable ϕ .

$$\overline{|V_{AB}|} = \frac{\phi}{360} V_H \quad (5)$$

where phase shift $\phi = 0 \sim 180^\circ$.

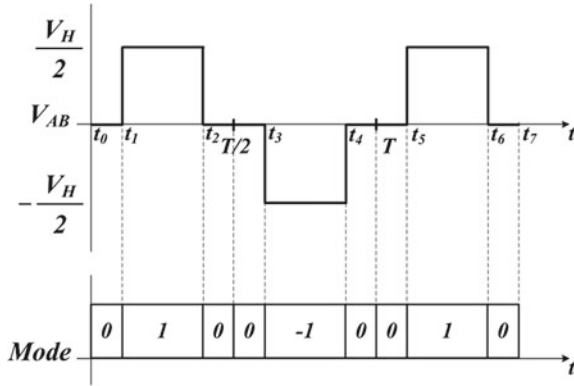


Fig. 3 Waveform of even topology

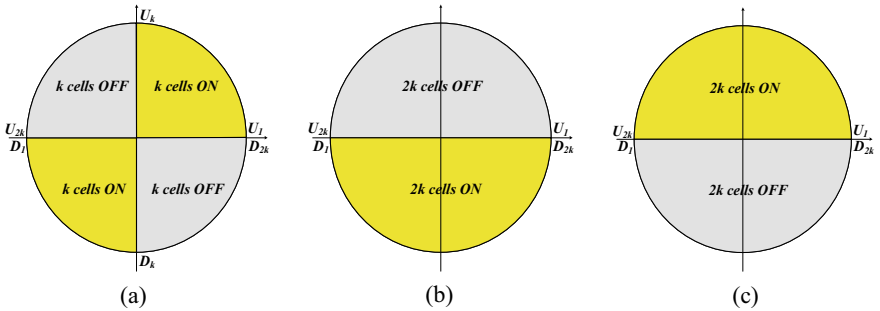


Fig. 4 Operational modes of even topology

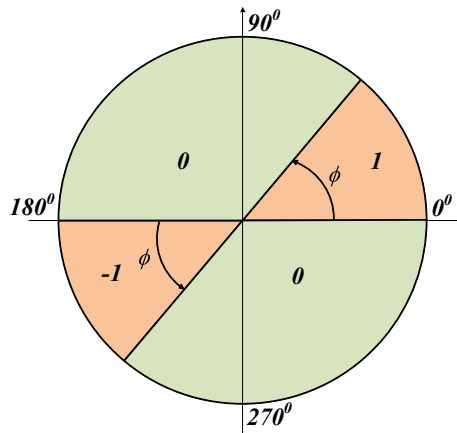


Fig. 5 Phase shift control of even topology

2.2.2 Odd Topology Configuration

In the odd-numbered configuration, the MMC cell numbers of the upper group and the lower group are odd ($2k + 1$), where k is a natural number and greater than 1. Each operating mode ensures that $(2k + 1)$ cells are turned on to ensure stable voltage and minimum reactive current across the capacitors of each cell. As shown in Fig. 6, each mode has four modes corresponding to four-level voltages: $-V_c$, $(-V_{dc})/2$, $(+V_{dc})/2$, $+V_c$. Therefore, there is no level 0 in this waveform. As shown in Fig. 6, the corresponding mode of input waveform and odd phase in primary winding analyze each mode of operation as well as the configuration. The voltage of the capacitor is $V_{dc}/(2k + 1)$ and the voltage of the point B is $V_{dc}/2$.

Figure 7 shows that the converter’s output voltage in odd-numbered phases is controlled by adjusting the ratio of mode 2, -2 versus mode 1, -1 to one cycle.

Fig. 6 Waveform of odd topology

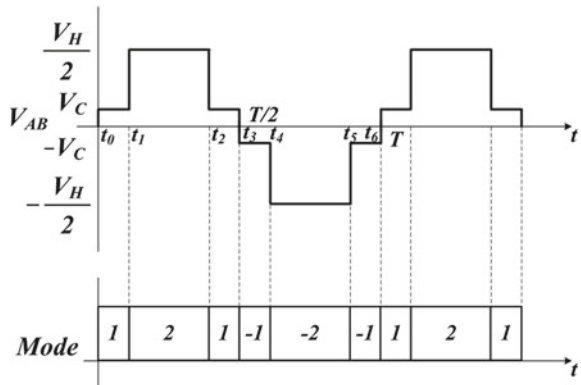
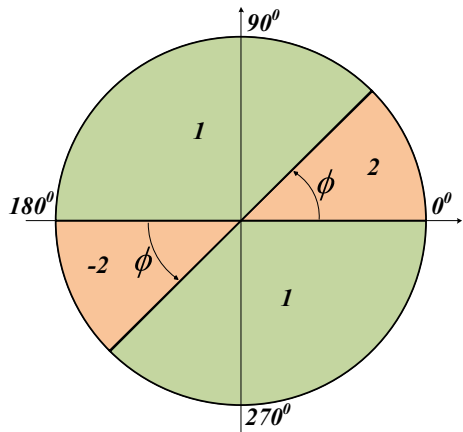


Fig. 7 Phase shift control of odd topology



$$|\overline{V_{AB}}| = V_C + \frac{\phi}{360} V_H \tag{6}$$

where V_c is the voltage across the capacitor and the phase shift.

2.2.3 Switching Pattern of the Proposed Converter

This control algorithm is represented by a figure in Fig. 8, which shows the switching pattern of the proposed topology with N of 4. This uses carrier (v_{car}) and four reference waveforms v_{ref1} through v_{ref4} . Compare all reference waves with the carrier waveform and generated switching signals (U_n and D_n).

$$v_{ref1}(t) = \left(1 - \frac{\phi}{360}\right)[u(t) - u(t - 2T)] + \frac{\phi}{360}[u(t - 2T) - u(t - 4T)] \tag{7}$$

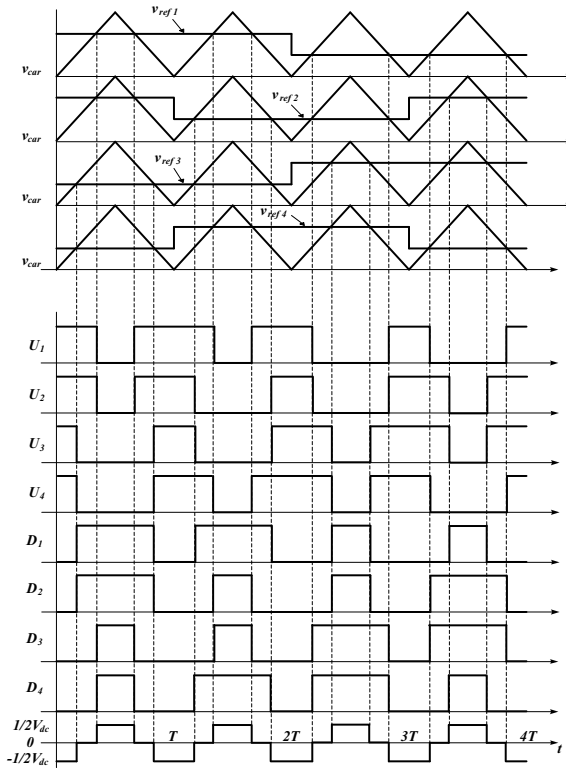


Fig. 8 Phase shift control of odd topology

$$v_{\text{ref}2}(t) = \left(1 - \frac{\phi}{360}\right)[u(t) - u(t - T) + u(t - 3T) - u(t - 4T)] \\ + \frac{\phi}{360}[u(t - T) - u(t - 3T)] \quad (8)$$

$$v_{\text{ref}3}(t) = \left(1 - \frac{\phi}{360}\right)[u(t - T) - u(t - 2T)] + \frac{\phi}{360}[u(t) - u(t - 2T)] \quad (9)$$

$$v_{\text{ref}4}(t) = \left(1 - \frac{\phi}{360}\right)[u(t - T) - u(t - 3T)] \\ + \frac{\phi}{360}[u(t) - u(t - T) + u(t - 3T) - u(t - 4T)] \quad (10)$$

3 Simulation and Results

Figure 9 shows the simulation results for voltage and gate driver signal waveforms. From top to bottom: V_p is the primary voltage, U1, U2, U3, U4 is gate driver signal.

Figure 10 shows the experimental results of even configuration when phase shift is 90° .

Figure 11 shows the simulation results for voltage and gate driver signal waveforms. From top to bottom: V_p is the primary voltage, U1, U2, U3, U4 is gate driver signal.

Figure 12 shows the experimental results of even configuration when phase shift is 90° .

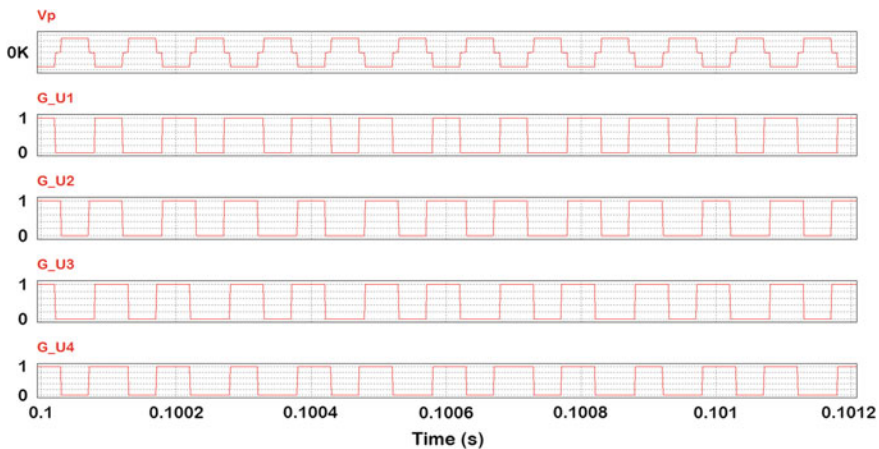


Fig. 9 Even configuration upper gate driver signals

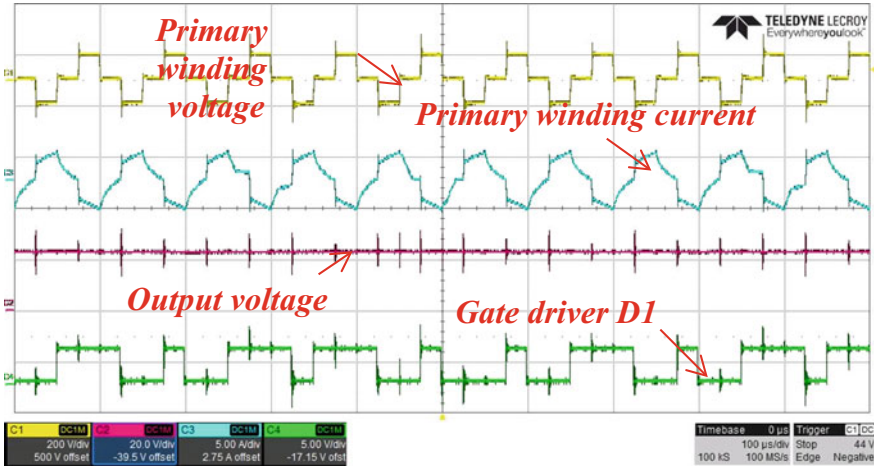


Fig. 10 Experimental results of voltage and current waveform

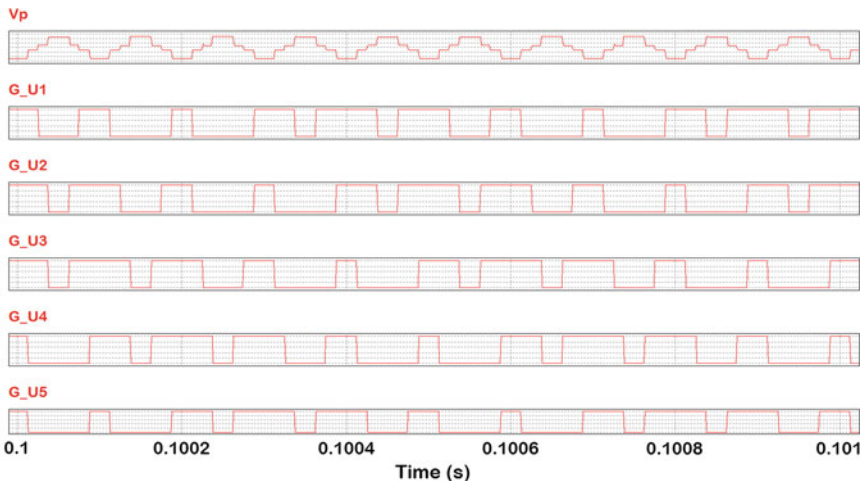


Fig. 11 Odd configuration upper gate driver signals

4 Conclusion

The proposed converter is based on the series-connected of MHCs, is capable of preventing spike voltages on the switch due to the availability characteristics of the configuration. Therefore, they can be connected into strings to handle higher voltage and to solve the problem of limiting the voltage capability of semiconductor switching devices. The proposed PWM cell-rotated selection control algorithm can solve capacitor voltages balance problem without voltage sensors on submodules.

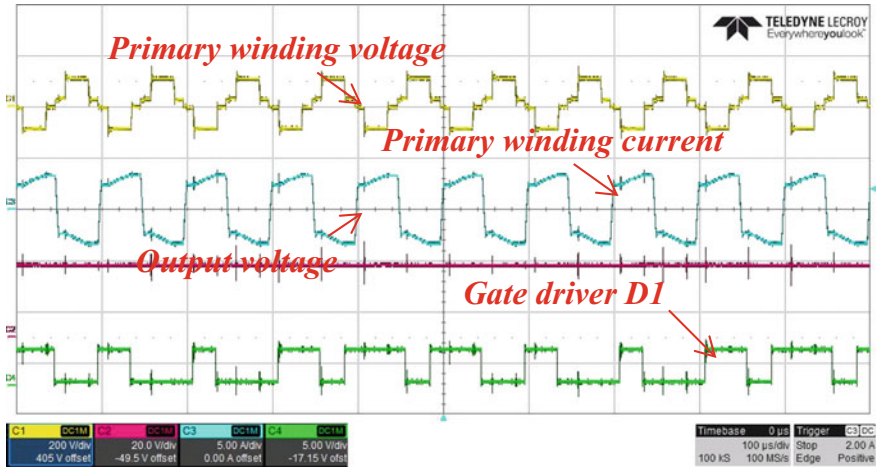


Fig. 12 Experimental results of voltage and current waveform

Acknowledgements This work was supported by the Korea Institute of Energy Technology Evaluation and Planning (KETEP) and the Ministry of Trade, Industry & Energy (MOTIE) of the Republic of Korea (No. 20183010141100).

References

1. Thoma J, Chilachava D, Kranzer D (2014) A highly efficient DC-DC-converter for medium-voltage applications. In: 2014 IEEE international energy conference, Cavtat, pp 127–131. <https://doi.org/10.1109/ENERGYCON.2014.6850417>
2. Mohammadzadeh Shahir F, Babaei E (2017) Application of high voltage gain DC-DC converter in photovoltaic system with energy storage. In: 2017 8th power electronics, drive systems & technologies conference, Mashhad, pp 265–269. <https://doi.org/10.1109/PEDSTC.2017.7910334>
3. REN21, Renewables 2018: Global status report. https://www.ren21.net/wp-content/uploads/2018/06/17-8652_GSR2018_FullReport_web_-1.pdf
4. Public electricity production from fossil fuels. IEA information paper in support of G8 plan of action
5. International Energy Agency, Energy Technology Perspectives 2017, IEA. <https://www.iea.org/publications/freepublications/publication/EnergyTechnologyPerspectives2017ExecutiveSummaryEnglishversion.pdf>
6. International Energy Agency, World Energy Outlook 2017. https://www.iea.org/publications/freepublications/publication/WEO_2017_Executive_Summary_English_version.pdf
7. Rudervall R, Charpentier J, Sharma R (2000) High voltage direct current transmission systems technology. ABB Power Systems Sweden, Review Paper
8. Blaabjerg F, Liserre M, Ma K (2012) Power electronics converters for wind turbine systems. IEEE Trans Ind Appl 48(2)
9. Meyer JM, Rufer A (2006) A DC hybrid circuit breaker with ultra-fast contact opening and integrated gate-commutated thyristors (IGCTs). IEEE Trans Power Deliv 21(2):646–651

10. Meyer C, De Doncker RWAA (2006) Solid-state circuit breaker based on active thyristor topologies. *IEEE Trans Power Electron* 21(2):450–458
11. Kirby N, Xu L, Siepmann W (2002) HVDC transmission options for large offshore windfarms. In: 35th IEEE IAS annual meeting. Industry applications conference, Stockholm, Sweden
12. Myrzik JMA, Calais M (2003) String and module integrated inverters for single phase grid connected photovoltaic systems—a review. In: *Proceeding of IEEE Bologna Power Tech*, vol 2

Narrowband-IoT Base Station Development for Green Communication



Subhankar Shome and Rabindranath Bera

Abstract IoT technology has already changed when and where the work has to be done, in almost every sector. By 2020, the number of IoT devices that are in use is expected to grow to 31 billion. This number of huge devices need connectivity, which means every connected device will emit a certain amount of power and will generate more e-waste every year. Ultra-narrowband (UNB) and narrowband Internet of things (IoT) is usually a technology deployment supporting low power communications which require very narrow spectrum channels. In comparison to normal broadband spectrum with high signal to noise ratio, narrowband signals with high signal to noise ratio (SNR) required very less transmission power because of its less-consumed spectrum allocation. Broadband spread spectrum option is there, which also required low power but in that case, spectrum is generally spread over a huge band. This spreading effect reduces the SNR level of the system and consumes less power, but due to huge band allocation, this type of system becomes very costly. So, low SNR-based spread spectrum system is not recommended for IOT application. In these researches, two major techniques are explored to make communication green, one is narrowband communication another is pulsed transmission which helps transmitter and receiver to go to sleep mode. Using these two, power consumption and emission can be very less which will save the environment.

Keywords IoT · NB-IoT · Green communication · Green IoT · MSR

1 Introduction

Internet of things is now everywhere in the society which has been incorporated over the last 10–20 years. Almost every useful thing for humans is now in always connected mode through IoT networks. Continuous monitoring and efficient control of every device are very much required to save resources in every sector. Expected

S. Shome (✉) · R. Bera
Sikkim Manipal Institute of Technology, Sikkim Manipal University, Sikkim, India
e-mail: subho.ddj@gmail.com

R. Bera
e-mail: rbera50@gmail.com

© Springer Nature Singapore Pte Ltd. 2020
A. K. Bhoi et al. (eds.), *Advances in Greener Energy Technologies*,
Green Energy and Technology, https://doi.org/10.1007/978-981-15-4246-6_27

growth in IoT network will reach 31 billion by 2020 and 75 billion by 2025 [1]. Growth in the IoT network means growth in interconnected devices. That means, by 2025, more than 75 billion IoT devices will be operational in the world (Fig. 1), which is going to be a big cause of e-waste generation and also going to be a reason for big amount of energy emission. Considering this issues a low power wide area network (LPWAN) can be a game changer for IoT industry [2].

Low power is very much essential to save battery life for remote devices. Applications like IoT which aim for long range, low power, and reliable communications, narrowband spectrum communication is the choice. One of the main key factors in LPWAN is spectrum selection. Mostly, three types of spectrum choice are there for communication system design. One is narrowband spectrum, second is a broadband spectrum, and third is spread spectrum which basically explores broadband spectrum. In spread spectrum technology, a narrow band spectrum is stretched over the broadband to reduce power consumption. This will be power efficient which is an aim of IoT but it will be an unnecessary spectrum allotment for a low chunk of control data which required a narrow band spectrum only. Also, this spread spectrum method reduced the SNR of the signal which is not recommended for very long distance communication. IoT base station will be designed to serve around 5–10 km of area for which spread spectrum will not be a choice. So the only choice is a narrowband spectrum for this LPWAN network, which will reduce spectrum cost, required low power than a normal broadband spectrum, will give sufficient SNR for long-range communication and will make efficient use of spectrum for low chunk control data. Different types of spectrum are shown in Fig. 2. Another efficient way

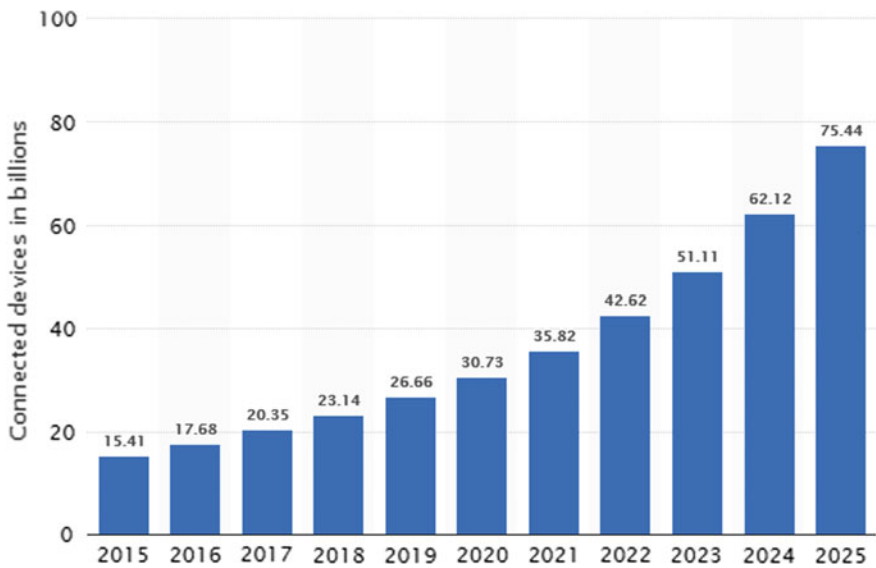


Fig. 1 Internet of things (IoT)-connected devices installed worldwide from 2015 to 2025 (in billions)

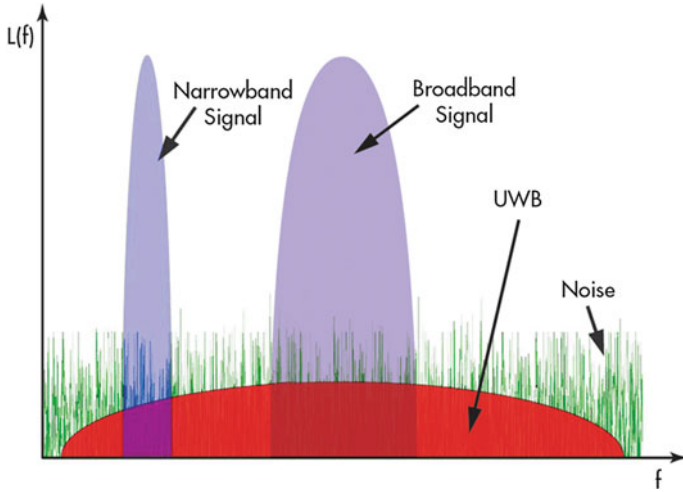


Fig. 2 Different types of spectrum available for communication

to reduce the power is pulsed transmission. In this mode, the IoT transmitter will not be ON for all the time, only when user will send the control information, the transmitted will be ON and rest of the time, transmitter will be on SLEEP mode. This is a well-established technology already present in TV remote control. This is why a battery of TV remote control runs over the year. One big aim of our research is to transfer this well-established technology into IoT devices. Pulsed transmission of the narrowband spectrum will maximize the battery life up to 10–15 years which turns IoT devices very environmental-friendly for green communication [3].

Living in the age of advanced wireless communication technology, the society is forwarding with the newly born requirements of cellular services which are not only confined in the periphery of Internet surfing, voice call but other significant issues. Presently, people are enjoying the VoLTE service provided by many of the Indian cellular service providers. Though the service providers have commissioned a large number of 4G/4G+ base stations throughout the country, the existing 4G band over 2.3 GHz uses a maximum of 20 MHz bandwidth for single-carrier technology. These base stations are designed to provide only mobile services (voice and data). But, cater to IoT services which are of control signals of very narrow bandwidths, future base station need to update in a way which can provide multiservice to the users. Basically, future base station will be going to provide broadband and narrowband spectrum simultaneously to support multiservice. Broadband spectrum will support mobile services like today and narrowband support future IoT needs. This narrowband spectrum can be inserted into the guard band or in band of the licensed 4G spectrum [4] (Fig. 3).

By installing the multi-purpose 4G LTE base station, the service provider is able to provide IoT services over the mobile network. But, keeping in mind about the future requirement of IoT devices to be installed throughout the country, it is already evident

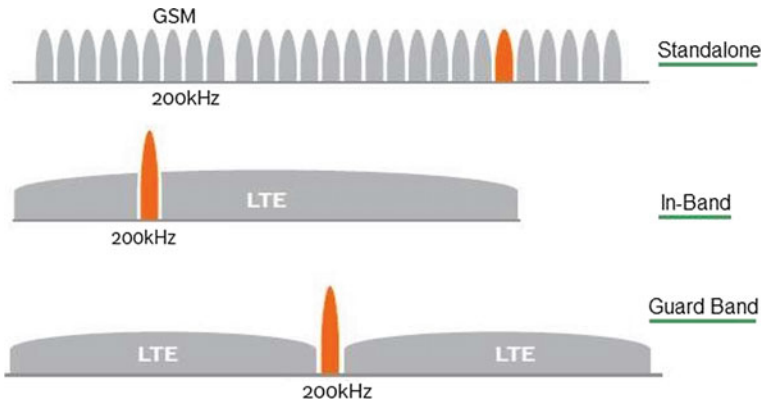


Fig. 3 Coexistence options for broadband and narrowband spectrum

by statistics that this much of LTE-A bandwidth will not be able to accommodate a large number of NB-IoT [5] devices which are going to be of the order of millions per cell. To accommodate the billions of IoT devices, within the country, the 4G/4G+ spectrum will not be sufficient in the future days. So, the authors have initiated the multipurpose base station design by introducing enhanced mobile broadband (eMBB) technology which is only possible by the revolutionary 5G communication technology [6].

In this paper, the major role of the authors is to develop multi-purpose base stations where one eMBB service is present for lightning speed multimedia and two different narrow bands IoT services have been integrated into the guard band of 5G eMBB spectrum. Multi-standard radio (MSR) base station development process is shown and discussed. In an MSR, transmitter and receiver are capable to process multiple carriers of different radio access technologies (RATs) simultaneously in a common active RF platform [7].

Finally, this base station will serve several Low power narrow band IoT devices which will be a very cost effective, low power consumed green communication system [8].

2 Background Motivation

Reliance Jio and Samsung's planned NB-IoT network is expected to be the first of its kind in the country. It will be designed to support a variety of consumer and enterprise use cases such as vehicle tracking, smart appliances, smart metering, security, and surveillance.

The NB-IoT network will utilize Reliance Jio's existing 4G/4G+ spectrum and base stations and will be supported by a new and dedicated Cellular IoT virtualized core.

The commercial NB-IoT network launched in Mumbai in February 2018 [9] and will soon be extended to other parts of the country. The Cat-M1/NB-IoT network will amplify opportunity for solutions such as smart metering for utilities, smart parking, smart bins, smart environmental sensors for smart cities, logistic solutions as well as other applications in agriculture and farming.

3 Model of Multi-Standard Radio

The multi-standard radio (MSR) [10] will be designed in the following way with the help of a signal combiner. The challenge is to combine multiple input signals with different sample rates, different characterization (carrier) frequencies, and different bandwidths into a single signal. So, the integration of three different signals is to be done in a software platform where the utility of specifying a row vector containing the desired set of sample rates, characterization RF carriers, bandwidths is important. The condition of specifying the sample rate is as below. Sample rate is an array parameter specifying the sample rate of each individual input signal. The order of the sample rate values in the array parameter must match the order of the input signals at the input multipoint. The similar condition will be adopted for specifying characterization RF carriers of each signal and bandwidth of each signal. The outgoing signal must be a single signal at the specified characterization frequency and sample rate. If the above conditions are fulfilled, the signal combiner [11] will be capable to automatically compute data flow production and consumption rates for individual input and output ports. Signal combiner resamples and recharacterizes the input signals to the output sample rate and output characterization frequency. It also synchronizes the resampled signals (due to different latencies introduced from different sample rates) before combining them into one signal. The combined signal is generated from the combined port characterized at output RF carrier (specified) and the output sample rate. Signal combiner also outputs each resampled and recharacterized signal at the output multipoint (characterized at output RF and the output sample rate). The order of the output signals from the output multipoint is in the same the order as the input signals at the input multipoint (Figs. 4, 5 and 6).

Following Eq. (2) depicts up conversion of baseband signal to RF via phase modulation

$$s(t)_{\text{FM}} = A_c \cos \left(2\pi f_c + 2\pi k_f \int_0^t m(t) \cdot dt \right) \quad (1)$$

$$s(t)_{\text{FM}} = A_c \cos \{ 2\pi (f_c + k_{f,q}) \cdot t \} \quad (2)$$

where f_c = carrier frequency and $k_{f,q}$ = frequency factor.

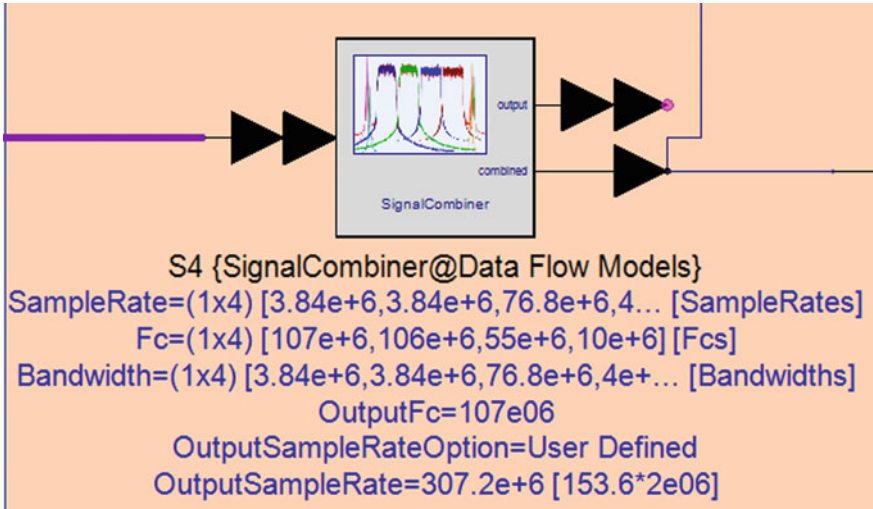


Fig. 4 Up conversion of baseband signal to RF via phase modulation

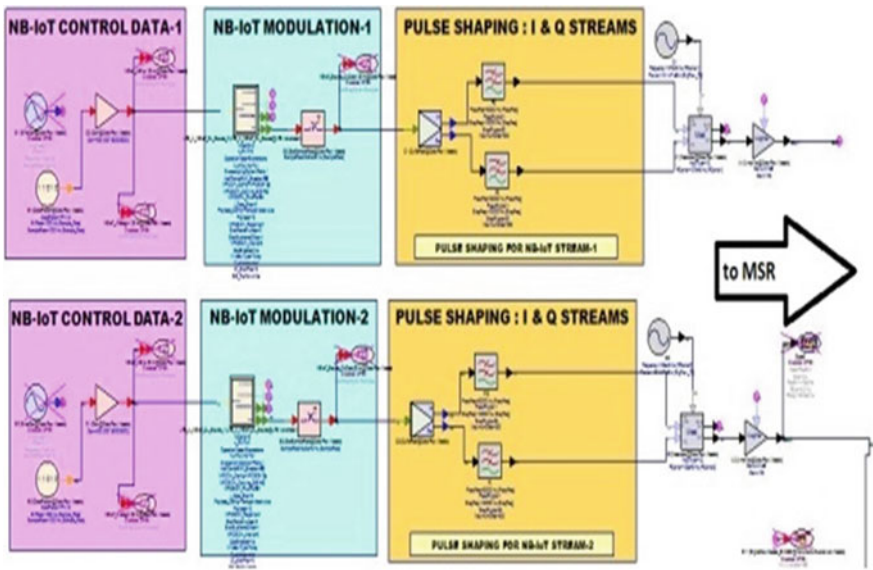


Fig. 5 NB-IoT signals generated in SystemVue, Keysight Technologies, Inc.

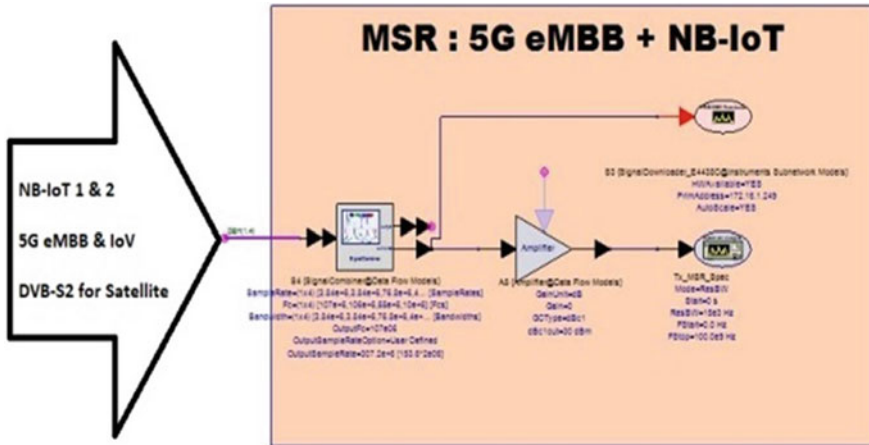


Fig. 6 All signals for respective services sent to MSR for dumping into VSG

4 Multi-Services Base Station Design, “NB-IoT as a Service”

To design a 5G-IoT base station with multiple services, a model is to be developed. Using the programming platform, three individual spectrums will be generated by following the 3GPP 5G-NR standard. The model will integrate the three services (i) 5G enhanced mobile broadband (eMBB) for faster Internet, (ii) Narrowband-IoT-based massive machine-type communications service for smart lamp control, and (iii) Narrowband-IoT-based massive machine-type communications service for smart fan control. The individual spectrum’s bandwidth is different and their corresponding sampling rates are also different. So, at the next step, a vector is to be settled containing the bandwidths, desired sample rates, and RF carriers for three different services to be undergone by multi-radio combiner functionality. Finally, the PHY layer will outcome a combined RF spectrum centered at the final characterization RF carrying three individual spectrum [12, 13] (Figs. 7 and 8).

4.1 NB-IoT Service Toward Green Communication

The advent of digital communications systems has led to the development of the vector signal generator, which is also known as a digital signal generator. These signal generators are capable of generating digitally modulated radio signals that may use any of a large number of digital modulation formats such as QAM QPSK, FSK, BPSK, and OFDM. The vector signal generator (VSG) used in the project is Agilent N5182A (100 kHz–3 GHz) MXG [14] and it is deployed as the 5G base stations. The basic digital modulation format used for NB-IoT signals is QPSK.

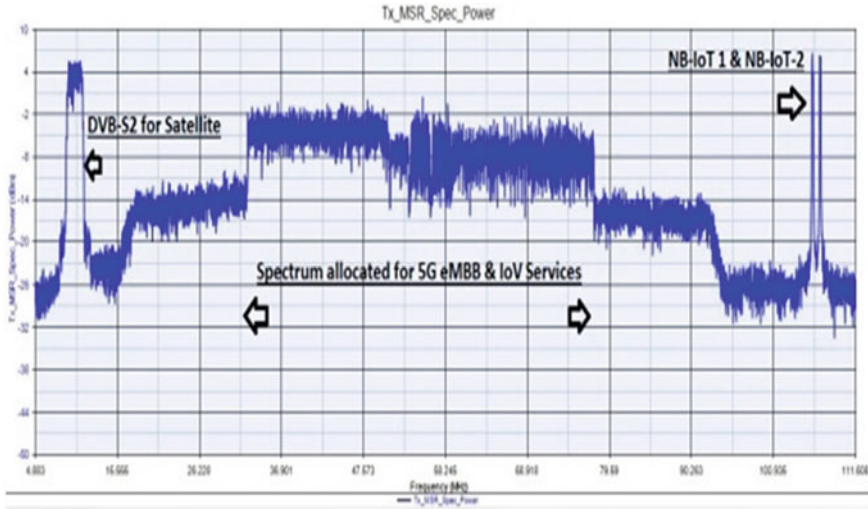


Fig. 7 The frequency spectrum of the signals sent for NB-IoT, eMBB & IoV and DVB-S2 services from 5G base stations



Fig. 8 4-in-1 multi-purpose 5G base station

Since 3GPP standard for NB-IoT has been followed, the basic 180 kHz bandwidth modulated data is underrun by OFDM and sent over radio frequencies 106 and 107 MHz in the guard bands of 55 MHz center frequency of Verizon standard 5G spectrum. The signals for the services NB-IoT 1 and 2, eMBB and IoV and DVB-S2 are multiplexed and transmitted from the VSG (Fig. 9).

The base station sends 180 kHz baseband NB-IoT signal over 107 MHz RF. Since this is in the range of FM radio (87–108 MHz), the signal is demodulated with the help of FM receiver and acquired by the server. Parallel, the analog signal is passed

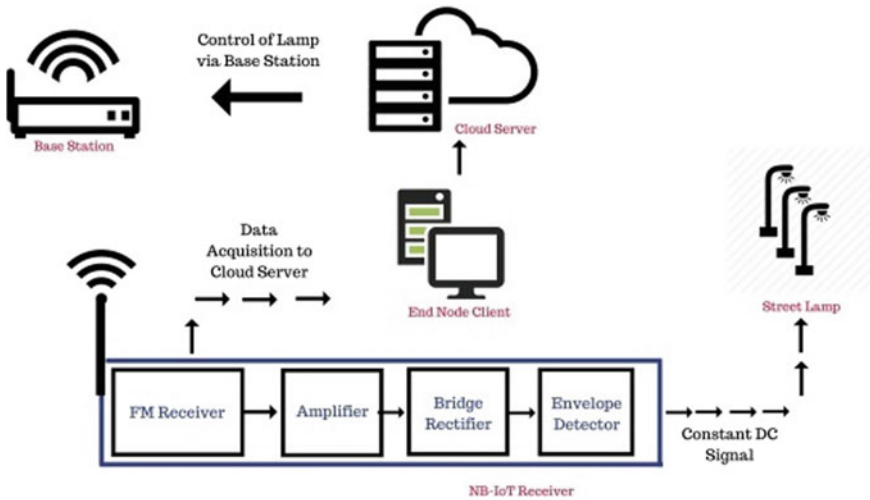


Fig. 9 Schematic for NB-IoT lamp

through a cascade of LM-741 op-amps for linear amplification. After that, it is sent to bridge rectifier and envelope detector circuit for AC to DC conversion which in turn drives a relay for turning the lamp ON and OFF (Fig. 10).

4.2 NB-IoT Over Millimeter Wave

It is a parallel development of standalone NB-IoT base station over millimeter-wave frequency. The modeling of narrowband Internet of things is done in Keysight SystemVue and the waveform achieved from this model is passed through the signal downloader (a part selector block available in the SystemVue library). The designed waveform is tested first in the simulation platform and validated through simulation to generate the bandwidth of 20 kHz. Using the Keysight Electronic Design Automation (EDA) tool, this method of validation helps to know about the performance of the NB-IoT spectrum. The characteristics of the waveforms can be analyzed in this simulation platform before sending it to the arbitrary waveform (ARB) memory of the actual hardware. Here, the generation side involves an Agilent vector signal generator which accepts the downloading of the designed waveform (from SystemVue platform) to the dynamic sequencing memory of the VSG. Once the waveform is downloaded into the ARB memory, the VSG will transmit the baseband samples through its In-Phase (I) and Quadrature Phase (Q) output. The I/Q OUT port signal is connected to the Mic input of the CPU-1 where a MATLAB script has been designed to capture the NB-IoT samples from the Mic In port and delivering it to the ethernet port of the same CPU by using MATLAB TCP-IP embedded function. Then, the signal gets in through the LAN-IN port of a Power Over Ethernet (PoE) adapter and coming out



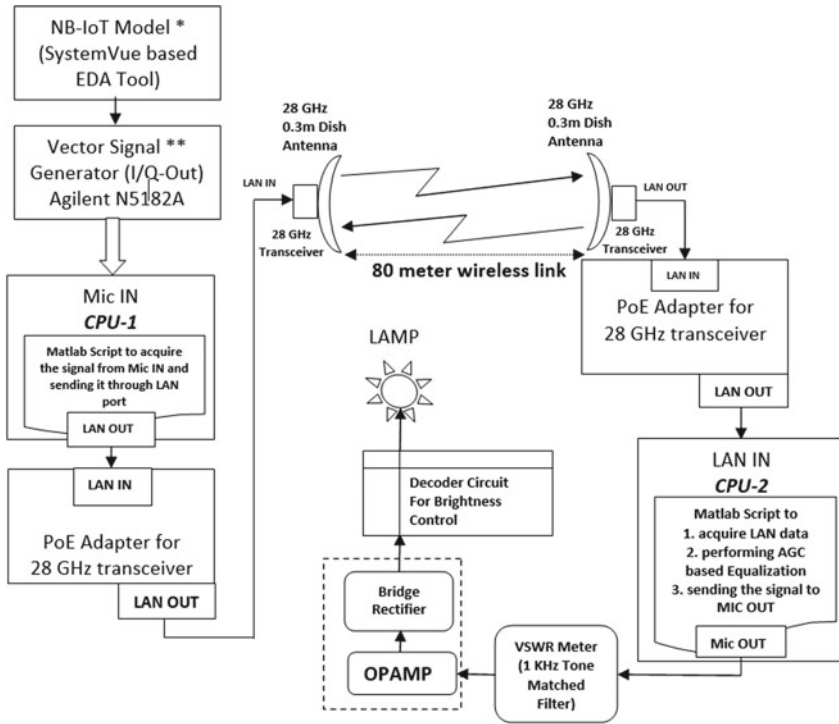
Fig. 10 NB-IoT smart lamp

of its LAN-OUT port. The same signal is directly inserted to the ethernet input of the 28 GHz transceiver where the digital modulation is done followed by the RF upconversion. The RF is radiated through a 0.3 m diameter dish antenna.

This NB-IoT waveform over 28 GHz is propagated over an 80 m wireless link (Fig. 11).

At the receiver side, another 28 GHz dish antenna receives the waveform and the 28 GHz transceiver down converts it into a baseband signal which is passed through Ethernet cable to the Ethernet port of CPU-2. A MATLAB script runs in the CPU-2 to accomplish the following activities. (i) To acquire the LAN data, (ii) To perform the auto-gain control (AGC)-based equalization and (iii) sending the signal to Mic Out.

After this, the narrowband signal is directly given to the input of a VSWR meter from which the integrated DC output comes out. The VSWR meter acts as the 1 kHz matched filter which helps to achieve a fluctuating DC output voltage carrying the signature of only 1 kHz baseband PRF code. This baseband code is fed to the input of an OPAMP for its amplification and passed through the bridge rectifier circuit to



* NB-IoT Model is designed in Keysight SystemVue. Its waveform is downloadable to Arbitrary waveform memory of VSG through Signal Downloader

** VSG is having the dynamic sequencing feature to play the downloaded waveform in its Arbitrary waveform memory

Fig. 11 Block diagram of NB-IoT system using 28 GHz millimeter wave

have a nearly steady DC voltage which is given to the relay circuit. If the DC voltage appears to the relay, the lamp will be glowing ON with certain brightness. A decoder circuit is inserted before the lamp for decoding the 1 kHz PRF signal. Depending upon the extracted code pattern, the brightness of the lamp is controlled.

5 Summary/Conclusion

Narrowband communication and broadband communication are two very useful techniques in today's world for sending information from one end to another. More information needs broadband spectrum to accommodate data chunks. Broadband communication causes more energy consumption in electronic circuitry. In case of control signal transmission, data chunks are less which is only for device control and

this type are communication is possible using very narrow band spectrum allocation. Narrow band spectrum consumes very less energy compare to broadband spectrum which increases the battery life for the IoT devices and also heat or carbon emission is very less which is a very good step toward green communication. Another advantage of this system is the pulsed mode communication. In this pulsed mode communication, transmitter is not always ON, it kept it in sleep mode always. When the control signal is sent by the user, then only the device get active and transmission will take place. The power consumption is high at this time only; when transmission is not there, the device will consume the minimum power and save lots of energy in term of battery life. In this type of system, battery life is expected to be 10 years or more. This type of systems is very much environment-friendly green system and will leads the future devices toward green communication.

Acknowledgements The authors are thankful to Dr. Ramdas Pai and Mrs. Vasanthi Pai Endowment Fund, for giving Project on 5G-IoT, which is running under Center of Excellence of Electronics and Communication Department, SMIT. Authors are also thankful to Honorable Vice Chancellor, SMU, Director SMIT, and all members of SMU family for their continuous support.

References

1. <https://www.statista.com/statistics/471264/iot-number-of-connected-devices-worldwide/>
2. GSMA Industry Paper, Mobile Internet of Things low power wide area connectivity. Access <https://www.gsma.com/iot/wp-content/uploads/2016/03/Mobile-IoT-Low-Power-Wide-Area-Connectivity-GSMA-Industry-Paper.pdf>
3. Andres-Maldonado P, Ameigeiras P, Prados-Garzon J, Navarro-Ortiz J, Lopez-Soler JM (2017) NarrowBand IoT data transmission procedures for massive machine type communications. *IEEE Netw* 31(6). <https://doi.org/10.1109/MNET.2017.1700081>
4. Ratasuk R, Tan J, Mangalvedhe N, Ng MH, Ghosh A (2017) Analysis of NB-IoT deployment in LTE guard-band. In: 2017 IEEE 85th vehicular technology conference (VTC Spring), NSW, Sydney, pp 1–5. <https://doi.org/10.1109/VTCSpring.2017.8108184>
5. 3GPP TS 36.211 (2016) E-UTRA physical channels and modulation–chap.10, Narrowband IoT
6. Chen M, Qian Y, Hao Y, Li Y, Song J (2018) Data-driven computing and caching in 5G networks: architecture and delay analysis. *IEEE Wirel Commun* 25(1)
7. 3GPP TR 37.900 V12.0.0 (2014-09) 3rd generation partnership project; Technical specification group radio access network; Radio frequency (RF) requirements for multicarrier and multiple radio access technology (Multi-RAT) base station (BS) (Release 12)
8. De Sanctis M, Cianca E, Joshi V (2011) Energy efficient wireless networks towards green communications. *Wirel Pers Commun* 59:537. <https://doi.org/10.1007/s11277-011-0244-4>
9. MWC 2018: Jio joins hands with Samsung over new IoT network in India: <https://www.indiatoday.in/technology/news/story/mwc-2018-jio-joins-hands-with-samsung-over-new-iot-network-in-india-1178384-2018-02-27>
10. Dogaru E, dos Santos FV, Rebernak W (2013) A RF BIST architecture for output stages of multistandard radios. In: 2013 military communications and information systems conference, St.-Malo, pp 1–8
11. Neog P, Bera R (2017) Multi-standard radio for 2G to 5G. In: 2017 2nd international conference on telecommunication and networks (TEL-NET), Noida, pp 1–5. <https://doi.org/10.1109/TEL-NET.2017.8343496>

12. Rates Crippa M, Arnold P, Friderikos V, Gaji B, Guerrero C, Holland O, Labradork I, Sciancalepore V, von Hugo D, Wong S, Yousaf FZ, Sayad B, Resource sharing for a 5G multi-tenant and multi-service architecture. Researchgate (Preprint)
13. Bockelmann C et al (2018) Towards massive connectivity support for scalable mMTC communications in 5G networks. IEEE Access 6:28969–28992. <https://doi.org/10.1109/ACCESS.2018.2837382>
14. <https://www.keysight.com/en/pd-797248-pn-N5182A/mxg-rf-vector-signal-generator?cc=US&lc=eng>
15. Khatun F, Islam MR (2018) Security in cloud computing-based mobile commerce. In: Advances in electronics, communication and computing. Lecture notes in electrical engineering, vol 443. Springer Nature, Singapore Pte Ltd. https://doi.org/10.1007/978-981-10-4765-7_20

Design and Prototype Implementation of a Renewable Energy-Powered Home with Home Automation System Using Internet of Things (IoT)



Dherendra Bhattarai, Amit Kumar Singh, Sanjeev Newpaney,
and Pawan Pyakurel

Abstract This paper presents a design and prototype implementation of a renewable energy-powered home with a basic home automation system using Internet Of things (IoT). The proposed system consists of two main parts; The first part consists of renewable energy (solar) power system where the power supplied to the house is produced from solar panel(s), which will be supplied to an inverter through a MPPT-based solar charge controller. A battery has been used in the system as a backup power supply which will be charged with the help of the charge controller. The excess power generated (when no home appliances are used and the battery is fully charged) will be supplied to the power grid or will be used to run an external AC motors such as water pumps. The second part consists of home automation using Internet Of things (IOT) using a Wi-Fi interface and an android application BLYNK. With the help of the mentioned android application BLYNK, the user will be able to know the current status of the lights and other electrical appliances of their house, whether the lights and other electrical appliances are turned on/off, and can remotely turn on/off the appliances and lights. The home automation in this prototype is focussed on the parts only where most of the energy could be wasted when we forget to turn off the lights, fan and power plugs while leaving the house and could be turned on/off remotely through an android app. The two subparts of the design will be finally combined to make a renewable energy-based smart home. Unlike the costly and sophisticated home automation systems available in the market, this design is cheap and simple, and can be easily implemented in our home.

D. Bhattarai · A. K. Singh (✉) · P. Pyakurel
Department of Electrical and Electronics Engineering, Sikkim Manipal Institute of Technology,
Sikkim Manipal University, Sikkim, India
e-mail: amit.s@smit.smu.edu.in

D. Bhattarai
e-mail: dherendra1993@gmail.com

P. Pyakurel
e-mail: pawan.p@smit.smu.edu.in

S. Newpaney
Department of Mechatronics, Advanced Technical Training Centre, Sikkim, India
e-mail: sanjeevnewpaney@yahoo.co.in

Keywords MPPT · IoT · BLYNK · Home automation · Buck converter · Photovoltaic (PV)

1 Introduction

When we think about renewable energy, the first image that comes to our mind is often large solar panels on rooftops. The solar panels, also known as photovoltaic (PV) modules, convert sunlight into electricity, and have been the backbone of renewable energy for years [1]. In very recent years, solar energy has gained wide popularity as an alternative way to produce electricity.

The Internet of things, commonly known as IoT, is an extension of connectivity of Internet to daily used objects, machines, people, animals, or things at our homes or any other place that have the ability to transfer and transmit data via a network without requiring any other means.

This project aims to design and implement a prototype of a renewable energy-powered home with a basic home automation system using Internet Of things (IoT). Here, an Arduino board will be used as the main controller of the system. A Wi-Fi module will be interfaced with the Arduino board so that the system can be controlled remotely via Internet and also when the solar battery gets fully charged, the excess energy form the solar panel could be used for other purposes like charging other batteries or running a motor, etc.

1.1 Literature Review

In this advancing world, advancement in wireless technologies is also growing rapidly. This swift development influences a person to use mobile phones. Implementation of wireless technologies and advanced home automation systems makes easier for people to control home appliances and especially, for disabled people [2]. Home automation is a challenging topic. The developer needs to make the system as per the user necessity. Since the user demand varies from person to person, developers of home automation face challenges on every system they develop. A paper proposed by Shopan Dey, Ayon Roy and Sandip Das on “Home Automation Using Internet of Thing”, we found that they were able to control various devices through webpage and android application with the help of Wi-Fi module connected to Internet and Raspberry pi as a controller [3].

Grid-connected inverters reduce a lot of energy bill at our homes and have a high reliability. A project design proposed by “Yanfeng Shen, Huai Wang, and Frede Blaabjerg” on reliability-oriented design of a “Grid Connected Photovoltaic Micro inverter” is found to have high reliability performance of grid-connected microinverters. To decrease the required maintenance and cost, reliability allocation is performed from the requirement of the system level to the component-level design objective [4].

The main quality of the new inverter topology is that it provides a larger AC output voltage compared to the DC input voltage, depending on the duty cycle at an instant. This quality of inverter is not found in the typical voltage source inverters, in which the DC input voltage is always higher than the AC output voltage. A sliding mode controller is proposed for enhancing the boost inverter dynamics, to work accurately in any working condition, with an advantage of control over the classical control robustness for changing plant parameter, which leads to non-changing dynamics and steady-state response in ideal running condition. The new inverter is proposed to be used in systems where a larger output AC voltage is needed to be compared with the input DC voltage [5].

Today, maximum photovoltaic models either do not precisely model the changing parameters of the maximum power point trackers, or they include extreme computations for this application. To solve this problem, a MATLAB/Simulink model of a single-phase grid-connected photovoltaic inverter was developed and tested by Michael E. Ropp, and Sigifredo Gonzalez. The development of the photovoltaic array, the integration of the MPPT algorithm with a DC–DC converter averaged model, and the Simulink design are discussed in their paper. It was experimentally shown and explained that the averaged model works properly for the prediction of general nature and performances of single-phase grid-connected photovoltaic systems [6]. A research paper on “Optimization of perturb and observe maximum power point tracking method” shows a theoretical study permitting the ideal selection of the two main parameters describing the Perturb and Observe algorithm, where as an example, a boost DC–DC converter has been examined [7].

The study of above-mentioned projects and papers have helped us to design and develop a prototype that could make a reliable and cost-saving renewable energy-based home automation-based using Internet Of things (IoT). This project is focussed on renewable energy and IoT because of their various advantages. Some of them are mentioned below:

Some basic advantages of using renewable energy are [8]:

- Renewable energy is sustainable and will never run out.
- It is cheaper or free once the system is installed. Only the initial installation cost is high.
- It produces little or no waste like carbon dioxide and other pollutants, so no harm is caused to the environment.

Some basic advantages of home automation are [9]:

- Power saving—When electrical appliances are left switched on while we are away from home, we can turn the appliances off remotely via a mobile application.
- Convenience—switches and appliances can be turned on/off using a mobile app from anywhere.
- Control—we can get information on which appliances/switches are on/off at anytime from anywhere and can control them.

These are just some of the basic advantages based on the prototype discussed in this paper. Other than these advantages, there are a lot more advantages of using renewable energy and home automation system. Keeping the advantages and cost factor in mind, an efficient system has been designed and discussed in this paper.

2 Proposed System Design

Figure 1 shows the basic proposed design of the prototype. Here, in this project, the battery is charged form a solar panel through a MPPT-based charge controller. The DC current of the battery is converted into AC current with the help of an Inverter. The driver unit consists of relays, optocouplers, etc. The inverter supplies the AC power to the load through the driver unit. The controller used here is an Arduino mega board. The battery and the controller are connected through driver unit for the purpose of battery feedback to the system so that the battery is cut-off from the charging unit after the battery is fully charged. The load block consists of fans and bulbs of the house. The controller is connected to a Wi-Fi module which will help in remote controlling of the system through Internet via an android application BLYNK. The system is also designed to feed the excess-generated power to other external batteries or to run a motor or to the grid.

A detail and sequential hardware design procedure according to the above block diagram of the prototype are discussed below.

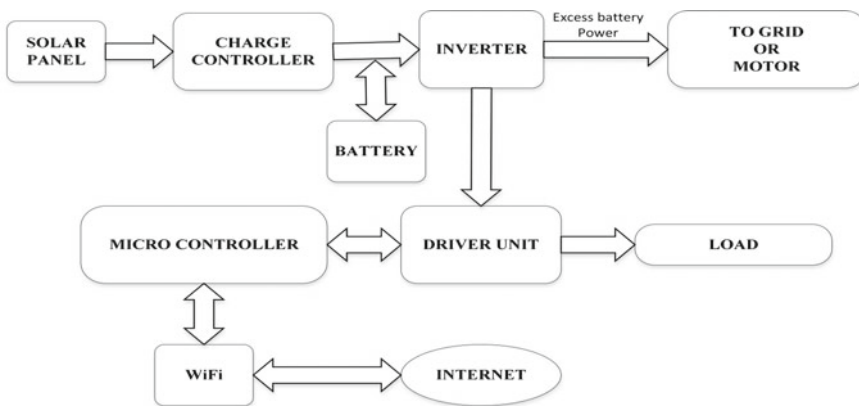


Fig. 1 Block diagram of proposed system

2.1 Charge Controller with Maximum Power Point Tracking (MPPT)

See Fig. 2.

2.1.1 Maximum Power Point Tracking (MPPT)

MPPT or maximum power point tracking algorithm is used to get a maximum output power from the photovoltaic panel. The MPPT algorithm basically helps to match the input impedance of a PV system with its output impedance to get a maximum power output. The relationship between output power, voltage and current of a PV cell is complex, thus producing a non-linear output. This output is shown as the current–voltage characteristic of the PV cell. With changes in outside conditions such as irradiance and temperature, the V–I curve shifts upwards and downwards. The output voltage of a PV cell is inversely proportional to the change in temperature and the output current change is directly proportional to the change in irradiance [10].

There are several types of MPPT methods: perturb and observe method (commonly known as P&O method), current sweep method, constant voltage method, temperature method, incremental conductance method, etc. But perturb and observe method is most commonly used method. In P&O method, the controller measures the power by adjusting the voltage by a small amount from the array, if the current power is greater than the previous power, the controller again tries for the next step in the same direction until the power stops increasing. This method is also known as hill-climbing method.

MPPT is basically applied to a DC–DC converter connected to the solar panel. Here, in this design a DC–DC boost converter has been used with an Arduino UNO as a controller. The flowchart in Fig. 3 describes the MPPT algorithm used in this project.

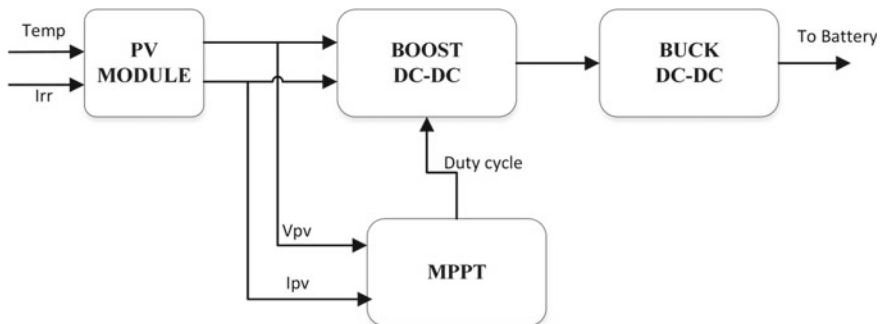


Fig. 2 Block diagram of charge controller

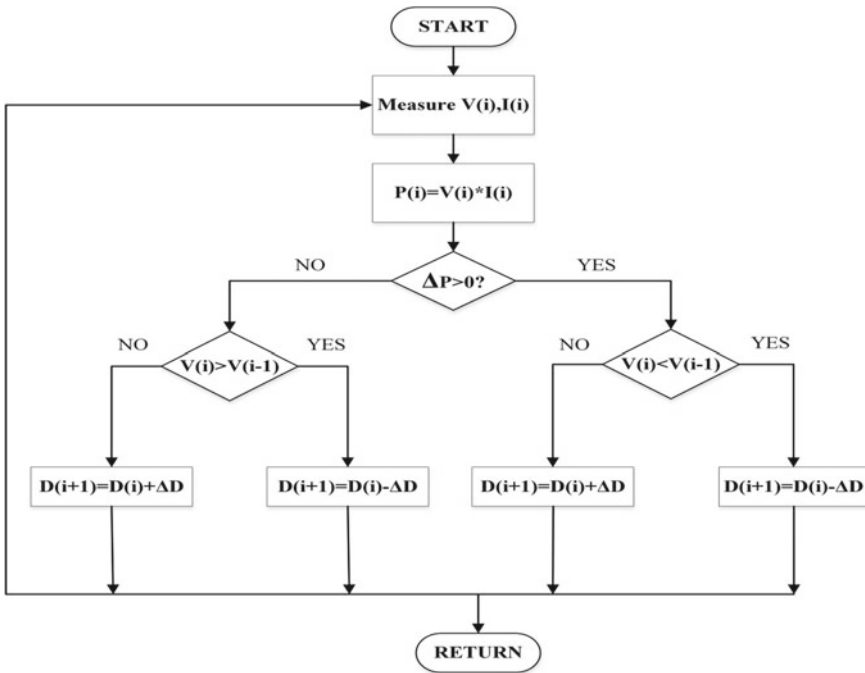


Fig. 3 MPPT (Perturb and Observe algorithm)

2.1.2 Boost Converter with MPPT

Figure 4 shows the circuit diagram of a boost DC–DC converter with an inductor and a capacitor of 12 mH and 2200 μf, 63 V, respectively. The boost converter input is supplied from the 12 V 35 W solar panel, through a current sensor and a voltage sensor in between. Here, a current sensor (ACS712) and a voltage sensor

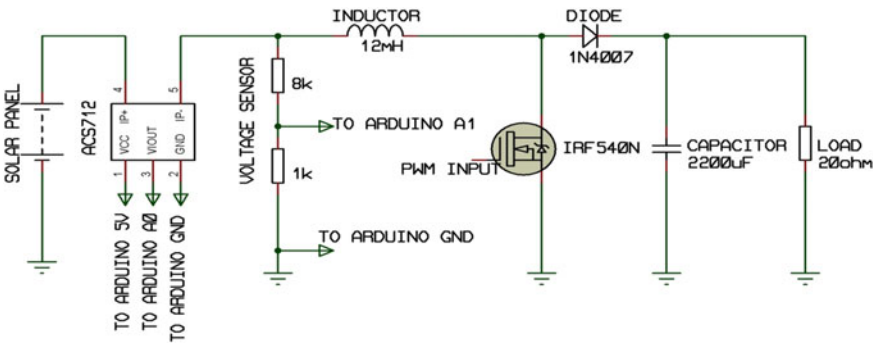


Fig. 4 Boost converter with current and voltage sensor

(Voltage divider) have been used to sense the current and voltage from the solar panel and provide the sensed voltage and current as inputs to the analog pins of the microcontroller (Arduino UNO). The MOSFET driver used in this schematic is an optocoupler (MCT2E).

The output voltage equation of the boost converter is given by:

$$V_{out} = \frac{V_{in}}{1 - D}$$

where

V_{out} the output voltage of the converter.

V_{in} the input voltage of the converter.

D the duty cycle of the PWM signal.

Here, the input voltage and duty cycle (D) cannot be controlled as they depend on the MPPT algorithm which tries to retain the output power of the PV panel at its maximum by changing the duty cycle of the pwm gate signal of the mosfet during varying external factors like temperature and irradiance of the panel, so the output voltage of the boost converter cannot be kept at a constant output voltage. So we need to cascade a DC–DC converter with the boost converter for a constant output voltage for battery charging. In this prototype, a closed-loop buck converter is designed and placed in cascade with the boost converter to give a constant output voltage of 13.8 V for charging the battery.

2.1.3 Closed-Loop Buck Converter

Figure 5 shows a closed-loop buck DC–DC converter with an inductor and a capacitor of 12 mH and 2200 μ f, 63 V, respectively. The input to the buck converter is the unregulated output of the boost converter. Here, two voltage sensors (Voltage divider), one at the input side and one at the output side, have been used to sense the voltage

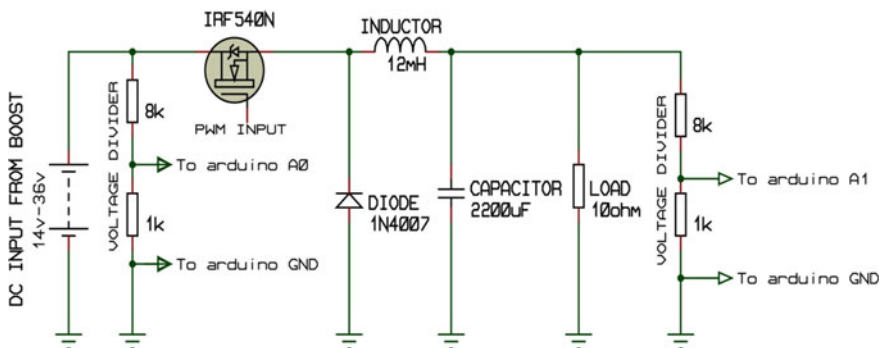


Fig. 5 Buck converter in closed loop

at the input and output of the converter, respectively, and adjust the duty cycle of the pwm gate signal to get a constant battery charging voltage of 13.8 V at the output. The output voltage equation of the buck converter is given by:

$$V_{out} = D \times V_{in}.$$

where

- V_{out} the output voltage of the converter.
- V_{in} the input voltage of the converter.
- D the duty cycle of the PWM signal.

The flow chart of the closed-loop buck converter is given in Fig. 6:

Thus, by combining two DC–DC converters in series (one for MPPT and the other one for constant output), the charge controller for 12 V battery is made and an output voltage of 13.8 V was obtained for successful charging of the battery.

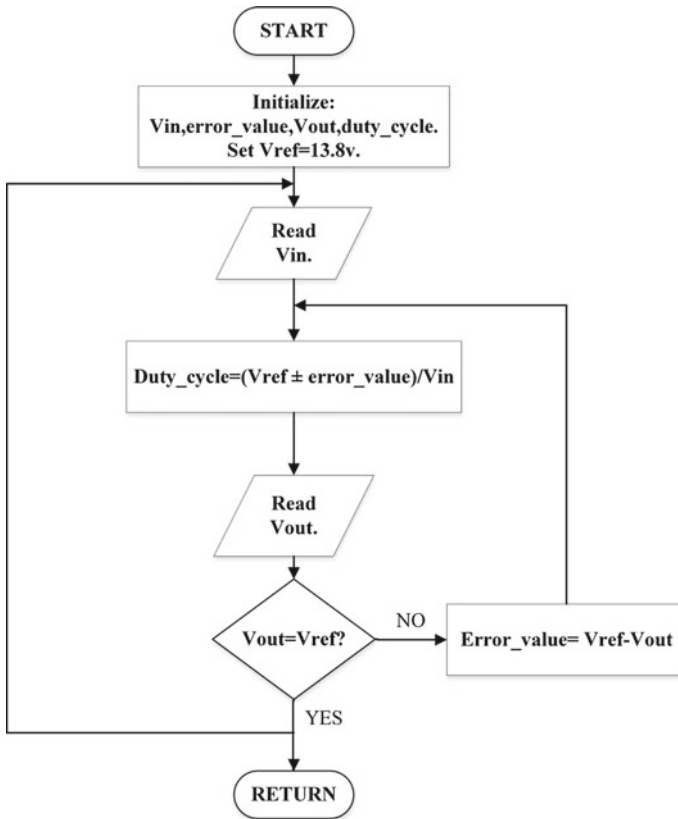


Fig. 6 Flowchart of closed-loop buck converter

The DC voltage of the battery now needs to be converted to AC to use it to power our electrical home appliances. For this, an inverter has been designed which will convert 12 V (DC) to 220 V (AC) with 50 Hz frequency.

2.2 Inverter Using IC CD-4047

Figure 7 shows a full wave inverter using a monostable/Astable multivibrator IC CD4047. The main purpose of this IC (CD4047) is to generate a square wave output of 50/60 Hz frequency for the inverter as because our household items work at this frequency. The frequency calculation for IC CD4047 is given by:

$$f = \frac{1}{4.4 \times R \times C}$$

where

$$R = 19 \text{ k}\Omega$$

$$C = 0.22 \text{ }\mu\text{F}$$

$$f = \frac{1}{4.4 \times 19 \times 10^3 \times 0.22 \times 10^{-6}}$$

$$= 54.37 \text{ Hz @ } 50 \text{ Hz (approx).}$$

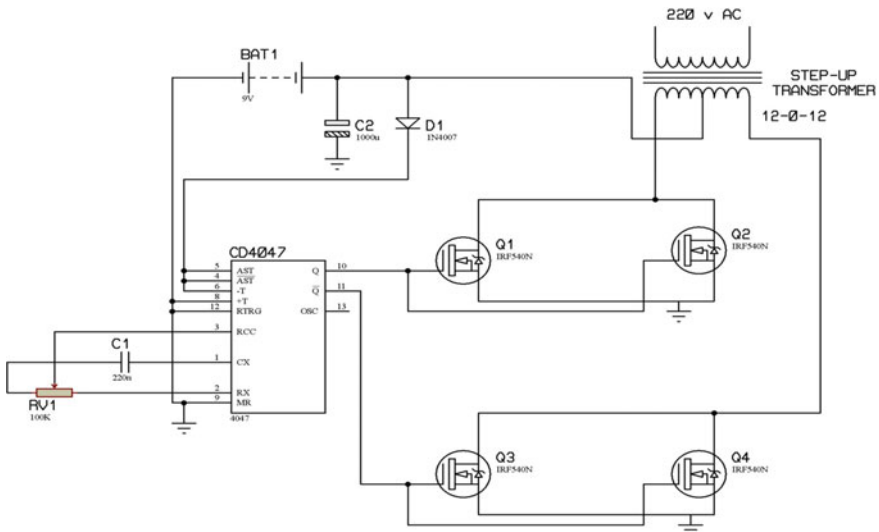


Fig. 7 Full Bridge inverter using CD4047

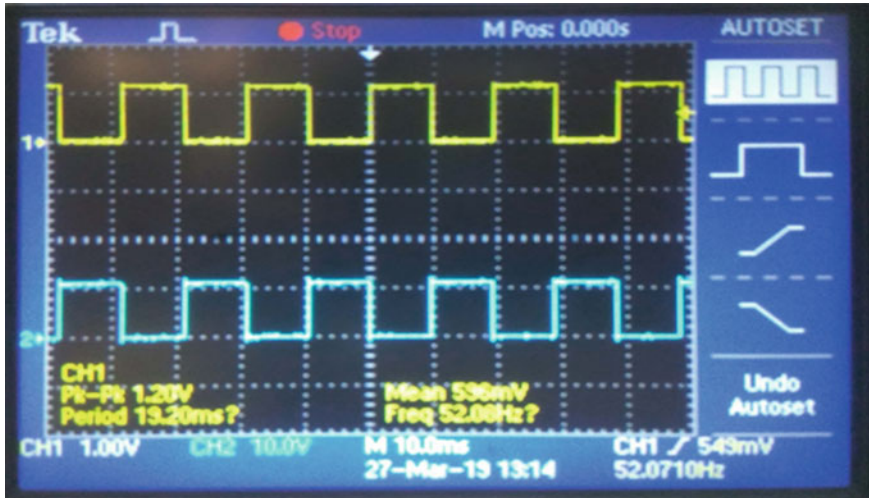


Fig. 8 Output waveforms of CD 4047

The IC CD4047 generates two square wave output from pin no. 10 and 11. The two square waves are of opposite polarities as shown in Fig. 8.

The full bridge inverter in the schematic model above consists of four numbers of Mosfets. The two generated square pulses are used as gate signals to Q1–Q2 and Q3–Q4, respectively. The DC voltage of 12 V is supplied to circuit through IC CD4047. The mosfet pairs [Q1, Q2] and [Q3, Q4] are turned ON and OFF alternately in a complementary manner at a frequency of 50 Hz.

A 12–220 V centre-tapped step-up transformer is connected at the drain terminals of the two mosfet pairs with its centre tap wire connected to the positive terminal of the battery. This inverter is able to power a load of 100 (approx.) watts at the output.

The AC loads to the inverter are connected to a Wi-Fi controlled home automation system where the household AC loads are turned ON/OFF using BLYNK framework with an android application—BLYNK.

2.3 Home Automation Using BLYNK

Figure 9 shows the connection and implementation of the home automation system. Here, an Arduino MEGA is used as a controller, a Wi-Fi module (ESP8266) is interfaced and connected to the controller so that the controller could be connected to the Wi-Fi of our house. An android application called BLYNK needs to be installed in the phone of the user. The user needs to create a BLYNK account with a unique network name and password and also enter the Wi-Fi module authentication code. The Wi-Fi of our house should be connected to the Internet in order to use this application to control the switches of the house. The Arduino Mega controller is

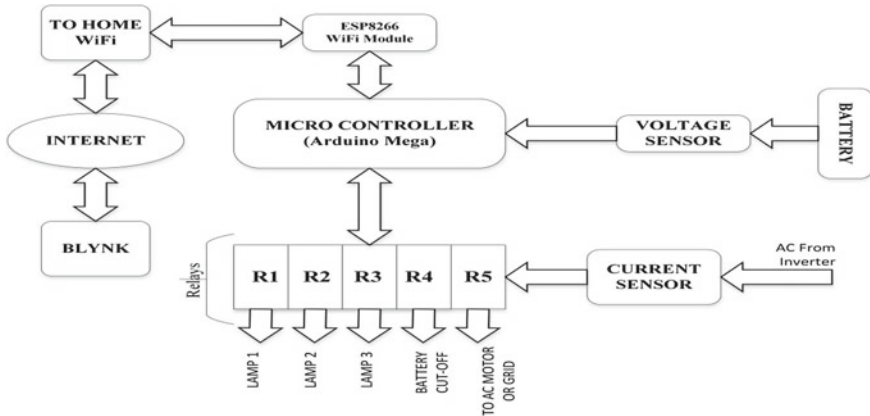


Fig. 9 Home automation using BLYNK

connected with five relay modules as shown in the block diagram above. The first three relays (R1, R2 & R3) are connected to lamps or switches, the fourth relay (R4) has been used as a circuit breaker when the voltage sensor senses full charge in the battery such that the solar panel voltage is directly fed to the inverter through the charge controller and the battery could be kept as a backup source. The relay R5 is the main relay in which is connected to a current sensor and supplies power to the other four relays. The relay R5 switches to grid supply or external AC motor load (for example: water pumps) when no load is used at the house, i.e. no current is drawn at the house hold load.

3 Hardware Fabrications and Connections

See Figs. 10, 11 and 12.

4 Output Results

4.1 Charge Controller with MPPT

The above three graphs show the output of boost converter with MPPT. The first graph (Fig. 13) shows the output power of the solar panel, the second graph (Fig. 14) and the third graph (Fig. 15) show the output voltage and output current of the solar panel, respectively. We can clearly see that with the MPPT algorithm even during large fluctuations in output voltage and current, the output power of the solar panel has low ripple as compared to the voltage and current graphs and is moreover kept at

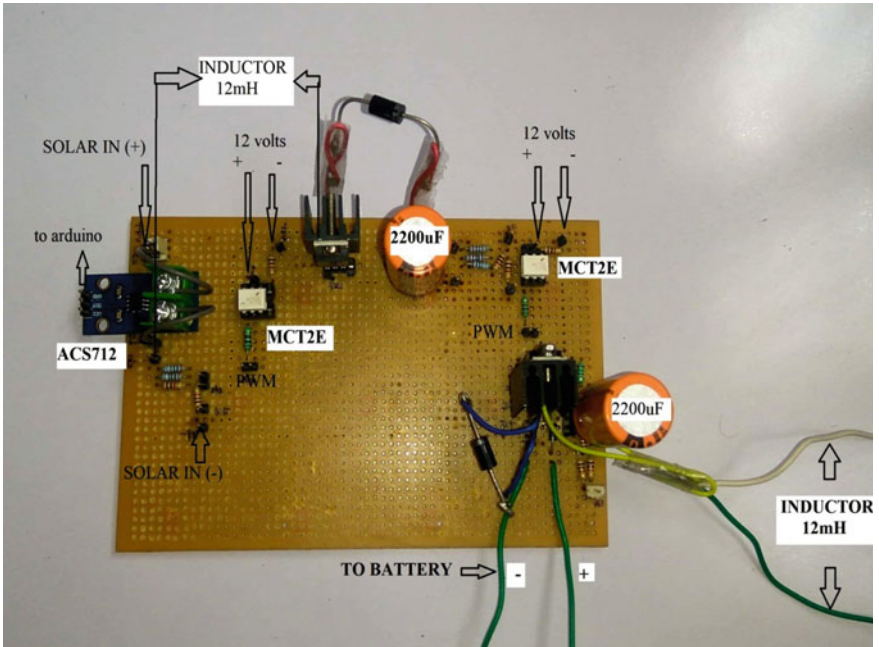


Fig. 10 Charge controller hardware

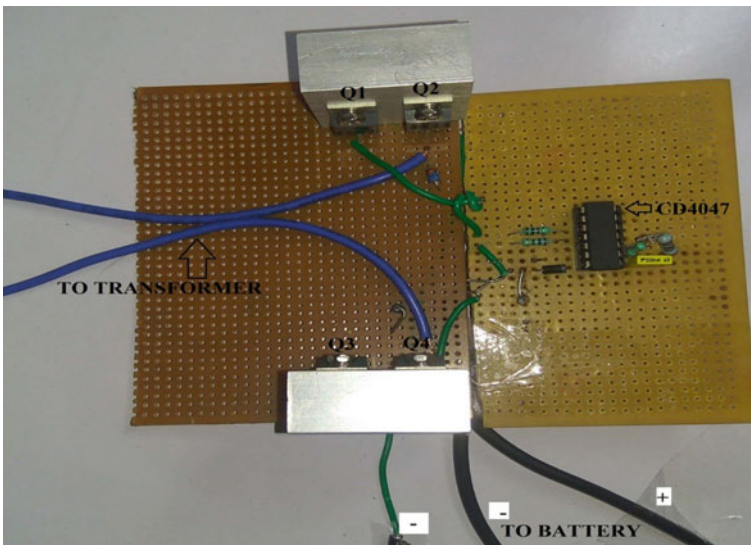


Fig. 11 Inverter hardware

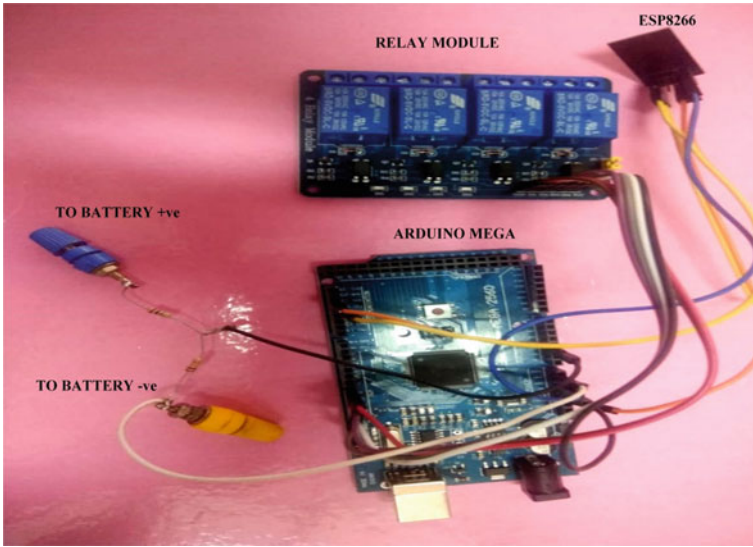


Fig. 12 Home automation hardware

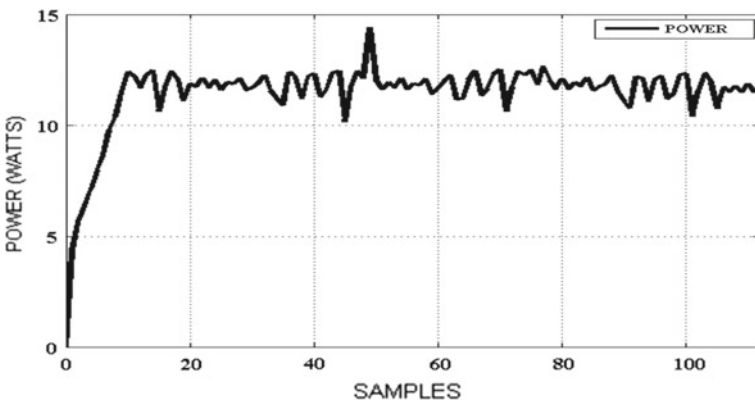


Fig. 13 MPPT (Power)

a constant range or at a maximum power with respect to the corresponding voltage and current at any instant.

4.2 BLYNK Application Screen

Figure 16 shows the screenshot of the android application BLYNK. Here, it shows the current battery voltage level as 12 V (i.e. the battery is fully charged) and three

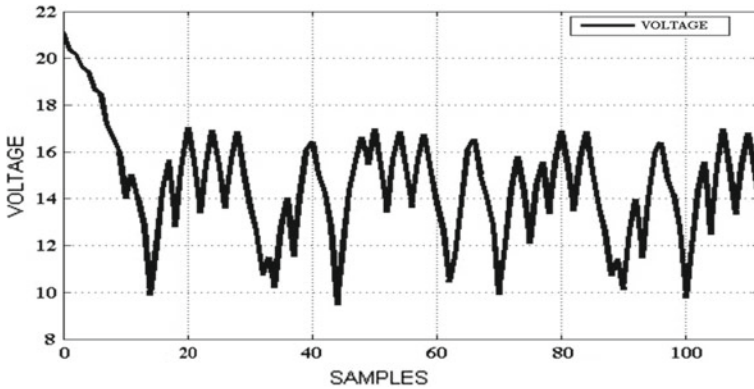


Fig. 14 MPPT (Voltage)

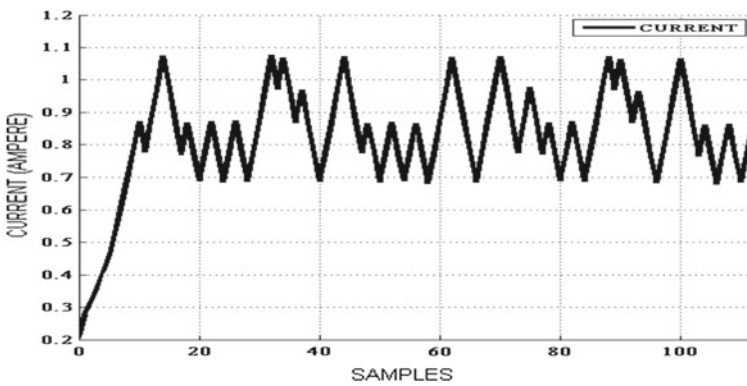


Fig. 15 MPPT (Current)

switches, namely LIGHT1, LIGHT2 and LIGHT3 where all the switches are turned ON. The user can remotely monitor the status of switches via this application and can accordingly turn ON/OFF switch(s) according to his requirement.

5 Summary/Conclusion

The prototype design and implementation of the renewable energy-based home automation system using IoT were successful. The MPPT results shown above were obtained on a cloudy day but using the MPPT algorithm helped us to get a constant power of 12–13 W at the output of charge controller even with a small solar panel of 12 V 35 W. The inverter using CD4047 IC produces a square wave at the output, so some noises are produced at the transformer due to the square wave. However,

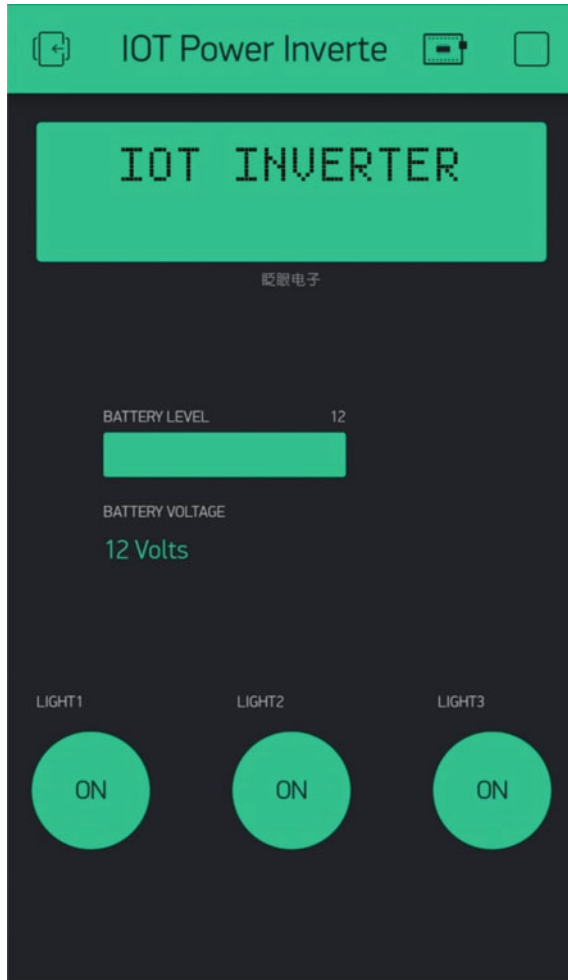


Fig. 16 BLYNK application screenshot

in future, this can be reduced by designing a LC filter circuit and placing it before the transformer to get a perfect sinusoidal signal so that it could be supplied to the grid. Also, in future, this design can be modified and implemented in a largescale and can be used any form of renewable energy as a power source. Implementation of this design in our homes will help us to do a better energy saving and management. Using renewable energy as a power source will not cost us much in terms of currency as renewable energies are free of cost and are available in abundance.

References

1. Green MA (2000) *Power to the people: sunlight to electricity using solar cells*. UNSW Press
2. Ransing RS, Rajput M (2015) Smart home for elderly care based on wireless sensor network. In: 2015 international conference Nascent technologies in the engineering field (ICNTE), pp 1–5
3. Dey S, Roy A, Das S (2016) Home automation using internet of thing. *IRJET* 2(3):1965–1970
4. Shen Y, Huai W, Frede B (2017) Reliability oriented design of a grid-connected photovoltaic micro inverter. In: 2017 IEEE 3rd international future energy electronics conference and ECCE Asia (IFEEC 2017-ECCE Asia). IEEE
5. Ramon OC, Barbi I (1999) A boost DC–AC converter: analysis, design, and experimentation
6. Ropp ME, Gonzalez S (2009) Development of a MATLAB/Simulink model of a single-phase grid-connected photovoltaic system
7. Femia N, Petrone G, Spagnuolo G, Vitelli M (2005) Optimization of perturb and observe maximum power point tracking method. *IEEE Trans Power Electron* 20(4):963–973
8. Schaber K, Steinke F, Mühlich P, Hamacher T (2012) Parametric study of variable renewable energy integration in Europe: advantages and costs of transmission grid extensions. *Energy Policy* 42:498–508
9. Li RYM (2013) The usage of automation system in smart home to provide a sustainable indoor environment: a content analysis in Web 1.0. Li, Rita Yi Man (2013), The Usage of Automation System in Smart Home to Provide a Sustainable Indoor environment: A Content Analysis in Web 1:47–60
10. Nedumgatt JJ, Jayakrishnan KB, Umashankar S, Vijayakumar D, Kothari DP (2011) Perturb and observe MPPT algorithm for solar PV systems-modeling and simulation. In: 2011 annual IEEE India conference. IEEE, pp 1–6

A Four-Switch-Type Converter Fed Improved Photovoltaic Power System



Neeraj Priyadarshi, Farooque Azam, Akash Kumar Bhoi,
and Amarjeet Kumar Sharma

Abstract The energy policy of India basically focused on renewable energy sources, and it comes after China, USA and Russia as far as energy production is concerned. In this paper, a four-switch-type converter is modeled, and the power loss model is described for improved photovoltaic (PV) power systems. The simulation responses are realized under different fault conditions. THD of grid voltage/current waveforms is found less than 5% which follow IEEE 519.

Keywords PV · Converter · THD

1 Introduction

The primary energy sources of India are crude oil, natural gas, coal, nuclear energy, hydroelectricity, wind power, biomass electricity and solar power, and up to 2030, India can import energy to fulfill its requirements [1–8]. Moreover, the country's energy dependency will increase by 53% of the total energy requirement. India economic sector is growing rapidly and anticipated to become the second highest contributor to fulfill required power globally by 2035.

Figure 1 shows the projected solar generation capacity in India. Ministry of New and Renewable Energy Department has been constructed in 1980 to preview of

N. Priyadarshi (✉) · A. K. Sharma
Department of Electrical Engineering, Birsa Institute of Technology (Trust),
Ranchi 835217, India
e-mail: neerajrjd@gmail.com

A. K. Sharma
e-mail: ermaxamar@gmail.com

F. Azam
School of Computing & Information Technology, REVA University, Bangalore 560064, India
e-mail: farooque53786@gmail.com

A. K. Bhoi
Department of Electrical & Electronics Engineering, Sikkim Manipal Institute of Technology,
Sikkim Manipal University, Gangtok, India
e-mail: akash730@gmail.com

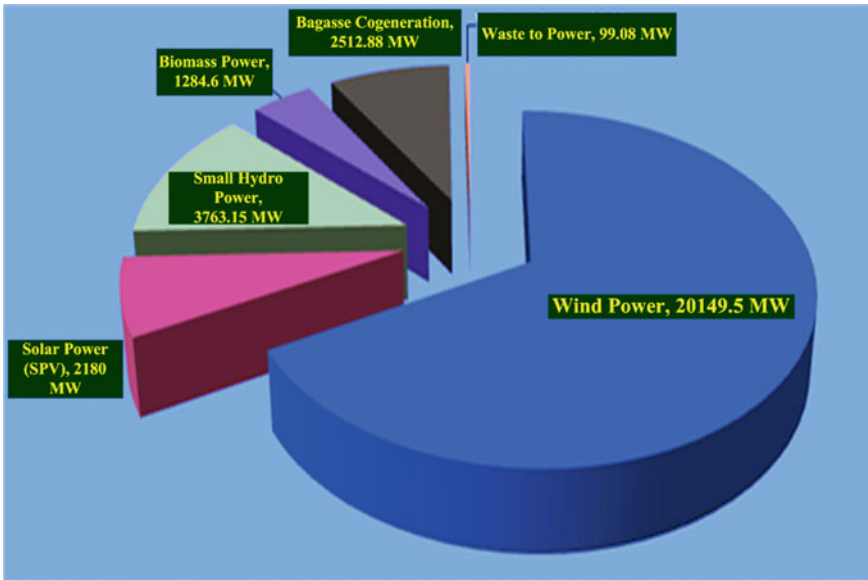


Fig. 1 Statistics of renewable energy sources in India

alternative energy sources. The total renewable generation of India capacity, 68.9 and 4.59%, comes from wind and solar renewable sources, respectively. India has efficient PV generation possibilities as about 365 days, and 300 sunny days are possible with solar irradiance lies in the range 4–7 kWh/m² [9–11].

1.1 Four-Switch-Type Converter Mathematical Modeling

Four-switch-type converter works in two modes of operation. In the first mode, switches K_1 and K_4 are ON and K_2 and K_3 are switched OFF and formed positive half cycle of the desired output voltage. In the second mode of operation, switches K_2 and K_3 are switched ON and switches K_1 and K_4 are switched OFF and formed a negative half cycle of the desired output voltage. Figure 2 represents the circuit diagram of four-switch-type converter.

Similarly, the average state-space model of four-switch-type converter is expressed as (Figs. 3 and 4)

$$\begin{bmatrix} \frac{dV_{CS}}{dt} \\ \frac{dI_{L1}}{dt} \\ \frac{dV_{C1}}{dt} \end{bmatrix} = \begin{bmatrix} -\frac{1}{R_S C_S} & -\frac{D}{C_S} & 0 \\ \frac{D}{L_1} & 0 & -\frac{(1-D)}{L_1} \\ 0 & \frac{(1-D)}{C_1} & -\frac{1}{R_L C_1} \end{bmatrix} \begin{bmatrix} V_{CS} \\ I_{L1} \\ V_{C1} \end{bmatrix} + \begin{bmatrix} \frac{D}{C_S} \\ 0 \\ 0 \end{bmatrix} I_S \quad (1)$$

$$V_S = V_{CS}$$

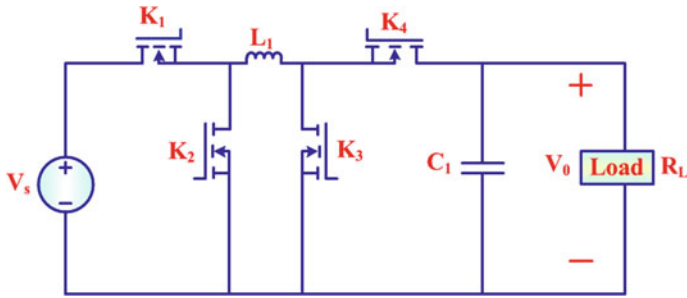


Fig. 2 Circuit diagram of four-switch-type converter

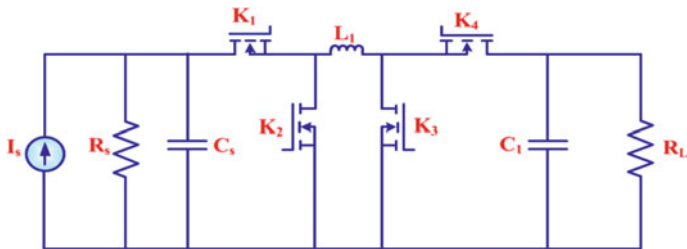


Fig. 3 Equivalent circuit of current-fed four-switch-type converter

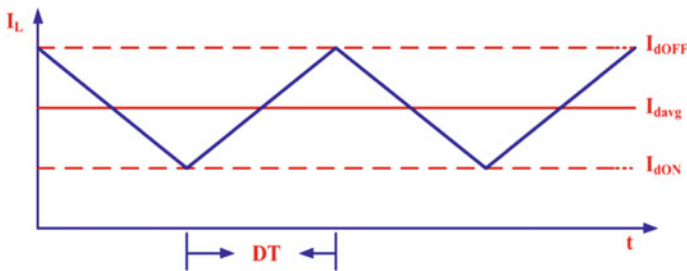


Fig. 4 Inductor current waveform

Similarly, the small signal dynamic model is:

$$\begin{bmatrix} \frac{d\tilde{V}_{CS}}{dt} \\ \frac{d\tilde{I}_{L1}}{dt} \\ \frac{d\tilde{V}_{C1}}{dt} \end{bmatrix} = \begin{bmatrix} -\frac{1}{R_S C_S} & -\frac{\tilde{D}}{C_S} & 0 \\ \frac{\tilde{D}}{L_1} & 0 & \frac{(1-\tilde{D})}{L_1} \\ 0 & \frac{(1-\tilde{D})}{C_1} & -\frac{1}{R_L C_1} \end{bmatrix} \begin{bmatrix} \tilde{V}_{CS} \\ \tilde{I}_{L1} \\ \tilde{V}_{C1} \end{bmatrix} + \begin{bmatrix} -\frac{\tilde{I}_{L1}}{C_S} \\ \frac{V_{CS}}{L_1} + \frac{\tilde{V}_C}{L_1} \\ -\frac{\tilde{I}_L}{C_1} \end{bmatrix} \tilde{d} \quad (2)$$

$$\tilde{V}_S = \tilde{V}_{CS}$$

1.2 Power Loss Model for Buck–Boost Converter

The above circuit shown is non-ideal buck/boost converter. Mathematically, power loss derivation for four-switch-type converter in continuous conducting mode is expressed as:

(i) MOSFET losses

In buck–boost converter MOSFET works as a switching device. MOSFET conduction loss (PCLM) is:

$$P_{\text{CLM}} = R_{\text{dSON}} I_{\text{dRMS}}^2 \quad (3)$$

$$\Rightarrow P_{\text{CLM}} = R_{\text{dSON}} D \left[I_o^2 + \frac{\Delta I^2}{12} \right] \quad (4)$$

where

- I_{dRMS} Drain to source RMS current.
- R_{dSON} Drain to source resistance.
- D Duty ratio.
- ΔI Induction ripple current.
- I_o Converter output current.

Total switching losses of MOSFET is the sum of turn-on loss (P_{ONL}) and turn-off loss (P_{OFFL}).

Total switching losses in MOSFET (P_{SL}).

$$P_{\text{SL}} = P_{\text{ONL}} + P_{\text{OFFL}} \quad (5)$$

where

$$P_{\text{ONL}} = \frac{1}{2} V_{\text{ds}} I_{\text{dON}} t_r f_s \quad (6)$$

$$P_{\text{OFFL}} = \frac{1}{2} V_{\text{ds}} I_{\text{dOFF}} t_f f_s \quad (7)$$

where

- V_{ds} Drain to source voltage.
- I_{dON} & I_{dOFF} MOSFET ON and OFF current.
- t_r · t_f MOSFET rise and fall time.
- f_s Switching frequency.

From the above figure, we can write:

$$I_{\text{dON}} = I_s - \frac{\Delta I}{2} \quad (8)$$

$$I_{dOFF} = I_S + \frac{\Delta I}{2} \quad (9)$$

$$V_{dS} = V_S \quad (10)$$

$$P_{ONL} = \frac{1}{2} V_S \left(I_S - \frac{\Delta I}{2} \right) t_r f_S \quad (11)$$

$$P_{OFFL} = \frac{1}{2} V_S \left(I_S + \frac{\Delta I}{2} \right) t_r f_S \quad (12)$$

(ii) Diode losses

Diode blocks reverse voltage and acts as a rectifier in power electronics converters. The consolidated power loss through the diode is the sum of conduction loss of diode (P_{CDL}), turn-on as well as turn-off losses. Since diode begun to conduct from OFF mode, turn-on loss of diode has been neglected.

Switching loss of diode (P_{SLD}) is:

$$P_{SLD} = \frac{1}{2} Q_{tr} V_{tr} f_S \quad (13)$$

where

Q_{tr} Diode reverse recovery charge.

V_{tr} Reverse recovery voltage.

Total power loss of diode = $P_{CDL} + P_{SLD}$

Total conduction loss of diode

$$P_{CDL} = V_{do} (1 - D) I_S + R_d (1 - D) I_S^2 \quad (14)$$

where

R_{DC} Inductor DC resistance.

R_d Diode on resistance.

(iii) Inductor losses

In the form of the magnetic field, the inductor stores energy. Total power loss in the inductor is the sum of core loss (P_{core}) and resistive losses [DC resistive loss ($P_{R_{DC}}$) + AC resistive loss ($P_{R_{AC}}$)]

$$P_{core} = \frac{V_S - I_S R_{dSON} - I_S R_{DC}}{R_C} \quad (15)$$

$$\text{DC resistive losses } (P_{R_{DC}}) = I_S^2 R_{DC} \quad (16)$$

$$\text{AC resistive losses } (P_{R_{AC}}) = \frac{\Delta I^2}{12} R_{AC} \quad (17)$$

(iv) Capacitor losses

Capacitor stores energy in the form of electric field: Total capacitor losses are the sum of DC resistance loss and AC resistance loss.

$$\text{DC resistive losses } (P_{DC}) = \frac{V_C^2}{R_P} \quad (18)$$

where

R_P Capacitor parallel resistance.

V_C Capacitor voltage.

AC resistive losses

$$(P_{AC}) = I_{C_{RMS}}^2 R_{Equivalent} \quad (19)$$

where

R_{Eq} Equivalent series resistance.

$I_{C_{RMS}}$ Capacitor RMS current.

Total power loss in the capacitor is the sum of DC resistance and AC resistance loss. Since P_{PC} is very small compared to P_{AC} , P_{DC} is neglected.

$$P_{Loss}(\text{capacitor}) = \frac{\Delta I^2}{12} R_{equivalent} \quad (20)$$

2 Dynamic Operation of Grid-Connected PV System When Fault Occurs

Under different fault conditions, the proposed PV power system has been integrated inverter for grid-connected photovoltaic system which is analyzed using MATLAB/Simulink environment. Proposed system is studied at constant insolation level 1000 W/m^2 and standard ambient temperature $25 \text{ }^\circ\text{C}$. Fault has been cleared on the grid side and has a time span of 0.2 s from 0.2 to 0.4 s.

When a three-phase fault occurs in the proposed system on the grid side, the corresponding variation in inverter current and grid currents is shown in Fig. 5. The fault is initiated at 0.2 s, while cleared at 0.4 s. The inverter voltage is negligible when fault occurs at the grid side. Due to the three-phase fault, the inverter current becomes asymmetrical since DC current is superimposed on AC current causing asymmetry. In case of emergency condition, a 3-phase circuit breaker is connected

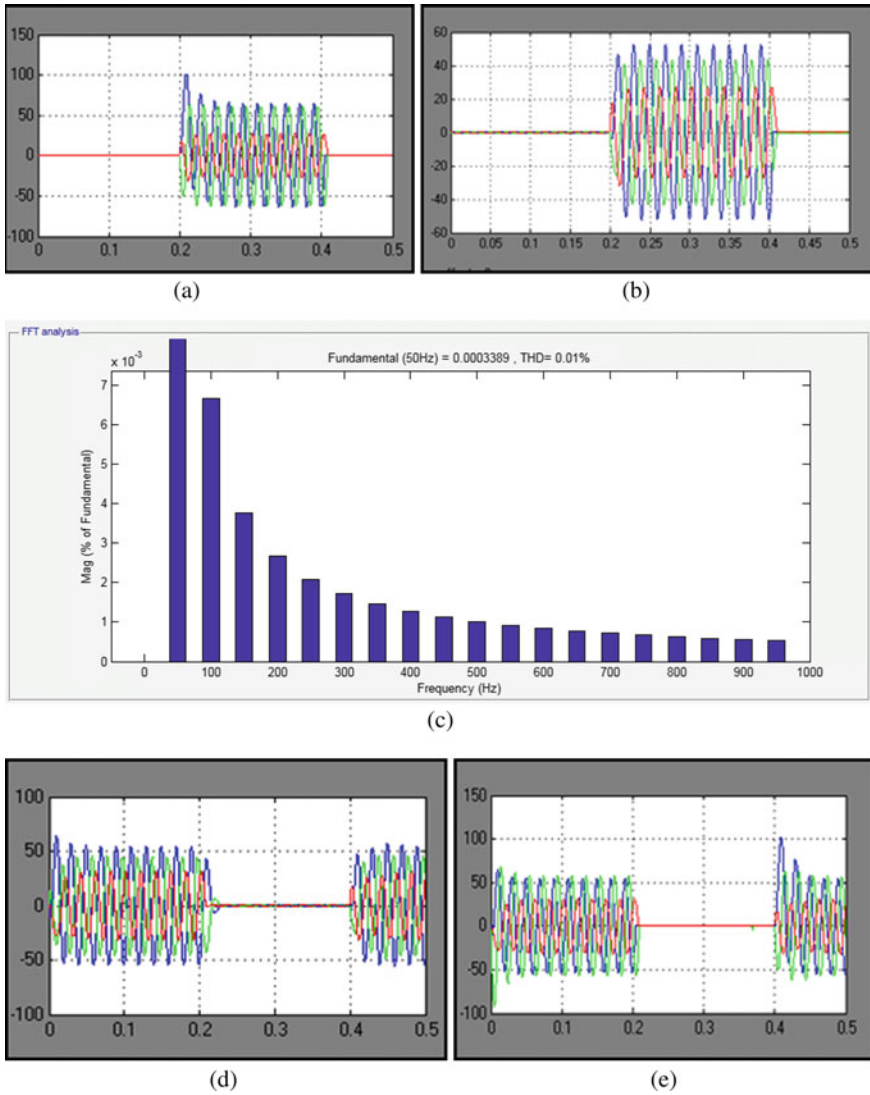


Fig. 5 **a** Inverter current, **b** grid current, **c** FFT inverter current **d** inverter current with circuit breaker, **e** grid current with circuit breaker

to the grid side to isolate the PV generation system from the distribution system. In case of line-to-ground fault, the magnitude of inverter current between 0.2 and 0.3 s is 50 A, while the grid current magnitude is around 60 A as shown in figure. From FFT analysis, the inverter current has total harmonic distortion 0.1%, and the inverter-side current and grid-side currents are also shown with circuit breaker.

3 Conclusion

This research work deals with mathematical modeling and power loss model of four-switch-type converter for improved photovoltaic (PV) power systems. The three-phase fault occurs in the proposed system on the grid side, the corresponding variation in inverter current and grid currents have been revealed and THD of these waveforms is less than 5% which follow IEEE 519. The simulation responses are realized under different fault conditions.

References

1. Priyadarshi N, Padmanaban S, Maroti PK, Sharma A (2018) An extensive practical investigation of FPSO-based MPPT for grid integrated PV system under variable operating conditions with anti-islanding protection. *IEEE Syst J* 1–11
2. Priyadarshi N, Padmanaban S, Bhaskar MS, Blaabjerg F, Sharma A (2018) A fuzzy SVPWM based inverter control realization of grid integrated PV-wind system with FPSO MPPT algorithm for a grid-connected PV/wind power generation system: hardware implementation. *IET Electric Power Appl* 1–12
3. Abderazak L, Dezso S, Josep MG, Laszlo M, Aissa B (2018) Discrete model predictive control-based maximum power point tracking for PV systems: overview and evaluation. *IEEE Trans Power Elec* 33:7273–7287
4. Bhim S, Chinmay J, Anmol B (2018) An improved adjustable step adaptive neuron based control approach for grid supportive SPV system. *IEEE Trans Ind Appl* 54:563–570
5. Priyadarshi N, Sharma AK, Priyam S (2018) An experimental realization of grid-connected PV system with MPPT using dSPACE DS 1104 control board. In: *Advances in smart grid and renewable energy*. Lecture notes in electrical engineering, vol 435. Springer, Singapore
6. Priyadarshi N, Sharma AK, Azam F (2017) A hybrid firefly-asymmetrical fuzzy logic controller based MPPT for PV-wind-fuel grid integration. *Int J Renew Energy Res* 7(4)
7. Priyadarshi N, Sharma AK, Priyam S (2017) Practical realization of an improved photovoltaic grid integration with MPPT. *Int J Renew Energy Res* 7(4)
8. Nishant K, Ikhlaiq H, Bhim S, Bijaya KP (2017a) MPPT in dynamic condition of partially shaded PV system by using WODE technique. *IEEE Trans Sustain Energy* 8:1204–1214
9. Nishant K, Ikhlaiq H, Bhim S, Bijaya KP (2017b) Rapid MPPT for uniformly and partial shaded PV system by using JayaDE algorithm in highly fluctuating atmospheric conditions. *IEEE Trans Ind Info* 13:2406–2416
10. Priyadarshi N, Padmanaban S, Mihet-Popa L, Blaabjerg F, Azam F (2018) Maximum power point tracking for brushless DC motor-driven photovoltaic pumping systems using a hybrid ANFIS-FLOWER pollination optimization algorithm. *MDPI Energies* 11(1):1–16
11. Priyadarshi N, Azam F, Bhoi AK, Alam S (2019) An artificial fuzzy logic intelligent controller based MPPT for PV grid utility. In: *Lecture notes in networks and systems* 46. https://doi.org/10.1007/978-981-13-1217-5_88

Impact of Power Factor Correction Methods on Power Distribution Network—A Case Study



Sudeep Pradhan, Dipanjan Ghose, and Amit Kumar Singh

Abstract To ensure proper conservation of electrical energy and the working of the instruments at maximum efficiency, it is essential to have a near-perfect power factor of one. Power factor correction (PFC) is normally done by supplying external reactive power to the system using capacitor banks of fixed ratings. The power distribution within the state of Sikkim has undergone a number of changes over the years in its infrastructure to ensure a higher working efficiency and reduce energy wastage; PFC methods are being one of them. An 11 kV/433 V substation within the SMIT campus was selected to perform the presented study, considering data of power factor, and active and reactive power both before and after PFC. The results obtained were used to give an estimation of the net kVA savings of the state of Sikkim, proving that PFC significantly aids in the reduction of production cost of electricity and increases efficiency of the system.

Keywords Power factor correction · Energy efficiency · Sustainable development · Power distribution · Monitoring · Sustainable industrial technology

1 Introduction

In general state, electric power generally undergoes three large processes: generation at a power house, its transmission to substations and finally distribution to consumers. The entire interconnected network, which involves the generation, transmission as well as distribution of electricity at consumer levels, falls under the definition of an

S. Pradhan · D. Ghose · A. K. Singh (✉)
Department of Electrical and Electronics Engineering, Sikkim Manipal Institute of Technology,
Sikkim Manipal University, Sikkim, India
e-mail: amit.s@smit.smu.edu.in

S. Pradhan
e-mail: sudeepradhan76@gmail.com

D. Ghose
e-mail: ghosedipanjan1998@gmail.com

electrical power system [1]. A typical power system comprises numerous interconnected devices, including generators, motors, isolators, circuit breakers, transformers, conductors and many more [1]. With advancement in technology, various ‘smart’ devices are also finding their place within power systems, accounting for better and more efficient supply of electrical power. Dividing the complex structure of a power system, we get certain subdivisions as follows:

Generating substation: The generating station is the beginning of a power system. It is the place where electricity is generated from other sources, like thermal, hydroelectric or renewable energy sources [2]. The law of energy conversion clearly mentions that there can be no process involving the independent creation or destruction of energy and it can only convert from one form to the other. A generating substation basically involves the usage of other energy forms to rotate or turn the turbine of an electric generator, ultimately leading to the generation of electricity which can be transmitted.

Transmission substation: The electric power generated in the generating substations is generally within the ranges from 11 to 25 kV [1]. Transmission of electricity in such low voltages involves higher amount of currents (as power = voltage \times current, so lesser the voltage, higher the current for a constant power) which are again associated with the necessity of thicker conductors, accounting for both expenses and heat losses. To avoid this, generally the electric power generated in the generating stations is stepped up using step-up transformers to higher voltages of 115, 132 or 400 kV which are then transmitted to reduce the losses due to higher current values [1].

Besides this, an electric substation also serves for number of other purposes, including isolation of circuits for both their maintenance and during sudden increase in the load demand to protect the generating stations and their equipment, presence of bus bars to enable the splitting of electric power for distribution purposes and housing safety devices for protection of the machineries like circuit breakers and fuses [2]. A substation also serves as the major purpose of improvising the power factor of the circuits. An inside study into the same has been presented later.

Subtransmission substation: A subtransmission substation basically is involved in stepping down the voltage received from the transmission substations making use of step-down transformers [1]. Its operation is somewhat similar to that of distribution systems, differing slightly on the grounds that they supply larger and higher loads, has a higher working voltage than a distribution system and supplies its power to other few substations, unlike distribution systems who supply to loads [1].

Distribution substation: As one of the final stages of a power system, distribution substations feed the substations which are very near the commercial consumers [1].

Besides being simply a measure of the cosine of the angle between voltage and current, power factor also determines the efficiency or effectivity of usage of electrical energy [3].

Under ideal conditions, the current and voltage of the circuit should be in phase, making the power factor a perfect unity. In practical situations, however, most of the loads in daily usage are reactive loads, that is, they are having both resistive and

inductive components [3]. It is during consideration of the ratio between the resistive and inductive loads that power factor come into play.

The presence of inductive loads in the circuit lowers the power factor as for every inductive load; the current lags the voltage by a certain angle. At an electrical perspective, a low power factor would mean that a comparatively greater amount of current is needed to supply the same power to the same equipment [3, 4], which is a crucial aspect leading to wastage of electricity, a valuable resource. Considering the huge number of loads present in the grid, and the similar losses associated with them due to a low power factor, the wastage of electricity would amplify to a tremendous amount, which is largely undesirable.

In simple words, the technique to increase the power factor of a system to get a value of power factor closer to 1 is termed as power factor correction [5]. Power factor correction techniques uses both active and passive approaches, reducing the input root mean square (RMS) current and decreasing the input apparent power and resultantly increasing the power factor [5]. Power factor correction ensures maximum and most efficient utilization of the AC supply power for the instrument. The reactive power component, present generally due to inductive loads, is the main cause for the fall of power factor as discussed earlier. Thus, there must be a compensatory source of capacitive power to make up for that loss. This is the basic idea behind most power factor correction approaches.

Recent developments in the generation and transmission sectors of electric power have led to a shift of focus to emphasize on the approaches and methodologies generally used in those areas to improvise on existing technologies, ensuring a more efficient supply system [6]. Again, installation of a compensatory system to cater for the power factor loss and ensure a greater efficiency demands an investment of a capital amount. The most economical solution for this would be to check that the initial investment for the equipment is largely profitable considering the overall savings achieved in the transmission of electric power resulting from that investment [7].

In small-to-very-small power handling situations (100 W or even less), a passive approach can be considered to correct the power factor by filtering the AC signal through a low-pass filter circuit, using inductors and capacitors as a series resonance circuit [8]. However, for most cases, the power being handled is way over 100 watts and active power factor correction comes into play, giving a more efficient correction along with the added boons of a light bulk-free circuit [5]. Active power factor correction methods can achieve power factors as high as 0.95 or even above in some situations besides having a wide range of AC input voltages and frequency for the system [5]. As of present records, out of the numerous methods of power factor correction used in the industry, attaching shunt capacitors within the circuitry at points near the loads is a proven approach to handle our situation [9]. Shunt capacitors generally draw a notable number of users towards itself because of its cheap availability and reasonably low costs. Besides, there are no moving parts present as well, giving the entire power factor correction method an easier solution to its problem [9]. There are numerous approaches adopted for power factor correction techniques including making use of analog controllers [10] and delay control [11]

along with other novel methods [12, 13]. However, on many grounds, conventional methods for the same stand exclusive in its standing as a well-adopted method.

On installation of a capacitor bank in a facility, they act as sources of reactive powers, so that the facility can draw the reactive power required to be supplied to the load from the capacitor banks itself instead of the utility [9]. Only the difference between the all the reactive power of the facility and the reactive power of the capacitor bank needs to be drawn from the utility supply, leading to savings of quite a large amount of power and monetary benefits as well. A lower necessity of the reactive power in a system accounts for lesser consumption of apparent power to the utility, thus releasing capacity in the system [9]. It is to be also noted that reactive power in a system does not account for any useful work, but is very essential for the operation of instruments. Most loads in a system being inductive in nature, they draw in both magnetizing and power-producing current, out of which the magnetizing current is responsible for the formation of electromagnetic field in the device, ultimately leading to the formation of reactive power. An inductive load is one in which the current lags the voltage; the amount of lag between the two components being the electrical displacement angle (phase angle).

1.1 Impact of Power Factor on Power Distribution Network:

In simple terms, the power factor ($\cos \emptyset$) can be defined as the ratio of the actual power that is dissipated in an AC circuit and the product of the root mean square (rms) values to the voltage and current in the circuit. In electrical engineering, the power factor can also be defined as the ration between the real power which is actually absorbed by the load to the apparent power which flows in the circuit, and the obtained power factor is a dimensionless number within the range from -1 to 1 . The AC portion of electric power can be mainly resolved as apparent, active and reactive powers (shown in Fig. 1), where

$$\text{Apparent Power } (S) = V_{\text{rms}} \times I_{\text{rms}} \quad (1)$$

$$\text{Active Power } (P) = V_{\text{rms}} \times I_{\text{rms}} \times \cos \emptyset \quad (2)$$

$$\text{Reactive Power } (Q) = V_{\text{rms}} \times I_{\text{rms}} \times \sin \emptyset \quad (3)$$

The three power types can be related as [14]:

$$S^2 = P^2 + Q^2 \quad (4)$$

While active power is the real power of the circuit, dissipated in the circuit resistance, reactive power accounts for the power developed in the circuit reactance. Apparent power is the idle or useless power of the circuit. Taking it a step ahead,

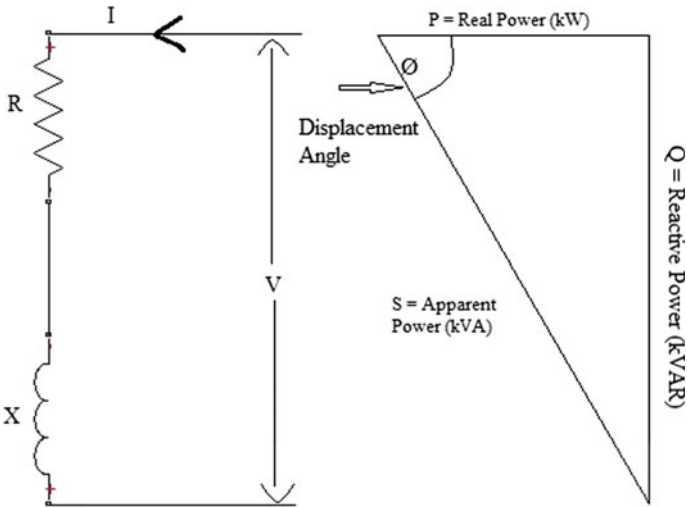


Fig. 1 Diagram showing the relation between the types of power (power triangle)

power factor can be determined as the ratio of the working power to the apparent power, with the formula $P F = \text{kW/kVA}$ [3].

In real world, every load is reactive in nature. If the load is inductive, then the current lags the voltage, implying that the power factor is lagging or positive, while a negative power factor occurs in case of a capacitive load where the current leads the voltage, resulting in a leading power factor. Most of the appliances used in everyday life are generally inductive loads. Thus, obtaining perfect power factor of 1 is ideally not possible.

A significantly low power factor has its impact on the recorded power, making the percentage of the measured kVA greater than the kW demand [15]. Besides, many electricity companies charge extra amounts for lower power factors. Adding power factor correction facilities within the system will aid to remove the power factor penalties from the electricity bill. Also, the reduced current which results from an improvised power factor allows new loads to be added without upgradation of the circuit infrastructure [15]. The voltage drop in the conductor is also reduced, improving the voltage at the equipment [15].

2 Calculations

2.1 Practical Instance on Savings Due to Power Factor Correction:

An 11 kV/440 V substation within the SMIT campus in Sikkim was considered. The substation had three transformers, two of which were of 1000 kVA capacity and the third was larger at 1600 kVA. Two 100 kVAR and one 200 kVAR capacity capacitor banks had been installed to facilitate the power factor correction process. During the course of the study, a 1000 kVA transformer was considered at its full load, along with its corresponding 100 kVAR capacitor bank as a supplier of reactive power in the circuit.

Figures 2 and 3 show brief schematic diagrams of the substation both before and after power factor correction.

The readings for the voltage, current and the power factor were obtained on a single day of study at intervals for two hours from 6:00 a.m. in the morning to 6:00 p.m. in the evening. The different timings of the data account for different demand for loads at different hours of the same day. The readings were taken for both before and after power factor correction had taken place in the substation. Using the voltage, current

Fig. 2 System diagram without capacitor bank

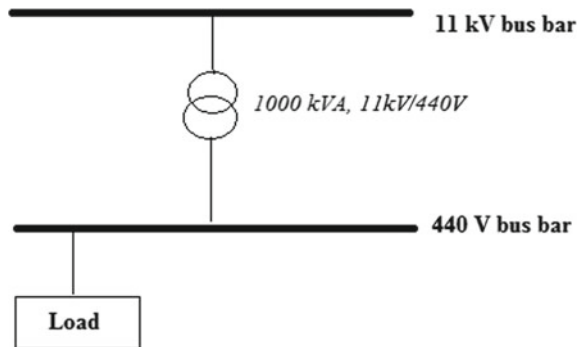


Fig. 3 System diagram with the capacitor bank

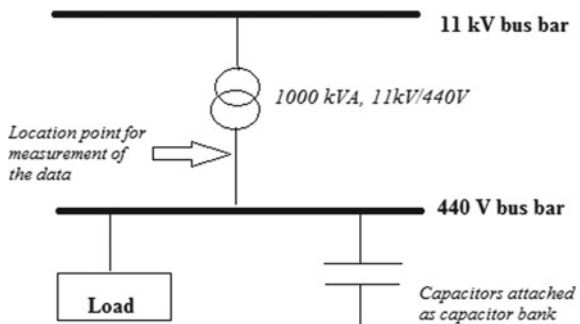


Table 1 Data obtained before power factor correction

Time (in h)	Power factor	Active power (P) (kW)	Reactive power (Q) (kVAR)	Apparent power (S) (kVA)	Current (I) (A)
06:00	0.7	50.66	51.391	72.168	172.34
08:00	0.89	42.06	21.268	47.136	112.53
10:00	0.69	50.99	53.213	73.704	175.97
12:00	0.88	52.20	27.884	59.189	146.49
14:00	0.80	52.84	52.841	74.730	153.61
16:00	0.88	48.49	25.900	54.980	134.41
18:00	0.88	47.27	25.250	53.598	132.98

Table 2 Data obtained after power factor correction

Time (in h)	Power factor	Active power (P) (kW)	Reactive power (Q) (kVAR)	Apparent power (S) (kVA)	Current (I) (A)
06:00	0.98	50.66	9.823	51.61	123.1
08:00	0.98	42.06	8.155	42.84	102.2
10:00	0.98	50.99	9.887	51.94	123.9
12:00	0.97	52.20	12.91	56.70	132.9
14:00	0.98	52.84	10.24	53.82	125.4
16:00	0.98	48.49	9.402	49.40	120.7
18:00	0.99	47.27	6.685	47.74	118.5

and power factor readings, the active, reactive and apparent powers of the system were calculated using the Eqs. (2), (3) and (4) for both before and after power factor correction.

The calculated data can be represented in tabular form as shown in Tables 1 and 2.

After having obtained the data, the following graphs were plotted using a Python programming-based interface for both before and after power correction, as depicted in Figs. 4, 5, 6 and 7.

3 Results

From the above graphs, the following deductions can be easily made:

1. There was an improvisation of 15.8% in the average power factor from 0.82 before correction to 0.98 after correction.

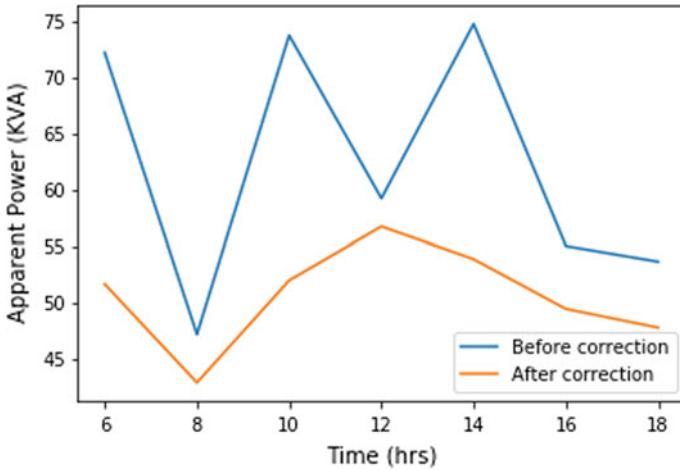


Fig. 4 Graph of apparent power versus time (extracted using Python programming)

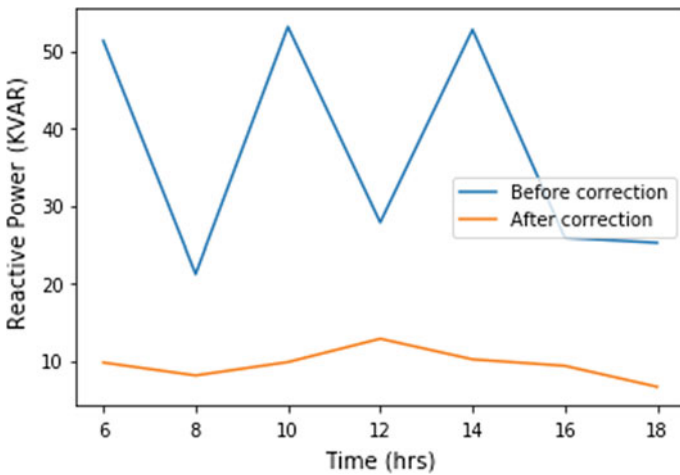


Fig. 5 Graph of reactive power versus time (extracted using Python programming)

2. The average transformer load underwent a reduction of 17.3%, from 62.215 kVA before correction to 51.43 kVA after power factor correction.
3. The cable losses also had a decrement of 17.6%, as the average current value in the cable reduced from 146.90 to 120.9 A.
4. Also, the compensated reactive power by the capacitor bank was 73.9%, with a reduction in the average reactive power in the system from 36.82 kVAR before correction to 9.586 kVAR after correction methodologies which were implemented.

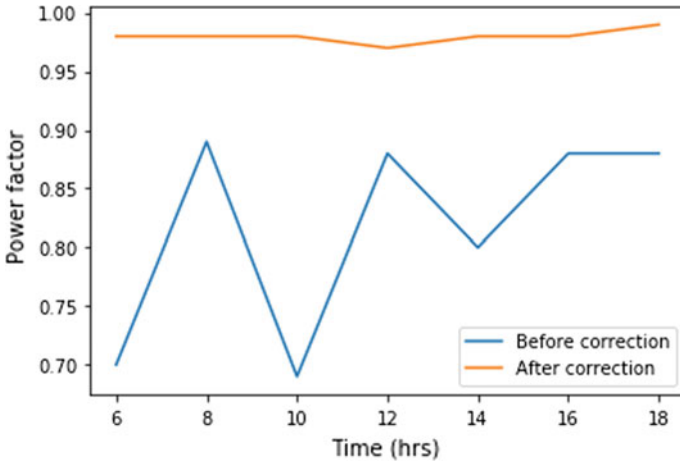


Fig. 6 Graph of power factor versus time (extracted using Python programming)

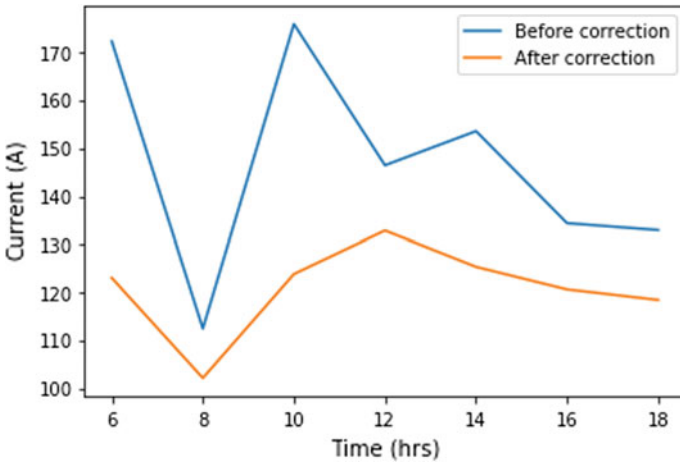


Fig. 7 Graph of current versus time (extracted using Python programming)

3.1 Capacity of the System:

As explained earlier, one of the main intentions to perform a power factor correction in a system is to permit the addition of extra loads to the same system. As depicted in the graphs, the average power factor had underwent an improvisation from 0.82 to 0.98 after correction, thus the demand which was decreased or the kVA of the transformers which was released can be depicted as in Eqs. (5) and (6):

$$X = \frac{\text{Initial Power Factor}}{\text{Final Power Factor}} \quad (5)$$

$$S_{\text{new}} = X \times S_{\text{old}} \quad (6)$$

On putting the value X is obtained as:

$$X = \left(\frac{0.82}{0.98} \right) = 0.836$$

And, $S_{\text{new}} = X \times 1000 = 836.73$ kVA.

Thus, on power factor improvement from 0.82 to 0.98, a capacity of 19.5% was released from the transformer, which is equal to 163.27 kVA.

3.2 Losses During Distribution:

The losses occurring in the distribution network within a network also undergoes a steady improvement once the power factor is improved. The total loss in a system can be calculated as the net total of the losses faced in the transformer and the losses faced in the cables. On a power factor correction method application in a system, there is a vent in the amount of current in the system as it undergoes a steady decrease. As a result, the losses often referred as ' I^2R losses' [16] also decrease, and their relationship being denoted as:

$$P = I^2R \quad (7)$$

Although the reduction in the amount of losses faced in the system alone does not justify the installation costs of installing a capacitor bank, it acts as an added benefit to its purpose. Once the current in the system flowing through the wires, conductors and transformers reduces, the losses in the system also undergo a reduction.

The percentage in the reduction of losses in the system is proportional to the square of the current, which is in turn proportional to the improved power factor [9] and hence can be related as:

$$\text{Percentage loss reduction} = [1 - X^2] \times 100 \quad (8)$$

where ' X ' can be obtained from Eq. (5) and its value is 0.836. Thus, the overall percentage loss reduction is obtained from Eq. (8) as 30.11%.

Again, due to improvisations in the power factor, the new current through the cables can also be obtained as:

$$\text{New Current} = \frac{S_{\text{new}}}{\sqrt{3} \times V} \quad (9)$$

where S_{new} is taken from Eq. (6) and its value has already been established as 836.73 kVA. Here, V is equal to 440 V. Thus, the new current from Equation (p) can be obtained as 1097.923 A.

3.3 Period of Payback:

Power factor correction is the combination of fixed cost and running cost. The fixed cost is essentially defined as the initial investment made for installation for any machinery in an industry. The established capacitor along with its appurtenance has a fixed cost of 70,000 INR (Indian Rupees). The annual maintenance cost of the installed machinery, here the capacitor, is defined as the running cost. Fixed cost is treated as the total invested cost.

$$\text{Released in kVA} = 1000 - 836.73 = 163.27 \text{ kVA}$$

$$\text{Approximate cost for 1 kVA} = 150 \text{ INR}$$

$$\text{Released kVA total cost} = 163.27 \times 150 = 24,490 \text{ INR}$$

$$\begin{aligned} \text{Payback Period} &= \frac{\text{Invested cost}}{\text{Saving cost}} \\ &= \frac{70,000}{24,490} = 2.85 \text{ years} \end{aligned}$$

4 Discussions

As already discussed, issues pertaining to improper power factor (less than 1) have long been a cause of discrepancy in power distribution networks since time of their implementation. In the research genre too, it has often been treated as a speculated topic and over times, numerous methodologies to tackle the problem have been introduced, with each procedure targeting to outrun the previous techniques in terms of efficiency and feasibility of their implementation in real world. The important and crucial role played by PFC methods in the electrical ecosystem has already been excavated [17]. Even automation in the field of PFC has been taken up and evaluated over time [18]. Usage of certain power electronic devices, like inverters for PFC of motors [19], also in switching mode power supplies [20] is not uncommon in the adopted PFC techniques. In fact, in recent times, a number of works have showcased the use of converters as a probable PFC methodology [21–23]. Along with boost converters [21, 22], even buck–boost converters are being implemented in applications like electric vehicles and battery charging [23]. Switching control by making use of magnetic recovery switches too is a novel method in this genre [24].

Suggesting a new novel methodology to handle PFC associated cases is clearly beyond the scope of this study. However, the work presented analyses critically a technique of PFC which has been adopted and used by numerous industries irrespective of the introduction of variegated techniques every year. The study establishes the cost related that is the economic savings associated with an industry on adoption of this methodology of PFC. There are still many machine-oriented factories who are yet to implement such systems within their ecosystem, so in some linguistic terms, the literature presented aims at bridging the research gap for such cases, overall promoting a perseverance of a sustainable environment.

5 Conclusion

In this study, it was found that for a good performance in terms of electricity supply system, it is necessary to have a power factor range of 0.9–0.95. This will help reduce the losses or waste in the electrical energy and substantially increase the output with no requirement to set up extra transformers and cables.

In distribution system, power factor correction will certainly release generation and transmission capacities. Furthermore, because of its tight interconnection character, the precise advantage due to capacity release is quite complicated to evaluate; hence, it is left out from the economic analysis of capacitor from the distribution system.

Power factor improvement results in:

- Plant efficiency improvement.
- Overloading of transformers, cables and switchgears is reduced.
- Capacity system is released.

The observation from the study shows that the improvement in the power factor saves quite an amount of money and also improves the efficiency of the system. Also, if this could be followed by the large industries, this would help them to a large extent.

The regular measuring and checking of the power factor by appointing a third party is highly recommended.

To let the effect extend to the upstream network, the capacitor should be installed in the distribution network not in the transmission network.

There might not be any direct benefit as increasing the power factor does not result in the reduction of the electricity consumption. Nevertheless, it will cut down the need for installation of new power stations which will act as a beneficiary to the environment in long run.

Acknowledgements For the conduction of the experiments especially for gathering of data, the 11 kV substation within the premises of the author's home institute, Sikkim Manipal Institute of Technology, Sikkim, India, was accessed. The authors remain indebted to the workers of the substation for their cooperation in every way. Also the authors express gratitude towards the institute for allowing them to access its resourceful libraries and research collections, without which the completion of this endeavour would not have been feasible.

References

1. Article: Power system. www.circuitglobe.com/power-system/htm
2. Article: Power distribution and transmission. www.brighthubengineering.com/power-generation-distribution
3. Article: Understanding power factor and why it's important. www.edistoelectric.com
4. Miller T (1982) Reactive power control in electric systems. Wiley, Hoboken
5. Article: What is power factor correction? www.sunpower-uk.com
6. Taufik O, Faraj O (2003) Effect of low power factor in Libyan electrical distribution system, CIRED
7. Onohaebi SO, Odiase OF, Osafehinti SI (2010) Improving the efficiency of electrical equipment by power factor correction—a case study on medium scale study in Nigeria. *J Math Technol*
8. Article: Passive power factor correction. www.radio-electronics.com/info/power-management/power-factor-correction-pfc/
9. Al-Naseem OA, Adi AK (2011) Impact of power factor correction on the electrical distribution network of Kuwait—a case study. *Online J Power Energy Eng (OJPEE)* 2(1)
10. Rim GH, Kim WH, Kang I (1995) A simplified analog controller for power factor correction converters. *IEEE Trans Industr Electron* 42(4):417–419
11. Lee KC, Choi HS, Cho BH (2000) Power factor correction converter using delay control. *IEEE Trans Power Electron* 15(4):626–633
12. Hsu SM, Ghosh A, Joshi A (2000) Discussion of A new approach to load balancing and power factor correction in power distribution system [Closure to discussion]. *IEEE Trans Power Delivery* 15(4):1325–1326
13. Lo KC, Lee TP, Wu KH (2008) Grid-connected photovoltaic system with power factor correction. *IEEE Trans Industr Electron* 55(5):2224–2227
14. Article: Electric power. www.circuitglobe.com/electric-power.htm
15. Article: 5 Benefits of power factor correction that can impact your utility bill. www.interstates.com/power-factor-correction/
16. Natarajan R (2005) Power system capacitors. Taylor and Francis, Abingdon
17. Zheng F, Zhang W (2017) Long term effect of power factor correction on the industrial load—a case study. In: Australasian Universities Power Engineering Conference. IEEE, Melbourne, Australia
18. Kabir Y, Mohsin YM, Khan MM (2017) Automated power factor correction and energy monitoring system. In: International Conference on Electrical, Computer and Communication Technologies, IEEE, Coimbatore, India
19. Mahendran S, Nagapavithra S, Umamaheshwari S (2017) Fuzzy based power factor correction for BLDC motor using hybrid inverter. In: Conference on emerging devices and smart systems, conference on emerging devices and smart systems, Tiruchengode, India
20. Mahmud MWB, Alum AHMZ, Rahman DA (2018) Improvement of active power factor correction circuit for switch mode power supply using fly back and boost topology. In: International Conference on Computer and Communication Engineering, IEEE, Kuala Lumpur, Malaysia
21. Vadde A, Sachin S, SitaramGupta VVSN (2017) Re-implementation of synchronous boost converter with controller for power factor correction. In: IEEE region 10 symposium, Cochin, India

22. Powniker S, Shelar S (2016) Development of active power factor correction controller using boost converter. In: IEEE International WIE Conference on Electrical and Computer Engineering, Pune, India
23. Mehta CP, Balamurugan P (2016) Buck-Boost converter as power factor correction controller for plug-in electric vehicles and battery charging application. In: International conference on power systems, IEEE, New Delhi, India
24. Garg RK, Nama JK, Gupta N, Gupta V (2017) Novel closed loop control for power factor correction using magnetic energy recovery switch. In: Innovations in power and advanced computing technologies, Vellore, India

Design of a Smart Energy Management Controller for Hybrid Energy System to Promote Clean Energy



Somudeep Bhattacharjee and Champa Nandi

Abstract Due to the emissions of greenhouse gases, the dangerous impacts of climate change are increasing. In order to combat climate change, hybrid energy system started playing a crucial role. Since individual renewable energy sources are not able to generate a fixed amount of power, the hybrid energy system is used to maintain continuity of power supply. For efficiently utilizing the energy from different renewable energy resources in the hybrid energy system, there has been a growing interest toward those algorithms that make controlling and management of hybrid renewable energy systems with conventional energy system easier and less complex for electricity generation. This chapter proposes the design of a smart energy management controller that uses an energy management algorithm to take decisions in order to integrate and utilize four different renewable energy technologies to reduce the contribution of thermal power generation. This controller stores a large amount of energy for electric vehicle charging. This chapter also proposes the design of an energy storage algorithm for effectively controlling the energy storage operation of the charging station for charging an electric vehicle. This book chapter also includes a detailed discussion on the role of the hybrid system to battle against climate change in Tamil Nadu with a detailed discussion on the scenario of climate change in Tamil Nadu. For analyzing the feasibility of the proposed hybrid system, a twenty-four hours case study analysis is done using the real-time data of renewable energy resources of a selected area in Tamil Nadu, India.

Keywords Renewable energy technologies · Hybrid energy system · Solar power plant · Hydroelectric power plant · Wind farm · Electric vehicle

S. Bhattacharjee · C. Nandi (✉)

Department of Electrical Engineering, Tripura University, Agartala, India

e-mail: cnandi@tripurauniv.in

S. Bhattacharjee

e-mail: somudeep.ee@tripurauniv.in

© Springer Nature Singapore Pte Ltd. 2020

A. K. Bhoi et al. (eds.), *Advances in Greener Energy Technologies*,

Green Energy and Technology, https://doi.org/10.1007/978-981-15-4246-6_31

1 Introduction

The weather of Tamil Nadu varies from dry sub-sticky to semi-parched. For energizing the water assets, the dependency of the state on the rainfall is very high. Therefore, rainstorm disappointments lead to intense water shortage and extreme dry season [1]. This makes the state highly prone to the impacts of climate change. Climate change fundamentally realizes changes in climatic conditions [2]. Primarily, the burning of fossil fuel for power production, cooking, vehicles, etc., causes massive climate changes by increasing the temperature [3]. The burning of fossil fuel causes emissions of greenhouse gases (GHGs), and these emissions are the main reason behind the massive climate changes on Tamil Nadu. These impacts are in the form of natural hazards such as sea level rise, cyclone, severe drought, increased flooding, heavy rainstorm and changes in the monsoon. Due to these natural hazards, the growth of the agriculture sector and infrastructure sector declines a lot.

In order to combat this climate change, the emissions of greenhouse gases need to be reduced. These greenhouse gases are mainly generated from the electricity and transportation sector. In the electricity sector, fossil fuel-based thermal power plants are mainly used. The main reason behind using thermal power plant is that they maintain continuity of power supply. On the other hand, individual renewable energy sources are not able to generate a fixed amount of power always as well as their power generation cost is high. But, these individual drawbacks of renewable energy technologies can be easily overcome by implementing the technology of the hybrid system. In addition, renewable energy technologies are upgrading every year and therefore their price of energy production also decreases in the future. This forces the world to shift its attention toward a grid-connected hybrid system that combines more than one power source for maintaining continuity of power supply by keeping at least one conventional energy source in the backup. Such kind of hybrid system reduces the dependency on thermal power plant and provides continuity of power supply. For efficiently utilizing the energy from different renewable energy resources in the hybrid energy system, there has been a growing interest toward those algorithms that make controlling and management of hybrid renewable energy systems with conventional energy system easier and less complex for electricity generation. One of the main concerns in the design is to effectively utilize the energy from different sources and use them as per requirement.

This chapter proposes the design of a smart energy management controller of the hybrid energy system that uses an energy management algorithm to take decisions in order to integrate and utilize four different energy technologies (i.e., solar, hydro, wind and thermal) to reduce the contribution of thermal power generation. This controller stores a large amount of energy in the battery bank for electric vehicle charging. This chapter also proposes the design of an energy storage algorithm for effectively controlling the operation of charging and discharging of the battery bank in the charging station. This chapter includes a twenty-four hours case study analysis which is done using the real-time data of renewable energy resources of the selected area in order to show the possibility of renewable power generation and check the

feasibility of the proposed hybrid system. The proposed hybrid system provides a continuous quantity of energy to fulfill the electric load as well as stores the desired quantity of energy in the battery bank of charging station for an electric vehicle which is only used for electric vehicle charging using wireless power transfer (WPT) technology or battery swapping technology. An innovative blueprint of a vehicle which utilizes an electric motor for converting electrical energy stored in the battery into mechanical energy that helps to run the vehicle is known as an electric vehicle [4]. The electric vehicle used electricity as a fuel, which reduces vehicle's pollution in the atmosphere. But after traveling a fixed amount of distance, an electric vehicle needs electricity for charging. This disadvantage is possible to eliminate using battery swapping station) or wireless power transfer (WPT) technology-based charging station for an electric vehicle. In BSS, the consumer's empty battery is replaced by means of a completely charged battery of a similar kind. With the help of battery swapping station (BSS) or wireless power transfer (WPT) technology based charging station, it was possible to diminish the tensions of consumers regarding extensive charging periods of electric vehicles and of containing sufficient stored power in the battery of an electric vehicle to complete a journey [5]. WPT technology-based stations charge the electric vehicle while traveling on a road without stopping them. This advances the efficient capacity of driving and also diminishes the weight of the battery [6]. Both these charging stations require continuous as well as large amounts of a power supply which are mainly provided by conventional energy sources. Therefore, if this power is produced from a hybrid energy system, then it supplies a continuous amount of power to them with less pollution. This chapter also suggests a smart business plan of selling the battery-stored power for electric vehicle charging in such a way that the energy prices lower than the grid energy prices, which promotes the use of electric vehicles in the area where it is placed as well as increases the profit of hybrid power plant. This book chapter also includes a detailed discussion of the theory of hybrid power system, need of hybrid power system, geography of Tamil Nadu, climate of Tamil Nadu, climate change and its impacts on Tamil Nadu, the future scenario of climate change in Tamil Nadu, need of renewable energy sources, necessity of hybrid energy system, the scenario of power generation in Tamil Nadu and the future extension.

2 The Scenario of Climate Change in Tamil Nadu

2.1 Geography and Climate of Tamil Nadu

One of the biggest territories of India is Tamil Nadu, which spreads a region of 130,058 km² (50,216 mi²). It shares borders with Karnataka toward the northwest, Kerala toward the west and the Bay of Bengal to the east. Also, it shares borders with the Indian Ocean toward the south and Andhra Pradesh toward the north. The dependency of Tamil Nadu on stormy downpours is very high. Therefore, when

the rainstorms come up short, the intensity of the dry season is very high. The weather of Tamil Nadu varies from dry sub-sticky to semi-parched. Tamil Nadu agribusiness is betting of a rainstorm. The state has particular times of rainfall, which are the proceeding rainstorm time frame. In the time period of June to September, a southwest rainstorm with solid southwest winds is there. In the time period of October to December, a northeast rainstorm with overwhelming winds is there. In the time period of January to May, the dry season is there. Tamil Nadu has a standard yearly rainfall of about 945 mm where 48% is contributed by the northeast rainstorm and 32% is contributed by the southwest rainstorm. Due to this full dependency of Tamil Nadu on rainfall for energizing its water assets, intense shortage of water with extreme dry season arises in case of rainstorm disappointments [1]. This makes the state highly prone to the impacts of climate change.

2.2 Climate Change in Tamil Nadu

Climate change fundamentally realizes changes in climatic conditions. Climate change is the net aftereffect of numerous factors caused by the consistent development of Planet Earth through numerous geographical periods [2]. A number of these climate changes have been because of natural causes yet others can be credited to human exercises, for example, deforestation, atmospheric emissions from industry and transport, which have prompted gases and aerosols being put away in the environment. These gases are known as greenhouse gases (GHGs) as they trap warmth and raise air temperatures close to the ground, acting like a greenhouse on the exterior of the planet [7]. Primarily, the burning of fossil fuel for power production, cooking, vehicles, etc., causes massive climate changes by increasing the temperature [3]. These emissions are the main reason behind the risky effects of environmental change on Tamil Nadu. These risky effects attack in the form of natural hazards such as sea level rise, cyclone, severe drought, increased flooding, heavy rainstorm and changes in the monsoon. Due to these natural hazards, the growth of the agriculture sector and infrastructure sector declines a lot. The damage of crop is a direct impact of climate change on Tamil Nadu, and other than that, there are many indirect impacts of it. These effects are revenue lost, deficiency of harvests, cost increment, joblessness, village to city mitigation, decreased personal satisfaction, mental pressure, credit hazard and so on. On March 30, 2012, strong winds and heavy rain damaged 15,000 banana trees in Theni district, which has a price of fifty lakh rupees. Similarly, strong winds and heavy rain damaged a large number of banana trees in Niligiri district on May 4, 2011. On August 7, 2012, again, strong winds and heavy rains damaged a large number of coconut trees, banana trees and drumstick trees in Theni district which has a price of 1.5 crores. There are some of the incidents of damage of crops in Tamil Nadu. In the case of infrastructure impact, damage to the road is the most common impact. The damage of road is a direct impact of climate change on Tamil Nadu as it wastes a large amount of money for their repair, and other than that, there are many indirect impacts of it. These impacts are street closing for over thirty days,

traffic redirection (more fuel required for the more drawn-out path), extensive traffic on the regions, increase air pollution due to heavy traffic of vehicles, government development budgets cutoff due to unexpected expenses, etc. [8].

2.3 *Future Scenario of Climate Change in Tamil Nadu*

In the time duration of November to December in the year 2015, Chennai and its neighboring areas face the extreme flood. This makes an individual of these regions vigilant about the predictions of the rainfall. But, after one year, the approach of these persons demonstrates a pendulum-like swing as they were rigidly expecting updates on the development of rainfall bearing clouds in the upcoming days. This swing indicates the unpredictability of weather conditions in Tamil Nadu. The approaching dry season of the mid-year is the third consecutive atmosphere-related event that the state has looked in the past 15 months. Other two events are typhoon Vardah and the floods of November–December 2015 which cause tremendous damage to property. Tamil Nadu might have weather-related occasions of extreme force in the upcoming years, as forecasted by Tamil Nadu State Action Plan on Climate Change (TNSAPCC). The normal yearly highest temperature increment by 3.1 °C by 2100 from the standard of 1970–2000, as per the quoting researches of Center for Climate Change and Adaption Research (CCCAR) of Anna University, TNSAPCC. Correspondingly, there may be an increment of 3.5 °C in the ordinary yearly least temperature. On the other hand, the normal yearly rainfall could diminish up to 9%. The pattern of rainfall might move to northeast monsoon. This may possibly cause extreme floods and cyclone events. The swings between floods, hurricane and dry season could turn out to be extremely severe due to environmental change. From the standard time duration of 1970–2000 in Tamil Nadu, the projections of most extreme temperature demonstrate an ascent of:

- 1 °C in the time duration of 2005–2035 (2020s),
- 2.2 °C in the time duration of 2035–2065 (2050s),
- 3.1 °C in the time duration of 2065–2095 (2080s).

Furthermore, the forecast of the least temperature shows an ascent of:

- 1.1 °C in the time duration of 2005–2035 (2020s),
- 2.4 °C in the time duration of 2035–2065 (2050s),
- 3.5 °C in the time duration of 2065–2095 (2080s).

Additionally, the forecast for yearly rain shows a decrease in:

- 2–7% in the time duration of 2005–2035 (2020s),
- 1–4% in the time duration of 2035–2065 (2050s),
- 4–9% in the time duration of 2065–2095 (2080s).

Similarly, the indications show a little decrease in the rainstorm occasions for the season of the southwest rainstorm and also show an ascent of growing intense

rainstorm occasions for the season of northeast rainstorm [9]. This scenario of intense situations strictly indicates that there is an urgent need to reduce the impacts of climate change.

3 Role of Hybrid Energy System to Combat Climate Change

3.1 Need of Renewable Energy Technologies

Nowadays, electricity is the most needed demand for our daily life. Electrical power plays a crucial role in the present life of a person. If this electrical power is not present, then it generates difficulties in the life of a person. It reduces the speed of the life of a person. Individuals need to figure out how to deliver power from sustainable power sources [10]. Since the demand of electrical load is increasing as well as the problem of global warming is rising, the interest of many individuals is shifting toward environmentally friendly solutions of energy to safeguard the earth for the future age [11]. In the present scenario, many renewable energy sources are also found and modified to meet the increasing load demand. Some of the major renewable power sources are solar power which utilizes the warmth from the sun, hydropower, which utilizes the intensity of running water to run the turbine and so forth. Thus, electrical power is an extraordinary aid of the general public from multiple points of view, and the accessibility of electric power prompted the advancement of electric instruments in the work environment, which could little more secure, and progressively dependable. At home, it gave warmth to make cooking simpler, and electric machines help to save time all through the house [12]. The social and economic advancement in mankind's history is dictated by the availability and accessibility of electrical energy. Hence, the solution was found out to fulfill the demand of energy for the necessity of general public and financial development. The safety of energy and the constancy of general public improvement infer into two directions [13]. These two directions are:

- Increasing the efficacy of using fossil fuel-based power generation.
- Extensive utilization of sustainable power sources.

Extensive utilization of sustainable (or renewable) power sources can expand the safety of energy for both the future and present society [13]. The utilization of clean energy has been increasing day by day with the focus on the different sustainable power sources. The innovations of sustainable power sources can provide clean and plentiful power which is collected from self-reestablishing assets, for example, sun, water, wind, earth and plants [14]. In the current circumstances, some of the major renewable energy technologies are based on solar, wind and hydropower sources. The utilization of renewable energy is the best option to combat climate change. Sun-based power is the transformation of energy from daylight into electrical power,

either straightforwardly utilizing photovoltaic (PV), in a roundabout way utilizing concentrated solar power, or a mix [15]. When the power is derived from the energy of wind flow, then it is known as wind power [16]. When the power is produced by utilizing the intensity of falling water or speedy running water, then it is known as hydropower [17].

3.2 Necessity of Hybrid Energy System

In the present situation, some of the major renewable energy technologies are based on solar, wind and hydropower sources. However, these technologies have some major drawbacks. Solar power is not continuous in nature throughout the day as well as not available at night. Also, solar power generation is affected during the rainy season when the sky is fully covered with clouds. The wind power plant also possesses some drawbacks like wind speed not always remain the same which affects its generation of power. The hydroelectric power plant at the same time possesses some major drawbacks like during summer season, it does not generate the rated amount of power with its installed capacity due to a shortage of water. These individual drawbacks of solar, wind and hydroelectric power plants can be easily overcome with the use of the hybrid energy system. At the point when a mix of at least two energy sources is utilized to create power, at that point, the general framework is known as a hybrid energy system. This kind of system increases the safety of energy to the next level. A combination of photovoltaic (PV) and wind turbines with a backup diesel generator is used as the most widely recognized hybrid energy system. The utilization of sustainable power technologies lessens the utilization of imported non-renewable energy sources, taking into account the cleaner production of electricity and the optimization of energy supply alternatives [18]. There are many benefits of the hybrid system. It helps to keep the environment clean by reducing the usage of non-renewable energy sources. It saves the fuel up to 50%. It requires low maintenance cost and it is a silent system. It is capable to maintain the continuity of power supply by connecting to other power supplies (wind turbines, solar panels, etc.). It provides low variability in the system efficiency and it provides more reliable results. It has a long life cycle as it can supply energy for more than 20–25 years [19, 20]. A hybrid power system gives a steady type of energy production. This kind of system is a cost-effective energy solution with high power quality and reliability. And, an individual energy system does not generate utilizable energy for a large portion of time during the year as compared to the hybrid energy system [14]. In addition, renewable energy technologies are upgrading every year and therefore their price of energy production also decreases in the future.

But still, there are many countries like India, where coal is used as the main energy source. India generates its major portion of power from coal thermal power plant, i.e., 58.3% [21]. Similarly, the contribution of thermal power generation is high in Tamil Nadu. Figure 1 indicates the scenario of the installed power capacity of Tamil Nadu in MW. This scenario indicates that the capacity of the thermal power

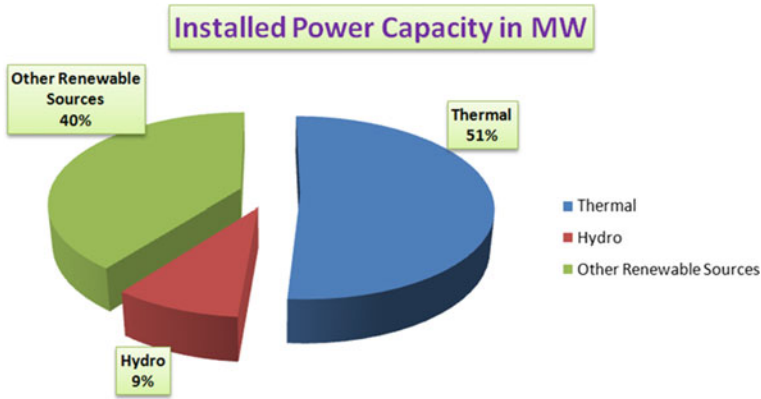


Fig. 1 Installed power capacity (MW) of Tamil Nadu

plant is 12,479 MW (51%), hydroelectric plant is 2208 MW (9%) and remaining sustainable (or renewable) power sources-based power plant is 9646 MW (40%) [22]. This shows that the contribution of the thermal power plant is very high, and therefore, it pollutes the environment by the emission of greenhouse gases. This indicates that the electricity sector of Tamil Nadu is one of the main reasons behind the dangerous impacts of climate change on Tamil Nadu. Therefore, it is very necessary to reduce this dependency, and for that, renewable energy technologies-based hybrid system plays a crucial role. The main reason behind using thermal power plant is that they maintain continuity of energy supply. Additionally, individual renewable power sources are not able to generate a fixed amount of power always as well as their power generation cost is high. This forces the world to shift its attention toward a grid-connected hybrid system which utilizes a mix of at least two energy sources for maintaining continuity of power supply by keeping at least one conventional energy source in the backup. It is true that the thermal power plants provide continuity of power supply, but this continuity is possible to achieve by using the hybrid system. With the help of one large-sized hybrid power plant where renewable energy sources contribute a major portion of power, it is possible to shut down nearby thermal power plants of small capacity.

4 System Description of Hybrid Energy System

4.1 Block Diagram

The block diagram of the grid-connected hybrid energy system is demonstrated in Fig. 2. This system utilizes four different energy technologies (i.e., solar, hydro, wind and thermal) to reduce the contribution of thermal power generation. This hybrid

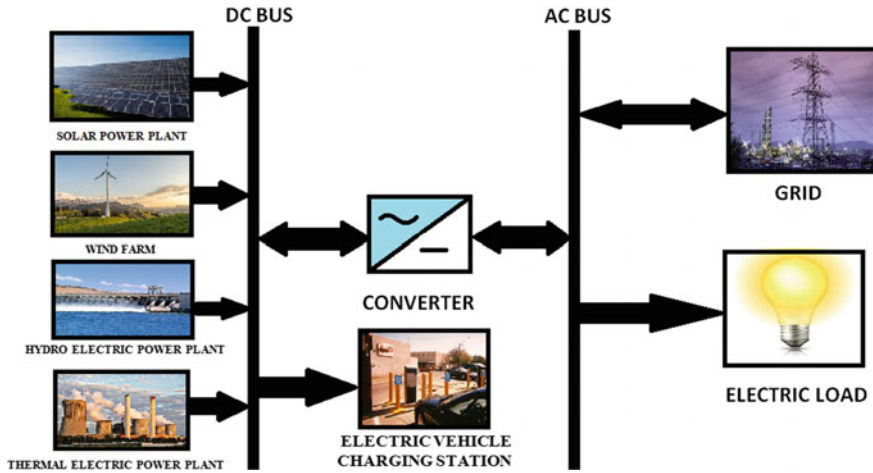


Fig. 2 Block diagram of grid-connected hybrid energy system

energy system utilizes a grid for consuming extra power and providing power for fulfilling the load demand during requirement. The main parts of this block diagram are the solar power plant, wind farm, grid, electric load, electric vehicle charging station and converter. Here, inverter is represented by a converter which is used to transform DC power into AC power. In this hybrid system, an energy management algorithm is used to manage and control the energy of all energy sources. In the electric vehicle charging station, an energy storage algorithm is used to store energy efficiently.

HVDC transmission is utilized in the hybrid energy system since it is progressively cost effective and endures minor losses of electrical energy for large distance transmission, yet at the same time, its expense is higher in small distance transmission. The problem of skin effect does not arise in HVDC transmission. DC transmission lines can take a greater amount of current in each conductor. The problem of synchronizing two distinct systems does not arise during connecting them due to the absence of frequency. Yet at the same time, an AC voltage is simpler to step up and step down. On the other hand, a DC voltage is not simpler to step up and step down [23, 24]. So, DC is used to connect and control all the energy sources and later converted into AC before sending to the grid and electric load.

4.2 Mathematical Modeling of Solar Power Plant

Solar cells are manufactured utilizing semiconductor materials (typically silicon). These materials are utilized to make an electric field, positive on one diode (flipside) and negative on the other (in the direction of the sun). When the sunshine falls on the solar cell, electrons are thumped free from the atoms which make electron-hole

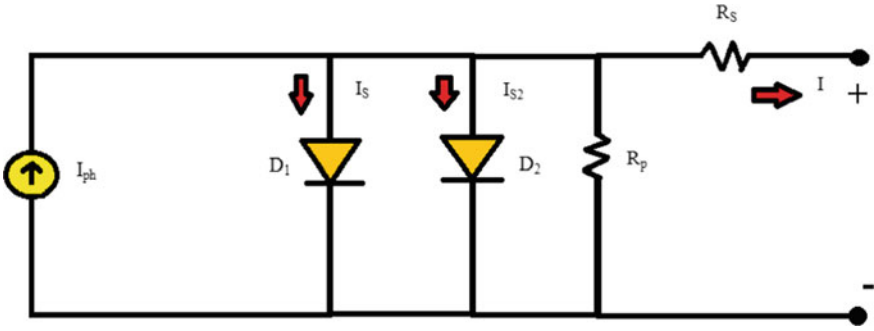


Fig. 3 Circuit diagram of a solar cell

pairs. At that time, if the electrical conductors are attached to the positive and negative sides of the solar cell, then it worked like an electrical circuit and generates electricity [25]. The circuit diagram of the solar cell is demonstrated in Fig. 3 [26].

Using Fig. 3, the final current is written as,

$$I = I_{ph} - I_{D1} - I_{D2} - I_{SH} \tag{1}$$

Here,

- I final current in amperes,
- I_{D1} diode D1 current (ampere),
- I_{D2} diode D2 current (ampere) and
- I_{SH} shunt current (ampere).
- I_{ph} solar-induced current, also known as photo-generated current in amperes.

Therefore,

$$I_{ph} = I_{ph0} \times [(I_r)/(I_{r0})] \tag{2}$$

Here,

- I_r indicates the solar irradiance in W/m^2 hitting the solar cell.
- I_{ph0} indicates the generated solar current (measured) for the irradiance I_{r0} .

Also, I_{D1} is given by

$$I_{D1} = I_S * (e^{[(V+I*R_s)/(N*V_t)]} - 1) \tag{3}$$

And I_{D2} is given by

$$I_{D2} = I_{S2} * (e^{[(V+I*R_s)/(N2*V_t)]} - 1) \tag{4}$$

Here,

- I_S indicates the saturation current of the first diode,
- I_{S2} indicates the saturation current of the second diode,
- V_t indicates the thermal voltage, $V_t = (kT/q)$,
- k indicates the Boltzmann constant,
- T indicates the simulation temperature of the device,
- q indicates the elementary charge on an electron,
- N indicates the quality factor of the first diode,
- $N2$ indicates the quality factor of the second diode,
- V indicates the voltage across the electrical ports of the solar cell.

Therefore, I_{Sh} is given by

$$I_{Sh} = (V + I * R_s) / R_p \quad (5)$$

where

- R_S Series resistance
- R_P Shunt resistance.

Using Eqs. (1), (2), (3), (4) and (5),

$$I = I_{ph} - I_S * (e^{[(V+I*R_s)/(N*V_t)]} - 1) - I_{S2} * (e^{[(V+I*R_s)/(N2*V_t)]} - 1) - [(V + I * R_s) / R_p] \quad (6)$$

Equation (6) is used to calculate the final current of a solar cell (also known as output current) [26]. The solar power plant includes a solar array where the desired number of series-connected solar modules is attached to a string, and every solar module comprises the desired number of solar cells connected in series. Also, the desired number of modules connected strings is connected in parallel. This solar array transforms the sunlight into electrical power. This power is then increased by maximum power point tracker (MPPT) with a boost converter. Here, a controllable DC-DC converter is utilized to find out the highest power point, and after that, the most extreme power of solar power plant is obtained.

4.3 Mathematical Modeling of Wind Farm

Because of the irregular warming of the climate of the earth by the sun, the revolution of the earth and the abnormalities of the surface of the earth, the winds are produced. Basically, it is a type of solar energy. The pattern of wind flow and speed vary differently in various parts of the earth [27]. When the power is derived from the energy of wind flow, then it is known as wind power [16]. For converting the kinetic energy into mechanical energy, wind turbines are used. Later, this mechanical energy is utilized by the generator to produce electrical energy [27]. In the present situation, wind power is getting more attention due to its ability to generate high power in an

efficient way [28]. When an object of mass m moving in the air with a speed v , then its kinetic energy E is given by,

$$E = (1/2)mv^2 \quad (7)$$

At a constant speed velocity, the power of the moving air is given by,

$$P_w = \frac{dE}{dt} = \frac{1}{2} \cdot m \cdot v^2 \quad (8)$$

Here, m indicates the mass flow rate for each second.

The power in the air when the air passes an area A (e.g., the area swept by the rotor blades) is given by,

$$P_w = \frac{1}{2} \cdot \rho \cdot A \cdot v^3 \quad (9)$$

Here, ρ indicates the air density.

The air density can be defined as an element of the turbine height above ocean level H

$$\rho = \rho_o - 1.194 \times 10^{-4} \quad (10)$$

Here, ρ_o indicates the air density at ocean level at temperature $T = 298$ K ($\rho_o = 1.225$ kg/m³).

The power obtained from the wind can be written as,

$$P_{\text{BLADE}} = C_P(\lambda, \beta) \cdot P_w = C_P(\lambda, \beta) \cdot \frac{1}{2} \cdot \rho \cdot A \cdot v^3 \quad (11)$$

The maximum theoretical value of power factor (i.e., C_p) is 0.593.

The torque of the rotor is given by

$$T_w = (P_{\text{BLADE}}/\omega_m) = \left[C_P(\lambda, \beta) \cdot \frac{1}{2} \cdot \rho \cdot A \cdot v^3 \right] / \omega_m \quad (12)$$

The area covered by the blades can be written as,

$$A = \pi R^2 \quad (13)$$

Therefore,

$$T_w = \left[C_P(\lambda, \beta) \cdot \frac{1}{2} \cdot \rho \cdot A \cdot v^3 \right] / \omega_m \quad (14)$$

where ω_m is the angular velocity of the rotor [29, 30].

In the vast majority of the wind power system, PMSG is utilized to convert the mechanical energy of wind turbine into electricity. The synchronous generator is utilized with a high number of poles in a direct-driven wind energy conversion system (WECS) [31]. In the case of PMSG, the magnetic field is acquired by utilizing a permanent magnet, however, not an electromagnet. In such a situation, the field flux stays steady, and the supply needed to energize the field winding which is not vital, and slip rings are not needed [32]. The wind farm comprises a fixed number of windmills. Every windmill comprises a wind turbine with PMSG which is utilized to produce AC power. The kinetic energy of wind is utilized by the wind turbine to generate mechanical power. This mechanical power is utilized by PMSG to generate AC power, and then, this power transforms into DC power using a rectifier. This power is then increased by MPPT with a boost converter. Here, a controllable DC-DC converter is utilized to find out the highest power point, and after that, the most extreme power of the wind farm is obtained.

4.4 Mathematical Modeling of Hydroelectric Power Plant

The hydraulic power in watt is given by

$$P_h = g\rho DH \quad (15)$$

where

D indicates the discharge of water through the turbine in m/s,

P indicates the density in kg/m^3 ,

H indicates the head in m and g is equal to 9.8 m/s^2 .

Thus, the hydraulic power in kW is given by

$$P_h = (9.8)DH \quad (16)$$

The total potential of the water is given by the following equation:

$$P_{\text{total}} = P_h * n_t * n_g \quad (17)$$

where

n_t turbine efficiency and

n_g generator efficiency.

Hence, the hydraulic power is given by:

$$P_h = P_c * e_w * g * h_f \quad (18)$$

Here,

- P_e indicates the coefficient of electrical discharge,
- e_w indicates the density of water,
- g indicates the gravitational acceleration,
- h_f indicates the water head [33].

The hydroelectric power plant involves a fixed number of units. Every unit contains a hydraulic turbine attached to a synchronous machine. Also, the synchronous machine is attached to a transformer. The hydraulic energy is utilized by the hydraulic turbine to generate mechanical energy. Then, this mechanical energy is utilized by the synchronous machine to produce electrical energy. This electrical energy is expanded utilizing a transformer. Since the synchronous machine produces AC power, so this power is transformed into DC power using a rectifier.

4.5 Mathematical Modeling of Thermal Electric Power Plant

The numerical modeling of the steam turbine is given underneath. In view of the continuity equation, the statement of mechanical power generated by the steam turbine:

$$\frac{dW}{dt} = V \frac{d\rho}{dt} = F_{in}(t) - F_{out}(t) \quad (19)$$

where

- W indicates the weight of steam in the turbine (kg),
- V indicates the volume of the turbine (m^3),
- ρ indicates the density of the steam (kg/m^3),
- F indicates the steam mass flow rate (kg/s),
- t indicates the time (second).

Assuming that the flow out of the turbine is proportional to the pressure in the turbine,

$$F_{out} = P \frac{F_0}{P_0} \quad (20)$$

Here,

- P indicates the pressure of the steam in the turbine (kPa),
- P_0 indicates the rated pressure,
- F_0 indicates the rated flow out of the turbine.

For constant temperature in the turbine,

$$\frac{d\rho}{dt} = \frac{dP}{dt} \cdot \frac{\partial \rho}{\partial P} \quad (21)$$

From Eqs. (19), (20) and (21), the mathematical model is written as:

$$F_{in}(t) - F_{out}(t) = V \frac{d\rho}{dt} = V \frac{dP}{dt} \cdot \frac{\partial \rho}{\partial P} = V \frac{\delta \rho}{\delta P} \cdot \frac{P_0}{F_0} \cdot \frac{dF_{out}}{dt} = T_T \frac{dF_{out}}{dt} \quad (22)$$

Therefore, using Eq. (22),

$$T_T \frac{dF_{out}}{dt} + F_{out}(t) = F_{in}(t) \quad (23)$$

The torque of turbine is proportional to the steam flow rate,

$$T_m(t) = kF(t) \quad (24)$$

Here, k represents the proportional constant [34].

The thermal electric power plant involves a fixed number of units. Every unit contains a steam turbine attached to a synchronous machine. Also, the synchronous machine is attached to a transformer. The steam energy is utilized by the steam turbine to generate mechanical energy. Then, this mechanical energy is utilized by the synchronous machine to produce electrical energy. This electrical energy is expanded utilizing a transformer. Since the synchronous machine produces AC power, so this power is transformed into DC power using a rectifier.

4.6 Mathematical Modeling of Electric Vehicle Charging Station

A battery bank of a lithium-ion battery is utilized for the storage system of the charging station as it requires low maintenance. Also, the rate of self-discharge for this battery is very low when contrasted with other battery cells, for example, NiMH and so forth. Also, its energy density is high [35]. The lithium-ion battery model uses these equations:

Discharge model ($i^* > 0$).

$$f_1(it, i^*, i) = E_0 - K \cdot \frac{Q}{Q - it} i^* - K \cdot \frac{Q}{Q - it} \cdot it + A \cdot \exp(-B \cdot it). \quad (25)$$

Charge model ($i^* < 0$).

$$f_2(it, i^*, i) = E_0 - K \cdot \frac{Q}{it + 0.1 \cdot Q} \cdot i^* - K \cdot \frac{Q}{Q - it} \cdot it + A \cdot \exp(-B \cdot it). \quad (26)$$

In the above equations,

- E_0 indicates the constant voltage, in V,
- K indicates the polarization constant in Ah^{-1} ,
- i^* indicates the low-frequency current dynamics in A,
- i indicates the battery current in Ah,
- it indicates the extracted capacity in Ah,
- Q indicates the maximum battery capacity in Ah,
- A indicates the exponential voltage in V,
- B indicates the exponential capacity in Ah^{-1} [36].

5 Research Methodology of Hybrid Energy System

The framework proposed by Somudeep Bhattacharjee et al. is used as a guideline to assess the design and implementation of this grid-connected hybrid energy system. In [37], Somudeep Bhattacharjee et al. designed an intelligent controller of a hybrid system that combines two renewable energy sources (solar and wind) with a conventional energy source (thermal) for maintaining the continuity of power supply in order to charge electric vehicle battery. In [37], the hybrid system tries to minimize the usage of the thermal power plant. This work likewise performs a case study analysis utilizing real-time information of solar irradiance and wind speeds of Delhi, India, to understand the feasibility of the hybrid system. This work mainly intends to decrease the utilization of pollution-generating energy sources by raising the utilization of renewable energy sources using the hybrid system. But, this work possesses many weaknesses which need to be addressed and solved for maintaining the continuity of power supply. In this work, the controller utilizes only two renewable energy sources (solar and wind) with a backup of the thermal power source; therefore, the utilization of thermal power is very high in the night when the wind power is not there. This limitation is very much necessary to be addressed and solved. In this book chapter, the work described in [37] is further extended by increasing the capability of smart energy management controller, which adds an additional stable renewable energy source of hydropower into the hybrid system. The energy management algorithm is used to design a smart energy management controller, which is used to integrate four different energy technologies (i.e., solar, hydro, wind and thermal). The utilization of hydropower minimizes the usage of thermal power in the night when both the solar and wind power are not there. In this chapter, an additional battery controller is designed which helps in the protection of the battery bank of the charging station from a low input voltage. The energy storage algorithm is used to design the battery controller of the charging station of an electric vehicle. The proposed hybrid system not only stores energy for electric vehicle charging, but also fulfills a large electric load demand and supplies extra energy to the grid. These controllers are designed using MATLAB/Simulink software. This technique is validated using the case study-based discussion. This case study is performed using real-time data on solar irradiance, real-time data on wind speed and real-time data of

stream flow of Kaveri River of a selected location of Mettur, Tamil Nadu, India, to understand the feasibility of the proposed hybrid system. The latitude and longitude of the selected location are $11^{\circ} 48.15$ min north and $77^{\circ} 48.36$ min east.

5.1 Formulation of Energy Management Algorithm

The energy management algorithm is used to design a smart energy management controller. This controller integrates and controls four different energy technologies (i.e., solar, hydro, wind and thermal). The flowchart of the energy management algorithm is demonstrated in Fig. 4.

Case 1: The controller first checks the solar power P_{SOLAR} and then calculates the required load utilizing the underneath equation:

$$\text{REQUIRED LOAD} = \text{LOAD} - (P_{\text{SOLAR}}) \quad (27)$$

LOAD indicates the total demand of electric power needed to fulfill, and P_{SOLAR} indicates the solar power produced from the solar power plant. If the required load of Eq. (27) is less than zero, then it shows that the solar power is capable to meet the demand of LOAD. In this situation, solar voltage is used to fulfill the requirement of the electric load, and the surplus solar energy is sent to the grid. At that time, the combined voltage of wind, thermal and hydropower plant was used to charge the battery bank of an electric vehicle charging station. This stored energy is later aimed to be utilized for charging the batteries of electric vehicles, utilizing WPT technology or battery swapping technology.

Case 2: When the required load of Eq. (27) is greater than zero, then it shows that the solar power is unable to meet the load demand. In this situation, the controller checks the wind power P_{WIND} and then calculates the required load utilizing the underneath equation:

$$\text{REQUIRED LOAD} = \text{LOAD} - (P_{\text{WIND}}) \quad (28)$$

LOAD indicates the total demand of electric power needed to fulfill, and P_{WIND} indicates the wind power produced from the wind farm. If the required load of Eq. (28) is less than zero, then it shows that the wind power is capable to meet the demand of LOAD. In this situation, wind voltage is used to fulfill the requirement of the electric load, and the surplus wind energy is sent to the grid. At that time, the combined voltage of solar, thermal and hydropower plant was used to charge the battery bank of an electric vehicle charging station. This stored energy is later aimed to be utilized for charging the batteries of electric vehicles, utilizing WPT technology or battery swapping technology.

Case 3: When the required load of Eq. (28) is greater than zero, then it shows that the wind power is unable to meet the load demand. In this situation, the controller

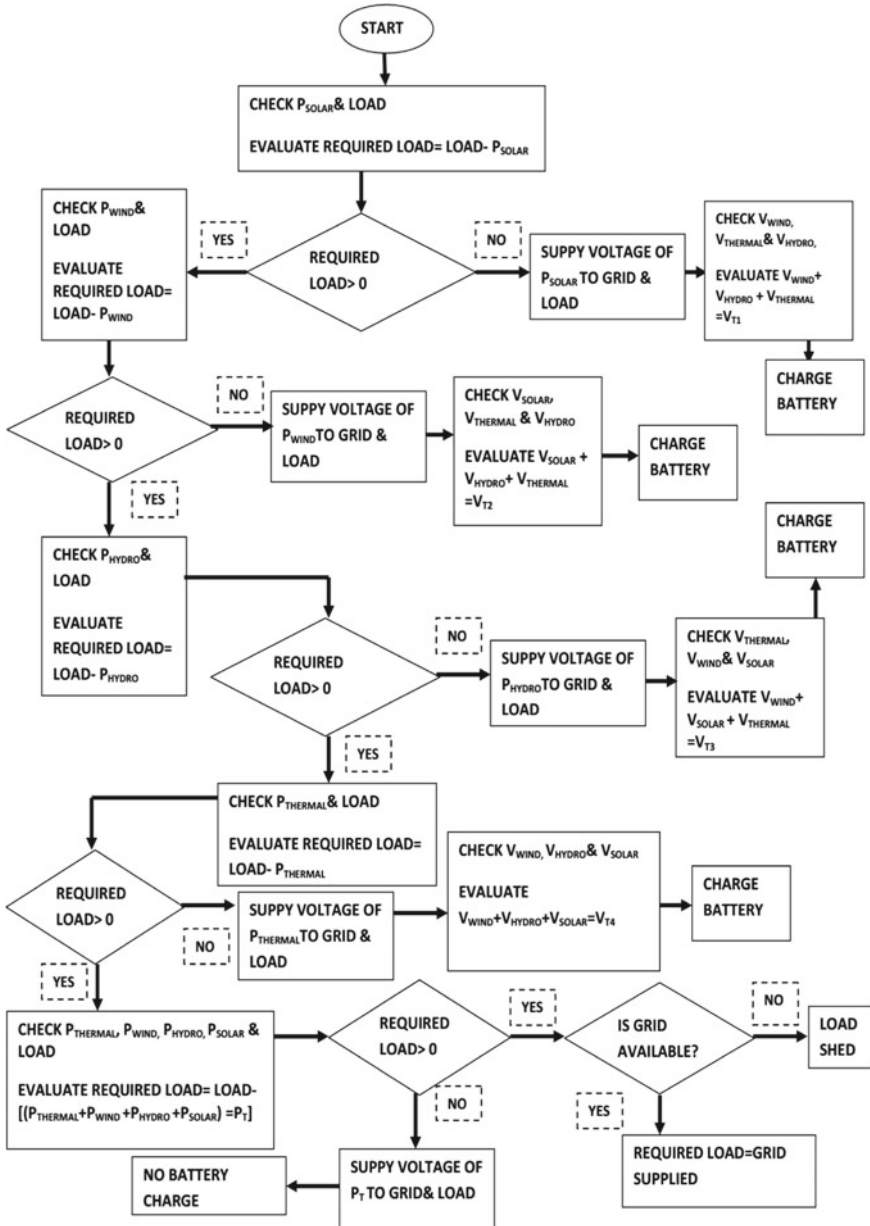


Fig. 4 Flowchart of energy management algorithm

checks the hydropower P_{HYDRO} and then calculates the required load utilizing the underneath equation:

$$\text{REQUIRED LOAD} = \text{LOAD} - (P_{\text{HYDRO}}) \quad (29)$$

LOAD indicates the total demand of electric power needed to fulfill, and P_{HYDRO} indicates the hydropower produced from the hydropower plant. If the required load of Eq. (29) is less than zero, then it shows that the hydropower is capable to meet the demand of LOAD. In this situation, hydrovoltage is used to fulfill the requirement of the electric load, and the surplus hydroenergy is sent to the grid. At that time, the combined voltage of wind, thermal and solar power plant was used to charge the battery bank of an electric vehicle charging station. This stored energy is later aimed to be utilized for charging the batteries of electric vehicles, utilizing WPT technology or battery swapping technology.

Case 4: When the required load of Eq. (29) is greater than zero, then it shows that the hydropower is unable to meet the load demand. In this situation, the controller checks the thermal power P_{THERMAL} and then calculates the required load utilizing the underneath equation:

$$\text{REQUIRED LOAD} = \text{LOAD} - (P_{\text{THERMAL}}) \quad (30)$$

LOAD indicates the total demand of electric power needed to fulfill, and P_{THERMAL} indicates the thermal power produced from the thermal power plant. If the required load of Eq. (30) is less than zero, then it shows that the thermal power is capable to meet the demand of LOAD. In this situation, thermal voltage is used to fulfill the requirement of the electric load, and the surplus thermal energy is sent to the grid. At that time, the combined voltage of wind, hydro and solar power plant was used to charge the battery bank of an electric vehicle charging station. This stored energy is later aimed to be utilized for charging the batteries of the electric vehicle, utilizing WPT technology or battery swapping technology.

Case 5: When the required load of Eq. (30) is greater than zero, then it shows that the thermal power is unable to meet the load demand. In this situation, the controller checks the solar power P_{SOLAR} , wind power P_{WIND} , hydropower P_{HYDRO} and the thermal power P_{THERMAL} and then calculates the required load utilizing the underneath equation:

$$\text{REQUIRED LOAD} = \text{LOAD} - (P_{\text{THERMAL}} + P_{\text{HYDRO}} + P_{\text{WIND}} + P_{\text{SOLAR}}) \quad (31)$$

LOAD indicates the total demand of electric power needed to fulfill, P_{SOLAR} indicates the solar power produced from the solar power plant, P_{WIND} indicates the wind power produced from the wind farm, P_{HYDRO} indicates the hydropower produced from the hydropower plant and P_{THERMAL} indicates the thermal power produced from the thermal power plant. If the required load of Eq. (31) is less than zero, then it shows that the combined power of all power plants is capable to meet the demand of LOAD. In this situation, the combined voltage of all power plants is used

to fulfill the requirement of the electric load, and the surplus energy is sent to the grid. At that time, no voltage sent for charging battery bank of an electric vehicle charging station. When the required load of Eq. (31) is greater than zero, then it shows that the combined power of all power plants is unable to meet the load demand. In this situation, grid power is used as the final backup energy source to fulfill the required load. But, if it is not available, then load shed occurs.

5.2 Formulation of Energy Storage Algorithm

The energy storage algorithm is used to design the battery controller of the charging station of an electric vehicle. The flowchart of the energy storage algorithm is demonstrated in Fig. 5. This controller disconnects the battery bank from the hybrid system during the discharging of the batteries. This controller fulfills two objectives. First, it protects the battery bank of the electric vehicle charging station from low voltage. Secondly, it helps to use battery power only for electric vehicle charging. In the normal condition, the power of the battery bank of the electric vehicle charging station is dissipated utilizing load resistor. This battery bank is charged by a DC voltage source (DC voltage of the hybrid system). In case of low voltage condition, the controller disconnects the battery bank from the hybrid system. If the battery SOC indicates 100%, battery controller then sends ‘1’ signal to the circuit breaker which results in circuit breaker to remain close, and this causes battery to remain connected to the hybrid system, and battery charging takes place. But, if the battery SOC decreases, the battery controller then sends ‘0’ signal to the circuit breaker

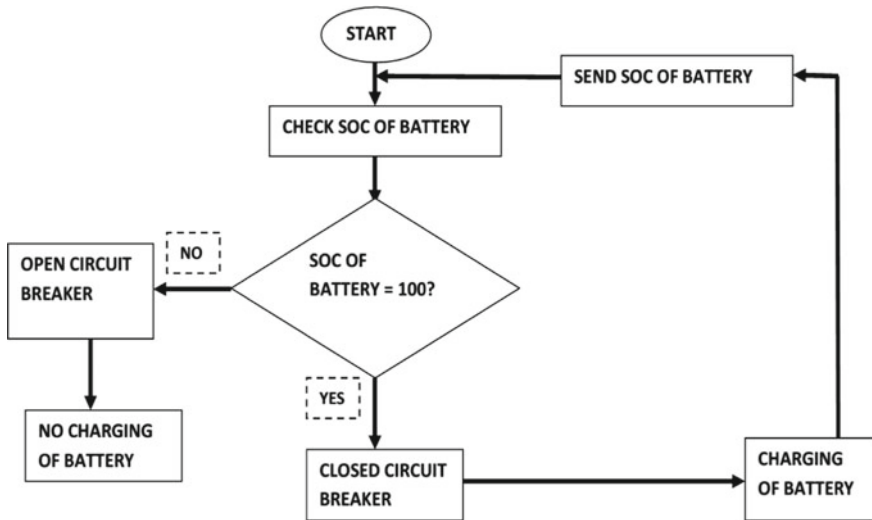


Fig. 5 Flowchart of energy storage algorithm

which results in its open, and this causes battery disconnected from the hybrid system during the discharging of the battery. If the battery SOC indicates 100%, then it means the battery is charging, and when SOC decreases, then it means battery starts discharging.

The battery storage power is only aimed to charge an electric vehicle, and so, this type of controller is designed. The battery controller helps to keep the battery power only for charging electric vehicle batteries and not for selling to the grid. The hybrid power plant can set up its own charging station of the electric vehicle and sell this power for electric vehicle battery charging. Moreover, the hybrid plant can sell this battery power to other private or government electric vehicle charging station with a lower price than the grid power price, so that they promote more electric vehicles in that area as well as it increases the profit of hybrid plant. Since the power price is less than the grid price, so it motivates different charging stations of an electric vehicle to buy this power from the hybrid system. This reduces vehicle pollution. Moreover, if the charging station uses WPT technology or battery swapping technology, then this power is used to charge those electric vehicles, which are present at a far location.

6 Simulation and Modeling of Hybrid System

The simulation model of the hybrid energy system is based on the block diagram of the grid-connected hybrid energy system and is designed using MATLAB/Simulink software. This simulation model includes seven major divisions. The solar power plant, hydroelectric power plant, wind farm, grid and electric load, a smart energy management controller, thermal electric power plant and electric vehicle charging station are the seven divisions. The simulation model of the grid-connected hybrid energy system is shown in Fig. 6.

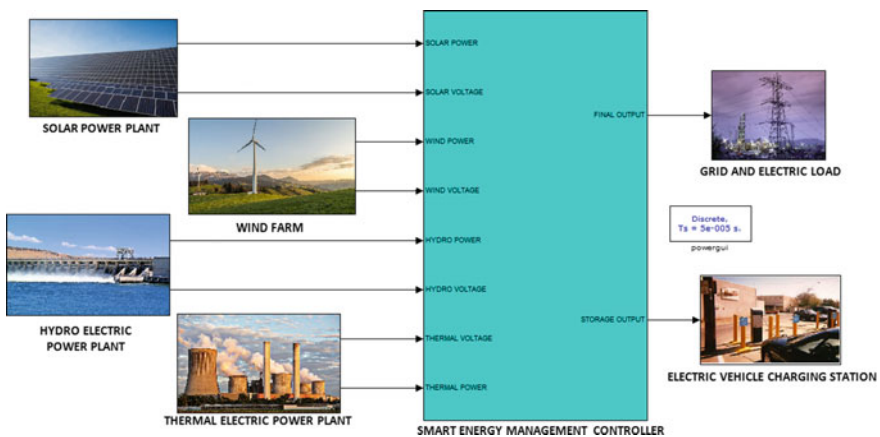


Fig. 6 Simulation model of grid-connected hybrid energy system

6.1 Solar Power Plant

The simulation model of the solar power plant includes a solar array. This solar array comprises 20,000 parallel strings, and in each string, 1500 solar modules are connected in series. Every module comprises 96 series-connected solar cells. The rated capacity of this solar array is 206.9 MW. The lifetime of this solar array is 25 years. This solar array transforms the sunlight into electrical power. This power is then increased by MPPT with a boost converter. Here, a controllable DC-DC converter is utilized to find out the highest power point, and after that, the most extreme power of solar power plant is obtained. Therefore, the rated capacity of the solar power plant with MPPT is 1.54 GW. Then, both the final voltage and final power are sent to the smart energy management controller.

6.2 Wind Farm

The simulation model of wind farm comprises 35 windmills. Every windmill comprises a wind turbine with PMSG which is utilized to produce AC power. The kinetic energy of wind is utilized by the wind turbine to generate mechanical power. This mechanical power is utilized by PMSG to generate AC power, and then, this power transforms into DC power using a rectifier. This power is then increased by MPPT with a boost converter. Here, a controllable DC-DC converter is utilized to find out the highest power point, and after that, the most extreme power of the wind farm is obtained. The rated capacity of one wind turbine (without MPPT) is 5 kW. The rated capacity of a wind farm with MPPT is 3 MW. Then, both the final voltage and final power are sent to the smart energy management controller.

6.3 Hydroelectric Power Plant

In the simulation model of a hydroelectric power plant, there are seven units. Every unit contains a hydraulic turbine attached to a synchronous machine. Also, the synchronous machine is attached to a transformer. The hydraulic energy is utilized by the hydraulic turbine to generate mechanical energy. Then, this mechanical energy is utilized by the synchronous machine to produce electrical energy. This electrical energy is expanded utilizing a transformer. Since the synchronous machine produces AC power, so this power is transformed into DC power using a rectifier. Then, both the final voltage and final power are sent to the smart energy management controller. The rated capacity of the hydroelectric power plant is 153 MW.

6.4 Thermal Electric Power Plant

In the simulation model of a thermal electric power plant, there are five units. Every unit contains a steam turbine attached to a synchronous machine. Also, the synchronous machine is attached to a transformer. The steam energy is utilized by the steam turbine to generate mechanical energy. Then, this mechanical energy is utilized by the synchronous machine to produce electrical energy. This electrical energy is expanded utilizing a transformer. Since the synchronous machine produces AC power, so this power is transformed into DC power using a rectifier. Then, both the final voltage and final power are sent to the smart energy management controller. The rated capacity of a thermal electric power plant is 120 MW.

6.5 Smart Energy Management Controller

The energy management algorithm is used to design a smart energy management controller. This controller integrates and controls four different energy technologies (i.e., solar, hydro, wind and thermal). In order to understand the working of smart energy management controller, there is a need to understand five main conditions. These conditions are:

- The smart energy management controller firstly checks the solar power from the solar power plant and checked that it is more than 100 kW or not. If it is more than 100 kW, then its voltage is first sent to fulfill the requirement of electric load of 100 kW, and the excess energy is sent to the grid. At that time, the total sum voltage of wind, thermal and hydropower plant is sent for charging battery bank of the electric vehicle charging station. This stored energy is later aimed to be utilized for charging the batteries of the electric vehicle, utilizing WPT technology or battery swapping technology.
- Secondly, if the solar power is less than 100 kW and the wind power is more than 100 kW, then the wind voltage is sent to fulfill the requirement of electric load of 100 kW, and the excess energy is sent to the grid. At that time, the total sum voltage of solar, thermal and hydropower plant is sending for charging battery bank of an electric vehicle charging station. This stored energy is later aimed to be utilized for charging the batteries of the electric vehicle, utilizing WPT technology or battery swapping technology.
- In the third condition, when both the solar power and wind power are individually less than 100 kW and the hydropower is more than 100 kW, then the controller sends the hydrovoltage to fulfill the requirement of electric load of 100 kW, and the excess energy is sent to the grid. At that time, the total sum voltage of solar, wind and thermal power plant is sending for charging battery bank of an electric vehicle charging station. This stored energy is later aimed to be utilized for charging the batteries of the electric vehicle, utilizing WPT technology or battery swapping technology.

- In the fourth condition, if all the renewable energy technologies (e.g., solar, wind and hydro) are individually less than 100 kW, then the thermal power from the thermal power plant is checked that it is more than 100 kW or not. If the thermal power is more than 100 kW, then it is sent to fulfill the requirement of electric load of 100 kW, and the excess energy is sent to the grid. At that time, the total sum voltage of solar, wind and hydropower plant is sending for charging battery bank of an electric vehicle charging station. This stored energy is later aimed to be utilized for charging the batteries of the electric vehicle, utilizing WPT technology or battery swapping technology.
- In the fifth condition, if the thermal power is not able to generate 100 kW, then the total sum voltage of solar, wind, thermal and hydropower plant is sent to fulfill the requirement of electric load of 100 kW, and the excess energy is sent to the grid. At that time, no voltage is sent for charging battery bank of charging station. Such condition is ideal and only done during an emergency or special requirement. If the total sum power of all the power plants is unable to meet the requirement of electric load of 100 kW, then the grid power is utilized to meet the demand of electric load (if the grid power is available); otherwise, load shed occurs. This condition is very rare because thermal power plant did not depend on nature for its generation just like other renewable energy sources.

6.6 Grid and Electric Load

In the simulation model of the grid and electric load, the DC final output voltage of the smart energy management controller is filtered using the LC filter. The filtered DC voltage is connected to an IGBT two-level inverter. The IGBT inverter utilizes pulse width modulation at a 2 kHz carrier frequency. The hybrid energy system is discretized at a sample time of 50 μ s. The load voltage is managed at 330 kV rms by a PI voltage controller utilizing abc_to_dq and dq_to_abc transformations. The first output of the voltage controller is a vector comprising the three modulating signals utilized by the PMW generator to produce the 6 IGBT pulses. The second output provides the modulation index. LC filter is used to reduce the harmonics produced by the inverter. Then, this AC voltage is passed from a 50 Hz transformer (330 kV/330 kV) of rating 200 MVA with Wye/Wye configuration in order to remove fluctuations of generating voltage and current. Then, the filtered AC voltage is sent to feed 50 Hz electric load of 100 kW. In order to maintain voltage stability in extreme conditions, a 50 Hz voltage source (representing grid) is connected near to an electric load of 100 kW. It helps to feed the electric load whenever required. The grid is mainly connected either to provide excess power to the grid or to utilize power from the grid.

6.7 *Electric Vehicle Charging Station*

The simulation model of the charging station of electric vehicle utilizes renewable voltage for charging the battery bank. A battery bank of a lithium-ion battery is utilized for the storage system of the charging station as it requires low maintenance. Also, the rate of self-discharge for this battery is very low when contrasted with other battery cells, for example, NiMH and so forth. In addition, its energy density is high [35]. Using the load resistor, the power of the battery bank is dissipated. This battery bank is charged by a DC voltage source (DC voltage of the hybrid system). The nominal voltage of the battery is 800 V. The rated capacity of the battery is 375,000 Ah. The stored energy is later aimed to be utilized for charging batteries of electric vehicles, utilizing WPT technology or battery swapping technology. For solving the overcharging problem, the large capacity battery bank is utilized. In order to safely charge a battery bank, the battery controller is designed. This battery controller is based on an energy storage algorithm. The main aim of this controller is to break the circuit when the battery starts discharging or when the input DC voltage goes below the nominal voltage of the battery bank. If the battery SOC indicates 100%, battery controller then sends '1' signal to the circuit breaker which results in remain close, and this causes battery to remain connected to the hybrid system, and battery charging takes place. But, if the battery SOC decreases, the battery controller then sends '0' signal to the circuit breaker which results in its open, and this causes battery disconnected from the hybrid system during the discharging of the battery. If the battery SOC indicates 100%, then it means the battery is charging, and when SOC decreases, then it means battery start discharging. In the battery controller, the battery SOC checked that it is less than 100 or not using relational operators. If it is not less than 100, then it sends a '0' signal to switch. Then, the switch checks the signal is greater than or equal to one or not. If it is not greater than one nor equal to one, then it sends a '1' signal as an output to the circuit breaker. In addition, if the battery SOC is less than 100, then it sends a '1' signal to switch. Then, the switch checks the signal is greater than or equal to one or not. If it is greater than or equal to one, then it sends a '0' signal as an output to the circuit breaker. The battery storage power is only aimed to charge an electric vehicle, and so, this type of controller is designed. The battery controller helps to keep the battery power only for charging electric vehicle batteries and not for selling to the grid. The hybridpower plant can set up its own charging station of the electric vehicle and sell this power for electric vehicle battery charging. With the help of the battery swapping technique or WPT technology, this hybrid system-based charging station can charge those electric vehicles which are at far locations.

7 Case Study on Mettur, Tamil Nadu

For analyzing the feasibility of the proposed hybrid energy system using the smart energy management controller at different situations, there is a need for hourly analysis of the proposed hybrid system using real-time statistics of solar, hydro and wind resources of the selected location. Therefore, a case study on Mettur, Tamil Nadu, was done. This case study is performed using real-time data of solar irradiance, real-time data on wind speed and real-time data of stream flow of Kaveri River of a selected location of Mettur, Tamil Nadu, India, to understand the feasibility of the proposed hybrid system. The latitude and longitude of the selected location are $11^{\circ} 48.15$ min north and $77^{\circ} 48.36$ min east. The selected location of Mettur, Tamil Nadu, is shown in Fig. 7 [38]. The main reason for selecting this location is its highest possibility of renewable power generation.

7.1 Solar Radiation, Wind Speed, Temperature and Stream Flow Data

The data on wind speed, temperature and solar radiation (or solar irradiance) of the selected location is obtained from the database of NASA surface meteorology and solar energy [39]. The average yearly solar radiation is found to be $5.12 \text{ kWh/m}^2/\text{day}$. The daily solar radiation varies from 4.220 to $6.500 \text{ kWh/m}^2/\text{day}$. The peak daily solar radiation of $6.500 \text{ kWh/m}^2/\text{day}$ is in the month of March as shown in Fig. 8. The clearness index is in the range of 0.431 – 0.641 with the highest daily solar radiation

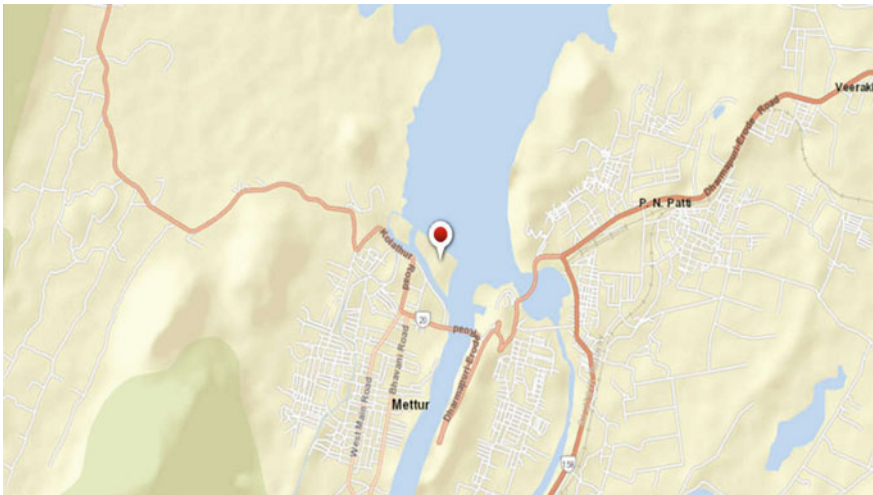


Fig. 7 Selected location of Mettur area in Tamil Nadu

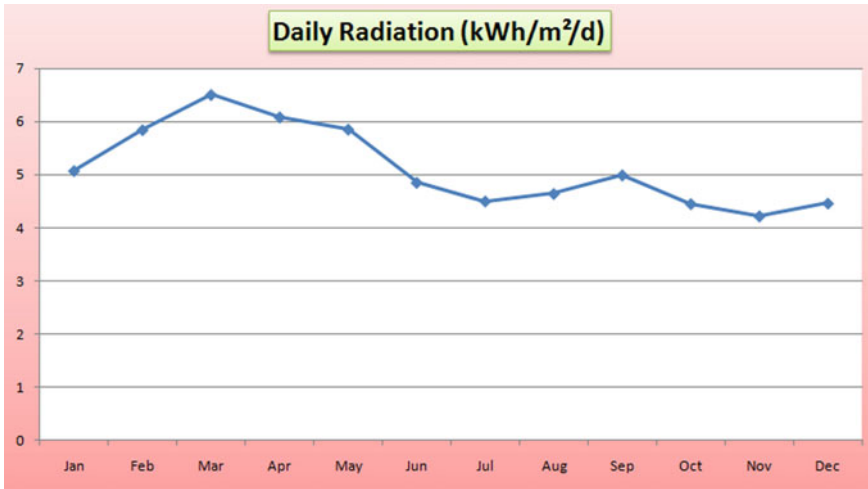


Fig. 8 Monthly average data for daily solar radiation

of 0.641 in the month of March which is shown in Fig. 9. Figure 8 represents the monthly average statistics of daily solar radiation [39, 40]. Figure 9 represents the monthly average statistics of the clearness index [39, 40].

Wind speed data is found to be at 50 m above the surface of the earth in the Mettur area. Figure 10 indicates that the average wind speed is in the range of 2.200–3.450 m/s. The average annual wind speed is found to be 2.75 m/s, and the peak wind speed of 3.450 m/s is in the month of June. Table 1 shows the ambient temperature in degree Celsius of the selected location of Mettur, Tamil Nadu. It indicates that the

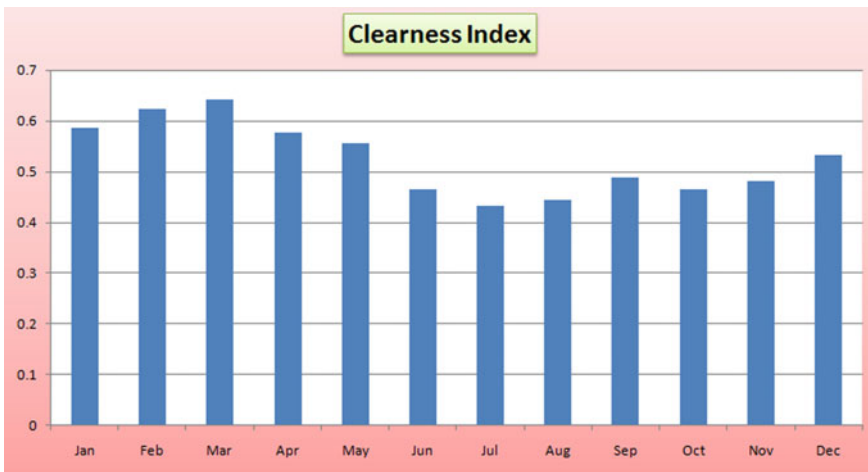


Fig. 9 Monthly average data for clearness index

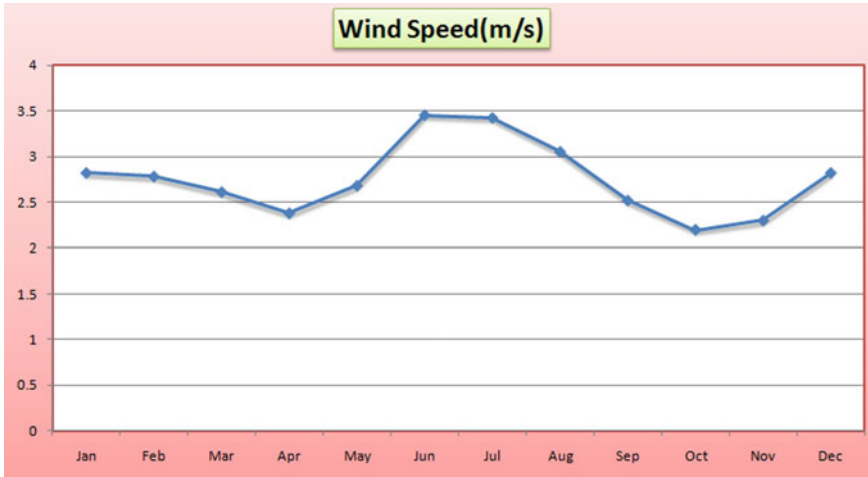


Fig. 10 Monthly average data for wind speed

Table 1 Monthly average data for ambient temperature in degree celsius

Month	Minimum temperature (°C)	Daily low temperature (°C)	Average temperature (°C)	Daily high temperature (°C)	Maximum temperature (°C)
January	23.3248	23.3248	23.3249	23.3248	23.3248
February	25.5853	25.5853	25.5852	25.5853	25.5853
March	27.6857	27.6857	27.6856	27.6857	27.6857
April	26.9255	26.9255	26.9256	26.9255	26.9255
May	26.3854	26.3854	26.3854	26.3854	26.3854
June	25.1752	25.1752	25.1751	25.1752	25.1752
July	24.9451	24.9451	24.9453	24.9451	24.9451
August	25.1452	25.1452	25.1452	25.1452	25.1452
September	25.6353	25.6353	25.6354	25.6353	25.6353
October	24.6951	24.6951	24.6951	24.6951	24.6951
November	23.6248	23.6249	23.625	23.6249	23.6248
December	22.9847	22.9847	22.9846	22.9847	22.9847
Annual	22.9847	25.176	25.1699	25.176	27.6857

temperature is in the range of 22.980–27.680 °C. The average annual temperature is found to be 25.17 °C with the highest temperature of 27.680 °C in the month of March [39, 40].

Figure 11 indicates that the average stream flow of Kaveri (anglicized as Cauvery) River is in the range of 21,249.686–578,498.925 L/s. The average annual stream flow is found to be 182,814.11 L/s with the highest average stream flow of 578,498.925 L/s

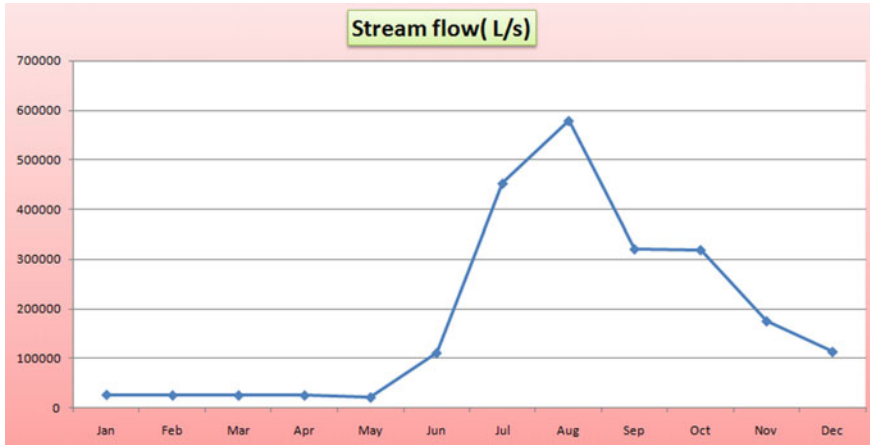


Fig. 11 Monthly average data for stream flow of Kaveri River

in the month of August. Using [40, 41], the real-time data of stream flow of Kaveri River of the selected location is obtained. The monthly average data for stream flow is shown in Fig. 11 [40, 41].

On the basis of Figs. 8, 9, 10, 11 and Table 1, this place possesses a huge possibility of renewable power generation. These figures mainly indicate that the possibility of solar, wind and hydropower generation in this location is very high.

7.2 Hourly Energy Generation Analysis

This case study analysis is mainly based on 24-h duration to understand all different situations. On the basis of the outcomes achieved from the simulation model of the hybrid energy system using real-time data in MATLAB/Simulink software, these case studies are done. These case studies use real-time data of temperature, wind speed, clearness index and solar radiation (or solar irradiance) of the selected location which is acquired from the database of NASA surface meteorology and solar energy [39]. These case studies also use real-time data of stream flow of Kaveri River. Using [40, 41], the real-time data of stream flow of Kaveri River of the selected location is obtained. Figure 12 shows the hourly generation of solar power in kW. Figure 13 shows the hourly generation of wind power in kW. Figure 14 shows the hourly hydropower generation in kW. Figure 15 shows the hourly thermal power generation in kW. Figure 16 shows the hourly excess power sending to a grid in kW. Figure 17 shows the hourly storage power sending to the electric vehicle charging station in kW. This analysis is mainly based on 24-h duration to understand all different situations. All these figures (Figs. 12, 13, 14, 15, 16 and 17) are mainly based on the 24-h real-time data on a day of January month. Using Figs. 12, 13, 14, 15, 16 and 17, it is easy

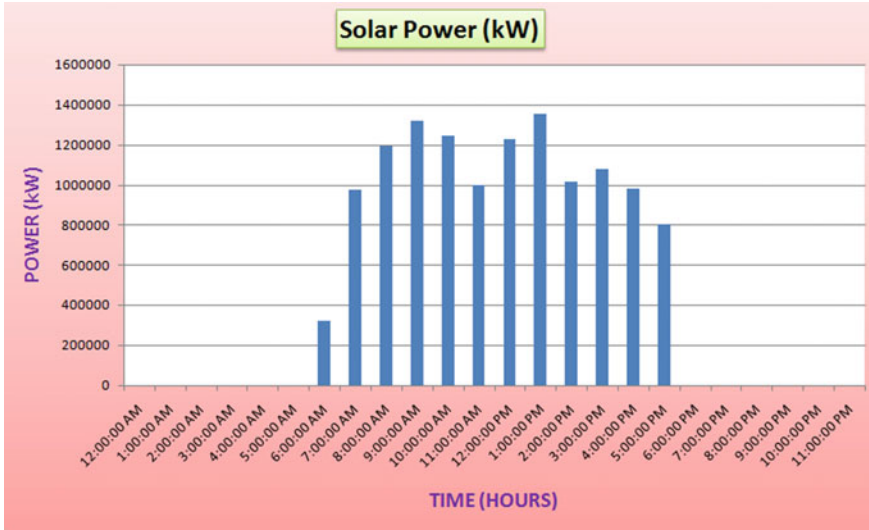


Fig. 12 Hourly solar power generation in kW

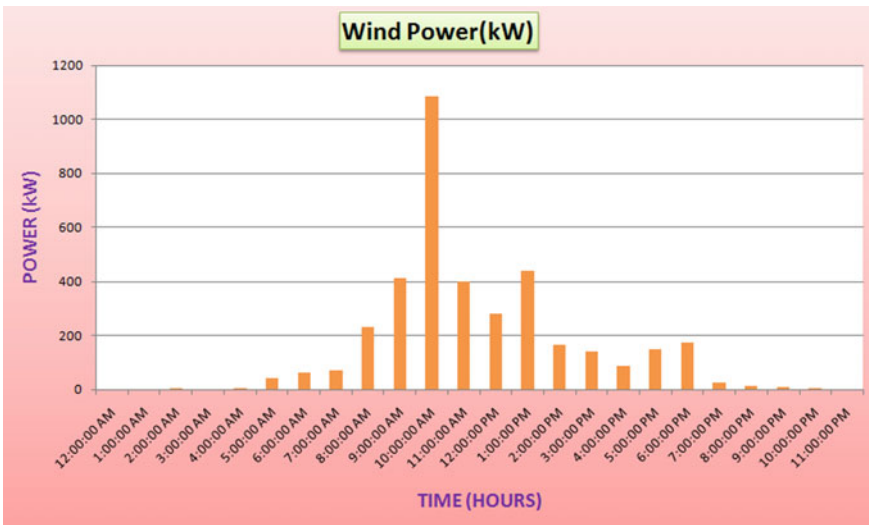


Fig. 13 Hourly wind power production in kW

to understand all different situations that the proposed hybrid system mainly faces. In the time duration of 6:00 AM–6:00 PM (first situation), solar power generation is high, so the excess solar power sending to a grid is very high after fulfilling the load demand of 100 kW. This results in hydropower, wind power and thermal power stored in the electric vehicle charging station. Since the production of hydropower,

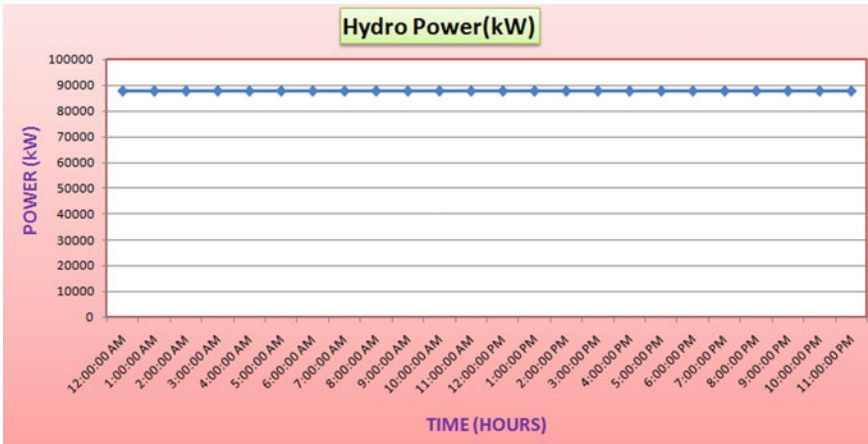


Fig. 14 Hourly hydropower production in kW

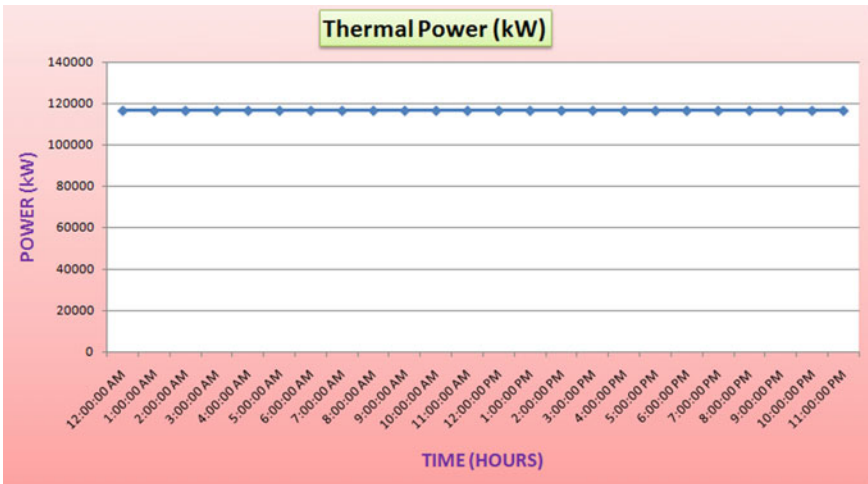


Fig. 15 Hourly thermal power generation in kW

wind power and thermal power was good at that time, so the storage power sending to the electric vehicle charging station is very high.

In the time duration of 6:00 PM–12:00 AM (second situation), the generation of both the solar and wind power are decreasing, so when both of them are less than 100 kW, then the hydropower is sent to fulfill the electric load demand, and excess hydropower is sent to the grid. Therefore, the excess power sending to a grid is still good but lowers to the first situation. This results in solar power, wind power and thermal power stored in the electric vehicle charging station. Since solar power generation is decreased to zero, and also, wind power generation is low, so thermal

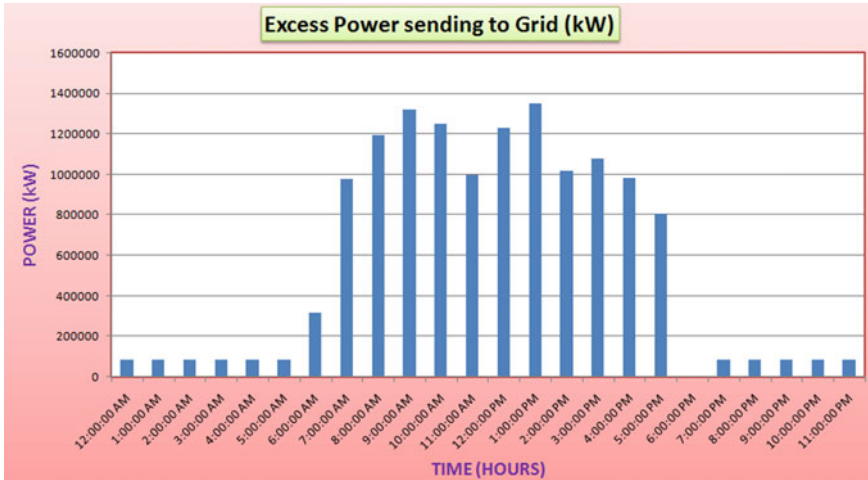


Fig. 16 Hourly excess power sending to grid in kW

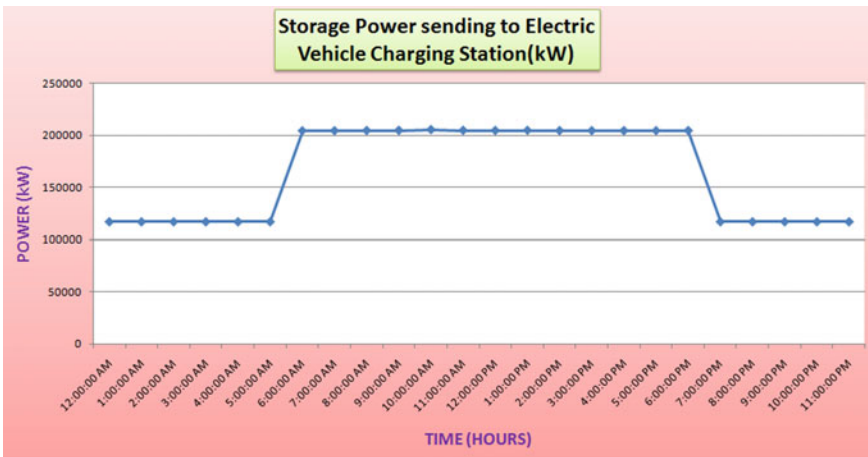


Fig. 17 Hourly storage power sending to electric vehicle charging station in kW

power is mainly stored in the electric vehicle charging station. Therefore, the storage power sending to an electric vehicle charging station is still good but lowers to the first situation.

At the time duration of 12:00 AM–4:00 AM (third situation), solar power generation is not there, and wind power generation is very low (less than 100 kW) which results hydropower sends to fulfill the electric load demand and excess hydropower is sent to the grid. Therefore, the excess power sending to the grid is similar to the second situation. This results in wind power, solar power and thermal power stored in the charging station. Since there is no generation of solar power and wind power

generation is very low, so the thermal power is mainly stored in the charging station of the electric vehicle. In this time duration, stored power sending to the electric vehicle charging station is at the lowest level compared to the first and second situations. In the time duration of 4:00 AM–6:00 AM, solar power generation is not present, and wind power generation is increasing (but still lower than 100 kW). This results hydropower is used to fulfill the load demand of 100 kW and the excess hydropower send to the grid. The excess hydropower sending to the grid is similar to the third situation. This results in wind power, solar power and thermal power stored in the electric vehicle charging station. Since the generation of solar power is not there and wind power generation is increasing, so the total storage power sending to the electric vehicle charging station is higher than the third situation. These situations are most common and mainly faced by the hybrid system.

In addition to the above situations, extra three situations are there. In the fourth situation, solar power generation is lower than 100 kW and wind power generation is more than 100 kW. At that time, wind power was used to meet the demand of the electric load, and excess wind power is sent to the grid. This results in thermal power, hydropower and solar power stored in the charging station. This situation mostly arises during night time. In the fifth situation, if the hydropower, wind power and solar power have individually produced less than 100 kW, then the thermal power is send to fulfill the electric load demand, and excess thermal power is sent to the grid. This results in solar power, hydropower and wind power stored in the electric vehicle charging station. This fifth situation is rare. In the sixth situation, if the wind power, solar power and thermal power are individually generating less than 100 kW, then the total power is sent to fulfill the electric load demand, and excess power is sent to the grid. This results in no power stored in the electric vehicle charging station. At that time, the battery controller disconnected the charging station from the hybrid system. In the present scenario, the sixth situation only occurs during a technical emergency. But, it is also true that the non-renewable energy sources are going to end in the future, so at that time, this situation may arise. It would be better to use a biogas in place of the thermal power plant in the future. With the help of this case study, it is easy to understand that the proposed location of India possesses a huge scope of renewable power generation which is needed to be used. Solar power generation is possible to a much larger extent as well as the scope of wind power generation is good which is proved by the case study analysis.

7.3 Total Energy Production and Consumption Analysis

The electrical production and consumption summary of the proposed hybrid system is shown in Table 2. It indicates the overall results of the case study analysis using the real-time data of the day of January month. This table indicates the overall optimization results of the proposed hybrid system. Based on this table, it is clear that the system is highly profitable. The proposed hybrid system fulfills a total load demand of 2400 kWh/day, and the total excess energy sent to the grid is very high

Table 2 Electrical production and consumption summary of hybrid system

Component	Production (kWh/day)	Percent (%)
<i>Production summary of system</i>		
Solar power plant	12,504,284	71.8215
Wind farm	3791.2465	0.0219
Hydroelectric power plant	2,106,144.7	12.0971
Thermal power plant	2,796,000	16.0595
Total	17,410,220	100
Total renewable energy	14,614,220	83.9405
<i>Consumption summary of system</i>		
AC primary load	2400	0.015
Total excess energy sends to grid	13,465,400	77.349
Total energy stored in electric vehicle charging station	3,940,620	22.636
Total	17,408,420	100

(i.e., 13,465,400 kWh/day). It provides a high-income benefit to the hybrid system. The total energy stored in the electric vehicle charging station is 3,940,620 kWh/day. Since this stored energy is present in a large amount, so it can be used to charge many electric vehicles. The hybrid power plant can set up its own charging station of the electric vehicle and sell this power for electric vehicle battery charging. Moreover, the hybrid plant can sell this battery power to other private or government electric vehicle charging station with a lower price than the grid power price, so that they promote more electric vehicles in that area as well as it increases the profit of hybrid plant. Since the power price is less than the grid price, so it is beneficial for charging station to utilize the energy of a hybrid system. This reduces vehicle pollution. Moreover, if the charging station uses WPT technology or battery swapping technology, then this power is used to charge those electric vehicles, which are present at a far location. This also provides a high-income benefit to the hybrid system. In the overall energy generation scenario, the contribution of the solar power plant is at the highest (i.e., 71.8215%), and the contribution of the wind farm is at the lowest (i.e., 0.0219%). In this generation scenario, the contribution of renewable energy is 83.9405%, and the contribution of non-renewable energy is 16.0595%. This system helps to protect the environment by reducing pollution without affecting the continuity of the power supply.

8 Conclusion

The weather of Tamil Nadu varies from dry sub-sticky to semi-parched. Due to climate change, the whole state is facing dangerous natural hazards such as sea level rise, cyclone, severe drought, increased flooding, heavy rainstorm and changes

in the monsoon. In order to combat climate change, hybrid energy system plays a crucial role in reducing the emissions of greenhouse gases. For efficiently utilizing the energy from different renewable energy resources in the hybrid energy system, there has been a growing interest toward those algorithms that make controlling and management of hybrid renewable energy systems with conventional energy system easier and less complex for electricity generation. This chapter has successfully designed a smart energy management controller of the hybrid energy system that uses an energy management algorithm to take decisions in order to integrate and utilize four different energy technologies (i.e., solar, hydro, wind and thermal) to reduce the contribution of thermal power generation. This controller successfully stores a good quantity of power in the battery bank of the charging station for charging an electric vehicle. This chapter has successfully designed a battery controller that uses an energy storage algorithm for effectively controlling the energy storage operation of the electric vehicle charging station. In this chapter, a twenty-four hours case study analysis is done using the real-time data of renewable energy resources of the selected area which shows that the possibility of renewable power generation is very high. This analysis shows that the proposed hybrid system is profitable and feasible. The proposed system successfully supplies a continuous amount of power to fulfill the electric load as well as stores a desired quantity of energy in the charging station for electric vehicle charging. This system is capable to protect the environment by reducing the pollution without affecting the continuity of power supply. It reduces the pollution generated from the electricity sector as well as the transportation sector. This work can be further extended by replacing the thermal power plant with the biogas plant of the same capacity.

9 Open Research Directions

In the proposed hybrid system, smart devices can be used to collect and send the data of electrical load to the smart energy management controller for better energy management. This advancement requires some changes in the energy management algorithm. The searching for all those areas which have a high capability of renewable energy production plays a crucial role in the future installation of a hybrid energy system [42]. Minimization of harmonics in the hybrid energy system is another open research direction of the hybrid energy system. To maintain power quality, minimization of harmonics is necessary [43]. The utilization of the blockchain concept in a hybrid energy system helps to improve the efficiency, and therefore, it indicates another open research direction of the hybrid energy system. Another open research direction includes the searching of all those places like school, offices, etc., which have a high capability of renewable energy production, and may also set up their personal charging station for an electric vehicle. It promotes the utilization of electric vehicles [44]. These research suggestions help to reduce the dangerous impacts of climate change and also provide a profitable business.

References

1. Geography of Tamil Nadu, https://en.m.wikipedia.org/wiki/Geography_of_Tamil_Nadu. Accessed on 1 Mar 2019
2. Statistics Related to Climate Change—India, <https://www.indiaenvironmentportal.org.in/files/file/climate%20change%20related%20statistics%20-%20india%2029nov13.pdf>. Accessed on 1 Mar 2019
3. Causes of Climate Change, https://19january2017snapshot.epa.gov/climate-change-science/causes-climate-change_.html. Accessed on 2 June 2018
4. Puriour Bjorg Guonadottir, Electric vehicles, T-611-NYTI-21652 New Technology, https://mafiadoc.com/electric-vehicles_599ef14d1723dd11409074ef.html. Accessed on 7 June 2018
5. Sarker MR, Pandzic H, Ortega-Vazquez MA (2013) Electric vehicle battery swapping station: business case and optimization model. In: International conference on connected vehicles and expo (ICCVE), pp 289–294
6. Vilathgamuwa DM, Sampath JPK (2015) Wireless power transfer (WPT) for electric vehicles (EVs)—present and future trends. In: Plug in electric vehicles in smart grids power systems. Springer, Singapore, pp 33–60. https://doi.org/10.1007/978-981-287-299-9_2
7. Statistics Related to Climate Change—India, https://www.mospi.gov.in/sites/default/files/publication_reports/climateChangeStat2015.pdf. Accessed on 1 Mar 2019
8. Climate Risk Assessment and Management: Tamil Nadu State Planning Commission and Regional Integrated Multi Hazard Early Warning Systems, <https://www.unescap.org/sites/default/files/Climate%20risk%20assessment%20tools%20for%20development%20planning%20by%20Sugato%20Dutt.pdf>. Accessed on 1 Mar 2019
9. Changing climate inflicts drought on Tamil Nadu, <https://indiaclimatedialogue.net/2017/01/23/changing-climate-inflicts-drought-tamil-nadu/>. Accessed on 5 Mar 2019
10. Importance of Electricity—How It Changed People’s Lives, <https://www.articlesfactory.com/articles/science/importance-of-electricity-how-it-changed-peoples-lives.html>. Accessed on 19 Nov 2017
11. Marisarla C, Kumar KR (2013) A hybrid wind and solar energy system with battery energy storage for an isolated system. *Int J Eng Innov Technol (IJEIT)* 3
12. How Did Electricity Impact Society?, <https://www.reference.com/history/did-electricity-impact-society-3d108662bc468b61>. Accessed on 19 Nov 2017
13. Vuc G, Borlea I, Jigoria-Oprea D, Teslovan R (2013) Virtual power plant strategy for renewable resources aggregation. *Eurocon, 2013. IEEE*, pp 737–743. <https://doi.org/10.1109/EUROCON.2013.6625065>
14. Advantages and Disadvantages of Hybrid Power Supply System, <https://www.storagebattery-factory.com/news/advantages-and-disadvantages-of-hybrid-power-supply-system.html>. Accessed on 19 Nov 2017
15. Solar power, https://en.m.wikipedia.org/wiki/Solar_power. Accessed on 18 Feb 2019
16. Wind power, https://en.m.wikipedia.org/wiki/Wind_power. Accessed on 13 July 2018
17. Hydro Power, <https://en.m.wikipedia.org/wiki/Hydropower>. Accessed on 13 July 2018
18. Bhikabhai Y (2005) Hybrid power system and their potential in the pacific island, SOPAC Miscellaneous Report 406, <https://docs.niwa.co.nz/library/public/SMR406.pdf>. Accessed on 19 Nov 2017
19. Chun SC (2015) Development of a hybrid solar wind turbine for sustainable energy storage, Kuala Lumpur, <https://eprints.uthm.edu.my/7849/>. Accessed on 19 Nov 2017
20. Advantages of the Hybrid Energy System of Generators, <https://www.inmesol.com/hybrid-system/advantages-of-the-hybrid-system.asp>. Accessed on 19 Nov 2017
21. Power Sector at a Glance ALL INDIA|Government of India|Ministry of Power, <https://powermin.nic.in/en/content/power-sector-glance-all-india>. Accessed on 20 May 2018
22. Power for All Tamil Nadu, https://powermin.nic.in/sites/default/files/uploads/Power_For_All_Tamilnadu_Signed.pdf. Accessed on 3 July 2018
23. High-Voltage Direct Current, https://en.wikipedia.org/wiki/High-voltage_direct_current. Accessed on 12 Nov 2017

24. When and Why Is DC Used Instead of AC for Long-Distance Electric Power Lines? Is DC Becoming More Common Now? What Are Its Advantages and Disadvantages?-Quora, <https://www.quora.com/When-and-why-is-DC-used-instead-of-AC-for-long-distance-electric-power-lines-Is-DC-becoming-more-common-now-What-are-its-advantages-and-disadvantages>. Accessed on 19 Nov 2017
25. Rao GJ, Shrivastava SK (2016) Modelling and implementation of hybrid solar wind-hydro renewable energy systems. *Int Adv Res J Sci Eng Technol* 3:63–69
26. Solar Cell Model—MATLAB—Math Works India, <https://in.mathworks.com/help/physmod/elec/ref/solarcell.html>. Accessed on 20 Nov 2017
27. How Do Wind Turbines Work?|Department of Energy, <https://energy.gov/eere/wind/how-do-wind-turbines-work>. Accessed on 20 Nov 2017
28. Ingole AS, Rakhonde BS (2015) Hybrid power generation system using wind energy and solar energy. *Int J Sci Res Publ* 5:2250–3153
29. Martinez J (2007) Modelling and control of wind turbines. Master, Thesis, Imperial College London, UK, <https://workspace.imperial.ac.uk/centreforprocesssystemsengineering/Public/MSc%20Thesis/2007%20MSc%20Thesis/2007.2%20-%20Martinez%20Jasmin.pdf>. Accessed on 16 Oct 2017
30. Implement Model of Variable Pitch Wind Turbine—Simulink—Math Works India, <https://in.mathworks.com/help/physmod/sps/powersys/ref/windturbine.html?requestedDomain=www.mathworks.com>. Accessed 20 Nov 2017
31. Simulation of Solar and Wind Power Plant Using MATLAB for Micro-Grid, <https://easychair.org/publications/paper/dC56>. Accessed on 20 Nov 2017
32. Kumar S (2017) Modelling and simulation of hybrid wind/photovoltaic stand-alone generation system. Master, Thesis, National Institute Technology, Rourkela, <https://ethesis.nitrkl.ac.in/6344/1/E-44.pdf>. Accessed on 20 Nov 2017
33. Singh V, Kumar A, Batish N (2014) Simulation and analysis of integrated wind power with small hydroelectric hybrid power system for transient stability. *Adv Res Electr Electron Eng* 1:42–48
34. Dulau M, Bica D (2014) Mathematical modelling and simulation of the behavior of the steam turbine. *Procedia Technol* 723–729. The 7th international conference inter disciplinarity in engineering. <https://doi.org/10.1016/j.protcy.2013.12.555>
35. Lithium Ion Battery Advantages & Disadvantages: Radio-Electronics.Com, <https://www.radio-electronics.com/info/power-management/battery-technology/lithium-ion-battery-advantages-disadvantages.php>. Accessed on 12 Feb 2018
36. Implement Generic Battery Model—Simulink—Math Works India, <https://in.mathworks.com/help/physmod/sps/powersys/ref/battery.html>. Accessed on 20 Nov 2017
37. Bhattacharjee S, Nandi C, Reang S (2018) Intelligent energy management controller for hybrid system. In: 3rd IEEE international conference for convergence in technology (I2CT), pp 1–7
38. HOMER Energy, <https://www.homerenergy.com>. Accessed on 07 June 2018
39. NASA Prediction of Worldwide Energy Resources, <https://power.larc.nasa.gov/>. Accessed on 15 July 2018
40. Nandi C, Bhattacharjee S, Reang S (2018) An optimization case study of hybrid energy system based charging station for electric vehicle on Mettur, Tamil Nadu. *Int J Adv Sci Res Manag* 3:225–231
41. Inter-State Water Disputes, <https://web.archive.org/web/20070212165529/http://wrmin.nic.in/cooperation/disputes.htm>. Accessed on 1 Feb 2019
42. Nandi C, Bhattacharjee S, Chakraborty S (2019) Climate change and energy dynamics with solutions: a case study in Egypt. In: *Climate change and energy dynamics in the Middle East*. Springer, Berlin, pp 225–257
43. Saha S, Das S, Nandi C (2014) Harmonics analysis of power electronics loads. *Int J Comput Appl* 92:32–36
44. Bhattacharjee S, Batool S, Nandi C, Pakdeetrakulwong U (2017) Investigating electric vehicle (EV) charging station locations for Agartala, India. In: *The 2nd international conference of multidisciplinary approaches on UN sustainable development goals (UNSDGs)*, pp 28–29

ZnO/rGO Nanocomposite for Supercapacitor Energy Storage Applications



Sumitra Nongthombam and Bibhu Prasad Swain

Abstract Supercapacitors as a new class of energy storage devices are of considerable attention owing to their exceptionally large power densities and wide range of operating temperature which significantly challenges in meeting the energy requirements for numerous applications. The chapter deals with the basic understanding of the electrochemical system—principles, thermodynamics, the components and its effects in implementing the device. The materials that are used as electrode for supercapacitor devices play a significant part in its capacitive behavior. Importance of making composites of different electrode materials in supercapacitors is overviewed in this chapter. Numerous researches have been conducted recently approaching different synthesis methods for preparing rGO/ZnO composite. Herein, a few methods are highlighted. Review on the composite reveals their positive synergistic effect suggesting it as an encouraging hybrid material for various applications including supercapacitors. Electrochemical characterization techniques are discussed which are necessary to evaluate capacitive properties.

Keywords Supercapacitors · Electrochemical energy storage · Green energy storage · rGO/ZnO · Electrode materials · Nanocomposites

1 Introduction

Supercapacitors are electrochemical capacitors which have numerous advantages over the conventional capacitors, fuel cells and batteries. The continuous exploitation of fossil fuels in support of the growing energy necessitates our continuously rising population, and even though energy is made to produce from renewable sources requires energy management and large energy storage systems [1]. This excites many researchers to explore for high power storage capacity with the great life cycle. Thus, supercapacitors emerge as an alternative energy source providing more sustainability and environmentally friendliness. Supercapacitors also called ultracapacitors are different from fuel cells and batteries in terms of generation of energy. In fuel cells

S. Nongthombam · B. P. Swain (✉)
Department of Physics, National Institute of Technology Manipur, Imphal, India
e-mail: bibhuprasad.swain@gmail.com

© Springer Nature Singapore Pte Ltd. 2020
A. K. Bhoi et al. (eds.), *Advances in Greener Energy Technologies*,
Green Energy and Technology, https://doi.org/10.1007/978-981-15-4246-6_32

and batteries, chemical reactions occurring via redox reaction cause the generation of electrical energy. Contrarily, in supercapacitors, energy is not liberated through redox reaction but due to diffusion of electroactive ions near the electrode forming electrical double layers [2, 3]. Fuel cells are limited to availability and produce low power density, insufficient cycles and less durability although it provides high energy density. Supercapacitors have a great ability to generate large amount of energy usually high power densities, excellent cyclability and durability in comparison with that of conventional batteries. Also, their higher energy density and specific capacitance being significantly higher than traditional capacitors make them applicable for energy storage independently or hybrids with batteries for enhanced applications. Exhibition of notable properties by supercapacitors as discussed above finds it useful in various fields, viz. electronic industry, hybrid transportation, electric rails, etc. [4, 5]. However, their energy density being lower than batteries limits to utilize them for battery replaceable energy source [6]. So, nanostructured materials are of recent interest as they have large surface area contributing to the higher capacitance values, thus improving the performance of supercapacitors. The ability of supercapacitors to generate energy within a short period, high capacity and large charging/discharging cycles made them particularly useful for storing energy.

The specific capacitive behavior of this system is varied by some factors including the type of electrolytes and the electrode materials used. Variations in the properties of supercapacitors arising due to different electrolytes and their specific capacitance are reported. Electrochemical tests conducted with composites of asymmetric materials resulted in better performance possessing higher energy density and specific capacitance values compared to supercapacitors with symmetric electrode materials as reviewed in the recent article [7]. Report on capacitance values of the hybrid of ZnO and rGO reveals the composite as a promising material for electrode usage in supercapacitors [8]. Various kinds of synthesis process of the composite are discussed here in this chapter [6, 9, 10]. Thermodynamics governing in supercapacitors is introduced. Different techniques for making electrochemical measurements are explained [11, 12].

Recently, various new materials that can be used as electrodes are investigated by much researchers for further advancement of supercapacitors [13]. Carbon-based materials deal a great interest for using it as electrode in supercapacitor applications owing to its wettability by large surface, highly conducting, chemically stable and porous nature [14]. Among them, graphene is of tremendous interest because of its exceptional properties including large surface area, excellent electrical conductivity, efficient functionalization with other materials and good optical properties. Other than carbon-based materials, conducting polymers and oxide materials yield suitable electrode for supercapacitor devices [15].

2 Supercapacitors

Supercapacitors are a special kind of capacitors having higher energy storage capacity and specific capacitance than the traditional capacitors. The difference is that supercapacitors have no dielectric unlike in capacitors and features thinner separation between the electrodes. Electrolyte used in supercapacitors employs a vital part in its conductivity. They can be aqueous, organic, liquid, etc. In choosing so, high voltage window, high electrochemical stability, the high concentration of ions and smaller size of ions, low resistivity and less toxicity should be taken into consideration. Aqueous electrolytes have a higher concentration of ions and lower resistance compared to other electrolytes and can be prepared more easily but is limited due to its small voltage window resulting in less energy density and power density.

2.1 Principle of Capacitors

Capacitor consists of two plates with a dielectric between the two plates separating them. When a capacitor is provided a voltage, charge of opposite polarity accumulates on the two plates leading to a difference in potential between them. Due to the presence of dielectric between them, charges are unable to migrate but rather accumulate on the surface of two plates, thus storing them in the form of electrical energy. The value of capacitance in a capacitor is given by

$$C = \frac{Q}{V} \quad (1)$$

where Q denotes charge on each electrodes and V represents resulting difference in potential between them.

For a parallel plate capacitor, capacitance is defined to be

$$C = \frac{\epsilon_r \epsilon_0 A}{D} \quad (2)$$

where A is the area of each electrode, ϵ_r is the relative permittivity of a material, ϵ_0 is the permittivity of free space and D is the distance between the electrodes.

2.2 Types of Supercapacitors

Depending on their charge storage properties, supercapacitors can be currently categorized as (1) electrochemical double-layer capacitors (ELDC), (2) pseudocapacitors and (3) hybrid capacitors. A typical schematic diagram for the three kinds of capacitors is shown below (Fig. 1).

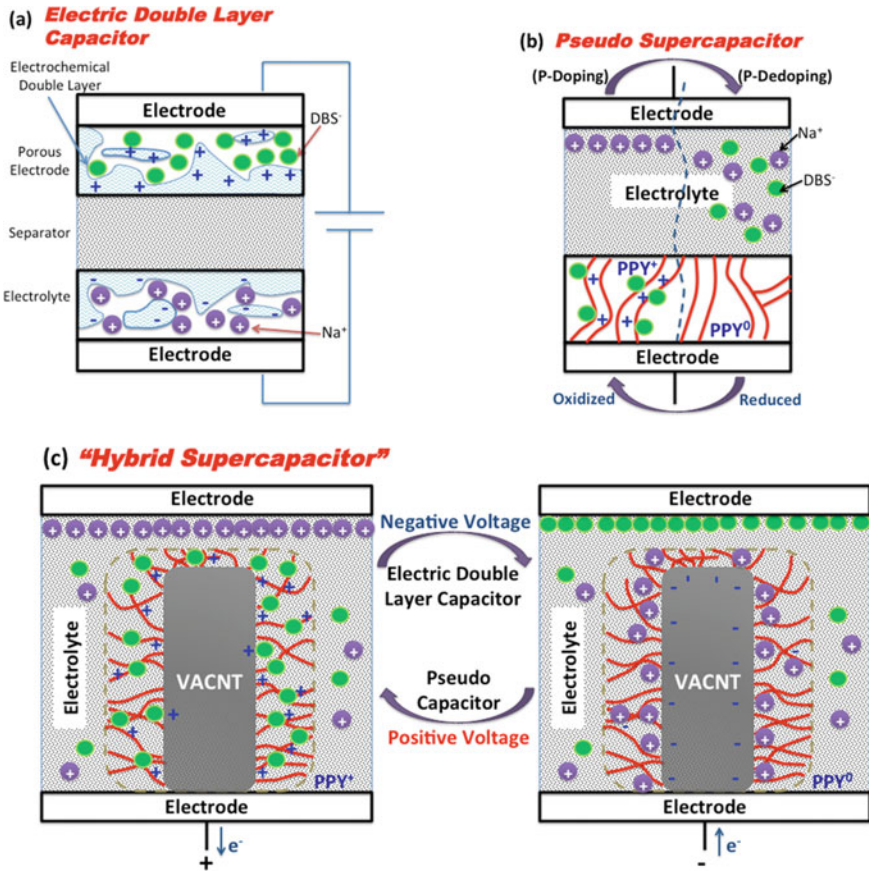


Fig.1 Schematic representation of EDLC, pseudocapacitor and hybrid supercapacitor [16]

EDLC is a kind of supercapacitor where the capacitance is generated through the diffusion of electrolyte ions near the electrode surface. Charge accumulates over the opposite electrodes forming electrical double layers, hence the name electrical double layer capacitor. It is a non-Faradaic process where various forms of carbon are the widely used electrode materials. Charge is not transferred between the electrodes in EDLC with the electrolyte remaining constant through the charge/discharge flow. The composition of the electrodes may change during the reaction. Carbon nanotubes, fullerene and graphene are some of the materials which can form electrical double layers.

The capacitance of pseudocapacitors arises from the Faradaic reversible process that takes place between the electrolyte and some electroactive species. Conducting polymers and metal oxides are commonly studied materials for pseudocapacitors.

Since they somewhat behave like a battery, they provide larger energy density as compared to EDLC. Some examples are PANI, MnO_2 , PEVOT, RuO_2 , etc.

In spite of their differences, both EDLCs and pseudocapacitors are dependent on the surface area as both phenomena occur across the surface throughout the charging–discharging reactions. Thus, to obtain large capacitance values, there is a need in increasing the specific surface area and proper control of the material pore size. Materials exhibiting pseudocapacitance which have lower cycle stability and lower power density are made a composite with carbon-based materials which possess relatively lower energy density to utilize the advantage of both the properties of electrolytic capacitors and battery-like behavior of pseudocapacitors. These hybrid materials which compensate the deficient properties of their individuals enhancing the performance of supercapacitors are called hybrid supercapacitors. Commonly studied hybrid materials are graphene-based and carbon nanotubes (CNT)-based composites with metal oxides or conducting polymers.

3 Overview of Different Electrode Materials

Carbon-based materials, for instance, graphene, fullerene, carbon nanotubes (CNT) and other forms of carbon, are mostly studied for making electrode materials because of their highly porous nature and excellent conducting properties for supercapacitor applications. Some promising electrode materials for energy storage applications include RuO_2 , MnO_2 , V_2O_5 , Fe_3O_4 , ZnO. Also, conducting polymers can make double-layer capacitance reporting a significant specific capacitance. Recently, functionalization of these various materials is the commonly investigated works for studying supercapacitor performance. Composites of CNT with electrically conducting polymers (ECPs) reported high specific capacitance with excellent cycle life [17]. The reason is due to the high doping level and high charge/discharge rate which makes it a significant advantage in supercapacitors although they are mechanically weak and poor cyclic stability. Thus, making hybrids with CNTs provides excellent mechanical properties in addition to the excellent conductivity and high charge/discharge cycle. Tremendous attention is in the study of graphene materials because of its superior electrical conductivity than the other carbon-based materials. The literature review on graphene reveals that it can produce specific capacitance of 117 Fg^{-1} in aq. H_2SO_4 at 100 mV/s scan rate when prepared with different methods [3]. rGO/ZnO nanocomposite shows large specific capacitance upto 314 Fg^{-1} with good cyclability synthesized by using supercritical method [9].

4 Synergetic Effect of ZnO/rGO Nanocomposite

Graphene is a promising material because of its notable properties including large surface area, highly conducting, good thermal, optical and mechanical exhibition.

For a single-layer graphene, its specific surface area is $2600 \text{ m}^2/\text{g}$ theoretically [18]. The specific capacitance of graphene-based EDLC is 550 Fg^{-1} theoretically, while electrochemical measurement using cyclic voltammetry shows 21 Fcm^{-2} in Song et al. work [19]. Nevertheless, due to the restacking of graphene sheets, the conductivity of graphene is reduced and has lesser specific capacitance. So, to improve their capacitive behavior, they are made composite with other capacitive materials. Composite with pseudocapacitive materials generates capacitance from redox charge transfer in addition to the double-layer capacitance. On the other hand, ZnO is a multifunctional material possessing 3.37 eV band gap, 60 mV exciton binding energy and excellent optical and electrical properties utilizing it on a broad range of applications including supercapacitors. In spite of the lower specific capacitance than other metal oxides, ZnO offers great advantage for studying supercapacitor applications due to their low cost, highly abundant and non-toxic behavior. Besides, ZnO being a suitable electron donor makes it an excellent combining material for graphene as it is a good acceptor of the electron. ZnO/G composite shows specific capacitance highest up to 122.4 F/g at a scan rate of 5 mV as reported by Suranya et al. [6].

5 Preparation Methods

5.1 Preparation of GO

Graphene oxide can be prepared from graphite oxide by some methods such as reduction process and ball milling. Hwang et al. describe the preparation of graphene oxide using modified Hummers process [20]. In brief, graphite powder about 4 and 2 g of NaNO_3 is added into 92 ml of H_2SO_4 solution, and the mixture is continuously stirred in a thermostat bath maintained at $3 \text{ }^\circ\text{C}$. Further, the solution is continuously stirred around 2 h by slowly adding 12 g of potassium permanganate into the solution. Then, the obtained solution is heated at $35 \text{ }^\circ\text{C}$ while stirring continuously for another 2 h . Subsequently, the temperature of the solution is heated at $75 \text{ }^\circ\text{C}$ while adding 184 mL of distilled water into the solution. Then, after stirring for 10 min , the mixture is slowly dropped to 5% H_2O_2 so that the undissolved KMnO_4 can be removed. The process continues until the above solution turns a brilliant yellow color.

5.2 Different Methods for Preparing ZnO/GO Nanocomposite

ZnO/graphene composite is prepared by Yubaraj et al. utilizing supercritical carbon dioxide (ScCO_2) [9]. A homogenous suspension is obtained by mixing 1 mL of ethanol in 20 mg GO which is then kept around 2 h in an ultrasonicator under room temperature. Another solution of ZnO precursor typically $\text{Zn}(\text{NO}_3)_2 \cdot 6\text{H}_2\text{O}$ (100 g)

and ethanol (1 mL) is prepared. The two solutions are mixed and put to a 20-mL stainless steel reactor. The reactor is maintained at a temperature of 300 °C and pressure of 9 MPa after it is charged with CO₂. The solution is stirred continuously for 6 h under ScCO₂ conditions. Then, CO₂ is slowly removed from the solution, and the ZnO/graphene composite is obtained.

The composite is also prepared by the microwave-assisted technique by some other researchers [10]. Here, 10 mL of hydrazine is dissolved in GO/Zn(OH)₂ and placed in a microwave system. The solution is maintained at a temperature of 150 °C for 2 min, thereby obtaining black color. The obtained solution is then repeatedly washed with DI, at a centrifuge speed of 10,000 rpm about 10 min so that the residuals are removed from the solution. The resulting product is then dried for 3 h at 100 °C in a hot air oven, and ZnO/graphene composite is synthesized.

Preparation of graphene/ZnO composite is described by Santhya et al. using solvothermal process [6]. Briefly, ethylene glycol about 2 ml is mixed with 5 mg of synthesized graphene, and the solution is transferred into a sonicator and kept for 1 h. The above solution is filled with 20 mL of ethylene glycol which is stirred continuously by dissolving 20 mg of zinc acetate into the solution. Then 0.1 M of NaOH dissolved in 5 mL DI is poured in the above solution under continuous stirring. After the solution is stirred for 30 min, it is poured in an autoclave at 160 °C for two days. After centrifuging the above solution, ethanol and DI are used for washing it thoroughly which is then dried for 24 h. The final product obtained is the graphene/ZnO.

6 Electrochemical Measurements

The conducting characteristics of supercapacitors are studied by electron impedance spectroscopy, cyclic voltammetry (CV) and galvanostatically charge/discharge. These techniques determine the specific capacitance of supercapacitors. The structure of an electrochemical system is composed of three electrodes—reference electrodes usually kept at a constant voltage, working electrode whose potential is determined with respect to the reference electrode and counter electrode to make a complete circuit. All electrochemical techniques are based on Ohm's law. In the CV method, response in current is measured as a function of the potential applied across the electrode. On the other hand, voltage is determined by controlling the current in the electrochemical cell in the galvanostatic method. The CV is measured at each of the electrodes at different scan rates. The scan rate varies inversely with specific capacitance. Lower the scan rate, higher is the specific capacitance. Scan rate determines how fast the voltage is scanned. Faster the scan rate, size of diffusion layer of the supercapacitor decreases followed by subsequent rise in current. Besides, energy density and power density of the electrodes are also responsible in altering the behavior of a supercapacitor. They vary inversely to each other. They can be measured from the two formulas given by

$$E = \frac{1}{2}C(\nabla V)^2 \quad (3)$$

$$P = E/t \quad (4)$$

Here, C denotes specific capacitance, t is discharge rate and ΔV symbolizes potential window.

6.1 Cyclic Voltammetry

This technique is used to determine the capacitive nature of various electrodes to be used in supercapacitors. In a typical CV experiment, the voltage supplied to an electrochemical cell is varied, and the resulting current is determined as time elapse. The variation in potential is shown in Fig. 2 where the applying voltage is made to decrease from E_1 to E_2 and then reverse back to E_1 . This voltage speed can be altered and is called the scan rate.

Fig. 2 Potential variation as a function of time during the cyclic voltammetry

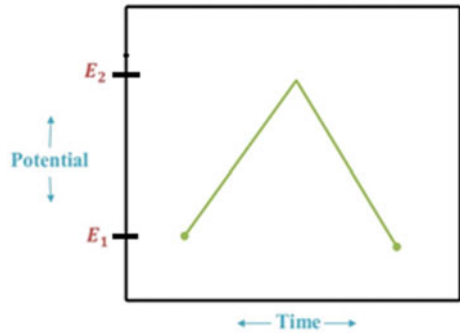


Fig. 3 Current versus potential plot in the cyclic voltammetry experiment

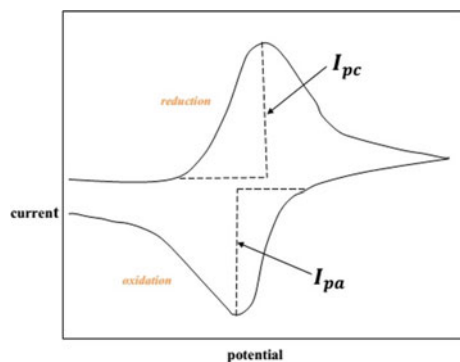


Figure 3 is the rough picture of cyclic voltammograms. Here, the voltage is the first scan negatively where the analyte gets more and more reduced on the electrode generating a reduction current. However, with further increase in the voltage, there is a decrease in current as diffusion of the analyte is increased forming a diffusion layer near the electrode. When a scan in the reverse direction the analyte reoxidizes the formerly reduced analyte to liberate the reduction current. I_{pc} and I_{pa} denote the cathodic peak current and anodic peak current during oxidation and reduction process, respectively. This peak current value varies linearly with the scan speed where the specific capacitance is determined using the formula

$$C = \frac{I_{pc} + I_{pa}}{\nu m} \quad (5)$$

where I_{pc} and I_{pa} are the current peak in the forward scan and reverse scan, respectively.

The pseudocapacitance of conducting polymers and metal oxides is evaluated with CV with appropriate electrolytes and at various scan rates. CV is the repeated alternate cycles of cathodic and anodic scans. The area of the current–potential curve of supercapacitor determines capacitance where larger area represents the better performance of a supercapacitor.

6.1.1 Nernst Equation

The equilibrium of the oxidized and reduced concentrations of the analytic in CV is described by the Nernst equation. The maximum amount of work done an electrochemical potential can perform is given by Gibbs free energy. Gibbs energy can determine the equilibrium composition of a reaction mixture by identifying the composition corresponding to the Gibbs energy minimum. By knowing the Gibbs energy at a specific composition, we can measure the zero current cell potential at that composition using the relation

$$\Delta G = -\nu F E \quad (6)$$

where ν is the number of electrons, F is the Faraday constant and E is the potential difference of the cell.

Considering the reduction reaction in the electrochemical cell $A^+ + e^- \rightarrow A$.

The applied cell potential can be described as an expression relating to the relative reduced and oxidized species of the analyte.

$$E = \frac{\Delta G}{\nu F} - \frac{RT}{\nu F} \ln Q \quad (7)$$

$Q = \frac{A}{A^+}$ is the reaction quotient.

The above equation can be written as

$$E = -E^0 - \frac{RT}{\nu F} \ln Q \quad (8)$$

where E^0 is the standard Gibbs energy expressed in potential.

This equation is known as the Nernst equation.

6.2 Galvanostatic Charge/Discharge Method

Galvanostatic charge/discharge method consists of a galvanostat for controlling current, and the resulting potential is measured. At constant current, the rate of change of voltage can be plotted. The nearly triangular shape obtained in the plot provides charge/discharge properties of the electrode material, and from the discharge, an internal resistance of the electrode material can also be measured. Apart from measuring specific capacitance of supercapacitor, GCD plot determines its energy and power density.

Using the CV and GCD curves, specific capacitance of supercapacitor can be calculated using relation (9).

$$C = \frac{I}{\frac{dV}{dt}} \quad (9)$$

I is the discharge current and $\frac{dV}{dt}$ gives the rate of discharge which is measured from the plot.

$$C_{sp} = \frac{4C}{m} \quad (10)$$

m is the mass of species of nanomaterials present on the electrodes.

Capacitance from the charge/discharge plot can be compared with that obtained by CV and analyze the capacitance values. In addition, the energy density and power density is also determined from the formula

$$E = \frac{CV^2}{2} \quad (11)$$

$$P = \frac{V^2}{4R} \quad (12)$$

where R is the equivalent series resistance.

6.3 Electrochemical Impedance Spectroscopy

This technique is a graphical method which is used to measure specific capacitance from impedance spectra. The impedance is measured by using Ohm's law. Impedance is plotted as a function of frequency varying over a wide range. At the lower frequency of the plot, a straight line is observed, whereas small semicircles are shown at higher frequencies. This indicates that some harmonics are present in the input signal at higher frequencies. The length of the semicircle gives charge transport of Faradaic resistance along with the solution resistance, and decrease in the Faradaic resistance increases the density in power. The capacitance can be evaluated using the relation

$$C = \frac{1}{2\pi f Z} \quad (13)$$

The impedance of the electrode materials is comprised of real part and imaginary part. Nyquist plot is the plot between the two terms. When heterogeneous electrodes are considered, Randles and Ershler model are usually helpful as they can be used to measure the interfacial properties of supercapacitors. The Randles–Ershler equivalent circuits are defined as

$$Z_{RE} = R_s + \left(j\omega C_d + \frac{1}{R_{CT} + ZW(\omega)} \right) \quad (14)$$

It determines the electrolyte charge resistance, Warburg impedance arising from the diffusion of electrolyte ions from the electrolyte to the electrode, double layer capacitance and electron transfer resistance. EIS determines characteristics of conduction and the charge transport in the electrode/electrolyte interface. It analyzes low resistance and charge transport from the electrode to the electrolyte.

7 Summary

Supercapacitors emerge as an essential energy source with an increasing number of applications in various fields leading to one of the versatile tools in modern technology. Both the two main kinds of capacitor, viz. pseudocapacitors and EDLC, are surface phenomena, and larger the surface area, more is the contribution to the specific capacitance of a supercapacitor. Electrodes made of hybrid materials in a supercapacitor provide large capacitance as both redox reactions and charge accumulation occur across the electrode surface. ZnO/graphene nanocomposite serves an efficient electrode material as it shows a high specific capacitance and cyclic stability. The composite made a synergistic effect as it attains higher specific capacitance compared to the individual electrode materials. Recombination of electron hole pairs takes place in the composite. The basic principles governing in supercapacitors are

the same as in conventional capacitors. Components in a supercapacitor play a key role in varying its capacitive performance. With the proper understanding of the principles and components of a supercapacitor, the device can be improved by carefully choosing electrode and electrolyte used.

References

1. Tan CW, Tan KH, Ong YT, Mohamed AR, Sharif Hussein SZ (2011) Carbon nanotubes applications: solar and fuel cells, hydrogen storage, lithium batteries, supercapacitors, nanocomposites, gas, pathogens, dyes, heavy metals and pesticides. *Environ Chem Sustain World* 3–46
2. Winter M, Brodd RJ (2004) What are batteries, fuel cells, and supercapacitors? *Chem Rev* 104:4245–4269
3. Vivekchand SRC, Rout CS, Subrahmanyam KS, Govindaraj A, Rao CNR (2008) Graphene-based electrochemical supercapacitors. *J Chem Sci* 120:9–13
4. Chen Y, Zhang Z, Hwang Z, Zhang H (2017) Effects of oxygen-containing functional groups on the supercapacitor performance of incompletely reduced graphene oxides. *Int J Hydrogen Energy* 42:7186–7194
5. Weinstock IB (2002) Recent advances in the US department of energy storage technology research and development programs for hybrid electric and electric vehicles. *J Power Sources* 110:471–474
6. Saranya M, Ramachandran R, Wang F (2016) Graphene-zinc oxide (G-ZnO) nanocomposite for electrochemical supercapacitor applications. *JS: AMD* 1:454–460
7. Muzaffar A, Ahamed MB, Deshmukh K, Thirumalai J (2019) A review on recent advances in hybrid supercapacitors: design, fabrication and applications. *Renew Sust Energy Rev* 110:123–145
8. Zhang Y, Li H, Pan L, Lu T, Sun Z (2009) Capacitive behavior of graphene–ZnO composite film for supercapacitors. *J Electroanal Chem* 634:68–71
9. Haldoraia Y, Voitb W, Shima J (2014) Nano ZnO@ reduced graphene oxide composite for high performance supercapacitor: green synthesis in supercritical fluid. *Electrochim Acta* 120:65–72
10. Ramadoss A, Kim SJ (2013) Facile preparation and electrochemical characterization of graphene/ZnO nanocomposite for supercapacitor applications. *Mater Chem Phys* 140:405–411
11. Dhillion S, Kant R (2017) Theory for electrochemical impedance spectroscopy of heterogeneous electrode with distributed capacitance and charge transfer resistance. *J Chem Sci* 129:1277–1292
12. Chen SM, Ramachandran R, Saraswathi V (2014) Recent advancements in electrode materials for the high performance electrochemical supercapacitors: a review. *Int J Electrochem Sci* 9:4072–4085
13. Conway BE, Birss V, Wojtowicz J (1997) The role and utilization of pseudocapacitance for energy storage by supercapacitors. *J Power Sources* 66:1–14
14. Frackowiak E, Khomenko V, Jurewicz K, Lota K, Beguin F (2006) Supercapacitors based on conducting polymers/nanotubes composites. *J Power Sources*. 153:413–418
15. Stankovich S, Dikin DA, Domment GHB, NaOH KM, Zimmey EJ, Stach EA, Piner RD, Nguyen SBT, Ruoff RS (2006) Graphene-based composite material. *Nature* 442:282–286
16. Sammoura FN, Teh KS, Kozinda A, Zang X, Lin L (2014) A hybrid supercapacitor using vertically aligned CNT-polypyrrole nanocomposite. In: *IEEE 27th international conference on micro electro mechanical systems (MEMS)*
17. Liu CG, Yu ZN, Deff D, Zhamu A, Jang BZ (2010) Graphene-based supercapacitor with an ultrahigh energy density. *Nano Lett* 10:4863–4868
18. Hummers WS, Offeman RE (1958) Preparation of graphene oxide. *J Am Chem Soc* 80:1339–1344

19. Song C, Yin X, Han M, Li X, Hou Z, Zhang L, Cheng L (2017) Three-dimensional reduced graphene oxide foam modified with ZnO nanowires for enhanced microwave absorption properties. *Carbon* 116:50–58
20. Huang Z, Zhang H, Chen Y, Wang W, Chen Y, Zhong Y (2013) Microwave-assisted synthesis of functionalized graphene on Ni foams electrodes for supercapacitor applications. *Electrochim Acta*. 108:421–428
21. Elgrishi N, Rountree KJ, McCarthy BD, Rountree ES, Eisenhart TT, Dempsey JL (2018) A practical beginner's guide to cyclic voltammetry. *J Chem Educ* 95:197–206
22. Vangari M, Pryor T, Jiang L (2013) Supercapacitors: review of materials and fabrication methods. *J Energy Eng* 139(2):72–79
23. Wang S, Wei T, Qi Z (2008) Supercapacitor energy storage technology and its application in renewable energy power generation system. In: *Proceedings of ISES world congress 2007*, vol I–V, pp 2805–2809
24. Lonkara SP, Pillaia V, Abdalab A (2019) Solvent-free synthesis of ZnO-graphene nanocomposite with superior photocatalytic activity. *Appl Surf Sci* 465:1107–1113
25. Lang X, Hirata A, Fujita T, Chen M (2011) Nanoporous metal/oxide hybrid electrodes for electrochemical supercapacitors. *Nat Nanotechnol* 6:232–236
26. Li Z, Zhou Z, Yun G, Kai Shi LX, Yang B (2013) High-performance solid-state supercapacitors based on graphene-ZnO hybrid nanocomposites. *Nanoscale Res Lett* 8:1–9
27. Pandolfo AG, Hollenkamp AF (2006) Carbon properties and their role in supercapacitors. *J Power Sources* 157:11–27
28. Hashim N, Muda Z, Hussein M, Isa IM, Mohamed A, Kamari A, Suriani SA, Mamat M, Jaafar AM (2016) A brief review on recent graphene oxide-based material nanocomposites: synthesis and applications. *J Mater Environ Sci* 7(9):3225–3243
29. Lonkara SP, Pillaia V, Abdalab A (2019) Solvent-free synthesis of ZnO-graphene nanocomposite with superior photocatalytic activity. *Appl Surf Sc* 465 1107–1113

Green IoT (G-IoT): An Insight on Green Computing for Greening the Future



T. Suriya Praba, S. Pooja Laxmi, T. Sethukarasi, R. D. Harshitha, and Veeramuthu Venkatesh

Abstract The smarter world is projected using an epoch in which things like smartwatches, mobile phones, desktop, laptops, vehicles and intelligent trains can inevitably and sensitively help people in a cooperative manner. With the proliferation in the number of desktops, the aggregate amount of energy depleted by them is on a substantial rise, which in turn is augmenting carbon content in the global atmosphere. With the consciousness of this problem, methods are being in use to diminish the power practice in computers. To solve this issue, green computing is the only solution. Green computing is the effective exploitation of computing assets while reducing environmental percussion and ensuring both financial and social safety. It is a well-adjusted ecological method toward attaining a healthier and innocuous environment without negotiating the technological prerequisites of the current and future generations. This chapter illustrates the overview of advances in green cloud computing technology and several other technologies and problems regarding green IoT and helps attain acme in all the future works and experiments that need to be covered to endure a sustainable green computing atmosphere. This in turn helps in establishing self-assured growth.

Keywords IoT · Green computing · Energy saving · Wireless sensor network · Green data centers

1 Introduction

Green computing is the study, research and implementation of environmentally friendly and sustainable computing [1–4]. The world’s environmental situation is

T. Suriya Praba · S. Pooja Laxmi · R. D. Harshitha · V. Venkatesh (✉)
SASTRA Deemed University, Thanjavur 613401, India
e-mail: venkatesh@cse.sastra.edu

T. Suriya Praba
e-mail: suriyapraba@cse.sastra.edu

T. Sethukarasi
R M K Engineering College, Chennai 601206, India

getting progressively worse, and as professionals and professionals-to-be in the IT field, we need to be mindful of the algorithms, architecture components, technology and hardware that we use. This is why we require green computing.

1.1 Need for Green Computing

The average computer consumes so much power than what is needed and emits a significant amount of CO₂. In addition to this, computers are also made up of hardware components that have toxic materials in them that make it harder to dispose of them. Figure 1 shows the composition of the average personal computer.

Computers are just about everywhere now, and it is high time we develop methods of using sustainable technologies. Figure 2 is given below which shows the power consumption in a typical working environment [5–8]. There are no offices in the

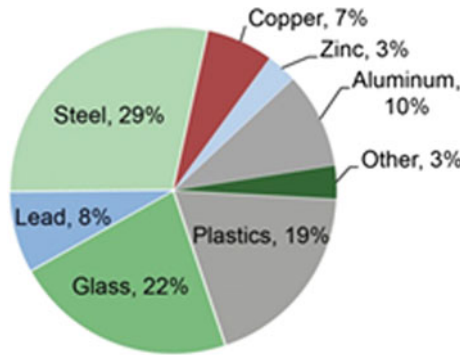


Fig. 1 Composition of the average personal computer

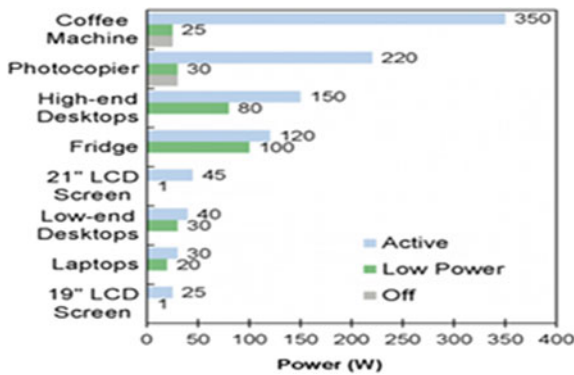


Fig. 2 Power consumption in a typical working environment

world that do not use computers, and all of them at least use this much power on an average; a plain end user does not know all that is involved. So, it lies in our hands to create and implement green and sustainable alternatives, this necessitates green computing.

1.2 Areas Addressed to Achieve Green Computing [5–9]

The chapter discusses various topics of the Internet of Things (IoT) such as green radio-frequency identification (RFID), green wireless sensor network (GWSN), green cloud computing (GCC), green edge computing (GEC), green data centers (GDC) and green machine-to-machine (GM2M) technologies which are diagrammatically represented in Fig. 3.

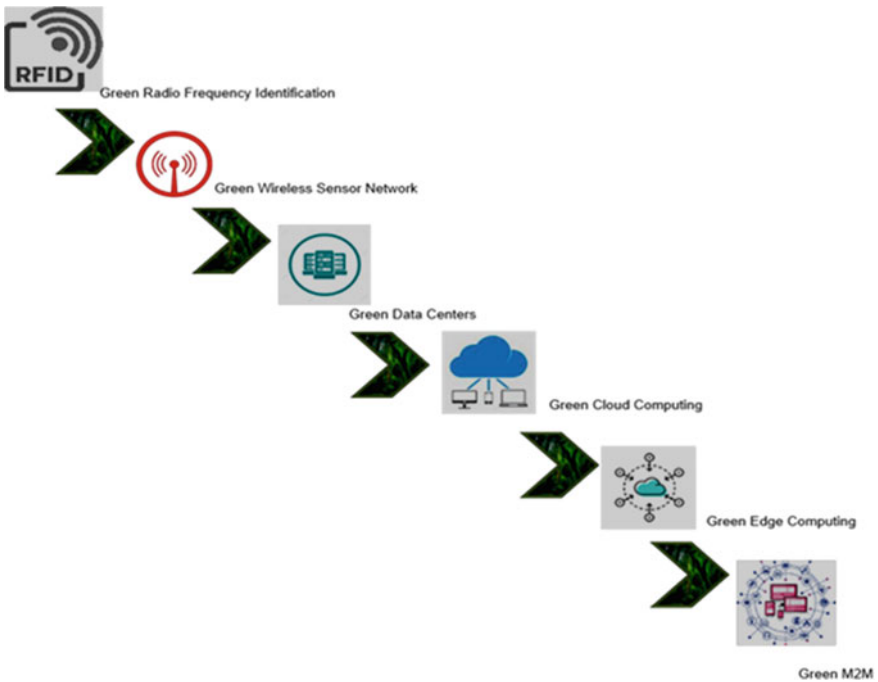


Fig. 3 Areas addressed to achieve green computing

2 Green Radio-Frequency Identification [10]

2.1 Introduction to RFID

It is one of the most primitive technologies. It has experienced a lot of advancements over the years. This topic discussed RFID and how it can be made greener and the advantages of doing so. It is the technology involved in identifying devices with the help of radio waves. In short, it is a sensing mechanism. The fact that it uses radio waves makes it unique and its architecture unique as well.

RFID consists of four different components; they are tag, reader, antenna and the station.

2.1.1 Tag

It is the key element for identifying devices. There are two different types of tags, active and passive tags. The active tags have their source of power, typically to transmit and receive signals to either send or receive messages. The passive tags do not have a source of power such as a battery; instead, they depend on the readers (readers will be discussed shortly); these signals help in generating electromagnetic energy that the tags use to power themselves.

2.1.2 Reader

If the tag is used for sending, then the RFID reader extracts the information sent by the tag. The communication between the tag and the reader is done through radio waves as mentioned above. Because of the range of radio waves, the tag and reader must be within the confines of the range for proper functioning.

2.1.3 Antenna

This is the component that bridges communication between the tag and the reader. This is at the heart of the RFID technology. It is a simple circuit that receives signals and converts them into radiations. Owing to the smaller size of RFID systems, the antennas are small as well. This results in both the wavelength and the bandwidth which are small.

2.1.4 Station

It is an intelligent self-standing component of the system that records the findings of the tags or the history of communication between the reader and the tag.

RFID is used in various domains; in the commerce field, it is used for asset tracking; in retail applications, it contributes to inventory control and keeping in check the new items added and old items that are removed. It finds purpose in the access control sector as a way of granting access to authorized users. Instead of a magnetic strip, barcodes are utilized to grant access to users with valid privilege. For example, the library cards issued need only to be placed in front of the reader, and the owner of it can enter if the reader returns assuring feedback. RFID is a simple, primitive and yet efficient technology.

As many advantages as there are, they impose some negative impacts on the environment. Green computing aims at developing computer systems and their components in such a way that from the manufacturing phase to the disposal phase, the systems involved are friendly to the environment and not leave any traces that cannot be reversed. In contrast, the components used in RFID are hard to recycle and are hazardous to the environment. This is a much serious issue since disposal or recycling are parts of the lifecycle of a technology's components. Many organizations have already taken to protests to reveal the serious impact of primitive RFID components, and many papers have been published to reiterate this fact.

Moreover, RFID is more expensive than barcoding and can in many cases be easily replaced by the use of barcode readers. It requires a lot of maintenance and needs to be checked frequently since it is a unique technology. The installation, implementation and monitoring of the reader need to be done by experts. The RFID components used now are not energy efficient in any manner. The algorithms and protocols used need to focus on eliminating tag collisions, manage the overheating issues and employ powerful dynamic algorithms to handle transmission and reception of signals. This topic discovers ways in which the negative effects of RFID on the environment can be removed. It searches for any modification that would result in improved efficiency.

2.2 Making RFID Green

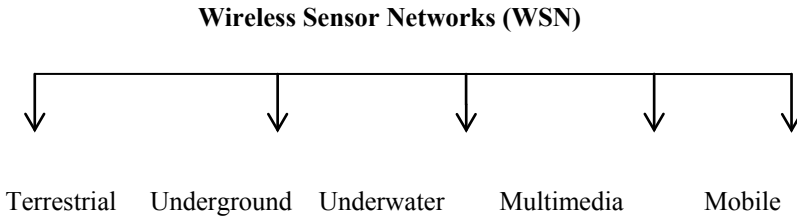
The usage of unmanned aerial vehicle (UAV) helped in increasing the range and identifying the readers a lot easier. The addition of just this one component makes it so much more efficient. The UAV and sensors help in delivering information from the readers, while the tags monitor the area the RFID is about to sense.

The RFID technology is less problematic compared to other technologies and is hence viewed as a benchmark for how green technology is supposed to be inherently.

3 Green Wireless Sensor Network [11–13]

Wireless sensor network (WSN) consists of many sensors spaced out across a network to monitor and store information based on what they were deployed for, and mostly, they record temperature, humidity, etc. Communication between different

sensors or nodes is wireless as the name suggests. There are different types of WSNs. They are terrestrial, underground, underwater, multimedia and mobile wireless sensor networks.



3.1 Types of Wireless Sensor Network

3.1.1 Terrestrial

These sensors are present in the land and make for great ground stations that facilitate communication. They span over target areas typically arranged either in a structured or unstructured way. The battery power is considerably low, but it can be enhanced with secondary sources of power.

3.1.2 Underground

This type of WSN is more expensive than its terrestrial counterpart. They need more in terms of attention, maintenance, cost and implementation. They prove to be extremely useful in monitoring underground conditions. Since these sensors are present underground, recharging them is hard. In addition to the existing problem, they have low battery power, and they suffer a significant amount of signal loss as well.

3.1.3 Underwater

Underwater sensors are effective in applications that call for monitoring the conditions in water bodies. A lot of applications revolve around the information provided by these sensors. A lot of the tech that can be used underwater is under development and need betterment. The underwater sensors are no exceptions. Also, they have a low battery life and cannot be recharged.

3.1.4 Multimedia

Multimedia WSNs monitor and respond to multimedia content such as images, video files and audio files. They are required in large numbers, and so, the sensors are low cost in most cases. They have components that facilitate receiving and transmitting multimedia content. This implies that it also requires high bandwidth and energy requirements.

3.1.5 Mobile

These sensors were primarily created to adapt, improve and overcome obstacles of static sensors. They are intelligent and are capable of providing better coverage due to their mobility. Optimization of power consumption is one of the many reasons why they are preferred.

This shows that WSNs are used in all walks of life without us even being aware of it. Since they are ubiquitous and are huge in number, they are bound to have some impacts on the environment. Not to mention some of them affect it negatively.

They have enormous power requirements but not enough performance which is not a desired property. They do not effectively utilize energy. Usage of batteries with a limited or very short-lived life span that is not friendly to the environment is some of the negative effects associated with mobile sensors. The rest of the topic discusses how these negative effects can be counteracted.

3.2 *Achieving Green Wireless Sensor Networks*

Making room for efficient usage of power is a plausible first move. The main reason why power management is not efficient in WSNs is that they are idle most of the time. Thus, putting these sensors in sleep mode during the time they are not being used and waking them up during transmission or reception is a useful addition. This not only improves efficiency but also makes the system smarter and greener. In addition to this, the sensors can take advantage of the environment they are deployed in. For example, terrestrial WSNs could make use of solar energy instead of short-lived batteries and mobile WSNs.

- Can utilize kinetic energy to recharge or back the sensors up. This not only explores renewable energy resource deployment but also makes the network green.
- The second move is to focus on improving the design of the network without affecting the quality of service. This involves replacing the existing constituents with their better counterparts. Such an architecture involves a hierarchical network design, wherein the smart, green (ones with sleep and wake states that are controlled by a microprocessor) nodes or sensors are placed in optimal places and clustered. The integration mechanism used in clustering is vital as it improves

the longevity of the sensor's life. The outcome of all this produced a design that showed a significant rise in performance, decrease in power consumption and cost which. Hence, this is an ideal indicator of a green alternative.

- The final step is improving performance while reducing CO₂ emissions. Incorporation of wake-up radios (WUR) in WSN for supporting the waking state of remote nodes is a valuable additive. The next scheme is wireless energy harvesting (WEH), which is the usage of unperishable resources as already seen before. Another additive is error control coding (ECC); now, this is something we have not addressed yet. Sensor networks such as the underground and underwater ones suffer a significant loss of signals due to which additional energy is used to retransmit. ECC strives to reduce the loss of signals by removing noise and ensures the reliability of the signals. These schemes make the network greener by reducing carbon emissions.

3.3 Advantages of Green Wireless Sensor Network

- Encourages the use of mobile sensors while ensuring unaltered and perhaps bettered performance and is widely available to everyone.
- Short-lived batteries made out of toxic materials are discarded.
- Power consumption is optimized, and no negative trade-offs are observed.
- Scope for renewable energy resources is explored and employed.
- CO₂ emissions are reduced.

In essence, green wireless sensor network is of great value to the Internet of things, and the improvements that have been made through years are clear sign to pursue it.

4 Green Data Centers [14, 15]

4.1 Data Centers

A data center is a common word in the tech world. Data centers are so large, complex and have huge requirements of resources because of which there are only about 390–400 around the world. By definition, a data center is a large group of networked computer servers typically used by organizations for the remote storage, processing or distribution of large amounts of data. They consist of either a small number of large servers or a large number of small servers all in a single building or room; for this reason, they are called server farms. It is already a known fact that a single computer on its own has a significant carbon footprint, so it is obvious that a large group of computers and servers will affect the environment badly. We shall explore

green data centers and understand why they are necessary and how they interact with the environment.

4.1.1 Importance of Data Centers

In the Internet world, data centers quite literally run everything, ranging from browsing to data storage to communication to e-commerce and so on. So, you can imagine how very powerful they are. In 2011, 1.8 ZB (Zetta Bytes) of digital data was generated by data centers, and consecutively in 2016, it was 2.8 ZB, and by 2020, it is estimated to be about 40 ZB. The processing power of data centers is excellent, and the demand for processing is very high. Technologies to improve the speed, quality and power are much sought after. In such a point in time, considering the Earth's needs and welfare should also be a concern, and more often than not, it is not. The advent of cloud computing also provoked the usage and need for data centers.

After this casual introduction, let us now get into details about the data center on a deeper level. Data centers are no different than regular offices in terms of the outward appearance, but the inside is filled with server stacks monitored and managed by a group of individuals assigned to them. As for the design, different organizations have different designs. The arrangement of servers, network topology used and the additional or complementary equipment used also vary based on the design, the organization, its needs, the services it caters and so on. This, of course, affects the speed, performance and efficiency.

Data centers can be categorized into three different types, distributed data centers, centralized data centers and cloud-enabled data centers.

Distributed DC: A series of data centers are interconnected or distributed over the network so that they can provide services round the clock whenever and wherever necessary.

Centralized DC: Data centers placed in different locations of the world that are part of the data center network might take up additional resources, to optimize the resource usage; they are all moved to a single location. This is known as data center consolidation.

Cloud-enabled DC: Cloud computing is a very up and coming technology which can be coupled with data centers to meet needs and services dynamically, so providing services from the data centers through a cloud and using the cloud as a means of remote storage is what this type of data centers are capable of performing.

One of the key reasons data centers require a lot of attention and resources is because they generate huge amounts of heat, and in order to cool them, they require further more resources.

4.2 Green Data Center

Green data center is a facility that utilizes energy efficient, sustainable and eco-friendly technologies. They try to incorporate new technologies as much as possible and remove older inefficient ones.

4.2.1 Impact of Green Data Centers

There are around 500–600 data centers all over the world. These server houses that contain hundreds of thousands of servers, all of them consuming huge amounts of power, emit just as much CO₂. Just to state the importance of green data centers and how much impact they have on the environment, here, Fig. 4 shows the need for data centers in America due to enormous amounts of power requirements.

If we wish to reduce the power that is consumed, we need to first analyze the power consumed by the individual sectors. The pie chart (Fig. 5) displays exactly that, and in the solution, we will be looking at solutions to optimize some of these sectors.

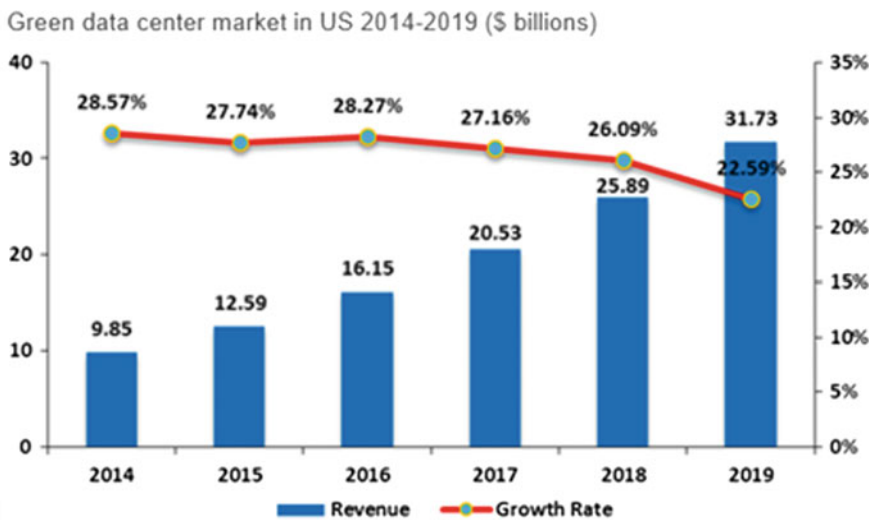
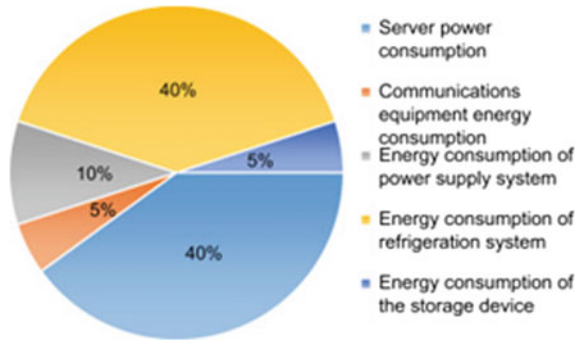


Fig. 4 Need for green data centers in the USA 2014–2019

Fig. 5 Power consumed by individual sectors



4.3 Making Data Centers Green

Data centers can be made greener by changing their in terms of hardware equipment used, cooling mechanisms, components used in the cooling towers or ‘chilling plants’ as they call it and usage of materials that fuel the uninterrupted availability of power. In essence what we are looking for are ways that promote reduced power consumption, better architecture plans, new models that implement said architectures and getting to the bottom of finding greener hardware alternatives. Exploring successful implementations gives us an idea as to how our goal can be accomplished. Some of the already established concepts are.

4.3.1 Virtualization

Virtualization is the mechanism by which a sort of illusion is created which makes it seem like there is more memory than what is physically there. Likewise, it can make a single server appear as multitude of servers. Data centers consist of a huge number of servers of varying sizes as mentioned earlier. This is implicative of the fact that virtualization could be an easy solution to the reduction in power consumption. Virtualization is implemented with the help of virtual machines; these machines are capable of performing or tending to different services at the same time which makes them efficient and important. Different parts of the machine such as the virtual machine monitor (VMM) and supervisor exist to make sure they all work seamlessly. Some of these machines are in sleep mode to preserve power and add to the conservation of energy by doing so.

4.3.2 Smart Sensors in Chilling Plants

To reduce the heat generated and the power consumed and to reduce the heat, chilling plants are used. There are many ways in which its functionality can be optimized. The location of the data center is a crucial decision which could take the efficiency

either environmentally conscious or reckless. Data centers in high positions or plains of colder regions of the world are very advantageous. One of the reasons being that cooling will be much easier as the normal temperature of the surrounding is cold. We can also use smart sensors to monitor the temperature inside and outside the data centers. In case the weather outside is cold, the outside air could be used to cool the server racks. This can lessen the power consumption as we might not require as many air conditioners as those required during a sunny day. Exploration of renewable resources like solar energy to provide power for the chilling plants is always possible. They are some simple yet very effective methods to save energy and yield great results when implemented on a large scale. Facebook is one of the famous organizations that consumes minimal energy compared to the by implementing these green alternatives.

4.3.3 Smart Architecture

A modified, efficient and modern architecture that can be used in data centers includes smart sensors. This time, it is used to control not just in the chilling plants. The sensors will alert in case of a crisis via an email or SMS or any other mode of indication there is. These sensors are used to observe the temperature and humidity as well. Based on the humidity, some defense mechanisms are deployed. Why? Because these sensors are only used to stable environments and might get heavily damaged under erratic conditions. Therefore, a humidity sensor is used to indicate the weather beforehand and tells us what has to be done. The sensors work in a two-part plan. One of the sensors that are outside the DC sends information regarding the status of the data center, its temperature to the other one inside the DC.

- The incorporation of virtual servers had reduced the energy costs by about 4%. This is a massive achievement, although any amount of improvement is appreciated. This benefits both the organization and the environment alike.
- When the temperature is really low, a lot of the air conditioners and in rare cases a whole unit of the chilling plant could be in sleep mode preserving so much power and cost.
- Parts of the data center could be dead/asleep when they are not required. At least one-fifth of the server population is asleep. This is good news because it adds to optimization and being aware of the power consumption.
- Heat generated by data centers is reduced naturally. This is the kind of impact technology is expected to depict, improvement with little to no damage to the Earth.
- The space consumed by green data centers is also lesser compared to normal data centers, and this benefits the organization greatly as is obvious.

5 Green Cloud Computing [16–19]

5.1 *Emergence of Cloud Computing*

Cloud computing broadens the horizon for remote access to huge amounts of data on the go, without having to be physically present or have a classical work environment. To understand the wonders cloud computing can do, knowing what it means is a good place to start. Cloud was coined to indicate the Internet, as clouds are present everywhere much like the Internet. Cloud computing is storing, processing and managing data from a remote location. Internet connection is a must for cloud computing. There are four different types of clouds: public, private, community and hybrid. Based on the requirements, users can choose their suitable cloud by purchasing it from a cloud provider of their choice.

5.1.1 Types of Cloud

- **Public cloud:** Anyone with an Internet connection can view and access the contents of your cloud.
- **Private cloud:** Only those who have been authorized to access your clouds, such as an organization, or a group of restricted users may access your cloud.
- **Community cloud:** As the name suggests, a group of organizations or a community of organizations access contents from the same cloud. The organizations can have control over how much of their contents can be accessed.
- **Hybrid cloud:** This is an amalgamation of different types of clouds.

5.1.2 Types of Cloud

Cloud computing is a much sought-after technology because of its numerous advantages like,

- **Affordability:** Smaller organizations that do not have enough resources to buy large physical storage areas can make use of the cloud at a much reasonable price.
- **Availability:** The data that is in the cloud is accessible by the home user, organization or a community of organizations at any point of time.
- **Simplicity:** The user needs to worry only about using the data and not about managing or organizing the data as the cloud provider takes care of all of that.

With the rise of such a revolutionary technology, there is bound to be a significant increase in energy and resource requirements. Moreover, it also poses some challenges to the environment. Some of the negative impacts of profuse power consumption are depletion of fossil fuels, water usage in cooling systems to compensate

for the heat generated by data centers; to overcome these disadvantages and be more environmentally conscious, green cloud computing came into existence.

5.2 Green Cloud Computing

Green cloud computing is a part of green computing that deals with two issues, energy reduction and increasing sustainability by implementing virtualization, effective algorithms and green data centers.

5.3 Achieving Green Cloud Computing

Green computing looks for strategies that can be implemented to develop computers that have little to no negative impacts on the environment from their components from the manufacturing process to the disposal process. The objective of green cloud computing is to remove the ill effects cloud computing has on the environment and if possible, explore further to improve the existing design in terms of efficiency. Several discoveries and ideas have already surfaced. We will now see a few of them in detail.

The multi-method data delivery coupled with sensor-cloud technology proved to have reduced the energy and power consumption. The multi-method programs involve more than one way of collecting data or analyzing data; to put it simply, it has different ways of doing the same activity and chooses one of those ways based on which fits best at a particular point in time. So, the MMDD introduces four different ways of delivering data in this case.

- Green wireless sensor network to sensor-cloud.
- Cloud to sensor-cloud.
- Cloudlet to sensor-cloud.
- Sensor-cloud users to other sensor-cloud users.

The introduction of this into the normal routine reduced the amount of energy that was consumed while maintaining low delivery rates. Many surveys were conducted from 2013–2016 which highlighted the changes in algorithms. All provided solutions to increase efficiency, while some supported resource management, and a few suggested solutions for improving operational costs. Only one provided solution for improving CO₂ emissions. Similarly, different architectures proposed also showed an increase in efficiency coupled with solutions for resource management. Some examples are,

5.3.1 Algorithm

Every cloud data center needs a job scheduler, to schedule jobs, and by using an algorithm with dynamic voltage frequency scaling (DVFS), technique has shown to improve the efficiency significantly with a much lesser emission of CO₂ and decreased energy consumption. This is one of the many algorithms that can be applied as a green alternative.

5.3.2 Design

Clouds rely on data centers to provide services in a pay-to-avail fashion. The components in data centers such as CPUs, memory stacks, communication lines are the significant power consuming factors; majority of which is needed by the CPUs, so applying the DVFS on the CPUs yields values approximately in linear power to the frequency in servers. The design of the data centers can be switched with green components to make a great difference in the environment and little discomfort to the systems.

5.4 *Advantages of Green Cloud Computing*

- Cloud computing largely depends on data centers to function. Although cloud computing aims at flexibility and availability of data, the data centers take up large spaces, demand over the top power resources and emit large amounts of CO₂. Therefore, the green substitutes are the optimal solutions.
- The green alternatives do not affect the quality of service as much while being environmentally friendly.
- Something as simple as a reduction of paper usage is notable too, as the documents and important, confidential files can be stored, even their backup can be in another cloud.
- Communication between employers and employees is possible from remote locations; for example, employees can work from home which greatly affects the environmental footprint in a positive way.
- This can be viewed as a much cheaper investment in the long run.

6 Green Edge Computing [20, 21]

Edge computing or fogging is the technology that distributes the computational load over a group of systems that are part of the fog. It could sometimes perform part of the computation and let the rest of the work be carried out in the cloud, or it could

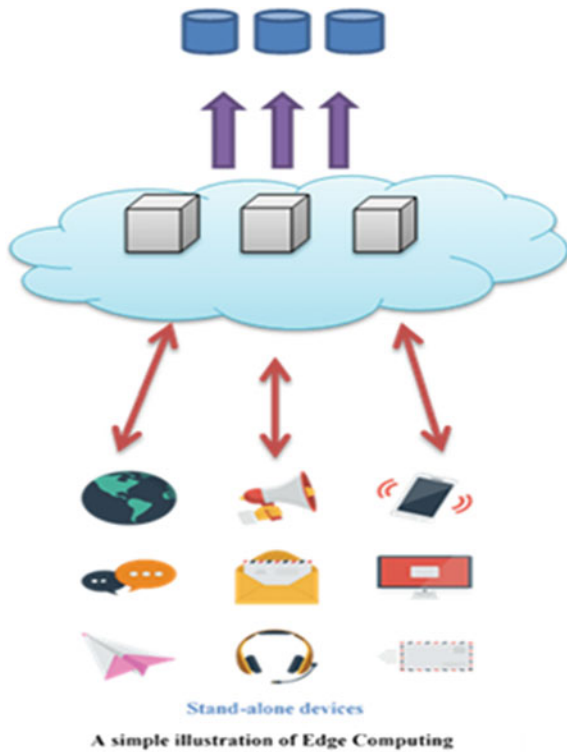
perform the whole processing job by sharing it with other edges (systems in the fog). It is used in any application that calls for cloud computing or data centers, which is almost everything these days.

6.1 Emergence of Edge Computing

Data centers and clouds that process huge amounts of data have increasing expectations placed on them such as speed and quality which is a complex task in itself. The users are not usually aware of these things, and there is no necessity for them to know the intricacies in order to work with cloud. This is where edge computing comes in; it finishes a part of the processing so that the load on the cloud can be lessened and the performance can be improved greatly while not having to give up much.

Here, Fig. 6 is a simple illustration of how we use edge computing in our day-to-day lives without even knowing it. Apart from what is mentioned above, edge computing is used in industrial applications such as MRI scanners, wind turbines, smart power grid and even smart traffic lights. It is not hard to see why it is important,

Fig. 6 Simple illustration of edge computing



and any kind of modification that increases efficiency is very much welcome. Since edge computing has a lot to do with cloud computing and data centers, it is obvious to see that it poses the same challenges to the environment that they do too. So, our focus shifts to solving these negative effects.

Edge computing when coupled with just the right technologies, architecture and algorithms could easily be efficient, green and sustainable. So, let us explore a distinct set of additives to edge computing that allows us to achieve our objective. Mind you, it is only one of the many amalgamations that have been suggested to improve efficiency while being conscious of the environment's needs.

6.2 Additives

- As more and more things are introduced into Internet of things (IoT), the number of devices that are part of it is increasing exponentially. Clouds are being recognized and used widely even if they are relatively new. So, the first ingredient or additive to a more efficient edge computing structure is cloud of things (CoTs). CoTs are used because the devices that do not have sufficient resources can utilize the cloud to increase the power of processing, and it helps in managing huge amounts of data at a relatively modest cost as well.
- Wireless optical broadband access networks (**WOBANS**) are at the back-end of the network, with wireless mesh network (WMN) which is located at the access points at the front end. WOBANs exhibit great reliability and have a wide reach or spread. Moreover, they also have reduced latency in comparison with other network architectures. In case of latency intolerant applications, such as stock updates, online gaming, this proves to be a valuable addition. It is economically safe and considerate as well.
- Edge caching suggests that data is to be cached to receive quick responses, increasing spectral efficiency (the rate at which data can be transmitted over a given bandwidth) and decreasing energy consumption. Caching is necessary in order to cope with the heterogeneity of devices that interact with the edge devices or the cloud. It is to be noted that collaborative edge computing, a collection of edges is also applied, which is implicit because edges consist of nodes that perform processing tasks beforehand as mentioned earlier.

6.2.1 Advantages

- Economically and environmentally friendly.
- Heterogeneous devices are not discriminated.
- Increased efficiency.
- Power requirements are significantly reduced.
- Faster response rates.

6.3 *Green Energy in Reality*

There are several leading international corporations that implement green energy as of now. They are some of the big names you would have probably heard such as.

- Intel
- Microsoft
- Apple
- Dell
- Google
- Sony

It is good to see that there are corporations that can afford to go green, and they make the civilized choice to do so. They make a great impact on the environment positively.

7 Green M2M

7.1 *Machine-To-Machine Technology*

Machine-to-machine technology in IoT is the tendency of machines to communicate between themselves without human-directed commands and course of actions [7]. The field of artificial intelligence is behind this; as we search for ways on how to make systems intelligent and self-sufficient, we then expect them to perform tasks based on gained knowledge that will exhibit better actions and results than what can be done by humans.

Intelligent machines need certain elements to communicate with other machines; some of these elements are a high-speed wireless Internet connection, sensors to share information based on the field in the discussion, RFID for sensing valid recipients and necessary communication links in the network. M2M technology is useful in ample ways. Any place where machines are being used, M2M can be implemented. M2M replaces the need for manual work in numerous areas; this is a godsend in places where humans cannot go or are dangerous for human exploration. As of now, M2M is already being used in some factories in the manufacturing phase. It could also be applied to regulating traffic maintaining how busy the roads are to prevent traffic jams. If M2M technology were to be applied in as many places as possible, it would be quite revolutionary adding to why it is on the rise now.

The M2M technology depends heavily on wireless networks as mentioned earlier, so we will now see some of the most efficient network architectures.

- **Cellular Network:**

This is the network architecture that is employed at large mainly due to its larger range and its presence almost everywhere. The disadvantages are that they rely on

battery life, which in many cases is short-lived; in addition to this, the technology of cellular network constantly goes through changes; a few years ago, GSM would have sufficed, but now, we are looking at LTE-M or 5G. So, the hardware used probably will not last as long, and has to be updated every once in a while.

- **Wi-Fi Network:**

Wireless fidelity (Wi-Fi) involves Wi-Fi chips which are cheap compared to other networks, and the power requirement is just as cheap. The chips go as far as to eliminate the need for specific Wi-Fi drivers or even computers when you can just use universal asynchronous receiver/transceiver (UART) instead. There is just one demerit; it does not have as good of a range as cellular networks do.

- **BLE Network:**

Bluetooth low-energy (BLE) networks are certainly better than Bluetooth networks, because they are more advanced, but one striking similarity is that the range and the amount of information that can be transmitted and received are very limited. They are great in place of applications that require only a small range and share smaller amounts of information such as pacers and heart rate monitors used in a hospital.

Some other networks are ZigBee, SIGFOX, LoRaWAN and Symphony Link which are quite popular and are used based on what the application calls for.

As wondrous as the potential of M2M technology is, it requires a lot of power to function; many of the machines used are battery powered, and they contribute to disposal problems. We will explore ways to make M2M technology green.

7.2 *Need for Green M2M*

As we know, M2M technology is on the rise and the communication of machines could be ubiquitous in a few years down the lane [8]. M2M is involved when any two machines communicate across a network. It is obvious to see how more and more devices come into play, and more and more energy and power requirements join the party as well. Our job as sensible creators is to develop devices and technologies that are beneficial and at the same time display sustainability.

7.3 *Making Machine to Machine Technology Green [22]*

There are various techniques that have actually worked, and they are listed below,

- As mentioned earlier, one of the reasons for unnecessary energy consumption is because of relay nodes. One way to go about it is to put a lot of the relays that are not active in sleep mode; another way is minimizing the number of relays used

between the source and destination nodes. There is another ingredient to make this more efficient. Along with any one of the ways mentioned above, we could also focus on minimizing the transmission energy shared by the selected or active relay nodes. The great thing about this approach is that it is balanced; it also tries not to let the quality of service (QoS) be affected.

- A lot of the information shared between different systems are often small in size and are transmitted in bursts and in erratic intervals; sometimes it could be regular, and suddenly, transmission happens after long intervals; in such cases, adaptive modulation and coding (AMC) and uplink power control (UPC) are employed to manage the sudden changes in the intervals. To see how AMC is a valuable addition, consider that AMC works in cohesion with modulation and coding scheme (MCS), which can be adjusted in such a way that the higher its value is, the lower the power consumed is, but the trade-off is that the error rate is just as high, so choosing an optimum MCS value with AMC manages the sudden bursts of small information extremely well. The erratic intervals can be managed by UPC, which helps the receiver always interpreting the same SINR. The only issue is that the sender must be capable of handling indifferent energy, and this rests on the transmission power of the channel, so if the channel was stable, an optimum MCS value could be attained. This is how both ACS and UPS work together to increase efficiency and reduce power consumption.
- While we are in the topic of improving the quality of the channels, it is worthy of mentioning cooperative communication. There are many strategies to implement this, some of them are,
 - **Single Input Single Output (SISO):** It is a multi-hop scheme which splits the distance between the source and the destination into multiple active relay nodes as the path and achieves lower power consumption than direct transmission.
 - **Cooperative Relay:** This method involves the same three components, but here, the data to be shared is split into two frames, and the source sends one frame to the destination directly, while the next frame is sent to the relay which forwards it to the destination. This occurs in parallel, so the error rates are reduced while the data reaches the destination faster and requires less power.
 - **Multiple Input Multiple Output (MIMO):** It is a single-hop scheme with two components remaining the same, the source and the destination nodes, but there are plenty of relay nodes involved. Many of them called the cooperative sources, and the rest are cooperative destinations. The source splits the data into multiple frames and forwards it to the cooperative sources, while they forward it to the cooperative destinations concurrently, which is then transmitted to the destination node. This method also reduces the room for error and power consumption.

7.4 Advantages of Green Machine-To-Machine Technology:

- M2M technology is revolutionary and can help devices all around the world become much smarter, which benefits every field of work.
- GM2M reduces energy consumption which opens it up to so many more ways of making IoT greener.
- GM2M explores the creation of green intelligent devices, thereby encouraging space and deep-sea exploration.
- It improves low mobile devices to be used optimally. For example, say a cargo ship dispatches some goods, the delivery truck needs only go to the docks when necessary, so the cargo ship could call for the truck only when it has reached the docks. This is just a speck of what M2M could achieve.
- The lifetime of devices used in M2M technology has a greater lifespan, is energy efficient and can be disposed of easily.

8 Conclusion

An invigorating and latest direction intended for research pertaining smarter world is discussed in this chapter. It talks about numerous engineerings and problems regarding green computing, which shows a noteworthy use in attaining a sustainable smart world. Go green is a conception which is practiced only in a few organizations, but if every individual uses its components, then it might benefit one and all irrespective of anything. The gains of green computing are unblemished. As the number of PCs has neared 2 Billion in 2015, the impending savings associated to energy use, e-waste and CO₂ are indubitable. The count is on a steady rise. Hence, proper enactment of green computing will be a facilitating hand when it comes to saving energy and eliminating the pollution and also helps establish a sustainable environment. Precisely, the overview concerning green and IoT has been achieved. The engineerings associated to green IoT which include six blistering green ICT (e.g., green DC, green CC, green M2M, green RFID, green WSN and green IoT) have been presented, with the compendious of overall green ICT ideologies. In accession, conferring particular responsiveness to sensor2cloud which is an innovative example in green IoT, the state-of-the-art advances nearly sensor2cloud have been presented, and the forthcoming sensor-cloud has been planned.

References

1. Li Q, Zhou M (2011) The survey and future evolution of green computing. In: Proceedings of the 2011 IEEE/ACM international conference on green computing and communications, pp 230–233

2. Min-yi G (2010) Green computing: connotation and tendency. *Comput Eng* 36:1–7
3. Wadhwa B, Verma A (2014) Energy and carbon efficient VM placement and migration technique for green cloud datacenters. In: 2014 seventh international conference on contemporary computing (IC3), pp 189–193
4. Wu J, Zhang Y, Zukerman M, Yung EK-N (2015) Energy-efficient base-stations sleep-mode techniques in green cellular networks: a survey. *IEEE Commun Surv Tutor* 17:803–826
5. Roy A, Datta A, Siddiquee J, et al (2016) Energy-efficient Data centers and smart temperature control system with IoT sensing. In: 2016 IEEE 7th annual information technology, Electronics and Mobile Communication Conference (IEMCON), pp 1–4
6. Mao Y, Zhang J, Letaief KB (2016) Dynamic computation offloading for mobile-edge computing with energy harvesting devices. *IEEE J Sel Areas Commun* 34:3590–3605
7. Wang L, Zhang X, Wang S, Yang J (2017) An online strategy of adaptive traffic offloading and bandwidth allocation for green M2M communications. *IEEE Access* 5:6444–6453
8. Elkheir GA, Lioumpas AS, Alexiou A (2011) Energy efficient AF relaying under error performance constraints with application to M2M networks. In: 2011 IEEE 22nd International symposium on personal, indoor and mobile radio communications, pp 56–60
9. Janhunen J, Mikhaylov K, Petäjäjärvi J, Sonkki M (2019) Wireless energy transfer powered wireless sensor node for green IoT: design Implementation and Evaluation. *Sensors* 19:90
10. Han C, Harrold T, Krikidis I et al (2011) Green radio: radio techniques to enable energy efficient wireless networks. *IEEE Commun Mag Spec Issue Green Commun* 49:46–54
11. Hasan Z, Boostanimehr H, Bhargava VK (2011) Green cellular networks: a survey, some research issues and challenges. *arXiv Prepr arXiv11085493*
12. Bianzino AP, Chaudet C, Rossi D, Rougier J-L (2012) A survey of green networking research. *IEEE Commun Surv Tutor* 14:3–20
13. Zhu C, Leung VCM, Shu L, Ngai EC-H (2015) Green Internet of Things for smart world. *IEEE Access* 3:2151–2162
14. Liu Q, Ma Y, Alhoussein M et al (2016) Green data center with IoT sensing and cloud-assisted smart temperature control system. *Comput Netw* 101:104–112
15. Peoples C, Parr G, McClean S et al (2013) Performance evaluation of green data centre management supporting sustainable growth of the Internet of Things. *Simul Model Pract Theory* 34:221–242
16. Farahnakian F, Ashraf A, Pahikkala T et al (2015) Using ant colony system to consolidate VMs for green cloud computing. *IEEE Trans Serv Comput* 8:187–198
17. Hou W, Ning Z, Guo L (2018) Green survivable collaborative edge computing in smart cities. *IEEE Trans Ind Informatics* 14:1594–1605
18. Ning Z, Kong X, Xia F et al (2019) Green and sustainable cloud of things: enabling collaborative edge computing. *IEEE Commun Mag* 57:72–78
19. Bonomi F, Milito R, Zhu J, Addepalli S (2012) Fog computing and its role in the internet of things. In: Proceedings of the first edition of the MCC workshop on Mobile Cloud Computing, pp 13–16
20. Sun X, Ansari N (2016) EdgeIoT: Mobile edge computing for the Internet of Things. *IEEE Commun Mag* 54:22–29
21. Yu W, Liang F, He X et al (2018) A survey on the edge computing for the Internet of Things. *IEEE Access* 6:6900–6919
22. Laya A, Alonso L, Alonso-Zarate J, Dohler M (2015) Green MTC, M2M, internet of things. *Green Commun Princ Concepts Pract* 217–236

An Overview of Green Energy Management Systems



J. Ajayan, P. Prakasam , and P. Mohankumar

Abstract Energy consumption is a key factor in measuring the economic growth of a city/country. Even after 2015, fossil fuels are supplying the major part of energy demanded by people from all over the world. Air pollution, water pollution, biodiversity loss, deforestation, and global warming due to carbon emissions and climate change are some of the negative aspects of consuming fossil fuels for meeting the energy demand. So, it is high time to generate renewable energy, also known as green energy. Green energy is defined as the energy generated from the renewable sources such as sunlight, wind, biomass, and geothermal energy. For household/commercial purpose, the most critical issue is the effective reduction in the cost of electricity. For saving energy in buildings, vehicles, communication networks, and industries/factories, it is important to develop an energy monitoring/management systems. Like energy production, energy saving is also equally important because the amount of energy saved can be considered as the amount of energy generated. Therefore, it is extremely important to save energy as much as possible in consumer/industrial applications.

Keywords Energy Management Systems (EMS) · Global Warming · Green Energy · Photovoltaic · Solar Cells

J. Ajayan

Department of Electronics and Communication Engineering, SNS College of Technology, Coimbatore, India

e-mail: email2ajayan@gmail.com

P. Prakasam (✉)

School of Electronics Engineering, Vellore Institute of Technology, Vellore, India

e-mail: prakasamp@gmail.com

P. Mohankumar

Department of Mechatronics Engineering, SNS College of Technology, Coimbatore, India

e-mail: mohankumareie@gmail.com

© Springer Nature Singapore Pte Ltd. 2020

A. K. Bhoi et al. (eds.), *Advances in Greener Energy Technologies*,

Green Energy and Technology, https://doi.org/10.1007/978-981-15-4246-6_34

1 Introduction

The quality of life and the global economy are strongly depending on the security and stability of energy supply. The demand of energy is continuously increasing due to the industrial revolution which is connected with economic development. For a bright and secure energy future, sustainable energy production, energy transmission, energy usage, and energy storage are required.

There are three main objectives for energy management and they are (i) to save energy, (ii) to minimize energy production/distribution/storage cost, and (iii) to minimize environmental effects. Renewable sources provide only a small fraction of the world's total electricity [1–3]. The use of solar cells is increasing day by day in recent years. However, these solar photovoltaic cannot compete with fossil fuels on economic basis. It is required to explore high efficiency, cost-effective, reliable photovoltaic materials for the successful use of solar photovoltaics instead of fossil fuels. Inexpensive transition metal oxides and sulfides can be used in solar energy converters such as photovoltaics, dye-sensitized solar cells (DSSCs), and photoelectron chemical cells (PECs).

A key challenge is to meet the future energy needs for the next generation. The population of the world will reach approximately 9.4 billion in 2050. That is, the world's population will be increased by 36% in the next three decades. Therefore, meeting future energy demand/needs will be a main obstacle in the road of national/international economic development. The world energy council (WEC) has estimated that the energy consumption will be increased by 61% in 2050. Electricity generation for meeting the future electricity demand will also be a key issue.

In 2010, the world's total electricity production was estimated to be 21.5 billion MWh and WEC expects that approximately 53.6 billion MWh electricity is required in 2050 to meet the electricity demand. The increase in energy production increases the carbon emissions which lead to the climate change [4–10]. So, it is important to generate energy without affecting the environment in the future which is a critical challenge. Today, solar energy and wind energy contribute only 4% of world's total energy, and however, it will increase to 20–40% by 2060.

Researchers are taking efforts to find new technologies to minimize the dependence of fossil fuels in order to ensure the safety of environment. Energy generated from natural renewable resources such as sunlight, wind, tides, rain, biomass, and geothermal heat and hydroelectric power plants is known as green energy. Compared to fossil fuels, renewable sources of energy have negligibly small impact on the environment. That is, green energy sources do not produce pollutants that lead to climate change. Solar power, wind power, hydropower, geothermal heat, biomass, biofuels, etc., are the typical green energy sources.

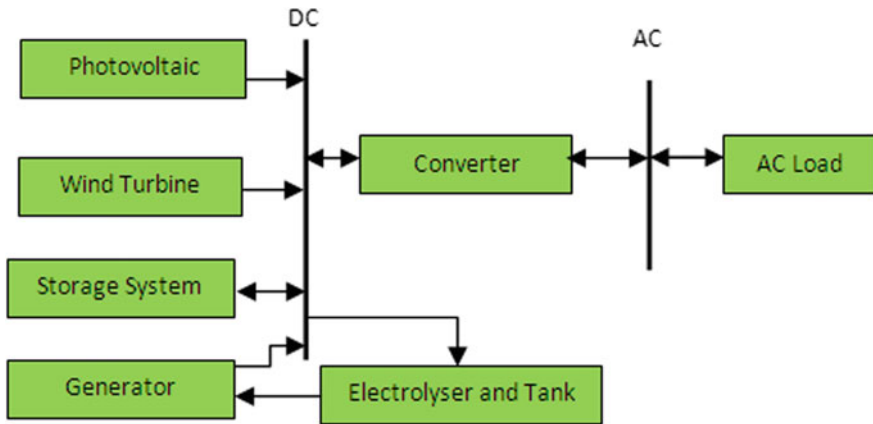


Fig. 1 Green energy system

2 Green Energy System

The block diagram of a green energy system is illustrated in Fig. 1. The main purpose of utilizing a green energy system is to minimize carbon dioxide (CO₂) emissions. Reduction of CO₂ emission helps to prevent global warming and climate change. The green energy system can also provide reliable and sustainable electricity. Renewable energy resources, energy backup systems like fuel cells and batteries, and converter systems are the key components of a green energy system.

A green energy system consists of semiconductor-based photovoltaic cells which is used to directly convert solar energy which is produced by solar cell into electrical energy, wind energy generated by wind turbine into electrical energy, geothermal heat generated by geothermal power plant into electrical energy, and kinetic energy of water generated by hydroelectric power plant into electrical energy.

In a green energy system, fuel cells and batteries can be used as energy storage systems and an inverter system is used to convert DC power into AC power. The electrolyser is used to supply hydrogen which is essential for the working of fuel cells. Electrolyser is used to produce oxygen and hydrogen from water. A hydrogen tank is used to collect the hydrogen generated by the electrolyser [5].

3 Green Energy Management System

3.1 Introduction

Maintenance and management of resources, saving energy, and reducing energy costs are the major issues in recent years. Both in household and commercial appliances,

reduction of energy costs and saving of energy are extremely important. Industries meant for manufacturing have become a fully automated industry using a lot of automated manufacturing machines. However, it consumes a large amount of electric energy which leads to an increase in expense for manufacturing industries. Hence, energy monitoring plays a vital role in those industries. Several research groups have developed energy monitoring/energy management systems in recent years [1–31]. These energy monitoring/management systems can record the data and can also provide the real-time status of the power sources.

The schematic representation of a green energy management system is depicted in Fig. 2. The solid arrow lines in Fig. 2 indicate the flow of power, and the dotted lines represent the flow of data. The green energy management system shown in Fig. 2 has mainly three parts and they are (1) renewable energy generation plants (wind turbine, PV plant, biomass plant, hydropower plant, etc.), (2) energy monitoring/management system (EMS) and their control signals, and (3) battery and grid system. The EMS consists of a data logger, battery state of charge (SOC) monitor, forecasting model predictor for power dispatching, and the security and safety system. If the total power/energy generated from the renewable energy generation plants reaches the upper limit of the battery energy storage system, then the rest of the power generating from the power plants can be fed to the grid. The renewable sources are acting as an input to the EMS system. The forecasting model predictor also records the amount of energy generated by the wind turbines, PV plant, biomass plant, and hydropower plant. Based on the previously recorded data, the model predictor will predict the wind speed, solar radiation intensity, etc. The EMS considers the forecasting results supplied by the model predictor for the effective management of renewable energy resources, meeting the energy demands and reducing the energy costs.

A smart green energy monitoring/management system implemented by United States Institute for Theatre Technology (USITT) based on DMX512 protocol has been reported in [11]. Based on the data obtained from different sensors through the channels of DMX512, the end user monitors the LED lamps and thereby manages the electric energy in [11].

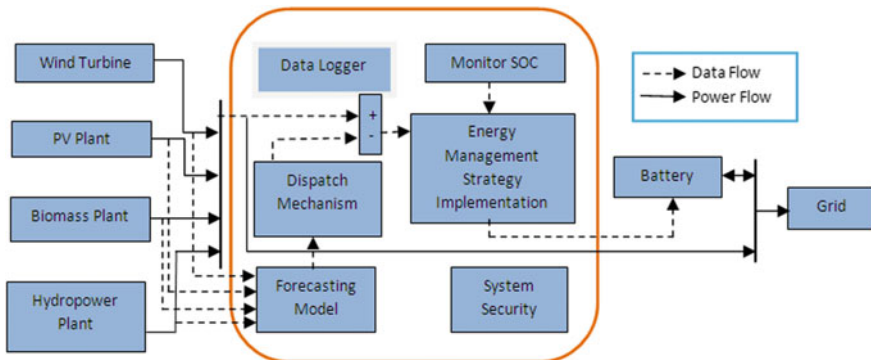


Fig. 2 Block diagram of energy monitoring system

An IEEE802.15.4- and ZigBee-based smart home energy management system (SHEMS) developed by Han and Lim is reported in [12]. The SHEMS developed by Han and Lim divides different home network tasks and allocate the small tasks to the suitable components by integrating various sensor systems. The SHEMS controls and manages the different home consumer devices with the help of these active sensor systems by using disjoint multipath-based routing.

Park and his fellow research members have developed a smart energy management system (SEMS) that monitors the energy consumption with the help of a motion sensor [13]. Yardi has reported a smart home energy management (HEM) system that controls the home appliances and monitors their electricity consumption [14] with the help of a smart meter and Internet. The HEM uses a smart meter to provide an interface between database and utility for energy consumption with the help of Internet connectivity.

3.2 Energy-Integrated Urban Planning and Managing Support System

Kim [4] from Sunkyunkwan University, Republic of Korea, and his fellow research members have successfully developed an EMS known as energy-integrated urban planning and managing support system [EnerISS]. Different types of energy sources in a city can be visualized and monitored using location-based sensor networks.

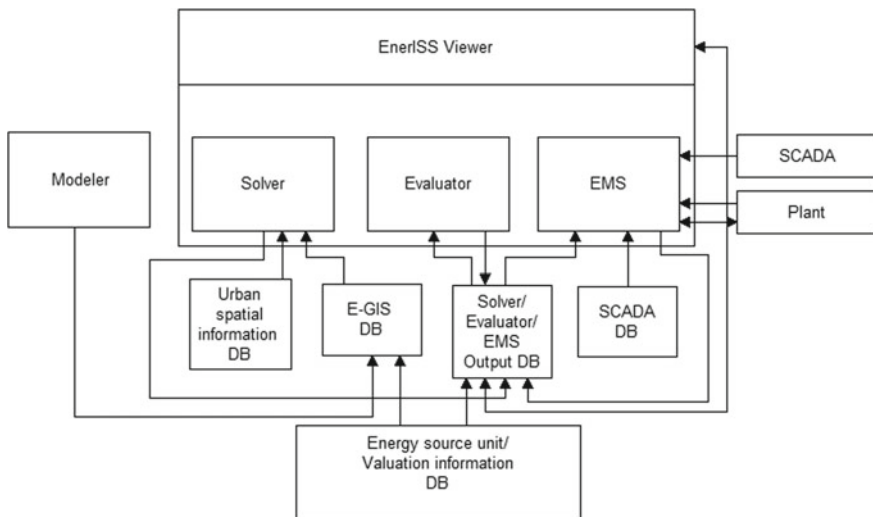


Fig. 3 Schematic representation of EnerISS

The schematic diagram of EnerISS energy management system is shown in Fig. 3. EnerISS consists of a modeler, energy monitoring and viewing system called EnerGIS, database (DB) module, and energy management system. This system can accurately estimate the energy demand using E-GIS database which helps to plan the energy supply through an energy management system (EMS). Energy consumption is the key parameter which determines the development of any city or a country [8–22].

3.3 Energy Management System for a Hybrid Power Source System

The block diagram representation of a hybrid power source system for vehicles is shown in Fig. 4. A hybrid power source system normally consists of a fuel cell stack, supercapacitors, and lithium-ion batteries. Fuel cell is considered as one of the most

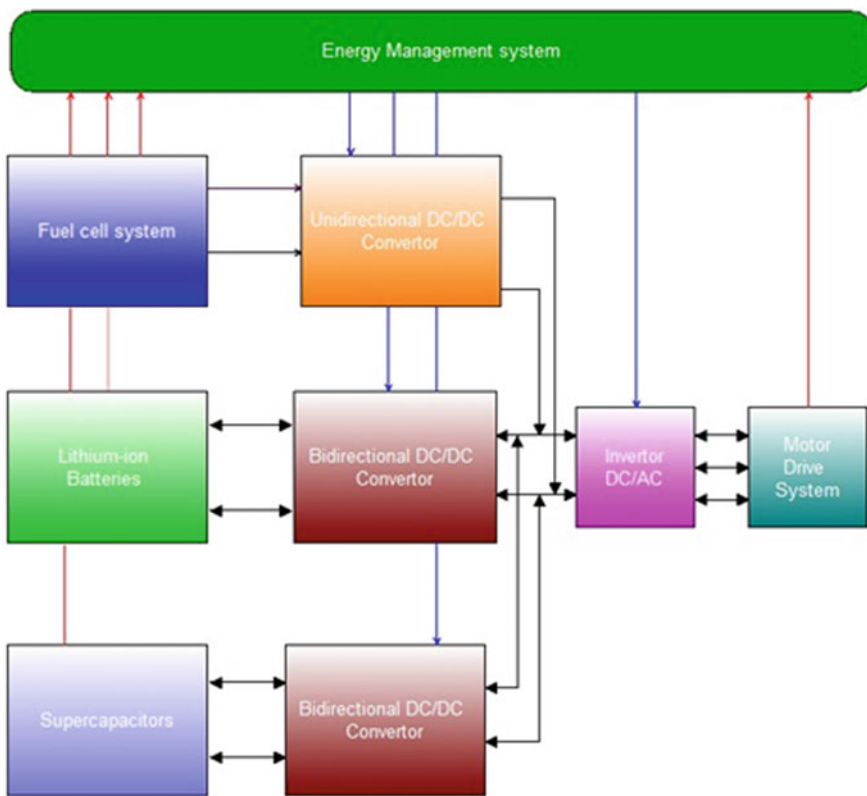


Fig. 4 Block diagram of a hybrid power source system for vehicles

attractive technologies for efficient and clean power generation. The two critical factors that are to be considered while designing a hybrid power source system are distribution and development of energy management systems. The reliability and life span of a hybrid power source system depends on the power distribution methods. A fuel cell is an electrochemical device that directly converts the chemical energy of the fuel into electrical energy. Alkaline fuel cells, solid oxide fuel cells, phosphoric acid fuel cells, and proton exchange membrane fuel cells are the various types of fuel cells available today. Among these fuel cells, proton-exchange membrane fuel cells have several advantages over other types of fuel cells like excellent dynamic characteristics, low temperature operation, and high power density. The energy management system plays a vital role in bringing a balance between the power sources in a hybrid power system and the load power [23]. The combination of fuel cell and unidirectional DC/DC converter provides required power for the vehicles. The lithium-ion battery together with bidirectional DC/DC converter provides required power for the start up of fuel cell, and the combination of supercapacitor and bidirectional DC/DC converter provides the required peak power to reduce the burden of fuel cell and lithium-ion batteries. The energy management system for a hybrid power source system is shown in Fig. 5. Host controller, fuel cell management unit, supercapacitor management unit, and lithium-ion battery management unit form the energy management system for a hybrid power source system. The controller area network manages the transmission of information in the system. The host controller interacts with the hybrid power sources and motor drive system to get the real-time status of the hybrid power source system and vehicle demand power. The management units are used to measure the key parameters such as state of voltage, state of charge, and maximum power capability and also to protect the power source systems. The energy management system used in a building is called building energy management system (BEMS). The energy management system used in industry/factory is known as industry energy management system (IEMS). Energy management systems save energy in a power source system [24–31] and the energy saving obtained by an energy management system can be expressed as [27]

$$\text{Energy saving (\%)} = \left(1 - \frac{\text{Energy usage after the implementation of EMS}}{\text{Energy usage before the implementation of EMS}} \right) \times 100$$

Energy management system plays a vital role in ensuring sustainability. Sustainability is defined as the ability to meet the present demands without compromising the capability of the next generation to meet the future needs. The three different forms of sustainability are environmental sustainability, social sustainability, and economic sustainability [28].

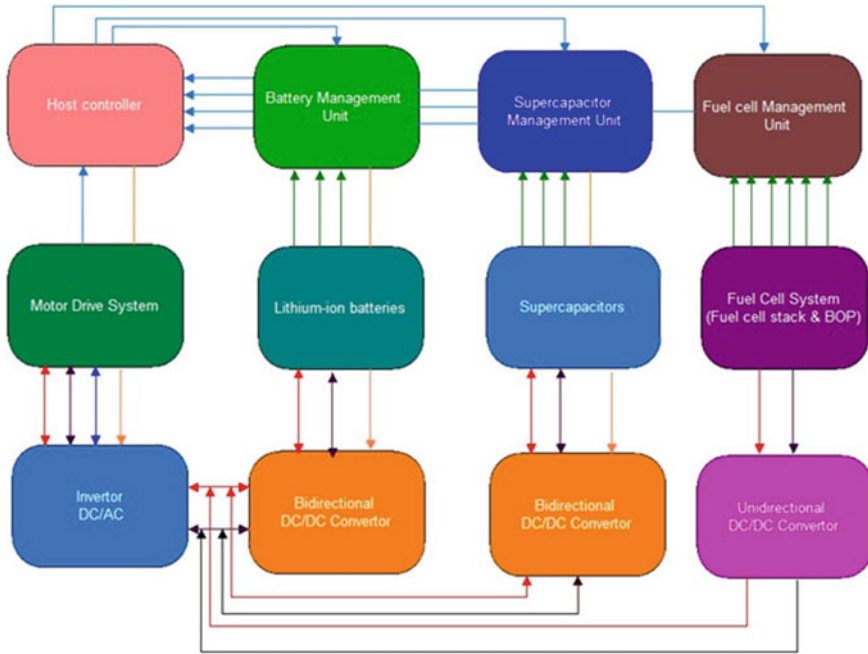


Fig. 5 Energy management system for a hybrid power source system

3.4 Green Energy Engineering and Green Energy Technology

Green energy engineering is a new field of engineering that explores the best ways to use renewable energy sources, efficient energy management and find solutions to economic, social, and environmental sustainability. The demand for energy is growing day by day. Therefore, it is very important to find new sources of energy which does not harm the environment. The term green represents healthy integration of human with the nature for a flourishing future [29]. Green energy engineering explores the generation of power from renewable energy sources like water, hydrogen, biomass, wind, geothermal, and sunlight. The relationship between green energy engineering and other engineering fields are shown in Fig. 6.

Green energy engineering is interrelated with renewable energy engineering and energy and power engineering. Energy and power are related to mechanical engineering, environmental engineering, and chemical engineering. Renewable energy engineering is related to mechanical engineering, environmental engineering, civil engineering, and bioengineering. Mechanical engineering is interrelated to the engineering fields of civil, forestry, industry, mining, nuclear, electrical, computer, marine, transport, electronic, agriculture, geothermal, and petroleum. Environmental engineering is related to other engineering fields such as civil, forestry, industry, mining,

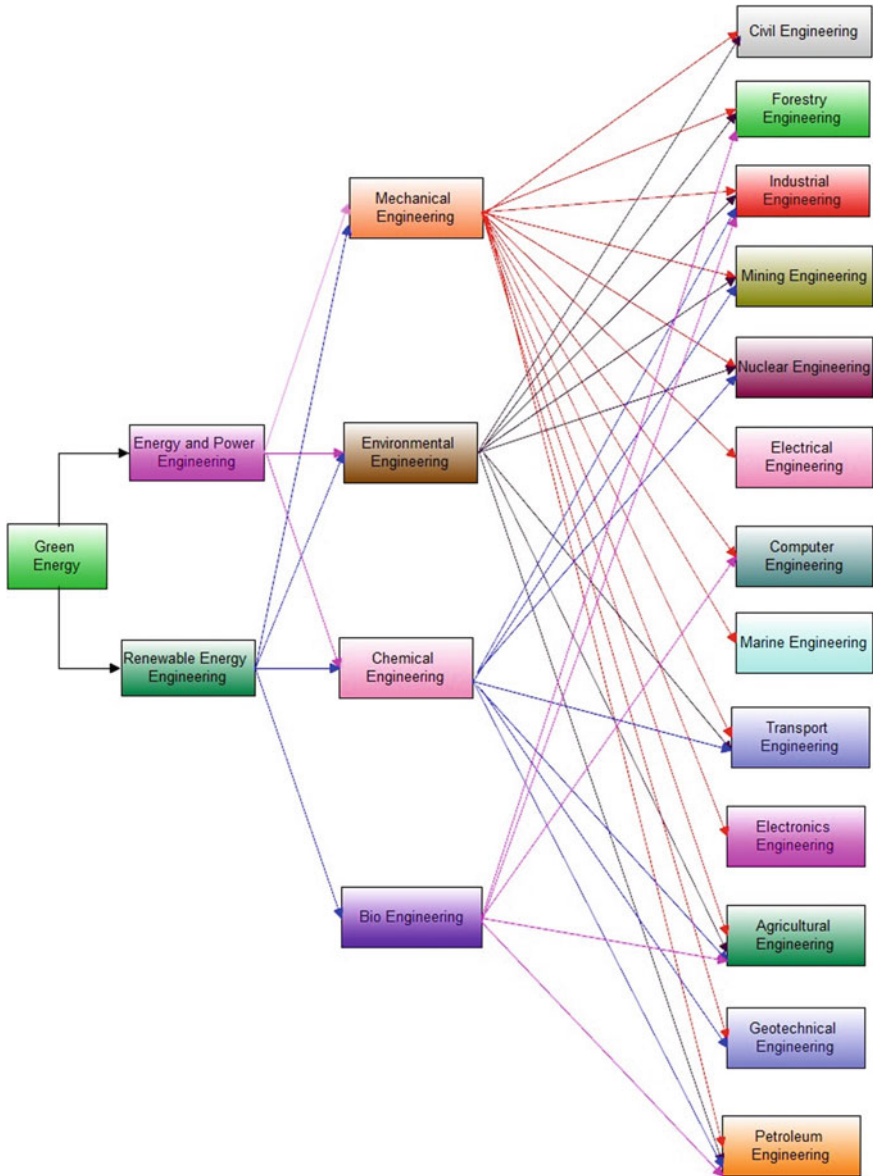


Fig. 6 Relationship between green energy and other engineering fields

nuclear, transport, agriculture, geothermal, and petroleum. Chemical engineering is related to industrial engineering, mining engineering, geothermal engineering, and petroleum engineering. Finally, bioengineering is interrelated with forestry engineering, industrial engineering, computer engineering, agriculture engineering, and petroleum engineering [29]. The green energy technology is defined as a technology that is used to save energy in the fields of industry, buildings, communication networks, and transport systems by exploring renewable energy sources. Green energy technology can increase the revenue and reduce the energy costs. Green energy technologies also help to reduce pollution [30].

3.5 Green Switch

Goiri et al. [15] have introduced the concept of a green switch to effectively manage the energy sources and workloads which is illustrated in Fig. 7. The predictor module evaluates the utilization of renewable energy and workload. Based on the predictor output and current battery charge level, the solver generates an energy source schedule and the workload schedule. The configure changes the configuration of the energy sources based on solver outputs [15, 16].

However, most of the systems so far mentioned solely monitor the key areas to calculate the total energy utilization. Hence, these systems do not estimate the detail consumption of electricity for individual components and evaluate the large historical information. Hence, the cloud- and virtual technology-based energy management systems play the major role.

The following two systems employ virtualization technology and cloud infrastructure to develop a cloud green energy management system. The cloud green EMS can perform the functions such as historical energy information analysis, prediction for machine breakdown and renewal, power adjustment in contract capability of

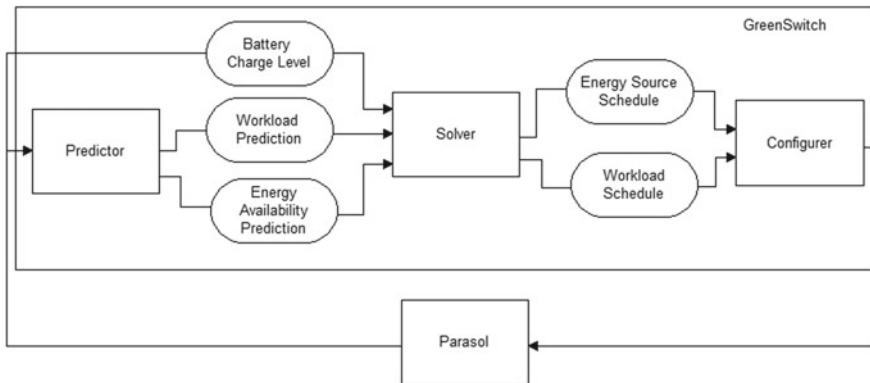


Fig. 7 Block diagram of green switch

electricity, power restoration, single device abnormal warning, and system electricity abnormal warning.

3.6 Robust Smart Green Management System

Parasol is solar-powered microdata centers which consist of photovoltaic cells, batteries, grid-tie, cooling unit, and an air conditioner. The block diagram of a robust smart green management system (R-SGEMS) developed by Okafor et al. [16] is shown in Fig. 8.

The R-SGEMS shown in Fig. 8 consists of an integrated energy management and monitoring module that utilizes a cloud computing data center. R-SGEMS can be realized using demand-side management (DSM) scheme. DSM is mainly used to force the customer to use minimum energy during peak hours [15, 20]. Advanced metering infrastructure (AMI) can be used to enhance the DSM and its energy efficiency.

Photovoltaic solar cells, current and voltage sensors, battery storage system, grid-to-inverter network, high-power switching controller, distribution grid network, smart meter, AMI RF interface IP demodulator sensors, and cloud computing data center are the key components of R-SGEMS. The advantages of R-SGEMS are given below.

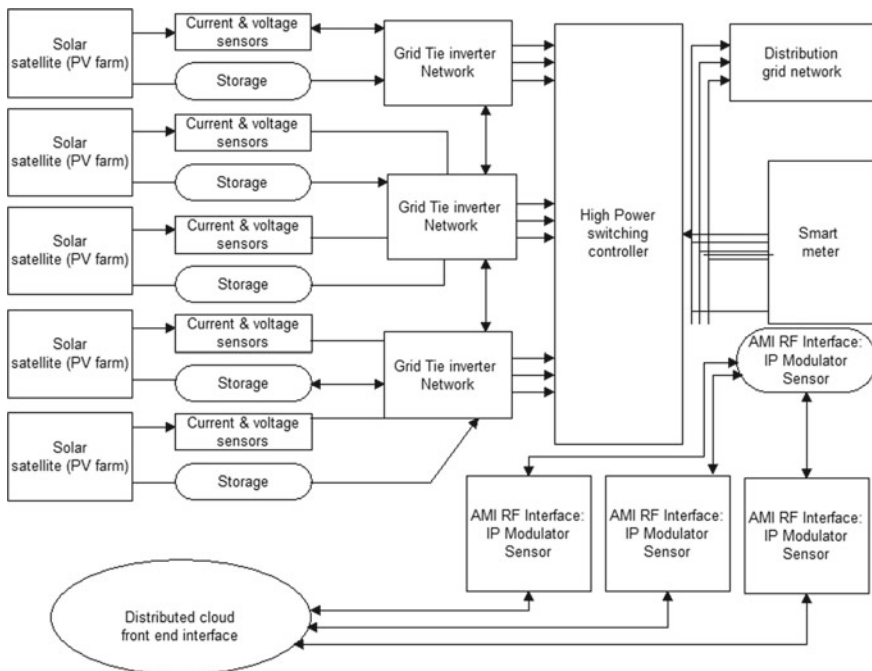


Fig. 8 Block diagram of a robust smart green management system (R-SGEMS)

1. The cost of implementation and management is very low
2. Greater reliability and Agility
3. Flexibility in network topology
4. Elasticity and scalability
5. Independent of location and device
6. Virtualization
7. Multitenancy
8. High Efficiency
9. Load adjustment and performance monitoring
10. Sustainability
11. Security.

3.7 i-Green Energy Management System

The one more system of cloud-based green energy management system iGEMS has been developed by Yang [21]. The block diagram of iGEMS is illustrated in Fig. 6. Cloud services, cloud platforms, and cloud infrastructure are the three important phases of iGEMS. Cloud infrastructure is considered as the heart of the iGEMS. Cloud infrastructure controls the management and deployment of virtual machines that can be used to increase the scalability of the systems [22].

According to the cloud infrastructure, both historical data and real-time data can be collected from energy meters and are processed to provide energy consumption behavior for early warning and real time. Apart from this, the environmental data and carbon emission data can also be collected and stored. In order to store and process the data, cloud computing and big data distributed database platforms can be used based on the infrastructure.

Data analysis service, data monitoring service, data collection service, and Web applications service are the four cloud services provided for the same. For increasing the feasibility of the EMS system, an open source is adopted to implement the above three phases as shown in Fig. 9.

The main features of the iGEMS systems are.

1. Data analysis for historical electricity
2. Abnormal warning for single devices
3. Abnormal warning for system electricity
4. Evaluation of pipeline failure
5. Restoration of power
6. Adjustment of power in contract capacity of electricity
7. Machine breakdown prediction and maintenance.

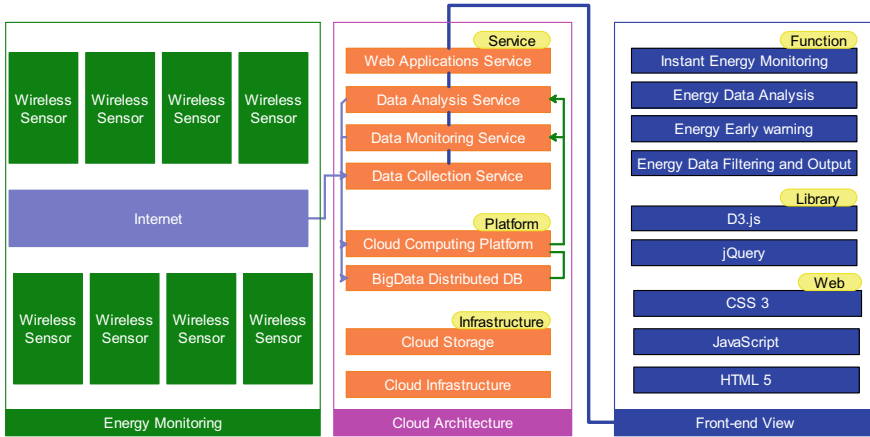


Fig. 9 Block diagram of iGEMS

4 Green Radio

About 2–3% of the total carbon dioxide emission is contributed by wireless mobile phone industries, and the mobile phone industries is also consuming huge amount of energy. Therefore, care must be taken to minimize the energy consumption of base stations. Trading bandwidth for energy efficiency, exploitation of multiuser diversity, and power efficient link adaptation are the three main strategies recommended by the radio resource management (RRM) for green radio [6]. The energy consumption rate (ECR) is a key factor which determines the transmit energy efficiency of a radio communication system.

$$ECR = \frac{PT}{RT} = \frac{P}{R} \tag{1}$$

In Eq. (1), P , R , and T , respectively, represent average transmit power, data rate, and time period of transmission. Link adaptation scheme can be used to save energy in communication systems, and saved energy using link adaptation technique can be calculated in terms of energy reduction game (ERG).

$$ERG = 1 - \frac{ECR_{TEST(LA)}}{ECR_{REF}} \% \tag{2}$$

In Eq. (2), ECR_{REF} and $ECR_{TEST(LA)}$ represent ECR of the reference system operated at fixed transmit power and ECR of the test system operated at desired transmit power, respectively [6]. The rapid development of mobile applications, cyber-physical systems, and wireless data networks leads to the increase in electricity consumption and energy costs. The increase in electricity consumption has an impact on environment and climate conditions. The minimization of energy cost is extremely

important in heterogeneous networks with hybrid power source systems. In a wireless network, the major part of energy is consumed by its base stations. Therefore, energy management systems are essential in wireless communication networks to reduce energy consumption and energy costs without affecting the network performance [31]. The computation tasks and data traffic in wireless networks will grow in the future that result in the increase of energy consumption and energy costs. Edge computing can be used to overcome this issue. In order to provide cloud services to the customers, edge computing uses the distributed resources in base stations, gateways, routers, and mobile devices. For sustainable green energy computing, it is best to increase the utilization of green energy. Energy Internet is a fast-growing technology that provides flexible and customizable energy scheduling in power grids. With the help of the energy Internet, it is possible to manage the computation task, data traffic, and green energy resources [24].

5 Summary

This chapter highlights the basics of green energy management systems and also various methods suggested by researchers. The utilization of renewable energy resources has to be improved in order to minimize the environmental effects. However, the effective management of green energy generated from renewable resources like sunlight, wind turbines, biomass, geothermal heat, etc., is required for the sustainability and reliability of green energy. In this chapter, green switch, green radio, and green energy management systems are discussed in detail. From the discussion, it has been found that cloud-based green energy management systems control the energy in an efficient manner.

References

1. Ahmad R, Jilani G, Arshad M, Zahir ZA, Khalid A (2007) Bio-conversion of organic wastes for their recycling in agriculture: an overview of perspectives and prospects. *Ann Microbiol* 57:471–479
2. Zalewski M, Santiago-Fandino V, Neate J (2003) Energy, water, plant interactions: ‘Green feedback’ as a mechanism for environmental management and control through the application of phytotechnology and ecohydrology. *Hydrol Process* 17:2753–2767
3. Skoulou V, Mariolis N, Zanakis G, Zabaniotou A (2011) Sustainable management of energy crops for integrated biofuels and green energy production in Greece. *Renew Sust Energy Rev* 15:1928–1936
4. Kim SA, Shin D, Choe Y, Seibert T, Walz Sp (2012) Integrated energy monitoring and visualization system for Smart Green City development—designing a spatial information integrated energy monitoring model in the context of massive data management on a web based platform. *Automation in Construction* 22:51–59
5. Ashourian MH, Cherati SM, Mohd Zin AA, Niknam N, Mokhtar AS, Anwari M (2013) Optimal green energy management for island resorts in Malaysia., *Renewable Energy*, vol. 51, pp. 36–45

6. Han C, Armour S (2011) Energy efficient radio resource management strategies for green radio. *IET Commun* 5(18):2629–2639
7. Barklund E, Pogaku N, Prodanovic M, Hernandez-Aramburo C, Green TC (2008) Energy management in autonomous microgrid using stability-constrained droop control of inverters. *IEEE Trans Power Electron* 23(5):2346–2352
8. Behrens P, van Vliet MTH, Nanninga T, Walsh B, Rodrigues JF (2017) Climate change and the vulnerability of electricity generation to water stress in the European Union. *Nat Energy* 2:1–7
9. Debnath KB, Mourshed M (2018) Challenges and gaps for energy planning models in the developing-world context. *Nat Energy* 3:172–184
10. Dieterich JM, Carter EA (2017) Quantum solutions for a sustainable energy future. *Nat Rev* 1:1–7
11. Wang S-F, Su Y-Z, Chu Y, Chau Y-F, Wei JH, Yang W, Liu A-L, Kao F-H (2014) Design of a smart green energy management system based on DMX512 Protocol. *Appl Mech Mater* 479–480: 1032–1037
12. Han D-M, Lim J-H (2010) Design and implementation of smart home energy management systems based on ZigBee. *IEEE Trans Consum Electron* 56:1417–1425
13. Park S, Choi M-I, Kang B, Park S (2013) Design and implementation of smart energy management system for reducing power consumption using ZigBee wireless communication module. *Procedia Comput Sci* 19:662–668
14. Yardi VS (2013) Design of smart home energy management system. *Int J Innova Res Comput Commun Eng* 3(3):1851–1857
15. Goiri I, Katsak W, Ley K, Nguyen T, Bianchini R (2013) Parasol and greenswitch: managing datacenters powered by renewable energy. *ASPLOS'13*, Houston, Texas, USA 16–20 March 2013
16. Okafor KC, Oparaku OU, Achumba IE, Ezech GN, Chilakpu KO (2015) R-SGEMS: a novel green energy management system for renewable energy utility. *Int J Energy Policy Manage* 1(1):6–19
17. Kuo PH, Huang CJ (2018) A green energy application in energy management systems by an Artificial Intelligence-based solar radiation forecasting model. *Energies* 11, 819–834
18. Jerez S, Tobin I, Vautard R, Monta´vez JP, Lo´pez-Romero JM, Thais F, Bartok B, Christensen OB, Colette A, De´que´ M, Nikulin G, Kotlarski S, van Meijgaard E, Teichmann C, Wild M (2015) The impact of climate change on photovoltaic power generation in Europe. *Nat Commun* 1–8
19. Trianna A, Cagno E, Bertolotti M, Thollander P, Andersson E (2019) Energy management: a practice-based assessment model. *Appl Energy* 235:1614–1636
20. Vale Z, Morais H, Faria P, Ramos C (2013) Distribution system operation supported by contextual energy resource management based on intelligent SCADA. *Renew Energy* 52:143–153
21. Yang CT, Yan Y-Z, Chen, S-T, Liu R-H, Ou J-H, Chen, K-L (2016) iGEMS: a cloud green energy management system in data center. *Lecture notes in computer science, green, pervasive, and cloud computing*, vol 9663, pp 82–89
22. Yang C-T, Liu J-C, Huang K-L, Jiang F-C (2014) A method for managing green power of a virtual machine cluster in cloud. *Future Gener Comput Syst* 37: 26–36
23. Wang Y, Sun Z, Chen Z (2019) Development of energy management system based on a rule-based power distribution strategy for hybrid power sources. *Energy* 175:1055e1066
24. Gu L, Cai J, Zeng D, Zhang Y, Jin H, Dai W (2019) Energy efficient task allocation and energy scheduling in green energy powered edge computing. *Future Gener Comput Syst* 95:89–99
25. Liu, P, Lin B, Wu X, Zhoud H (2019) Bridging energy performance gaps of green office buildings via more targeted operations management: a system dynamics approach. *J Environ Manage* 238:64–71
26. De Courchelle I, Gu´erout T, Da Costa G, Monteil T, Labit Y (2019) Green energy efficient scheduling management. *Simul Model Practice Theory* 93:208–232

27. Lee D, Cheng CC (2016) Energy savings by energy management systems: a review. *Renew Sustain Energy Rev* 56: 760–777
28. Mustapha MA, Manan ZA, Alwi SR (2017) Sustainable green management system (SGMS)—an integrated approach towards organisational sustainability. *J Cleaner Prod* 146:158–172
29. Oncel SS (2017) Green energy engineering: opening a green way for the future. *J Cleaner Prod* 142(4): 3095–3100
30. Stucki T (2019) Which firms benefit from investments in green energy technologies?—The effect of energy costs. *Research Policy*. 48(3): 546–555
31. Wang B, Yang Q, Deng X (2017) Energy management for cost minimization in green heterogeneous networks. *Future Gener Comput Syst*

Two-Stage DC-AC Quadratic Boost Inverter for Renewable Energy Applications



Rajat Kumar Sah, Namit Wadhawan, Akansha, and P. Sriramalakshmi

Abstract This paper proposes a new two-stage DC-DC-boosted inverter circuit. The new class of inverter topology is formed by cascading an existing fifth-order quadratic boost converter with a single-phase H-bridge inverter. This quadratic boost inverter is capable of producing a high peak AC voltage, with a high conversion ratio at high efficiency. In this research work, a single switch with less duty ratio is used in the DC-DC converter stage to obtain high boost factor, and maximum modulation index is used to get high AC voltage gain. The two-stage DC-AC power conversion system is simulated in MATLAB/Simulink environment, and it is validated with the experimental results.

Keywords Quadratic boost inverter (QBI) · New quadratic boost converter (NQBC) · Electromagnetic interference (EMI) · Conventional quadratic boost converter (CQBC)

1 Introduction

Currently, a large number of renewable energy sources (RES) are being employed to meet the rising demand under all possible circumstances but all such sources lack one property of all and that is often to meet the demand in terms of efficiency. The light is put in the development of converters for point-of-load applications with special attention on realization of goals such as higher power density, better conversion efficiency

R. K. Sah · N. Wadhawan · Akansha · P. Sriramalakshmi (✉)
School of Electrical & Electronics Engineering, Vellore Institute of Technology, Chennai 600127,
Tamil Nadu, India

e-mail: sriramalakshmi.p@vit.ac.in

R. K. Sah
e-mail: rajatkumar.sah2015@vit.ac.in

N. Wadhawan
e-mail: namit.wadhawan2015@vit.ac.in

Akansha
e-mail: akansha.2015@vit.ac.in

© Springer Nature Singapore Pte Ltd. 2020

A. K. Bhoi et al. (eds.), *Advances in Greener Energy Technologies*,
Green Energy and Technology, https://doi.org/10.1007/978-981-15-4246-6_35

at full-load, and low electromagnetic interference (EMI). The design challenges of renewable energy applications include forming non-isolated topology which is free of transformers, minimum ripples content in the inductor current, capacitor voltage, and reduction in the filtering component sizes to reduce the impact of EMI. The low-loss magnetic materials and high-frequency switching are widely adopted in DC-DC converters. In addition, these converters are smaller in size and lighter in weight, with enhanced power density. Many power electronic converters and DC-DC conversion systems are capable of producing stable voltages to drive the DC loads. They are basically classified as buck converter, boost converter, buck–boost converter, and other higher-order converter circuits [1–4]. High-voltage gain applications [5–10] have a lot of restrictions and one such restriction happens to be the low efficiency. The dynamic and steady-state performances are of equal importance in the new topological evolutions. In view of all the aforementioned requirements, there is a need to evolve single-switch quadratic-type boost topologies with more steady-state voltage gain and better efficiency. So, not only DC-DC conversion takes place but also the H-bridge inverter connected through DC link helps in receiving proper AC output voltage.

In this paper, an existing DC-DC converter topology, the new quadratic boost converter (NQBC) [11], is cascaded with a single-phase H-bridge inverter to obtain a high peak AC output voltage. A 48 V DC voltage is supplied to NQBC to boost the voltage to 160 V with the duty ratio of 0.36, and peak AC voltage of 160 V is obtained with the modulation index of 1. The topology is simulated in MATLAB/Simulink and is experimented in the laboratory with the same design parameters. The operating modes, steady-state analysis simulation, experimental results, and performance evaluation are presented in detail.

2 Two-Stage DC-AC Quadratic Boost Inverter Topology

Figure 1 illustrates the proposed topology of two-stage DC-AC quadratic boost inverter.

The two-stage quadratic boost inverter topology is obtained by connecting NNQBC [11] and an H-bridge inverter in cascaded form. The DC-DC conversion part is followed by DC-AC inversion. The DC voltage supply is given to NNQBC [11] and the boosted DC output voltage is given to the H-bridge inverter through the DC link as input. This topology is based on the fifth-order quadratic boost converter proposed in [11] to achieve the required DC output voltage. Due to the arrangement of the passive components in NQBC [11], the ripple content is reduced. Hence, it is better in comparison with other boost inverter topologies.

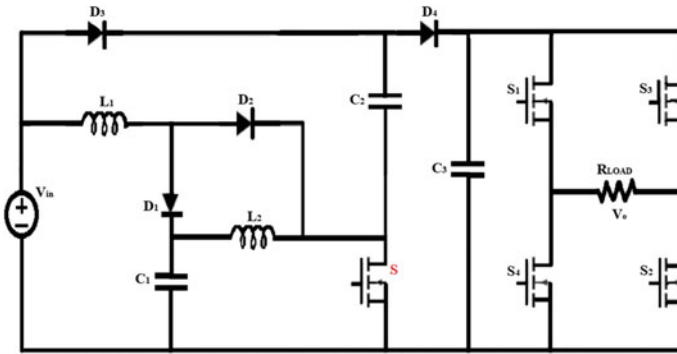


Fig. 1 Two-stage quadratic boost inverter

3 Modeling of Quadratic Boost Converter

An existing fifth-order boost quadratic boost converter is used, and the modes of operations are discussed in the succeeding sections. The conventional quadratic boost converter is combined with an additional capacitor and diode. The conventional QBC (CQBC) is a fourth order circuit while the NQBC is a fifth order one due to the presence of the additional charging and discharging components. This increased order helps in obtaining the increased voltage gain in comparison to CQBC. Due to the arrangement of L- and C-elements, the NQBC [11] provides higher boosting at low duty ratio. It is easily controllable due to the presence of a single switch. Figure 2 shows the modified quadratic boost converter.

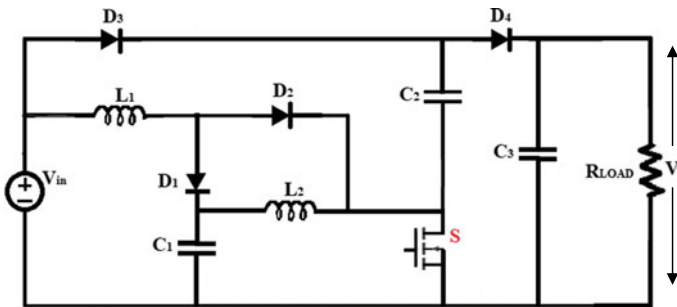


Fig. 2 New quadratic boost converter (NQBC)

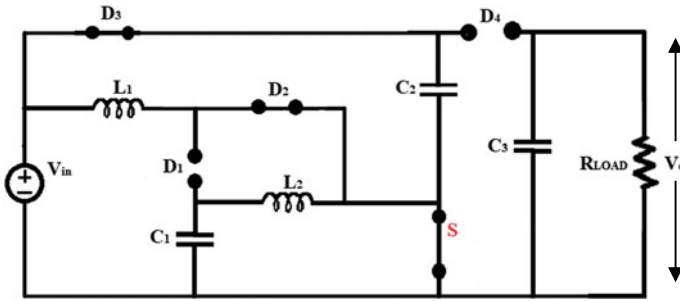


Fig. 3 Equivalent circuit when S is ON

4 Steady-State Performance Analysis

In this section, time domain analysis is presented to show the steady-state performance of the DC-DC NQBC converter. As the NQBC [11] uses a single switch for control, the operating modes of the converter are entirely based on the ON and OFF states of the switch S.

4.1 When Switch ‘S’ is ON

During this mode of operation, switch (S) is turned on. The equivalent circuit during this time interval is shown in Fig. 3. The energy is stored in the energy storage elements, L_1 and C_2 while L_2 and C_2 will exchange the energy. Diodes D_2 and D_3 are forward biased and act as closed circuit, while diodes D_1 and D_4 are reversed biased and act as open circuit.

During this mode, the inductor voltage and capacitor voltage values are obtained as follows:

$$V_{L1} = V_{in} \tag{1}$$

$$V_{L2} = V_{C1} \tag{2}$$

4.2 When Switch ‘S’ is OFF

During this mode of operation, switch (S) is turned off. The equivalent circuit during this time interval is shown in Fig. 4. The stored energy is transferred to load through

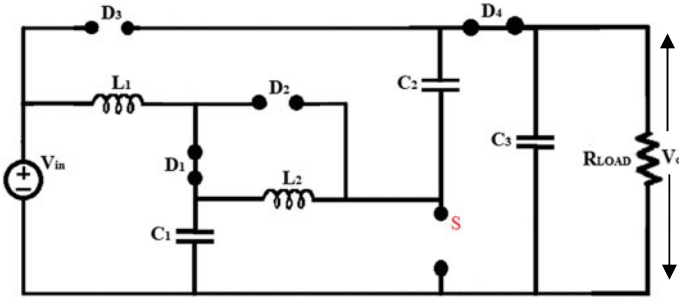


Fig. 4 Equivalent circuit when switch ‘S’ is OFF

L_1 , L_2 , and C_2 elements. Diodes D_2 and D_3 are reversed biased while diodes D_1 and D_4 are forward biased.

In this state, the inductor voltage and capacitor voltage values are obtained as:

$$V_{L1} = V_{in} - V_{C1} \tag{3}$$

$$V_{L2} = V_{C1} + V_{C2} - V_o \tag{4}$$

Applying volt-second balance using Eqs. (1)–(4) gives design equations in terms of ripple currents and ripple voltages,

$$L_1 = \frac{V_g D}{(f_s \Delta i_1)^2} \tag{5}$$

$$L_2 = \frac{V_{C1} D}{(f_s \Delta i_2)^2} \tag{6}$$

$$C_1 = \frac{[(D^2 - 2D + 2)V_g]}{[(1 - D)^2 R f_s \Delta v_{c1}]} \tag{7}$$

$$C_2 = \frac{[(D^2 - 2D + 2)V_g]}{[R f_s \Delta v_{c2}]} \tag{8}$$

$$C_3 = \frac{[(1 - D)^2 V_o D]}{[8L_2 [(D^2 - 2D + 2) f_s \Delta v_{c3}]]} \tag{9}$$

$$\text{Boost Factor} = \frac{D^2 - 2D + 2}{(1 - D)^2} \tag{10}$$

5 Simulink Diagram of Two-Stage Quadratic Inverter

In the proposed topology, an input supply of 48 V is given as the input and peak AC output voltage of 160 V appears across a resistive load. The simulation parameters are listed below in Table 1. The MATLAB/Simulink diagram is shown in Fig. 5.

Table 1 Simulation design specifications

Parameters	Attributes
Input voltage (V_{in})	48 V
Fundamental frequency (f_o)	50 Hz
Converter switching frequency (f_s)	50 kHz
Inverter switching frequency (f_S)	10 kHz
Duty ratio of shoot-through (D)	0.36
Modulation index (M)	1
Inductor ($L1$)	250 μ H
Inductor ($L2$)	250 μ H
Capacitor ($C1$)	47 μ F
Capacitor ($C2$)	47 μ F
Capacitor ($C3$)	100 μ F
Load resistance (R_L)	260 Ω

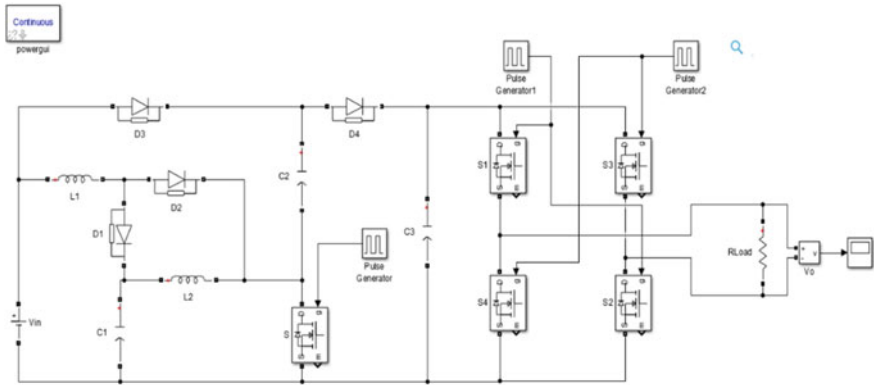
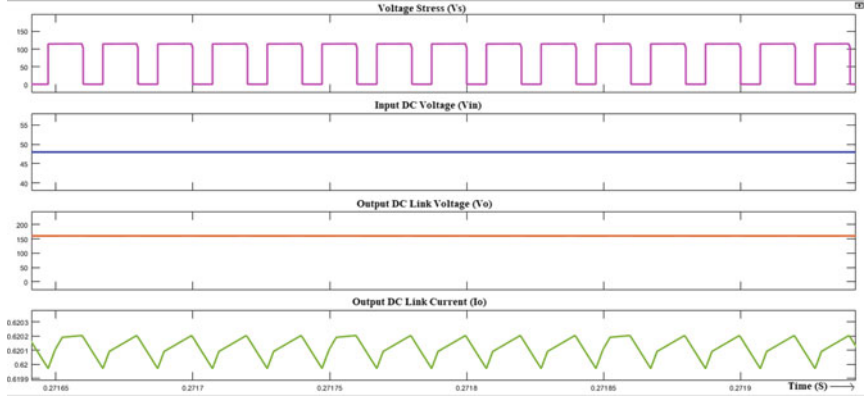
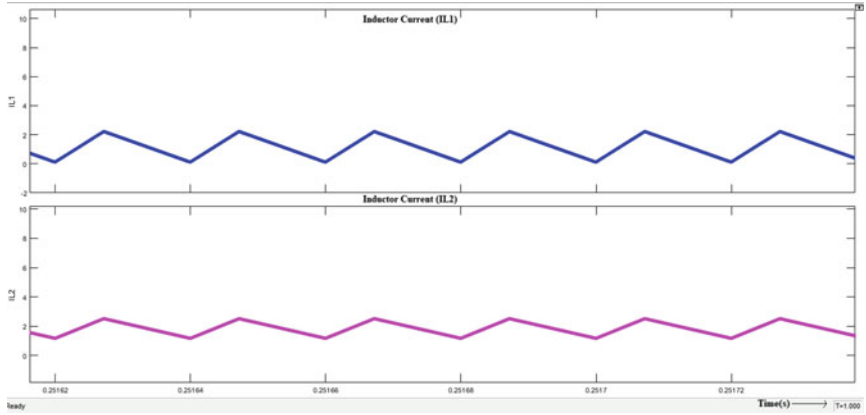


Fig. 5 Simulink diagram of two-stage NQBC boost inverter

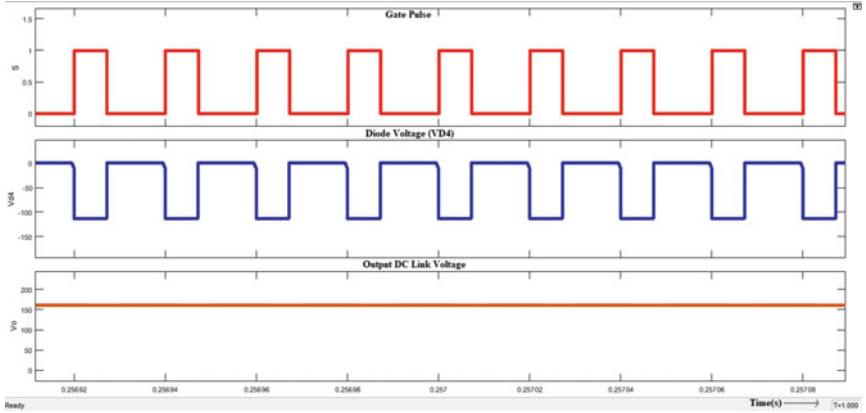
(a)

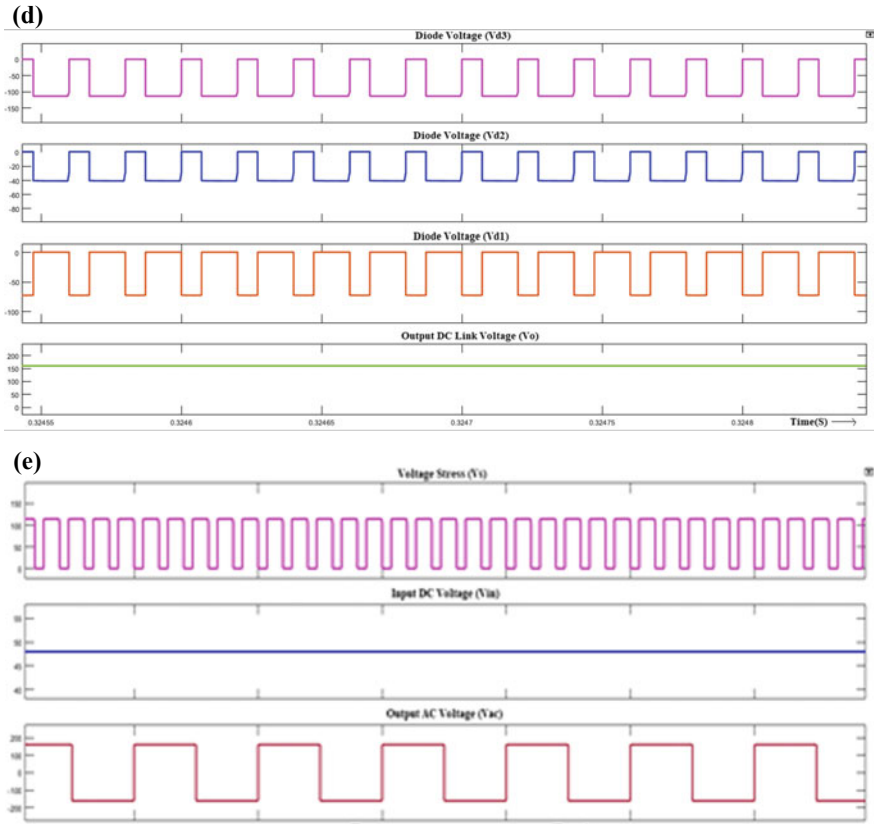


(b)



(c)





◀**Fig. 6** a Voltage stress of switch (V_S), input DC voltage (V_{in}), DC link voltage (V_o), and DC link current (I_o). b Voltage stress of switch (V_S), inductor currents of $L1$ (I_{L1}) and $L2$ (I_{L2}). c Gate pulse (S), diode (V_{D4}) voltage, and DC link voltage (V_o). d Voltage stress across the diode V_{D1} , V_{D2} , V_{D3} and output DC link voltage (V_o). e Voltage stress of switch (V_S), input DC voltage (V_{in}), and output AC load voltage (V_{AC})

5.1 Simulation Results

The analysis of this novel topology is performed in MATLAB/Simulink. Figure 6a–e exhibit the simulated results of the quadratic boost inverter (QBI) topology.

Figure 6a shows the voltage stress across boost converter switch (V_S), input DC voltage (V_{in}), DC link voltage (V_o), and DC link current (I_o) waveforms of the converter. Input voltage of 48 V is given and DC link voltage of 160 V is obtained across the inverter.

Figure 6b shows the waveform of both the inductors current I_{L1} and I_{L2} which shows the charging and discharging of both inductors.

Figure 6c shows the waveforms of gate pulse across the switch (S), diode (V_{D4}) voltage, and the 160 V DC link voltage (V_o) which is given to the inverter as input.

Table 2 Component stress of conventional topologies with NQBCs

Parameters	CQBC [5]	Modified NQBC [6]	NQBC [11]
V_{Gain}	2.44	2.44	3.44
Peak voltage stress (PVS)	160	160	112
Buffer capacitor voltage stress	75	27	75

$$V_{in} = 48 \text{ V}, D = 0.36, \text{ and } V_o = 160 \text{ V}$$

Figure 6d shows the waveform of the diode voltages (V_{D1} , V_{D2} , V_{D3}) and the 160 V DC link voltage (V_o) as input for inverter.

Figure 6e shows a peak unfiltered output AC voltage (V_{AC}) of 160V which is obtained across the load. The peak load current (I_{AC}) of 0.62 A is obtained.

Table 2 shows the comparison of voltage gain, peak voltage stress, and buffer capacitor voltage stress across the existing conventional topologies as per the theoretical calculations by considering the same design specifications mentioned below.

6 Experimental Verification

A prototype of QBI is designed as shown in Fig. 7 to offer the output power of 100 W and peak AC voltage of 160 V. Its performance is tested experimentally.

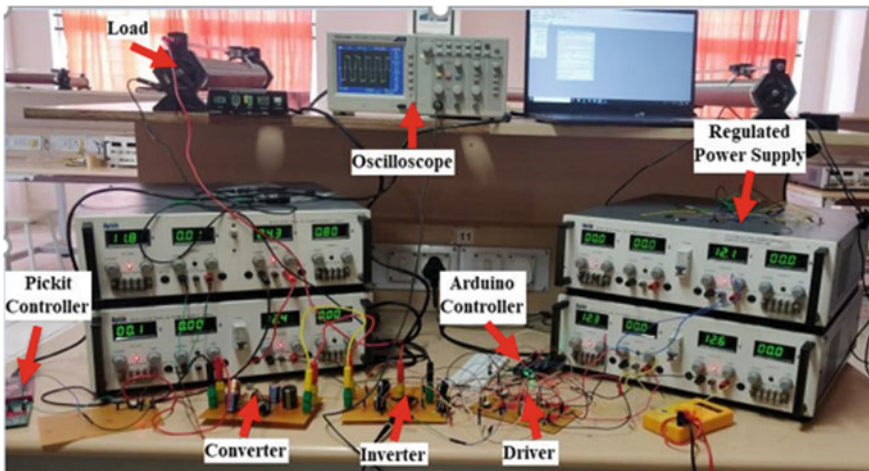


Fig. 7 Hardware experimental setup

Table 3 Hardware design specifications

Parameters	Attributes
Input voltage (V_g)	48 V
Fundamental frequency (f_o)	50 Hz
Converter switching frequency (f_S)	50 kHz
Inverter switching frequency (f_S)	10 kHz
Duty ratio of shoot-through (D)	0.36
Modulation index (M)	1
MOSFET	IRF840, 8 A, 600 V
Diodes	MUR860, 4 A, 600 V
Inductor ($L1$)	250 μ H, 8 A
Inductor ($L2$)	250 μ H, 8 A
Capacitor ($C1$)	47 μ F, 450 V
Capacitor ($C2$)	47 μ F, 450 V
Capacitor ($C3$)	100 μ F, 400 V
Capacitor (driver circuit)	0.1 μ F, 50 V
Resistance (driver circuit)	33 Ω
Resistance (driver circuit)	330 Ω
Resistance (driver circuit)	1 k Ω
MOSFET driver	TLP250H
Load resistance (R_L)	260 Ω

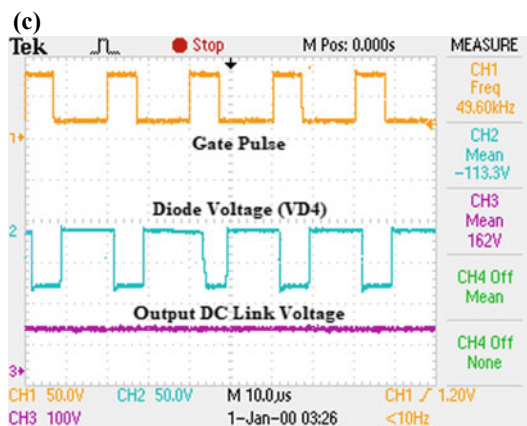
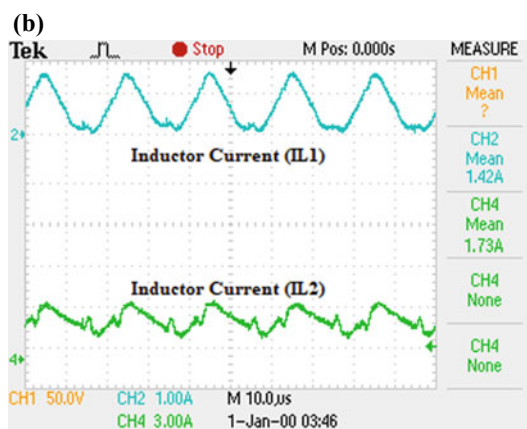
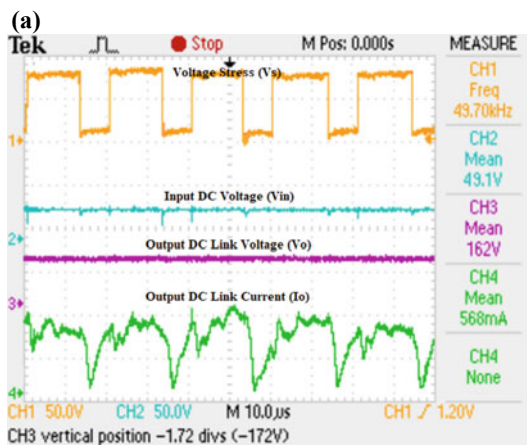
The hardware prototype specifications are listed in Table 3. For the duty ratio 0.36, an unfiltered output AC voltage of 160 V is obtained across the 260 Ω load. The efficiency of the prototype is 84.30% which is better when compared to conventional DC-DC-boosted inverter topology. A high gain of 3.33 is achieved for low duty cycle of 0.36.

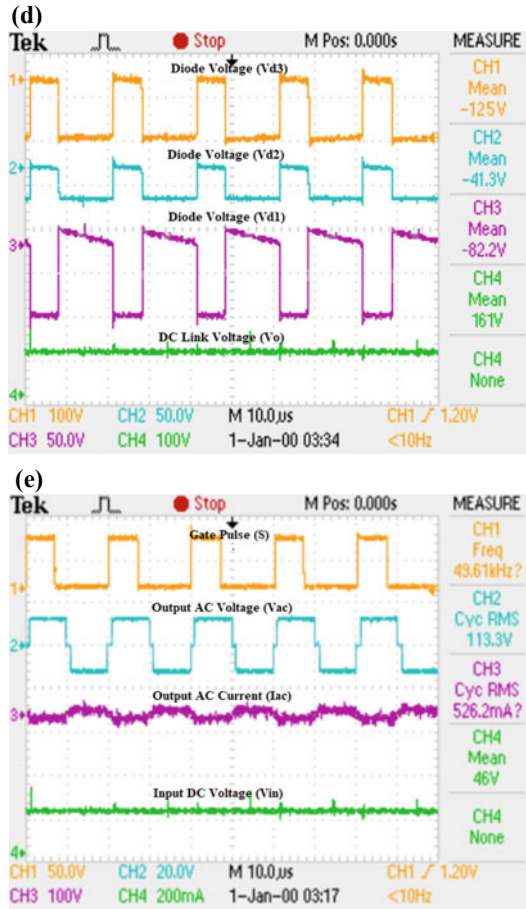
6.1 Hardware Results

The performance of the proposed two-stage boost inverter topology is tested and the results are presented. Figure 8a–e exhibit the experimental results of the QBI topology.

Figure 8a shows the voltage stress across switch (V_S), input DC voltage (V_{in}), DC link voltage (V_o), and DC link current (I_o) waveforms of the converter. Input voltage of 48 V is given and 160 V DC link voltage is obtained.

Figure 8b shows the waveform of both the inductors current I_{L1} and I_{L2} which shows the charging and discharging of both inductors. The average inductor current of 1.4 A is obtained.





◀**Fig. 8** **a** Voltage stress of switch (V_S), input DC voltage (V_{in}), DC link voltage (V_o), and DC link current (I_o). **b** Inductor currents of L_1 (I_{L1}) and L_2 (I_{L2}). **c** Gate pulse (S), diode ($D4$) voltage, and DC link voltage (V_o). **d** Voltage stress across the diode V_{D1} , V_{D2} , V_{D3} and output DC link voltage (V_o). **e** Gate pulse (S), input DC voltage (V_{in}), output AC load voltage (V_{AC}), and output AC load current (I_{AC})

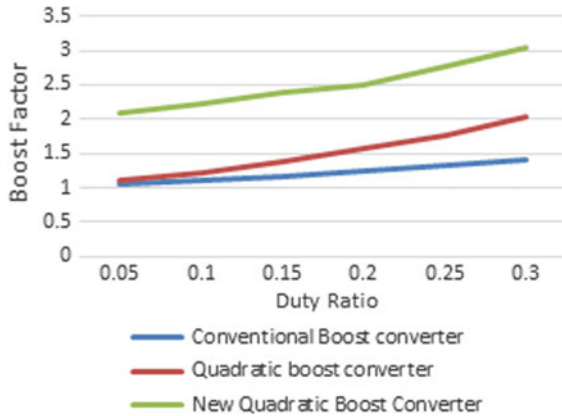
Figure 8c shows the waveform gate pulse across the switch (S), voltage stress across diode ($D4$), and the 160 V DC link voltage (V_o) which is given to the inverter as input.

Figure 8d shows the waveform of the diodes voltages (V_{D1} , V_{D2} , V_{D3}) which is negative and the 160V DC link voltage (V_o) as input for inverter. Figure 8e shows a peak unfiltered output AC voltage (V_{AC}) of 160 V, and the peak load current (I_{AC}) of 0.526 A is obtained across the load.

Table 4 Expressions for boost factor in terms of duty ratio

S. No.	Parameters	Conventional boost converter [12–15]	QBC [5]	NQBC [11]
1	B (in terms of D)	$\frac{1}{1-D}$	$\frac{1}{(1-D)^2}$	$\frac{D^2-2D+2}{(1-D)^2}$

Fig. 9 Boost factor versus duty ratio



7 Performance Comparison of Conventional Boost Converter, Fourth-Order QBC, and NQBC

The performance comparison of conventional boost converter, QBC, and NQBC are presented in Fig. 7. The graph is plotted between the boost factor (B) Versus duty ratio (D) of the mentioned topologies. Table 4 presents the expressions used for obtaining the plots between the conventional boost converter, QBC, and modified NQBC.

It is understood from Fig. 9 that the boost factor is high for NQBC when compared to NQBC-based inverter and conventional boost converter for the same value of duty ratio.

8 Conclusion

This paper discusses the operating principle and analysis of the two-stage quadratic boost inverter. The input voltage of 48 V produces a peak AC load voltage of 160 V. A small value of shoot-through duty ratio $D = 0.36$ can provide a high gain of 3.33. The voltage stress across the devices is less and so higher efficiency of 84.30% is obtained. The performance comparison is presented between conventional boost converter, QBC and NQBC. Hence, the topology is suitable whenever a small DC voltage needs to be boosted and inverted to meet the demand of low-voltage and medium power applications.

References

1. Hwu KI, Tu WC (2012) Voltage-boosting converters with hybrid energy pumping. *IET Power Electron* 5(2):185–195
2. Li K, Ioinovici A (2014) Large DC gain non isolated converter based on a new L-C-D step-up switching cell. In: *Proceedings of IEEE APCCAS*, pp 284–287
3. Zhang S, Xu J, Yang P (2012) A single-switch high-gain quadratic boost converter based on voltage-lift-technique. *Proceedings of IEEE IPEC*, pp 71–75
4. Hwu KI, Yau YT (2010) A KY boost converter. *IEEE Trans Power Electron* 25(11):2699–2703
5. Morales-Saldana JA, Loera-palolo R, Palacios-Hernandez E, Gonzalez-Martinez JL (2014) Modelling and control of a dc-dc quadratic boost converter with R2P2. *IET Power Electron* 7(1):11–22
6. Ye Y-M, Cheng KWE (2014) Quadratic boost converter with low buffer capacitor stress. *IET Power Electron* 7(5):1162–1170
7. Kadri R, Gaubert J-P, Champenios G, Mostefai M (2010) Performance analysis of transformerless single switch quadratic boost converter for grid connected photovoltaic systems. In: *Proceeding of IEEE ICEM*, pp 1–7
8. Diaz-saldierna L-H, Langarica-cordoba D, Leyva-Ramos J (2015) Loop-shaping control of high-step converters for fuel-cell applications. In: *Proceedings of IEEE Mediterranean conference on control and automation*, pp 789–795
9. Zhao Y, Li W, Deng Y, He X (2011) High step-up boost converter with passive lossless clamp circuit for non-isolated high step-up applications. *IET Power Electron* 4(8):851–859; Jovicic D (2010) Step-up DC–DC converter for megawatt size applications. *Power Electron* 3 (3):369–378
10. Chen S-M, Liang T-J, Yang L-S, Chen J-F (2011) A cascaded high step-up DC–DC converter with single switch for micro source applications. *IEEE Trans Power Electron* 26(4):1146–1153
11. Veerachary M (2015) Analysis of a new fifth-order boost converter. In: *Proceedings of IEEE Conference on SPICES*, pp 1–5
12. Rai JN, Gupta N, Bansal P (2016) Design and analysis of DC-DC boost converter. *Int J Adv Res Innov* 4(3):499–502
13. Nicolae D, Richards C, van Rensburg J (2010) Boost converter with improved transfer ratio. In: *Proceedings of IEEE IPEC*, pp 76–81
14. Mohan N et al (1989) *Power electronics*. Wiley
15. Bhimra PS (1990) *Power electronics*. Khanna publishers, New Delhi, India

Maximum Power Point Tracking for Wind Energy Conversion System



Monika Vardia, Neeraj Priyadarshi, Irfan Ali, Farooque Azam,
and Akash Kumar Bhoi

Abstract This work mainly focuses on the development of adaptive fuzzy logic controller-based control strategy for indirect matrix converter in wind energy generation system for targeting the maximum energy development. Indirect matrix converter and its adaptive fuzzy controls provide the basic platform to accomplish the research objectives in both hardware and software aspects. Here, WT emulator system consisting of DC drive is built to reproduce similar behavior like that of real WT to the wind generation system. The wind velocity changes and load switching conditions are performed using the wind turbine emulator. It calculates the wind speed values to calculate the torque command of the WT together with the wind characteristics.

1 Introduction

With the development of technology and increase in world population with high living standards, the need for energy is increasing drastically. In the last 20 years, with the increase in necessity of economics and secure energy sources and negative impacts of nuclear energy and increase in energy demand all over the world have attracted many researchers to work and studies about the different methods of renewable energy. The sources of renewable energy have major merits like abundance in nature with lack of harmful emissions [1–6].

M. Vardia · I. Ali
Geetanjali Institute of Technical Studies, Udaipur 313001, India

N. Priyadarshi (✉)
Birsra Institute of Technology (Trust), Ranchi 835217, India
e-mail: neerajrjd@gmail.com

F. Azam
School of Computing & IT, REVA University, Bangalore 560064, India

A. K. Bhoi
Department of Electrical & Electronics Engineering, Sikkim Manipal Institute of Technology,
Sikkim Manipal University, Majhitara, India
e-mail: akash.b@smit.smu.edu.in

© Springer Nature Singapore Pte Ltd. 2020

A. K. Bhoi et al. (eds.), *Advances in Greener Energy Technologies*,
Green Energy and Technology, https://doi.org/10.1007/978-981-15-4246-6_36

In this new world, microgrid and distributed generation applications are attracted attraction to gradually increment of reliability and efficiency of the modern power system. The power modulator is one of the most important components of the renewable energy systems. However, these power converters must meet certain criteria and standards such as IEEE 1547, IEEE 929-2000, IEC61727, EN61000-3-2, EN 50330-1 and US National Electrical Code (NEC) 690 which defines some properties of the power converter such as pf, PQ, RFI/EMI. WTs are the emerging source of renewable energy with ratings of commercial WTs now exceeding 10 MW. Also, it is the highest cost competitive among all the environmental clean and safe sources of renewable energy in the world.

2 Maximum Power Point Tracking Algorithm for Wind Power

Apart from the strength of the wind, maximum extractable energy depends on the operating point of the system also. So, the maximum power point tracking (MPPT) is of critical importance in WECS for minimizing the return time of the installation cost as well as maximizing the system's efficiency [7–11]. In MPPT, generator speed and the wind velocity are related intercepted by WT is optimized such that the output power is maximized. For this purpose, accurate calibration of mechanical sensors, like encoders/resolvers and anemometers, is required to get the information about generator rotor position/speed and wind velocity. However, the utility of mechanical sensors always increases the overall cost, failure rate and complexity of the hardware system.

Sensorless MPPT control schemes are effectively used nowadays due to the advancement in the technologies for wind industry. Due to the advancement in power electronics and microcontroller technologies, sensorless control for WECS has become easy and feasible. Presently, the control methods for wind speed sensorless MPPT control can be divided into five major categories: optimal torque (OT) control, perturbation and observation (P&O) control, power signal feedback (PSF) control, wind speed estimation (WSE)-based control, and the fuzzy logic (FL) control.

The P&O method which is also known as hill-climb search (HCS) method is widely used in wind generation system to extract maximum power and energy. Its merit is that its implementation does not depend on various informations like wind speed and turbine characteristics. Here, a simple hill climbing control is applied by perturbing the control variable and observing the resulting increase or decrease in power.

In OT control method, the torque of the generator is adjusted according to lookup table or optimal reference torque curve, which is calculated through hardware tests, but its efficiency is affected with the age of the system. In PSF control method, the wind turbine shaft speed is measured or estimated to calculate the optimal power for the MPPT control during operation which requires a pre-programmed 2D lookup

table with stored values of PMS generator speed and capture maximum power at different wind speed. In the WSE-based control method of MPPT, the estimation of the wind speed is used to compute the optimal rotor speed command from the optimal TSR.

The FL control method is very effective in MPPT techniques as it does not require the knowledge of WT characteristics and various wind velocities. For the universal control algorithm, fast convergence, insensitive parameters, and good noise immunity and inaccuracy of signals. For the fast convergence of the output is achieved by adaptively decreasing the step size during the search process. With the information of the increment/decrement of the PMSG rotor speed, by increase/decrease the electrical output power of the generator is calculated.

Among the existing wind speed sensorless maximum power point techniques, the PSF and OT are the two emerging techniques, but their implementation needs good knowledge of WECS. Also, the accuracy of these methods is affected by system parameter variations caused due to aging of the system. Therefore, this is an open area to further study and carry out research to combine the existing techniques, like the combination of HCS and PSF or HCS and OT.

Therefore, now new technology generators, power electronic devices and control solutions have to be implemented and developed to improve the characteristics of the wind energy conversion system and make it more advanced to be integrated into the power grid. Also, there are also introducing some emerging technology challenges and its needed to be further clarified, investigated and implemented. To the best knowledge of the candidate, very few studies have been done on the development, evaluation and experimental investigation of IMC interfaced synchronous generator for WECS incorporated with adaptive fuzzy logic control and space vector PWM under different conditions.

3 Details of Implemented Wind Energy Generation System

Figure 1 presents the schematic diagram of the practically implemented wind generation system consisting of indirect matrix converter (IMC) interfaced synchronous generator. The power from wind turbine is directly transmitted to the generator and is converted into electrical power. The generated power is transmitted to the utility grid through IMC.

The indirect matrix converter is exactly controlled to guarantee different speed operations with MPPT control. The IMC manages the power transfer. It is also applied for interfacing with the grid and space vector pulse width modulation (SVPWM) control is mostly used to getting the low harmonic output characteristics. It controls the power factor and the reactive power. It applies the “perturb and observe” MPPT technique by limiting the shaft speed to capture maximum output energy at various wind velocities. In these sections, various elements of the proposed system are described as follows:

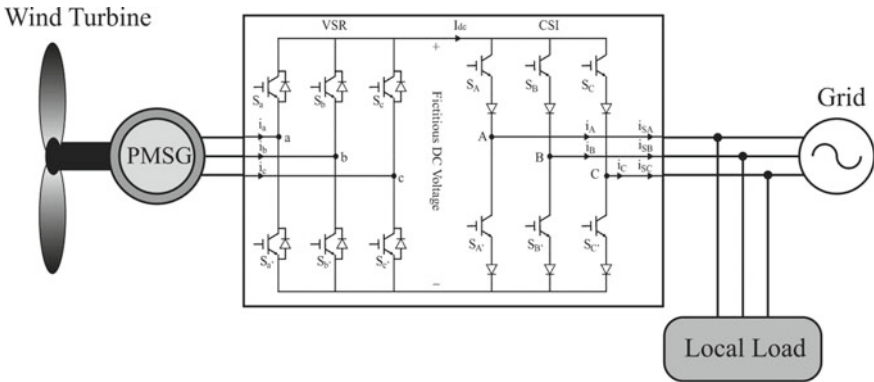


Fig. 1 Proposed wind energy conversion system

3.1 Wind Turbine Model

Here, a DC motor controller-based WT emulator which drives the generator is used for practical experimentation as shown in Fig. 2. It is used to achieve different wind speeds along with load switching methods. The real-time board which is dSPACE DS1104 is used to control this chopper-based direct current motor drive which calculates the torque demand using wind turbine characteristics for different values of wind speeds to reproduce the behavior of wind turbines to WECS.

The aerodynamic mechanical torque (T_m) and output power (P_0) by WT are expressed as follows:

$$T_m = \frac{1}{2} \pi \rho C_p(\lambda) R_w^3 V_w^2 \tag{1}$$

$$P_0 = \frac{1}{2} \rho C_p A_r V_w^3 \tag{2}$$

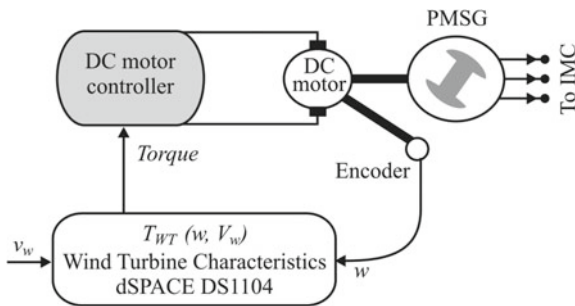


Fig. 2 Wind turbine emulator system

Figure 3 shows the steady-state output power/wind speeds at different wind speeds (marked with star). And, the power coefficient represents the TSR λ and rotor blade pitch angle θ according to Eq. (3) as shown in Fig. 4.

$$C_p(\lambda, \theta) = 0.73 \left(\frac{151}{\lambda_i} - 0.58\theta - 0.002\theta^{2.14} - 13.2 \right) e^{-18.4/\lambda_i} \tag{3}$$

where

$$\lambda_i = \frac{1}{\frac{1}{\lambda - 0.02\theta} - \frac{0.003}{\theta^3 + 1}} \tag{4}$$

and

$$\lambda = \frac{\omega R_r}{V_\omega} \tag{5}$$

In (5), ω is the turbine shaft-angular speed. From Eqs. (2) and (5), we get

Fig. 3 Power-speed characteristics of a WT at different wind speeds

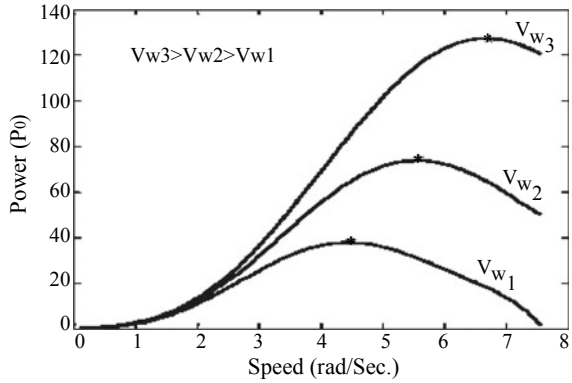
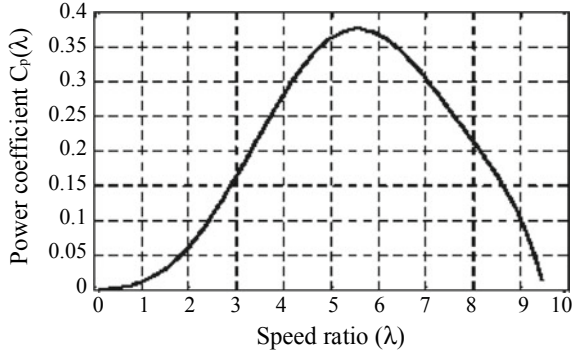


Fig. 4 $C_p-\lambda$ characteristics of wind turbine



$$P_0 = \frac{1}{2} \rho C_p A_r \left(\frac{\omega R_r}{\lambda} \right)^3 \quad (6)$$

At different wind speed, the maximum power can be captured if shaft speed is adjusted. The novel idea of this work is to change the angular frequency of PMSG by the SVPWM control of indirect matrix converter to capture the shaft speed to get the maximum power of WT at different times.

4 Response Under Varying Wind Speed Condition

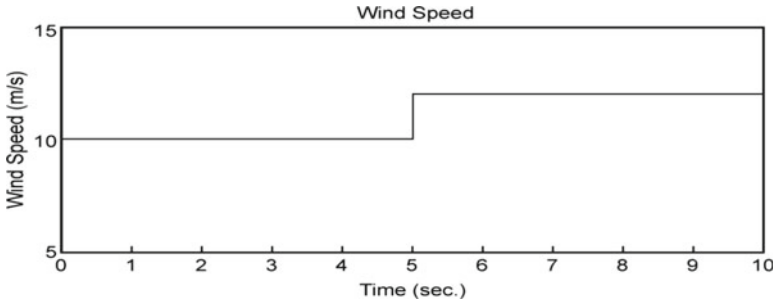
Response of system with a wind speed, which fluctuates with a mean value near 10 m/s and at 5 s, following an almost step change, rises to a mean value near 12 m/s, as shown in Fig. 5a. The simulated results in Fig. 5 show the wind speed, generator, electrical torque, mechanical torque and aerodynamic torque of generator, injected grid current, grid active power, IMC voltage, voltage, frequency of injected grid power.

As the wind speed increases, the generator speed also increases accordingly as shown in Fig. 4b. The corresponding changes in aerodynamic, mechanical and electrical torque are shown in Fig. 4c, d. With the decrease or increase of wind velocity, the values of output real power from the generator decrease or increase.

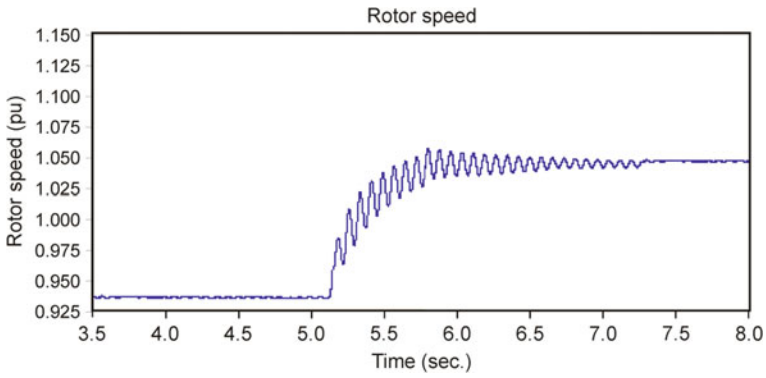
From Fig. 5b, we see that ω always depends on ω_{ref} which is rising, trying to capture its reference value for the specific wind velocity. On fault, ω maintains close to ω_{ref} and increases until it is equal to reference value. When this addition, output power and ω reach a new steady-state value, which indicates the maximum absorption of real power from the wind power turbines.

From the results of Fig. 5b, it is evident that the generator depends on the angular frequency for max-efficiency of aerodynamics (ω_{ref}) to achieve maximum power point very nearly. Also, AC voltage regulator of adaptive fuzzy logic control keeps the IMC injected grid voltage regulated. When the wind velocity increases, adaptive fuzzy logic control-based MPPT algorithm generates the phase shift signal $\Delta\delta$ of the phase angle δ through fuzzy logic controller FC₁, after differentiating current angular frequency at the terminal of generator (ω) with angular frequency for max. aerodynamic efficiency (ω_{ref}), and by giving rise to new value of the phase angle (δ) and modulation index (MI) is produced to operate at maximum aerodynamic efficiency to capture maximum energy with regulated output grid voltage, respectively. Thus, the proposed MPPT algorithm provides faster tracking, resulting in more energy yield.

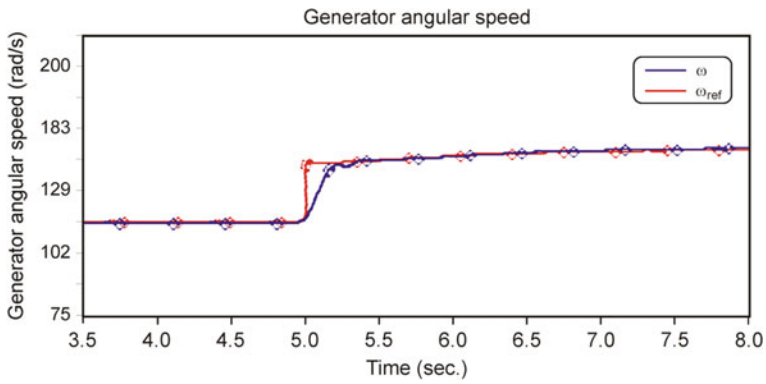
As shown in Fig. 5g the real power tracks its reference value when wind speed varies, whereas the reactive power fluctuates within limits. From the simulated waveforms in Fig. 5e, it is evident that proposed adaptive control is effective to maintain a constant grid voltage under varying wind conditions. The effect of fluctuating wind speed can also be verified from the amount of active power and current injected into the grid by the voltage-boosted IMC-based wind generation system as shown in Fig. 5f, h.



(a) Wind Speed

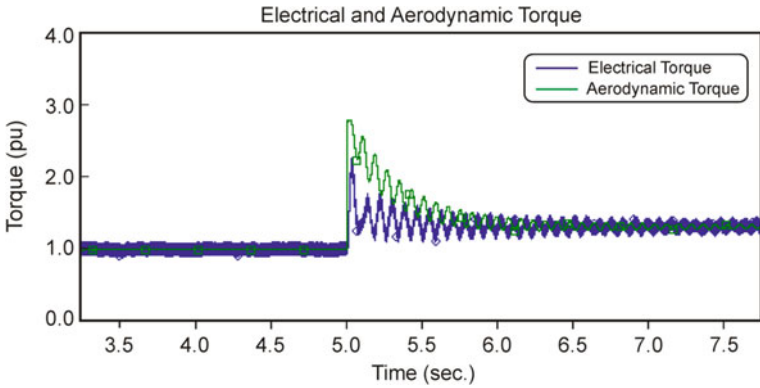


(b) Rotor Speed

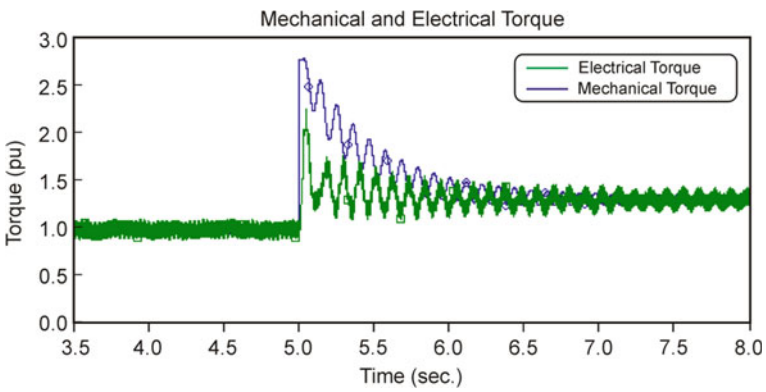


(c) Angular Speed of Generator

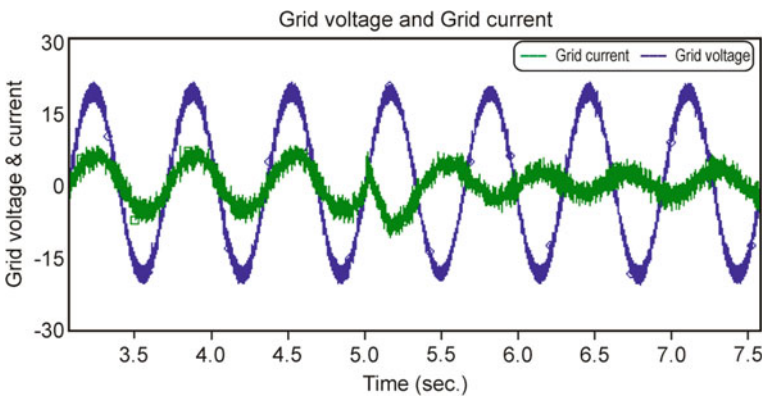
Fig. 5 Simulation responses during change in wind velocity



(d) Electrical and Aerodynamic Torque of Generator

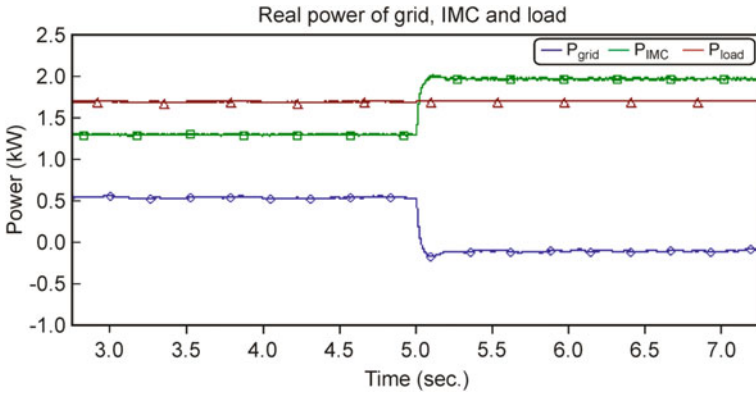


(e) Mechanical and Electrical Torque of Generator

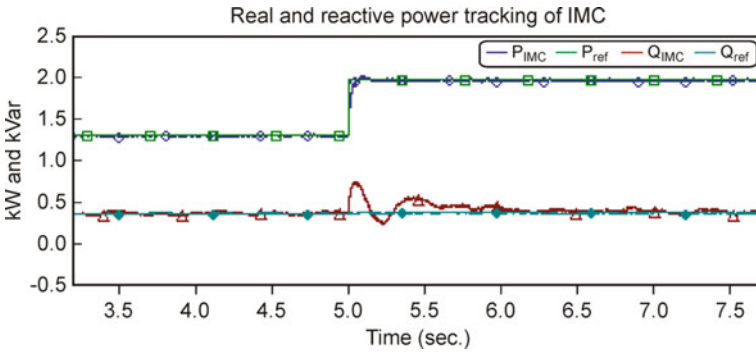


(f) Grid Voltage and Current

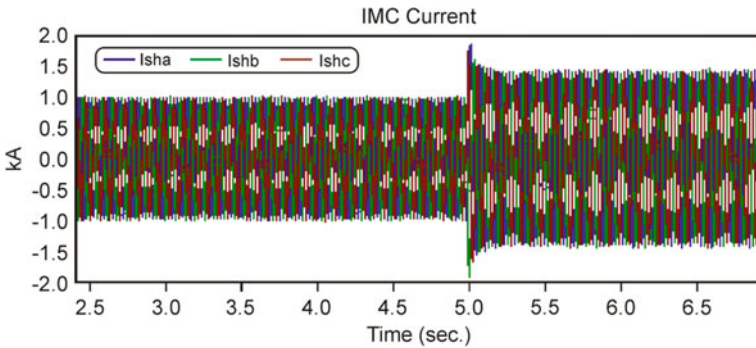
Fig. 5 (continued)



(g) Real Power of Grid, IMC, and Load



(h) Real and Reactive Power Tracking Capability of IMC



(i) Three-phase Current Injected into Grid by the Wind Generation System

Fig. 5 (continued)

5 Conclusion

For implementation of the maximum power point tracking (MPPT) capability of the proposed adaptive fuzzy-based controller, wind energy generation system has been examined under varying wind velocity conditions. This system simulates under suddenly raising of the wind velocity to validate the output response of the developed control system. The designed wind energy conversion systems worked at high tracking efficiency under changing wind velocity.

References

1. Priyadarshi N, Padmanaban S, Maroti PK, Sharma A (2018) An extensive practical investigation of FPSO-based MPPT for grid integrated PV system under variable operating conditions with anti-islanding protection. *IEEE Syst J*, 1–11
2. Priyadarshi N, Padmanaban S, Bhaskar MS, Blaabjerg F, Sharma A (2018) A fuzzy SVPWM based inverter control realization of grid integrated PV-wind system with FPSO MPPT algorithm for a grid-connected PV/wind power generation system: hardware implementation. *IET Electr Power Appl*, 1–12
3. Priyadarshi N, Anand A, Sharma AK, Azam F, Singh VK, Sinha RK (2017) An experimental implementation and testing of GA based maximum power point tracking for PV system under varying ambient conditions using dSPACE DS 1104 controller. *Int J Renew Energy Res* 7(1):255–265
4. Priyadarshi N, Kumar V, Yadav K, Vardia M (2017) An experimental study on zeta buck-boost converter for application in PV system. In: *Handbook of distributed generation*. Springer. https://doi.org/10.1007/978-3-319-51343-0_13
5. Priyadarshi N, Sharma AK, Priyam S (2018) An experimental realization of grid-connected PV system with MPPT using dSPACE DS 1104 control board. In: *Advances in smart grid and renewable energy. Lecture notes in electrical engineering*, vol 435. Springer, Singapore
6. Priyadarshi N, Sharma AK, Azam F (2017) A hybrid firefly-asymmetrical fuzzy logic controller based MPPT for PV-wind-fuel grid integration. *Int J Renew Energy Res* 7(4)
7. Priyadarshi N, Sharma AK, Priyam S (2017) Practical realization of an improved photovoltaic grid integration with MPPT. *Int J Renew Energy Res* 7(4)
8. Priyadarshi N, Sharma AK, Bhoi AK, Ahmad SN, Azam A, Priyam S (2018) MATLAB/Simulink based fault analysis of PV grid with intelligent fuzzy logic control MPPT. *Int J Eng Technol* 7:198–204
9. Priyadarshi N, Sharma AK, Bhoi AK, Ahmad SN, Azam A, Priyam S (2018) A practical performance verification of AFLC based MPPT for standalone PV power system under varying weather condition. *Int J Eng Technol* 7:338–343
10. Priyadarshi N, Padmanaban S, Mihet-Popa L, Blaabjerg F, Azam F (2018) Maximum power point tracking for brushless DC motor-driven photovoltaic pumping systems using a hybrid ANFIS-FLOWER pollination optimization algorithm. *MDPI Energies* 11(1):1–16
11. Priyadarshi N, Azam F, Bhoi AK, Alam S (2019) An artificial fuzzy logic intelligent controller based MPPT for PV grid utility. In: *Lecture notes in networks and systems*, vol 46. https://doi.org/10.1007/978-981-13-1217-5_88

A Study on Frequency Regulation Energy Storage System Design in Island Power System



Jaewan Suh, Seungmin Jung, and Minhan Yoon

Abstract The necessity and installation of energy storage device are increasing due to the change of power system such as an increase in large-capacity distributed power source, and therefore, it is required to study the power system analysis and control method considering energy storage system (ESS). The type of grid-connected converter of the battery system is assumed to be the voltage source converter. The controller is configured to allow independent control of P and Q , as the effective power output controller of the energy storage device according to the frequency change of the power system, the droop control method using the controllable droop coefficient was used. In this paper, we compare and analyze the effects of fixed and adaptive droop control methods on the stability of the independent power system in the transient situations such as the dropout of generators. A method has been studied to improve system stability by appropriately controlling ESS using adaptive droop control. Simulations showed the adverse effects of inappropriate control on the power system stability. An adequate capacity and droop control for an ESS active power control depending on the power system operation condition has been studied, and the effectiveness of the droop control was verified by simulation. The adaptive droop control strategy can appropriately adjust the droop coefficient according to the system condition so that the ESS contributes appropriately to the stability improvement of the power system.

Keywords (5–6) ESS · Frequency regulation · Adaptive droop control · Active power control · Power system stability

J. Suh

Department of Electrical Engineering, Dongyang Mirae University, Seoul 08221, South Korea
e-mail: jwsuh@dongyang.ac.kr

S. Jung

Department of Electrical Engineering, Hanbat National University, Daejeon 34158, South Korea
e-mail: seungminj@hanbat.ac.kr

M. Yoon (✉)

Department of Electrical Engineering, Kwangwoon University, Seoul 01897, South Korea
e-mail: minhan.yoon@gmail.com

© Springer Nature Singapore Pte Ltd. 2020

A. K. Bhoi et al. (eds.), *Advances in Greener Energy Technologies*,

Green Energy and Technology, https://doi.org/10.1007/978-981-15-4246-6_37

1 Introduction

Recently, volatilities and uncertainties in power system operation have increased due to various distributed power sources including renewable energy sources and fluctuated loads such as electric vehicle charging [1]. Energy storage systems (ESS) have studied and applied as a solution to compensate for these phenomena. Lithium-ion battery (LIB), which has recent energy density efficiency and a rapid decline in cost, is becoming a popular trend among chemical storage methods [2]. For pumped storage power generation, there is a problem in terms of ease of charging and discharging and quick reactivity for use in FR. Compressed air storage devices, flywheels, supercapacitors, and superconducting energy storage devices are still in need of technical maturity.

Increasingly, battery ESS (BESS) is being installed in the location where large-scale renewable energy sources exist and power system operators provide incentives [3, 4]. On the other hand, a large amount of ESS is applied and demonstrated to compensate for the frequency variation of the power system [5, 6]. In order to compensate for the fluctuating frequency, an appropriate amount of active power must be extracted through converter control, where the converter controller is an outer controller for correcting errors in the basic AC and DC systems and an inner controller for generating the firing signal can be configured [7]. Typically, the part of the ESS related to the compensating control of the varying frequency is performed at the higher-level master controller level than the outer control. In case that several devices are controlled for the same purpose, the droop control method is used when they are located in the same system. Depending on the requirements of the power system operator, the droop coefficient is usually set to be changed. The droop may have one value at all times or at an emergency, and the response characteristic may be changed by applying a different value.

In this paper, we conducted a study on the power system condition based on the adaptive droop control and the estimation of the proper droop compared to the ESS capacity.

2 Frequency Regulation Energy Storage System

This study assumes that the BESS is used for frequency regulation purposes. As shown in Fig. 1, many BESSs use a large-capacity lithium-ion battery that is connected to the system using a voltage source converter recently. The advantage of the VSC is that it can operate within a defined limit from the P and Q in positive and negative ratings. Therefore, when AC voltage control is applied, it is possible to compensate for the fluctuating frequency by controlling only the active power while maintaining the voltage of the system [8].

However, in the normal case, the converter rating is allocated to the active power as much as possible due to the problem of the converter size, and the power factor is

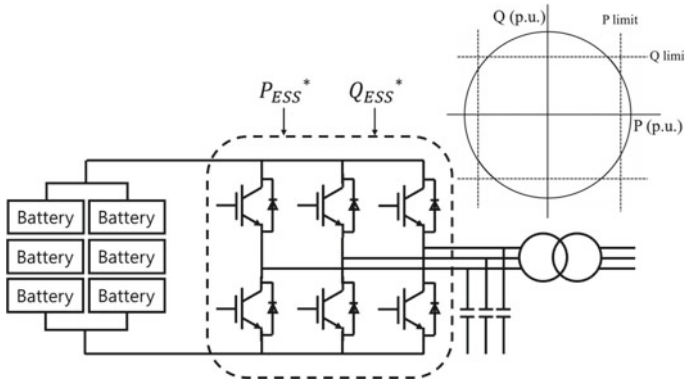


Fig. 1 BESS system configuration

used close to 1.0. In this paper, a system stability dynamic simulation is performed using a constant power factor control scheme.

This frequency regulation (FR) ESS replaces the governor-free operation of power plants using instantaneous active power control capability. Such a power control function stabilizes the system when properly operated, but may otherwise adversely affect the system stability. Especially, the smaller scale and the less robust system, the stable control of the large-capacity ESS becomes the important factor in the system operation.

Therefore, current power system conditions such as short-circuit capacity or spinning reserve power and the active capacity of the ESS installed in the grid are important key factors in determining the active power output by the ESS.

2.1 FR-ESS Control Scheme

In this study, as a kind of adaptive droop control, the operation of FR-ESS is divided into three modes, steady state, transient state, and exit state as shown in Fig. 2 [9]. The steady state is the stable operation without any disturbance in the power system,

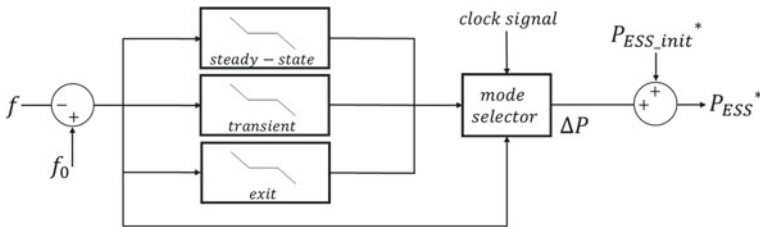


Fig. 2 FR-ESS master control configuration

and the transient state causes a large variation in frequency such as the dropout of the generator. The exit state refers to the state in which the ESS is recovering after a certain period of time in the transient state.

The appropriate ESS active power output calculation value for each state is continuously calculated in accordance with the frequency error signal of the reference frequency of the current power system and the measured frequency. The input signal for the master controller of the ESS to determine these three states is the frequency error value and the time synchronization signal.

2.2 Steady-State Control Mode

In the steady-state ESS control, the ESS exchanges only a small amount of power for maintaining the stage of charge (SoC) in the frequency dead-band region within a certain range ($f_{db.min} < f < f_{db.max}$), and when the measured frequency is out of range, it outputs the output with the frequency deviation by the predetermined slope of power–frequency curve.

The ratio K of the output relative to the frequency input deviation can be calculated by Eq. (1). It is a parameter representing the relationship between the power generation power of the power system and the amount of frequency variation due to the imbalance of the demand amount. $P_{ESS.rated}$ is the rated capacity of the FR-ESS, δ is the speed droop coefficient of the ESS device. f_N is the base frequency. Therefore, the output ΔP of the ESS versus the frequency change Δf is defined as Eq. (2).

$$K = \frac{100 \cdot P_{ESS.rated}}{\delta \cdot f_N} \quad (1)$$

$$\Delta P = \frac{\delta \cdot K}{100} \cdot \Delta f \quad (2)$$

$$\begin{cases} f < f_{db.min} \\ f > f_{db.max} \end{cases}$$

2.3 Transient-State Control Mode

The transient condition occurs mainly when large-capacity generators are tripped due to an accident or the like. This can be done to help reduce the rate of change of frequency (RoCoF) or relief frequency nadir by applying a large K_{tran} value to the ESS to give a greater output for the frequency drop than to control it with the same K_{ss} value as the steady state.

The transient-state determination is performed in the mode selector that it is assumed to operate when the frequency drop width is consistently larger than the specified value R_{tran} (Hz/s) for X steps based on the frequency error signal and time synchronization signal.

2.4 Exit-State Control Mode

If the transient-state control mode of the ESS is utilized, the K value is maintained at a high value even if the frequency is restored after the accident, so that the ESS can be discharged rapidly. Also, if the frequency regulation continues at a high K value, the degraded frequency will return to the base frequency, and the excessive output change of the ESS may adversely affect the frequency stability.

The normal state switching control (exit control mode) by the speed droop rate at the end of the transient state is performed. The exit mode condition is that the system frequency above than f_{exit} (Hz) and the rising condition are maintained for more than t_{exit} (s).

2.5 FR-ESS Control Algorithm

Figure 3 shows the algorithm for performing the FR-ESS controls described in Sects. 2.1–2.4.

Step 1: Basically, it will continue to discriminate the frequency dead-band, and if it goes out of the band, it will perform the frequency regulation in the steady-state control mode.

Step 2: If the measured RoCoF exceeds the R_{tran} value more than X step, the speed droop is increased from steady-state K_{ss} to the transient K_{tran} . At this time, the transient mode duration t_{tran} is reset to zero and synchronized in time.

Step 3: When the system frequency is recovered above an exit mode frequency f_{exit} and the transient mode duration t_{tran} exceeds the specified $t_{\text{tran.out}}$, the control mode is changed to the exit control mode. The speed droop is decreased from transient K_{tran} to the exit K_{exit} . At this time, the exit mode duration t_{exit} is reset to zero and synchronized in time.

Step 4: If the frequency is recovered within the dead-band and the exit mode duration t_{exit} exceeds $t_{\text{exit.out}}$, the ESS performs the SoC recovery control again.

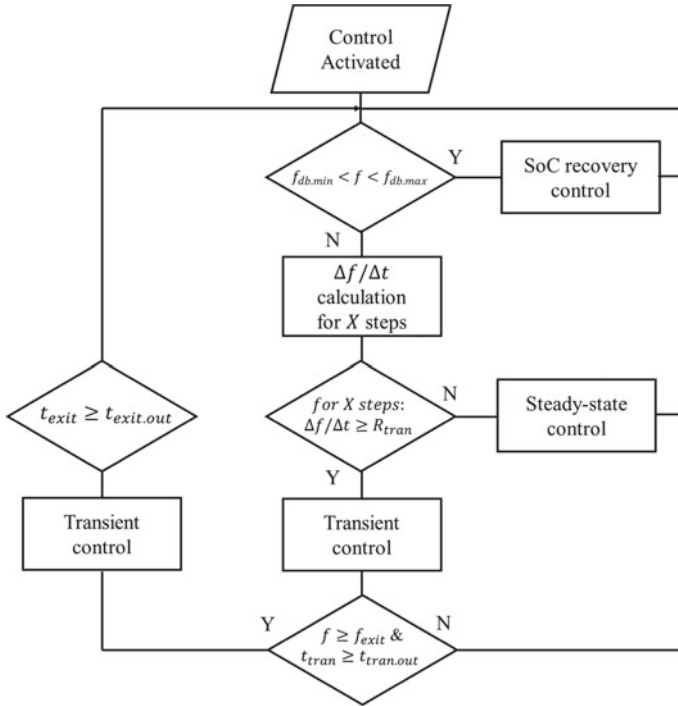


Fig. 3 FR-ESS control algorithm

3 Case Study

3.1 System Description

In this paper, the droop control method has been studied that considers the variable power system condition. We carry out case studies on the different FR-ESS capacity and various droop coefficients considering of power system data of Korea Electric Power Cooperation (KEPCO). The KEPCO system is an island power system independent of neighboring countries. Therefore, there is no way to compensate for the frequency fluctuation except for the spinning reserve that it has. If the frequency is high, it is possible to lower the frequency back to the base frequency by detecting the generation power [10]. In the opposite case, however, the additional power supply is required, and the KEPCO system order that the generators in operation are always reserved for 1500 MW.

For the case study, the test system used is 70% load case in 2019 as a typical representative case. Information on the system is shown in Table 1. The case where the generator disconnected assumes 1000 MW dropout case, which is the case of one unit of maximum thermal generator case.

Table 1 Test system for case study

Generation	66,259.9 MW + 18,039.1 MVar
Load	65,310.1 MW + 16,322.3 MVar
Losses	949.8 MW
ESS capacity	376/700 MW
Steady-state K_{ss}	23.8
Transient K_{tran}	7870
Exit K_{exit}	41.67

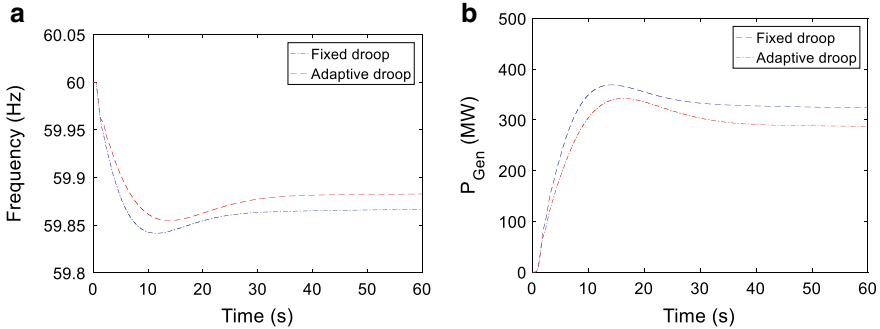


Fig. 4 a Frequency, b power output of generators

3.2 Simulation Result

3.2.1 376 MW ESS Capacity

It is assumed that an ESS with a capacity of 376 MW, which is about 0.5% of the total generation capacity of the system, is connected to the system. The fixed droop case using the existing single droop is called the steady-state case, and the other one is the case using the adaptive droop is called the transient case.

As shown in Fig. 4a, in case that adaptive droop control is applied, it is confirmed that RoCoF is smaller and frequency nadir is larger than fixed droop control. Figure 5a, b show that the ESS is operating in transient control mode after a certain period of time elapses after generator outage, so that other generators such can reduce the governor-free operation as shown in Fig. 4b.

3.2.2 700 MW ESS Capacity

The second case study investigates the effect of doubling ESS capacity as 700 MW in the same system condition. In this case, the ESS is installed in 1% of the total power generation, and the effect can be increased as shown in Figs. 6, 7. When shifting from the transient control mode to the exit control mode, we can see that the system

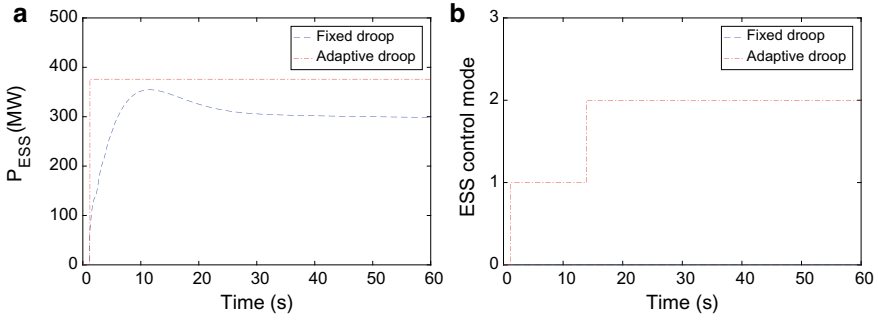


Fig. 5 a ESS power output, b ESS control mode

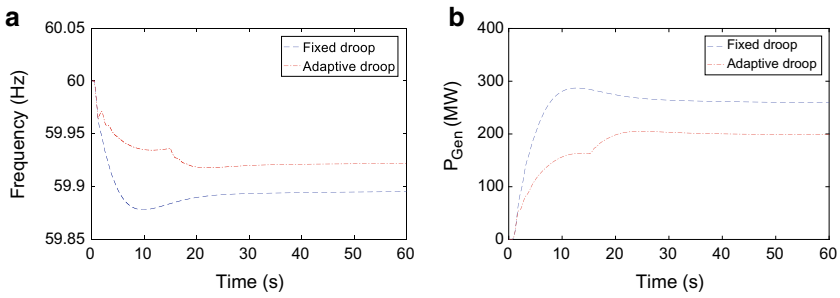


Fig. 6 a Frequency, b ESS power output

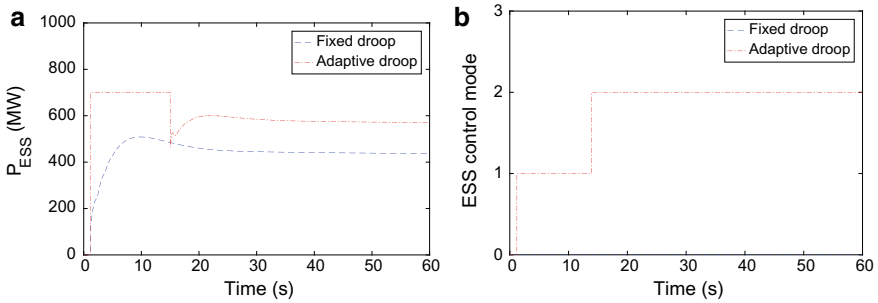


Fig. 7 a ESS power output, b ESS control mode

frequency once again drops significantly. However, in terms of RoCoF, frequency nadir, and converged frequency, it can be seen that it contributes more to maintaining stable frequency stability than fixed droop.

4 Conclusion

In this paper, we have studied the control methods to smooth the power system frequency adjustment through the utilization of ESS. The adaptive droop control method that controls the speed droop according to the frequency condition of the system was applied to compare with the fixed droop method. At this time, we could confirm through the case study that adaptive droop control is better in terms of frequency nadir, RoCoF, and converged frequency. However, when the same adaptive droop method is applied, it is found through simulation that when the capacity of the ESS increases, the frequency is fluctuated when the transient control mode and the exit control mode are changed. Therefore, when using this method, the droop should be determined by considering the short-circuit capacity of the system and the capacity of the ESS relative to the inertia. In the future, a study should be conducted to estimate the appropriate droop coefficient.

Acknowledgements This work was supported by the Korea Institute of Energy Technology Evaluation and Planning (KETEP) and the Ministry of Trade, Industry and Energy (MOTIE) of the Republic of Korea (No. 20182410105330), and National Research Foundation (Grant No. 2017R1C1B5018073) funded by the Korean government.

References

1. IEA (2018) Renewables 2018: market analysis and forecast from 2018 to 2023. [Internet]. Available from: <https://www.iea.org/renewables2018/> (website)
2. Chen H, Cong TN, Yang W, Tan C, Li Y, Ding Y (2009) Progress in electrical energy storage system: a critical review. *Prog Nat Sci* 19(3):291–312
3. Le HT, Santoso S, Nguyen TQ (2012) Augmenting wind power penetration and grid voltage stability limits using ESS: application design, sizing, and a case study. *IEEE Trans Power Syst* 27(1):161–171
4. Divya KC, Østergaard J (2009) Battery energy storage technology for power systems—an overview. *Electr Power Syst Res* 79(4):511–520
5. Oudalov A, Chartouni D, Ohler C (2007) Optimizing a battery energy storage system for primary frequency control. *IEEE Trans Power Syst* 22(3):1259–1266
6. Choi W, Yu G, Kook K (2016) Operating method of BESS for providing AGC frequency control service considering its availability maximization. *Trans Korean Inst Electr Eng* 65(7):1161–1168
7. Jung S, Yoon YT, Jang G (2016) Adaptive curtailment plan with energy storage for AC/DC combined distribution systems. *Sustainability* 8(8):818
8. Yoon M, Yoon YT, Jang G (2015) A study on maximum wind power penetration limit in island power system considering high-voltage direct current interconnections. *Energies* 8(12):14244–14259
9. Lu X, Sun K, Guerrero JM, Vasquez JC, Huang L (2014) State-of-charge balance using adaptive droop control for distributed energy storage systems in DC microgrid applications. *IEEE Trans Ind Electron* 61(6):2804–2815
10. Kottick D, Blau M, Edelstein D (1993) Battery energy storage for frequency regulation in an island power system. *IEEE Trans Energy Convers* 8(3):455–459

A Fuzzy Logic Control Based Vibration Control System for Renewable Application



Tarunkumar Choudhary, Neeraj Priyadarshi, Piyush Kumar, Farooque Azam, and Akash Kumar Bhoi

Abstract The main purpose of this thesis is to propose an active vibration control system to minimize the vibration of the structure. Vibration control is still the challenging problem in the field of control engineering. In this thesis, two electromagnetic actuators are used to minimize the vibration of the structure. Fuzzy logic control techniques are adopted here as the control system. Two electromagnets are placed at the midpoint of the beam, one above the structure and one below the structure. The beam model is first deriving analytically according to the Euler–Bernoulli beam theory. A noncontact displacement sensor is used to measure the displacement of the mid-span of the beam. The fuzzy logic control technique is used as controller to decide the output direct current (D.C.) passing through the coils of the electromagnet based on velocity and displacement of midpoint of the beam. When any external disturbance load is applied at midpoint of the beam, then beam starts to oscillate in upward and downward directions from static equilibrium position. During the upward displacement of the beam from the static equilibrium position, the bottom electromagnet actuator is switched on and electromagnet will give a magnetic force in the opposite direction of motion of the beam. Similarly, during the downward movement of the beam below the static equilibrium position, the top electromagnetic actuator is switched on and electromagnet will give a magnetic force in the opposite downward motion of the beam. In this thesis, it is shown that the proposed damper successfully

T. Choudhary · P. Kumar
Department of Mechanical Engineering, Birsa Institute of Technology (Trust),
Ranchi 835217, India

N. Priyadarshi (✉)
Department of Electrical Engineering, Birsa Institute of Technology (Trust),
Ranchi 835217, India
e-mail: neerajrjd@gmail.com

F. Azam
School of Computing and IT, REVA University, Bangalore 560064, India

A. K. Bhoi
Department of Electrical and Electronics Engineering, Sikkim Manipal Institute of Technology,
Sikkim Manipal University, Gangtok, India
e-mail: akash730@gmail.com

© Springer Nature Singapore Pte Ltd. 2020

A. K. Bhoi et al. (eds.), *Advances in Greener Energy Technologies*,
Green Energy and Technology, https://doi.org/10.1007/978-981-15-4246-6_38

minimizes the amplitude of vibration of the beam due to the action of step excitation and chirp signal excitation.

Keywords Photovoltaic (PV) · Fuzzification · Stiffness · Scope · Crisp

1 Introduction

Nowadays, due to depleting nature of conventional energy sources, the demand of renewable energy is increasing. The photovoltaic, wind energy, biomass, tidal and geothermal energy sources are the major source of renewable power. Among different renewable sources, the solar energy sources are the major promising technology because of the environmental friendliness behavior [1–7]. However, electrical power using wind energy sources has been considered for this research work, and vibration control system has been discussed for mechanical design.

Active vibration control (AVC) has been used to minimize the undesired vibrations in different systems for many years. The problems of undesired vibration have unfavorable results on equipments; thus, it can be needed to control the vibration. Vibration has two different methods, one is the active vibration, and the other one is passive vibration. Passive vibration control is less effective and has some limits to their effectiveness.

Nowadays, active vibration control is more common, and they have many control methods to minimize the vibration. Active control is based on overlying secondary sound or vibration source on primary sources to obtain a least amount of residual signal. AVC is the currently also commercially used for minimization of vibration in automobiles, helicopters, aircraft structure, satellites, civil (bridges), etc. It offers good comfort with less weight than conventional passive technologies.

1.1 Beam

Beams are most common element of many architectural, civil and mechanical engineering structures. Beams are frequently classified on the basis of supports or reactions. A beam having many types of support by pins, roller or smooth surface at end is called a beam. But here, we use simple beam to control active vibration of control beam, the simple beam is a beam that has pinned support at one end and roller support at other end and also has a load carried at midpoint of the beam. A simply supported beam is largely used in machine as transmission of power, gear train and link which having different loads that can generate vibration. These active vibrations are needed to control for comfort and long life for machine. From these produced vibration, a noise will generate.

1.1.1 Vibration Control of Simple Beam

Active vibration control technique is developed for controlling vibration using smart materials in real time. The vibration control is still a challenging control engineering problem in various sectors like machines, automobile, space and satellites and aircraft structure, bridge, etc., where there is a major problem from undesired vibration. Under such conditions, it is required to apply different control techniques. It has been demanding various methods to control vibration according to wide range of application. The major vibrations effects are like space structure having specific behavior of the structure is desire methods, and it may be required to control it with major expense. Many researchers are establishing new methods to control this area and implementing it in many practical systems. Mostly, active vibration control techniques are applied for smart materials and are attracting intents around the world. The former is usually managed as a dynamic problem and aims to minimize vibration in terms of displacement or noise. Most of the machines and structures are necessary to control the low levels of vibration such as smooth running leads to reduce fatigue and stress and some little noise. Active vibration control (AVC) systems have developed as variable equipment to fill for low-frequency gap.

Moreover, in vibration control application, it is generally held that vibration reduction would intrinsically reduce fatigue damage in structure. Although this may be generally true, there are some examples in which this assumption is no longer valid. This example could be found in conditions where low displacement vibration hides high structure stress, or in applications showing significant spillover problems. Furthermore, even if it is on a particular application vibration control would improve the point of view and probably the control logic that could be further improved to minimize fatigue damage.

1.2 Fuzzy Logic

Fuzzy logic is a method to compute based on “degrees of truth” rather than the usual “true or false” (1 or 0) Boolean logic which is based on the modern computer and many control techniques. It has generalization of the fuzzy sets rule to deal with approximation rather than precise. In difference, with fuzzy sets having fuzzy rules, it is also known as crisp logic [8–11].

The fuzzy logic has fuzzy set made up of many membership values of 0 and 1 only. This fuzzy logic is applied to change from control theory to artificial intelligence for most of the mathematicians, who prefer Bayesian logic. Many researcher engineers develop some control technique, which prefers traditional two values. The fuzzy set theory has membership value range between 0 and 1.

2 Modeling and Analysis

Analytical study of vibration damper is made up of a noncontact electromagnet actuator to minimize the vibration of the beam. A displacement sensor is also used to measure displacement of beam. Magnetic actuators have been extensively used to excite and control the vibration of beam. It has the advantage of applying noncontact actuating force to control and excite structures. The magnetic force turns out to be different from a simple force because of the fact that it also changes the stiffness of the system. A fuzzy logic control technique is applied here to minimize the vibration of the beam. We use two electromagnetic actuators that are applied at above and bottom of the midpoint of the simply supported beams, both having same dimension and function. When the external force (F_e) applied at midpoint of the beam, then it starts to oscillate upward and downward directions, having velocity and displacement. These oscillations of beam create vibration and noise, which need to be minimized for better performance in their applications.

Fuzzy logic controller is used as a controller which having two input, velocity and displacement (x), and has one output as current (i). This current is used to pass through the coils of the electromagnets to generate forces from the electromagnetic actuators, and this actuating forces act on the beam to minimize the amplitude of vibration. During the upward movement of the beam from static equilibrium position, the bottom actuator pulls down the beam. Similarly, when it moves downward, the upper actuating force will be applied on the beam to minimize the vibrational amplitude of it.

In fuzzy logic controller, it has two inputs as current and displacement, which has a range of deflection when load is applied. It has memberships function as small, medium and high. It has fuzzy sets having fuzzy rules (if-then) that are applied to define output current as either high or low current flow to actuators for minimization of active vibration of beam by the actuating force developed in actuators.

2.1 Beam Model

Let us consider an equation of simply supported beam in single degree of freedom (SDOF) model,

$$m\ddot{x} + c\dot{x} + kx = F_e(t) - F_b(t) + F_t(t) \quad (1)$$

$$\ddot{x} + \frac{c}{m}\dot{x} + \frac{k}{m}x = \frac{F_e}{m} - \frac{F_b}{m} + \frac{F_t}{m}$$

$$\begin{bmatrix} 1 & 0 \\ 0 & 1 \end{bmatrix} \begin{Bmatrix} \ddot{X} \\ \dot{X} \end{Bmatrix} + \begin{bmatrix} \frac{c}{m} & \frac{k}{m} \\ -1 & 0 \end{bmatrix} \begin{Bmatrix} \dot{X} \\ X \end{Bmatrix} = \begin{bmatrix} \frac{1}{m} & \frac{1}{m} & \frac{-1}{m} \\ 0 & 0 & 0 \end{bmatrix} \begin{bmatrix} F_e \\ F_t \\ F_b \end{bmatrix}$$

$$\begin{aligned} \begin{Bmatrix} \ddot{X} \\ \dot{X} \\ X \end{Bmatrix} &= - \begin{bmatrix} \frac{c}{m} & \frac{k}{m} \\ -1 & 0 \end{bmatrix} \begin{Bmatrix} \dot{X} \\ X \end{Bmatrix} + \begin{bmatrix} \frac{1}{m} & \frac{1}{m} & \frac{-1}{m} \\ 0 & 0 & 0 \end{bmatrix} \begin{bmatrix} F_e \\ F_t \\ F_b \end{bmatrix} \\ A &= - \begin{bmatrix} \frac{c}{m} & \frac{k}{m} \\ -1 & 0 \end{bmatrix}, \quad B = \begin{bmatrix} \frac{1}{m} & \frac{1}{m} & \frac{-1}{m} \\ 0 & 0 & 0 \end{bmatrix}, \quad C = \begin{bmatrix} 1 & 0 \\ 0 & 1 \end{bmatrix} \text{ and } D = \begin{bmatrix} 0 & 0 & 0 \\ 0 & 0 & 0 \end{bmatrix} \\ Y &= \begin{bmatrix} 1 & 0 \\ 0 & 1 \end{bmatrix} \begin{Bmatrix} \dot{X} \\ X \end{Bmatrix} + \begin{bmatrix} 0 & 0 & 0 \\ 0 & 0 & 0 \end{bmatrix} \begin{bmatrix} F_e \\ F_t \\ F_b \end{bmatrix} \end{aligned}$$

In multi-degrees of freedom model (MDOF), let us consider a simply supported beam having same displacement which contains $\times 1$ vector $\{x\}$ when actuating force is applied $F_e(t)$. If there is mass $[M]$, stiffness $[K]$ and damping matrices $[C]$ of size $n \times n$, then the main equation of motion for the beam is represented as

$$[M]\{\ddot{X}\} + [C]\{\dot{X}\} + [K]\{X\} = F_e(t) + F_t(t) - F_b(t) \tag{2}$$

where

$[f_t]$ is the force which is applied on top electromagnetic actuator,

$[f_b]$ is the force which is applied in bottom actuator.

In state-space notation,

$$\begin{Bmatrix} \ddot{X} \\ \dot{X} \\ X \end{Bmatrix} = - \begin{bmatrix} [M]^{-1}[C] & [M]^{-1}[K] \\ [-1] & [0] \end{bmatrix} \begin{Bmatrix} \dot{X} \\ X \end{Bmatrix} + \begin{bmatrix} [M]^{-1} & [M]^{-1} & [-M]^{-1} \\ 0 & 0 & 0 \end{bmatrix} * \begin{bmatrix} F_e \\ F_t \\ F_b \end{bmatrix}$$

Or,

$$[\dot{X}] = [A]\{X\} + [B]\{U\} \tag{3}$$

2.2 Analysis

Figure 1 shows the working principle of the double electromagnetic actuators to control the vibration of the simple beam. The beam has pinned support at one end, and the other end has roller support which has external disturbance load at midpoint of the beam. It is known that the external force exerted on the beam by a single actuator is directly proportional to the square of the direct current (i) and inversely proportional to the square of the gap between the actuator and the beam. If the force exerted on the beam is denoted as F , then.

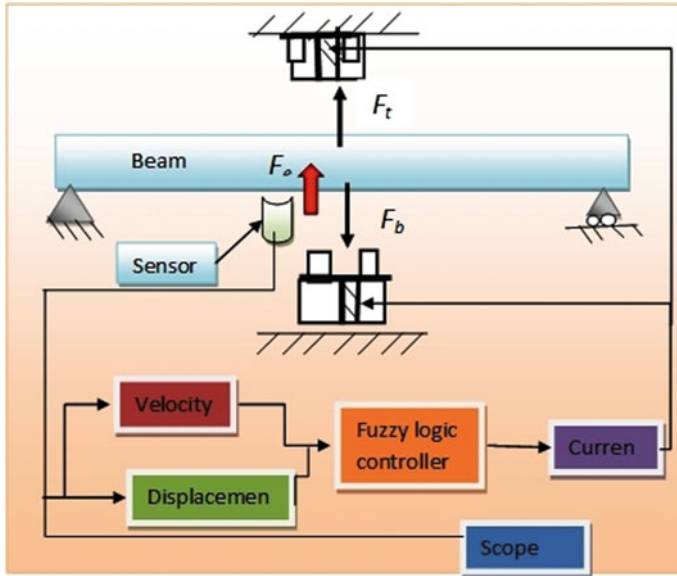


Fig.1 Schematic diagram showing the arrangement of the beam with actuator and sensor

$$F = K \frac{i^2}{(x_0 - x)^2} \tag{4}$$

where i is the current of coil of magnetic actuator, x_0 is the initial gaps between the beam and the actuator and x is the displacement of the beam after applying force. And the constant,

$$K = \frac{\mu_0 n^2 A_m}{4} \tag{5}$$

where μ_0 is the permeability of free space = $4\pi \times 10^{-7}$ N/A², n is the number of turns in the coil of electromagnet and A_m is the cross-sectional area of the electromagnet.

3 Modeling of Fuzzy Logic Controller

Fuzzy logic is a similar impression to human beings’ feeling and reasoning process. The elementary idea behind fuzzy logic control exists to cooperate the “expert experience” of a human operation in the design of a fuzzy controller in controlling a process whose input–output relationship is well-defined by a collection of fuzzy control rules (if–then rules) including linguistic variables.

Fuzzy logic controller has four parts:

Fuzzification: It means to transform input into proper linguistic value, so that it can be equated to the rule in rule base system of fuzzy logic. It includes the transformation of the input/output signals into a number of fuzzy-represented values (fuzzy sets).

Rule base: It contains the knowledge in form of a set of rule to control the artificial system. It is the collection of rules. The basic main function of rule base is to provide the desired information to fuzzification module, the rule base module and the defuzzification module. ‘If’ part is called antecedent, and ‘then’ part is called consequent.

Inference engine: If control rules are relevant, then it decides the input to the plant. The inference mechanism provides the mechanism for invoking or referring to the rule base such that the appropriate rules are fired on the simulation presented in Fig. 2.

Defuzzification: It converts fuzzy output to crisp output. Here, centroid method is used for defuzzification. Defuzzification interprets membership’s degree in the fuzzy sets into a specific action or real value.

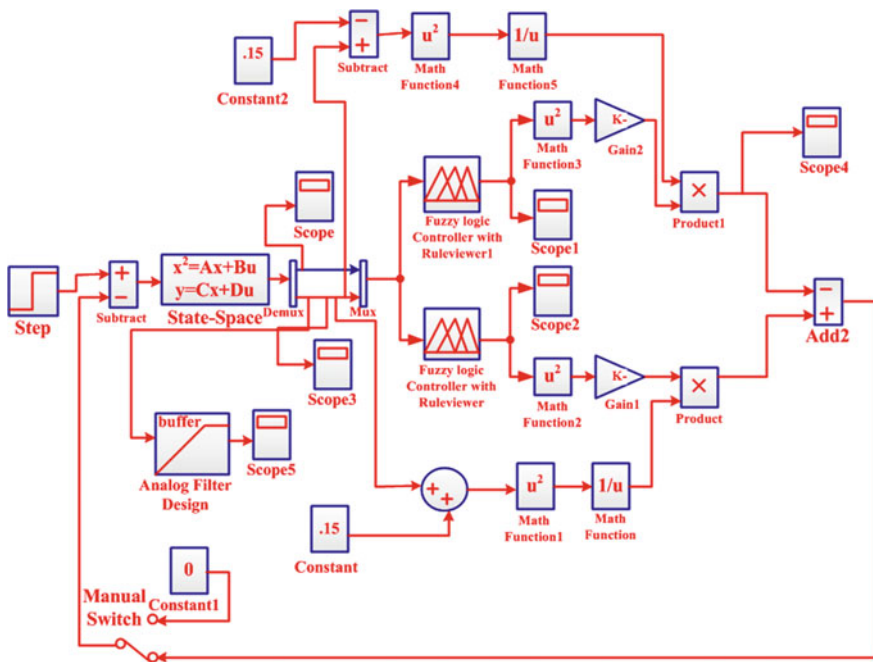


Fig. 2 Simulink model

4 MATLAB Simulink Model

For the analytical study of the active vibration control system, a Simulink model has been made with double electromagnetic actuators to minimize the vibration in MATLAB simulation. The block diagram of Simulink model is shown in Fig. 2. The state-space block contains A, B, C, D matrices of the beam. The input of the state-space block is velocity and displacement of the mid-span of the beam. These parameters are the input parameters of fuzzy logic block. Based on these parameters, D.C. current will be passed through the coil of the electromagnet which will be responsible to produce electromagnetic force. Finally, the displacement of the beam is observed in Scope3.

4.1 Fuzzy Rules

There are two electromagnetic actuators which are used, and they have different rules as follows which are presented with results in Figs. 3 and 4.

4.1.1 Rules for Top Actuator

If velocity is negative and displacement is positive, then current is zero to make the beam closer to reference position.

If velocity is zero and displacement is positive, then current is also zero to make the beam closer to reference position.

If velocity is PS and displacement is positive, then current is zero to make the beam closer to reference position.

If velocity is NM and displacement is positive, then current is zero to make the beam closer to reference position.

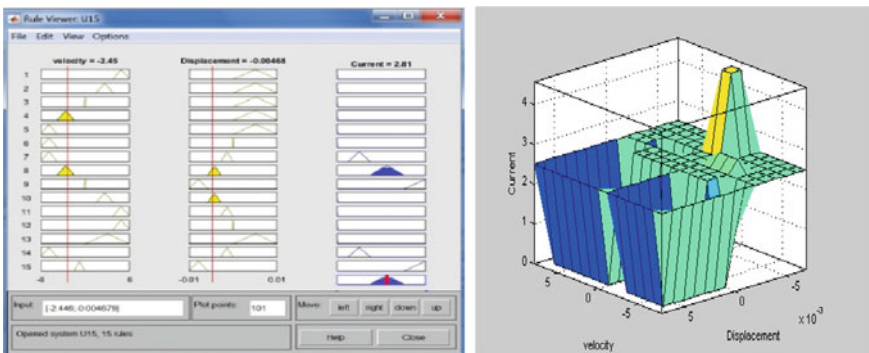


Fig.3 Ruler viewer and surface viewer of top actuator of fuzzy logic controller

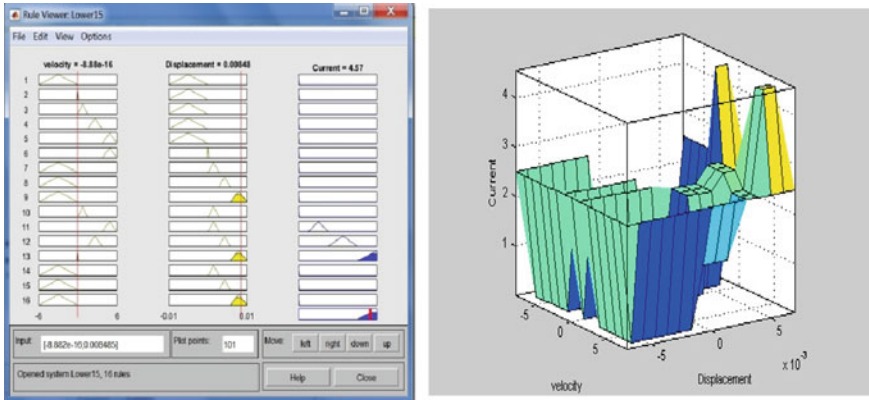


Fig.4 Ruler viewer and surface viewer of bottom actuator of fuzzy logic controller

If velocity is NB and displacement is positive, then current is zero to make the beam closer to reference position.

If velocity is NB and displacement is zero, then current is zero to make the beam closer to reference position.

If velocity is NB and displacement is NS, then current is PS to make the beam closer to reference position.

If velocity is NM and displacement is NM, then current is PM to make the beam closer to reference position.

If velocity is zero and displacement is NB, then current is PB to make the beam closer to reference position.

If velocity is PM and displacement is NM, then current is zero to make the beam closer to reference position.

If velocity is PB and displacement is NS, then current is zero to make the beam closer to reference position.

If velocity is PB and displacement is zero, then current is zero to make the beam closer to reference position.

If the velocity is anyone and displacement is positive, then current is zero to make the beam closer to reference position.

4.1.2 Rules for Bottom Actuator

If the velocity is negative and displacement is negative, then current is zero to make the beam closer to the reference positions.

If the velocity is zero and displacement is negative, then current is zero to make the beam closer to the reference positions.

If the velocity is PS and displacement is negative, then current is zero to make the beam closer to the reference positions.

If the velocity is PM and displacement is negative, then current is zero to make the beam closer to the reference positions.

If the velocity is PB and displacement is negative, then current is zero to make the beam closer to the reference positions.

If the velocity is PB and displacement is zero, then current is zero to make the beam closer to the reference positions.

If the velocity is negative and displacement is PS, then current is zero to make the beam closer to the reference positions.

If the velocity is negative and displacement is PM, then current is zero to make the beam closer to the reference positions.

If the velocity is negative and displacement is PB, then current is zero to make the beam closer to the reference positions.

If the velocity is PS and displacement is PS, then current is zero to make the beam closer to the reference positions.

If the velocity is PB and displacement is PS, then current is PS to make the beam closer to the reference positions.

If the velocity is PM and displacement is PM, then current is PM to make the beam closer to the reference positions.

If the velocity is zero and displacement is PB, then current is PB to make the beam closer to the reference positions.

If the velocity is negative and displacement is PS, then current is zero to make the beam closer to the reference positions.

If the velocity is negative and displacement is PM, then current is zero to make the beam closer to the reference positions.

If the velocity is negative and displacement is PB, then current is zero to make the beam closer to the reference positions.

5 Results and Conclusion

5.1 Numerical Study

A simply supported beam of following parameter is considered as a model to minimize the vibration using twin electromagnetic actuators (Table 1).

Initially, the beam is disturbed by a chirp signal having magnitude 195 to 250 Hz. The first natural frequency of beam is found to be 200 Hz. Therefore, we observe the peak at the resonance of the beam, and the frequency of the chirp signal is said from 195 to 250 Hz. The beam's controlled and uncontrolled responses of the mid-span of the beam are shown in Figs. 5 and 6.

It is seen from Fig. 6 that the twin actuators successfully control the vibration of simply supported beam, and then the beam is excited by an impulse load of 500 N. The step time is set at 0.1 s and shows the response due to controlled and uncontrolled conditions. Figure 6 indicates the controlled and uncontrolled responses of the beam.

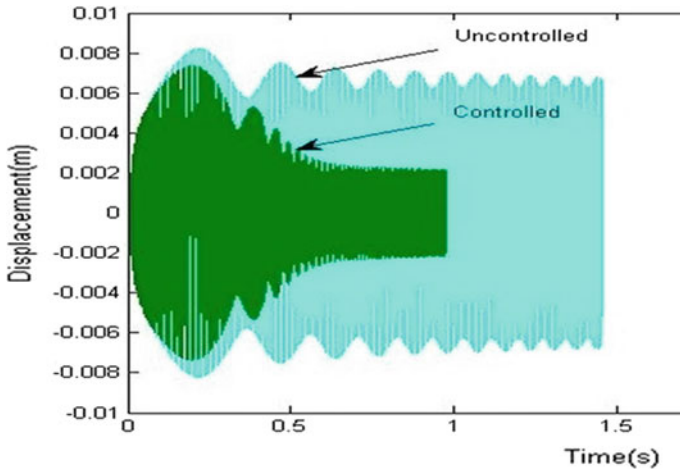


Fig.5 Uncontrolled and controlled responses of the midpoint of the beam under the action of chirp signal excitation

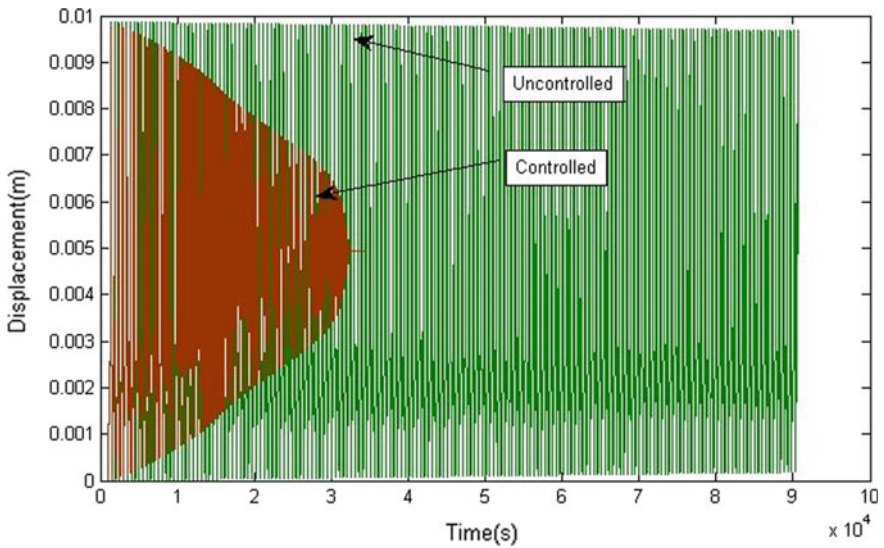


Fig.6 Controlled and uncontrolled responses of the beam under the step excitation

It is clearly observed that in case of uncontrolled of the beam due to the presence of internal materials damping considered, the displacement decreases very slowly, whereas in case of controlled response, the displacement quickly reduces.

Therefore, from these above-mentioned data, it can be concluded that the proposed twin actuator fuzzy logic control system can be able to minimize vibration due to the different types of external loading.

Table 1 Parameters of beam

S no.	Parameter	Dimensions
1	Beam length (L)	20 cm
2	Cross-sectional area (A)	$1.5 \times 0.5 \text{ cm}^2$
3	Young's modulus (E)	$200 \times 10^9 \text{ N/m}^2$
4	Density (ρ)	7850 kg/m^3
5	No. of turns of wire on the electromagnet (n)	100 turns
6	Cross-sectional area of the core (A_m)	2 cm^2

6 Conclusion

In this paper, an active vibration control system has been proposed to minimize the amplitude of vibration of a simply supported beam. This system has two electromagnetic actuators that are placed at top and bottom of the beam to minimize of the vibration. A fuzzy logic control system is adopted to decide, whether top or bottom actuator is switched on. Based on the displacement and velocity of the beam, current is passed through the coil of the electromagnets and damping force is applied against the direction of the motion of the beam. It has been shown that in this thesis, the proposed active vibration control system successfully controls the vibration of the beam. This active vibration control system can be applied to minimize the vibration of other structures like different types of beam or rotor structure.

References

1. Priyadarshi N, Padmanaban S, Marcoti PK, Sharma A (2018) An extensive practical investigation of FPSO-Based MPPT for grid integrated PV system under variable operating conditions with anti-islanding protection. *IEEE Syst J* 1–11
2. Priyadarshi N, Padmanaban S, Bhaskar MS, Blaabjerg F, Sharma A (2018) A Fuzzy SVPWM based inverter control realization of grid integrated PV-wind system with FPSO MPPT algorithm for a grid-connected PV/Wind power generation system: hardware implementation. *IET Electric Power Appl* 1–12
3. Priyadarshi N, Anand A, Sharma AK, Azam F, Singh VK, Sinha RK (2017) An experimental implementation and testing of GA based maximum power point tracking for PV system under varying ambient conditions using dSPACE DS 1104 controller. *Int J Renew Energy Res* 7(1):255–265
4. Priyadarshi N, Kumar V, Yadav K, Vardia M (2017) An experimental study on Zeta buck-boost converter for application in PV system. In: *Handbook of distributed generation*, Springer. https://doi.org/10.1007/978-3-319-51343-0_13
5. Priyadarshi N, Sharma AK, Priyam S (2018) An experimental realization of grid-connected PV system with MPPT using dSPACE DS 1104 control board. In: *Advances in smart grid and renewable energy. Lecture notes in electrical engineering*, vol 435, Springer, Singapore
6. Priyadarshi N, Sharma AK, Azam F (2017) A hybrid firefly-asymmetrical fuzzy logic controller based MPPT for PV-wind-fuel grid integration. *Int J Renew Energy Res* 7(4)

7. Priyadarshi N, Sharma AK, Priyam S (2017) Practical realization of an improved photovoltaic grid integration with MPPT. *Int J Renew Energy Res* 7(4)
8. Priyadarshi N, Sharma AK, Bhoi AK, Ahmad SN, Azam A, Priyam S (2018) MATLAB/Simulink based Fault Analysis of PV Grid with Intelligent Fuzzy Logic Control MPPT. *Int J Eng Tech* 7:198–204
9. Priyadarshi N, Sharma AK, Bhoi AK, Ahmad SN, Azam A, Priyam S (2018) A practical performance verification of AFLC based MPPT for standalone PV power system under varying weather condition. *Int J Eng Tech* 7:243–338
10. Priyadarshi N, Padmanaban S, Mihet-Popa L, Blaabjerg F, Azam F (2018) Maximum power point tracking for brushless DC motor-driven photovoltaic pumping systems using a hybrid ANFIS-FLOWER pollination optimization algorithm. *MDPI Energies* 11(1):1–16
11. Priyadarshi N, Azam F, Bhoi AK, Alam S (2019) An artificial fuzzy logic intelligent controller based MPPT for PV grid utility. *Lecture notes in networks and systems*, vol 46. https://doi.org/10.1007/978-981-13-1217-5_88

Experimental Investigation and Fuzzy-Based Modeling of Micro-EDM Process Parameters



I. Shivakoti, G. Kibria, B. B. Pradhan, and A. Sharma

Abstract Micro-EDM process has become a potentially important advanced machining process for producing accurate and complex three-dimensional structural micro-features. The present paper investigates the influence of mixing of NaNO_3 salt in oxy-based de-ionized water fluid on micro-EDM performance. The D3 die steel work material was selected for hole drilling. The L9 Taguchi design was implemented for experimental design considering micro-EDM variables. Peak current, pulse-on-time and salt (NaNO_3) concentration were taken into consideration as process variables. For achieving the accurate micro-hole during micro-EDM process, the responses were selected as tool wear rate, material erosion rate, hole overcut and through-hole taper. Regression models are developed based on experimental results of responses. Further, fuzzy-based models are developed using MATLAB logic toolbox. The comparative analysis of experimental, fuzzy predicted and regression predicted was done using comparative plots. Comparative results confirm that fuzzy-based model (prediction error = 1.98%) provides better results than the regression model (prediction error = 4.87%) developed.

Keywords Micro-EDM · Fuzzy logic · D3 die steel · Dielectric fluid · De-ionized water · Taguchi method

I. Shivakoti (✉) · B. B. Pradhan · A. Sharma
Mechanical Engineering Department, Sikkim Manipal Institute of Technology (SMIT), Sikkim
Manipal University, Gangtok, Sikkim, India
e-mail: ishwar.siwa@gmail.com

B. B. Pradhan
e-mail: bbpradhan1@rediffmail.com

A. Sharma
e-mail: ashz_1974@yahoo.com

G. Kibria
Department of Mechanical Engineering, Aliah University, Kolkata 700160, India
e-mail: prince_me16@rediffmail.com

1 Introduction

From the last quarter of the previous century, miniaturization has been a major issue, and at the end of the last decade, the research into various micro-machining processes got the momentum to unfold a new era of manufacturing due to several industrial applications. The miniaturization poses unique demands and challenges to manufacturing engineers for continuous improvements in micro-manufacturing technologies which can process difficult-to-machine materials and alloys [1]. In the literature, several research issues on micro-machining technologies have been reported ranging from mechanical micro-machining techniques to non-conventional micro-machining technologies and precision finishing processes [2]. Among several micro-machining processes, micro-EDM has the capability of manufacturing micro-sized feature in hard and electrically conductive materials. Basically, micro-EDM is a thermal-erosive micro-machining technique, and due to non-contact-type material removal process, the machining process does not offer any chatter or vibration to the machine element. In addition, very hard materials like nickel alloys, titanium alloys, etc., can be machined with ease. In this process, discrete electrical discharges are made to generate between two electrodes within inter-electrode gap, and due to generation of plasma channel in the discharge zone, material from workpiece is melted and vaporized. The tiny debris is removed by collapsing the plasma channel and flushing jet of dielectrics [3].

The nature of dielectric fluid plays important role in micro-EDM while machining operation as various dielectrics possesses various chemical composition, cooling rate, dielectric strengths and viscosity. Therefore, the process responses are abundantly affected by properties of dielectric used. Kerosene is commonly used dielectric medium in conventional EDM process. However, use of kerosene creates several environment and machining issues such as (a) degradation of dielectric molecules, (b) generation of CO and CH₄ vapors which pollutes the machining environment and (c) carbon particles gets adhere onto the work material, etc. [4–6]. These cause unstable discharge between micro-tool and workpiece and ultimately result low machining efficiency. Therefore, it is urgently required to search alternate dielectric fluid, which may overcome the problems created by the hydrocarbon-based dielectric fluid. De-ionized water is an alternative dielectric in micro-EDM instead of kerosene. In comparison with hydrocarbon-type dielectrics, de-ionized water provides better and safe machining in terms of environment as well as machining efficiency. Further, de-ionized water possesses enhanced cooling and flushing properties, which enhances the material removal efficiency [7]. Several researchers have conducted experimental research and analysis of the effect of de-ionized water during micro-EDM to explore the impact of dielectric fluid on micro-EDM performance [3, 8–19]. From these literatures, it is revealed that the use of de-ionized water has significant effect on the micro-EDM performances. Furthermore, the dielectric strength of the dielectric fluid has significant contributions in discharge stability and machining efficiency. The literature review revealed that there exists an extensive significance of various dielectrics

as well as mixing of additives in dielectrics on micro-EDM process during micro-machining of difficult-to-cut alloys and superalloys. Furthermore, mixing of various types of minerals may have significant effect on performance criteria. Mixing of ions in dielectric fluid results in increase of electrical conductivity of the inter-electrode gap, and breakdown may occur at lower value of discharge voltage setting. This phenomenon can cause narrow discharge or plasma channel at the spark gap. Moreover, the mixing of salt at various concentrations can cause precipitate of reactive products on the micro-tool and further can reduce the amount of tool wear during micro-hole machining. Considering those gaps and requirement of alternate dielectric other than hydrocarbon-based fluid, a well-structured process methodology has been formulated to understand the significance of NaNO_3 salt-mixed de-ionized water during machining. To explore the effect of mixing of NaNO_3 salt in de-ionized water on micro-EDM performance, in the present research work, micro-EDM process of D3 die steel has been conducted utilizing NaNO_3 salt-mixed de-ionized water. Furthermore, fuzzy-based modeling has been conducted on the basis of experimental data achieved. Lotfi A. Zadeh has introduced the term “fuzzy logic” and fuzzy set theory in 1965 [20]. It provides an efficient way of dealing with the vague and uncertain information. The manufacturing processes were greatly improved by integrating fuzzy with gray relational analysis [21, 22]. In this paper, Taguchi-based design has been employed for experiments. The mathematical modeling has been done for each process responses. Further, fuzzy logic-based models are developed. Moreover, regression models have been developed, and the fuzzy-predicted, regression-predicted and experimental data has been compared using various plots of micro-EDM performance measures.

2 Materials and Methods

2.1 Experimental Planning

A traditional die-sinking EDM machine (ZNC spark erosion machine, model: ZNC-S-50, manufactured by Sparkonix India Pvt. Ltd., Pune, India) was used to perform the experiments. The EDM system conventionally uses kerosene as dielectric fluid for electrical discharge machining operation. To facilitate the micro-hole machining using NaNO_3 salt-mixed de-ionized water dielectric, a different dielectric circulating system was developed, so that it does not affect the existing EDM machine. The dielectric supply and circulating system consists of pump, pressure-regulating valve, pressure gauge, dielectric reservoir and dielectric supply and exit pipes. In this experimentation, the cylindrical shape through micro-holes was machined on D3 die steel plates (dimension of 20 mm \times 15 mm \times 1 mm). Solid cylindrical copper rod of diameter 300 μm and length of 20 mm were used as micro-tool during machining. The experiment was conducted at various concentrations of NaNO_3 salt mixed in de-ionized water. In the present set of experiments, pulse-on-time, peak current and salt concentration are considered as process variables. The values and range of these

Table 1 Micro-EDM process parameters with levels for experimentation

Micro-EDM parameters	Unit	Levels		
		L1	L2	L3
Peak current	A	0.5	1.0	1.5
Pulse-on-time	μs	8	12	16
Salt concentration	g/l	1	4	8

three process parameters were taken considering the past literature review of micro-EDM research. Taguchi-based L9 experimental planning was done for conducting an experiment. Table 1 depicts the micro-EDM parameters and their levels. At each process parametric combination, the average of three experimental runs was considered for further analysis. Tool wear rate (TWR), overcut (OC), material removal rate (MRR) and micro-hole taper were taken as response criteria. The material removed per unit machining time is termed as material removal rate. Similarly, tool wear rate also calculated considering material removed from tool electrode. These two responses were calculated after measuring the tool and workpiece weights by high precision balance (make—Mettler Toledo, Switzerland).

The overcut is the measure of diameter difference of hole generated and electrode tip. The amount of overcut for the micro-holes generated was measured using precision optical measuring microscope of resolution 0.1 μm (STM7, made by Olympus, Japan). Equation 1 was followed for calculating the micro-hole taper. The properties of D3 die steel are given in Table 2. The parametric settings for the Taguchi experiments are given in Table 3. The micro-hole machining that has been performed at various parametric combinations is given in Table 4 as designed by Taguchi experimental design.

$$\text{Taper} = \frac{\text{Entry hole dia.}(D_{\text{EN}}) - \text{Exit hole dia.}(D_{\text{EX}})}{2 \times \text{Thickness}(t)} \tag{1}$$

Table 2 Mechanical and physical properties of work material (D3 die steel)

Property	Value
Specific heat (Cal/g °C)	0.110
Elastic modulus (GPa)	190
Tensile strength (MPa)	640
Density (g/cm ³)	7.86
Rockwell hardness C	58–64
Thermal conductivity (W/m-K)	7.2

Table 3 Parametric setting for the present experimentation

Condition	Description
Workpiece material	D3 die steel plate, positive terminal, dimension: 20 mm × 15 mm × 1 mm
Tool material	Copper, 300 μm diameter, solid
Dielectric fluid	De-ionized water
Additive in dielectric	NaNO ₃ salt
Duty ratio	95%
Flushing pressure	0.5 kgf/cm ²
Resistivity of dielectric	4.2 MΩ-cm

Table 4 L9 Taguchi design showing process parametric combinations and corresponding experimental results of responses [24]

Exp. No.	Input factor			Responses			
	Peak current (A)	Pulse-on-time (μs)	Salt concentration (g/l)	Material removal rate (MRR) (mg/min)	Tool wear rate (TWR) (mg/min)	Overcut (OC) (mm)	Taper
1	0.5	8	1	0.003625	0.002856	0.067543	0.03895
2	0.5	12	4	0.004814	0.001837	0.079255	0.04059
3	0.5	16	8	0.004157	0.002000	0.083751	0.05130
4	1	8	4	0.006632	0.002874	0.068327	0.05630
5	1	12	8	0.005901	0.002311	0.056521	0.06102
6	1	16	1	0.004524	0.002434	0.066410	0.06475
7	1.5	8	8	0.005334	0.002487	0.072310	0.05955
8	1.5	12	1	0.006586	0.003331	0.069640	0.06314
9	1.5	16	4	0.007135	0.002046	0.053125	0.06571

2.2 Taguchi Methodology

The experiment was designed based on Taguchi L9 DoE. The L9 orthogonal array with actual values of different levels of process variables is given in Table 4. As material removal rate is a response of “larger-the-better” type, therefore, the *S/N* ratios are evaluated as per Eq. 2. However, tool wear rate, overcut and taper are “smaller-the-better” type, and the *S/N* ratios of these responses are evaluated as per Eq. 3.

$$\text{Larger is better: } S/N \text{ ratio} = \eta = -10 \log_{10} \left[\frac{1}{n} \sum_{i=1}^n \frac{1}{y_i^2} \right] \tag{2}$$

$$\text{Smaller is better: } S/N \text{ ratio} = \eta = -10 \log_{10} \left[\frac{1}{n} \sum_{i=1}^n y_i^2 \right] \tag{3}$$

2.3 Fuzzy Logics

Employing MATLAB software, fuzzy logic has been introduced for selection of output responses utilizing three basic steps fuzzification, fuzzy inference and defuzzification. In fuzzification, for each input and the output parameters of the micro-EDM process, membership functions are assigned. After fuzzification, fuzzy rule base is formed. Let, the input variables are X_1, X_2 and X_3 . These three variables are linked with process parameters as described in Table 1. Let, the output variables are Y_1, Y_2, Y_3 and Y_4 . These four variables are linked with output responses as described in Table 4. Figure 1 represents the schematic view of fuzzy logic used for the present experimentation for the input–output variables of micro-EDM process.

The input variables were divided into low, medium and high levels. The output variables are divided into nine levels—VVS, VS, S, ML, M, MH, H, VH and VVH. The membership functions were accordingly assigned to each of the inputs and outputs equal to the number of levels they have.

The membership functions for each of the process parameters are shown below in Figs. 2, 3 and 4, respectively. The membership functions of the responses are shown in Figs. 5, 6, 7 and 8, respectively.

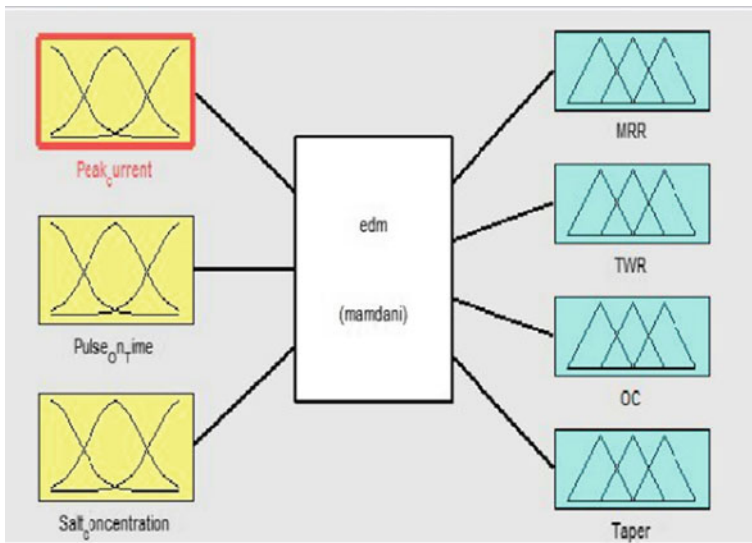


Fig. 1 Input–output relationship based on implemented fuzzy logics

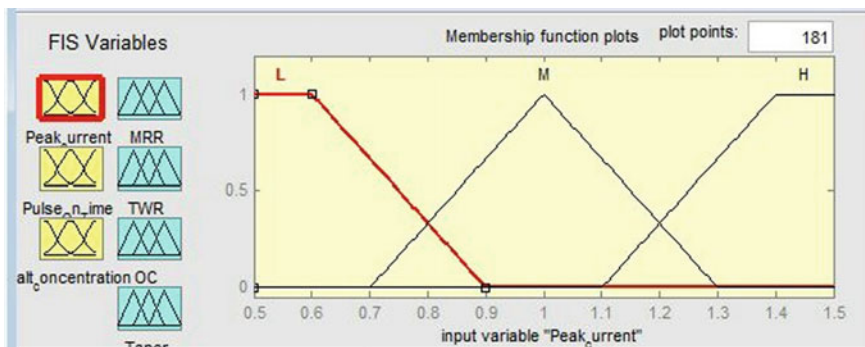


Fig. 2 Relationship function plot for peak current

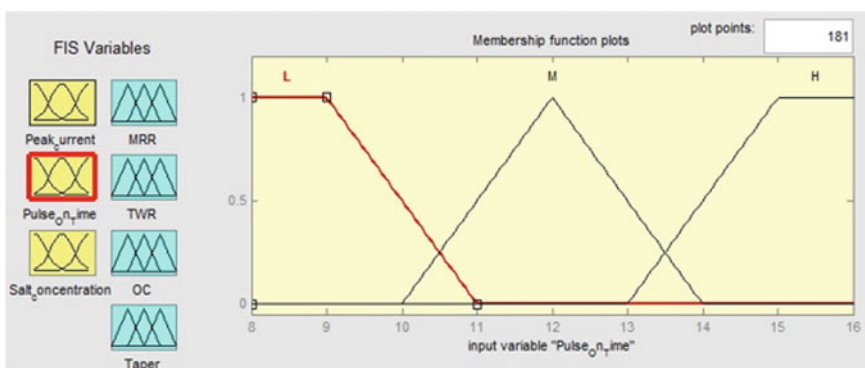


Fig. 3 Relationship function plot for pulse-on-time

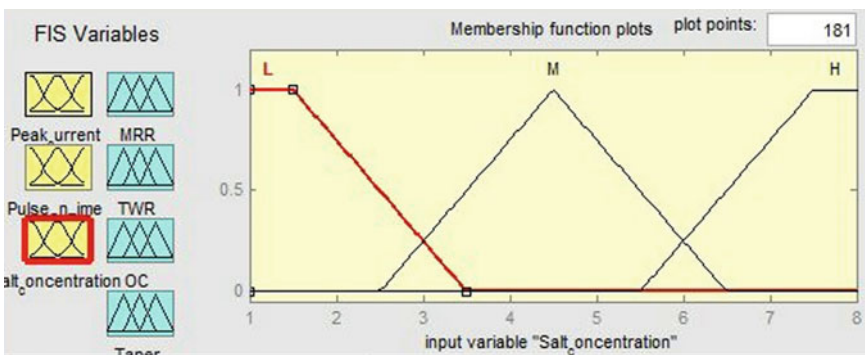


Fig. 4 Relationship function plot for salt concentration

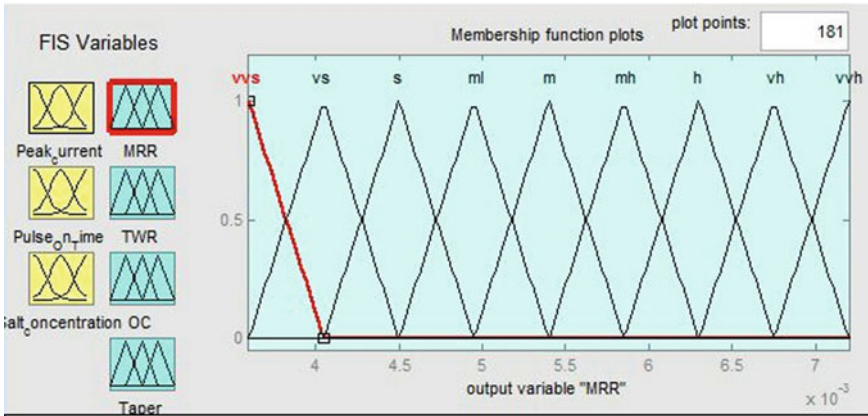


Fig. 5 Relationship function plot for material removal rate (MRR)

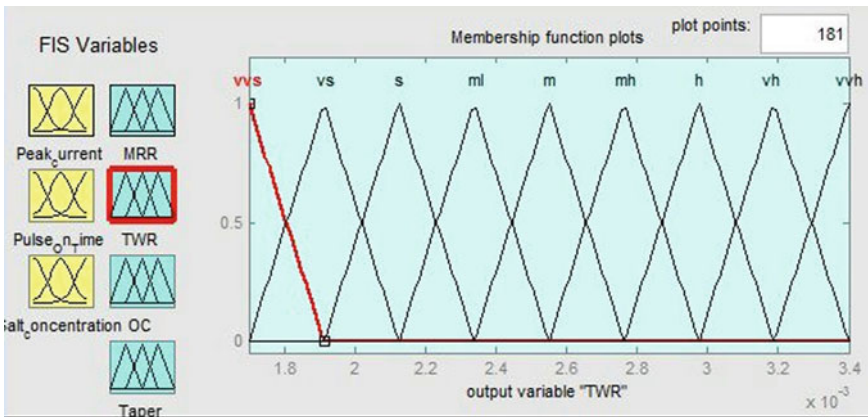


Fig. 6 Relationship function plot for tool wear rate (TWR)

The control rule which plays in fuzzy is “if-then.” The variables which are included in fuzzy are X_1, X_2, X_3 as input and several output $Y (Y_1, Y_2, Y_3 \text{ and } Y_4)$ [22, 23]. In Rule 1, if we consider X_1 to be A_1, X_2 to be B_1 and X_3 to be C_1 , then Y is D_1 , otherwise, Rule 2 will be followed. Rule 2 states that if X_1 to be A_2, X_2 to be B_2 and X_3 to be C_2 , then Y is D_2 . These rules will be continued until Rule n comes. Rule n states that if X_1 to be A_n, X_2 to be B_n and X_n to be C_n , then Y is D_n . Here, $A_i, B_i, C_i, D_i, E_i, F_i$ and G_i are the fuzzy subsets. A, B, C are the fuzzy sets of the micro-EDM process parameters, i.e., peak current, pulse-on-time and salt concentration, respectively. And D, E, F and G are the fuzzy sets of response criteria as mentioned in Table 4. Now, the rules are evaluated and the results so obtained are analyzed. This process is called fuzzy inference. The output is obtained as fuzzy variables. Conversion of fuzzy variables to absolute value is defuzzification.

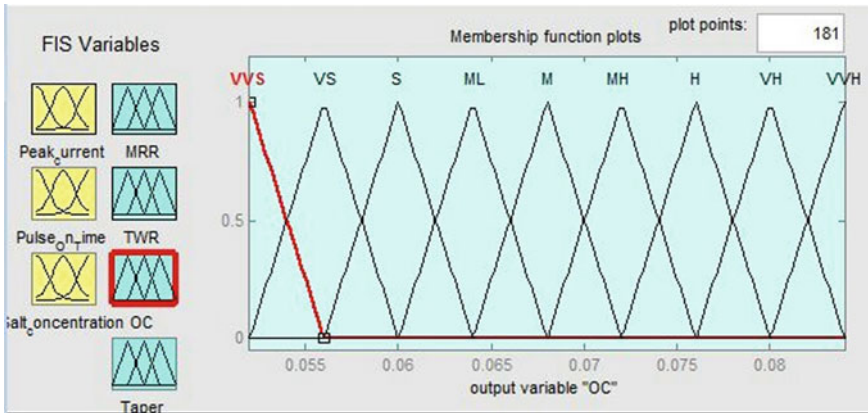


Fig. 7 Relationship function plot for overcut (OC)

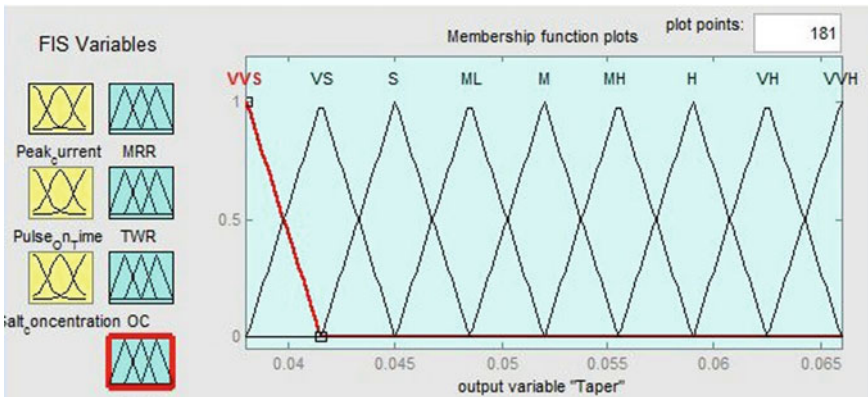


Fig. 8 Relationship function plot for taper

3 Results and Discussion

3.1 Analysis Based on Taguchi Experimentation

From Table 4, the experimental data were analyzed by MINITAB™ statistical software. The detailed analysis of the three micro-EDM parameters, namely pulse-on-time, peak current and salt concentration, on the four responses has been done. The statistical regression technique is used to establish relationships between the considered process parameters and response criteria. The regression equations shown in Eqs. 4–7 have been formulated based on the experimental data achieved in Taguchi-based experimentation.

$$\begin{aligned} \text{MRR}(y) = & 0.00752 - 0.00459 \times x_1 - 0.000755 \times x_2 + 0.00236 \times x_3 \\ & + 0.000864 \times x_1x_2 - 0.000082 \times x_2x_3 - 0.00111 \times x_1x_3 \end{aligned} \quad (4)$$

$$\begin{aligned} \text{TWR}(y) = & 0.00253 + 0.00252 \times x_1 - 0.000045 \times x_2 - 0.000272 \times x_3 \\ & - 0.000127 \times x_1x_2 + 0.000019 \times x_2x_3 - 0.000075 \times x_1x_3 \end{aligned} \quad (5)$$

$$\begin{aligned} \text{OC}(y) = & 0.0132 + 0.0818 \times x_1 + 0.00635 \times x_2 - 0.0080 \times x_3 \\ & - 0.00788 \times x_1x_2 + 0.000385 \times x_2x_3 + 0.00152 \times x_1x_3 \end{aligned} \quad (6)$$

$$\begin{aligned} \text{Taper}(y) = & 0.0156 + 0.0138 \times x_1 + 0.00107 \times x_2 + 0.0070 \times x_3 \\ & + 0.00093 \times x_1x_2 - 0.000331 \times x_2x_3 - 0.00244 \times x_1x_3 \end{aligned} \quad (7)$$

Here, x_1 , x_2 and x_3 correspond to peak current, pulse-on-time and salt concentration, respectively, and $0.5 \leq x_1 \leq 1.5$ (A), $8 \leq x_2 \leq 16$ (μs) and $1 \leq x_3 \leq 8$ (g/l). The above-mentioned regression equations have been used to predict the values of response criteria at all the parametric combinations as per Taguchi L9 design of experiments. Table 5 shows the predicted results of responses using regression Eqs. 4, 5, 6 and 7, respectively.

Table 5 Regression-predicted results of responses and corresponding calculated prediction errors

Exp. No.	Predicted results from regression				Error of prediction (%)			
	MRR (mg/min)	TWR (mg/min)	OC (mm)	Taper	MRR	TWR	OC	Taper
1	0.00379	0.00276	0.0692	0.0379	4.54	3.2	2.4	2.66
2	0.00463	0.00216	0.0725	0.0481	3.83	17.6	8.4	18.6
3	0.00400	0.00201	0.0840	0.0509	3.75	0.44	0.3	0.71
4	0.00617	0.00289	0.0691	0.0530	6.85	0.68	1.2	5.77
5	0.00636	0.00203	0.0617	0.0581	7.87	11.9	9.2	4.79
6	0.00461	0.00225	0.0702	0.0606	1.93	7.30	5.7	6.32
7	0.00527	0.00256	0.0710	0.0615	1.10	3.10	1.7	3.36
8	0.00683	0.00332	0.0691	0.0652	3.82	0.10	0.6	3.33
9	0.00682	0.00222	0.0501	0.0679	4.37	8.40	5.6	3.35
	Average prediction errors				4.20	5.90	3.9	5.43
	Total average prediction error				4.87			

3.2 Fuzzy-Based Modeling

Fuzzy logic-based models are developed to establish relationships between the micro-EDM parameters considered and output performance criteria. The fuzzy-predicted data is compared with both the experimental and the regression-predicted results at all the parametric combinations of L9 experimentation. The fuzzy-predicted data is given in Table 6. Utilizing comparative plots as shown in Figs. 9, 10, 11, and 12, the fuzzy- and regression-predicted results have been compared with the experimentally obtained results. From these plots, it is observed that the fuzzy- and regression-predicted results values are in close range in comparison with the experimental results.

It is also observed that fuzzy provides better results as well as better prediction as compared to regression. The prediction errors calculated based on regression are 4.20, 5.90, 3.9 and 5.43%, respectively, for MRR, TWR, OC and taper. However, the prediction errors calculated based on fuzzy-based model are as 1.85, 3.29, 1.58 and 1.20%, respectively. In the current fuzzy-based model, it is calculated that the overall prediction error (1.98%) of responses is much less than the overall prediction error (4.87%). Therefore, it is confirmed that fuzzy-based model predicts better results than regression model during micro-EDM of D3 die steel in the considered range of process parameters.

Table 6 Fuzzy-predicted results of responses and corresponding calculated prediction errors

Exp. No.	Predicted results from fuzzy				Error of prediction (%)			
	MRR (mg/min)	TWR (mg/min)	OC (mm)	Taper	MRR	TWR	OC	Taper
1	0.00374	0.00276	0.0680	0.0391	3.17	3.36	0.67	0.03
2	0.00495	0.00177	0.0800	0.0415	2.80	3.59	0.94	2.23
3	0.00405	0.00191	0.0800	0.0520	2.57	4.54	4.47	1.36
4	0.00675	0.00276	0.0680	0.0555	1.78	2.96	0.48	1.42
5	0.00585	0.00234	0.0560	0.0625	0.86	1.25	0.92	2.40
6	0.00450	0.00255	0.0640	0.0649	0.55	4.72	3.62	0.22
7	0.00540	0.00255	0.0720	0.0590	1.23	2.53	0.43	0.92
8	0.00675	0.00333	0.0680	0.0625	2.49	0.03	2.35	1.02
9	0.00705	0.00191	0.0533	0.0649	1.19	6.69	0.33	1.23
Average prediction errors					1.85	3.29	1.58	1.20
Total average prediction error					1.98			

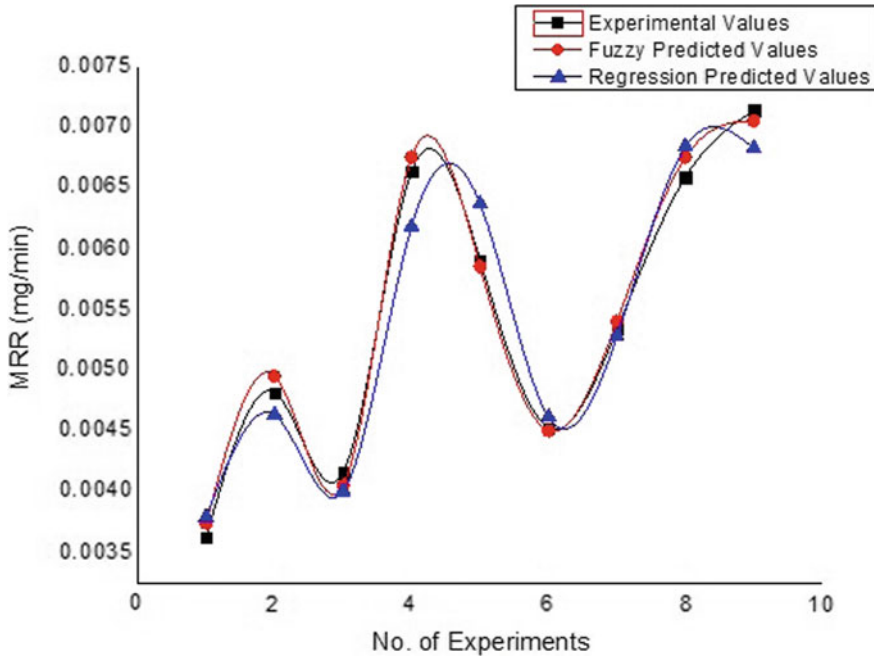


Fig. 9 Assessment plot of experimental, fuzzy-predicted and regression-predicted results for MRR

3.3 Experimentation Based on Significant Parameters

From the Taguchi-methodology-based experimentation and statistical analysis (ANOVA), it is revealed that peak current is the most effective variable on material removal rate and micro-hole taper. However, pulse-on-time is the dominant micro-EDM parameter for variation of tool wear rate and taper. Salt concentration is the significant parameter on MRR and OC. Figure 13 shows the percentage of contributions of the considered process parameters on the process criteria. Based on this, further experimentation is conducted by varying these significant process parameters. Figure 14a, b shows the variation of material removal rate and micro-hole taper while varying peak current parameter. The plots depict that with increase of peak current value, material removal rate and taper both are increased, and these trends are very obvious from the literature study. Figure 15a, b shows the variation of tool wear rate and micro-hole taper while with pulse-on-time. Tool wear rate decreases substantially with increase of pulse-on-time, whereas variation in micro-hole taper shows irregular trend in Fig. 15b. Figure 16 shows the variation of material removal rate and overcut with salt concentration. Figure 17 shows the microscopic view of entry side micro-hole machined at two parametric combinations of peak current, pulse-on-time and salt concentration of (a) 1 A/8 μ s/4 g/l and (b) 1.5 A/12 μ s/1 g/l.

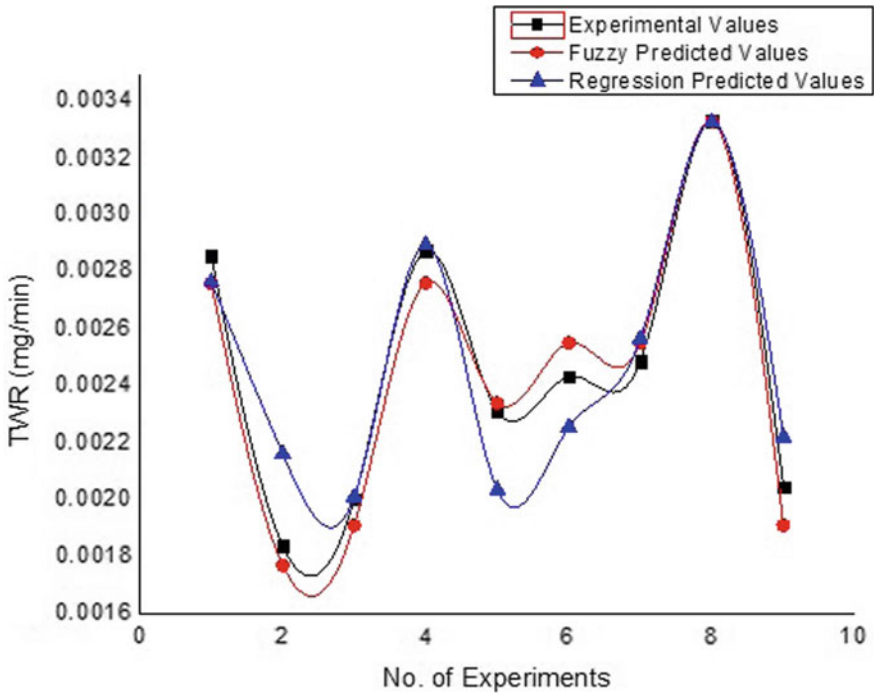


Fig. 10 Assessment plot of experimental, fuzzy-predicted and regression-predicted results for TWR

From these views, it is concluded that NaNO_3 salt-mixed de-ionized water has great influence for generating high-quality micro-holes.

4 Conclusions

In this paper, D3 die steel material was machined by micro-EDM considering parametric design based on L9 Taguchi methodology. NaNO_3 salt-mixed de-ionized water was employed. Further, based on experimental data, fuzzy-based models are established and fuzzy-predicted results were evaluated. The important findings of the present work are as follows:

- (i) For material removal rate and taper, most significant process parameter is peak current. In addition, for tool wear rate and taper, greatly influencing process parameter is pulse-on-time. Salt concentration has most contributing effect on MRR and overcut.

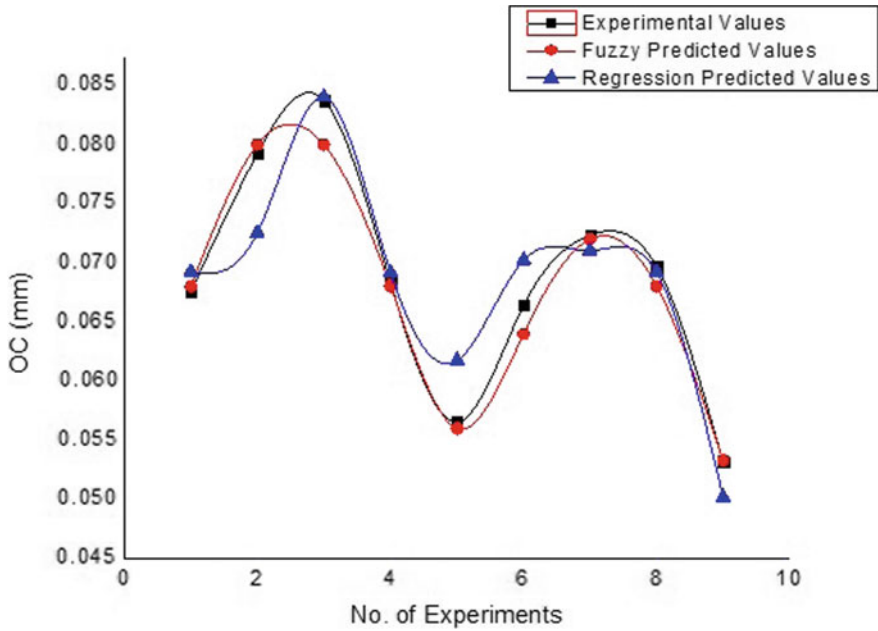


Fig. 11 Assessment plot of experimental, fuzzy-predicted and regression-predicted results for OC

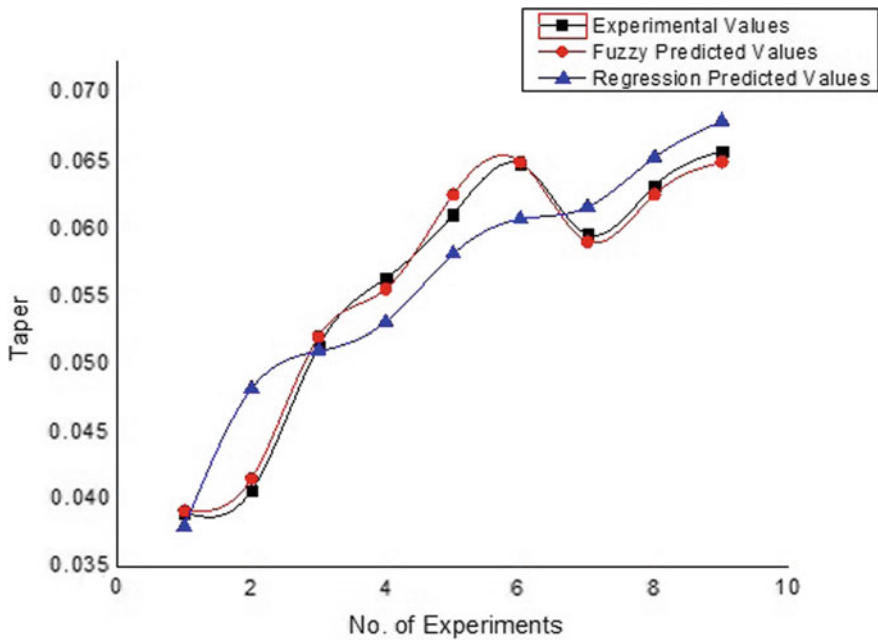


Fig. 12 Assessment plot of experimental, fuzzy-predicted and regression-predicted results for taper

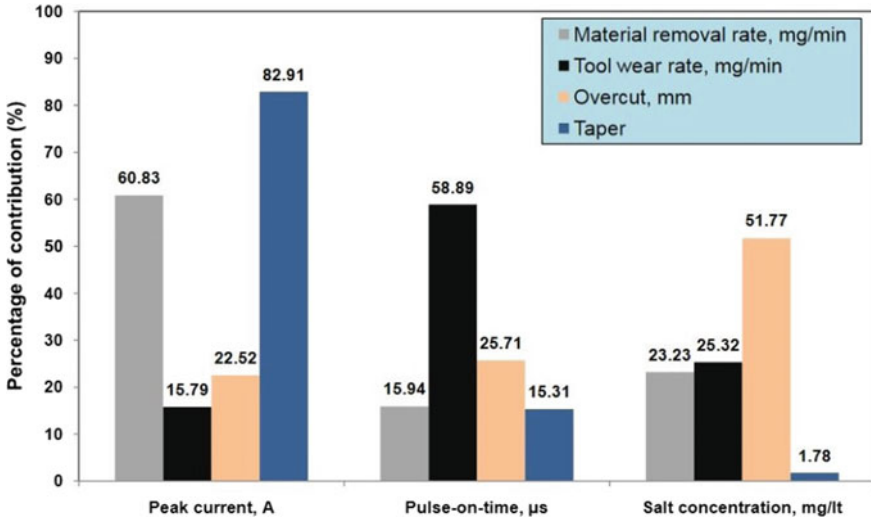


Fig. 13 Percentage contributions of process parameters on process performances

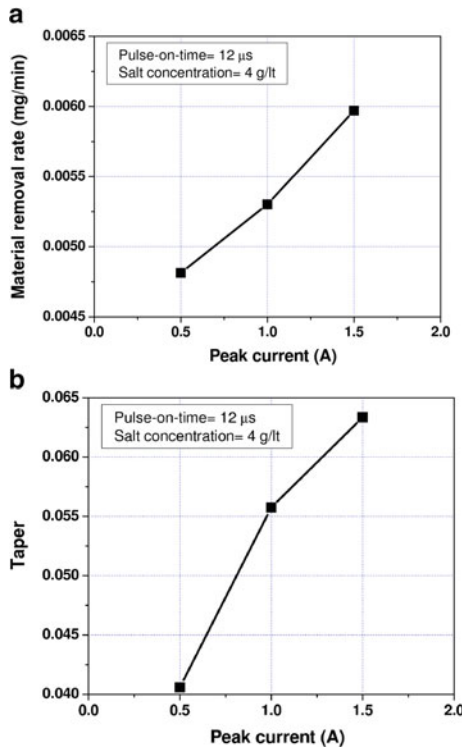


Fig. 14 Effect on a material removal rate and b taper by peak current

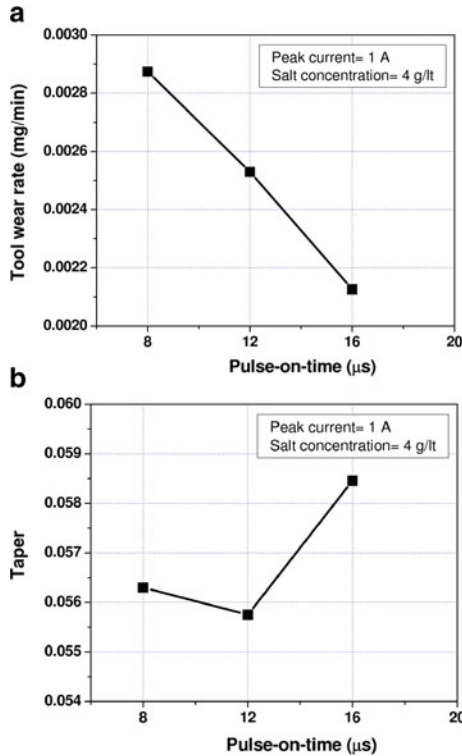


Fig. 15 Effect on **a** tool wear rate and **b** taper by pulse-on-time

- (ii) One of the striking contributions of the present research is the study of effect of mixing of NaNO_3 salt during micro-hole machining in D3 die steel workpiece. It is found from the experimental investigation that salt-mixed dielectric fluid has great influence during micro-hole machining. Tool wear rate decreases when the salt concentration increased from 1 to 4 g/l, thus improving the accuracy of micro-hole and productivity as well.
- (iii) Fuzzy-based model is developed for predicting the values of considered responses at various parametric combinations. Moreover, regression-based models of the responses are also developed, and the values of responses were predicted at all parametric combinations of process parameters.
- (iv) The overall percentage of prediction error of responses for fuzzy-based model is 1.98%, which is much less than the overall prediction error calculated (4.87%) based on regression model equations. These results confirm that fuzzy-based modeling provides better results than the regression model during micro-EDM of D3 die steel in the considered range of micro-EDM parameters. Furthermore, additional experiments were conducted to explore the consequence of one factor variation keeping other variables constant.

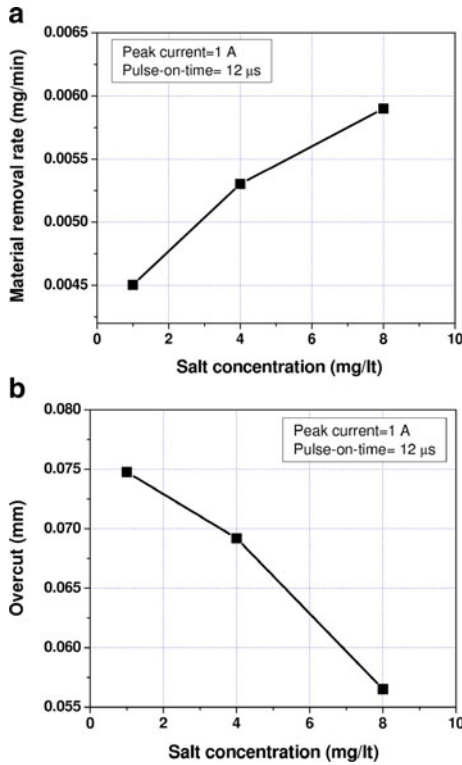


Fig. 16 Effect on a material removal rate and b overcut by salt concentration

In the present research, authors attempted to produce quality and accurately shaped micro-hole by micro-EDM process employing NaNO_3 salt-mixed de-ionized water. The present research study of micro-EDM operation on D3 die steel may be utilized for further research in the area of micro-machining of difficult-to-cut materials.

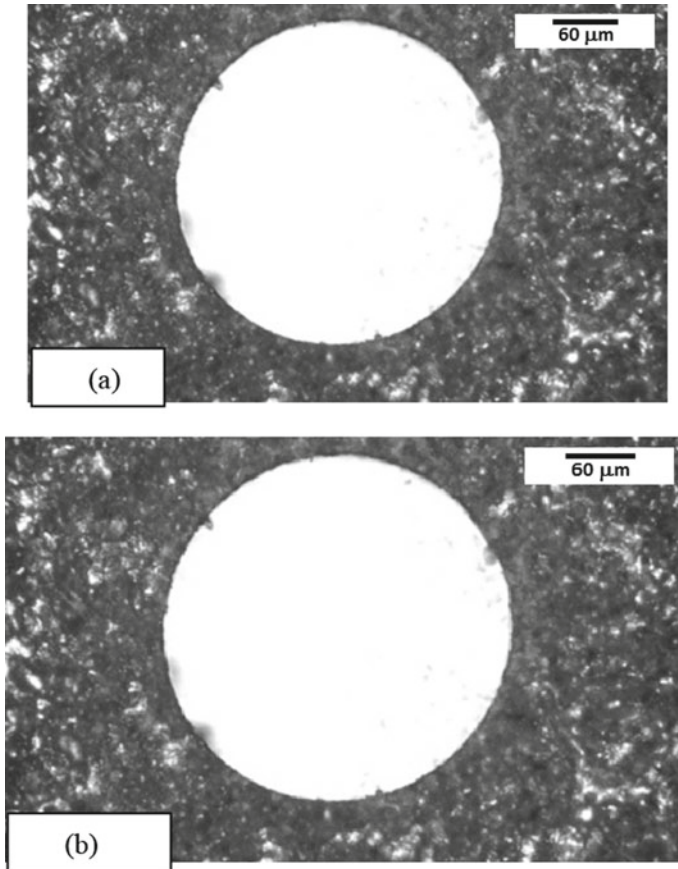


Fig. 17 High-resolution view of micro-hole machined at parametric combinations of peak current, pulse-on-time and salt concentration of **a** 1 A/8 μ s/4 g/l, **b** 1.5 A/12 μ s/1 g/l

References

1. Masuzawa T (2000) State of the art of micromachining. *CIRP Ann* 49(2):473–488
2. Gentili E, Tagaglio L, Aggogeri F (2005) Review on micromachining techniques. In: *Proceedings of the 7th international conference on advance manufacturing systems and technology*, vol 486, pp 387–396
3. Kibria G, Sarkar BR, Pradhan BB, Bhattachayya B (2010) Comparative study of different dielectrics for micro-EDM performance during microhole machining of Ti-6Al-4V alloy. *Int J Adv Manuf Technol* 48:557–570
4. Kibria G, Bhattacharyya B (2011) Investigation into micro-hole geometrical accuracy during micro-EDM of Ti-6Al-4V employing different dielectrics. *Int J Mach Mach Mater* 10(4):310–325
5. Zhang QH, Du R, Zhang JH, Zhang Q (2006) An investigation of ultrasonic-assisted electrical discharge machining in gas. *Int J Mach Tools Manuf* 46:1582–1588

6. Vajta L, Siklos P, Nagy L (1967) Study on the decomposition of kerosene used as a dielectric medium in spark machining, vol 11, no 3–4. *Periodica Polytech*, Budapest, Hungary, pp 263–274
7. Jeswani ML (1981) Electrical discharge machining in distilled water. *Wear* 72:81–88
8. Rashed CAA, Romoli L, Tantussi F, Fuso F, Burgener M, Cusanelli G, Allegrini M, Dini G (2013) Water jet guided laser as an alternative to EDM for micro-drilling of fuel injector nozzles: a comparison of machined surfaces. *J Manuf Process* 15(4):524–532
9. Chung DK, Shin HS, Kim BH, Park MS, Chu CN (2009) Surface finishing of micro-EDM holes using deionized water. *J Micromech Microeng* 19(4):1–7
10. Nguyen MD, Rahman M, Wong YS (2012) An experimental study on micro-EDM in low-resistivity deionized water using short voltage pulses. *Int J Adv Manuf Technol* 58(5–8):533–544
11. Kagaya K, Oishi Y, Yada K (1986) Micro-electrodischarge machining using water as a working fluid—I: micro-hole drilling. *Precis Eng* 8(3):157–162
12. Jilani ST, Pandey PC (1984) Experimental investigations into the performance of water as dielectric in EDM. *Int J Mach Tool Des Res* 24(1):31–43
13. Lin CT, Chow HM, Yang LD, Chen YF (2007) Feasibility study of micro-slit EDM machining using pure water. *Int J Adv Manuf Technol* 34(1):104–110
14. Chen SL, Yan BH, Huang FY (1999) Influence of kerosene and distilled water as dielectrics on the electric discharge machining characteristics of Ti-6Al-4 V. *J Mater Process Technol* 87(1–3):107–111
15. Chung DK, Kim BH, Chu CN (2007) Micro electrical discharge milling using deionized water as a dielectric fluid. *J Micromech Microeng* 17:867
16. Song KY, Chung DK, Park MS, Chu CN (2009) Micro electrical discharge drilling of tungsten carbide using deionized water. *J Micromech Microeng* 19(4). <https://doi.org/10.1088/0960-1317/19/4/045006>
17. Chung DK, Shin HS, Kim BH, Park MS, Chu CN (2009) Surface finishing of micro-EDM holes using deionized water. *J Micromech Microeng* 19(4). <https://doi.org/10.1088/0960-1317/19/4/045025>
18. Chen SL, Huang FY, Suzuki Y, Yan BH (1997) Electrical discharge machining characteristics of Ti-6Al-4V alloy using distilled water as a dielectric fluid. *J Jpn Inst Light Metals* 47(4):226–231
19. Chung DK, Shin HS, Chu CN (2012) Modeling and experimental investigation for electrolytic corrosion prevention in high frequency micro EDM using deionized water. *Microsyst Technol* 18(6):703–712
20. Zadeh LA (1965) Fuzzy sets. *Inf Control* 8(3):338–353
21. Lin CL, Lin JL, Ko T (2002) Optimisation of the EDM process based on orthogonal array with fuzzy logic and grey relational analysis method. *Int J Adv Manuf Technol* 19:271–277
22. Lin JL, Lin CL (2004) The use of grey fuzzy logic for optimization of manufacturing process. *J Mater Process Technol* 160:9–14
23. Nandi AK, Prathihar DK (2004) Automatic design of fuzzy logic controller using a genetic algorithm to predict power requirement and surface finish in grinding. *J Mater Process Technol* 148:288–300
24. Shivakoti I, Kibria G, Diyaley S, Pradhan BB (2003) Multi-objective optimization and analysis of electrical discharge machining process during micro-hole machining of D3 die steel employing salt mixed de-ionized water dielectric. *JCARME* 3:27–39

Experimental Study on PV Degradation Loss Assessment of Stand-Alone Photovoltaic (SAPV) Array in Field: A New Simplified Comparative Analytical Approach



Rohit Tripathi, Rakhi Sharma, and G. N. Tiwari

Abstract In the present study, a comparative study has been made on some quality factors: PV production factor, PV degradation loss factor and PV temperature-dependent factors of on-field PV array, placed at Centre for Energy Studies, Indian Institute of Technology Delhi, New Delhi, India. Three PV arrays are installed in IIT Delhi, named as: subarray (make1-Siemens), subarray (make2-CEL) and entire PV array (combination of both subarrays). A new terminology PV degradation loss factor has been proposed. The concept of overall PV degradation loss factors due to the combined effect of various constant losses due to long-term exposure of existing PV arrays as well as variable losses and operating temperature have been introduced. An attempt has been made to develop a new simplified methodology to evaluate the overall PV degradation loss factors (due to the combined effect of various monthly variable losses and the constant (fixed) losses) for on-field PV array/subarrays on the basis of observations measured during experimentation and numeric computations. In the observation, subarray (make1-Siemens) is found to be higher for generating high electrical energy on-field condition.

Keywords Solar irradiance · PV array · Degradation loss factor · Electrical energy/power

R. Tripathi (✉)

School of Electrical, Electronics & Communication Engineering, Galgotias University,
Greater Noida, UP 201307, India
e-mail: rohitrtripathi30.iitd@gmail.com

R. Tripathi · G. N. Tiwari

Centre for Energy Studies (CES), Indian Institute of Technology Delhi, Hauz Khas, New Delhi
110016, India

R. Sharma

School of Engineering & Technology, Indira Gandhi National Open University, Maidan Garhi,
New Delhi 110068, India

© Springer Nature Singapore Pte Ltd. 2020

A. K. Bhoi et al. (eds.), *Advances in Greener Energy Technologies*,

Green Energy and Technology, https://doi.org/10.1007/978-981-15-4246-6_40

1 Introduction

With the developing concerns of environmental issues, clean energy generation has acquired added importance. Solar radiation is environmentally benign and a sustainable source of energy [1]. In most sections of India, clear, sunny conditions are experienced 250–300 days in a year [2]. Latter the growth of PV technology and its function in space applications, it is now being utilized for terrestrial applications, e.g. rural usages, solar water pumping, space heating, lighting, communications, refrigeration, utility grids and other household appliances. For commercial applications, it is utterly necessary to bring down the cost of high-efficiency solar cells, which will match the affordability criteria [3]. A PV array [4, 5] comprises a group of PV cells that are connected in series and parallel combination. These PV cells are basically p - n diodes that convert the incident irradiance into the electrical gain. Stand-alone photovoltaic (SAPV) systems with a suitable energy storage mechanism have turned into one of the most hopeful ways out for the urgent electrical problem of many remote consumers worldwide [6, 7]. Considering the long-term use of photovoltaic arrays, many losses in the integrated PV system and the outside conditions, the measuring factors of photovoltaic arrays and performance of array cannot obtain the desired value. Therefore, PV system design plays an important role in achieving the desired effect by considering the standard parameters of PV arrays.

As compared to rated/max. PV performance indices (as estimated with newly installed PV system), continuous fall in on-field PV performance indices can be observed in system lifetime due to different losses in a PV array that are induced by the long-term use of photovoltaic array with long-term exposure of PV modules in changing climatic conditions. Various sources of PV degradation are there, out of which one is preliminary photon degradation related to a physical process in the solar cell itself [8], this effect is normally observed in beginning hours of PV operation, and the other is related to long-term weathering and degradation of the module [9] such as system ages.

Degradation of the PV modules and subsequent losses in the generation of electrical energy can have a serious impact on PV array potential electrical energy generation. However to know the progressive degradation of photovoltaic modules, detailed, analytic data is not readily obtainable [10]. In this manuscript, performance indices such as electrical gain and degradation loss factors have been calculated from the experimentally measured outside performance of a photovoltaic array. Knowledge of these actual on-field performances of PV array/subarrays can be very useful for system designers, professionals, operators and users in their efforts to realize successful PV system. This paper presents analytical mathematical modelling to evaluate annual on-field electrical energy output of existing stand-alone PV array on the basis of daily and subsequently monthly electrical energy production. Further, a new methodology has been established for calculating degradation loss factors of entire PV array with its constituent subarrays. Mostly available literature presents causes for different PV losses, but the literature which proposes an evaluation of these losses independently or overall losses after year's outdoor exposure/ageing of PV array is rarely available.

2 Outdoor Photovoltaic System

PV system is an assembly of PV cells and Tedlar, glass and frames which was designed for conversion of solar irradiance into electrical energy. Combination of series- and parallel-connected PV modules is combined in one and formed a PV array; PV array may consist of no. of subarrays for desired output or application. In this paper, a stand-alone photovoltaic array of 2.32 kW_p placed at IIT Delhi, India, as represented by Fig. 1a has been considered for experimental analysis. This proposed PV array system comprises two subarrays of ratings 1.2 and 1.12 kW_p each.

These subarrays, PV subarray1 and PV subarray2, consist of 16 modules (make1, 75 W_p each, 15 years old) and 32 modules (make2, 35 W_p each, 25 years old), respectively. The modules consist of 36 monocrystalline silicon cells per module. Figure 1b, c represents a photograph of PV cells/ modules (make1) in subarray1 and a photograph of PV cells/modules (make2) in subarray2, respectively. Other important components of the 2.32 kW_p photovoltaic system are an inverter (3 kVA), DC power storage batteries (360 Ah, 48 V), charge controller (40 A, 48 V). During daytime operation, electrical energy generated by PV array is fed into the battery bank through solar charge controller and excess electrical energy is directly fed into the inverter for supplying electrical power to the connected electrical loads. Storage batteries supply electrical power only during night or during low sunshine period when the power supplied by the array is less than the power demand by the loads.

In the existing outdoor PV system, a fixed metal-supporting structure is used for mounting photovoltaic arrays and inclination of the supporting frame is maintained at around latitude of the place to get maximum annual average solar radiations [11]. In order to supply the power generated from the 2.23 kW_p system for the uses in the solar house at Indian Institute of Technology Delhi, a proper connection was made between the inverter and the general switching board by making use of electric cable. The necessary electrical energy to the different connected loads of mud house such as tube lights, ceiling fan, computer, submersible water pump and CFLs for streetlight is provided through this photovoltaic system. Design parameters for PV module/subarrays of 2.32 kW_p PV array are given in Table 1. For monocrystalline silicon cell, temperature coefficient (β) is considered 0.45% per °C [12].

3 Experimental Observations for Performance Evaluation

For on-field, outdoor experimental set-up at solar house of IIT Delhi as shown in Fig. 2 [13], the data was obtained for each hour during the whole day of experimentation for two individual PV subarrays that have PV modules of two companies, here named as make1 and make2. To estimate electrical gain and PV degradation loss factors of existing outdoor PV array with its constituent subarrays, experiments have been conducted for clear sky days of each month throughout the year for measuring required experimental parameters. Hourly variation of required experimental

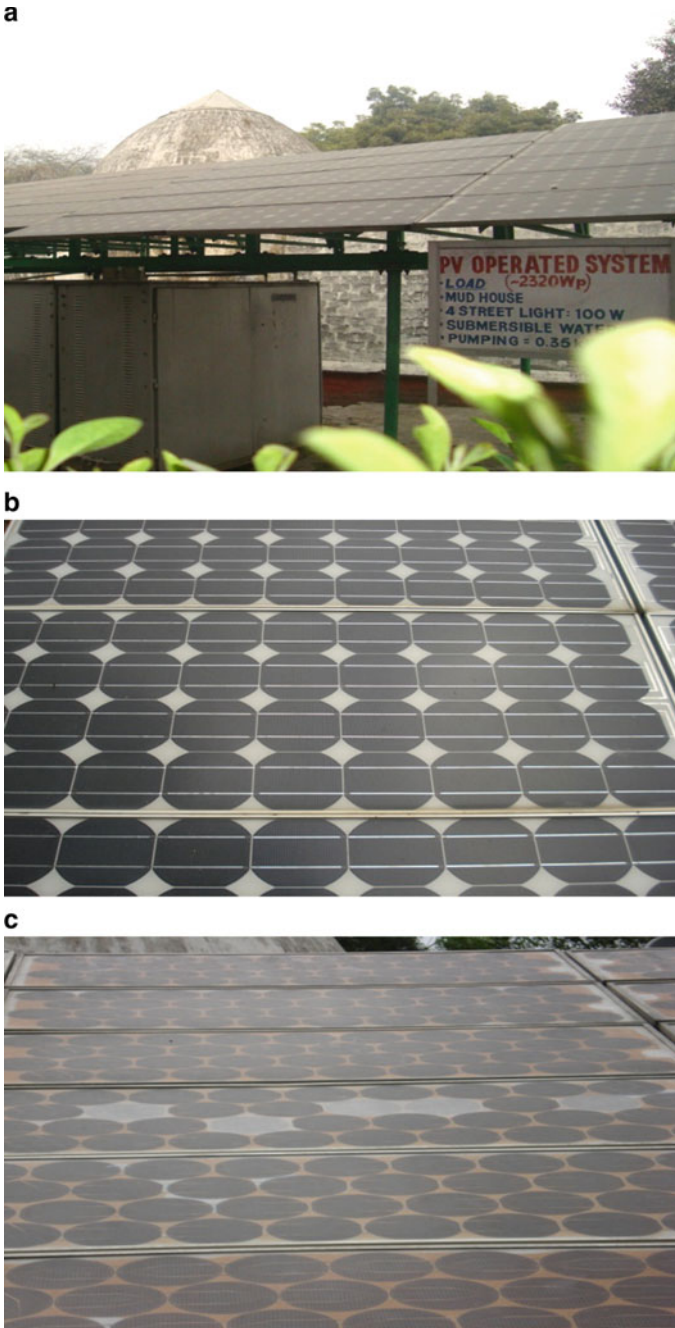


Fig. 1 **a** Photograph of stand-alone photovoltaic system (2.32 kW_p) at CES, IIT Delhi, India. **b** Photograph of PV cells/ modules (Siemens) in subarray1. **c** Photograph of PV cells/modules (CEL) in subarray2

Table 1 Design parameters for subarrays of 2.32 kW_p photovoltaic array

PV array (2.32 kW _p)	PV subarray1 (1.2 kW _p)	PV subarray2 (1.12 kW _p)
PV modules	Made by Siemens	Made by Central Electronics Ltd.
Specifications	Peak power—75 W _p	Peak power—35 W _p
	$I_{sc} = 4.8 \text{ A}$	$I_{sc} = 2.35 \text{ A}$
	$V_{oc} = 21.7 \text{ V}$	$V_{oc} = 20.5 \text{ V}$
	$I_{max} = 4.4 \text{ A}$	$I_{max} = 2.1 \text{ A}$
	$V_{max} = 17 \text{ V}$	$V_{max} = 16.5 \text{ V}$
	Area = 0.605 m ²	Area = 0.4 m ²
No. of PV modules	16	32
No. of series and parallel modules	4 parallel strings with 4 series modules in each	8 parallel strings with 4 series modules in each

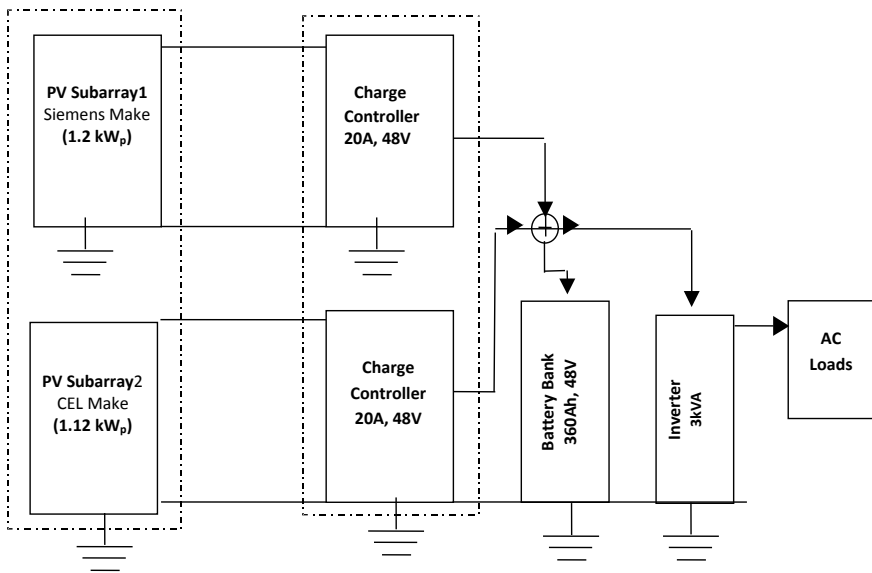


Fig. 2 Block diagram of 2.32 kW_p stand-alone PV system [13]

parameters, e.g. open-circuit voltage, short-circuit current, solar intensity, ambient and PV operating temperature, has been measured in clear sky days of each month over a year for PV subarrays, i.e. make1 (subarray1) and make2 (subarray2) of the entire PV array. To determine monthly performance indices of the existing SAPV system, the number of clear days in each month was recorded for New Delhi climate conditions.

Table 2 exhibits a sample of daily investigational data for existing PV array system that is obtained in a clear sky day for the month of May at CES, IIT Delhi (India).

Table 2 Hourly variation of various measured parameters on experimental set-up of PV array for a clear sky day of May (summer month)

Time (hour)	Subarray1		Subarray2		Ambient air temp T_{amb} (°C)	PV operation temp. T_{or} (°C)	Average solar intensity I_{ave} (W/m^2)
	Short-circuit current I_{sc} (A)	Open-circuit voltage V_{oc} (V)	Solar intensity I_1 (W/m^2)	Short-circuit current I_{sc} (A)			
8:00 am	4.3	71.0	360	2.6	68.0	33.0	355
9:00 am	6.3	70.8	530	3.9	68.0	34.0	525
10:00 am	7.0	70.8	550	4.2	67.8	35.0	550
11:00 am	9.9	70.6	750	5.8	67.8	36.0	750
12:00 pm	11.7	70.6	850	6.6	67.8	36.6	850
1:00 pm	11.6	70.5	840	6.5	67.7	37.0	840
2:00 pm	9.9	70.5	730	5.7	67.7	36.0	730
3:00 pm	7.6	70.0	600	4.4	67.3	36.0	600
4:00 pm	5.3	69.9	410	3.1	67.2	35.0	410
5:00 pm	3.2	69.0	190	1.9	67.0	34.0	190

While carrying out experiments on PV array, daily hourly observations for I_{sc} and V_{oc} of both subarrays were measured through a digital tong metre (least count 0.001 V, 0.1 A). Solar intensity on both subarrays and temperature were measured while carrying out on-field tests, with the help of calibrated portable solar metre (least count 20 W/m²), calibrated thermometer (least count 1 °C) and digital infrared laser thermometer (least count 0.1 °C), respectively.

4 Concept of Overall Pv Degradation Loss Factor

Solar cells/modules/array degradation may be caused by various factors such as front surface soiling, optical degradation, partial shading, AR coating degradation, mismatch cells due to manufacturing defects, connection losses, ageing effect or long-term exposure of PV modules. For example, PV degradation due to front surface soiling can be detected by in-field visual inspection of the modules/array. The accumulated dirt may, however, partially shade a cell in the module causing it to produce less current in cell than the other string cells. PV cell/module transmittance decreases by the dirt gathering on modules, and this causes electrical power losses and consequently daily energy losses. Piliouguine et al. [14] estimated that with a new self-cleaning coating film, year average daily energy soiling losses were 2.5%, whereas for the non-coated modules losses were 3.3%, on the basis of yearly measured electrical parameters on the Silicon modules installed on the roof of a university laboratory under open-air conditions in Malaga, Spain. In areas that experience frequent rains, assumption about soiling losses is in the range from 1 to 4% on annual basis [15]. However, in climates with infrequent rain, soiling losses of up to 20% on a monthly basis and 7% on an annual basis have been measured [16].

Energy conversion losses from the solar cell surface are also caused by the reflection of incident solar intensity from the cell surface. The conversion efficiency of solar cell is improved by using antireflective (AR) coating on the solar cell surface. This AR coating not only lessens the reflection losses but also lowers the surface recombination velocity. Poor performance of this AR coating after long-term environmental exposure/ageing of solar cell/module may cause degradation losses. Wilhelm Durisch et al. [17] evaluated the CIS module outdoor annual performance on the basis of developed semi-empirical efficiency model and reported the output reduction of the module at STC by 9% from 42.4 W down to 38.6 W [17]. For more than 20 years old, 3 BP PV modules, experimental analysis that is carried out using a series of $I-V$ experiments under on-field conditions, pointed out the causes of power degradation and especially of its extent were junction's damage, discolouring, humidity ingress, delamination of encapsulate, hot spots, etc. [18].

For over an expected life of 30 years of successful PV operations, much research is needed in all aspects of PV system. Van Dyk et al. [19] calculated the performance of usual modules for 15-month duration and that of a PV concentrator array for 13-month duration, and results show that the meteorological surroundings could cause 18% decrease in potential power of modules. Guenounou et al. [20] compared the

performance of four different technologies of PV panels for one year of outdoor exposure conditions of a coastal region. Kichou et al. [21] studied the degradation of tandem micromorph thin-film photovoltaic (TFPV) modules located in Jaén (Spain) under long-term outdoor exposure and addressed its impact on the output power of a PV array. This has been reported that the extended outdoor exposure times also cause degradation of module and can decrease the module efficiency as much as one by half [22].

Solar cells/modules/array degradation causes losses in PV electrical energy generation. For the system installed in actual outdoor practical conditions, it is most difficult to predict and evaluate PV degradation losses caused by each factor independently. Therefore, a new concept for evaluation of overall PV degradation loss factors has been developed, which accounts for the constant (fixed) losses, mainly caused by long-term exposure of PV modules such as PV system ages and variable losses mainly caused by unequal front surface soiling, variable operating temperature, etc.

5 Methodology for Evaluating Overall PV Degradation Loss Factor

To evaluate overall PV degradation loss factor for stand-alone PV array, the simplified computation method has been developed with the help of obtained on-field energy enactment of existing PV array. Overall PV degradation loss factors are evaluated for subarray1 (make1) and subarray2 (make2) and for entire existing PV array of 2.32 kW_p with the help of electrical energy gain in outdoor conditions calculated by using parameters measured during on-field experimentation at IIT Delhi over a year.

5.1 Evaluation of On-Field Performance of PV Array/subarrays

The following two computational methods are used to evaluate monthly electrical energy gain during a year and further will be used to evaluate overall PV degradation loss factors.

5.1.1 Computational Method 1

The daily electrical gain of a PV array depends on solar irradiance and cell temperature. Short-circuit current obtained from PV array is directly proportional to the variation in solar intensity on PV array. The V_{oc} , however, depends logarithmically on intensity of irradiance [19]. The minor variation in open-circuit voltage (V_{oc}) in

the day is observed due to ambient temperature changes and cloud effects. By continuous observation of I_{sc} and V_{oc} of the PV array, PV efficiency and degradation or zero power output can be freely observed [23].

Using experimentally measured observations daily, subsequent monthly and then yearly electrical gain of PV array/subarrays can be evaluated. In order to obtain monthly electrical energy gain of n th month, experimentally calculated average daily electrical gain in a particular n th month ($n = 1, 2, 3 \dots 0.12$) is multiplied by the no. of clear sky days in that month (D_n). Similarly, monthly electrical energy output of entire PV array can be expressed by Eq. (1) as a sum of experimentally calculated monthly electrical gain of individual PV subarray1 and subarray2 [13].

$$\begin{aligned}
 (E_{PV \text{ array}})_{\text{monthly},n} = & \left\{ \sum_{\text{hourly}} (\text{FF} \times V_{oc} \times I_{sc})_{\text{subarray1}} \right\}_n \\
 & \times D_n + \left\{ \sum_{\text{hourly}} (\text{FF} \times V_{oc} \times I_{sc})_{\text{subarray2}} \right\}_n \times D_n \quad (1)
 \end{aligned}$$

where $(E_{PV \text{ array}})_{\text{monthly},n}$ represents the monthly electrical energy gain of on-field PV array in n th month (kWh), I_{sc} represents short-circuit current, V_{oc} is known as open-circuit voltage, FF is fill factor for subarray and D_n represents number of clear sky days in a n th month of a year.

The fill factor (FF) of a PV module is an important performance indicator as it represents the sharpness of knee in the I - V curve. The actual magnitude of the FF depends strongly on module technology, design and the quality of junction of PV cell. Ideally, FF should be high.

5.1.2 Computational Method 2

On-field electrical energy gain of PV array/subarrays can also be evaluated by using a presented mathematical model, which includes the concept of overall PV degradation loss factor and actual measured climatic parameters of a given location. The final expression of PV array/subarray actual on-field electrical energy output has been established in step (iii), after following the steps (i) and (ii) as explained below:

(i) *Estimation of rated electrical gain of on-field PV array at STC*

Estimation of PV electrical gain of the PV array and subarrays is valuable in finding the PV performance evaluation and possible amendments. Peak power (P_m) from the array is at standard test condition (STC) as per rated specifications given by manufacturer. STC for PV system can be stated by 100 mW/cm² (1000 W/m²) irradiance meeting the requirements of standard reference AM 1.5 G spectrum and ambient temperature 298.16 K (25 °C). The usable is found very appropriate, as the efficiency in per cent is identically same to power output in mW/cm² [24].

Monthly electrical energy gain from existing outdoor PV array can be estimated by getting mathematical product of daily electrical energy gain and number of clear days in n th month as expressed by Eq. (2). Here, daily electrical energy gain is attained by multiplying the given rated/peak power of PV module given at STC (in W_p) with the on-field condition in hhours/d [25].

$$(\xi_{\text{rated}})_{\text{monthly},n} = P_m \times h_{\text{EFS}_n} \times D_n \quad (2)$$

where $(\xi_{\text{rated}})_{\text{monthly},n}$ represents rated monthly electrical energy gain of on-field PV array in n th month (kWh), P_m represents peak power of array measured in STC (W_p) and h_{EFS_n} represents equivalent hours for a clear sky day in n th month (hours/day).

Equivalent hours of full sun radiation (h_{EFS}) are considered by the number of hours of incident irradiance at an object if the intensity of irradiance is been constant at its peak value of 1000 W/m^2 that delivers the same gain obtained from sunrise to sundown. h_{EFS} for a specific day can be attained by the integration of area under the solar intensity and time curve. For obtaining the actual value of h_{EFS} for a particular location, we use the experimentally measured daily hourly variation of solar intensity incidents on the PV.

(ii) ***Estimation of maximum electrical gain with on-field PV operating temperature correction***

It is important to measure on-field PV operating temperature (T_{OT}) as PV operating temperature (T_{OT}) significantly affects the output power of solar PV array. Expressions are available to show the significant decrease in PV power output with increase in PV operating temperature [25]. Consequence of counting the effect of operating temperature of PV in the potential (rated) monthly output of electrical energy has been presented by Eq. (3).

$$(\xi_{\text{max}})_{\text{monthly},n} = P_m \times h_{\text{EFS}_n} \times D_n \times \{1 - \beta(T_{\text{OT}_n} - T_{\text{STC}})\} \quad (3)$$

where $(\xi_{\text{max}})_{\text{monthly},n}$ represents estimated maximum monthly electrical energy output gain of PV array/subarray in n th month (kWh), T_{OT_n} represents daily mean of PV operating temperature in n th month ($^{\circ}\text{C}$) and T_{STC} represents temperature at standard rated condition.

(iii) ***Estimation of actual electrical energy output with overall PV degradation loss correction***

In this section, concept of overall degradation loss caused by on-field solar cells/modules/array degradation has been incorporated and finally a new method for evaluating PV degradation loss factor has been developed. Modified expression of the daily electrical energy gain of PV array has been developed after combining the effect of PV operating temperature, incident solar intensity and PV cell/module degradation losses. Maximum monthly electrical gain with PV operating temperature correction as given in Eq. (3) is further corrected for overall PV degradation by

multiplying this by a factor ϵ_o . Here, Eq. (4) expresses the estimated actual daily electrical energy gain from the PV array comprises two subarrays with overall PV degradation loss correction. Summation of electrical energy gain from two subarrays provides the total electrical energy gain from the entire PV array.

$$\begin{aligned}
 (\xi_{pv \text{ array}})_{\text{daily}} = & [P_m \times h_{EFS} \times \{1 - \beta(T_{OT} - T_{STC})\} \times \epsilon_o]_{\text{subarray1}} \\
 & + [P_m \times h_{EFS} \times \{1 - \beta(T_{OT} - T_{STC})\} \times \epsilon_o]_{\text{subarray2}} \quad (4)
 \end{aligned}$$

where ϵ_o expresses PV production factor which can be defined as the ratio of actual on-field array output and maximum annual array output estimated with existing on-field environmental conditions (i.e. PV operating temperature that depends on ambient air temperature and solar intensity; full sunshine equivalent hours that depend on the received solar intensity) for a particular location. In actual field condition, this production factor is found less than one due to PV degradation losses. Here, δ_o represents the overall PV degradation loss factor and can be expressed by Eq. (5).

$$\delta_o = 1 - \epsilon_o \quad (5)$$

Overall PV degradation loss factor (δ_o) represents the ratio of total losses in PV array electrical energy output and maximum electrical energy output with existing on-field. The losses are due to combined effect of various constant losses, mainly caused by long-term exposure of installed PV modules/array such as the system ages and short-term variable losses mainly caused by unequal soiling, etc.

For estimating annual electrical energy output from PV array using mathematical model, average values of h_{EFS} and T_{OT} for clear day of each month over a year are evaluated using observations as obtained while carrying out experimentation. Expressions to estimate on-field monthly electrical energy gain of PV array/subarrays have been developed as given below by Eq. (6).

$$\begin{aligned}
 (\xi_{pv \text{ array}})_{\text{monthly},n} = & [P_m \times (h_{EFS_n} \times D_n) \times \{1 - \beta(T_{OT_n} - T_{STC})\} \times \epsilon_{o_n}]_{\text{subarray1}} \\
 & + [P_m \times (h_{EFS_n} \times D_n) \times \{1 - \beta(T_{OT_n} - T_{STC})\} \times \epsilon_{o_n}]_{\text{subarray2}} \quad (6a)
 \end{aligned}$$

where $(\xi_{pv \text{ array}})_{\text{monthly}}$ represents actual on-field electrical energy output of the PV array for n th month with overall PV degradation loss correction; here, for January $n = 1$ and for December $n = 12$. h_{EFS_n} is average value of equivalent hours of full sunshine obtained for clear days in n th month, and T_{ON_n} is daily mean value of PV operating temperature measured in n th month. ϵ_{o_n} is the PV production factor in n th month; here, overall PV degradation loss factor calculated in n th month (δ_{O_n}) is expressed by

$$\delta_{O_n} = 1 - \epsilon_{O_n} \quad (6b)$$

Expressions to estimate on-field annual electrical energy output of PV array/subarrays have been developed as given by Eq. (7).

$$\begin{aligned}
 (\xi_{pv\ array})_{annual} &= \sum_{n=1}^{12} [P_m \times (h_{EFS_n} \times D_n) \times \{1 - \beta(T_{OT_n} - T_{STC})\} \times \epsilon_{o_n}]_{subarray1} \\
 &+ \sum_{n=1}^{12} [P_m \times (h_{EFS_n} \times D_n) \times \{1 - \beta(T_{OT_n} - T_{STC})\} \times \epsilon_{o_n}]_{subarray2}
 \end{aligned}
 \tag{7}$$

Terms $\xi_{pv\ array}$ and h_{EFS_n} are also very important parameters for sizing work of PV components.

5.2 Evaluation of Overall PV Degradation Loss Factor

Overall PV degradation loss factor δ_o accounts for the power conversion losses due to solar cells/modules/array degradation caused by various factors, and these losses in turn reduce the electrical energy output from the PV array. These losses can be named as constant losses (long term) and variable losses (short term) as it is difficult to evaluate the losses caused by each factor independently for the system installed in actual outdoor field conditions.

To know the overall PV degradation loss factor for the entire PV array and for more reliable performance evaluation, overall PV degradation loss factor for both subarray1 and subarray2 has been evaluated separately. To evaluate the overall PV degradation loss factors, expressions presented by Eqs. (1) and (6) for evaluating monthly electrical energy generation by PV array/subarrays have been equated separately for individual component subarrays. These developed expressions are expressed by Eqs. (8) and (9). In these expressions, parameters either are known or can be obtained experimentally for subarray1 and subarray2, in order to evaluate the unknown parameter of overall PV degradation loss factor, for respective subarray.

Overall PV degradation loss factor for subarray1 in n th month is obtained by Eq. (8a) and (b).

$$\begin{aligned}
 &\left\{ \sum_{hourly} (FF \times V_{oc} \times I_{sc})_{subarray1} \right\}_n \times D_n \\
 &= [P_m \times (h_{EFS_n} \times D_n) \times \{1 - \beta(T_{OT_n} - T_{STC})\} \times \epsilon_{o_n}]_{subarray1}
 \end{aligned}
 \tag{8a}$$

and

$$(\delta_{o_n} = 1 - \epsilon_{o_n})_{subarray1}
 \tag{8b}$$

Similarly, overall PV degradation loss factor for subarray2 in n th month is obtained by Eq. (9a) and (9b).

$$\left\{ \sum_{\text{hourly}} (\text{FF} \times V_{\text{oc}} \times I_{\text{sc}})_{\text{subarray2}} \right\}_n \times D_n = [P_m \times (h_{\text{EFS}_n} \times D_n) \times \{1 - \beta(T_{\text{OT}_n} - T_{\text{STC}})\} \times \epsilon_{o_n}]_{\text{subarray2}} \tag{9a}$$

and

$$(\delta_{o_n} = 1 - \epsilon_{o_n})_{\text{subarray2}} \tag{9b}$$

Approximate value of degradation loss factor for entire PV system on the basis of annual performance can be evaluated with the help of average of all monthly degradation loss factors evaluated over a year for the constituent subarray1 and subarray2 of entire PV array. To obtain maximum on-field electrical energy production, ideal value of PV production factor (ϵ_o) is 1 and the ideal value of PV degradation loss factor (δ_o) is 0.

In the present study to obtain more effective results, overall PV degradation loss factors for PV array/subarrays have been evaluated with the help of monthly on-field electrical energy output measured by rigorous on-field experimentation during typical clear days in each month over a year. The same analysis has been applied only for typical clear days on-field experimental data in order to get of the overall PV degradation loss factor for an outdoor existing PV array/subarrays.

If high variability in degradation loss factors is obtained during monthly analysis, then necessary measures may also be taken to improve the poor performance of PV array/subarrays by applying high degree of maintenance. Developed expressions can be used for any kind of PV array system, which comprises any number of subarrays.

6 Evaluation of Temperature-Dependent Loss Factor

PV module/array rated performance is specified by the manufacturer at a standard test condition (STC) at temperature of 25 °C and solar intensity of 1000 W/m². However, in actual field conditions PV operating temperature for a given location does not remain as 25 °C and causes deviation in its specified rated performance. High PV operating temperature significantly affects the output power of PV array and causes an overall reduction in electrical power output. PV module temperature profile in non-steady conditions was studied for cloudy and clear days, and it was observed that the PV module temperature variation was from 27 to 52 °C with an ambient temperature of 24.5 °C [26]. Here, the temperature-dependent loss factor for PV array/subarrays can be calculated by using Eq. (10).

$$\delta_{T_n} = \{1 - \beta(T_{OT_n} - T_{STC})\} \tag{10}$$

where δ_{T_n} represents the temperature-dependent loss factor for PV array/subarrays obtained in n th month, T_{OT_n} represents daily mean of PV operating temperature in n th month and T_{STC} represents temperature at standard rated condition (25 °C).

7 Results and Discussion

As explained in Sect. 3, experimental observations have been recorded in the existing SAPV array system for clear day of each month over a year to evaluate the energy performance of the PV array system. The experimentally calculated daily electrical energy generated by the PV array system in a typical day of the month of May was calculated as 6.047 kWh. Two individual component subarrays contribute 3.896 kWh/day and 2.178 kWh/day for subarray1 (make1) and subarray2 (make2), respectively. Figure 3 shows the monthly variation of average solar intensity on entire PV array over a year.

Electrical energy generated by the PV array greatly depends on the incident solar irradiation as one of the parameters short-circuit current has a linear relationship with solar intensity. Equivalent hours of full sunshine (h_{EFS}) for both subarrays have been calculated for each month using measured received solar energy on the individual subarrays.

To obtain the equivalent hours of full sunshine (h_{EFS}) for entire PV array, average of h_{EFS} values obtained for both subarrays is considered. Figure 4 shows the variation of the average value of h_{EFS} obtained for clear day of each month over a year for the existing PV array. Figure 5 depicts the monthly variation of average daily values of ambient temperature and PV operating temperature of on-field PV array.

In existing outdoor PV system, two subarrays are placed adjacent to each other (side by side at equal height and same environmental conditions). In the present manuscript, parameters that affect the PV array performance like ambient temperature, PV operating temperature, solar intensity and equivalent hours of full sunshine

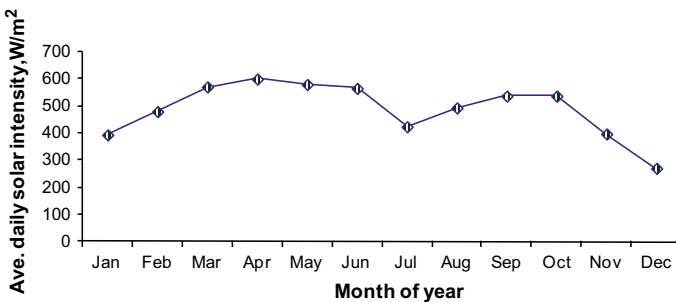


Fig. 3 Monthly variation of average solar intensity on existing PV array

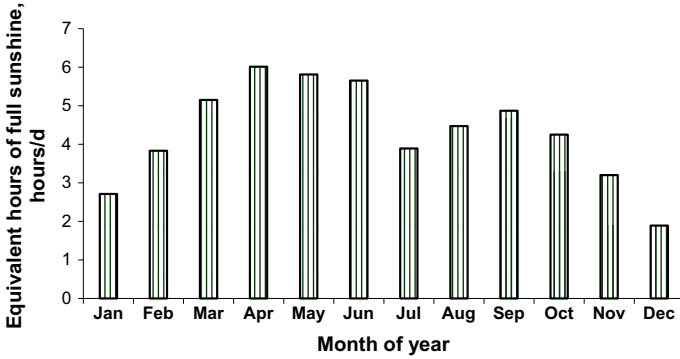


Fig. 4 Monthly variation of full sunshine/irradiance (h_{EFS}) for PV array

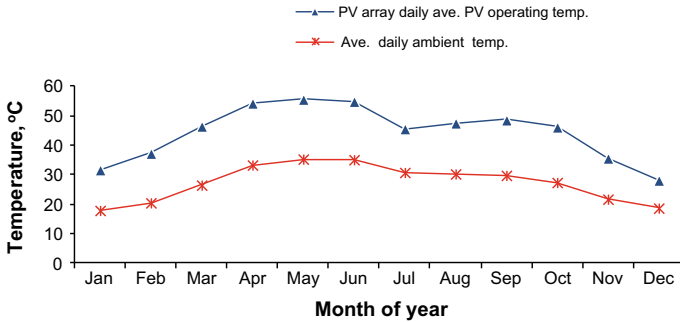


Fig. 5 Monthly variation of average daily values of ambient air temperature and operating temperature of PV array

on both subarrays are measured and found almost same (or slight change) for both subarray1 and subarray2. Because of this, average value of these parameters of both constituent subarrays has been shown to present the entire 2.32 kW_p PV array system parameters, and that average values for entire PV array parameters come very close to the values of parameters of constituent subarrays.

$I-V$ characteristic of PV expresses the FF as ratio of V_m and I_m (maximum power from max. voltage and current) to V_{oc} , I_{sc} (product of open-circuit voltage and short-circuit current). Value of fill factor (FF) has been considered 0.73 as obtained from the module technical specification details for the given PV subarray1 and subarray2 as mentioned in Table 1. The common value of fill factor for crystalline silicon cell is 0.67–0.80. A number of clear days in each month that are useful for PV power generation under New Delhi climatic conditions and experimentally obtained daily electrical energy gain (kWh/d) have been given in Table 3. The monthly variation of experimentally obtained electrical energy gain using Eq. (1) is shown in Fig. 6 for both individual subarrays and entire 2.32 kW_p PV array of existing set-up. Figure 7 depicts experimentally obtained actual annual electrical energy gain performance

Table 3 Average daily electrical energy gain for considering outdoor PV arrays (kWh/day) in each month during a year (experimentally)

Months	No. of clear days	PV subarray1, daily electrical energy gain	PV subarray2, daily electrical energy gain	Complete PV array, daily electrical energy gain
January	22	2.2	1.3	3.5
February	25	2.9	1.7	4.6
March	29	3.5	2.2	5.7
April	28	4.0	2.2	6.2
May	30	3.9	2.2	6.1
June	25	3.7	2.2	5.9
July	16	2.5	1.9	4.4
August	17	3.4	2.1	5.5
September	23	3.7	2.3	6.0
October	25	3.2	2.1	5.3
November	22	2.7	1.6	4.3
December	20	1.6	1.0	2.6

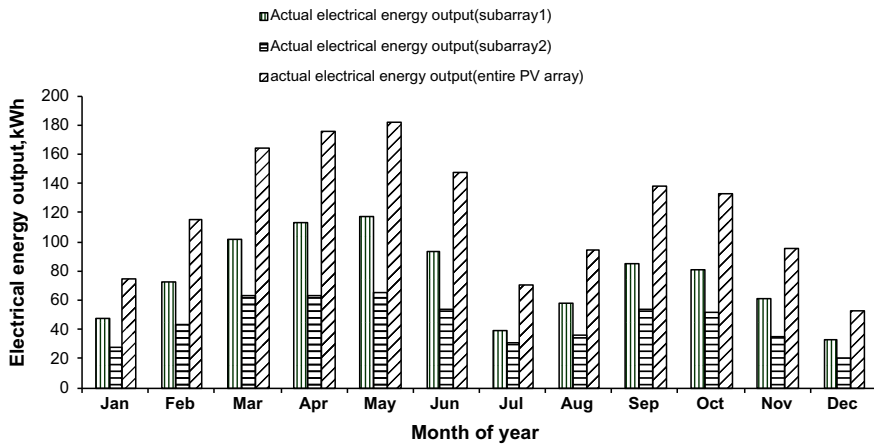


Fig. 6 Monthly variation of obtained actual electrical energy gain of PV array/subarrays (experimentally)

using Eq. (1) with respect to the estimated rated annual electrical energy gain performance of on-field at STC using Eq. (2). It is observed that on-field measured actual electrical energy gain for entire PV array/subarrays is obtained quite less as compared to rated electrical energy gain for the same existing PV array/subarrays, obtained by using the parameter specifications given by the manufacturer at STC.

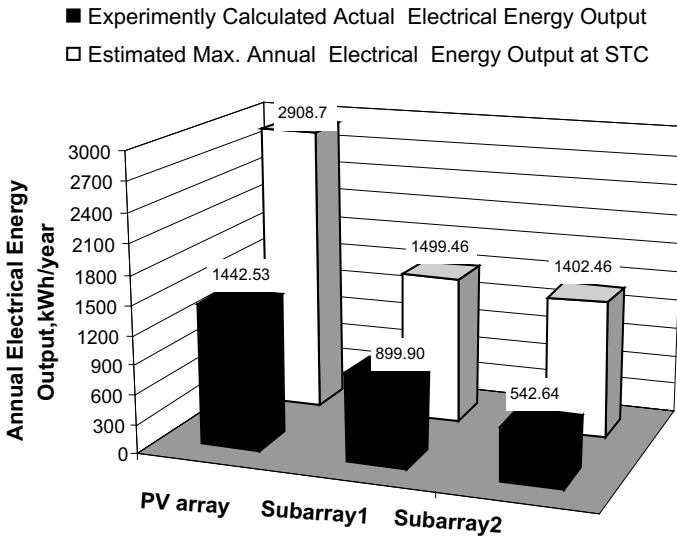


Fig. 7 Annual electrical energy gain for PV array/subarrays

Equations (4, 5, 6 and 7) represent set of computational model that has been developed to estimate actual electrical energy output on a daily, subsequently monthly and thereafter an annual basis and incorporate the concept of overall PV degradation loss factor that causes losses in electrical energy production. Continuous degradation in PV module/array due to long-term exposure of on-field installed PV array such as system ages results in constant (fixed) losses in electrical power generation, whereas small monthly variation in PV degradation loss factor during a year represents the PV degradation caused by different variable factors such as unequal front surface soiling and partial shading.

Reduction in electrical energy output is obtained due to the high PV degradation losses, mainly caused by long-term on-field exposure/ageing effect of on-field PV modules/array. Overall PV degradation loss factors and PV production factors for PV subarray1 and subarray2 are determined using Eq. (8) and Eq. (9), respectively. These values for existing PV array/subarrays are given in Table 4.

Variations in overall PV degradation loss factors for existing PV array/subarrays over the year are plotted as shown in Fig. 8. Plot of Fig. 8 shows quite high value of overall PV degradation loss factor for subarray2 as compared to overall PV degradation loss factor obtained for subarray1. This is because of the higher degradation of subarray2 PV modules as compared to subarray1 PV modules. This high overall PV degradation loss factor for subarray2 causes high power conversion losses and in turn low electrical power output from the subarray2. This performance of subarray2 is decreased due to the long-term exposure/ageing problem of existing PV modules of subarray2, and this is causing a significant reduction in entire PV array average performance.

Table 4 PV production factor and overall PV degradation loss factor for PV array/subarrays

Months	PV production factor			Overall PV degradation loss factor		
	Subarray1 (make1)	Subarray2 (make2)	Entire array	Subarray1 (make1)	Subarray2 (make2)	Entire array
January	0.654	0.418	0.556	0.346	0.582	0.444
February	0.665	0.421	0.549	0.335	0.579	0.451
March	0.629	0.419	0.526	0.371	0.581	0.474
April	0.644	0.383	0.516	0.356	0.617	0.484
May	0.65	0.389	0.522	0.35	0.611	0.478
June	0.571	0.352	0.462	0.429	0.648	0.538
July	0.607	0.495	0.537	0.393	0.505	0.463
August	0.77	0.503	0.637	0.23	0.497	0.363
September	0.715	0.482	0.595	0.285	0.518	0.405
October	0.72	0.485	0.595	0.28	0.515	0.405
November	0.764	0.468	0.615	0.236	0.532	0.385
December	0.723	0.473	0.605	0.277	0.527	0.395
Ave	0.676	0.441	0.560	0.324	0.559	0.440

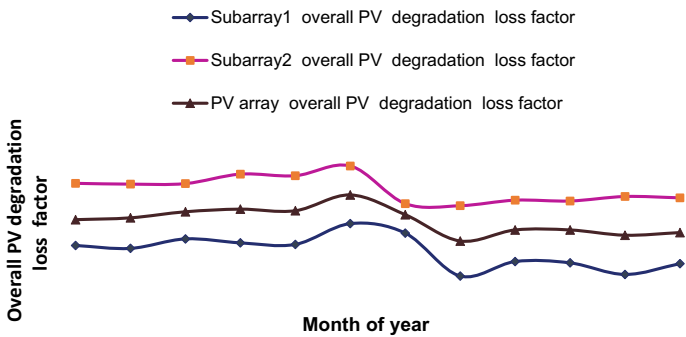


Fig. 8 Variation of overall PV degradation loss factors for existing PV array/ subarrays

Overall PV degradation loss factors due to the combined effect of various monthly variable losses and the constant (fixed) losses caused by long-term exposure/ageing effect of existing PV array/subarrays were found in the range of 0.230–0.429 for subarray1 and 0.497–0.648 for subarray2 of the entire existing PV array of 2.32 kW_p.

Small variations in evaluated overall PV degradation loss factors from min. to max. are observed during a year, and this can be concluded that the minimum obtained values of overall PV degradation loss factors (0.230 and 0.497 for subarray1 and subarray2, respectively) indicate towards the constant (fixed) losses due to PV degradation caused by ageing effect, whereas small monthly variation in evaluated overall PV degradation loss factors of PV array/subarrays from its fixed value indicates

towards the variable losses due to PV degradation caused by variable factors such as unequal front surface soiling of existing PV array/subarrays, partial shading (tree leaves and bird dropping) and self-cleaning due to rain. Minimum values of variable losses were obtained in the month of August because of self-cleaning of modules due to rain (Fig. 7).

Constant PV degradation losses due to the long-term exposure/ageing of existing PV array/subarrays were found almost 23% for subarray1 (make1, 15 years old) and 49.7% for subarray2 (make2, 25 years old) of entire existing PV array of 2.32 kW_p (make1 and make2). Similarly, monthly variation in PV degradation losses that are mainly caused by unequal front surface soiling of existing PV array/subarrays and self-cleaning due to rain and varying PV operating temperature was found almost in the range of 0–19.9% for subarray1 and 0–15.1% for subarray2 of entire existing PV array of 2.32 kW_p. These all losses have been expressed with respect to PV array/subarray maximum or potential electrical energy output performance estimated for same actual experimental environmental conditions.

Equation (10) determines the PV temperature-dependent loss factors for both PV subarrays. Temperature-dependent loss factors for entire PV array have been obtained by taking the average of temperature-dependent loss factors of both subarrays, and obtained data is given in Table 5 on the basis of experimental calculations carried out for clear day observations in each month over a year.

Figure 9 shows the monthly variation of temperature-dependent loss factors for the existing PV array. In existing on-field PV array set-up, both subarrays have almost same PV operating temperature as they are installed at the equal height under same environmental conditions. The low value of a temperature-dependent loss factor during winter months causes low losses in electrical energy output due to low operating

Table 5 Temperature-dependent loss factor for PV array/subarrays

Months	Temperature-dependent loss factor		
	Subarray1 (make1)	Subarray2 (make2)	Entire PV array
January	0.029	0.031	0.030
February	0.055	0.055	0.055
March	0.097	0.096	0.096
April	0.132	0.131	0.132
May	0.138	0.137	0.138
June	0.134	0.134	0.134
July	0.094	0.091	0.093
August	0.102	0.101	0.101
September	0.107	0.105	0.106
October	0.096	0.094	0.095
November	0.048	0.047	0.048
December	0.014	0.014	0.014
Ave	0.087	0.086	0.0868

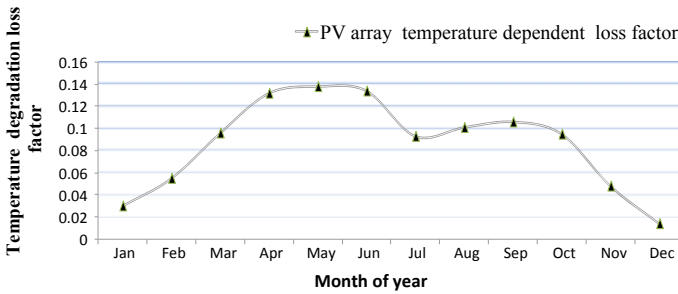


Fig. 9 Variation of temperature-dependent loss factors for existing entire PV array

temperature, and its high value during summer months causes relatively high losses in electrical energy output. Monthly variation of temperature-dependent loss factor for PV array/subarrays has been obtained in the range of 0.014–0.138. It obtained 0.014 (minimum) in December month and 0.138 (maximum) in May month of a year. Fifty percentage losses in the environmentally exposed ageing PV system cause only 50% electrical power output, and such old PV system will not be sufficient to fulfil all electrical power requirements of connected load for which it was initially designed. A threshold is considered, where up to a point, over all degradation losses are tolerable and depends on the end user connected load requirement for useful electrical power and overall PV system operational maintenance cost incurred. One of the factors that decide the cost of electricity is photovoltaic module lifetime, and this lifetime of module is decided by degradation. By specifying the guarantee of PV module, PV manufacturers point towards the extent to which the PV module will degrade.

Year's outdoor operations of modules indicate electrical power output degradation. It has been experienced that module quality plays a significant role in determining the level of degradation. PV degradation has been reduced considerably with technology improvements and quality assurance. With the advancement of PV module technology, most of the manufacturers now offer 25-year guarantee for standard solar module and indicate that after 25 years electrical power output of PV should not be less than 80% of rated power.

8 Conclusions

Accurate prediction of PV system energy performance at design phase is crucial for both economic and long-term technical performance evaluations.

- Based on annual experimental observations and numeric computations, overall PV degradation loss factors for existing PV array/subarrays have been evaluated. With long-term use of the PV array, there are constant PV degradation losses caused by extended exposure/ageing of PV modules. Other variable PV degradation losses

are mainly caused by unequal front surface soiling, variable operating temperature, etc.

- Higher electrical energy production factor has been obtained for subarray1 (make1), which is 1.5 times higher than for subarray2 (make2), and lower PV degradation loss factor has been found for subarray1 (make1) (1.7 times lower to make2).
- The temperature-dependent loss has been obtained more or less same for both different makes (1–2) which results that make1 is better PV array for high electrical energy production.

References

1. Joshi AS, Dincer I, Reddy BV (2009) Thermodynamic assessment of photovoltaic systems. *Sol Energy* 83:1139–1149
2. Jain A, Mehta R, Mittal SK (2011) Modelling impact of solar radiation on site selection for solar PV power plants in India. *Int J Green Energy* 8(4):486–498
3. Tripathi R, Tiwari GN, Dwivedi VK (2016) Overall energy, exergy and carbon credit analysis of N partially covered Photovoltaic Thermal (PVT) concentrating collector connected in series. *Sol Energy* 136:260–267
4. Dumas LN, Shumka A (1982) Photovoltaic module reliability improvement through application testing and failure analysis. *IEEE Trans Reliab* 31(3):228–234
5. Al-Aloud A, Zhang L (2000) Application of radial basis function networks for solar-array modeling and maximum power-point prediction. *IEEE Trans Distrib* 147(5):310–316
6. Kazmerski LL (2006) Solar photovoltaic's R&D at the tipping point: a technology overview. *Electron Spectrosc Relat Phenom* 150:105–135
7. Albrecht J (2007) The future role of photovoltaics: a learning curve versus portfolio perspective. *Energy Policy* 35:296–304
8. Knobloch J, Glunz SW, Henniger V, Warta W, Wettling W (1995) 21% efficient solar cells processed from czochralski grown silicon. In: *Proceeding 13th EU PVSEC, Nice, France*
9. Bishop J, Ossenbrink HA (1995) Five years of module qualification testing. In: *Proceeding of 13th EU PVSEV Nice, vol 2. France, p 104*
10. Quintana MA, King D, McMahon TJ, Osterwald CR (2002) Commonly observed degradation in field-aged photovoltaic modules. In: *Proceeding 29th IEEE PVSEC, New Orleans, p 1436*
11. Messenger R, Ventre J (2000) Photovoltaic's systems engineering. CRC Press LLC, Florida, pp 3–5
12. Tripathi R, Tiwari GN, Al-Helal IM (2016) Thermal modelling of N partially covered photovoltaic thermal (PVT)–Compound parabolic concentrator (CPC) collectors connected in series. *Sol Energy* 123:174–184
13. Sharma R, Tiwari GN (2012) Technical performance evaluation of stand-alone photovoltaic array for outdoor field conditions of New Delhi. *Appl Energy* 92:644–652
14. Piliouguine M, Cañete C, Moreno R, Carretero J, Hirose J, Ogawa S, Sidrach-de-Cardona M (2013) Comparative analysis of energy produced by photovoltaic modules with anti-soiling coated surface in arid climates. *Appl Energy* 112:626–634
15. Hammond R, Shrinivasan D, Harris A, Whitfield K, Wohlgemuth J (1997) Effects of soiling on PV Module and radiometer performance. In: *26th IEEE PVSC, Anaheim, California*
16. Tripathi R, Tiwari GN (2017) Annual performance evaluation (energy and exergy) of fully covered concentrated photovoltaic thermal (PVT) water collector: an experimental validation. *Sol Energy* 146:180–190

17. Wilhelm D, King-Hang L, Josie C (2006) Efficiency and degradation of a copper indium diselenide photovoltaic module and yearly output at a sunny site in Jordan. *Appl Energy* 83(12):1339–1350
18. Kaplanis S, Kaplanis E (2011) Energy performance and degradation over 20 years performance of BP c-Si PV modules. *Simul Model Pract Theory* 19(4):1201–1211
19. Van Dyk EE, Meyer EL, Vorster FJ, Leitch AWR (2002) Long-term monitoring of photovoltaic devices. *Renew Energy* 25(2):183–197
20. Guenounou A, Malek A, Aillerie M (2016) Comparative performance of PV panels of different technologies over one year of exposure: application to a coastal Mediterranean region of Algeria. *Energy Convers Manage* 114:356–363
21. Kichou S, Abaslioglu E, Silvestre S, Nofuentes G, Torres M, Ramírez, Chouder A (2016) Study of degradation and evaluation of model parameters of micromorph silicon photovoltaic modules under outdoor long term exposure in Jaén, Spain. In: *Energy conversion and management*, vol 120, pp 109–119
22. Meyer EL, Van Dyk EE (2016) Assessing the reliability and degradation of photovoltaic module performance parameters. *IEEE Trans Reliab* 53:83–92
23. Meyer EL, Van Dyk EE (2000) Monitoring I, V and performance parameters of photovoltaic modules. In: *17th European photovoltaic solar energy conference (PSEC)*, pp 524–527
24. Tripathi R, Tiwari GN, Bhatti TS, Dwivedi VK (2017) 2-E (Energy-Exergy) for partially covered concentrated photovoltaic thermal (PVT) collector. *Energy Procedia* 142:616–623
25. Tripathi R, Tiwari GN, Dwivedi VK (2017) Energy matrices evaluation and exergoeconomic analysis of series connected N partially covered (glass to glass PV module) concentrated-photovoltaic thermal (C-PVT) collector: at constant flow rate mode. *Energy Convers Manage* 145:353–370
26. Saini V, Tripathi R, Tiwari GN, Al-Helal IM (2018) Electrical and thermal assessment of N partially covered PVT-compound parabolic concentrator collector connected in series, for different solar cell materials. *Appl Therm Eng* 128:1611–1623

Design of Wind Energy Conversion System Under Different Fault Conditions



Monika Vardia, Neeraj Priyadarshi, Irfan Ali, Farooque Azam,
and Akash Kumar Bhoi

Abstract This work demonstrates an experimental setup of a wind emulator, which is tested over abnormal conditions like sudden change in wind speed, miscommutation in the converter, sudden outage, dynamic change in load, etc. The control system is built with dSPACE DS1104 IC-based real-time board. Simulation and experimental results are obtained from a laboratory 1.2 kW prototype of WECS to show the results under steady-state and dynamic balanced/unbalanced conditions. It also shows the various and comparative experimental and simulation results for developed control system under different situations to demonstrate the robust enhancement in the steady-state and dynamic performance of proposed adaptive fuzzy logic control over traditional system.

1 Introduction

Nowadays, innovations in wind power are growing in the global market. Even 10% potential of wind power, if used properly, can meet world electricity needs. However, the main drawback of wind energy is its unpredictable availability, and it requires other sources as well. Figure 1 illustrates the worldwide wind power capacity. Even with different challenges which the WT industry is facing, it would reach to 760 GW by the year 2020 as per reports of Executive Summary Power Sector, September 2018 [1–6].

M. Vardia · I. Ali
Geetanjali Institute of Technical Studies, Udaipur 313001, India

N. Priyadarshi (✉)
Birsra Institute of Technology (Trust), Ranchi 835217, India
e-mail: neerajrjd@gmail.com

F. Azam
School of Computing and Information Technology, REVA University, Bangalore 560064, India

A. K. Bhoi
Department of Electrical and Electronics Engineering, Sikkim Manipal Institute of Technology,
Sikkim Manipal University, Gangtok, India
e-mail: akash730@gmail.com

© Springer Nature Singapore Pte Ltd. 2020

A. K. Bhoi et al. (eds.), *Advances in Greener Energy Technologies*,
Green Energy and Technology, https://doi.org/10.1007/978-981-15-4246-6_41

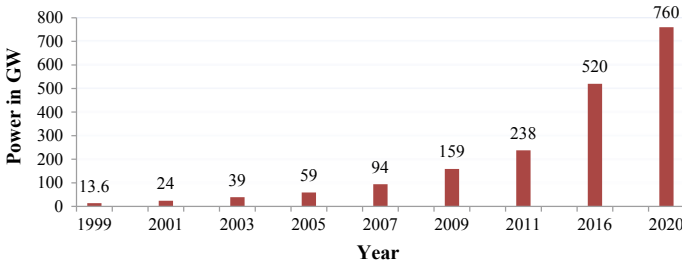


Fig. 1 Cumulative capacity of wind power globally

With 13.1 GW capacity, USA has become the largest market in 2012 in wind power, whereas China is with 13 GW and the EU with 11.9 GW. These three almost constitute about 87% of the global market. As far as manufacturers are concerned, Vestas which is a Danish company is on the prior position as manufacturers since 2000, whereas GE is on the second position because of the strong U.S. market since 2012.

The worldwide top manufacturers of WTs in the year 2018 have been illustrated in Fig. 2, where it can be seen that in the top 10 manufacturers there are four Chinese companies with a total percent share of 17.1% according to reports of Executive Summary Power Sector, September 2017. Also, Fig. 3 presents the growing trends of size of emerging turbine between the years 1980 and 2018.

In the last few years, the wind power has emerged significantly in our country also. India is the fourth largest in the world as far as installed wind power capacity is concerned according to the Renewable Global Status Report, 2018. As of June 30, 2018, the total installation capacity has reached to 34.2 GW and that too mainly across southern, western and northern regions of the country. Tamil Nadu is the largest wind

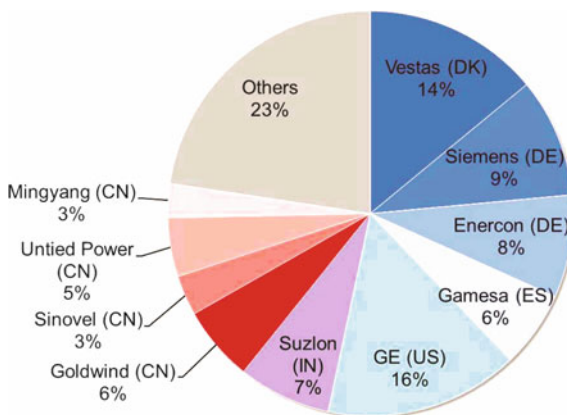


Fig. 2 Distribution of share of market share by the manufacturers of turbines in 2017 (REN21—Renewables 2016 Global Status Report, 2017)

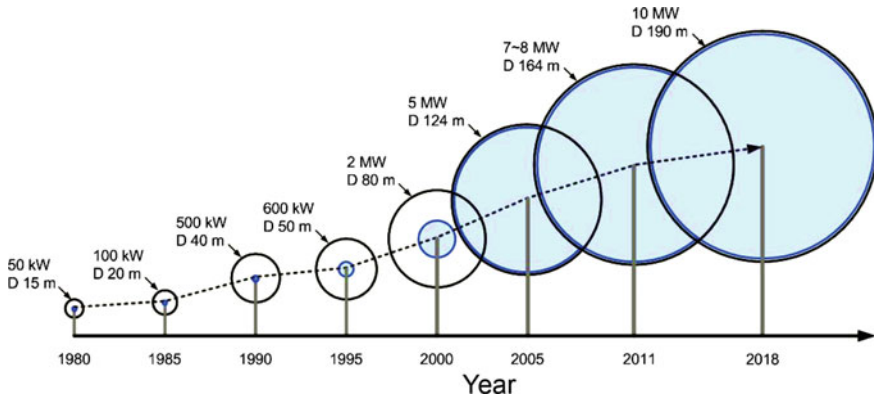


Fig. 3 Scenario of trends in WT size with its rating

power generating state which accounts for nearly 30% of the total, followed by other states as shown in Fig. 4.

It has been predicted that 6000 MW of additional power from wind will be added in our country by 2019. The cost of energy from wind in our country is decreasing rapidly day by day. Wind power tariff is kept low around ₹2.43 per kWh during the auctions for wind projects in December 2018. In December 2018, the government devised some guidelines for wind power tariff so that auctions are clear with minimum risks to the developer. Indian company named Suzlon has emerged globally in the past decade with market share of almost 7.7% in global WT sales. Presently, it is the leading manufacturer of WTs for the Indian market, holding around 43% of market share in our country.

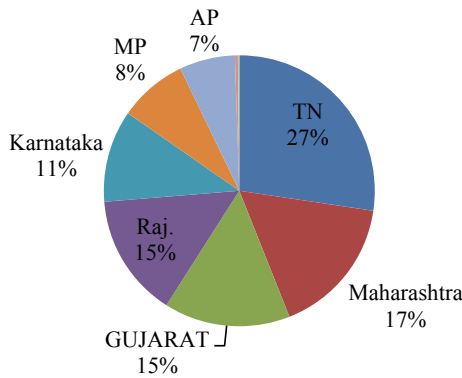


Fig. 4 Top states share in wind power as on December, 2018

2 Power Semiconductor Devices and Converters for WECS

The semiconductor devices serve the base for various power converter configurations used for harnessing the wind energy. It determines several critical performances like cost, reliability, etc. The main technologies for such applications are press-pack packaging IGCT, the modular IGBT and the press-pack designed IGBT. But now, there is tremendous development in SiC devices, which mainly finds like metal oxide semiconductors and diodes. The pressure contact for eliminating the base plate has become the main trends in improving the packaging technology of IGBT module which includes base plate soldering.

In last 45 years, trends in technologies of power electronics have changed dramatically. Initially, it was simply a soft starter which then changed to simple thyristors in 1980s. Later, more advanced diode bridges with a chopper came in the market, and almost 15 years back, more advanced topologies of rectifier–inverter set commonly called as back-to-back power converters were evolved for the WTs. In last five to ten years back, more advanced converters with fast controllers have been tested and commercialized for application in wind power to meet the strict grid code requirements laid down by different governments. Different converter structures have been proposed and developed by different researchers as shown in Figs. 5 and 6.

Figure 5 presents structure of a direct-drive synchronous-generator-interfaced wind generation system, where the power modulator system consists of the rectifier–inverter set and the DC link, where role of rectifier is to regulate output power of the generator [7–11].

Also, the grid-side converter can achieve power or torque control through torque control. The main role of grid-side inverter is to maintain DC-link voltage constant with control of reactive power. Traditionally, the AC/DC/AC or back-to-back converter was adopted for WECS, where GSC is a diode-rectifier oriented with a boost converter, and PWM rectifier is said as voltage source converter (VSC) or a multilevel converter as shown in Fig. 6.

Though AC/DC/AC or back-to-back power converter is cheaper with high density of power, but it has several demerits. It has the demerit of high weight, the poor line pf and large physical dimensions with large DC-link electrolytic capacitor or the

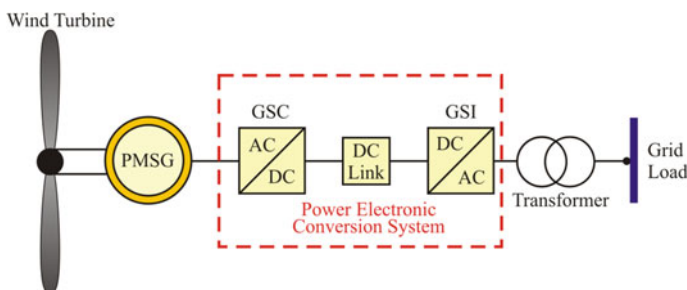


Fig. 5 Block diagram of grid connected wind energy conversion system

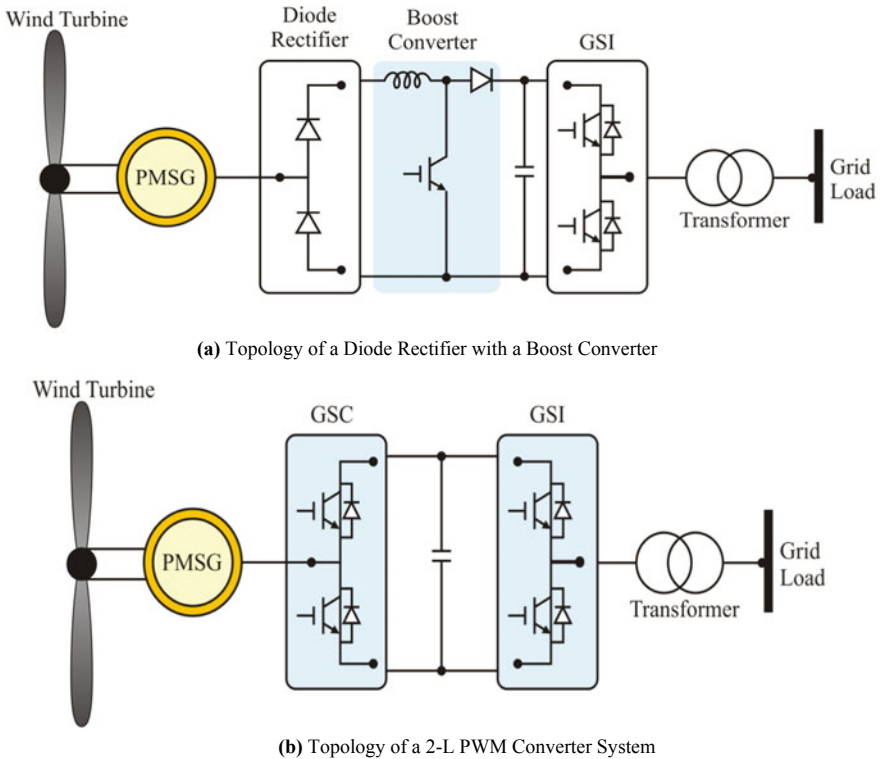


Fig. 6 Topology of direct-drive wind generation system

inductor. Therefore, it is necessary to eliminate the DC capacitor or inductor, which is better power electronics converter topology called as the matrix converter (MC) which has high merit over the conventional back-to-back or the AC/DC/AC converter in terms of compact in size, lightweight, high reliability, etc., as reported by several researchers.

3 Response of Single-Phase Fault Condition

The developed IMC interfaced WECS has been run using MATLAB/Simulation and Sim Power System Toolbox under single-phase faults, which is only because of dips in the system. Single-phase-to-ground fault is applied at time $t = 5$ s for the duration of 0.2 s near to the grid of WECS. The overall response of grid voltage, currents and power during the fault condition is important to be determined in order to develop the ride through various capabilities of the proposed wind energy generation system.

Figure 7 shows the simulated response of various parameters like real and reactive power of IMC, grid and load; IMC currents and voltage, grid currents and voltage

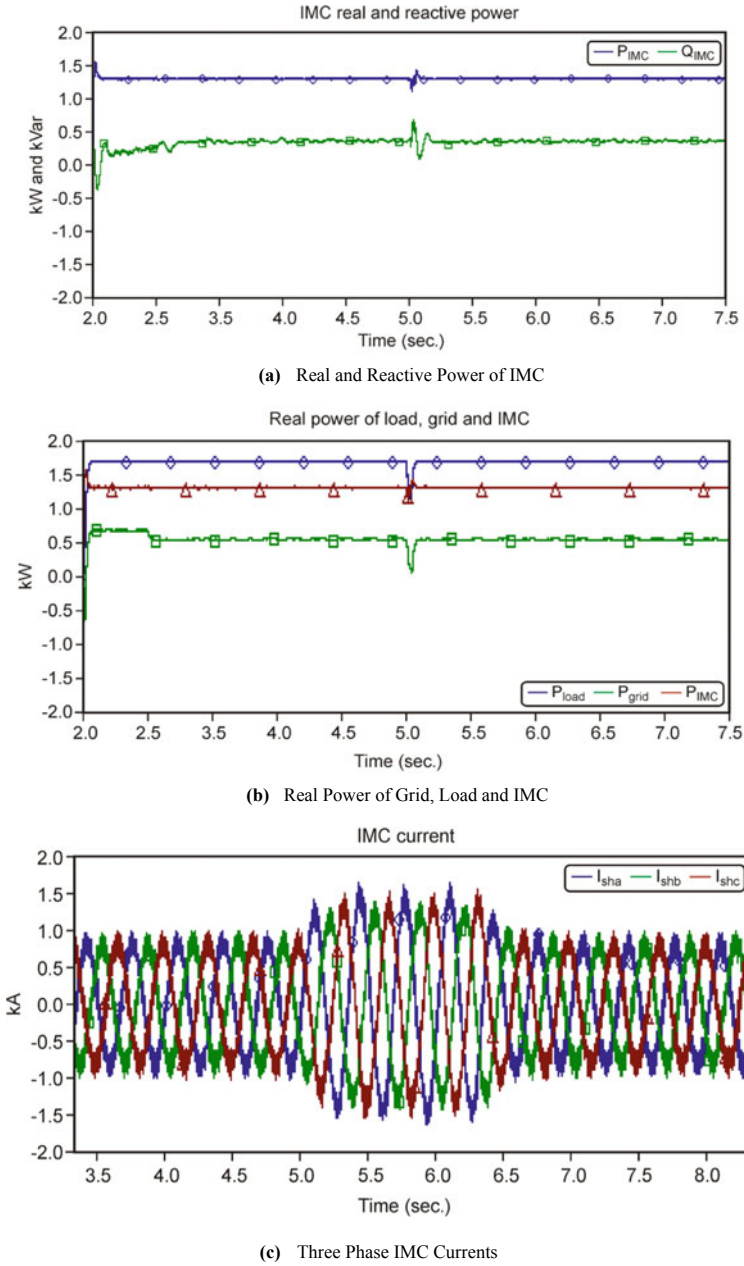
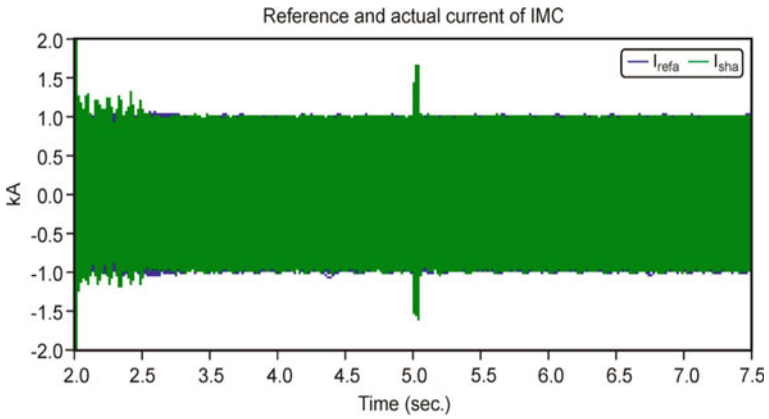
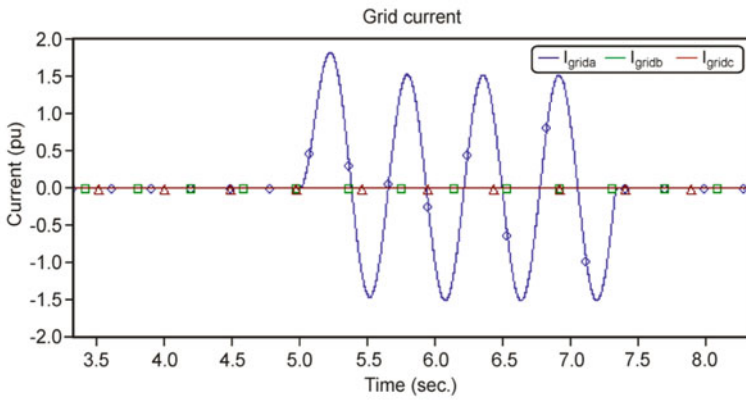


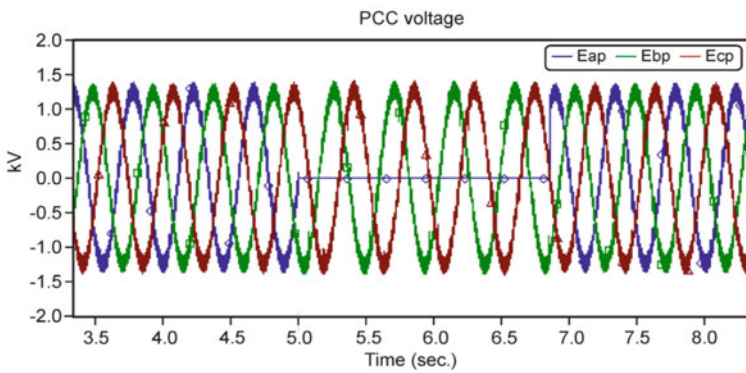
Fig. 7 Simulated responses during single-phase-to-ground fault condition. **a** Real and reactive power of IMC, **b** real power of grid, load and IMC, **c** three-phase IMC currents, **d** reference and actual current of IMC, **e** grid current, **f** grid voltage, **g** output voltage and current of IMC, **h** generator speed



(d) Reference and Actual Phase Current of IMC



(e) Grid Current



(f) Grid voltage

Fig. 7 (continued)

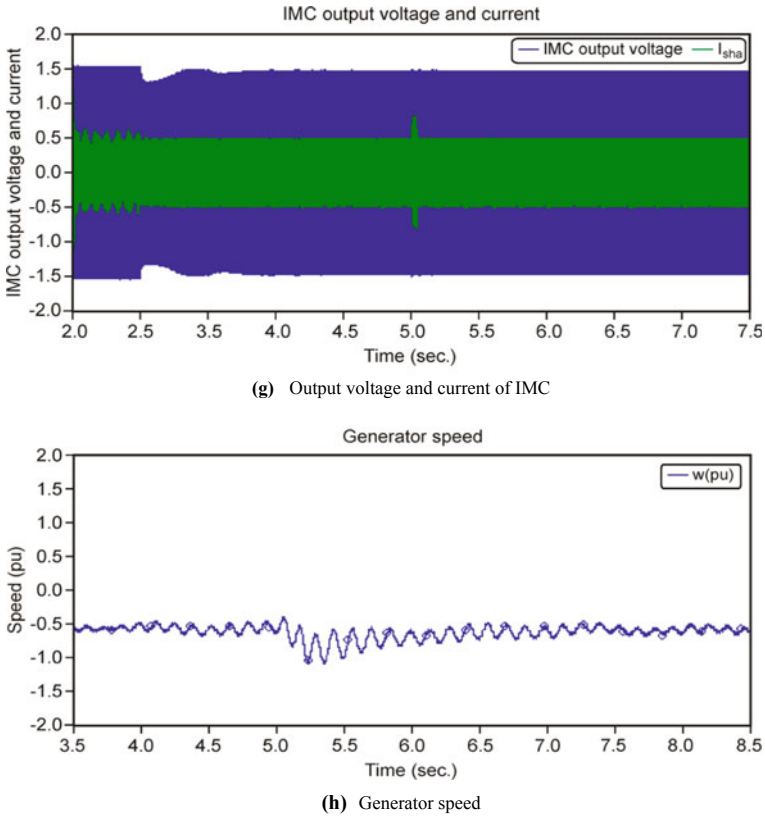


Fig. 7 (continued)

and generator speed of the proposed IMC interfaced grid-connected wind generation system during fault conditions. As shown in Fig. 7a and b, the real power remains almost constant, whereas the reactive power varies within limits during single-phase fault condition. The current supplied by the wind generation system during the fault does not increase beyond the limit set by the controller. The current follows the reference current as shown in Fig. 7d.

The current of faulty phase in grid increases abruptly but within safe limits as shown in Fig. 7e. Figure 7f shows the response of grid voltage during the fault. The generator speed slightly reduces during the fault period, as shown in Fig. 7h. Hence, it can be seen that THD of the grid voltage and current is less than 5% which consent with permissible limits of the IEEE-519 standards.

In Fig. 7f, in proposed adaptive fuzzy logic control system, the grid voltage completely recovers after the fault, so the meeting of grid codes and the wind turbine do not trip. Also, the simulation output waveforms of Fig. 7 shows that the wind energy generation system is not electrically stressed, and by getting the result, it remains connected during and after the fault, thus increasing the transient stability of the

control system. The current of wind generation system also maintains quite below the limit. Also, the grid voltage remains unchanged as observed from waveform. The active power produced by the wind energy generation system makes a small dip and covers in less than 0.15 s as demonstrated in Fig. 7b, and thereby meets the grid code requirement of control system.

It is notified that though the grid currents during the fault increases; but in the proposed adaptive fuzzy logic control system, the unbalance and distortion levels are smaller. About the grid and IMC voltages, the behavior is already acceptable and good as the ripple during the transient that is not bigger than 4.3%, except at the beginning. Also, for the result of the optimal control, the power extracted from the wind is stored in the generator and it causes to speed up.

4 Conclusion

The adaptive fuzzy logic control system detects the optimum blocking period for as per severity of the fault. This proposed adaptive fuzzy logic control system detects the low severity and estimates blocking period of 0.2 ms in order to avoid the extra variations that would be caused by the blocking of the indirect matrix converter valves. MCs have gained increased attention in industry and academia as one of the preferred choices for power electronics converter due to its above-mentioned advantages. Some studies are done on matrix-converter-based wind energy conversion system (WECS) using simulation environment, but still matrix converter hardware prototypes have not been developed and investigated in detail for wind power applications.

References

1. Priyadarshi N, Padmanaban S, Maroti PK, Sharma A (2018) An extensive practical investigation of FPSO-based MPPT for grid integrated PV system under variable operating conditions with anti-islanding protection. *IEEE Syst J* 1–11
2. Priyadarshi N, Padmanaban S, Bhaskar MS, Blaabjerg F, Sharma A (2018) A fuzzy SVPWM based inverter control realization of grid integrated PV-wind system with FPSO MPPT algorithm for a grid-connected PV/wind power generation system: hardware implementation. *IET Electr Power Appl* 1–12
3. Priyadarshi N, Anand A, Sharma AK, Azam F, Singh VK, Sinha RK (2017) An experimental implementation and testing of GA based maximum power point tracking for PV system under varying ambient conditions using dSPACE DS 1104 controller. *Int J Renew Energy Res* 7(1):255–265
4. Priyadarshi N, Kumar V, Yadav K, Vardia M (2017) An experimental study on zeta buck-boost converter for application in PV system. In: *Handbook of distributed generation*. Springer, Berlin. https://doi.org/10.1007/978-3-319-51343-0_13
5. Priyadarshi N, Sharma AK, Priyam S (2018) An experimental realization of grid-connected PV system with MPPT using dSPACE DS 1104 control board. In: *Advances in smart grid and renewable energy*. Lecture notes in electrical engineering, vol 435. Springer, Singapore

6. Priyadarshi N, Sharma AK, Azam F (2017) A hybrid firefly-asymmetrical fuzzy logic controller based MPPT for PV-wind-fuel grid integration. *Int J Renew Energy Res* 7(4)
7. Priyadarshi N, Sharma AK, Priyam S (2017) Practical realization of an improved photovoltaic grid integration with MPPT. *Int J Renew Energy Res* 7(4)
8. Priyadarshi N, Sharma AK, Bhoi AK, Ahmad SN, Azam A, Priyam S (2018) MATLAB/Simulink based fault analysis of PV grid with intelligent fuzzy logic control MPPT. *Int J Eng Tech* 7:198–204
9. Priyadarshi N, Sharma AK, Bhoi AK, Ahmad SN, Azam A, Priyam S (2018) A practical performance verification of AFLC based MPPT for standalone PV power system under varying weather condition. *Int J Eng Tech* 7:338–343
10. Priyadarshi N, Padmanaban S, Mihet-Popa L, Blaabjerg F, Azam F (2018) Maximum power point tracking for brushless DC motor-driven photovoltaic pumping systems using a hybrid ANFIS-FLOWER pollination optimization algorithm. *MDPI Energies* 11(1):1–16
11. Priyadarshi N, Azam F, Bhoi AK, Alam S (2018) An artificial fuzzy logic intelligent controller based MPPT for PV grid utility. *Lecture notes in networks and systems*, vol 46. https://doi.org/10.1007/978-981-13-1217-5_88

A New Wake-Up Modem for Low-Power Communications



Gun-Ho Lee and Eui-Rim Jeong

Abstract The demand for the Internet of things (IoT) technologies is growing rapidly. Hence, it is of paramount importance to address the battery problem associated with IoT devices. Although the required battery life of most of these devices is two or three years, in practice, the battery can last only a few months. The research presented in this paper aims to reduce the power consumption of IoT devices by using the wake-up modem proposed herein. To design low-power IoT devices, we analyze which parts of the devices consume the most power. Based on findings in the literature, the conventional IoT devices account for 60% of the total power consumption in the communication subsystem. Hence, the design of a low-power communication subsystem is critical for the low-power design of IoT devices. IoT devices have a very small amount of data for transmission; besides, data communication occurs very occasionally. Thus, the IoT device is in a standby mode most of the time. To reduce the standby mode power consumption, we propose a wake-up modem and verify its effectiveness and efficiency via computer simulation. Moreover, this paper suggests separating the wake-up modem to detect the wake-up preamble and the main modem for data recovery. While the detection block of the wake-up preamble is working in standby mode, only wake-up receiver blocks are operated, and the remaining receiver blocks are turned off. This greatly reduces the standby mode power consumption. In addition, the wake-up receiver can decrease the portion of the data receiver to the total receiver power consumption, which enables the data transceiver design without considering power consumption. The main radio is turned on when a wake-up preamble is detected. Considering that IoT devices are in standby mode most of the time, the proposed scheme can significantly reduce the overall power consumption since the proposed wake-up modem can reduce power consumption in standby mode significantly. Therefore, by applying the proposed scheme, the total power consumption for

G.-H. Lee

Department of Mobile Convergence Engineering, Hanbat National University,
Daejeon, South Korea
e-mail: rjsg4100@gmail.com

E.-R. Jeong (✉)

Department of Information and Communication Engineering, Hanbat National University,
Daejeon, South Korea
e-mail: erjeong@hanbat.ac.kr

© Springer Nature Singapore Pte Ltd. 2020

A. K. Bhoi et al. (eds.), *Advances in Greener Energy Technologies*,

Green Energy and Technology, https://doi.org/10.1007/978-981-15-4246-6_42

717

communication can be minimized in communication systems whose data transaction does not frequently occur, for example, IoT devices.

Keywords Wake-up modem · Wake-up preamble · Low power · 1-bit quantization · Binary FSK

1 Introduction

The Internet of things (IoT) technology is classified into short-distance communication, such as Zigbee [1], Bluetooth [2], and Wi-Fi [3]; and long-distance communication, such as Narrowband IoT (NB-IoT) [4], LoRa [5], and Sigfox [6]. In this paper, we propose a low-power long-distance transmission structure that consumes much less standby power than existing IoT technologies. Unlike the conventional IoT communication system with a single modulation scheme, the proposed transmission scheme has two blocks. One is a wake-up preamble to determine whether a valid frame signal is received, and the other is a data frame to transmit messages. In the standby state, the receiver checks whether the valid frame is received or not; however, in the standby mode, we propose that only the wake-up preamble search circuit operates and the other radio frequency unit for data reception is turned off. By using the proposed standby operation, power consumption can be reduced remarkably [7]. Once the arrival of the wake-up preamble is confirmed, the power of the data-receiving units is turned on, and data reception begins. The IoT device, in general, has a very small amount of data for transmission; besides, data communication is performed occasionally. Therefore, if the wake-up preamble and the corresponding wake-up reception block are designed to consume very low power, the battery life of the device will be increased significantly.

In this paper, we propose a frequency-shift keying-based wake-up preamble transmission structure and a corresponding low-power wake-up preamble receiver. To reduce the complexity and power consumption of the wake-up receiver, the proposed receiver has a non-coherent receiver structure and reduces the complexity of the correlator to detect the wake-up preamble by using 1-bit quantization of the received signal [8, 9]. Although the 1-bit quantization reduces wake-up performance by 1 dB compared to multi-bit quantization, the benefits of reducing the receiver complexity and power consumption are much greater.

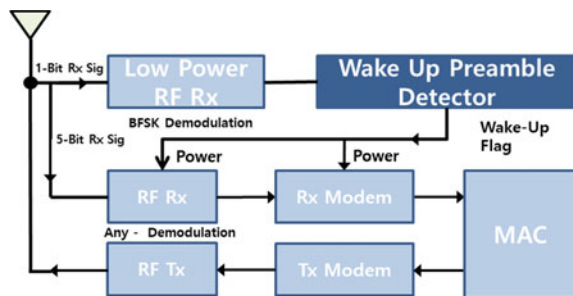
2 Proposed Low-Power Wake-Up Modem

In this section, first, we present the overall structure of the low-power modem proposed in this paper. Then, we explain the wake-up modem in the sequel. Specifically, we describe the modulation and demodulation method of the wake-up modem and the structure of the wake-up preamble detector.

2.1 Overall Receiver Structure and Operation

Figure 1 shows the block diagram of the proposed low-power modem. Herein, we propose a heterogeneous frame structure. Specifically, the transmission frame comprises the wake-up preamble and data. The wake-up preamble uses binary frequency-shift keying (BFSK) modulation, whereas the data use any other modulation technique. The reason for choosing BFSK modulation for the wake-up preamble is that a simple and low-power analog demodulator can be implemented at the receiver. Most existing IoT devices employ a single modem structure for their preamble and data. However, the proposed receiver consists of a wake-up detector and a main receiver. The wake-up detector performs BFSK demodulation and preamble detection, while the main receiver functions to restore data. A heterogeneous frame structure consisting of a wake-up modem and a main modem is characterized by the fact that the preamble and data can employ different modulation techniques. The modulation technique for the preamble should focus on receiver sensitivity and low-power consumption. On the other hand, the modulation scheme for data should consider the receiver sensitivity and spectral efficiency. The proposed transmitter transmits the wake-up preamble at the front of the frame, followed by the data. For the wake-up preamble, a binary pseudo-noise (PN) signal is modulated with the BFSK and then transmitted. The operation of the receiver is as follows. The receiver continuously checks whether the wake-up preamble arrives in the receiver standby mode. A confirmation of the detection of the wake-up preamble indicates the reception of a valid packet. In the receiver standby mode, which continuously checks whether a packet is received, all receiver blocks except the wake-up receiver are turned off. This enables the design of a low-power receiver without considering the power consumption of the remaining data-receiving blocks. This is because the remaining blocks are needed only after a valid preamble arrives. Unlike the conventional communication system, most IoT communication systems operate in the standby mode rather than in the transmission/reception mode. Therefore, if the power consumption of the wake-up preamble detector is reduced, the overall receiver power consumption can be decreased as well.

Fig. 1 Overall structure of the proposed transmitter and receiver



2.2 Wake-Up Transmitter

A transmission frame consists of the wake-up preamble and data. The wake-up preamble is the beginning of the frame, and it is used to indicate packet initialization, whereas data are used for message transmission. We utilize BFSK to modulate the wake-up preamble. Although the BFSK is not the best option to ensure communication performance, such as receiver sensitivity, it is one of the best that guarantees low-power implementation. In this study, we choose BFSK for the preamble because it enables a significant reduction in power consumption in standby mode [10]. Furthermore, data are transmitted using a different modulation scheme while focusing on spectral efficiency and receiver sensitivity.

Figure 2 is a block diagram of the preamble generation architecture. As mentioned earlier, we design the preamble with the PN signal. The initial state is [0 0 0 0 0 0 0 0 0 0 0 0 0 0 1]. The 15th and 14th bits are transmitted as the wake-up preamble after the exclusive disjunction process. By using the above PN generator, a PN sequence up to $2^{15} - 1$ length can be generated.

Figure 3 shows the spectrum of the BFSK modulated wake-up preamble. The figure on the left-hand side shows the spectrum of the transmitted signal, while the figure on the right-hand side shows that of the received signal at a signal-to-noise ratio (SNR) of 15 dB, that is, $SNR = 15$ dB. Since the BFSK modulation scheme is used, the spectrum of the received signal appears as two blue tones, as shown in

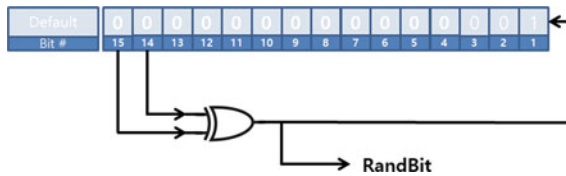


Fig. 2 Wake-up preamble generation block

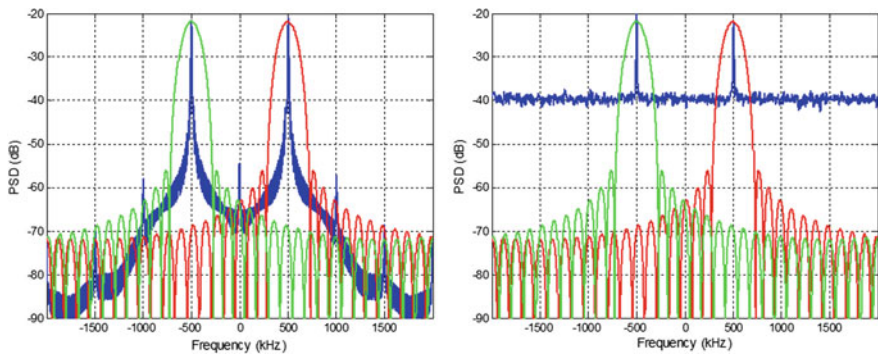


Fig. 3 Wake-up spectrum of the BFSK modulated wake-up signal when SNR is infinite (left) and SNR is 15 dB (right)

the figure. The center frequency represents binary data. Moreover, bits 0 and 1 are assigned to low and high frequencies, respectively.

2.3 Wake-Up Receiver

In this section, we describe the BFSK demodulation and the wake-up preamble detector.

2.3.1 BFSK Demodulation

Figure 4 shows the proposed low-power BFSK demodulation block diagram. The transmit wake-up preamble is BFSK modulated at the following two frequencies: 919 and 921 MHz. Furthermore, the receiver has two band-pass filters (BPFs) for the two frequencies. The envelopes of the two BPF outputs are subtracted, and the resulting single output is used to detect the wake-up preamble.

Figure 5 shows the signals of the two-envelope detector output. Two envelopes are inverted against each other. Unlike the case where the SNR is infinite when the SNR is 15 dB, the envelope detector output is contaminated by the noise. If the envelope of

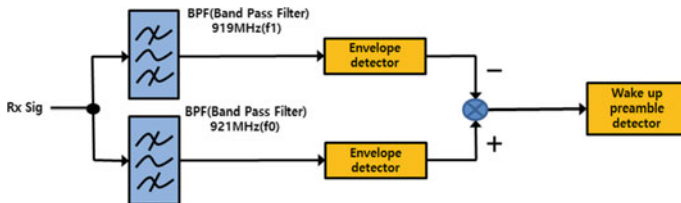


Fig. 4 BFSK demodulation block diagram

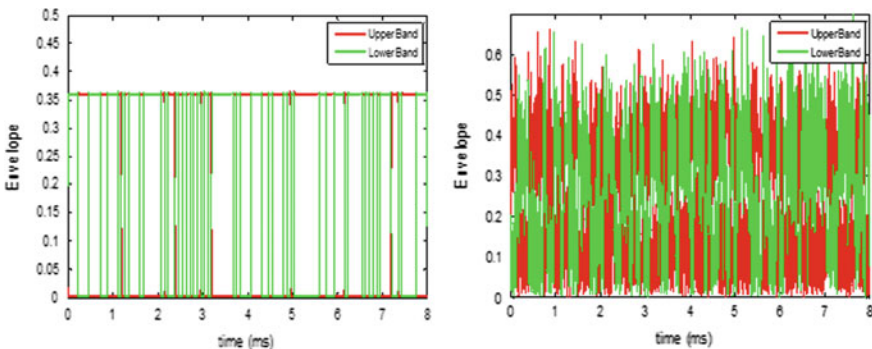


Fig. 5 Overall envelope detector output signal (left: infinite SNR; right: SNR of 15 dB)

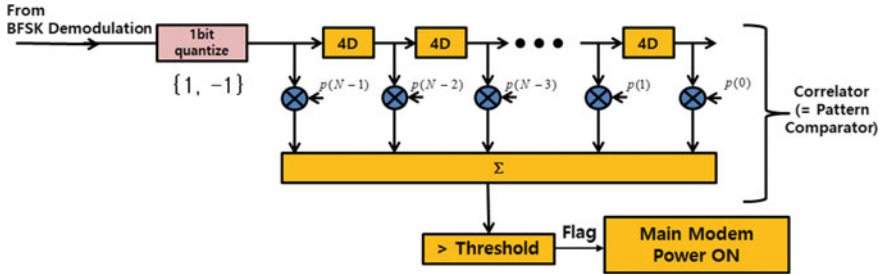


Fig. 6 Wake-up preamble detector structure block diagram

a low frequency is subtracted from that of a high frequency, a positive signal occurs when 1 is received, while a negative signal occurs when 0 is received.

2.3.2 Wake-Up Preamble Detector

After the outputs of the two-envelope detectors pass through the differential element, this signal is subjected to 1-bit quantization, as shown in Fig. 6; that is, only the sign information of the received signal is used. During the 1-bit quantization, the preamble detection performance is degraded due to quantization noise. However, if the length of the wake-up preamble is sufficiently long, quantization noise or loss can be minimized. It should be noted that 1-bit quantization is used because, here, low-power consumption is of more interest than efficient performance. Further, the 1-bit quantization output is input to the cross-correlator. In the cross-correlator, the correlation is calculated by XNOR operation between the 1-bit quantized signal and the transmitted wake-up preamble. Since the transmission preamble is a binary signal that uses the PN sequence and the received signal is a 1-bit quantized output, the correlation can be obtained by an XNOR operation rather than a multiplication operation. This is important to reduce power consumption. In addition, in the 1-bit quantization, the output of the cross-correlator is compared with a threshold value to determine whether a wake-up preamble has arrived or not; besides, this threshold value can be any fixed constant value. If the received signal is quantized to a multi-bit, the threshold should be selected as a function of the SNR. To this end, a block to estimate the SNR of the received signal should be additionally implemented. However, since the threshold can be fixed through 1-bit quantization, power consumption reduction and receiver simplification can be achieved simultaneously.

3 Simulation Results for Wake-Up Preamble Detector

To verify the performance of the wake-up preamble detector, in this section, we conduct a computer simulation. Furthermore, we compare and analyze the frame

detection error ratio (FER) versus the wake-up preamble length and FER performance versus multi-bit quantization. The simulation environments are as follows: the bit rate is 50 kbps, the received sampling clock is 200 kHz (4-times oversampling), the tone spacing is 1 MHz, and the channel is an additive white Gaussian noise.

Figure 7 shows the wake-up preamble detection performance. The X-axis denotes the SNR, while the Y-axis represents the FER. From the figure, one observes that the wake-up preamble detection performance improves as the preamble length increases. For example, if the preamble length is 4095, the FER is below 1E-3 at SNR = 0 dB. This figure indicates that by increasing the preamble length, one can detect the arrival of a packet at a very low SNR.

Figure 8 shows the FER performance with respect to the preamble length and multi-bit quantization. When the preamble length is 63 or 255, wake-up preamble detection is possible at high SNRs over 6 dB. Also, when the preamble length is 1023 or 4095, preamble detection is possible at low SNRs. Therefore, the preamble length can be designed based on intended applications, such as short- or long-distance communication. Furthermore, the 1-bit quantization indicates performance loss due to quantization noise; besides, the loss is about 1 dB. However, if a sufficiently long preamble length is used as described above, the preamble detection performance can be sufficiently improved. Regarding multi-bit quantization, the deterioration in performance due to quantization noise is smaller than the 1-bit quantization since the preamble length becomes longer. By using 1-bit quantization throughout the simulation, we found that it is possible to design a communication system by varying the quantization bit and the preamble length following the designer’s specifications.

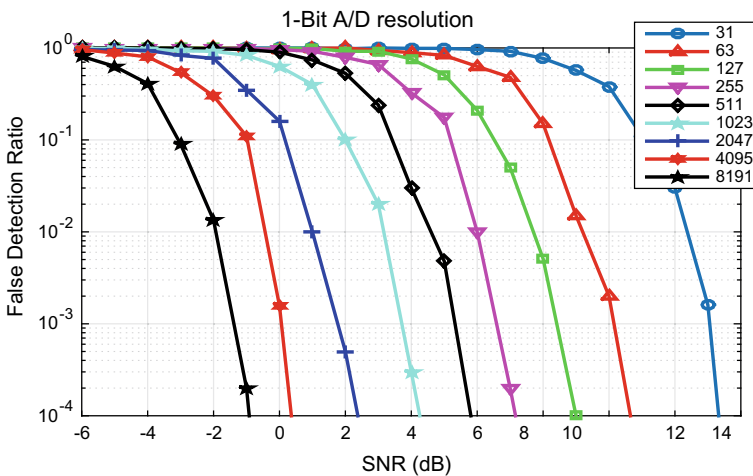


Fig. 7 Simulation to determine the performance of FER based on the wake-up preamble length

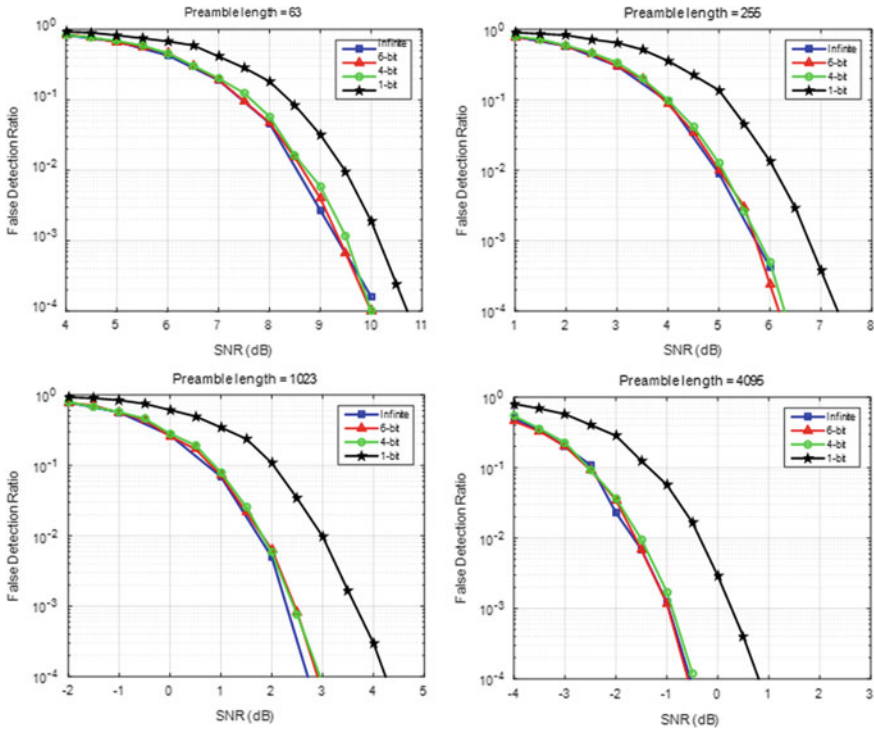


Fig. 8 Simulation of FER performance by N -bit quantization

4 Summary/Conclusion

In this paper, we have proposed a low-power wake-up preamble and detector and found that it is possible to reduce the complexity and power consumption in the standby mode. The proposed architecture can serve as an alternative to the IoT communication solution for limited power applications.

References

1. Wang W, He G, Wan J (2011) Research on Zigbee wireless communication technology. In: IEEE 2011 international conference on electrical and control engineering, no. 51077079, pp 1245–1249
2. Sairam KVSSSS, Gunasekaran N, Redd DR (2002) Bluetooth in wireless communication. IEEE Commun Mag 40:90–96
3. Chou C-M, Li C-Y, Chien W-M, Lan K-C (2009) A feasibility study on vehicle-to-infrastructure communication: WiFi vs. WiMAX. In: IEEE 2009 tenth international conference on mobile data management: systems, services and middleware

4. Ratasuk R, Vejlggaard B, Mangalvedhe N, Ghosh A (2016) NB-IoT system for M2M communication. In: IEEE wireless communications and networking conference (WCNC), pp 1–5
5. Petric T, Goessens M, Nuaymi L, Toutain L, Pelov A (2016) Measurements, performance and analysis of LoRa FABIAN, a real-world implementation of LPWAN. In: IEEE 27th annual international symposium on personal, indoor, and mobile radio communications (PIMRC), pp 1–7
6. Lauridsen M, Vejlggaard B, Kovács I, Nguyen HC, Mogensen PE (2017) Interference measurements in the European 868 MHz ISM band with focus on LoRa and SigFox. In: IEEE wireless communication and networking conference (WCNC), pp 1–6
7. Lee I, Sylvester D, Blaauw D (2017) A subthreshold voltage reference with scalable output voltage for low-power IoT systems. *IEEE J Solid-State Circuits* 52:1443–1449
8. Boufounos PT, Richard G (2008) 1-Bit compressive sensing. In: IEEE 2008 42nd annual conference on information sciences and systems
9. Rabbachin A, Stoica L, Tiuraniemi S, Oppermann I (2004) A low cost, low power UWB based sensor network. International workshop on wireless ad-hoc networks (IWVAN)
10. Ayers J, Mayaram K, Fiez TS (2007) A low power BFSK super-regenerative transceiver. In: 2007 IEEE international symposium on circuits and systems, pp 3099–3102

Effective and Reactive Power Measurement Technique Using a Phase Angle of Voltage-Based Current DFT



Ji-Hoon Yang, Seong-Mi Park, and Sung-Jun Park

Abstract Background/Objectives: Recently, customers have asked for highly reliable quality power and various energy operation services. To meet this expectation, it is necessary to investigate a new energy operation paradigm integrating information telecommunications technology. The present government, too, actively, promotes commercialization of green power IT technology and export industrialization as part of “low-carbon green growth” and “green energy industrial development strategy.” Methods/Statistical analysis: This paper could detect the current information as a result of the application of DFT algorithm based on the measured voltage phase. At this time, as a result of a simulation using PSIM tool, it could simply be separated into the term of effective power component and the term of reactive power component, and it was noted that it had an excellent rapid response in detecting effective power as compared to the existing method. In addition, the below conclusions could be drawn as a result of the production of an actual digital measuring system and the application of it to a single-phase power measurement. Findings: This paper measured the current, applying a DFT algorithm based on the angle of the voltage phase to detect power information about the fundamental harmonic component. At this time, in applying the DFT algorithm, terms in Fourier series can be separated into an effective current component with the same phase as the voltage and reactive current component with a phase difference of 90° with voltage. Thus, the proposed power measurement technique can make simple calculations, not applying “zero-level detection method” and “phase angle detection method through software” in reactive power detection. Thus, this study could express reactive power as an algebraic sum in calculating it and could reduce the complexity. Improvements/Applications: It is expected that the

J.-H. Yang · S.-J. Park (✉)

Department of Electrical Engineering, Chonnam National University, Gwangju, Korea
e-mail: sjpark1@jnu.ac.kr

J.-H. Yang

e-mail: mydream1120@naver.com

S.-M. Park

Department of Lift Design Engineering, Korea Lift College, Geochang 50141, Korea
e-mail: seongmi@klc.ac.kr

© Springer Nature Singapore Pte Ltd. 2020

A. K. Bhoi et al. (eds.), *Advances in Greener Energy Technologies*,

Green Energy and Technology, https://doi.org/10.1007/978-981-15-4246-6_43

power measurement technique proposed in this paper will be utilized as a power measurement technique through its advantages that it has less complexity as compared to the existing method and can be composed simply.

Keywords Discrete Fourier transform (DFT) · Power measurement method · Phase angle of the voltage · Green energy industrial · IT technology

1 Introduction

Recently, customers have asked for highly reliable quality power and various energy operation services. To meet this expectation, it is necessary to investigate a new energy operation paradigm integrating information telecommunications technology. The present government, too, actively, promotes commercialization of green power IT technology and export industrialization as part of “low-carbon green growth” and “green energy industrial development strategy” [1–3]. For the optimization of power operation, it is essential to develop a digital power measurement device integrating IT technology. Especially, when harmonic content flows into voltage and current, distortion of waveform takes place, and as pulsation component exists in the effective/reactive power, there is a difficulty in power operation. Thus, for the optimized power operation, it is essential to develop a measuring system that can detect power information about fundamental harmonic components [4–6].

This paper measured the current, applying a DFT algorithm based on the angle of the voltage phase to detect power information about the fundamental harmonic component. At this time, in applying the DFT algorithm, terms in Fourier series can be separated into an effective current component with the same phase as the voltage and reactive current component with a phase difference of 90° with voltage. Thus, the proposed power measurement technique can make simple calculations, not applying “zero-level detection method” and “phase angle detection method through software” in reactive power detection. Thus, this study could express reactive power as an algebraic sum in calculating it and could reduce the complexity [7–9].

2 Single-Phase Power

2.1 General Single-Phase Power Measurements

Figure 1 shows the general measurement principle of the calculation of power with the measured values of alternating voltage and current. In general, instantaneous power is expressed as the times of voltage and current, and the average power in one cycle is defined as Eq. (1).

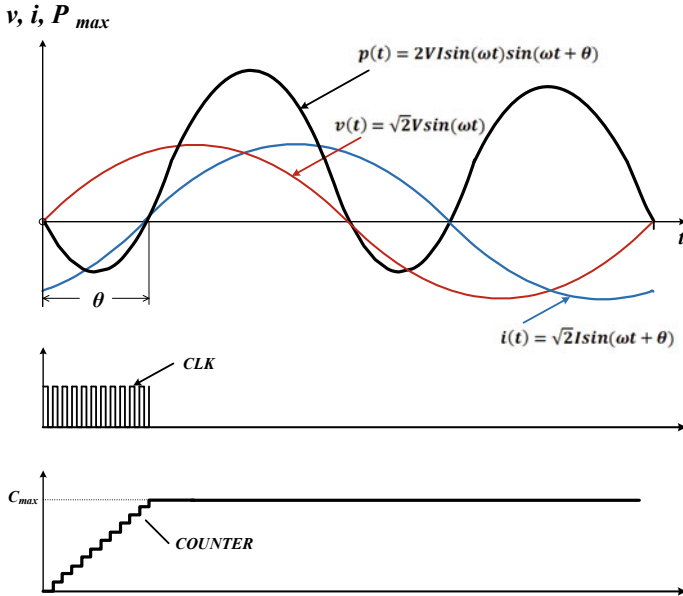


Fig. 1 Voltage, current, power and phase angle waveforms

$$p = \frac{1}{T} \int_0^T v(t) \cdot i(t) dt \tag{1}$$

In addition, effective values of voltage and current for one cycle are defined as Eqs. (2) and (3) below.

$$V_{rms} = \sqrt{\frac{1}{T} \int_0^T v^2(t) dt} \tag{2}$$

$$i_{rms} = \sqrt{\frac{1}{T} \int_0^T i^2(t) dt} \tag{3}$$

To calculate volt-ampere [VA] from the effective values of voltage and current, it is defined as Eq. (4).

$$P_a = \sqrt{\frac{1}{T} \int_0^T V^2(t) dt} \sqrt{\frac{1}{T} \int_0^T i^2(t) dt} = \frac{1}{T} \sqrt{\int_0^T V^2(t) dt \cdot \int_0^T i^2(t) dt} \tag{4}$$

However, reactive power cannot be calculated through waveform composition, unlike effective power or volt-ampere. Thus, as mentioned previously, the general reactive power measurement method is classified into a phase angle detection method through a zero-level detection method and phase angle detection method through software. As for zero-level detection method, the phase can be measured like Fig. 1. CLK is counted through a digital counter like Fig. 1. Counting begins at the point in time when the voltage cycle begins and stops at the point in time when the current cycle begins. At this time, from the proportional relationship of the entire CLK, the phase differences of voltage and current can be defined as Eq. (5) [10, 11].

$$\theta = \frac{\text{CLK}_N}{\text{CLK}_{\text{Total}}} \times 360[^\circ] \tag{5}$$

Meanwhile, the phase detection method through software is done with the ratio of effective power to volt-ampere, which can be defined as Eq. (6).

$$\cos \theta = \frac{P}{P_a} \tag{6}$$

Previously, the phase angle was detected with this method to calculate the reactive power.

Figure 2 shows the block diagram of the general power measurement device. The general power measurement device consists of an AD conversion part, a phase lag compensation part by a filter, a digital filter part, sensors and an AD offset part, a gain compensation part and a calculation part. At this time, the calculation part detects the phase angle to measure effective/reactive power, and power calculation is made through trigonometric function. Like this, sinusoidal values have disadvantages that it takes much time to calculate them since there is much complexity.

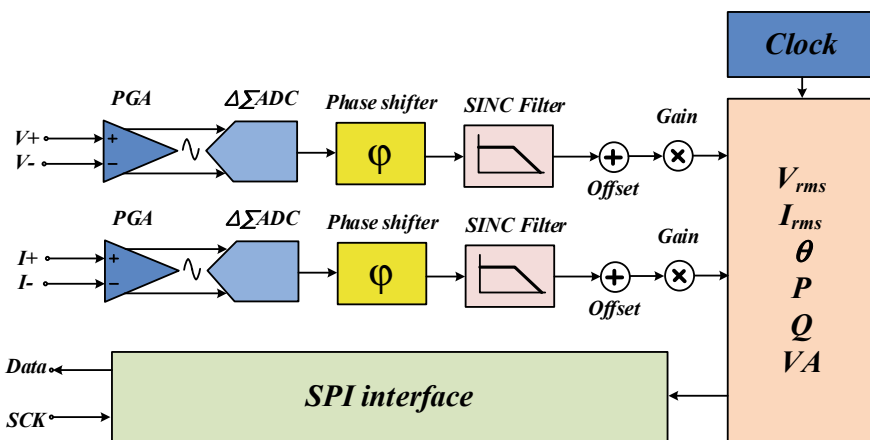


Fig. 2 Typical power meter block diagram

2.2 Single-Phase Power Measurement of the Proposed Scheme

All periodic functions can be expressed like Eq. (7) through a Fourier series.

$$f(\theta) = a_0 + \sum_{n=1}^{\infty} [a_n \cdot \cos(n \cdot \theta) + b_n \cdot \sin(n \cdot \theta)] \tag{7}$$

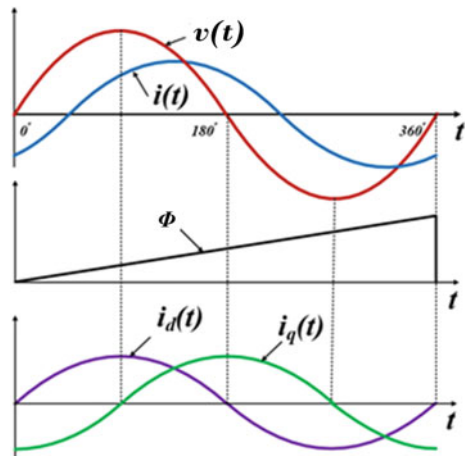
Like Eq. (7), if there is a fundamental harmonic component only, of the DC component, fundamental harmonic component and harmonic content, it can be defined as Formula (8) through Fourier series. At this time, the phase angle θ is a random reference angle.

$$f(\theta) = a_1 \cdot \cos(\theta) + b_1 \cdot \sin(\theta) \tag{8}$$

θ in Eq. (8) is selected as the voltage phase and can be expressed as term a_1 with a phase difference of 90° with voltage and b_1 with the same phase with the voltage. Thus, if Eq. (8) is the same as the current flowing into the load, the load current can simply be expressed as the reactive current term and the effective current term. Figure 3 is the result of DFT of current based on voltage phase.

Figure 4 shows a block diagram of the proposed power measurement device. Like Fig. 4, the phase angle is detected, applying PLL to voltage. It is noted that current information is calculated, applying the DFT algorithm based on voltage phase. The voltage interaction formula is expressed as Eq. (9). At this time, the expression of the fundamental harmonic component, while developing the current with Fourier series, can be defined like Eq. (10).

Fig. 3 Voltage phase angle based current DFT



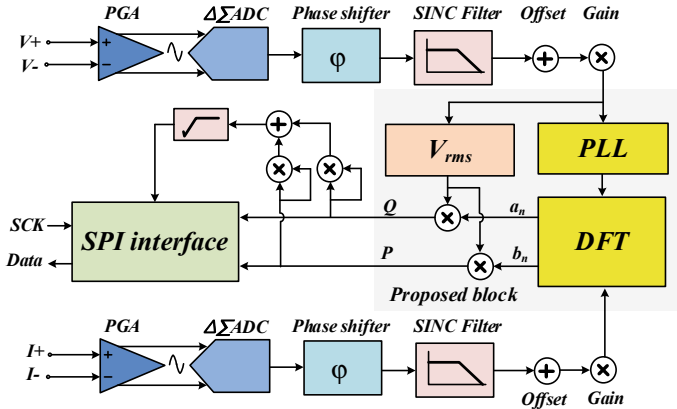


Fig. 4 Block diagram of proposed power meter

$$V(\theta) = A \cdot \sin(\theta) \tag{9}$$

$$i(\theta) = a_1 \cdot \cos(\theta) + b_1 \cdot \sin(\theta) = I_q \cdot \cos(\theta) + I_d \cdot \sin(\theta) \tag{10}$$

From Eq. (10), effective current term I_d with the same phase as the voltage and reactive current term I_q with a phase difference of 90° with voltage can be expressed. Thus, effective power, reactive power and volt-ampere are expressed like Eqs. (11), (12) and (13).

$$P = \frac{1}{2} \cdot A \cdot b_1[\text{W}] \tag{11}$$

$$P_r = \frac{1}{2} \cdot A \cdot a_1[\text{VAR}] \tag{12}$$

$$P_a = \sqrt{p^2 + P_r^2}[\text{VA}] \tag{13}$$

Methods adapted (pl include reference), any modification of regular methods, the extraction methodology/simulation models, the growth conditions and measurement of plants/animals should be stated. Wherever necessary provide (citation) references1.

3 Simulation and Experimental Results

Figure 6 is the resulting waveform of the simulation of the proposed power measurement technique. Figure 6a is the waveform of voltage and current. Phase difference occurred between voltage and current by RL load. In addition, the load was changed

by adding an RC load in parallel after 100 [ms]. Figure 6b is the waveform as a result of the DFT of current based on the phase angle of the voltage in Fig. 6a for high-precision power measurement. It can be divided into an effective current I_d with the same phase as voltage and a reactive current I_q with a phase difference of 90° with voltage. Figure 6c shows the actual current wave and the current wave applying DFT algorithm. When the load changes, it is noted that it follows the fundamental harmonic component of the actual current normally after one cycle. Figure 6c and d, respectively, show the waveform of power measured through the existing method and the proposed method. It was noted that the reactive power measurement was similar to the existing method, but effective power was measured faster than in the existing method. Figure 6e shows term a_1 with the same phase as the voltage and term b_1 with a phase difference of 90° with voltage in applying the actual DFT algorithm. As a result of a simulation, effective power can be calculated with the times of the effective value of the voltage and the effective value of the effective current equivalent to the term of the effective value of the effective current. Reactive power can be calculated with the times of the effective value of voltage and the effective value of reactive current equivalent to the term of the effective value of the reactive current (Fig. 5).

Figure 7 shows a digital power measurement device that applies the power measurement technique proposed in this study. The external structure of the digital power measurement device consists of a display that shows voltage, current, phase and impedance and behavior switches to operate the measuring system. The internal structure consists of an MCU module for the control and operation of the measuring system, a voltage sensing part, a current sensing part, a digital output part, external devices, a Bluetooth communication module for communication and SMPS for

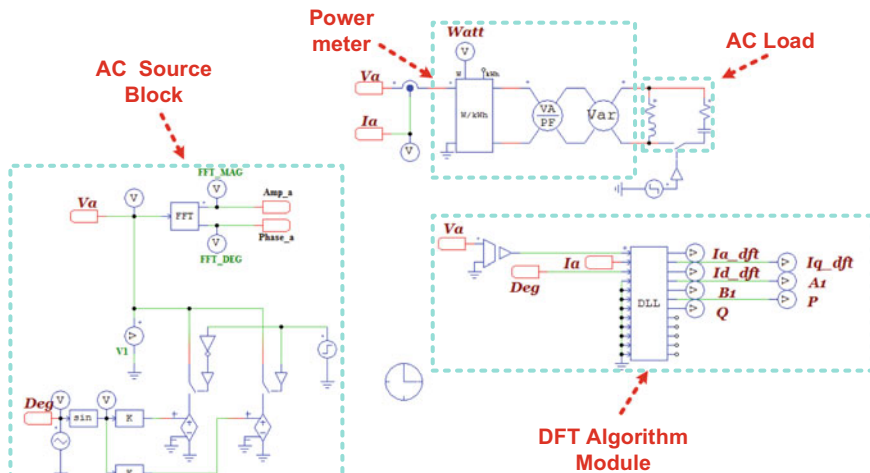


Fig. 5 Simulation circuit diagram of the proposed power measurement technique

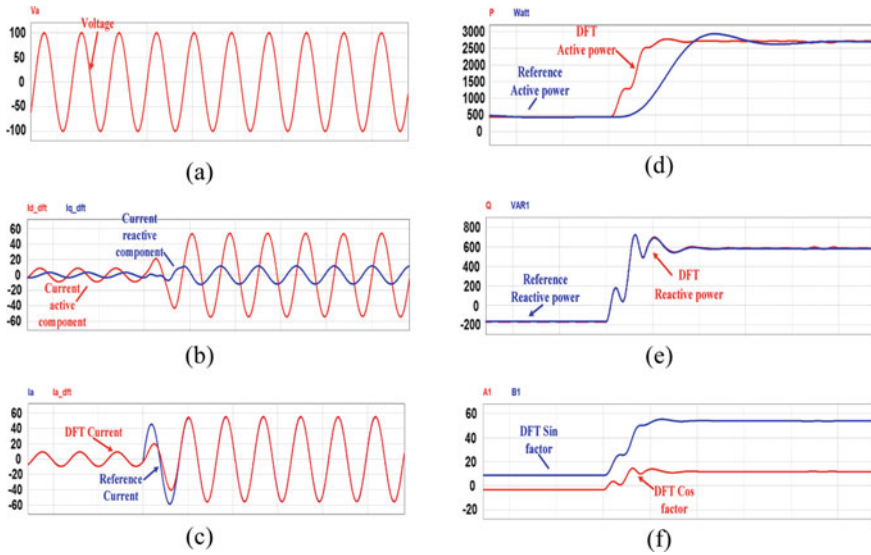
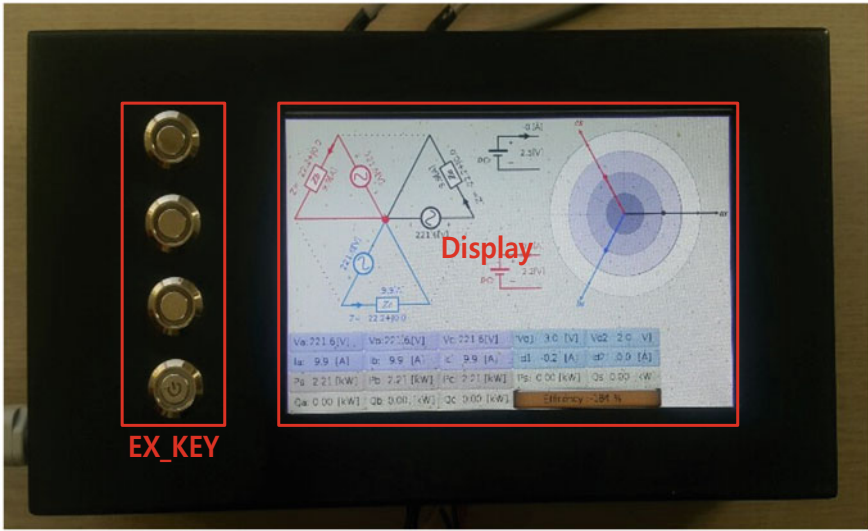


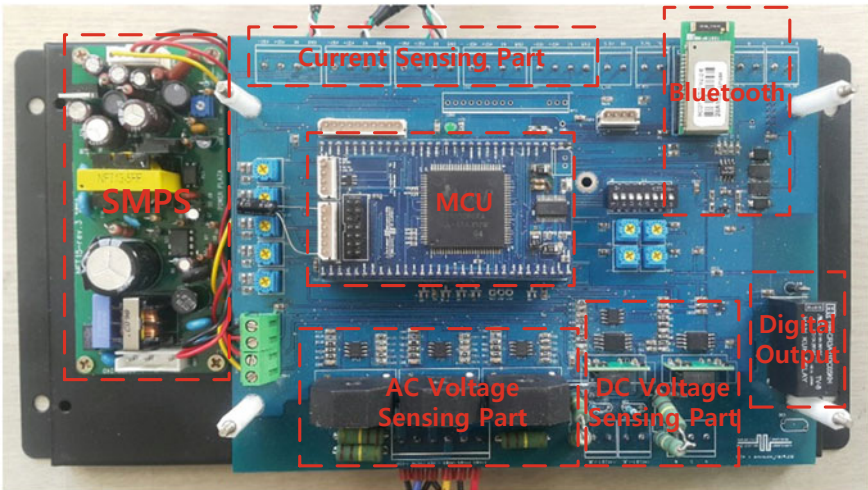
Fig. 6 Simulation results of the proposed power measurement technique waveform

the power supply of the measuring system. It is a structure in which a sensing port is connected to the voltage and current points to measure the sensing port to measure single-phase and three-phase voltage, current and power. Four-channel port was prepared to observe internal values.

Figure 8 is the waveform as a result of the experiment applying the proposed power measurement technique. Figure 8a shows the actual voltage, the actual current and waveforms of I_q and I_d . Voltage and current were measured, applying single-phase AC power to the actual RL load. As a result, there were phase differences in voltage and current by the inductive load. The voltage and current were measured by the produced power measurement device, and the proposed power calculation algorithm using DFT was applied. As a result, it was found out through the experiment that it could be separated into effective current component I_d with the same phase as the voltage and reactive current component I_q with a phase difference of 90° . Figure 8b shows the waveforms of effective power P , reactive power P_r and coefficients a_n and b_n measured using D/A converter applying the proposed power measurement algorithm. It was found out through an experiment that for effective/reactive power and coefficients a_n and b_n , stable power values could be drawn as 20 [ms] passed after the measurement began.



(a) External structure



(b) Internal structure

Fig. 7 Proposed power meter architecture

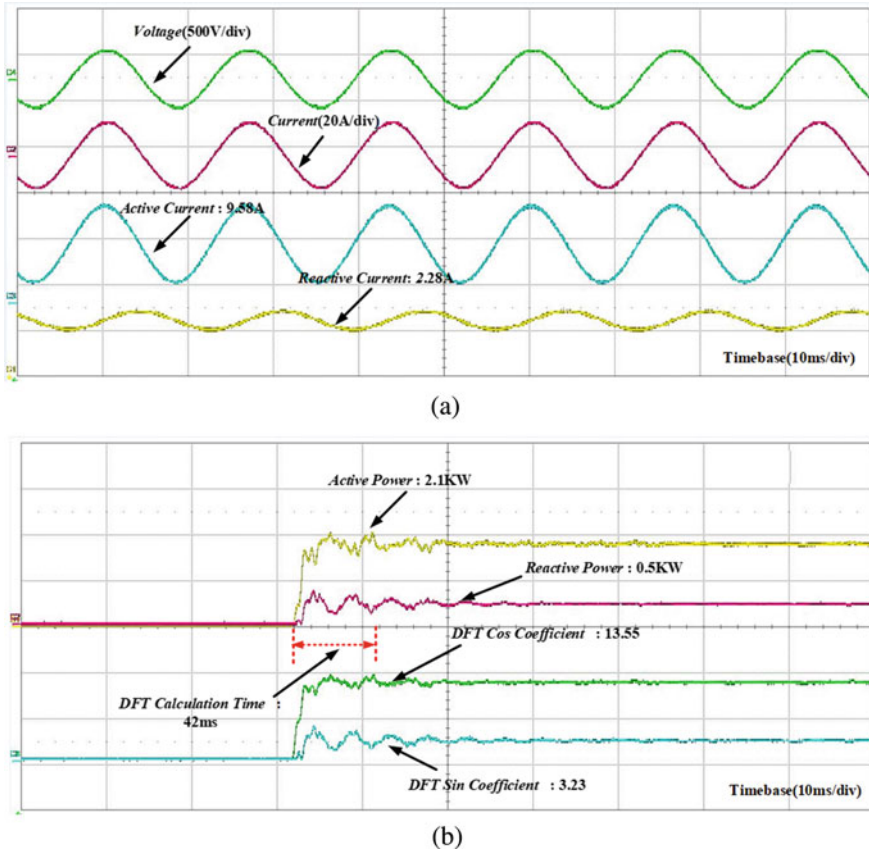


Fig. 8 Experimental results of the proposed power measurement technique waveform

4 Conclusion

This paper could detect current information as a result of the application of DFT algorithm based on the measured voltage phase. At this time, as a result of a simulation using PSIM tool, it could simply be separated into the term of effective power component and the term of reactive power component, and it was noted that it had an excellent rapid response in detecting effective power as compared to the existing method. In addition, the below conclusions could be drawn as a result of the production of an actual digital measuring system and the application of it to a single-phase power measurement.

First, the proposed power measurement algorithm is a new power measurement technique that should not consider the phase contrast of voltage and current. Thus, the time of operation could be reduced to below 30% as compared to the existing method, not applying the trigonometric function.

Second, the proposed power measurement algorithm could increase the sampling frequency by 1.3 times as compared to the existing method and could accordingly enhance precision by 7% as compared to the existing power measurement method.

Lastly, this power measurement device provides various energy operation services by allowing remote control, equipped with mode bus and the Bluetooth function.

Therefore, it is expected that the power measurement technique proposed in this study will be utilized as a power measurement technique through its advantages that it has less complexity as compared to the existing method and can be composed simply.

Acknowledgements This research was supported by Korea Electric Power Corporation. (Grant number:R18XA04).

References

1. Lin C-C, Deng D-J, Kuo C-C, Liang Y-L (2018) Optimal charging control of energy storage and electric vehicle of an individual in the internet of energy with energy trading. *IEEE Trans Industr Inf* 22:2570–2578
2. Serrano-Sanchez C, Olmeda-Delgado M, Petrakopoulou F (2019) Energy and economic evaluation of a hybrid power plant coupling coal with solar energy. *Appl Sci* 9:850
3. Yang X, Song Y, Wang G, Wang W (2010) A comprehensive review on the development of sustainable energy strategy and implementation in China. *IEEE Trans Sustain Energy* 1:57–65 (Institute of Electrical and Electronics Engineers)
4. Renga D, Hassan HAH, Meo M, Nuaymi L (2018) Energy management and base station on/off switching in green mobile networks for offering ancillary services. *IEEE* 2:868–880
5. Jung N-J, Yang I-K, Choi S-H, Jin Y-T, Park S-J (2012) A Study on the requirements analysis and design for system development of remote firmware upgrade management system based-on AMI. *Power Electron Annu Conf* 61:155–161
6. Yoon W-K, Devaney MJ (1996) Power measurement using the wavelet transform. *Korean Ins Illumination Electr Installation Eng* 47:1205–1210
7. Angrisani L, Apuzzo D, Vadursi M (2015) Power measurement in digital wireless communication systems through parametric spectral estimation. *IEEE Instrum Meas Technol Conf Proc* 55:1051–1058
8. Rong-Ching Wu, Chiang C-T (2010) Analysis of the exponential signal by the interpolated DFT algorithm. *Korean Inst Electr Eng* 59:3306–3317
9. Belega D, Petri D (2006) Accuracy analysis of the multicycle synchrophasor estimator provided by the interpolated DFT algorithm. *Inst Electr Electron Eng* 62:942–953
10. Hao H, Bracewell RN (1987) A three-dimensional DFT algorithm using the fast Hartley transform. *Inst Electr Electron Eng* 75:264–266
11. Bjoerk G, Soederholm J (1999) Phase-difference measurements, distributions and the phase-difference minimum uncertainty states. *J Opt B Quantum Semiclassical Opt* 1:315–319

A Preventive Control Strategy of Embedded VSC HVDC in a Large-Scale Meshed Power System



Jaehyeong Lee, Sungchul Hwang, Soseul Jung, Gilsoo Jang, Seungmin Jung, and Minhan Yoon

Abstract When VSC HVDC is applied to the meshed power system, if the appropriate operating point is not determined, it is adversely affected to the total power system. To avoid the side effects of HVDC operation, this paper proposes a method to determine the proper operating point of VSC HVDC. Especially, the control of the VSC HVDC can be a burden for the system operator. In order to alleviate this burden, preventive control should be applied to reduce the burden on system operators. The danger of overloading of the AC line is predicted in advance, so that the operating point at which overload does not occur after an accident is determined as the operating point of VSC HVDC. The typical conventional VSC HVDC control methods are constant active/reactive power control and remedial action scheme. In the former case, there is no control after the contingency, which can cause AC overload or overvoltage problems. The latter controls the operating point for system reliability, but it can be a burden for the system operator and can cause problems in the system in case of communication failure. On the other hand, when applying the preventive control, it is possible to determine an operating range in which the AC load and the overvoltage do not occur even after $N - 1$ contingency in the operating range of VSC HVDC. In addition, in this paper, we proposed an operating point that minimizes the

J. Lee · S. Hwang · S. Jung · G. Jang
School of Electrical Engineering, Korea University, Seongbuk-gu 02841, South Korea
e-mail: bluesky6774@korea.ac.kr

S. Hwang
e-mail: adidas@korea.ac.kr

S. Jung
e-mail: jss928@korea.ac.kr

G. Jang
e-mail: gjang@korea.ac.kr

S. Jung
Department of Electrical Engineering, Hanbat National University, Daejeon 34158, South Korea
e-mail: seungminj@hanbat.ac.kr

M. Yoon (✉)
Department of Electrical Engineering, Kwangwoon University, Seoul 01897, South Korea
e-mail: minhan.yoon@gmail.com

system's total losses in the area. The proposed control strategy can reduce the burden on the VSC HVDC operation and can also provide economic benefits by reducing losses. This will be one of the VSC HVDC operation plans that can be selected by the system operator in the future.

Keywords Embedded VSC HVDC · HVDC operation · Preventive control · System loss minimization · VSC HVDC

1 Introduction

In recent years, as the use of electricity as the final form of energy has increased, such as electric motors and heating and air conditioning equipment, electricity demand is also steadily increasing, making it a large and complex power transmission and distribution system to supply demand from remotely located power plants [1]. As the power system becomes more complicated and larger, there is a problem of large-scale fault current, vulnerabilities on voltage stability and transmission line overloading in urban area power system where the loads are concentrated. In the Seoul metropolitan area, the problems as mentioned earlier are occurring simultaneously [2]. As a solution, the grid segmentation and flexibility improvement through the application of voltage-sourced converter (VSC) high-voltage direct current (HVDC) have been examined [3–5]. The VSC HVDC is a powerful facility that can independently control active power and reactive power. In the case of embedded VSC HVDC in the middle of the system, if it is not properly controlled, it can adversely affect the system [6]. There can be variable control schemes on VSC HVDC. In this paper, we have proposed the stable operation strategy that the system operator does not have to take any additional action for the $N - 1$ contingency and verify it through simulation.

2 VSC HVDC Control Strategy

The operation control strategies of VSC HVDC can be classified into three as follows. The first is constant power control, which is used to maintain constant power output from the generator in one direction [7]. In this method, the output is generally kept below the HVDC rated capacity to bear the output from the remaining line if $N - 1$ DC contingency occurs [8]. This control method is mainly applied to the purpose of generator lead-out line, and when applied to a VSC HVDC in a complex system, there is a problem because there is no additional control according to the system change. In order to solve this problem, a second control strategy, the remedial action scheme (RAS), can be applied. RAS is a control strategy that changes the operating point of the VSC HVDC to ensure system reliability when a disturbance occurs in the system. In practice, many VSC HVDC projects use RAS, to relieve overload of alternating current (AC) system or secure voltage stability [9, 10]. This RAS maintains the

operating point of the VSC HVDC for any purpose in normal operation, and in a transient condition, it changes the operating point only, which is advantageous in terms of economic efficiency or system reliability. However, this control strategy can be an operational burden for system operators. The AC system changes power flow and voltage in response to changes in the system, but because VSC HVDC is not possible, it can be a problem with the system when the appropriate operating point change is not applied. Also, HVDC control is difficult to be performed even if there is a problem with the disturbance communication system of the system.

2.1 Preventive Control Strategy

In order to reduce the burden on the system operator, this paper applies the third control strategy, the preventive control strategy. The prevention control is defined as “The purpose of preventive control is to prepare the system while it is still in steady-state so that the system can adequately handle future uncertainty” in the literature [11]. By applying preventive control to embedded VSC HVDC, it is possible to set the VSC HVDC operation area to maintain reliability standard after AC contingencies in advance and to determine the operating point, so that the operation can be coped with the disturbance without any control. The stable power control range of the VSC HVDC for the $N - 1$ contingencies that can occur in the AC transmission line is shown in Fig. 1. The system operator considers a large number of contingencies, so that the area where overload does not occur even after the contingencies is determined as the normal operation area. Within this operating range, the optimal operating point can be determined by minimizing losses or leveling the line utilization, etc.

However, not all overloads can be eliminated for preventive control. First, it is impossible to control power flow for AC lines that are not sensitive to HVDC control. This is not a disadvantage, but it can also be an advantage, as the uncontrollable lines are not considered a monitoring line for HVDC operation, which is also convenient for the grid operator. Second, there may not be an operating area that can mitigate all

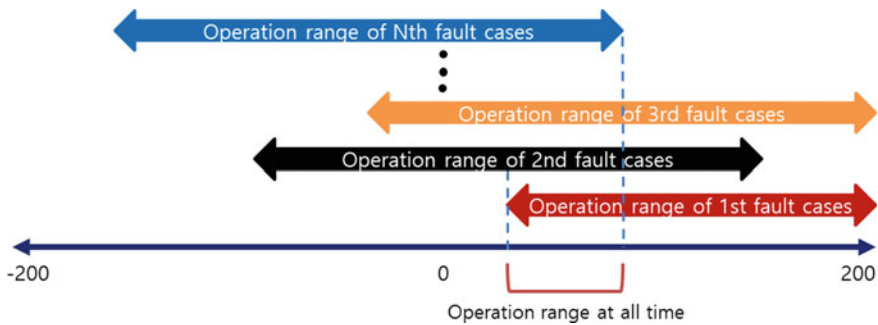


Fig. 1 Overload relief operation range among multiple study cases

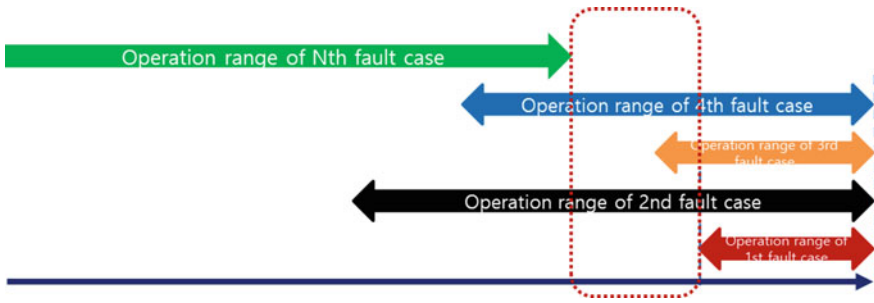


Fig. 2 Non-existence of the overload relief operation range among multiple study cases

overloads after $N - 1$ contingencies. Figure 2 shows the operating range of the HVDC which cannot eliminate the overload when faults occur. In this case, it is necessary to determine the priority of contingencies, which includes the number of overloads that can be eliminated, failure history, the severity of overload and importance of maintaining the transmission line. This criterion should be considered by the system operator in the process of determining the operating point.

2.2 Determination of Optimal Operating Point

In this paper, three factors were considered when determining the optimum operating point (the active and reactive power flow level) for the VSC HVDC: relieving thermal overload, minimizing system losses and minimal adjustment to the VSC HVDC operating point among various operating conditions. In this section, determination of the optimum operating point(s) for the VSC HVDC is discussed. The method used for determining the optimum operating point is as follows. To help explain the process, Fig. 3 shows a flowchart of the process used in this analysis.

- (1) Determine the operating point (active and reactive power flow level for the VSC HVDC) which minimizes the system losses for each studied case.
- (2) Check the overloaded lines and transformers under studied contingencies at the operation point which was determined in (1).
- (3) If there is any overload in the results, determine the operation range of the HVDC which can mitigate the overload in each case.
- (4) Determine the operating point to minimize the system losses within the HVDC operating range that eliminates all overloads in a study case.
- (5) Repeat step 3–4 to determine the operating range which can mitigate all overloads in all studied cases.
- (6) Determine the optimum operating point to minimize system losses within the identified operating ranges that mitigated contingency overloads.
- (7) Loss calculation was for the entire test system. Automatic $N - 1$ and $N - 2$ contingencies were evaluated.

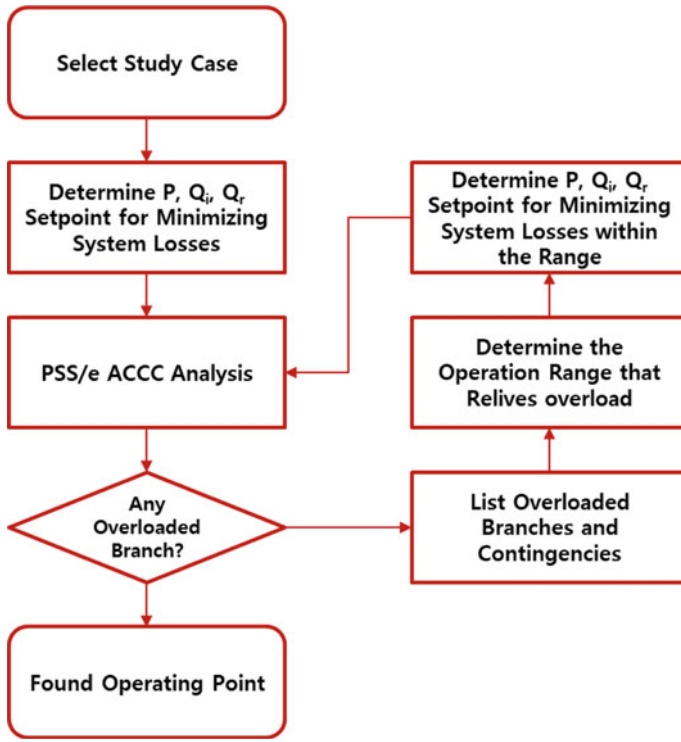


Fig. 3 Flowchart for determining operating point

Equations (1–5) shows an equation for calculating the system total losses. The constraint conditions for the equations in the determination of the operating point include the post-contingency operation region considered in the preventive control and the maintenance of the reliability criterion in normal operation. $Loss_{total}$ is the system total losses, $Loss_{AC}$ is the AC system losses, $Loss_{DC}$ is the HVDC line losses, $Loss_{DC,conv}$ is the HVDC conversion loss, $P_{r,AC}$, $P_{r,DC}$ are the AC/DC line flow active powers at the receiving end, $P_{s,DC}$ is the DC line flow active powers at the sending end, Q_r is the AC line flow reactive powers at the receiving end, $V_{r,AC}$, $V_{r,DC}$ is the AC/DC voltage at the receiving end, and ω is the loss rate of the converter.

$$Loss_{Total} = Loss_{AC} + Loss_{DC} \tag{1}$$

$$Loss_{AC} = \frac{p_{r,AC}^2 + Q_r^2}{V_{r,AC}^2} \cdot R_{AC} \tag{2}$$

$$Loss_{DC} = Loss_{DC,line} + Loss_{DC,conv} \tag{3}$$

$$\text{LOSS}_{\text{DC,line}} = \frac{P_{r,\text{DC}}^2}{V_{r,\text{AC}}^2} \cdot R_{\text{DC}} \quad (4)$$

$$\text{LOSS}_{\text{DC,conv}} = (P_{r,\text{DC}} + P_{s,\text{DC}}) \cdot \omega \quad (5)$$

3 Case Study

3.1 System Description

Korea Electric Power Corporation's (KEPCO's) power system in the metropolitan area has multiple loops to improve system reliability. However, this configuration led to increased fault current, and the fault current levels are becoming a concern. Another known issue in the metro area is related to voltage stability, particularly in the northern part of the metro area where there is concentrated power generation. Additionally, there is a concern of thermal overload. In order to solve these problems, KEPCO is proposing to segment the grid using a BTB VSC HVDC in the northern part of the metro area. The DC system can reduce fault current by segmenting AC networks which potentially alleviate AC system thermal overload by carrying controlled amount of active power through HVDC and improve voltage stability with VSC's reactive power support capability. In this study, the evaluated BTB VSC HVDC was connected between Yangju 154 kV buses. Table 1 and Fig. 4 show the assumed specifications of the Yangju BTB VSC HVDC and system diagram. In this paper, a simulation is conducted to determine the operating point of Yangju BTB VSC HVDC in the Korean system in 2021.

Table 1 Specification of BTB VSC HVDC

Active power capacity	200 MW
Reactive power capacity	100 MVAR
MVA rating	224 MVA
DC voltage	100 kV
Configuration	Symmetric monopole
Conversion loss	2.4% of active power
AC voltage setpoint	1.04 p.u

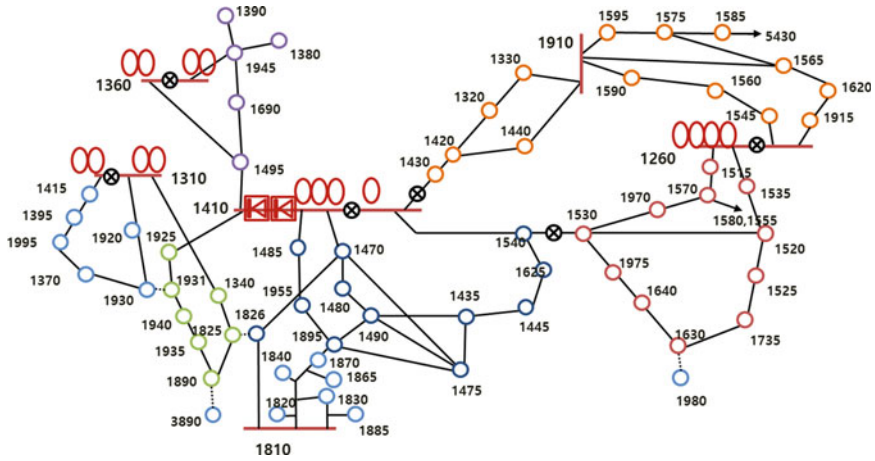


Fig. 4 Northern part of the metropolitan area

Table 2 Operation for loss minimization (without preventive control)

Load condition (%)	Operation for loss minimization (MW, MVAR)		
	P	Q_r	Q_i
100	130	100	100
90	30	100	100
80	20	100	100

3.2 Simulation Result

For the comparison with the optimal operating point applying the preventive control, the operating point of the HVDC considering only the loss minimization was calculated. The results are given in Table 2. When the load conditions of the system are 100, 90 and 80%, the operating point for system total loss minimization at each condition is 1542.79 MW, 1355.75 MW and 1207.38 MW, respectively. However, the losses without HVDC were 1543.84 MW, 1357.09 MW and 1208.79 MW, respectively, and the overall loss was decreased. For comparison, the loss minimization operating point considering preventive control at each load condition was determined.

3.2.1 Load Condition: 80%

The minimum loss operating point within the operating range in which overload does not occur in the event of contingency is determined as follows.

- (1) Optimum active power setpoint identified earlier without consideration of thermal overload: Yangju \rightarrow Yangju S (20 MW).

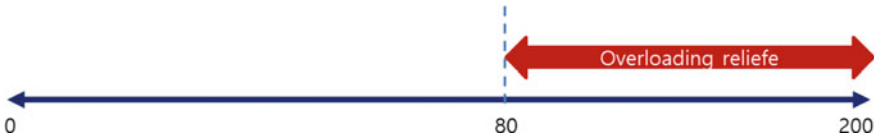


Fig. 5 Operation range to eliminate overload (80%)

Table 3 Comparison of the system losses in the 80% case

System losses		
Without HVDC	With HVDC	
	Before	After (preventive control)
1208.79 MW	1207.38 MW	1207.45 MW (+0.07 MW)

- (2) It was found that the identified overloads can be eliminated if the VSC HVDC operates in the direction of Yangju → Yangju S in 80–200 MW range, as shown in Fig. 5.
- (3) Identified minimum system loss operating point within the range: Yangju → Yangju S (80 MW).
- (4) Rerun ACCC with the VSC HVDC at the new operating point: No overload was found.

Results for 80% case are summarized in Table 3. It shows that system losses are 0.07 MW more when considering the elimination of thermal overload than without the consideration. But losses are still less than those in the case without the HVDC, and buses 1411, 1410 are disconnected.

3.2.2 Load Condition: 90%

At this stage, the minimum loss operating point within the operating range in which overload does not occur in the event of contingency is determined as follows. Since the overload occurs in the case of four contingencies, the range that all overload cases can be resolved is reviewed.

- (1) Previous control: Yangju → Yangju S (30 MW)
- (2) Set the operating range where the overload can be resolved against the contingency: As shown in Fig. 6, all the overloading cases are eliminated when controlling in the direction of Yangju → Yangju S in 140–200 MW.
- (3) The minimum loss operating point within the range: Yangju → Yangju S (140 MW)
- (4) Rerun the ACCC at new operating point: No overload cases

The system loss is increased by 0.01 MW but less than the bus separation case. The results for 90% case are summarized in Table 4.

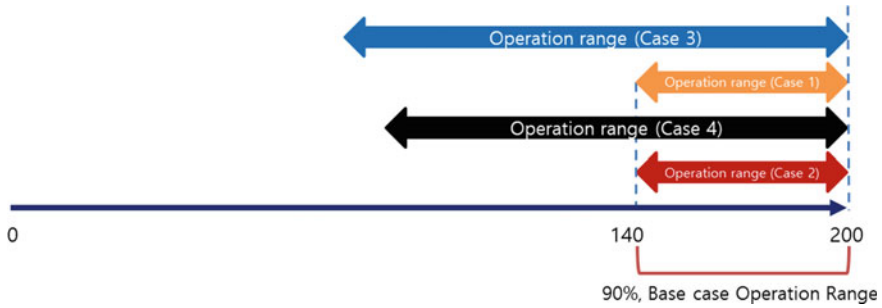


Fig. 6 Operation range to eliminate overload (90%)

Table 4 Comparison of the system losses in the 90% case

System loss	With HVDC		
	Without HVDC	With HVDC	
		Before	After (preventive control)
1357.09 MW		1355.75 MW	1356.00 MW (+0.25 MW)

3.2.3 Load Condition: 100%

There are a number of overloading cases at peak loading condition. At this stage, the minimum loss operating point within the operating range in which overload does not occur in the event of contingency is determined as follows. Since the overload occurs in the case of four contingencies, the range that all overload cases can be resolved is reviewed.

- (1) Previous control: Yangju → Yangju S (130 MW).
- (2) Set the operating range where the overload can be resolved against the contingency: Overloading cannot be eliminated with BTB VSC HVDC capacity.
- (3) It should be operated with the minimum loss operating point.

4 Conclusion

In this paper, we have proposed a VSC HVDC active power control strategy as preventive control for $N - 1$ contingencies in AC transmission line system. We have analyzed the stable operation schemes for the $N - 1$ contingencies and verified that the corresponding operation strategy is suitable through the power flow simulation. Simulation results show that the proposed operation strategy cannot achieve the maximum advantage in terms of loss, but it is possible to obtain an effect of reducing the loss while increasing the convenience of the system operator. In some cases, a new operating point was not proposed, but if the HVDC specification is further

increased, a new operating point will be found. Additional studies that can further improve the efficiency of HVDC while still considering the convenience of the grid operator are still required. In addition to preventive control, RAS also needs control research that enables HVDC to operate and maintain the reliability of the system without the intervention of the system operator.

Acknowledgements This research was supported by Korea Electric Power Corporation (R18XA06-62) and National Research Foundation Grant (No. 2017R1C1B5018073) funded by the Korean government.

References

1. Global energy statistical yearbook 2018 [Internet]. Enerdata; c2019 [cited 5 Feb 2019]. Available from: <https://yearbook.enerdata.net/>
2. Yoon M, Park J, Jang G (2012) A study of HVDC installation in Korean capital region power system. In: Power and Energy Society General Meeting, 1–5 July 2012. <https://doi.org/10.1109/PESGM.2012.6345290>
3. Lee JH, Yoon M, Jung S, Jang G (2015) System reliability enhancement in a metropolitan area using HVDC technology. *J Int Counc Electr Eng* 5(1):1–5. <https://doi.org/10.1080/22348972.2015.1011771>
4. Vovos PN, Song H, Cho K-W, Kim T-S (2013) A network reconfiguration algorithm for the reduction of expected fault currents. In: 2013 IEEE power & energy society general meeting, 1–5 July 2013. <https://doi.org/10.1109/PESMG.2013.6673000>
5. Tongsir S, Hoonchareon N (2011) Fault current limitation in metropolitan power system using HVDC link. In: The 8th Electrical Engineering/Electronics, Computer, Telecommunications and Information Technology (ECTI) Association of Thailand—Conference 2011, 2011 May, pp 840–844. <https://doi.org/10.1109/ECTICON.2011.5947971>
6. Hazra J, Phulpin Y, Ernst D (2009) HVDC control strategies to improve transient stability in interconnected power systems. In: 2009 IEEE Bucharest PowerTech, 1–6 June 2009. <https://doi.org/10.1109/PTC.2009.5281816>
7. Asplund G, Eriksson K, Svensson K (1997) DC transmission based on voltage source converters. *CIGRE SC14 Colloquium* 1–7
8. Frey K, Rudion K, Christian J (2015) Automated operation approach for embedded HVDC links during (N – 1)-conditions in the AC system. In: 2016 IEEE International Energy Conference (ENERGYCON), 1–6 April 2015. <https://doi.org/10.1109/ENERGYCON.2016.7514117>
9. Johnson RK, Klemm NS, De Laneuville, H, Koetschau SG, Wild G (1989) Power modulation of Sidney HVDC scheme. I. RAS control concept, realization and field tests. *IEEE Trans Power Deliv* 4(4):2145–2152. <https://doi.org/10.1109/61.35641>
10. Johnson RK, Klemm NS, Schilling KH, Thumm G (1989) Power modulation of Sidney HVDC scheme. II. Computer simulation. *IEEE Trans Power Deliv* 4(4):2153–2161. <https://doi.org/10.1109/61.35642>
11. Wehenkel L, Pavella M (2004) Preventive vs. emergency control of power systems. In: IEEE PES power systems conference and exposition, 2004, pp 1665–1670. <https://doi.org/10.1109/PSCE.2004.1397528>

Development of BESS Design Plan for Wind Power System Using Short-Term Capacity Factor



Minhan Yoon, Jaewan Suh, and Seungmin Jung

Abstract By comparison with other renewable resources, wind energy penetration has increased significantly in conventional power system. Due to the variability of wind power system, development of wind power system management technologies and compensation devices have been receiving attention in the field of power industries. With storage, the output of the wind farm can be controlled for improving reliability and also having more economic utilization. A new design plan in this paper based on capacity factor for wind system is to consider actual power supply pattern. In this paper, the energy capacity calculation process based on the specific capacity factor of wind farm for micropower system is introduced, and verification processes are performed through PSCAD/EMTDC by using Jeju Island information which is operated in South Korea. The calculation process is considering surplus power which is occurred between generating power and consumption power according to the independent power system operation characteristics and reserve power of the small-scale power system.

Keywords ESS application · Curtailment · Microgrid · Capacity calculation · EMS

1 Introduction

In order to generate the output power efficiently and smoothly, large-scale wind power system is being integrated continuously, and the wind power penetration is also being increased. In the aspect of power system, this state has a possibility about

M. Yoon

Department of Electrical Engineering, Kwangwoon University, Seoul 01897, Korea
e-mail: minhan.yoon@gmail.com

J. Suh

School of Electrical Engineering, Dongyang Mirae University, Seoul 08221, Korea
e-mail: jwsuh@dongyang.ac.kr

S. Jung (✉)

Department of Electrical Engineering, Hanbat National University, Daejeon 305-719, Korea
e-mail: seungminj@hanbat.ac.kr

© Springer Nature Singapore Pte Ltd. 2020

A. K. Bhoi et al. (eds.), *Advances in Greener Energy Technologies*,

Green Energy and Technology, https://doi.org/10.1007/978-981-15-4246-6_45

occurrence of several reliability issues to entire power system due to the system dependency on environmental factor. Most of all, large amounts of wind power penetration can make huge impact to the utility power grid because wind turbine has the characteristics of output fluctuation according to the wind energy environment [1, 2]. In addition, various problems are existed such as reactive power issues and maximum wind speed limitation problem in case of turbulence situation. To solve this kind of issue, a prediction system regarding wind resources has been developed to reduce error between real output power and prediction power [3–5]. Furthermore, several compensation devices have been receiving attention in the wind power system sector, as the previous cost issue had reduced according to the technological developments.

Among the various applications in power system, battery energy storage system (BESS) is one of the most efficient equipments for energy industries. To improve performance of wind power system, application methods of BESS have been developed with various directions. In order to supply wind power to power system appropriately and efficiently, not only technical issue of wind turbine but also comprehensive scheme of integrated energy storage system is being studied. Through integration with BESS, which has fast characteristics of charging and discharging, large-scale wind farm could act flexibly with regarding reactive power or active power about wind power output. The gap between forecasting output and real output is able to reduce with BESS, and the reaction about instantaneous profile of wind power is feasible as well [6, 7]. With this application, the demand response process is expected to be flexible in the future power system which will include large wind power penetration [8–11]. Recently, in case of permanent magnet synchronous generator-based wind turbine (PMSG), the plan to make the output power of wind system smoothly by utilizing BESS at the DC control section is being considered [12, 13].

Since the price issue of the BESS is the greatest point to be considered in real system, the entire capacity calculation and design are significantly influenced by the efficiency of integrated system. For BESS, the peak power reduction is a tough issue because the large-scale system configuration is hard to be considered. This paper is focused on the BESS capacity calculation for large-scale wind farm to reduce output fluctuation which is occurred by uncertainty of wind speed. It is important to determine appropriate capacity by considering scale of wind farm and condition of power grid; nevertheless, there are many controversies about appropriate BESS capacity between wind turbine owner and power system operator. However, there is no appropriate calculation method because each power system has unique characteristic, and specific calculation plan cannot deal with every characteristic.

In this paper, pre-calculation process about BESS capacity is introduced by considering surplus power which is related capacity factor of wind farm. The surplus power is the energy gap between generated power and required load at the target system. By considering this energy, the BESS can be designed in simulation process and should compensate instantaneous power fluctuation in target power grid. The capacity factor, which is utilized as a main parameter, considers abundant wind condition because the BESS should be operated under severe environment. In addition, the proposed system suggests that the suitable proportion of the BESS capacity in reserve power by focusing on the small power system. By using this proposed

calculation process, a microgrid system, which is expected to integrate large-scale wind farm with relatively small consumption power, can calculate BESS capacity in advance. The entire simulation process is based on PSCAD/EMTDC to confirm the electric supply condition.

2 System Description

Wind turbines are connected to utility grid with various ways, but a specific wind farm is usually designed by using one connection topology and same type turbine generator. Along with the cost of permanent magnet material and weight decrease, PMSGs are becoming attractive and receiving attention due to the suitability for composing large-scale wind farm. Figure 1 represents that the composed wind turbine which is integrated with BESS. The wind farm composed by PMSG turbine and the output electrical power is denoted by P_{WT} .

2.1 BESS System Configuration

The $P_B(t)$ is the charging/discharging output power of the BESS and limited by the rated capacity of inverter. Generally, the BESS in power system industry has a similar design including a point of connection (PoC). The BESS should be operated according to a condition of local network to determine whether it is absorbing the released energy from the grid or not. In this paper, the simulation is composed to store the surplus output power of integrated system, and this scheme is formulated with a bidirectional power conversion system (PCS).

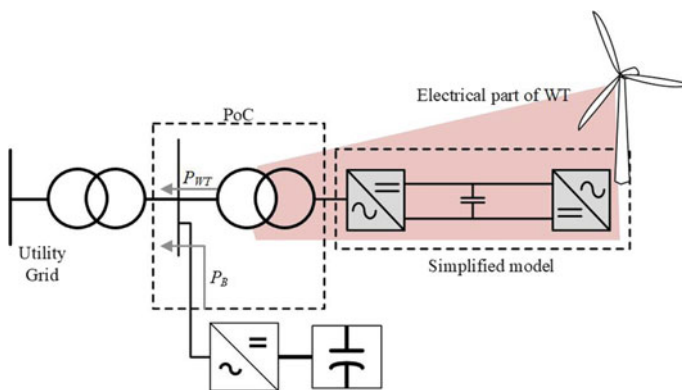


Fig. 1 Design of integrated model and power flow

To consider the battery condition appropriately, state of charge (SOC) of the BESS should be calculated every second by considering the integral output power. The SOC of the BESS cannot exceed certain operational point due to its own lifecycle. This paper is focusing on the output power at PoC, and the relationship is defined as Eq. (1). Also, the relation about the output power by wind farm and ESS is defined as Eq. (2).

$$P_{PoC} = P_{WF} + P_B \tag{1}$$

$$P_{PoC} = P_{WT1} + P_{WT2} + \dots + P_{WTn} + P_B \tag{2}$$

where P_{PoC} is the output profile of connection point. The proposed calculation process is focused on the automatic maximum power point tracking (MPPT) control with BESS to focus on generated surplus power. When it is described as a time function, the relationship can be rewritten as follows:

$$P_B(t) = P_{PoC}(t) - P_{WF}(t) \tag{3}$$

$$P_B(t + 1) = \begin{cases} P_{Load}(t) - P_{min} - P_{WF}(t), & (P_{Load} \geq P_{PoC}) \\ P_{min} + P_{WF}(t) - P_{Load}(t), & (P_{Load} < P_{PoC}) \end{cases} \tag{4}$$

where P_{Load} is the local load of the system and P_{min} is the must-run capacity.

2.2 BESS Charging/Discharging Strategy

Figure 2 shows the basic concept of the BESS control scheme with pre-calculated BESS capacity by considering surplus power of the entire system. Basically, each

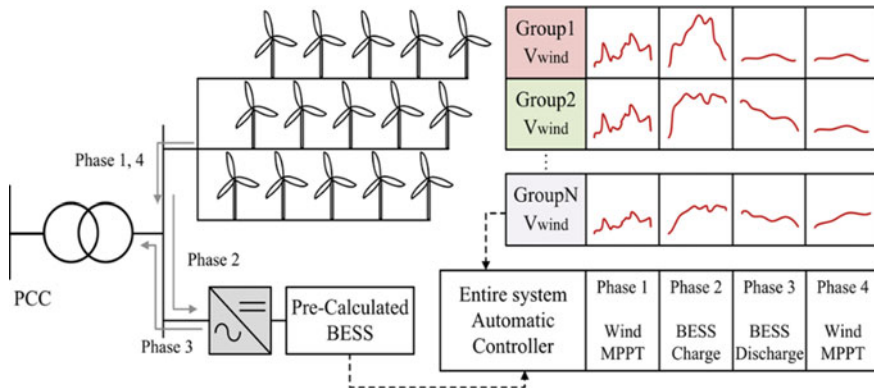


Fig. 2 Concept of MPPT control system integrated with pre-calculated BESS

wind turbine is operated using MPPT control scheme, and the BESS is focusing in active power balance of entire system. Each turbine has different operation status regarding tip speed ratio according to the changed wind speed. The verification process can be performed by composing several wind turbines as a group which is on similar condition with nearby environment characteristic.

The BESS should reply to active power gap between generating power and local demand. However, when total active power exceeds the demand load, the active pitch control has to be utilized to shed off the aerodynamic energy by turning blades. In this paper, the pitch angle is kept zero during the normal operation, but several wind turbines would be controlled using pitch angle control. It would be operated if additional control is required according to the existence of surplus power.

2.3 BESS Capacity Calculation

The capacity factor (CF) is an important parameter which is used in determining the annual energy output of wind power system. It is a significant index of productivity and efficiency of a wind power system. Usually, it shows the fraction of the entire energy delivered over a year. Therefore, it can be formulized by dividing the total output power of certain wind system with the maximum energy assumed by rated power. The capacity factor is defined as follows:

$$CF = \frac{E_{total}}{E_{rate}} = \frac{\text{Total generated power(MWh)}}{P_{rate}(\text{MW}) \cdot t(h)} \quad (5)$$

where E_{Load} is the total output energy of wind system, E_{rate} is maximum output energy of wind system and $P_{rate}(t)$ is maximum output power of wind system. Since the BESS is integrated to mitigate power fluctuation, the realistic output power consideration is required. The capacity factor is closely related with realistic wind system operation because this factor is based on actual output power. However, this factor does not consider an intensity of wind speed that closely relates with specific season. Since the proposed method is focused on the severe environment situation at the minimum load condition, the utilization process regarding capacity factor should consider high wind speed penetration. To utilize this factor in the calculation process appropriately, a classification process about specific period regarding the intensity of wind power fluctuation is required. In this paper, the capacity factor is classified by considering the intensity of wind speed environment. The process includes several wind environment characteristics such as continuity of wind stream during a specific period variability according to seasonal difference.

The process calculates capacity factor by dividing annual data to three sections: high, middle and low. Each capacity factor is defined as follows:

- The high capacity factor (HCF) defines the highest capacity factor section which is linked hours (month interval). That value is used for basic BESS capacity

design; it can be formulized by using minimum output power of local generator and minimum load. The basic BESS energy capacity is composed as follows:

$$C_{\text{BESS}}(\%) = \frac{P_{\text{HCF}} + P_{\text{min}} - P_{\text{Lmin}}}{P_{\text{rate}}} \times 100 \quad (6)$$

where C_{BESS} is the total output energy of wind system, PHCF is wind output power by calculating HCF and P_{Lmin} is minimum load power.

- To apply suitable value for BESS system, other capacity factor sections have to be applied to calculation process. The low capacity factor (LCF) is estimated by using same liked duration with HCF, but it defines the lowest capacity factor. That value is used to calculate minimum BESS capacity by considering possibility factor of minimum load occurrence which is directly related with surplus power. It could be determined by using estimated wind velocity parameter, and transmission system operator (TSO) should select the value by considering entire system load fluctuation.

$$C_{\text{min}}(\%) = \frac{P_{\text{LCF}} + P_{\text{min}} - \beta P_{\text{Lmin}}}{P_{\text{rate}}} \times 100 \quad (7)$$

where C_{min} is minimum BESS capacity and β is load factor of target system.

- In sequence, residual time sections are used to calculate middle capacity factor (MCF), and it is used to prevent excessive energy capacity. The limitation should be determined by considering the fluctuation because the degree is related with rated value of compensation devices. The finalized BESS system would be performed as a reserve device. Therefore, the previous entire reserve power can be used as a value for reducing the BESS capacity. It can be expressed as follows by including above-introduced values:

$$C_{\text{lim}}(\%) = \frac{P_{\text{rate}} + (\text{HCF} - \text{MCF})}{P_{\text{rate}} + P_{\text{rsv}}} \times 100 \quad (8)$$

where C_{lim} is limited BESS capacity and P_{rsv} is reserve power of target system.

3 Data Configuration

The proposed case study is focused on surplus power generated during midnight power service period when having significant possibility of minimum load condition.

Table 1 Power network data of Jeju Island

Year	HVDC capacity (MW)	Min. supply (MW)	Max. supply (MW)	Min. demand (MW)	Max. demand (MW)
2016	400	170	975	410	829
2017	600	170	1175	428	866
2018	600	170	1175	447	905
2019	600	170	1175	466	942

Table 2 Wind capacity growth/prediction data of Jeju

Year	Reserve power (MW)	Controllable power (MW)	Wind capacity prediction (MW)
2016	805	975	564
2017	1005	1175	680
2018	1005	1175	890
2019	1005	1175	1300

In addition, the gap between minimum load and generating power including wind power system is relatively huge in the small-scale power system. This paper plans to introduce the proposed method in the Jeju Island which is operated in South Korea. The system has local generator as controllable reserve power and considers large-scale wind power construction at nearby place. The system characteristics are applied by using the information which is referred in fifth power supply planning of South Korea.

The Jeju Island is interconnected with main power grid of South Korea by HVDC. Although the target system can be supplied with electricity through connection line, the capacity of the line is limited, and the connection line is usually operated as a supply power mode. Owing to the complexity of conversion process for receiving power mode, system operator generally considers the HVDC capacity as a reserve power. Table 1 represents several information of the Jeju Island power system between 2016 (historical data) ~2019 (predicted data) which is handled in simulation process.

The maximum supply power is including HVDC, and the maximum demand power is not exceeding the range of available supply power. Therefore, the case of supply power deficiency is not considered in the configured simulation. The wind power capacity is assumed based on the prediction reports of local government of Jeju Island. The wind power construction capacity is represented in Table 2.

3.1 Simulation Configuration

By considering the Jeju wind farm, case studies were configured by using PSCAD/EMTDC. Figure 3 shows the designed flowchart in this paper. Two different

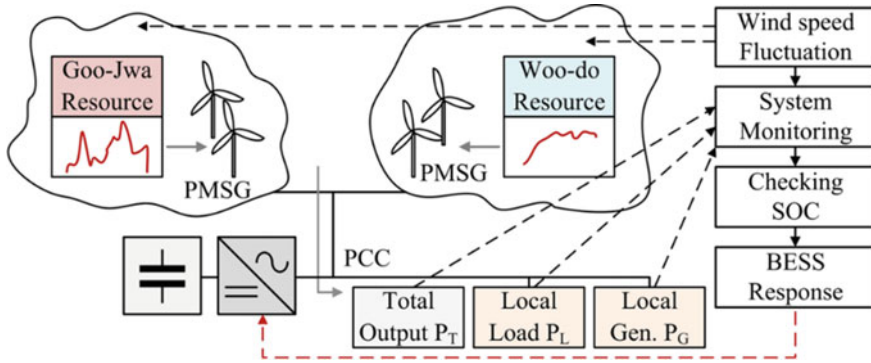


Fig. 3 Data exchange flowchart in PSCAD simulation

regions, Goo-jwa and Woo-do, are applied to reflect different local characteristics. Each wind speed is individually inserted as a signal in the simulation. Table 3 shows each capacity factor data calculated by the proposed equations, and Table 4 shows the related BESS capacity according to the formed percentages. The HCF/LCF is calculated based on linked two months, and the MCF is calculated by using other residual sections. The verification processes for the suitability were performed according to the measured wind data represented in Fig. 4 (January and May). We chose these two cases which represent the highest and the lowest wind potential for simulation progress to verify its availability.

In case of wind farm, the NREL 5 MW PMSG wind turbine is utilized. Taking into account the performance of the PMSG wind turbine, the charging/discharging

Table 3 Calculated capacity factor data

Year	Reserve power (MW)	Controllable power (MW)	Wind capacity prediction (MW)
2016	805	975	564
2017	1005	1175	680
2018	1005	1175	890
2019	1005	1175	1300

Table 4 Designated BESS capacity for each year ($\beta = 0.6$)

Year	Reserve power (MW)	Controllable power (MW)	Wind capacity prediction (MW)
2016	805	975	564
2017	1005	1175	680
2018	1005	1175	890
2019	1005	1175	1300

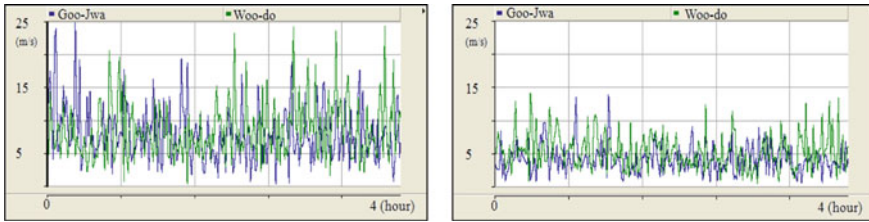


Fig. 4 Designed wind speed data of January and May

processes are carried out by BESS. The battery charging algorithm always focuses whether the entire system meets the balance between supply/demand.

3.2 Simulation Results

In the configured simulation, charging process would be started when the surplus power is generated. The surplus power is expected to exist during the midnight electricity time when considering the power system characteristic. To consider these severe situations, the case studies were mainly focused on the situation by using minimum demand power state.

The generated surplus power could be stored promptly, and it is extracted from wind turbines that utilize MPPT control scheme. The energies stored in the BESS must be consumed in the next discharging phase preferentially to prepare about the next charging process. Figure 5 includes the entire power curve in January case with simulated power system. In the simulation, owing to the wind energy potential difference, BESS charging/discharging processes were continuously operated. In power curve, the brown curve represents the total extracted wind power from the system without BESS. In the case at 2016, surplus power was not produced with BESS, and charged power is consumed at the next phase as shown in green curve. However, in case after 2016, the surplus power is generated during the simulation due to the high wind potential. The blue curve represents required mechanical control power due to the limitation of SOC. Except the blue marked section, excessive power does not occur in the other section.

In Korea, the TSO officially considers two hours for emergency situations that may provide time to respond to the operation of other fuel generators. Therefore, as described in the figure (dashed lines), the BESS compensation is available in the intended strong wind condition. In May, since the wind profile is low, the excess energy was not generated even in 2019 as separately depicted in Fig. 5. It is expected that the composite capacity will provide a suitable solution to cover the excess power generated in normal operation.

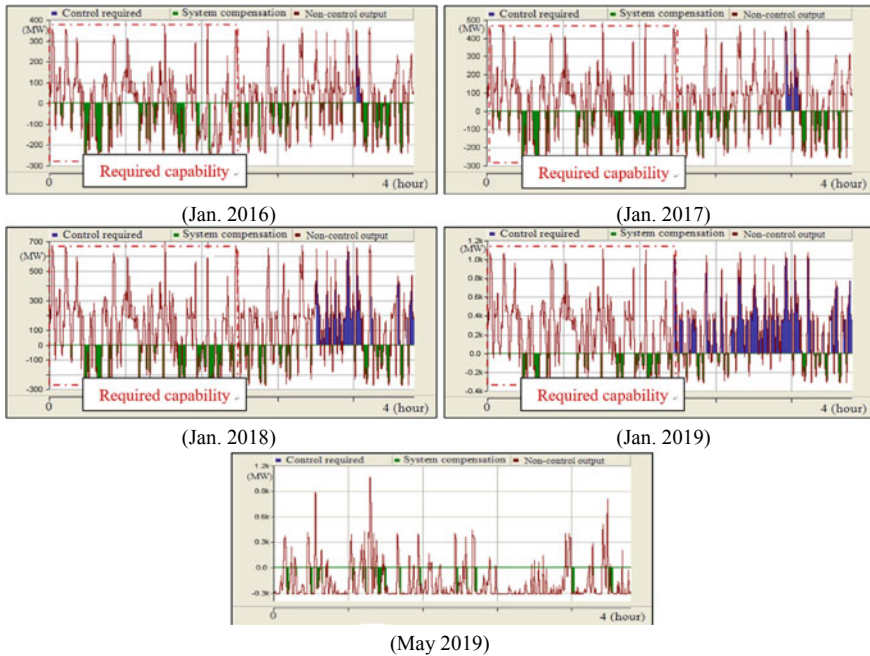


Fig. 5 Total power curve in the simulation

4 Conclusion

This paper deals with BESS estimation method for wind turbines to compensate for excess power generated. The designed formulas were derived taking into account the minimum load power state, which relates to the factor of excess power. The wind turbine and the BESS were simulated by PSCAD. The analysis was conducted considering the real energy system in Korea. In the simulation, the excess power in the normal wind potential state is successfully compensated. The months which were greatly used for calculating HCF generate huge surplus power, and it cannot be wholly compensated by using calculated BESS. In Korea, however, the TSO considers two hours for emergency situations that may provide time to respond to the operation of other fuel generators. The verification process is considering severe load condition which is using minimum load quantity during every midnight electricity section. It is clear that the compensation process could be achieved about short time severe surplus power by using calculated BESS capacity. In case of real power system, the minimum load is existed at short time duration and the compensation process could be performed more appropriately.

Acknowledgment This work was supported by National Research Foundation Grant (No. 2018R1C1B5030524) and Korea Electric Power Corporation Grant (R18XA06-40) funded by the Korean government.

References

1. Kusiak A, Zheng H, Song Z (2009) Short-term prediction of wind farm power: a data mining approach. *IEEE Trans Energy Convers* 24(1):125–136
2. Li W, Joos G, Belanger J (2010) Real-time simulation of a wind turbine generator coupled with a battery supercapacitor energy storage system. *IEEE Trans Ind Electron* 57(4):1137–1145
3. Gökçek M, Bayülken A, Bekdemir S (2007) Investigation of wind characteristics and wind energy potential in Kırklareli Turkey. *Renew Energy* 32:1739–1752
4. Goel PK, Singh B, Murthy SS, Kishore N (2011) Isolated wind-hydro hybrid system using cage generators and battery storage. *IEEE Trans Ind Electron* 58(4):1141–1153
5. Eskin N, Artar H, Tolun S (2008) Wind energy potential of Gökçeada Island in Turkey. *Renew Sustain Energy Rev* 12:839–851
6. Shi G, Zhang J, Cai X, Zhu M (2016) Decoupling control of series-connected DC wind turbines with energy storage system for offshore DC wind farm. In: 2016 IEEE 7th international symposium on power electronics for distributed generation systems (PEDG). Vancouver, BC, pp 1–6
7. Vargas LS, Bustos-Turu G, Larraín F (2015) Wind power curtailment and energy storage in transmission congestion management considering power plants ramp rates. *IEEE Trans Power Syst* 30(5):2498–2506
8. Ye W, Herman B, Maria G (2015) Method for assessing available wind primary power reserve. *IEEE Trans Sustain Energy*. 6(1):272–280
9. Vidyanandan KV, Nilanjan S (2013) Primary frequency regulation by deloaded wind turbines using variable droop. *IEEE Trans Power System* 28(2):837–846
10. Nayeem RU, Torbjorn T, Daniel K (2008) Temporary frequency control support by variable speed wind turbines potential and application. *IEEE Trans Power System*. 23(2):601–612
11. Ekamayake JB, Jenkins N, Strbac G (2008) Frequency response from wind Turbines. *Wind Eng* 32(6):537–586
12. Wang Y, Meng J, Zhang X et al (2015) Control of PMSG-based wind turbines for system inertial response and power oscillation damping. *IEEE Trans Sustain Energy* 6(2):565–574
13. He W, Yuan X, Hu J (2016) Inertia provision and estimation of PPL-based DFIG wind turbines. *IEEE Trans Power System* 32(1):510–521

A Feasibility Study About Capacity Factor-Based BESS Design Plan by State of Charge Analysis



Yunhwan Lee, Minhan Yoon, Jaewan Suh, and Seungmin Jung

Abstract Wind power plant is focused on the improvement of reliability and stability issues which can make impact not only nearby distribution system but also the entire utility grid. Among the compensation devices, utilizing battery energy storage system (BESS) in a wind farm is being considered in many fields to alleviate the fluctuation. It is required to appropriate capacity calculation process for application of the BESS in the wind power system because calculating BESS capacity was not formulated and several algorithms have no adoptability for the various wind farm characteristics. In this paper, a state of charge analysis is progressed based on previous pre-calculation method of BESS capacity. By configuring various wind fluctuating conditions, the feasibility studies about not only historical data and expected condition including power system are constructed. According to the state of charge analysis, a severe surplus power can be covered during certain section which is proposed by power system operator. The electrical supply analysis was progressed by PSCAD/EMTDC.

Keywords ESS application · Curtailment · Micro-grid · Capacity calculation · EMS

Y. Lee

System Planning Team, Korea Power Exchange, Naju, Korea
e-mail: yunan2@kpx.or.kr

M. Yoon

Department of Electrical Engineering, Tongmyong University, Busan 48520, Korea
e-mail: minhan.yoon@gmail.com

J. Suh

Department of Electrical Engineering, Kwangwoon University, Seoul 01897, Korea
e-mail: jwsuh@dongyang.ac.kr

S. Jung (✉)

Department of Electrical Engineering, Hanbat National University, Daejeon 305-719, Korea
e-mail: seungminj@hanbat.ac.kr

© Springer Nature Singapore Pte Ltd. 2020

A. K. Bhoi et al. (eds.), *Advances in Greener Energy Technologies*,

Green Energy and Technology, https://doi.org/10.1007/978-981-15-4246-6_46

1 Introduction

To make wind power profile efficiently and smoothly, various industrial operators have continuously composed large-scale wind farm system, and the spread of wind farm is also progressed. In terms of the power system, depending on the environmental factors, there may be some reliability problems across the power grid. Among them, wind turbines have characteristics of output variation according to geographical environments, so it is possible that large amounts of wind penetration could significantly affect the connected power grid. Therefore, in case of turbulent flow, various issues such as reactive power support or curtailment problems could be existed. In order to solve such problems, a few of accurate prediction methods for wind power generation have been considered to reduce the error between actual and predicted profiles. In addition, in the field of wind power generation systems, as the entire cost of compensation device has been reduced along with technology development, several storage basis solutions are attracting attention. Especially, the Battery Energy Storage System (BESS) is considered as attractive devices for the energy industry. Several BESS application methods have been utilized in different ways to improve the performance of the wind turbine system in terms of both stability and efficiency issues. As described in [1] and [2], the charging/discharging schemes have been focused on power system flexibility to enhance demand response. As general storage system has flexible operational scheme in terms of power supply issue, generated fluctuation due to wind farm is expected to be reduced with appropriate control scheme [3–5]. The error reduction and improving the instantaneous accuracy of the wind power profile can be realized with that application according to the Refs. [6] and [7]. With an appropriate storage capacity calculation, furthermore, the overspecified construction can be reduced, and securing necessary reserve power for uncertainty/variability of wind power can be feasible.

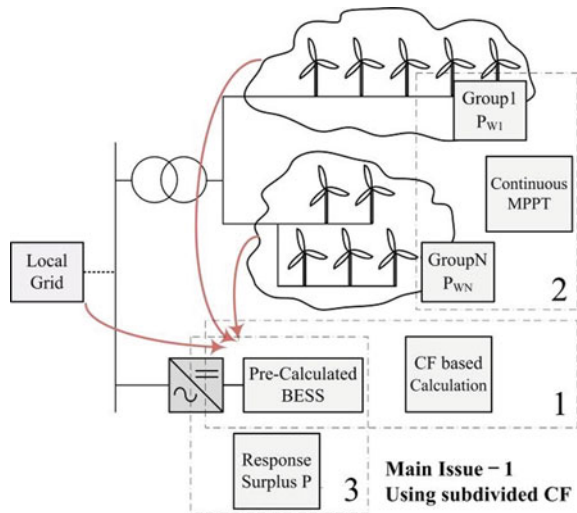
Currently, type IV wind turbines have variously been utilized in power generation system for smoothing profile with own DC-powered section as described in [8, 9]. This generation system applies internal DC network which has grid-friendly operating condition. Because the stability issue of those renewable resources is the largest factor to consider in an actual system, the overall farm design heavily considers the BESS integrated system. The condition of peak power reduction in the daily response is too complex for the design of the BESS to adequately contribute to the real system due to the limitation of the economic feasibility. The previous studies focus on the BESS capacity calculation for a large-scaled wind power plants to reduce the power variation that occurs due to uncertainty. It is important to decide an appropriate energy capacity taking into account not only the scale of wind farm but also the condition of the connected power grid, as the reliability of the BESS is closely related and much controversy arises between the owner of the wind turbine and the grid operator in terms of the corresponding [10].

In this work, a pre-calculation procedure for the BESS capacity is utilized by taking into account the excess power associated with the defined capacity factor of certain wind farm. Surplus power means the energy differences generated from daily power consumption, which are normally considered as generated quantity and minimum load of the target system. The previous system allocated an available proportion of the BESS capacity to use it as a reserve power for small power network. Using the previous power consumption patterns, a micro-grid system, which is considered to integrate a number of wind turbines with relatively small-scaled power consumption, is used to confirm state of charge (SOC) variation with concerning integrated power system including load condition. The entire simulation process is based on PSCAD, and the wind variation is generated by MATLAB.

2 Framework of Applied System

In case of type IV, which generally named as permanent magnetic synchronous generator (PMSG), the stable AC frequency is distributed to the power grid with a full converter. The connection point of wind turbine is considered for BESS integrating point as well. Figure 1 shows a developed wind farm integrated with a BESS. The wind farm is composed of several groups of wind turbines, and the output profile of each group is denoted as PWN. Since multiple wind turbines should be considered for different environmental factors, the PMSG converter is simplified to handle the entire system properly in the EMTDC simulation. Firstly, each wind turbine in the farm considers two options, which are divided to extracting maximum power with imposed wind speed or curtailment of own profile according to order by the

Fig. 1 Three stages for BESS configuration plan



system operator. Within the BESS operation range, which depends on SOC, the available power of wind system will be continuously extracted, and the capacity needs pre-calculation method by estimation process. In this process, we adopt capacity factor-based calculation method which is represented in Ref. [11]. The aim of this paper is to verify the SOC feasibility by applying severe wind condition in Korea. The verification process cannot be performed for every wind turbine; however, an estimated simulation can be performed by composing several groups operating in approximately similar environments.

The BESS should respond to the real power gap relating to demand of local power network and generated wind power. Because the concept does not consider a supervisory control scheme such as active curtailment methods, the wind turbines preferentially follow the maximum power point tracking (MPPT). Yet, in the case of an excess of real power compared to the load demand, a pitch control is used to eliminate the aerodynamic energy by shedding off the blades. In this study, the pitch angle is maintained at zero during normal operation. Multiple wind turbines in the farm could be controlled with pitch angle control in an event of excessive power, and the energy amount should be estimated to check whether additional control is required or not.

2.1 BESS Charging/discharging Strategy

To check the capacity condition of storage, the SOC of the BESS needs to be defined during the entire simulation. The SOC of previous state would be estimated every second. The SOC of the BESS can be defined as follows:

$$\text{SOC}(t + 1) = \begin{cases} \text{SOC}(t) - \frac{E_B(t)}{\eta E_{\max}}, & (P_B(t) \geq 0) \\ \text{SOC}(t) - \frac{\eta E_B(t)}{E_{\max}}, & (P_B(t) < 0) \end{cases} \quad (1)$$

where E_B is the electrical energy calculated by $P_B(t)$ and E_{\max} is the maximum electrical energy of BESS. The BESS control scheme is applied according to the existence of excess power, and the SOC should be the main control value of the control processes. Figure 2 represents a flow chart of the proposed control algorithm for the BESS operation. Each charging/discharging operation is assigned to a few phases that occur depending on the situation. The local fuel generator serves as the reserve power used for the BESS operation criteria. By using the minimum generation power of the local generators as a standard, the charge/discharge operation is differed at every operating time.

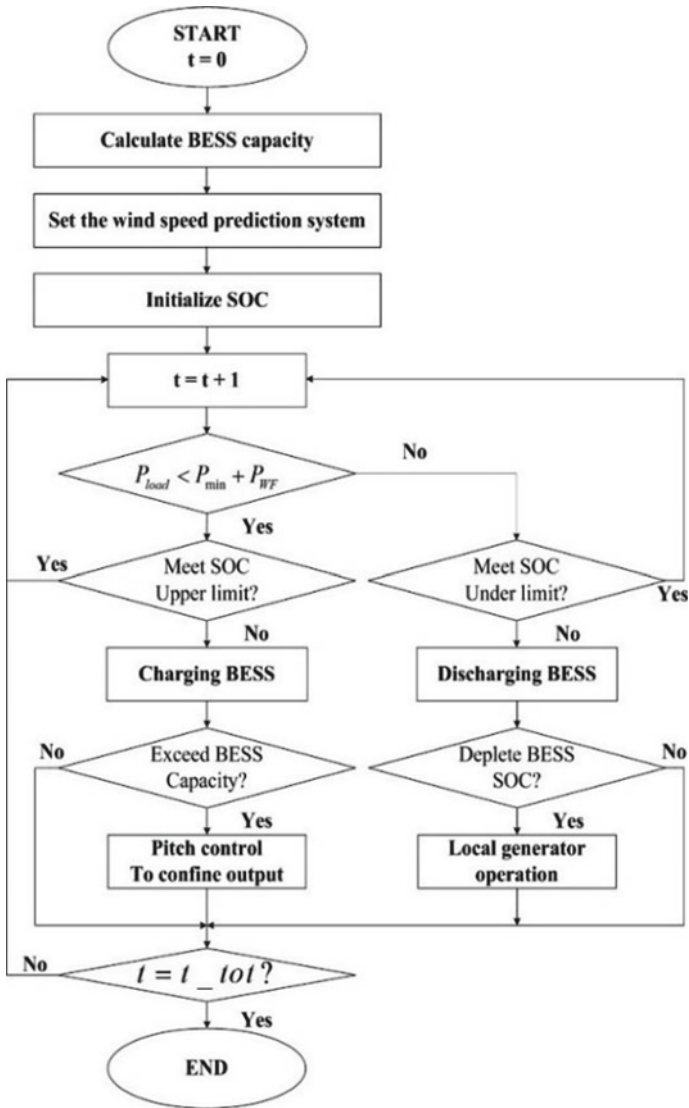


Fig. 2 Flow chart of control algorithm for BESS

2.2 Wind Data Construction

To properly calculate a capacity of the BESS system in advance, the wind prediction system should be put together to check the correctness of the formula. The prediction system consists of the Weibull distribution function to describe wind speed data. The descriptive data has reasonable performance in terms of agreement with an

experimental data. The Weibull distribution function is expressed as:

$$f(v) = \frac{k}{c} \left(\frac{v}{c}\right)^{k-1} e^{-\frac{v}{c}^k} \quad (2)$$

where c is Weibull scale parameter (m/s), k is Weibull shape parameter and v is wind speed. Until recently, numerous methods have been proposed to estimate Weibull parameter. This paper uses selected parameter which is used in Rayleigh distribution formula represented as follows:

$$f(v) = \frac{\pi v}{2\bar{v}^2} e^{-\frac{\pi v^2}{4\bar{v}^2}} \quad (3)$$

where \bar{v} is Weibull scale parameter (m/s). It is widely known that the power of the wind which flows at speed v through a blade sweep area A increases as the cubic of its velocity and is given by using the following equation:

$$P(v) = \frac{1}{2} \rho A \bar{v}^3 \quad (4)$$

where ρ is the air density (kg/m^3). A is the sweep area (m^2). The average wind power density of target place based on Weibull probability density function could be expressed as:

$$P_m = \frac{1}{2} \rho \bar{v}^3 \frac{\Gamma\left(1 + \frac{3}{k}\right)}{\left[\Gamma\left(1 + \frac{1}{k}\right)\right]^3} \quad (5)$$

where Γ means Gamma function. Wind velocity data is extrapolated by considering following power-law formula:

$$\frac{v_1}{v_2} = \left(\frac{h_1}{h_2}\right)^\alpha \quad (6)$$

where v_1 means the wind velocities (at height h_1), v_2 means the wind velocities (at height h_2) and α means the roughness factor. The wind data and information are utilized to measure the data by the automatic weather system in meteorological administration of South Korea. By utilizing wind speed data for every 10 min, the random wind speed prediction process could be performed. The processes predict wind speed by every 1 min according to the Rayleigh distribution formula ($\alpha = 0.1$).

Table 1 Power network data of JEJU Island

Year	HVDC capacity (MW)	Min. supply (MW)	Max. supply (MW)	Min. demand (MW)	Max. demand (MW)
2016	400	170	975	410	829
2017	600	170	1175	428	866
2018	600	170	1175	447	905
2019	600	170	1175	466	942

Table 2 Wind farm composition data of JEJU (including prediction)

Year	Grid reserve (MW)	Controllable quantity (MW)	Wind installation (MW)
2016	805	975	564
2017	1005	1175	680
2018	1005	1175	890
2019	1005	1175	1300

3 Case Study

3.1 Power System Modelling

To verify the availability of the mentioned calculation process, an integration test for the wind farm system in PSCAD was carried out. This document deals with BESS charge/discharge testing focused on long-term compensation. The general power system including BESS capacity is based on the test system in Ref. [11] and established with a simplified model. The wind farm modelling is created by placing electrical components of the user-defined libraries in PSCAD. By using realistic wind resource environments, each wind turbine generates power according to the MPPT control, and the BESS works to verify the current SOC level, which is the main objective of the proposed process. Table 1 represents general power system data of the JEJU Island between 2016 (historical data) and 2019 (predicted data) which is handled in simulation process. The wind power capacity is assumed based on the reports by the local government of JEJU. The constructed/predicted wind power construction capacities are represented in Table 2.

3.2 Simulation Configuration

According to the capacity calculation method in Ref. [11], a BESS system is constructed and changed each year as represented in Table 3. As the wind power increases drastically, the energy capacity of the BESS has been increased by the specified percentages. The wind prediction model in 2.2 was used to establish verification

Table 3 Designed BESS energy capacity about each year

Year	2016	2017	2018	2019
C _{BESS} (%)	2.015	2.725	7.046	8.584
BESS capacity (MWh)	11.364	18.532	62.713	111.5913

Table 4 Composed wind data for designed case study

Case	Goojwa (m/s)			Woodo (m/s)		
	Minimum	Maximum	Average	Minimum	Maximum	Average
1	0.87	20.56	7.29	0.26	22.27	6.83
2	0.23	26.72	6.49	0.41	29.52	10.54

processes. Two selected regions, Goojwa and Woodo, are applied to consider local characteristics. Each wind speed is individually inserted as a signal in the simulation shown in Table 4.

In case of a wind turbine, simulated farm consists of NREL 5 MW PMSG wind turbine. By considering type IV wind turbine, the BESS will respond to compensate according to the defined references. Battery charging system has to be considered for the entire system that should meet power demand–supply.

As the main aim of this paper is to confirm SOC variation, the SOC of the battery is estimated in the overall simulation process. When an excessive wind energy is generated in simulation, the pitch control by multiple turbines is promoted. Taking into account the required minimum power, the total simulation time is 4 h between 12 o'clock and 4 o'clock in the evening.

3.3 Simulation Results

The SOC variation according to the charging/discharging process for Cases 1 and 2 was shown in Figs. 3, 4, 5 and 6. According to the SOC curve, the battery capacity demands are gradually increased due to the wind power capacity. At the early state, the charging/discharging processes were progressed efficiently, but the BESS system

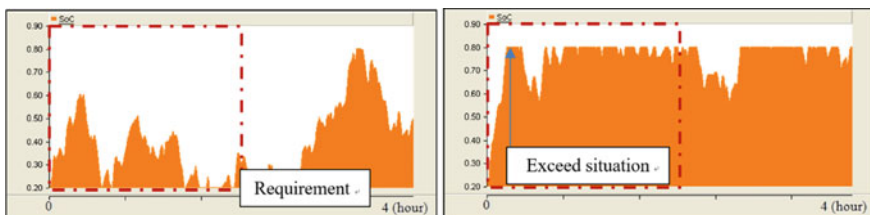


Fig. 3 SOC fluctuation curves about case studies in 2016 (Case 1: left, Case 2: right)

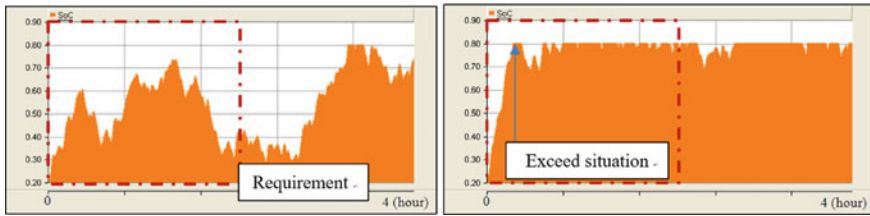


Fig. 4 SOC fluctuation curves about case studies in 2017 (Case 1: left, Case 2: right)

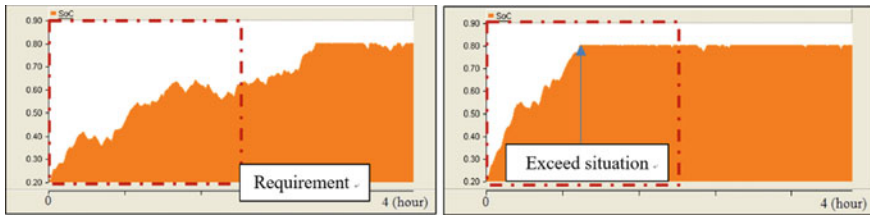


Fig. 5 SOC fluctuation curves about case studies in 2018 (Case 1: left, Case 2: right)

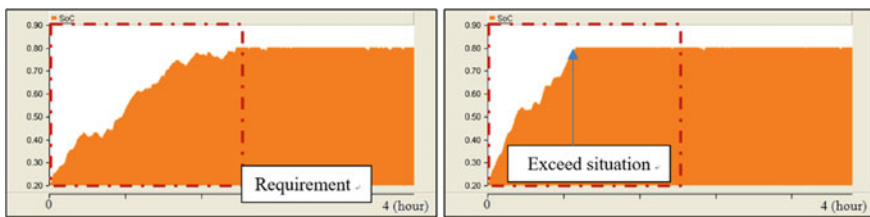


Fig. 6 SOC fluctuation curves about case studies in 2019 (Case 1: left, Case 2: right)

continuously reaches the SOC limitation as the wind power capacity grows drastically and BESS capacity cannot increase by reaching the limitation to consider economic feasibility.

The SOC curve in Cases 1 and 2 represents the effect of wind potential on energy utilization. As described in Fig. 3, the low average wind speed of Case 1 produces an appropriate SOC curve, and the excess power was not generated within two hours. However, in Case 2, because of the high wind potential, the SOC reaches the limitation point at an early stage. In 2016, the BESS capacity is 11,364 MWh, and the SOC deviation is strongly indicated in both cases.

The SOC operating status is displayed in a similar manner in all simulated years. Although the SOC almost reaches the limit, in Case 1 the SOC is adequately compensated within two hours, which is designated requirement by TSO in Korea. As the SOC is gradually increased according to the growth of the wind system (111.5913 MWh in 2019), the SOC variation is smoothed as shown in Fig. 6. By

Table 5 Simulation result of proposed method

Year	Case	Number of charging complete	Number of discharging complete	Converted amount (MWh)	Required power capacity (MW)	Controlled amount (MWh)
2016	1	0	0	70,346	117.2	0
	2	9	0	53,879	89.6	31,774
2017	1	4	0	87,063	145.2	3866
	2	7	0	67,780	112.8	46,652
2018	1	0	0	134,301	223.8	0
	2	1	0	157,314	262.1	15,930
2019	1	0	0	231,813	386.4	0
	2	2	0	259,345	432.2	42,774

taking advantage of this capacity, Case 2 in 2018 and 2019 shows another compensatory feasibility. However, the simulations display SOC limit exceed situation in both years as well.

The number of charging/discharging completion, the total amount of energy conversion and the control quantity of wind turbine were represented in Table 5. The range of SOC is designated within 20 and 80 percentage to protect battery life cycle. In case of Cases 1 and 2, control required power exists every simulated year and gradually increases because the wind speeds are almost occurred above rated speed. However, the TSO in Korea considers two hours for emergency situations that may provide time to respond to the operation of other fuel generators. Therefore, as described in the figure (dashed lines), the BESS compensation is available in the intended strong wind condition. The surplus powers in Cases 1 and 2 which are generated with highest wind potential cannot be compensated with calculated capacity, and the control required quantity is gradually increased.

4 Conclusion

This paper addresses the previously used BESS capacity prediction plan for relatively large-scaled wind farm to compensate for the expected extra power production. The designed systems were established in PSCAD and testified with the developed wind production theory to estimate SOC variations. The previous PSCAD-based power system uses a composite real wind condition which described in this paper. In the simulation, the SOC curves are maintained within two hours considering the designed normal wind potential. Since the TSO in Korea determines the requirement as two hours, it is expected that the composite BESS capacity can handle the generated excess power. When a high wind potential is taken into account, however, strong overshoot conditions were generated in the simulation. The numerical result of the

simulation indicates a significant control quantity for maintaining a power system. It is clear that the high wind potential in the simulation is a serious condition that cannot be sustained for more than one hour. In the case of a general power system, furthermore, the load at minimum state is only founded shortly during a day time; the planned severe condition is difficult to form in the operating condition. Nevertheless, the BESS should prepare the condition by considering the realistic wind condition to secure a certain balance of the power grid.

Acknowledgements This work was supported by National Research Foundation Grant (No. 2018R1C1B5030524) and Korea Electric Power Corporation Grant (R18XA06-40) funded by the Korean government.

References

1. Goel PK, Singh B, Murthy SS, Kishore N (2011) Isolated wind-hydro hybrid system using cage generators and battery storage. *IEEE Trans Ind Electron* 58(4):1141–1153
2. Vargas LS, Bustos-Turu G, Larrain F (2015) Wind power curtailment and energy storage in transmission congestion management considering power plants ramp rates. *IEEE Trans Power Syst* 30(5):2498–2506
3. Eskin N, Artar H, Tolun S (2008) Wind energy potential of Gökçeada Island in Turkey. *Renew Sustain Energy Rev* 12:839–851
4. Shi G, Zhang J, Cai X, Zhu M (2016) Decoupling control of series-connected DC wind turbines with energy storage system for offshore DC wind farm. In: 2016 IEEE 7th international symposium on Power Electronics for Distributed Generation Systems (PEDG), Vancouver, BC, pp 1–6
5. Ye W, Herman B, Maria G (2015) Method for assessing available wind primary power reserve. *IEEE Trans Sustain Energy* 6(1):272–280
6. Nayeem RU, Torbjorn T, Daniel K (2008) Temporary frequency control support by variable speed wind turbines potential and application. *IEEE Trans Power System* 23(2):601–612
7. Ekamayake JB, Jenkins N, Strbac G (2008) Frequency response from wind turbines. *Wind Eng* 32(6):537–586
8. Wang Y, Meng J, Zhang X et al (2015) Control of PMSG-based wind turbines for system inertial response and power oscillation damping. *IEEE Trans Sustain Energy* 6(2):565–574
9. He W, Yuan X, Hu J (2016) Inertia Provision and estimation of PPL-based DFIG wind turbines. *IEEE Trans Power System* 32(1):510–521
10. Vaclav K, Sanjay K, Remus T et al (2016) Sizing of an energy storage system for grid inertial response and primary frequency reserve. *IEEE Trans Power System* 31(5):3447–3456
11. Seungmin J (2018) Development of complementary operation plan for wind power fluctuation based on small-scale ESS. *Int J Eng Technol* 7(3.24):344–348

Design and Implementation of DC–DC Boost Converter for Solar Application



Ashutosh Jha, Anilanshu Singh, and S. Angalaeswari

Abstract Nowadays, there has been an increasing concern and demand for renewable energy. The top contender for which is solar energy—it is cheap, available everywhere and readily convertible to useful electrical energy by photovoltaic panels. It has been estimated that for meeting the world’s power requirement, an area of the size of Spain is required to be covered completely with solar panels. Thus, in order to efficiently utilize this resource, various methods like MPPT, etc., are defined. By utilizing maximum power point tracking, we can utilize the energy that would be wasted from the solar panel by increasing or decreasing the duty cycle. For that, an efficient and stable power electronics converter is required. In this paper, the designing and testing of such a boost converter are discussed.

Keywords DC–DC boost converter · Solar panel · MPPT · Duty cycle · Hardware

1 Introduction

The conversion of renewable energy is obligatory in the present power sector to meet the supply and demand. The power generated through conventional sources is not enough to meet the growing power demand [1]. The main advantages of distributed sources is its location which can be placed nearer to the consumer load so as to reduce the transmission losses, producing a low voltage that can be readily accessible to the consumers by reducing the conversion losses, utilization of the renewable sources which is pollution free, available in nature, maintenance cost, etc. [2]. Solar power is preferable among all other sources due to its availability throughout the year, easy to convert and cheap. But the solar output voltage is very less which cannot be used

A. Jha · A. Singh · S. Angalaeswari (✉)
School of Electrical Engineering, Vellore Institute of Technology, Chennai, India
e-mail: angalaeswari.s@vit.ac.in

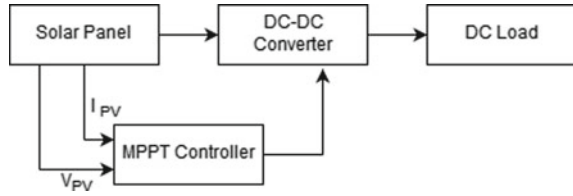
A. Jha
e-mail: ashutoshjha98@hotmail.com

A. Singh
e-mail: anilanshusingh15@gmail.com

© Springer Nature Singapore Pte Ltd. 2020

A. K. Bhoi et al. (eds.), *Advances in Greener Energy Technologies*,
Green Energy and Technology, https://doi.org/10.1007/978-981-15-4246-6_47

Fig. 1 Block diagram of the system



directly. The power extracted from solar has to be maximum so that its efficiency has been improved. There are many maximum power point tracking (MPPT) techniques available to extract the maximum power. The various MPPT techniques have been discussed in [3]. The voltage has to be boosted up using DC–DC boost converter. A converter can be acting either in buck or boost mode depending upon whether the voltage has to be increased or decreased at the output side. Keeping in consideration that the converter will feed DC appliances and inverters, a suitable LC filter is also designed and implemented to keep output ripple as low as possible [4]. The filter design is required in the hardware implementation so as to reduce the THD and keep it within IEEE1547 and IEEE519 norms [5, 6].

The main motivation behind this work is the hardware implementation of solar-based system using boost converter by reduced harmonics in the output voltage. The block diagram of the system is shown in Fig. 1.

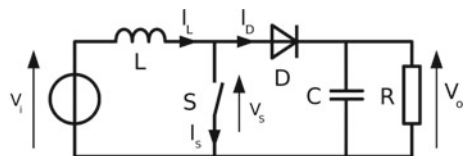
In a purely inductive filter, the ripple factor depends on the load resistance proportional and in a capacitor filter; it is inversely proportional to the load resistance. Hence, the combination of inductor and capacitor has been employed here to make the ripple factor independent of load filter [7, 8].

2 Design of Boost Converter

A boost converter can operate in two modes—continuous and discontinuous mode. When it operates in continuous mode, the inductor current (I_L) never falls to zero. The schematic diagram of the boost converter is shown in Fig. 2. When the switch S is closed in ON mode, the input voltage (V_i) appears across the inductor. The inductor current (I_L) changes during a time period (t) by the formula as given below:

$$\frac{\Delta I_L}{\Delta t} = \frac{V_i}{L} \tag{1}$$

Fig. 2 Schematic diagram of boost converter



where L is the value of the inductor.

At the end of the On-state, the current increase in I_L is therefore:

$$\Delta I_{L_{ON}} = \frac{1}{L} \int_0^{DT} V_i dt = \frac{DT}{L} V_i \quad (2)$$

where D represents the duty cycle. It is the ratio of the commutation period T during On-state. Therefore, the duty cycle ranges from 0% (S is never on) to 100% (S is always on).

During the Off-state, the switch S is open, hence, the current in the inductor starts to flow through the load. If zero voltage drop is considered in the diode, and a capacitor which is large enough for its voltage to remain unchanged, the evolution of I_L is:

$$V_o - V_i = L \frac{dI_L}{dt} \quad (3)$$

Therefore, the change in I_L during the Off-period is:

$$\Delta I_{L_{off}} = \int_{DT}^T \frac{(V_i - V_o)dt}{L} = \frac{(V_i - V_o)(1 - D)T}{L} \quad (4)$$

The converter is operating in steady-state conditions; the amount of energy stored in all the components has to be the same at the start and at the end of a commutation cycle. Energy stored within the inductor is given by:

$$E = \frac{1}{2} L I_L^2 \quad (5)$$

So, the current in the inductor is same at the beginning and end of the commutation cycle. This means the overall change in the current (the summation of the changes) is zero:

$$\Delta I_{L_{ON}} + \Delta I_{L_{OFF}} = 0 \quad (6)$$

Substituting $\Delta I_{L_{ON}}$ and $\Delta I_{L_{OFF}}$ by their expression yields:

$$\Delta I_{L_{ON}} + \Delta I_{L_{OFF}} = \frac{V_i DT}{L} + \frac{(V_i - V_o)(1 - D)T}{L} = 0 \quad (7)$$

This can be written as:

$$\frac{V_o}{V_i} = \frac{1}{1 - D} \quad (8)$$

Table 1 Specifications and ratings of components calculated from the derived formulae

Description	Value
Switching frequency	50 kHz
Power inductor	330 mH, 11.5 A max
Capacitor	1 μ F
Load	100 Ω
Output current (50% duty cycle, 10 V_{in})	0.2 A

The equation given above depicts that the output voltage is always greater than the input voltage (as the duty cycle changes from 0 to 100%), and that it increases with duty cycle, theoretically to infinity as duty cycle reaches 100%. That is why this converter is referred to as a step-up converter.

The duty cycle can be calculated from the equation given above:

$$D = 1 - \frac{V_i}{V_o} \tag{9}$$

The specifications of the components are given in Table 1.

3 Simulation Results

For designing and testing the circuit, MATLAB/Simulink software has been used. The simulation circuit is shown in Fig. 3. For the simulation purpose, the solar model has been considered as a constant DC voltage source. It is connected to the boost converter circuit through the inductor. The load has been connected to the output of

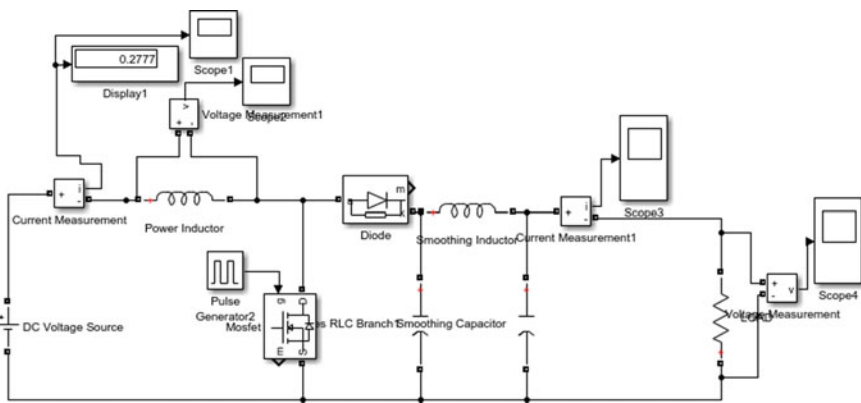


Fig. 3 Simulink diagram of the proposed system

the converter. Resistive load is considered for the analysis. In this work, the open-loop system is taken for both simulation and hardware implementations. The pulse for the boost converter has been generated from the pulse generator for various duty cycles. The results have been validated with simulation results.

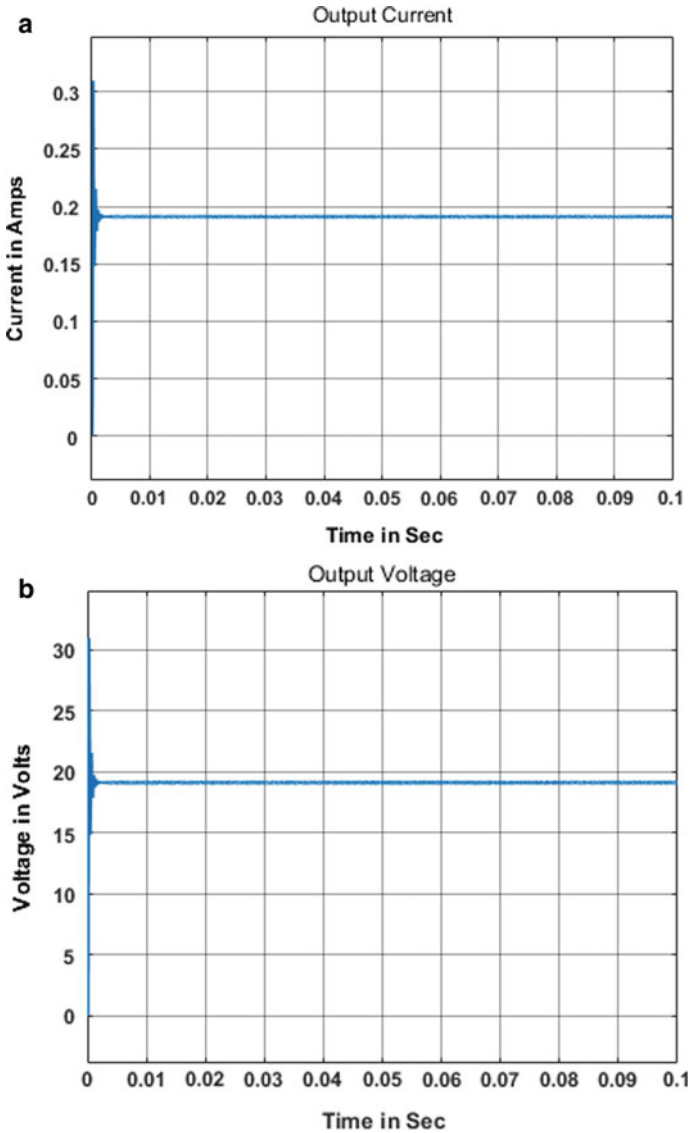


Fig. 4 a Current through the load. b Voltage across the load

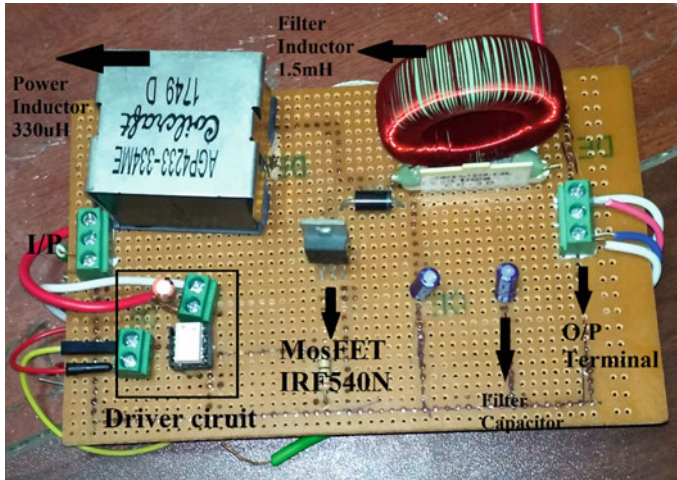


Fig. 5 Hardware implementation

The output voltage and output current have shown in Fig. 4a, b. The current through the load has been observed as 0.1911 A and the voltage across the load as 19.11 V as shown below.

4 Hardware Implementation and Its Results

The hardware implementation of the system is shown in Fig. 5. The PCB fabrication has been done in the laboratory and the components have been soldered. The testing and validation have been done and the hardware results have compared with the simulation results. In hardware, the switching frequency has been considered as 41.87 kHz. The duty cycle diagram is shown in Fig. 6. The output voltage for the input of 5 V and duty cycle of 50% is shown in Fig. 7. The circuit has been tested with various duty cycles and the output voltage for various duty cycles has been plotted in Fig. 8. The input voltage has been varied as solar voltage is viable depending on its irradiation. The extension of this work is to test the circuit with solar input and implement the closed-loop control.

5 Conclusion

A stable, low THD boost converter was designed and implemented. The converter has high power rating owing to the high current carrying capacity of individual

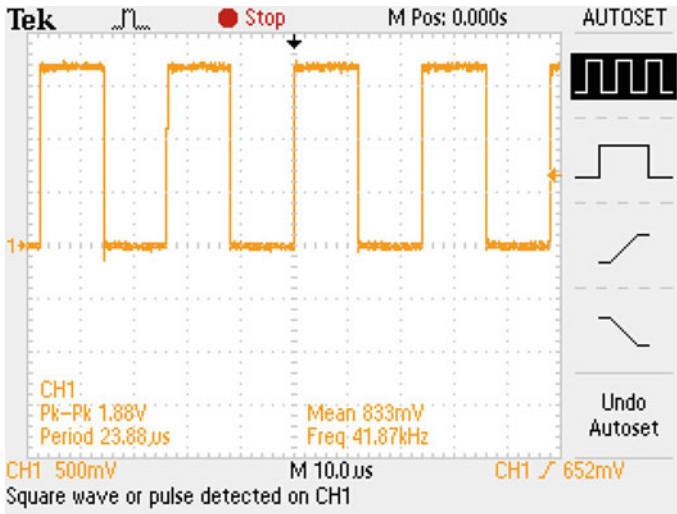


Fig. 6 Gating pulse given by Arduino Uno R3

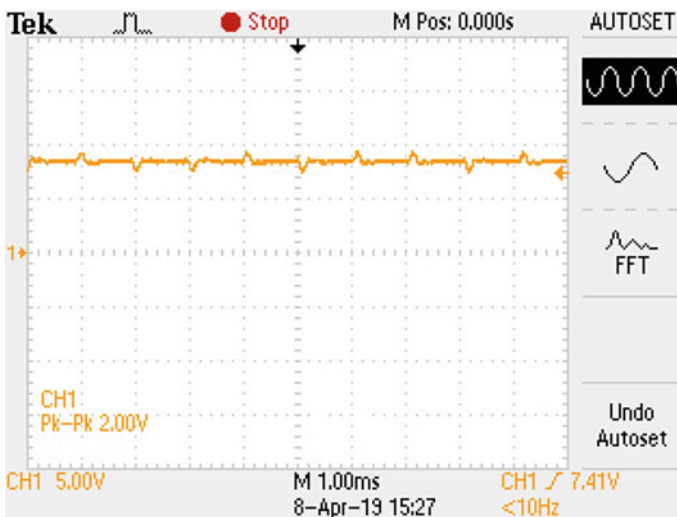


Fig. 7 Output voltage for input value of 5 V and 50% duty cycle

components. The $6'' \times 4''$ converter is capable of delivering 144 W of power theoretically and 100 W with active cooling element (typically fan) attached. The converter is ideal for implementing MPPT as its duty cycle can be varied easily by using feedback from current and voltage sensors. Also, due to its LC low pass filter, the stability is not affected even at changing duty cycles and loads as required in practical implementation.

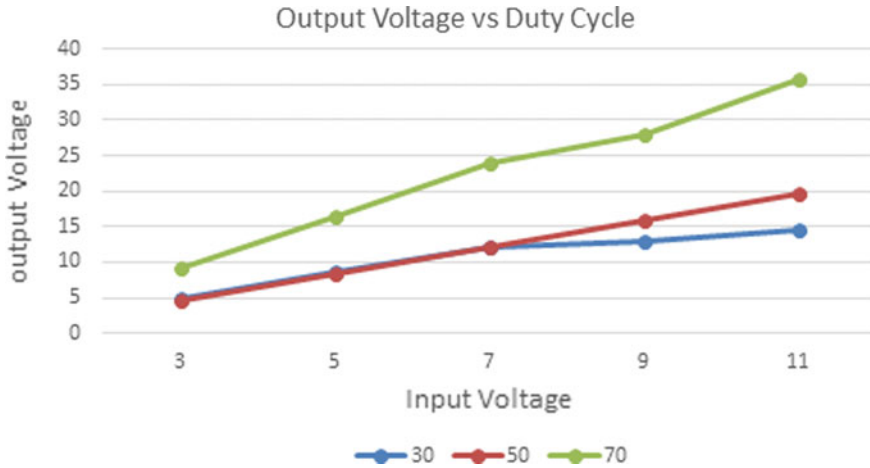


Fig. 8 Output voltages at various duty cycles and input voltages

References

1. Angalaeswari S, Jamuna K (2015) Optimal placement and sizing of real power supporting DG in radial distribution networks. In: IEEE conference on women in engineering (WIECON-ECE 2015), pp 342–345
2. Angalaeswari S, Jamuna K (2017) Constrained power loss minimization of DC micro grid using particle swarm optimization. In: Proceedings of the international conference on data engineering and communication technology, advances in intelligent systems and computing, vol 468. Springer, Berlin, pp 379–389
3. Karami N, Moubayed N, Outbib R (2017) General review and classification of different MPPT Techniques. *Renew Sustain Energy Rev* 68:1–18
4. Huangfu Y, Pang S, Nahid-Mobarakeh B, Guo L, Rathore AK, Gao F (2018) Stability analysis and active stabilization of on-board DC power converter system with input filter. *IEEE Trans Ind Electron* 65(1):790–799
5. Rangarajan SS, Collins ER, Fox JC (2017) Detuning of harmonic resonant modes in accordance with IEEE 519 standard in an exemplary north American distribution system with PV and wind. In: 2017 IEEE 6th international conference on renewable energy research and applications (ICRERA), pp 435–440
6. Zong XJ, Gray PA, Lehn PW (2016) New metric recommended for IEEE standard 1547 to limit harmonics injected into distorted grids. *IEEE Trans Power Delivery* 31(3):963–972
7. McLyman CWT (2016) Transformer and inductor design handbook. CRC press, Boca Raton
8. Fang J, Li H, Tang Y (2017) A magnetic integrated LLCL filter for grid-connected voltage-source converters. *IEEE Trans Power Electron* 32(3):1725–1730

Real-Time Implementation of Solar-Based Water Irrigation System



S. Angalaeswari, Suvrason Mookherjee, and K. Jamuma

Abstract In this period of proper usage of energy and economy, solar energy comes in scene which is abundant in nature. Converting this abundant energy into useable form will reduce the burden on other fossil fuels and at the same time increase our energy needs. In this paper, a system comprising of solar as the primary source and battery as backup has been modeled for the solar irrigation purpose where the conventional power supply may not available in rural areas. The energy derived from the cell is used to power the load. A DC-DC boost converter has been used to boost the voltage from solar and battery. A single-phase full-bridge inverter has been used between the DC-DC boost converter and the load to convert the DC voltage into AC voltage. Filter circuit has been proposed to reduce the harmonics in the inverter voltage. Since solar irradiation is variable in nature, a conventional proportional-integral (PI) controller has been implemented for the DC-DC boost converter, so as to make the output DC voltage as constant. The modeling has been done in MATLAB/Simulink, and simulation analysis has been done. In order to validate the performance of the system in real time, the system has been evaluated in OPAL RT software. Rapid control prototype (RCP) has been developed for improving the control strategies while reducing the risk, cost and time. The closed-loop feedback has been implemented using Arduino with real-time simulator. The simulation and real-time results show that the proposed system is highly suitable for the irrigation purpose and have effective and efficient results with variable irradiation.

Keywords Renewable sources · Real-time implementation · Closed-loop voltage control · Simulator · Controller

S. Angalaeswari (✉) · S. Mookherjee · K. Jamuma
Vellore Institute of Technology, Chennai, Tamil Nadu, India
e-mail: angalaeswari.s@vit.ac.in

S. Mookherjee
e-mail: suvsom@gmail.com

K. Jamuma
e-mail: jamuna.k@vit.ac.in

© Springer Nature Singapore Pte Ltd. 2020

A. K. Bhoi et al. (eds.), *Advances in Greener Energy Technologies*,
Green Energy and Technology, https://doi.org/10.1007/978-981-15-4246-6_48

1 Introduction

Solar energy is the primary source of renewable energy which is eternal. The need for converting solar energy to usable form arises due to the exhaustion of fossil fuels. A solar cell serves this purpose. The real-time implementation of the solar-based circuit is required for the effective validation of the microgrid by reducing the complexity [1]. Before implementation of the microgrid in the actual manner, digital simulation using real-time simulator is a requisite in beneficial way [2]. The paper aims at the modeling and simulation of a PV system using a DC-DC converter in MATLAB/Simulink. A solar cell has been used to convert solar energy into electrical energy by photovoltaic effect. A photovoltaic cell is made up of two layers: n-layer and p-layer, respectively. The p-layer which is thinner than the n-layer is exposed to sunlight. The photons from the sunlight are absorbed by the semiconducting material, thereby exciting the free electrons to travel from n-layer to p-layer. Hence, there is a flow of current in the circuit.

The solar photovoltaic system suffers from two major drawbacks. Firstly, output current is dependent on weather condition which is unpredictable. Secondly, the conversion efficiency is very less. The behavior changes with changing solar irradiance and temperature. Based on the region, the output of the panel will change, for example, in tropical subtropical region, incident radiation and temperature will be higher compared to other regions. Hence, to improve the performance of the PV system, a controller and a DC-DC converter are employed. The controller system is responsible to feedback and transfers it to the load. The DC-DC boost converter is used to improve the strength of the source voltage. Boost converter output voltage is used as input of single-phase inverter to supply AC voltage load. Later, we run whole system in RT LAB for real-time implementation.

Rajasthan state in India has dry and hot weather conditions. According to 2018 monsoon report, average rainfall in Rajasthan is 9% less than last year. Two out of third farmers depend on rain for irrigation purpose in the state. To bring easiness in farmers life, government provide canal network to fulfill irrigation needs. Time slots are allotted to every farmer for taking water from canal. An uncertain power cut due to coal storage is another problem to farmer who depends on electricity to run irrigation pump. Economically backward farmers, who cannot afford generator, suffer more when there is power cut in their slot time. So, our project is an approach to help them by building such system that runs pump by solar energy and by a battery when solar cannot. The main objectives of this paper are to design a solar-based irrigation system and to implement a suitable controller for efficient operation of the above system using RT LAB.

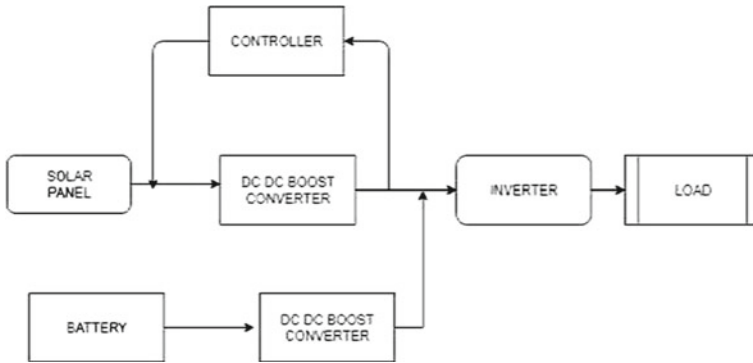


Fig. 1 Block diagram

2 Description of Microgrid

The microgrid has been modeled with solar panel, battery and inverter with AC load as shown in Fig. 1. This microgrid is able to operate only in islanded mode of operation. The solar panel gives the output voltage of 96 V at 500 W/m² irradiance and that voltage is given to DC-DC boost converter for boosting it to 220 V. A battery is also attached to system for backup purpose. Battery’s output voltage is also fed to DC-DC boost converter that gives 220 V. A single-phase full-bridge inverter is converting this DC voltage into fully sine wave 220 V AC output. This voltage is supplied to load of 0.5 HP motor.

RT LAB software had been used for real-time implementation of microgrid model [3]. OP4500 (hardware-in-loop system) is connected to computer by Internet by its IP address. Analog and digital ports of OP4500 are used for interfacing. Arduino UNO is used as controller to regulate the boost converter voltage. Analog port’s pin 1 is connected to Arduino pin 9, and analog port’s pin 20 is connected to Arduino’s GND. Digital port requires 5 V supply to function, so regulated power supply is connected to it. Digital port’s pin 1 is connected to pin 9 of Arduino, and digital port’s GND is connected to GND of Arduino. Digital signal oscilloscope is used to monitor the waveform of connections between Arduino and both ports. The hardware interfacing diagram of OPAL RT simulator is shown in Fig. 2.

3 Descriptions of Components

The project consists of six parts/modules

- Solar panel
- DC-DC boost converter
- Battery

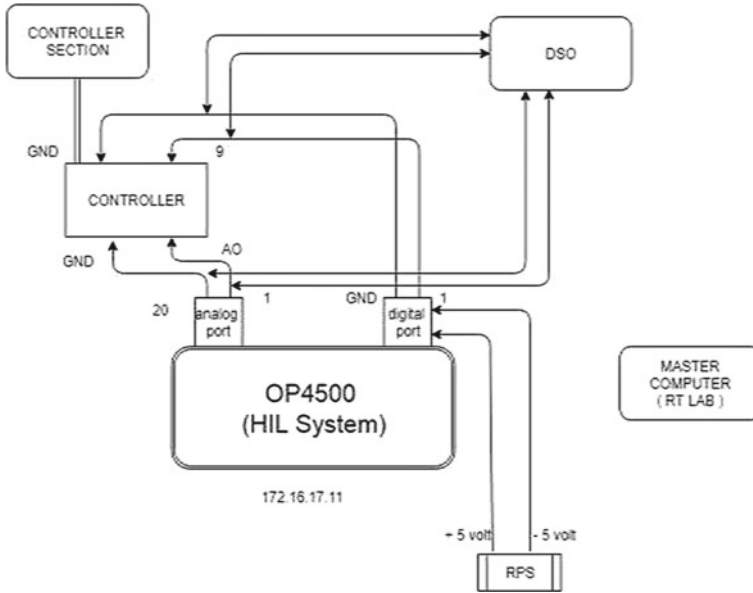


Fig. 2 Hardware interfacing block diagram

- Inverter
- Arduino UNO
- OP4500.

3.1 Solar Panel

The solar panel consists of a combination of p–n junction arranged in a particular order. When solar radiation falls on the photosensitive p–n junction, an electron hole pair is created. The electron hole pair moves across the space charge region which results in flow of current. As the irradiance increases, the number of electron hole pair created increases. So, the overall number of charge particles moving increases; hence, an increase in photocurrent takes place (Table 1).

The equation of a PV cell with its characterization is:

$$I_{ph} = I_{scr} + K_i(T - 298) * \eta \tag{1}$$

- k Boltzmann’s constant, i.e., 1.38×10^{-23} J/K;
- q Electron charge, i.e., 1.6×10^{-19} C;
- K_i Short-circuit current temperature coefficient at I_{scr} ;
- Lambda Solar irradiation in W/m^2 ;

Table 1 Block parameters of solar cell

Parameters	Value
Number of cells per module	51
Number of series-connected modules per string	3
Number of parallel string	66
Series resistance	0.037
Module specification [V_{oc} , I_{sc} , V_{mp} , I_{mp}]	[60.2, 4.68, 50.7, 5.58]

- I_{scr} Short-circuit current at 25 °C;
- I_{ph} Light-generated current;
- E_{go} Band gap for silicon;
- T_r Reference temperature;
- I_{or} Cell saturation current at T_r ;
- R_{sh} Shunt resistance;
- R_s Series resistance.

3.2 DC-DC Boost Converter

A boost converter is a voltage step-up converter. It is a sort of exchanged mode power supplied or SMPS that holds at any rate a diode and a transistor and in any event a vitality putting away components like capacitor, inductor or together. Channels developed utilizing capacitors which in some cases are utilized within synthesis with inductors have been added to converter yield to lessen yield voltage swell [4, 5]. The

Fig. 3 Boost converter schematics

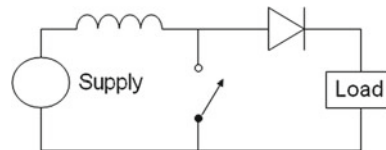


Table 2 Specifications of the DC-DC boost converter

Description	Rating
Resistance R_{on} (Ω)	0.001
Inductance L_{on} (H)	0
Forward voltage V_f (V)	0.8
Snubber resistance R_s (Ω)	500
Snubber capacitance (F)	250e-9

Table 3 Battery's parameters

Battery type	Nickel metal hydride
Nominal voltage (V)	96
Rated capacity (Ah)	100
Initial state-of-charge	50

boost converter equivalent circuit is shown in Fig. 3. Table 2 gives the specifications of boost converter.

3.3 Battery

Battery is placed in system to supply the load when solar cell cannot, like in rainy and cloudy days or in night. The battery type used in this work is nickel–metal hydride. Its nominal voltage is 96 V that is boosted by DC-DC boost converter to 205 V. Table 3 gives the specifications of the battery.

3.4 Inverter

Inverter is a power electronic device which converts a DC input voltage to a symmetric AC voltage of required magnitude and frequency at the output end. This power electronic is also known as a DC-AC converter. Ideal and practical inverter has sinusoidal and non-sinusoidal waveforms at output. If the input DC is a voltage source, the inverter is called a voltage source inverter (VSI). One can similarly use a current source inverter (CSI), where the input to the circuit is a current source. The VSI circuit has direct control over “output (AC) voltage,” whereas the CSI directly controls output (AC) current. We used VSI single-phase full-bridge inverter that can be simply justified with a switching scheme of full-bridge converter. This inverter circuit converts DC to AC. It achieves this by closing and opening the switches in the right sequence. It has four different operating states which are based on which switches are closed [6].

4 Results and Discussion

According to the OP4500 interface and pin configuration, digital in and analog out pin had been inserted. All wire connections are done according to it. Analog out's pin 20 is connected to Arduino's GND. Analog out's pin 1 is connected to Arduino's pin A0. Digital in and Arduino' GND is connected to each other. Digital in's pin 1 is connected to Arduino's pin 9. RPS is connected digital In +5 volt and GND.

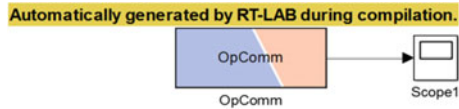


Fig. 4 RT LAB compilation window

4.1 Simulation Results

The compilation of the model has been taking place after arranging all the hardware components, and then, the simulation is carried out. The task is to compile, simulate it, load model and execute the simulation. Then, the simulator has to interact with the model in the simulation process. This is an automated process which will be started by simply clicking the compile button in the main control panel. Once the code has been generated and model compiled; the execution options can be set up before starting the simulation [7]. Figure 4 shows the compilation window in real-time simulator.

The hardware setup of this work is shown in Fig. 5. The desktop shown in Fig. 5 represents the master system having the entire model in it. The Simulink file has been opened from the OPAL RT software, and building process is taking place. The

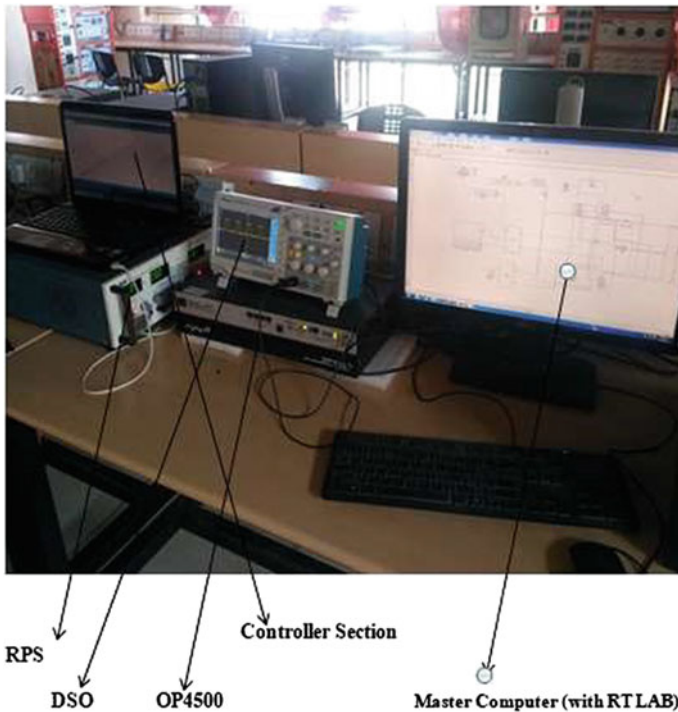


Fig. 5 Hardware setup of the solar-based system

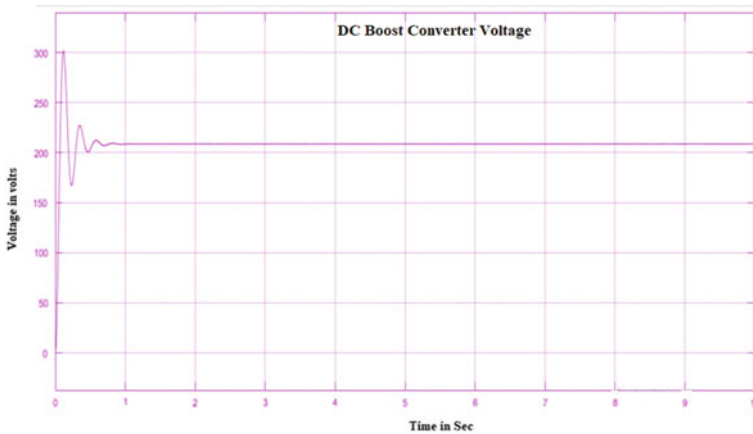


Fig. 6 Boost converter output

simulator has the hardware implementation of the controller which is in real time. This is based on rapid control prototype (RCP) where except the controller all other components such as solar, boost converter, battery, inverter and load are kept in simulation. The output voltage at DC-DC boost converter is taken outside, and it is compared with the reference voltage in Arduino controller. The controller has been programmed such that the voltage has to be maintained within the limits. The output from the controller has again given to the simulator, from where the pulses have been given to the boost converter in the Simulink diagram. The laptop shown in Fig. 5 is the controller part where the Arduino coding has been implemented. The simulator, power supply and the oscilloscope are shown in Fig. 5. The oscilloscope is giving the results of the controller as pulses.

The output DC voltage of boost converter is shown in Fig. 6. The voltage is boosted to 205 V, and it is given into the inverter operation. The pulses for the converter have been produced from the Arduino controller.

The inverter output voltage is shown in Fig. 7. Since it is a real-time simulation, the time taken is infinity. To project the output from the circuit, the simulation time has been set as 10 s and the scope results have highlighted. The system has been tested with variable irradiation with different input voltages, and the output voltage at DC link capacitor and the load voltage are within the limits (Figs. 8, 9, 10, 11, 12 and 13).

5 Conclusion

The solar irrigation system in real-time simulation has been modeled with OPAL RT simulator. Battery has been considered as the backup source. The DC-DC boost converter has been used to boost the low voltage from solar to meet out the load

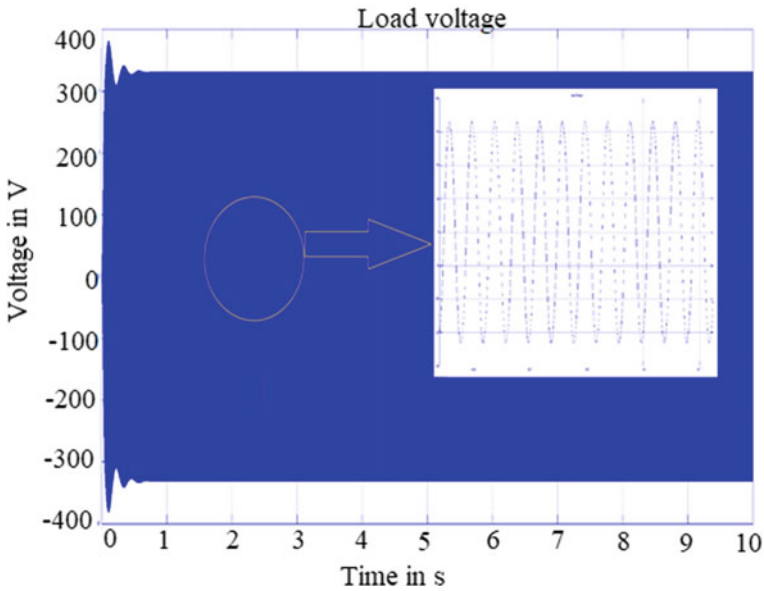


Fig. 7 Inverter output



Fig. 8 OP4500 hardware kit

requirement. Rapid control prototype method of simulation has been carried out in the simulator where the controller has been developed in hardware, and remaining others are in the simulation. The results obtained using Arduino has efficiently control the boost converter output voltage within the limits. The system has been validated for various input voltages. In this period of proper use of energy and cost cutting, solar energy comes into the scenery which is abundant in nature. Conversion of this abundant available energy into useable form will reduce the burden on fossil fuels, while at the same time expand our energy content. In this paper, a system comprising of solar as the primary source and battery as backup has been modeled for the solar irrigation purpose where the conventional power supply may not available in rural areas. The energy derived from the cell is used to power the load. A DC-DC boost

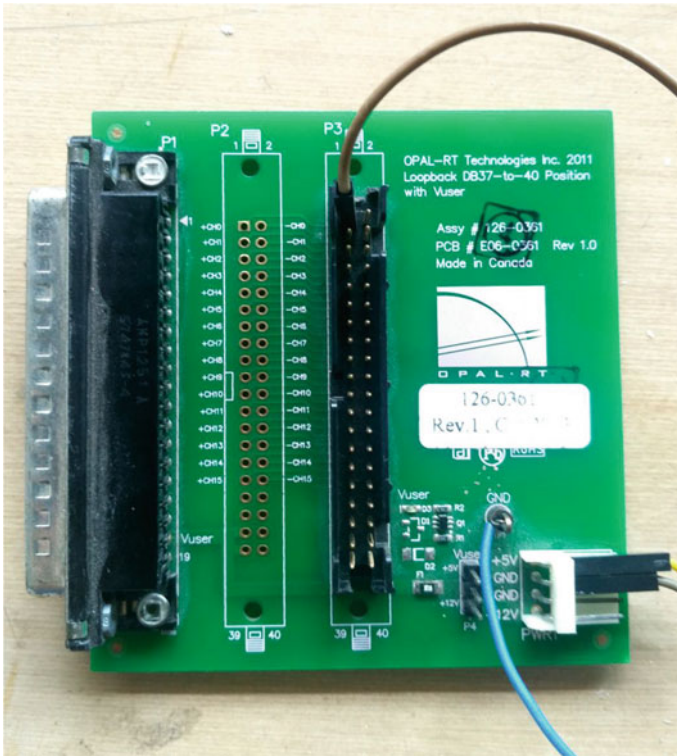


Fig. 9 Digital in board

converter has been used to boost the voltage from solar and battery. A single-phase full-bridge inverter has been used between the DC-DC boost converter and the load to convert the DC voltage into AC voltage. Filter circuit has been proposed to reduce the harmonics in the inverter voltage at the output end. Solar has thus come to the scene with extreme efficient use of it for proper usage of various day-to-day used devices.

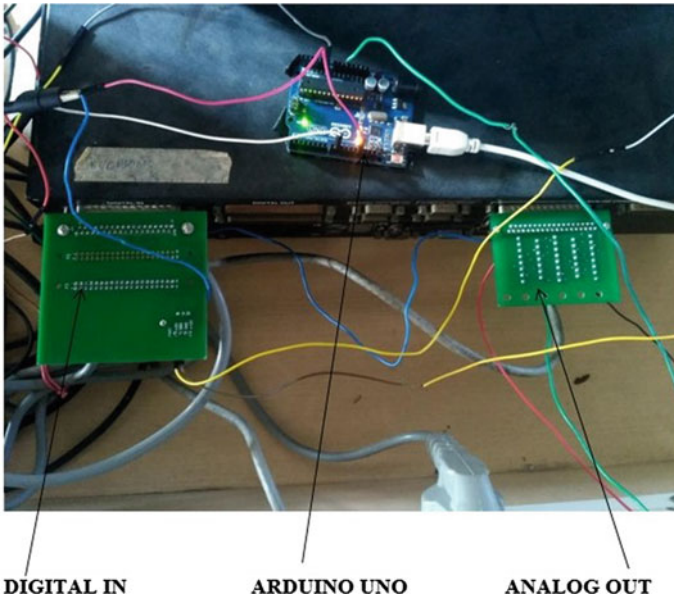


Fig. 12 Hardware connections of boards

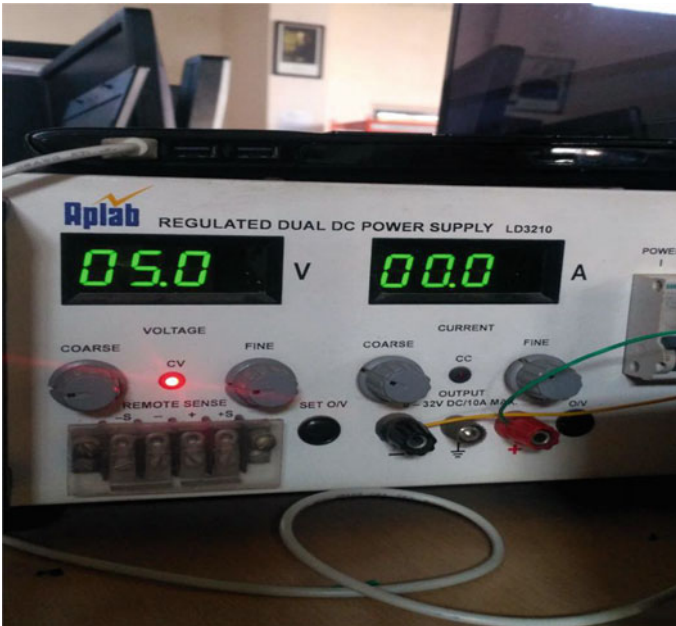


Fig. 13 Power supply for digital board

References

1. Lu L-Y, Liu J-H, Chu C-C, Wu Y-C, Cheng P-T (2012) Realtime simulations of a laboratory-scale micro-grid system in Taiwan. In: 2012 IEEE 13th workshop on control and modeling for power electronics (COMPEL), Kyoto, pp 1–8
2. Farzinfar M, Jazaeri M, Nair NC, Razavi F (2014) Stability evaluation of MicroGrid using real-time simulation. In: 2014 Australasian universities power engineering conference (AUPEC), Perth, WA, pp 1–6
3. Mikkili S, Panda AK, Prattipati, J (2014) Review of real-time simulator and the steps involved for implementation of a model from MATLAB/SIMULINK to real-time. The Institution of Engineers (India)
4. Tolia ND, Lo DP, Ajudia HA (2014) Study of boost converter with inverter for stand alone solar applications. *Int J Eng Res Technol (IJERT)* 3(5)
5. Siddhartha Bhatt M, Indira MS (2015) A study of boost converter with solar photovoltaic system for maximum energy efficiency. *The J CPRI* 11(1):133–138
6. Kumari P, Keshari RK, Banerjee S (2017) Design and implementation of photovoltaic module using multilevel inverter and boost converter. *Int Res J Eng Technol (IRJET)* 04(11)
7. Wanik MZC, Bousseham A, Elrayyah A (2016) Real-time simulation modeling for PV-battery based micro grid system. In: 2016 IEEE international conference on power system technology (POWERCON), Wollongong, NSW, pp 1–6

MPPT in Partially Shaded PV System with the Use of WODE Technique



K. R. Sugavanam, A. Mutharasan, J. Prakash, P. Gowtham,
M. Ramprasanth, and U. Vinay Sahoo

Abstract Maximum power point tracking (MPPT) in solar PV is necessary as it influences the total power extracted from a solar array. This paper introduces one technique for the tracking of the maximum power point in a partially shaded PV system under both dynamic and steady-state conditions. This paper elaborates on the use of the whale optimization and differential evolution (WODE) algorithm in MPPT in a PV system. This technique is a hybrid algorithm. This technique is free from the general drawbacks of evolutionary techniques such as slower convergence rate, large number of searching agents, large computational burden and oscillations that causes power losses at the output. This technique has been successfully implemented in MATLAB simulation with variation in various parameters of the solar panel, and it has also been tested on hardware consisting of various peaks indicating the change in partial shading with time. It is found that the technique gives a better efficiency in about half the time taken by the other algorithms currently used. The hybrid technique, it takes lesser time to converge; it has the capability to overcome the difficulties of each other.

K. R. Sugavanam (✉) · J. Prakash
Jaya College of Engineering and Technology, Chennai, India
e-mail: sugavanamkr@gmail.com

J. Prakash
e-mail: prakash_ies@yahoo.co.in

A. Mutharasan
Vel Tech Rangarajan Dr. Sagunthala R&D Institute of Science and Technology, Chennai, India
e-mail: mutharasanm@gmail.com

P. Gowtham · M. Ramprasanth · U. V. Sahoo
Vel Tech High Tech Dr. Rangarajan Dr. Sakunthala Engineering College, Chennai, India
e-mail: gowtham31798@gmail.com

M. Ramprasanth
e-mail: ramprasanth3104@gmail.com

U. V. Sahoo
e-mail: vinaysahoo77@gmail.com

© Springer Nature Singapore Pte Ltd. 2020

A. K. Bhoi et al. (eds.), *Advances in Greener Energy Technologies*,
Green Energy and Technology, https://doi.org/10.1007/978-981-15-4246-6_49

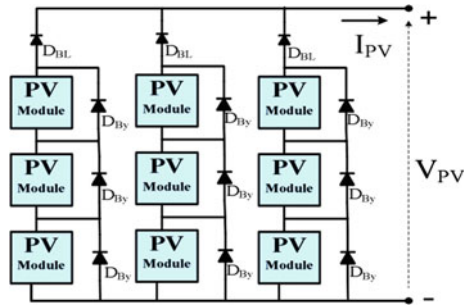
Keywords Solar PV · MPPT · Partial shading · Whale optimization · Differential evolution

1 Introduction

In day-to-day life, we totally dependent on electric power.. The power is extracted by burning coal, by burning fuels and gases, by nuclear fuels and a part of the same power we use also comes from renewable sources such as solar power, hydropower plants and wind energy systems. The power that we generate from non-renewable sources maybe high and the power generated may be making our lives better but at the same time, it also pollutes the environment we are living in and it is making the place we live in unliveable. What we mean to say is that the pollution caused by these non-renewable energy sources is making our living difficult day by day. As a solution to it, we have started taking steps towards the use of renewable energy sources for generating electrical power. The well-known sources of renewable energy are solar-, wind- and waterborne sources. Hydropower plants are conventional sources of energy and have already developed a lot. But the other sources such as solar and wind energy sources are more recent and a lot of research is being conducted in these. Out of these two, solar energy is given more importance as it is a static and more reliable source of energy when compared to the wind energy source. This is one of the reasons why people are being attracted towards the field of energy production with solar energy; more and more people are investing in making solar farms, and people are installing solar PV panels of smaller capacity even at their homes.

Efforts are being made in extracting maximum power out of solar PV panels. That is, efforts are being made to run the solar panels at their maximum power point (MPP). To find MPPs, the maximum power point tracking (MPPT) algorithms are used [1]. Basically, MPPT algorithms find the instantaneous power by using the voltage and current in the system. The voltage and the current are sensed by separate sensors and the data is fed as input parameters to the MPPT. The MPPT finds the most appropriate voltage reference or the best duty cycle for the converter to produce the maximum power. Generally, a solar farm or array has a number of solar panels which are connected in parallel and series combinations. This is done because the output of a single panel is too small to be given to any load. Hence, solar panels are added in series to increase the voltage provided with bypass diodes across each panel and these strings of series panels are connected in parallel to add up the current provided with blocking diodes in series with each string. Generally, when the sunlight is uniform across the solar PV array, that is, when the solar irradiance is uniform across each panel, there usually occurs only one peak in the power–voltage curve. But in practical conditions due to shadows of various objects such as clouds, buildings and trees on the various panels, there is non-uniformity in the irradiance and there are various peaks in the power–voltage curve of the solar PV array [2]. Any change in the pattern of the shadows on the solar PV array decides the pattern of the power–voltage curve (Fig. 1).

Fig. 1 Solar PV array



Global MPP tracking becomes a difficult and tedious task when it has to be done in the partially shaded conditions. The generally used MPPT methods are perturb and observe (P&O), hill climbing, etc. [3]. They are useful when utilized for solar PV systems with uniform irradiation throughout the system, and these are good to track MPP only and are usually unable to differentiate between GMPP and LMPP, and as a result, they stagnate at the first peak in power–voltage curve. As the GMPP is not tracked and the algorithm gets stagnated at the first peak itself, irrespective of it being the GMPP or LMPP, the losses in these systems are high. Therefore, to find out the GMPP and reduce losses, use of fuzzy logic was introduced in MPPT [4]. Fuzzy logic gave better results but they caused heavy computational burden on the processor that used to use up much space due to the fuzzification and defuzzification. Alternately, use of neural network required huge data. This caused the people to turn towards more evolutionary techniques such as the particle swarm optimization (PSO). This technique was very useful in finding the GMPP but the only disadvantage it had was that it took a large count of iterations to converge. If the velocity of the search was increased, the technique never converged, and at the same time, if the velocity of the operation was decreased too much, the convergence would take long time to occur. With these difficulties in mind, researchers made modifications to the classical PSO and found the Adaptive perceptive PSO (APPSO) and modified PSO. These techniques were better as they provided separate search space for each particle, but they also required a large number of particles to search the whole region and it also increased the complexity and load on the processor. Researchers still kept developing the technique and brought out improved PSO (IPSO) [5], novel PSO, etc. Those modifications improved the working performance of the whole power extraction system by improving its ability to search but they also created large oscillations. This made the system unstable. Other than PSO, numerical approach and simulated annealing are also being used for finding the GMPP. These techniques were efficient but did not make much of a difference.

Grey wolf optimization (GWO) is a technique developed by Mirjalili which had comparatively lesser oscillations and computational burden and enhanced searching ability. Mohanty proposed MPPT algorithm which worked based on GWO [6]. This algorithm was inspired from the hunting behaviour of grey wolf. It consisted of tracking, encircling and attacking its prey. This technique was better than the previous

ones but still stagnated on LMPP if the difference between the LMPP and GMPP was too small.

Therefore, Mirjalili once again came up with a better method called the ‘Whale optimization (WO)’ algorithm [7]. This method has lower probability of stagnating at the LMPP. This technique is developed based on the bubble net hunting technique of humpback whales. In this technique, the trajectory path is depending upon the shrinking circling movement. Because of such tracking mechanism, the whole search space is covered. The movement of the whale consists of a spiral movement and also a linear inward movement. The probability of finding the GMPP is based on random numbers. This is a probabilistic algorithm in which the chance of finding the GMPP is greater than or equal to 50% and the chances of stagnating at the LMPP is less than or equal to 50%. The chances of success can be increased by increasing the count of searching whales in the algorithm, but this brings out problems of large initial oscillations, computational burden and makes the system unstable.

In this paper, we have introduced a technique which combines differential evolution (DE) technique with the whale optimization algorithm. This new technique overcomes the problem of excessive number of spiralled paths in the WOA, the need for excessive number of searching whales in the WOA and also eliminates the chances of stagnation at LMPP. The DE has a strong searching mechanism and a high agility. All DE does is that it chooses one best position of the whale, out of the three positions provided by the WOA. The DE includes three processes such as the mutation, the crossover and the selection. The WODE does not have the common disadvantages of other evolutionary algorithms like the larger convergence period, big counts of searching particles, high stress, steady-state stability on the processor, etc., that causes power loss, oscillations and delays in output. The WODE algorithm with these advantages favours the tracking of GMPP easily within the shortest possible time and with least number of search particles. This method is simulated in MATLAB (Fig. 2).

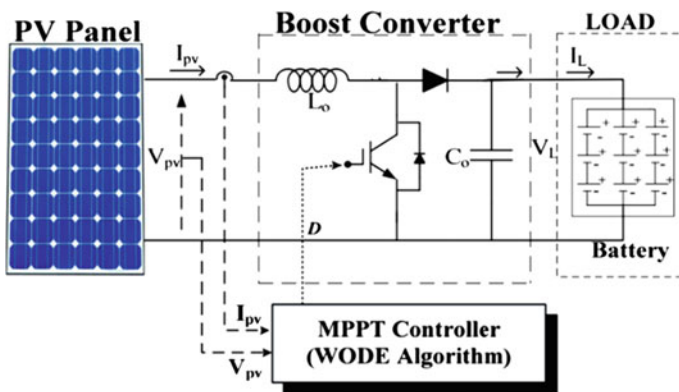


Fig. 2 Basic layout of a solar PV system

A solar PV farm or an array has a number of solar panels connected in parallel and series combinations. During normal operating conditions the solar irradiance on the panels is uniform and the power produced by them is uniform, but in partially shaded conditions the power produced by each panel is not uniform. Power generated by the solar PV panels that are shaded is less compared to the panels which are not shaded; the panels in the shaded region produce lesser current. This produces a voltage drop in the system and reduces the output power. To eradicate this problem, we use bypass diodes (D_{By}) across each panel in a series of panels. When these series of panels are connected in parallel, due to the drop in voltage, a circulating current flows through the system. To eradicate this problem, blocking diodes (D_{BL}) are used in series to the strings of the series of panels.

2 WODE Algorithm

The WODE is the combination of two revolutionary techniques. It combines the properties of the WOA with the strong and fast searching properties of the DE technique. The algorithm runs in cycle in which the WOA is first executed and then the DE is screens out the best starting point for WOA. The objective function of WODE (f) is given as,

$$f(D) = \max P_{PV}(D)$$

$$P_{PV}(D) = V_{PV}(D) * I_{PV}(D)$$

where $P_{PV}(D)$, $V_{PV}(D)$ and $I_{PV}(D)$ are instantaneous value of power, instantaneous value of voltage and instantaneous value of current at duty cycle D .

Where $0 \leq D \leq 1$.

2.1 Whale Optimization

This algorithm has been developed by observing the behaviour of the humpback whales for hunting. This attack technique is known as bubble net feeding. It is shown in the figure below. It mainly consists of three actions: (1) searching for the prey; (2) encircling the prey; and (3) bubble net attack.

2.1.1 Searching

Initially, the system has a vast number of possible solutions, that is, initially the algorithm searches for a solution randomly. Later on, the WOA searches on a global

level with the help of the random coefficient vector (A). When $|A| > 1$, the humpback whale starts searching for optimum value of GMPP in the entire region. Here,

$$D_{ij}(G + 1) = D_{\text{rand}} - A * d_{ij}$$

$$d_{ij} = |C * D_{\text{rand}} - D_{ij}(G)|$$

$$A = 2 * \alpha * \text{rand} - \alpha$$

$$\alpha = 2 - 2 * G/g$$

where

D_{rand} is random duty cycle.

$D_{ij}(G + 1)$ is $G + 1$ th iteration's duty cycle.

d_{ij} is coefficient vector of j th whale and i th agent of DE.

rand and C are random numbers where rand lies between 0 and 1 and $C = 2 * \text{rand}$.

α is a linear iteration-dependent number.

i is Current Population.

G represents the present iteration number.

g is the maximum number of iteration.

2.1.2 Encircling

Here, whale finds the most optimum prey and starts to move towards it. That is, the algorithm finds an appropriate GMPP and moves towards it. This happens when $|A| < 1$. Here,

$$d_{ij} = |C * D_{\text{best}}(G) - D_{ij}(G)|$$

$$D_{ij}(G + 1) = D_{\text{best}} - A * d_{ij}$$

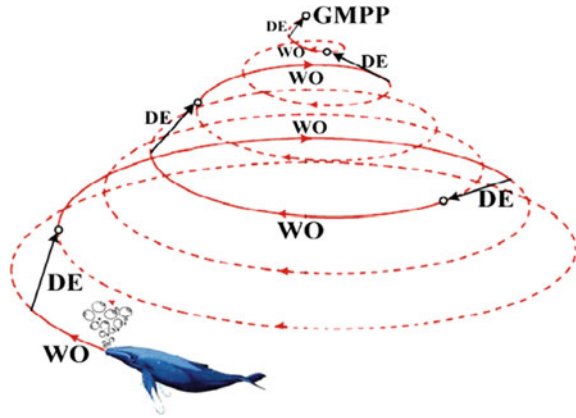
where

$D_{\text{best}}(G)$ is known as best duty cycle after the G th iteration.

2.1.3 Bubble Net Attack

During the bubble net attack, whale is driven in two directions: (1) linear motion of the whale and (2) circular motion of the whale. Both have a 50–50% probability of occurrence of both the types of movement (Fig. 3).

Fig. 3 Bubble net attack of a whale with the linear and spiralling motion as in the WODE



$$D_{ij}(G + 1) = \begin{cases} D_{\text{best}}(G + 1) - A * d_{ij} & \text{if } P_C < 0.5 \\ d'_{ij} * e^{bL} * \cos(2\pi L) + D_{\text{best}}(G) & \text{if } P_C \geq 0.5 \end{cases}$$

2.2 Differential Evolution

DE is used here in order for enhancing the working ability of the WOA. It is a probabilistic method. It takes up the three output vectors of the WOA ($D_{i1}(G)$, $D_{i2}(G)$ and $D_{i3}(G)$) and then processes them to produce another vector that is closer to the GMPP. The processes under the DE are (1) mutation, (2) crossover and (3) selection.

2.2.1 Mutation

The mutation produces a trial vector ($U_i(G)$) from the output vectors of WOA ($D_{i1}(G)$, $D_{i2}(G)$ and $D_{i3}(G)$) otherwise called the parent vector. This is done with reference to the scale factor of mutation (ξ). The mutation given as

$$U_{ij}(G) = D_{ij}(G) + \xi * (D_{i2}(G) - D_{i3}(G))$$

2.2.2 Crossover

Here, a child vector ($D'_i(G)$) is selected from either of the two vectors (trial vector ($U_i(G)$) or the best parent vector ($D_{i1}(G)$)). Crossover is done by using crossover probability (ρ).

$$D'_i(G) = \begin{cases} U_i(G) & \text{if rand} \leq \rho \\ D_{i1}(G) & \text{if rand} \leq \rho \end{cases}$$

2.2.3 Selection

The DE part chooses the most appropriate option ($D_i(G + 1)$) for the next iteration. This selection is done based on the best value of objective function (f) (Fig. 4).

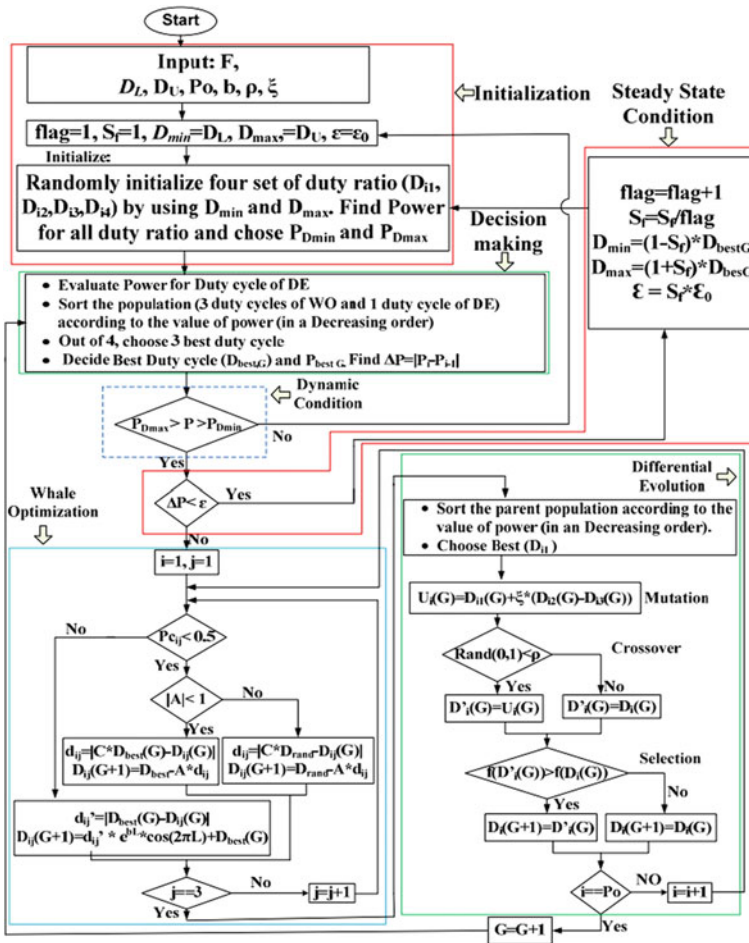


Fig. 4 Complete flowchart of WODE algorithm

$$D_i(G + 1) = \begin{cases} D'_i(G) & \text{if } f(D'_i(G) > D_{i2}(G)) \\ D_{i1}(G) & \text{otherwise} \end{cases}$$

2.3 Selection of Control Parameters

The control variables have an important part in an algorithm. By choosing the appropriate control parameters, the algorithm can run easily. The three control parameters that control the working of WODE are (1) shape constant (b), (2) scaling factor (ξ) and (3) crossover probability (ρ).

2.3.1 Shape Constant (b)

This variable determines the radius and the shape of the spiral net in the WO. If b is small the accuracy of the algorithm increases, but if the value of b is too small the convergence rate decreases thereby taking long to find the GMPP. Therefore, the optimum range of b is [0.1–1].

2.3.2 Scaling Factor (ξ)

In simple terms, it is an amplification factor. It controls the differential variations in the DE. If small ξ is taken, the differential variation is reduced but has a bigger convergence time, facilitating exploration on large scale. It may also cause overshoot of optimum result. The optimum range is [0–5].

2.3.3 Crossover Probability (ρ)

It affects the diversity of DE. For a higher value of ρ , the diversity, exploration and convergence rate in DE are more, but search robustness is less. For smaller values, the search robustness increases but the rate of convergence becomes low. The optimum value of ρ lies in the range of [0.1–1].

The value of the control parameters is decided in two steps:

Step-1: The limit of optimum constants ($b \in [0.1, 1]$, $\xi \in [0, 5]$ and $\rho \in [0.1, 1]$) is separated into 10 equal sections and samples are made with the combinations. Now, we have 1000 combinations. All the combinations are tested 20 times by simulation, and the average tracking duration is calculated. The result to the first step is the combination of the control parameters with the least average tracking time. An example is shown below (Fig. 5).

Fig. 5 MPPT tracking time for step 1

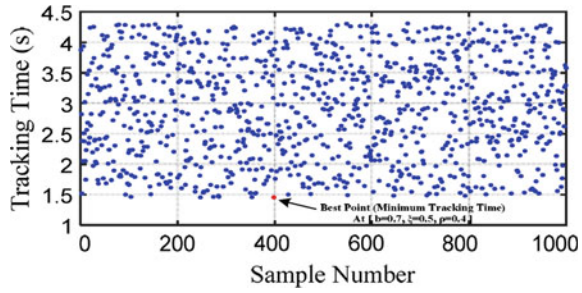
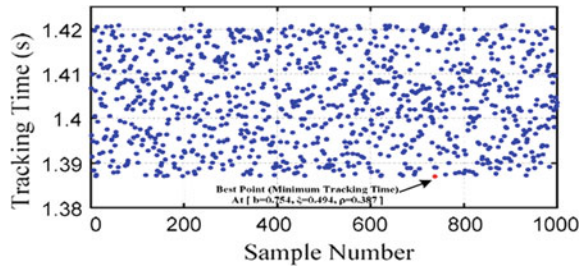


Fig. 6 MPPT tracking time for step 2



The above figure shows the tracking duration changes from 1.451 to 4.319 s and the most appropriate set of constant values is $b = 0.7$, $\xi = 0.5$ and $\rho = 0.4$ for the mean tracking duration of 1.451 s.

Step-2: The best values (result) of the previous step are again separated into a range of 10 more steps ($b \in [0.63, 0.77]$, $\xi \in [0.45, 0.55]$ and $\rho \in [0.36, 0.44]$). Now again we have 1000 combinations and all the combinations are again tested 20 times by simulation and the mean tracking duration is calculated. The solution to this step is the mixture with the least mean tracking duration (Fig. 6).

The above figure shows that the tracking duration varies from 1.387 to 1.421 s and the most appropriate set of constants is $b = 0.754$, $\xi = 0.494$ and $\rho = 0.387$ for the mean tracking duration of 1.387 s. The gap between the lowest and highest results in the second step is small (34 ms), so the results of the second step can be taken for global use. But, in case the gap between is more, the step-2 is reiterated with the solution of step-2 itself.

3 Results and Conclusion

The WODE has been implemented successfully and runs on simulation using MATLAB. The power waveform and the duty cycle waveform are shown below for an example simulation run. From the power waveform, we can clearly say that the WODE tracks the GMPP in the least time, thereby reducing the loss of power (Figs. 7 and 8).

Fig. 7. Power waveform

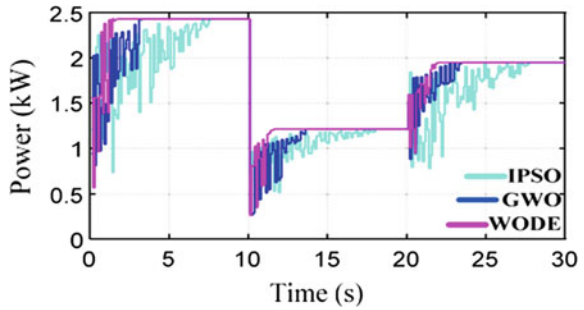
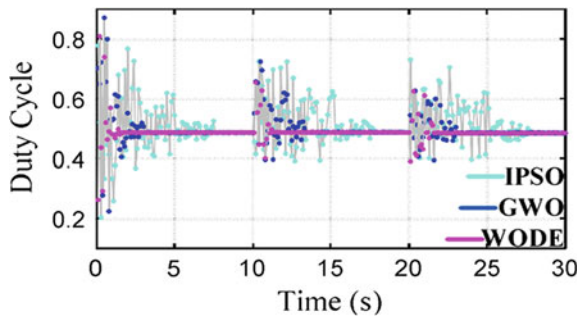


Fig. 8 Duty cycles



The output of WODE has been compared with other techniques and the comparison has been tabulated below. The comparison is done depending on factors such as convergence time, efficiency and average number of iterations (Table 1).

From the above table, we can clearly infer that WODE algorithm is far better compared to the other well-known techniques such as the GWO and the IPSO. The WODE takes about a quarter the time used up by the IPSO to track the GMPP and about half the time used up by the GWO algorithm. Its efficiency is higher than the others too. The average number of iterations taken by the WODE is lesser to the others too. The stagnation of the tracking algorithm at the LMPP is not seen in WODE. Based on the comparison, we can surely say that WODE has lot many advantages over the other well-known algorithms. It is showing such results because of the combination of the two efficient and strong algorithms (WO & DE). This gives it a good steady-state and dynamic stability.

Table 1. Comparison of WODE with other well-known algorithms


Methods	Average number of iterations	Average % efficiency	Average tracking time (s)
IPSO	29	87.967	8.01
GWO	15	95.167	3.57
WODE	7	98.844	1.36

References

1. Subudhi B, Pradhan R (2013) A comparative study on maximum power point tracking techniques for photovoltaic power systems. *IEEE Trans Sustain Energy* 4(1):89–98
2. Patel H, Agarwal V (2008) Maximum power point tracking scheme for pv systems operating under partially shaded conditions. *IEEE Trans Industr Electron* 55(4):1689–1698
3. Kollimalla SK, Mishra MK (2014) Variable perturbation size adaptive P&O MPPT algorithm for sudden changes in irradiance. *IEEE Trans Sustain Energy* 5(3):718–728
4. Guruambeth R, Ramabadran R (2016) Fuzzy logic controller for partial shaded photovoltaic array fed modular multilevel converter. *IET Power Electron* 9(8):1694–1702
5. Ishaque K, Salam Z, Amjad M, Mekhilef S (2012) An improved particle swarm optimization (PSO)-based MPPT for PV with reduced steady-state oscillation. *IEEE Trans Power Electron* 27(8):3627–3638
6. Mohanty S, Subudhi B, Ray PK (2016) A new MPPT design using grey wolf optimization technique for photovoltaic system under partial shading conditions. *IEEE Trans Sustain Energy* 7(1):181–188
7. Prakash P, Mohana Sundaram K, Anto Bennet M (2017) Parameter estimation of carbon nano tubes field effect transistor (CNFET) using whale optimization algorithm. In: International conference on energy, data analytics and soft computing (ICECDS-2017)

A Case Study on Implementation of an Efficient and Cost-Effective Solar Power Generation System for Irrigation Purpose



K. S. Tamilselvan , G. Mageshkumar, S. Suthagar, and G. Murugesan

Abstract In present days, it is a great need and urgency for an alternate source for energy conservation. As the limitations of conventional energy are more such as availability, generation cost, and utilization, it is an urge to go for nonconventional energy. In non-conventional energy sources, solar plays a major role, particularly in countries like India as surplus solar energy is freely available. In this chapter, the authors present “an efficient and cost-effective solar power generation system for irrigation purpose.” The case study includes design, development, and implementation of insulated gate bipolar junction transistor (IGBT)-based solar energy conversion to run a three-phase motor for irrigation applications. The highlight of the design is the use of a minimum number of solar panels for the design. Solar power is effectively utilized to run the motor with the help of specially designed drives. Sufficient protection and security are also provided. The proposed design uses a 1.8 kW solar panel for 3 HP power rating motor. Three different control stages are used in the design, namely pulse width modulator (PWM) stage, variable frequency drive (VFD) stage that is voltage to frequency converter and maximum power point tracking (MPPT). The control techniques are provided by using a high-speed processor. The authors designed and fabricated the solar power system and verified the performance. A three-phase induction motor was successfully run from 8.00 am to 5.00 pm with normal sunlight. Running status of the motor including ON/OFF status, water throughput, load current, frequency, and voltage are informed to the farmer with the help of GSM module. This chapter provides an efficient and economically viable solution for farmers.

Keywords Insulated gate bipolar junction transistor · Pulse width modulator stage · Variable frequency drive · Maximum power point tracking

K. S. Tamilselvan (✉)
Department of ECE, KPR Institute of Engineering and Technology, Coimbatore, India
e-mail: kstamilselvan@gmail.com

G. Mageshkumar · S. Suthagar · G. Murugesan
Department of ECE, Kongu Engineering College, Perundurai, India
e-mail: magesh.me.est@gmail.com

1 Introduction

Many renewable energy sources are available in present days, but out of all the sources, photovoltaic principle-based power generation plays an important role. The reason behind these phenomena is the utilization of solar power, which is available freely. Using a large array of PV systems for solar power generation has its own limitations when connected to the stand-alone load or to the power grids such as voltage fluctuations and a high-frequency deviation [1]. The implementation of PV-based systems in electrical power generation will make a high impact on the overall power system in future. If such impact is made, then the dependency on non-renewable resources will be reduced. Proper measures should be carried out in order to maintain high reliability of power system when we combine two or more PV systems [2]. DC voltage generated by the solar panel is converted into AC power which in turn is used to run a three-phase induction motor. The reason for choosing a three-phase induction motor over single-phase induction motor is that it has less severe effects on starting current. This system requires variable speed control techniques because the sun constantly changes its position and the power generated by the stationary PV cells varies accordingly. From the observation, in different voltage situation, the motor does not produce maximum torque in specific supply frequency. Therefore, the supply frequency should be changed to achieve maximum power. A three-phase induction motor controller (inverter) was developed to drive the motor in variable frequency from 15 to 50 Hz.

2 Materials and Methods

The block diagram of the proposed system is shown in Fig. 1. The following text explains the functionality of individual blocks in the design. This design is capable

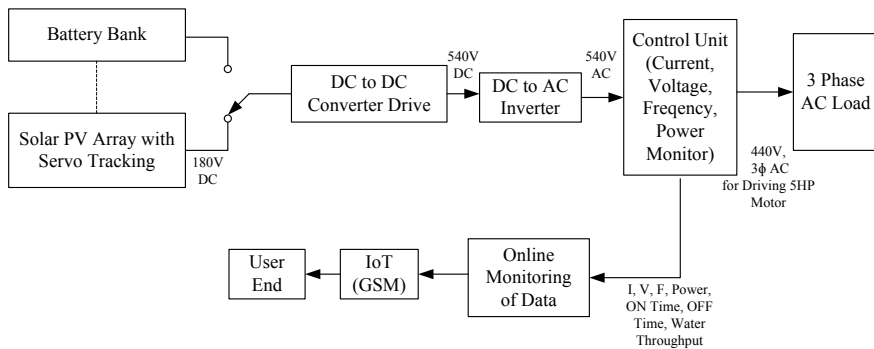


Fig. 1 Block diagram of solar-power generation system

of generating power from solar panels in an effective manner even with low sunlight. The following are the blocks in the design,

- Solar Panel Array
- Servo motor
- DC–DC Converter Drive
- DC–AC Inverter
- Control Unit
- Online Data Monitoring
- GSM for IoT
- Battery Bank.

2.1 Solar PV Array and Battery Bank

The solar photovoltaic array converts the sunlight into electrical energy. An array of six elements of 30 V and 250 W high-efficiency polycrystalline solar panels is connected in series to generate 180 V DC. According to the power requirement, another array of solar panels shall be connected in parallel to the first array of solar panels to increase the current rating, thereby increasing the power delivered by the array (Fig. 2).

The tracking of sunlight is provided with a light-dependent resistor (LDR). The solar panel is mounted on a frame that has servo motors attached to it that will turn the solar panels to face the sunlight directly from morning to evening. The servo motor setup ensures that the source is utilized to maximum efficiency. The voltage generated by the solar array is used for driving the motor as well as to charge the battery bank. The battery bank ensures that the uninterrupted power is delivered to the load. When the sunlight is not sufficient to generate power that could drive an AC



Fig. 2 Solar photo-voltaic array (six panels)

load, then the design automatically switches from the solar power mode to battery-operated mode. In such a situation, an SMS is sent to the user to intimate that the power mode is changed. The user can reply to that SMS and choose to turn OFF the load/ keep the load ON.

2.2 DC–DC Converter

In DC–DC converter block, 180 V DC input is converted into 540 V DC output using the boost converter. The generalized circuit diagram for a DC–DC converter is shown in Fig. 3. In the circuit when the switch SW1 is open, the capacitor C1 gets charged to V_{in} , and if the switch SW1 is closed, the current flow through the inductor L1 increases in a linear manner. During this period, the energy stored in the capacitor C1 gets discharged and flows through the load R_L [3]. The diode D1 prevents the discharge of current through D1. When the switch SW1 is opened again, the charge stored in the inductor decreases linearly through diode D1 to load R_L . The diode D1 is called as a freewheeling diode which acts as forward biased for the energy from the inductor, and it acts as reverse biased for the energy from the capacitor, thereby ensuring that the current through the load R_L remains undisturbed.

From the description above, we can infer that the load current varies linearly depending on the switch positions (ON/OFF). When the switch is ON, the load current increases linearly, and when the switch is OFF, the load current decreases linearly [4, 5]. The rate of increment and decrement depends on how fast the switching happens. In order to achieve a high output voltage, the switch can be replaced with high power and high speed switching transistors such as 2N3055 and BU508. The transistor can be turned ON and OFF using a programmable pulse generator.

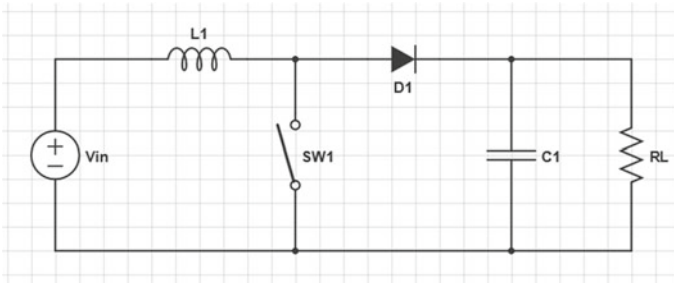


Fig. 3 DC–DC boost converter

2.3 DC–AC Inverter

An inverter is a circuit that converts DC into AC. In this design, an inverter stage is used. The circuit is intended to drive an AC load, a 3 hp three-phase induction motor. The power requirement for the load is 2.25 kW. The designed inverter can deliver the required power. If the power delivered is less than the requirement, then the control unit will take care of the necessary safety precaution measures to protect the motor [6].

2.4 Control Unit

The control unit is designed using a PIC microcontroller (PIC18F2550). The control unit monitors the running status of the AC load. The designed system is tested with a 3 hp, three-phase induction motor for irrigation purpose. The parameters that are monitored by the microcontroller unit are voltage, load current, frequency, and power delivered [7, 8]. The control unit also has the features of over-voltage protection, short-circuit protection and overload protection. In case of any undesirable operational conditions, the control unit disconnects the motor and ensures the safety of the load connected to it. The user, based on the climatic conditions of the particular area, can adjust the threshold levels of the parameters [9].

2.5 Data Monitoring

The status of the system is displayed in a 4×16 LCD. The data monitored by the control unit is sent to the user through an SMS at regular intervals. The following are the kinds of messages that are can be sent to the user:

- Input Voltage = 180 V
- Output Voltage = 430 V
- Frequency = 50 Hz
- Load Current = 20 A
- Motor ON Time 09:47 AM
- Motor OFF Time 12:03 PM

3 Implementation

The above-discussed design was practically implemented and tested in a private agricultural field in Kodaikanal Hills, India. The system was tested to be successfully

delivering the required power for running a 3 hp, three-phase induction motor for watering the agricultural field. Figure 4 shows the IGBT section of DC-to-AC inverter where the high voltage DC is converted into a high voltage AC sufficient to drive the motor for irrigation purpose. The control unit section of the system is shown in Fig. 5.



Fig. 4 Insulated gate bipolar junction transistor section of DC-AC inverter

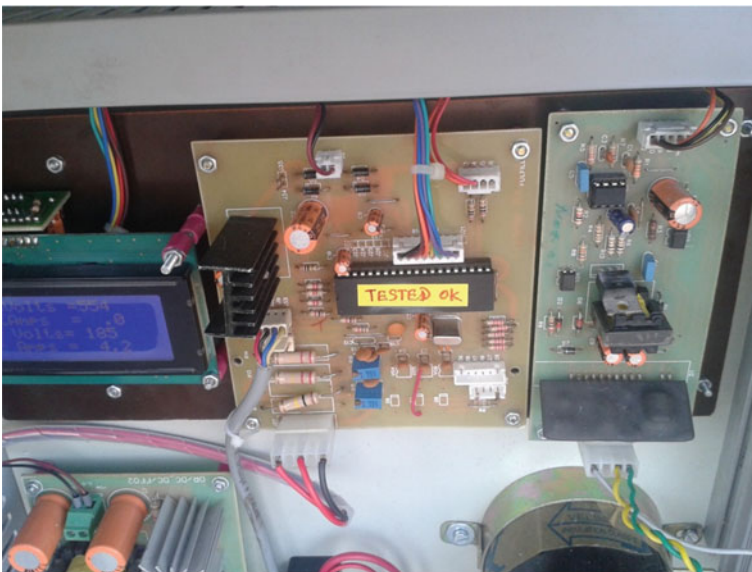


Fig. 5 PCB of control unit

4 Result

Table 1, shows the results of the implemented solar power generation system. The energy obtained from the solar panel will be maximum during the time between 11:30 am to 3:00 pm. The table displays the readings of input voltage, input current and calculated DC power from the solar panel to the designed system. The formula for calculating the DC power (P_{dc}) is shown in Eq. (1).

$$P_{dc} = V_{dc} * I_{dc} \tag{1}$$

In the above equation, V_{dc} and I_{dc} correspond to the DC voltage and DC current obtained from the solar panel at different times in a day starting from 07:00 am to 05:30 pm.

The inverter block in the system converts the DC power into AC power. The AC voltage and AC current at the output are measured, and AC power (P_{ac}) is calculated using the formula given below.

$$P_{ac} = \sqrt{3} * V_{ac} * I_{ac} \tag{2}$$

In the above equation, V_{ac} and I_{ac} correspond to the AC voltage and AC current obtained from the inverter output at different times in a day starting from 07:00 am to 05:30 pm.

The efficiency (η) of the inverter system is calculated using the Eq. (3) given below,

$$\eta = \left(\frac{P_{ac}}{P_{dc}} \right) * 100\% \tag{3}$$

Table 1 Implementation results of solar power generation system

Time at which data are acquired	Input DC voltage from solar panel (V_{dc})	Input DC current (I_{dc})	Input DC power $P_{dc} = V_{dc} * I_{dc}$	Output AC voltage (V_{ac})	Output AC current (I_{ac})	Output AC power $P_{ac} = \sqrt{3}(V_{ac} * I_{ac})$	Efficiency $\eta = \left(\frac{P_{ac}}{P_{dc}} \right) * 100\%$
07:00 am	34	0.50	17.00	25	0.32	13.856	81.51
10:00 am	130	0.75	97.50	75	0.71	92.229	94.59
12:30 pm	180	0.96	172.80	119	0.83	171.000	98.96
02:00 pm	158	0.85	134.30	95	0.80	131.630	98.01
04:00 pm	108	0.65	70.20	59	0.58	60.290	85.88
05:30 pm	72	0.60	43.20	41	0.51	36.216	83.83

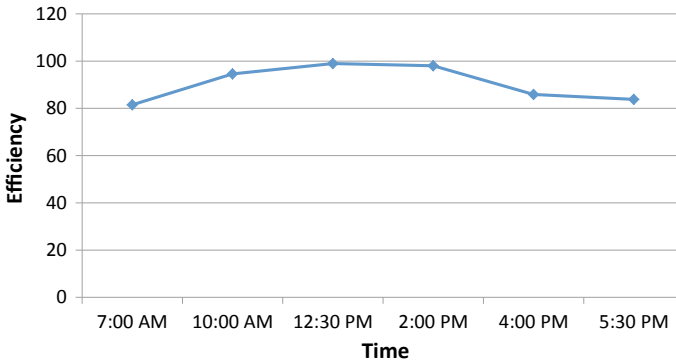


Fig. 6 Time versus efficiency of the system

From the table, it is inferred that the efficiency of the inverter system is maximum during the midday. The power generated by the system is capable of running a 3 hp motor, from 08:00 am till 05:00 pm. The throughput of water pumped by the motor is low when the sunlight is lesser, and it is higher during the midday. The system works even when the availability of sunlight is less on a cloudy day.

The graph in Fig. 6. represents the variation of efficiency of the designed solar power generation system with respect to time in a day at a private form in Kodaikanal. The efficiency is observed from the graph that it maximum during midday and reduces as the time varies in both directions.

5 Conclusion

The designed system consists of individual sub-modules that can be interconnected into a complete unit. If one part of the design fails, then that particular module alone can be tested and rectified. At every stage of development of the system, the modules are tested to give the desired voltage, current, frequency and power ratings. This design is highly suitable for tribal villages in hill areas where the electrical facility is difficult to establish. The design also has some limitations considering the low light conditions in hill areas that the power delivered to the load may be reduced. Although the power delivered is low, the system will not affect the load. The reason for this is that the power to the load will be disconnected automatically when the power goes down below the threshold value set by the user. In future, some additional facilities such as dry run prevention and pushing the parameters into the cloud with IoT application for future reference.

References

1. Sharma A, Parakh A (2018) Design of solar powered induction motor drive for pumping application. *Int J Latest Trends Eng Technol* 10:228–237
2. Mahitha M, Tejasw G (2016) Grid interfaced 3-phase solar inverter with MPPT by using boost converter. *Int J Modern Trends Sci Technol* 2:21–26
3. Arul DS, AmmasaiGounden N (2004) A novel hybrid isolated generating system based on PV Fed inverter-assisted wind driven induction generators. *IEEE Trans EC* 19:416–422
4. Yousuf NB, Salim KM, Haider R, Alam MR, Zia FB (2012) Development of a three phase induction motor controller for solar powered water pump. In: 2nd international conference on the developments in renewable energy technology
5. Coelho RF, Concer FM, Martins DC (2010) A simplified analysis of DC–DC converters applied as maximum power point tracker in photovoltaic systems. In: IEEE international symposium on power electronics for distributed generation systems
6. Raj CT, Srivastava SP, Agarwal P (2009) Energy efficient control of three-phase induction motor. *Int J Comput Electr Eng* 1
7. Philip J, Jain C, Kant K (2016) Control and implementation of a standalone solar photo-voltaic hybrid system. *IEEE Trans Ind Electron* 52:3472–3479
8. Mastromauro RA, Liserre M, Dell'Aquila A (2007) Single-phase grid-connected photovoltaic systems with power quality conditioner functionality. In: 12th European conference on power electronics and applications, Aalborg
9. Borgum FJ, Nijhof EBG (1980) Inverter circuit for a PWM motor speedcontrol system. *Electron Compon Appl* 2:130

Augmented Yield Productivity of Solar Still Using Energy Storage Materials: Experimental Investigation Under the Climatic Conditions of Rajasthan



Amrit Kumar Thakur, M. Ponrajan Vikrama, and S. Christopher

Abstract Freshwater scarcity and growing vitality essential are among the most important issues around the world. In the current work, an effort is made to improve the yield of existing single-slope single-basin solar still (SS) with basin area of 1 m^2 using various energy absorbing material such as black granite stone, metal scrap of mild steel and nanoparticle Al_2O_3 in the water basin, and the freshwater yield was compared with and without the energy storing material (ESM) for the water depth of 0.01 m. Yield of freshwater augmented by 11.6%, 25.1% and 33.5% by using metal scrap, black granite and nanofluid Al_2O_3 inside the water basin, respectively, and the full day efficiency augmented by 15.5%, 26.8% and 33.6% as compared to the conventional SS. It was concluded that the solid nanometric size particle Al_2O_3 inside the water basin helps in achieving the maximum yield of the freshwater. SS is also proficient to eliminate the impurities of brackish water and convert it to pure and distilled water with PPM ranging below 50 and makes it ideal for the rural Indian villages with economical and hygienic point of view.

Keywords Solar still · Nanofluid · Desalination · Evaporation · Condensation

Nomenclatures

q_{rws}	Rate of radiative heat transfer (W/m^2)
q_{ews}	Rate of evaporative heat transfer (W/m^2)
h_{rws}	Radiation heat transfer coefficient ($\text{W}/\text{m}^2 \text{ k}$)
h_{cws}	Convection heat transfer coefficient ($\text{W}/\text{m}^2 \text{ k}$)
h_{ews}	Evaporative heat transfer coefficient ($\text{W}/\text{m}^2 \text{ k}$)
h_{lws}	Total inner surface heat transfer coefficient ($\text{W}/\text{m}^2 \text{ k}$)
P_{ts}	Total partial pressure of solar still (N/m^2)
P_{bws}	Partial pressure of basin (N/m^2)

A. K. Thakur (✉) · M. P. Vikrama · S. Christopher
Department of Mechanical Engineering, Anna University (CEG Campus),
Chennai 600025, India
e-mail: amritt1@gmail.com

© Springer Nature Singapore Pte Ltd. 2020

A. K. Bhoi et al. (eds.), *Advances in Greener Energy Technologies*,
Green Energy and Technology, https://doi.org/10.1007/978-981-15-4246-6_51

P_{gs}	Partial pressure of glass (N/m^2)
A_{bws}	Area of water basin (M^2)
T_{bws}	Temperature of water basin ($^{\circ}C$)
T_{gs}	Temperature of glass ($^{\circ}C$)
M_{ws}	Molecular weight of water
M_{as}	Molecular weight of air
M_{ews}	Hourly yield production of distilled water (l)
M_d	Full day yield production of distilled water (l)
C_{pa}	Specific heat capacity ($J/kg\ k$)
LW	Latent heat of vaporization (J/kg)
I	Solar radiation (W/m^2)

Greek Letters

ϵ_{eff}	Emissivity of glass surface
σ	Stefan–Boltzmann constant = $5.669 \times 10^{-8} W/m^2 K^4$
η	Efficiency (%)
Δt	Time step (second)

1 Introduction

Clean consumable water is a fundamental need for human being alongside air and food. Direct employments of the water from source like lake, rivers, ocean and groundwater stores are not generally prudent, due to the closeness of higher quantity salt/high dissolved impurities/harmful organisms. Developing populaces, expanding financial exercises and an adjustment in atmosphere have prompted to genuine shortage of drinking water in numerous nations [1]. 79% of the world's surface is encased with water, however, lesser than 1% of the all out accessible water is perfect water, a large portion of which is accessible in waterways, lakes and underground and just around a 33% of this freshwater must be utilized for human needs. A propos 1.1 billion populace in the world has admittance to sufficient drinking water safety issues [2] and no less than 80% of dry and semi-dry nations have severe cyclical droughts. In India, the lack of clean water is a serious issue in the beach front district, especially in the remote waterfront area. Sunlight-based refining is the strategy where sun essentialness is utilized to create clean water from salty/harsh water for drinking, local and different utilizations. There are various refining methods urbanized for desalination that is basic and financially savvy. Among these available methods, solar distillation is most practical and economical, especially for freshwater production from brackish water [3]. India, as a moist nation, has plenitude of daylight and the normal consistently sun powered vitality vary between 4 and 7 KWh/m^2 in various

areas of the nation. Generally of a normal premise, nation has 250–300 clear, bright days in a year, and along these lines, nation gathers a propos 5000 trillion kilowatt-long periods of sun powered vitality a year [4]. Desalination procedure is believed to be a standout among the least perplexing and extensively gotten frameworks for changing over saline water into freshwater. One of the primary focal points of the purifying procedure is that it needs warming just up to 120 °C, which can be provided from sun-based vitality. Conventional desalination techniques used are costly to produce a small quantity of freshwater. In addition, the utilization of conventional vitality sources is not for eternity environmentally friendly. In desalination processes, solar still can be used to generate clean water from briny water source. Mostly for purifying water with very economical and simple constructional mechanism, solar still is preferred. Major drawback of solar still is its productivity and overall efficiency. Many researchers have investigated the effects of a variety of parameters such as glass cover, inclination angle, insulation, basin design and energy absorbing material on the solar still productivity.

These parameters help into analysis, so that the enhancement in the yield productivity rate and effectiveness of the solar still can be made. Thakur et al. [5] contrasted the profitability of SS and water profundity of 0.01 m having nanofluid Al_2O_3 inside the basin water and contrasted these outcomes with phase change materials (PCM) for same profundity. It was experiential that the yield of the SS achieves most noteworthy esteem when nano-sized particles Al_2O_3 is utilized in water bowl as contrast with customary SS and SS with PCM. Thakur et al. [6] fabricated SS and created black nano-paint (Al_2O_3 mixed with black paint) and covered it inside the bowl and internal walls of the SS. Al_2O_3 was situated in the inside of the water bowl to absorb the maximum solar vitality and attributable to this, yield expanded. Thakur et al. [7] streamlined SS and approved the trial results with CFD device for the water profundity of 0.01, 0.02 and 0.03 m. It was seen that most acute yield was accomplished when water profundity had a base respect, i.e., 0.01 m. Rajvanshi [8] present the intelligent and preliminary examination of the effect of including dyes to a sun controlled desalination unit. Unique hues like dark naphthylamine, red carmoisine and dim green used. It was seen that black naphthylamine shading saw to be for the most part apt which augmentation the yield productivity of SS by 29%. The precise portrayal saw that increase of the neighboring temperature by 40% expand the yield productivity by 27% and augmentation of yield by around 10% with a wind speed increase from 1 to 32 km/h. The development of the distillate with developing mindfulness of dye up to 500 ppm, after which it is sovereign of the mindfulness. Sodha et al. [9] were abuse red, dark and violet colors for insightful the effect of colors on the recitation of SS. Result exhibits that the dark and violet colors are more effective than other shadings. It increase the benefit of the SS. Bilal et al. [10] assessed the effect of various retaining materials in a sun-based still and thus improves the gainfulness of refined water. Dark ink, black elastic matt and black colors were used as a part of the examination. The results show that the proficiency of distill water using an enrapturing dark elastic matt extended the entire day creation of water by 38%. Using dark ink extended the proficiency by 45% and black colors delayed profitability by 60%, and it was presumed that black color is the best material in utilizing stipulations of crisp

water yield. Nafey et al. [11] did review of the benefit of the SS, distinctive size of rubber, black in color having thickness of 2, 6 and 10 mm and black rock matter (7–12, 12–20 and 20–30 mm) measure used as essentialness stockpiling materials. Dark elastic with measurement of 10 mm thickness, upgrade the effectiveness by 20% at saline water amount condition of 60 l/m² and rock material with a size of 20–30 mm improve the productivity by 19% at bitter arrangement sum structure 20 l/m², and furthermore, dark shake material retains and release occurrence sun-based essentialness faster than dark elastic. Sakthivel et al. [12] were used dark color stone as vitality stockpiling material to watch the presentation of the SS. An examination was driven with different profundities of the stone layer in ventures of 12, 18, 20 and 25 mm. It was seen that the gainfulness of the SS for entire day with the stone extended by around 17%. SS yield was 3.9 kg/m² every day, which is progressed than that of the SS with imperativeness retaining material dark elastic sheet. Sathyamurthy et al. [13] examined a portable SS with vaporization and condensation compartment. A particular incline portable SS with paraffin wax as PCM was considered and placed between evaporating and condensing chamber. The greatest efficiency of the SS with PCM was 14%. It was seen that subsequent to the day's end PCM acts as a heat resource, and more than 34% of totality yield was achieved, and everyday yield achieved with PCM was 52% more effective than found without PCM. Ravi et al. [14] suggested an experimental method to improve the productivity of sun-based still using heat storage properties of material during daylight times when solar incidence energy has a high value which would be useful for later use when sunlight intensity reduces. Thermal energy storage (TES) was involved with the variation of enthalpy of storage matter. Sensible warmth storage was related by means of the temperature augment of the storage media. Well-organized storage technology was essential to store the energy for 24 h cycle to meet up vitality demand. Experimental outcome of a SS in presence of various kinds of PCM such as magnesium sulfate heptahydrate, potassium dichromate and sodium acetate was used. Among PCMs, magnesium sulfate heptahydrate gives an enhanced yield of potable water. Naima et al. [15] experimentally investigated the performance of SS using different size charcoal as energy storage material and reported its effect on yield of SS. It has been uncovered that the SS with charcoal particles as an imperativeness retaining medium demonstrates a 15% change in productivity over the wick-type still. In like manner coarse size, charcoal particles give praiseworthy results at high stream rates. Sahota et al. [16] considered the deviation of the maximum temperature variation among water and nanofluid assisting Al₂O₃, TiO₂ and CuO nanoparticle. Maximum temperature difference is set up to elevated for Al₂O₃–water-based nanoparticle dispersed fluid go after by TiO₂ and CuO–water-based nanofluids for each one having a concentration of 0.2, 0.25 and 0.3%. This result was achieved just because metallic nanoparticle at high concentration extends more in the specified capacity of the nano-liquid of the passive double slope SS and the facade area for heat transport from nanoparticle to nano-liquid increases which confine elevate the warmth of the nano-liquid. It has been theoretical that involvement gives an augmentation of 13.11, 19.03 and 28.90% for and CuO, TiO₂ and Al₂O₃, water-based nanofluid.

From the above literature review, it was observed that there are mainly a few major category of energy storage material, firstly which is easily and naturally available such as black granite stone, dyes and metal scrap. Other than that nanofluid is also served as energy absorbing material. Many researchers compare the productivity of solar still by using a combination of naturally available ESM while other has compared various nanofluids for productivity enhancement. Very few performances and design details of solar still has been found where nanofluid Al_2O_3 has been compared with naturally or cheaply available energy storage material black granite stone and metal scrap made of mild steel. The major aspire of the current effort is to study:

- Comparison of yield productivity of single-slope SS with energy absorbing material nanofluid Al_2O_3 , black granite stone and metal scrap of mild steel-based SS with same depth of water 0.1 m.
- Full day efficiency comparison of SS for all cases.
- Yield production comparison of calculated and observed data.
- Distilled output water quality level achieved in parts per million (PPM) for all cases using total dissolved solid TDS meter.

2 Experimental System and Procedure

The comprehensive arrangement of investigational setup is revealed in Fig. 1a, b, where the water basin is painted black as well as absorbed plate are black painted

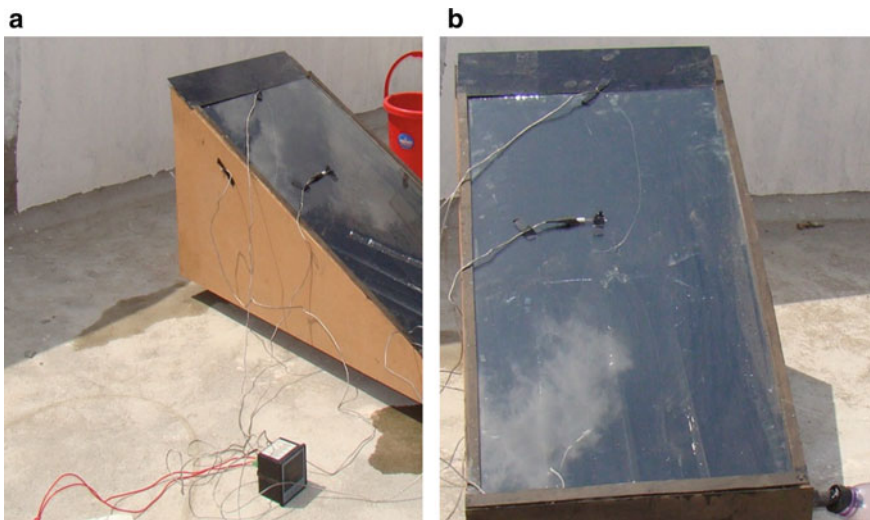


Fig. 1 a, b Photographic view of the fabricated Test setup

in order to augment the fascinating power of basin area. J-type thermocouple with temperature range of 0–250 °C and accurateness range of ± 1 °C in each 0–150 °C is used for measuring temperature of various regions of SS. The experimental has been fabricated and installed in Jaipur, Rajasthan, India with 26.9144° N latitude and 75.7863° E longitude. Glass surface of the SS is south facing in order to collect maximum amount of solar emission. The SS contain the basin area of 1 m² with the absorber plate is made using an aluminum sheet 1.7 mm. In order to decrease heat transfer fatalities, all the boundaries of the water basin of SS are insulated through a 2.5 cm thick plywood and thermocol and the glass surface of the SS is made by simple window glass having very good emissivity value of 4 mm thickness and tending at the angle of 26°.

Experimentations are performed for June 25 to June 28, 2017 in interim time of 7:00 AM–6:00 PM for on normal sunny days. On 25 June, simple solar still yield production has been tested while on 26 June, 2 kg metal scrap made up of mild steel (M.S) is used inside the water basin. Observation has been made on 27 June when 4 kg black granite stone of size 10–15 mm was used in water basin while on 28 June, nanoparticle Al₂O₃ of size 50 nm to 100 mixed with base fluid as water is used in water basin. The temperatures at various locations in the SS are tracked by J-type thermocouples. The surrounding temperature is evidence by utilizing thermocouple (J-type). Pyrometer coupled to an solar radiation meter with precision of ± 30 W/m² and scope of 0–1850 W/m² has been utilized to screen the solar emission. A measuring jar of 1000 ml was used to accurately measure the quantity of fresh water collected from the glass upper surface of the SS. Digital anemometer of model number EQ 619B, equinox has been used to measure wind speed with range 0.40–30 m/s and accuracy level of $\pm 3\%$. In order to measure the hardness of output water from SS. TDS meter of HM Digital manufacturer Inc. with range 0–1200 ppm and accuracy level $\pm 2\%$ full scale has been used.

3 Mathematical Modeling

Sun-oriented radiation esteem is commonly most elevated in evening from 12 noon to 2.30 PM. What is more, in the midst of the time, as the temperature of the inside surface of the glass spread increase; the energetic promptness of buildup diminishes. Along these lines, the energetic promptness of vanishing of water will be extra than the rate of buildup on the glass spread, which impacts the enlargement in temperature of the air vapor space among the water surface and the glass spread. In this technique, to expand the rate of refined water yield in the SS, changes are being made to (i) enlargement the temperature of salty water in the bowl, (ii) dropping the temperature of the glass front of SS and (iii) decline the warmth misfortune and utilize the most noteworthy vitality accessible for the dissipation of water from the water bowl. For this creative investigation, SS viability is improved and to store the over the top possible sun-based vitality in daylight times for the continuation of the vaporization progression at nightfall and evening time. For accomplishing this target so as to

increase the efficiency of the SS, vitality stockpiling materials are utilized in the inside of the water bowl of SS. Following are the condition used to infer determined profitability and proficiency of sun-based still.

3.1 Radiative Heat Transfer

To estimate the slope point of outer glass surface of the SS, the water basin and outer glass cover were considered to be in parallel interminable surface. The rate of radiative heat transfer from water basin to glass cover can be presented as follows

$$q_{rws} = h_{rws}(T_{bws} - T_{gs}) \tag{1}$$

Rate of heat transport coefficient during emission is shown as [17]

$$h_{rws} = \epsilon_{\text{eff}} \cdot \sigma \left[(T_{bws} + 273)^2 + (T_{gs} + 273)^2 \right] [T_{bws} + T_{gs} + 546] \tag{2}$$

where Stefan–Boltzmann constant $\sigma = 5.669 \times 10^{-8} \text{ W/m}^2 \text{ K}^4$.

3.2 Convective Heat Transfer

Heat exchange inside the SS happened because of free convection exchange and it is brought about by the force of buoyancy, convective ebb and flow have been created and it routes from bowl water to the inward glass cover surface. In this manner, the convective heat exchange from water bowl to the inward glass surface spread is given by Dunkle [18]

$$h_{cws} = 0.884 \left[\frac{(T_{bws} - T_{gs}) + (P_{bws} - P_{gs})(T_{bws} + 273.15)}{268,900 - P_{bws}} \right]^{2/3} \tag{3}$$

3.3 Evaporative Heat Transfer

The rate of evaporative heat transfer from the water basin to the inner glass surface is specified by Malik et al. [19]

$$q_{ews} = h_{ews} \cdot A_{bws}(P_{bws} - P_{gs}) \tag{4}$$

The evaporative heat transfer coefficient is given Malik et al. [19]

$$h_{ews} = \frac{(M_{ws} \cdot L_w \cdot P_{ts}) \cdot (h_{cws})}{M_{as} \cdot C_{pa}(P_{ts} - P_{bws})(P_{ts} - P_{gs})} \quad (5)$$

The entirety internal heat transfer coefficient from basin water plane to the condensing glass surface cover is given by

$$h_{1ws} = h_{cws} + h_{rws} + h_{ews} \quad (6)$$

The hourly freshwater productivity can be obtained by Tiwari [20]

$$M_{ews} = (q_{ews}/L_w) \times 3600 = [h_{ews}(T_{bws} - T_{gs})/L_w] \times 3600 \quad (7)$$

Full day yield productivity of solar still is given as

$$M_d = \sum_{24h} M_{ews} \quad (8)$$

Efficiency of solar still is given as

$$\eta_d = \frac{M_d \times L_w}{A_{bws}(\sum I)\Delta t} \times 100\% \quad (9)$$

4 Results and Discussion

Solar energy is the most significant parameter in the calculation of distillate yield from a solar still. The clean water yield relies on the solar energy got for the period of the day. Highest freshwater yield is accomplished when the concentration of solar emission and the surrounding atmosphere warmth are comparatively high. Variability of solar radiation and daytime is appeared in graphical frame in Fig. 2, recorded at 0.01 m water profundity with various cases. In all cases, maximum radiation available was in time among 11 AM–2 PM. Maximum radiation among all the cases was observed 918.17 W/m² for the when nanoparticles-based fluid Al₂O₃ is used in the basin water at 12 noon and minimum of 858.06 W/m² was observed for simple solar still with metal scrap of M.S at same time. Deviation of the ambient temperature w.r.t instance is shown in graphical form in Fig. 3, recorded at water depth of 0.01 m, with and without energy absorbing material, and it was observed that ambient temperature is maximum between 1 and 2 PM and highest value of ambient temperature was observed for nanofluid inside water basin and lowest was observed for solar still with metal scrap of M.S inside water basin.

Fig. 2 Deviation of the solar radiation w.r.t time at 0.01 m water depth

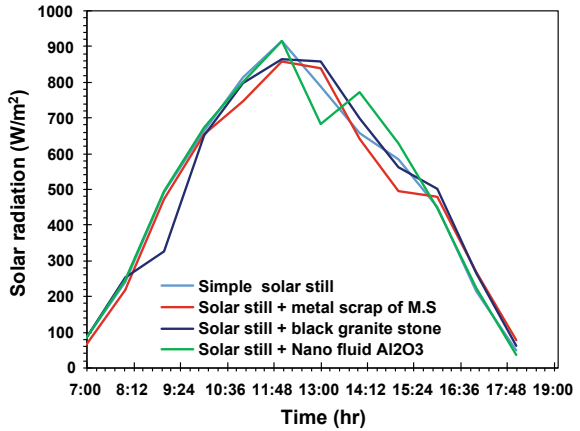


Fig. 3 Difference of ambient temperature w.r.t time at 0.01 m water depth

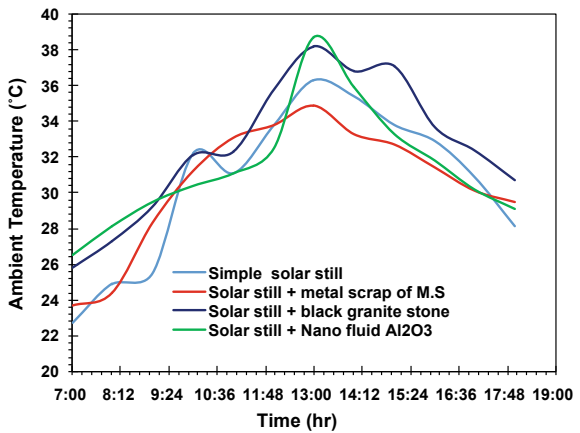


Fig. 4 Deviation of the glass cover temperature w.r.t time at 0.01 m water profundity

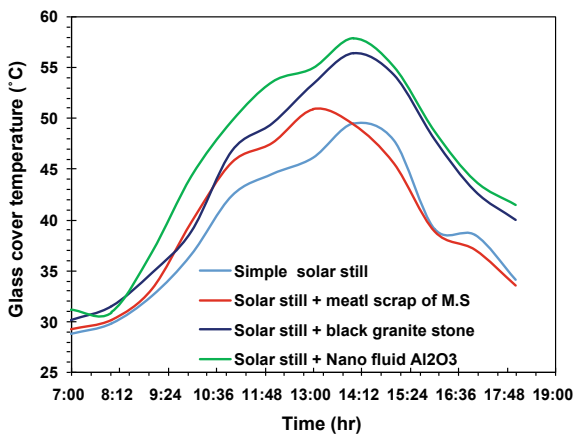


Fig. 5 Deviation of the water basin temperature w.r.t time at 0.01 m water profundity

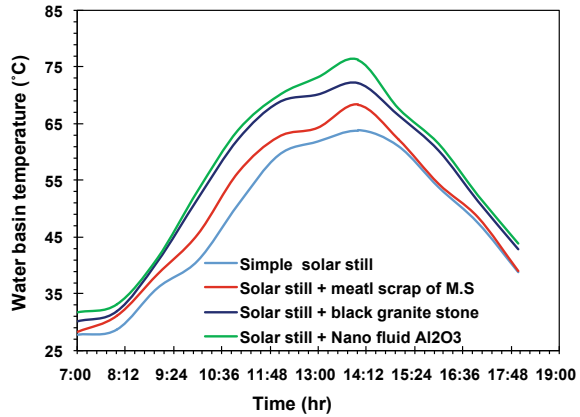
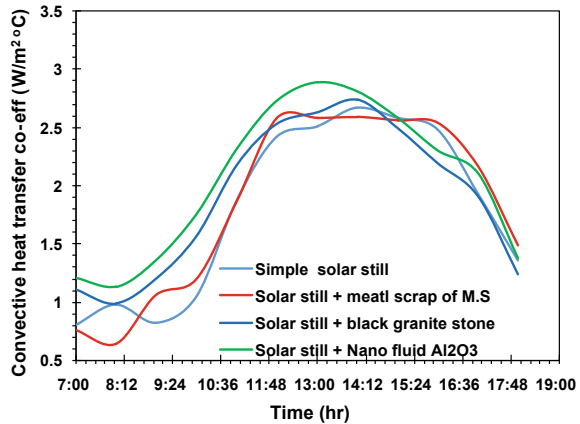


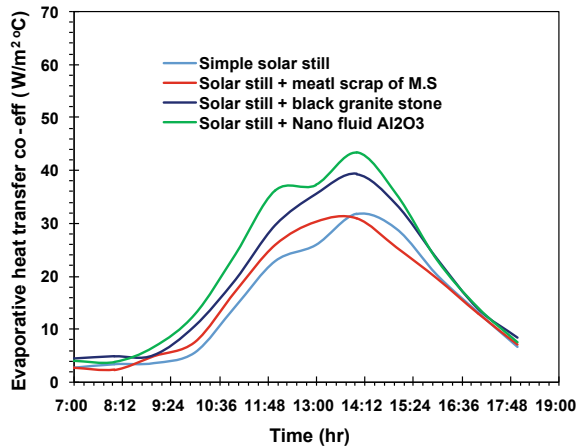
Fig. 6 Deviation of the convective heat transfer coefficient w.r.t time at 0.01 m water depth



Variability of the glass cover temperature and time is appeared in Fig. 4, recorded at 0.01 m water profundity for all four cases. Glass cover temperature increases as the surrounding temperature increments with time.

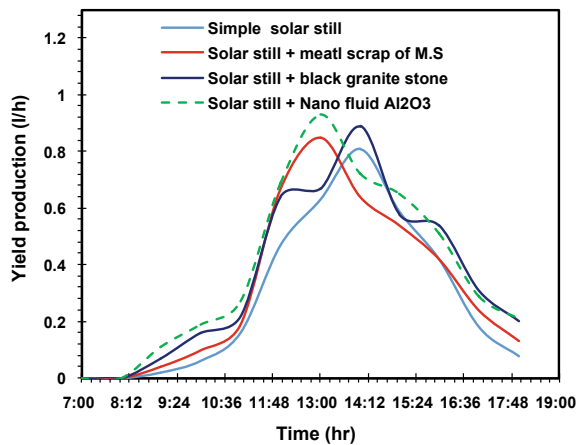
Wind speed plays a very vital role in decreasing outer glass cover temperature and by this condensation rate of heat transfer increases and final yield production of solar still increases. It be noted to maximum glass temperature of 57.9 °C was achieved for nanofluid inside water basin at 2 PM and lowest was achieved for simple solar still with 49.5 °C at 2 PM. As seen in Fig. 5, the highest water basin temperature is achieved using nanofluid Al₂O₃ inside water basin due to its higher thermal conductivity than metal scrap of M.S and black granite and minimum for simple solar still exclusive of any vitality storage material. Figures 6 and 7 show the standards of evaporative and convective heat transfer coefficient w.r.t time. In order to achieve highest yield production of solar still, this coefficient should have high value to augment the rate of heat transfer and by this final productivity of the SS improves. It was also observed

Fig. 7 Deviation of evaporative heat transfer coefficient w.r.t time at 0.01 m water profundity



as of the consequences that evaporative and convective heat transfer coefficient has maximum value for the SS, when nanofluid Al₂O₃ was used in basin water and minimum heat transfer coefficient was achieved for simple solar still without ESM. Figure 8 shows the deviation of the yield production with respect to time. It was observed that surrounding temperature starts increasing w.r.t time, both surrounding temperature and glass cover temperature start increasing consequently, but the water gets heated before the glass, hence, the variance in water basin temperature and glass temperature rises and that results into increment in distillate output. Maximum distilled output of water was achieved for solar still with nanofluid Al₂O₃ inside water basin as energy absorbing material, and minimum yield was achieved for simple solar still with any energy storing medium. Figure 9 shows the wind variation on different days when experiment was performed with time.

Fig. 8 Deviation of the yield production with time at 0.01 m water profundity



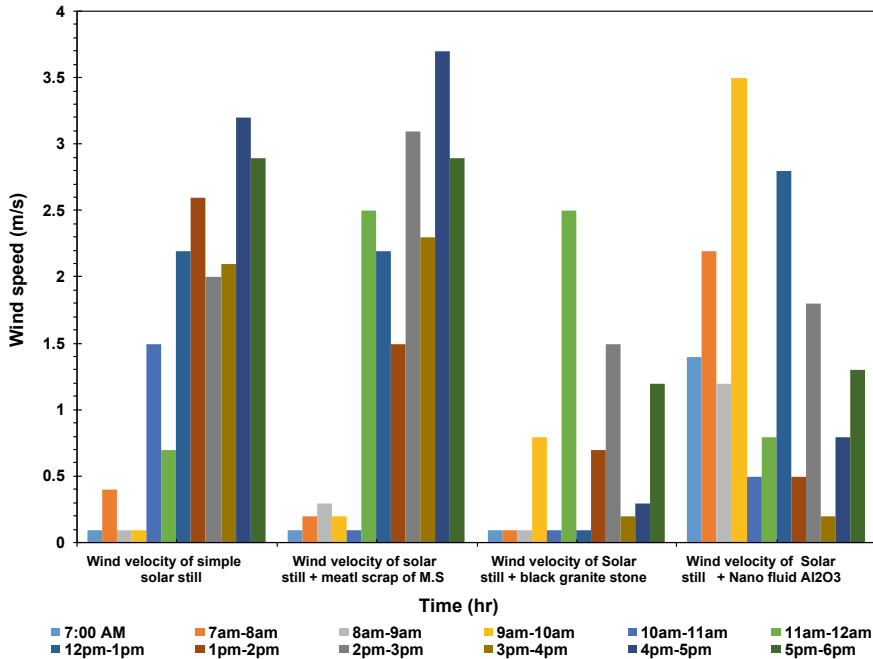


Fig. 9 Variation of the wind velocity with time at 0.01 m water profundity

Wind velocity increases the condensation rate of vapor and the freshwater yield of the SS increased with the addition of solid nanometric size particle Al₂O₃ in water basin, and also it was observed that the yield productivity of the clean/distilled water was enhanced by wind speed which creates the higher difference of temperature among glass surface and the basin water.

Figure 10 demonstrates the deviation of the entire day proficiency with time. It was seen that effectiveness of SS straightforwardly relies upon entire day yield generation and sun-based radiation. It was seen that the most astounding yield profitability of crisp water was accomplished, when nanofluid Al₂O₃ was utilized inside water bowl, and furthermore, entire day productivity was accomplished greatest for a similar case (Table 1).

Yield productivity of solar still has been calculated as well as practically it was measured by measuring jar in liter per hour. Due to various factors such as atmospheric condition, heat losses due to proper insulation, calculated value and observed value differ in case of solar still. As the output achieved by solar still is distilled water, so the hardness level of water will be zero but due to some impurity on measuring jar and due to environment condition, harness level of very minute value is achieved. Table 2 has compared the observed and calculated value of yield production. Table 3 shows the comparison of the total dissolved solid (TDS) value of inlet water sample of solar still and water output achieved from solar still. Inlet water sample has been collected from various water sources at different regions in Jaipur, Rajasthan.

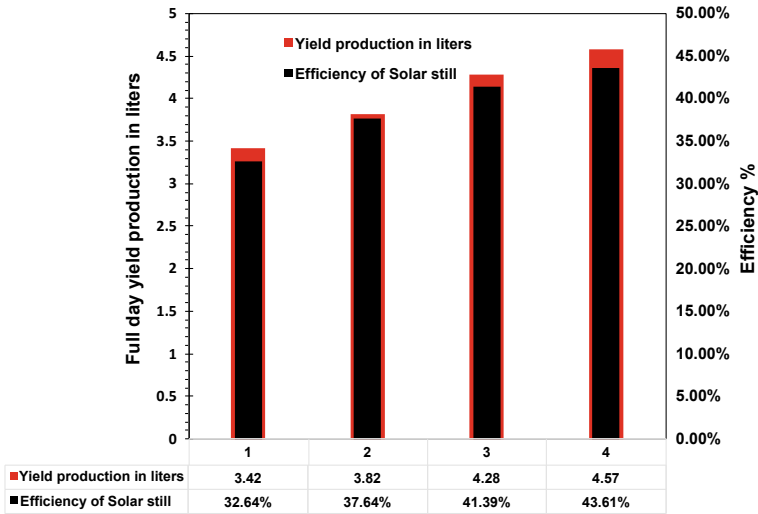


Fig. 10 Variation of the full day efficiency with time at 0.01 m water depth

Table 1 Demonstrates the assessment of observed full day freshwater yield and entire day efficiency of SS

Type of solar still	Observed full day yield production in liter	Entire day efficiency (%)
Simple solar still	3.42	32.64
Solar still + metal scrap of M.S inside basin	3.82	37.64
Solar still + black granite stone inside basin	4.28	41.39
Solar still + nanofluid Al ₂ O ₃ inside basin	4.57	43.61

Table 2 Comparisons of freshwater yield of SS for calculated and observed data

S. No.	Parameter at depth of water 0.1 m	Distillate output in liter	
		Calculated	Observed
1	Simple solar still	3.78	3.42
2	Solar still + metal scrap of M.S inside water basin	4.09	3.82
3	Solar still + black granite stone inside water basin	4.49	4.28
4	Solar still + nanofluid Al ₂ O ₃ inside water basin	4.80	4.57

Table 3 Comparisons of TDS value of input and output water of solar still

S. No.	Parameter at water depth of 0.1 m	Water hardness in PPM of dissolved salts	
		Sample water inside basin	Collected water at output
1	Simple solar still	962	23
2	Solar still + metal scrap of M.S	1083	17
3	Solar still + black granite stone inside water basin	1076	14
4	Solar still + nanofluid Al ₂ O ₃ inside water basin	1089	16

5 Conclusion

The SS with the basin area 1 m² has been fabricated and freshwater yield was investigated experimentally using various energy storage materials. The subsequent conclusions have been arrived base on the investigational outcome.

- Energy is stored by the materials placed inside the basin during peak hours of solar radiation mainly during 11 AM to 2 PM and then later it is released to basin water of SS in order to achieve a better yield even in evening and night.
- Yield of freshwater augmented by 11.6%, 25.1% and 33.5% by using metal scrap, black granite and nanofluid Al₂O₃ inside the water basin, respectively.
- Nanofluid Al₂O₃ used in water basin of the SS given the highest yield productivity of freshwater among all the storage materials. A yield improvement of 33.5% and full day efficiency improvement of 33.6% were observed as compared to conventional SS.
- Wind velocity assumes a noteworthy function in delivering temperature contrast between glass surface and water bowl, which aides in improved yield of clean/distilled water.
- Freshwater received after desalination given minimum TDS values and it was observed that SS is capable of producing freshwater from brackish water ranging from 900 to 1100 PPM in the experimental trial.

6 Future Recommendation

- Optimization of the quantity, density and size of the energy absorbing material is possible to achieve more variation in results.
- Aluminum is used as absorbing plate of inside basin can be replaced by higher thermal conductive material such as copper for yield production increment.

References

1. Wang L, Wang M, Huang ZH, Cui TX, Gui XC, Kang FY, Wang KL, Wu DH (2011) *J Mater Chem* 21:18295–18299
2. Tabrizi FF, Dashtban M, Moghaddam H, Razzaghi K (2010) Effect of water flow rate on internal heat and mass transfer and daily productivity of a weir-type cascade solar still. *Desalination* 260:239–247
3. Saidur R, Elcevvadi E, Mekhilef S, Safari A, Mohammed H (2011) An overview of different distillation methods for small scale applications. *Renew Sustain Energy Rev* 15:4756–4764
4. Arjunan T, Aybar H, Nedunchezhian N (2009) Status of solar desalination in India. *Renew Sustain Energy Rev* 13:2408–2418
5. Thakur AK, Khandelwal P, Sharma B (2018) Productivity comparison of solar still with nano fluid and phase changing material with same depth of water. In: Anand G, Pandey J, Rana S (eds) *Nanotechnology for energy and water*. ICNEW 2017. Springer proceedings in energy. Springer, Cham
6. Thakur AK, Agarwal D, Khandelwal P, Dev S (2018) Comparative study and yield productivity of nano-paint and nano-fluid used in a passive-type single basin solar still. In: Sen Gupta S, Zobia A, Sherpa K, Bhoi A (eds) *Advances in smart grid and renewable energy*. Lecture Notes in Electrical Engineering, vol 435. Springer, Singapore
7. Thakur AK, Pathak SK (2017) Single basin solar still with varying depth of water: optimization by computational method. *Iran J Energy Environ* 8(3):216–223
8. Rajvanshi AK (1981) Effect of various dyes on solar distillation. *Sol Energy* 27:51–65
9. Sodha MS, Kumar A, Tiwari GN (1980) Effects of dye on the performance of a solar still. *Appl Energy* 7:147–162
10. Akash BA, Mohsen MS, Osta O, Elayan Y (1998) Experimental evaluation of a single-basin solar still using different absorbing materials. *Renew Energy* 14:307–310
11. Nafey AS, Abdelkader M, Abdelmotalip A, Mabrouk AA (2001) Solar still productivity enhancement. *Energy Convers Manage* 42:1401–1408
12. Sakthivel M, Shanmugasundaram S (2008) Effect of energy storage medium (black granite gravel) on the performance of a solar still. *Energy Res* 32:68–82
13. Sathyamurthy R, El-Agouz S, Dharmaraj V (2015) Experimental analysis of a portable solar still with evaporation and condensation chambers. *Desalination* 367:180–185
14. Gugulothua R, Somanchia NS, Devi RSR, Banothc HB (2015) Experimental Investigations on Performance Evaluation of a Single Basin Solar Still Using Different Energy Absorbing Materials. *Aquat Procedia* 4:1483–1491
15. Naima MM, El Kawi MAA (2002) Non-conventional solar stills Part 1. Non-conventional solar stills with charcoal particles as absorber medium. *Desalination* 153:55–64
16. Sahota L, Tiwari GN (2016) Effect of nano fluids on the performance of passive double slope solar still: A comparative study using characteristic curve. *Desalination* 388:9–12
17. Sharma V, Mallick S (1991) Estimation of heat transfer coefficients, upward heat flow and evaporation in a solar still. *ASME (Solar Energy)*
18. Dunkle RV (1961) Solar water distillation; the roof type still and a multiple effect diffusion still. In: *International developments in heat transfer*, ASME proceedings of international heat transfer, Part V. University of Colorado
19. Malik MAS, Tiwari GN, Kumar A, Sodha MS (1982) *Solar distillation*. Pergamon Press, UK
20. Tiwari GN (2014) *Solar energy*. Narosa Publishing House, p 290

Massive MIMO for Green Communication



Samarendra Nath Sur

Abstract Demand for a high-speed communication system is increasing day by day, and in order to match up with the demand, researchers are continuously exploring new technology, signal processing algorithms, high-speed hardware platform, etc. In these regards, massive multi-input and multi-output (MIMO) become a front runner for the successful deployment of the future wireless communication system. But in order to deal with the environmental effect, the development of energy efficient and green communication system has become utmost necessary. This paper represents a general idea of massive MIMO and its prospect for the successful deployment of green communication.

Keywords Green communication · MIMO · LTE · Energy efficiency · Networks

1 Introduction

The information and communication technology (ICT) industry is looking for energy-efficient and high-speed communication networks, namely fifth-generation (5G) wireless networks [1]. It can boost up the capacity by 100-fold in comparison with the existing networks and also aiming to connect 100 billion devices worldwide. The efficient use of ICT is becoming important [2] and wireless communication is the most essential and vital element. And power consumption is the most important factor for proper deployment of the future generation communication networks.

Therefore, the concept of green information and communications technologies comes into play and it nothing but the joint development of green communication and green computing [3, 4]. The requirement of development of green communication become so important that, in 2015, the IEEE Technical Committee on Green Communications and Computing (TCGCC), Green ICT Standardizations and Big Data (TSCBD) jointly came forward for the Green Standardization and Industry Issues for ICT and Relevant Technologies.

S. N. Sur (✉)

Department of Electronics and Communication Engineering, Sikkim Manipal Institute of Technology, Sikkim Manipal University, Majitar, Rangpo, East Sikkim 737136, India
e-mail: samar.sur@gmail.com

© Springer Nature Singapore Pte Ltd. 2020

A. K. Bhoi et al. (eds.), *Advances in Greener Energy Technologies*,

Green Energy and Technology, https://doi.org/10.1007/978-981-15-4246-6_52

In these regards, massive MIMO/millimeter wave (mmWave) are the key technologies [5, 6]. The performance of the system can be enhanced by exploiting the unused and unlicensed spectrum and by utilizing large numbers of antennas [5]. But the capacity gain due to massive MIMO comes at the expense of system complexity. It includes growing power consumption in the RF section of the circuits. As per the study, it increases linearly with the number of antennas. Therefore, it is required to focus on the design of an energy-efficient 5G communication network [7, 8]. Today, energy consumption has become a prime area of concern to design a wireless communication system. Same is true for the massive MIMO. And this paper represents the utility of the massive MIMO for the green communication deployment.

The rest of the paper is organized as follows: Sect. 2 presents an overview of the massive MIMO system and its basic architecture. Section 3 discusses the requirement of green communication and related technologies involved. At last, how massive MIMO can be utilized for the future generation green communication is discussed in Sect. 4. In Sect. 5, we have the conclusion of the paper.

2 Massive MIMO

Over few decades, MIMO has been considered as a subject because of its ability to increase the wireless data traffic and to enhance the reliability of wireless systems [9]. Considering the recent technologies, the spectral efficiency can be improved by scaling up the available systems by increasing the number of antennas. And this has given the birth of massive MIMO systems [9–11] and the growth in the data rate is presented in Fig. 1.

Massive MIMO (large-scale antenna) systems are an encouraging solution to fulfilling the demand of the future generation communication system goal [11, 12]. Massive MIMO system enhanced the desired degree of service with respect to the number antennas. Increase in antenna number is always advantageous in term of throughput, reduction in radiated power, providing reliable quality of service, and very simple implementable signal processing techniques [13, 14]. A typical scenario of massive MIMO systems for uplink and downlink are shown in Figs. 2 and 3, respectively.

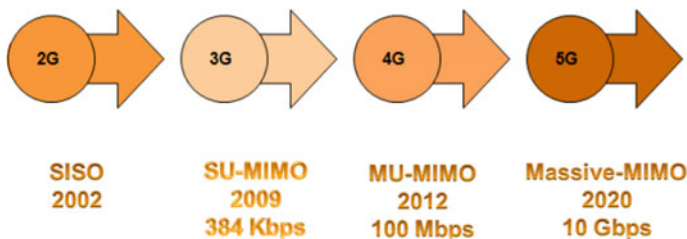


Fig. 1 Wireless communication system speed evolution [10]

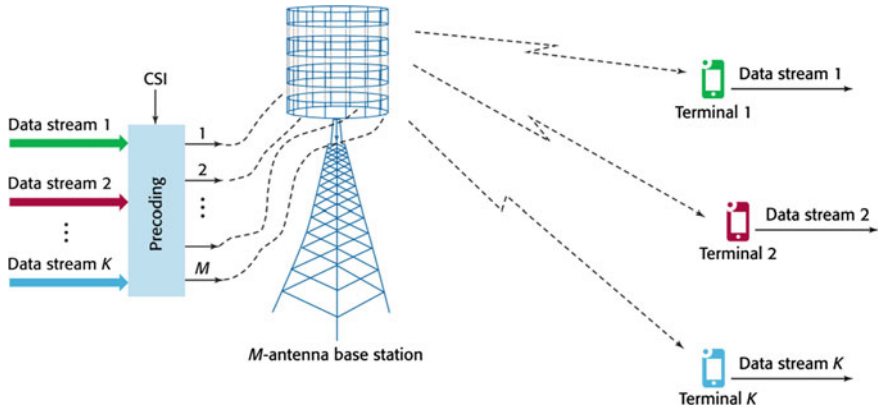


Fig. 2 Downlink scenario of a massive MIMO system [9]

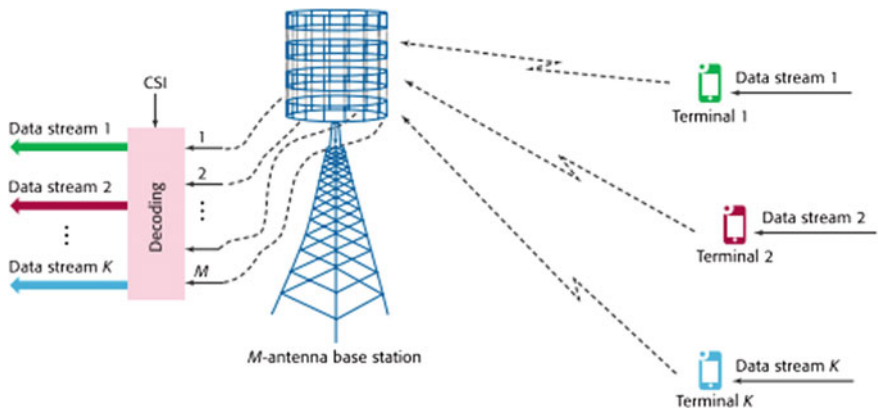


Fig. 3 Uplink scenario of a massive MIMO system [9]

Figures 2 and 3, represent the downlink and uplink scenario for a massive MIMO system respectively [10]. Linear precoding techniques are introduced to channelize the signal in the desired direction and to get ride-off from the mutual interference [10]. Therefore, to enhance the system performance, the receiver should have the intelligence to understand the non-stationary behavior of the wireless channel. And to do so, it is required to estimate the channel at the receiver side after each coherence time interval. Initially, massive MIMO systems were proposed with TDD mode of operation, with periodic channel estimation and compensation. Figure 4 shows the essential components of a massive MIMO system.

As in the figure, the proper contamination of pilot symbol is a critical problem in massive MIMO [10]. Lots of methods have been proposed to solve the problem, such as based on the channel state information, based on the cooperative method for optimum pilot design, time-shifted pilot method, etc. From the perspective of the MIMO

Fig. 4 Massive MIMO system components [10]



encoding, some well-known techniques have been proposed and widely used, such as Vertical-Bell Laboratories Layered Space-Time (VBLAST), space-time block codes (STBC) and space-time trellis coding [15]. But, in order to encounter the severe channel condition, MIMO is combined with orthogonal frequency-division multiplexing (OFDM) or Filter Bank Multicarrier (FBMC) for the future generation communication system (5G). The choice of these encoding techniques is depending on the requirements of high data rate and the reliability of the system.

For massive MIMO system, system complexity is the main concern from the point of view of implementation. Design of low-complex encoder and decoder is of utmost important. In comparison with the conventional MIMO, massive MIMO depends on the linear receiver system, such as maximum ratio combining (MRC), matched filtering, conjugate beamforming, minimum mean squared error (MMSE) receive combining and zero-forcing (ZF).

Till today, lots of receiver algorithms have been proposed and implemented. Linear detection techniques such as ZF, MMSE, successive interference cancelation (SIC) and ordered SIC (OSIC) present a performance clearly inferior to the maximum likelihood (ML) detector [16]. At the same time, as in [17], the sphere decoding (SD) produces near-optimal performance but its complexity becomes comparable to the ML detector. For large MIMO systems, several detection schemes have been proposed such as detection based on local search [18, 19]; meta-heuristics [20, 21]; via message passing on graphical models [22, 23]; lattice reduction (LLR)-aided detection [24, 25]; detection using Monte Carlo sampling [26]. However, in order to have near-ML performance with such receiver, the system required large numbers of antennas.

3 Green Communication

With the growth in communications usage, the time has come take to necessary steps to have energy-efficient communications system. In these regards, the cellular network is the main area of concerned [27–29].

According to a study by Ericsson, mobile operators are investing almost half of their total expenses for network energy costs. Therefore, cellular networks/telecommunications applications have a significant role for lowering greenhouse gas emissions and power consumption. Therefore, a proper deployment of radio networks can enhance the energy efficiency of the networks and can fulfill the goal of green communication. And this will be beneficial for the environment.

As a part of the deployment of the green communications, a number of technical approaches have been taken into an account, such as energy-efficient network architecture and protocols, energy-efficient wireless transmission techniques, cross-layer optimization methods and opportunistic spectrum sharing. The same is depicted in Fig. 5.

Time-domain solutions are based on the optimized use of the power amplifier (PA) in a communication system. It actually reduces the PA operating time, and therefore, using this approach, a considerable amount of energy can be saved during the PA off time [30–32]. This approach is based on the reduction in control signals with respect to the reference signals (RSs). Basically, there are three ways to achieve the goal, such as normal unicast, multicast broadcast single-frequency networks (MBSFN) and cell discontinuous transmission (DTX). This approach can be proven to be good in an idle traffic case. Therefore, it is more suitable for the rural area [30, 33].

In cellular networks, a large amount of power is wasted because of constant power supply to the unused wireless resources and devices. In these regards, cell switch on/off has become a widely used technique to reduce the power consumption in a cellular network. And this approach depends on the traffic load situation. It can be implemented for both single layer (macrocell) and multilayer networks (such as heterogeneous networks, HetNet). As it is based on the traffic condition, some

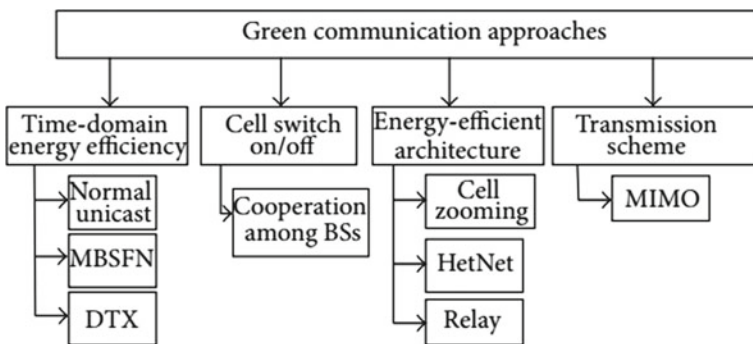


Fig. 5 Classifications of green communication technologies [30]

cells will be active and some not. Therefore, the active cells will increase the power transmission to cover the area, but all the base station are power limited and put a limitation on this approach [30].

Energy-efficient architecture is basically an extension of the previous approach. This approach is based on the cooperation between the BSs and re-sizing the cell based on the traffic load [34]. As mentioned in Fig. 5, it is having some components such as cell zooming, HetNets and relay techniques. To accomplish the power reduction, heterogeneous network architecture is having different types of cell size. And those are designated as macro, micro, pico and femto cell architecture [35]. This kind of cell structure is having different types of cell size and transmission power and results show a tremendous reduction in the energy consumption. Similarly, the relay approach can be used to save energy. The main goal of the relay approach is to save energy. In a relay, the system throughput is increased by utilizing short and repeated transmission. And this repeated transmission interns reduced the path loss. And research output proves the fact that cooperative rely improves the system performance but with less energy. But it depends on the optimal deployment of the relay nodes [30].

Lastly, MIMO has become the foremost ingredient for the next generation of wireless networks. MIMO improves the system without increasing either the bandwidth or the transmission power. The main goal of this paper is to discuss the role of MIMO/massive MIMO toward the green communication.

4 Massive MIMO (M-MIMO) in Green Communication

Future generation communication system needs to be highly spectrum efficient and also energy efficient, which is the goal of 5G communication [5, 36] (Fig. 6).

Technology	High EE at	Coverage	Transmit power	Circuit power	Challenges
mmWave	BS and UT	200 m	Low	High	Transceiver design
LTE-U	BS and UT	500 m	Moderate	Moderate	Coexistence design
UDNs	UT	10–200 m	Low	High	Interference management, backhaul, user association, on-off switching
D2D	BS	2–100 m	Low	Low	Interference management, cooperative design
M-MIMO	UT	1000 m	Low	High	Signal processing, CSI, antenna cost

Fig. 6 Comparison of green 5G technologies [5]

In this regard, massive MIMO is the key enabler for 5G is MIMO technology, where the BSs are having a large number of antennas (more than 10 to be called as massive MIMO). This is in order to achieve high spectral and energy efficiency gain over the current 4G communication system. And to enable the scope of the green communication, massive MIMO operates with millimeter wave and heterogeneous network architecture [37].

In comparison with the conventional MIMO system, massive MIMO system is more energy efficient because of its architecture. For example, in order to achieve a throughput, the massive MIMO system required less transmission power in user terminal (UEs) because the same can be adjusted by having larger antennas at the BSs. And secondly, as massive MIMO system can have the same BER performance with the linear receiver processing, therefore, it required low levels of circuit power expenditure.

Lots of research work is going on to make the massive MIMO system an energy-efficient green system. Lots of methods have been proposed such as multi-user detection, precoding, user scheduling, antenna selection, transceiver redesign, improving resource utilization and power amplifier redesign, etc.

In these regards, FDD technique is best suitable for the massive MIMO operation. Now, with the increased number of BSs antennas, the system throughput is also improved but at the cost off increased circuit power consumption. Then, also the massive system can be called as energy efficient if the system throughput is large enough to counter the circuit power consumption [35].

Similarly, researchers are also looking for redesigning the baseband and RF chain to minimize the power requirement. In conventional approach, MIMO precoding and beamforming are the part of digital baseband processing.

Now in conventional MIMO, for each antenna, there is a dedicated baseband and RF chain. Such a design is not valid for massive MIMO. In massive MIMO it is required to minimize the requirement of RF chain. The only way to do so is to include hybrid precoding, antenna selection and transceiver redesign as in Fig. 7.

So far, we have discussed numerous prospects for developing green communication system using conventional massive MIMO system systems. Several other technologies, such as mmWave, HetNet, energy harvesting (EH) and cloud-based radio access, are also considered to be enabler on green communication system.

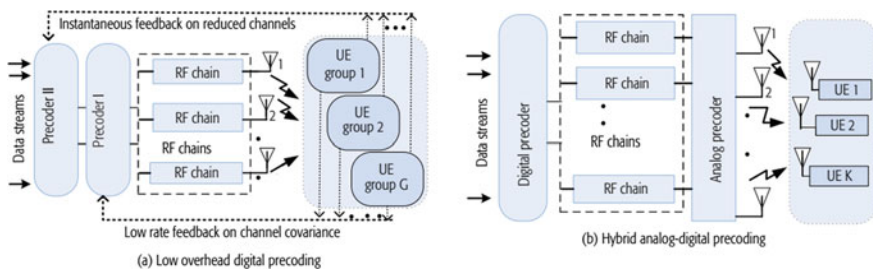


Fig. 7 Precoding techniques for mmWave massive MIMO systems [35]

Although the massive MIMO is the key enabler, it has a sustainable solution for the green communication, and the system should come up with the diverse applications and heterogeneous networks to support the varied user requirements.

5 Conclusion

Massive MIMO is a promising and best solution toward the successful implementation of the goal of 5G communication. This technology offers both spectral efficiency and energy efficiency in comparison with the present 4G system. This paper deals with the overview of the green communication system and massive MIMO system along with its constituent technologies. Because of its inherited features, a massive MIMO system provides enough energy efficiency to fulfill the requirement of the green communication, furthermore, the goal of 5G system. But this deployment put forwards some challenges for the researchers such as low-complex signal processing algorithms, circuit architecture with low power consumption, scale down the requirement of the RF chains and minimizing the losses related to the high power amplifiers.

References

1. Prasad KNRSV, Hossain E, Bhargava VK (2017) Energy efficiency in massive MIMO-based 5G networks: opportunities and challenges. *IEEE Wirel Commun* 24(3):86–94. <https://doi.org/10.1109/MWC.2016.1500374WC>
2. Commission of the European Communities Staff Working Document (2012) Exploiting the Employment Potential of ICTs
3. Wu J, Rangan S, Zhang H (2012) Green communications: theoretical fundamentals, algorithms, and applications. CRC Press
4. Murugesan S, Gangadharan GR (2012) Harnessing green IT: principles and practices. Wiley
5. Wu Q, Li GY, Chen W, Ng DWK, Schober R (2017) An overview of sustainable green 5G networks. *IEEE Wirel Commun* 24(4):72–80. <https://doi.org/10.1109/MWC.2017.1600343>
6. Chen Y et al (2011) Fundamental trade-offs on green wireless networks. *IEEE Commun Mag* 49(6):30–37
7. Han S et al (2015) Large-scale antenna systems with hybrid analog and digital beamforming for millimeter wave 5G. *IEEE Commun Mag* 53(1):186–194
8. Zeng Y, Zhang R (2016) Millimeter wave MIMO with lens antenna array: a new path division multiplexing paradigm. *IEEE Trans Commun* 64(4):1557–1571
9. Marzetta TL (2015) Massive MIMO: an introduction. *Bell Labs Tech J* 20:11–22. <https://doi.org/10.15325/BLTJ.2015.2407793>
10. Hassan N, Fernando X (2017) Massive MIMO wireless networks: an overview. *Electronics* 6:63
11. Larsson EG, Edfors O, Tufvesson F, Marzetta TL (2014) Massive MIMO for next generation wireless systems. *IEEE Commun Mag* 52(2):186–195. <https://doi.org/10.1109/MCOM.2014.6736761>
12. Hoydis J, Ten Brink S, Debbah M (2013) Massive MIMO in the UL/DL of cellular networks: how many antennas do we need? *IEEE J Sel Areas Commun* 31(2):160–171

13. Björnson E, Larsson EG, Marzetta TL (2016) Massive MIMO: ten myths and one critical question. *IEEE Commun Mag* 54:114–123
14. Rusek F, Persson D, Lau BK, Larsson EG, Marzetta TL, Edfors O, Tufvesson F (2013) Scaling up MIMO: opportunities and challenges with very large arrays. *IEEE Signal Process Mag* 30(1):40–60
15. Chockalingam A, Rajan BS (2014) *Large MIMO systems*. Cambridge University Press, Cambridge, UK
16. Li H, He W, He Q, He J (2017) The application and development of SIC technology in wireless communication system. In: 2017 IEEE 9th international conference on communication software and networks (ICCSN), Guangzhou, pp 565–570. <https://doi.org/10.1109/ICCSN.2017.8230175>
17. Barbero L, Thompson J (2008) Fixing the complexity of the sphere decoder for MIMO detection. *IEEE Trans Wirel Commun* 7(6):2131–2142
18. Vardhan KV, Mohammed SK, Chockalingam A, Rajan BS (2008) A low-complexity detector for large MIMO systems and multicarrier CDMA systems. *IEEE J Sel Areas Commun* 26(3):473–485
19. Li P, Murch RD (2010) Multiple output selection-LAS algorithm in large MIMO systems. *IEEE Commun Lett* 14(5):399–401
20. Datta T, Srinidhi N, Chockalingam A, Rajan BS (2010) Random-restart reactive tabu search algorithm for detection in large-MIMO systems. *IEEE Commun Lett* 14(12):1107–1109
21. Srinidhi N, Datta T, Chockalingam A, Rajan BS (2011) Layered tabu search algorithm for large-MIMO detection and a lower bound on ML performance. *IEEE Trans Commun* 59(11):2955–2963
22. Goldberger J, Leshem A (2011) MIMO detection for high-order QAM based on a Gaussian tree approximation. *IEEE Trans Inf Theory* 57(8):4973–4982
23. Narasimhan TL, Chockalingam A (2014) Channel hardening-exploiting message passing (CHEMP) receiver in large-scale MIMO systems. *IEEE J Sel Topics Signal Process* 8(5):847–860
24. Wubben D, Seethaler D, Jalden J, Matz G (2011) Lattice reduction. *IEEE Signal Process Mag* 28(3):70–91
25. Zhou Q, Ma X (2013) Element-based lattice reduction algorithms for large MIMO detection. *IEEE J Sel Areas Commun* 31(2):274–286
26. Datta T, Kumar NA, Chockalingam A, Rajan BS (2013) A novel Monte Carlo-sampling-based receiver for large-scale uplink multiuser MIMO systems. *IEEE Trans Veh Technol* 62(7):3019–3038
27. Department for Culture, Media and Sport & Department for Business, Innovation and Skills (2009) Digital Britain final report, pp 1–245; Available (Accessed Dec 2011). <https://www.official-documents.gov.uk/>
28. Phippa A (2009) Who makes IT professionals environmentally aware? European community in information technology (ERCIM) News 79, Special Theme: Towards Green IT, p 16
29. The Climate Group (2008) Smart 2020: enabling the low carbon economy in the information age, pp 1–87
30. Alsharif MH, Nordin R, Ismail M (2013) Survey of green radio communications networks: techniques and recent advances. *J Comput Netw Commun* 2013, 13p. Article ID 453893. <https://doi.org/10.1155/2013/453893>
31. Chen T, Yang Y, Zhang H, Kim H, Horneman K (2011) Network energy saving technologies for green wireless access networks. *IEEE Wirel Commun* 18(5):30–38
32. 3GPP R1–100387 (2010) Extended cell DTX. <https://www.3gpp.org/fp/tsgan/WG1RL1/TSGR159b/Docs/R1-100387.zip>
33. Imran M, Ambrosy A, Blume O et al (2012) Final integrated concept. EARTH Project Report, Deliverable D6(4):1–95
34. Niu Z, Wu Y, Gong J, Yang Z (2010) Cell zooming for cost-efficient green cellular networks. *IEEE Commun Mag* 48(11):74–79

35. Auer G, Blume O, Giannini V et al (2012) Energy efficiency analysis of the reference systems, areas of improvements and target breakdown. EARTH Project Report, Deliverable D2(3):1–68
36. Wang C et al (2014) Cellular architecture and key technologies for 5G wireless communication networks. *IEEE Commun Mag* 52(2):122–130. <https://doi.org/10.1109/MCOM.2014.6736752>
37. Liu W, Han S, Yang C, Sun C (2013) Massive MIMO or small cell network: Who is more energy efficient? In: 2013 IEEE wireless communications and networking conference workshops (WCNCW), Shanghai, pp 24–29. <https://doi.org/10.1109/WCNC>

Evaluation of Leakage Current in Single-Phase H-Type Transformerless Inverters for PV Grid System



Mohammed Imran and Manjula Mane

Abstract The mathematical evaluation of different types of single-phase H-type transformerless inverters for PV grid system is introduced in this chapter. When a PV system is interfaced with utility grid with the help of transformerless inverter, a parasitic capacitance is formed between the PV and the ground resulting in the flow of leakage currents; as a result, the leakage currents must be in permissible limits to reduce injection of DC current into AC grid. In this paper, the mathematical analysis of H-bridge transformerless inverter is performed to understand on which factors the leakage current depends. Further, MATLAB simulation is performed for H4, H5, H6 and H6-I topologies of inverter to analyze the value of leakage current. In view of local residential loads, the PV system is designed for 2.5 KW which is usually in the capacity range of 1–5 KW where leakage currents are found to be severe.

Keywords Leakage current (I_{leakage}) · Common-mode voltage (V_{CM}) · Differential mode voltage (V_{DM}) · Parasitic capacitance (C_{PV})

1 Introduction

In order to minimize the leakage current flow within allowable limit, various topologies for transformerless PV grid inverter have been described in literature. To reduce leakage current, topologies are further categorized into three different groups. The first group of topologies derived from the basic H-type inverter depicted in Fig. 1. The first group tries to keep V_{CM} constant by isolating the PV from the grid for unipolar and hybrid SPWM strategies. The aforementioned isolation can be realized by adding additional switch(es) in the DC or in the AC side of the basic H-bridge inverter circuit. The power circuit configurations of two schemes, wherein additional switch(es) are employed in the DC side of the inverter are depicted in Fig. 10

M. Imran (✉) · M. Mane
Electrical Engineering Department, UCOE, Osmania University, Hyderabad, India
e-mail: imraneed@mjcollege.ac.in

M. Mane
e-mail: manjulagooga@gmail.com

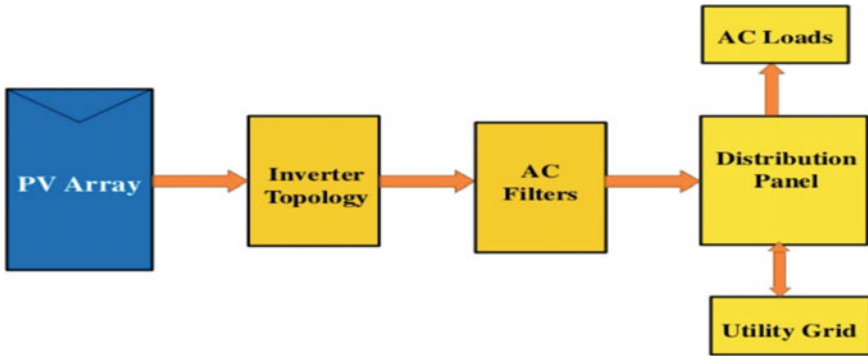


Fig. 1 Basic view of PV model interfaced to utility grid

and Fig. 12. The power circuit configurations of two schemes, wherein additional switch(es) are employed on the AC side of the inverter are depicted in Fig. 14.

2 Leakage Current in H-Type Transformerless PV Grid Inverter

The cause of $I_{Leakage}$ flow is due to the presence of capacitance between the panel and the ground. The equivalent model of PV panel showing the presence of the parasitic capacitance is depicted in Fig. 2.

The magnitude of this C_{PV} relies on several factors, viz. (a) PV panel and frame structure, (b) surface area of the cells and distance between the cells, (c) structure of the module frame, (d) weather conditions, (e) humidity, (f) dust or salt covering the PV panel, and (g) type of electromagnetic compatibility (EMC) filter. The approximate

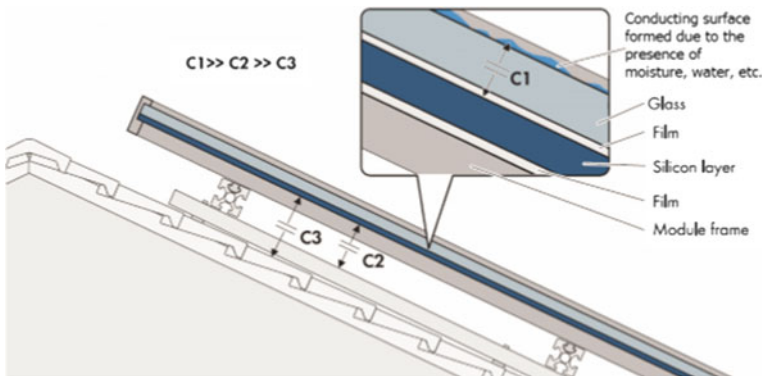


Fig. 2 PV panel structure depicting presence of C_{PV} [1]

value of this parasitic capacitance is about 70–120 nF/kW for crystalline silicon cells (polycrystalline), whereas it increases to 110–170 nF/kW for CdTe-based solar cells.

The path of leakage current through C_{PV} in a standard H-type transformerless inverter is depicted in Fig. 3. Here, $I_{Leakage}$ is the leakage current, C_{PV} is parasitic PV capacitance of the PV panel, and L_1, L_2 are the filter inductances. Though only one inductor would have been sufficient to serve the purpose of filtering, two inductors are employed for this purpose the reason for which is discussed later in this section.

An equivalent mathematical model of Fig. 3 to evaluate the leakage current is depicted in Fig. 4a. Here, Z_1 and Z_2 are the impedances of the inductors, L_1 , and L_2 , respectively. Applying Millman’s/Thevenin theorem this model can be simplified.

From Fig. 4b, the equation of V_x is

$$V_x = \frac{\frac{V_{AO}}{Z_1} + \frac{V_{BO}}{Z_2}}{\frac{1}{Z_1} + \frac{1}{Z_2}} = \frac{V_{AO}Z_2 + V_{BO}Z_1}{Z_1 + Z_2} = V_{AO}\frac{Z_2}{Z_1 + Z_2} + V_{BO}\frac{Z_1}{Z_1 + Z_2} \quad (1)$$

$$= V_{AO}\frac{Z_2}{Z} + V_{BO}\frac{Z_1}{Z} \quad (2)$$

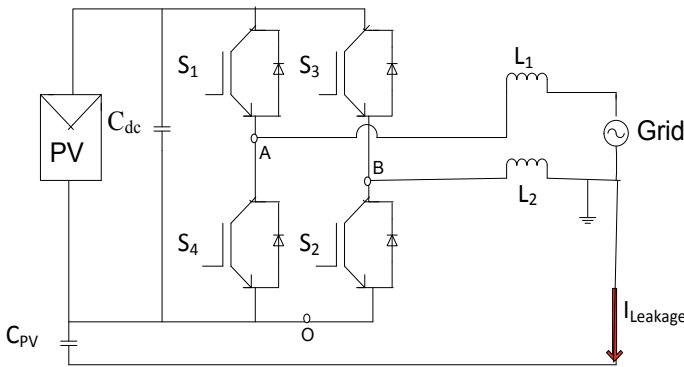


Fig. 3 Transformerless standard H-bridge inverter depicting leakage current path through PV parasitic capacitance

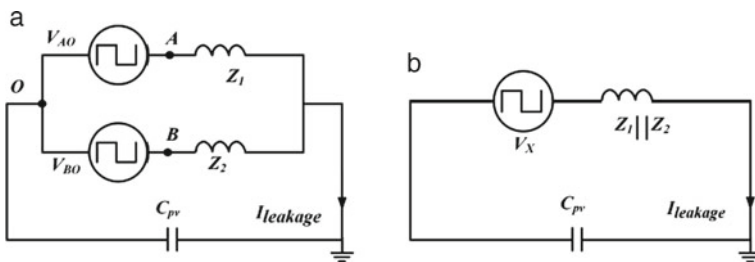


Fig. 4 Equivalent mathematical model depicting leakage current path in a standard H-bridge inverter: **a** actual model and **b** simplified model

wherein $Z = Z_1 + Z_2$. Rearranging/modifying (2),

$$\begin{aligned} &= V_{AO} \frac{Z_2}{Z} - V_{AO} \frac{Z_1}{Z} + V_{AO} \frac{Z_1}{Z} + V_{BO} \frac{Z_1}{Z} \\ &= V_{AO} \frac{Z_2 - Z_1}{Z} + (V_{AO} + V_{BO}) \frac{Z_1}{Z} \end{aligned} \quad (3)$$

Again rearranging/modifying (2)

$$\begin{aligned} &= V_{AO} \frac{Z_2}{Z} - V_{BO} \frac{Z_1}{Z} + V_{BO} \frac{Z_2}{Z} - V_{BO} \frac{Z_2}{Z} \\ &= (V_{AO} + V_{BO}) \frac{Z_2}{Z} - V_{BO} \frac{Z_2 - Z_1}{Z} \end{aligned} \quad (4)$$

Adding (3) and (4),

$$\begin{aligned} 2V_x &= V_{AO} \frac{Z_2 - Z_1}{Z} + (V_{AO} + V_{BO}) \frac{Z_1}{Z} + (V_{AO} + V_{BO}) \frac{Z_2}{Z} - V_{BO} \frac{Z_2 - Z_1}{Z} \\ &= (V_{AO} + V_{BO}) + (V_{AO} - V_{BO}) \frac{Z_2 - Z_1}{Z} \\ V_x &= \frac{(V_{AO} + V_{BO})}{2} + \frac{(V_{AO} - V_{BO})}{2} \frac{Z_2 - Z_1}{Z} \end{aligned} \quad (5)$$

$$V_x = V_y + \frac{V_z}{2} \frac{Z_2 - Z_1}{Z} \quad (6)$$

wherein,

$$\begin{aligned} V_y &= \frac{(V_{AO} + V_{BO})}{2} \\ V_z &= V_{AO} - V_{BO} \end{aligned} \quad (7)$$

Multiplying (7) with $\frac{Z_1}{Z}$,

$$V_z \frac{Z_1}{Z} = V_{AO} \frac{Z_1}{Z} - V_{BO} \frac{Z_1}{Z} \quad (8)$$

Multiplying (7) with $\frac{Z_2}{Z}$,

$$V_z \frac{Z_2}{Z} = V_{AO} \frac{Z_2}{Z} - V_{BO} \frac{Z_2}{Z} \quad (9)$$

Adding (2) and (8),

$$V_x + V_z \frac{Z_1}{Z} = V_{AO} \frac{Z_2}{Z} + V_{BO} \frac{Z_1}{Z} + V_{AO} \frac{Z_1}{Z} - V_{BO} \frac{Z_1}{Z} \quad (10)$$

$$V_{AO} = V_x + V_z \frac{Z_1}{Z} \text{ Adding (2) and (9),}$$

$$\begin{aligned} V_x + V_z \frac{Z_2}{Z} &= V_{AO} \frac{Z_2}{Z} + V_{BO} \frac{Z_1}{Z} + V_{AO} \frac{Z_2}{Z} - V_{BO} \frac{Z_2}{Z} \\ V_x + V_z \frac{Z_2}{Z} &= V_{AO} \frac{2Z_2}{Z} + V_{BO} \frac{Z_1 - Z_2}{Z} \\ V_x + V_z \frac{Z_2}{Z} &= \left(V_x + V_z \frac{Z_1}{Z} \right) \frac{2Z_2}{Z} + V_{BO} \frac{Z_1 - Z_2}{Z} \\ V_x \left(1 - \frac{2Z_2}{Z} \right) + \left(V_z \frac{Z_2}{Z} - \frac{2Z_1 Z_2}{Z^2} \right) &= V_{BO} \frac{Z_1 - Z_2}{Z} \\ V_x \left(\frac{Z_1 - Z_2}{Z} \right) + V_z \left(\frac{Z_2(Z_2 - Z_1)}{Z} \right) &= V_{BO} \frac{Z_1 - Z_2}{Z} \\ V_x - V_z \frac{Z_2}{Z} &= V_{BO} \end{aligned} \quad (11)$$

Substituting expression of V_x from (6) in (10),

$$\begin{aligned} V_{AO} &= V_Y + \frac{V_z}{2} \frac{Z_2 - Z_1}{Z} + V_z \frac{Z_1}{Z} \\ V_{AO} &= V_Y + \frac{V_z}{2} \end{aligned} \quad (12)$$

Substituting expression of V_x from (6) in (11),

$$\begin{aligned} V_{BO} &= V_Y + \frac{V_z}{2} \frac{Z_2 - Z_1}{Z} - V_z \frac{Z_2}{Z} \\ V_{BO} &= V_Y - \frac{V_z}{2} \end{aligned} \quad (13)$$

From (12) and (13), it can be observed that the term ' V_Y ' is common for both input voltages, V_{AO} and V_{BO} in the equivalent mathematical model are shown in Fig. 4a. Hence, V_Y is termed hereafter as the common-mode voltage for the system, V_{CM} . From (7), it can be observed that the term ' V_Z ' is the potential difference between the two voltages V_{AO} and V_{BO} . Hence, V_Z is termed hereafter as the differential mode voltage for the system, V_{DM} .

Substituting the expressions for V_{AO} and V_{BO} from (12) and (13), respectively, Fig. 4 can be redrawn as shown in Fig. 5. Applying Millman's/Thevenin theorem.

The model is shown in Fig. 5 can be simplified further as shown below (Fig. 6).

It is seen that the voltages, V_Y (or V_{CM}) and V_Z (or V_{DM}) act as a forcing function for the flow of leakage current. Hence, the leakage current flow be minimized/eliminated if the aforementioned forcing functions can be made either of the

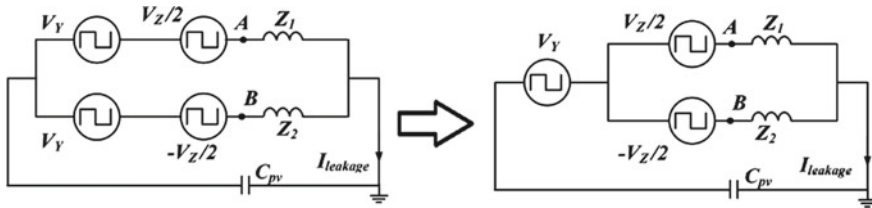


Fig. 5 Equivalent mathematical model depicting leakage current path in a standard H-bridge inverter in terms of V_{CM} and V_{DM}

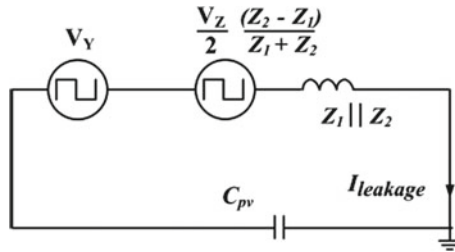


Fig. 6 Simplified mathematical model depicting leakage current path in a standard H-type inverter

following: (a) zero, (b) constant dc, or (c) having only low-frequency components as the impedance offered by C_{PV} is very large at low frequency. Another possibility to minimize leakage current is to ensure that the parasitic capacitances of PV are impressed with either zero or fixed DC voltage as impedance offered by the capacitor to the DC voltage is infinite.

3 Evaluation of Leakage Current in H-Type Transformerless Grid-Connected Inverter Using MATLAB

The MATLAB simulations for H4, H5, H6 and H6-I topologies of transformerless inverters for PV grid system have been performed to evaluate leakage currents. The below simulations have been obtained using 2.5 KW PV panel.

The V_{CM} and V_{DM} characteristics with leakage current for H4, H5, H6 and H6-I topologies [2] have been shown below.

The H-bridge inverter shown in Fig. 2 is realized using different PWM (unipolar, bipolar, and hybrid PWM) switching techniques (Figs. 7, 8 and 9).

H5 topology has one additional switch in comparison with H4 topology and is shown in Fig. 10 (Fig. 11).

H6 inverter type model has two extra switches on the DC side in comparison with H4 topology and is shown in Fig. 12 (Fig. 13).

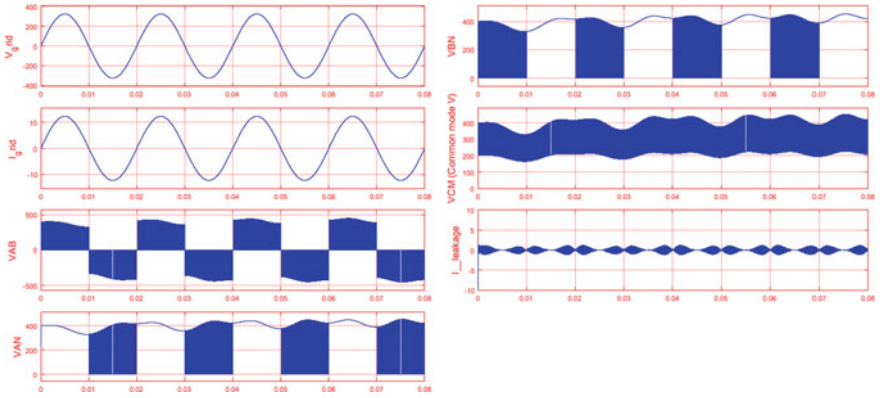


Fig. 7 H4 topology results with unipolar PWM switching

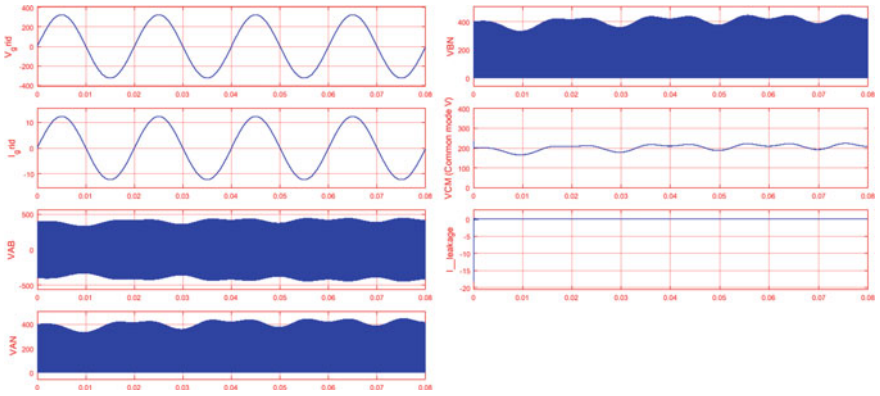


Fig. 8 H4 topology results with bipolar PWM switching

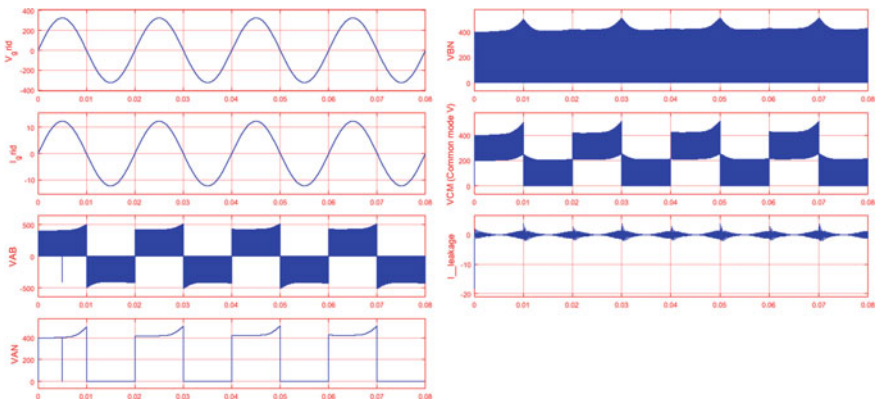


Fig. 9 H4 topology results with hybrid PWM switching

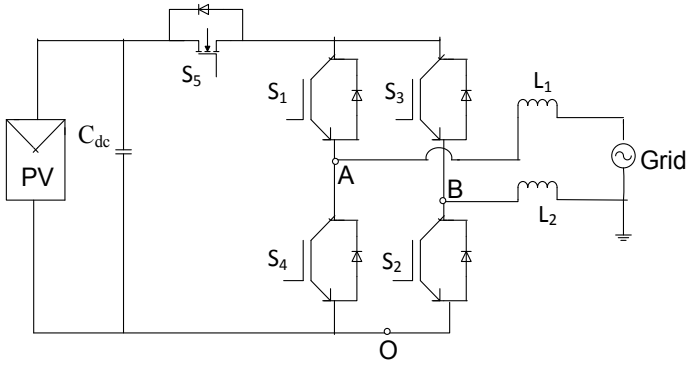


Fig. 10 H5 topology

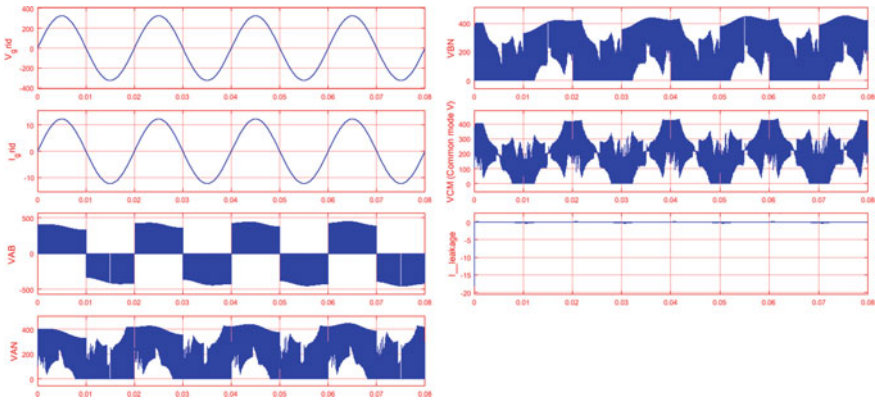


Fig. 11 H5 inverter output waveforms

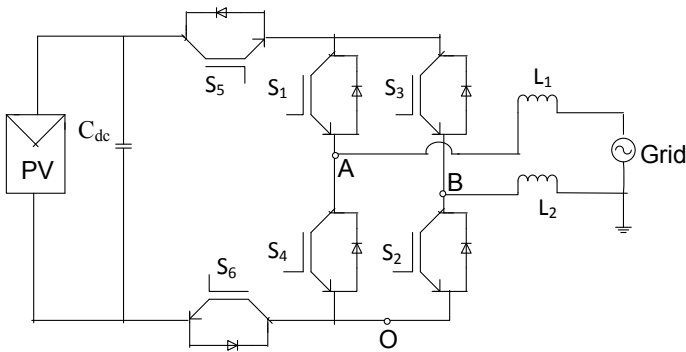


Fig. 12 H6 topology inverter output waveforms

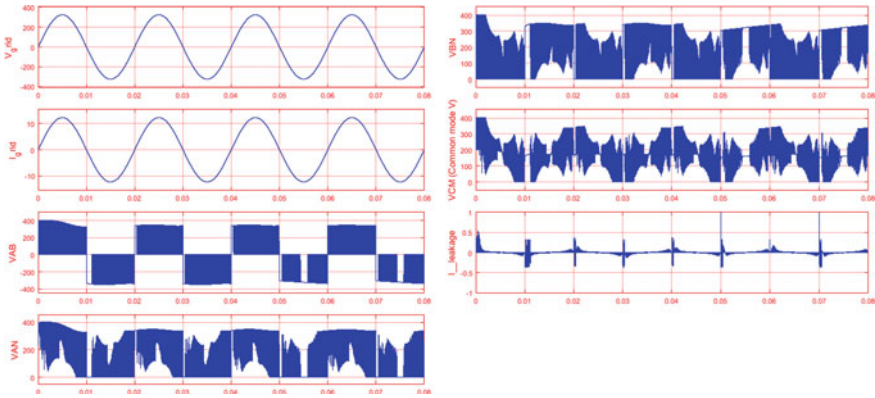


Fig. 13 H6 topology output waveforms

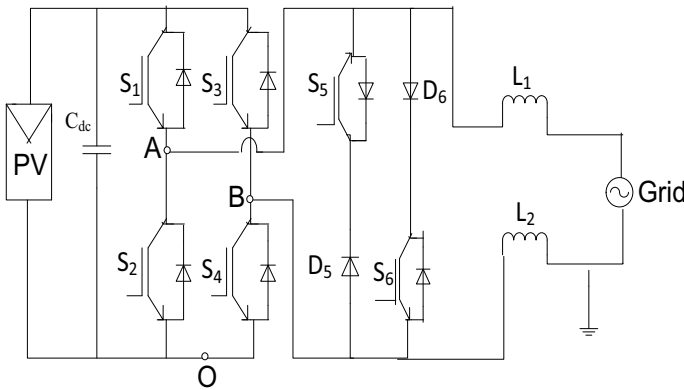


Fig. 14 H6-I topology

H6-I topology has two additional switches with diodes on the AC side in comparison with H4 topology and is shown in Fig. 14 (Fig. 15).

4 Effect of PWM Switching Strategies on Leakage Current in H-Bridge Inverter

In H-bridge inverter-based transformerless grid-connected schemes, the filter inductances, L_1 and L_2 , are kept equal so as to ensure $Z_1 = Z_2$. This eliminates the portion of forcing function involving V_Z shown in Fig. 6. Hence, the flow of leakage current, in this case, relies on the frequency and value of V_Y (or V_{CM}). The switching strategy for H-bridge single-phase inverter is generally realized by either of the following:

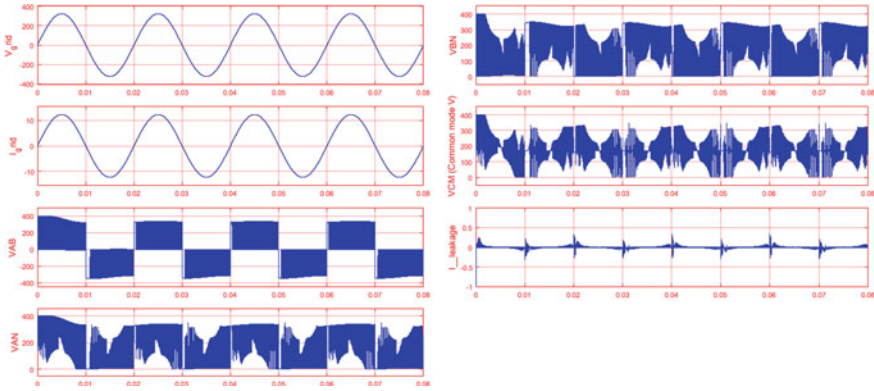


Fig. 15 H6-I topology inverter output waveforms

1. Bipolar,
2. Unipolar, and
3. Hybrid SPWM [3].

The magnitude of V_{CM} for these modulation techniques are given in Table 1, which shows V_{CM} is constant over a grid cycle in bipolar SPWM technique, and hence this PWM technique generates negligible leakage current. In case of unipolar as well as in hybrid PWM technique, V_{CM} has inverter switching frequency components. Hence, wherein these PWM techniques are employed, there will be a considerable value of leakage current as less impedance is offered by C_{PV} for high-frequency components present in V_{CM} . Thus, among the three modulation techniques, only bipolar technique can be employed for transformerless H-bridge inverter to restrict leakage current within a permissible limit. However, the efficiency of the inverter gets reduced if bipolar PWM is employed instead of unipolar or hybrid PWM-based switching logic. As efficiency is a major concern in transformerless grid-connected systems, bipolar technique is seldom employed. To achieve high efficiency and acceptable magnitude of leakage current, various topologies are presented in the literature.

5 Conclusion

The mathematical analysis of H-type proposed system for grid is performed to understand on which factors the leakage current depends and how it can be eliminated for the better performance of transformerless inverters, which has been studied and clearly indicated in this chapter.

The impact of different PWM strategies on H-bridge inverter is studied.

The leakage current has been evaluated for different H-type inverters using MATLAB and Simulink models and it is found to be nearly zero. The value of leakage current slightly differs in each case. The analysis is carried out for 2.5 KW PV panel

Table 1 Common-mode voltage generated in three commonly employed modulation techniques for H-bridge inverter

Positive half cycle		Negative half cycle				
<i>Bipolar SPWM technique</i>						
Switching states in switching cycle	V_{AO}	V_{BO}	$V_{CM} = \frac{V_{AO}+V_{BO}}{2}$	Switching states in switching cycle	V_{AO}	$V_{CM} = \frac{V_{AO}+V_{BO}}{2}$
S1, S2 ON	V_{PV}	0	$\frac{V_{PV}}{2}$	S1, S2 ON	V_{PV}	0
S3, S4 ON	0	V_{PV}	$\frac{V_{PV}}{2}$	S3, S4 ON	0	V_{PV}
<i>Unipolar SPWM technique</i>						
Switching states in switching cycle	V_{AO}	V_{BO}	$V_{CM} = \frac{V_{AO}+V_{BO}}{2}$	Switching states in switching cycle	V_{AO}	$V_{CM} = \frac{V_{AO}+V_{BO}}{2}$
S1, S2 ON	V_{PV}	0	$\frac{V_{PV}}{2}$	S3, S4 ON	0	$\frac{V_{PV}}{2}$
S2, S4 ON	0	0	0	S1, S3 ON	V_{PV}	V_{PV}
S1, S2 ON	V_{PV}	0	$\frac{V_{PV}}{2}$	S3, S4 ON	0	$\frac{V_{PV}}{2}$
S1, S3 ON	V_{PV}	V_{PV}	V_{PV}	S2, S4 ON	0	0
<i>Hybrid SPWM technique</i>						
Switching states in switching cycle	V_{AO}	V_{BO}	$V_{CM} = \frac{V_{AO}+V_{BO}}{2}$	Switching states in switching cycle	V_{AO}	$V_{CM} = \frac{V_{AO}+V_{BO}}{2}$
S1, S2 ON	V_{PV}	0	$\frac{V_{PV}}{2}$	S3, S4 ON	0	$\frac{V_{PV}}{2}$
S2, S4 ON	0	0	0	S1, S3 ON	V_{PV}	V_{PV}

as the leakage currents are usually severe for PV system designed in the power range of 1–5 KW for local residential purposes.

The leakage current is evaluated keeping unity power factor in mind. Hence, there is an utmost need for designing of transformerless inverters for PV applications with a new inverter topology with modified PWM switching techniques to nullify leakage currents below VDE 0126-1-1 standards with variable power factor control.

References

1. SMA AG Solar Technology. Technical information—capacitive leakage currents—information on the design of transformerless inverters of type Sunny Boy, Sunny Mini Central, Sunny Tripower
2. Rizzoli G et al (2016) Comparison of single-phase H4, H5, H6 inverters for transformerless photovoltaic applications. In: IECON proceedings (Industrial electronics conference)
3. Zeb K et al (2018) A review on recent advances and future trends of transformerless inverter structures for single-phase grid-connected photovoltaic systems. *Energies* 11(8)
4. Zhang L, Sun K, Xing Y, Zhao J (2015) Parallel operation of modular single-phase transformerless grid-tied PV inverters with common DC bus and AC bus. *IEEE J Emerg Sel Top Power Electron* 3(4):858–869
5. Yang B, Li W, Gu Y, Cui W, He X (2012) Improved transformerless inverter with common-mode leakage current elimination for a photovoltaic grid-connected power system. *IEEE Trans Power Electron* 27(2):752–762
6. Ün E, Hava AM (2009) A near-state PWM method with reduced switching losses and reduced common-mode voltage for three-phase voltage source inverters. *IEEE Trans Ind Appl* 45(2):782–793
7. Sonti V, Jain S, Bhattacharya S (2017) Analysis of the modulation strategy for the minimization of the leakage current in the PV grid-connected cascaded multilevel inverter. *IEEE Trans Power Electron*
8. Reed LE (1998) Performing a literature review
9. Dastagiri Reddy B, Selvan MP, Moorthi S (2015) Design, operation, and control of s3 inverter for single-phase microgrid applications. *IEEE Trans Ind Electron*
10. Rahimi R, Afshari E, Farhangi B, Farhangi S (2015) Optimal placement of additional switch in the photovoltaic single-phase grid-connected transformerless full bridge inverter for reducing common mode leakage current. In: 2015 IEEE conference on energy conversion, CENCON 2015
11. Rahimi R, Farhangi B, Farhangi S (2016) New topology to reduce leakage current in three-phase transformerless grid-connected photovoltaic inverters. In: 7th power electronics, drive systems and technologies conference, PEDSTC 2016
12. Rahimi R et al (2018) H8 inverter to reduce leakage current in transformerless three-phase grid-connected photovoltaic systems. *IEEE J Emerg Sel Top Power Electron*
13. Moradi GR, Afshari E, Rahimi R, Farhangi B, Farhangi S (2016) Improvement of the modulation method for single-phase transformerless photovoltaic conergy inverter for reactive power injection capability. In: 2016 24th Iranian conference on electrical engineering, ICEE 2016
14. Lorenzani E, Concari C, Barater D, Franceschini G, Buticchi G (2016) Recent advances in single-phase transformerless photovoltaic inverters. *IET Renew Power Gener*
15. Lokhande NM, Phadnis GS (2007) Website: www.ijirset.com. *Int J Innovative Res Sci Eng Technol* (An ISO 3297: 2007 Certified Organization)
16. Lee JS, Lee KB (2013) Modulation technique to reduce leakage current in transformerless photovoltaic systems using a three-level inverter. In: Conference proceedings—IEEE applied power electronics conference and exposition—APEC

17. Suan FTK, Rahim NA, Ping HW (2013) Three-phase transformerless grid-connected photovoltaic inverter to reduce leakage currents. In: CEAT 2013—2013 IEEE conference on clean energy and technology
18. Kerekes T (2009) Analysis and modeling of transformerless photovoltaic inverter systems. Aalborg University, Aalborg
19. Karasani RR, Borghate VB, Meshram PM, Suryawanshi HM, Sabyasachi S (2017) A three-phase hybrid cascaded modular multilevel inverter for renewable energy environment. *IEEE Trans Power Electron*
20. Hu Y, Xiao W, Cao W, Ji B, John Morrow D (2015) Three-port DC-DC converter for stand-alone photovoltaic systems. *IEEE Trans Power Electron*
21. Hou CC, Shih CC, Cheng PT, Hava AM (2013) Common-mode voltage reduction pulsewidth modulation techniques for three-phase grid-connected converters. *IEEE Trans Power Electron*
22. Hava AM, Ün E (2009) Performance analysis of reduced common-mode voltage PWM methods and comparison with standard PWM methods for three-phase voltage-source inverters. *IEEE Trans Power Electron* 24(1):241–252
23. Guo X (2017) Three-phase CH7 inverter with a new space vector modulation to reduce leakage current for transformerless photovoltaic systems. *IEEE J Emerg Sel Topics Power Electron* 5(2):708–712
24. Guo X et al (2016) Leakage current elimination of four-leg inverter for transformerless three-phase PV systems. *IEEE Trans Power Electron*
25. Guo X, Jia X (2016) Hardware-based cascaded topology and modulation strategy with leakage current reduction for transformerless PV systems. *IEEE Trans Ind Electron* 63(12):7823–7832
26. González R, López J, Sanchis P, Marroyo L (2007) Transformerless inverter for single-phase photovoltaic systems. *IEEE Trans Power Electron* 22(2):693–697
27. Freddy TKS, Rahim NA, Hew WP, Che HS (2015) Modulation techniques to reduce leakage current in three-phase transformerless H7 photovoltaic inverter. *IEEE Trans Ind Electron*
28. Fernandes BG, Anandababu C (2016) Leakage current generation in view of circuit topology of non-isolated full-bridge neutral point clamped grid-tied photovoltaic inverters. *IET Power Electron* 9(8):1571–1580
29. Eggum EG (2015) Application of modular multilevel converter for interfacing grid-connected photovoltaic conversion plants.
30. Dutta S, Debnath D, Chatterjee K (2018) A grid-connected single-phase transformerless inverter controlling two solar PV arrays operating under different atmospheric conditions. *IEEE Trans Ind Electron*
31. Debnath D, Chatterjee K (2015) Two-stage solar photovoltaic-based stand-alone scheme having battery as energy storage element for rural deployment. *IEEE Trans Ind Electron*
32. Debnath D, Chatterjee K (2013) Transformer coupled multi-input two stage standalone solar photovoltaic scheme for rural areas. In: IECON proceedings (Industrial electronics conference)
33. Debnath D, De P, Chatterjee K (2016) Simple scheme to extract maximum power from series connected photovoltaic modules experiencing mismatched operating conditions. *IET Power Electron* 9(3):408–416
34. Debnath D, Chatterjee K (2013) A buck-boost integrated full bridge inverter for solar photovoltaic based standalone system. In: Conference record of the IEEE photovoltaic specialists conference
35. Chen Y, Xu D, Xi J (2016) Common-mode filter design for a transformerless ZVS full-bridge inverter. *IEEE J Emerg Sel Topics Power Electron*
36. Cavalcanti MC et al (2010) Modulation techniques to eliminate leakage currents in transformerless three-phase photovoltaic systems. *IEEE Trans Ind Electron*
37. Campanhol LBG, Da Silva SAO, Bacon VD, Azauri AO (2016) Three-phase grid-connected PV system operating with feed-forward control loop and active power-line conditioning using NPC inverter. In: IECON proceedings (Industrial electronics conference)
38. Bradaschia F et al (2011) Modulation for three-phase transformerless z-source inverter to reduce leakage currents in photovoltaic systems. *IEEE Trans Ind Electron* 58(12):5385–5395

39. Anandababu C, Fernandes BG (2017) Neutral point clamped MOSFET inverter with full-bridge configuration for nonisolated grid-tied photovoltaic system. *IEEE J Emerg Sel Topics Power Electron*
40. Afshari E et al (2017) Control strategy for three-phase grid-connected PV inverters enabling current limitation under unbalanced faults. *IEEE Trans Ind Electron* 64(11):8908–8918
41. Afshari E, Rahimi R, Farhangi B, Farhangi S (2015) Analysis and modification of the single phase transformerless FB-DCB inverter modulation for injecting reactive power. In: 2015 IEEE conference on energy conversion, CENCON 2015
42. Inverter for transforming a DC voltage into an AC current or an AC voltage, 3933146623 (2003)
43. Chapter 3 review of carrier based PWM methods and development of analytical PWM tools 3.1 VSI operation and the volt-seconds principle
44. 林伸行 (2017) 病院・介護施設におけるノロウイルス感染症の拡大防止対策を目的とした吐物の飛散状況に関する研究. *感染症誌* 91:399–404
45. Серебрякова ОЕ (2014) Взаимосвязь полиморфизма гена фактора некроза опухоли альфа с риском развития метаболического синдрома и, “ВЗАИМОСВЯЗЬ ПОЛИМОРФИЗМА ГЕНА ФАКТОРА НЕКРОЗА ОПУХОЛИ АЛЬФА С РИСКОМ РАЗВИТИЯ МЕТАБОЛИЧЕСКОГО СИНДРОМА И АТЕРОСКЛЕРОЗА, p 131
46. Zhang L, Sun K, Feng L, Wu H, Xing Y (2013) A family of neutral point clamped full-bridge topologies for transformerless photovoltaic grid-tied inverters. *IEEE Trans Power Electron*
47. Zeb K et al (2018) A comprehensive review on inverter topologies and control strategies for grid connected photovoltaic system. *Renew Sustain Energy Rev* 94:1120–1141
48. Yang T et al (2018) Hybrid modulation strategy to eliminate current distortion for PV grid-tied H6 inverter. *Appl Sci* 8(12):2578
49. Whiteley Z (1994) *Curriculum vitae*
50. Wang H, Blaabjerg F, Simões MG, Yang Y (2016) Power control flexibilities for grid-connected multi-functional photovoltaic inverters. *IET Renew Power Gener* 10(4):504–513
51. Vazquez G, Martinez-Rodriguez PR, Sosa JM, Escobar G, Juarez MA (2014) Transformerless single-phase multilevel inverter for grid tied photovoltaic systems. In: *IECON proceedings (Industrial electronics conference)*, pp 1868–1874
52. Teodorescu R, Blaabjerg F (2004) *Kunst-Wilson.Zajonc.1980.Pdf*, pp 580–586
53. Tarnini MY, Abdel-Karim N, Chahine K (2017) Simulation of leakage current and THD compensation in a large PV system. *Int J Appl Eng Res* 12:8602
54. Sharma R (2007) Single-phase transformerless unipolar switched inverters for utility-connected photovoltaic applications, p 265
55. Raju A. Analysis and validation of reactive power compensation by transformerless multilevel inverter using SPWM and modified SVPWM strategies
56. *The Pcs*, Chapter 2 overview of grid connected solar, pp 16–41
57. Panda A, Pathak MK, Srivastava SP (2016) A single phase photovoltaic inverter control for grid connected system. *Sadhana Acad Proc Eng Sci* 41(1):15–30
58. Mukherjee S (2017) Advanced control architectures for grid connected and standalone converter systems
59. Meza C, Biel D (2008) Analysis and control of a single-phase single-stage grid-connected photovoltaic inverter outline
60. Maknouninejad A, Simoes MG, Zolot M (2009) Single phase and three phase p+resonant based grid connected inverters with reactive power and harmonic compensation capabilities. In: 2009 IEEE international electric machines and drives conference, IEMDC '09, no 1, pp 385–391
61. Liu B et al (2017) Combined reactive power injection modulation and grid current distortion improvement approach for H6 transformer-less photovoltaic inverter. *IEEE Trans Energy Convers* 32(4):1456–1467
62. Liao Z, Song Z, Xu D, Mei C, Liu G (2014) Unifying electrical engineering and electronics engineering, vol 238

63. Kadam A, Shukla A (2017) A multilevel transformerless inverter employing ground connection between PV negative terminal and grid neutral point. *IEEE Trans Industr Electron* 64(11):8897–8907
64. Jekel TB (2008) *Fundamentals of power electronics*, 2nd edn.
65. Jankovic Z, Nasiri A, Wei L (2015) Robust H_∞ controller design for microgrid-tied inverter applications. In: 2015 IEEE energy conversion congress and exposition, ECCE 2015, pp 2368–2373
66. Islam M, Mekhilef S, Hasan M (2015) Single phase transformerless inverter topologies for grid-tied photovoltaic system: a review. *Renew Sustain Energy Rev* 45:69–86
67. Islam M, Afrin N, Mekhilef S (2016) Efficient single phase transformerless inverter for grid-tied PVG system with reactive power control. *IEEE Trans Sustain Energy* 7(3):1205–1215
68. Islam M, Mekhilef S (2015) A new high efficient transformerless inverter for single phase grid-tied photovoltaic system with reactive power control. In: Conference proceedings—IEEE applied power electronics conference and exposition—APEC, vol 2015, pp 1666–1671
69. Hassaine L, Olias E, Quintero J, Salas V (2014) Overview of power inverter topologies and control structures for grid connected photovoltaic systems. *Renew Sustain Energy Rev* 30:796–807
70. Han D, Li S, Lee W, Sarioglu B (2017) Achieving zero common mode voltage generation in a balanced inverter with neutral-point diode-clamping. In: 2017 IEEE energy conversion congress and exposition, ECCE 2017, vol 2017, Janua, pp 4351–4357
71. Hamrouni N, Jraidi M, Chérif A (2008) New control strategy for 2-stage grid-connected photovoltaic power system. *Renew Energy* 33(10):2212–2221
72. González R, Gubía E, López J, Marroyo L (2008) Transformerless single-phase multilevel-based photovoltaic inverter. *IEEE Trans Ind Electron* 55(7):2694–2702
73. GERC (2016) Regulations for net metering rooftop solar PV grid interactive systems, pp 1–29
74. Driels M (1996) *Linear control systems engineering*, vol 5, pp 569–573
75. Deepa R, Nagashree AN, Anand K (2016) Transformerless grid connected single phase inverter for power system application. In: 2015 international conference on emerging research in electronics, computer science and technology, ICERECT 2015, pp 418–422
76. Ciobotaru M, Teodorescu R, Blaabjerg F (2006) Control of single-stage single-phase PV inverter. *EPE J (Eur Power Electron Drives J)* 16(3):20–26
77. Calais M, Agelidis VG, Dymond MS (2001) Cascaded inverter for transformerless single-phase grid-connected photovoltaic systems. *Renew Energy* 22(1):255–262
78. Ardashir JF, Siwakoti YP, Sabahi M, Hosseini SH, Blaabjerg F (2016) S4 grid-connected single-phase transformerless inverter for PV application. In: IECON proceedings (Industrial electronics conference), pp 2384–2389
79. Anthony CJ (2016) Single phase transformer less grid connected PV inverter: a review
80. Almasoudi F, Matin M (2018) An improved proposed single phase transformerless inverter with leakage current elimination and reactive power capability for PV systems application. *J Low Power Electron Appl* 8(3):29
81. Alawieh H, Arab Tehrani K, Azzouz Y, Dakyo B (2014) A new active common-mode voltage elimination method for three-level neutral-point clamped inverters. In: IECON proceedings (Industrial electronics conference), pp 1060–1066
82. Aider JL, Danet A, Lesieur M (2007) Large-eddy simulation applied to study the influence of upstream conditions on the time-dependant and averaged characteristics of a backward-facing step flow. *J Turbul* 8:1–30
83. Ahmad Z, Singh SN (2017) Comparative analysis of single phase transformerless inverter topologies for grid connected PV system. *Solar Energy* 149:245–271